MRI of the Liver

Imaging Techniques
Contrast Enhancement
Differential Diagnosis

2nd Edition

Editors
G. Schneider
L. Grazioli
S. Saini

Springer

MRI of the Liver - 2nd Edition

Imaging Techniques, Contrast Enhancement, Differential Diagnosis

Günther Schneider • Luigi Grazioli • Sanjay Saini (Eds.)

MRI of the Liver

2nd Edition

Imaging Techniques, Contrast Enhancement,
Differential Diagnosis

Springer

EDITORS

Günther Schneider, M.D.
Clinic for Diagnostic and Interventional Radiology
University Hospital of Saarland
66421 Homburg/Saar, Germany

Luigi Grazioli, M.D.
Department of Radiology
University of Brescia
Piazzale Spedali Civili 1
25023 Brescia, Italy

Sanjay Saini, M.D.
Emory University School of Medicine
Department of Radiology
1364 Clifton Road, NE
Atlanta GA 30322, USA

CONTRIBUTORS

M.A. Kirchin
P. Fries
M.P. Bondioni
A. Massmann
K. Altmeyer
L. Olivetti
L. Romanini
R. Seidel
D.R. Martin
A. Luca
M. Harisinghani
R.V. D'Souza
D. Sahani

Library of Congress Control Number: 2005937525

ISBN 88-470-0209-5 (1st ed.) Springer Milan Berlin Heidelberg New York

ISBN-10 88-470-0335-0 (2nd ed.) Springer Milan Berlin Heidelberg New York
ISBN-13 978-88-470-0335-4 (2nd ed.) Springer Milan Berlin Heidelberg New York

Springer is a part of Springer Science+Business Media
springer.com

Printed in Italy

Cover design: Simona Colombo, Milan
Typesetting: Compostudio, Cernusco s/N (Milan)
Printing and binding: Arti Grafiche Nidasio, Assago (Milan)

Preface to the Second Edition

The practicing radiologist is continually challenged to update his/her competencies so as to deliver state-of-the-art radiological care. Nowhere is this truer than in the rapidly evolving world of magnetic resonance imaging, where innovations in both technology and diagnostic pharmaceuticals have dramatically altered the landscape of practice.
MR imaging plays an important role in the management of patients with liver disease, permitting not only the detection of benign and malignant hepatic masses but also the characterization of focal and diffuse liver lesions in a single non-invasive examination. The excellent soft tissue contrast achievable on MR imaging permits accurate assessment of both the full extent of tumor infiltration and of the relationship of tumors to adjacent vascular structures. This information is vital for decisions as to the appropriate course of treatment for a given patient. With this in mind, this book is aimed at assisting busy radiologists to incorporate the experience of experts in MR imaging of the liver into their daily practice. The contributors to this book are highly acclaimed radiologists with extensive personal experience in abdominal imaging in general and liver MR imaging in particular. The product of their efforts is a book that comprehensively reviews the many diseases that affect the liver, and describes in detail the typical enhancement features of these diseases on MR imaging. Because a number of very different MR contrast agents are now available for use in MR imaging of the liver, a feature of this book is the comparative enhancement behavior of lesions on post-contrast imaging after administration of these agents. For completion, comparison is also made with the typical enhancement behavior of lesions on alternative diagnostic imaging modalities, namely ultrasound and computed tomography.

This second edition of "MRI of the Liver" is a revised and extensively updated version of the first edition published in 2003. The chapters included in the first edition have been enriched with the most recent information available in the literature, and by the inclusion of many additional images; the opportunity to directly observe the characteristic features of the lesions under discussion represents a very efficient learning tool for practicing radiologists.

Additional chapters included in the second edition are dedicated to MR imaging of hepatic pseudolesions (Chapter 5), MR imaging of the biliary tree and gallbladder (Chapter 7), MR imaging of the liver in pediatric patients (Chapter 10) and MR angiography in liver disease (Chapter 12). Finally, an entire chapter is dedicated to comparing the available contrast agents for imaging of specific liver lesions (Chapter 8).

Much of the additional information available in this edition highlights the potential of MR imaging to be a "one-stop shop" procedure for the comprehensive evaluation of the liver, hepatic vasculature, and biliary tract. This information is essential in transplant patients and can also contribute to reducing overall health-care costs by reducing the number of imaging studies and avoiding unnecessary surgery.

The editors owe a debt of gratitude to the contributors to this book for sharing their extensive knowledge with the wider radiology community. We are also grateful to Bracco for supporting this educational endeavor. Indeed, this kind of academic-industrial partnership is what helps us provide the best care for our patients. We hope readers find the contents of this book beneficial, and we welcome feedback on how we might continue to facilitate the transfer of essential knowledge in the radiological community.

November, 2005

Sanjay Saini, M.D.
Atlanta, USA

Foreword to the First Edition

It is with pleasure that I am writing the foreword for this textbook entitled "MRI of the Liver: Imaging Techniques, Contrast Enhancement, Differential Diagnosis" by Drs. Schneider, Grazioli and Saini.

If the liver has become the key organ to image in the abdomen, magnetic resonance (MR) imaging has become an indispensable modality for its evaluation. The absence of ionizing radiation, unparalleled soft tissue contrast, inherent multiplanar capability and high temporal resolution in dynamic gadolinium-enhanced imaging are major advantages over other imaging techniques. Furthermore, the introduction of contrast agents with liver specific properties has increased the usefulness of MRI for the detection and characterization of liver lesions.

This book fills a void in the current literature, giving radiologists and other physicians (primarily hepatologists and liver surgeons) interested in liver diseases the opportunity to have an up-to-date, single source of knowledge on MRI applied to the liver. This book is a combination of a manual, a reference textbook and an atlas. The first chapter constitutes a manual of liver MRI including modern imaging techniques and sequences. By including common imaging protocols tailored for the main manufacturers, it offers to practicing radiologists cookbook recipes to obtain superb liver MRI studies like the ones obtained by experts such as the authors. Current approaches to MRI of the liver using phased-array multicoils, enhanced gradients and motion reduction techniques allow us to have images with superb contrast resolution and acceptable spatial and temporal resolution. In chapter two, the authors cover the contrast administration strategy for MRI of the liver, detailing the use of both extracellular and liver specific contrast agents. The reasoning for the intravenous administration of extracellular gadolinium contrast agents as a useful adjunct in liver MRI is discussed. The increase in differences in signal intensity between normal hepatic parenchyma and hypo- or hypervascular neoplastic tissues is discussed, as are the specific enhancement patterns observed in different phases of perfusion following gadolinium administration. In addition, the rationale for using liver specific MR contrast agents is presented, with examples given for both manganese and iron oxide-based agents.

Chapter three presents a detailed overview of the histological classification of focal and diffuse liver pathologies, focusing on the essential needs of radiologists. In addition, possible classifications of focal liver lesions are presented based on their appearance on both unenhanced and contrast-enhanced MRI. Specifically, flow charts and tables for the differential diagnoses of liver lesions are presented, thereby consolidating in a single source the charts and tables found in a multiplicity of books and articles on abdominal and hepatobiliary imaging.

Chapters four and five constitute a reference on liver MRI of focal liver disease, discussing the radiological features of benign and malignant focal lesions in a systematic fashion. All benign and malignant primary liver lesions are presented from the most common such as hemangioma or hepatocellular carcinoma to the rarest such as nodular regenerative hyperplasia or epithelial hemangioendothelioma. Both pediatric and adult liver tumors are included. The sections on secondary liver lesions cover not only metastases and lymphoma, but also inflammatory and parasitic lesions. Where appropriate, the imaging features observed with other techniques (computed tomography and ultrasound) are presented for comparison.

The role of MRI in the characterization and monitoring of diffuse liver disease is recognized with a whole chapter dedicated to cirrhosis, iron overload and vascular pathol-

ogy. For completion a chapter is included on MRI of the liver post-surgery/post-ablation, an increasing challenge for abdominal radiologists given the increased frequency with which these techniques are performed.

This textbook is very well illustrated with more than 600 figures of high quality, which allow it to be seen as an atlas on liver MRI.

This textbook on MRI of the liver taps on the expertise of three obvious leaders in liver imaging, namely Drs. Günther Schneider, Luigi Grazioli and Sanjay Saini. Their respective institutions, the University Clinic of Homburg-Saar, Germany, the University Hospital of Brescia, Italy, and the Mass. General Hospital in Boston, USA, are well-known for their interest in liver radiology and, specifically, liver MRI. This truly international effort has produced a fully-encompassing source for radiologists anywhere with current and practical information. I predict that this book will influence the way we practice liver imaging: the protocols will be improved, the differential diagnosis charts will be copied and pinned up in reading rooms in many departments and overall it will have a beneficial impact.

I invite you to read the work of Drs. Schneider, Grazioli and Saini with the certainty that you will enjoy their material and information.

November, 2002 **Pablo R. Ros, MD, MPH**

Contents

Contributors

Günther Schneider, M.D.
Clinic for Diagnostic and Interventional Radiology
University Hospital of Saarland
66421 Homburg/Saar, Germany

Luigi Grazioli, M.D.
Department of Radiology
University of Brescia
Piazzale Spedali Civili 1
25023 Brescia, Italy

Sanjay Saini, M.D.
Emory University School of Medicine
Department of Radiology
1364 Clifton Road, NE
Atlanta GA 30322, USA

Miles A. Kirchin, Ph.D.
World Wide Medical Affairs
Bracco Imaging SpA
Via E. Folli 50
Milan, Italy

Peter Fries, M.D.
Clinic for Diagnostic and Interventional Radiology
University Hospital of Saarland
66421 Homburg/Saar, Germany

Maria Pia Bondioni, M.D.
Department of Radiology
University of Brescia
Piazzale Spedali Civili 1
25030 Brescia, Italy

Alexander Massmann, M.D.
Clinic for Diagnostic and Interventional Radiology
University Hospital of Saarland
66421 Homburg/Saar, Germany

Katrin Altmeyer, M.D.
Clinic for Diagnostic and Interventional Radiology
University Hospital of Saarland
66421 Homburg/Saar, Germany

Lucio Olivetti, M.D.
Department of Radiology
Istituti Ospedalieri di Cremona
Viale Concordia 1
26100 Cremona, Italy

Laura Romanini, M.D.
Department of Radiology
University of Brescia
Piazzale Spedali Civili 1
25023 Brescia, Italy

Roland Seidel, M.D.
Clinic for Diagnostic and Interventional Radiology
University Hospital of Saarland
66421 Homburg/Saar, Germany

Diego R. Martin, M.D.
Emory Healthcare
The Emory Clinic, Inc.
Department of Radiology
1364 Clifton Road, NE
Atlanta, GA 30322, USA

Angelo Luca, M.D.
Department of Radiology
ISMETT - Mediterranean Institute
for Transplantation and Advanced
Specialized Therapies
Via Tricomi 1
90127 Palermo, Italy

Mukesh Harisinghani, M.D.
Division of Abdominal Imaging
Department of Radiology
Massachusetts General Hospital
and Harvard Medical School
White 270, 55 Fruit Street
Boston, MA 02114, USA

Roy V. D'Souza, M.D.
Division of Abdominal Imaging
Department of Radiology
Massachusetts General Hospital
and Harvard Medical School
White 270, 55 Fruit Street
Boston, MA 02114, USA

Dushyant Sahani, M.D.
Clinical Instructor
Harvard Medical School
Assistant Radiologist in Abdominal
and Interventional Radiology
Massachusetts General Hospital
White 270, 55 Fruit Street
Boston, MA 02114, USA

Acknowledgements

We are indebted to Diane Wagner-Jochem (University Hospital Homburg/Saar, Germany) and Antonella Cerri (Springer-Verlag Italia, Milan) for their beyond-the-call-of-duty efforts to get this book published in a timely manner.
Our sincere thanks go also to Anne M. Johnston, Gianni Chiappella and Patrizia Andreoni for their precious support in the preprint processes of copyediting and typesetting, respectively, and Alexandra Davies and John R. Parker for their contributions to proofreading.

November, 2005 **The Editors**

1

Techniques for Liver MR Imaging

CONTENTS

1.1 Introduction

Magnetic resonance imaging (MRI) is establishing a role as a primary diagnostic technique with evidence showing MR to have advantages over computer tomography (CT) as regards diagnostic sensitivity and specificity for many pathologies of solid organs, bile and pancreatic ducts, bowel, peritoneum, and retroperitoneum. MRI is particularly well-suited to the evaluation of liver pathology due to an ability to generate contrast by a variety of mechanisms. This allows specific evaluation of important diffuse processes such as abnormal fat, as may be seen in non-alcoholic steatohepatitis, or iron accumulation as seen in hemochromatosis. The use of intravenous gadolinium-based contrast agents allows evaluation of the vascular supply to benign and malignant tumors, yielding important diagnostic information. Similarly, perfusion and interstitial distribution of gadolinium contrast agent in the liver parenchyma may be valuable for sensitive evaluation of the acute and chronic changes of hepatitis, including cirrhosis. Dynamic perfusion analysis is obtained by the acquisition of a series of scans at multiple times (see Chapt. 3). No other imaging technique can provide the comprehensive evaluation of liver disease possible on MRI. Use of contrast-enhanced CT for multiphase examinations is associated with an ionizing radiation burden that is proportional to the number of scans obtained during the study. There are increasing concerns regarding the risks of radiation and the iodinated contrast agents associated with CT imaging of the abdomen. For example, the National Academy of Science has released BEIR VII, the seventh in a series of consensus reports on radiation risks, which includes a section on radiation from diagnostic CT. In brief, assuming the demographic distribution of the U.S. population, a single dose of 100 mSv is associated with an estimated lifetime attributable risk (LAR) for developing a solid cancer or leukemia of 1 in 100 while a single dose of 10 mSv is associated with a LAR of 1 in 1000 for developing a cancer. Given that it is estimated that 60 million CT examinations are performed per year and that utilization is increasing [5], the potential tumor burden to the population should be an important consideration in determining practice patterns for liver evaluation. The incidence of contrast-induced nephropathy associated with iodinated contrast agents used for CT scanning is difficult to ascertain. Although the risk of renal insufficiency for the general population is estimated at below 2%, risk factors including pre-existing impaired renal function, diabetes mellitus, and high contrast agent volume may significantly elevate the likelihood [16]. Patients with diabetes and mild to moderate renal insufficiency have been estimated to have a 9%-40% risk, and this estimated risk has been reported to increase to 50%-90% in various studies [17, 27]. Conversely, the injectable gadolin-

ium contrast agents used for MRI have an excellent safety history, with no significant nephrotoxic effects.

1.2 MR Imaging Techniques and Concepts

One of the major challenges of MRI in the abdomen has centered on the problem of acquiring data from tissue that normally moves in relation to respiration, with additional undesirable effects from cardiovascular pulsation and bowel peristalsis. MRI of the liver initially relied upon standard spin-echo (SE) T1-weighted and T2-weighted methods. However, since these are sequences that acquire data over a long time window relative to respiratory movement [3, 8, 13] they require supplemental techniques of respiratory gating, which in turn adds to the total acquisition time. Moreover, the reliability of the examination is reduced as even minor inconsistent respiratory gating can yield non-diagnostic images. Use of these techniques can lead to total procedure times in excess of 60 min. Currently employed MR techniques focus on shorter sequences that can be completed within a breath-hold. These include T1-weighted fast spoiled gradient echo (SGE) and breath-hold half-Fourier transform single shot spin-echo (HASTE or ssfse) methods [3, 8,18, 31, 38, 39] (Fig. 1). Tables 1 and 2 summarize the nomenclature for the majority of the currently employed recommended sequences. The single shot spin-echo sequences are slice selective, performing all of the preparation and acquisition for an individual slice in approximately 1 sec, with the central k-space data acquired over a fraction of that time. As the image contrast is derived from the central k-space, single shot techniques are remarkably motion insensitive, and have respiratory-independent characteristics that are useful in non-compliant patients [39]. T1-weighted 2-dimensional (2D) or 3-dimensional (3D) gradient echo sequences tend to be motion sensitive as these techniques use interleaved phase lines: the phase lines are collected from each image slice one phase line at a time moving from slice-to-slice. A consequence is that even transient motion occurring during only a fraction of the acquisition will affect all the slices. T1-weighted techniques with motion insensitive properties are also available. These use the same basic concept applied to the T2-weighted single shot technique: 2D data with rapid filling of the central k-space are acquired by preparing and analyzing one slice at a time. In this case, however, spoiled gradient echo sequences that utilize an inversion or saturation pre-pulse are used to generate the T1 contrast [7, 35, 42]. These sequences have been referred to as turbo fast low-angle shot (turboFLASH) and fast inversion-recovery motion-insensitive (FIRM). Another development has been the application of 3D gradient echo sequences modified from MR angiographic techniques. These have various vendor-specific names, including the first description of this technique, known as Volumetric Interpolated Breath-hold Examination (VIBE) [33]. This approach facilitates the generation of high-resolution images of the liver, particularly out-of-phase resolution, with the ability to generate near isotropic voxel sizes in the order of 2-3 mm when combined with interpolation techniques. Such an approach allows better evaluation of hepatic vascular anatomy, and generates volumetric datasets that can be used for multiplanar reconstruction.

Another critical element in T1-weighted breath-hold imaging is the use of intravenously-administered gadolinium contrast agents (see Chapt. 3). These agents shorten the T1 relaxation rate of tissues resulting in marked elevation of signal on T1-weighted images. They are used to assess focal liver lesions based upon characteristic vascular enhancement patterns which can be distinguished from adjacent normal hepatic parenchyma [33, 36]. The liver is unique in having a dual blood supply, receiving 70-80% of afferent blood flow from the portal vein, and the remainder from the hepatic artery. Hepatic tumors develop selective portal-venous or hepatic arterial blood supply based on their specific characteristics. Tumors that derive blood supply from hepatic arterial branches are best visualized during the hepatic arterial dominant phase of liver enhancement. Hypovascular tumors are predominantly supplied by portal-venous branches, and demonstrate enhancement-time curves that are different from normal liver, having slower and less intense enhancement, which is in part due to the lack of contribution from the hepatic arterial supply, and in part to their lower total intravascular volume per gram of tissue. Over time, measured in units of minutes, the gadolinium concentration may slowly increase in a non-uniform pattern within these tumors due to leakage of the contrast agent into the interstitial spaces. Therefore, a key to diagnostic MR liver exams is dynamic multiphase post-gadolinium SGE imaging, which provides information regarding the time intensity curves of hepatic lesions (Fig. 1 and Fig. 2) [20, 21, 26]. Gadolinium contrast agents are extremely safe; the risk of serious reactions is estimated at around 1 per million while the risk for mild reactions is estimated at around 2.5%.

Although contrast agents based on super-paramagnetic iron oxide (SPIO) and manganese have also been developed for MR imaging of liver lesions [11, 12, 19, 30, 46], gadolinium-based agents are

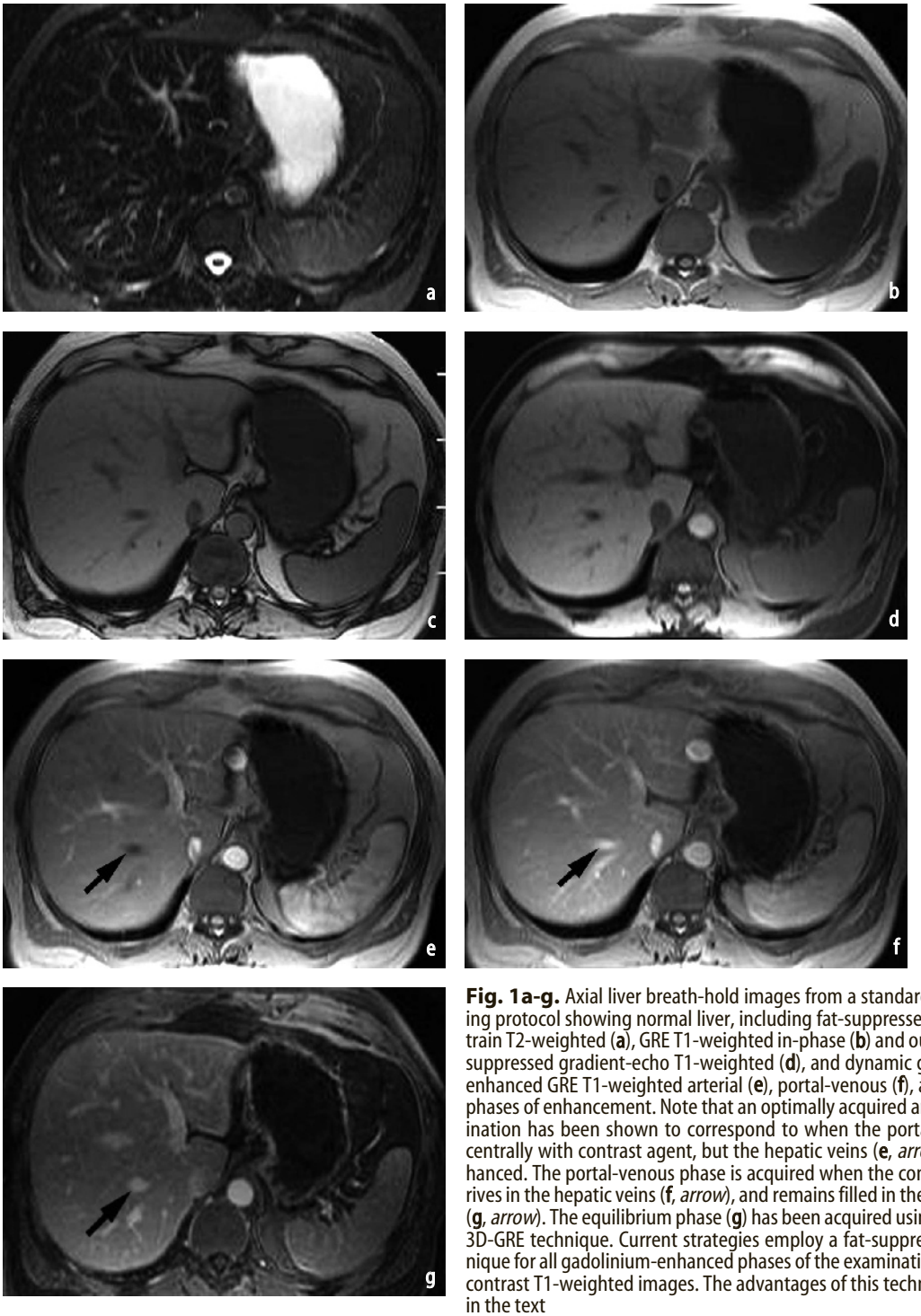

Fig. 1a-g. Axial liver breath-hold images from a standard abdominal imaging protocol showing normal liver, including fat-suppressed single shot echo-train T2-weighted (**a**), GRE T1-weighted in-phase (**b**) and out-of-phase (**c**), fat-suppressed gradient-echo T1-weighted (**d**), and dynamic gadolinium-chelate enhanced GRE T1-weighted arterial (**e**), portal-venous (**f**), and equilibrium (**g**) phases of enhancement. Note that an optimally acquired arterial phase examination has been shown to correspond to when the portal veins have filled centrally with contrast agent, but the hepatic veins (**e**, *arrow*) are not yet enhanced. The portal-venous phase is acquired when the contrast bolus first arrives in the hepatic veins (**f**, *arrow*), and remains filled in the equilibrium phase (**g**, *arrow*). The equilibrium phase (**g**) has been acquired using a fat-suppressed 3D-GRE technique. Current strategies employ a fat-suppressed 3D-GRE technique for all gadolinium-enhanced phases of the examination, and for the pre-contrast T1-weighted images. The advantages of this technique are discussed in the text

Table 1. Acronyms and abbreviations for commonly used sequences

Acronym	Philips	GE	Siemens
Fast Spin-Echo	TSE	FSE	TSE
Single Shot Fast Spin-Echo	SSh TSE	SSFSE/RARE	HASTE
Snapshot / Ultrafast Gradient Echo	TFE	Rapid SPGR	TurboFlash
		FIRM	MP RAGE
3D Turbo Field Echo with fat suppression	THRIVE	FAME/LAVA	VIBE
Fast Field Echo	FFE	SPGR FSPGR GRASSE GRE	FLASH FISP GRE
Steady State Fast Field Echo	Balanced FFE (bFFE, bTFE)	FIESTA	True FISP
Saturation Bands	REST	SAT	PreSAT
Spectrally Selective Fat Suppression	SPIR SPAIR	CHEMSAT	FATSAT
Water Excitation Fat Suppression	Proset		QuickFatSat

Table 2. Definition List of Abbreviations

ceMRA	Contrast-enhanced magnetic resonance angiography
CSE	Conventional spin-echo
FISP	Fast imaging with steady precession
FLASH	Fast low-angle shot
FID EPI	Echo planar imaging readout of the free induction decay
FSE	Fast spin-echo
FSPGR	Fast spoiled gradient-recalled acquisition into steady state
GRASE	Gradient and spin-echoes
GRASS	Gradient-recalled acquisition in the steady state
GRE	Gradient-echo imaging, gradient-recalled echo
GRE EPI	Echo planar imaging solely using gradient echoes (readout of the free induction decay)
HASTE	Half-Fourier acquired single-shot turbo spin-echo
HASTIRM	Half-Fourier acquired single-shot turbo spin-echo with preceding inversion pulse, utilizing only magnitude information
IR	Inversion recovery
MP RAGE (3D)	Magnetization prepared rapid acquired gradient echoes
MRCP	Magnetic resonance cholangiopancreatography
RARE	Rapid acquisition with relaxation enhancement
SAR	Specific absorption rate
SE EPI	Echo planar imaging readout module under a spin-echo technique
SPAIR	Spectral Attenuated Inversion Recovery
SPIR	Spectral Inversion Recovery
SPGR	Spoiled GRASS
SP GRE (SGE)	Spoiled gradient (recalled) echo
SSFP	Steady-state free precession
TFL	Turbo FLASH
TrueFISP	True fast imaging with steady precession
TSE	Turbo spin echo
T1 FFE	T1-weighted fast field echo
T2 FFE	T2-weighted fast field echo

generally considered to be the most useful and practical, particularly for lesion characterization.

A review of the enhancement characteristics of benign and malignant lesions reveals that most diagnostically important information can be derived from SGE images acquired during the hepatic arterial phase after the bolus injection of a gadolinium contrast agent. Most of the information required for making a specific diagnosis of cyst, hemangioma, hamartoma, hypervascular FNH or adenoma, or of a hypervascular HCC in cirrhosis, versus a hyper- or hypovascular metastasis, is present on these images. T2-weighted imaging is predominantly used not for lesion detection, but rather for lesion characterization, to demonstrate high water content, which is usually associated with benign cysts, hemangiomas, or bile duct hamartomas. However, hypervascular metastases can also demonstrate elevated signal on T2-weighted images.

The time delay between initiation of contrast agent administration and initiation of the SGE scan for optimal hepatic arterial dominant phase SGE images is critical, with a narrow time window of 18-20 sec noted for most patients. Visually, this can be verified on the resulting images with ideal results showing contrast enhancement of the central portal veins, while the hepatic veins remain completely unenhanced (Fig. 1). The optimal time for the portal-venous dominant phase is less critical; typically the timing delay is 45-60 sec, with ideal images showing recent filling of the hepatic veins. The time delay for equilibrium phase images is the least critical, and can be performed anytime from 1.5-2 min after contrast agent injection. Although the hepatic arterial dominant phase is diagnostically critical, one of the great strengths of MR imaging is the availability of multiple sequences, each delineating different components of normal and pathological tissues [32].

Improving disease conspicuity involves maximizing the difference in signal intensities between diseased tissues and the background tissue. For disease processes situated within or adjacent to fat, this is readily performed by manipulating the signal intensity of fat, which can range from low to high on both T1-weighted and T2-weighted images. For example, disease processes that are low in signal intensity on T1-weighted images, such as peritoneal fluid or retroperitoneal fibrosis, are most conspicuous on T1-weighted sequences in which fat is high in signal intensity (i.e., sequences without fat suppression). Conversely, disease processes that are high in signal intensity, such as subacute hemorrhage or proteinaceous fluid, are more conspicuous if fat is rendered low in signal intensity with the use of fat suppression techniques. On T2-weighted images, features that are low in signal intensity, such as fibrous tissue, are most conspicuous with sequences that render the background fat high in signal intensity, such as echo-train spin-echo sequences. Features that are moderate to high in signal intensity on T2-weighted images, such as lymphadenopathy or ascites, are most conspicuous with sequences in which fat signal intensity is rendered low, such as fat-suppressed sequences.

Gadolinium chelate enhancement is routinely useful because it permits visualization of the pattern of blood delivery (i.e., capillary enhancement) and the size and/or rapidity of drainage of the interstitial space (i.e., interstitial enhancement) both of which improve the detection and characterization of disease [4, 37]. Arterial-phase image acquisition is achieved using a short-duration sequence initiated immediately after gadolinium injection. A spoiled gradient-echo (SGE) sequence, performed as a multisection 2D or 3D acquisition, is an ideal sequence to use for arterial phase imaging. The majority of focal mass lesions are best evaluated in the arterial phase of enhancement, particularly lesions that do not distort the margins of the organs in which they are located (e.g., focal liver, spleen, or pancreatic lesions). Images acquired 1.5-10 min after contrast administration are in the equilibrium phase of enhancement, with the optimal window being 2-5 min after contrast agent administration. Diseases that are superficial, spreading, or inflammatory in nature are generally well-shown on equilibrium phase images. The concomitant use of fat suppression serves to increase the conspicuity of disease processes characterized by increased enhancement on equilibrium phase images including peritoneal metastases, cholangiocarcinoma, ascending cholangitis, inflammatory bowel disease, and abscesses [8, 18].

The majority of liver diseases can be characterized by defining their appearance on pre-contrast (unenhanced) T1- and T2-weighted images and on T1-weighted images acquired during the hepatic arterial, portal-venous and equilibrium phases after the injection of a gadolinium-based contrast agent. With the recent approval by the U.S. Food and Drug Administration (FDA) of Gadolinium-BOPTA, a gadolinium-based T1-shortening MR contrast agent is now available in the USA which permits additional contrast-enhanced T1-weighted imaging during a delayed time-frame for the improved detection and further characterization of liver lesions (Fig. 2). This is discussed in detail in Chapter 3.

1.2.1 T1-Weighted Sequences

T1-weighted sequences are routinely useful for investigating diseases of the abdomen, and they supplement T2-weighted images for investigating dis-

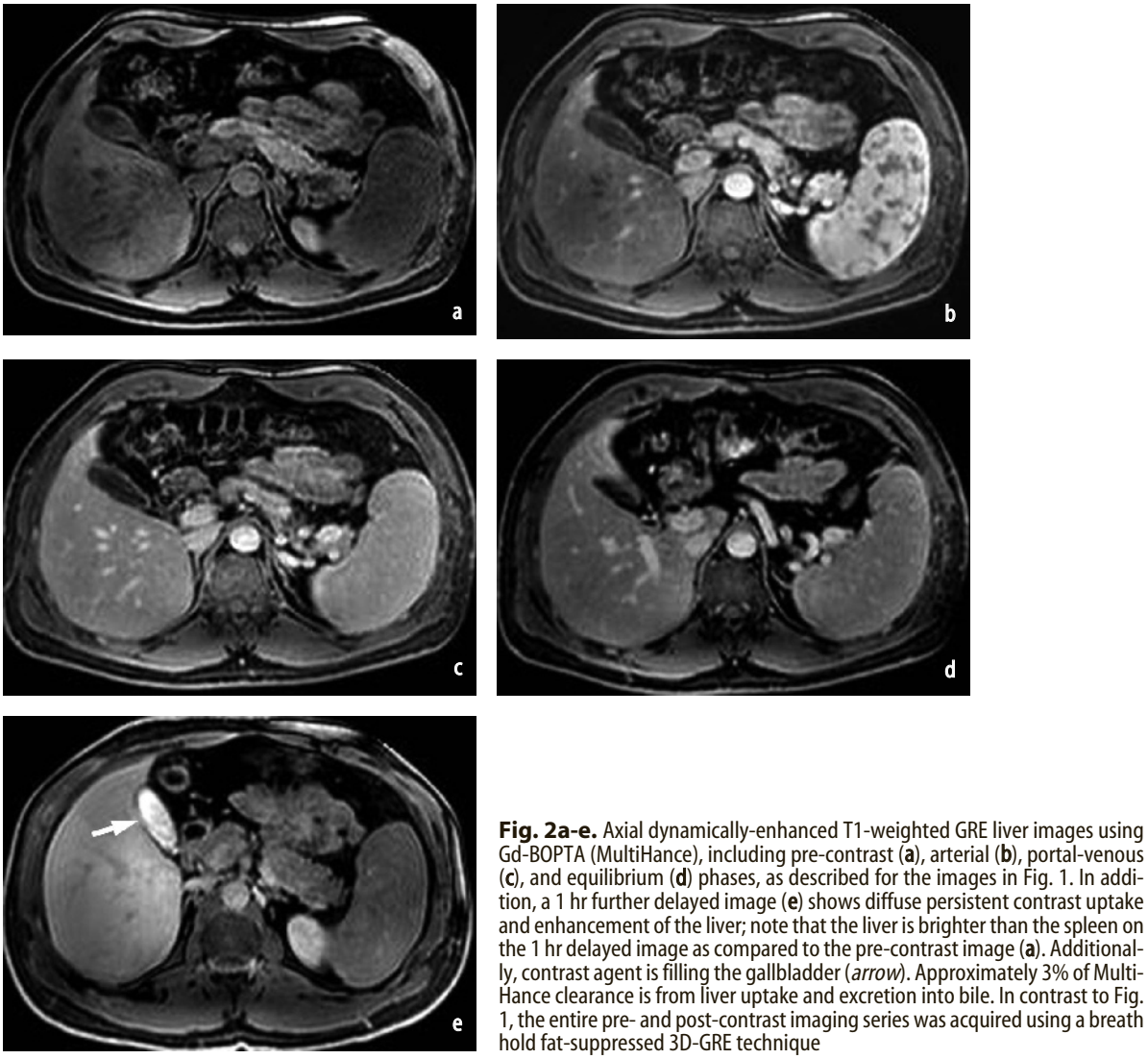

Fig. 2a-e. Axial dynamically-enhanced T1-weighted GRE liver images using Gd-BOPTA (MultiHance), including pre-contrast (**a**), arterial (**b**), portal-venous (**c**), and equilibrium (**d**) phases, as described for the images in Fig. 1. In addition, a 1 hr further delayed image (**e**) shows diffuse persistent contrast uptake and enhancement of the liver; note that the liver is brighter than the spleen on the 1 hr delayed image as compared to the pre-contrast image (**a**). Additionally, contrast agent is filling the gallbladder (*arrow*). Approximately 3% of MultiHance clearance is from liver uptake and excretion into bile. In contrast to Fig. 1, the entire pre- and post-contrast imaging series was acquired using a breath hold fat-suppressed 3D-GRE technique

eases of the pelvis. The primary information that precontrast T1-weighted images provide includes: 1) information on abnormally increased fluid and fibrous tissue content which appears low in signal intensity on T1-weighted images; and 2) information on the presence of subacute hemorrhage or concentrated protein, which are both high in signal intensity. T1-weighted sequences obtained without fat suppression also demonstrate the presence of fat as high signal intensity tissue. The routine use of an additional fat attenuating technique facilitates reliable characterization of fatty lesions. When gadolinium-enhanced imaging is performed, fat-suppression is critical for improving the contrast between enhancing soft tissue structures and adjacent fat. Examples of such soft tissue structures include retroperitoneal vasculature and lymph nodes, mesenteric lymph nodes, the pancreas, and the peritoneum.

1.2.1.1 Spoiled Gradient-Echo (SGE) Sequences

T1-weighted SGE sequences are the most important and versatile sequences for studying abdominal disease. In combination with a phased-array multi-coil, these sequences may be used to replace longer duration sequences such as T1-weighted spin-echo (SE) sequences. SGE sequences are characterized by a relatively long repetition time (TR) (approximately 150 msec) to maximize signal-to-noise (SNR) ratio and the number of sections that can be acquired in one multisection acquisition, and a short in-phase echo time (TE) (approximately 4.2-4.5 msec at 1.5 Tesla (T)). At 1.5 T, protons in a voxel containing 100% fat will precess approximately 220-230 Hz more slowly than protons in a voxel comprising 100% water. The result is that the precession of protons becomes increasingly

out-of-phase. The time required for protons to regain a full in-phase orientation is approximately 4.4 msec at 1.5 T. After 2.2 msec (i.e., half this time) the precession of protons in water and fat will be 180° out-of-phase. The current generation of MR software incorporates dual-echo breath-hold SGE sequences that can acquire two sets of 2D k-space data and two sets of images, one in-phase and the other out-of-phase, with spatially matched slices [34]. The flip angle should be approximately 70-90˚, to maximize the T1-weighted signal. With the use of phased-array surface coils, section thicknesses of 5-7 mm result in diagnostically adequate images. On new MRI machines, more than 22 sections may be acquired in a 20 sec breath-hold, or 44 paired sections when using the dual-echo technique.

1.2.1.2 Out-of-Phase SGE Sequences

Low levels of intracellular fat accumulation may be detected on out-of-phase (opposed-phase) SGE images. This is useful for demonstrating diseased tissue in which mixtures of fat and water protons are present within the same voxel (Fig. 3). A voxel containing predominantly fat or water will not demonstrate diminished signal on out-of-phase images. On the other hand, cells that accumulate lipid, such as hepatocytes with abnormally elevated cytosolic lipid vacuoles, or lipid-laden adrenal adenomas, can be found to have a diminished signal on out-of-phase images, compared to in-phase images [45]. This is due to a mixed aqueous-lipid environment within the cells. Lipid in subcutaneous or intra-abdominal adipocytes has very little free water available, and thus the out-of-phase effect does not occur.

Another use of dual-echo imaging is to identify paramagnetic effects associated with iron (Fig. 4) [41]. Abnormally elevated liver iron deposition may develop in iron overload from increased red cell turnover, or from genetic hemochromatosis (see Chapt. 9, Section 9.4) [2, 9, 10, 14, 40 44]. To different degrees this may also involve the spleen and pancreas. On the longer second echo (4.4 msec at 1.5 T) image, iron will lead to the loss of tissue signal due to T2* effects [1, 2, 9, 10, 14, 15]. Similarly, paramagnetic surgical clips may be seen to cause blooming of a dark focus around the clip on the longer second echo image. At 1.5 T, both fat and iron cause liver signal decrease on out-of-phase images acquired using a TE of 6.6 msec, relative to the in-phase images acquired with a TE of 4.4 msec. Conversely, on 2.2 msec out-of-phase TE images fat is darker and iron is brighter, relative to 4.4 msec TE images. This is the most important reason for always adjusting the dual echo acquisitions to obtain the out-of-phase echo at a shorter TE than the in-phase echo. Generally, using the shortest possible out-of-phase and in-phase echo times will assure the best quality images, with better signal and fewer susceptibility artifacts.

1.2.1.3 Fat Suppressed SGE Sequences

Fat suppressed (FS) SGE images are routinely acquired before contrast injection for evaluating the pancreas [23] and for the detection of subacute hemorrhage [29]. Fat suppression is generally achieved on SGE images by selectively stimulating slower-precessing protons associated with fat using a tuned radio-frequency (RF) pulse, prior to performing the gradient echo imaging components of the sequence. The image parameters are similar to those for standard SGE sequences. It may be advantageous to employ a lower out-of-phase echo time (2.2-2.5 msec at 1.5 T) to benefit from additional fat-attenuating effects and also to increase the SNR ratio and the number of sections per acquisition. On current MRI machines, fat-suppressed SGE permits the acquisition of 22 sections in a 20 sec breath-hold with reproducible uniform fat suppression. One method that modern systems use to reduce the amount of additional time that fat suppression adds to the SGE sequence, and to acquire a greater number of slices per breath-hold, is to perform a fat suppression step after several phase encoding steps, rather than after every phase encode. Another approach is to selectively tune the stimulation RF pulse to activate protons in water, but not in fat. This eliminates the need to add fat saturation pulses [22].

Fat-suppressed SGE images are used to improve the contrast between intra-abdominal fat, diseased tissues and blood vessels on interstitial-phase gadolinium-enhanced images. Gadolinium enhancement generally increases the signal intensity of blood vessels and disease tissue, and fat suppression diminishes the competing high signal intensity of background fat.

1.2.1.4 3D SGE Sequences

3D SGE imaging has been used extensively for MR angiography (MRA), but only recently has it evolved into an accepted technique for soft-tissue imaging in the abdomen and pelvis. This development has partly been achieved simply by reducing the flip angle from the 70-90˚ used for MRA to 12-15˚. Advantages include the ability to acquire a volumetric dataset that can be sectioned into thinner

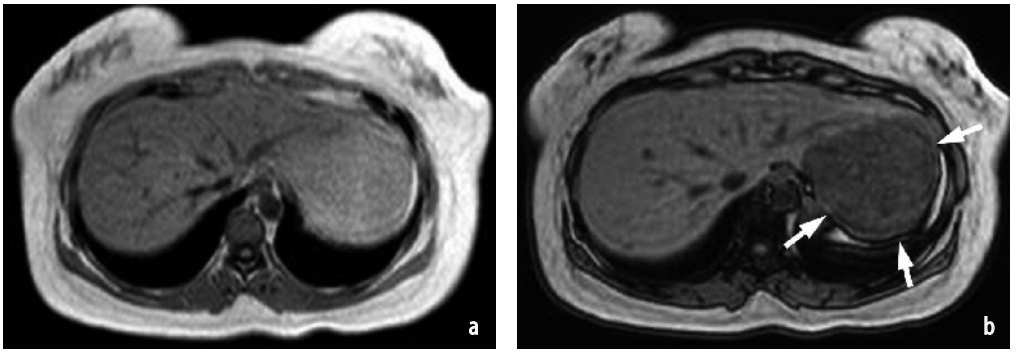

Fig. 3a, b. Axial breath-hold in-phase (**a**) and out-of-phase (**b**) T1-weighted GRE images through the liver with geographic fatty accumulation and enlargement of the lateral segments of the left liver lobe. Note that the lateral left lobe segments show conspicuous signal drop on the out-of-phase image (**b**, *arrows*) as compared to the relatively uninvolved adjacent liver and in comparison to the paraspinal muscles

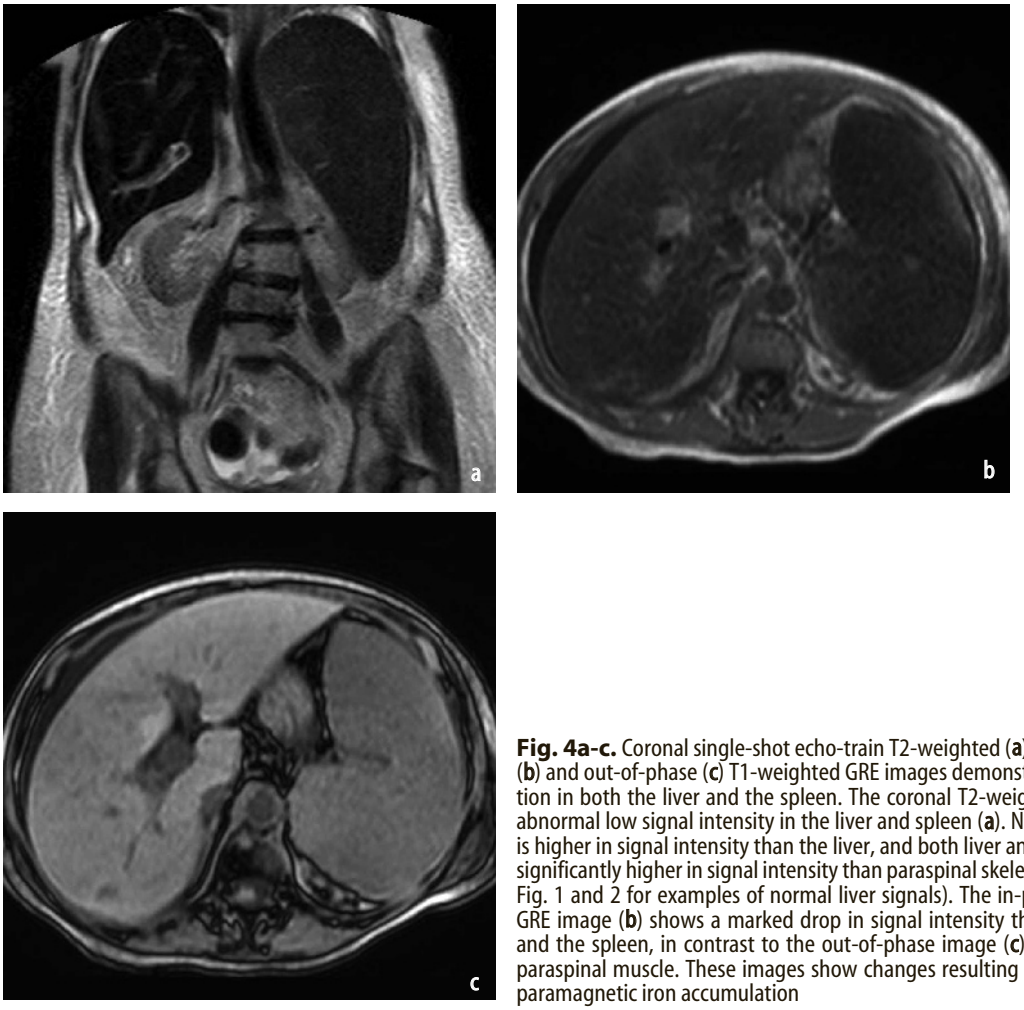

Fig. 4a-c. Coronal single-shot echo-train T2-weighted (**a**) and axial in-phase (**b**) and out-of-phase (**c**) T1-weighted GRE images demonstrating iron deposition in both the liver and the spleen. The coronal T2-weighted image shows abnormal low signal intensity in the liver and spleen (**a**). Normally, the spleen is higher in signal intensity than the liver, and both liver and spleen should be significantly higher in signal intensity than paraspinal skeletal muscle (Refer to Fig. 1 and 2 for examples of normal liver signals). The in-phase T1-weighted GRE image (**b**) shows a marked drop in signal intensity throughout the liver and the spleen, in contrast to the out-of-phase image (**c**) and in contrast to paraspinal muscle. These images show changes resulting from T2* effects of paramagnetic iron accumulation

sections than typically acquired for 2D images (generally in the 2.5-3.0 mm per slice range) and to post-process the data into other imaging planes. Although there are differences between some of the sequence features on different MR systems, fat suppression tends to be superior with greater uniformity compared to 2D SGE. On some MR systems, it is also possible to image a larger volume of tissue during the same breath-hold period than with 2D SGE. A potential limitation of 3D SGE imaging is diminished contrast-to-noise. However, this can be improved with the use of gadolinium enhancement.

The very short TR and TE values achieved with this technique using the latest generation high-speed gradients results in significant advantages: imaging with a greater number of thinner slices while contiguously covering a larger volume of tissue during a single breath-hold; fat-suppression without compromising the required slice coverage; reduction of paramagnetic image artifacts.

1.2.1.5 Motion-Insensitive SGE

Limitations of both 2D and 3D SGE imaging are a degree of sensitivity to motion and a requirement for the patient to cooperate by following breathing instructions. In uncooperative patients, the SGE sequence may be modified to achieve respiratory-independent images (Fig. 5). Typically, a single shot approach using the minimum TR possible is utilised. Such sequences include the so-called magnetization prepared rapid acquisition gradient echo (MP-RAGE), and turbo-fast low angle shot (Turbo FLASH) sequences. These techniques use magnetization-prepared SGE, in which an inversion pre-pulse improves the T1-weighted contrast during a short single slice acquisition. As the protons recover magnetization, a single slice SGE imaging sequence with short TR is performed. An inversion time of around 0.5 sec provides optimal T1-weighted contrast, and sufficient time to allow the protons to recover between slices leads to an effective slice-to-slice TR of approximately 1.5 sec. This technique can depict blood flowing through the imaging plane as either bright or dark, by making the pre-pulse slice-selective or non slice-selective, respectively [24] . A limitation of this technique is the inability to obtain as high a T1-weighted contrast as with standard SGE. Another limitation is that the magnetization-prepared slice-by-slice technique cannot be used for dynamic gadolinium-enhanced imaging of the liver, particularly during the hepatic arterial dominant phase. As each slice requires around 1.5 sec to acquire, the time difference accumulated between the top and bottom liver slices is too great to capture the entire liver in the arterial phase of enhancement. In contrast, the standard SGE sequences, although motion sensitive, offer superior time resolution for the entire volume of tissue imaged, with the critical contrast data acquired in less than 5 sec. With these data time-averaged throughout the entire set of slices, the entire liver can be imaged in the same phase of contrast enhancement.

An alternative strategy developed to deal with motion is based on motion correction. Older methods using slow spin-echo sequences that required several minutes per acquisition used bellows applied around the patient's lower chest to detect the respiratory cycle, in order to trigger acquisition of data only during end-expiration. Although similar in strategy, a more accurate method has been developed in conjunction with rapid imaging sequences. With this approach a rapid acquisition MP-RAGE type sequence is used to acquire a continuous series of sagittal images across the right hemi-diaphragm at a rate of greater than one image per second. The liver-lung interface produces a high contrast border that can be automatically detected by the specialized software, and used to trigger image acquisition at the same phase of the respiratory cycle. Another approach uses phase accumulation during motion of the tissue in order to calculate a correction factor, which is then used to restore the detected signal to the location from where it would have originated had there not been any movement. These methods are still considered to be under development.

1.2.1.6 Contrast-Enhanced SGE

In addition to its use in precontrast T1-weighted imaging, SGE sequences are routinely used for multi-phase image acquisition after intravenous administration of gadolinium contrast agents for investigation of the liver, spleen, pancreas, and kidneys (Fig. 6). An important feature of the multisection acquisition of SGE images is that the central phase-encoding steps are generally used to fill the central k-space, which determines image contrast. This contrast component of the dataset is acquired over a 4-5 sec period for the entire dataset, and is essentially shared by each individual section. As a result, data acquisition is sufficiently short for the entire dataset to isolate a distinct phase of enhancement (e.g., hepatic arterial dominant phase). This ensures that images of organs, such as liver, are shown in the same phase of contrast enhancement uniformly throughout the volume of the tissue.

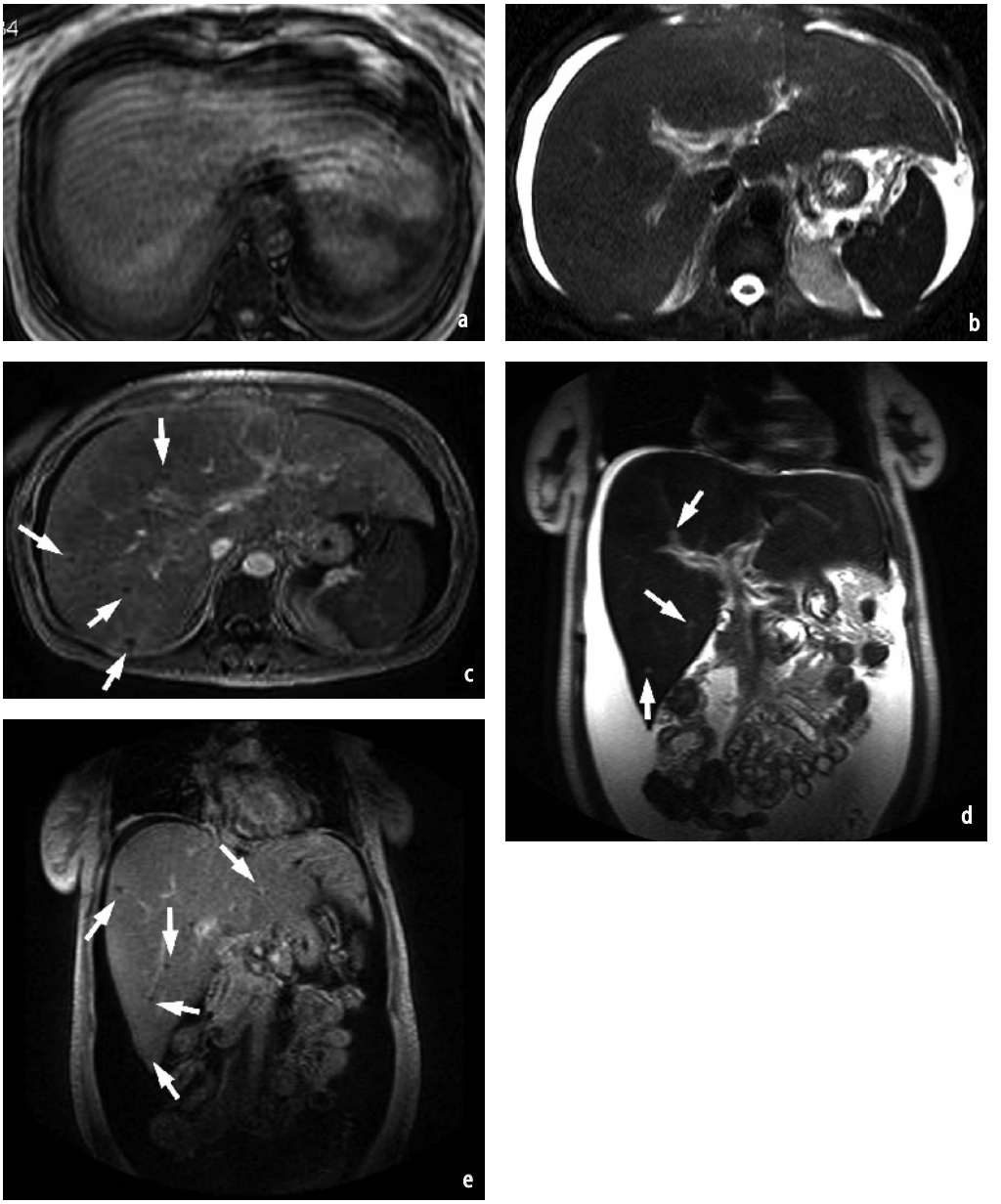

Fig. 5a-e. Uncooperative patient examination of a critically ill patient with immunodeficiency and liver fungal micro-abscesses, including standard axial T1-weighted GRE (**a**), axial single-shot echo-train fat-suppressed T2-weighted (**b**), axial magnetization-prepared gadolinium contrast-enhanced T1-weighted GRE (**c**), and the corresponding coronal T2-weighted (**d**) and T1-weighted (**e**) images. This patient was unable to breath-hold, and was examined while breathing freely throughout the study. Standard T1-weighted GRE technique (**a**) shows marked image motion-related deterioration, rendering the image non-diagnostic. However, single shot T2-weighted images (**b** and **d**) are inherently resistant to motion-related deterioration, and provide reproducibly high diagnostic quality images, in this case showing ascites, dark liver and spleen due to abnormal iron accumulation from prior blood transfusions, and tiny sub-centimeter high signal foci in the liver corresponding to micro-abscesses. As an alternative to standard T1-weighted GRE imaging, magnetization-prepared GRE imaging is relatively insensitive to motion-related deterioration (compare contrast-enhanced image (**a**) to images (**c**) and (**e**)). The magnetization-prepared enhanced images (**c** and **e**) show multiple micro-abscesses as non-enhancing tiny foci (*arrows*) surrounded by mild perilesional enhancement

1.2.2 T2-Weighted Sequences

Typical information available on T2-weighted sequences includes: the presence of increased fluid in acutely inflamed diseased tissue, which has high signal intensity; the presence of chronic non-inflammatory fibrotic tissue [25], which has low signal intensity; and the presence of iron deposition or heme products, which has very low signal intensity.

1.2.2.1 Standard Spin-Echo and Fast Spin-Echo Sequences

Standard T2-weighted spin-echo or fast spin-echo sequences have relatively long acquisition times (several minutes are needed to acquire slices through the abdomen or pelvis) but the achieved-contrast-to-noise ratio is good. Unfortunately, breathing-related motion precludes use of these sequences for abdominal imaging, unless used in conjunction with a motion correction method, such as respiratory gating. Not only does this add to the total scan time, but the achieved motion correction is not reliable or accurate: usually mild edge blurring leads to deteriorated resolution. Typical scan times are 5-7 min, depending on the respiratory rate and pattern. However, it is not unusual for the acquisition to fail, necessitating repetition. Pelvic imaging can be performed without breath-holding in most patients, with little image deterioration due to breathing-related motion relative to the upper abdomen. Motion due to bowel contraction can cause image deterioration, and can be reduced using intravenous or intramuscular glucagon. The latest generation fast spin-echo techniques inlcude sequences called turbo spin-echo, or fast spin-echo-xl which are based on intermediate length echo-trains. With these sequences acquisition times can be reduced to as low as 2.5 min for the pelvis.

1.2.2.2 Echo-Train Spin-Echo Sequences

Echo-train spin-echo sequences are single shot fast spin-echo, turbo spin-echo, or rapid acquisition with relaxation enhancement (RARE) sequences. The principle of echo-train spin-echo sequences is to sum multiple echoes within the same repetition time interval, leading to decreased examination time, increased spatial resolution, or both. This is a slice-by-slice technique, in which a single slice-selective excitation pulse is followed by a series of echoes, typically 180° pulses, each separated by around 3 msec, to fill in the k-space for the entire slice. Although the theoretical TR is infinite, each slice requires around 1.2-1.5 sec, before continuing to the next slice. Since the motion sensitive component represents only a small fraction of the entire acquisition period, this technique is relatively insensitive to breathing artifacts. Echo-train spin-echo has achieved widespread use because of this advantage. In contrast, conventional T2-weighted spin-echo sequences are lengthy and suffer from patient motion and increased examination time. The major disadvantage of echo-train sequences is that T2 differences between tissues are decreased. Although this is usually not problematic in the pelvis because of the substantial differences in T2 values between diseased and normal tissue, in the liver the T2 difference between diseased and background normal liver may be small, and thus a decreased T2 difference may result from the T2-averaging effects of summed multiple echoes. This may result in relatively diminished lesion conspicuity for lesions with mildly elevated T2-weighted signal intensity, such as HCC, as compared to standard spin-echo sequences. Fortunately, diseases with T2 values similar to those of liver generally have longer T1 values than liver, so that lesions that are poorly visualized on echo-train spin-echo are generally well-visualized on native SGE or immediate post-gadolinium SGE images as low-signal lesions.

Echo-train spin-echo, and T2-weighted sequences in general, are important for evaluating the abdomen and pelvis. For liver masses, it is predominantly T2-weighted images that are important for lesion characterization, while T1-weighted images are important for both lesion detection and characterization. T2-weighted images are also important for the assessment of diffuse liver disease, including iron deposition (Fig. 4), edema related to active liver disease (Fig. 6), and fibrosis. Echo-train T2-weighted sequences are important for the assessment of fluid-filled structures, including bile ducts, gall bladder, pancreatic duct, stomach and bowel, as well as cysts or cystic masses, abscesses or free fluid in the abdomen or pelvis. The relative resistance of echo-train images to motion degradation (Fig. 5) generally yields better resolution of structures internal to cystic masses, such as the septations within a pancreatic serous or mucinous tumor. MR cholangiopancreatography (MRCP) is based on modified echo-train sequences, in which the effective TE is longer, in the order of 250-500 msec. Lengthening the TE results in heavily T2-weighted high contrast images that make most soft tissues dark, while the fluid in bile ducts, gallbladder, and the pancreatic duct is very bright. MRCP can be performed in thin sections of

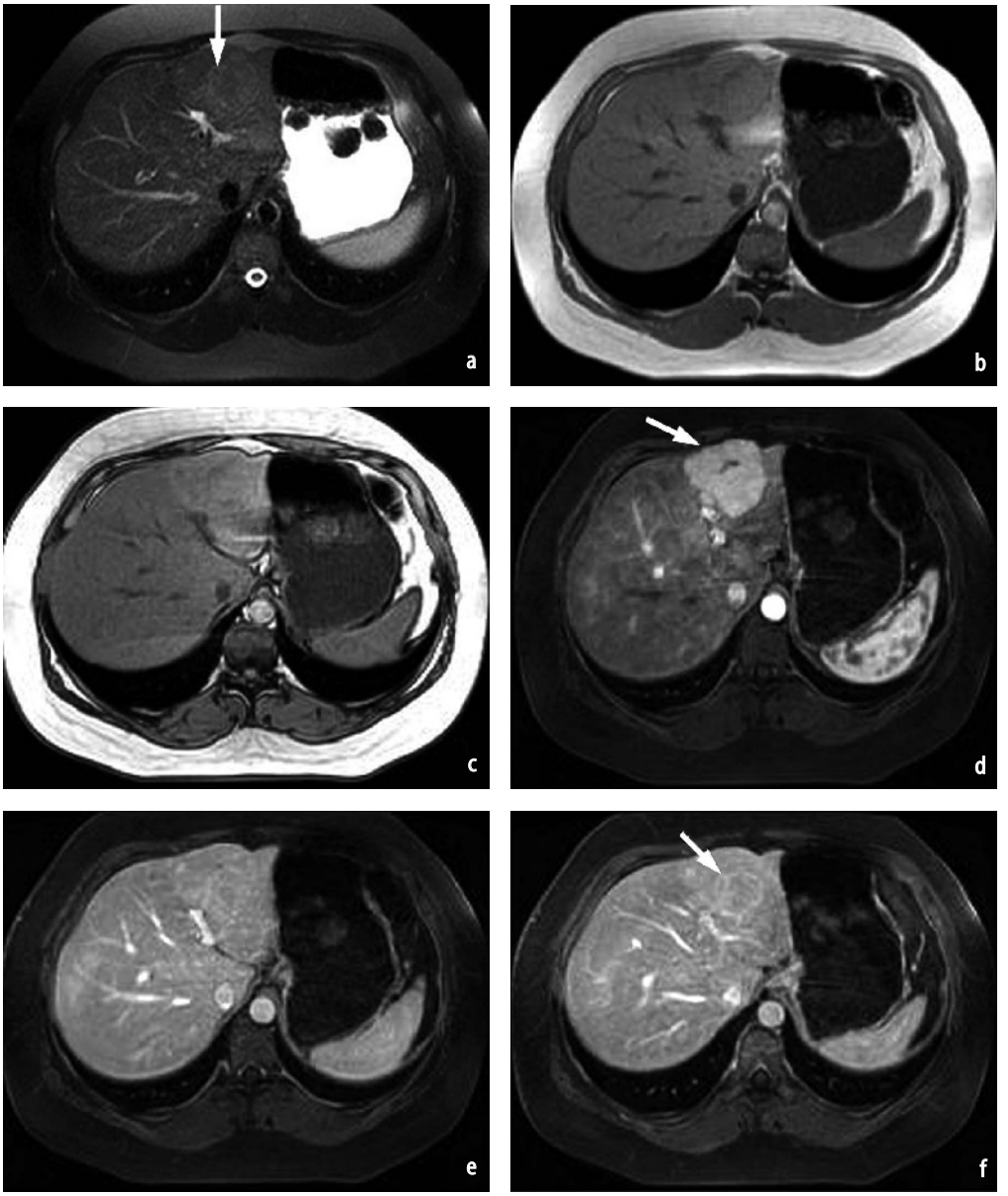

Fig. 6a-f. Axial liver breath-hold images of an intra-hepatic FNH, in the setting of a diffusely abnormal liver with features of steatohepatitis on fat-suppressed single-shot T2-weighted (**a**), in-phase (**b**) and out-of-phase (**c**) T1-weighted, and dynamically gadolinium-enhanced T1-weighted arterial (**d**), portal-venous (**e**), and equilibrium (**f**) phase images. A subtle drop in liver signal intensity is noted in contrast from in-phase (**b**) to out-of-phase images (**c**) (compare liver to paraspinal muscle where the liver is hyperintense compared to muscle on the in-phase image (**b**), and isointense compared to muscle on the out-of-phase image (**c**)). This is indicative of diffuse fatty liver accumulation. In addition, the arterial phase image (**d**) shows diffuse heterogeneous liver enhancement with patchy areas of hyper-enhancement noted towards the periphery of the liver, a finding that has been described in connection with acute hepatitis [28]. This patient also has a mass in the left hepatic lobe (**a**, **d**, and **f**, *arrows*) showing features typical of a benign FNH. In particular, the mass demonstrates a central focus of high signal on the T2-weighted image (**a**, *arrow*), that corresponds to a slowly enhancing central fibrovascular scar; compare the arterial phase (**d**, *arrow*) to the equilibrium phase (**f**, *arrow*). This case serves to demonstrate the critical information delineated on the arterial phase image (**d**). If this component of the gadolinium-enhanced tissue perfusion was not included, or incorrectly timed, the abnormal liver enhancement of hepatitis and the arterial phase-dominant characteristics of the FNH would not be recognized, as these are transient features

3-4 mm for higher spatial resolution, or by using a single thick slab of 3-4 cm if the need is to include the majority of the pancreatic and bile duct in a single image. As a result of the repeated refocusing echo pulses, echo-train imaging is relatively insensitive to respiratory motion and bowel peristalsis. Combined with its relative resistance to the paramagnetic distortion effects of intraluminal bowel gas, echo-train imaging is therefore particularly well-suited to imaging the bowel.

Fat is high in signal intensity on echo-train spin-echo sequences in comparison to conventional spin-echo sequences, in which fat is intermediate in signal intensity. The MR imaging determination of recurrent malignant disease versus fibrosis for pelvic malignancies illustrates this difference. Recurrent malignant disease in the pelvis (e.g., cervical, endometrial, bladder, or rectal cancer) generally appears high in signal intensity on conventional spin-echo sequences because of the higher signal intensity of the diseased tissue relative to the moderately low-signal intensity fat. In contrast, fat is high in signal intensity on echo-train spin-echo images, and recurrent disease will commonly appear relatively low in signal intensity. Unfortunately, the fact that abnormal tissue is not high in signal intensity on echo-train T2-weighted images relative to fat is not specific for neoplasm, as fibrosis can have a similar appearance. This is particularly problematic in post-therapy patients.

Fat may also be problematic in the liver because fatty liver is high in signal intensity on echo-train spin-echo sequences, thereby diminishing contrast with the majority of liver lesions, which are also generally high in signal intensity on T2-weighted images. It is often necessary to use fat suppression on T2-weighted echo-train spin-echo sequences for liver imaging. Fat suppression should generally be applied to at least one set of images of the abdomen or pelvis, to ensure optimal contrast between high signal abnormalities, such as fluid collections or cystic masses, and adjacent intra-abdominal or pelvic fat.

1.2.3 The Uncooperative Patient Examination

The single shot T2-weighted technique can acquire each slice in less than 1 sec, and the critical data for creating the image during only a small fraction of that time, rendering this technique relatively insensitive to image deterioration resulting from respiratory motion (Fig. 5). Breath-hold examination is preferable to reduce spatial misregistration between adjacent slices. However, if a patient is incapable of following breath-hold instructions, a free breathing technique can be utilized as part of an "uncooperative" examination. Gradient echo T1-weighted techniques are sensitive to motion and will suffer from respiratory-related image deterioration. However, magnetization-prepared gradient echo sequences, for example TurboFLASH, which operates as a slice-by-slice single shot technique, can generate T1-weighted images that are resistant to deterioration from respiratory motion. Unfortunately, a limitation of magnetization-prepared gradient echo sequences is that the contrast-to-noise ratio is inferior to regular gradient echo, and that the time to image the entire liver is typically 15-20 sec, making it impossible to acquire all of the liver in the optimal arterial capillary phase of contrast enhancement after administration of gadolinium contrast agent. However, in the setting of an uncooperative patient, this technique provides an alternative that can yield some of the diagnostic data required from pre- and post-contrast T1-weighted images.

1.3 Technical Factors

1.3.1 Surface Coils

Phased-array surface coils provide on average a three-fold improvement in SNR and should be considered essential for optimal imaging of the abdomen and liver. New technical developments include increased numbers of coil receiver elements associated with magnets that are engineered with a greater number of receiver channels. In combination with parallel processing techniques such as SENSE and SMASH [43], these represent methods that use coil element sensitivity profiles to obtain spatial information that can lead to reduced acquisition times for gradient echo imaging. As the number of coil elements and receiver channels are increased, the degree of acceleration may be increased. In addition, improved coil system designs facilitate more rapid imaging of multiple body regions in combination, such as the abdomen and pelvis.

1.3.2 Magnetic Field Strength

The magnetic field strength of choice currently employed for body MRI is 1.5 T. At the current state of development, this field strength provides an optimal combination of SNR and speed, allowing optimization of rapid acquisition techniques while staying within government institution-determined energy deposition-rate limits. These systems also provide a good balance between T1 values, that are dependent on field strength, and

achievable contrast effects. In addition, field distortion and paramagnetic effects that increase with increasing field strength possibly resulting in undesirable image artifacts remain within tolerable limits at 1.5 T. There are theoretical considerations favouring development of higher field systems for body MRI and efforts are well underway to transfer techniques used at 1.5 T to 3 T. However, it has become apparent that the approaches used previously to migrate from lower to higher (1.5 T) field systems have not proven successful in migrating from 1.5 T to 3 T. The relative strengths of higher field imaging at 3 T, in general, are more easily realized when using longer acquisition techniques such as fast spin echo (FSE) T1- and T2-weighted images, or multi-excitation gradient echo with oversampling. This explains the relative ease with which implementation of 3 T imaging has occurred for brain, spine, and musculoskeletal applications where longer acquisition imaging is used predominantly (in the order of minutes) and the relative difficulty in implementing 3 T imaging for the abdomen, where faster acquisition sequences are needed (in the order of seconds). Specific challenges for body imaging at 3 T are detailed below.

1.3.2.1 SAR and RF Power Deposition

At 3 T the Specific Absorption Ratio (SAR), a measure of RF energy deposited in the body, increases by a factor of four, and has an undesirable impact on essential image characteristics including contrast, acquisition time, and resolution. The SAR thresholds as per Food and Drug Administration guidelines are 2 W/kg in the normal mode and 4 W/kg in the first level-controlled mode [6].

1.3.2.2 Magnetic Field Distortions

Susceptibility effects are greater at 3 T. In body imaging these may arise from surgical clips or hardware or from air-soft tissue interfaces that arise from the lungs, gastrointestinal tract or irregular skin surfaces.

1.3.2.3 Field-of-View

Fields-of-view in excess of 35-40 cm are commonly used for body imaging in the z-direction, placing high demand on static magnetic field homogeneity over a large area. Field homogeneity is significantly more challenging at 3 T.

1.3.2.4 Motion

Motion from respiration, heart and bowel peristalsis may cause marked image deterioration. At 3 T fast acquisition techniques may be limited by SAR concerns.

1.3.2.5 Contrast

Sequences have been optimized at 1.5 T to achieve a balance between speed of acquisition and image contrast. At 3 T, image contrast may suffer from a combination of compromises arising from SAR limitations. In addition, adjustments are required to adapt to the longer T1 and shorter T2 of soft tissues at 3 T.

1.3.2.6 Signal-to-Noise Ratio

RF signal generated at 3 T is four times stronger than at 1.5 T. However, a simultaneous increase in noise by a factor of two results in a net SNR ratio increase of only two. A challenge is to be able to realize this theoretical benefit as the increase in SNR at 3 T is balanced against losses from adjustments for limitations related to SAR.

1.3.2.7 Dielectric Effect

This phenomenon is seen as a loss of signal when the transmitted wavelength approaches the size of the body structure [47]. For a circular body habitus there is loss of signal at the periphery, while for an oval body habitus the signal loss occurs at the periphery of the short axis. To a certain extent this can be corrected using phantom-derived algorithms like body-tuned CLEAR (Philips Medical Systems).

1.4 Summary

Abdominal MRI should be considered a primary imaging method for many important disease processes, and the method of choice for imaging of both diffuse diseases and tumors of the liver. Reproducible diagnostic quality liver imaging with rapid acquisition techniques is feasible using the techniques discussed in this chapter. Gadolinium-enhancement is the key to a comprehensive examination and dynamically acquired images should include, at a minimum, the capillary-arterial, por-

tal-venous and equilibrium-interstitial phases. An additional benefit of the rapid imaging strategies discussed in this chapter is shortened examination times. Ongoing technological developments may provide greater degrees of simplicity, reproducible quality, faster examinations, and accessibility to a broader range of imaging centers, including those with less experience in MRI.

References

1. Alustiza JM, Artetxe J, Castiella A. MR quantification of hepatic iron concentration. Radiology 2004;230:479-484
2. Bonetti MG, Castriota-Scanderbeg A, Criconia GM, et al. Hepatic iron overload in thalassemic patients: proposal and validation of an MRI method of assessment. Pediatr Radiol 1996;26:650-656
3. Bradley, WG. Optimizing lesion contrast without using contrast agents. J Magn Reson Imaging 1999;10:442-449
4. Braga L, Semelka RC, Pietrobon R, Martin DR, de-Barros N, Guller U. Does hypervascularity of liver metastases as detected on MRI predict disease progression in breast cancer patients? Am J Roentgenol 2004;182:1207-13
5. Brenner DJ, Elliston CD. Estimated radiation risks potentially associated with full body CT screening. Radiology 2004;232:735-738
6. Brix B, Seebass M, Hellwig G, Griebel J. Estimation of heat transfer and temperature rise in partial-body regions during MR procedures: an analytical approach with respect to safety considerations. Magn Reson Imaging 2002;20:65-76
7. Chien D, Edelman RR. Ultrafast imaging using gradient echoes. Magn Reson Q 1991;7:31-56
8. Coates GG, Borrello JA, McFarland EG, et al. Hepatic T2-weighted MRI: a prospective comparison of sequences, including breath-hold, half-Fourier turbo spin echo (HASTE). J Magn Reson Imaging 1998;8:642-649
9. Engelhardt R, Langkowski JH, Fischer R, et al. Liver iron quantification: studies in aqueous iron solutions, iron overloaded rats, and patients with hereditary hemochromatosis. Magn Reson Imaging 1994;12:999-1007
10. Ernst O, Sergent G, Bonvarlet P, et al. Hepatic iron overload: diagnosis and quantification with MR imaging. AJR Am J Roentgenol 1997;168:1205-1208
11. Ferrucci JT. Advances in abdominal MR imaging. Radiographics 1998;18:1569-1586
12. Fretz CJ, Stark DD, Metz CE, et al. Detection of hepatic metastases: comparison of contrast-enhanced CT, unenhanced MR imaging, and iron oxide-enhanced MR imaging. AJR Am J Roentgenol 1990;155:763-770
13. Gaa J, Hutabu H, Jenkins RL, et al. Liver masses: replacement of conventional T2-weighted spin echo MR imaging with breath-hold MR imaging. Radiology 1996;200:459-464
14. Gandon Y, Guyader D, Heautot JF, et al. Hemochromatosis: diagnosis and quantification of liver iron with gradient-echo MR imaging. Radiology 1994;193:533-538
15. Gandon Y, Olivie D, Guyader D. Non-invasive assessment of hepatic iron store by MRI. The Lancet 2004;363:357-62
16. Gleeson TG, Bulugahapitiya S. Contrast-Induced Nephropathy. AJR 2004;183 (6):1673-1689
17. Harkonen S, Kjellstrand CM. Exacerbation of diabetic renal failure following intravenous pyelography. Am J Med 1977;63:939-946
18. Helmberger TK, Schroder J, Holzknecht N, et al. T2-weighted breathold imaging of the liver: a quantitative and qualitative comparison of fast spin echo and half Fourier single shot fast spin echo imaging. Magma 1999;9:42-51
19. Imai Y, Murakami T, Yoshida S, et al. Superparamagnetic iron oxide-enhanced magnetic resonance images of hepatocellular carcinoma: correlation with histological grading. Hepatology 2000;32:205-212
20. Imam K, Bluemke DA. MR imaging in the evaluation of hepatic metastases. Magn Reson Imaging Clin N Am 2000;8(4):741-56
21. Kelekis NL, Semelka RC, Worawattanakul S, et al. Hepatocellular carcinoma in North America: a multiinstitutional study of appearance on T1-weighted, T2-weighted, and serial gadolinium-enhanced gradient-echo images. AJR Am J Roentgenol 1998;170:1005-1013
22. Kier R, Mason BJ. Water-suppressed MR imaging of focal fatty infiltration of the liver. Radiology 1997;203:575-577
23. King LJ, Scurr ED, Murugan N, et al. Hepatobiliary and pancreatic manifestations of cystic fibrosis: MR imaging appearances. Radiographics 2000;20:767-777
24. Koolpe HA, Koolpe L. Portal hypertension: angiographic and hemodynamic evaluation. Radiol Clin North Am 1986;24:369-381
25. Kreft B, Dombrowski F, Block W, et al. Evaluation of different models of experimentally induced liver cirrhosis for MRI research with correlation to histopathologic findings. Invest Radiol 1999; 34:360-366
26. Low RN. Current uses of gadolinium chelates for clinical magnetic resonance imaging examination of the liver. Top Magn Reson Imaging 1998;9:141-166
27. Manske CL, Sprafka JM, Storry JT, Wang Y. Contrast nephropathy in azotemicdiabetic patients undergoing coronary angiography. Am J Med 1990; 89:615-620
28. Martin DR, Seibert D, Yang M, et al. Reversible Heterogeneous Arterial Phase Liver Perfusion. Associated With Transient Acute Hepatitis: Findings on Gadolinium-Enhanced MRI. JMRI 2004;20:838-842
29. Mitchell DG. Chemical shift magnetic resonance imaging: applications in the abdomen and pelvis. Top Magn Reson Imaging 1992;4:46-63
30. Muller RD, Vogel K, Neumann K, et al. SPIO-MR imaging versus double-phase spiral CT in detecting malignant lesions of the liver. Acta Radiol 1999;40:628-635
31. Naganawa S, Jenner G, Cooper TG, et al. Rapid MR imaging of the liver: comparison of twelve techniques for single breath-hold whole volume acquisition. Radiat Med 1994;12:255-261
32. Noone TC, Semelka RC, Siegelman ES, et al. Budd-Chiari syndrome: spectrum of appearances of acute, subacute, and chronic disease with magnet-

ic resonance imaging. J Magn Reson Imaging 2000;11:44-50
33. Rofsky NM, Lee VS, Laub G, et al. Abdominal MR imaging with a volumetric interpolated breath-hold examination. Radiology 1999;212:876-884
34. Rofsky NM, Weinreb JC, Ambrosino MM, et al. Comparison between in-phase and opposed-phase T1-weighted breath-hold FLASH sequences for hepatic imaging. J Comput Assist Tomogr 1996; 20:230-235
35. Semelka RC, Balci NC, Op de Beeck B, et al. Evaluation of a 10-minute comprehensive MR imaging examination of the upper abdomen. Radiology 1999;211:189-195
36. Semelka RC, Brown ED, Ascher SM, et al. Hepatic hemangiomas: a multi-institutional study of appearance on T2- weighted and serial gadolinium-enhanced gradient-echo MR images. Radiology 1994;192:401-406
37. Semelka RC, Chung JJ, Hussain SM, et al. Chronic hepatitis: correlation of early patchy and late linear enhancement patterns on gadolinium-enhanced MR images with histopathology initial experience. J Magn Reson Imaging 2001;13:385-391
38. Semelka RC, Kelekis NL, Thomasson D, et al. HASTE MR imaging: description of technique and preliminary results in the abdomen. J Magn Reson Imaging 1996;6:698-699
39. Semelka RC, Martin DR, Balci C, et al. Focal liver lesions: Comparison of dual-phase CT and multi-sequence multiplanar MR imaging including dynamic gadolinium enhancement. J Magn Reson Imaging 2001;13:397-401
40. Siegelman ES, Mitchell DG, Semelka RC. Abdominal iron deposition: metabolism, MR findings, and clinical importance. Radiology 1996;199:13-22
41. Siegelman ES. MR imaging of diffuse liver disease: Hepatic fat and iron. Magn Reson Imaging Clin N Am 1997;5:347-365
42. Siewert B, Muller MF, Foley M, et al. Fast MR imaging of the liver: quantitative comparison of techniques. Radiology 1994;193:37-42
43. Sodickson DK, McKenzie CA. A generalized approach to parallel magnetic resonance imaging. Mec Phys 2001;28:1629-43
44. Thomsen C, Wiggers P, Ring-Larsen H, et al. Identification of patients with hereditary haemochromatosis by magnetic resonance imaging and spectroscopic relaxation time measurements. Magn Reson Imaging 1992;10:867-879
45. Thu HD, Mathieu D, Thu NT, et al. Value of MR imaging in evaluating focal fatty infiltration of the liver: preliminary study. Radiographics 1991; 11:1003-1012
46. Torres CG, Lundby B, Sterud AT, et al. Mn-DPDP for MR imaging of the liver. Results from the European phase III studies. Acta Radiol 1997;38:631-637
47. Tropp J. Image brightening in samples of high dielectric constant. J Magn Reson 2004;167:12-24

2

Histopathologic Classification of Liver Pathologies

CONTENTS

2.1 Benign and Malignant Nodular Hepatocellular Lesions

2.1.1 Regenerative Lesions

Generally, a regenerative nodule is a well-circumscribed area of parenchyma showing enlargement as a response to necrosis, altered circulation or other stimuli.

2.1.1.1 Monoacinar Regenerative Nodule

A monoacinar regenerative nodule is a regenerative nodule limited to one portal tract. Usually, multiple nodules are found involving most of the liver. This is referred to as diffuse nodular hyperplasia [184].

Diffuse Nodular Hyperplasia without Fibrous Septa (Nodular Regenerative Hyperplasia, NRH)

Diffuse nodular hyperplasia can be subdivided into nodular regenerative hyperplasia in which no fibrous septa can be found, or diffuse nodular hyperplasia containing fibrous septa or occuring in coexisting cirrhosis.

Nodular hyperplasia is defined by the presence of non-neoplastic nodules that are not limited by fibrous septa (Fig. 1). The cells of the surrounding parenchyma are atrophic (Fig. 2). Nodular hyperplasia is usually a regenerative response occurring after circulatory stress. Portal vein obstruction may be responsible for widespread hepatocellular atrophy and secondary hepatic arterial dilatation (Fig. 3). Increased arterial flow and possible hepatotropic factors cause hepatocellular hyperplasia and nodule formation.

Monoacinar regenerative nodules may also occur in cases of disturbed circulation, such as hepatic vein obstruction and circulation disorders of the sinusoids. However, the resulting nodules are less uniformly distributed and are accompanied by more congestion and fibrous septa.

The term NRH was originally applied to livers with minimal or no parenchymal fibrosis. NRH can be found in up to 5% of the older population. A higher prevalence occurs in patients with concomitant systemic diseases associated with vasculopathy, such as polycythemia, rheumatoid arthritis and polyarteritis nodosa.

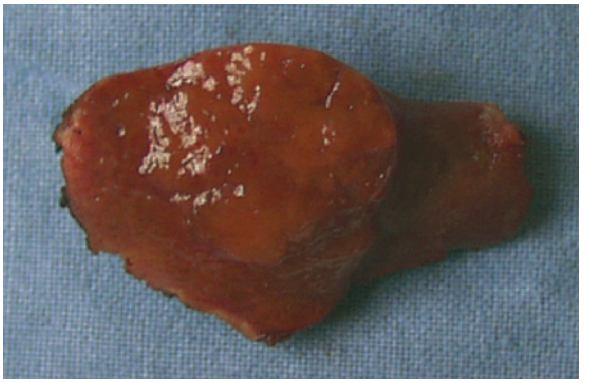

Fig. 1. Cut surface of a nodular regenerative hyperplasia (NRH)

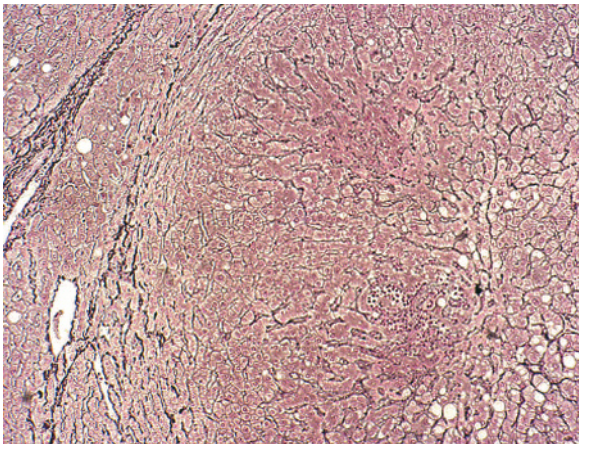

Fig. 2. Nodular regenerative hyperplasia demonstrating a non-neoplastic nodule with hyperplastic liver cells surrounded by atrophic parenchyma

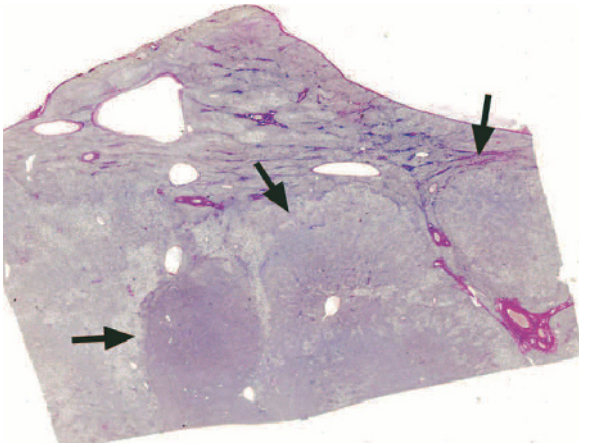

Fig. 3. Histology of diffuse nodular regenerative hyperplasia with demonstration of multiple nodules (*arrows*) surrounded by atrophy in adjacent liver tissue caused by Budd-Chiari syndrome

Clinical symptoms, which aid the diagnosis in affected patients, include esophageal varices, splenomegaly, moderate increased alkaline phosphatase and ascites [118, 176].

Diffuse Nodular Hyperplasia with Fibrous Septa or in Cirrhosis

As described above, this lesion corresponds to nodular regenerative hyperplasia with concomitant fibrous septa, or which is superimposed on a previous hepatic cirrhosis [177, 184].

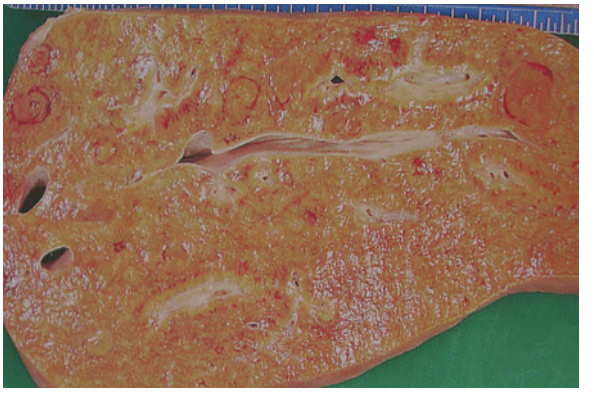

Fig. 4 . Nodular regenerative hyperplasia with a diffuse micronodular pattern

2.1.1.2 Multiacinar Regenerative Nodule

A regenerative nodule involving more than one solitary portal tract is called a multiacinar regenerative nodule. Normally, it presents in livers with pre-existing pathology such as cirrhosis, or in cases of severe disease of the portal veins, hepatic veins, or sinusoids. Usually, multiple nodules occur within the liver and these can correspond to cirrhotic nodules if they are surrounded by fibrous septa. If larger than most cirrhotic nodules of the same liver or measuring at least 5 mm in diameter, multiacinar regenerative nodules are also called large regenerative nodules or macroregenerative nodules [172] (Fig. 4).

2.1.1.3 Lobar or Segmental Hyperplasia

Lobar or segmental hyperplasia is defined as the enlargement of an entire lobe or the major part of a lobe in one or several liver segments, while other parts of the liver show atrophy, necrosis or fibrosis. This pathologic pattern has also been described as atrophy-hypertrophy complex [71].

Lobar or segmental hyperplasia may occur in Budd-Chiari syndrome or in primary sclerosing cholangitis involving the hepatic veins or bile ducts. It introduces both a hyperplasia and an atrophy or fibrosis into the liver parenchyma. As hyperplasia typically arises in regions with increased blood flow in Budd-Chiari syndrome, the caudate lobe often presents as hyperplastic because the drainage of this part of the liver is usually independent of the main hepatic veins. Normally lobar or segmental hyperplasia measures at least several centimeters in diameter but consists of histologically normal liver cells [164].

2.1.1.4 Cirrhotic Nodule (Monoacinar Cirrhotic Nodule / Multiacinar Cirrhotic Nodule)

Generally, a cirrhotic nodule is defined as a regenerative nodule in which hepatocytes are partially or completely surrounded by fibrous septa. It can be subdivided according to its expansion. Thus, a monoacinar cirrhotic nodule contains no more than one terminal portal tract, whereas a multiacinar cirrhotic nodule is composed of two or more portal tracts. However, this definition is not in accordance with the classifications micronodule and macronodule that exist in cirrhosis. This is usually defined by size with a division point at 3 mm in diameter [14].

2.1.1.5 Focal Nodular Hyperplasia (FNH)

Focal nodular hyperplasia is defined as a nodule that consists of benign-appearing hepatocytes which are accompanied by fibrous stroma and which may contain ductules that form a characteristic central stellate scar. It usually occurs in an otherwise histologically normal or nearly normal liver.

Similar to adenoma (2.1.2.1), FNH is predominantly found in female patients. Although oral contraception does not seem to be causal, continuous enlargement of lesions has been reported concomitant with the taking of birth-control pills and during pregnancy [182].

Multiple FNH occur in 10-20% of all cases while an association with hemangioma occurs in 5-10% of cases [78, 107].

Macroscopically, FNH shows septations and, in classical cases, a central scar. However, in up to 30% of all cases a central scar is not present. In contrast to fibrolamellar carcinoma (2.1.2.5), the

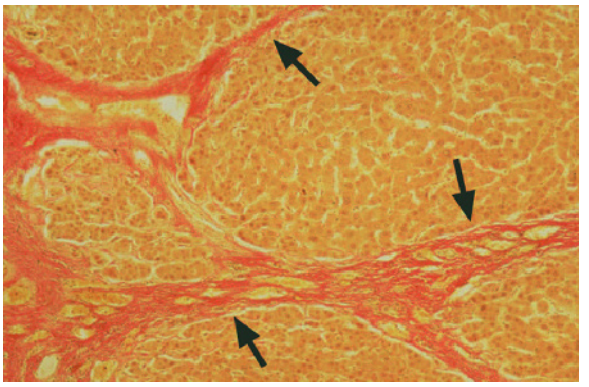

Fig. 5. Focal nodular hyperplasia consists of liver nodules which are separated by fibrous septa (*arrows*). Bile ducts, sometimes numerous, are always present at the interface between liver nodules and septa.

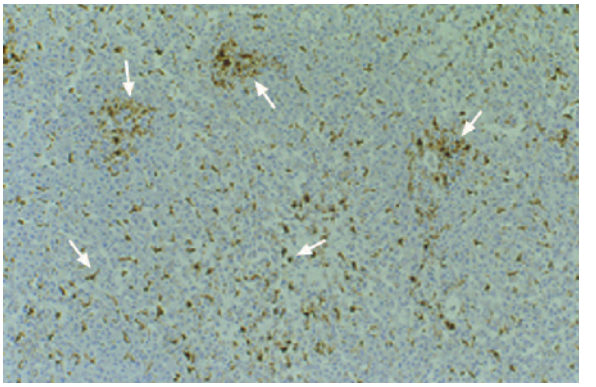

Fig. 6. Histology of focal nodular hyperplasia demonstrating Kupffer cells (*arrows*)

scar is not a true one, but rather congeries of blood vessels and bile ducts and sometimes a focal area of cirrhosis. An elevated fat- and glycogen-content can often be demonstrated. FNH is thought to derive from an initial regional vascular arteriovenous (AV) malformation which undergoes consecutive localized overgrowth of all liver constituents. Thus, histologically, FNH consists of abnormally arranged normal liver cells (Fig. 5). In contrast to adenoma, small bile ductules that do not communicate with larger bile ducts are found. Kupffer cells are also present although their function is frequently deficient (Fig. 6).

FNH is currently divided into a classic and a non-classic type. The classic type presents with an abnormal nodular architecture, malformed vessels, and cholangiocellular proliferation. The non-classic type can be further subdivided into

a) teleangiectatic FNH,
b) FNH with cytologic atypia and
c) mixed hyperplastic and adenomatous FNH [178].

The gross appearance of classic FNH consists of nodules surrounded by fibrous septations in a radiating appearance originating from the central scar. On histologic examination there is nodular hyperplastic parenchyma and often moderately thickened hepatic plates with normal hepatocytes. The central scar consists of fibrous tissue, cholangiocellular proliferation with surrounding inflammation and malformed vessels of different calibres. In contrast to adenoma, the blood flows centrifugally from anomalous central arteries in FNH.

Non-classic FNH typically does not show a central scar formation, its appearance is variable, and often resembles adenoma. The teleangiectatic type presents with atrophic hepatic plates separated by dilated sinusoids. Short fibrous septa and bile-duct proliferation is always found in teleangiectatic FNH.

FNH with cytologic atypia typically exhibit the appearance of classic FNH, but contain areas of cell dysplasia.

Mixed hyperplastic and adenomatous FNH presents features of the teleangiectatic type as well as a resemblance to adenoma.

A so-called FNH syndrome is present if more than two FNH co-exist with intracerebral vascular malformations, meningioma or astrocytoma. If any of the associated lesions are found in the presence of a solitary FNH, the syndrome is probably present with incomplete expression. Since the risk of rupture is quite low and patients usually do not present relevant symptoms (90% of all FNH are discovered by chance), surgical intervention is not mandatory [88].

Focal Nodular Hyperplasia, Solid Type

The solid type of FNH occurs most commonly. Solitary lesions are observed in two thirds of individuals, while two or more lesions may be present in the remaining one third of individuals.

On cut sections most solid FNH have a central fibrous stalk region (Figs. 7, 8). However, this is often absent in lesions smaller than 1 cm in diameter. The stalk region contains an artery that typically is larger than expected considering its localization. Degenerative changes such as post-thrombotic arterial fibrosis and cholestasis may be observed in larger lesions.

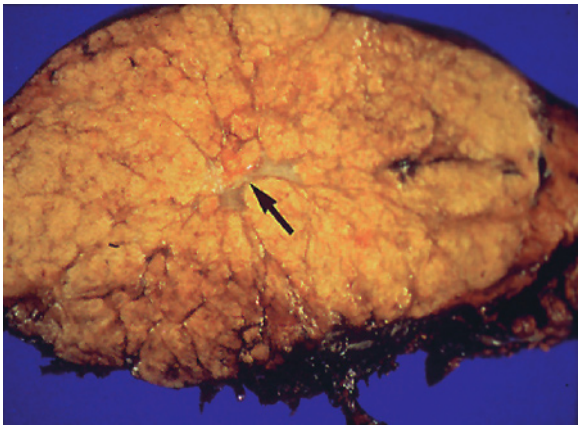

Fig. 7. Focal nodular hyperplasia with characteristic central fibrous region (*arrow*) and radiating fibrous cords

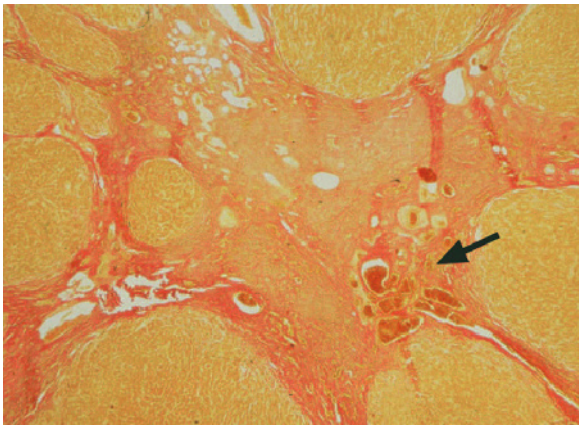

Fig. 8. Histology of a central stellate scar in FNH demonstrating thick-walled vessels (*arrow*) of a large arterial malformation surrounded by fibrous tissue

Focal Nodular Hyperplasia, Teleangiectatic Type

This type of FNH shows multiple dilated blood spaces near the center of the lesion, so that large lesions may resemble hemangioma or peliosis. Compared with solid FNH, the arteries in the central region are small and numerous. The teleangiectatic type of FNH is usually observed in cases of multiple FNH syndrome.

2.1.2 Dysplastic or Neoplastic Lesions

2.1.2.1 Hepatocellular Adenoma

Liver cell adenoma has an incidence of 1/1,000,000 and is mainly found in women of child-bearing age [65].

In contrast to the situation with FNH, oral contraceptives seem to lead to an increased incidence of hepatocellular adenoma [16]. Moreover, both lesion size and complication rate seem to correlate positively with the duration of oral contraception [26]. Some authors have noted tumor regression after discontinuation of oral contraceptives [43].

Androgen therapy, familial insulin-dependent diabetes, Fanconi anemia and some glycogen storage diseases tend to predispose subjects to adenoma [61].

If subjects have more than ten hepatic adenomas the condition is referred to as liver adenomatosis. This entity is independent of gender or hormone therapy and seems to be associated with an elevated complication rate.

Adenomas are unencapsulated tumors of light brown or yellow colour in gross specimen, with compressed adjacent liver tissue that may mimic capsule formation.

Biopsy of adenoma reveals enlarged and glycogen-rich hepatocytes, sometimes surrounded by a capsule (Fig. 9). Portal tracts and bile ducts are characteristically absent and, in contrast to FNH, there is a substantially increased risk of spontaneous bleeding [121] (Fig. 10). Hepatocytes are normal in appearance, but the typical acinar architecture is missing. Mitoses are often absent.

The missing bile ducts enable the differential diagnosis of adenoma from FNH on hepatobiliary sequence scintigraphy. Around 80% of patients with liver cell adenoma complain of abdominal symptoms, which are typically caused by compression, intratumoral bleeding or even rupture and hemoperitoneum [154].

Patients with liver cell adenoma should undergo resection to avoid these complications, and female patients should discontinue oral contraception. Some authors report individual cases of malignancy developing in liver cell adenoma, however, as yet, there is no valid proof of malignant transformation [60].

On rare occasions it may be impossible to distinguish adenoma from well-differentiated hepatocellular carcinoma (HCC) on biopsy.

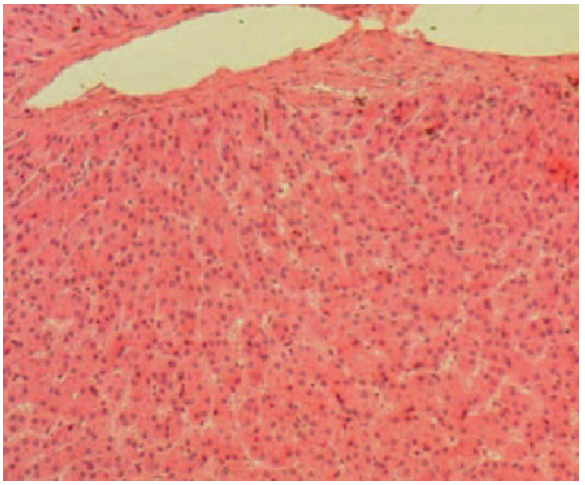

Fig. 9. Histology of hepatic adenoma arranged in plates that are two to three cells thick, separated by sinusoids

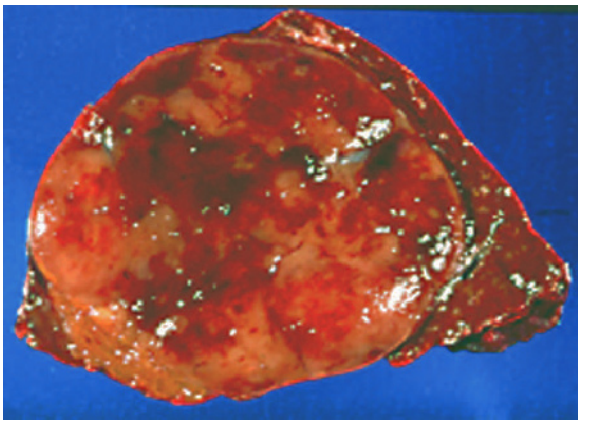

Fig. 10. Macroscopic aspect of liver adenoma with large intralesional hemorrhage

2.1.2.2 Dysplastic Focus

Dysplastic focus is defined as congeries of hepatocytes, measuring less than 1 mm in diameter, which show dysplasia but no histological signs of malignancy. Dysplastic foci generally occur in cirrhosis of any origin and are extremely rare in non-cirrhotic livers. In addition, patients suffering from α-1-antitrypsin deficiency, tyrosinemia or chronic viral hepatitis B or C demonstrate a comparatively high prevalence of dysplastic foci. Usually, serum α-fetoprotein is normal or minimally increased. However, in patients with tyrosinemia, high levels of serum α-fetoprotein can be found even before nodules are macroscopically visible [12, 181].

2.1.2.3 Dysplastic Nodule

A dysplastic nodule is defined as a nodular region of hepatocytes, measuring at least 1 mm in diameter showing signs of dysplasia but no definite histological signs of malignancy. These nodules are usually found in cirrhotic livers. Dysplastic nodules may be differentiated into two subgroups on the basis of the degree of cellular dysplasia [59, 165].

Dysplastic Nodule, Low-grade

A low-grade dysplastic nodule is a lesion with a mild degree of atypia.

Dysplastic Nodule, High-grade

High-grade dysplastic nodules are lesions with at least a moderate degree of atypia insufficient for the diagnosis of malignancy. However, this type of lesion can be considered a precursor to HCC and thus resection should be considered. These lesions may be of any size within the grossly visible range (Fig. 11), however, as the size of the lesion increases, so too does the likelihood that high-grade or malignant lesions are present: benign lesions are usually not greater than 20 mm in diameter. Necrosis and hemorrhage are not usually seen in high-grade dysplastic nodules.

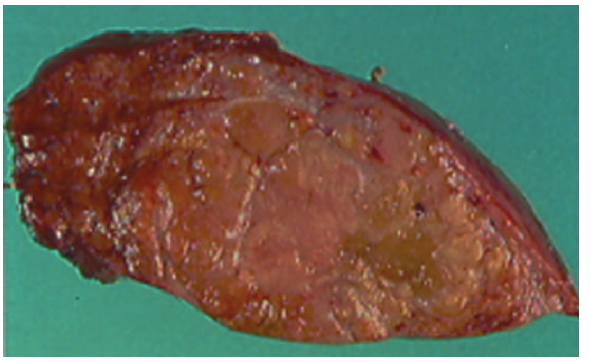

Fig. 11. Cross section of a large high-grade dysplastic nodule in a cirrhotic liver, which can only be differentiated microscopically from a HCC

2.1.2.4 Hepatocellular Carcinoma (HCC)

In Europe and North America the incidence of HCC is generally below 3/100,000 inhabitants, while in parts of Asia and Africa it is about thirty times higher. The endemic occurrence of chronic hepatitis B and exposure to Aflatoxin B1 seem to be primary reasons for this [8]. In Europe and Japan the leading cause of HCC is chronic hepatitis C with consecutive cirrhosis [53].

Patients with chronic hepatitis or hemochromatosis have the highest risk of developing HCC. On the other hand, alcohol-induced cirrhosis, autoimmune hepatitis and α-1-antitrypsin-deficiency do not seem to increase the risk significantly. Similarly, primary biliary cirrhosis and Wilson's disease do not predispose subjects to an increased incidence of HCC [135].

Generally, the prognosis for patients with HCC is poor, and is largely dependent upon the extent of surgical intervention, the size of tumor growth, the functionality of the remaining liver parenchyma and the possibility of infiltration of the portal vein [199] (Fig. 12).

Whereas the ultimate procedure for the potential cure of patients with HCC remains liver transplantation [153], possibilities for palliative treatment include intraarterial injection of ^{131}Iod-Lipiodol or alcohol [55].

The macropathological division of HCC, which dates from the beginning of the 20th century, correlates relatively well with imaging findings. Three main types can be distinguished:

- the multinodular type with multiple, sharply-demarcated tumor nodules,
- the massive type with one single tumor node and smaller satellite nodules,
- the diffuse type with tumor areas interspersed throughout the liver.

Additionally, an encapsulated tumor type can be distinguished, which seems to be an early phase of the other histological types. Unfortunately, there doesn't seem to be a correlation between these morphological criteria and epidemiological findings or prognosis. The new World Health Organisation (WHO) classification presents a more differentiated set of criteria for HCC characterization [81].

Apart from the above-mentioned pathologies, it is evident that almost any chronic liver disease leading to cirrhosis may be complicated by HCC. Neoplastic development in the liver can be seen as a multi-step process that is triggered by a variety of events. Normal liver is mitotically inactive, but when cells are stimulated to divide as occurs in a variety of conditions, including liver cirrhosis, the liver becomes sensitive to carcinogenesis. However, HCC also occurs in the absence of cirrhosis in a small but significant (about 7%) proportion of cases [100].

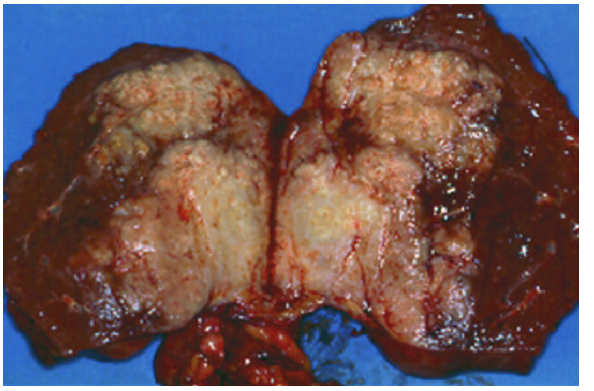

Fig. 12. Cut surface of a hepatocellular carcinoma without a capsule, infiltrating the liver parenchyma

A proposal as to how the multi-step development of HCC can be interpreted is presented in Table 1. However, it is important to realize that reliable differentiation between pre-cancerous developments, such as high-grade dysplastic nodules, and well-differentiated HCC is not always possible [58, 142].

Microscopically, HCC has several patterns. HCC is composed of malignant hepatocytes that differentiate into normal liver structures and mimic normal hepatocyte growth, but do not form normal hepatic acini (Fig. 13). Cells in well-differentiated HCC are difficult to distinguish from normal hepatocytes or hepatocellular adenoma cells. Malignant hepatocytes may even produce bile (Fig. 14). In other cases, there are microscopic variations, with HCC containing fat (Fig. 15), tumoral secretions (large amounts of watery material), fibrosis, necrosis and amorphous calcifications (Figs. 16, 17). This variable microscopic presentation gives rise to different appearances according to the imaging techniques employed.

Table 1. HCC development and liver cirrhosis

Macro-regenerative nodule
⇓
Low-grade dysplastic nodule
⇓
High-grade dysplastic nodule
⇓
Well-differentiated HCC
⇓
Undifferentiated HCC

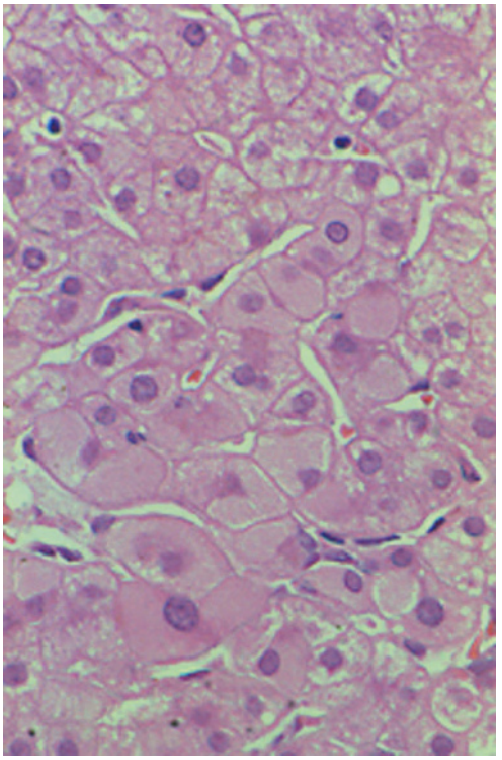

Fig. 13. Grade 1 HCC consisting of small liver-like tumor cells arranged in thin trabecular layers, which may be difficult to distinguish from liver-cell adenomas and atypical hyperplastic nodules

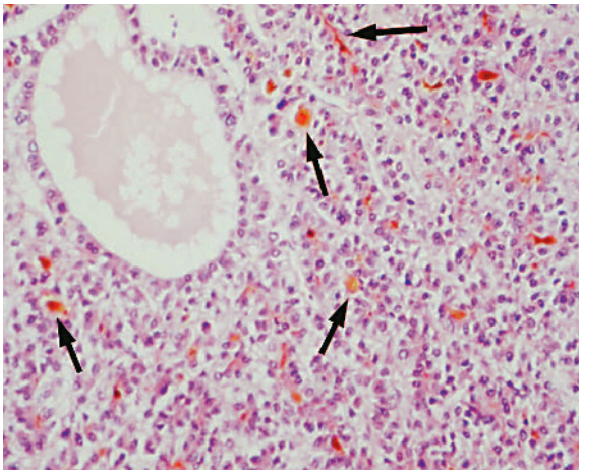

Fig. 14. Histological aspect of a well-differentiated HCC showing bile production (*arrows*)

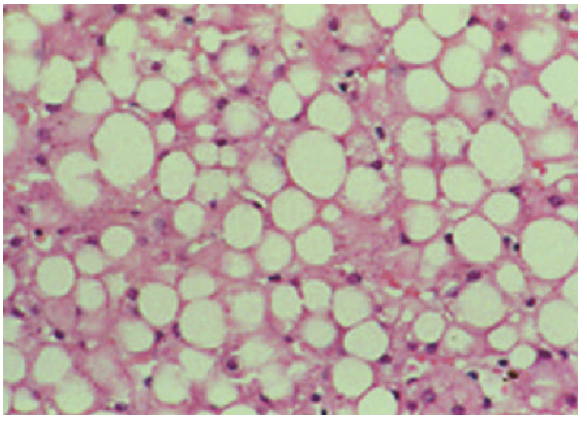

Fig. 15. HCC with fatty metamorphosis

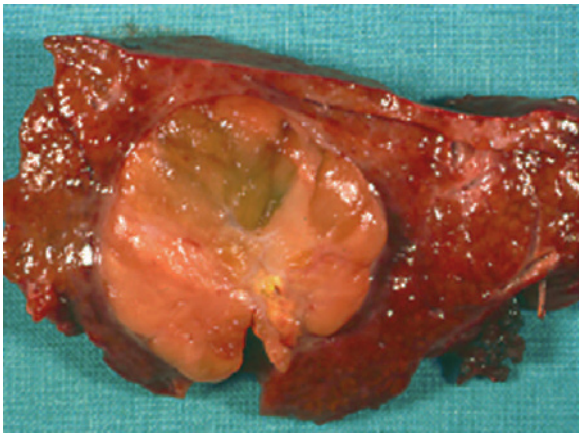

Fig. 16. Cut section of a HCC with a mosaic pattern containing fat, solid nodules, necroses, fibrosis and cystic areas

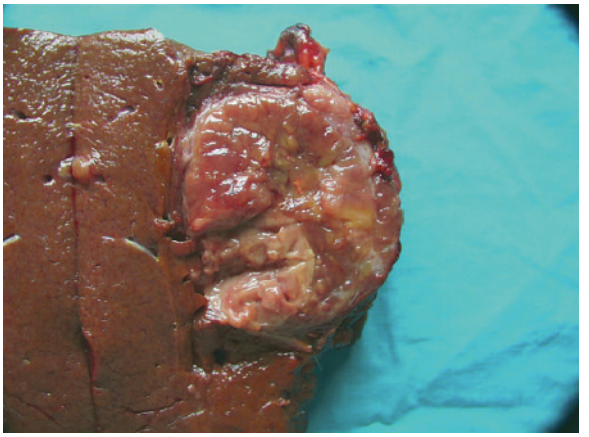

Fig.17. Cut section of a HCC with mosaic pattern, note the fatty and fibrous areas

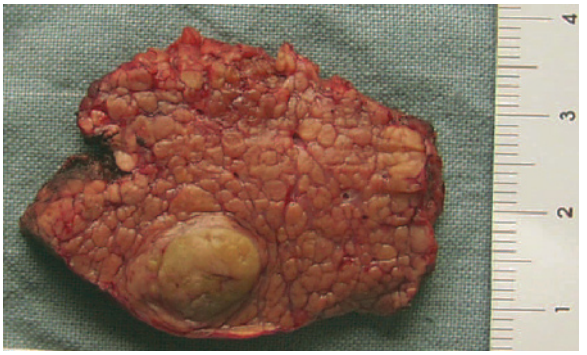

Fig. 18. Cut section of a HCC with a nodular pattern and fibrous capsule

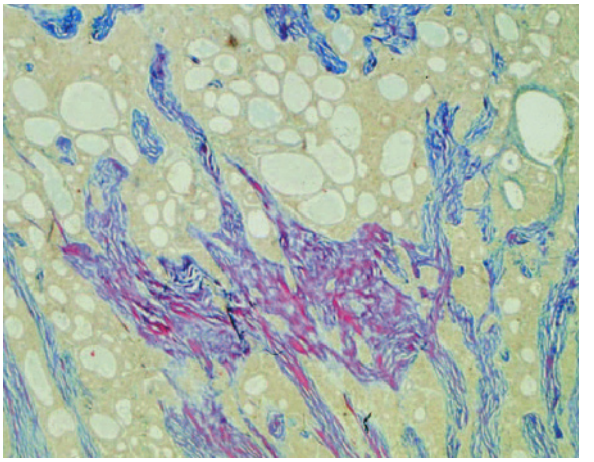

Fig. 19. Histology of a fibrolamellar carcinoma demonstrating tumor cells separated by characteristic parallel lamellae of coarse, ropy collagen

Macroscopically, there are also several patterns of growth. HCC is referred to as single or massive when there is either a solitary small or a large mass, with or without a capsule (Fig. 18). Multifocal HCC, the second most common pattern, is characterized by multiple separate nodules. The least common pattern of diffuse or cirrhotomimetic growth consists of multiple small tumoral foci distributed throughout the liver, mimicking the nodules of cirrhosis. HCC is said to be encapsulated when it is completely surrounded by a fibrous capsule. Patients with encapsulated HCC have a better prognosis due to the increased possibilities for resection. However, vascular invasion of intrahepatic vessels (portal hepatic vein branches) and perihepatic vessels (inferior vena cava and portal vein) is common.

2.1.2.5 Fibrolamellar Carcinoma (FLC)

This type of hepatocellular carcinoma occurs both in male and female patients, typically under the age of 25 years. In contrast to HCC, underlying cirrhosis is not usually present in FLC. Pain in the right upper abdominal quadrant, nausea and weight loss are the leading symptoms, while jaundice is quite rare. Often the tumors are relatively large (> 15 cm) at the time of detection. If resected early, the five year survival rates are about 50%. Metastases from FLC are mostly located in the lymph nodes and lungs, and, in roughly half of the cases, metastatic lymph nodes are present at the time of diagnosis. Macroscopically, the tumors have a lobular appearance with fibrous septa and a central scar, which, in contrast to that in FNH, is a true scar.

FLC lesions have a distinctive microscopic pattern and are composed of eosinophilic, malignant hepatocytes containing prominent nuclei. FLCs express hepatic as well as biliary keratin. The fibrous component accounts for 50% of the tumoral mass

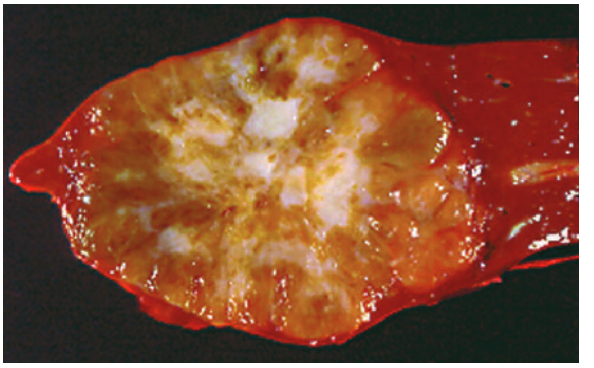

Fig. 20. Cut section of a fibrolamellar carcinoma with a lobular arrangement with interconnecting fibrous septa and a central stellate scar

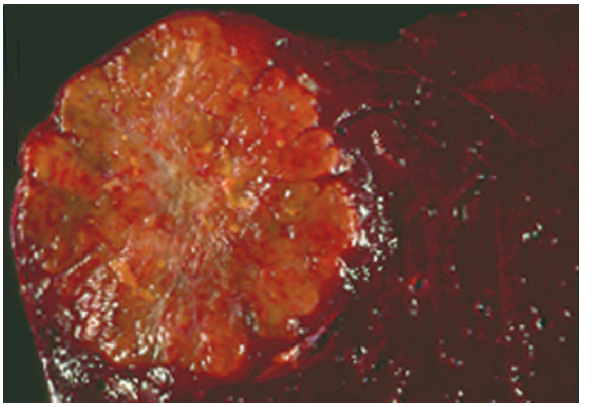

Fig. 21. Cut section of a fibrolamellar carcinoma with a nodular appearance but with minimal demonstration of a central stellate scar

and is distributed in multilamellar strands (Fig. 19), except in larger tumors containing large central scars (Fig. 20). Satellite nodules are often present. The appearance of FLC can be similar to that of FNH as both tumors have a central scar and multiple fibrous septa (Fig. 21). In FLC, hemorrhage is rare, while necrosis and coarse calcifications are often present, especially in the central scar (in approximately 30% of cases). The origin of FLC is still to be clearly defined, although mixed FLC/HCC types seem to exist [38].

2.2 Benign and Malignant Tumors of the Biliary Tract

2.2.1 Bile Duct Adenoma

This tumor is found mainly by chance and its maximal size does not usually exceed 2 cm. Microscopically, small bile ducts lined by mucin-producing cells are embedded in a fibrous stroma. A malignant transformation has not yet been reported [3].

2.2.2 Bile Duct Cystadenoma

Hepatic cystadenoma is a very rare tumor, although analogous forms are quite common in the pancreas and ovaries. Most of the patients are women in their fifth decade of life, and the major symptoms include pain and jaundice. Infection, rupture and malignant transformation of these slowly growing tumors may occur. Surgical resection is the therapy of choice [98] (Fig. 22).

Microscopically, cystic spaces filled with viscous yellowish or reddish fluid can be seen. The most common mucinous type should be distinguished from the serous and papillary cystic types. The tumoral stroma may consist of only a thin hyaline rim, but it may also appear as a compact layer [79].

2.2.3 Biliary Papillomatosis

About 50 cases of multiple small papillomas of the intra- and extrahepatic bile ducts have been described. Jaundice may be the only presenting symptom, although sepsis and hemobilia with a subsequent fatal outcome may result. A temporary biliary stoma may bring about some relief, although the only curative method to date involves liver transplantation. The presence of biliary papillomas seems to coincide with ulcerative colitis, Caroli's syndrome and polyposis coli [124].

2.2.4 Bile Duct Carcinoma (Cholangiocarcinoma, CCC)

Bile duct carcinomas are divided according to their location, into intrahepatic cholangiocarcinoma [9], hilar adenocarcinoma (Klatskin tumor) [91] and carcinoma of the extrahepatic bile ducts [5].

On cut sections, CCC is characterized by the presence of large amounts of whitish fibrous tissue (Fig. 23). Inside the tumor, especially in large examples, a variable amount of central necrosis may be present, while hemorrhage is rare. Histologically, the tumor is an adenocarcinoma with a glandular appearance and cells that resemble biliary epitheli-

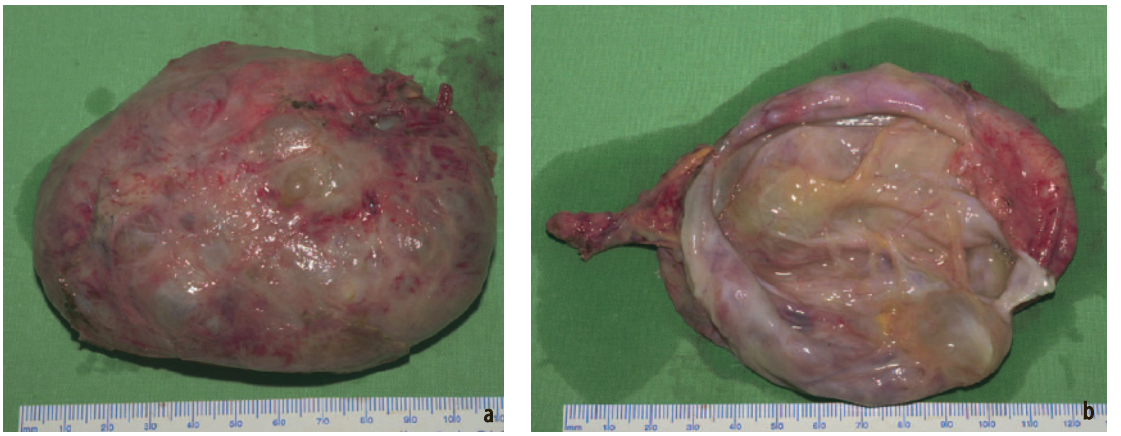

Fig. 22a, b. Biliary cystadenoma. The resected tumor (**a**) is well-defined and shows a thick capsule. The cut surface (**b**) of a biliary cystadenoma, in contrast to congenital simple cysts, demonstrates a multilocular appearence. Cysts may show hemorrhage and fluid-fluid levels

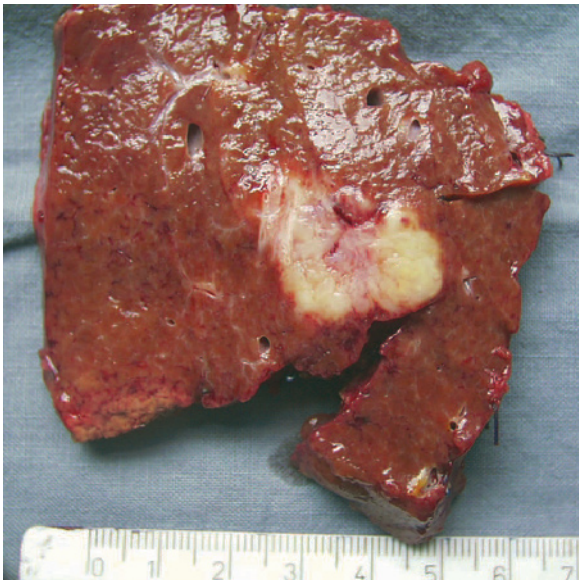

Fig. 23. Cut section of a intrahepatic cholangiocellular carcinoma diffusely infiltrating the liver with finger-like extensions and central sclerosis

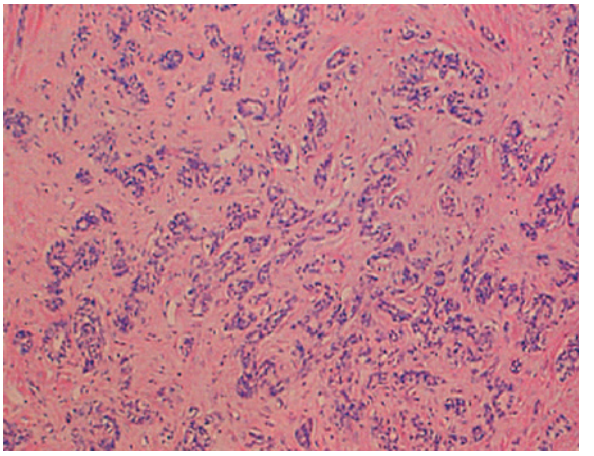

Fig. 24. Histology of the periphery of a CCC which demonstrates tumor cells in a tubular pattern in an abundant fibrous stroma entrapping normal liver cells

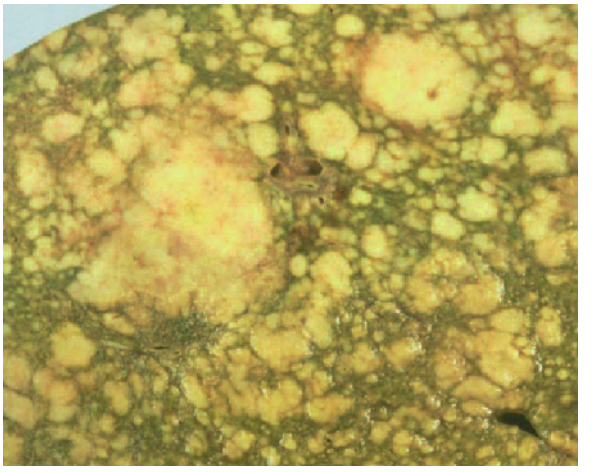

Fig. 25. Macroscopic distribution of diffuse hepatic metastases of a CCC

um with fibrous stroma (Fig. 24). Mucin production and calcification can sometimes be demonstrated. At autopsy there is often a layer of atypical cells surrounding the main tumor, which probably propagates relapsing tumor growth after an initial curative resection. Overall the prognosis is poor.

A large desmoplastic reaction is typical of CCC. Diagnostic studies often reveal lymph node metastases and hematogeneous spread to the lungs, bones, adrenals, spleen and pancreas. Intrahepatic carcinomas often arise in the fifth or sixth decades of life, and usually later in life than HCC. Non-specific signs such as pain and weight loss are typical, while jaundice is generally atypical. The tumor is usually hypovascular, but it may show late enhancement in cases of desmoplastic changes. Early signs of metastases include finger-like extensions along lymphatic channels and represent another reason for the poor prognosis of intrahepatic CCC (Fig. 25). Infections with *Clonorchis sinensis* and *Opisthorchis viverrini*, hepatolithiasis and congenital anomalies of the bile ducts predispose subjects to bile duct carcinoma. Other risk factors include Caroli's syndrome, sclerosing cholangitis and congenital hepatic fibrosis [18, 93, 94, 136].

The most common extrahepatic locations of CCC are along the common hepatic duct and the cystic duct. In these cases, painless jaundice is the leading symptom. Associations with choledochal cysts, congenital malformations of the bile ducts and ulcerative colitis have been reported. CCC with a high cuboid epithelium located in the liver hilum is typically referred to as Klatskin tumor [91].

2.2.5 Bile Duct Cystadenocarcinoma

In contrast to bile duct carcinoma, the prognosis for patients with this tumor is somewhat better. Bile duct cystadenocarcinoma is quite rare and metastases are only seldom found. It is usually diagnosed by histologic analysis of a resected cystic mass lesion.

The majority of bile duct cystadenocarcinomas occur in middle-aged women and cause no symptoms until they are quite large in size. Since local or metastatic spread is quite rare, patients are usually referred for surgery [79, 108].

2.2.6 Gallbladder Carcinoma

This tumor is mainly found in female patients predominantly in the sixth decade of life. The main symptoms include right upper abdominal quadrant pain, nausea and jaundice. Patients frequently have gallstones or, on occasion, a so-called "porcelain" gallbladder caused by recurrent inflammation [84].

Whereas adenocarcinoma growth usually involves just the gallbladder, squamous cell carcinoma and undifferentiated carcinoma often infiltrate neighboring structures. Local complications involving fistula, perforation or empyema may arise. Distant metastases typically occur in advanced cases [70, 87].

Other quite rare tumor types in the gallbladder include sarcoma, primary malignant melanoma, carcinoid and lymphoma [111, 193, 198].

2.3 Benign Non-Epithelial Tumors

2.3.1 Hemangioma

The most common liver lesions are hemangiomas, which are found with a prevalence of 0.4-7.3% and only rarely cause any clinically relevant symptoms [78]. Thus, they are most often detected by chance. Small capillary hemangiomas need to be distinguished from larger cavernous hemangiomas, which are frequently categorized as benign congenital hamartomas. Macroscopically, cystic blood-filled spaces can be visualized. When detected intraoperatively, these lesions can be diagnosed as hemangiomas by simple palpation. The lining of these spaces consists of endothelial cells and thin fibrous walls. With increasing tumor size, central thrombosis with consecutive fibrosis, myxoid changes or calcification may occur.

Therapeutic intervention should only be considered in cases of symptomatic or giant hemangioma (larger than 10 cm) [192].

Complications such as rupture, thrombocytopenia or disseminated intravascular coagulation (DIC), caused by stasis of blood flow in the dilated vessels, may occur on rare occasions. Multiple hemangiomas are considered part of the syndrome of systemic hemangiomatosis. Fine needle biopsy should be avoided because of possible bleeding and because in many cases only blood is aspirated, which leads to poor diagnostic results. The diagnosis can usually be established by means of blood pool scintigraphy [166] or MRI.

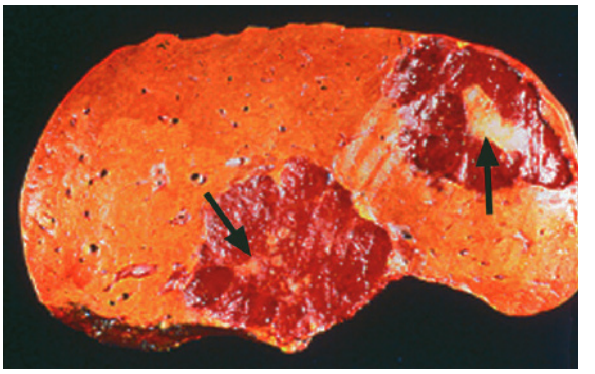

Fig. 26. Cut section of two large hepatic hemangiomas showing central fibrosis and hyalin changes (*arrows*)

On cut sections, larger hemangiomas almost always present a heterogeneous composition with areas of fibrosis, necrosis and cystic changes and intratumoral coarse calcifications (Fig. 26). In some cases abundant fibrous tissue completely replaces the lesion.

2.3.2 Infantile Hemangioendothelioma (IHE)

Most of these infantile mesenchymal tumors are found during the first six months of life, and there seems to be a slight female predominance [157].

Common symptoms include hepatomegaly or a palpable mass, sometimes together with diminished growth or high-output cardiac failure caused by shunting. Rupture, thrombocytopenia and hypofibrinogenemia may occur on rare occasions. Surgical intervention may be avoided if no life-threatening complications appear, as the tumor tends to regress gradually. Therapeutic strategies may consist of steroids, chemo- or radiotherapy, embolization or resection. Macroscopically, IHEs are usually multiple and diffuse. A solitary lesion is an uncommon variant. The nodules vary from a few millimeters to 15 cm or more in size, and are round, reddish-brown and spongy, or white-yellow with fibrotic predominance in mature cases.

Microscopically, two types can be distinguished:

- Type 1 has intercommunicating vascular channels with a single-layered endothelial lining. Thrombosis and infarction in cavernous spaces is quite frequent, as is extramedullary hematopoesis.
- Type 2 demonstrates nuclear atypia and a multi-layered endothelial lining. There seems to be some resemblance to angiosarcoma, but the finding of a metastasizing IHE has not yet been reported [46].

2.3.3 Lymphangioma

Hepatic lymphangioma are congeries of dilated lymphatic channels containing proteinaceous fluid or blood. Lymphangiomas in the liver occur most frequently as multiple masses, although solitary lesions are found on occasions. In some cases concomitant hemangiomas can be found. When diagnosing hepatic lymphangioma, whole body cross-sectional imaging is indicated because multiple organs and tissues, (i.e. spleen, kidneys, lungs, gastrointestinal tract and skeleton), are usually involved, particularly in children. Thus, the condition is often referred to as lymphangiomatosis [72, 170].

2.3.4 Angiomyolipoma

Angiomyolipomas are rare soft tissue tumors found most frequently in the kidneys and occasionally also in the liver. There is an increased incidence of these tumors in association with tuberous sclerosis [24, 67, 122].

Angiomyolipomas consist of blood vessels, fat and smooth muscle [66] (Fig. 27).

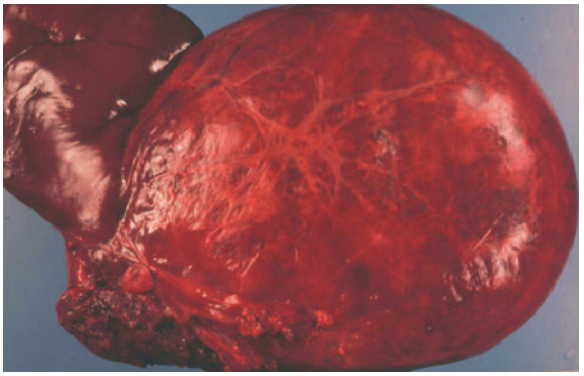

Fig. 27. Macroscopic aspect of an angiomyolipoma of the liver

2.4 Malignant Non-Epithelial Tumors

2.4.1 Angiosarcoma

These tumors are the most frequent sarcomas of the liver and arise typically in the sixth and seventh decades of life, predominantly in male subjects. Exposure to thorotrast, monomers of vinyl chloride, steroids, radium and chronic arsenic intoxication is known to be associated with angiosarcoma. Liver cell hyperplasia with dilatation of the sinusoids and increased fibrosis leading to portal hypertension are typical early stages of tumor growth. Macroscopically, angiosarcomas are ill-defined sponge-like hemorrhagic tumors (Fig. 28). They are composed of malignant endothelial cells lining vascular channels of variable size, from cavernous to capillary, which attempt to form sinusoids. Metastases to lymph nodes, spleen, lung, bone and adrenals are rarely found.

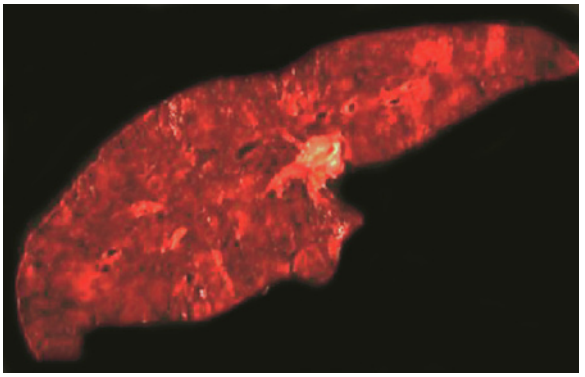

Fig. 28. Cut section of a diffuse infiltrating hepatic angiosarcoma

Thorotrast particles can be found within the malignant endothelial cells in cases of Thorotrast-induced angiosarcoma. The majority of angiosarcomas present as multiple nodules, often with areas of internal hemorrhage. When angiosarcoma appears as a single, large mass, it does not have a capsule and frequently contains large cystic areas filled with blood debris [125, 152, 163, 194].

2.4.2 Malignant Epithelioid Hemangioendothelioma (EHE)

This tumor most often arises in female patients in the fifth decade of life. Patients complain of weight loss and right upper abdominal quadrant pain, sometimes in combination with jaundice. There may be an association with oral contraceptives. The tumor is most frequently located at subcapsular sites (50-65%) and macroscopically, it is a solid, fibrous mass, sometimes with calcifications and encased by vessels. In contrast to angiosarcoma, the prognosis seems to be better; increasingly patients are undergoing hepatectomy and consecutive liver transplantation. Grossly, two different types of EHE have been described: an early stage nodular type with small subcapsular lesions, which in a later stage of the disease tend to become diffuse with confluent lesions along the hepatic or portal veins. Typically, in malignant EHE a retraction of the liver surface can be noted (Fig. 29). The only other primary liver lesion in which this sign is observed is CCC. Microscopically, EHEs are com-

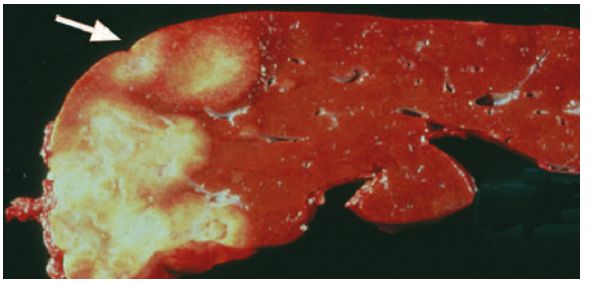

Fig. 29. Cut section of a subcapsular-located malignant epithelioid hemangioendothelioma showing a characteristic retraction of the liver surface (*arrow*)

posed of epithelioid and dentritic cells within a tumor matrix that may become sclerotic, hyalinized and calcified. Intratumoral necrosis and hemorrhage are common findings [54, 80].

2.4.3 Undifferentiated (Embryonal) Sarcoma

Along with hepatoblastoma and IHE this is one of the most frequent primary malignant hepatic tumors in children, arising typically between the ages of six and ten. Increased girth and weight loss are common symptoms and a newly discovered heart murmur induced by a tumor thrombus may be present on rare occasions. Macroscopically, sarcomas have solid and cystic areas, hemorrhage or necroses, and are sometimes surrounded by a pseudocapsule. In 50% of all cases, extramedullary hematopoesis can be demonstrated. Complete tumor resection followed by chemotherapy and radiation can increase the five year survival rate to about 15% [160, 173].

2.4.4 Rhabdomyosarcoma (Sarcoma Botryoides)

Hepatic rhabdomyosarcoma is a tumor typically found in children below the age of five. Only on very rare occasions do they arise in adults. Typically, the tumor has a grape-like appearance and grows in the lumina of larger bile ducts. Its presence leads to intermittent icteric episodes, fever and weight loss.

The prognosis and treatment modalities are similar to those of undifferentiated embryonal sarcoma [76].

2.4.5 Other Primary Sarcomas

Almost every type of sarcoma has been reported in the liver. They usually occur in middle and old age, in either sex, and are typically large and at an advanced stage when discovered. Although most of the tumors are slow-growing, in most cases prognosis is poor as complete excision is seldom possible due to the size and degree of advancement. Leiomyosarcomas may arise from the ligamentum teres, the portal and hepatic veins, as well as from the liver capsule. Other rare malignant soft-tissue tumors of the liver include fibrosarcoma, malignant fibrous histiocytoma, liposarcoma, osteosarcoma, malignant hemangiopericytoma and sarcomas with divergent cell lines (malignant mesenchymoma).

2.4.6 Primary Lymphoma of the Liver

Hodgkin's lymphoma, non-Hodgkin's lymphoma and leukaemia, as well as histiocytosis and mastocytosis, may affect the liver secondarily. Nevertheless, an increasing number of primary lymphomas of the liver are being described [139, 150]. The recognition of primary hepatic lymphoma is important as treatment often has a favorable outcome. The tumor may occur at any age, from childhood to adolescence, and is around four times more likely to occur in males. Patients present with abdominal pain, hepatomegaly or a mass. Additional B-symptoms (fever, weight loss) are found in 50% of cases. On rare occasions the tumor may be associated with autoimmune disorders, chronic hepatitis, cirrhosis, infection with hepatitis B virus

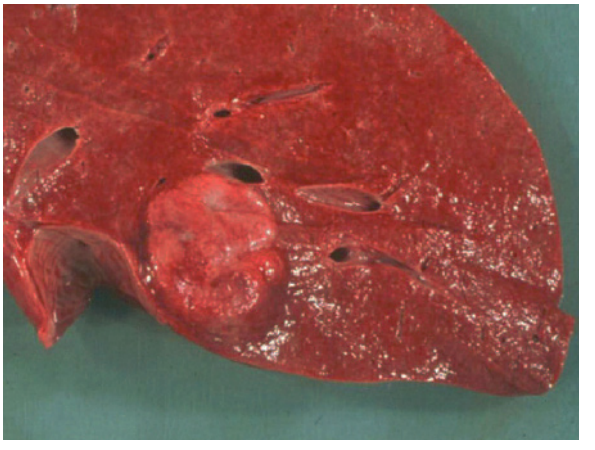

Fig. 30. Macroscopic presentation of a solid solitary primary hepatic manifestation of Hodgkin's disease

(HBV) or the human immunodeficiency virus (HIV). Although the tumors most frequently present as solitary (Fig. 30) or multiple masses, diffuse infiltration can also be found on occasions. Upon histology, most non-Hodgkin lymphomas are described as high-grade. Possible misdiagnoses include metastatic carcinoma, chronic hepatitis and inflammatory pseudotumor.

Surgical resection gives the best prognosis although multi-agent chemotherapy and/or radiation therapy are also often worthwhile [83].

2.5 Hepatoblastoma

Hepatoblastoma is typically found in young children. Up to one third of patients have concomitant anomalies such as hemihypertrophy, cleft palate, Beckwith-Wiedemann or Down's syndrome. The tumors are often palpable, while failure to thrive and weight loss, together with extremely elevated α-fetoprotein (AFP) levels, are typical symptoms. Cystic, necrotic and/or hemorrhagic areas as well as fibrosis and calcifications are common, while the tumor may also be partially encapsulated. In 20% of cases the tumors are multifocal.

Most tumors are of the epithelial, mixed or mesenchymal type. In very rare cases of teratoid or even chondroid hepatoblastoma, muscle or neuronal cells may be found. Epithelial hepatoblastoma is composed of fetal and/or embryonal malignant hepatocytes. A mixed hepatoblastoma has both an epithelial (hepatocyte) and a mesenchymal component consisting of primitive mesenchymal tissue. Amorphous calcifications are seen in about 30% of cases. This histological classification has prognostic implications: the epithelial type has a better prognosis than the other forms, especially when there is a predominant hepatocyte presence. Embryonal epithelial cells are more primitive than fetal epithelial and mesenchymal cells and tumors with the former histological type carry a poorer prognosis.

Surgical resection is the primary treatment although operative mortality is high (about 25%). Accurate tumor staging is essential to determine the need for additional chemo- or radiotherapy. The long term survival rate is about 15-35%. Factors that contribute to a worse prognosis are age under one year, large tumor size, involvement of vital structures and the predominance of anaplastic cells [77, 95, 183].

2.6 Tumor-like Lesions

2.6.1 Cysts

The etiology and pathogenesis of solitary liver cysts have not yet been totally clarified. Moreover, it is uncertain whether they are developmental or neoplastic in origin.

2.6.1.1 Non-Parasitic Cysts

Primary, non-parasitic liver cysts are subdivided into unilocular and multilocular varieties. Whereas unilocular cysts are more likely to be developmental in origin, multilocular cysts may be neoplastic with an increased, but nevertheless very low potential for malignant change (Fig. 31). Primary, non-parasitic liver cysts may occur at any age although the peak incidence is between the fourth and sixth decades of life with a male to female ratio of 4-5:1. Liver cysts smaller than 8-10 cm seldom cause symptoms and are therefore most often diagnosed by chance. In cases of symptomatic cysts, patients present with an upper abdominal mass and fullness, nausea and occasional vomiting. An acute abdominal crisis may be due to torsion, strangulation, hemorrhage into the cyst or rupture [143].

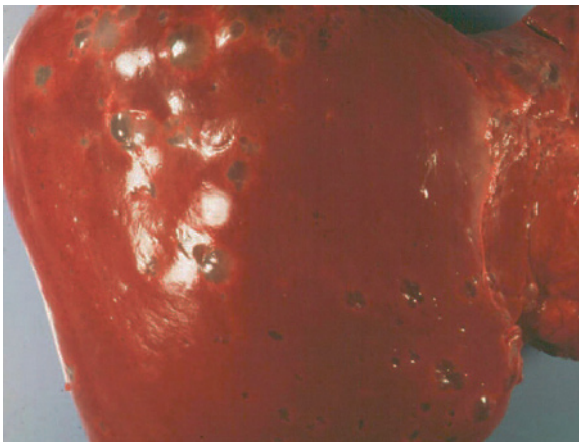

Fig. 31. Liver surface with diffuse distribution of non-parasitic uncomplicated liver cysts

Symptomatic large solitary cysts are twice as likely to be found in the right lobe as in the left. Jaundice is a frequent complication. Whereas excision has often been the treatment of choice, aspiration and injection of sclerosing agents such as alcohol, polidocanol or minocyclin chloride represent an accurate therapeutic option in many cases [52, 63].

Malignant tumors arising from either type of solitary cyst may occur on very rare occasions. Although these tumors are usually adenocarcinomas, squamous cell carcinomas and even carcinoids have been reported [20, 167].

2.6.2 Mesenchymal Hamartoma

Mesenchymal hamartoma most likely represents a localized abnormality of ductal plate development that precedes birth. They occur almost exclusively in young children with an average age of 15 months and have a predominance in males to females of 2:1. Association with polycystic kidney disease, congenital hepatic fibrosis and biliary hamartoma has been described. Children typically present with progressive abdominal enlargement and imaging techniques show a cystic mass which is usually large. Microscopically, a variable mixture of liver tissue is seen. Extramedullary hematopoiesis is commonly present. Surgical excision is curative and malignant transformation has not been reported [49, 161].

2.6.3 Biliary Hamartoma

Biliary hamartomas often occur as small lesions, found by chance on fine needle biopsy. They contain irregularly-formed dilated bile ducts in a fibrous stroma and may occur together with cystic kidneys. It is still unclear as to whether cholangiocarcinomas arise from these lesions [50].

2.6.4 Inflammatory Pseudotumor (IPT)

A rare differential diagnosis among solid liver tumors is the so-called IPT. This lesion may appear in almost any tissue and anatomic location and on diagnostic imaging mimics other common histological and imaging findings. Despite numerous reports, the pathogenesis of IPT remains unclear. Recent publications have explained the etiology of this lesion as either a post-inflammatory regenerative process or a primary neoplastic process [11, 34, 47].

The suspicion of neoplasm is based on histologic findings in which an IPT is shown to consist of myofibroblasts, fibroblasts, lymphocytes and plasma cells. In such cases the pathologist may be persuaded to diagnose a sarcoma with primary benign clinical behavior. The suspicion that the lesion is of true neoplastic origin may be reinforced by the presence of histiocytes and spindle cells and when immunohistochemical and ultrastructural examinations reveal signs of benign as well as malignant growth [36].

However, examination of IPT of the ileo-caecum have shown that they may be associated with infection. The histology of this lesion was shown to be comparable with that of mycobacterial pseudotumors of the lymph nodes, spleen and lung in a patient infected with HIV [101].

From this observation it was concluded that the immune system plays an important role in the pathogenesis of this kind of mass lesion. Additionally, electron microscopy may demonstrate intracellular bacilliform organisms. Molecular analysis of DNA fragments was able to identify *Pseudomonas* sub-populations that were not known to be infectious in humans. In this regard, pathogenic organisms such as Epstein-Barr virus, *actinomyces* and *nocardia*, especially in hepatic lesions, are suspected to contribute to the development of IPT [187].

2.6.5 Other Tumor-like Lesions: Peliosis Hepatis

The microscopic type is characterized by an area of absent reticulin fibers, thus resulting in a dilation of the sinusoids, which are normally lined by endothelium [196]. Two varieties have been described: the phlebectatic type, in which the blood-filled spaces are lined with endothelium and are based on aneurysmal dilatation of the central veins, and the parenchymal type, in which the blood spaces are not lined with endothelium and are usually associated with hemorrhagic parenchymal necrosis.

There seems to be an increased incidence of peliosis with thiopurine, anabolic steroids, vitamin A and thorotrast. The macroscopic type of peliosis shows cystic blood-filled spaces, which occur in malnutrition, leukemias, tuberculosis, some forms of vasculitis, lepra and HIV. Due to the large cystic blood-filled areas, imaging studies may lead to the misinterpretation of the lesion as hemangioma [48, 149, 155, 195].

These lesions typically have no clinical relevance, but may cause some difficulties in the differential diagnosis of focal liver lesions.

2.7 Infectious Diseases of the Liver

2.7.1 Liver Abscess

A liver abscess generally develops by one of three different routes:

- ascending infection of the bile ducts,
- hematogeneous spread in endocarditis, pneumonia and pulmonary AV-malformations,
- purulent infections draining to the portal vein, e.g. diverticulitis.

The origins of pyogenic abscesses within the liver are usually not obvious. Contributory factors include diabetes mellitus, perforated duodenal ulcer or diverticulosis. The most common pathogenic germs are *E. coli*, other coliforms, and *Streptococcus milleri*. Anaerobes are being reported with increasing frequency. However, amebiasis and several worm infections (ascariasis, clonorchiasis, fascioliasis) of the biliary tree, which predispose subjects to bacterial cholangitis, should be considered as possible pathogenic agents in the differential diagnosis of pyogenic liver abscesses [68].

Infection spread via the biliary tree may be due to an acute ascending cholangitis complicating a large bile duct obstructed by stones. In addition, suppurative cholecystitis, post-operative biliary stricture, acute or chronic pancreatitis and tumors in the biliary tree and pancreas may cause focal inflammation that spreads to the liver.

Today, bacterial infection via the portal vein is less common in industrialized nations. Hepatic spread arises from inflammatory processes in the appendix, the colon (as in diverticulitis) and the pancreas, leading to septic portal thrombophlebitis and thereafter to liver abscesses. In developing countries, umbilical sepsis plays a leading role and is the source of portal pyemia which may also induce splenic vein occlusion leading to splenomegaly.

An arterial spread of infection to the liver is common. Patients usually develop clinical symptoms before a visible abscess can be depicted. Pathogenic germs include *Staphylococcus*, *Neisseria gonorrhoeae* and *Chlamydia trachomatis* which may induce complicated pelvic infections. Chronic granulomatosis disease facilitates arterial septic spread to the liver [119].

On rare occasions, acute cholecystitis or liver trauma may be the cause of a liver abscess. Amebic abscesses are not very frequent in Europe. While abscesses might not have a fibrous capsule initially, they tend to form coagulative necrosis and subsequently liquefy (Figs. 32, 33). Thereafter, abscesses may rupture and induce peritonitis, which usually has a bad prognosis.

Hepatic *Aspergillus* infection typically demonstrates multiple small hemorrhagic necrosis. Hyphae may also obstruct vessels and lead to infarction.

Multiple portal or periportal abscesses with granuloma formation are typical of *Candida*. In *Cryptococcus* infections large abscesses are absent, but small foci of necrosis may be observed which sometimes follow the bile ducts in a manner similar to sclerosing cholangitis [10].

Patients under immunosuppression or with hematologic disease are particularly at risk of developing hepatic abscesses.

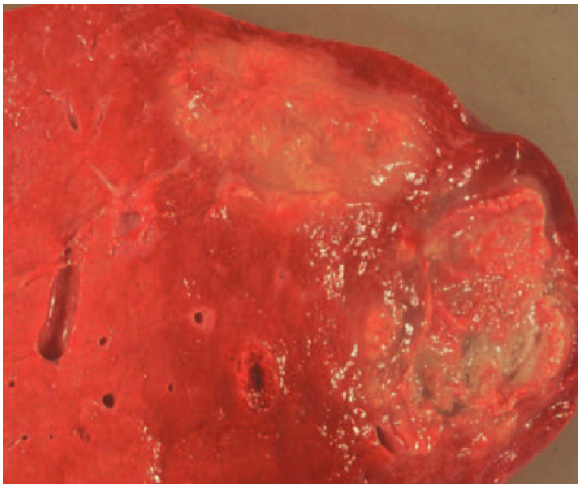

Fig. 32. Macroscopic aspect of an early-stage intrahepatic abscess formation with the beginning of central necrosis, in a patient with immune deficiency

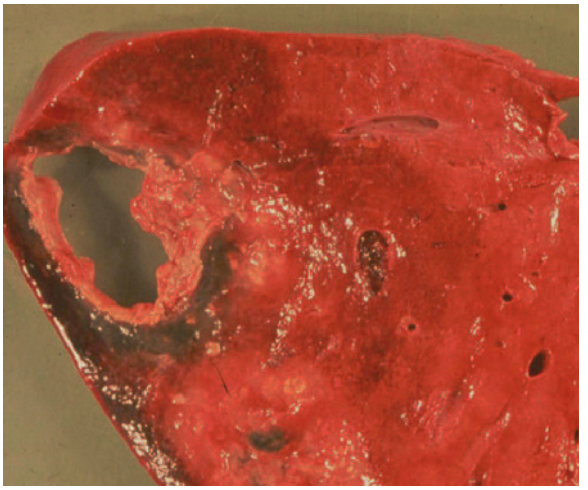

Fig. 33. Abscess formation with central liquified necrosis caused by septic emboli in a patient with AV-malformations of the pulmonary vasculature

2.7.1.1 Abscess Formation in Bile Ducts

Usually a cholangitis is induced by biliary obstruction caused by lithiasis or strictures, and more rarely by a malignant neoplasm. Ascension from the gastrointestinal tract is the typical route of spread.

2.7.2 Helminthic Infections

2.7.2.1 Nematodes (Ascariasis)

Transmission of helminths is usually by the fecal-oral route. Hepatomegaly with an eosinophilic granulomatous reaction may be present during migration of the larvae. This may lead to mechanical obstruction of the bile or pancreatic ducts and subsequent cholecystitis, hepatic abscesses and septicemia [89].

2.7.2.2 Cestodes (*Echinococcus*)

Echinococcus granulosus, which is the cause of the unilocular hydatosis, is found throughout Europe and is mainly transmitted by contact with dogs. The larval oncospheres reach the hepatic parenchyma via the portal vein. There they form slowly growing cysts, which may lead to compression or bacterial infection of the bile ducts. The cysts may grow to a size of 30 cm, and are typically surrounded by a fibrous rim which may calcify. Daughter cysts may also occur. A liver biopsy should be avoided because of the potential risk of peritoneal spread, anaphylactic reactions and dissemination of disease. Partial liver resection or sucking of the cysts and treatment with Albendazole may bring about remission.

Unlike the situation with *E. granulosus* infection, patients with *E. multilocularis* infection typically complain of jaundice and ascites. Untreated alveolar hydatidosis is frequently fatal. Cysts may rupture spontaneously. There are typically multiple irregularly formed cysts with a malignant-like tendency to invade surrounding parenchyma [2, 25] (Fig. 34).

2.7.2.3 Trematodes (Schistosomiasis)

Worldwide, schistosomiasis is the leading cause of portal hypertension. Typically, there is a latency between infection and the phase when trematodes

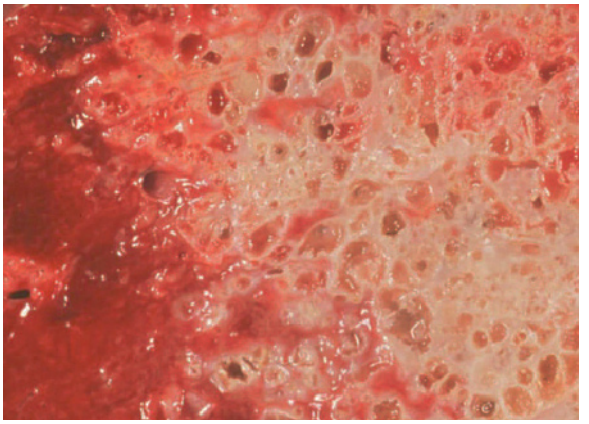

Fig. 34. Cut section of a hepatic infection with *Echinococcus alveolaris*. Congeries of small hepatic cysts are present which infiltrate the liver parenchyma

(*S. mansoni, S. japonicum, S. mekongi*) are found in the portal vein, where the female schistosoma begins egg-laying. This may lead to the so-called Katayama fever and transient hepatosplenomegaly. In advanced schistosomiasis, microscopic examination reveals a periportal fibrosis (Symmers' clay-pipe stem fibrosis), which follows the periportal tracts. Concomitant granulomatous inflammation occurs with scarring. This leads to the typical portal hypertension of the presinusoidal type. The length and intensity of infection correlates positively with the degree of portal hypertension [42, 171].

2.8 Parenchymal Disease

2.8.1 Hemochromatosis

In hemochromatosis there is typically an increased uptake of iron in the small intestine despite already adequate iron storage. This leads to iron deposition in the liver, pancreas, joints, myocardium and hypophysis. There is both an inherited and a transfusion-induced type of hemochromatosis. Typical symptoms include diabetes, arthralgias, cardiac insufficiency and hypogonadism. To avoid permanent organic deficiency it is important to diagnose the inherited type. Whereas blood examination is able to hint at the possibility of hemochromatosis, a liver biopsy with increased iron storage in hepatocytes establishes the diagnosis [56, 144] (Fig. 35).

In MRI the increased iron content can be demonstrated by calculation of the T2 relaxation time. This allows diagnosis as well as follow-up un-

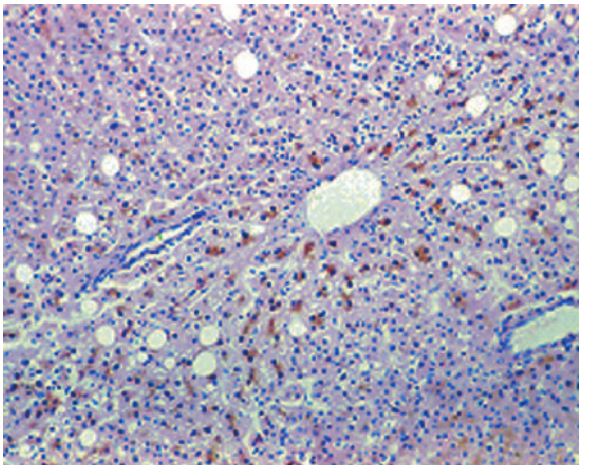

Fig. 35. Histology of hepatic parenchyma affected by hemochromatosis. Hemosiderin is predominantly accumulated in periportal parenchymal cells, which is in contrast to siderosis of the liver in which iron is stored predominantly in Kupffer cells

der therapy to be assessed. Patients suffering from untreated hemochromatosis typically develop liver cirrhosis and are at high risk of HCC development. Consequently, regular imaging studies should be initiated.

2.8.2 Transfusional Iron Overload (Hemosiderosis)

In some aplastic or hemolytic anemias frequent transfusions are necessary, which lead to increased iron storage in the spleen, liver, lymph nodes and bone marrow. This induces fibrosis of the hepatic parenchyma. If there is additional iron uptake in the intestine, such as in thalassemia, there is the possibility of liver cirrhosis even in young patients [99].

2.8.3 Fatty Liver

Pathologically there are two types of fatty liver: the macrovesicular type in which there are large fat deposits, and the microvesicular type. Imaging is unable to distinguish between the two types. Focal fatty liver on histology typically shows macrovesicular fat deposits. Generally, these lesions do not cause any symptoms and may be solitary or multiple. A general disposition to steatosis (see Table 2) or a localized hypoxia may be the cause, although focal fatty infiltration of the liver may also occur in patients after chemotherapy.

There is a distinct disease entity called non-alcohol induced steatohepatitis (NASH) which demonstrates the transition from steatosis to hepatitis and cirrhosis. This was first described in adipose patients after gastrointestinal bypass (see Table 3) [7].

Table 2. Causes of steatosis hepatis

- Diabetes mellitus
- Obesity
- Kwashiorkor
- Alcohol- or drug-induced liver injury
- Chronic inflammatory bowel disease
- Hepatitis C
- Malaria
- Immotile cilia syndrome
- Fatty liver in pregnancy
- Reye's syndrome
- Heat-stroke
- SIDS
- Insect bites
- Chronic hepatitis B and C in transplanted livers
- Wolman's disease
- Chemotherapy

Table 3. Causes of non-alcohol induced steatohepatitis (NASH)

- Morbid obesity
- Gastroplasty, gastro-intestinal bypass
- Diabetes mellitus type II
- Drug-induced liver injury
- Parenteral nutrition
- Weber-Christian disease
- Abetalipoproteinemia

2.8.4 Wilson's Disease

Wilson's disease is an inherited autosomal-recessive disease typically associated with increased intestinal uptake of copper and subsequent deposition in the liver, basal ganglia and other organs. There may be an acute or even fulminant hepatitis, chronic inflammation or cirrhosis. In contrast to hemochromatosis, these patients do not demonstrate an increased risk of developing HCC.

Wilson's disease should be considered when a low level of coeruloplasmin (less than 1.3 mmol/l) and an increased quantity of copper is present in the liver (greater than 250 mg/g dry weight) [159].

Clinical symptoms of patients suffering from Wilson's disease seem to be directly related to the accumulation of copper in the brain, cornea, liver

and kidneys. Liver cirrhosis induced by Wilson's disease is normally macronodular. However, a mixed type or a micronodular type can also be observed. Histology reveals nodules of variable size separated by fibrous septa with minimal cholangiocellular proliferation and varying signs of inflammation [109].

However, the distribution of copper deposition does not correlate with the pattern of nodules [162].

The current treatment of choice is D-Penicillamin, which chelates unbound copper for urinary excretion [146].

However, liver transplantation can also be considered as an ultimate therapeutic option [129].

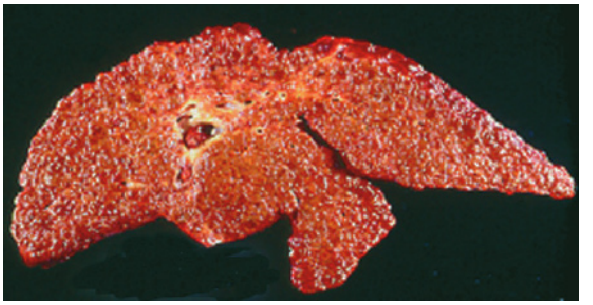

Fig. 36. Cut section of liver affected by macronodular cirrhosis with a marked variation in size and shape. This is accentuated by the intervening fibrous stroma which varies from broad scars to thin delicate bands of fibrotic tissue

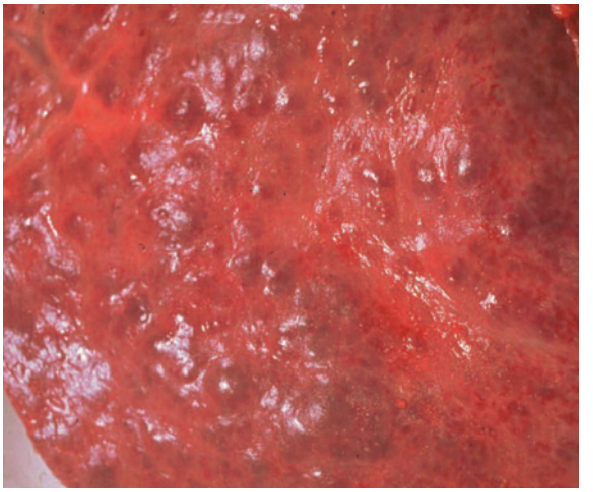

Fig. 37. Large nodules in a macronodular cirrhosis on the capsular surface of the liver

2.8.5 Primary Sclerosing Cholangitis

An unspecific inflammatory fibrosis of the intermediate and large bile ducts leads to irregular stenosis and ectasia of the intra- and extrahepatic bile ducts. This often remains completely asymptomatic and is only diagnosed because of increased levels of alkaline phosphatase (AP), although chronic fatigue, stomach pain and intermittent jaundice may also result [104, 179, 189].

Typically, primary sclerosing cholangitis predominates among male patients in their fifth decade of life [188].

The clinical course can be variable, with many patients dying due to progressive hepatic insufficiency. The only curative treatment is liver transplantation. About 10% of all patients with primary sclerosing cholangitis subsequently develop cholangiocarcinoma or HCC [32].

An association with chronic inflammatory bowel disease (such as Colitis ulcerosa) has also been reported. Primary sclerosing cholangitis has to be distinguished from secondary types of sclerosing cholangitis, such as those induced by surgical intervention, cholelithiasis and even cholangiocarcinoma [128].

2.8.6 Cirrhosis

Hepatic cirrhosis is the endpoint of different toxic, autoimmune, congenital or infectious diseases (see Table 4). Typically it is a diffuse process involving fibrosis and nodule formation [13].

Macropathologically, there are micronodular (nodules < 3 mm), macronodular (nodules > 3 mm) and mixed types of cirrhosis. In micronodular cirrhosis the liver normally displays no irregularity of shape and there is an increased fibrotic reaction compared to the macronodular type (Fig. 36). Although hepatomegaly is frequently seen in the early stages, the size of the liver subsequently decreases. The macronodular type typically displays an irregular surface (Fig. 37) and large fibrotic bands. A transition from the micro- to the macronodular type of cirrhosis sometimes occurs in patients under treatment or after alcohol abstinence [14].

Although many definitions of cirrhosis can be found in the literature, the most appropriate and concise of these states that cirrhosis is "a diffuse process characterized by fibrosis and a conversion of normal architecture into structurally abnormal nodules". Essential for the diagnosis of cirrhosis is the presence of both fibrosis and nodules throughout the entire liver. However, regeneration should not be present and this must be taken into account when evaluating histopathologic specimens from needle biopsies. For this reason, liver cirrhosis is a diagnosis that should only be assigned by the pathologist; cross-sectional imaging indicates only the diffuse nature of the process.

Table 4. Different pathologies leading to hepatic cirrhosis

• **Toxic**	
Alcohol	Methotrexate
Isoniazid	Methyldopa
Amiodarone	
• **Infections**	
Hepatitis B and C	Schistosomiasis
• **Autoimmune**	
Chronic active hepatitis	Primary biliary cirrhosis
• **Metabolic**	
Wilson's disease	Hemochromatosis
α-1-antitrypsin-deficiency	Galactosemia
Glycogen storage disease	Tyrosinemia
Diseases of urea cycle	Abetalipoproteinemia
• **Biliary obstruction**	
Atresia	Cystic fibrosis
Cholelithiasis	Strictures
Sclerosing cholangitis	
• **Vascular**	
Budd-Chiari syndrome	Veno-occlusive disease
Chronic cardiac insufficiency	Hereditary hemorrhagic teleangiectasia with AV-shunts
• **Others**	
Neonatal hepatitis-syndrome	Indian childhood cirrhosis
Intestinal bypass	Sarcoidosis

Fibrosis is an integral part of cirrhosis and differentiates it from nodular regenerative hyperplasia. Structurally abnormal nodules may often occur but sometimes they can only be identified by means of subtle architectural changes, such as a disordered or compressed cell plate pattern. Although abnormalities in vasculature and blood flow are very important, they are not included in the definition since these changes are a consequence of the other pathologic features rather than primary abnormalities. Equally, true regenerative nodules can be a late occurrence in cirrhosis and therefore regeneration is also excluded from the definition. Although regeneration is not essential for the diagnosis of cirrhosis, it is important to point out that regeneration is a critical factor influencing the evolution of cirrhosis [13, 147].

2.8.7 Primary Biliary Cirrhosis

This disease, whose etiology remains obscure, typically affects small hepatic ducts which become surrounded by chronic inflammatory infiltrations and are eventually destroyed. Microscopic examination frequently reveals portal tracts without bile ducts. Women in the fourth and fifth decades of life are most commonly affected and there seems to be an association with autoimmune disorders such as Sjögren's syndrome, Sicca complex, CREST syndrome and vasculitis. Typical symptoms include cholestasis, progredient fibrosis and cirrhosis [39, 86, 133].

2.8.8 Secondary Biliary Cirrhosis

This type of cirrhosis is induced by obstruction of the extrahepatic bile ducts. Choledocholithiasis as well as benign strictures or malignant neoplasms may be the cause. Since regenerative nodules are typically absent, the condition is more a diffuse regenerative process than a true cirrhosis. Portal hypertension without typical morphological signs of liver cirrhosis is frequently observed [137, 151, 185].

2.8.9 Reye's Syndrome

Reye's syndrome is an acute fatty degeneration of the liver occurring together with encephalopathy. It typically affects children with viral infections (influenza B or varicella) who have been treated with acetylic salicylic acid. There is only limited hepatomegaly and the steatosis seems to be intermittent. Hence, the only decisive finding for prognosis is the extent of the neurological symptoms [31, 132].

2.8.10 Caroli's Syndrome

This cystic ectasia of small intrahepatic ducts is typically found diffusely, although cases of segmental occurrence may also be observed. Cholelithiasis leads to an intermittent obstructive jaundice with pain and fever and concomitant cholangitis. Possible complications are similar to those of choledochal cysts. In cases of segmental occurrence, a partial hepatic resection is curative. There is an association with congenital hepatic fibrosis and Potter's sequence [28, 113].

Patients with Caroli's syndrome have an increased risk of intrahepatic cholangiocellular carcinoma, and thus regular imaging studies should be performed (Fig. 38).

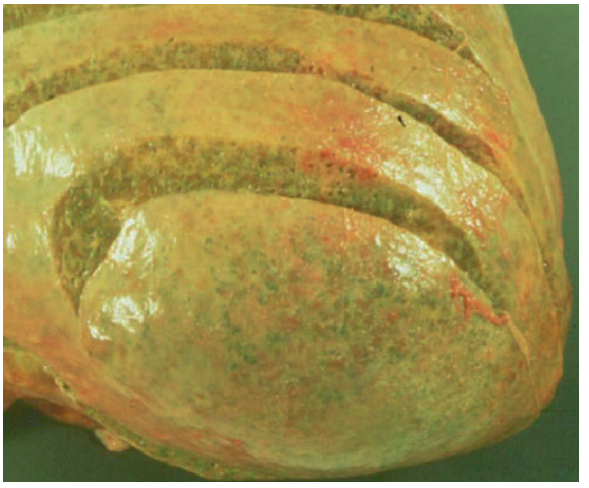

Fig. 38. Macroscopic aspect of a liver affected by Caroli's disease. The parenchyma shows yellowish changes due to cystically dilated bile-ducts and congestion of bile

2.8.11 Liver Disease in Patients with Cystic Kidneys

2.8.11.1 Cystic Liver Disease in Combination with Cystic Kidney Disease

Liver cysts are associated with the autosomal dominant as well as the recessive type of renal cysts. In the dominant type there are hepatic cysts at birth of up to 10 cm in size, which usually become symptomatic in the fifth decade of life. The most common symptoms are hepatomegaly, pain, and fever in cases of infection. Women seem to be affected more frequently than men, and there is a correlation with the number of pregnancies. Diverticles of the colon, a vitium cordis, ovarian cysts, inguinal herniation or intracranial aneurysms may occur concomitantly. Von Meyenburg complexes, which involve irregularly-dilated bile ducts, seem to be associated with the development of liver cysts in autosomal dominant cystic kidney disease [112, 130].

In the autosomal recessive type of disease the degree of hepatic involvement may vary. Infants with the perinatal type typically do not live long because of pulmonary complications.

In the neonatal and infantile type there is a tendency to portal fibrosis and cystic dilation of bile ducts in combination with renal insufficiency. The juvenile type presents with portal hypertension. Microscopically, there is an increased number of bile ducts in the portal tracts, which are irregularly formed and linked together [21].

2.8.11.2 Congenital Hepatic Fibrosis and Cystic Kidneys

Congenital hepatic fibrosis together with cystic kidneys is a distinct entity. Symptoms of cholangitis and portal hypertension are relevant findings. Patients typically present late with esophageal variceal bleeding. Macroscopically, the liver seems to be enlarged and tough, and cysts are not visible. Concomitant congenital malformations may be found [64, 96] (see Table 5).

Table 5. Pathologies and syndromes with concomitant hepatic cirrhosis

- Congenital hepatic fibrosis
- Familial congenital heart disease
- Pulmonary arterivenous fistula
- Gastric ulcers
- Protein-losing enteropathies syndrome
- Laurence-Moon-Biedl-syndrome

- Similar changes
- Meckel's syndrome
- Ivemark's syndrome
- Ellis-van-Crefeld syndrome
- Nephronophthisis – congenital hepatic fibrosis
- Jeune syndrome
- Vaginal atresia syndrome
- Tuberous sclerosis
- Medullary cystic disease

2.8.12 Langerhans Cell Histiocytosis

Liver involvement in histiocytosis is found in 29-71% of all cases. The leading symptoms are sclerosing cholangitis with cholestasis, progressive decrease of intrahepatic bile ducts and fibrosis with portal hypertension. Systemic chemotherapy may lead to an improvement, but in severe pediatric cases transplantation may be the only curative treatment [69, 120].

2.8.13 Storage Diseases

2.8.13.1 Glycogen Storage Disease

The different forms of glycogen storage disease are all autosomal recessive inherited diseases. Glycogen storage disease should always be considered in children with hepatomegaly, hypoglycemia, growth retardation, an unproportional distribution of body fat and increased transaminases [117, 140] (Table 6).

2.8.13.2 Galactosemia

Galactosemia is an inherited autosomal-recessive condition that manifests primarily through the first exposure to galactose via lactose in fed milk. The cause and effect of this disease are mostly due to a defect in the enzyme galactose-1-phosphate uridyl transferase [82].

Children with this disease typically present shortly after birth with growth retardation, nausea, vomiting, diarrhea and jaundice. If untreated, a cirrhosis may develop by the age of six months [156].

Table 6. Overview of glycogen storage diseases

Type	Hepatic manifestation	Other manifestations
• **Ia (von Gierke)**	Hepatomegaly, HCC, hepatic adenoma	Growth retardation, seizures, hypoglycemia, osteoporosis, gout, glomerulonephritis, amyloidosis
• **Ib**	Hepatomegaly, HCC, hepatic adenoma	Growth retardation, seizures, hypoglycemia, osteoporosis, gout, glomerulonephritis, amyloidosis, neutropenia and frequent infections
• **II (Pompé)**	Microscopic changes, hepatomegaly	Hypotonia, respiratory and cardiac insufficiency (infantile type)
• **III (Forbes)**	Hepatomegaly, cirrhosis, hepatic adenoma	Hypoglycemia, muscle weakness, growth retardation
• **IV (Anderson)**	Hepatomegaly, cirrhosis, focal fatty areas	Growth retardation, cardiac insufficiency
• **VI & IX**	Hepatomegaly	Growth retardation, mild hypoglycemia, hyperlipidemia

2.8.13.3 Hereditary Intolerance of Fructose

This inherited disorder of fructose metabolism is either caused by a deficiency of fructose-1-phosphate aldolase or is due to a dysfunction of the enzyme fructose-1,6-biphosphatase [15, 62].

Primary symptoms include poor feeding, vomiting and failure to thrive. Additionally, hepatosplenomegaly, hemorrhage, jaundice, fever and ascites can be found. Cases with acute liver failure may occur, and there is frequently steatosis and subsequent cirrhosis [123].

2.8.13.4 Mucopolysaccharidosis

Mucopolysaccharidosis is due to the deficient activity of enzymes responsible for the catabolism of glucosaminoglycans. It involves the accumulation of excessive amounts of mucopolysaccharides in the somatic and visceral tissue and the excretion of partial metabolites in the urine. Additionally, accumulations of gangliosides can be found. Mucopolysaccharidosis may be subdivided into six different disorders with each one presenting different clinical features. Although the same catabolic pathway is affected, each case involves a different specific enzyme. The types that manifest in the liver are type I (Hurler), II (Hunter), III (Sanfilippo), VI (Maroteaux-Lamy) and VIIb. Macroscopically, the liver becomes enlarged and extensive fibrosis or cirrhosis may occur. When present, the fibrosis is generally diffuse with heavy deposits of collagen bundles and gradual microdissection of parenchyma into nodules. Cirrhosis in mucopolysaccharidosis can present as either a macronodular or a micronodular type [180].

2.8.14 Viral Hepatitis

2.8.14.1 Acute Hepatitis

The various forms of viral hepatitis induced by different viruses have a similar morphology. Macroscopically, there is hepatomegaly with an edematous capsule, and distinct necrotic areas which lead to surface irregularities. In fulminant hepatitis, necrosis results in liver shrinkage and a relevant loss of parenchymal volume, however, there might be complete restitution. If necrosis occurs there may be scar formation, which is morphologically similar to that in cirrhosis. Cirrhosis typically develops in cases of chronic hepatitis [126, 169].

2.8.14.2 Chronic Hepatitis

An inflammatory process which lasts longer than six months without signs of regression is referred to as chronic hepatitis. Histologically, chronic hepatitis is a necro-inflammatory, primarily hepatocytic disease with or without cirrhosis, in which lymphocytes clearly dominate the inflammation. There is a gradation regarding the degree of inflammation, its localization and the subsequent fibrosis.

Macroscopically, an enlarged liver can be demonstrated in the acute phase caused by edematization. Ascites and splenomegaly are signs of a more fulminant course [45]. The main etiological categories for chronic hepatitis in addition to virus infection are listed in Table 7.

Table 7. Etiological categories of chronic hepatitis

• Viral (HBV, HDV, HCV)
• Autoimmune (classic lupoid-type and subtypes)
• Autoimmune overlap syndromes
• Drug induced (e.g. nitrofurantoin, α-methyldopa, isoniazid and others)
• Cryptogenic

2.8.15 Liver Disease in Congestive Heart Disease

Chronic failure of the right heart leads to an enlarged liver via congestion. Diffuse cell necrosis may develop due to the decreased blood flow, increased blood pressure and resulting hypoxemia (Fig. 39). Cell necrosis thereafter induces a fibrosis which resembles micronodular cirrhosis. However, in contrast to other forms of cirrhosis, the microscopic architecture remains intact [97].

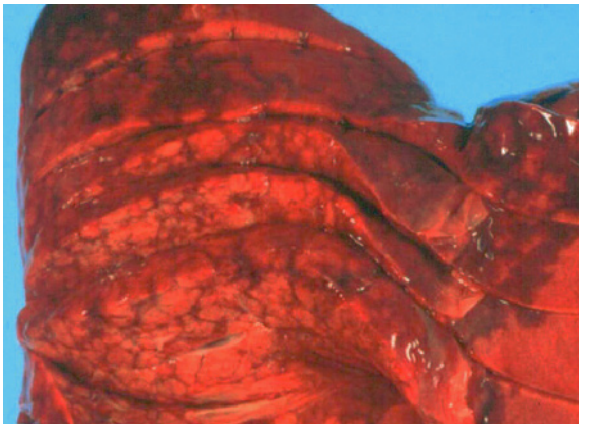

Fig. 39. Macroscopic aspect of cardiac liver cirrhosis based on congestive heart disease, leading to increased intrahepatic blood pressure and reduced flow with subsequent cirrhosis

2.9 Vascular Changes

2.9.1 Thrombosis of the Portal Vein

According to Virchow's triad there are three main mechanisms leading to a thrombosis: hypercoagulability, stasis and injury to the vascular endothelium (see Table 8). Obstruction of the portal vein may be intermittent, as can be shown in ultrasonographic and histologic studies. Recanalization is quite rare once the thrombus formation has reached the smaller portal branches [19, 168].

2.9.2 Obstruction of Smaller Portal Branches

The type of portal hypertension caused by obliteration of the smaller portal branches sometimes occurs in systemic vasculitis or rheumatic disease and may be found prior to a manifest cirrhosis in primary sclerosing cholangitis (PSC), primary biliary cholangitis (PBC) or sarcoidosis. An infection with schistosoma – with eggs of the parasite causing a chronic inflammatory reaction – may lead to thrombosis and fibrosis. Acute thrombosis of a small portal vein causes a so-called pseudo-infarction (Zahn infarction), while thrombosis of larger branches may induce more diffuse atrophy with subsequent regenerative hyperplasia [6, 51, 134].

2.9.3 Budd-Chiari Syndrome

The combination of portal hypertension and hepatomegaly caused by an obstruction of venous drainage was first described by Budd in 1845. This obstruction may be located intrahepatically in the small hepatic veins or extrahepatically in the larger veins or the inferior caval vein (Fig. 40). The type of obliterative endophlebitis of small hepatic veins described by Chiari is called "veno-occlusive disease". A principal clinical symptom is slowly increasing portal hypertension. Only a few patients develop a fulminant disease with acute liver failure, hepatic encephalopathy and coagulopathy, and this arises from the sudden obstruction of all larger hepatic veins. This may be caused by any coagulation disorder which predisposes subjects to a thrombosis, or by a growing neoplasm, a hypertrophied caudate lobe or membrane formation in the inferior caval vein. Treatment options include anticoagulation, resection of a mechanical obstruction or porto-systemic shunting. The last approach may involve liver transplantation. In acute obstruction

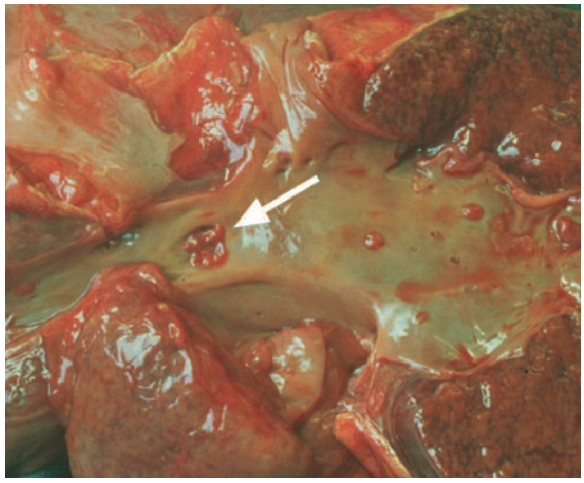

Fig. 40. Cut section of a liver from a patient with Budd-Chiari syndrome demonstrating thrombus formation in a large hepatic vein (*arrow*)

Table 8. Etiological factors leading to portal vein thrombosis

• **Hypercoagulability**	
Polycythaemia vera	Idiopathic thrombocytosis
Paroxysmal nocturnal hemoglobinuria	CML
Subclinical myeloproliferative disease	Oral contraceptives
Pregnancy	Protein C deficiency
Antithrombin III deficiency	
• **Stasis**	
Cirrhosis	HCC
Pancreatic carcinoma	Splenectomy
• **Vascular injury**	
Sepsis of the umbilical veins	Pylephlebitis
Trauma	Catheterization
Schistosomiasis	Chronic inflammatory bowel disease

Table 9. Etiological factors leading to thrombosis of the hepatic veins

• **Hypercoagulability**	
Polycythemia vera	Subclinical myeloid dysplasia
Paroxysmal nocturnal hemoglobinuria	Promyelocytic leukemia
Chronic myeloid leukemia	Oral contraceptives
Pregnancy	Anticardiolipin antibodies
Idiopathic thrombozytopenic purpura	Protein C deficiency
Antithrombin III deficiency	
• **Stasis**	
Membranous obstruction of the inferior caval vein	Congenital anomalies
Cirrhosis	Cardiac insufficiency
Constrictive pericarditis	Obstruction of the superior caval vein
Atrial myxoma	Sickle cell anemia
HCC	Hypernephroma
Adrenal carcinoma	Hodgkin's disease
Wilms' tumor	Leiomyoma and leiomyosarcoma
Metastasizing neoplasms	Hydatid cysts
Abscess formation	Hematoma
• **Vascular injury**	
Trauma	Catheterization
Amyloidosis	Vasculitis
Tuberculosis	Behçet's disease
Sarcoidosis	Filariasis
• **Others**	
Chronic inflammatory bowel disease	Protein-losing enteropathy
Multiple myeloma	

the liver seems to be enlarged because of a dilation of the sinusoids. If there is only a partial obstruction there might be hypertrophy of the areas with diminished drainage [92, 114, 175] (see Table 9).

2.9.4 Veno-Occlusive Disease (VOD)

A fibrotic obstruction of the small (< 1 mm) liver veins leads to hepatomegaly with congestion of the sinusoids. If longstanding, this results in liver fibrosis. Causative agents include pyrrolizidine alkaloids, which are found in exotic teas and as contamination in cereals. Azathioprin and cysteamin are also known to induce VOD, while whole body irradiation, together with intensive chemotherapy, is thought to lead to injury of the endothelium of small hepatic veins. Acute symptoms include sudden onset of pain with hepatomegaly and ascites. More than 50% of all bone marrow-transplanted patients show signs of VOD. Typical symptoms in these cases are weight gain, jaundice, thrombocytopenia and early stage liver failure. A similar disease is seen in patients treated with Dacarbazine, although histologically there is a thrombosis, rather than fibrotic obstruction, probably induced by an allergic reaction [23, 40, 57, 186].

2.9.5 Lobular or Segmental Atrophy

Thrombosis of the portal or hepatic veins may lead to focal atrophy with subsequent compensatory hypertrophy of the neighboring segments. This is especially common in patients with cirrhotic livers. Syphilis and metastatic carcinoma are known to cause so-called hepar lobatum. Segmental atrophy may also be due to a congenital anomaly [71, 127].

2.9.6 Infarction / Ischemia

Usually, an obstruction of the hepatic artery does not induce hepatic ischemia, as the blood flow via the portal vein is sufficient to guarantee parenchymal supply. Large infarcts are only possible if both

vessels have a diminished flow, as occurs in shock, chronic portal vein thrombosis or cirrhotic livers. Here, the increased portal tension induces a reduction of blood flow in the portal vessels. Intravasal coagulation may also cause liver infarctions [33, 141].

2.10 HIV-associated Liver Diseases

The liver in HIV is mainly affected by opportunistic infections. About half of all patients with seroconversion into mononucleosis-like disease have hepatomegaly. In almost all HIV patients there are non-specific hepatic findings such as granulomatous inflammation, peliosis hepatis or amyloidosis [37, 41].

2.10.1 Kaposi's Sarcoma

About 20% of all HIV-infected patients develop Kaposi's sarcoma of the liver, which typically grows from the portal tracts along the bile ducts. Parenchymal lesions are typically small (5-10 mm), and are located subcapsularly [74].

2.10.2 Primary Lymphoma of the Liver

Primary liver lymphomas are found more frequently in HIV-infected patients than in non-infected individuals. There may be focal lesions with necrotic centers, or a more diffuse infiltration of the liver parenchyma as well as lymphoma of bile ducts, which may resemble a sclerosing cholangitis [27, 85].

2.10.3 Cholangitis

Cryptosporidiae and *Microsporidiae* may induce a cholangitis especially if CD4+ counts are below 4/mm^3. Sclerosis leads to pain, fever and cholestasis. Furthermore, there is an increased incidence of bacterial cholangitis, induced by gram-negative agents [17, 110].

2.10.4 Fungal Infections

Generally, fungal infections are a major problem in HIV-positive patients and in patients with manifest AIDS. In these cases fungal infections may occur either focally or as disseminated infections in which the liver may be affected. The most important pathogenic germs are *Candida albicans*, *Cryptococcus neoformans*, *Histoplasma capsulatum*, *Pneumocystis carinii* and *Aspergillus*. A liver biopsy should be performed for an accurate diagnosis. However, the most sensitive techniques to classify the fungi responsible for the infection are blood culture and blood antigenemia tests [73, 190].

2.10.5 Protozoal Infections

Protozoal infections which may affect the liver of HIV-positive patients include *Toxoplasma gondii*, *Leishmania* species and *Cryptosporidium parvum*.

HIV-associated toxoplasmosis usually presents with focal lesions in the brain. Disseminated toxoplasmosis outside this location is uncommon in AIDS patients and is only occasionally found by chance or in autopsy material [22].

As the infection with *Leishmania* depends on the geographical distribution of this pathogenic germ; HIV-associated leishmaniosis only occurs in endemic regions such as southern Europe, South America and Africa. Inoculated parasites may persist latently in the body for several years, manifesting only as the immunodeficiency progresses [4].

2.10.6 Bacterial Infections

Bacterial infections which show an increased incidence in HIV-positive patients and which may manifest in the liver include tuberculosis, infections with atypical *Mycobacteria*, bacillary angiomatosis, cat-scratch disease and Q fever.

Hepatic foci of tuberculosis may appear as single or multiple mass lesions as well as miliary tuberculosis. Recent studies have revealed that active tuberculosis is present in 50% of adults dying of AIDS and that the liver is involved in 85% of these cases. Thus, tuberculosis represents the most important and most frequent hepatotropic HIV-associated disease [103].

HIV-associated infection with atypical *Mycobacteria*, such as *M. avium* and *M. intracellulare*, depends on geographic distribution and correlates with the CD4+ lymphocyte count. Infections within the liver manifest with increased serum alkaline phosphatase indicating either an obstruction of the bile ducts by enlarged lymph nodes in the liver hilum, or obstruction of the terminal ductules by intrahepatic *M. avium* granulomas. Thus, infections with atypical *Mycobacteria* should also be considered in cases of intrahepatic abscess formation in HIV-positive patients [106, 174].

2.11 Hepatic Trauma

The spleen and liver are the organs most frequently involved in trauma by car accident or penetration. Up to 60% of all patients with hepatic trauma are hemodynamically unstable and up to 45% have concomitant splenic involvement. The right liver lobe is the most frequently traumatized area. Subcapsular hematoma often results in a more restricted blood loss and is typically lens-shaped and causes compression of the neighbouring parenchyma. Rib fractures are a frequent finding. Parenchymal contusions and hematoma are less sharply demarcated. Parenchymal tears of the area nuda typically run parallel to hepatic veins and may remain undiscovered in peritoneal lavage. There may be some intraparenchymal or subcapsular air formation one to two days after trauma in necrotic areas. Trauma of the bile ducts may cause bile leakage which, on occasion, leads to formation of a demarcated bilioma. Hemorrhage in bile ducts may be suspected in cases of increased bile density. Generally, acute trauma most often presents with areas of high bile density, which in the course of time may lead to the development of more cystic lesions [29, 30, 44].

2.12 Metastases

Liver metastases are the most frequent malignant liver lesions. Between 24% and 36% of all patients who die of a malignancy are known to have hepatic metastases which frequently are below 1 cm in size [148].

In order of decreasing frequency, the principal organs which harbour the primary tumors of origin are the colon, stomach, pancreas, breast and lung. Hematogeneous spread via the portal vein is usually found in malignancies of the gastrointestinal tract, whereas lymphogeneous spread occurs in bile duct and pancreatic carcinoma. Primary tumors such as lung cancer seem to metastasize via the arterial blood supply of the liver. Hematologic disease such as lymphoma or leukemia may also infiltrate the hepatic parenchyma.

Metastases vary in size, consistency, uniformity of growth, stromal response and vascularity and can be either infiltrative or expansive. The appearance of metastases depends on the primary source and mode of propagation. Metastatic adenocarcinomas from the gallbladder and colon often contain calcifications and have a slimy cut surface due to mucin production. Tumors that are expanding and massive, such as colon cancer metastases, often have central liquefactive necrosis (Fig. 41). Metastases that have significant necrosis and/or fibrosis can umbilicate the surface of the liver capsule, which is helpful for differentiation from HCC, where umbilication rarely occurs (Fig. 42). Poorly-differentiated tumors such as seminomas, oat-cell carcinomas, non-Hodgkin's lymphomas and undifferentiated sarcomas tend to have a uniformly soft, "fish flesh-like" consistency. Squamous cell carcinomas have a granular and caseous central portion that lacks the shiny appearance of most adenocarcinomas. Individual metastases in the same liver can vary greatly in appearance because of differences in blood supply, hemorrhage, cellular differentiation, fibrosis and necrosis.

Most metastases maintain the microscopic features of the primary tumor, including the degree of stromal growth. Approximately 7-15% of patients with metastatic liver disease have tumor thrombi that occlude the portal and/or hepatic veins.

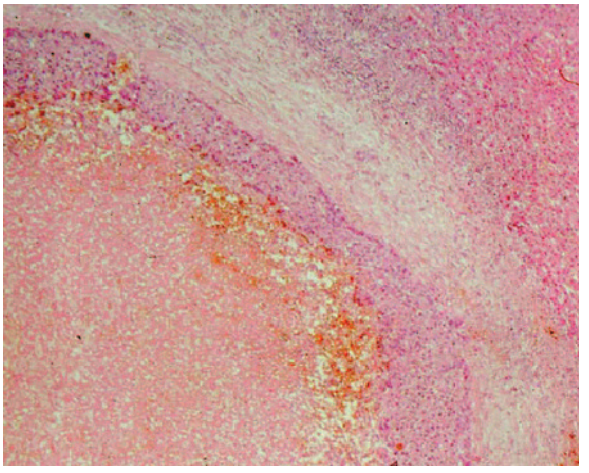

Fig. 41. Histology of a liver metastasis of a colorectal adenocarcinoma. Note the central necrosis surrounded by a rim of viable tumor tissue

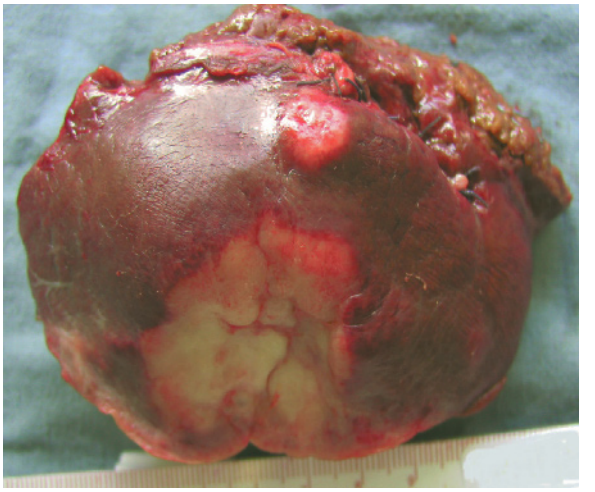

Fig. 42. Liver surface with metastasis of a colon carcinoma demonstrating a typical umbilicus formation

Metastases that penetrate the large portal veins disseminate through peripheral portal branches. The vascular supply of liver metastases is virtually all arterial and this is the basis of imaging strategies and therapeutic modalities. Although hepatic metastases from the splanchnic bed originally derive their blood supply from the portal vein, the blood supply becomes progressively arterial.

2.12.1 Metastases of Colorectal Adenocarcinoma

Colorectal carcinoma is the second most common carcinoma in men and women. 15% of all patients initially present with hepatic metastases due to vascular drainage via the portal vein (Fig. 43). Thereafter, local recurrence or distant metastases can occur during the first two years after the intended curative resection of the primary tumor. Their prevalence depends on TNM stage and is about 14% [191, 198].

A second surgical intervention is the only treatment that seems to be beneficial to patients with hepatic metastases despite the relatively low five year survival rate of 25% [145]. It seems that survival increases with the latency of the recurrent tumor growth [158].

Alternative palliative treatment modalities which may be relevant include chemotherapy with 5-Fluorouracil and Levamisol [115], embolization of arterial tumor vessels [35], and cryotherapeutic intervention [138].

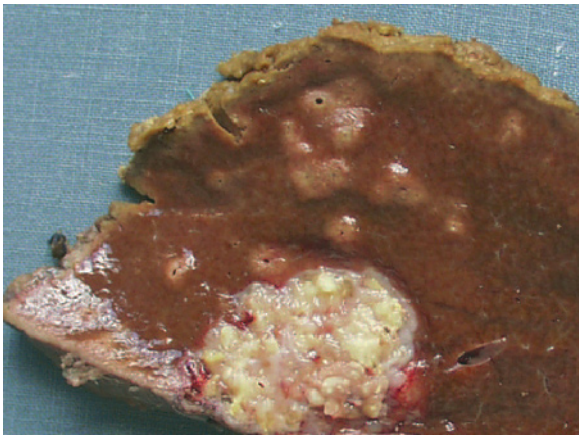

Fig. 43. Cut section of the liver in metastatic liver disease in a patient with primary colon carcinoma, demonstrating subcapsular as well as diffuse intrahepatic metastases

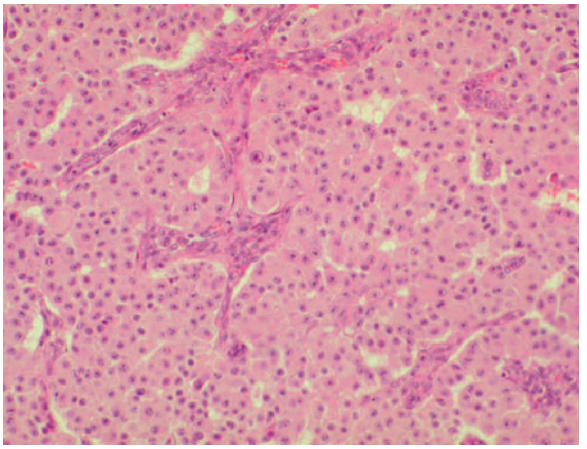

Fig. 44. Histology of hepatic metastasis of a neuroendocrine tumor with glandular differentiation and no signs of tumor necrosis

2.12.2 Metastases of Breast Carcinoma

Breast cancer is one of the most frequent malignancies in female patients in the western world. Patients with known hepatic metastases die rapidly if no therapy is initiated [75]. However, regional chemotherapy alone or in combination with partial hepatic resection does not seem to be of benefit [102]. Systemic chemotherapy only induces a partial remission in 30-40% of all patients.

2.12.3 Carcinoid Metastases

Almost two thirds of all carcinoids are found in the appendix, while up to one third are located in some other part of the small intestine. The course of disease and hence both life expectancy and quality is mainly dependent upon the extent of metastatic growth. Typical flush symptoms can often be relieved by a reduction of the hepatic tumor burden. The five year survival of patients with hepatic metastases is about 21% if no therapy is initiated [116]. Hemihepatectomy or segmental resection in patients with metastatic growth in one liver lobe and intermittent embolization of hepatic arteries in disseminated disease may improve the survival to up to 70% [1]. As carcinoid tumors usually display relatively slow tumor growth, liver transplantation in patients with diffuse metastases may be another treatment modality. Chemotherapy with 5-Fluorouracil, Streptozotocine, Doxorubicine or Dacarbacine as a monotherapy is of no benefit alone [116], although there may be some tumor regression when conducted in combination with embolization (Fig. 44).

2.13 Infiltration of the Liver in Hematologic Diseases

2.13.1 Non-Hodgkin's Lymphoma (NHL)

The primary hepatic manifestation in NHL must be distinguished from secondary involvement. Patients with primary lymphoma seem to have a favorable prognosis when initial resection is followed by chemotherapy. Typically, well-demarcated lesions with surrounding necrosis are found, and diffuse infiltration is rare [150].

However, secondary liver infiltration seems to occur quite frequently. Well-differentiated B-cell lymphomas tend to form multiple small nodules, whereas more undifferentiated types show a more diffuse manifestation that is hard to identify on imaging studies. Unlike other solid metastatic diseases of the liver, an involvement of both liver and spleen is typically found in lymphoma [90].

2.13.2 Hepatic Hodgkin's Lymphoma

Secondary infiltration of the hepatic parenchyma also occurs in patients with Hodgkin's lymphoma. Fever and hepatomegaly with jaundice may result. The morphology varies from diffuse infiltration to large well-demarcated areas or small nodules. In some patients there may be concomitant peliosis hepatis [83, 97].

References

1. Ahlman H, Westberg G, Wangberg B, Nilsson O, Tylen U, Schersten T, Tisell LE. Treatment of liver metastases of carcinoid tumors. World J Surg 1996 Feb;20(2):196-202
2. Akinoglu A, Demiryurek H, Guzel C. Alveolar hydatid disease of the liver: a report on thirty-nine surgical cases in eastern Anatolia, Turkey. Am J Trop Med Hyg 1991 Aug;45(2):182-9
3. Allaire GS, Rabin L, Ishak KG, Sesterhenn IA. Bile duct adenoma. A study of 152 cases. Am J Surg Pathol 1988 Sep;12(9):708-15
4. Alvar J, Gutierrez-Solar B, Molina R, Lopez-Velez R, Garcia-Camacho A, Martinez P, Laguna F, Cercenado E, Galmes A. Prevalence of Leishmania infection among AIDS patients. Lancet 1992 Jun 6;339 (8806):1427
5. Anderson JB, Cooper MJ, Williamson RC. Adenocarcinoma of the extrahepatic biliary tree. Ann R Coll Surg Engl 1985 May;67(3):139-43
6. Andrade ZA, Peixoto E, Guerret S, Grimaud JA. Hepatic connective tissue changes in hepatosplenic schistosomiasis. Hum Pathol 1992 May;23(5):566-73
7. Angulo P. Nonalcoholic fatty liver disease. N Engl J Med 2002 Apr 18;346(16):1221-31
8. Anonymous. Hepatocellular cancer: differences between high and low incidence regions. Lancet 1987 Nov 21;2(8569):1183-4
9. Anthony PP. Primary carcinoma of the liver: a study of 282 cases in Ugandan Africans. J Pathol 1973 May;110(1):37-48
10. Anthony PP. A guide to the histological identification of fungi in tissues. J Clin Pathol 1973 Nov;26(11):828-31
11. Anthony PP. Inflammatory pseudotumour (plasma cell granuloma) of lung, liver and other organs. Histopathology 1993 Nov;23(5):501-3
12. Anthony PP, Vogel CL, Barker LF. Liver cell dysplasia: a premalignant condition. J Clin Pathol 1973 Mar;26(3):217-23
13. Anthony PP, Ishak KG, Nayak NC, Poulsen HE, Scheuer PJ, Sobin LH. The morphology of cirrhosis: definition, nomenclature, and classification. Bull World Health Organ 1977;55(4):521-40
14. Anthony PP, Ishak KG, Nayak NC, Poulsen HE, Scheuer PJ, Sobin LH. The morphology of cirrhosis. Recommendations on definition, nomenclature, and classification by a working group sponsored by the World Health Organization. J Clin Pathol 1978 May;31(5):395-414
15. Baker L, Winegrad AI. Fasting hypoglycaemia and metabolic acidosis associated with deficiency of hepatic fructose-1,6-diphosphatase activity. Lancet 1970 Jul 4;2(7662):13-6
16. Baum JK, Bookstein JJ, Holtz F, Klein EW. Possible association between benign hepatomas and oral contraceptives. Lancet 1973 Oct 27;2(7835):926-9
17. Beaugerie L, Teilhac MF, Deluol AM, Fritsch J, Girard PM, Rozenbaum W, Le Quintrec Y, Chatelet FP. Cholangiopathy associated with Microsporidia infection of the common bile duct mucosa in a patient with HIV infection. Ann Intern Med 1992 Sep 1;117(5):401-2
18. Belamaric J. Intrahepatic bile duct carcinoma and C. sinensis infection in Hong Kong. Cancer 1973 Feb;31(2):468-73
19. Belli L, Romani F, Sansalone CV, Aseni P, Rondinara G. Portal thrombosis in cirrhotics. A retrospective analysis. Ann Surg 1986 Mar;203(3):286-91
20. Bloustein PA, Silverberg SG. Squamous cell carcinoma originating in an hepatic cyst. Case report with a review of the hepatic cyst-carcinoma association. Cancer 1976 Nov;38(5):2002-5
21. Blyth H, Ockenden BG. Polycystic disease of kidney and liver presenting in childhood. J Med Genet 1971 Sep;8(3):257-84
22. Bonacini M, Kanel G, Alamy M. Duodenal and hepatic toxoplasmosis in a patient with HIV infection: review of the literature. Am J Gastroenterol 1996 Sep;91(9):1838-40
23. Brooks SE, Miller CG, McKenzie K, Audretsch JJ, Bras G. Acute veno-occlusive disease of the liver. Fine structure in Jamaican children. Arch Pathol 1970 Jun;89(6):507-20
24. Bruneton JN, Kerboul P, Drouillard J, Menu Y, Normand F, Santini N. Hepatic lipomas: ultrasound and computed tomographic findings. Gastrointest Radiol 1987;12(4):299-303

25. Bryan RT, Schantz PM. Echinococcosis (hydatid disease). J Am Vet Med Assoc 1989 Nov 1;195(9):1214-7
26. Buhler H, Pirovino M, Akobiantz A, Altorfer J, Weitzel M, Maranta E, Schmid M. Regression of liver cell adenoma. A follow-up study of three consecutive patients after discontinuation of oral contraceptive use. Gastroenterology 1982 Apr;82(4):775-82
27. Caccamo D, Pervez NK, Marchevsky A. Primary lymphoma of the liver in the acquired immunodeficiency syndrome. Arch Pathol Lab Med 1986 Jun;110(6):553-5
28. Caroli J. Diseases of the intrahepatic biliary tree. Clin Gastroenterol 1973 Jan;2(1):147-61
29. Carrillo EH, Richardson JD. The current management of hepatic trauma. Adv Surg 2001;35:39-59
30. Carrillo EH, Wohltmann C, Richardson JD, Polk HC Jr. Evolution in the treatment of complex blunt liver injuries. Curr Probl Surg 2001 Jan;38(1):1-60
31. Casteels-Van Daele M, Van Geet C, Wouters C, Eggermont E. Reye's syndrome. Lancet 2001 Jul 28;358(9278):334
32. Chapman RW. Aetiology and natural history of primary sclerosing cholangitis—a decade of progress? Gut 1991 Dec;32(12):1433-5
33. Chen V, Hamilton J, Qizilbash A. Hepatic infarction. A clinicopathologic study of seven cases. Arch Pathol Lab Med 1976 Jan;100(1):32-6
34. Cheuk W, Woo PCY, Yuen KY, Yu PH, Chan JKC. Intestinal inflammatory pseudotumour with regional lymph node involvement: identification of a new bacterium as the aetiological agent. J Pathol 2000; 192: 289-292
35. Chuang VP, Wallace S. Hepatic artery embolization in the treatment of hepatic neoplasms. Radiology 1981 Jul;140(1):51-8
36. Coffin CM, Humphrey PA, Dehner LP. Extrapulmonary inflammatory myofibroblastic tumor: a clinical and pathological survey. Semin Diagn Pathol. 1998; 15: 85-101
37. Cozzi PJ, Abu-Jawdeh GM, Green RM, Green D. Amyloidosis in association with human immunodeficiency virus infection. Clin Infect Dis 1992 Jan;14(1):189-91
38. Craig JR, Peters RL, Edmondson HA, Omata M. Fibrolamellar carcinoma of the liver: a tumor of adolescents and young adults with distinctive clinicopathologic features. Cancer 1980 Jul 15;46(2):372-9
39. Culp KS, Fleming CR, Duffy J, Baldus WP, Dickson ER. Autoimmune associations in primary biliary cirrhosis. Mayo Clin Proc 1982 Jun;57(6):365-70
40. Culvenor CC, Edgar JA, Smith LW, Kumana CR, Lin HJ. Heliotropium lasiocarpum Fisch and Mey identified as cause of veno-occlusive disease due to a herbal tea. Lancet 1986 Apr 26;1(8487):978
41. Czapar CA, Weldon-Linne CM, Moore DM, Rhone DP. Peliosis hepatis in the acquired immunodeficiency syndrome. Arch Pathol Lab Med 1986 Jul;110(7):611-3
42. Da Silva LC, Carrilho FJ. Hepatosplenic schistosomiasis. Pathophysiology and treatment. Gastroenterol Clin North Am 1992 Mar;21(1):163-77
43. Daldrup HE, Reimer P, Rummeny EJ, Fischer H, Bocker W, Peters PE. The regression of a hepatocellular adenoma after the withdrawal of hormonal contraception. Rofo Fortschr Geb Rontgenstr Neuen Bildgeb Verfahr 1995 Nov;163(5):449-51
44. David Richardson J, Franklin GA, Lukan JK, Carrillo EH, Spain DA, Miller FB, Wilson MA, Polk HC Jr, Flint LM. Evolution in the management of hepatic trauma: a 25-year perspective. Ann Surg 2000 Sep;232(3):324-30
45. De Groote J. Classification of Chronic Hepatitis. Ann Clin Res 1976 Jun;8(3):130-8
46. Dehner LP, Ishak KG. Vascular tumors of the liver in infants and children. A study of 30 cases an review of the literature. Arch Pathol 1971 Aug;92(2):101-11
47. Dehner LP. The enigmatic inflammatory pseudotumour: the current state of our understanding or misunderstanding. J Pathol. 2000. Nov, 192(3): 277-9
48. Delas N, Faurel JP, Wechsler B, Adotti F, Leroy O, Lemerez M. Association of peliosis and necrotizing vasculitis. Nouv Presse Med 1982 Sep 25;11(37):2787
49. DeMaioribus CA, Lally KP, Sim K, Isaacs H, Mahour GH. Mesenchymal hamartoma of the liver. A 35-year review. Arch Surg 1990 May;125(5):598-600
50. Desmet VJ. Cholangiopathies: past, present, and future. Semin Liver Dis 1987 May;7(2):67-76
51. Devaney K, Goodman ZD, Epstein MS, Zimmerman HJ, Ishak KG. Hepatic sarcoidosis. Clinicopathologic features in 100 patients. Am J Surg Pathol 1993 Dec;17(12):1272-80
52. Deziel DJ, Rossi RL, Munson JL, Braasch JW, Silverman ML. Management of bile duct cysts in adults. Arch Surg 1986 Apr;121(4):410-5
53. Di Bisceglie AM. Hepatitis C and hepatocellular carcinoma. Semin Liver Dis 1995 Feb;15(1):64-9
54. Dietze O, Davies SE, Williams R, Portmann B. Malignant epithelioid haemangioendothelioma of the liver: a clinicopathological and histochemical study of 12 cases. Histopathology 1989 Sep;15 (3):225-37
55. Ducreux M, Lartigau E, Eschwege F, Etienne JP. Radiotherapy of malignant tumors of the liver. Gastroenterol Clin Biol 1995 Apr;19(4):350-60
56. Edwards CQ, Dadone MM, Skolnick MH, Kushner JP. Hereditary haemochromatosis. Clin Haematol 1982 Jun;11(2):411-35
57. Fajardo LF, Colby TV. Pathogenesis of veno-occlusive liver disease after radiation. Arch Pathol Lab Med 1980 Nov;104(11):584-8
58. Farber E. Hepatocyte proliferation in stepwise development of experimental liver cell cancer. Dig Dis Sci 1991 Jul;36(7):973-8
59. Ferrell L, Wright T, Lake J, Roberts J, Ascher N. Incidence and diagnostic features of macroregenerative nodules vs. small hepatocellular carcinoma in cirrhotic livers. Hepatology 1992 Dec;16(6):1372-8
60. Foster JH, Berman MM. The malignant transformation of liver cell adenomas. Arch Surg 1994 Jul;129(7):712-7
61. Foster JH, Donohue TA, Berman MM. Familial liver-cell adenomas and diabetes mellitus. N Engl J Med 1978 Aug 3;299(5):239-41
62. Froesch ER, Wolf HP, Baitsch H. Hereditary fructose intolerance. An inborn defect of hepatic fructose-1-phosphatase splitting aldolase. Am J Med 1963;34:151-167

63. Furuta T, Yoshida Y, Saku M, Honda H, Muranaka T, Oshiumi Y, Kanematsu T, Sugimachi K. Treatment of symptomatic non-parasitic liver cysts—surgical treatment versus alcohol injection therapy. HPB Surg 1990 Oct;2(4):269-77; discussion 277-9
64. Gang DL, Herrin JT. Infantile polycystic disease of the liver and kidneys. Clin Nephrol 1986 Jan; 25(1):28-36
65. Gonzalez A, Canga F, Cardenas F, Castellano G, Garcia H, Cuenca B, Sanchez F, Solis-Herruzo JA. An unusual case of hepatic adenoma in a male. J Clin Gastroenterol 1994 Sep;19(2):179-81
66. Goodman ZD, Ishak KG. Angiomyolipomas of the liver. Am J Surg Pathol 1984 Oct;8(10):745-50
67. Grasso S, Manusia M, Sciacca F. Unusual liver lesion in tuberous sclerosis. Arch Pathol Lab Med 1982 Jan;106(1):49
68. Greenstein AJ, Lowenthal D, Hammer GS, Schaffner F, Aufses AH Jr. Continuing changing patterns of disease in pyogenic liver abscess: a study of 38 patients. Am J Gastroenterol 1984 Mar;79(3):217-26
69. Grundy P, Ellis R. Histiocytosis X: a review of the etiology, pathology, staging, and therapy. Med Pediatr Oncol 1986;14(1):45-50
70. Guo KJ, Yamaguchi K, Enjoji M. Undifferentiated carcinoma of the gallbladder. A clinicopathologic, histochemical, and immunohistochemical study of 21 patients with a poor prognosis. Cancer 1988 May 1;61(9):1872-9
71. Hadjis NS, Blumgart LH. Clinical aspects of liver atrophy. J Clin Gastroenterol 1989 Feb;11(1):3-7
72. Haratake J, Koide O, Takeshita H. Hepatic lymphangiomatosis: report of two cases, with an immunohistochemical study. Am J Gastroenterol 1992 Jul;87(7):906-9
73. Harding CV. Blastomycosis and opportunistic infections in patients with acquired immunodeficiency syndrome. An autopsy study. Arch Pathol Lab Med 1991 Nov; 115(11): 1133-6
74. Hasan FA, Jeffers LJ, Welsh SW, Reddy KR, Schiff ER. Hepatic involvement as the primary manifestation of Kaposi's sarcoma in the acquired immune deficiency syndrome. Am J Gastroenterol 1989 Nov;84(11):1449-51
75. Hoe AL, Royle GT, Taylor I. Breast liver metastases-incidence, diagnosis and outcome. J R Soc Med 1991 Dec;84(12):714-6
76. Horowitz ME, Etcubanas E, Webber BL, Kun LE, Rao BN, Vogel RJ, Pratt CB. Hepatic undifferentiated (embryonal) sarcoma and rhabdomyosarcoma in children. Results of therapy. Cancer 1987 Feb 1;59(3):396-402
77. Ishak KG, Glunz PR. Hepatoblastoma and hepatocarcinoma in infancy and childhood. Report of 47 cases. Cancer 1967 Mar;20(3):396-422
78. Ishak KG, Rabin L. Benign tumors of the liver. Med Clin North Am 1975 Jul;59(4):995-1013
79. Ishak KG, Willis GW, Cummins SD, Bullock AA. Biliary cystadenoma and cystadenocarcinoma: report of 14 cases and review the literature. Cancer 1977 Jan;39(1):322-38
80. Ishak KG, Sesterhenn IA, Goodman ZD, Rabin L, Stromeyer FW. Epithelioid hemangioendothelioma of the liver: a clinicopathologic and follow-up study of 32 cases. Hum Pathol 1984 Sep;15 (9):839-52
81. Ishak KG, Anthony PP, Sobin LH. Histological typing of tumours of the liver. World Health Organization International Histological Classification of Tumours, 2nd edn. Berlin: Springer-Verlag, 1994
82. Isselbacher KJ, Anderson ER, Kurakoski K, Kalckar HM. Congenital galactosemia, a single enzymatic block in galactose metabolism. Science 1956; 123: 635
83. Jaffe ES. Malignant lymphomas: pathology of hepatic involvement. Semin Liver Dis 1987 Aug;7(3):257-68
84. Jones RS. Carcinoma of the gallbladder. Surg Clin North Am 1990 Dec;70(6):1419-28
85. Kaplan LD, Kahn J, Jacobson M, Bottles K, Cello J. Primary bile duct lymphoma in the acquired immunodeficiency syndrome (AIDS). Ann Intern Med 1989 Jan 15;110(2):161-2
86. Kaplan MM. Primary biliary cirrhosis. N Engl J Med 1987 Feb 26;316(9):521-8
87. Karasawa T, Itoh K, Komukai M, Ozawa U, Sakurai I, Shikata T. Squamous cell carcinoma of gallbladder—report of two cases and review of literature. Acta Pathol Jpn 1981 Mar;31(2):299-308
88. Kerlin P, Davis GL, McGill DB, Weiland LH, Adson MA, Sheedy PF 2nd. Hepatic adenoma and focal nodular hyperplasia: clinical, pathologic, and radiologic features. Gastroenterology 1983 May;84(5 Pt 1):994-1002
89. Khuroo MS, Zargar SA, Mahajan R. Hepatobiliary and pancreatic ascariasis in India. Lancet 1990 Jun 23;335(8704):1503-6
90. Kim H, Dorfman RF. Morphological studies of 84 untreated patients subjected to laparotomy for the staging of non-Hodgkin's lymphomas. Cancer 1974 Mar;33(3):657-74
91. Klatskin G. Adenocarcinoma of the hepatic duct at its bifurcation within the porta hepatis. Am J Med 1965; 38: 241-256.
92. Klein AS, Sitzmann JV, Coleman J, Herlong FH, Cameron JL. Current management of the Budd-Chiari syndrome. Ann Surg 1990 Aug;212(2):144-9
93. Koga A, Ichimiya H, Yamaguchi K, Miyazaki K, Nakayama F. Hepatolithiasis associated with cholangiocarcinoma. Possible etiologic significance. Cancer 1985 Jun 15;55(12):2826-9
94. Kurathong S, Lerdverasirikul P, Wongpaitoon V, Pramoolsinsap C, Kanjanapitak A, Varavithya W, Phuapradit P, Bunyaratvej S, Upatham ES, Brockelman WY. Opisthorchis viverrini infection and cholangiocarcinoma. A prospective, case-controlled study. Gastroenterology 1985 Jul;89(1):151-6
95. Lack EE, Neave C, Vawter GF. Hepatoblastoma. A clinical and pathologic study of 54 cases. Am J Surg Pathol 1982 Dec;6(8):693-705
96. Landing BH, Wells TR, Claireaux AE. Morphometric analysis of liver lesions in cystic diseases of childhood. Hum Pathol 1980 Sep;11(5 Suppl):549-60
97. Lefkowitch JH, Falkow S, Whitlock RT. Hepatic Hodgkin's disease simulating cholestatic hepatitis with liver failure. Arch Pathol Lab Med. 1985 May;109(5):424-6
98. Lewis WD, Jenkins RL, Rossi RL, Munson L, ReM-

ine SG, Cady B, Braasch JW, McDermott WV. Surgical treatment of biliary cystadenoma. A report of 15 cases. Arch Surg 1988 May;123(5):563-8
99. Ley TJ, Griffith P, Nienhuis AW. Transfusion haemosiderosis and chelation therapy. Clin Haematol 1982 Jun;11(2):437-64
100. Libbrecht L, Craninx M, Nevens F, Desmet V, Roskams T. Predictive value of liver cell dysplasia for development of hepatocellular carcinoma in patients with non-cirrhotic and cirrhotic chronic viral hepatitis. Histopathology 2001 Jul;39(1):66-73
101. Logani S, Lucas DR, Cheng JD, Ioachim HL, Adsay NV. Spindle cell tumours associated with mycobacteria in lymph nodes of HIV-positive patients: 'Kaposi sarcoma with mycobacteria' and 'mycobacterial pseudotumour'. Am J Surg Pathol; 1999;23:656-661
102. Lorenz M, Wiesner J, Staib-Sebler E, Encke A. Regional therapy breast cancer liver metastases. Zentralbl Chir 1995;120(10):786-90
103. Lucas SB, Hounnou A, Peacock C, Beaumel A, Djomand G, N'Gbichi JM, Yeboue K, Honde M, Diomande M, Giordano C, et al. The mortality and pathology of HIV infection in a west African city. AIDS 1993 Dec;7(12):1569-79
104. Ludwig J, MacCarty RL, LaRusso NF, Krom RA, Wiesner RH. Intrahepatic cholangiectases and large-duct obliteration in primary sclerosing cholangitis. Hepatology 1986 Jul-Aug;6(4):560-8
105. Mackay IR, Gershwin ME. Primary biliary cirrhosis: current knowledge, perspectives, and future directions. Semin Liver Dis 1989 May;9(2):149-57
106. Massenkeil G, Opravil M, Salfinger M, von Graevenitz A, Luthy R. Disseminated coinfection with Mycobacterium avium complex and Mycobacterium kansasii in a patient with AIDS and liver abscess. Clin Infect Dis 1992 Feb;14(2):618-9
107. Mathieu D, Zafrani ES, Anglade MC, Dhumeaux D. Association of focal nodular hyperplasia and hepatic hemangioma. Gastroenterology 1989 Jul;97 (1):154-7
108. Matsumoto J, Kondo S, Okushiba S, Morikawa T, Sugiura H, Omi A, Hirano S, Ambo Y, Katoh H, Fujita M, Shimizu M. Biliary cystadenocarcinoma with superficial spread to the extrahepatic bile duct. Hepatogastroenterology 2001 May-Jun;48 (39):647-9
109. McCullough AJ, Fleming CR, Thistle JL, Baldus WP, Ludwig J, McCall JT, Dickson ER. Diagnosis of Wilson's disease presenting as fulminant hepatic failure. Gastroenterology 1983 Jan;84(1):161-7
110. McGowan I, Hawkins AS, Weller IV. The natural history of cryptosporidial diarrhoea in HIV-infected patients.AIDS 1993 Mar;7(3):349-54
111. McLean CA, Pedersen JS. Endocrine cell carcinoma of the gallbladder. Histopathology 1991 Aug;19(2):173-6
112. Melnick PJ. Polycystic liver. Arch Pathol 1955; 59: 162-172
113. Mercadier M, Chigot JP, Clot JP, Langlois P, Lansiaux P. Caroli's disease. World J Surg 1984 Feb;8(1):22-9
114. Mitchell MC, Boitnott JK, Kaufman S, Cameron JL, Maddrey WC. Budd-Chiari syndrome: etiology, diagnosis and management. Medicine (Baltimore) 1982 Jul;61(4):199-218
115. Moertel CG, Fleming TR, Macdonald JS, Haller DG, Laurie JA, Goodman PJ, Ungerleider JS, Emerson WA, Tormey DC, Glick JH, et al. Levamisole and fluorouracil for adjuvant therapy of resected colon carcinoma. N Engl J Med 1990 Feb 8;322(6):352-8
116. Moertel CG, Johnson CM, McKusick MA, Martin JK Jr, Nagorney DM, Kvols LK, Rubin J, Kunselman S. The management of patients with advanced carcinoid tumors and islet cell carcinomas. Ann Intern Med 1994 Feb 15;120(4):302-9
117. Moses SW. Pathophysiology and dietary treatment of the glycogen storage diseases. J Pediatr Gastroenterol Nutr 1990 Aug;11(2):155-74
118. Nakanuma Y. Nodular regenerative hyperplasia of the liver: retrospective survey in autopsy series. J Clin Gastroenterol 1990 Aug;12(4):460-5
119. Nakhleh RE, Glock M, Snover DC. Hepatic pathology of chronic granulomatous disease of childhood. Arch Pathol Lab Med 1992 Jan;116(1):71-5
120. Nezelof C, Frileux-Herbet F, Cronier-Sachot J. Disseminated histiocytosis X: analysis of prognostic factors based on a retrospective study of 50 cases. Cancer 1979 Nov;44(5):1824-38
121. Nichols FC 3rd, van Heerden JA, Weiland LH. Benign liver tumors. Surg Clin North Am1989 Apr;69(2):297-314
122. Nishizaki T, Kanematsu T, Matsumata T, Yasunaga C, Kakizoe S, Sugimachi K. Myelolipoma of the liver. A case report. Cancer 1989 Mar 1;63(5):930-4
123. Odievre M, Gentil C, Gautier M, Alagille D. Hereditary fructose intolerance in childhood. Diagnosis, management, and course in 55 patients. Am J Dis Child 1978 Jun;132(6):605-8
124. Okulski EG, Dolin BJ, Kandawalla NM. Intrahepatic biliary papillomatosis. Arch Pathol Lab Med 1979 Nov;103(12):647-9
125. Popper H, Thomas LB, Telles NC, Falk H, Selikoff IJ. Development of hepatic angiosarcoma in man induced by vinyl chloride, thorotrast, and arsenic. Comparison with cases of unknown etiology. Am J Pathol 1978 Aug;92(2):349-69
126. Proujansky R, Vinton N. Acute Hepatitis. Adolesc Med 1995 Oct;6(3):437-446
127. Qizilbash A, Kontozoglou T, Sianos J, Scully K. Hepar lobatum associated with chemotherapy and metastatic breast cancer. Arch Pathol Lab Med 1987 Jan;111(1):58-61
128. Rabinovitz M, Gavaler JS, Schade RR, Dindzans VJ, Chien MC, Van Thiel DH. Does primary sclerosing cholangitis occurring in association with inflammatory bowel disease differ from that occurring in the absence of inflammatory bowel disease? A study of sixty-six subjects. Hepatology 1990 Jan;11(1):7-11
129. Rakela J, Kurtz SB, McCarthy JT, Ludwig J, Ascher NL, Bloomer JR, Claus PL. Fulminant Wilson's disease treated with postdilution hemofiltration and orthotopic liver transplantation. Gastroenterology 1986 Jun;90(6):2004-7
130. Ramos A, Torres VE, Holley KE, Offord KP, Rakela J, Ludwig J. The liver in autosomal dominant polycystic kidney disease. Implications for pathogenesis. Arch Pathol Lab Med 1990 Feb;114(2):180-4
131. Rappaport AM, MacPhee PJ, Fisher MM, Phillips MJ. The scarring of the liver acini (Cirrhosis).

Tridimensional and microcirculatory considerations. Virchows Arch A Pathol Anat Histopathol 1983;402(2):107-37
132. Reye RDK, Morgan G, Baral J. Encephalopathy and fatty degeneration of the viscera, a disease entity in childhood. Lancet 1963;2:749-752
133. Reynolds TB, Denison EK, Frankl HD, Lieberman FL, Peters RL. Primary biliary cirrhosis with scleroderma, Raynaud's phenomenon and telangiectasia. New syndrome. Am J Med 1971 Mar; 50(3):302-12
134. Reynolds WJ, Wanless IR. Nodular regenerative hyperplasia of the liver in a patient with rheumatoid vasculitis: a morphometric study suggesting a role for hepatic arteritis in the pathogenesis. J Rheumatol 1984 Dec;11(6):838-42
135. Riegler JL. Preneoplastic conditions of the liver. Semin Gastrointest Dis 1996 Apr;7(2):74-87
136. Rossi RL, Silverman ML, Braasch JW, Munson JL, ReMine SG. Carcinomas arising in cystic conditions of the bile ducts. A clinical and pathologic study. Ann Surg 1987 Apr;205(4):377-84
137. Rubin E, Popper H. The evolution of human cirrhosis deduced from observations in experimental animals. Medicine (Baltimore) 1967 Mar; 46(2):163-83
138. Ruers T, Bleichrodt RP. Treatment of liver metastases, an update on the possibilities and results. Eur J Cancer 2002 May;38(7):1023-33
139. Ryan J, Straus DJ, Lange C, Filippa DA, Botet JF, Sanders LM, Shiu MH, Fortner JG. Primary lymphoma of the liver. Cancer 1988 Jan 15;61(2):370-5
140. Ryman BE. The glycogen storage diseases. J Clin Pathol Suppl (R Coll Pathol) 1974;8:106-21
141. Saegusa M, Takano Y, Okudaira M. Human hepatic infarction: histopathological and postmortem angiological studies. Liver 1993 Oct;13(5):239-45
142. Sakamoto M, Hirohashi S, Shimosato Y. Early stages of multistep hepatocarcinogenesis: adenomatous hyperplasia and early hepatocellular carcinoma. Hum Pathol 1991 Feb;22(2):172-8
143. Sanfelippo PM, Beahrs OH, Weiland LH. Cystic disease of the liver. Ann Surg 1974 Jun;179(6):922-5
144. Schafer AI, Cheron RG, Dluhy R, Cooper B, Gleason RE, Soeldner JS, Bunn HF. Clinical consequences of acquired transfusional iron overload in adults. N Engl J Med 1981 Feb 5;304(6):319-24
145. Scheele J, Stang R, Altendorf-Hofmann A, Paul M. Resection of colorectal liver metastases. World J Surg 1995 Jan-Feb;19(1):59-71
146. Scheinberg IH, Sternlieb I, Schilsky M, Stockert RJ. Penicillamine may detoxify copper in Wilson's disease. Lancet 1987 Jul 11;2(8550):95
147. Scheuer PJ. Liver biopsy in the diagnosis of cirrhosis. Gut 1970 Mar;11(3):275-8
148. Schulz W, Borchard F. The size of the liver metastases in a low metastatic count. A quantitative study of postmortem livers. Rofo Fortschr Geb Rontgenstr Neuen Bildgeb Verfahr 1992. Apr;156(4):320-4
149. Scoazec JY, Marche C, Girard PM, Houtmann J, Durand-Schneider AM, Saimot AG, Benhamou JP, Feldmann G. Peliosis hepatis and sinusoidal dilation during infection by the human immunodeficiency virus (HIV). An ultrastructural study. Am J Pathol 1988 Apr;131(1):38-47
150. Scoazec JY, Degott C, Brousse N, Barge J, Molas G, Potet F, Benhamou JP. Non-Hodgkin's lymphoma presenting as a primary tumor of the liver: presentation, diagnosis and outcome in eight patients. Hepatology 1991 May;13(5):870-5
151. Scobie BA, Summerskill WHJ. Hepatic cirrhosis secondary to obstruction of the biliary system. Am J Dig Dis 1965;10:135-146
152. Selinger M, Koff RS. Thorotrast and the liver: a reminder. Gastroenterology 1975 Apr;68(4 Pt 1):799-803
153. Senninger N, Langer R, Klar E, Otto G, Kraus T, Baas J, Herfarth C. Liver transplantation for hepatocellular carcinoma. Transplant Proc 1996 Jun;28(3):1706-7
154. Shortell CK, Schwartz SI. Hepatic adenoma and focal nodular hyperplasia. Surg Gynecol Obstet 1991 Nov;173(5):426-31
155. Simon DM, Krause R, Galambos JT. Peliosis hepatis in a patient with marasmus. Gastroenterology 1988 Sep;95(3):805-9
156. Smetana HF, Olen E. Hereditary galactose disease. Am J Clin Pathol 1962;38:3-25
157. Stanley P, Geer GD, Miller JH, Gilsanz V, Landing BH, Boechat IM. Infantile hepatic hemangiomas. Clinical features, radiologic investigations and treatment of 20 patients. Cancer 1989 Aug 15;64(4):936-49
158. Steele G Jr, Ravikumar TS, Benotti PN. New surgical treatments for recurrent colorectal cancer. Cancer 1990 Feb 1;65(3 Suppl):723-30
159. Sternlieb I. Evolution of the hepatic lesion in Wilson's disease (hepatolenticular degeneration). Prog Liver Dis 1972;4:511-25
160. Stocker JT, Ishak KG. Undifferentiated (embryonal) sarcoma of the liver: report of 31 cases. Cancer 1978 Jul;42(1):336-48
161. Stocker JT, Ishak KG. Mesenchymal hamartoma of the liver: report of 30 cases and review of the literature. Pediatr Pathol 1983 Jul-Sep;1(3):245-67
162. Stromeyer FW, Ishak KG. Histology of the liver in Wilson's disease: a study of 34 cases. Am J Clin Pathol 1980 Jan;73(1):12-24
163. Tamburro CH. Relationship of vinyl monomers and liver cancers: angiosarcoma and hepatocellular carcinoma. Semin Liver Dis 1984 May; 4(2):158-69
164. Tavill AS, Wood EJ, Kreel L, Jones EA, Gregory M, Sherlock S. The Budd-Chiari syndrome: correlation between hepatic scintigraphy and the clinical, radiological, and pathological findings in nineteen cases of hepatic venous outflow obstruction. Gastroenterology 1975 Mar;68(3):509-18
165. Terada T, Terasaki S, Nakanuma Y. A clinicopathologic study of adenomatous hyperplasia of the liver in 209 consecutive cirrhotic livers examined by autopsy. Cancer 1993 Sep 1;72(5):1551-6
166. Trampert L, Benz P, Ruth T, Oberhausen E. Nuclear medicine diagnosis of focal liver lesions. Nuklearmedizin 1993 Aug;32(4):174-7
167. Ueyama T, Ding J, Hashimoto H, Tsuneyoshi M, Enjoji M. Carcinoid tumor arising in the wall of a congenital bile duct cyst. Arch Pathol Lab Med 1992 Mar;116(3):291-3
168. Valla D, Casadevall N, Huisse MG, Tulliez M, Grange JD, Muller O, Binda T, Varet B, Rueff B,

Benhamou JP. Etiology of portal vein thrombosis in adults. A prospective evaluation of primary myeloproliferative disorders.Gastroenterology 1988 Apr;94(4):1063-9
169. Valla D, Flejou JF, Lebrec D, Bernuau J, Rueff B, Salzmann JL, Benhamou JP. Portal hypertension and ascites in acute hepatitis: clinical, hemodynamic and histological correlations. Hepatology 1989 Oct;10(4):482-7
170. Van Steenbergen W, Joosten E, Marchal G, Baert A, Vanstapel MJ, Desmet V, Wijnants P, De Groote J. Hepatic lymphangiomatosis. Report of a case and review of the literature. Gastroenterology 1985 Jun;88(6):1968-72
171. Van Wijk HB, Elias EA. Heptatic and rectal pathology in Schistosoma intercalatum infection. Trop Geogr Med 1975 Sep;27(3):237-48
172. Wada K, Kondo F, Kondo Y. Large regenerative nodules and dysplastic nodules in cirrhotic livers: a histopathologic study. Hepatology 1988 Nov-Dec;8(6):1684-8
173. Walker NI, Horn MJ, Strong RW, Lynch SV, Cohen J, Ong TH, Harris OD. Undifferentiated (embryonal) sarcoma of the liver. Pathologic findings and long-term survival after complete surgical resection. Cancer 1992 Jan 1;69(1):52-9
174. Wallace JM, Hannah JB. Mycobacterium avium complex infection in patients with the acquired immunodeficiency syndrome. A clinicopathologic study.Chest 1988 May;93(5):926-32
175. Wang ZG. Recognition and management of Budd-Chiari syndrome. Experience with 143 patients. Chin Med J (Engl) 1989 May;102(5):338-46
176. Wanless IR. Micronodular transformation (nodular regenerative hyperplasia) of the liver: a report of 64 cases among 2,500 autopsies and a new classification of benign hepatocellular nodules. Hepatology 1990 May;11(5):787-97
177. Wanless IR. Portal vein thrombosis is associated with large regenerative nodules and diffuse nodular hyperplasia in cirrhotic livers. Hepatology 1994;20:412A
178. Wanless IR, Albrecht S, Bilbao J, Frei JV, Heathcote EJ, Roberts EA, Chiasson D. Multiple focal nodular hyperplasia of the liver associated with vascular malformations of various organs and neoplasia of the brain: a new syndrome. Mod Pathol 1989 Sep;2(5):456-62
179. Warren KW, Athanassiades S, Monge JI. Primary sclerosing cholangitis. A study of forty-two cases. Am J Surg 1966 Jan;111(1):23-38
180. Warzok R, Seidlitz G. Mucopolysaccharidoses. Genetics, clinical pathology, therapeutic regimes. Zentralbl Pathol 1992 Jun;138(3):226-34
181. Watanabe S, Okita K, Harada T, Kodama T, Numa Y, Takemoto T, Takahashi T. Morphologic studies of the liver cell dysplasia. Cancer 1983 Jun 15;51(12):2197-205
182. Wedig MP, Altmann C. Hormonal contraception and focal nodular hyperplasia. Zentralbl Gynakol 1991;113(24):1399-402
183. Weinberg AG, Finegold MJ. Primary hepatic tumors of childhood. Hum Pathol 1983 Jun;14(6):512-37
184. Weinbren K, Mutum SS. Pathological aspects of diffuse nodular hyperplasia of the liver. J Pathol 1984 Jun;143(2):81-92
185. Weinbren K, Hadjis NS, Blumgart LH. Structural aspects of the liver in patients with biliary disease and portal hypertension. J Clin Pathol 1985 Sep;38(9):1013-20
186. Weitz H, Gokel JM, Loeschke K, Possinger K, Eder M. Veno-occlusive disease of the liver in patients receiving immunosuppressive therapy. Virchows Arch A Pathol Anat Histol 1982;395(3):245-56
187. White JE, Chase CW, Kelley JE, Brock WB, Clark MO, Inflammatory pseudotumour of the liver associated with extrahepatic infection. South Med J 1997; 90: 23-29
188. Wiesner RH, LaRusso NF. Clinicopathologic features of the syndrome of primary sclerosing cholangitis. Gastroenterology 1980 Aug;79(2):200-6
189. Wiesner RH, LaRusso NF, Ludwig J, Dickson ER. Comparison of the clinicopathologic features of primary sclerosing cholangitis and primary biliary cirrhosis. Gastroenterology 1985 Jan;88(1 Pt 1):108-14
190. Wilkins MJ, Lindley R, Dourakis SP, Goldin RD. Surgical pathology of the liver in HIV infection. Histopathology 1991 May;18(5):459-64
191. Willett CG, Tepper JE, Cohen AM, Orlow E, Welch CE. Failure patterns following curative resection of colonic carcinoma. Ann Surg 1984 Dec;200(6):685-90
192. Yamagata M, Kanematsu T, Matsumata T, Utsunomiya T, Ikeda Y, Sugimachi K. Management of haemangioma of the liver: comparison of results between surgery and observation. Br J Surg 1991 Oct;78(10):1223-5
193. Yasuma T, Yanaka M. Primary sarcoma of the gallbladder—report of three cases. Acta Pathol Jpn 1971 May;21(2):285-304
194. Zafrani ES. Update on vascular tumours of the liver. J Hepatol 1989 Jan;8(1):125-30
195. Zafrani ES, Degos F, Guigui B, Durand-Schneider AM, Martin N, Flandrin G, Benhamou JP, Feldmann G. The hepatic sinusoid in hairy cell leukemia: an ultrastructural study of 12 cases. Hum Pathol 1987 Aug;18(8):801-7
196. Zak FG. Peliosis hepatis. Am J Pathol 1950; 26: 1-15
197. Zavadsky KE, Lee YT. Liver metastases from colorectal carcinoma: incidence, resectability, and survival results. Am Surg 1994 Dec;60(12):929-33
198. Zhang ZD, Myles J, Pai RP, Howard JM. Malignant melanoma of the biliary tract: a case report. Surgery 1991 Mar;109(3 Pt 1):323-8
199. Zieren J, Zieren HU, Muller JM. Liver resections for primary liver malignancies. Personal results and analysis of the literature. Langenbecks Arch Chir 1994;379(3):159-67

3

Contrast Agents for Liver MR Imaging

CONTENTS

3.1 Introduction

The imaging evaluation of patients with suspected liver masses has three principal purposes:

- lesion detection,
- lesion characterization,
- evaluation of the intra- and extrahepatic extent of tumor.

All three of the major non-invasive imaging modalities have roles to play in liver imaging.

Ultrasound (US) has traditionally been used for the primary screening of patients with abdominal pain, but the advent of contrast-enhanced US techniques now makes it a highly capable methodology for both the characterization and improved detection of liver masses [60, 93]. Computed tomography (CT) has generally been considered the imaging approach of choice for the detection of liver masses principally because of the ease of performing and interpreting large numbers of examinations, its widespread availability, and its generally acknowledged superior ability to evaluate the extra-hepatic abdomen [15]. However, until the advent of multi-detector CT (MDCT), the value of conventional CT for the characterization of focal liver lesions was generally considered to be inferior to that of contrast-enhanced magnetic resonance imaging (MRI) [123]. With the recent developments in MDCT technology, particularly the emergence of 16- and 64-row scanners combined with highly concentrated iodinated contrast agents, the impact of CT in both detection, and to a lesser extent, characterization of focal liver lesions has markedly improved [30, 61, 117]. In particular, CT has substantially shorter acquisition times, the possibility to acquire thin sections on a routine basis within a single breath-hold, the opportunity to retrospectively calculate thinner or thicker sections from the same raw data, and improved 3D-postprocessing techniques. These features now permit the acquisition of similar diagnostic information to that attainable on contrast-enhanced MRI with conventional extracellular gadolinium contrast agents, where information derives from differential blood flow between the tumor and surrounding normal liver parenchyma. However, unlike the situation in MRI, there are as yet no hepatospecific contrast agents available for CT. Hence, additional information based on the functionality of liver lesions, which is attainable with MRI, is not yet attainable with MDCT. Moreover, concern over the nephrotoxicity of certain iodinated contrast agents [128] and the requisite use of ionizing radiation in CT examinations are factors which should always be considered when referring patients for diagnostic evaluation of the liver.

In contrast to the situation in CT, several different classes of contrast agent are available for routine clinical use in MRI of the liver [39, 43, 70, 105, 122]. These include non-specific materials that distribute extracellularly in a manner similar to that of the iodinated agents used in CT, materials that are taken up specifically by hepatocytes and ex-

creted in part through the biliary system, and materials that are targeted specifically to the Kupffer cells of the reticuloendothelial system (RES) (Tables 1, 2). The differential use of these agents, depending on the clinical purpose, can maximize the diagnostic information available to the investigating radiologist. This chapter describes the properties and indications for each category of contrast agent for MRI of the liver.

3.1.1 Non-Specific Gadolinium Chelates

Chelates of the paramagnetic gadolinium ion that distribute solely to the extracellular space (i.e. do not have any tissue-specific biodistribution) have been commercially available since 1986 [113, 136, 147]. The four non-specific gadolinium chelates approved in the USA are gadopentetate dimeglumine (Magnevist®, Gd-DTPA; Berlex Laboratories/Schering AG), gadoteridol (ProHance®, Gd-HP-DO3A; Bracco Diagnostics), gadodiamide (Omniscan®, Gd-DTPA-BMA; GE Healthcare), and gadoversetamide (Optimark®, Gd-DTPA-BMEA; Mallinckrodt). Other non-specific gadolinium agents currently approved only in Europe include gadoterate meglumine (Dotarem®, Gd-DOTA; Guerbet) and gadobutrol (Gadovist®, Gd-BT-DO3A; Schering AG) (Table 2). Although the safety profiles of these agents are all extremely attractive, especially in comparison to iodinated x-ray contrast agents [39, 54, 70, 79, 80, 82, 105, 107, 127, 132], possible problems associated with the least stable of these agents (gadodiamide and gadoversetamide) [54] have recently come to light. Specifically, both gadodiamide and gadoverse-

Table 1.

Contrast agent type	Manufacturer	Principal Mechanism
Extracellular Gd agents		
Gadopentetate dimeglumine; Gd-DTPA (Magnevist®)	Schering[1] / Berlex[2]	T1 shortening
Gadoteridol; Gd-HP-DO3A (ProHance®)	Bracco[3,4]	T1 shortening
Gadodiamide; Gd-DTPA-BMA (Omniscan®)	GE Healthcare[5]	T1 shortening
Gadoversetamide; Gd-DTPA-BMEA (OptiMARK®)	Tyco Healthcare[6]	T1 shortening
Gadoterate meglumine; Gd-DOTA (Dotarem®)	Guerbet[7]	T1 shortening
Gadobutrol; Gd-BT-DO3A (Gadovist®)	Schering[1]	T1 shortening
Hepatobiliary agent		
Mangafodipir trisodium; Mn-DPDP (Teslascan®)	GE Healthcare[5]	T1 shortening
Combined extracellular / hepatobiliary agents		
Gadobenate dimeglumine; Gd-BOPTA (MultiHance®)	Bracco[3,4]	T1 shortening
Gadoxetate; Gd-EOB-DTPA (Primovist®)	Schering[1] / Berlex[2]	T1 shortening
SPIO agent		
AMI-25; Ferumoxides (Feridex®; Endorem®)	Berlex[8] / Guerbet[7]	T2 shortening
USPIO agents		
SH U 555 A (Resovist®)	Schering[1]	T1 & T2 shortening
AMI-227 (Combidex®; Sinerem®)	Advanced Magnetics[8] / Guerbet[7]	T1 & T2 shortening

1 = Berlin, Germany; 2 = Wayne NJ, USA; 3 = Milano, Italy; 4 = Princeton NJ, USA; 5 = Chalfont St. Giles, UK; 6 = St. Louis MO, USA; 7 = Aulnay-Sous-Bois, France; 8 = Cambridge MA, USA

Table 2. Physicochemical characteristics of commercially-available T1-shortening MR contrast agents

Characteristic		Extracellular agents						Combined extracellular / hepatobiliary agents		Hepatobiliary agent
		Magnevist (0.5 mol/L)	ProHance (0.5 mol/L)	Omniscan (0.5 mol/L)	OptiMARK (0.5 mol/L)	Dotarem (0.5 mol/L)	Gadovist (1.0 mol/L)	MultiHance (0.5 mol/L)	Primovist (0.25 mol/L)	Teslascan (0.05 mol/L)
Molecular structure		Linear, ionic	Cyclic, non-ionic	Linear, non-ionic	Linear, non-ionic	Cyclic, ionic	Cyclic, non-ionic	Linear, ionic	Linear, ionic	Not applicable
Thermodynamic stability constant (log K_{eq})		22.1	23.8	16.9	16.6	25.8	21.8	22.6	23.4	Not applicable
Conditional stability constant at pH 7.4		18.1	17.1	14.9	15.0	18.8	N/A	18.4	18.7	Not applicable
Osmolality (Osm/kg)		1.96	0.63	0.65	1.11	1.35	1.6	1.97	0.69	0.30
Viscosity (mPa•s at 37°C)		2.9	1.3	1.4	2.0	2.0	4.96	5.3	1.19	0.8
r1 relaxivity in plasma (L/mmol•s^{-1})	0.2 T	4.7[a]	NA	NA	NA	NA	5.5[a]	10.9[a]	NA	NA
	0.47 T	4.8[b], 3.8[c], 4.9[d]	4.9[b], 4.8[c]	4.4[b], 4.4[c]	5.7[c]	4.3[c]	5.6[b], 6.1[c]	9.2[c], 9.7[d]	8.7[c], 8.7[e]	3.6[c]
	1.5 T	3.9[a], 4.1[c]	4.1[c]	4.3[c]	4.7[c]	3.6[c]	4.7[a], 5.2[c]	8.1[a], 6.3[c]	6.9[c]	3.6[c]
	3 T	3.3[a], 3.7[c]	3.7[c]	4.0[c]	4.5[c]	3.5[c]	3.6[a], 5.0[c]	6.3[a], 5.5[c]	6.2[c]	2.7[c]
r2 relaxivity in plasma (L/mmol•s^{-1})	0.2 T	9.6[a]	NA	NA	NA	NA	10.1[a]	18.9[a]	NA	NA
	0.47 T	4.1[c], 6.3[d]	6.1[c]	4.6[c]	5.7[c]	5.5[c]	7.4[c]	12.9[c], 12.5[d]	13.0[c], 8.7[e]	4.3[c]
	1.5 T	5.3[a], 4.6[c]	5.0[c]	5.2[c]	6.6[c]	4.3[c]	6.8[a], 6.1[c]	18.7[a], 8.7[c]	8.7[c]	7.1[c]
	3 T	5.2[a], 5.2[c]	5.7[c]	5.6[c]	5.9[c]	4.9[c]	6.3[a], 7.1[c]	17.5[a], 11.0[c]	11.0[c]	9.3[c]

NA = not available ; a = Pintaske et al [88].; b = Vogler et al [141]; c = Rohrer et al.[100]; d = De Haen et al.[20], e = Schuhmann-Giampieri [119]
n.b. r1 and r2 relaxivity values from Rohrer et al. were determined from curves of relaxation rate versus concentration for just two concentrations of contrast agent and hence are subject to variability. Values from Pintaske et al. were determined for a minimum of eight contrast agent concentrations.

tamide, but none of the other approved gadolinium agents, have been shown to cause spurious hypocalcemia as a result of interference with laboratory tests for serum calcium [25, 54, 71, 90, 91]. The issue of gadolinium chelate stability in the case of gadodiamide has also been raised in a study to determine the extent to which gadolinium is deposited in bone following intravenous injection of this agent [33].

As paramagnetic compounds, gadolinium chelates shorten T1 tissue relaxation times when injected intravenously. At recommended doses of 0.1-0.3 mmol/kg their principal effect is to shorten the T1 relaxation time resulting in an increase in tissue signal intensity. This effect is best captured on heavily T1-weighted images [64, 69, 124]. Due to rapid redistribution of gadolinium chelates from the intravascular compartment to the extracellular space, the contrast agents must be administered as a rapid bolus, typically at 2-3 ml/sec. Thereafter, imaging of the entire liver is performed in a single breath-hold during the dynamic phase of contrast enhancement. This is most commonly undertaken with a 2D or 3D T1-weighted spoiled GRE sequence with serial imaging in the arterial dominant phase (25-30 sec post-injection), the portal-venous phase (60-80 sec post-injection), and the equilibrium phase (3-5 min post-injection).

A schematic representation of the enhancement behavior seen after the bolus injection of non-specific extracellular gadolinium chelates is shown in Fig. 1. In the hepatic arterial dominant phase, enhancement occurs principally in the arterial tree and mainly in arterially-perfused tissues and tumors [22, 72, 81, 148, 150]. This is important since most focal lesions, especially primary liver tumors like hepatocellular carcinoma (HCC) and metastases are supplied primarily via the hepatic arteries [41, 72, 148]. Enhancement during the arterial dominant phase is important in order to detect perfusion abnormalities. For example, transient increased segmental enhancement in liver segments may indicate that portal-venous flow is compromised due to compression or thrombosis [114, 152]. This can be of value in patients where findings on unenhanced images are equivocal.

Typically, maximal enhancement of the hepatic parenchyma is seen in the portal-venous phase. In this phase, hypovascular lesions such as cysts, hypovascular metastases and scar tissue are most clearly revealed as regions of absent or diminished enhancement [41]. Patency or thrombosis of hepatic vessels is also best shown during this phase.

Enhancement of tissues with enlarged extracellular spaces, such as focal liver lesions and scars of focal nodular hyperplasia (FNH), is usually best seen in the equilibrium phase. Likewise, typical signs of malignancy, such as peripheral wash-out in colorectal metastases, are best seen during the equilibrium phase. Such features frequently contribute to accurate lesion characterization [73, 74].

Imaging with gadolinium during the arterial phase has been shown to improve the rate of detection of suspected HCC in cirrhotic patients compared to unenhanced imaging [81, 150, 152]. For lesion characterization, characteristic enhancement patterns have been identified for a variety of benign and malignant masses (Figs. 2, 3) of both hepatocellular and non-hepatocellular origin [26, 41, 42, 72–74, 148].

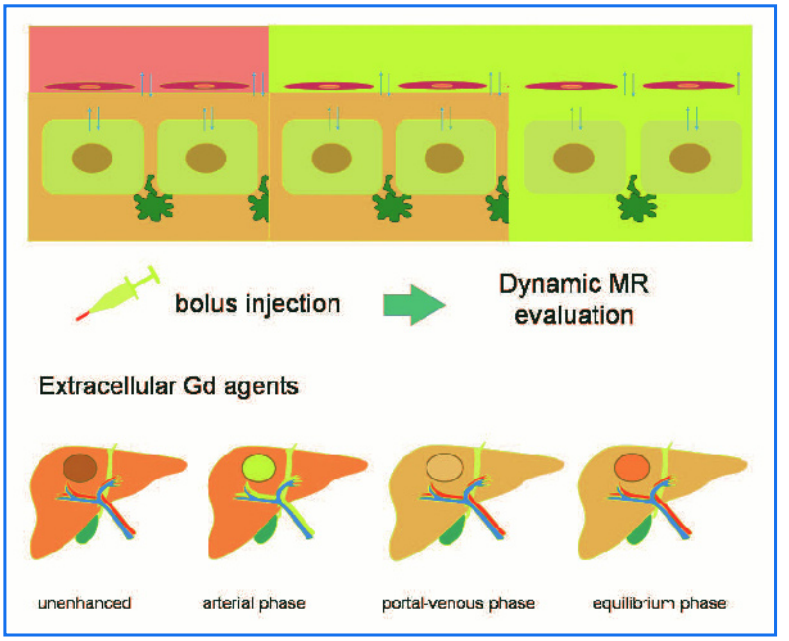

Fig 1. Enhancement scheme of the liver after injection of extracellular gadolinium chelates. Extracellular Gadolinium chelates initially distribute to the intravascular space and then rapidly filter into the extracellular space of normal tissue

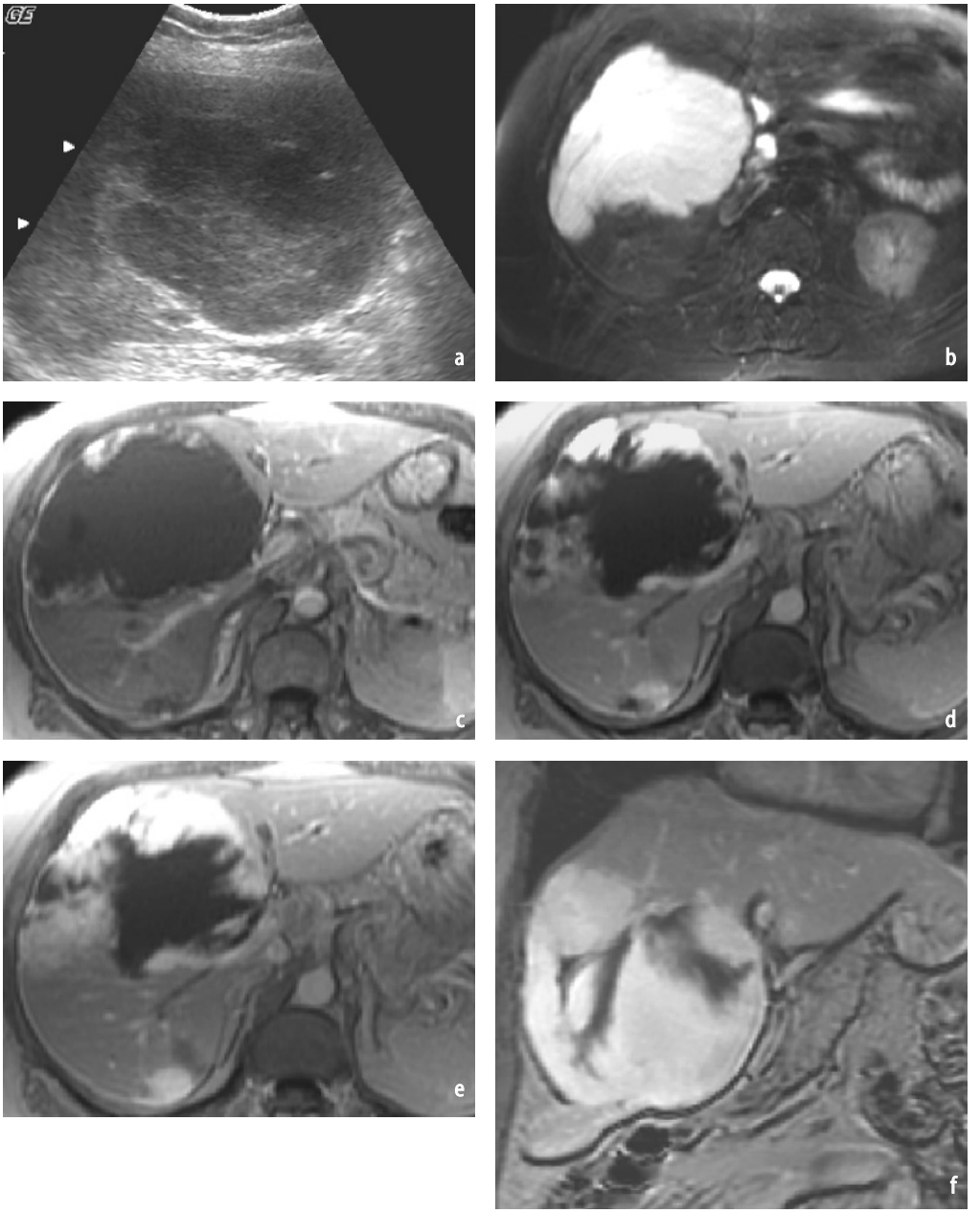

Fig. 2a-f. Hemangioma. A large hypoechoic mass noted in the liver on ultrasound (**a**) is seen as hyperintense on the T2-weighted MR image (**b**). With dynamic T1-weighted imaging following the bolus administration of Gd-DTPA, the lesion demonstrates intense peripheral nodular enhancement with progressive filling-in on the arterial (**c**), early and late portal-venous (**d** and **e**, respectively) and equilibrium (**f**) phase images. The enhancement pattern is characteristic of a benign hemangioma

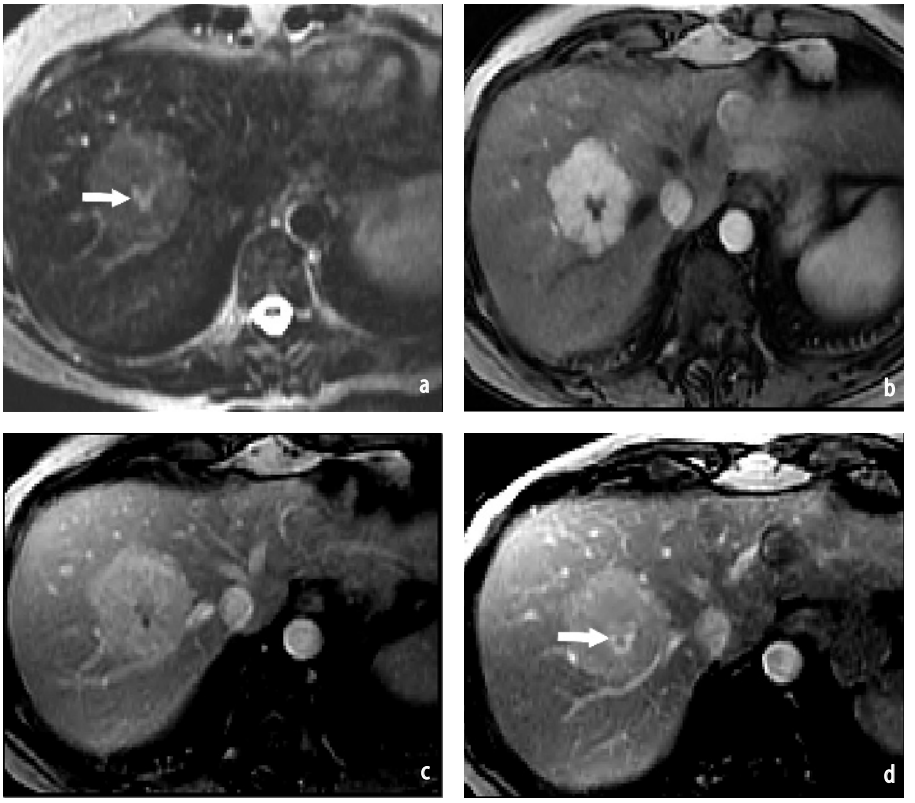

Fig. 3a-d. Focal nodular hyperplasia. A large well-defined mass in the liver is seen as hyperintense in comparison to the normal background parenchyma on the T2-weighted fast spin-echo image (**a**). A bright central scar (*arrow*) is also evident. Dynamic T1-weighted imaging following the administration of Gd-DTPA reveals that the lesion shows intense enhancement during the arterial phase (**b**) followed by rapid wash-out during the portal-venous (**c**) phase. The central scar is seen as hypointense on the arterial phase image and as hyperintense on the equilibrium phase image (**d**) (*arrow*)

3.1.2 Hepatocyte-Targeted Contrast Agents

Hepatocyte-selective contrast agents are taken up by hepatocytes and are eliminated, at least in part, through the biliary system. A prototypical, dedicated hepatocyte-selective contrast agent is mangafodipir trisodium (Teslascan®, Mn-DPDP; GE Healthcare) which was approved for clinical use in 1997 [23, 42, 70, 98, 105, 122, 143]. As with gadolinium chelates, mangafodipir trisodium is considered to have an acceptable safety profile although injection-related minor adverse events such as flushing, nausea and dizziness are relatively common [5, 27, 67, 98]. Moreover, Mn-DPDP dissociates rapidly following administration to yield free Mn^{++} ions [31]) which, in patients with hepatic impairment, may be associated with increased neurological risk [44, 77].

Like the gadolinium agents, mangafodipir trisodium is a paramagnetic contrast agent and primarily affects T1 relaxation times [135]. The increased signal intensity generated in functioning hepatocytes improves the contrast against non-enhancing tissues on T1-weighted images [5, 9, 27, 78, 108, 137]. A schematic representation of the enhancement behavior seen after administration of hepatobiliary agents such as mangafodipir trisodium is shown in Fig. 4.

This agent is administered as a slow intravenous infusion over 1-2 min, which unfortunately precludes dynamic phase imaging in the manner performed with gadolinium-based agents [5, 47]. Moreover, because the 5-10 mmol/kg dose of mangafodipir is 10% or less than that of the gadolinium agents, imaging with mangafodipir during its distribution phase in the extracellular fluid compartment does not contribute to diagnosis. Doses above 10 mmol/kg also do not contribute any additional enhancement [5, 143]. Liver enhancement is maximal within 10 min of mangafodipir trisodium infusion and persists for several hours. Since dynamic images are not acquired with this agent, any T1-weighted sequences can be used. Fat saturation has been shown to improve contrast [99, 108, 137]. More importantly, higher spatial resolu-

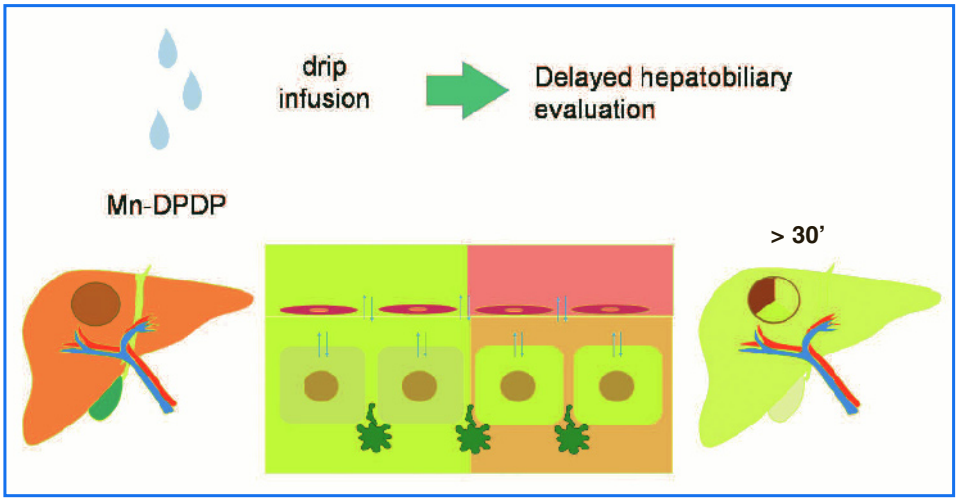

Fig. 4. Hepatobiliary agents such as mangafodipir trisodium (Mn-DPDP, Teslascan®) are taken up by hepatocytes and imaging is performed during a delayed hepatobiliary phase

tion imaging can be used effectively even if the entire liver cannot be covered in one data acquisition. On state of the art scanners, a useful sequence would be a 2D or 3D spoiled GRE sequence with a matrix size of 512/256 x 512 (Fig. 5).

Because liver enhancement in patients with cirrhosis is limited with mangafodipir trisodium [69], liver lesion detection on mangafodipir-enhanced MR imaging is primarily effective in patients with normal liver parenchyma. In these patients, non-hepatocellular focal lesions generally appear hypointense compared to the normal liver on post-contrast T1-weighted images [6, 144].

Several studies have shown a benefit for liver lesion detection with mangafodipir-enhanced hepatic MR imaging compared with unenhanced MRI [5, 6, 27, 137, 143, 144]. Moreover, since hepatocellular lesions such as FNH, hepatic adenoma and HCC generally enhance with mangafodipir, it is frequently possible to differentiate lesions of hepatocellular origin from lesions of non-hepatocellular origin [78, 83, 102]. Unfortunately, because mangafodipir often causes the enhancement of both benign and malignant lesions of hepatocellular origin, it is not always possible to differentiate between benign and malignant lesions [16]. In a study of 77 patients with histologically-confirmed diagnoses, the sensitivity and specificity of mangafodipir-enhanced MRI for the differentiation of histologically-confirmed malignant versus benign lesions was 91% and 67%, respectively, while that for the differentiation of hepatocellular versus non-hepatocellular lesions was 91% and 85%, respectively [83]. Enhancement of both benign and

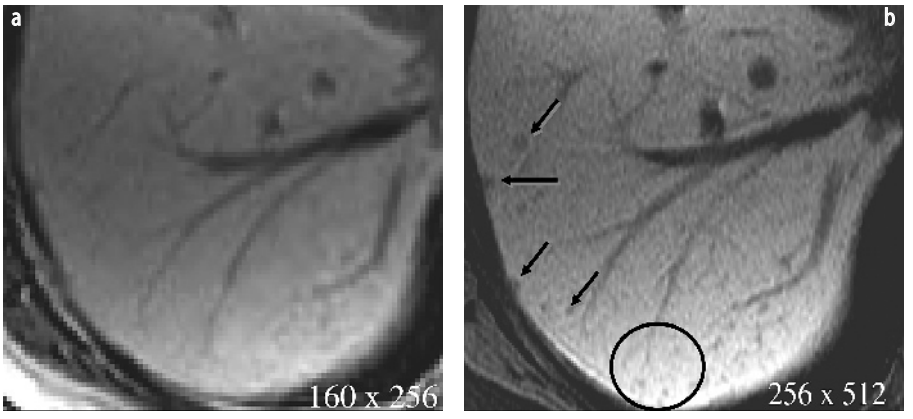

Fig. 5a, b. Detection of liver metastasis with mangafodipir trisodium in a young male patient with primary colorectal cancer. Post-mangafodipir-enhanced images obtained with standard (128 x 256) resolution (**a**) and high (256 x 512) resolution (**b**) are shown. Compared to the routine T1-weighted gradient-echo image more lesions (*arrows, circle*) are seen with the high resolution technique

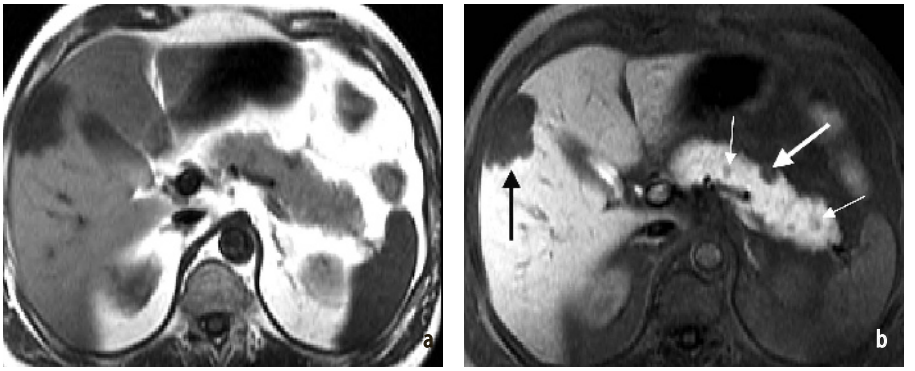

Fig. 6a, b. Mangafodipir-enhanced MRI of the pancreas in a middle-aged man with a history of sarcoma. Compared to the pre-contrast T1-weighted image (**a**) strong enhancement of the pancreas is seen on delayed images after the administration of mangafodipir (**b**). Multiple metastatic deposits in the pancreas (*white arrows*) are much better appreciated on the T1-weighted fat-suppressed post-contrast image. Additionally, the conspicuity of the lesions in the liver is improved (*black arrow*)

malignant hepatocellular neoplasms limits the usefulness of this agent for the accurate differentiation of hepatocellular lesions and this, combined with the frequent need for delayed imaging at 4-24 hrs post-contrast [102], represents the principal shortcoming of this agent [9, 16, 78, 83, 99] .

Apart from the inability to adequately differentiate benign from malignant lesions of hepatocellular origin, a further potential limitation of mangafodipir-enhanced liver MRI appears to be inadequate characterization of non-hepatocellular lesions. Common benign tumors such as hemangiomas and cysts, as well as non-neoplastic masses such as focal fatty infiltration and focal fat sparing may mimic malignancy in patients with known or suspected cancer. In these settings Gd-chelate-enhanced dynamic multiphase MRI is invaluable for satisfactory lesion characterization.

Although mangafodipir trisodium is primarily considered an agent for MRI of the liver, a number of early studies demonstrated a potential usefulness for imaging of the pancreas (Fig. 6) as well [32, 68, 76].

Moreover, since the Mn^{++} ion is excreted in part through the biliary system, mangafodipir trisodium may prove effective for biliary tract imaging [65].

3.1.3 Agents with Combined Extracellular and Hepatocyte-Specific Distribution

In 1998, gadobenate dimeglumine (MultiHance®, Gd-BOPTA; Bracco Imaging SpA) became available in Europe for MRI of the liver. Today, gadobenate dimeglumine is approved in Europe and other parts of the world for MRI of the liver, and in the United States, Europe and other parts of the world for MRI of the central nervous system and related tissues [2, 17, 18, 19, 58, 103, 115]. It is also under development for other indications including MR angiography and MRI of the breast and heart [3, 14, 55, 57, 59, 62, 86, 92, 111, 112, 115, 142, 149].

Gadobenate dimeglumine differs from the purely extracellular gadolinium agents as it combines the properties of a conventional non-specific gadolinium agent with those of an agent targeted specifically to hepatocytes [2, 52, 98]. With this agent it is possible to perform both dynamic phase imaging as performed with conventional gadolinium-based agents, and delayed phase imaging as performed with mangafodipir trisodium [37, 49, 50, 51, 87, 89]. Thus, arterial, portal-venous and equilibrium phase images are readily attainable using identical sequences to those employed with the conventional non-specific gadolinium agents [116]. Unlike the conventional agents, however, approximately 3-5% of the injected dose of gadobenate dimeglumine is taken up by functioning hepatocytes and ultimately excreted via the biliary system [129]. As with mangafodipir, a result of the hepatocytic uptake is that the normal liver parenchyma shows strong enhancement on delayed T1-weighted images that is maximal approximately 1 hr after administration [11, 129, 130].

A schematic representation of the enhancement behavior seen after administration of dual agents such as gadobenate dimeglumine is shown in Fig. 7.

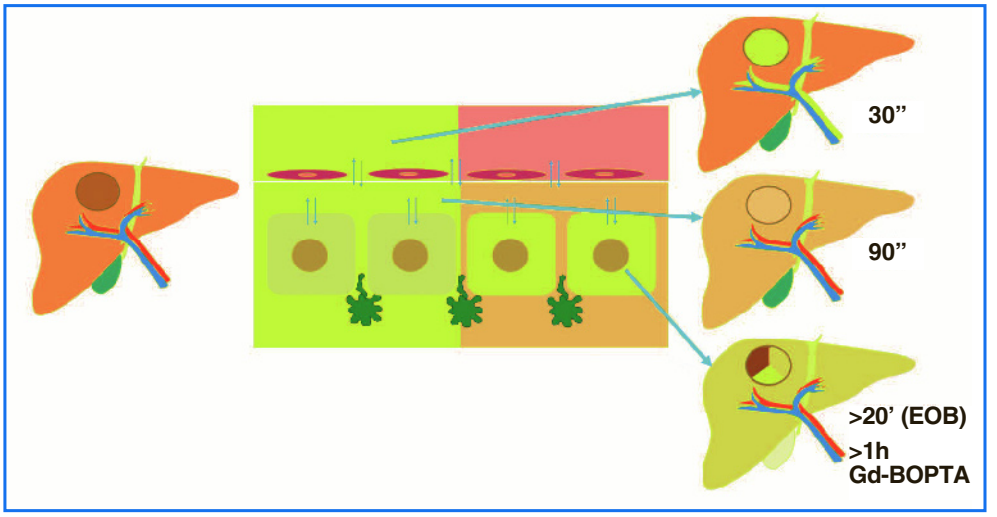

Fig. 7. Combined extracellular/hepatobiliary agents such as Gd-BOPTA and Gd-EOB-DTPA distribute initially to the intravascular and extravascular spaces and then, like Mn-DPDP, are taken up by hepatocytes via a specific transporter

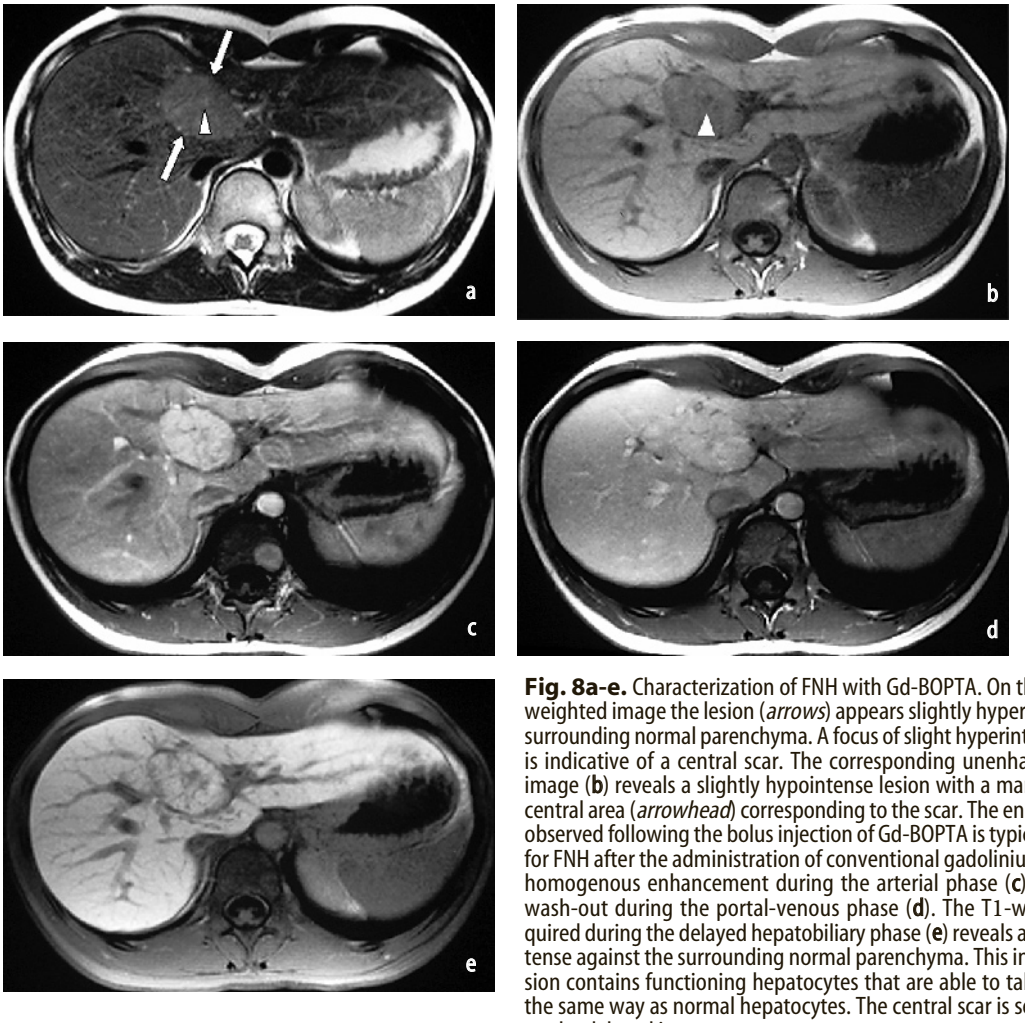

Fig. 8a-e. Characterization of FNH with Gd-BOPTA. On the unenhanced T2-weighted image the lesion (*arrows*) appears slightly hyperintense against the surrounding normal parenchyma. A focus of slight hyperintensity (*arrowhead*) is indicative of a central scar. The corresponding unenhanced T1-weighted image (**b**) reveals a slightly hypointense lesion with a markedly hypointense central area (*arrowhead*) corresponding to the scar. The enhancement pattern observed following the bolus injection of Gd-BOPTA is typical of that observed for FNH after the administration of conventional gadolinium agents, i.e. rapid homogenous enhancement during the arterial phase (**c**) followed by rapid wash-out during the portal-venous phase (**d**). The T1-weighted image acquired during the delayed hepatobiliary phase (**e**) reveals a lesion that is isointense against the surrounding normal parenchyma. This indicates that the lesion contains functioning hepatocytes that are able to take up Gd-BOPTA in the same way as normal hepatocytes. The central scar is seen as hypointense on the delayed image

A second feature unique to gadobenate dimeglumine is that the contrast-effective moiety of this agent interacts weakly and transiently with serum albumin [12, 20]. This interaction slows the tumbling rate of the Gd-BOPTA chelate and results in a longer rotational correlation time with inner shell water protons for Gd-BOPTA compared to gadolinium agents that do not interact with serum albumin. This in turn results in a T1 relaxivity in human plasma that is approximately twice that of the conventional gadolinium agents [20, 88] (Table 2). Not only does this increased relaxivity permit lower overall doses to be used to acquire the same information in the dynamic phase as available with conventional agents at a standard dose of 0.1 mmol/kg [116], it also facilitates the improved performance of gadobenate dimeglumine for both intra- and extrahepatic vascular imaging [57, 92].

A principal advantage of the selective uptake by functioning hepatocytes is that the normal liver enhances, while tumors of non-hepatocytic origin, such as metastases (Fig. 9) and cholangiocellular carcinoma (Fig. 10), as well as non-functioning hepatocytic tumors that are unable to take up Gd-BOPTA (Fig. 11), remain unenhanced, thereby increasing the liver-lesion contrast-to-noise ratio (CNR) and hence the ability to detect lesions [11, 89, 104, 129].

Imaging is typically performed with 2D or 3D T1-weighted GRE sequences while the use of fat saturation has been shown to improve CNR on delayed, hepatobiliary phase images. In the delayed hepatobiliary phase, high-resolution imaging is recommended.

Clinical studies and routine clinical practice have shown that dynamic phase imaging is particularly important for lesion characterization (Fig. 12), while delayed phase imaging in the hepatobiliary phase increases the sensitivity of MRI for liver lesion detection [11, 87, 89]. However, delayed phase imaging can also contribute to the improved characterization of lesions, particularly when the results of unenhanced and dynamic imaging are equivocal or when atypical enhancement patterns are noted on dynamic imaging [35, 36]. A particularly interesting and clinically important finding concerning the characterization of lesions on delayed hepatobiliary phase imaging after gadobenate dimeglumine administration is that focal nodular hyperplasia can be accurately differentiated from hepatic adenoma, thereby eliminating the need for lesion biopsy [37].

In addition to the hepatic imaging capability of this agent, its partial biliary excretion also facilitates its use for biliary tract imaging (Fig. 13), while the increased relaxivity deriving from weak protein interaction may prove beneficial for hepatic MR angiography (Fig. 14). Both of these features have proven advantageous for the pre-operative evaluation of potential liver donors in transplant surgery [34, 66]. Finally, preliminary studies have already indicated its potential for MR colonography [56].

A second agent with combined extracellular and hepatobiliary properties is gadolinium ethoxybenzyldiethylenetriaminepentaacetic acid (Primovist®, Gd-EOB-DTPA; Schering AG, Germany) which has recently been approved for use in Europe, albeit at a formulation of only 0.25 mol/L and at an approved dose of only 0.025 mmol/kg bodyweight [40, 97, 140] (Table 2). Like Gd-BOPTA, this agent has a higher T1 relaxivity compared to the conventional extracellular agents [97] and distributes initially to the vascular and interstitial compartment after bolus injection. However, whereas only 3-5% of the injected dose of Gd-BOPTA is taken up by hepatocytes and eliminated in the bile, in the case of Gd-EOB-DTPA, 50% of the injected dose is taken up and eliminated via the hepatobiliary pathway after approximately 60 min [40, 118]. The maximum increase of liver parenchyma signal intensity is observed approximately 20 min after injection and lasts for approximately 2 hrs [40, 106, 118, 119, 120, 140].

As with Gd-BOPTA, the dynamic enhancement patterns seen during the perfusion phase after injection of Gd-EOB-DTPA are similar to those seen with Gd-DTPA. During the hepatobiliary phase, Gd-EOB-DTPA-enhanced images have been shown to significantly improve the detection rate of metastases, HCC, and hemangiomas (Figs.15, 16), compared with unenhanced and Gd-DTPA-enhanced images [45, 46, 97, 140]. Moreover, Gd-EOB-DTPA may also be a suitable agent for biliary imaging [10].

Like Gd-BOPTA [53], Gd-EOB-DTPA has a safety profile that is not dissimilar from those of the conventional extracellular gadolinium agents [8, 40, 97].

3.1.4 RES-Specific Contrast Agents

Iron oxide particulate agents are selectively taken up by Kupffer cells of the reticulo-endothelial system (RES), primarily in the liver [39, 121], but also in the spleen and the bone marrow. Iron oxide particles of different sizes have been developed which are referred to as superparamagnetic iron oxides (SPIO, mean size > 50 nm) and ultrasmall superparamagnetic iron oxides (USPIO, mean particle size < 50 nm). Of the various formulations, two have so far been developed clinically for MR imaging: ferumoxides (Feridex®, Berlex Laboratories and Endorem®, Laboratoire Guerbet) which has particles ranging between 50 and 180 nm and SH U 555 A (Resovist®, Schering AG) which has

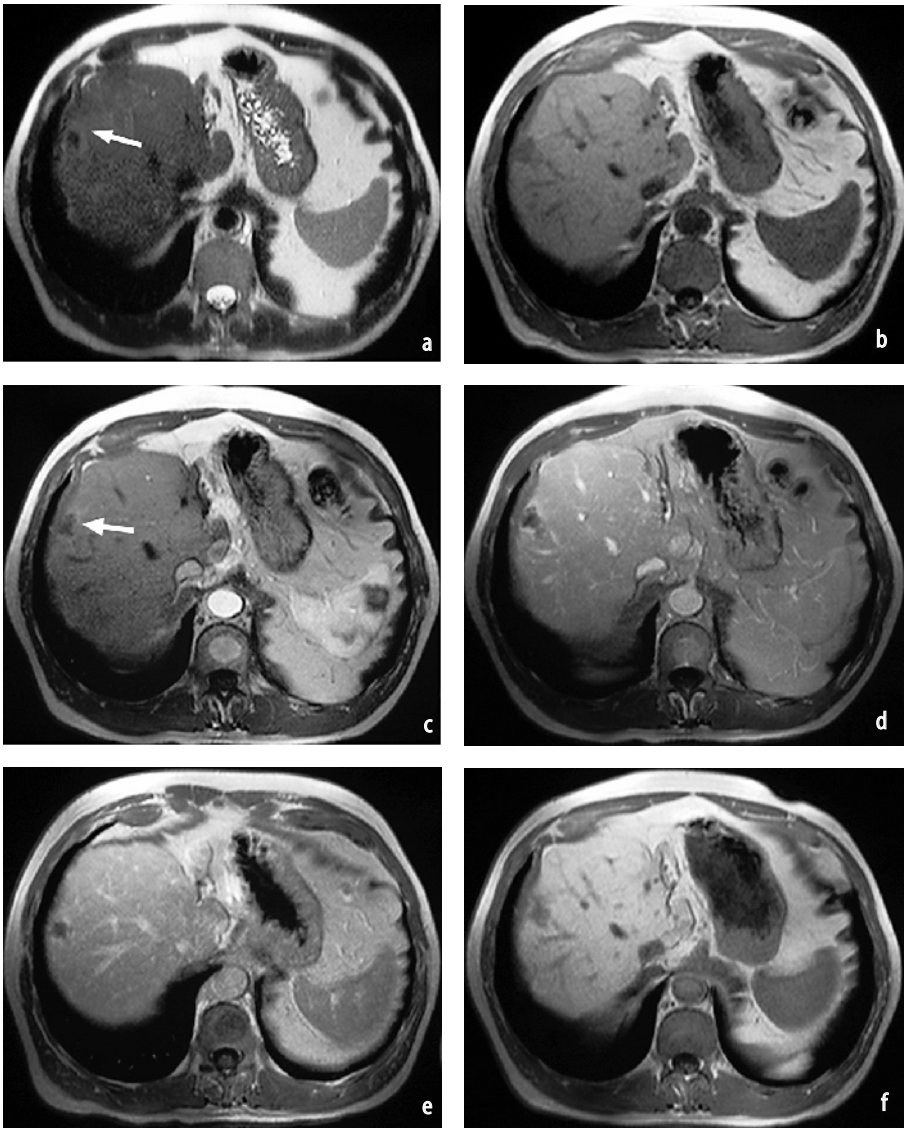

Fig. 9a-f. Characterization of hypovascular metastasis with Gd-BOPTA. Unenhanced T2-weighted and T1-weighted images (**a** and **b**, respectively) both reveal a lesion that is hypointense against the normal liver parenchyma (*arrow* in **a**). The lesion remains hypointense with a hyperintense peripheral rim on arterial (*arrow* in **c**), portal-venous (**d**) and equilibrium (**e**) phase images acquired after the administration of Gd-BOPTA. The hyperintense appearance of the rim is due to the presence of peripheral edema. On the T1-weighted image acquired during the delayed hepatobiliary phase (**f**) the lesion is still hypointense against a strongly enhanced surrounding normal parenchyma. This indicates that the lesion does not take up Gd-BOPTA and is therefore malignant in nature

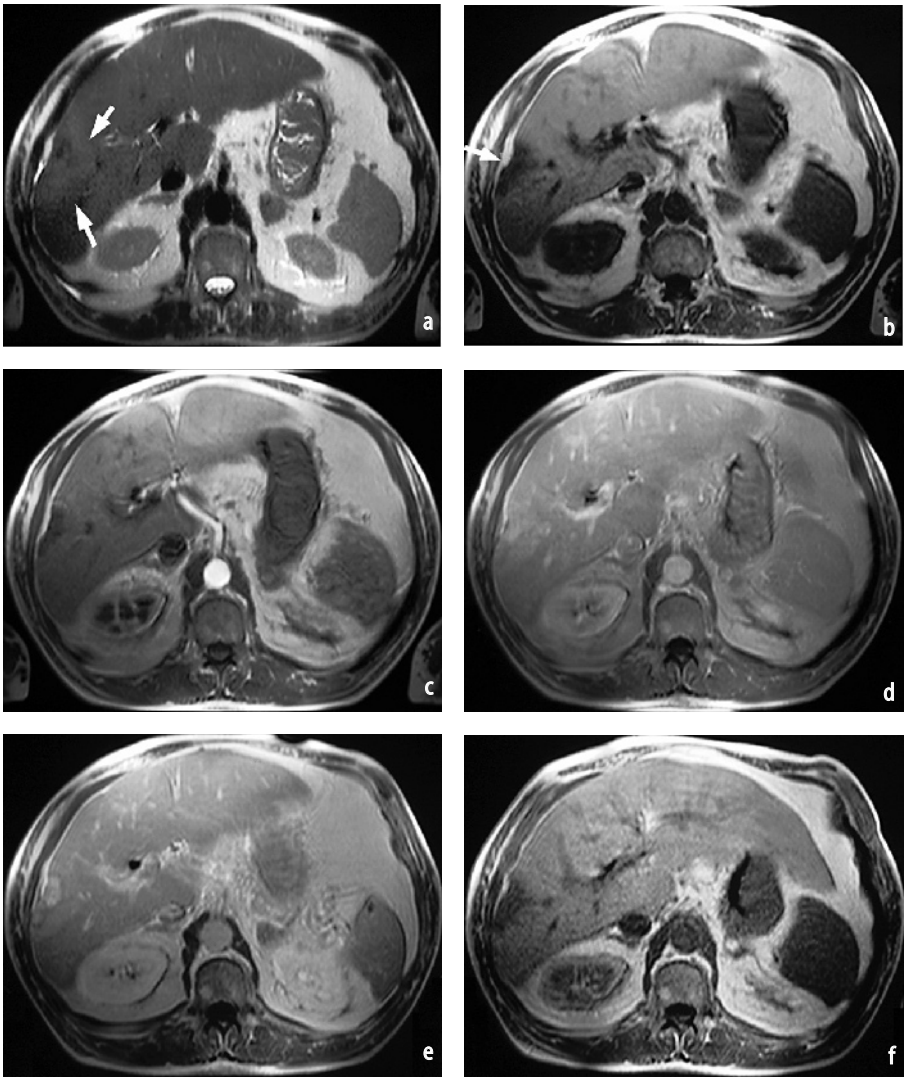

Fig. 10a-f. Characterization of cholangiocellular carcinoma with Gd-BOPTA. The unenhanced T2-weighted image (**a**) reveals a liver of low signal intensity in which a faint area of high signal intensity can be seen in the right lobe (*arrows*). On the unenhanced T1-weighted image (**b**) a marked area of hypointensity is apparent. In addition, capsular retraction is evident (*arrow*). The lesion retains an initial hypointense appearance on the T1-weighted arterial phase image acquired after the bolus administration of Gd-BOPTA (**c**), but thereafter demonstrates progressive delayed heterogeneous enhancement during the portal-venous and equilibrium phase images (**d** and **e**, respectively). On the T1-weighted image acquired during the delayed hepatobiliary phase (**f**) the lesion is again hypointense compared to surrounding normal parenchyma indicating that the lesion is malignant in nature

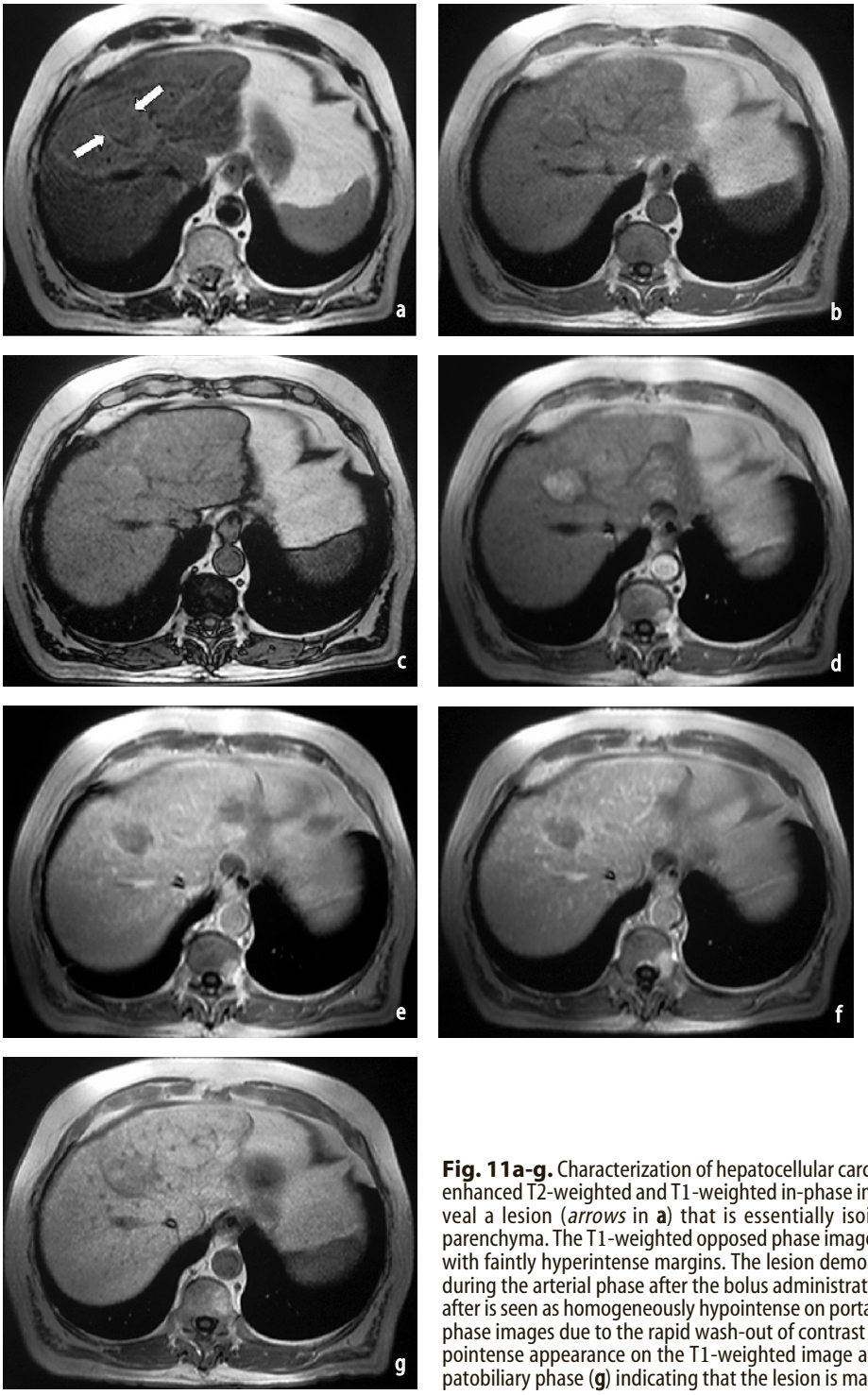

Fig. 11a-g. Characterization of hepatocellular carcinoma with Gd-BOPTA. The unenhanced T2-weighted and T1-weighted in-phase images (**a** and **b**, respectively) reveal a lesion (*arrows* in **a**) that is essentially isointense with the normal liver parenchyma. The T1-weighted opposed phase image (**c**) reveals an isointense lesion with faintly hyperintense margins. The lesion demonstrates marked hyperintensity during the arterial phase after the bolus administration of Gd-BOPTA (**d**), but thereafter is seen as homogeneously hypointense on portal-venous (**e**) and equilibrium (**f**) phase images due to the rapid wash-out of contrast agent. The lesion retains its hypointense appearance on the T1-weighted image acquired during the delayed hepatobiliary phase (**g**) indicating that the lesion is malignant in nature

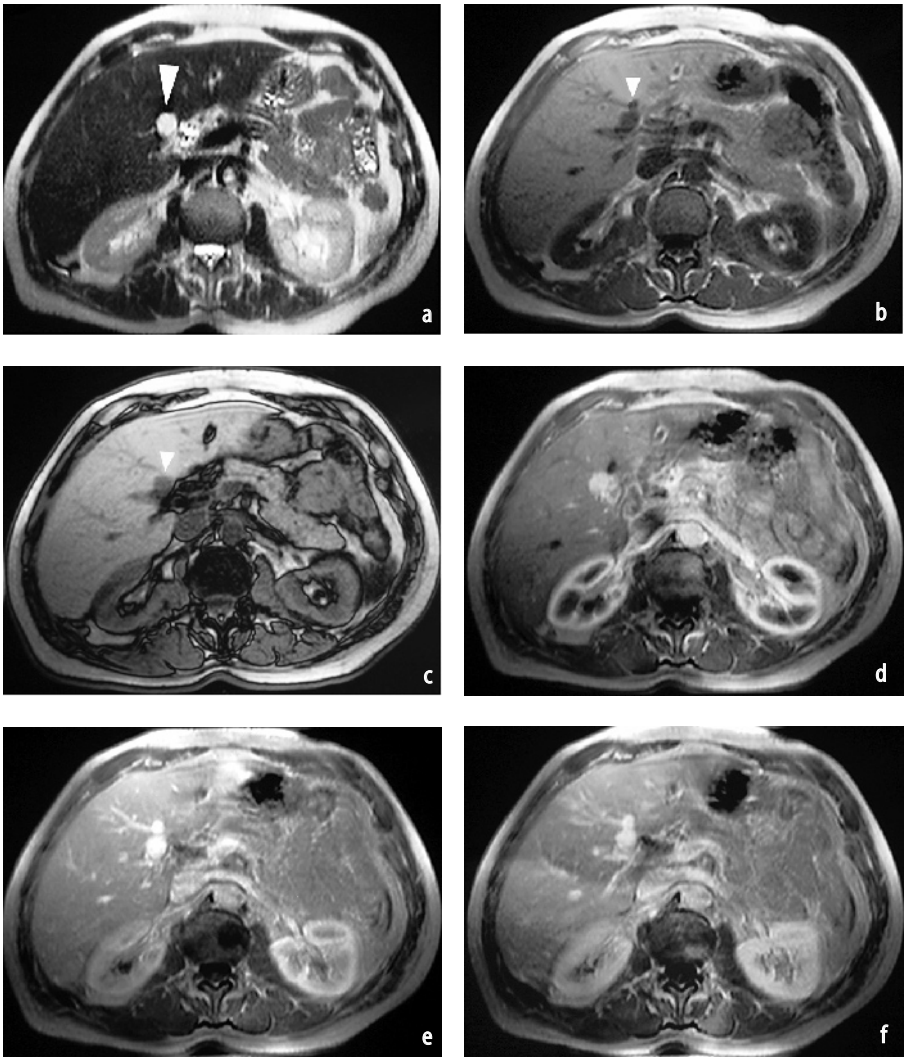

Fig. 12a-f. Characterization of capillary hemangioma with Gd-BOPTA. A markedly hyperintense lesion (*arrowhead*) on the unenhanced T2-weighted image (**a**) is seen as hypointense on the unenhanced T1-weighted in-phase and opposed phase images (**b** and **c**, respectively, *arrowheads*). The lesion demonstrates marked hyperintensity during the arterial phase after the bolus administration of Gd-BOPTA (**d**) and retains this hyperintense appearance on the subsequent portal-venous (**e**) and equilibrium (**f**) phase images. The persistent hyperintense appearance on the equilibrium phase image is an indication of the benign nature of the lesion

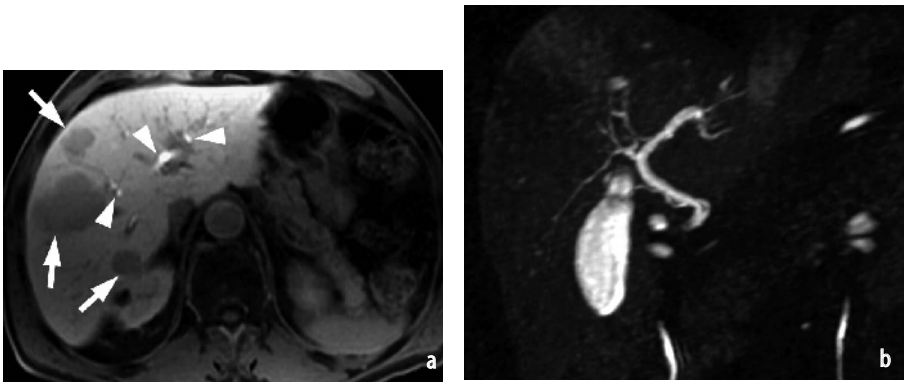

Fig. 13a, b. The T1-weighted fat-suppressed image (**a**) in the hepatobiliary phase after injection of Gd-BOPTA depicts multiple hypointense liver metastases (*arrows*). In addition, the bile ducts (*arrowheads*) are shown with a high SI due to the hepatobiliary excretion of the contrast agent. This high SI of the bile ducts allows for T1-weighted 3D-GRE imaging with calculation of MIP images (**b**) from the 3D raw data. Continuity and normal functionality of the bile duct structures as far as the papillary region is demonstrated due to excretion of the contrast agent with the bile. For bile duct imaging it is advisable to inject a dose of 0.1 mmol/kg bodyweight Gd-BOPTA and to perform imaging approximately 1.5-2 hours post-contrast agent injection to reduce the signal from the background

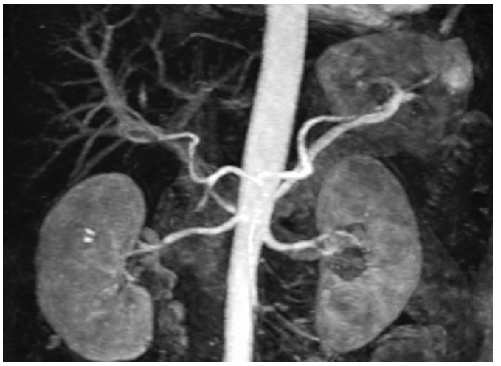

Fig. 14. Contrast-enhanced MR angiography (MRA) after injection of Gd-BOPTA demonstrating normal hepatic vasculature

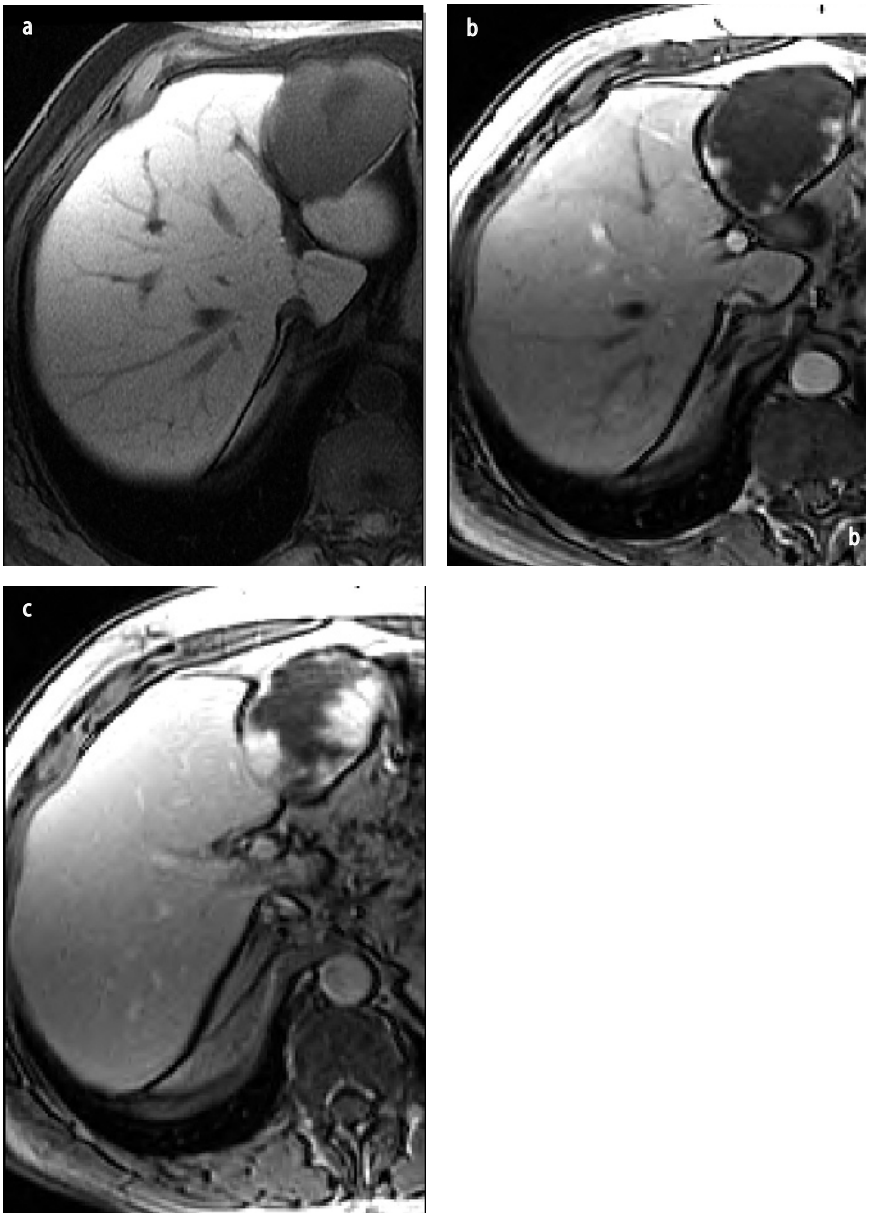

Fig. 15a-c. Hemangioma after Gd-EOB-DTPA. A hypointense lesion on the unenhanced T1-weighted image (**a**) demonstrates the enhancement pattern (peripheral nodular enhancement with progressive filling-in) typical of hemangioma on T1-weighted images acquired during the arterial (**b**) and portal-venous (**c**) phases after the administration of Gd-EOB-DTPA

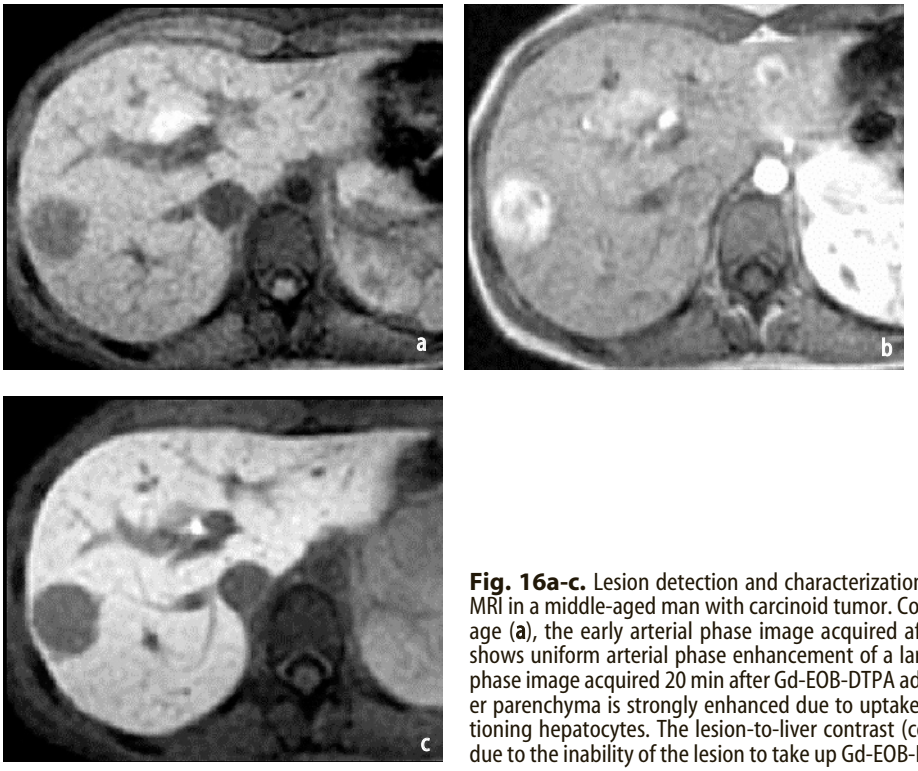

Fig. 16a-c. Lesion detection and characterization with Gd-EOB-DTPA-enhanced MRI in a middle-aged man with carcinoid tumor. Compared to the pre-contrast image (**a**), the early arterial phase image acquired after Gd-EOB-DTPA injection (**b**) shows uniform arterial phase enhancement of a large liver lesion. On the delayed phase image acquired 20 min after Gd-EOB-DTPA administration (**c**), the normal liver parenchyma is strongly enhanced due to uptake of the contrast agent by functioning hepatocytes. The lesion-to-liver contrast (conspicuity) is greatly improved due to the inability of the lesion to take up Gd-EOB-DTPA

particles ranging between 45 and 60 nm. The safety profiles of these agents are less attractive than those of the paramagnetic contrast agents: although serious adverse events are rare, with Endorem® approximately 3% of patients experience severe back pain while the contrast agent is being administered [4, 101].

The principal superparamagnetic effect of the larger SPIO particles is on T2 relaxation and thus MRI is usually performed using T2-weighted sequences in which the tissue signal loss is due to the susceptibility effects of iron [28, 29, 94, 96] (Fig. 17). Enhancement on T1-weighted images can also be seen [84] although this tends to be greater for the smaller SPIO and especially for the USPIO formulations [95]. Since there is an overall decrease in liver signal intensity, T2-weighted imaging with SPIO agents requires excellent imaging techniques that are free of motion artifacts. Typically, moderate T2-weighting (TE of approximately 60-80 msec) is adequate for optimizing lesion-liver contrast. Since the larger SPIO agents need to be administered by slow infusion to reduce side effects, for these agents imaging is generally performed some 20-30 min after administration [21, 101, 125]. Thus, scanning speed is not important and both fast breath-hold and conventional SE imaging can be employed. Pulse sequences that are sensitive to magnetic field heterogeneity tend to be sensitive to the presence of iron oxide. T2*-weighted gradient echo images are very sensitive to SPIO agents [21, 28, 29, 84, 101]. T2-weighted spin-echo sequences are more sensitive than T2-weighted fast (turbo) spin-echo sequences, because the multiple rephasing pulses used in the latter tend to obscure signal losses arising from local variations in the magnetic environment [21]. Administration protocols vary but typically precontrast T1- and T2-weighted imaging is followed by post-contrast T2-weighted imaging. Schematic representations of the enhancement behavior seen after administration of SPIO and USPIO agents are shown in Figs. 18 and 19.

Since SPIO particles are removed by the RES, the application of these agents is similar to the use of Tc-sulfur colloid in nuclear scintigraphy. Lesions that contain negligible or no Kupffer cells remain largely unchanged, while the signal intensity of the normal liver is reduced on T2-weighted images. As a result the CNR between the normal liver parenchyma and focal liver lesion is increased [21, 29, 84, 96, 101].

Many well-controlled studies using surgical pathology or intraoperative ultrasound (IOUS) as gold standards have supported the efficacy of SPIO-enhanced MRI [21, 29, 84, 96, 101]. For example, an early multi-center Phase III study showed more lesions in 27% of cases than unenhanced MR and in 40% of cases compared to CT [101]. On the other hand, other early studies were not able to demonstrate a significant benefit over

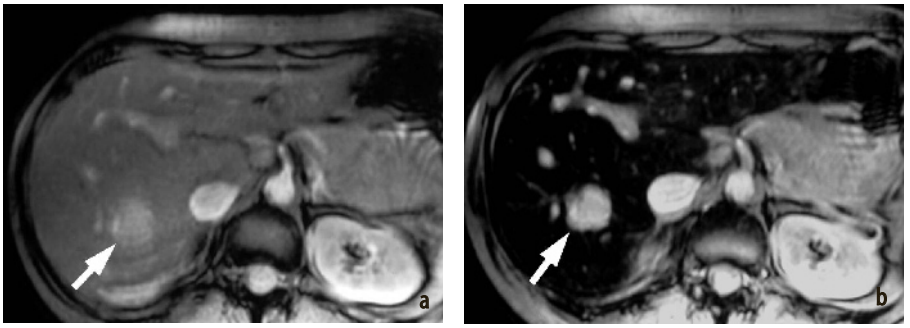

Fig. 17a, b. On the unenhanced T2*-weighted image (**a**) a liver metastasis (*arrow*) from breast cancer is shown with a slightly increased signal intensity. A drop of liver signal intensity is noted on the corresponding T2*-weighted image acquired after the administration of SPIO (**b**). This is due to the uptake of iron oxide particles by the Kupffer cells of the RES in normal liver parenchyma. The liver lesion does not show significant uptake of SPIO particles, hence the contrast between the metastasis and surrounding normal liver parenchyma is significantly increased after the injection of SPIO

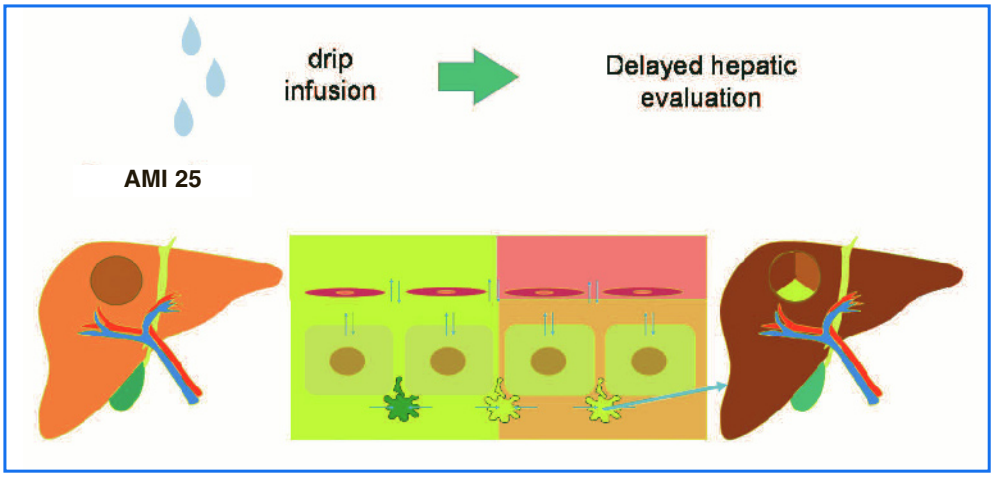

Fig. 18. Larger SPIO particles such as ferumoxides are administered by drip infusion and T2-weighted images are acquired more than 20 min after injection

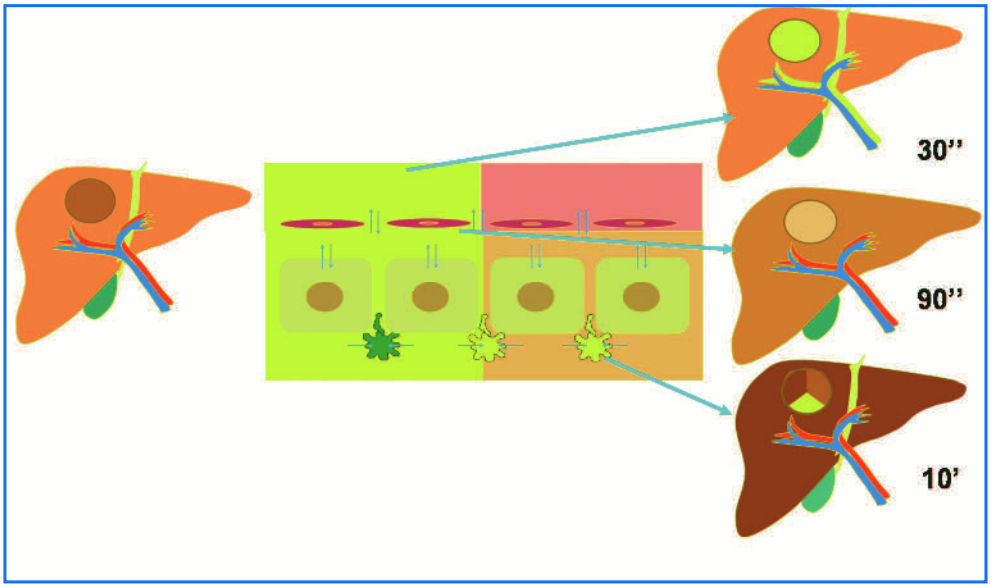

Fig. 19. Smaller USPIO particles such as SH U 555 A can be administered as a bolus, whereupon they distribute initially in the intravascular-extravascular space permitting dynamic T1-weighted imaging. Thereafter, like ferumoxides, SH U 555 A particles are taken up by Kupffer cells allowing T2-weighted delayed imaging

unenhanced imaging for the depiction of hepatic tumors [21]. More recent studies, however, have shown that SPIO-enhanced MRI has significantly greater detection capability for liver malignancies compared to spiral CT [125, 134, 145, 146]. Although comparisons of SPIO-enhanced MRI with other gadolinium-enhanced MR techniques have been somewhat limited until recently [7, 38, 48, 49, 50, 85, 133, 139], the general conclusion is that gadolinium-enhanced imaging is the more valuable approach for the detection of hepatocellular lesions such as HCC and FNH [38, 85, 133].

Limitations of SPIO-enhanced MRI include an increased incidence of false positive lesions due to the possibility of vessels mimicking lesions against a background of black liver, and a longer imaging protocol that requires pre- and post-contrast imaging over a period of 30 min or more. Furthermore, the use of SPIO in patients with cirrhosis is also challenging due to the diminished uptake and heterogeneous signal arising from fibrosis [24, 151]. However, in this regard a recent study has suggested a lower dose of SPIO agent might be useful in patients with cirrhotic liver [1].

The availability of SH U 555 A may go some way towards overcoming the problems inherent to the larger SPIO agents in that this agent can be administered as a fast bolus in order to observe the early perfusion characteristics of the liver using T1- or T2*-weighted sequences [95, 96, 126] (Fig. 20). This, combined with the enhancement patterns observed on delayed T1-weighted and T2-weighted images (Figs. 21, 22) may prove clinically useful for both the detection and characterization of lesions. Unfortunately, the enhancement observed on SH U 555 A-enhanced dynamic im-

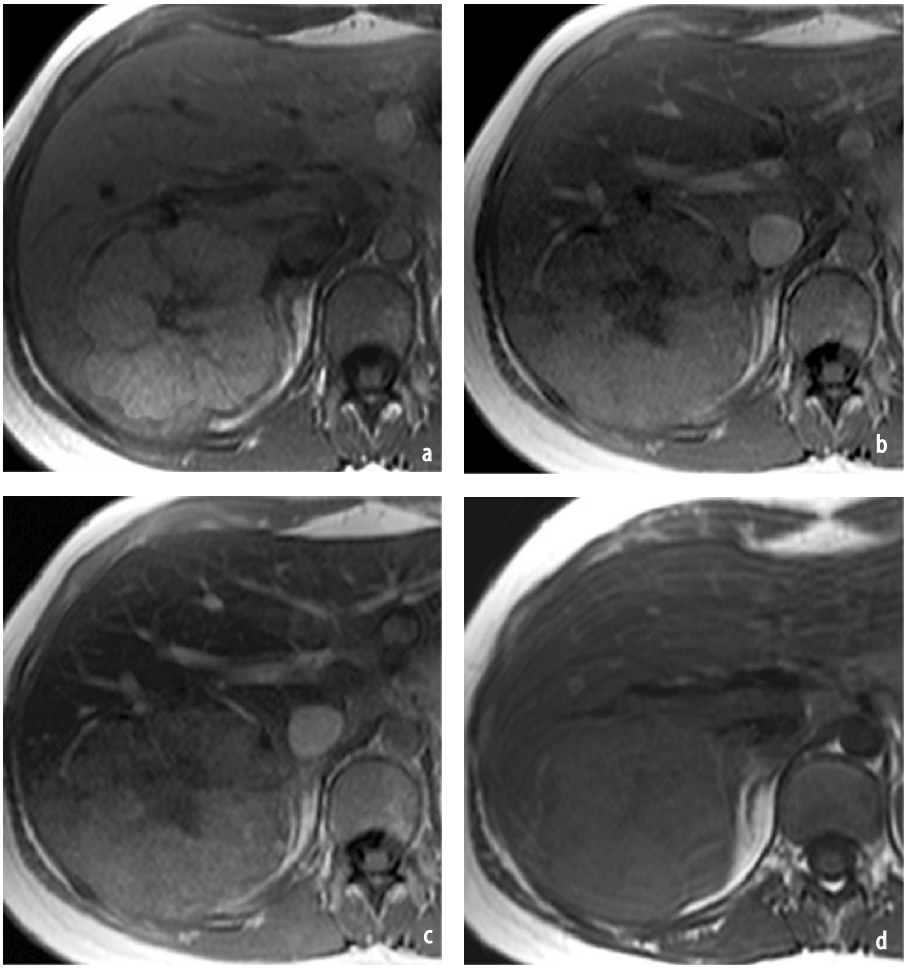

Fig. 20a-d. Dynamic T1-weighted MR imaging of focal nodular hyperplasia with SH U 555 A. A large homogeneously hyperintense lesion can be seen on the arterial phase T1-weighted GRE images acquired 30 sec after the administration of SH U 555 A (**a**). A central hypointense scar is also apparent on this image. On the portal-venous (**b**) and equilibrium (**c**) phase images acquired after 75 sec and 4 min, respectively, the lesion is seen as slightly hyperintense compared to the surrounding parenchyma. On the delayed phase image acquired after 10 min (**d**), the lesion appears isointense compared to the surrounding parenchyma while the central scar is seen as slightly hypointense. The isointense appearance on the delayed T1-weighted GRE image indicates that the lesion contains functioning Kupffer cells that are able to take up SH U 555 A. This suggests the lesion is benign in nature

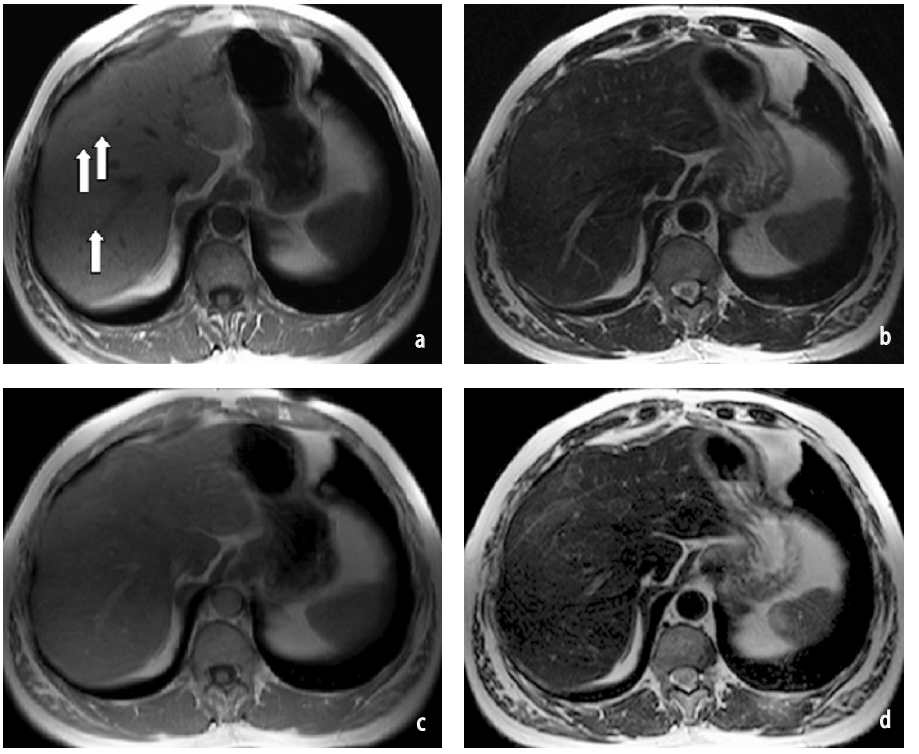

Fig. 21a-d. T2-weighted and T1-weighted MR imaging of nodular regenerative hyperplasia with SH U 555 A. The unenhanced GE T1-weighted image (**a**) reveals several faintly hyperintense nodules (*arrows*) in the right liver lobe. On the corresponding unenhanced TSE T2-weighted image (**b**) these nodules are again seen as slightly hyperintense. On the T1-weighted and T2-weighted images acquired 10 min after the administration of SH U 555 A (**c** and **d**, respectively) the nodules appear slightly hypointense against the surrounding parenchyma. This indicates that the lesions are able to take up contrast agent and are therefore likely to be benign in nature

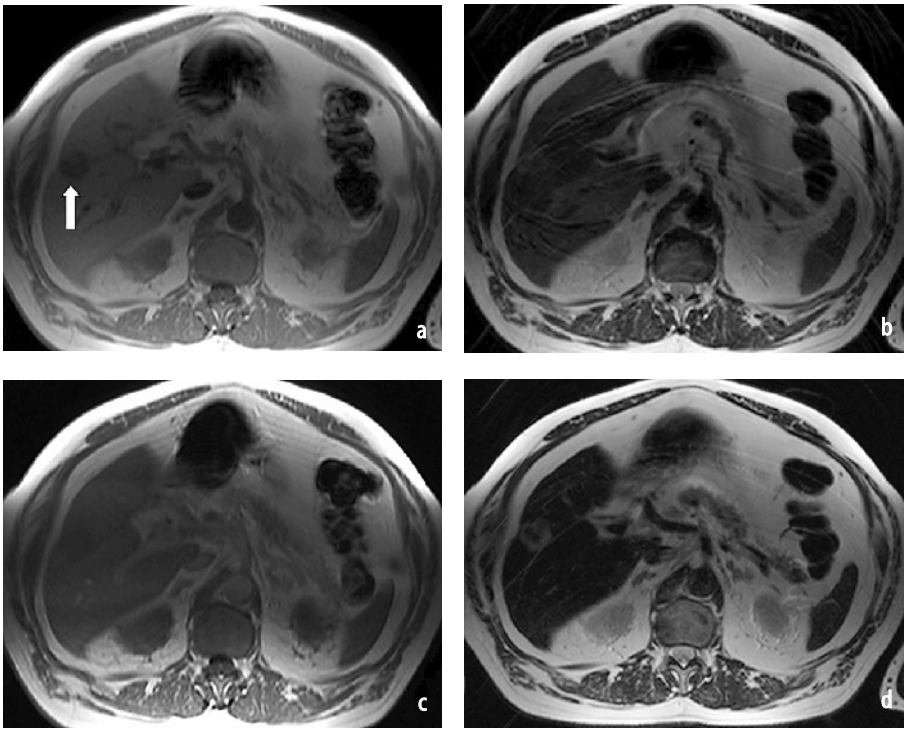

Fig. 22a-d. T2- and T1-weighted MR imaging of peripheral cholangiocellular carcinoma with SH U 555 A. The unenhanced GE T1-weighted image (**a**) reveals a hypointense mass (*arrow*) in the right liver lobe. Slight capsular retraction is also apparent. The lesion is less well seen on the corresponding unenhanced TSE T2-weighted image (**b**). The lesion does not indicate a capacity to take up the contrast agent on the delayed T1-weighted image acquired 10 min after the administration of SH U 555 A (**c**) and remains slightly hypointense compared to the surrounding parenchyma. On the corresponding post-contrast T2-weighted image (**d**) the lesion is clearly delineated with a peripheral hyperintense rim. This enhancement pattern indicates that the lesion is likely to be malignant in nature

ages is relatively weak due to the small dose (1 ml) that is injected from the prefilled syringes. Thus, it remains to be seen whether this agent will have widespread clinical impact on MRI of the liver.

In addition to possessing both T1 and T2 effects, the newer ultrasmall formulations currently under development have a longer intravascular residence than the larger SPIO agents. As with the larger SPIO particles, the Kupffer cells of the RES take up and eventually clear these USPIO particles over a period of about 24 hrs. The prolonged imaging window, however, allows for more favorable image resolution and signal-to-noise ratio because the acquisition parameters are less constrained by time. For liver imaging, the blood pool effect and combined T1 and T2 effects have shown promise for the detection and characterization of lesions [42, 110]. A specific advantage is that vessels and lesions show opposite enhancement. On T1-weighted images vessels are bright while lesions are dark, whereas on T2-weighted images the reverse is true. An additional advantage is that MR angiography may also be performed with these agents. An early study to evaluate the abdominal vasculature on delayed (45 min) images acquired following the infusion of AMI-227 revealed significant enhancement of all vessels [75]. Similarly, time of flight (TOF) MR angiography prior to and following AMI-227 administration demonstrated that the depicted renal artery lengths increased significantly following contrast administration [131]. Unfortunately, the use of blood pool agents is hindered at the present time by the presence of increased background signals and the superimposition of venous structures.

3.2 Injection Schemes for Liver MRI with Different Contrast Agents

Non-Specific Gadolinium Chelates

Gadopentetate dimeglumine (**Magnevist**®, Gd-DTPA; Berlex Laboratories/Schering AG)
Gadoteridol (**ProHance**®, Gd-HP-DO3A; Bracco Diagnostics),
Gadodiamide (**Omniscan**®, Gd-DTPA-BMA; GE Healthcare)
Gadoversetamide (**Optimark**®, Gd-DTPA-BMEA; Mallinckrodt)
Gadoterate meglumine (**Dotarem**®, Gd-DOTA; Guerbet)
Gadobutrol (**Gadovist**®, Gd-BT-DO3A; Schering AG)

These contrast agents are injected as a bolus, typically at a dose of 0.1 mmol/kg bodyweight and at a flow-rate of 2-3 ml/sec. The injection of the contrast agent should be followed by a saline flush of 20 ml at the same injection rate.

Contrast enhanced T1-weighted or T1-weighted fat-suppressed imaging of the entire liver is typically performed in a single breath-hold at:

20-25 sec post-injection	(Arterial phase imaging)
60-80 sec post-injection	(Portal-venous phase imaging)
3-5 min post-injection	(Equilibrium phase imaging)

Hepatocyte-Targeted Contrast Agents

Mangafodipir trisodium (**Teslascan**®, Mn-DPDP; GE Healthcare)

This agent has to be administered as a drip infusion over a period of approximately 10 min at a dose of 5 µmol/kg bodyweight (0.5 mL/kg; maximum dose, 50 mL). Alternatively, some investigators have used a hand injection over a 1 or 2 min period, followed by a flush of 10 mL of normal saline. However, when this fast injection scheme is employed, there is potentially an increased incidence of adverse events.

Imaging with T1-weighted and T1-weighted fat-suppressed sequences is usually performed at 15-20 min post-injection.

Agents with Combined Extracellular and Hepatocyte-Specific Distribution

Gadobenate dimeglumine (**MultiHance**®, Gd-BOPTA; Bracco Imaging SpA)
Gadolinium ethoxybenzyldiethylenetriaminepentaacetic acid (**Primovist**®, Gd-EOB-DTPA; Schering AG, Germany)

Imaging with contrast agents that have a combined extracellular and hepatocyte-specific distribution can be performed during the dynamic phase of contrast enhancement in a manner identical to that used with the non-specific Gd-chelates that have a purely extracellular distribution. For this purpose, these agents are injected as a bolus, typically at a dose of 0.05-0.1 mmol/kg BW (0.1-0.2 mL/kg bodyweight) for Gd-BOPTA and 0.025 mmol/kg BW (0.1 mL/kg bodyweight) for Gd-EOB-DTPA, at a flow-rate of 2-3 ml/sec. The injection of the contrast agent should be followed by a saline flush (0.9% sodium chloride solution) of 20 ml at the same injection rate.

Contrast enhanced T1-weighted or T1-weighted fat-suppressed imaging of the entire liver is

typically performed in a single breath-hold at:

20-25 sec post-injection	(Arterial phase imaging)
60-80 sec post-injection	(Portal-venous phase imaging)
3-5 min post-injection	(Equilibrium phase imaging)

In addition to imaging in the dynamic phase of contrast enhancement, the hepatocyte-specific distribution of these agents permits imaging to be performed in a more delayed hepatobiliary phase. Hepatobiliary imaging after injection of Gd-BOPTA is typically performed at 45 min to 3 hrs post-injection. Conversely, with Gd-EOB-DTPA imaging in the hepatobiliary phase is usually performed between 20 min and 2 hrs post-injection.

Typically 2D or 3D T1-weighted and T1-weighted fat-suppressed GRE images are acquired in the hepatobiliary phase.

RES-Specific Agents

SPIO Agents:

Ferumoxides (**Feridex**®, Berlex Laboratories and **Endorem**®, Laboratoire Guerbet)

A SPIO dose of 15 µmol/kg of bodyweight from the stock solution (0.075 mL/kg bodyweight) is diluted in 100 mL of a 5% glucose solution, before being administered as a drip infusion over a period of at least 30 min.

The incidence and severity of adverse events such as back pain, thoracic pain or decreased blood pressure correlates with the speed of infusion. Therefore, if patients experience side effects, the drip infusion should be stopped until the symptoms disappear and then recommenced at a lower infusion speed under medical supervision. However, if reactions such as nausea, urticaria or other allergic skin reactions occur, the administration should be stopped immediately and not recommenced.

The optimal time-point for imaging in the accumulation phase after SPIO administration is between 30 min and 6 hrs after injection of the complete dose of contrast medium.

Imaging protocols typically include T2-weighted TSE sequences, T2*-weighted sequences and in certain cases T1-weighted GRE sequences.

USPIO Agents:

SH U-555 A (**Resovist**®, Schering AG)

Unlike Ferumoxides, this iron oxide-based agent can be administered as a bolus.

The dose for patients with a bodyweight of less than 60 kg is 0.9 mL (total iron dose 0.45 mmol); patients with a bodyweight of more than 60 kg receive a dose of 1.4 mL (total iron dose 0.7 mmol). The contrast agent is administered as a bolus using an included 5 µm-filter followed by a saline flush (0.9% sodium chloride solution) of approximately 20 mL.

Following bolus injection, dynamic contrast-enhanced T1-weighted or T2*-weighted GRE imaging of the entire liver is typically performed in a single breath-hold at:

20-25 sec post-injection	(Arterial phase imaging)
60-80 sec post-injection	(Portal-venous phase imaging)
3-5 min post-injection	(Equilibrium phase imaging)

The time-point for imaging in the accumulation phase after USPIO injection is between 10 min and 8 hrs post-administration of the contrast medium.

At this time point T2-weighted or T2*-weighted SE or TSE images should be acquired. If information about the intrahepatic vessels is needed, the imaging study can be augmented by a TOF MR angiography sequence within the first 20 min after injection. During this time span a fraction of the administered dose of USPIO is still circulating in the blood thereby increasing the vessel signal on TOF images.

3.3 Radiologic Classification of Focal Liver Lesions on Unenhanced and Contrast-Enhanced MRI

Liver lesions can be classified on the basis of both unenhanced and contrast-enhanced images (Table 3). On unenhanced imaging, classification can be based upon the signal intensity and delineation of lesions on conventional T2-weighted and T1-weighted images as well as on opposed phase T1-weighted images or T1-weighted images acquired with fat suppression. Tables 4 and 5 show the characteristic appearances of many of the more common lesion types on unenhanced T2-weighted and T1-weighted images, respectively. Thus, on unenhanced imaging, lesions with a high fluid content, lesions containing fat and lesions with internal hemorrhage can be detected and readily diagnosed. Unfortunately, unenhanced imaging alone cannot always differentiate reliably between benign and malignant lesions and, in many cases, addi-

tional information from contrast-enhanced imaging is necessary for accurate differential diagnosis.

The availability of contrast agents with markedly different properties means that lesions can be classified on the basis of different enhancement patterns on contrast-enhanced imaging (Table 3). Thus, lesions can be classified according to their behavior on dynamic imaging following the administration of extracellular contrast agents (in a similar manner to that which occurs on dual phase spiral CT imaging), and to their behavior on delayed imaging following the administration of contrast agents targeted either to the hepatocytes or the Kupffer cells.

In the dynamic phase of contrast enhancement after the administration of gadolinium-based contrast agents, lesions can be classified according to whether they demonstrate hypervascular or hypovascular enhancement patterns or delayed persistent enhancement on T1-weighted acquisitions during the arterial, portal-venous and equilibrium phases, respectively (Table 6). Within these three major groups of lesions, lesions can be classified further according to the presence or absence of certain characteristic features. For example, a central scar within a hypervascular lesion in a non-cirrhotic liver that shows low signal intensity on T1-weighted images and high signal intensity on T2-weighted images may be indicative of FNH (Table 7). Similarly, a hypovascular lesion with a hypervascular rim that shows contrast agent washout at 10-15 min post-injection and a dough-nut or halo sign on T2-weighted images may be indicative of a metastasis of adenocarcinoma (Table 8). Finally, a lesion that shows nodular enhancement in the arterial phase followed by centripetal filling-in in the subsequent phases and high signal intensity on T2-weighted images may be indicative of a hemangioma (Table 9).

Whereas the enhancement seen on dynamic T1-weighted imaging gives information on the morphologic characteristics of lesions, that seen on delayed phase images after the injection of agents targeted either to the hepatocytes (e.g. Gd-BOPTA (Table 10), Gd-EOB-DTPA (Table 11), Mn-DPDP (Table 12)) or Kupffer cells (SPIO agents (Table 13), USPIO agents (Table 14, 15 and 16)) gives information on the cellular content and cellular functionality of lesions. In the case of Gd-BOPTA, the information gained in the delayed phase is additional to that seen in the dynamic phase and may serve to distinguish lesions of hepatocellular origin such as FNH that may be able to take up the agent, from lesions of hepatocellular origin such as HCC that have lost this ability and lesions of non-hepatocellular origin that are also unable to take up the agent (Table 10). Similarly, lesions can be classified into different groups on the basis of their ability to take up Gd-EOB-DTPA (Table 11), Mn-DPDP (Table 12) and iron oxide particles (Tables 13, 14, 15 and 16). However, the lack of a dynamic imaging capability combined with the sometimes overlapping levels of enhancement of different primary benign and malignant liver lesions often makes accurate differential diagnosis difficult with these agents.

The tables that follow demonstrate schematically an approach to the classification of liver lesions based on imaging features on unenhanced MR imaging and enhanced imaging after administration of both extracellular and liver-specific contrast agents.

3.4 Summary

Various categories of MR contrast agents are available for clinical use, all of which permit the demonstration of more liver lesions than can be depicted on unenhanced imaging alone. The biggest impediment to the more widespread use of contrast agents for liver imaging in the USA in particular is that reimbursement schemes have not yet been established. Thus, these products have so far received only a cautious welcome in the market place. In addition, the added cost of the extended imaging time needed for the tissue-specific (RES and hepatocyte) agents makes their use less attractive at the current time. On the other hand, it is possible the added value and cost-effectiveness of some of the newer agents will become apparent through clinical use.

Until recently, the absence of an approved contrast agent with combined extracellular and hepatobiliary distribution in the USA led various authors to propose sequential same-session imaging with both a tissue-specific agent and an extracellular gadolinium agent to improve liver lesion detection and characterization [63, 109]. The downside of this approach, however, is the need for two injections of two different contrast agents and the associated additional costs involved. The development of contrast agents such as gadobenate dimeglumine, which has the characteristics of both extracellular and hepatobiliary agents, allows functional information to be gained on hepatobiliary phase imaging in addition to that gained on standard dynamic phase imaging. In this regard, the use of agents with combined extracellular/hepatobiliary properties would appear to offer advantages not only in comparison to other MR contrast agents, but also in comparison to other imaging modalities such as MDCT.

Table 3. Classification of focal liver lesions

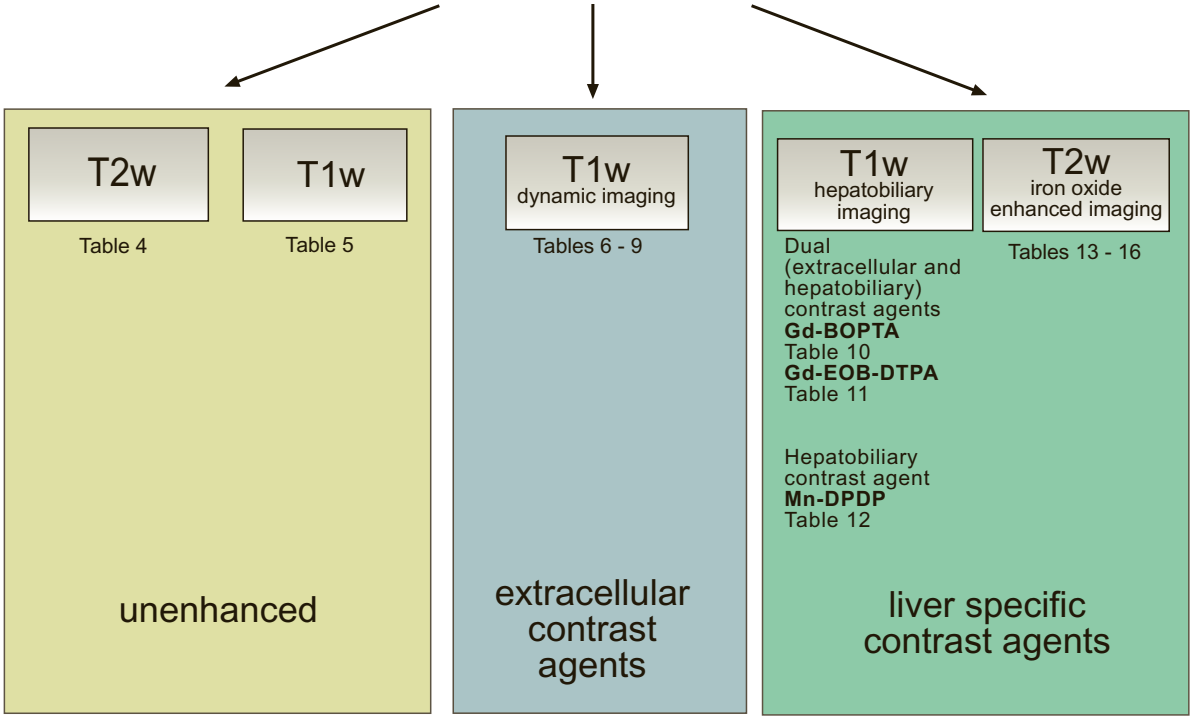

Table 4. DDX of focal liver lesions on T2w imaging

hyperintense	slightly hyperintense	isointense	hypointense
Cysts	Metastases of adenocarcinoma (e.g., colorectal), "halo-sign", "doughnut-sign"	FNH	Regenerative nodules (low signal caused by hemosiderin deposits)
Hemangioma	Undifferentiated HCC	Adenoma	Calcification
Metastases of neuroendocrine tumors	Focal Fatty Liver	Well-differentiated HCC	AV malformation with high flow (flow void)
Cystic metastases		Metastases of neuroendocrine tumors after chemotherapy	Fibrosis
Bilioma			Non-acute hemorrhage
AV malformation (low flow)			
Hemangiosarcoma			

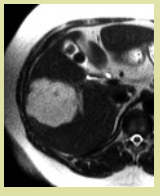
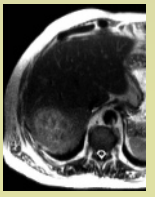
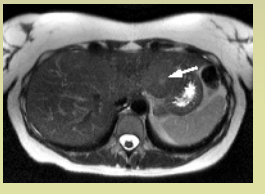
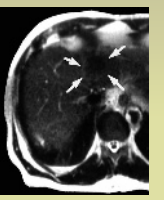

Table 5. DDX of focal liver lesions on T1w images

hyperintense

- fat
  - fs and/or opposed phase imaging
  - SI ↓
- hemorrhage
  - fs imaging
  - SI ↑
  - (due to magnetic field inhomogeneities = susceptibility artefacts)
- fluid with high protein content
  - fs imaging
  - SI ↔
- hemosiderotic nodules in cirrhotic liver
  - fs imaging
  - SI ↔
  - regenerative nodule (T2w SI ↓)

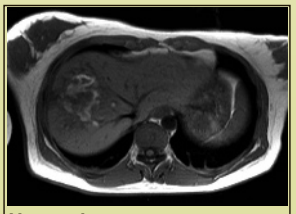

Hemorrhage

isointense or slightly hypointense

- with radiating septa +/- central scar
  - FNH
- NRH
- Adenoma
- HCC (well-differentiated)
- FNH (atypical)

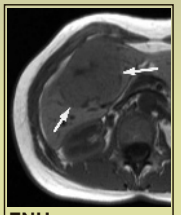

FNH

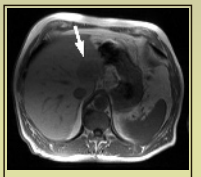

HCC

hypointense

most benign and malignant focal liver lesions

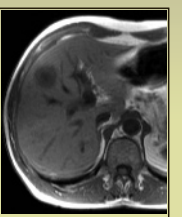

Mets

Table 6. DDX of focal liver lesions on T1w dynamic imaging (extracellular Gd-chelates (e.g., Gd-DTPA), dual Gd-chelates (e.g., Gd-BOPTA))

hypervascular liver lesions in arterial phase

Table 7

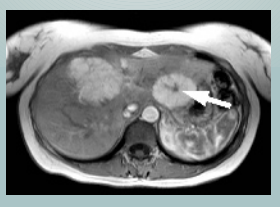

hypovascular liver lesions in arterial / portal venous phase

Table 8

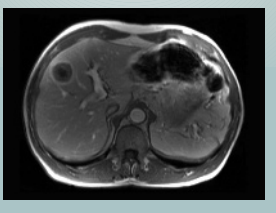

liver lesions with delayed persistent enhancement in equilibrium phase

Table 9

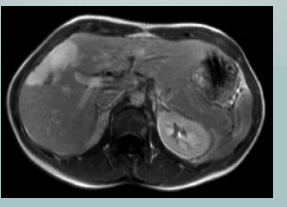

Table 7. DDX of hypervascular liver lesions on dynamic imaging

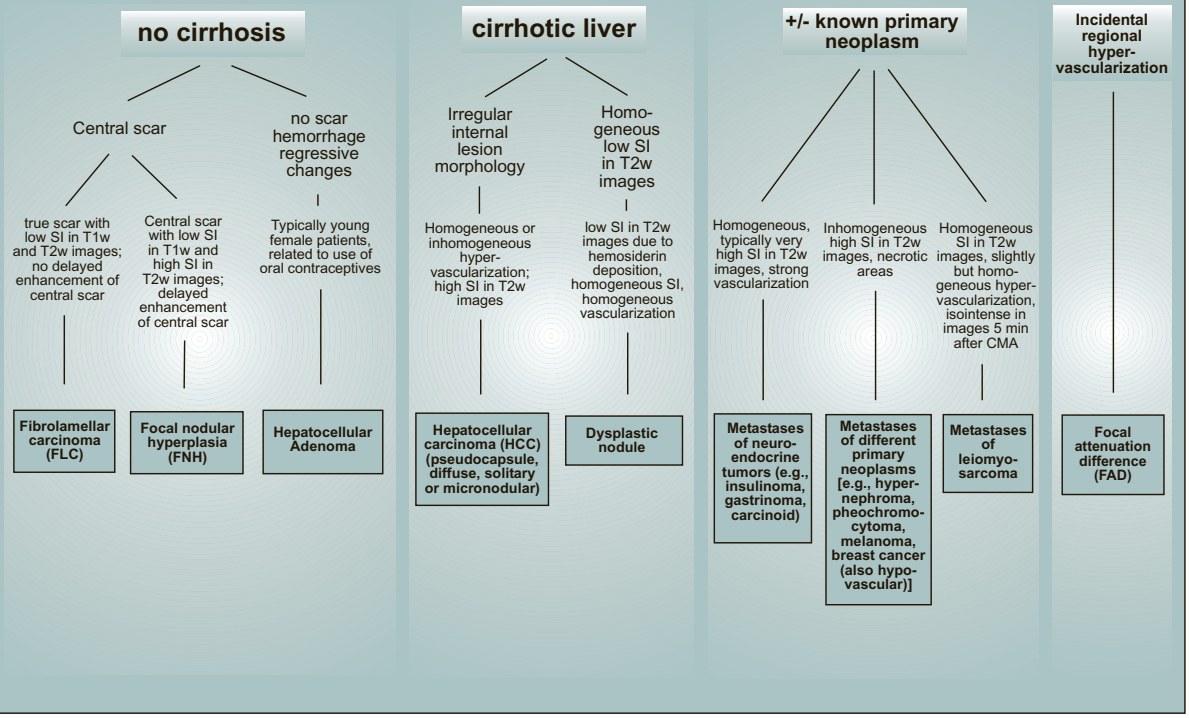

Table 8. DDX of hypovascular liver lesions on dynamic imaging

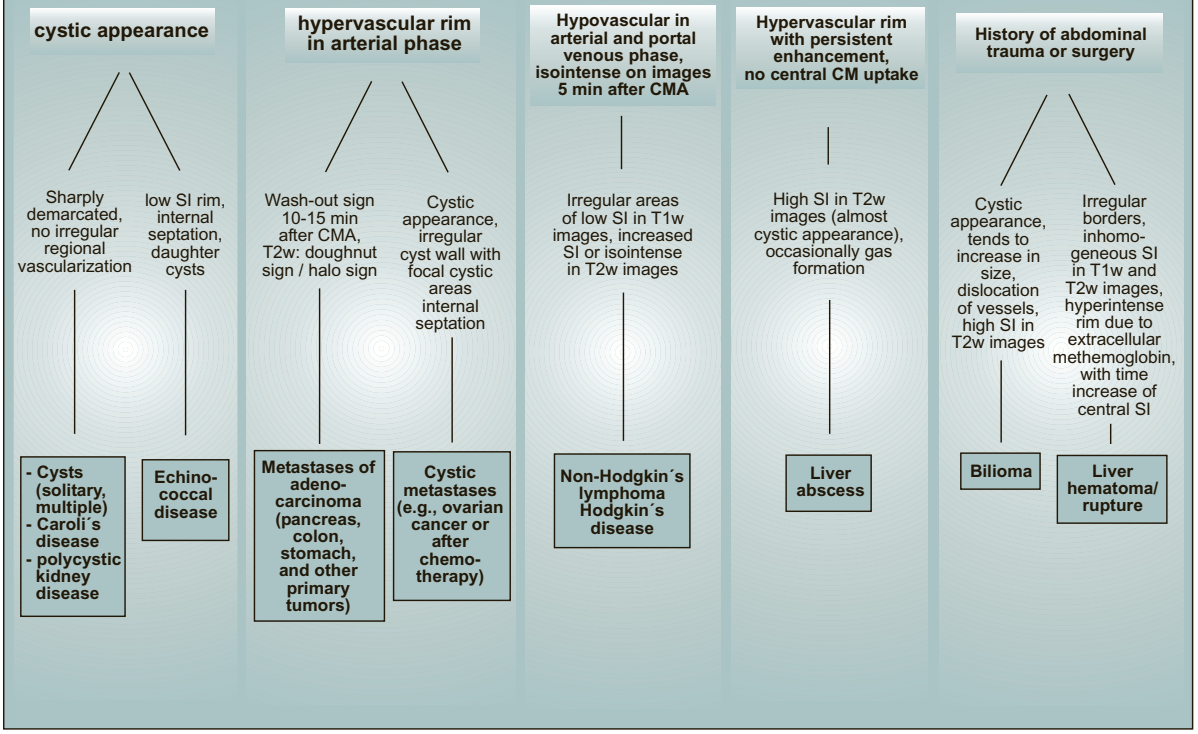

Table 9. DDX of liver lesions with delayed persistent enhancement

Nodular peripheral enhancement in arterial phase, centripetal filling	infiltrating along portal tracts, segmental biliary obstruction	+/- known primary neoplasm	Irregular, partially nodular enhancement in arterial phase, irregular filling	Homogeneous, sometimes early enhancement, irregular shape
High SI in T2w images (light bulb appearance), in large lesions central areas may remain unenhanced after CM application due to thrombosis/fibrosis sharply demarcated	Hypovascular with hypervascular peripheral enhancement in arterial phase	Hypo- or slightly hypervascular in arterial phase, low SI in T1w and high SI in T2w images, sometimes peripheral wash-out	Centrifugal or irregular filling, irregular borders	High SI in T2w images, iso- or hyperintense in delayed-phase images
Hemangioma	**Intrahepatic cholangiocellular carcinoma (CCC)**	**Metastases of leiomyosarcoma and gastrointestinal stromal tumors (GIST)**	**- Hemangiosarcoma - Hemangioendothelioma - Hemangiopericytoma**	**Peliosis hepatis**

Table 10. DDX of focal liver lesions in the hepatobiliary phase after Gd-BOPTA

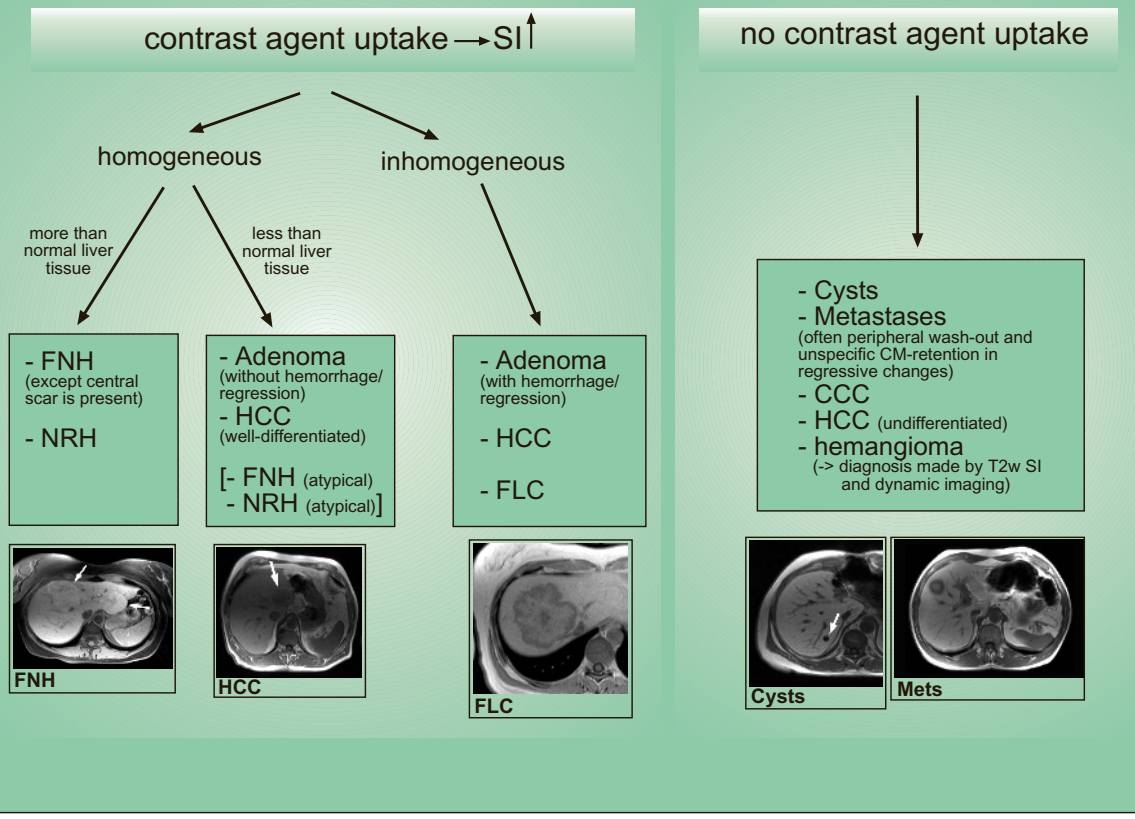

Table 11. DDX of focal liver lesions in the hepatobiliary phase after Gd-EOB-DTPA

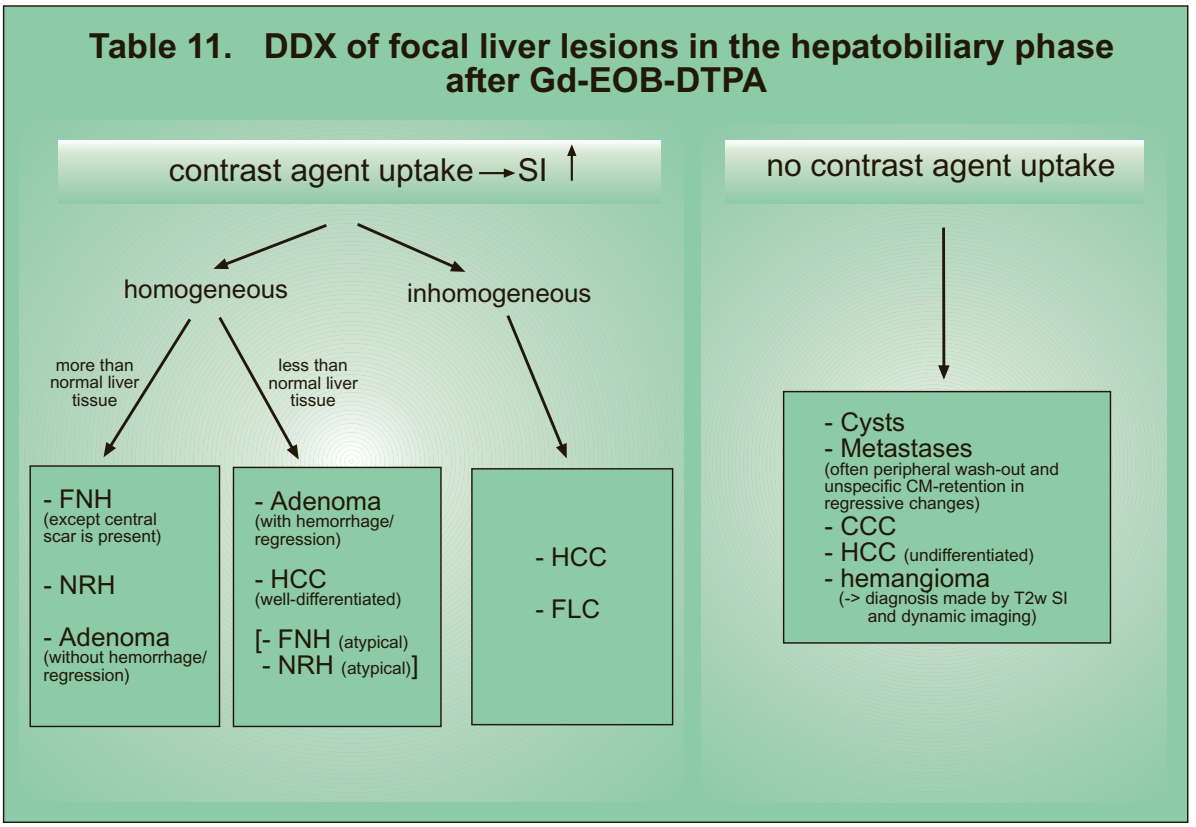

Table 12. DDX of focal liver lesions in the hepatobiliary phase after Mn-DPDP

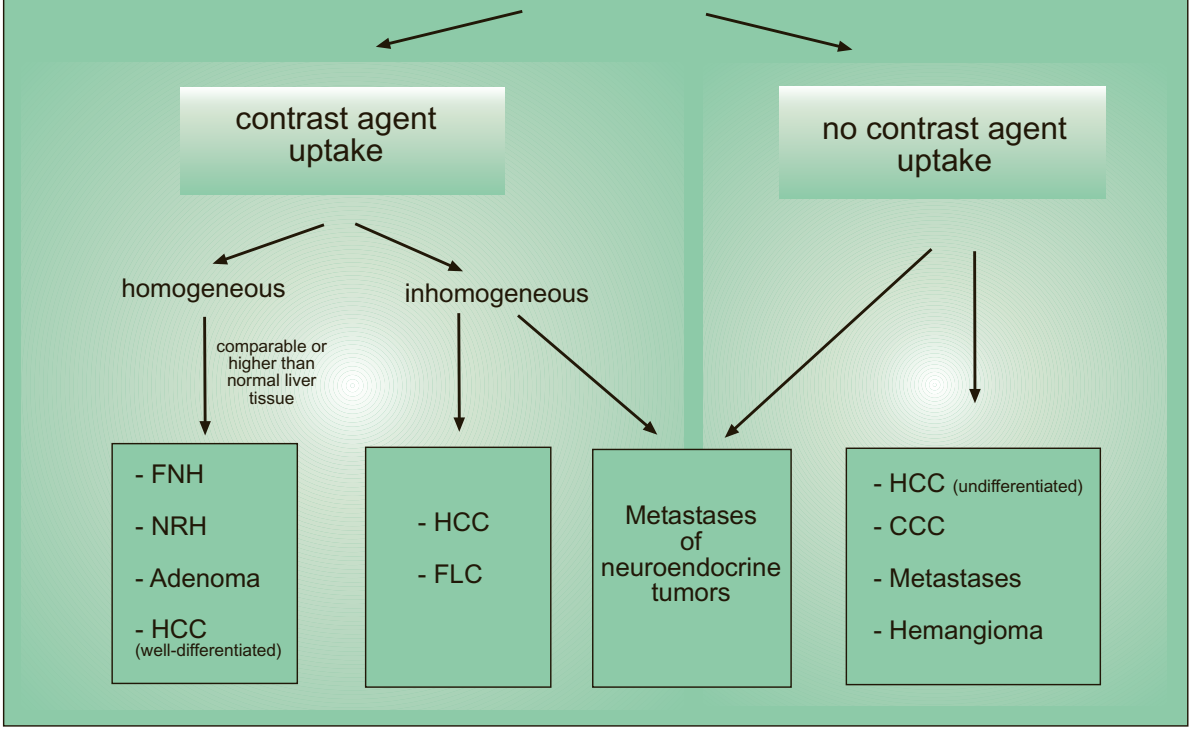

Table 13. DDX of focal liver lesions on SPIO enhanced T2w images in the RES-specific phase

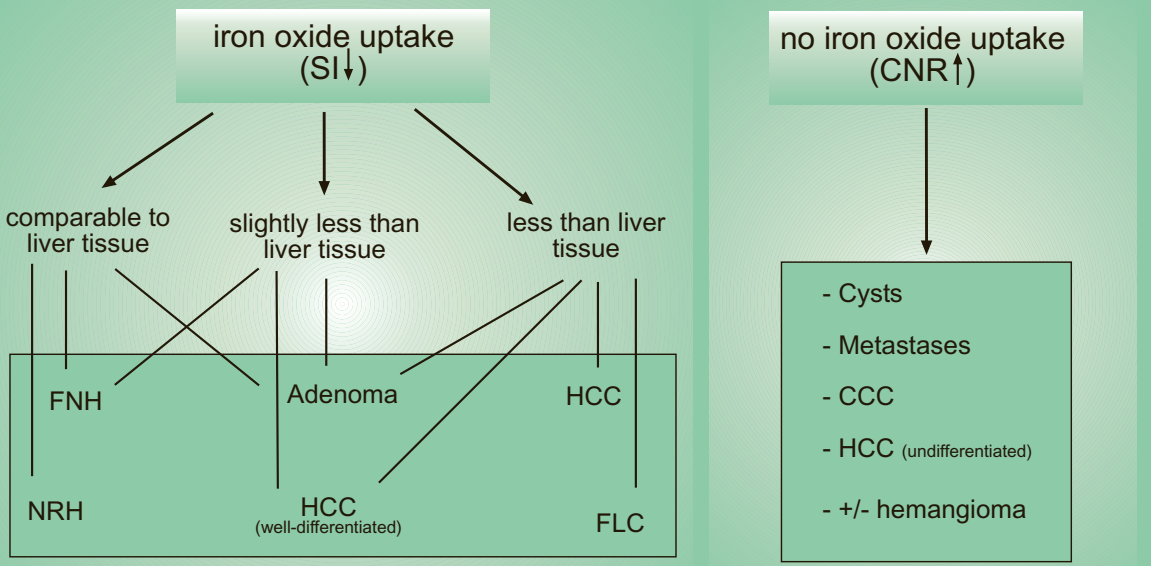

Table 14. DDX of focal liver lesions on USPIO enhanced T1w and T2*w dynamic CE imaging

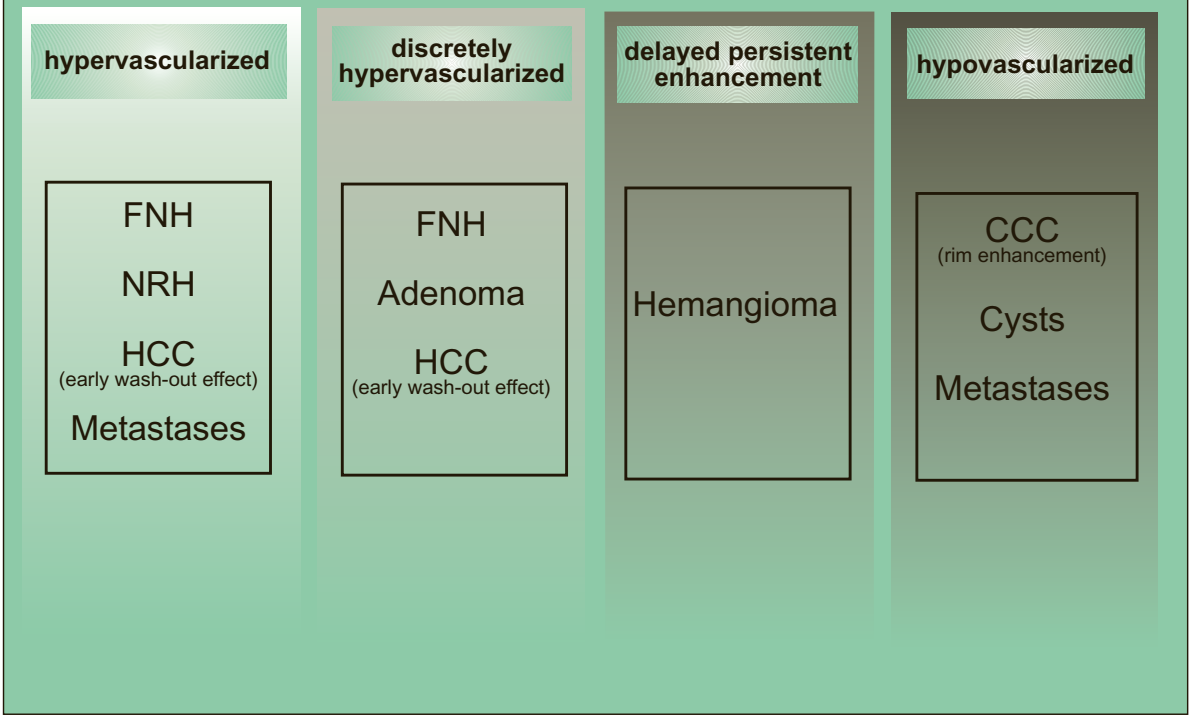

Table 15. DDX of focal liver lesions on USPIO enhanced T1w images in the RES-specific phase

hyperintense	slightly hyperintense	isointense	hypointense
FNH NRH Hemangioma	FNH Adenoma HCC (well-differentiated)	FLC Adenoma HCC (well-differentiated)	CCC Cysts HCC (undifferentiated) Metastases

Table 16. DDX of focal liver lesions on USPIO enhanced T2w/T2*w images in the RES-specific phase

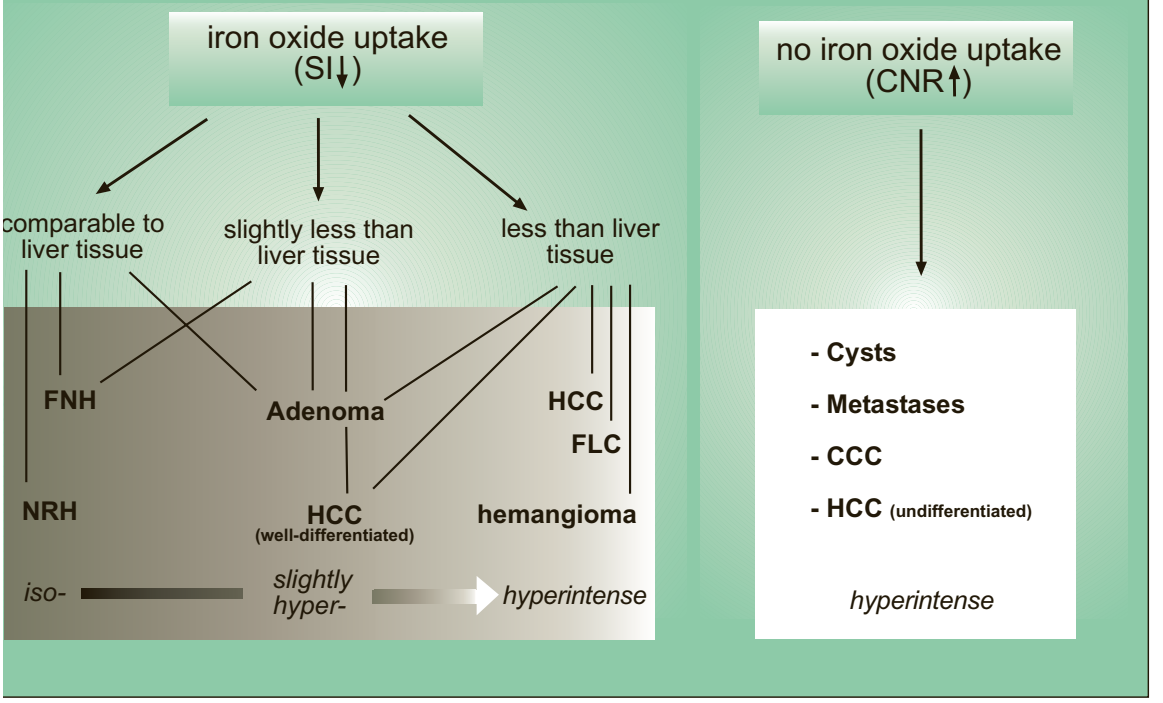

References

1. Arnold P, Ward J, Wilson D, Ashley Guthrie J, Robinson PJ. Superparamagnetic iron oxide (SPIO) enhancement in the cirrhotic liver: a comparison of two doses of ferumoxides in patients with advanced disease. Magn Reson Imaging 2003; 21(7):695-700
2. Baleriaux D, Colosimo C, Ruscalleda J, Korves M, Schneider G, Bohndorf K, Bongartz G, van Buchem MA, Reiser M, Sartor K, Bourne MW, Parizel PM, Cherryman GR, Salerio I, La Noce A, Pirovano G, Kirchin MA, Spinazzi A. Magnetic resonance imaging of metastatic disease to the brain with gadobenate dimeglumine. Neuroradiol 2002; 44:191-203
3. Bartolozzi C, Spinazzi A. MultiHance: help or hype? J Comput Assist Tomogr 1999; 23(Suppl. 1):151-159
4. Bellin MF, Zaim S, Auberton E, Sarfati G, Duron JJ, Khayat D, Grellet J. Liver metastases: Safety and efficacy of detection with superparamagnetic iron oxide in MR imaging. Radiology 1994; 193:657-663
5. Bernardino ME, Young SW, Lee JK, Weinreb JC. Hepatic MR imaging with Mn-DPDP: Safety image quality and sensitivity. Radiology 1992; 183:53-58
6. Birnbaum BA, Weinreb JC, Fernandez MP, Brown JJ, Rofsky NM, Young SW. Comparison of contrast enhanced CT and Mn-DPDP enhanced MRI for detection of focal hepatic lesions. Initial findings. Clin Imaging 1994; 18:21-27
7. Blakeborough A, Ward J, Wilson D, Griffiths M, Kajiya Y, Guthrie JA, Robinson PJ. Hepatic lesion detection at MR imaging: A comparative study with four sequences. Radiology 1997; 203:759-765
8. Bluemke DA, Sahani D, Amendola M, et al. Efficacy and safety of MR imaging with liver-specific contrast agent: U.S. multicenter phase III study. Radiology 2005; 237(1):89-98
9. Braga HJV, Choti MA, Lee VS, Paulson EK, Siegelman ES, Bluemke DA. Liver lesions: manganese-enhanced MR and dual-phase helical CT for preoperative detection and characterization-comparison with receiver operating characteristic analysis. Radiology 2002; 223:525-531
10. Carlos RC, Branam JD, Dong Q, Hussain HK, Francis IR. Biliary imaging with Gd-EOB-DTPA: is a 20-minute delay sufficient? Acad Radiol 2002; 9(11):1322-5
11. Caudana R, Morana G, Pirovano GP, Nicoli N, Portuese A, Spinazzi A, Di Rito R, Pistolesi GF. Focal malignant hepatic lesions: MR imaging enhanced with gadolinium benzyloxypropionictetra-acetate (BOPTA) - preliminary results of phase II clinical application. Radiology 1996; 199:513-520
12. Cavagna FM, Maggioni F, Castelli PM, Dapra M, Imperatori LG, Lorusso V, Jenkins BG. Gadolinium chelates with weak binding to serum proteins. Invest Radiol 1997; 32:780-796
13. Chang CA. Magnetic resonance imaging contrast agents. Design and physicochemical properties of gadodiamide. Invest Radiol 1993; 28:21-7
14. Cherryman GR, Pirovano G, Kirchin MA. Gadobenate Dimeglumine in MR imaging of Acute Myocardial Infarction: Results of a Phase III study comparing Dynamic and Delayed Contrast Enhanced MR Imaging with EKG, 201Tl SPECT and Echocardiography. Invest Radiol 2002; 37:135-145
15. Chezmar JL, Rumaneik WM, Megibow AJ. Liver and abdominal screening in patients with cancer: CT versus MR imaging. Radiology 1987; 165:399-406
16. Coffin CM, Diche T, Mahfouz A, Alexandre M, Caseiro-Alves F, Rahmouni A, Vasile N, Mathieu D. Benign and malignant hepatocellular tumors : evaluation of tumoral enhancement after mangafodipir trisodium injection on MR imaging. Eur Radiol 1999; 9:444-449
17. Colosimo C, Demaerel P, Tortori-Donati P, Christophe C, Van Buchem M, Högström B, Pirovano G, Shen N, Kirchin MA, Spinazzi A. Comparison of gadobenate dimeglumine (Gd-BOPTA) with gadopentetate dimeglumine (Gd-DTPA) for enhanced MR imaging of brain and spine tumors in pediatric subjects. Pediatr Radiol 2005; 35:501-510
18. Colosimo C, Knopp MV, Barreau X, Gerardin E, Kirchin MA, Guezenoc F, Lodemann KP. A comparison of Gd-BOPTA and Gd-DOTA for contrast-enhanced MRI of intracranial tumours. Neuroradiology 2004; 46:655-665
19. Colosimo C, Ruscalleda J, Korves M, La Ferla R, Wool C, Pianezzola P, Kirchin MA. Detection of intracranial metastases: a multi-center, intra-patient comparison of gadobenate dimeglumine-enhanced MRI with routinely used contrast agents at equal dose. Invest Radiol 2001; 36:72-81
20. De Haën C, Cabrini M, Akhnana L, Ratti D, Calabi L, Gozzini L. Gadobenate dimeglumine 0.5M solution for injection (MultiHance): pharmaceutical formulation and physicochemical properties of a new magnetic resonance imaging contrast medium. J Comput Assist Tomogr 1999; 23(Suppl. 1):161-168
21. Denys A, Arrive L, Servois V, Dubray B, Najmark D, Sibert A, Menu Y. Hepatic tumors: detection and characterization at 1T MR imaging with AMI-25. Radiology 1994; 193:665-669
22. Earls JP, Rofsky NM, DeCorato DR, Krinsky GA, Weinreb JC. Hepatic arterial–phase dynamic gadolinium-enhanced MR imaging: optimization with a test examination and a power injector. Radiology 1997; 202:268-273
23. Elizondo G, Fretz CJ, Stark DD, Rocklage SM, Quay SC, Worah D, Tsang YM, Chen MC, Ferrucci JT. Preclinical evaluation of MnDPDP: new paramagnetic hepatobiliary contrast agent for MR imaging. Radiology 1991; 178(1):73-8
24. Elizondo G, Weissleder R, Stark DD, Guerra J, Garza J, Fretz CJ, Todd LE, Ferrucci JT. Hepatic cirrhosis and hepatitis: MR imaging enhanced with superparamagnetic iron oxide. Radiology 1990; 174:797-801
25. Emerson J, Kost G. Spurious hypocalcemia after Omniscan - or OptiMARK-enhanced magnetic resonance imaging - An algorithm for minimizing a false-positive laboratory value. Arch. Pathol Lab Med 2004; 128:1151-1156
26. Fan ZM, Yamashita Y, Harada M, Baba Y, Yamamoto H, Matsukawa T, Arakawa A, Miyazaki T, Takahashi M. Intrahepatic cholangiocarcinoma : spin echo and contrast-enhanced dynamic MR imaging. Am J Roengenol 1993; 161:313-317
27. Federle MP, Chezmar JL, Rubin DL, Weinreb JC, Freeny PC, Semelka RC, Brown JJ, Borello JA, Lee JK, Mattrey R, Dachman AH, Saini S, Harmon B, Fenstermacher M, Pelsang RE, Harms SE, Mitchell DG, Halford HH, Anderson MW, Johnson CD, Fran-

cis IR, Bova JG, Kenney PJ, Klippenstein DL, Foster GS, Turner DA. Safety and efficacy of Mangafodipir Trisodium (Mn-DPDP) Injection for hepatic MRI in adults: results of the U.S. multicenter Phase III clinical trials (safety). J Magn Reson Imaging 2000; 12:186-197
28. Fretz CJ, Elizondo G, Weissleder R, Hahn PF, Stark DD, Ferrucci JT Jr. Superparamagnetic iron oxide – enhanced MR imaging: Pulse sequence optimization for detection of liver cancer. Radiology 1989; 172:393-397
29. Fretz CJ, Stark DD, Metz CE, Elizondo G, Weissleder R, Shen JH, Wittenberg J, Simeone J, Ferrucci JT. Detection of hepatic metastases: Comparison of contrast-enhanced CT, unenhanced MR imaging and iron-oxide-enhanced MR imaging. AM J Roentgenol 1990; 155:763-770
30. Furuta A, Ito K, Fujita T, Koike S, Shimizu A, Matsunaga N. Hepatic enhancement in multiphasic contrast-enhanced MDCT: comparison of high- and low-iodine-concentration contrast medium in same patients with chronic liver disease. AJR Am J Roentgenol 2004; 183(1):157-62
31. Gallez B, Bacic G, Swartz HM. Evidence for the dissociation of the hepatobiliary MRI contrast agent Mn-DPDP. Magn Reson Med 1996; 35:14-19
32. Gehl HB, Vorwerk D, Klose KC, Gunther RW. Pancreatic enhancement after low dose infusion of Mn-DPDP. Radiology 1991; 180:337-339
33. Gibby WA, Gibby KA, Gibby WA. Comparison of Gd DTPA-BMA (Omniscan) versus Gd HP-DO3A (ProHance) retention in human bone tissue by inductively coupled plasma atomic emission spectroscopy. Invest Radiol 2004; 39(3):138-42
34. Goyen M, Barkhausen J, Debatin JF, Kuhl H, Bosk S, Testa G, Malago M, Ruehm SG. Right-lobe living related liver transplantation: evaluation of a comprehensive magnetic resonance imaging protocol for assessing potential donors. Liver Transpl 2002; 8(3):241-50
35. Grazioli L, Morana G, Caudana R, Benetti A, Portolani N, Talamini G, Colombari R, Pirovano G, Kirchin MA, Spinazzi A. Hepatocellular Carcinoma: Correlation between gadobenate dimeglumine-enhanced MRI and pathologic findings. Invest Radiol 2000; 35:25-34
36. Grazioli L, Morana G, Federle MP, Brancatelli G, Testoni M, Kirchin MA, Menni K, Olivetti L, Nicoli N, Procacci C. Focal nodular hyperplasia: morphological and functional information from MR imaging with gadobenate dimeglumine. Radiology 2001; 221:731-739
37. Grazioli L, Morana G, Kirchin MA, Schneider G. Accurate differentiation of focal nodular hyperplasia from hepatic adenoma at gadobenate dimeglumine-enhanced MR imaging: prospective study. Radiology 2005; 236:166-177
38. Grazioli L. Morana G, Kirchin MA et al. MR Imaging of focal nodular hyperplasia (FNH) with gadobenate dimeglumine (Gd-BOPTA) and SPIO (Ferumoxides): an intra-individual comparison. J Magn Reson Imaging 2003; 17:593-602
39. Hahn PF, Saini S. Liver-specific MR imaging contrast agents. Radiol Clin North Am 1998; 36:287-297
40. Hamm B, Staks T, Muhler A, Bollow M, Taupitz M, Frenzel T, Wolf KJ, Weinmann HJ, Lange L. Phase I clinical evaluation of Gd-EOB-DTPA as a hepatobiliary MR contrast agent: safety, pharmacokinetics and MR imaging. Radiology 1995; 195:785-792
41. Hamm B, Thoeni RF, Gould RG, Bernardino ME, Luning M, Saini S, Mahfouz AE, Taupitz M, Wolf KJ. Focal liver lesions: characterization with nonenhanced and dynamic contrast material–enhanced MR imaging. Radiology 1994; 90:417-423
42. Harisinghani MG, Jhaveri KS, Weissleder R, Schima W, Saini S, Hahn PF, Mueller PR. MRI contrast agents for evaluating focal liver lesions Clin Radiol 2001; 56:714-725
43. Harisinghani MG, Saini S, Weissleder R, Halpern EF, Schima W, Rubin DL, Stillman AE, Sica GT, Small WC, Hahn PF. Differentiation of liver hemangiomas from metastases and hepatocellular carcinoma at MR imaging enhanced with blood-pool contrast agent Code-7227. Radiology 1997; 202:687-691
44. Hauser RA, Zesiewicz TA, Rosemurgy AS, Marinez C, Olanow CW. Manganese intoxication and chronic liver failure. Ann Neurol 1994; 36:871-875
45. Huppertz A, Balzer T, Blakeborough A, et al. Improved detection of focal liver lesions at MR imaging: multicenter comparison of gadoxetic acid-enhanced MR images with intraoperative findings. Radiology 2004; 230(1):266-75
46. Huppertz A, Haraida S, Kraus A, Zech CJ, Scheidler J, Breuer J, Helmberger TK, Reiser MF. Enhancement of focal liver lesions at gadoxetic acid-enhanced MR imaging: correlation with histopathologic findings and spiral CT-initial observations. Radiology 2005; 234(2):468-78
47. Kettritz U, Schlund JF, Wilbur K, Eisenberg LB, Semelka RC. Comparison of gadolinium chelates with manganese-DPDP for liver lesion detection and characterization: preliminary results. Magn Reson Imaging 1996; 14:1185-1190
48. Kim MJ, Kim JH, Chung JJ, Park MS, Lim JS, Oh YT. Focal hepatic lesions: detection and characterization with combination gadolinium- and superparamagnetic iron oxide-enhanced MR imaging. Radiology 2003; 228(3):719-26
49. Kim YK, Kim CS, Lee YH, Kwak HS, Lee JM. Comparison of superparamagnetic iron oxide-enhanced and gadobenate dimeglumine-enhanced dynamic MRI for detection of small hepatocellular carcinomas. AJR Am J Roentgenol 2004; 182:1217-1223
50. Kim YK, Lee JM, Kim CS, Chung GH, Kim CY, Kim IH. Detection of liver metastases: gadobenate dimeglumine-enhanced three-dimensional dynamic phases and one-hour delayed phase MR imaging versus superparamagnetic iron oxide-enhanced MR imaging. Eur Radiol 2005; 15:220-228
51. Kim YK, Lee JM, Kim CS. Gadobenate dimeglumine-enhanced liver MR imaging: value of dynamic and delayed imaging for the characterization and detection of focal liver lesions. Eur Radiol 2004; 14:5-13
52. Kirchin MA, Pirovano G, Spinazzi A. Gadobenate dimeglumine (Gd-BOPTA): an overview. Invest Radiol 1998; 33:798-809
53. Kirchin MA, Pirovano G, Venetianer C, Spinazzi A. Safety assessment of gadobenate dimeglumine (Multihance): extended clinical experience from phase I studies to post-marketing surveillance. J Magn Reson Imaging 2001; 14:281-294

54. Kirchin MA, Runge VM. Contrast agents for magnetic resonance imaging: safety update. Top Magn Reson Imaging 2003; 14:426-435
55. Knopp MV, Bourne MW, Sardanelli F, et al. Gadobenate dimeglumine in contrast-enhanced magnetic resonance imaging of the breast: a dose response analysis and comparison with gadopentetate dimeglumine. Am J Roengenol 2003; 181:663-676
56. Knopp MV, Giesel FL, Radeleff J, von Tengg-Kobligk H. Bile-tagged 3D magnetic resonance colonography after exclusive intravenous administration of gadobenate dimeglumine, a contrast agent with partial hepatobiliary excretion. Invest Radiol 2001; 36:619-623
57. Knopp MV, Giesel FL, von Tengg-Kobligk H, Radeleff J, Requardt M, Kirchin MA, Hentrich HR. Contrast-enhanced MR Angiography of the Run-off Vasculature: Intraindividual comparison of gadobenate dimeglumine with gadopentetate dimeglumine. J Magn Reson Imaging 2003; 17:694-702
58. Knopp MV, Runge VM, Essig M, Hartman M, Jansen O, Kirchin MA, Moeller A, Seeberg AH, and Lodemann K-P. Primary and Secondary Brain Tumors at MR Imaging: Bicentric Intraindividual Crossover Comparison of Gadobenate Dimeglumine and Gadopentetate Dimeglumine. Radiology 2004; 230:55-64
59. Knopp MV, Schoenberg SO, Rehm C et al. Assessment of Gadobenate Dimeglumine (Gd-BOPTA) for MR Angiography: Phase I Studies. Invest Radiol 2002; 37:706-715
60. Konopke R, Kersting S, Saeger HD, Bunk A. Kontrastmittelsonographie in der Detektion von Leberraumforderungen - Vergleich zum intraoperativen Befund. Detection of liver lesions by contrast-enhanced ultrasound - comparison to intraoperative findings. Ultraschall Med 2005; 26(2):107-113
61. Kopp AF, Heuschmid M, Claussen CD. Multidetector helical CT of the liver for tumor detection and characterization. Eur Radiol 2002; 12(4):745-52
62. Kroencke TJ, Wasser MN, Pattynama PMT et al. Gadobenate dimeglumine - enhanced magnetic resonance angiography of the abdominal aorta and renal arteries. AJR 2002; 179:1573-1582
63. Kubaska S, Sahani DV, Saini S, Hahn PF, Halpern E. Dual contrast enhanced magnetic resonance imaging of the liver with superparamagnetic iron oxide followed by gadolinium for lesion detection and characterization. Clin Radiol 2001; 56:410-415
64. Larson RE, Semelka RC, Bagley AS, Molina PL, Brown ED, Lee JK. Hypervascular malignant liver lesions: comparison of various MR imaging pulse sequences and dynamic CT. Radiology 1994; 192:393-399
65. Lee VS, Rofsky NM, Morgan GR, Teperman LW, Krinsky GA, Berman P, Weinreb JC. Volumetric mangafodipir trisodium-enhanced cholangiography to define intrahepatic biliary anatomy. Am J Roentgenol 2001; 176:906-908
66. Lim JS, Kim MJ, Kim JH, Kim SI, Choi JS, Park MS, Oh YT, Yoo HS, Lee JT, Kim KW. Preoperative MRI of potential living-donor-related liver transplantation using a single dose of gadobenate dimeglumine. AJR Am J Roentgenol 2005; 185(2):424-31
67. Lim KO, Stark DD, Leese PT, Pfefferbaum A, Rocklage SM, Quay SC. Hepatobiliary MR imaging: first human experience with MnDPDP. Radiology. 1991; 178(1):79-82
68. Liou J, Lee JK, Borrello JA, Brown JJ. Differentiation of hepatomas from nonhepatomatous masses: use of Mn-DPDP-enhanced MR images. Magn Reson Imaging 1994; 12:71-79
69. Low RN, Francis IR, Sigeti JS, Foo TK. Abdominal MR imaging: comparison of T2-weighted fast conventional spin-echo, and contrast-enhanced fast multiplanar spoiled gradient-recalled imaging. Radiology 1993; 186:803-811
70. Low RN. Contrast agents for MR imaging of the liver. J Magn Reson Imaging 1997; 7:56-67
71. Löwe A, Balzer T, Hirt U. Interference of gadolinium-containing contrast-enhancing agents with colorimetric calcium laboratory testing. Invest Radiol 2005; 40:521-525
72. Mahfouz AD, Hamm B, Taupitz M, Wold KJ. Hypervascular liver lesions: differentiation of focal nodular hyperplasia from malignant tumors with dynamic gadolinium-enhanced MR imaging. Radiology 1993; 186:133-138
73. Mahfouz AE, Hamm B, Wolf KJ. Peripheral washout: a sign of malignancy on dynamic gadolinium-enhanced MR images of focal liver lesions. Radiology 1994; 190:49-52
74. Mathieu D, Rahmouni A, Anglade MC, Falise B, Beges C, Gheung P, Mollet JJ, Vasile N. Focal nodular hyperplasia of the liver: assessment with contrast-enhanced Turbo-FLASH MR imaging. Radiology 1991; 180:25-30
75. Mayo-Smith WW, Saini S, Slater G, Kaufman JA, Sharma P, Hahn PF. MR contrast material for vascular enhancement: value of supermagnetic iron oxide. Am J Roentgenol 1996; 166:73-77
76. Mayo-Smith WW, Schima W, Saini S, Slater GJ, McFarland EG. Pancreatic enhancement and pulse sequence analysis using low dose mangafodipir trisodium. Am J Roentgenol 1998; 170:649-652
77. Misselwitz B, Muhler A, Weinmann HJ. A toxicological risk for using manganese complexes? A literature survey of existing data through several medical specialities. Invest Radiol 1995; 30:611-620
78. Murakami T, Baron RL, Peterson MS, Oliver JH 3rd, Davis PL, Confer SR, Federle MP. Hepatocellular carcinoma: MR imaging with mangafodipir trisodium (Mn-DPDP). Radiology 1996; 200:69-77
79. Nelson KL, Gifford LM, Lauber-Huber C, Gross CA, Lasser TA. Clinical safety of Gd-DTPA. Radiology 1995; 196: 439-443
80. Niendorf HP, Kallend D. Gadolinium chelates: adverse reactions. In: Dawson P, Cosgrove DO, Grainger RG (eds): Textbook of contrast media. ISIS Medical Media, Oxford, UK; 1999,323-332
81. Oi H, Murakami T, Kim T, Matsushita M, Kishimoto H, Nakamura H. Dynamic MR imaging and early-phase helical CT for detection small of intrahepatic metastases of hepatocellular carcinoma. Am J Roentgenol 1996; 366:36-374
82. Olukotun AY, Parker JR, Meeks MJ, Lucas MA, Fowler DR, Lucas TR. Safety of gadoteridol injection: U.S. clinical trial experience. J Magn Reson Imaging 1995; 5:17-25
83. Oudkerk M, Torres CG, Song B, Konig M, Grimm J, Fernandez-Cuadrado J, Op de Beeck B, Marquardt M, van Dijk P, Cees de Groot J. Characterization of

liver lesions with mangafodipir trisodium-enhanced MR imaging : multicenter study comparing MR and dual-phase spiral CT. Radiology 2002; 223:517-524
84. Oudkerk M, van den Heuvel AG, Wielopolski PA, Schmitz PIM, Borel Rinke IHM, Wiggers T. Hepatic lesions: detection with ferumoxide-enhanced T1-weighted MR imaging. Radiology 1997; 203:449-456
85. Pauleit D, Textor J, Bachmann R, Conrad R, Flacke S, Layer G, Kreft S, Schild H. Hepatocellular carcinoma: detection with gadolinium- and ferumoxides-enhanced MR imaging of the liver. Radiology 2002; 222:73-80
86. Pediconi F, Catalano C, Occhiato R, Venditti F, Fraioli F, Napoli A, Kirchin MA, Passariello R. Breast lesion detection and characterization at contrast-enhanced MR mammography: gadobenate dimeglumine versus gadopentetate dimeglumine. Radiology 2005; 237:45-56
87. Petersein J, Spinazzi A, Giovagnoni A, Soyer P, Terrier F, Lencioni R, Bartolozzi C, Grazioli L, Chiesa A, Manfredi R, Marano P, Van Persijn Van Meerten EL, Bloem JL, Petre C, Marchal G, Greco A, McNamara MT, Heuck A, Reiser M, Laniado M, Claussen C, Daldrup HE, Rummeny E, Kirchin MA, Pirovano G, Hamm B. Evaluation of the Efficacy of Gadobenate Dimeglumine in MR Imaging of Focal Liver Lesions: a Multicenter Phase III Clinical Study. Radiology 2000; 215:727-736
88. Pintaske J, Martirosian P, Graf H, et al. Relaxivity of gadopentetate dimeglumine (Magnevist®), gadobutrol (Gadovist®) and gadobenate dimeglumine (MultiHance®) in human blood plasma at 0.2 T, 1.5 T and 3 T. Invest Radiol 2006; In press.
89. Pirovano G, Vanzulli A, Marti-Bonmati L, Grazioli L, Manfredi R, Greco A, Holzknecht N, Daldrup-Link HE, Rummeny E, Hamm B, Arneson V, Imperatori L, Kirchin MA, Spinazzi A. Evaluation of the accuracy of gadobenate dimeglumine-enhanced MR imaging in the detection and characterization of focal liver lesions. Am J Roentgenol 2000; 175:1111-1120
90. Prince MR, Erel HE, Lent RW, et al. Gadodiamide administration causes spurious hypocalcemia. Radiology 2003; 227:639-646
91. Proctor KAS, Lokinendi VR, Roberts WL. Gadolinium magnetic resonance contrast agents produce analytic interference in multiple serum assays. Am J Clin Pathol 2004; 121:282-292
92. Prokop M, Schneider G, Vanzulli A, Goyen M, Ruehm SG, Douek P, Dapra M, Pirovano G, Kirchin MA, Spinazzi A. Contrast-enhanced MR Angiography of the Renal Arteries: Blinded Multicenter Crossover Comparison of Gadobenate Dimeglumine and Gadopentetate Dimeglumine. Radiology 2005; 234:399-408
93. Quaia E, Calliada F, Bertolotto M, Rossi S, Garioni L, Rosa L, Pozzi-Mucelli R. Characterization of focal liver lesions with contrast-specific US modes and a sulfur hexafluoride-filled microbubble contrast agent: diagnostic performance and confidence. Radiology 2004; 232(2):420-30
94. Reimer P, Kwong KK, Weisskoff R, Cohen MS, Brady TJ, Weissleder R. Dynamic signal intensity changes in liver with superparamagnetic MR contrast agents. J Magn Reson Imaging 1992; 2:177-181
95. Reimer P, Muller M, Marx C, Wiedermann D, Muller R, Rummeny EJ, Ebert W, Shamsi K, Peters PE. T1 effects of a bolus-injectable superparamagnetic iron oxide, SH U 555 A: dependence on field strength and plasma concentration – preliminary clinical experience with dynamic T1-weighted MR imaging. Radiology 1998; 209:831-836
96. Reimer P, Rummeny EJ, Daldrup HE, Balzer T, Tombach B, Berns T, Peters PE. Clinical results with Resovist: A phase II clinical trial. Radiology 1995; 195:489-496
97. Reimer P, Rummeny EJ, Shamsi K, Balzer T, Daldrup HE, Tombach B, Hesse T, Berns T, Peters PE. Phase II clinical evaluation of Gd-EOB-DTPA: dose, safety aspects, and pulse sequences. Radiology 1996; 199:177-183
98. Reimer P, Schneider G, Schima W. Hepatobiliary contrast agents for contrast-enhanced MRI of the liver: properties, clinical development and applications. Eur Radiol 2004; 14(4):559-78
99. Rofsky NM, Earls JP. Mangafodipir trisodium injection. A contrast agent for abdominal MR imaging. Magn Reson Imaging Clin North Am 1996; 4:73-85
100. Rohrer M, Bauer H, Mintorovitch J, Requardt M, Weinmann HJ. Comparison of magnetic properties of MRI contrast media solutions at different magnetic field strengths. Invest Radiol 2005; 40:715-724.
101. Ros PR, Freeny PC, Harms SE, Seltzer SE, Davis PL, Chan TW, Stillman AE, Muroff LR, Runge VM, Nissenbaum MA, et al. Hepatic MR imaging with ferumoxides: a multicenter clinical trial of the safety and efficacy in the detection of focal hepatic lesions. Radiology 1995; 196:481-488
102. Rummeny EJ, Torres CG, Kurdziel JC, Nilsen G, Op de Beeck B, Lundby B. Mn-DPDP for MR imaging of the liver. Results of an independent image evaluation of the European Phase III studies. Acta Radiol 1997; 38:638-642
103. Runge VM, Armstrong MR, Barr RG, Berger BL, Czervionke LF, Gonzalez CF, Halford HH, Kanal E, Kuhn MJ, Levin JM, Low RN, Tanenbaum LN, Wang AM, Wong W, Yuh WT, Zoarski GH. A clinical comparison of the safety and efficacy of MultiHance (gadobenate dimeglumine) and Omniscan (gadodiamide) in magnetic resonance imaging in patients with central nervous system pathology. Invest Radiol 2001; 36:65-71
104. Runge VM, Lee C, Williams NM. Detectability of small liver metastases with gadolinium BOPTA. Invest Radiol 1997; 32:557-565
105. Runge VM, Pels Rijcken TH, Davidoff A, Wells JW, Stark DD. Contrast-enhanced MR imaging of the liver. J Magn Reson Imaging 1994; 4:281-289
106. Runge VM. A comparison of two MR hepatobiliary gadolinium chelates: Gd-BOPTA and Gd-EOB-DTPA. J Comput Assist Tomogr 1998; 22:643-650
107. Runge VM. Safety of approved MR contrast media for intravenous injection. J Magn Reson Imaging 2000; 12:205-213
108. Sahani DV, O'Malley ME, Bhat S, Hahn PF, Saini S. Contrast-enhanced MRI of the liver with mangafodipir trisodium: imaging technique and results. J Comput Assist Tomogr 2002 26:216-22
109. Sahani DV, Saini S, Kalra MK, Michael M, Hahn

PF. Liver lesion detection and characterization with sequential use of hepatobiliary contrast agent mangafodipir trisodium and gadolinium-DTPA in a single imaging protocol. Acad Radiol 2002; 9 (Suppl 2):460-2
110. Saini S, Edelman RR, Sharma P, Li W, Mayo-Smith W, Slater GJ, Eisenberg PJ, Hahn PF. Blood–pool MR contrast agent material for detection and characterization of focal hepatic lesions. Initial clinical experience with superparamagnetic iron oxide (AMI-227). Am J Roentgenol 1995; 164:1447-1152
111. Sandstede JJW, Beer M, Lipke C, Pabst T, Kenn W, Harre K, Neubauer S, Hahn D. Time course of contrast enhancement patterns after Gd-BOPTA in correlation to myocardial infarction and viability: a feasibility study. JMRI 2001; 14:789-794
112. Sardanelli F, Iozzelli A, Fausto A, Carriero A, Kirchin MA. Gadobenate dimeglumine-enhanced MR imaging breast vascular maps: association between invasive cancer and ipsilateral increased vascularity. Radiology 2005; 235:791-797
113. Schering AG, Berlin. Magnevista. Nierengängiges paramagnetisches Kontrastmittel für die magnetische Resonanztomographie (MRT). 1987
114. Schlund JF, Semelka RC, Kettritz U, Eisenberg LB, Lee JKT. Transient increased segmental hepatic enhancement distal to portal vein obstruction on dynamic gadolinium-enhanced gradient echo MR images. J Magn Reson Imaging 1995; 4:375-377
115. Schneider G, Kirchin MA, Pirovano G, Colosimo C, Ruscalleda J, Korves M, Salerio I, La Noce A, Spinazzi A. Gadobenate dimeglumine-enhanced magnetic resonance imaging of intracranial metastases: effect of dose on lesion detection and delineation. J Magn Reson Imaging 2001; 14:525-539
116. Schneider G, Maas R, Schultze Kool L, Rummeny E, Gehl HB, Lodemann K, Kirchin MA. Low-dose gadobenate dimeglumine versus standard dose gadopentetate dimeglumine for contrast-enhanced magnetic resonance imaging of the liver: an intra-individual crossover comparison. Invest Radiol 2003; 38:85-94
117. Schoellnast H, Brader P, Oberdabernig B, Pisail B, Deutschmann HA, Fritz GA, Schaffler G, Tillich M. High-concentration contrast media in multiphasic abdominal multidetector-row computed tomography: effect of increased iodine flow rate on parenchymal and vascular enhancement. J Comput Assist Tomogr 2005; 29(5):582-7
118. Schuhmann-Giampieri G, Mahler M, Röll G, Maibauer R, Schmitz S. Pharmacokinetics of the liver-specific contrast agent Gd-EOB-DTPA in relation to contrast enhanced liver imaging in humans. J Clin Pharmacol 1997; 37:587-596
119. Schuhmann-Giampieri G, Schmitt-Willich H, Press WR, Negishi C, Weinmann HJ, Speck U. Preclinical evaluation of Gd-EOB-DTPA as a contrast agent in MR imaging of the hepatobiliary system. Radiology 1992; 183:59-64
120. Schuhmann-Giampieri G. Liver contrast media for magnetic resonance imaging. Interrelations between pharmacokinetics and imaging. Invest Radiol 1993; 28:753-761
121. Schwartz LH, Seltzer SE, Tempany CM, Silverman SG, Piwnica-Worms DR, Adams DF, Herman L, Herman LA, Hooshmand R. Superparamagnetic iron oxide hepatic MR imaging: efficacy and safety using conventional and fast spin-echo pulse sequences. J Magn Reson Imaging 1995; 5:566-570
122. Semelka RC, Helmberger TKG. Contrast agents for MR imaging of the liver. Radiology 2001; 218:27-38
123. Semelka RC, Martin DR, Balci C, Lance T. Focal liver lesions: comparison of dual-phase CT and multisequence multiplanar MR imaging including dynamic gadolinium enhancement. J Magn Reson Imaging 2001; 13(3):397-401
124. Semelka RC, Worawattanakul S, Kelekis NL, John G, Woosley JT, Graham M, Cance WG. Liver lesion detection, characterization, and effect on patient management: comparison of single-phase spiral CT and current MR techniques. J Magn Reson Imaging 1997; 7:1040-1047
125. Seneterre E, Taourel P, Bouvier Y, Pradel J, Van Beers B, Daures JP, Pringot J, Mathieu D, Bruel JM. Detection of hepatic metastases: ferumoxides-enhanced MR imaging versus unenhanced MR imaging and CT during arterial portography. Radiology 1996; 200:785-792
126. Shamsi K, Balzer T, Saini S, Ros PR, Nelson RC, Carter EC, Tollerfield S, Niendorf HP. Superparamagnetic iron oxide particles (SH U 555 A): evaluation of efficacy in three doses for hepatic MR imaging. Radiology 1998; 206:365-371
127. Shellock FG, Kanal E. Safety of magnetic resonance imaging contrast agents. J Magn Reson Imaging 1999; 10:477-484
128. Solomon R. The role of osmolality in the incidence of contrast induced nephropathy: a systematic review of angiographic contrast media in high risk patients. Kidney International 2005; 68:2256-2263
129. Spinazzi A, Lorusso V, Pirovano G, Kirchin M. Safety, tolerance, biodistribution and MR imaging enhancement of the liver with gadobenate dimeglumine. Acad Radiol 1999; 6:282-291
130. Spinazzi A, Lorusso V, Pirovano G, Taroni P, Kirchin M, Davies A. MultiHance clinical pharmacology: biodistribution and MR enhancement of the liver. Acad Radiol 1998; 5:86-89
131. Stillman AE, Wilke N, Li D, Haacke M, McLachlan S. Ultrasmall superparamagnetic iron oxide to enhance MRA of the renal and coronary arteries: Studies in human patients. J Comput Assist Tomog 1996; 20:51-55
132. Swan SK, Baker JF, Free R, Tucker RM, Barron B, Barr R, Seltzer S, Gazelle GS, Maravilla KR, Barr W, Stevens GR, Lambrecht LJ, Pierro JA. Pharmacokinetics, safety and tolerability of gadoversetamide injection (Optimark) in subjects with central nervous system or liver pathology and varying degrees of renal function. J Magn Reson Imaging 1999; 9:317-321
133. Tang Y, Yamashita Y, Arakawa A, Namimoto T, Mitsuzaki K, Abe Y, Katahira K, Takahashi M. Detection of hepatocellular carcinoma arising in cirrhotic livers : comparison of gadolinium- and ferumoxides-enhanced MR imaging. Am J Roentgenol 1999; 172:1547-1554
134. Tanimoto A, Wakabayashi G, Shinmoto H, Nakat-

suka S, Okuda S, Kuribayashi S. Superparamagnetic iron oxide-enhanced MR imaging for focal hepatic lesions: a comparison with CT during arterioportography plus CT during hepatic arteriography. J Gastroenterol 2005; 40(4):371-80
135. Tirkkonen B, Aukrust A, Couture E, Grace D, Haile Y, Holm KM, Hope H, Larsen A, Lunde HS, Sjogren CE. Physicochemical characterization of mangafodipir trisodium. Acta Radiol 1997; 38:780-9
136. Tweedle MF. Physicochemical properties of gadoteridol and other magnetic resonance contrast agents. Invest Radiol 1992; 27:1-6
137. Vogl TJ, Hamm B, Schnell B, Eibl-Eibesfeldt B, Steiner S, Lissner J. Focal liver lesions: MR imaging with Mn-DPDP - initial clinical results in 40 patients. Radiology 1991; 182:167-174
138. Vogl TJ, Hammerstingl R, Schwarz W, Kummel S, Muller PK, Balzer T, Lauten MJ, Balzer JO, Mack MG, Schimpfky C, Schrem H, Bechstein WO, Neuhaus P, Felix R. Magnetic resonance imaging of focal liver lesions: comparison of the superparamagnetic iron oxide Resovist versus gadolinium in the same patient. Invest Radiol 1996; 31:696-708
139. Vogl TJ, Hammerstingl R, Schwarz W, Mack MG, Muller PK, Pegios W, Keck H, Eibl-Eibesfeldt A, Hoelzl J, Woessmer B, Bergman C, Felix R. Superparamagnetic iron oxide-enhanced versus gadolinium-enhanced MR imaging for differential diagnosis of focal liver lesions. Radiology 1996; 198:881-887
140. Vogl TJ, Kummel S, Hammerstingl R, Schellenbeck M, Schumacher G, Balzer T, Schwarz W, Muller PK, Bechstein WO, Mack MG, Sollner O, Felix R. Liver tumors: comparison of MR imaging with Gd-EOB-DTPA and Gd-DTPA. Radiology 1996; 200:59-67
141. Vogler H, Platzek J, Schuhmann-Giampieri G, Frenzel T, Weinmann HJ, Raduchel B, Press WR. Pre-clinical evaluation of gadobutrol: a new, neutral, extracellular contrast agent for magnetic resonance imaging. Eur J Radiol 1995; 21:1-10
142. Völk M, Strotzer M, Lenhart M, Seitz J, Manke C, Feuerbach S, Link J. Renal time-resolved MR angiography: quantitative comparison of gadobenate dimeglumine and gadopentetate dimeglumine with different doses. Radiology 2001; 220:484-488
143. Wang C, Ahlstrom H, Ekholm S, Fagertun H, Hellstrom M, Hemmingsson A, Holtas S, Isberg B, Jonnson E, Lonnemark-Magnusson M, McGill S, Wallengren NO, Westman L. Diagnostic efficiency of Mn-DPDP in MR imaging of the liver: a phase III multicenter study. Acta Radiol 1997; 38:643-649
144. Wang C, Ahlstrom H, Eriksson B, Lonnemark M, McGill S, Hemmingsson A. Uptake of mangafodipir trisodium in liver metastases from neuroendocrine tumors. J Magn Reson Imaging 1998; 8:682-686
145. Ward J, Niak KS, Guthrie JA, Wilson D, Robinson PJ. Hepatic lesion detection: comparison of MR imaging after the administration of superparamagnetic iron oxide with dual-phase CT by using alternative - free response receiver operating characteristic analysis. Radiology 1999; 210:459-466
146. Ward J, Robinson PJ, Guthrie JA, Downing S, Wilson D, Lodge JP, Prasad KR, Toogood GJ, Wyatt JI. Liver metastases in candidates for hepatic resection: comparison of helical CT and gadolinium- and SPIO-enhanced MR imaging. Radiology 2005; 237(1):170-80
147. Weinmann HJ, Bauer H, Gries H, Radüchel B, Platzek J, Press WR. New contrast agents for MRI. In: Rinck PA (ed): Contrast and contrast agents in magnetic resonance imaging.: European Workshop on Magnetic Resonance in Medecine, State University Mons, Belgium, 1989:135-48
148. Whitney WS, Herfkens RJ, Jeffrey RB, McDonnell CH, Li KC, Van Dalsem WJ, Low RN, Francis IR, Dabatin JF, Glazer GM. Dynamic breath-hold multiplanar spoiled gradient-recalled MR imaging with gadolinium enhancement for differentiating hepatic hemangiomas from malignancies at 1.5 T. Radiology 1993; 189:863-870
149. Wikström J, Wasser MN, Pattynama PMT et al. Gadobenate dimeglumine - enhanced magnetic resonance angiography of the pelvic arteries. Invest Radiol 2003; 38:504-515
150. Yamashita Y, Mitsuzaki K, Yi T, Ogata I, Nishiharu T, Urata J, Takahashi M. Small hepatocellular carcinoma in patients with chronic liver damage: prospective comparison of detection with dynamic MR imaging and helical CT of the whole liver. Radiology 1996; 200:79-84
151. Yamashita Y, Yamamoto H, Hirai A, Yoshimatsu S, Baba Y, Takahashi M. MR imaging enhancement with superparamagnetic iron oxide in chronic liver disease: Influence of liver dysfunction and parenchymal pathology. Abdom Imaging 1996; 21:318-323
152. Yoshida H, Itai Y, Ohtomo K, Kokubo T, Minami M, Yashiro N. Small hepatocellular carcinoma and cavernous hemangioma; differentiation with dynamic FLASH MR imaging with Gd-DTPA. Radiology 1989; 171:339-342

4

Imaging of Benign Focal Liver Lesions

CONTENTS

4.1 Primary Benign Liver Lesions

Each of the cellular components of the liver - hepatocytes, biliary epithelium and mesenchyme - can give rise to benign tumors.

It is possible to classify these tumors based on their cellular origin:

Hepatocellular Origin
- Hepatocellular adenoma
- Hepatocellular hyperplasia
  - Focal nodular hyperplasia (FNH)
  - Nodular regenerative hyperplasia

Cholangiocellular Origin
- Hepatic cyst
  - Simple hepatic cyst
  - Congenital hepatic fibrosis or polycystic liver disease

Mesenchymal Origin
- Mesenchymal hamartoma
- Hemangioma
- Lipoma, Angiomyolipoma, Myelolipoma
- Leiomyoma

Most benign tumors are incidental findings during abdominal ultrasonography. The most common entities are simple cysts, cavernous hemangiomas, and focal nodular hyperplasia.

4.1.1 Hemangioma

Hepatic hemangioma is the most common primary liver tumor; the incidence of this lesion in the general population varies in published reports from 0.4% to 20%. Hemangiomas may be multiple in up to 50% of cases, but may also be found in conjunction with other neoplasms. An association with focal nodular hyperplasia occurs in 10-20% of cases [18, 53].

There are two forms of this neoplasm: those that occur in childhood and those that occur in adults. Infantile hepatic hemangioma frequently resolves spontaneously. However, it may also become life-threatening due to arterio-venous shunting and resulting cardiac failure. In such cases, the lesion requires aggressive surgical intervention. Hemangiomas in adults occur most frequently in the fourth and fifth decades of life and there is a much higher incidence in women (about 80%). Estrogen replacement therapy may play a role in the pathogenesis of this type of tumor [24]. Hemorrhage is the most common reason for prophylactic resection, although this occurs relatively infrequently.

Hemangioma, whether solitary or multiple, is a well-defined lesion that ranges in size from a few mm to more than 20 cm. Hemangiomas larger

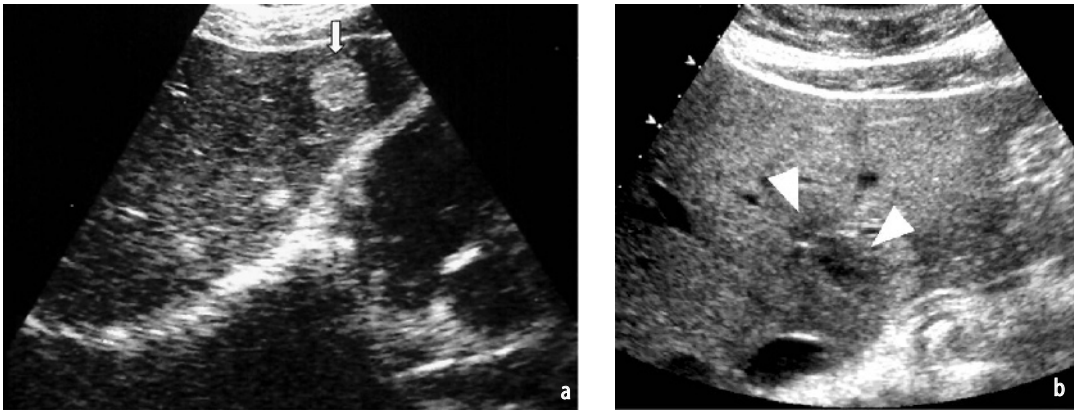

Fig. 1a, b. Hemangioma on US: ultrasound reveals (**a**) a well-defined homogeneously hyperechoic lesion (*arrow*) or (**b**) a tumor with heterogeneous echogenicity (*arrowheads*)

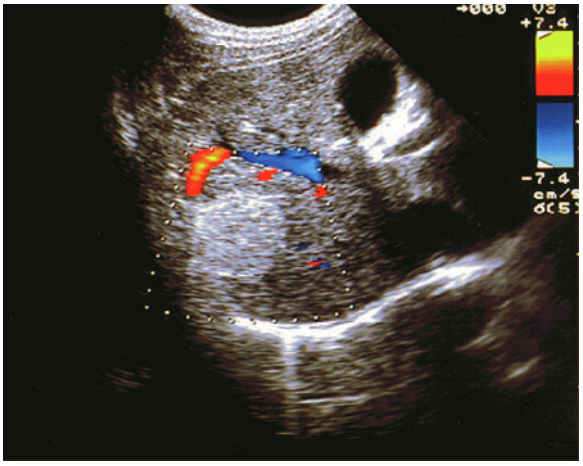

Fig. 2. Hemangioma on color Doppler US. On color Doppler ultrasound the lesion demonstrates a homogeneous structure with no flow within the nodule

than 10 cm are considered "giant" hemangiomas. Microscopically, they are tumors composed of multiple vascular channels lined by a single layer of endothelial cells supported by a thin, fibrous stroma. Large lesions almost always have a heterogeneous composition with areas of fibrosis, necrosis, cystic changes and intratumoral coarse calcifications. In some cases, abundant fibrous tissue completely replaces the lesion [1, 107].

As demonstrated in many studies on the natural history of hemangioma, a large proportion are asymptomatic, and liver function tests are normal. Nevertheless, in some cases, symptoms of liver hemangioma may be misleading. Rarely, patients present with abdominal pain, and in exceptional cases, with fever, leukocytosis, thrombocytopenia, consumptive coagulopathy (Kasabach-Merritt Syndrome) or cholestasis. Occasionally, very large hemangiomas may cause symptoms by compressing adjacent organs [80].

On ultrasound (US) examination, hemangiomas are typically homogeneously hyperechoic with well-defined margins, and may exhibit faint acoustic enhancement. The echogenicity may vary because these tumors may contain cystic and fibrotic regions; this is especially true in large hemangiomas (Fig. 1). Color Doppler US demonstrates filling vessels in the periphery of the tumor but no significant Color Doppler flow deep within the hemangioma itself (Fig. 2).

Power Doppler, however, may detect flow within hemangiomas but the pattern is non-specific and can also be seen in other primary hepatic liver lesions such as hepatocellular carcinoma (HCC) and focal nodular hyperplasia (FNH) [23].

Contrast-enhanced US allows monitoring of the dynamic enhancement behavior of hemangioma. During the arterial phase, both capillary and cavernous hemangiomas generally demonstrate an early and strong peripheral enhance-

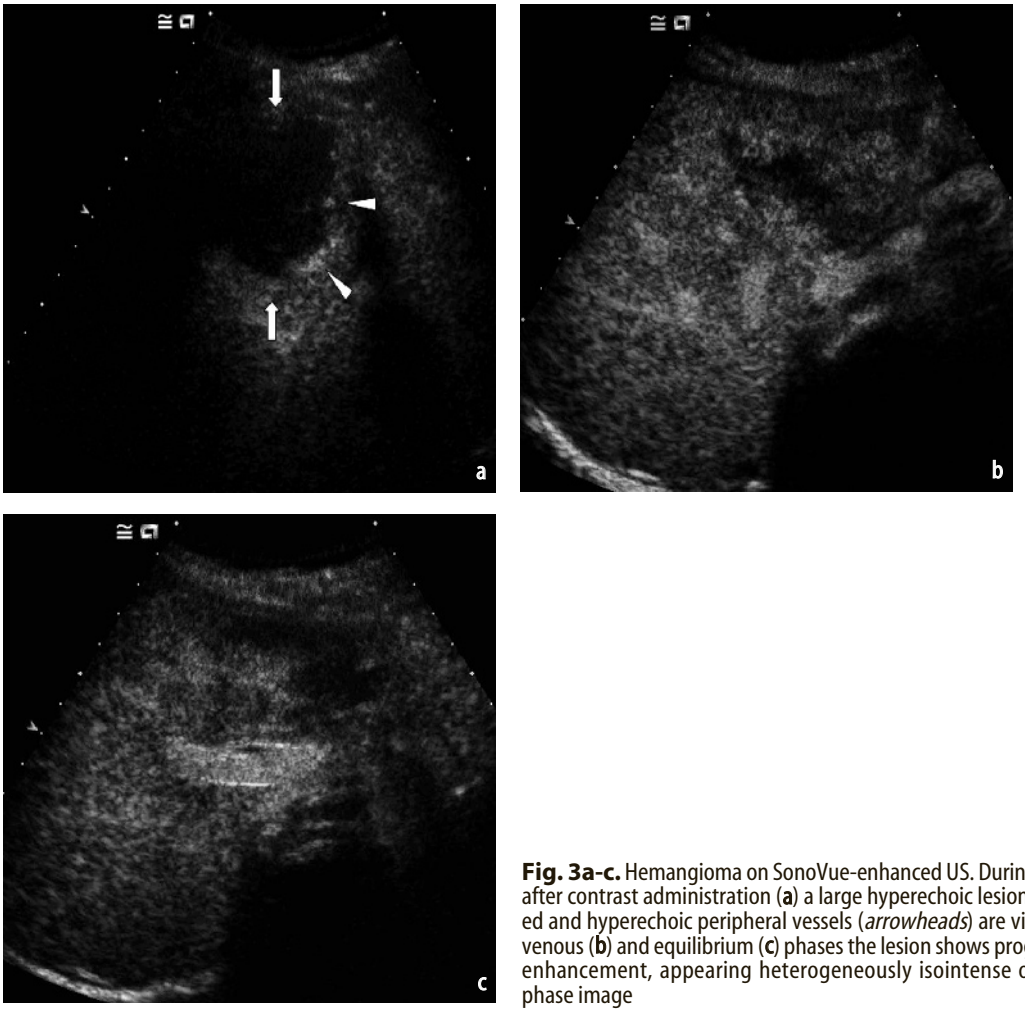

Fig. 3a-c. Hemangioma on SonoVue-enhanced US. During the arterial phase after contrast administration (**a**) a large hyperechoic lesion (*arrows*) id detected and hyperechoic peripheral vessels (*arrowheads*) are visible. In the portal-venous (**b**) and equilibrium (**c**) phases the lesion shows progressive centripetal enhancement, appearing heterogeneously isointense on the equilibrium phase image

ment. In the portal-venous phase, hemangiomas show a tendency for centripetal filling, and during the late phase, the vascular components of both capillary and cavernous hemangiomas tend to appear hyperechoic compared to the surrounding normal liver parenchyma. In the late phase, however, cavernous hemangiomas tend to be more heterogeneous due to incomplete filling of the lesion (Fig. 3) [7, 56].

Hemangiomas typically appear as low density masses on computed tomography (CT) imaging, with well-defined lobulated margins on unenhanced scans. During the arterial phase, hemangiomas demonstrate an initial peripheral nodular enhancement on spiral CT; this enhancement is isodense with the the aorta and progresses centrally with time. On delayed scans, the lesion becomes hyperdense or isodense compared with normal liver parenchyma (Fig. 4). The early nodular peripheral enhancement corresponds to large peripheral feeding vessels. The presence of nodular enhancement which is isodense with the aorta has been found to be about 70% sensitive and 100% specific in differentiating hemangioma from hepatic metastases [59]. Although small lesions often fill-in rapidly and completely (Fig. 5), large tumors may show central non-enhanced areas corresponding to scar tissue, myxoid changes or cystic cavities (Fig. 4) [118].

Hemangiomas are revealed as focal defects on both hepatobiliary and sulfur colloid scans against underlying liver which shows normal isotope uptake. Tagged red blood cell scans can be virtually diagnostic of this lesion; there is a defect in the early phases that shows prolonged and persistent "filling-in" on delayed scans [41].

Evaluation of hemangiomas of the liver is one of the major applications of magnetic resonance (MR) imaging, particularly in oncology patients with atypical hemangiomas detected on CT or US examinations (Fig. 6).

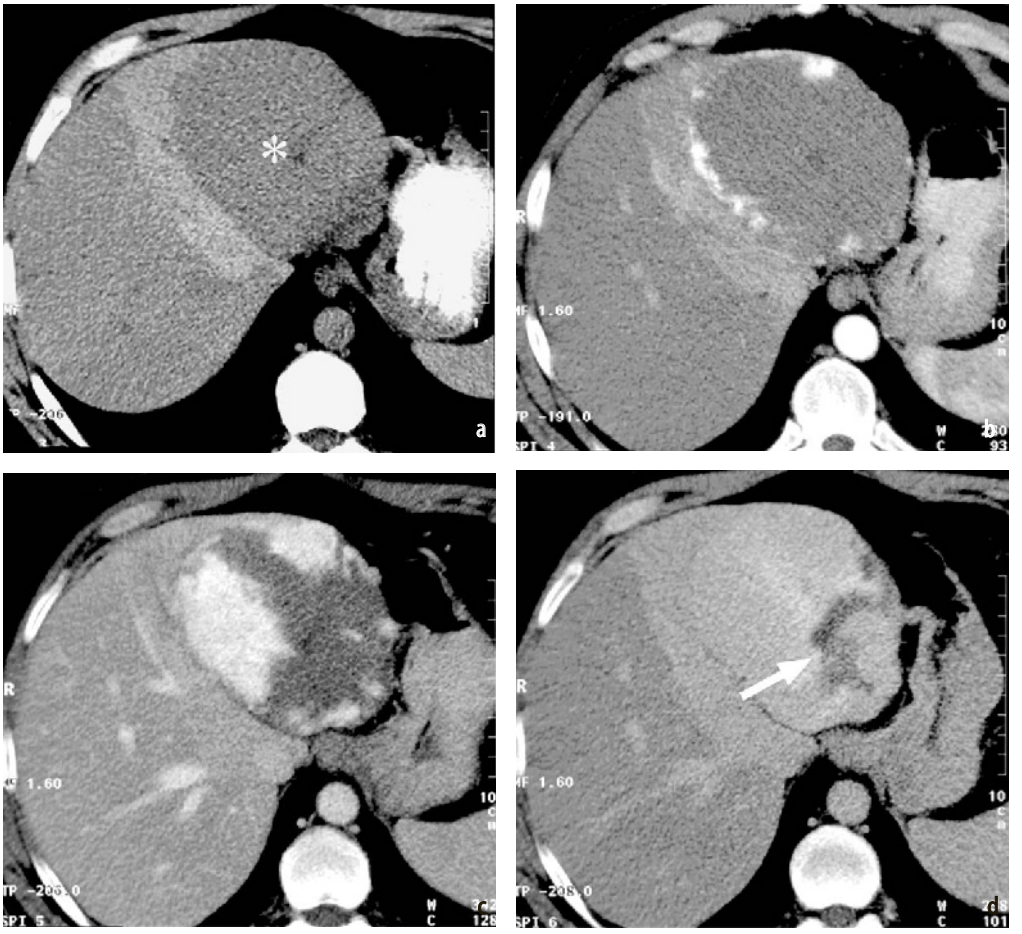

Fig. 4a-d. Cavernous hemangioma. On the unenhanced CT scan (**a**) the lesion (*asterisk*) is homogeneously hypodense with well-defined margins. During the arterial phase (**b**), hyperdense peripheral nodular enhancement is seen, which progresses centrally during the portal-venous phase (**c**). Stromal components within the lesion are demonstrated during the equilibrium phase (**d**), as areas of incomplete filling-in (*arrow*)

On unenhanced T1-weighted MR images, hemangiomas are most commonly visualized as well-defined, typically homogeneous, hypointense masses with lobulated borders. On T2-weighted images they characteristically show marked homogeneous hyperintensity with occasional low signal intensity areas corresponding to areas of fibrosis (Fig. 7) [63, 92].

After administration of an extracellular Gd-agent, or an agent with both extracellular and liver-specific properties, three types of enhancement pattern may be seen, depending on the size of the lesion. The majority of small lesions under 1.5 cm in diameter show uniform early enhancement during the arterial phase at 25–30 sec post-contrast, or peripheral nodular enhancement progressing centripetally to uniform enhancement in the late arterial and portal-venous phases (Fig. 8).

The second pattern is frequently seen in medium-size lesions between 1.5 and 5 cm, but may also be seen in large hemangiomas. These lesions typically show a peripheral nodular enhancement that progresses centripetally to a uniform enhancement in the equilibrium phase at 3-5 min post-contrast. In particular, large hemangiomas may show peripheral nodular enhancement with persistent central hypointensity corresponding to fibrosis and or cystic areas (Fig. 9).

Peripheral nodular enhancement, in particular, detected during the arterial phase of dynamic MR

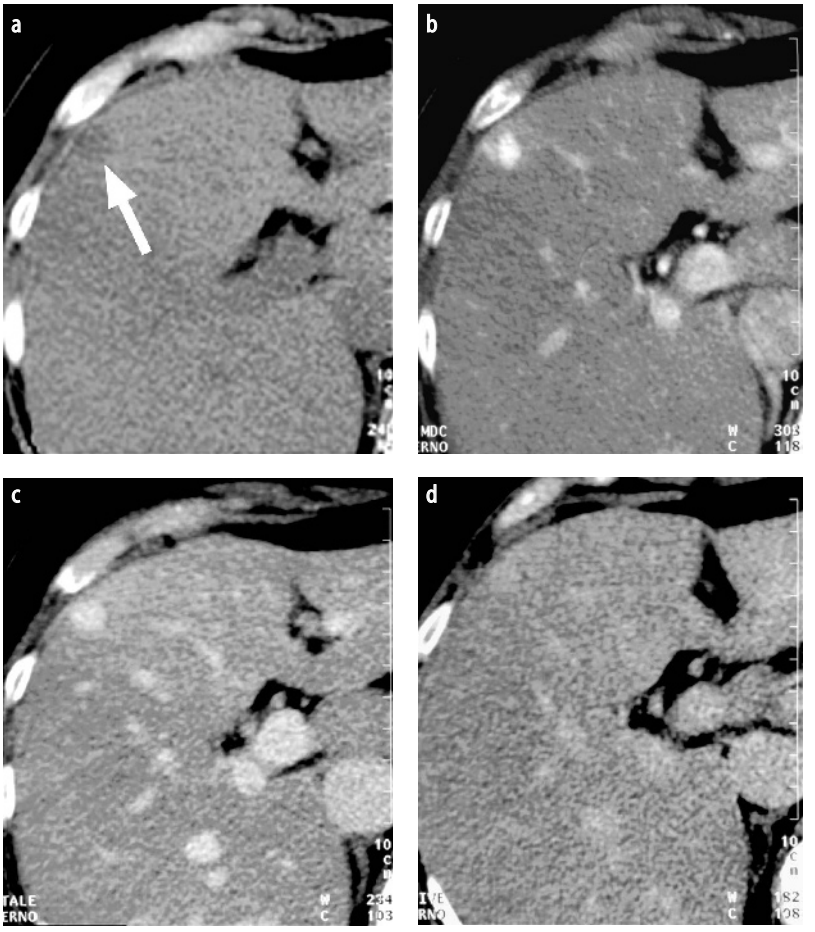

Fig. 5a-d. Hypervascular hemangioma. On the unenhanced CT scan (**a**) the hemangioma appears slightly hypodense (*arrow*). Rapid filling-in is seen in the arterial phase (**b**), which persists into the portal-venous phase (**c**). During the delayed phase (**d**) the hemangioma is isodense with the surrounding liver tissue

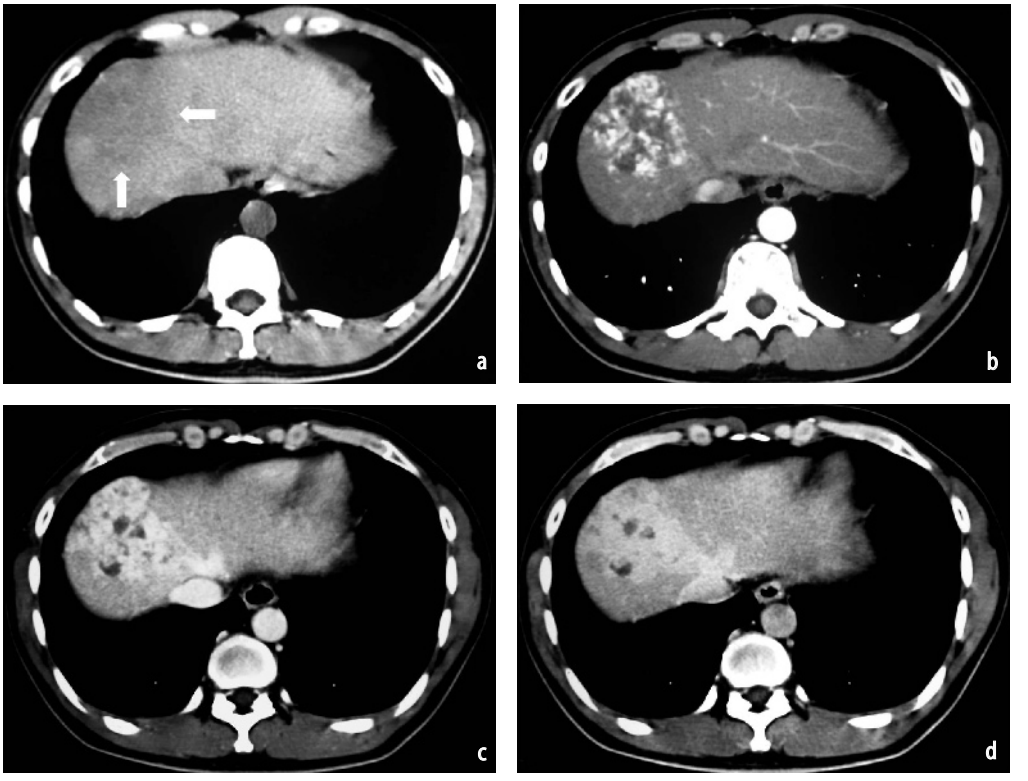

Fig. 6a-d. Atypical hemangioma. Patient with history of renal cell carcinoma. The precontrast CT scan (**a**) shows a large, slightly hypodense lesion (*arrows*) located in segment VIII of the right liver lobe. In the arterial phase of the dynamic study after contrast medium administration (**b**) the hemangioma demonstrates an irregular and marked enhancement with progressive but incomplete filling in the portal-venous (**c**) and equilibrium (**d**) phases

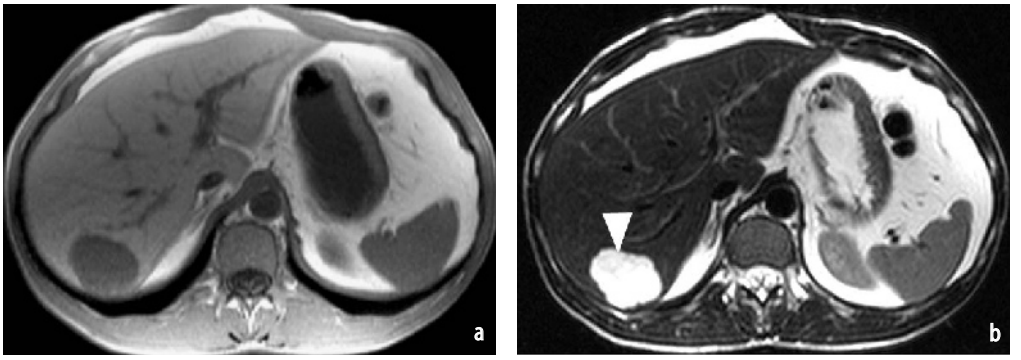

Fig. 7a, b. Hemangioma. On the unenhanced GE T1-weighted MR image (**a**), the hemangioma is seen as a well-defined hypointense mass. Conversely, on the T2-weighted image (**b**), the lesion (*arrowhead*) is markedly hyperintense

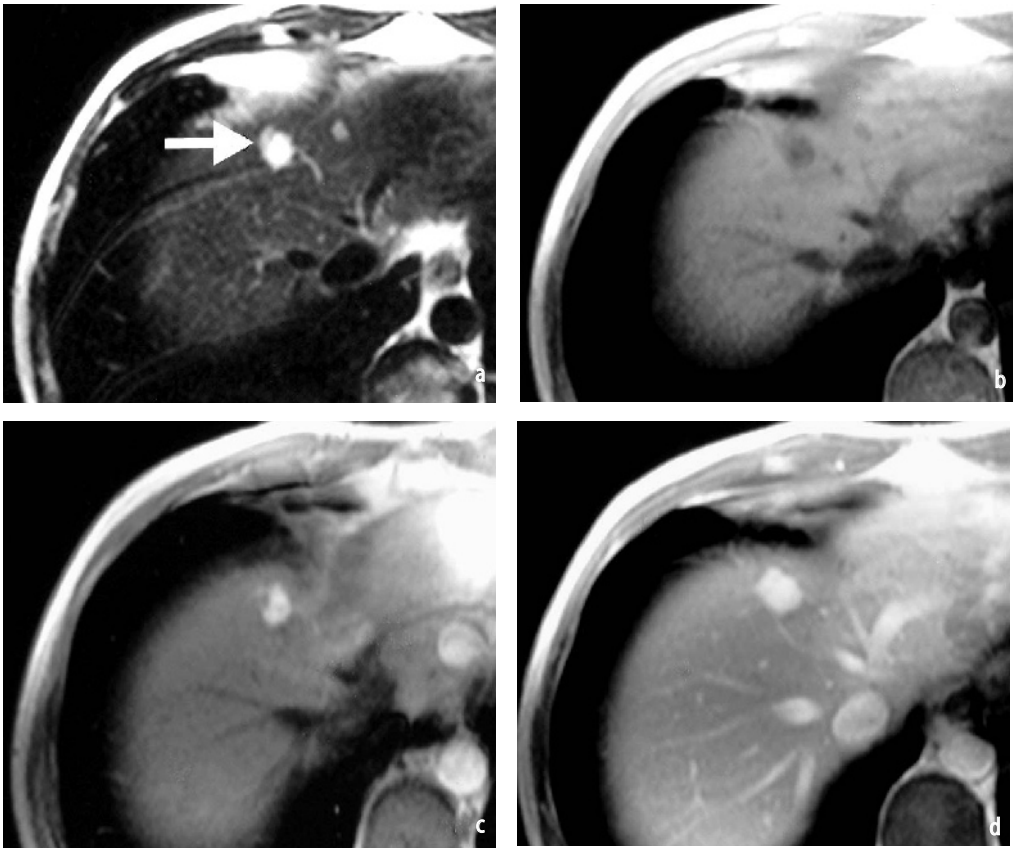

Fig. 8a-d. Hypervascular hemangioma after Gd-BOPTA .The lesion is markedly hyperintense (*arrow*) on the Turbo SE T2-weighted image (**a**) and hypointense on the GE T1-weighted image (**b**). Rapid enhancement on images acquired during the arterial phase (**c**) after the bolus injection of Gd-BOPTA is noted, which persists and becomes homogeneous during the portal-venous phase (**d**)

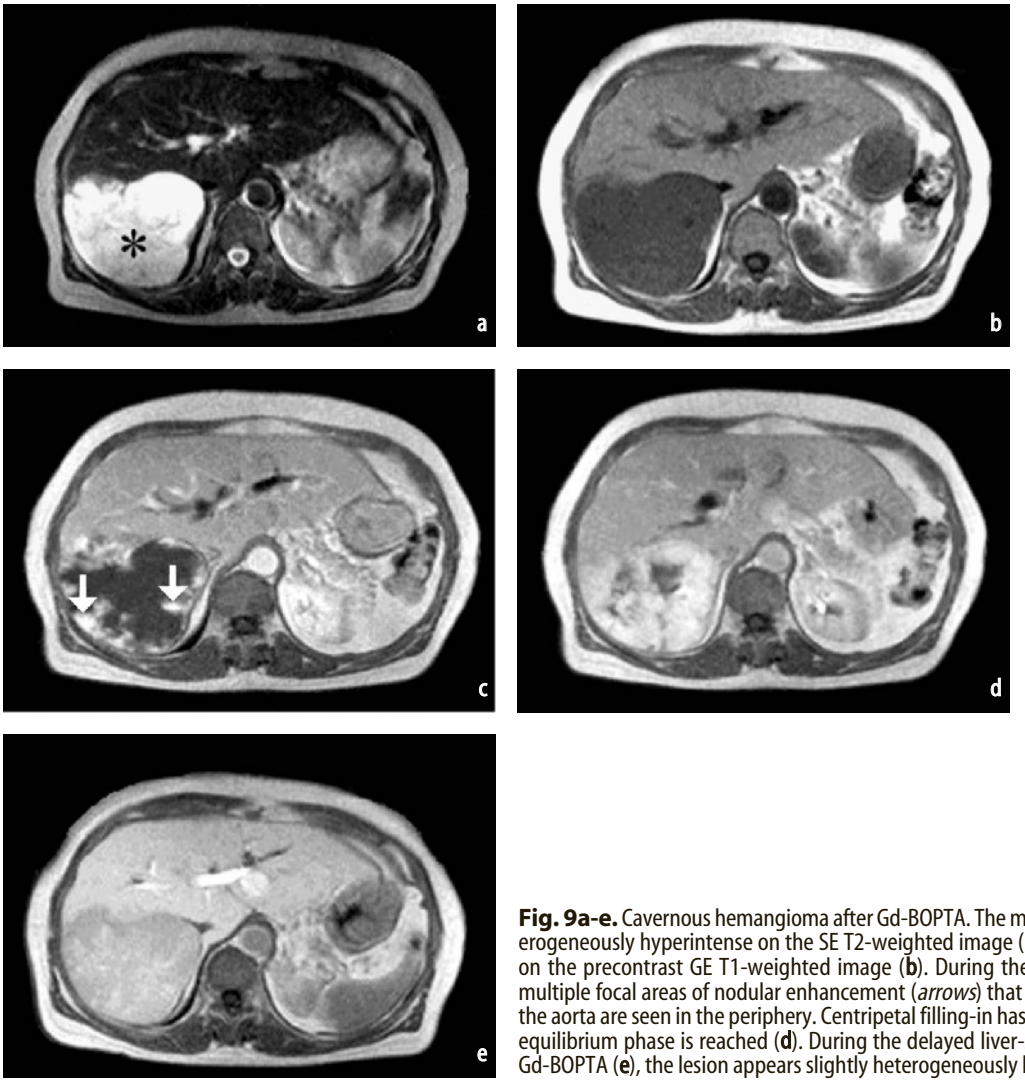

Fig. 9a-e. Cavernous hemangioma after Gd-BOPTA. The mass (*asterisk*) is heterogeneously hyperintense on the SE T2-weighted image (**a**) and hypointense on the precontrast GE T1-weighted image (**b**). During the arterial phase (**c**), multiple focal areas of nodular enhancement (*arrows*) that are isointense with the aorta are seen in the periphery. Centripetal filling-in has occurred when the equilibrium phase is reached (**d**). During the delayed liver-specific phase after Gd-BOPTA (**e**), the lesion appears slightly heterogeneously hypointense

imaging of the liver, is a very useful discriminating feature for the differential diagnosis of hemangiomas and metastases [59]. The third pattern of enhancement includes lesions that enhance homogeneously and thus may be difficult to differentiate from hypervascular metastases, which may demonstrate similar enhancement behavior. For these lesions, the combination of T2-weighted and serial dynamic post-contrast T1-weighted images facilitates a confident diagnosis of hemangioma (Fig. 10) [94].

Liver-specific contrast agents have also been evaluated for the characterization of hemangiomas. As in the case of purely extracellular Gd agents, a "nodular" centripetal pattern of enhancement on dynamic imaging after Gd-BOPTA and Gd-EOB-DTPA administration is considered highly specific for hemangioma in a manner similar to the finding of rim enhancement in the case of liver metastases. In the delayed liver-specific phase, hemangiomas tend to be isointense or hypointense compared to the surrounding liver parenchyma, and often contain low intensity areas indicative of fibrotic or cystic components. While contrast agent pooling of intralesional components may be seen a peripheral wash-out as observed in metastases is not observed in hemangiomas.

Superparamagnetic iron oxide (SPIO) contrast agents have also been evaluated for the characterization of hemangiomas, especially when these appear atypical on other imaging modalities. After administration of SPIO, hemangiomas appear hyperintense on post-contrast T1-weighted images compared to surrounding liver parenchyma, the reverse of their appearance on pre-contrast T1-

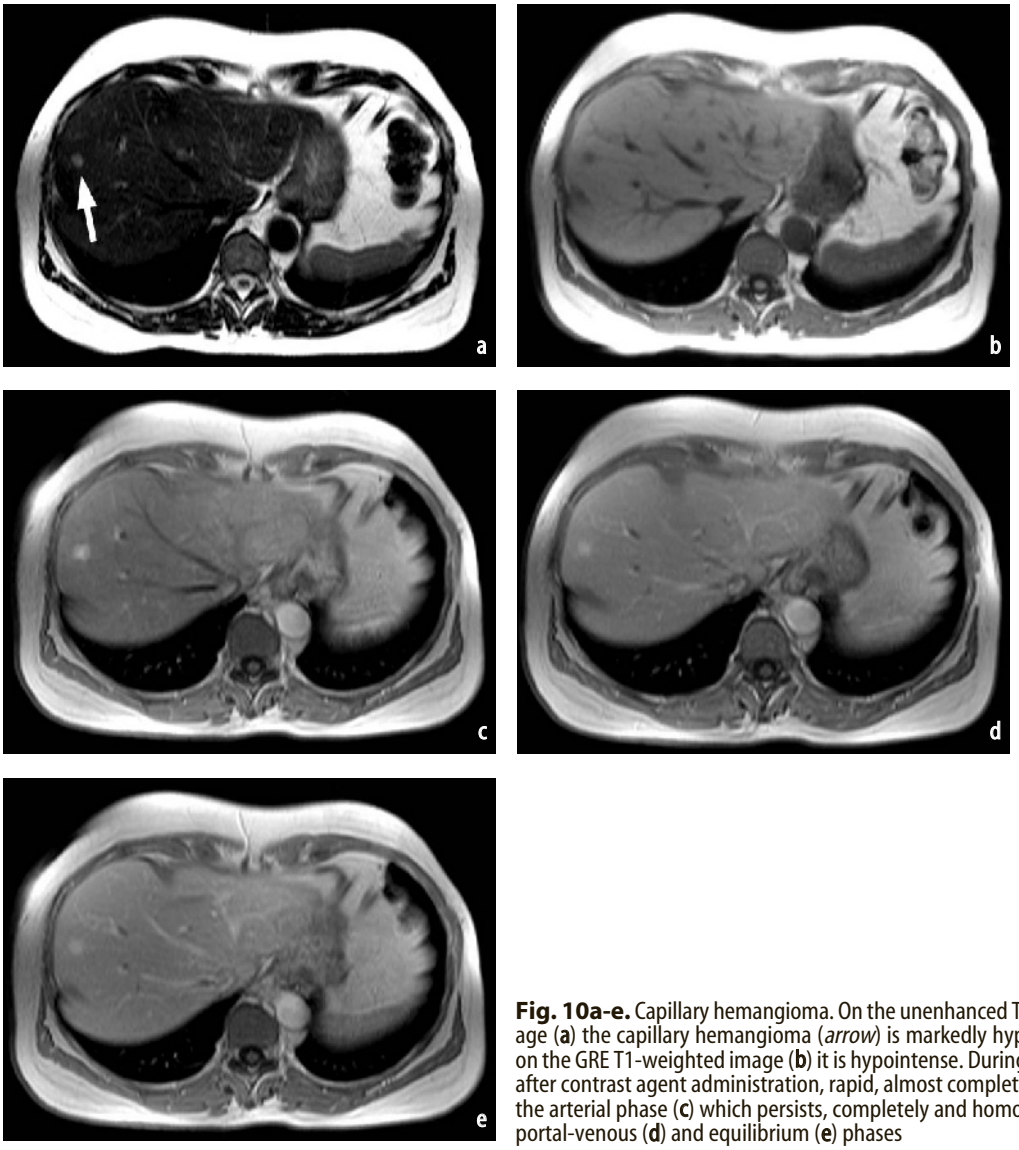

Fig. 10a-e. Capillary hemangioma. On the unenhanced T2-weighted TSE image (**a**) the capillary hemangioma (*arrow*) is markedly hyperintense, whereas on the GRE T1-weighted image (**b**) it is hypointense. During the dynamic study after contrast agent administration, rapid, almost complete filling-in is seen in the arterial phase (**c**) which persists, completely and homogeneously, into the portal-venous (**d**) and equilibrium (**e**) phases

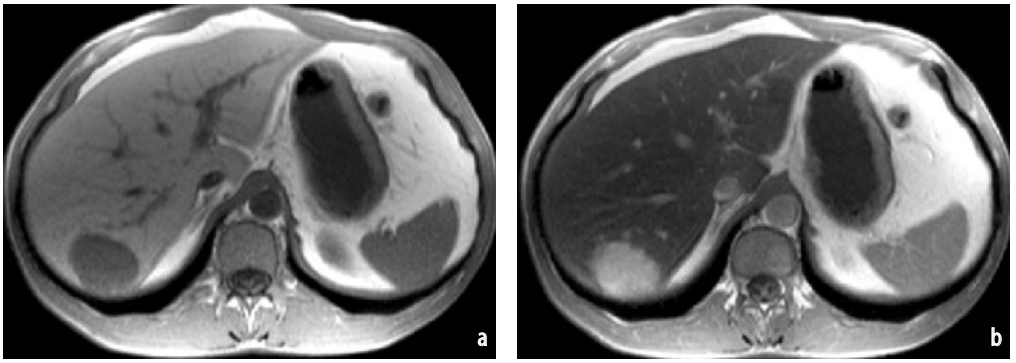

Fig. 11a, b. Hemangioma after SPIO. On the unenhanced GE T1-weighted image the hemangioma appears hypointense (**a**). On the post-contrast T1-weighted image after SPIO administration (**b**) the lesion shows increased signal intensity compared to the surrounding liver tissue (T1 effect)

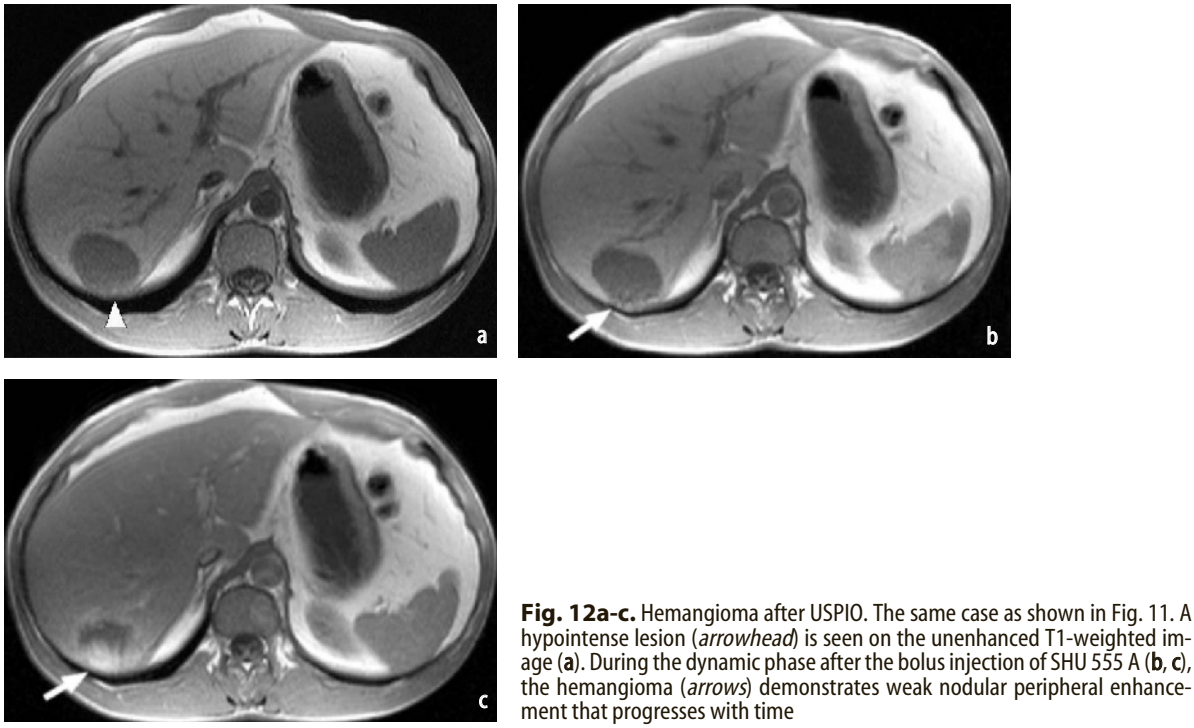

Fig. 12a-c. Hemangioma after USPIO. The same case as shown in Fig. 11. A hypointense lesion (*arrowhead*) is seen on the unenhanced T1-weighted image (**a**). During the dynamic phase after the bolus injection of SHU 555 A (**b**, **c**), the hemangioma (*arrows*) demonstrates weak nodular peripheral enhancement that progresses with time

weighted images. This signal enhancement is caused by a T1 effect due to low SPIO concentration in the vascular channels of hemangiomas. However, this effect can only be observed on T1-weighted delayed phase images, which are not routinely acquired after administration of SPIO (Fig. 11) [35].

With the use of ultrasmall superparamagnetic iron oxide (USPIO) contrast agents, which are ultimately cleared by the reticuloendothelial system but which reside in the intravascular compartment immediately after injection, hemangiomas enhance on T1-weighted dynamic images and appear hyperintense compared with the normal liver parenchyma (Fig. 12). On T2-weighted scans the lesions decrease in signal intensity and, at higher doses of USPIO, may become isointense with the liver [90].

Hemangiomas usually do not contain significant amounts of Kupffer cells or normal hepatocytes and therefore do not take up SPIO particles or Mn^{++} after the infusion of mangafodipir trisodium. Specifically, on delayed phase T2-weighted images after SPIO administration, hemangiomas appear hyperintense, whereas on T1-weighted images in the hepatobiliary phase after administration of mangafodipir trisodium hemangiomas generally appear hypointense.

4.1.2 Focal Nodular Hyperplasia

FNH is a benign tumor-like lesion of the liver which is considered to be the result of a hyperplastic response of the hepatocytes to the presence of a pre-existing vascular malformation. It is thought that increased arterial flow hyperperfuses the local parenchyma leading to secondary hepatocellular hyperplasia [111].

In support of this theory, FNH has been found in association with cavernous hemangioma and in some cases FNH has been associated with vascular malformations of various other organs and with neoplasms of the brain (Fig. 13) [111].

In frequency, FNH is the second most common benign hepatic tumor after hemangioma and has been shown to constitute about 8% of primary hepatic tumors at autopsy. It usually occurs in women of childbearing- and middle-age, but cases have been reported in men and children as well. Most investigators agree that oral contraceptives are not the causal agents of FNH [9]. However estrogens could have a trophic effect on FNH by increasing the size of nodules and contributing to the vascular changes [111].

Clinically, this tumor is usually an incidental finding at autopsy, elective surgery or on diagnos-

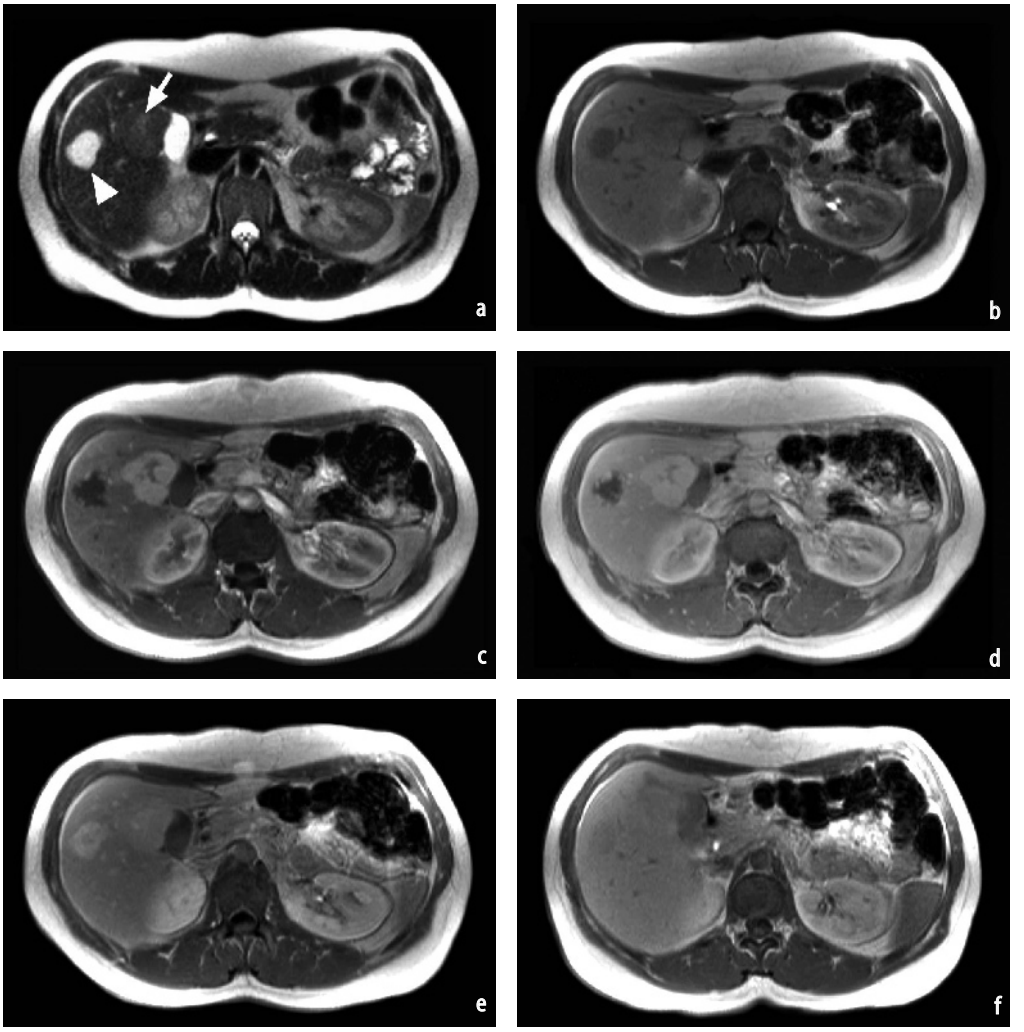

Fig. 13a-f. Focal nodular hyperplasia (FNH) / Hemangioma. Unenhanced T2-weighted images (**a**) show a slightly hyperintense lesion with a small hyperintense central scar (*arrow*) compressing the gallbladder. An additional subcapsular lesion (*arrowhead*) with homogeneous high signal intensity (light-bulb phenomenon indicative of hemangioma) can be seen. On the unenhanced T1-weighted GE echo image (**b**), the suspected hemangioma appears homogeneously hypointense with distinct borders while the lesion compressing the gallbladder shows isointense signal intensity and lobulation. On arterial phase images after the bolus administration of Gd-BOPTA (**c**), the lesion located near the gallbladder shows strong hyperintensity with a central hypointense scar. On portal-venous phase images (**d**), this lesion is still hyperintense and clearly delineated and the central scar is still hypointense. The second lesion demonstrates nodular peripheral enhancement typical of hemangioma. Imaging during the equilibrium phase 5 min after Gd-BOPTA administration (**e**) reveals enhancement of the central scar, a typical enhancement pattern of pseudoscar formation in FNH. The second lesion shows homogeneous contrast agent uptake. In the hepatobiliary phase (**f**), the lesion close to the gallbladder appears isointense compared to the surrounding parenchyma, indicating a lesion consisting of functioning hepatocytes able to take up Gd-BOPTA. The imaging pattern is consistent with that of an FNH. The second lesion is again hypointense and the imaging pattern is consistent with that of a hemangioma

tic liver imaging performed for other reasons. Less than one third of cases are discovered because of clinical symptoms, usually comprising right upper quadrant or epigastric pain. Although most patients are asymptomatic at discovery, in symptomatic cases pain is usually caused by larger lesions, which expand the Glisson capsule or have a focal mass effect on surrounding organs.

The natural history of FNH is characterized by the absence of complications. Therefore, typical asymptomatic FNH should be managed conservatively in association with the discontinuation of oral contraceptives. Rarely, when symptoms are particularly severe, surgical resection may be indicated.

FNH is usually a solitary, subcapsular nodular mass, but cases with several nodules have been described (Fig. 14). FNH is a homogeneous tumor, which only infrequently demonstrates hemorrhage and necrosis. On cut section the majority of these tumors have a central fibrous scar and although the margin is sharp, generally there is no capsule [19].

Often FNH has a mean diameter of 5 cm at the

time of diagnosis, although sometimes it is possible to find neoplasms that replace an entire lobe of the liver, as in the lobar FNH form.

Currently, FNH is divided into two types, classic and non-classic. Classic FNH is characterized by the presence of abnormal nodular architecture, malformed vessels, and cholangiocellular proliferation. The non-classic type comprises three subtypes: a) teleangiectatic FNH, b) FNH with cytologic atypia and c) mixed hyperplastic and adenomatous FNH.

Non-classic FNH may lack the nodular abnormal architecture and malformed vessels, which characterize the classic type, but they always show bile ductular proliferation [73].

The gross appearance of classic FNH consists of lobulated contours and parenchyma that is composed of nodules surrounded by radiating fibrous septa originating from a central scar that contains malformed vessels. A classical form of FNH with a stellate scar is seen in about 50% of cases; however, variant lesions are increasingly being detected. These variant lesions are often small with atypical features, such as the absence of a central scar or teleangiectatic changes. The most characteristic microscopic features of classic FNH are fibrous septa and cellular areas of hepatic proliferation. The hepatic plates may be moderately thickened and contain normal hepatocytes. The central scar typically consists of fibrous connective tissue, cholangiocellular proliferation with inflammatory infiltrates and malformed vessels, including tortuous arteries, capillaries and veins.

The arterial blood in FNH, as opposed to that in adenoma, flows centrifugally from the anomalous central arteries. Both classic and non-classic types contain a variable content of Kupffer cells.

In contrast, the gross appearance of non-classic FNH is heterogeneous and globally resembles that of adenoma, with lobulated contours and no macroscopic central scar. The histological findings of non-classic FNH depend on the subtype [9, 73]. The teleangiectatic type consists of hepatic plates that frequently appear atrophic. The plates are one cell thick and are separated by dilated sinusoids. Fibrous septa can be found in all cases of teleangiectatic FNH that contain some degree of bile duct proliferation. In this type of FNH arteries have a hypertrophic muscular media but no intimal proliferation. In contrast to the classic form, these abnormal vessels drain directly into the adjacent sinusoids, while in classic FNH connections to the sinusoids are almost never seen. Necrotic areas and hemorrhage can be found within teleangiectatic FNH; these features are often responsible for the appearance of the tumor and the presence of abdominal pain [73, 111]. FNH with cytological atypia have the gross and histological features of classic FNH but contain areas of large cell dysplasia. The mixed hyperplastic and adenomatous form of FNH has two variants, one resembling the teleangiectatic type, the other simulating adenoma [73].

When multiple, FNH lesions tend to be associated with other lesions, such as hepatic hemangioma, meningioma, astrocytoma, teleangiectasia of the brain, and systemic arterial dysplasia. FNH has also been described in association with hepatocellular adenoma and liver adenomatosis. In these cases it appears that FNH lesions may be secondary to systemic and local abnormalities of vascular growth induced by oral contraceptives, tumor-induced growth factors, thrombosis or local arteriovenous shunting [9].

On US images, classic FNH appears as a homogeneous well-demarcated nodule which may be hypoechoic, isoechoic or slightly hyperechoic relative to the normal liver parenchyma (Fig. 15). Displacement of contiguous hepatic vessels may be the only detectable abnormality. Some lesions may show a hypoechoic halo surrounding the lesion; this halo most likely represents compressed hepatic parenchyma and is more evident around nodules with fatty infiltration or which are located in steatotic liver tissue.

The central scar and the fibrous septa are often difficult to visualize on US. However, when apparent, the central scar is usually hyperechoic while the fibrous septa are hypoechoic. Characteristic findings at color Doppler US include the presence of a central feeding artery with a stellate or spoke-wheel pattern, which corresponds to vessels running into the radiating fibrous septa from the central scar (Fig. 16). The spectral analysis may show an intratumoral pulsatile waveform with high diastolic flow and low resistive index corresponding to malformed arteries, and a continuous waveform which could represent a draining vein of the neoplasm [112]. US in general is a non-specific imaging method for the characterization of non-classic FNH.

The hypervascularity of the lesion is detected using SonoVue-enhanced US. In the arterial phase of the dynamic study the intralesional vessels are typically of the stellate or spoke-wheel configuration and the lesion appears homogeneously hyperechoic compared to the normal liver parenchyma. In the portal-venous phase, FNH remains hyperechoic and the nodule gradually becomes isoechoic with the adjacent liver in the later phases of dynamic imaging. Conversely the central scar is depicted as a hypo- or anechoic area within the hyperechoic lesion during both the arterial and portal-venous phases, while it shows uptake of contrast in the later phases (Fig. 17) [57].

On unenhanced CT FNH is usually isoattenuating or slightly hypoattenuating. When the lesion is isoattenuating compared to the normal liver parenchyma, it may be detectable only because of

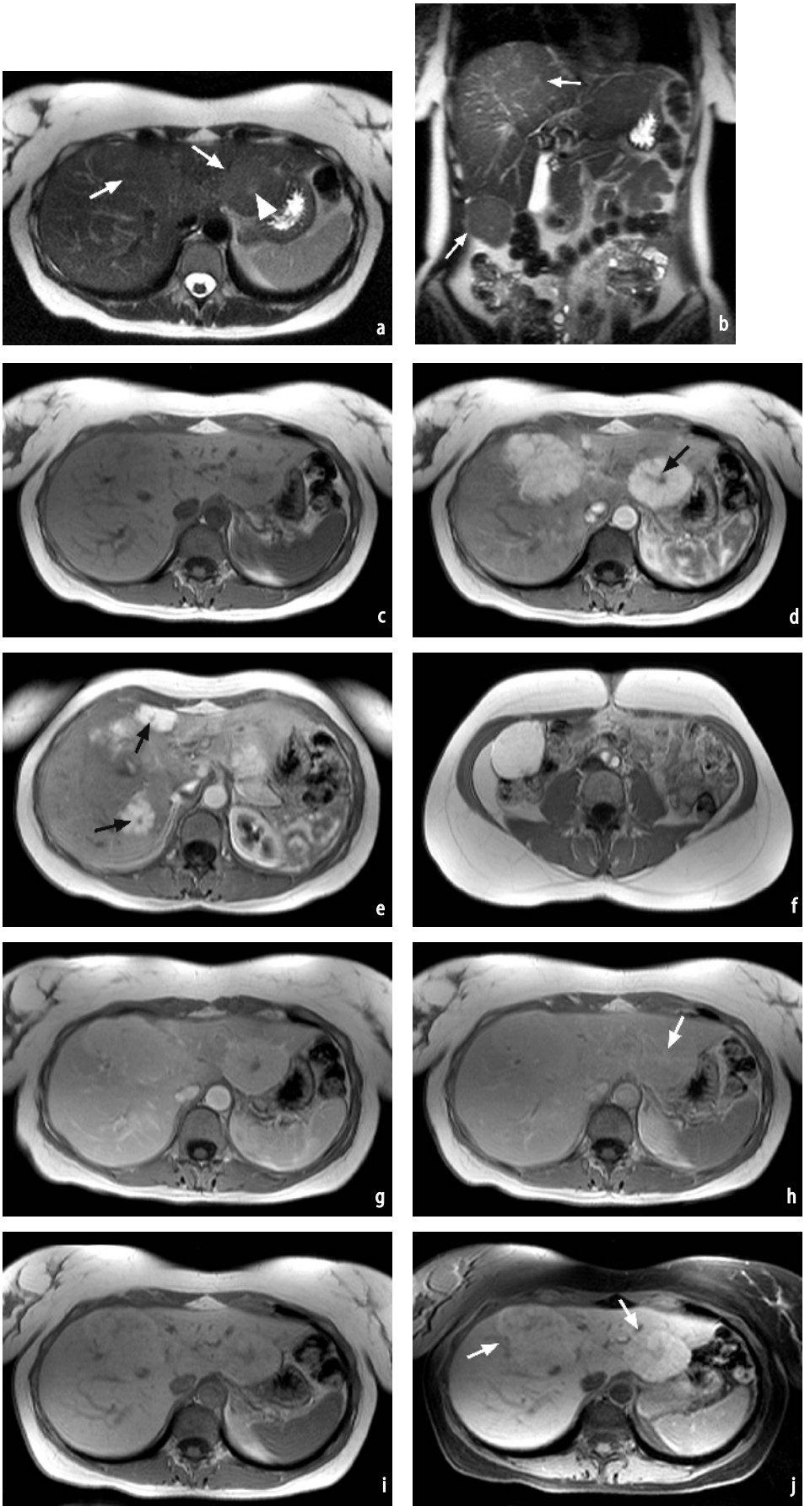
a
b
c
d
e
f
g
h
i
j

Fig. 14a-j. Multiple focal nodular hyperplasia. Unenhanced axial and coronal T2-weighted images (**a**, **b**) reveal several slightly hyperintense liver lesions (*arrows*) with one lesion in the left liver lobe demonstrating a central scar (*arrowhead*). On the unenhanced T1-weighted image (**c**) the lesions are slightly hypointense. Arterial phase images acquired after the bolus injection of Gd-BOPTA reveal strong hypervascularization of all the lesions (**d**-**f**), and a central scar in three of the lesions (*arrows*). In the portal-venous phase (**g**) the lesions are slightly hyperintense. In the equilibrium phase (**h**), the central scar of the lesion in the left liver lobe shows late enhancement (*arrow*). This is typical for FNH in which the central scar is more an arterio-venous malformation than a true scar. T1-weighted images acquired during the hepatobiliary phase (**i**), show enhancement of the liver lesions. This is more obvious on T1-weighted fs images (*arrows*) acquired at the same time point (**j**) and is indicative of the lesions containing functioning hepatocytes that are able to take up Gd-BOPTA. The fact that the lesions enhance to a higher degree than the surrounding liver tissue is indicative of the benign nature of the lesions and of the fact that the biliary system of FNH is malformed, leading to a slowing of biliary excretion

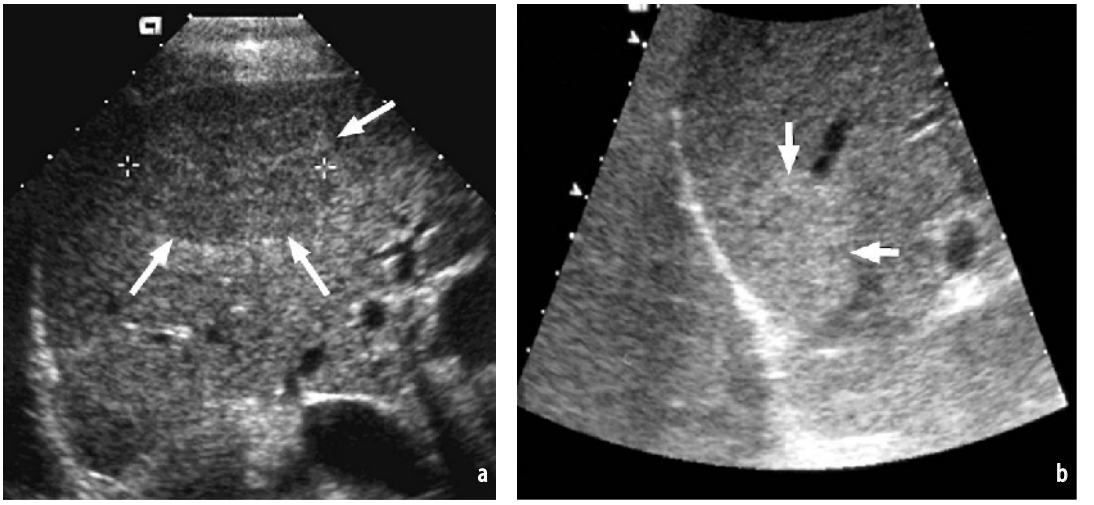

Fig.15a, b. Classic focal nodular hyperplasia on US. The ultrasound examination reveals a homogeneous lesion (*arrows*) that is either hypoechoic (**a**) or hyperechoic (**b**) compared to the surrounding normal liver tissue

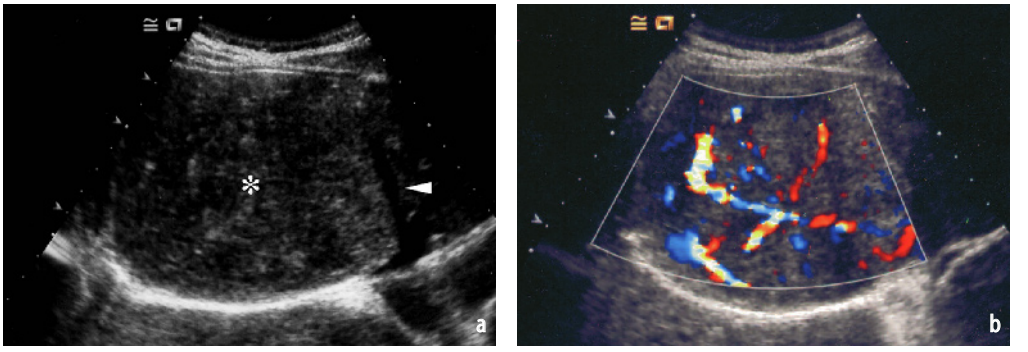

Fig. 16a, b. Classic focal nodular hyperplasia on color Doppler US. On ultrasound (**a**) the lesion (*asterisk*) is isoechoic and only a displacement of the middle hepatic vein is appreciable (*arrowhead*). Color Doppler US (**b**) shows vascularization within the lesion, corresponding to vessels running in the radiating fibrous septa, demonstrating a spoke-wheel pattern

its mass effect. FNH generally only appears hyperattenuating to unenhanced liver when there is hepatic steatosis or when the liver is otherwise abnormally decreased in attenuation. However, in rare cases FNH may still be isoattenuating or hypoattenuating on unenhanced CT in patients with hepatic steatosis when there is fatty infiltration of the FNH itself [67]. In a third of cases, a low-density central area is seen, corresponding to the central scar [95].

During the arterial phase of contrast-enhanced CT, FNH enhances rapidly and becomes hyperdense compared to normal liver. The low-attenuation scar appears conspicuous against the hyperdense tissue, and foci of enhancement representing feeding arteries may be seen within the scar. In the portal-venous phase of enhancement, the difference in attenuation between FNH and normal liver decreases and FNH may become isodense with normal liver parenchyma. The central scar is almost always seen as hypoattenuating to the remainder of the FNH on unenhanced and enhanced dynamic phase scans. On delayed scans, however, there is retention of contrast material within the fibrous scar, giving it an isoattenuating or, more frequently, a hyperattenuating appearance (Fig. 18). Detection of the central scar is related to the size of the lesion; while a central scar may be identified in as many as 65% of larger FNH, it may be seen in only about 35% of lesions smaller than 3 cm in diameter [15, 19]. 3D multidetector CT angiography is very useful in demonstrating the intratumoral vascularization of FNH which is characterized by hepatic venous drainage and by the absence of portal-venous supply (Fig. 19) [17].

On MR, FNH are considered classic when they appear as homogeneously isointense or slightly hyperintense on T2-weighted images, and isointense or slightly hypointense on T1-weighted images before contrast agent administration. Typical behavior during the dynamic phase of contrast enhancement is marked and homogeneous signal intensity enhancement during the arterial phase, rapid and homogeneous signal intensity wash-out during the portal-venous phase, and signal isointensity (with the exception of the scar) during the equilibrium phase (Fig. 20). A typical scar appears as a hyperintense central stellate area on T2-weighted images and as a hypointense area on T1-weighted images. During the dynamic phase of contrast enhancement a typical scar is hypointense during the arterial and portal-venous phases and slightly hyperintense in the equilibrium phase (Fig. 20).

Atypical features of FNH generally consist of le-

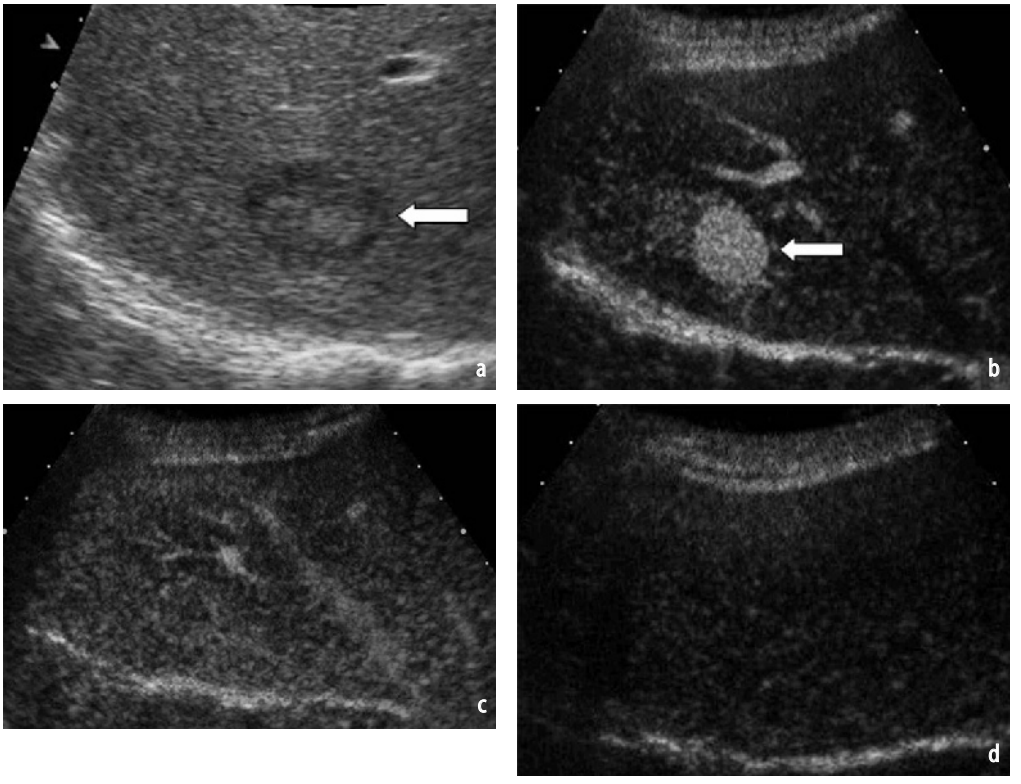

Fig. 17a-d. Focal nodular hyperplasia with SonoVue. Precontrast US (**a**) reveals a well defined isoechoic nodule (*arrow*) surrounded by a hypoechoic halo. In the arterial phase (**b**) after SonoVue administration the FNH (*arrow*) appears homogeneously hyperechoic compared to the normal liver parenchyma. Rapid contrast wash-out occurs in the portal-venous (**c**) and equilibrium (**d**) phases

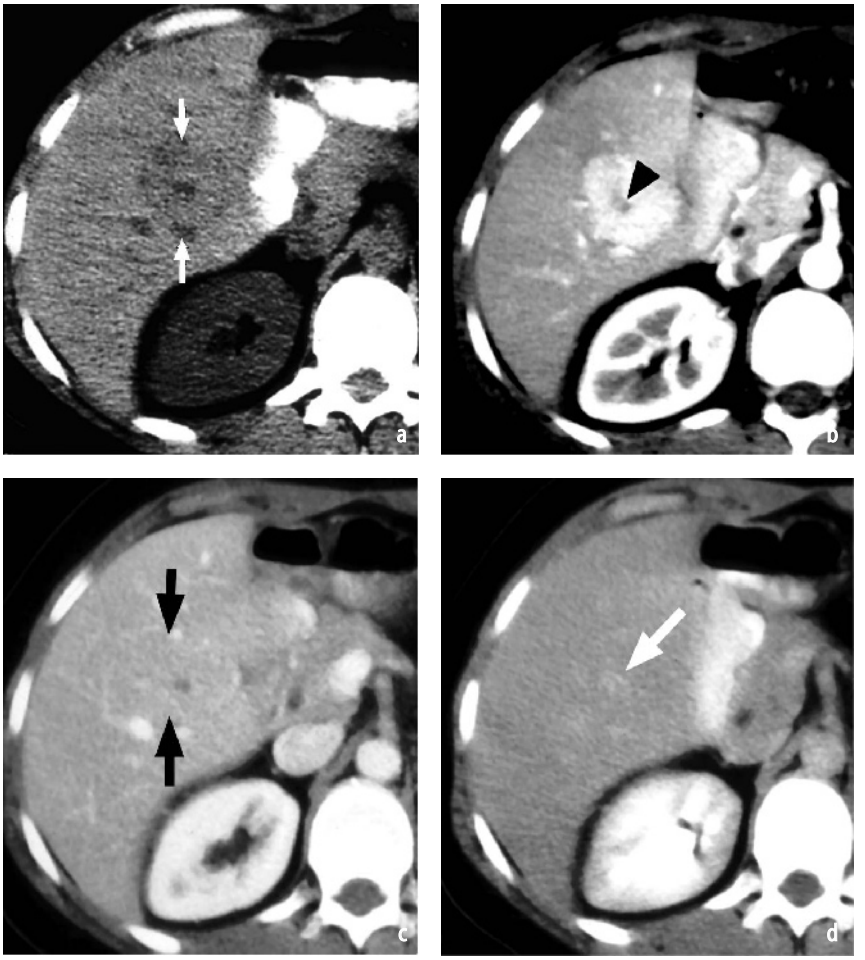

Fig. 18a-d. Focal nodular hyperplasia on CT. On the unenhanced CT scan (**a**) the FNH (*arrows*) is isoattenuating to the liver. During the arterial phase (**b**) after contrast medium administration, the nodule enhances rapidly and homogeneously while the central scar (*arrowhead*) remains hypodense. In the portal-venous and equilibrium phases (**c** and **d**, respectively) the FNH appears isodense compared to the normal liver parenchyma (*arrows* in **c**). In the equilibrium phase (**d**) the central scar is depicted as hyperattenuating (*arrow*)

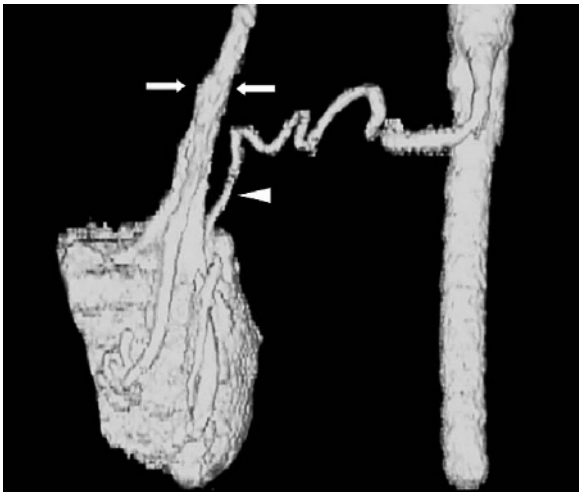

Fig. 19. Focal nodular hyperplasia on 3D multidetector CT angiography. 3D multidetector CT angiography shows the intratumoral vascularization, characterized by an arterial vessel leading directly into the lesion (*arrowhead*) and hepatic venous drainage (*arrows*)

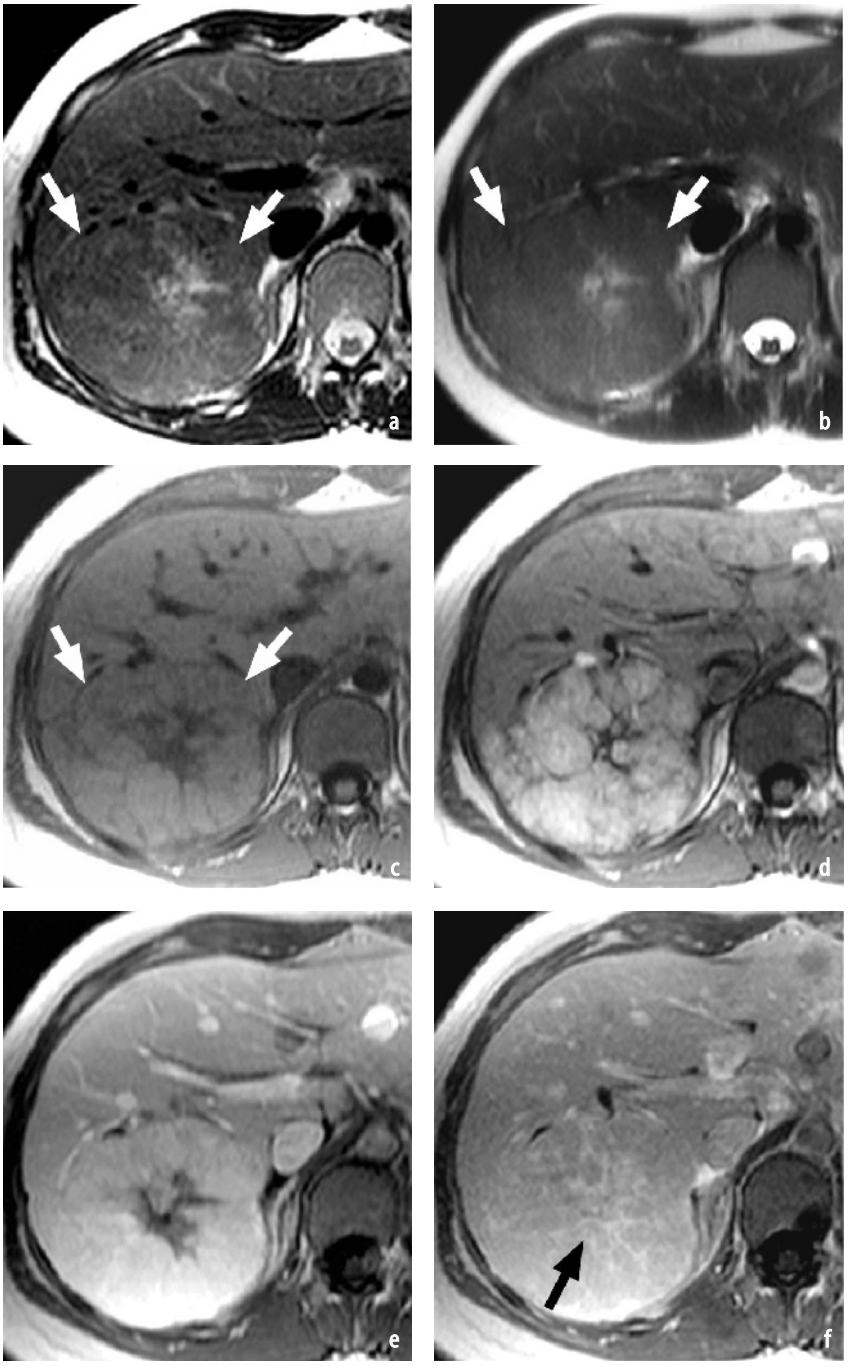

Fig. 20a-f. Focal nodular hyperplasia. On the Turbo SE T2-weighted and HASTE T2-weighted images (**a** and **b**, respectively), the nodule (*arrows*) is isointense compared to the surrounding liver tissue and possesses a hyperintense "stellate" central scar. On the unenhanced T1-weighted image (**c**), the FNH (*arrows*) appears as an isointense lesion with a hypointense central scar. This lesion shows intense and homogeneous enhancement during the arterial phase after contrast agent administration (**d**) and rapid wash-out in the portal-venous phase (**e**). In the equilibrium phase (**f**), the lesion is again isointense. The central scar is typically hypointense during the arterial and portal-venous phases. However, it appears hyperintense (*arrow*) in the equilibrium phase comparable to that seen in CT imaging

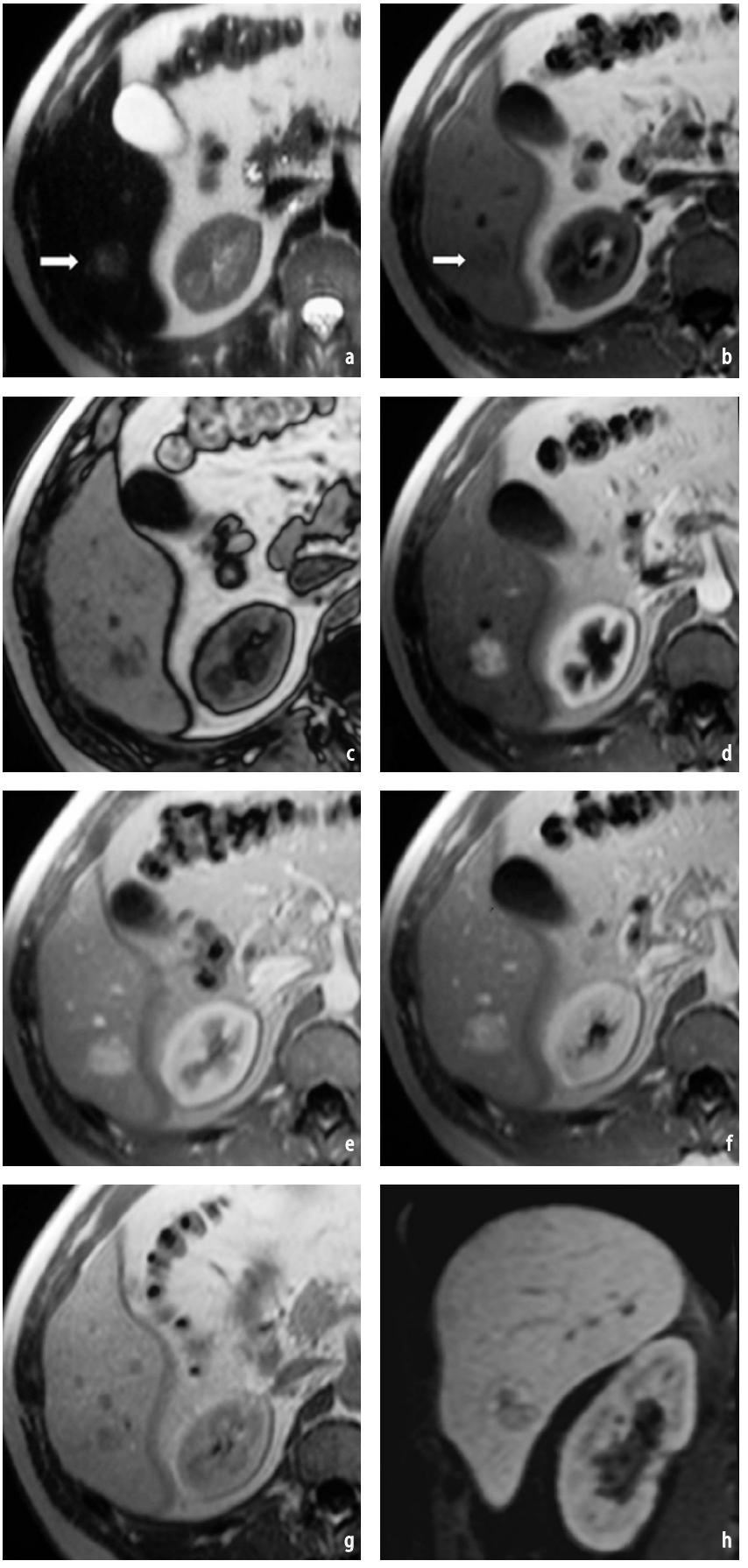

Fig. 21a-h. Atypical focal nodular hyperplasia with Gd-DTPA. On the precontrast HASTE T2-weighted image (**a**) the nodule (*arrow*) is slightly hyperintense compared to the surrounding normal liver parenchyma, whereas on the GRE T1-weighted "in-phase" image (**b**) it appears heterogeneously isointense (*arrow*). On the GRE T1-weighted "out-of-phase" image (**c**) it appears heterogeneously hypointense. In the arterial phase of the dynamic evaluation after contrast agent administration (**d**) the lesion shows marked enhancement, with persistent uptake of contrast material in the portal-venous (**e**) and equilibrium (**f**) phases. On late GRE T1-weighted "in-phase" (**g**) and "out-of-phase" (**h**) images the nodule appears as a well defined, slightly hypointense lesion. This behavior could be related to sinusoidal dilatation

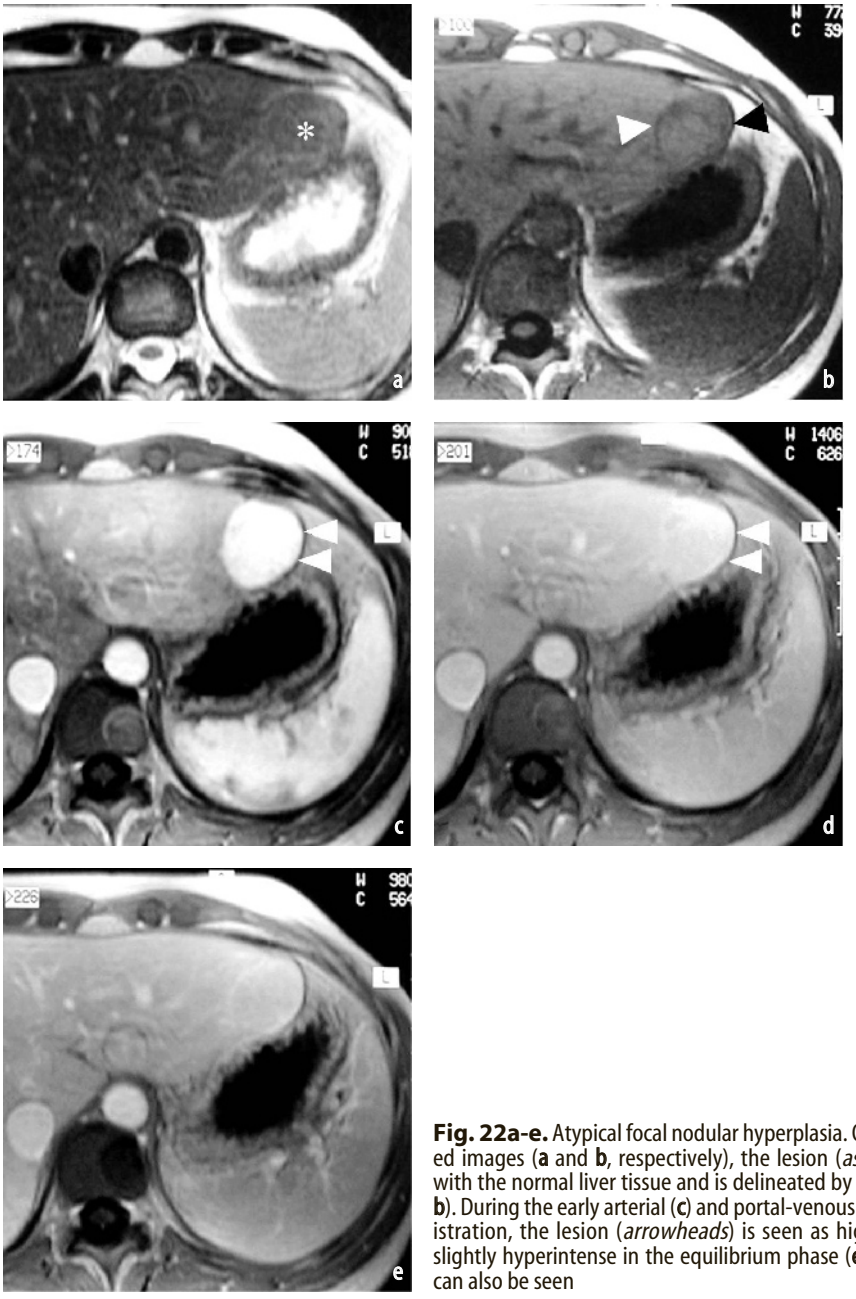

Fig. 22a-e. Atypical focal nodular hyperplasia. On the unenhanced T2- and T1-weighted images (**a** and **b**, respectively), the lesion (*asterisk* in **a**) is isointense as compared with the normal liver tissue and is delineated by a thin hypointense rim (*arrowheads* in **b**). During the early arterial (**c**) and portal-venous (**d**) phases after contrast agent administration, the lesion (*arrowheads*) is seen as highly vascularized. The lesion remains slightly hyperintense in the equilibrium phase (**e**) when a hyperintense peripheral rim can also be seen

sion heterogeneity, hyperintensity on T1-weighted images, strong hyperintensity on T2-weighted images and hypointensity in the portal-venous or equilibrium phases. Hyperintensity on T1-weighted images may be due to different pathologic changes, including fat deposition, copper accumulation, high protein concentration, blood degradation products or sinusoidal dilatation. Persistent contrast agent uptake in teleangiectatic FNH could be related to sinusoidal dilatation (Fig. 21).

Other atypical features include the absence of a central scar in a lesion greater than 3 cm in size, scar hypointensity on T2-weighted images and scar hypointensity in the equilibrium phase following injection of contrast agent. Finally, the presence of a pseudocapsule, seen as a complete hyperintense perilesional ring during the equilibrium phase can be considered atypical (Fig. 22) [38]. In rare cases, hemorrhage, calcification, or necrosis can be observed in non-classic forms of FNH.

The use of contrast-enhanced dynamic MR imaging provides the greatest diagnostic sensitivity among the imaging techniques in current use, especially when combined with the information available on precontrast T1- and T2-weighted im-

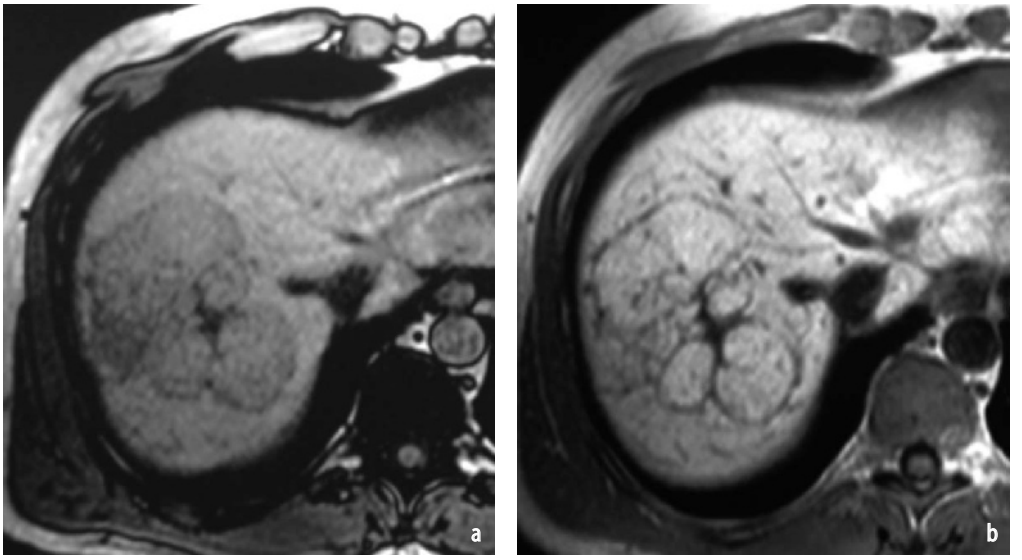

Fig. 23a, b. Focal nodular hyperplasia after mangafodipir trisodium administration. On the precontrast T1-weighted image (**a**), the FNH is seen as isointense with a stellate hypointense central scar. On the delayed image after mangafodipir administration (**b**), the lesion is again isointense compared to the surrounding parenchyma

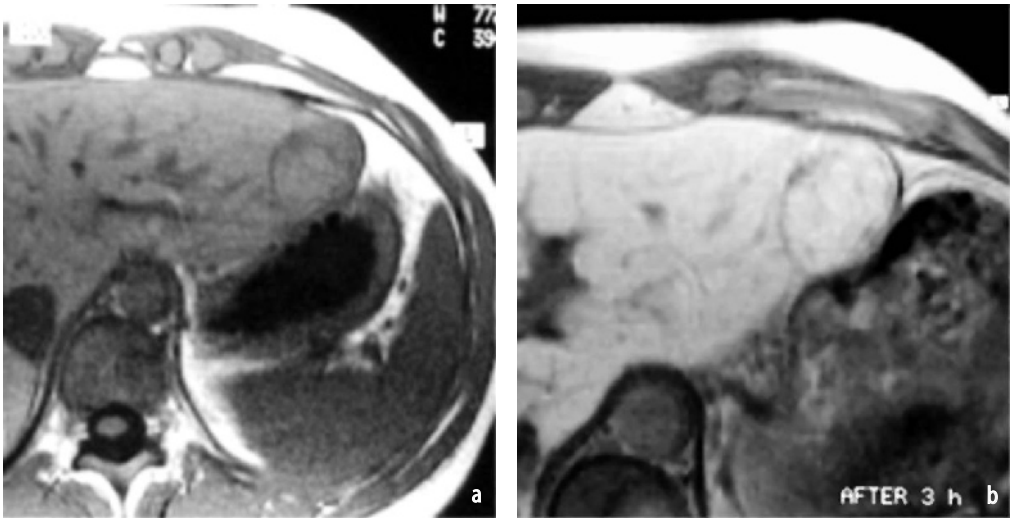

Fig. 24a, b. Atypical focal nodular hyperplasia after Gd-BOPTA. The same case as presented in Fig. 22. On the precontrast T1-weighted image (**a**) the FNH is isointense to partially slightly hypointense compared to the normal liver tissue. During the hepatobiliary phase 3 h after the bolus administration of Gd-BOPTA (**b**), the lesion is again isointense to the surrounding liver parenchyma, indicating functioning hepatocytes. This enables the diagnosis of FNH

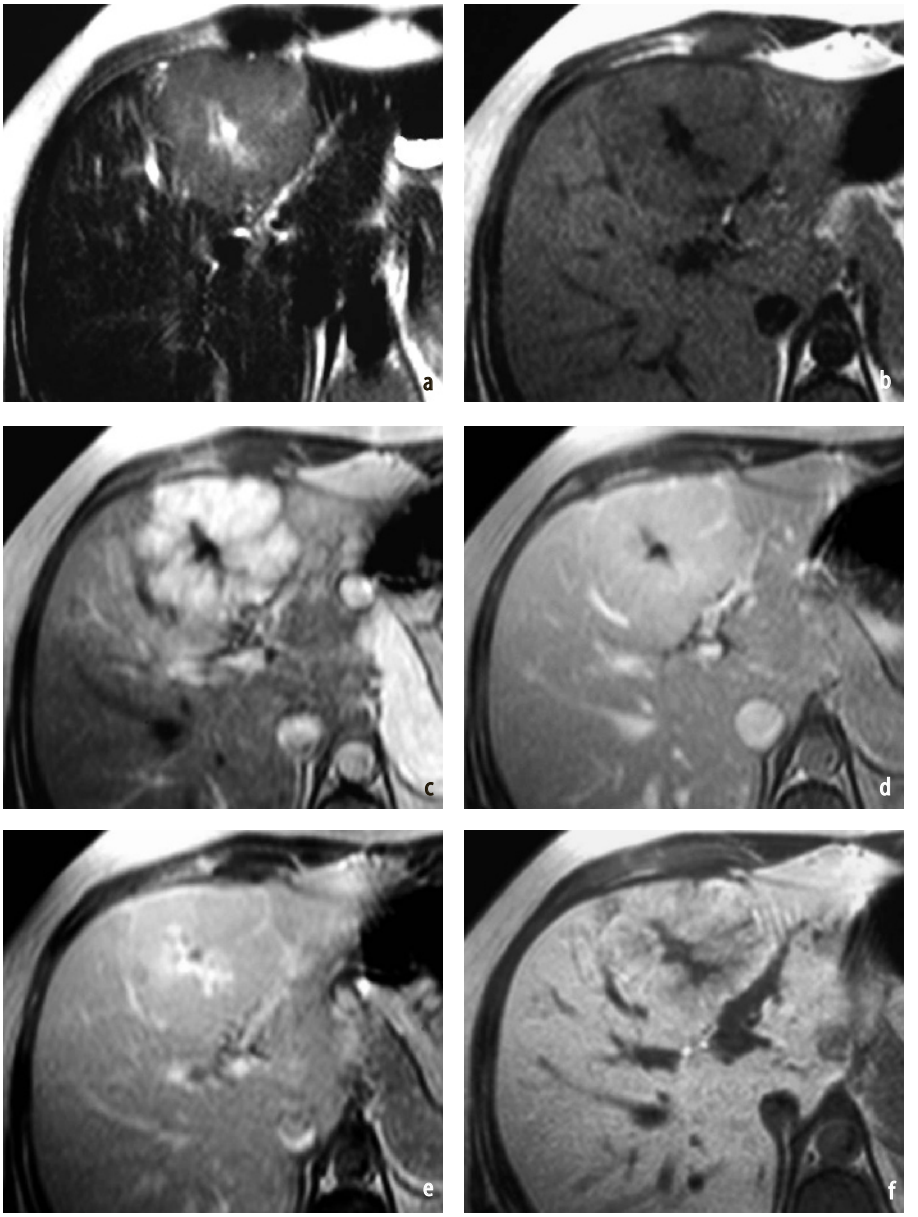

Fig. 25a-f. Focal nodular hyperplasia after Gd-BOPTA. On the unenhanced T2-weighted HASTE and T1-weighted GE images (**a**, **b**) as well as on post-contrast T1-weighted images acquired during the dynamic (**c**, **d**, **e**) and delayed (**f**) phase after administration of Gd-BOPTA, typical findings of FNH are clearly depicted. Importantly, it is possible to characterize the nodule according to both morphological and functional criteria

ages. However, the high frequency of atypical features does not permit the accurate characterization of FNH in every case. In this regard diagnosis on dynamic MR imaging with conventional extracellularly-distributed Gd agents relies on the same morphologic and hemodynamic features as helical CT [38].

The availability of liver-specific MR contrast agents increases the potential for accurate lesion characterization. FNH are depicted as either hyperintense or isointense during the delayed phase after administration of Gd-BOPTA, Gd-EOB-DTPA or Mn-DPDP, reflecting the abnormal biliary drainage within the lesion (Figs. 23, 24).

Gd-BOPTA in particular offers both a dynamic and delayed phase imaging capability, thereby permitting both morphological and functional information to be acquired for the characterization of these lesions (Figs. 25, 26) [38].

In the same way, Gd-EOB-DTPA is helpful in the characterization of FNH because FNH contains hepatocytes that take up this agent, resulting in

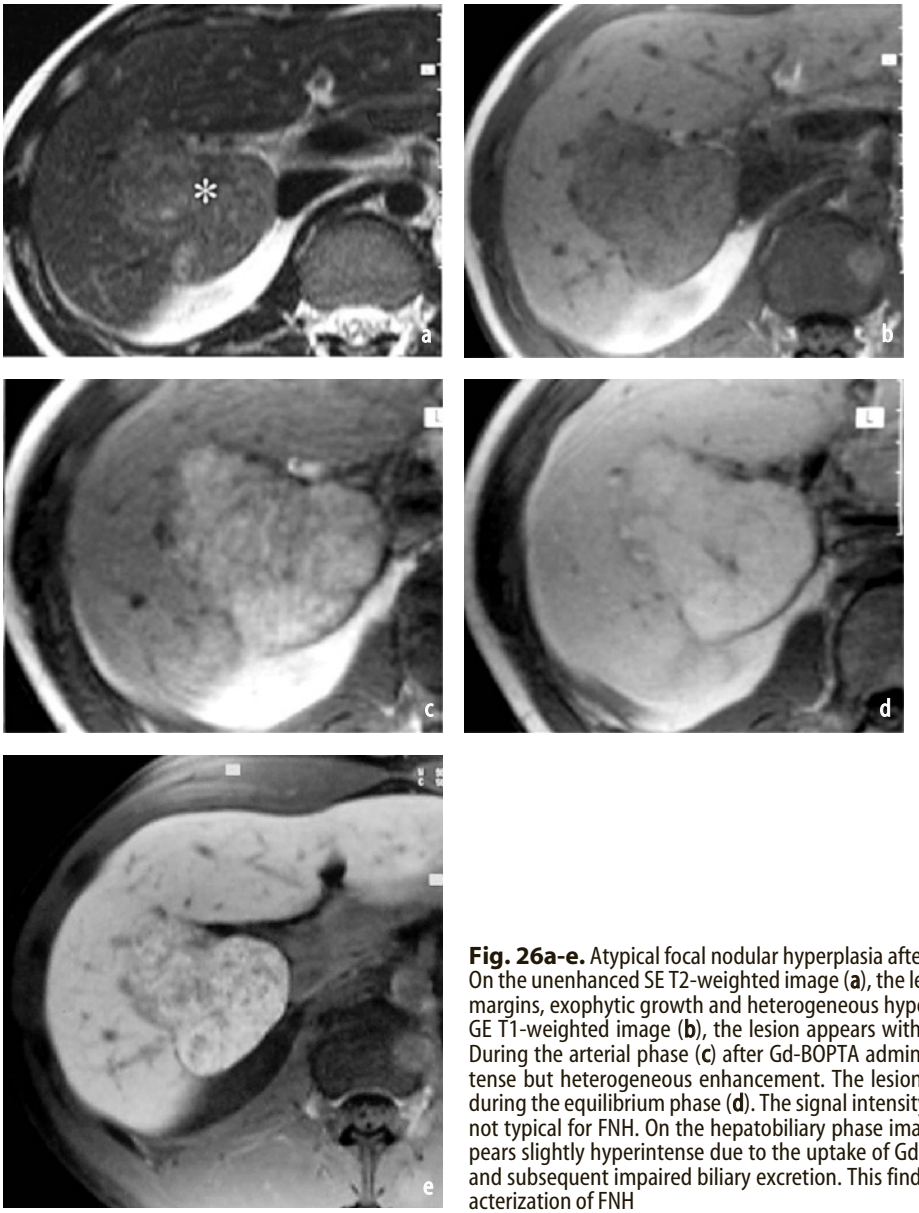

Fig. 26a-e. Atypical focal nodular hyperplasia after Gd-BOPTA
On the unenhanced SE T2-weighted image (**a**), the lesion (*asterisk*) shows lobulated margins, exophytic growth and heterogeneous hyperintensity. On the pre-contrast GE T1-weighted image (**b**), the lesion appears with heterogeneous hypointensity. During the arterial phase (**c**) after Gd-BOPTA administration, the nodule shows intense but heterogeneous enhancement. The lesion remains slightly hyperintense during the equilibrium phase (**d**). The signal intensity and enhancement pattern are not typical for FNH. On the hepatobiliary phase image (**e**), however, the lesion appears slightly hyperintense due to the uptake of Gd-BOPTA by normal hepatocytes and subsequent impaired biliary excretion. This finding is consistent with the characterization of FNH

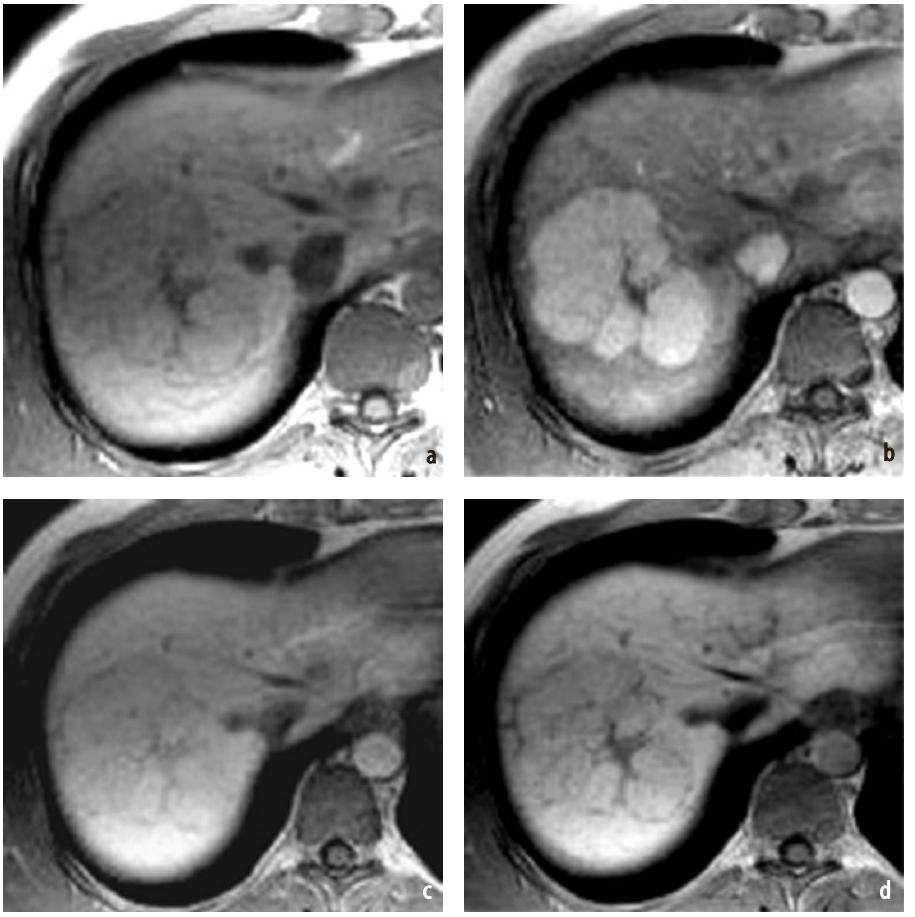

Fig. 27a-d. Focal nodular hyperplasia after Gd-BOPTA. On the pre-contrast T1-weighted image (**a**) the FNH is seen as isointense compared with surrounding liver tissue. The intense and homogeneous enhancement seen during the arterial and portal-venous phases (**b** and **c**, respectively), as well as the delayed isointensity demonstrated during the hepatobiliary phase (**d**), is typical for FNH

iso- or hyperintensity of the lesion compared with the normal liver parenchyma on delayed T1-weighted images; the enhancement pattern is very similar to that which is observed after Gd-BOPTA administration (Figs. 27, 28) [62].

On delayed phase T2-weighted images after SPIO administration, typical FNH demonstrate a loss of signal due to uptake of iron oxide particles by Kupffer cells within the lesion (Fig. 29) [34]. The degree of signal loss on SPIO-enhanced T2-weighted images is significantly greater than that in other focal liver lesions such as HCC and hepatocellular adenoma; however, overlap may occur due to the lack of function of Kupffer cells in some FNH [75].

In a large series it was demonstrated that only 39% of FNH showed significant signal drop after SPIO. The remaining 61% of nodules did not show significant signal drop and appeared homogeneously, but more frequently heterogeneously, hyperintense on T2-weighted images after SPIO (Fig. 30) [39].

On dynamic T1-weighted images after bolus USPIO administration (SH U 555 A), FNH in many cases demonstrate an initial, moderate signal increase followed by an early decrease of signal intensity due to contrast pooling (Fig. 31). The hypervascularity depicted on arterial phase images is generally inferior compared to that observed on Gd-enhanced arterial phase imaging. On dynamic T2-weighted images after USPIO administration, FNH demonstrate a decrease of signal intensity over time [44].

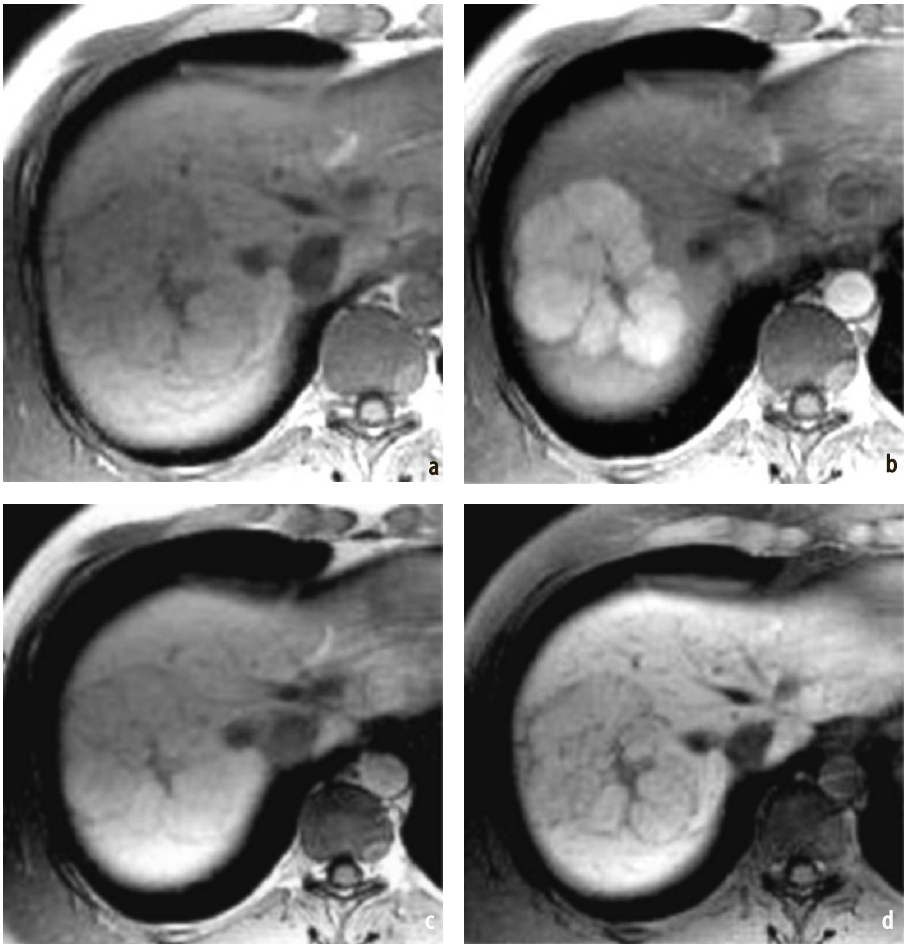

Fig. 28a-d. Focal nodular hyperplasia after Gd-EOB-DTPA. The same case as shown in Fig. 27. The enhancement pattern after Gd-EOB-DTPA is very similar to that observed after Gd-BOPTA; a slightly hypointense lesion on the unenhanced T1-weighted image (**a**) demonstrates strong hyperintensity during the arterial phase (**b**) after the administration of Gd-EOB-DTPA. The subsequent portal-venous phase image (**c**) reveals persistent enhancement typical of FNH. On the hepatobiliary phase image (**d**) the lesion demonstrates an iso/slightly hypointense appearance compared with the surrounding parenchyma. With this contrast agent the hepatobiliary phase image was acquired after 20 min

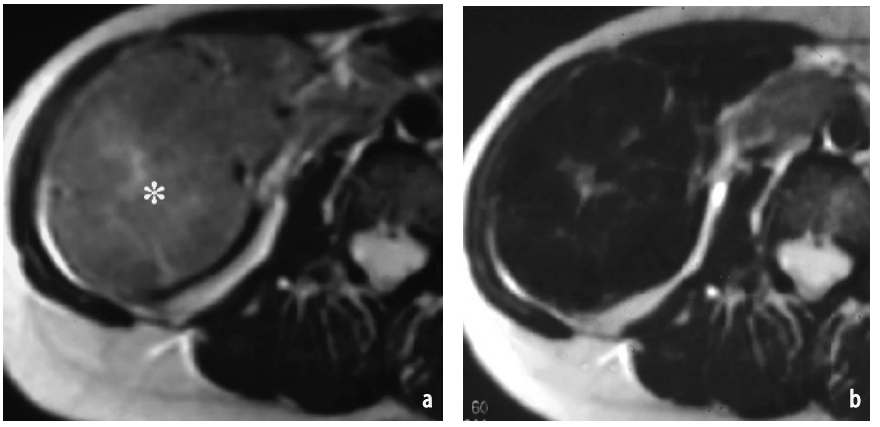

Fig. 29a, b. Focal nodular hyperplasia before (**a**) and after (**b**) SPIO administration. After SPIO administration (**b**), the FNH (*asterisk* in **a**) shows significant signal drop compared with that seen on the pre-contrast image (**a**)

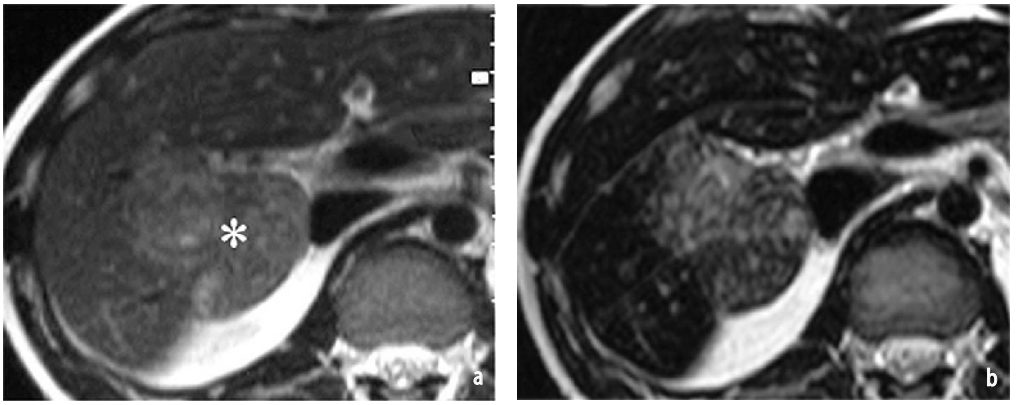

Fig. 30a, b. Focal nodular hyperplasia before (**a**) and after (**b**) SPIO administration. The same case as shown in Figure 26. The FNH (*asterisk*) appears slightly heterogeneously hyperintense on the SE T2-weighted image (**a**). After SPIO administration (**b**), the nodule is still heterogeneously hyperintense compared to the surrounding normal liver. Note that compared with the unenhanced image (**a**), the signal drop in FNH is less pronounced than in normal liver parenchyma

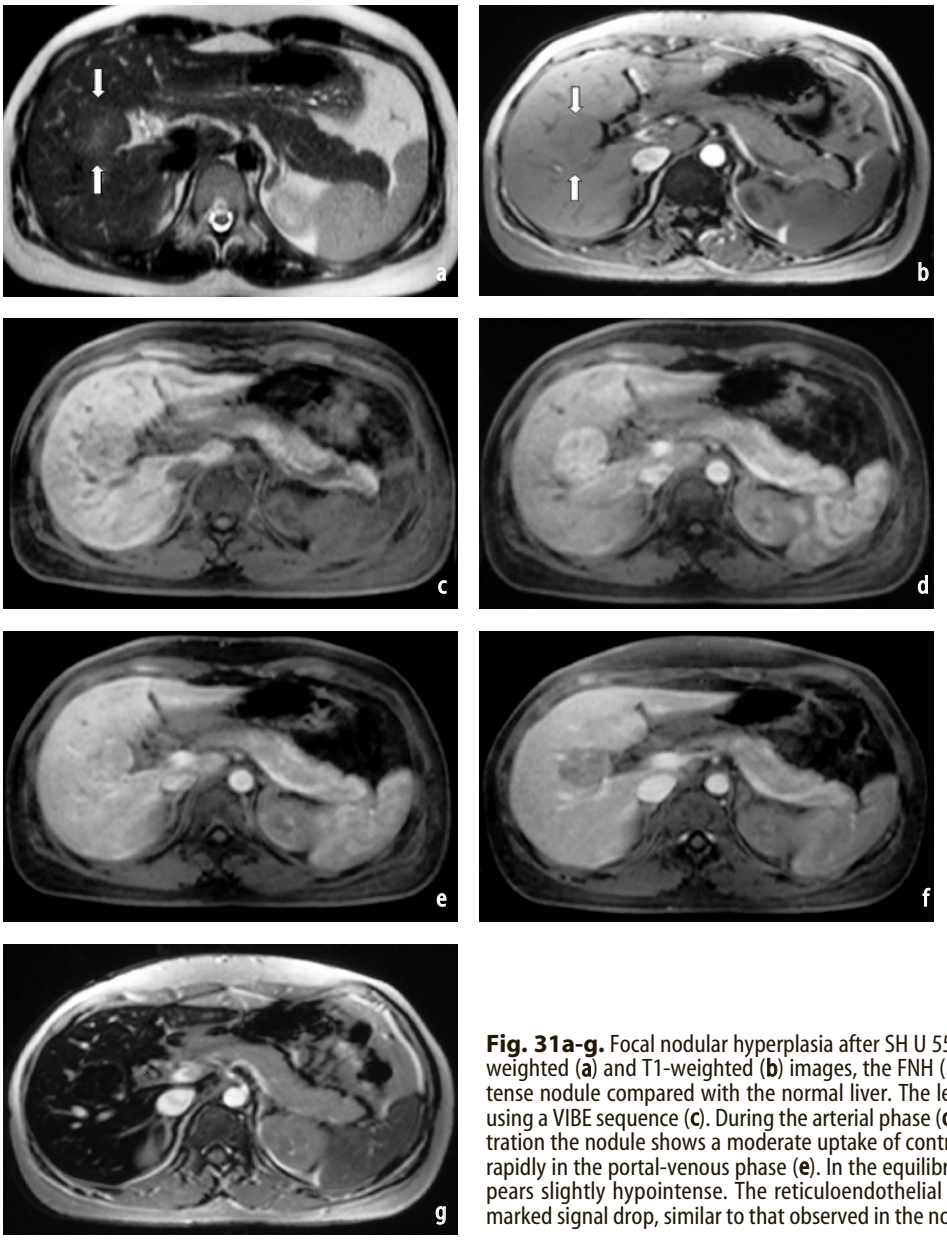

Fig. 31a-g. Focal nodular hyperplasia after SH U 555 A. On precontrast TSE T2-weighted (**a**) and T1-weighted (**b**) images, the FNH (*arrows*) appears as an isointense nodule compared with the normal liver. The lesion is slightly hypointense using a VIBE sequence (**c**). During the arterial phase (**d**), after SH U 555 A administration the nodule shows a moderate uptake of contrast agent witch washes out rapidly in the portal-venous phase (**e**). In the equilibrium phase (**f**) the lesion appears slightly hypointense. The reticuloendothelial phase (**g**) reveals a typical, marked signal drop, similar to that observed in the normal liver

4.1.3 Hepatocellular Adenoma

Hepatocellular adenoma (HA) is a rare benign tumor of hepatocellular origin which is most common in middle-aged women. The term HA is used to describe a spectrum of lesions associated with different pathological and etiological factors that give rise to a variety of histological forms. A new classification of adenomas has been proposed, according to which anabolic steroid-associated type HA is considered separate from the classical form [55]. This is due to its distinct histologic appearance, which often resembles that of hepatocellular carcinoma. An additional separate form is liver adenomatosis (LA) which is characterized by the presence of ten or more adenomas within an otherwise normal liver, without a history of glycogen storage disease or chronic anabolic steroid use.

Typical HA is defined as a tumor composed of hepatocytes arranged in cords, that only occasionally produces bile. The tumor lacks portal tracts and terminal hepatic veins [65]. Although the precise pathogenic mechanism of HA is unknown, the use of estrogen-containing [110] or androgen-containing [98] steroid medications clearly increases their prevalence, number and size within the affected population and often within individual patients. Moreover, this causal relationship is related to dose and duration, with the greatest risk encountered in patients taking large doses of estrogen or androgen for prolonged periods of time [98]. In women who have never used oral contraceptives the annual incidence of HA is about 1 per million. This increases to 30-40 per million in long-term users of oral contraceptives [83]. Withdrawal of estrogen derivates may result in regression of the HA.

Another risk group for HA are patients affected by glycogenosis, in particular, type I glycogen storage disease. In these patients, the possible pathogenetic mechanisms include glucagon/insulin imbalance, cellular glycogen overload, and protooncogene activation [8]. The adenomas are also more likely to be multiple and to undergo malignant transformation, although the latter is still quite rare. Patients with diabetes mellitus have decreased circulating insulin levels and elevated serum glucose, therefore they share a similar pathogenetic mechanism as patients affected by glycogenosis.

A recognized association is that of congenital or acquired abnormalities of the hepatic vasculature. An association with portal vein absence or occlusion [71] or portohepatic venous shunts [54] has been noted, particularly in patients with LA [37]. Although the adenomas in LA are histologically similar to other adenomas, they are not steroid-dependent, but are multiple, progressive, symptomatic, and more likely to lead to impaired liver function, hemorrhage, and perhaps malignant degeneration [26, 37].

Recently, some authors [11, 22] have suggested a genetic alteration in the origin of HA. Specifically, a combination of a β-catenin mutation and a deletion locus on chromosome 12 was found in patients with HA.

An association with pregnancy has also been described, probably due to increased levels of endogenous steroid hormones [103]. HA occurs sporadically in patients without known predisposing factors and rarely in children and adult males.

Most patients with only one or few HA are asymptomatic and almost invariably have normal liver function and no elevation of serum tumor markers such as α-fetoprotein. Large HA may cause a sensation of right upper quadrant fullness or discomfort. However, the classic clinical manifestation of HA is spontaneous rupture or hemorrhage, leading to acute abdominal pain and possibly progressing to hypotension and even death [58].

HA is solitary in 70-80% of cases, but it is not unusual to encounter two or three HA in one patient, particularly at multiphasic CT or MR imaging [49, 77]. Patients with glycogen storage disease or LA may have dozens of adenomas detected at imaging and even more at close examination of resected specimens [26, 37, 86]. Individual lesions vary in size from less than 1 cm to more than 15 cm. The typical steroid-related adenoma often comes to clinical attention when it reaches about 5 cm in diameter. Large and multiple lesions are more prone to spontaneous hemorrhage [58]. The propensity to hemorrhage reflects the histological characteristics of HA, in which the cord-like arrangement of cells structured in large plates are separated by dilated sinusoids. Because adenomas lack a portal-venous supply, they are perfused by arterial pressure derived solely from peripheral arterial feeding vessels. The extensive sinusoids and feeding arteries contribute to the hypervascular nature of HA, which together with the poor connective tissue support, predisposes the lesions to hemorrhage. Because a tumor capsule is usually absent or incomplete, hemorrhage may spread into the liver or abdominal cavity [65].

Kupffer cells are often found in adenomas, but in some cases can be reduced in number and with little or no function, as reflected by absent or diminished uptake of technetium (Tc)-99m sulfur colloid [89]. A key histological feature that helps distinguish HA from FNH is the notable absence of bile ductules in HA [13]. Adenoma cells are generally larger than normal hepatocytes and may contain large amounts of glycogen and lipid. Intra- and intercellular lipid may manifest as macroscopic fat deposits within the tumor [49] and are responsible

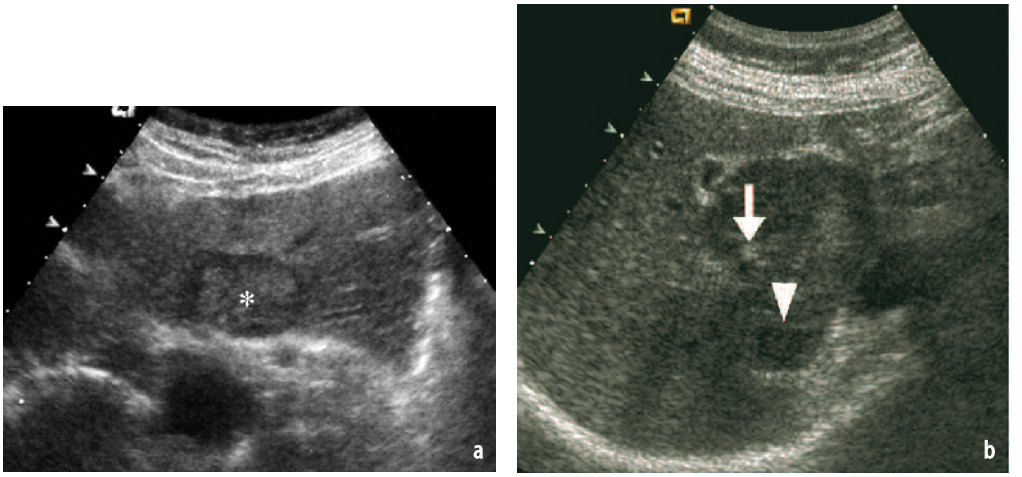

Fig. 32a, b. Hepatocellular adenoma on US. A small, non-complicated adenoma (**a**) is shown as a homogeneous, isoechoic nodule (*asterisk*) with a thin, hypoechoic peripheral rim. Larger adenomas are often heterogeneous in echogenicity (**b**), with both hyperechoic (*arrow*) and hypoechoic areas (*arrowhead*), which correspond to areas of hemorrhage, necrosis and fatty infiltration

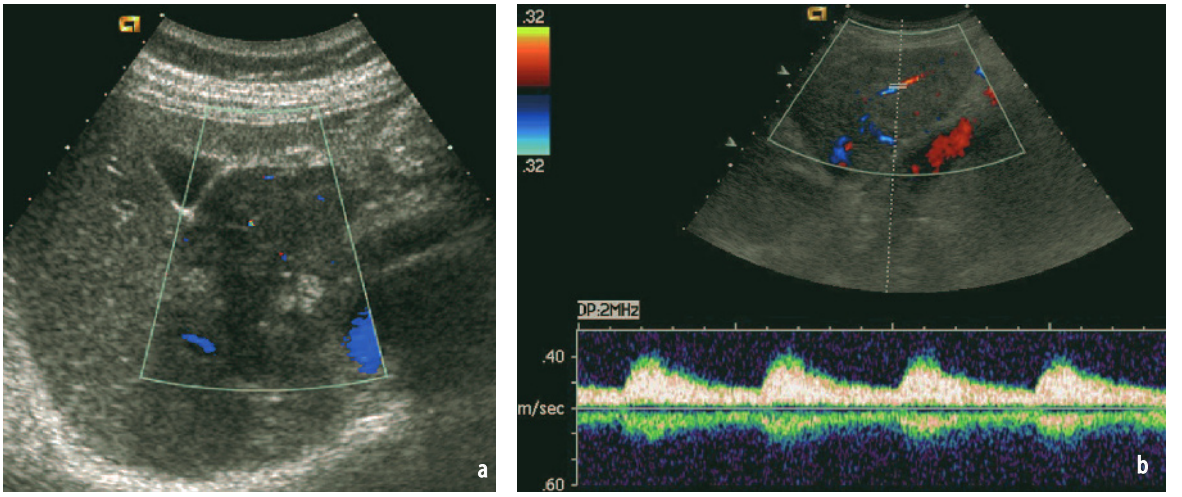

Fig. 33a, b. Hepatocellular adenoma on color Doppler US. Color Doppler ultrasound (**a**) reveals the intratumoral and peripheral vessels characterizing this lesion as hypervascular. A Color Doppler scan (**b**) reveals the presence of arterial vessels within the lesion, together with a characteristic arterial Doppler-spectrum

for the characteristic yellow appearance of the cut surface of adenoma. Evidence of lipid at CT or MR imaging can be helpful in diagnosing HA.

In many cases HA is seen as a large, predominantly hypoechoic lesion on US with central anechoic areas corresponding to areas of internal hemorrhage (Fig. 32) [117]. Adenomas may undergo massive necrotic and hemorrhagic changes which give the lesion a complex appearance on US with large cystic components. Non-complicated HA may appear as an iso- or hypoechoic mass with a relatively homogeneous aspect (Fig. 32a). However, fatty components within the lesion may result in focal hyperechogenicity. A peripheral pseudocapsule, which is present in about one third of HA lesions, is seen as a hypoechoic peripheral rim on US.

Color Doppler US reveals peripheral arteries and veins which correlate well with both gross and angiographic findings. In addition, Color Doppler may identify intratumoral arteries. This finding is absent in FNH and may be a useful discriminating feature for HA (Fig. 33) [30]. Contrast-enhanced US allows depiction of the characteristic vascular behavior of HA. During the arterial phase, an early and homogenous enhancement of non-necrotic, non-hemorrhagic portions of the tumor can be seen. Pericapsular feeding blood vessels are best

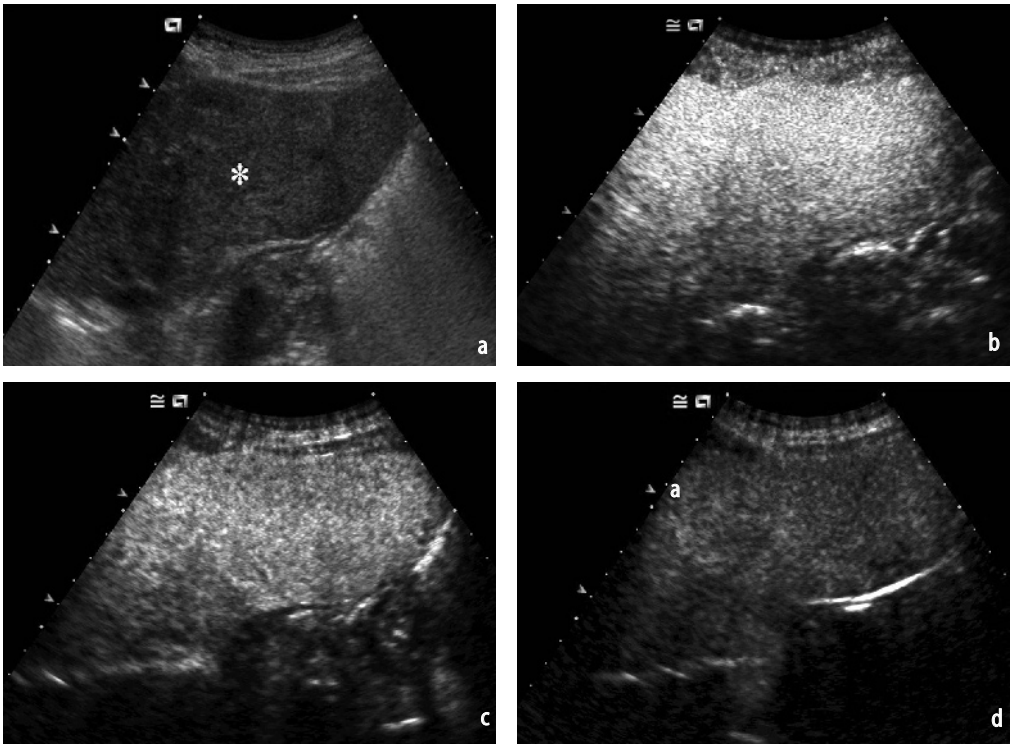

Fig. 34a-d. Hepatocellular adenoma with SonoVue. The precontrast US examination (**a**) shows an isoechoic lesion (*asterisk*) with lobulated margins, located in the left lobe of the liver. Dynamic evaluation after SonoVue administration reveals homogeneous enhancement of the nodule in the arterial phase (**b**) and rapid wash-out in the portal-venous (**c**) and equilibrium (**d**) phases

visualized during the early arterial phase. In the late arterial phase and in the early portal-venous phase, the contrast wash-out of HA is initially faster than the progressive wash-in of the surrounding liver parenchyma; therefore the neoplasm remains slightly hypoechoic. In the late portal-venous and sinusoidal phases, HA generally shows the same behavior as the surrounding liver parenchyma (Fig. 34).

On unenhanced CT, HA may appear as a hypodense mass due to the presence of fat and glycogen within the tumor. However, hyperdense areas corresponding to acute or subacute hemorrhage can be noted frequently in large, complicated lesions (Fig. 35). On contrast-enhanced dynamic CT scanning, non-complicated HA generally enhances rapidly and homogeneously and have increased attenuation relative to the liver. A pseudocapsule is frequently seen in larger lesions as a hypodense and hyperdense rim on non-contrast and equilibrium phase CT images, respectively (Fig. 36) [46]. The enhancement in adenomas typically does not persist because of arteriovenous shunting [88]. Larger or complicated HA may have a more heterogeneous appearance than smaller lesions (Fig. 37) [46].

On MR images, HA frequently show heteroge-

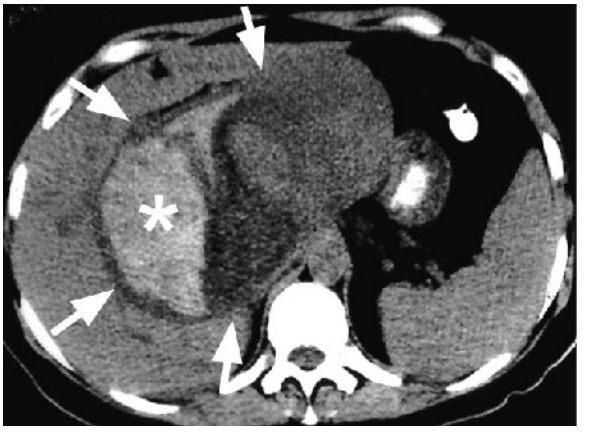

Fig. 35. Hemorrhagic hepatocellular adenoma. The pre-contrast CT scan reveals a large and inhomogeneous hypodense lesion (*arrows*) with a hyperdense component (*asterisk*) corresponding to acute hemorrhage

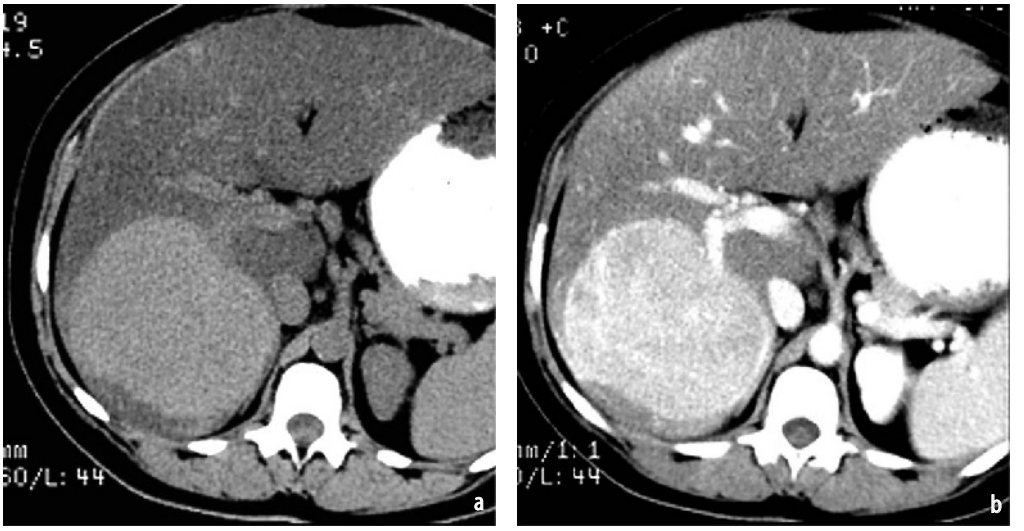

Fig. 36a, b. Non-complicated hepatocellular adenoma. On the pre-contrast CT scan (**a**), the mass appears homogeneously hyperdense compared to the surrounding liver tissue, demonstrating fatty changes. During the arterial phase after the administration of contrast medium (**b**), the density of the lesion markedly increases in a homogeneous manner

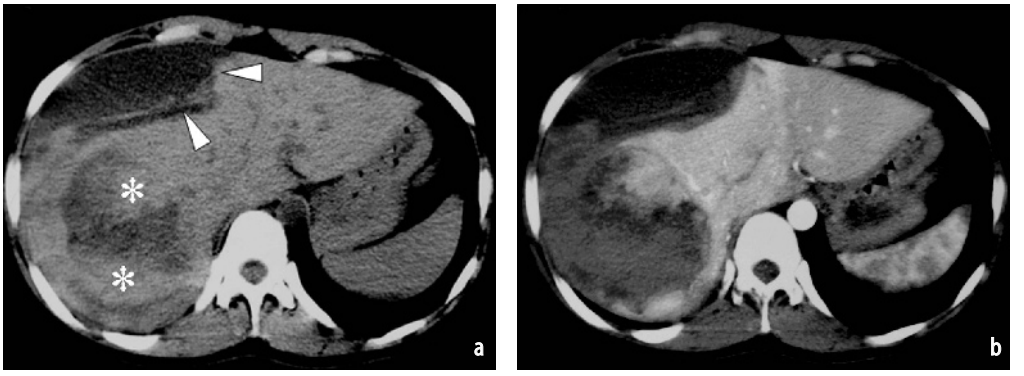

Fig. 37a, b. Complicated hepatocellular adenoma. On the precontrast CT scan (**a**) the mass (*asterisks*) appears heterogeneously hyperdense due to intratumoral hemorrhage. Associated subcapsular hematoma (*arrowheads*) can also be seen. Due to the degenerative changes, the lesion shows heterogenous enhancement in the portal-venous phase (**b**)

neous hyperintensity on unenhanced T2-weighted images and heterogeneous hypointensity on unenhanced T1-weighted images. Areas of increased signal intensity on T1-weighted images indicate the presence of fat and hemorrhage, while areas of reduced signal intensity indicate necrosis (Fig. 38) [77]. Sometimes HA have a hypointense peripheral rim, corresponding to a fibrous capsule. In most cases, the rim is of low signal intensity on both T1- and T2-weighted images (Fig. 38) [3]. Because non-complicated HA frequently have a homogeneous iso- or slightly hyperintense signal on T2-weighted images and an iso- or hypointense signal on T1-weighted images they may be hard to distinguish from surrounding normal liver parenchyma (Fig. 39). The presence of glycogen in HA may increase the signal intensity on T1-weighted images. Similarly, the homogeneous or heterogeneous appearance of HA may be determined by the presence of intranodular fat (Fig. 40).

Dynamic MR imaging is able to demonstrate the early arterial enhancement that results from the presence of large subcapsular feeding vessels. This finding, however, is not specific for HA; the

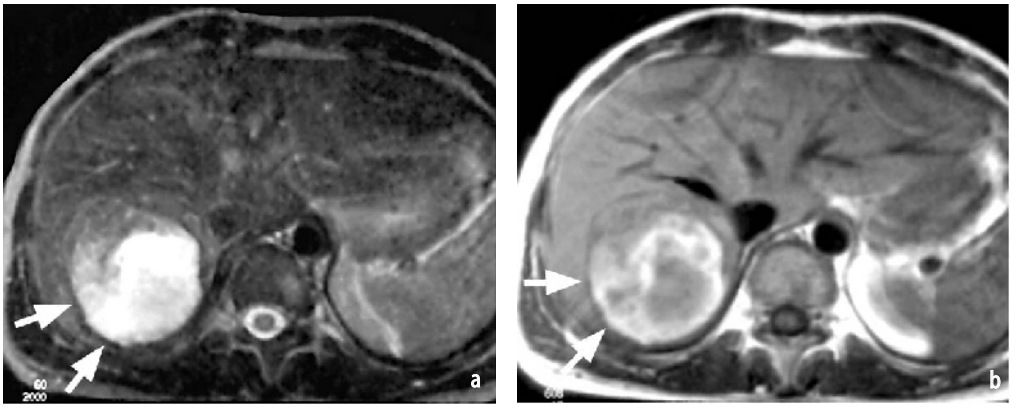

Fig. 38a, b. Complicated hepatocellular adenoma. Diffuse intratumoral hemorrhage within the lesion appears heterogeneously hyperintense on the T2-weighted spin-echo image (**a**) and heterogeneously hypointense on the corresponding unenhanced T1-weighted spin-echo image (**b**). A peripheral hypointense rim (*arrows*) representing a fibrous capsule is visible on both images

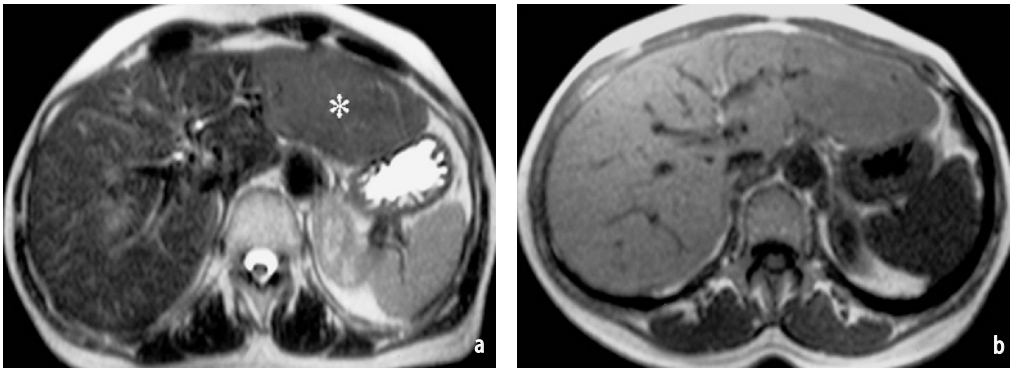

Fig. 39a, b. Non-complicated hepatocellular adenoma. A non-complicated HA (*asterisk*) located in the left lobe of the liver, appears slightly hyperintense on the unenhanced HASTE T2-weighted image (**a**) and isointense on the corresponding unenhanced GRE T1-weighted image (**b**)

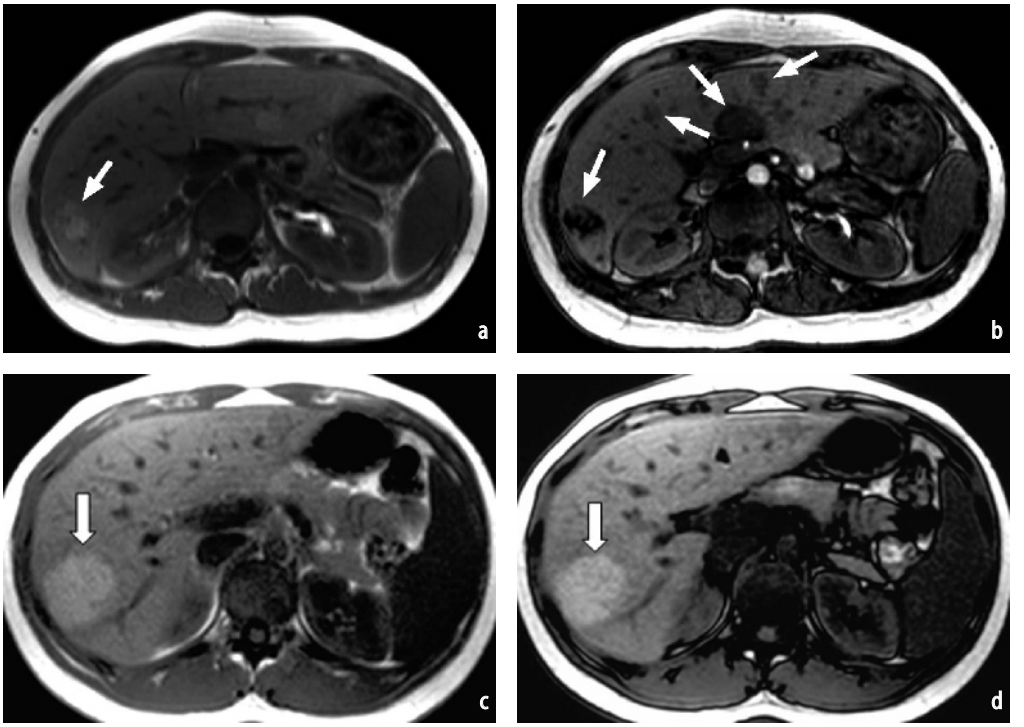

Fig. 40a-d. Non-complicated hepatocellular adenoma. (**a**) and (**b**) represent a case of liver adenomatosis (LA) in which one lesion shows a hyperintense signal (*arrow*) on the "in-phase" T1-weighted image (**a**) because of intronodular fat. On the corresponding "out-of-phase" image (**b**) the lesion shows a signal drop because of the intranodular fat. Multiple other fat-containing lesions of LA can also be seen (*arrows* in **b**). (**c**) and (**d**) in contrast demonstrate a case of HA with intranodular glycogen. Due to the T1-effect of intranodular glycogen, the HA (*arrow*) appears as a slightly hyperintense nodule on the T1-weighted "in-phase" image (**c**). On the corresponding "out-of-phase" image (**d**), in contrast to the case of LA, no signal-drop is visible since the high signal of the nodule is caused by intranodular glycogen, rather than intranodular fat

specific MR appearance of HA is generally that of a fat-containing or hemorrhagic lesion with increased peripheral vascularity. On portal-venous and equilibrium phase images HA generally appear isointense or slightly hypointense, with focal heterogeneous hypointense areas of necrosis, calcification or fibrosis.

On delayed liver-specific phase images after Gd-BOPTA administration, the common appearance is hypointensity of the solid, non-hemorrhagic components of the lesion (Figs. 41, 42). This is one of the main features that differentiates FNH from HA in non-complicated, but also in calcified lesions. The hypointensity of HA reflects the lack of biliary ducts. This enhancement pattern of HA in the liver-specific phase after injection of Gd-BOPTA is opposite to that observed in FNH. The overall difference in enhancement behavior of FNH and HA on hepatobiliary phase images can be ascribed to the different structural and functional features of the lesions; in HA the absence of biliary ductules within the lesion results in altered hepatocellular transport compared with that occurring in normal hepatocytes. Thus, while the mechanism of entry of Gd-BOPTA into the hepatocytes of HA may be unaltered, the absence of the intracellular transport gradient due to the lack of any active transport across the sinusoidal membrane manifests as hypointensity against enhanced normal liver parenchyma on images acquired in the hepatobiliary phase.

A recent study has highlighted the ability of Gd-BOPTA to accurately differente of FNH from HA [40]: at 1-3 hours after Gd-BOPTA administration almost all FNH appeared hyper- or isointense, while all HA appeared hypointense.

Conversely, after mangafodipir trisodium administration HA appear iso- or slightly hyperintense, similar to the appearance of FNH (Figs. 41, 42). This limits the possibility to make a correct differential diagnosis.

Dynamic T1-weighted imaging after USPIO administration can reveal slight arterial enhancement which in some cases is better seen at the periphery of the lesion and corresponds to the prominent vascular portion of the adenoma. The uptake of SPIO in the accumulation phase depends on the amount and functional status of the Kupffer cells in the tumor as well as in the periphery of the lesion (Fig. 43) [44].

Adenomas in some cases may take up SPIO, re-

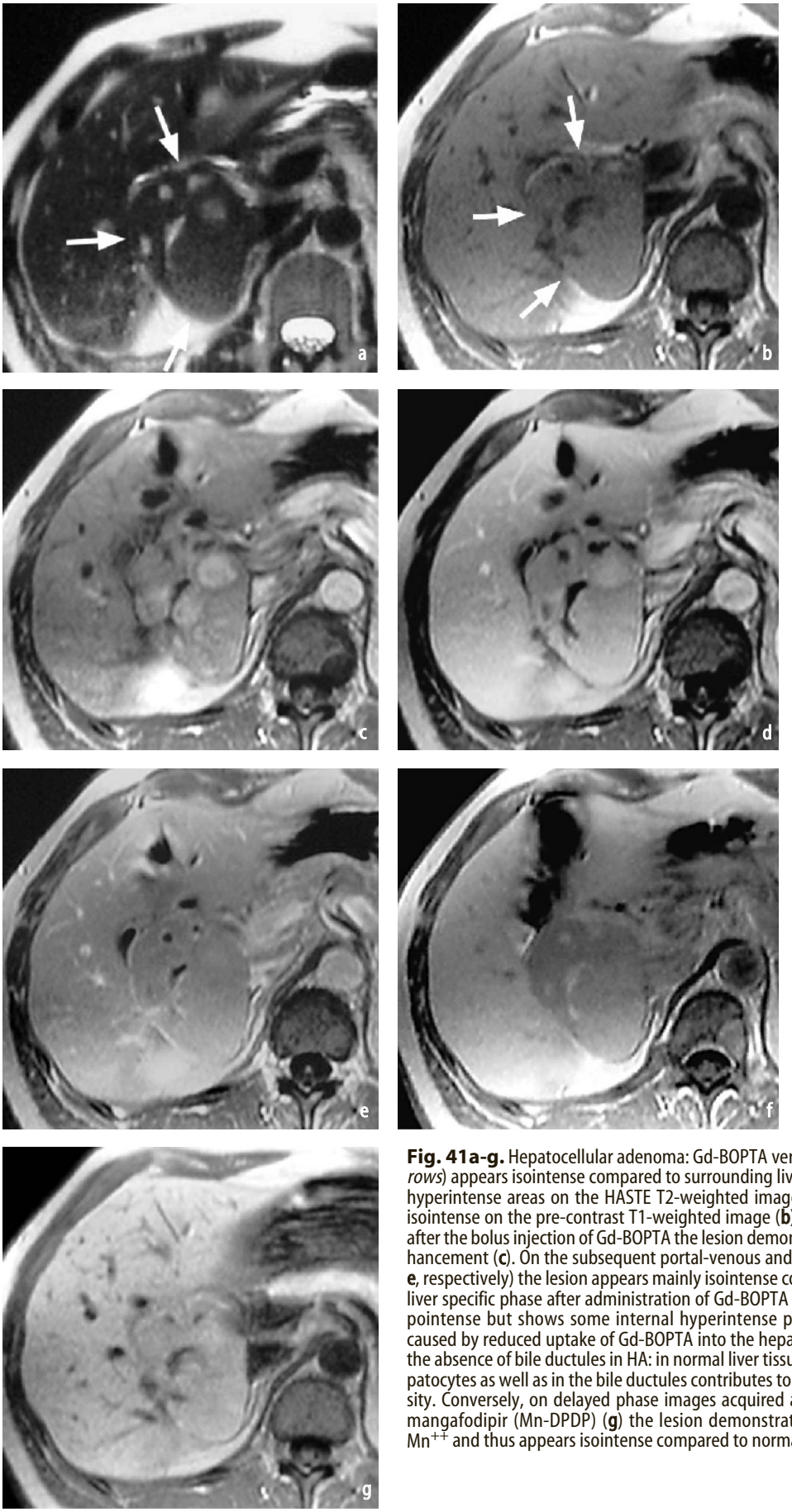

Fig. 41a-g. Hepatocellular adenoma: Gd-BOPTA versus Mn-DPDP. A lesion (*arrows*) appears isointense compared to surrounding liver tissue with intratumoral hyperintense areas on the HASTE T2-weighted image (**a**) and heterogeneously isointense on the pre-contrast T1-weighted image (**b**). During the arterial phase after the bolus injection of Gd-BOPTA the lesion demonstrates heterogeneous enhancement (**c**). On the subsequent portal-venous and equilibrium phases (**d** and **e**, respectively) the lesion appears mainly isointense compared to the liver. In the liver specific phase after administration of Gd-BOPTA (**f**) the lesion is seen as hypointense but shows some internal hyperintense peliotic areas. This may be caused by reduced uptake of Gd-BOPTA into the hepatocytes in HA as well as by the absence of bile ductules in HA: in normal liver tissue contrast agent in the hepatocytes as well as in the bile ductules contributes to the increased signal intensity. Conversely, on delayed phase images acquired after the administration of mangafodipir (Mn-DPDP) (**g**) the lesion demonstrates non-specific uptake of Mn^{++} and thus appears isointense compared to normal liver tissue

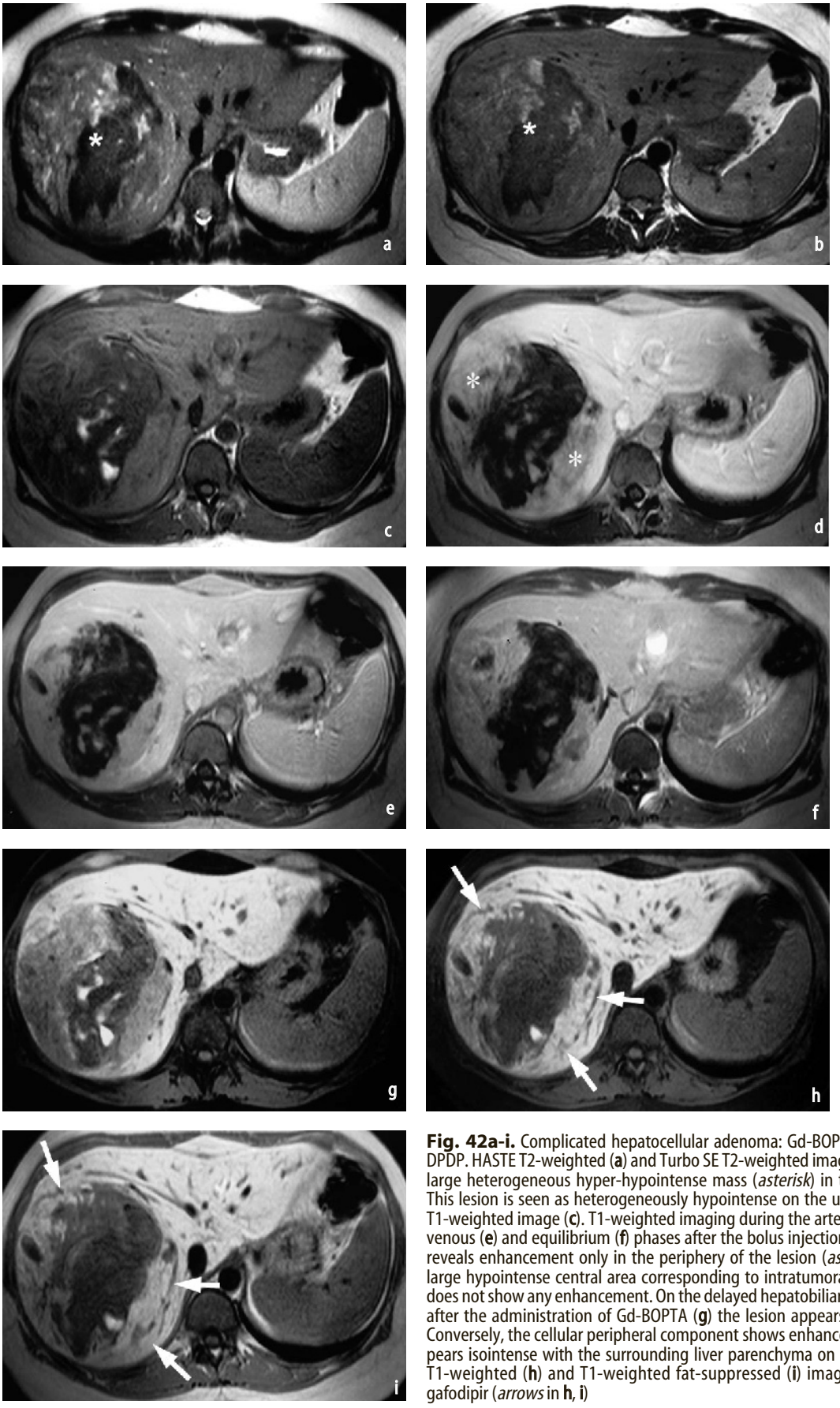

Fig. 42a-i. Complicated hepatocellular adenoma: Gd-BOPTA versus Mn-DPDP. HASTE T2-weighted (**a**) and Turbo SE T2-weighted images (**b**) reveal a large heterogeneous hyper-hypointense mass (*asterisk*) in the right lobe. This lesion is seen as heterogeneously hypointense on the unenhanced GE T1-weighted image (**c**). T1-weighted imaging during the arterial (**d**), portal-venous (**e**) and equilibrium (**f**) phases after the bolus injection of Gd-BOPTA reveals enhancement only in the periphery of the lesion (*asterisks* in **d**); a large hypointense central area corresponding to intratumoral hemorrhage does not show any enhancement. On the delayed hepatobiliary phase image after the administration of Gd-BOPTA (**g**) the lesion appears hypointense. Conversely, the cellular peripheral component shows enhancement and appears isointense with the surrounding liver parenchyma on delayed phase T1-weighted (**h**) and T1-weighted fat-suppressed (**i**) images after mangafodipir (*arrows* in **h**, **i**)

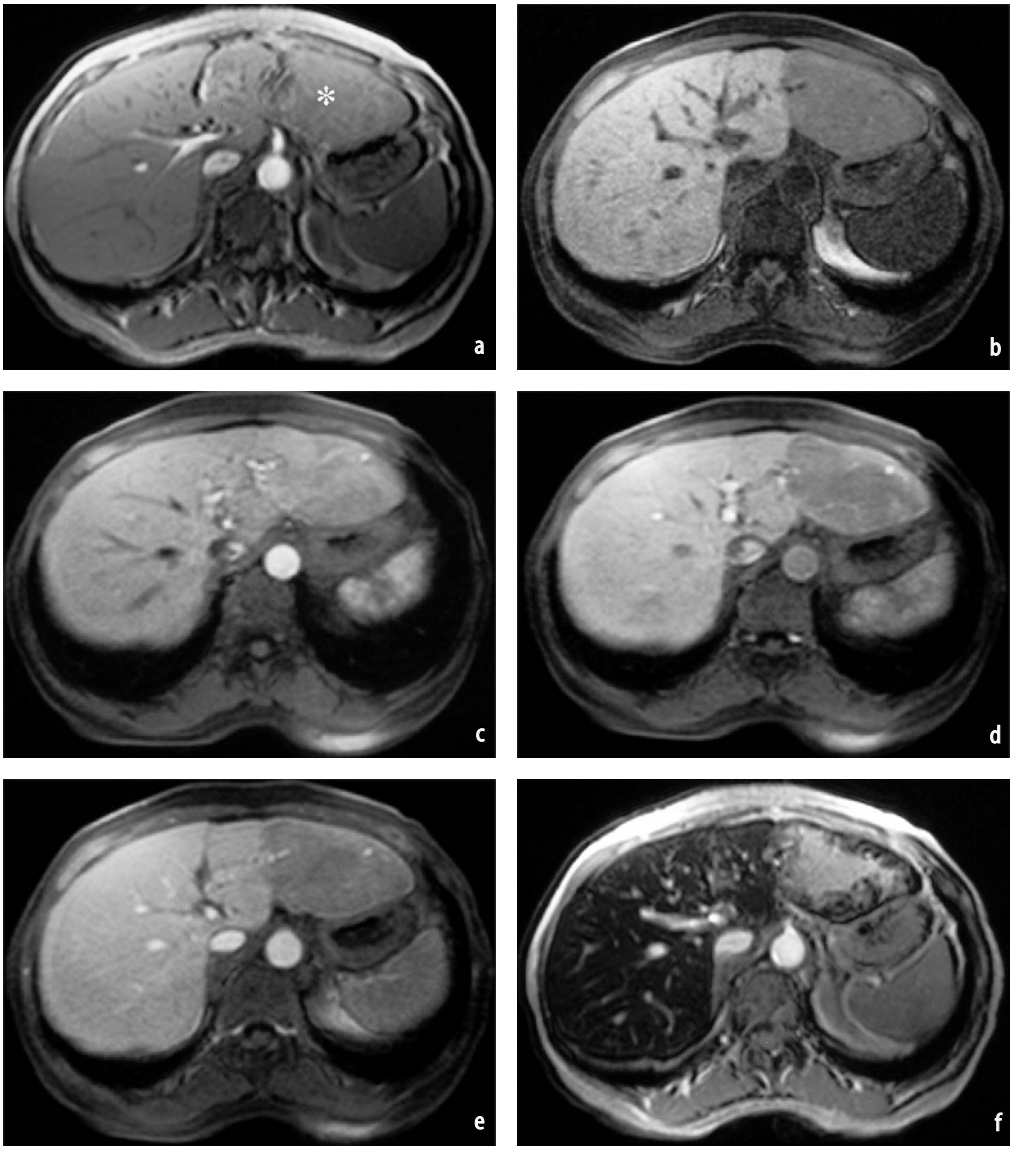

Fig. 43a-f. Non-complicated adenoma after USPIO. Same case as shown in Fig. 39. The nodule (*asterisk*) appears isointense with the normal liver tissue on the precontrast T2-weighted image (**a**), and slightly hypointense on the precontrast VIBE image (**b**). The lesion does not show significant enhancement on arterial phase images after SH U 555 A administration (**c**), whereas in the portal-venous (**d**) and equilibrium (**e**) phases the HA appears hypointense. On the accumulation phase (**f**) the HA appears heterogeneously hyperintense due to a reduced number of Kupffer cells, which are more frequent at the periphery of the lesion

sulting in a decreased signal on T2-weighted images. However the uptake of SPIO is usually poor in HA compared to FNH [108].

LA is a separate clinical entity which is characterized by the presence of multiple (>10) adenoma lesions, by the absence of any correlation with steroid medication, by its equal presence in both men and women, and by abnormal increases in serum alkaline phosphatase and γ-glutamyltransferase levels [26].

The conditions that may predispose patients to LA are poorly understood, although one of the more intriguing speculations is that congenital or acquired abnormalities of the hepatic vasculature may be involved [37]. Other investigators [27, 49] have noted that both FNH and HA occur more often in patients who have coexistent vascular tumors, portal-venous absence or occlusion, or hepatic portovenous shunts. It is thought that a focal disturbance of the hepatic blood supply somehow facilitates the hyperplastic development of these two similar benign liver lesions [37].

Patients with LA are at increased risk for development of HCC, and should be closely monitored with CT or MR imaging and by serum α-fetoprotein or other tumor marker examinations [58, 86].

Clinically, patients with LA can be asymptomatic or have chronic or acute abdominal pain.

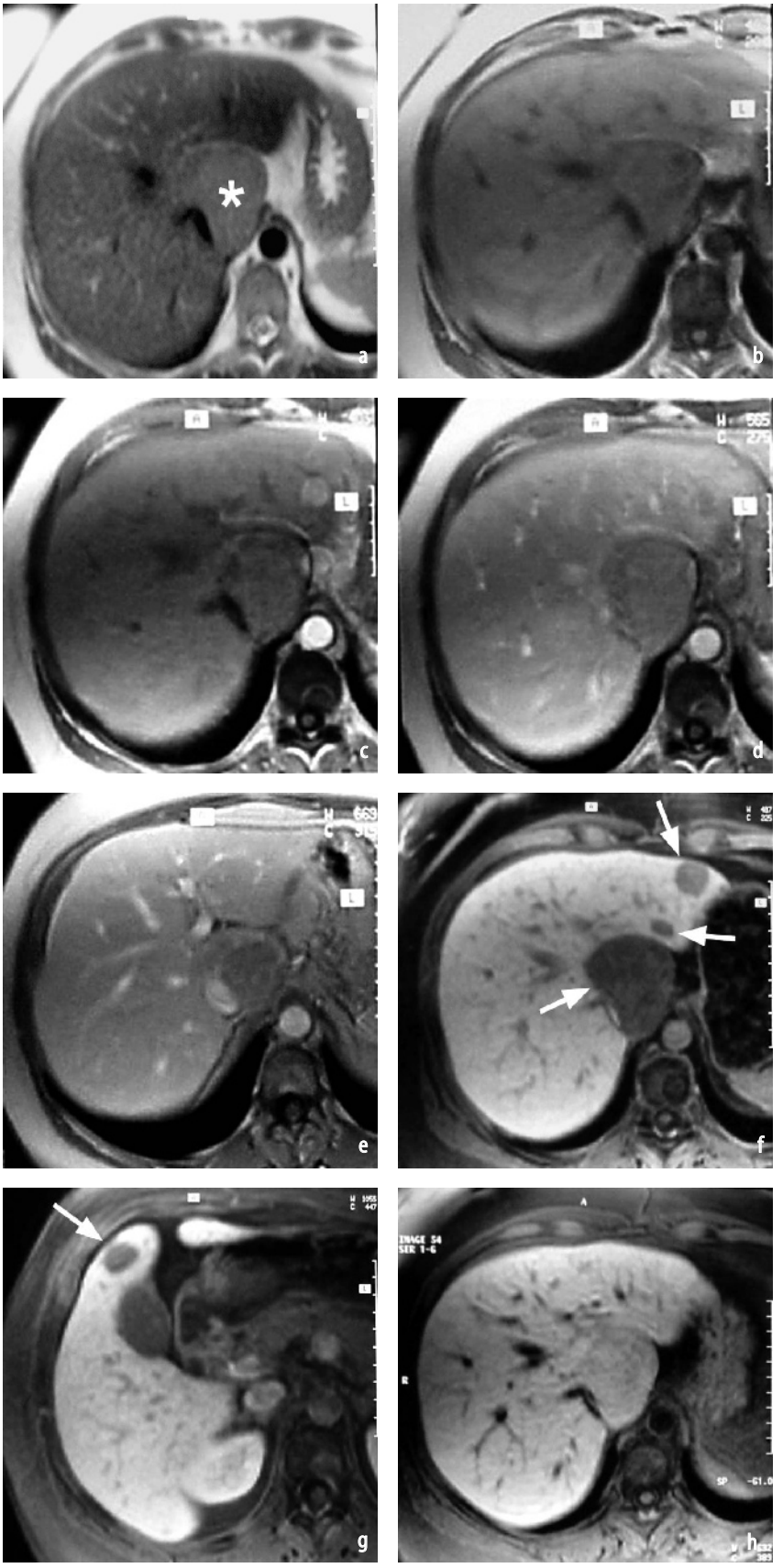
a
b
c
d
e
f
g
h

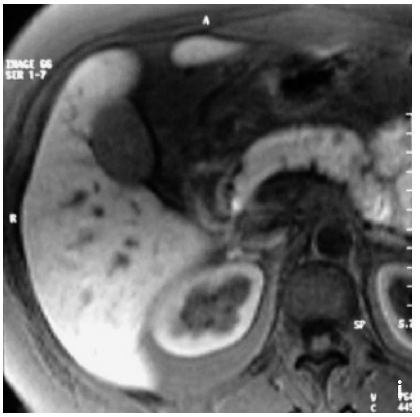

Fig. 44a-i. Liver Adenomatosis: Gd-BOPTA versus Mn-DPDP. The HASTE T2-weighted image (**a**) reveals several large, slightly hyperintense nodules with the biggest (*asterisk*) located in the caudal lobe. These nodules appear isointense compared with the surrounding parenchyma on the unenhanced GE T1-weighted image (**b**). The lesions do not show significant enhancement on arterial phase images acquired after the bolus administration of Gd-BOPTA (**c**), whereas on the portal-venous (**d**) and equilibrium (**e**) phase images the lesions appear iso- to hypointense. On delayed phase images acquired after the administration of Gd-BOPTA (**f** and **g**), several hypointense nodules (*arrows*) are visible. Conversely, after mangafodipir administration (**h** and **i**), the lesions are isointense with the normal liver and not clearly delineated

The multiple adenomas in LA may have a variety of appearances, but the CT and MR characteristics of individual lesions are similar to those reported for sporadic or solitary HA (Fig. 44) [49, 77].

Management of LA remains difficult because there is no predictive sign of its potential complications other than the size of the individual lesions. Therefore close follow-up is mandatory to evaluate progression. Liver resection is the preferred option because LA is essentially a benign disease that does not impair hepatocellular function. Liver transplantation remains a difficult decision, although it is sometimes the last option in progressive forms, or in liver disease that impairs socio-professional day-to-day life in young patients, particularly in young women trying to become pregnant [4].

4.1.4 Nodular Regenerative Hyperplasia

Nodular regenerative hyperplasia (NRH) of the liver is a condition characterized by diffuse micronodular transformation of the hepatic parenchyma without the formation of fibrous septa between the nodules [115].

The nodules vary in size (0.1 to 3 cm) but are usually smaller than 1 cm. Various systemic diseases and drugs are often associated with NRH: myeloproliferative syndromes (polycythemia vera, chronic myelogenous leukemia, and myeloid metaplasia); lymphoproliferative syndromes (Hodgkin's and non-Hodgkin's lymphoma, chronic lymphocytic leukemia, and plasma cell dysplasia); chronic vascular disorders (polyarteritis nodosa); rheumatologic disorders (rheumatoid arthritis, Felty's syndrome, scleroderma, calcinosis cutis, Raynaud's phenomenon, sclerodactyly and teleangiectasia), lupus erythematosus; steroids and anti-neoplastic medication [25, 99, 114].

Disturbance in the hepatic microcirculation is believed to be the primary cause of NRH [115]. Several different combinations of vascular obliteration can lead to a variegated parenchyma with atrophy and secondary hyperplasia [116]. The particular pattern of obliteration determines the size and distribution of the nodules. Uniform small nodules are usually produced by small portal vein obliteration. This commonly occurs because of inflammatory lesions in the small portal tracts, typically in early-stage primary biliary cirrhosis and various rheumatologic conditions. In these two examples, the primary lesion involves small ducts and small arteries, respectively, and the obliteration of the adjacent portal veins is a bystander effect. Because the tissue involvement is patchy, some small portal veins remain patent, giving a variegated pattern of patent and obliterated veins, which explains the presence of both atrophy and hyperplasia. Increased flow through the portal vein in the presence of splenomegaly could exacerbate nodule formation in those acini with a patent portal vein [10]. After thrombosis of large portal veins, there are often large contiguous regions of parenchyma near the hilum that retain portal flow and escape atrophy. This situation also leads to large regenerative nodules (macronodular hyperplasia, partial nodular transformation). This variant is characterized by large nodules several centimeters in diameter near the large portal tracts, and atrophy together with small nodules in peripheral parts of the liver [50, 66, 96, 102].

In addition to this simple response to variegated portal vein flow, secondary arterial hyperemia and arterial growth may enhance the topographic variegation of blood flow. Arterial growth leads to large regenerative nodules that resemble FNH [100]. In non-cirrhotic conditions, the hepatic venules are usually normal despite severe portal vein disease. Nodular hyperplasia may result from primary outflow obstruction with either hepatic vein thrombosis or congestive heart failure [14]. In these situations, the nodules are less uniformly

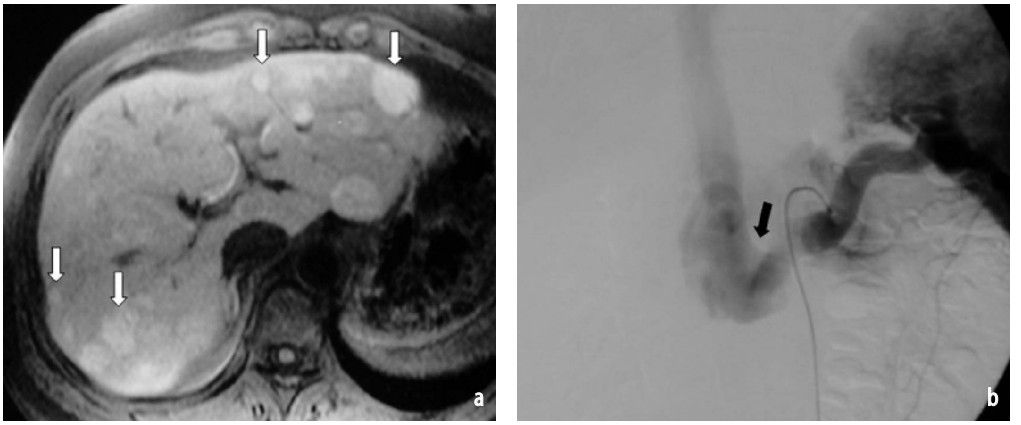

Fig. 45a, b. Nodular regenerative hyperplasia. A T1-weighted fat suppressed MR image (**a**) in the hepatobiliary phase after injection of Gd-BOPTA shows multiple, well-defined, hyperintense nodules (*arrows*) in both lobes of the liver. Note as well the absence of portal vein branches in the liver parenchyma. Portography (**b**) confirms the absence of the portal vein and the presence of a shunt (*arrow)* between the splenic vein and the inferior caval vein

distributed and are accompanied by sinusoidal congestion and fibrous septation [100, 113].

NRH occurs in all ages with a mean age of 50 years, with no gender predilection. It is rarely reported in childhood but when present, it is associated with portal vascular abnormalities, such as congenital absence of the portal vein (Fig. 45) [36]. It may also occur in the setting of diffuse fatty liver due to toxic or hormonal changes (Fig. 46).

The lesions are frequently found incidentally during surgery or imaging studies. Symptoms and signs, when present, can be divided into the following broad categories:

- symptoms of the underlying disease (Felty's syndrome, myeloproliferative disorders),
- manifestations of portal hypertension such as esophageal varices, splenomegaly and ascites,
- hepatic failure,
- acute abdominal crisis following rupture of a large nodule with hemoperitoneum,
- symptoms of hypersplenism.

Liver function tests are usually either normal or

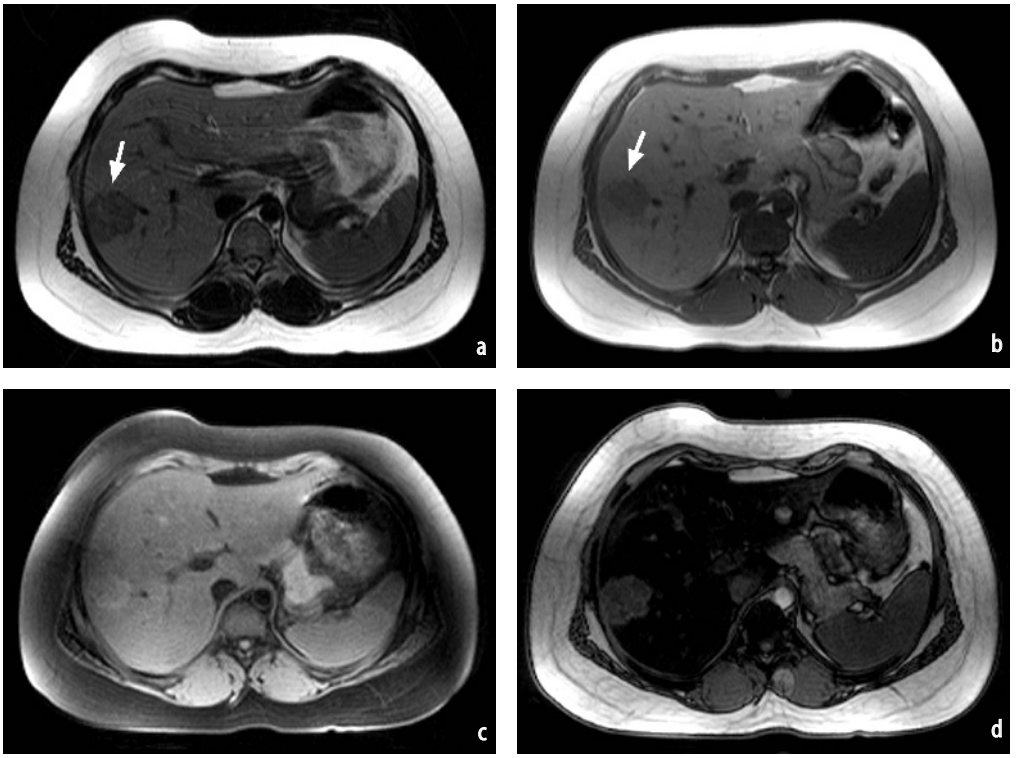

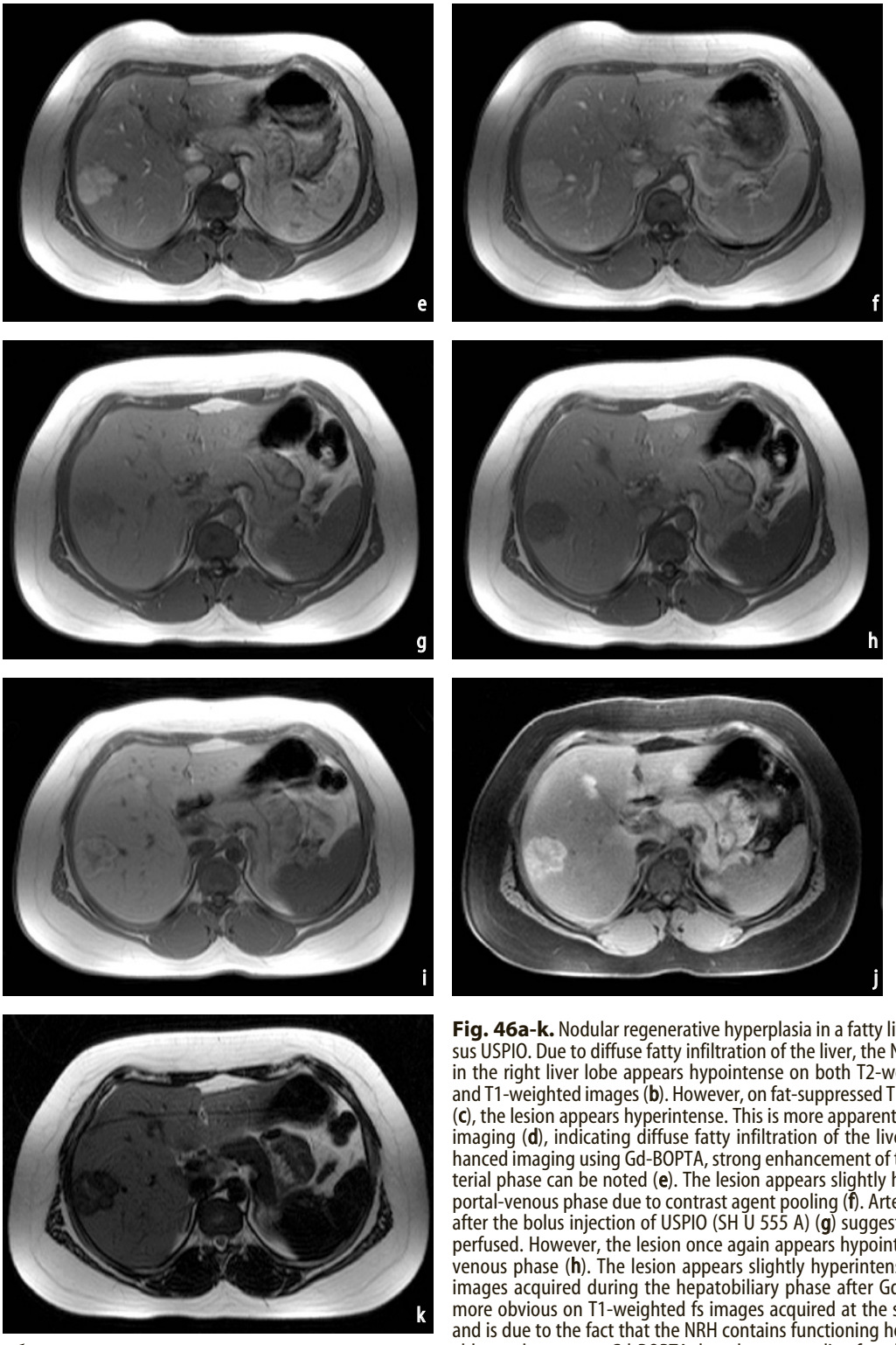

Fig. 46a-k. Nodular regenerative hyperplasia in a fatty liver: Gd-BOPTA versus USPIO. Due to diffuse fatty infiltration of the liver, the NRH nodule (*arrow*) in the right liver lobe appears hypointense on both T2-weighted images (**a**) and T1-weighted images (**b**). However, on fat-suppressed T1-weighted images (**c**), the lesion appears hyperintense. This is more apparent on opposed phase imaging (**d**), indicating diffuse fatty infiltration of the liver. On contrast enhanced imaging using Gd-BOPTA, strong enhancement of the lesion in the arterial phase can be noted (**e**). The lesion appears slightly hyperintense in the portal-venous phase due to contrast agent pooling (**f**). Arterial phase imaging after the bolus injection of USPIO (SH U 555 A) (**g**) suggests that the lesion is perfused. However, the lesion once again appears hypointense in the portal-venous phase (**h**). The lesion appears slightly hyperintense on T1-weighted images acquired during the hepatobiliary phase after Gd-BOPTA (**i**). This is more obvious on T1-weighted fs images acquired at the same time point (**j**) and is due to the fact that the NRH contains functioning hepatocytes that are able to take up more Gd-BOPTA than the surrounding fatty liver tissue. This behavior clearly underlines the diagnosis of a benign lesion. On T2-weighted images acquired after SH U 555 A injection (**k**) the lesion is even more hypointense compared with unenhanced images (**a**). This indicates that the lesion contains functioning Kupffer cells

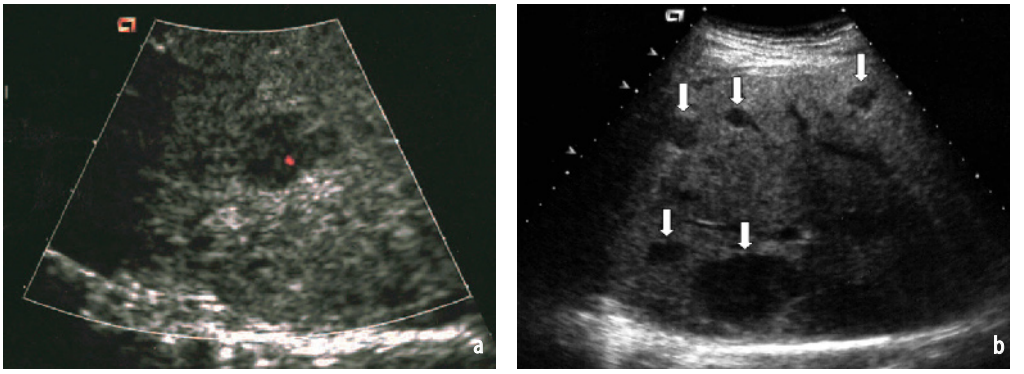

Fig. 47a, b. Nodular regenerative hyperplasia on US. An ultrasound scan (**a**) reveals a well demarcated homogeneous hypoechoic nodule. Color Doppler may show vascularity within the lesion. NRH may also appear as multiple, well-delineated, hypoechoic nodules (*arrows*) of variable size (**b**)

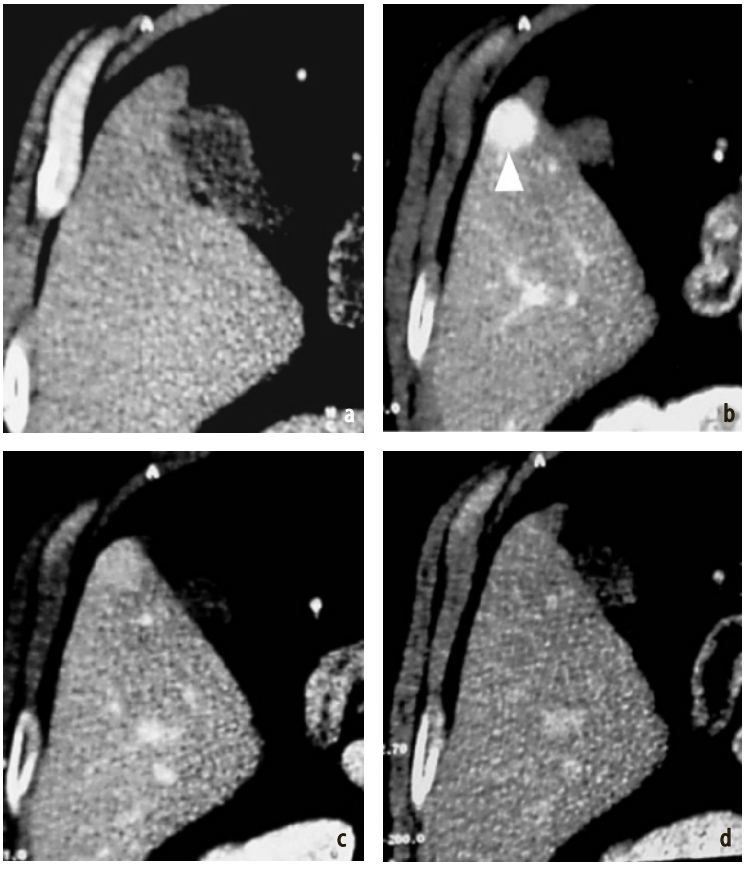

Fig. 48a-d. Nodular regenerative hyperplasia on CT. Whereas the pre-contrast CT scan (**a**) appears normal, on arterial phase images acquired after the administration of contrast medium (**b**), the NRH nodule (*arrowhead*) enhances markedly and homogeneously. In the portal-venous (**c**) and equilibrium (**d**) phases, the nodule is seen as slightly hyperdense and isodense, respectively

may be slightly altered. The most common abnormalities observed are elevation of alkaline phosphatase and γ-glutamyltransferase (GGT) levels.

In most cases NRH is not visible on US due to the same echogenecity as the surrounding parenchyma. In other cases, well-delineated hypoechoic or isoechoic nodules can be seen (Fig. 47) [76, 105].

Hyperechoic nodules have been reported on very rare occasions [20] while on other occasions, a diffusely heterogeneous hepatic parenchyma can be seen. Color Doppler examination in many cases demonstrates arterial supply within the nodules.

On CT imaging, approximately half of the cases appear normal, while the nodules in the remaining cases are typically hypoattenuating relative to the

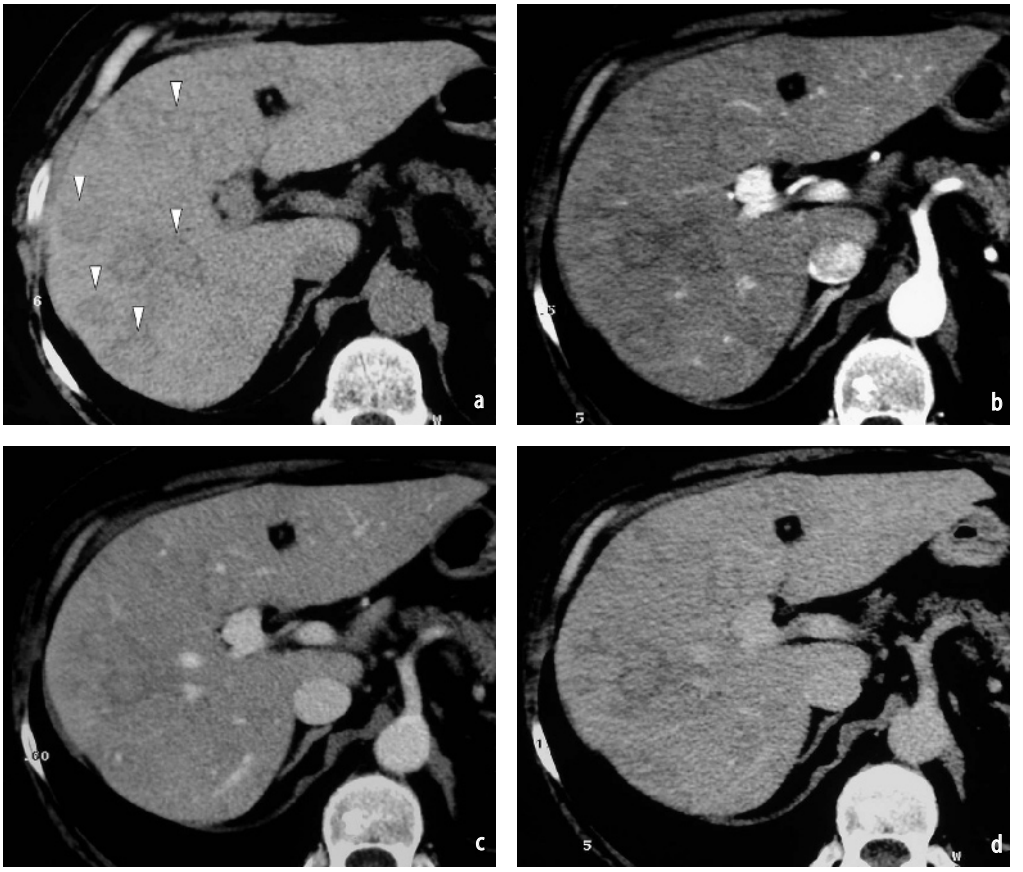

Fig. 49a-d. Nodular regenerative hyperplasia on CT. The pre-contrast CT examination (**a**) reveals numerous nodules (*arrowheads*), that are slightly hyperdense compared to the normal liver and surrounded by a thin hypodense rim. Weak enhacement is seen during the dynamic study after contrast medium administration (**b**-**d**). Note that the thin hypodense rim is well appreciable in all phases

adjacent normal hepatic parenchyma [25, 78]. Usually the nodules enhance homogeneously to different degrees after the intravenous administration of contrast media (Figs. 48, 49) [16].

On unenhanced T1-weighted MR images the lesions are generally almost isointense or slightly hyperintense compared to the surrounding liver parenchyma, while on unenhanced T2-weighted images the nodules appear iso- or slightly hypointense. A peripheral hypointense rim is often visible in large lesions on T1- and T2-weighted images. On dynamic MR imaging, the nodules are usually hyperintense in the arterial phase, and iso- or slightly hyperintense in the portal-venous and equilibrium phases. In the delayed, liver-specific phase after Gd-BOPTA administration, the lesions may appear isointense or hyperintense since they consist of benign hepatocytes with abnormal biliary system drainage (Fig. 50). The peripheral hypointense rim is better seen in larger lesions, particularly in the liver-specific phase, and probably represents an ischemic perinodular area (Fig. 51) [16].

After injection of iron oxide particles, the lesions usually show a significant uptake of contrast agent due to the presence of abundant Kupffer cells within the nodule (Fig. 52).

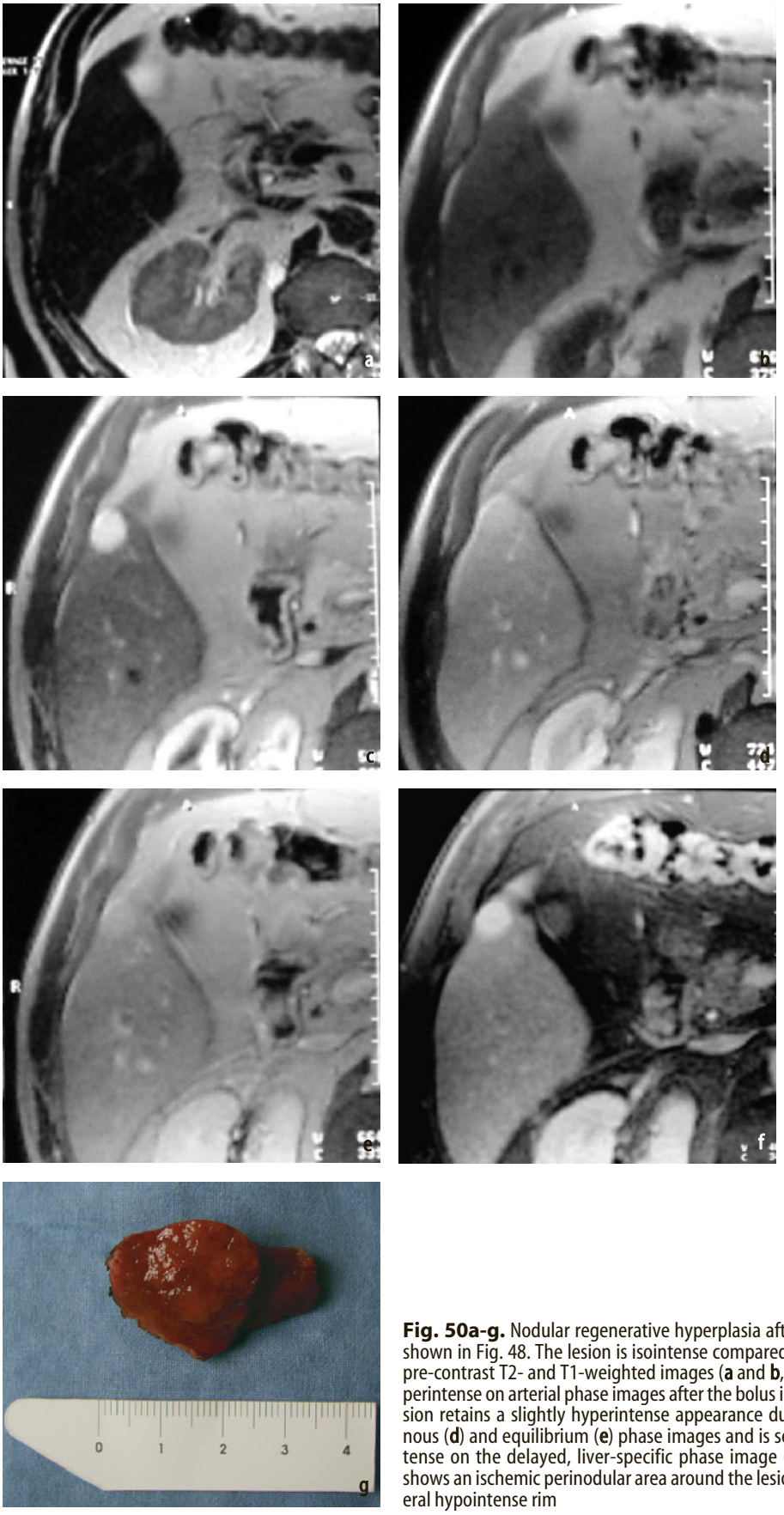

Fig. 50a-g. Nodular regenerative hyperplasia after Gd-BOPTA. The same case as shown in Fig. 48. The lesion is isointense compared with normal liver tissue on the pre-contrast T2- and T1-weighted images (**a** and **b**, respectively) but is strongly hyperintense on arterial phase images after the bolus injection of Gd-BOPTA (**c**). The lesion retains a slightly hyperintense appearance during the subsequent portal-venous (**d**) and equilibrium (**e**) phase images and is seen as homogeneously hyperintense on the delayed, liver-specific phase image (**f**). Gross pathology of NRH (**g**) shows an ischemic perinodular area around the lesion, corresponding to the peripheral hypointense rim

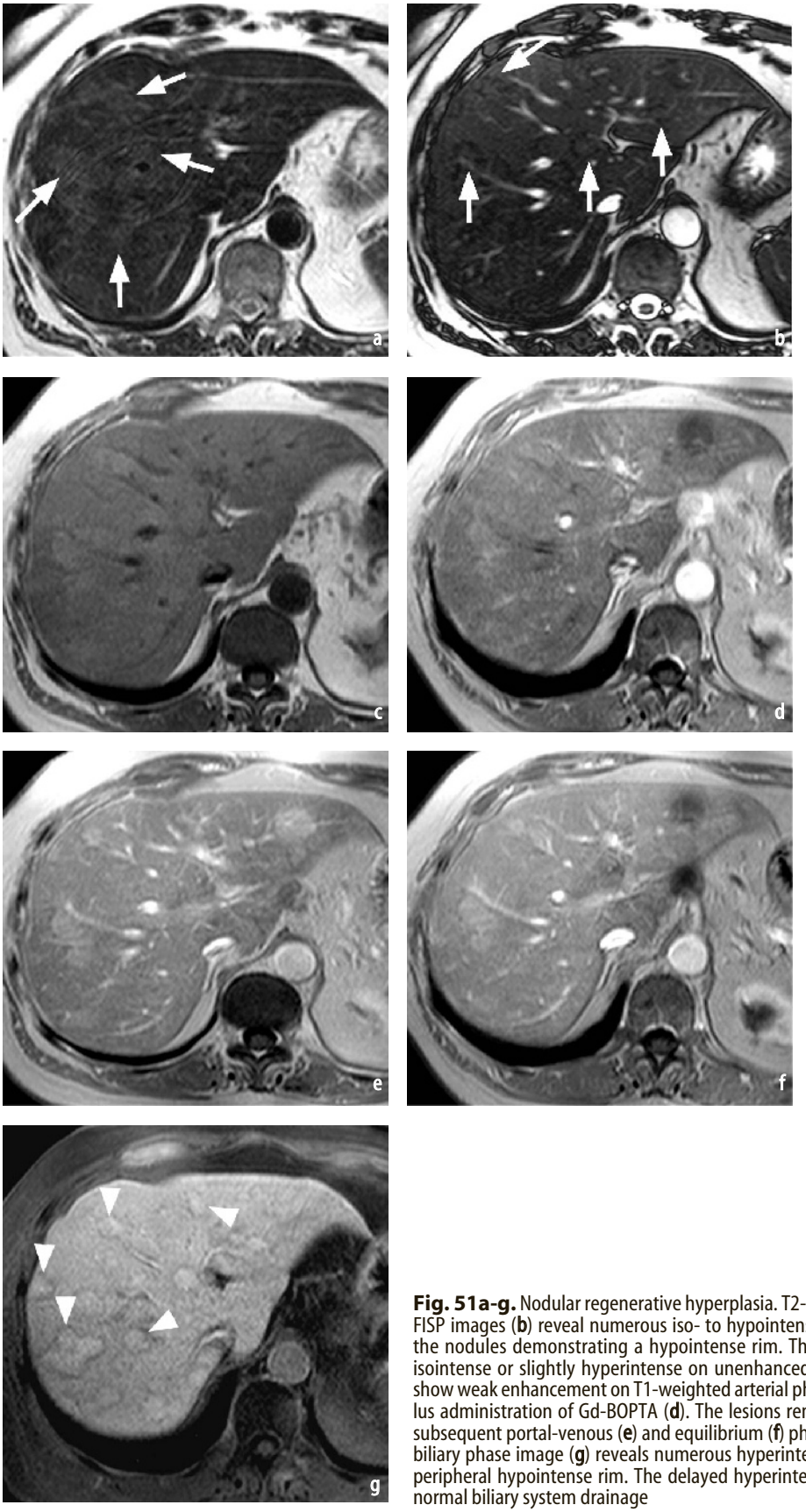

Fig. 51a-g. Nodular regenerative hyperplasia. T2-weighted TSE images (**a**) and True FISP images (**b**) reveal numerous iso- to hypointense nodules (*arrows*) with some of the nodules demonstrating a hypointense rim. These nodules are homogeneously isointense or slightly hyperintense on unenhanced T1-weighted GE images (**c**) and show weak enhancement on T1-weighted arterial phase images acquired after the bolus administration of Gd-BOPTA (**d**). The lesions remain slightly hyperintense on the subsequent portal-venous (**e**) and equilibrium (**f**) phase images. The delayed, hepatobiliary phase image (**g**) reveals numerous hyperintense nodules (*arrowheads*) with a peripheral hypointense rim. The delayed hyperintensity after Gd-BOPTA reflects abnormal biliary system drainage

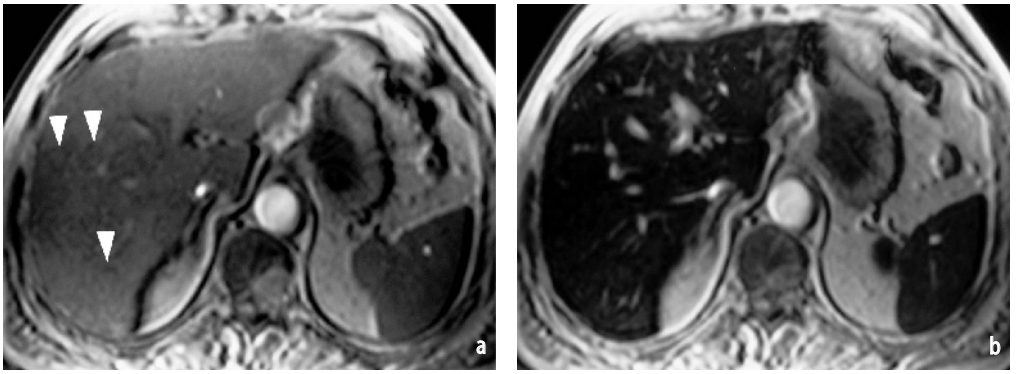

Fig. 52. Nodular regenerative hyperplasia on pre-contrast T2*-weighted (**a**) and post-contrast USPIO-enhanced T2*-weighted images (**b**). The isointensity of the nodules (*arrows* in **a**) on SH U 555 A enhanced images is related to the presence of abundant Kupffer cells

4.1.5 Cysts

Primary hepatic cysts should be distinguished from other cystic masses of the liver. A true cyst of the liver or bile duct is defined by the presence of an epithelial lining on the inner surface of the cyst. A simple hepatic cyst, on the other hand, is defined as a single unilocular cyst with a wall composed of a thin layer of fibrous tissue. If more than 10 cysts are seen, adult polycystic kidney and/or liver disease should be considered. The incidence of simple hepatic cysts is about 15% in autopsy series and they are more common in women than in men. Cysts are usually discovered incidentally, although up to 20% have been reported in surgical series of patients who presented with symptoms caused by mass effect such as abdominal pain, and jaundice [91].

On US examination, uncomplicated simple cysts present as anechoic, round, well-defined lesions with smooth borders, no septations and no mural calcifications. Although there is no acoustic shadow, often an acoustic enhancement can be observed.

On CT uncomplicated hepatic cysts are seen as round, well-defined water attenuation masses with smooth thin walls, and no internal septa or solid nodules. They show no enhancement after administration of contrast medium.

On T2-weighted MR images simple uncomplicated hepatic cysts are extremely hyperintense with a homogeneous appearance. On T1-weighted images they typically have a homogeneous hypointense appearance. However, the intensity of the cysts on T1-weighted images can vary if protein and/or hemorrhage are present within cyst fluid. These materials can shorten the T1-relaxivity and therefore cause a hyperintense appearance.

Congenital hepatic fibrosis is part of the spectrum of hepatic cystic disease, and is characterized by aberrant bile duct proliferation and periductal fibrosis. Cysts are usually not visible due to their very small size in typical congenital hepatic fibrosis (Fig. 53). In polycystic liver disease, numerous large and small cysts coexist with fibrosis. In cases of polycystic liver and/or kidney disease, the liver parenchyma surrounding the cyst is not normal, frequently containing von Meyenburg complexes and increased fibrous tissue (Fig. 54) [55].

Hepatic involvement occurs in approximately 30-50% of patients with polycystic kidney disease. Clinically, the majority of patients present in childhood, when congenital hepatic fibrosis predominates with bleeding, varices and other manifestations of portal hypertension. In patients with predominating polycystic liver disease, the lesions are usually identified incidentally. Approximately 70% of patients with polycystic liver disease also have adult polycystic kidney disease. Congenital hepatic fibrosis is also related to Caroli's disease. Cross-sectional images reveal multiple cysts in the liver that are often associated with multiple renal cysts [12]. In this clinical setting, the cysts may have variable signal intensity, presumably caused by proteinaceous content within the cysts and/or intracystic hemorrhage.

Acquired hepatic cysts, also called peribiliary cysts, are more conspicuous in the peribiliary tissue, and are associated with chronic diseases such as cirrhosis, ascending cholangitis, obstructive

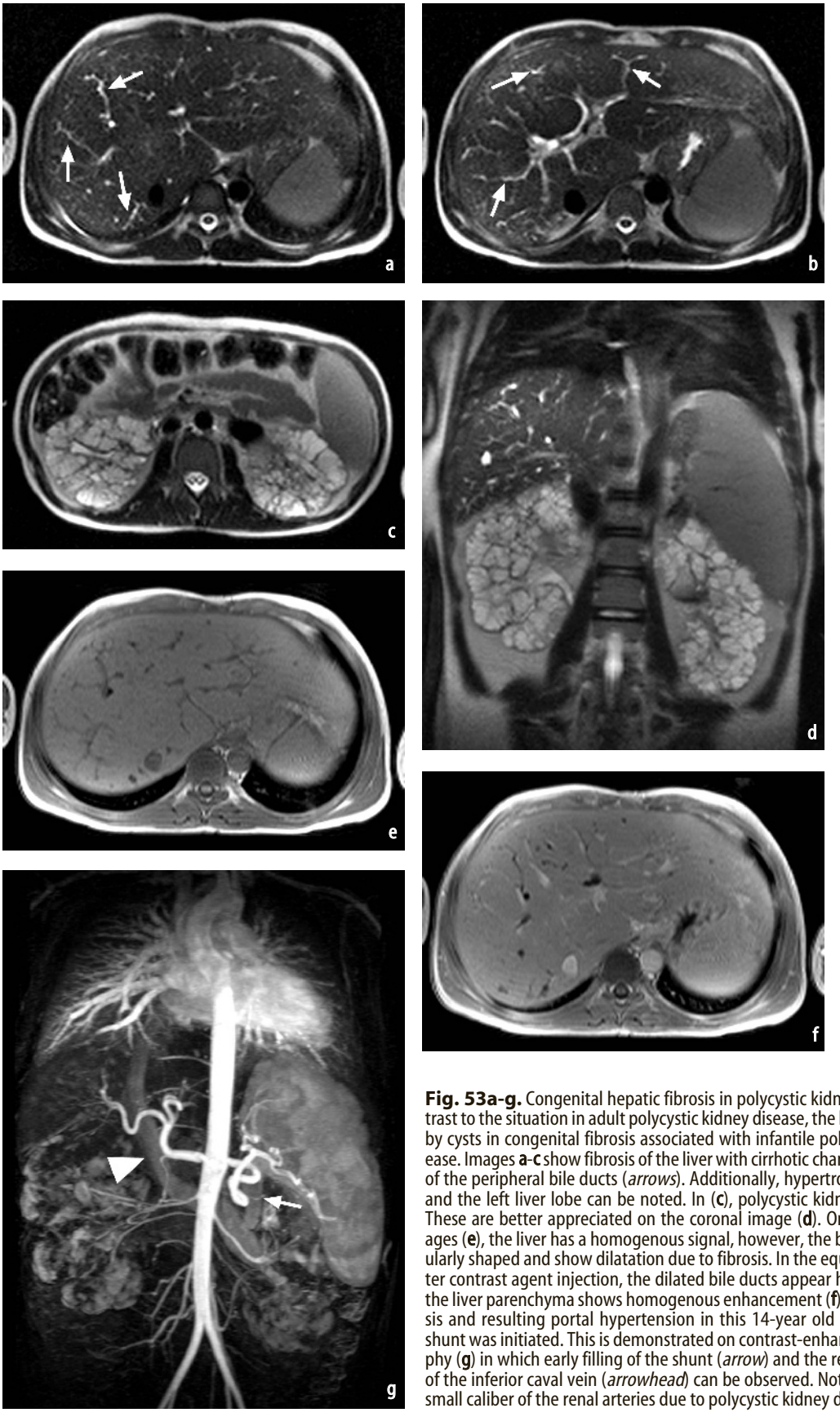

Fig. 53a-g. Congenital hepatic fibrosis in polycystic kidney disease. In contrast to the situation in adult polycystic kidney disease, the liver is not affected by cysts in congenital fibrosis associated with infantile polycystic kidney disease. Images **a**-**c** show fibrosis of the liver with cirrhotic changes and dilatation of the peripheral bile ducts (*arrows*). Additionally, hypertrophy of Segment 1 and the left liver lobe can be noted. In (**c**), polycystic kidneys are displayed. These are better appreciated on the coronal image (**d**). On T1-weighted images (**e**), the liver has a homogenous signal, however, the bile ducts are irregularly shaped and show dilatation due to fibrosis. In the equilibrium phase after contrast agent injection, the dilated bile ducts appear hyperintense while the liver parenchyma shows homogenous enhancement (**f**). Due to liver fibrosis and resulting portal hypertension in this 14-year old girl, a splenorenal shunt was initiated. This is demonstrated on contrast-enhanced MR angiography (**g**) in which early filling of the shunt (*arrow*) and the renal vein as well as of the inferior caval vein (*arrowhead*) can be observed. Note additionally, the small caliber of the renal arteries due to polycystic kidney disease

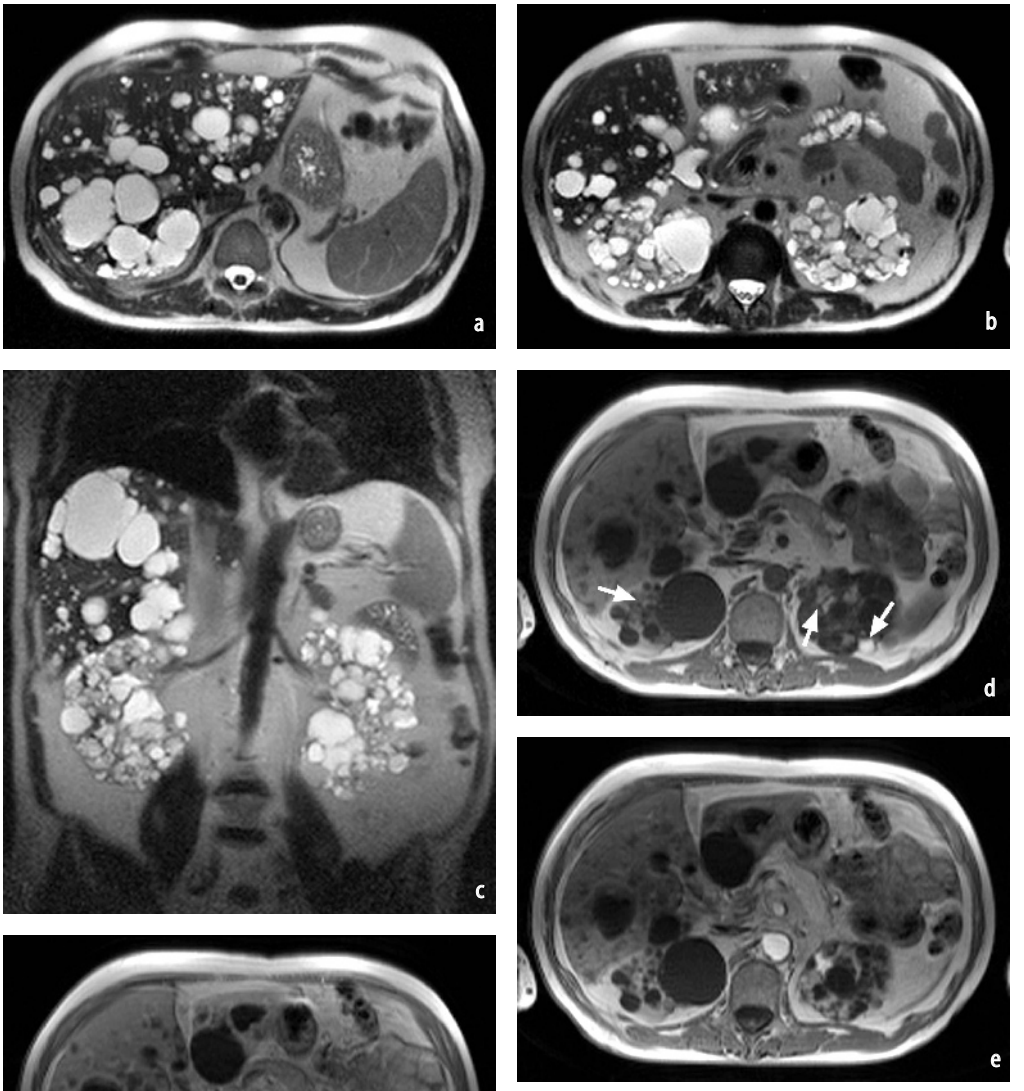

Fig. 54a-f. Polycystic liver and kidneys in adult polycystic kidney disease. Both the kidneys and the liver show multiple high signal intensity cysts on T2-weighted images (**a**-**c**). On T1-weighted images (**d**) the liver cysts appear hypointense whereas some of the kidney cysts appear hyperintense due to hemorrhage (*arrows*). After contrast medium injection, homogenous enhancement of liver parenchyma can be noted in both the arterial phase (**e**) and portal-venous phase (**f**). The remaining kidney parenchyma also shows homogenous enhancement. Since the risk of developing renal cell carcinoma is increased in patients with polycystic kidney disease, a very precise evaluation of the renal cysts is necessary

jaundice, systemic infections and in patients with polycystic liver disease and portal hypertension. Microscopically, acquired cysts are serous or mucinous in content and are caused by periductal gland obstruction.

Peribiliary cysts are generally located near the intra- and extrahepatic main ducts.

Although patients are usually asymptomatic, large lesions can cause biliary obstruction and jaundice (Figs. 55, 56).

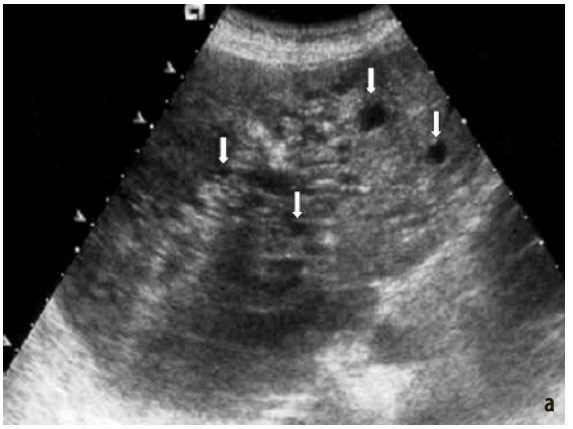

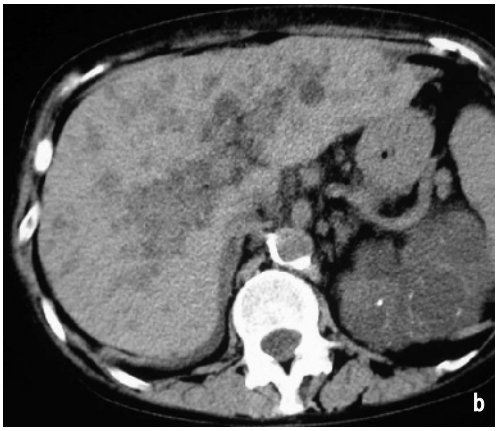

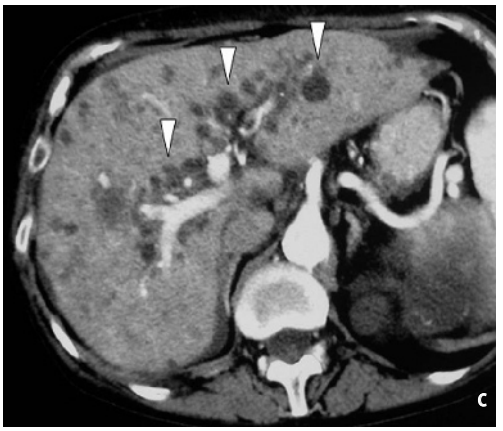

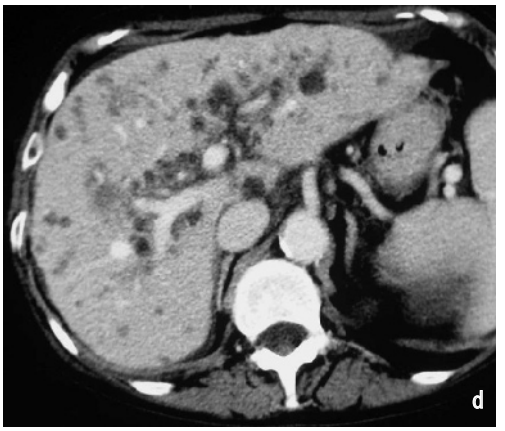

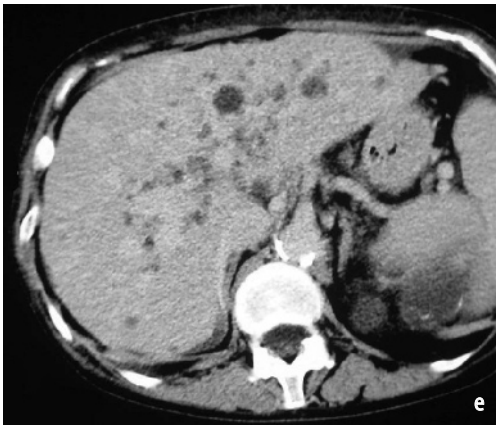

Fig. 55a-e. Peribiliary cysts on US and CT. On the US scan (**a**) numerous small, well-defined, hypo- to anechoic lesions (*arrows*) are demonstrated. On the pre-contrast CT scan (**b**), the cysts appear as hypodense, round lesions. They do not show significant enhancement after contrast medium administration (**c**-**e**). Note the "rosary beads" - like arrangement (*arrowheads* in **c**) of the cysts

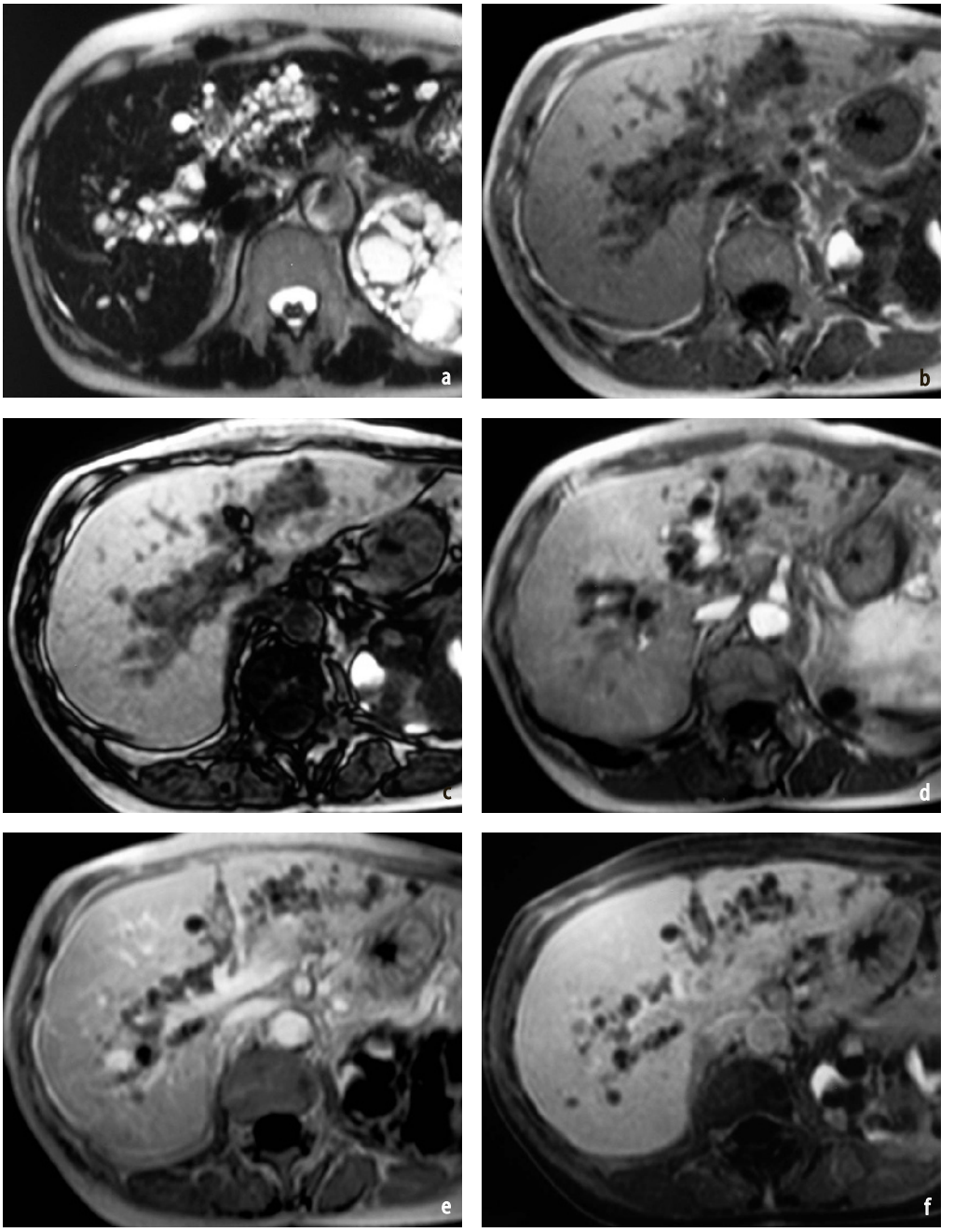

Fig. 56a-f. Peribiliary cysts on MR after Gd-BOPTA. On MR imaging, peribiliary cysts are characteristically markedly hyperintense lesions on T2-weighted images (**a**), and hypointense on T1-weighted GE "in-phase" (**b**) and "out-of-phase" (**c**) images. The cysts remain hypointense during the dynamic study after bolus administration of Gd-BOPTA (**d**, **e**) and do not show enhancement in the hepatobiliary phase (**f**) due to the absence of communication between the cysts and the biliary tree

4.1.6 Miscellaneous Tumors

4.1.6.1 Lipomatous Tumors

Benign hepatic tumors composed of fat cells include lipoma, and combined tumors such as angiomyolipoma (fat and blood vessels), myelolipoma (fat and hematopoietic tissue) and angiomyelolipoma [32].

Grossly, lipomatous tumors are usually solitary, round and well-circumscribed masses occuring in non-cirrhotic livers [31]. They contain variable proportions of adipose and smooth muscle tissue with thick-walled blood vessels. Flow cytometry shows a DNA-diploid pattern consistent with a benign lesion [104]. Hematopoietic foci may be present, and when prominent, the term myelolipoma [74] or angiomyelolipoma is used.

Angiomyolipomas are rare, usually asymptomatic solitary tumors. However, these tumors occasionally bleed, causing abdominal pain. Liver angiomyolipomas usually range in diameter from 0.3 to 36 cm and occur predominantly in women [47].

Liver angiomyolipomas may occur in association with Bourneville-Pringle syndrome. In this clinical setting, the lesions are generally multiple, progressive, and symptomatic.

Angiomyolipomas are often highly echogenic on US and are essentially indistinguishable from hemangiomas, although they may also present a mixed hyper-hypoechoic pattern (Fig. 57) [81].

Density measurements on unenhanced CT are characteristic of fat (–20 to –115 HU). Pure lipomas do not enhance, but variable enhancement occurs in lesions containing angiomatous elements (Fig. 58) [51, 81].

On MR imaging, the fatty and angiomatous components of angiomyolipomas lead to a high signal intensity on both T1- and T2-weighted images [69]. Hepatocellular carcinomas containing fat deposits may have a similar appearance. The early phase of contrast-enhanced dynamic CT or MR imaging may be useful in discriminating between angiomyolipomas and HCC with fat, because the fatty areas of angiomyolipoma are well-vascularized and enhance early. Conversely, the areas of fatty changes in HCC are relatively avascular, and enhancement is less obvious.

MR imaging with fat suppression techniques is useful to characterize hepatic angiomyolipomas, since lipid components show a typical signal drop with these sequences [48]. In contrast to the high signal intensity on T1- and T2-weighted images, the lesions appear hypointense compared to the

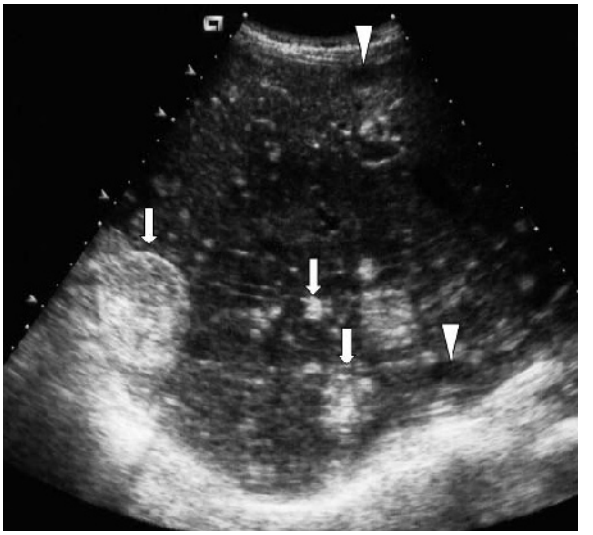

Fig. 57. Lipomatous tumors in Bourneville-Pringle syndrome on US. On US, multiple well-defined, hyperechoic (*arrows*) as well as small hypoechoic lesions (*arrowheads*) can be seen

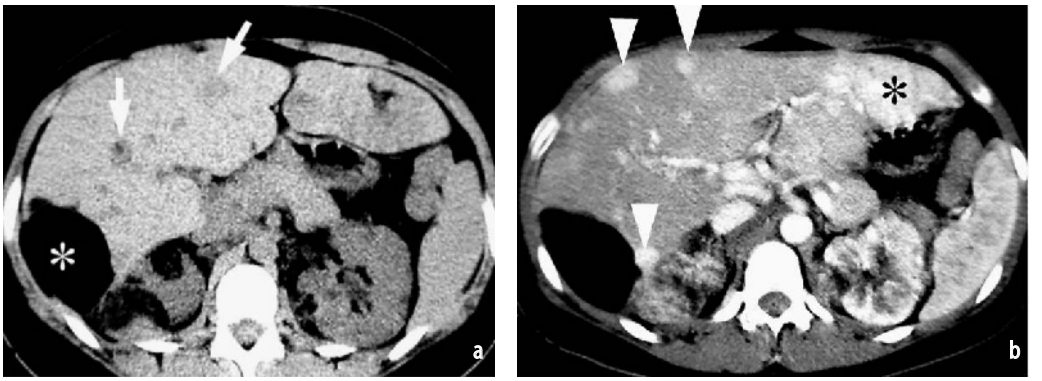

Fig. 58a, b. Lipomatous tumor in Bourneville-Pringle syndrome on CT. Pre-contrast CT (**a**) reveals multiple hypodense lesions (*asterisk*) and mixed lesions (*arrows*). The hypodensity of the largest lesion reflects the abundant fatty content. After administration of contrast medium (**b**), some nodules enhance homogeneously (*arrowheads*) whereas others enhance heterogeneously (*asterisk*). Note the presence of angiomyolipomas in both kidneys as well

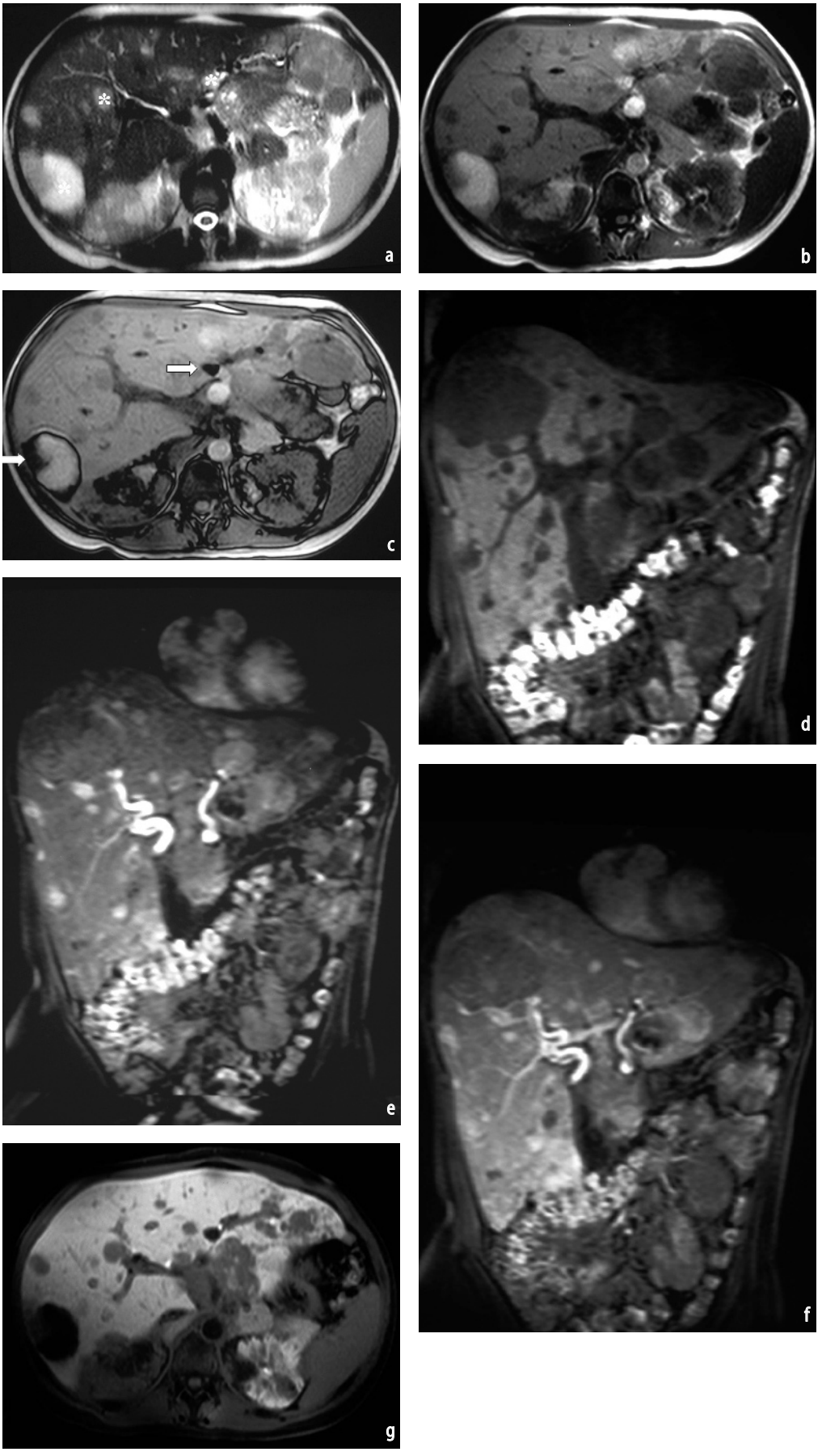
a
b
c
d
e
f
g

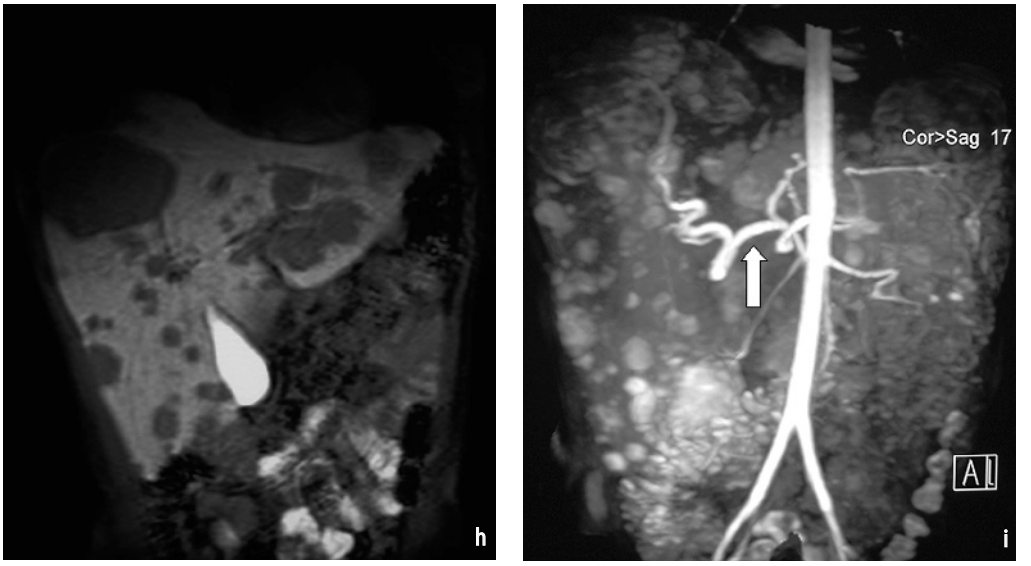

Fig. 59a-i. Lipomatous tumor in Bourneville-Pringle syndrome. Same case as shown in Fig. 58. On the unenhanced HASTE T2-weighted image (**a**) numerous hyperintense lesions (*asterisks*) can be seen in the liver. On the unenhanced GE T1-weighted image (**b**) some of the lesions are hypointense. Several of these lesions (*arrows*) demonstrate a decrease of signal intensity on the T1-weighted "out-of-phase" images due to the fat component (**c**). On the unenhanced coronal VIBE image (**d**) the nodules are seen as predominantly hypointense. Some lesions are seen as hypointense while others are hyperintense during the arterial phase after the administration of Gd-BOPTA (**e**). Numerous lesions remain hyperintense on the portal-venous phase image (**f**). On GE T1-weighted axial (**g**) and coronal (**h**) fat-suppressed images acquired during the delayed hepatobiliary phase, all of the lesions appear hypointense. MR angiography obtained with the VIBE sequence (**i**) reveals dilated and tortuous tripod celiac and hepatic arteries (*arrow*)

normal liver parenchyma on images obtained with fat suppression.

The appearance on contrast-enhanced MR imaging with gadolinium agents may mimic the pattern observed in hemangioma with peripheral nodular enhancement or irregular non-nodular vascular enhancement. However, arterial hyperintensity is also a common pattern of enhancement (Fig. 59).

4.1.6.2 Leiomyoma

This extremely rare lesion is a well-circumscribed smooth muscle tumor arising in the liver [45]. Several cases of leiomyoma have been reported in adults and children infected with the human immunodeficiency virus, suggesting that there may be a clinical association between these two entities [68, 109].

Leiomyoma has non-specific radiological characteristics. On US, leiomyomas may appear solid or hypoechoic with internal echoes [85, 109]. Leiomyomas are of low attenuation relative to normal liver on unenhanced CT scans, but following contrast agent administration, may display two distinct enhancement patterns: either peripheral rim enhancement, similar to that seen in abscesses, or homogeneous enhancement, which may sometimes be delayed [68, 109]. On MR imaging, leiomyomas are hypointense relative to the liver on T1-weighted images and hyperintense on T2-weighted images [85, 109]. Enhancement patterns after contrast agent administration are similar to those described for CT imaging.

4.2 Secondary Benign Liver Lesions

4.2.1 Pyogenic Abscess

Abscesses of the liver may be caused by bacterial, amebic or fungal infections, resulting in the localized collection of inflammatory cells and destruction of the surrounding parenchyma [82]. Hepatic abscesses can develop via five major routes [29]:

- the biliary route, due to ascending cholangitis, benign or malignant biliary obstruction and choledocholitisis,
- the portal vein route, due to pylephlebitis from appendicitis diverticulitis, proctitis, infected hemorrhoids, inflammatory bowel disease and others,
- the hepatic artery route, subsequent to septicemia,

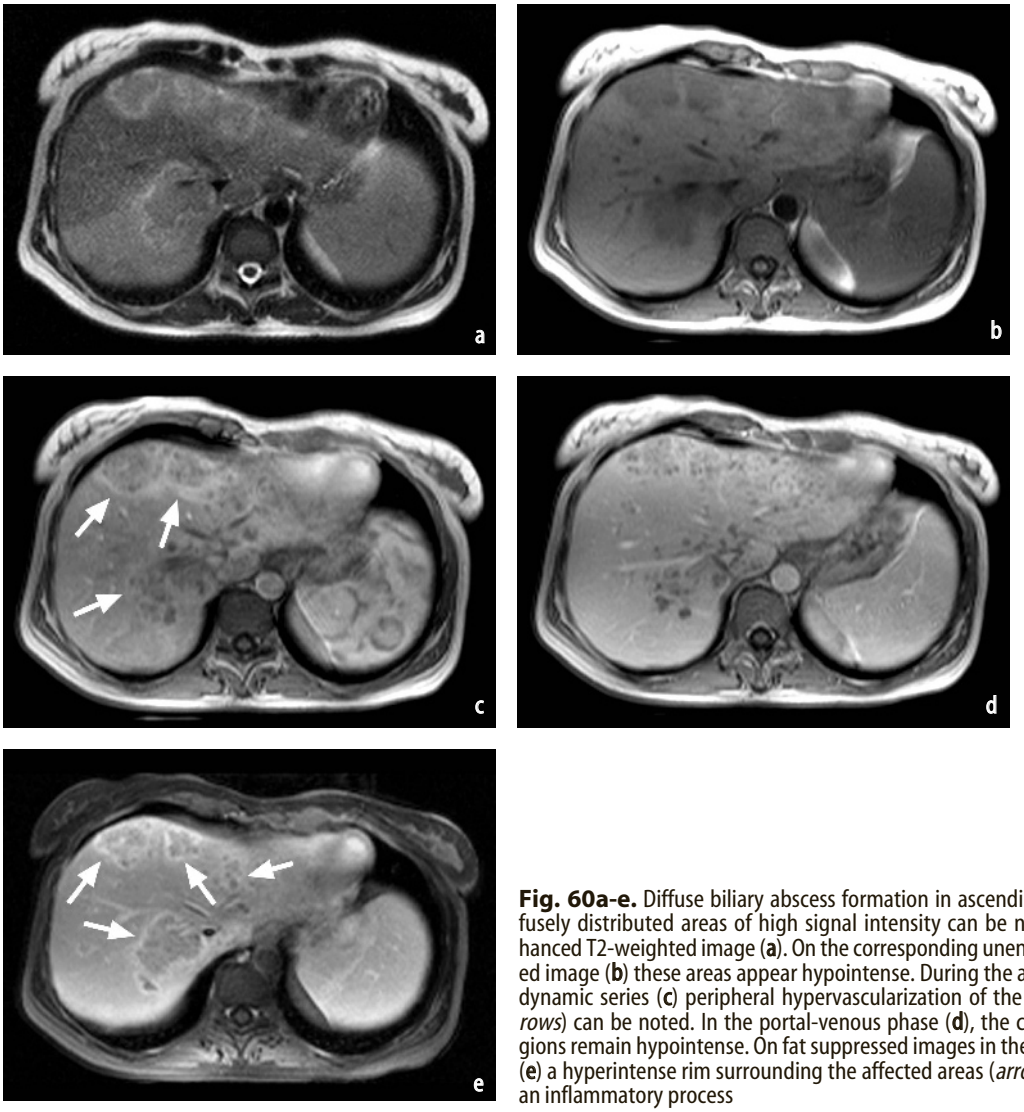

Fig. 60a-e. Diffuse biliary abscess formation in ascending cholangitis. Diffusely distributed areas of high signal intensity can be noted on the unenhanced T2-weighted image (**a**). On the corresponding unenhanced T1-weighted image (**b**) these areas appear hypointense. During the arterial phase of the dynamic series (**c**) peripheral hypervascularization of the affected areas (*arrows*) can be noted. In the portal-venous phase (**d**), the cystic-appearing regions remain hypointense. On fat suppressed images in the equilibrium phase (**e**) a hyperintense rim surrounding the affected areas (*arrows*) is indicative of an inflammatory process

- the direct extension route, from contiguous organ infections,
- the traumatic route, from blunt or penetrating injuries.

Before the era of antibiotics, pylephlebitis of the portal vein through seeding from appendicitis or diverticulitis was the most common cause of hepatic abscesses. Pyogenic abscesses today are most often associated with benign or malignant obstruction with cholangitis. About 50% of pyogenic abscesses are caused by anaerobic organisms or mixed anaerobic and aerobic organisms. *Escherichia Coli* is most frequently isolated in adults, while *Staphylococci* organisms are most often isolated from hepatic abscesses in children. Abscesses of biliary tract origin are multiple and frequently involve both hepatic lobes (Fig. 60). Abscesses of portal vein origin are often solitary and mainly localized in the right lobe.

The clinical symptoms of patients with hepatic abscesses include fever, malaise, abdominal pain in the right upper quadrant, nausea and vomiting. Tender hepatomegaly is the most common clinical sign and leukocytosis, elevated serum alkaline phosphatase levels and hypoalbuminemia are the most common laboratory abnormalities. Generally the onset of symptoms is acute [29].

Ultrasound can detect hepatic abscesses as small as 1.5 cm with a sensitivity of up to 90%. Pyogenic hepatic abscesses are extremely variable in shape and echogenicity and may appear as anechoic (50%), hyperechoic (25%) or hypoechoic (25%) (Fig. 61). Septa and fluid-fluid internal necrosis are frequently seen, while calcifications

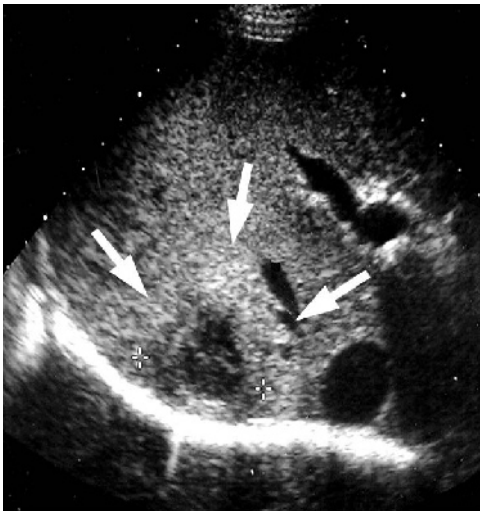

Fig. 61. Pyogenic abscess on US. Ultrasound reveals a heterogeneous hypo- to isoechoic lesion with ill-defined margins (*arrows*)

and gas may also be detected. Early lesions tend to be echogenic and poorly demarcated [72].

CT is a valid method for detecting hepatic abscesses with high sensitivity. On CT, hepatic abscesses appear as hypodense lesions with an internal pattern of varying density. The lesions generally appear as rounded masses that show minimal contrast enhancement. Most abscesses have a peripheral rim that shows contrast enhancement predominantly in the equilibrium phase. The "cluster" sign is suggestive for abscesses and represents smaller lesions surrounding a large abscess. Another CT sign, the "double target", is seen with early abscesses, and represents a hypodense lesion surrounded by a hyperdense rim, and an outer low-density region (Fig. 62). The presence of central gas, either air bubbles or an air-fluid level, is a specific sign of pyogenic hepatic abscess, but is present in fewer than 20% of cases [6, 87].

On MR imaging pyogenic abscess appears as an area of decreased signal intensity on T1-weighted images and increased signal intensity on T2-

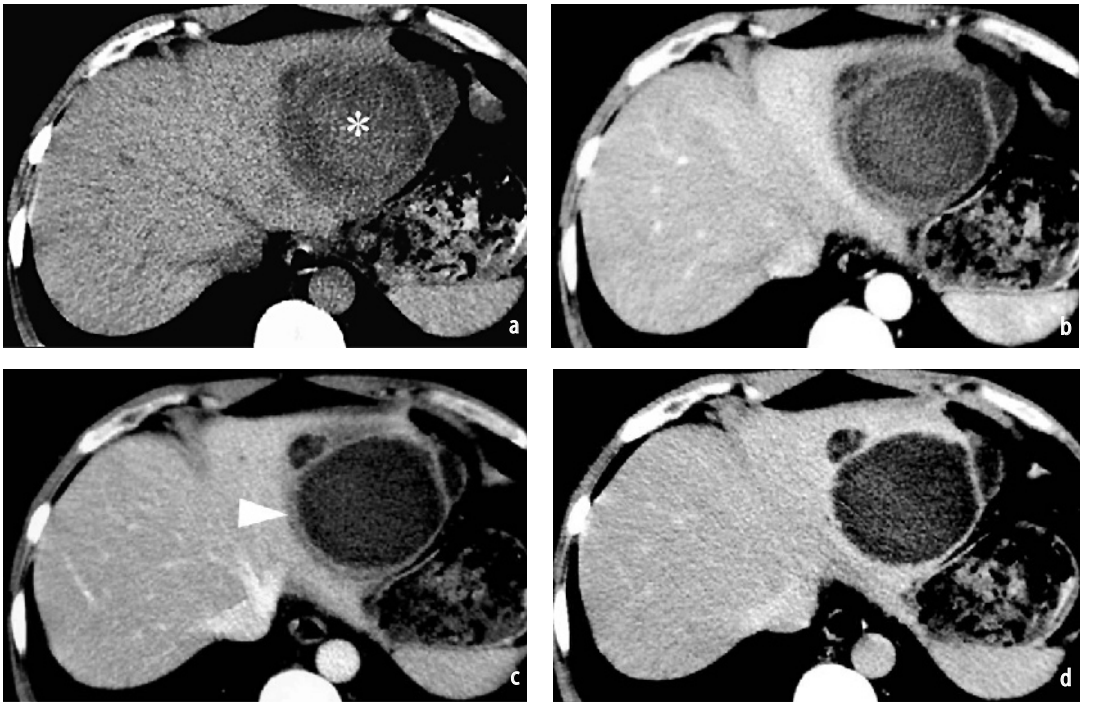

Fig. 62a-d. Pyogenic abscess on CT. On an unenhanced CT scan (**a**) the abscess (*asterisk*) appears as a heterogeneously iso- to hypodense lesion. Peripheral rim enhancement is seen on the arterial phase image after the administration of contrast medium (**b**). This is better seen in the portal-venous (**c**) and equilibrium phase (**d**) images due to peripheral edema (*arrowhead* in **c**)

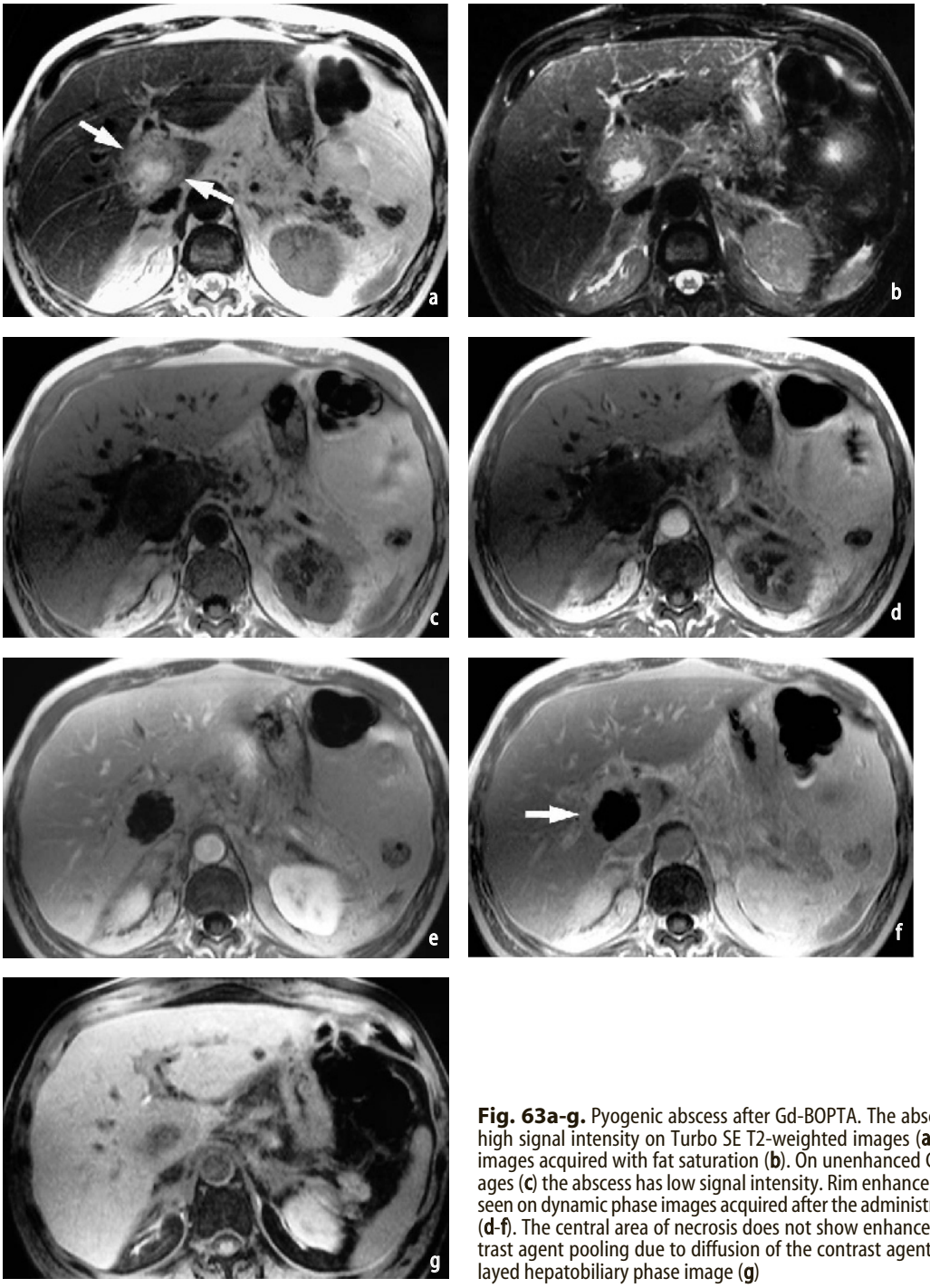

Fig. 63a-g. Pyogenic abscess after Gd-BOPTA. The abscess (*arrows*) has a high signal intensity on Turbo SE T2-weighted images (**a**) and T2-weighted images acquired with fat saturation (**b**). On unenhanced GE TI-weighted images (**c**) the abscess has low signal intensity. Rim enhancement (*arrow* in **f**) is seen on dynamic phase images acquired after the administration of Gd-BOPTA (**d**-**f**). The central area of necrosis does not show enhancement. Central contrast agent pooling due to diffusion of the contrast agent is seen on the delayed hepatobiliary phase image (**g**)

weighted images. Perilesional edema, characterized by high signal intensity on T2-weighted images, is seen in one third of cases. The abscess cavity may appear with homogeneous or heterogeneous signal intensity. After administration of contrast material, abscesses typically show rim enhancement followed by a slower increase in signal intensity within the center of the lesion (Fig. 63). Small lesions may enhance homogeneously in a manner similar to that seen with small hemangiomas [5].

Peripheral edema may be seen on delayed phase images as a rim of high signal intensity after administration of contrast agents with hepatobiliary properties. Similarly, decreased signal intensity after SPIO administration may be indicative of peripheral edema due to the high content of Kupffer cells and macrophages.

4.2.2 Amebic Abscess

Amebiasis caused by the parasite *Entamoeba histolytica* is an endemic disease of tropical areas, such as Mexico, Central and South America, Africa and Asia. Amebic liver abscess develops after infestation of colonic mucosa by the parasites, which lodge in the portal system. The liver can be invaded in one of three ways:

- via the portal vein (most common),
- through lymphatics,
- via direct extension through the colon wall into the peritoneum and then through the liver capsule.

Amebic liver abscess is the most common extraintestinal manifestation. Most patients with amebic liver abscesses present with a tender liver and abdominal pain in the right upper quadrant. Amebae are not usually found in the stool of patients with an amebic liver abscess. Because the clinical features and findings of stool examinations for amebae are usually not specific or are negative, serologic tests are helpful in detecting suspected amebic abscess; such tests are positive in about 90% of patients [61, 84].

On US studies, amebic abscesses are usually large, round, sharply-defined, hypoechoic masses with fine, low-level internal echoes at high gain settings (Fig. 64) [64].

The CT appearance of amebic abscess is nonspecific and variable; the lesion is usually round or oval and demonstrates peripheral hypodensity. A slightly hyperdense peripheral rim can be seen on unenhanced scans, which generally shows marked enhancement after administration of contrast material (Fig. 65). Lesions may appear as unilocular or multilocular masses, with internal debris and nodularity of the margins [106].

Amebic abscesses are well-defined structures with rim-like areas of varying signal intensity on both T1- and T2-weighted MR images. Within the abscess cavity, the signal intensity is decreased on T1-weighted images compared with the normal hepatic parenchyma. On T2-weighted images the lesion is hyperintense with a homogeneous or heterogeneous appearance and is often surrounded by areas of even higher signal intensity that correspond to edema within the normal liver tissue. No enhancement is seen in the central necrotic area after contrast agent administration, whereas heterogeneous enhancement can be observed at the periphery of the lesion, corresponding to inflammatory tissue. Persistent enhancement on late hepatobiliary phase images can be observed in this inflammatory tissue when contrast agents with hepatobiliary properties are used (Fig. 66). MR also offers the advantage of multiplanar capabilities to clearly depict the extension of the lesion. It is also helpful in follow-up studies to evaluate response to therapy.

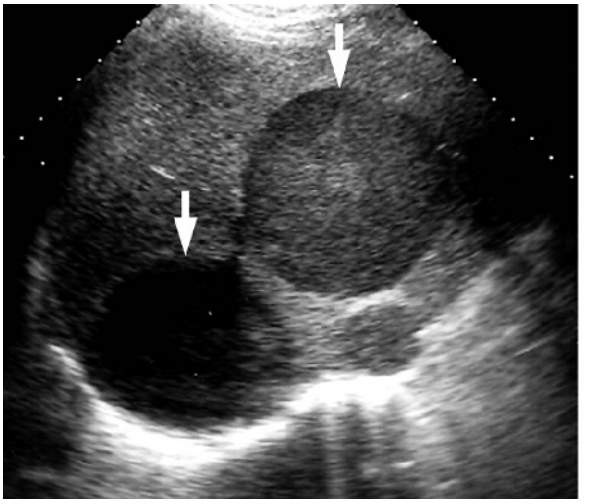

Fig. 64. Amebic abscess on US. The ultrasound scan reveals two large lesions (*arrows*) with different echogenicity

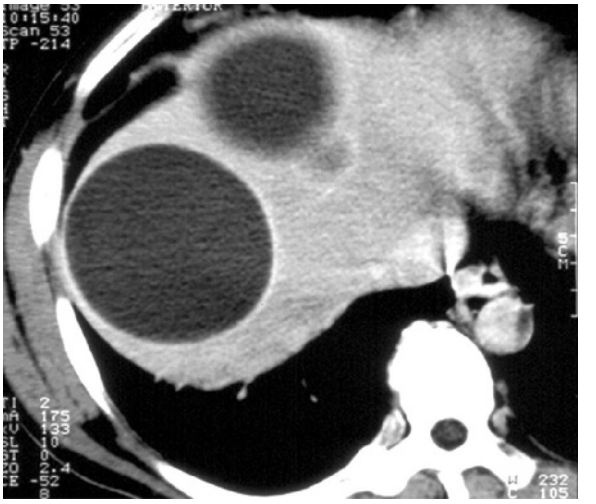

Fig. 65. Amebic abscess on CT. The CT scan reveals hypodense lesions with a thin hyperdense peripheral rim. The hypodense appearance is due to the high liquid content

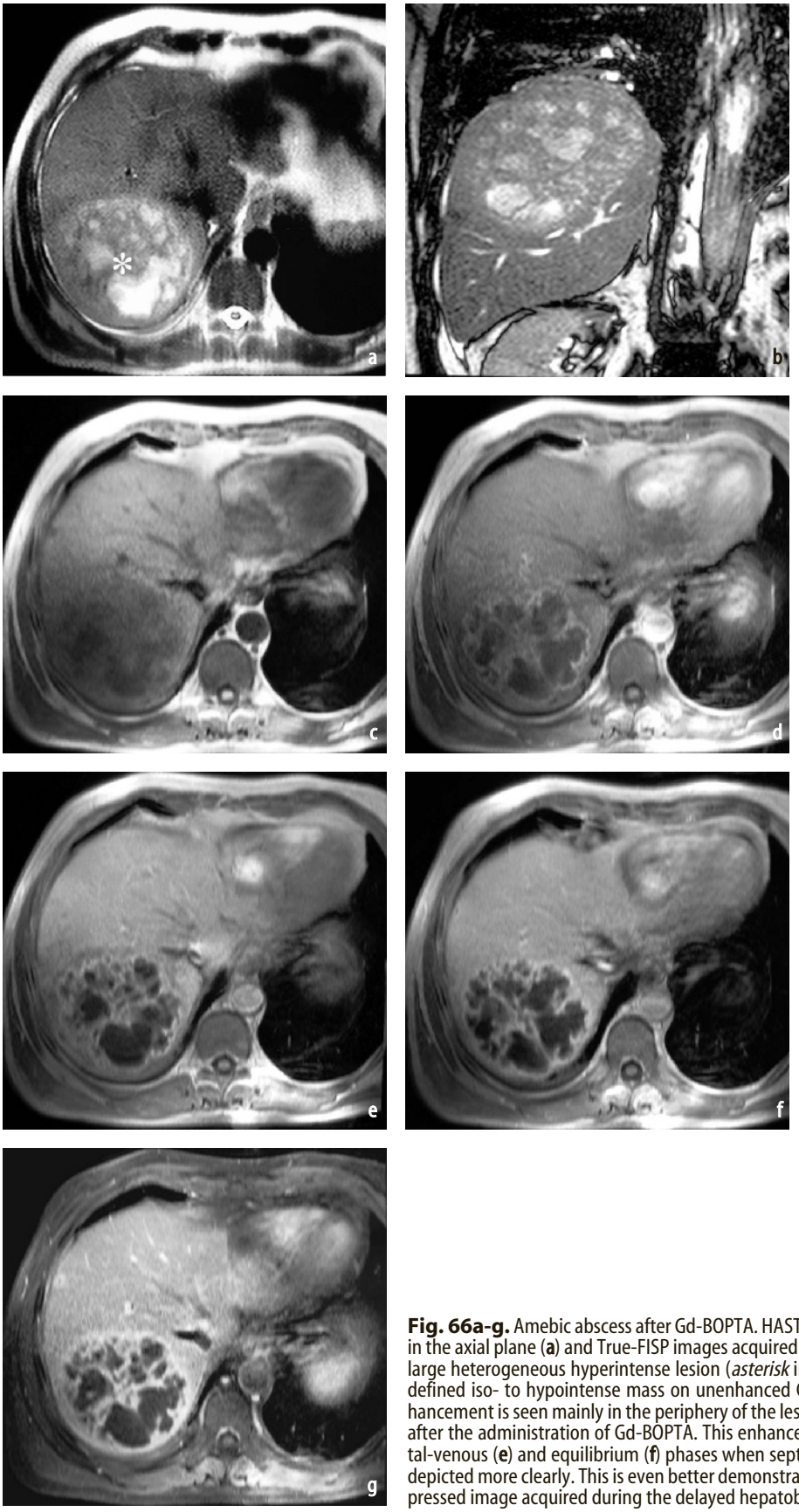

Fig. 66a-g. Amebic abscess after Gd-BOPTA. HASTE T2-weighted images acquired in the axial plane (**a**) and True-FISP images acquired in the coronal plane (**b**) reveal a large heterogeneous hyperintense lesion (*asterisk* in **a**). The lesion is seen as an ill-defined iso- to hypointense mass on unenhanced GE T1-weighted images (**c**). Enhancement is seen mainly in the periphery of the lesion during the arterial phase (**d**) after the administration of Gd-BOPTA. This enhancement increases during the portal-venous (**e**) and equilibrium (**f**) phases when septations and internal necrosis are depicted more clearly. This is even better demonstrated on the T1-weighted fat suppressed image acquired during the delayed hepatobiliary phase (**g**)

4.2.3 Candidiasis Infection

Hepatic candidiasis is relatively frequent in immunocompromised patients and it is found in more than 50% of patients with acute leukemia or lymphoma.

On US scans, three major patterns of candidiasis are seen:

- "wheel within a wheel", in which a peripheral zone surrounds an inner echogenic area,
- "Bull's eye", a lesion with a hyperechoic center surrounded by a hypoechoic rim,
- uniformly hypoechoic, the most common appearance, attributable to progressive fibrosis.

After therapy, the lesions may increase in echogenicity and decrease in size, although in some cases sonographic heterogeneity of the liver may persist for several years after treatment [33].

On CT the abscesses are generally multiple, small round hypodense areas on both pre- and post-contrast images. Calcifications can be seen within the lesions [97].

On MR imaging, candida lesions are generally hyperintense on fat suppressed T1-weighted images and have variable signal intensity on conventional T1-weighted spin-echo images. Contrast agent administration leads to the detection of more lesions, which are mainly round, ill-defined, focal hypointense areas. Frequently, percutaneous needle biopsy is needed to achieve a definitive diagnosis [93].

4.2.4 Echinococcal Cyst

Hydatid disease is caused by the parasite *Echinococcus granulosus*. The disease is mainly present in rural areas where dogs are used for herding live stock, especially sheep, and occurs frequently in Mediterranean countries, in Australia, and in South America.

Dogs are the normal host for the adult parasite, and hundreds of worms may exist in their intestinal tract. Sheep, cattle, herbivores and humans are intermediate hosts for the parasite and are infected after contact with dog feces. In heavily endemic areas, about 50% of dogs and up to 90% of sheep and cattle are infected with *E. granulosus*. Eggs are passed by the dogs and can be ingested by intermediate hosts.

Once inside the intermediate host, the parasitic eggs hatch and embryos penetrate the intestinal mucosa to enter lymphatic and venous channels. Most embryos are filtered by the liver and lungs with the remaining parasites reaching other organs, including the brain, spleen, kidneys, and the musculoskeletal system. Viable embryos transform into cysts which grow at a rate of approximately 1 cm per year. The wall of the hydatid cyst is composed of two layers: the endocyst, a germinal layer, and the ectocyst, a proteinaceous membrane. A dense fibrous capsule containing collagen, the pericyst, is formed by the host.

Echinococcal cysts usually develop in the liver (75% of cases) but may occur in any part of the body. The lesions are often asymptomatic for many years and are discovered incidentally on US or CT scans. Hydatidosis can also be detected by serologic tests. Classic symptoms of hepatic hydatid cyst include upper abdominal pain and hepatomegaly [2, 60].

Treatment consists of surgical removal of the cyst or antiparasitic drug therapy. If left untreated, a hepatic hydatid cyst may rupture into surrounding structures such as the liver parenchyma, biliary system, peritoneum, GI tract, or pleura. Hydatic cyst rupture is the major complication of echinococcal disease [2, 21, 87].

On abdominal plain film, curvilinear or ring-like calcifications can be seen in the right upper abdominal quadrant in about 20–30% of cases. However, calcifications do not necessarily indicate death of the parasite.

The appearance of the hydatic cyst on US is variable and depends on the stage of evolution and maturity. The lesion may appear as a well-defined anechoic cyst, as an anechoic cyst except for hydatid sand, as a multiseptate cyst with daughter cysts, as a cyst with a floating membrane, or finally, as a densely calcified mass (Fig. 67) [21, 42].

US has also been used to monitor the efficacy of medical antihydatid therapy: positive responses include cyst size reduction, membrane detachment, increased echogenicity and mural calcification.

On CT, hydatid disease appears as unilocular or multilocular well-defined cysts. Daughter cysts are seen as areas of lower density and are usually oriented towards the periphery of the lesion (Fig. 68). Daughter cysts can also float in the lumen of the mother cyst. Curvilinear ring-like calcification or grossly diffuse calcification are also common features. The peripheral walls may show enhancement after contrast medium administration (Fig. 69) [70, 87].

On MR imaging, the cystic component of echinococcal disease is similar to that of other cysts, with long T1 and T2 relaxation times. A low intensity rim around the cyst is present in most cases and is more conspicuous on T2- than T1-weighted sequences. This rim corresponds to the pericyst which is rich in collagen and has a short T2 relaxation time [2]. This rim and a multiloculated or multicystic appearance are distinctive features (Fig. 70). Floating membranes have low signal intensity on both T1- and T2-weighted images (Fig.

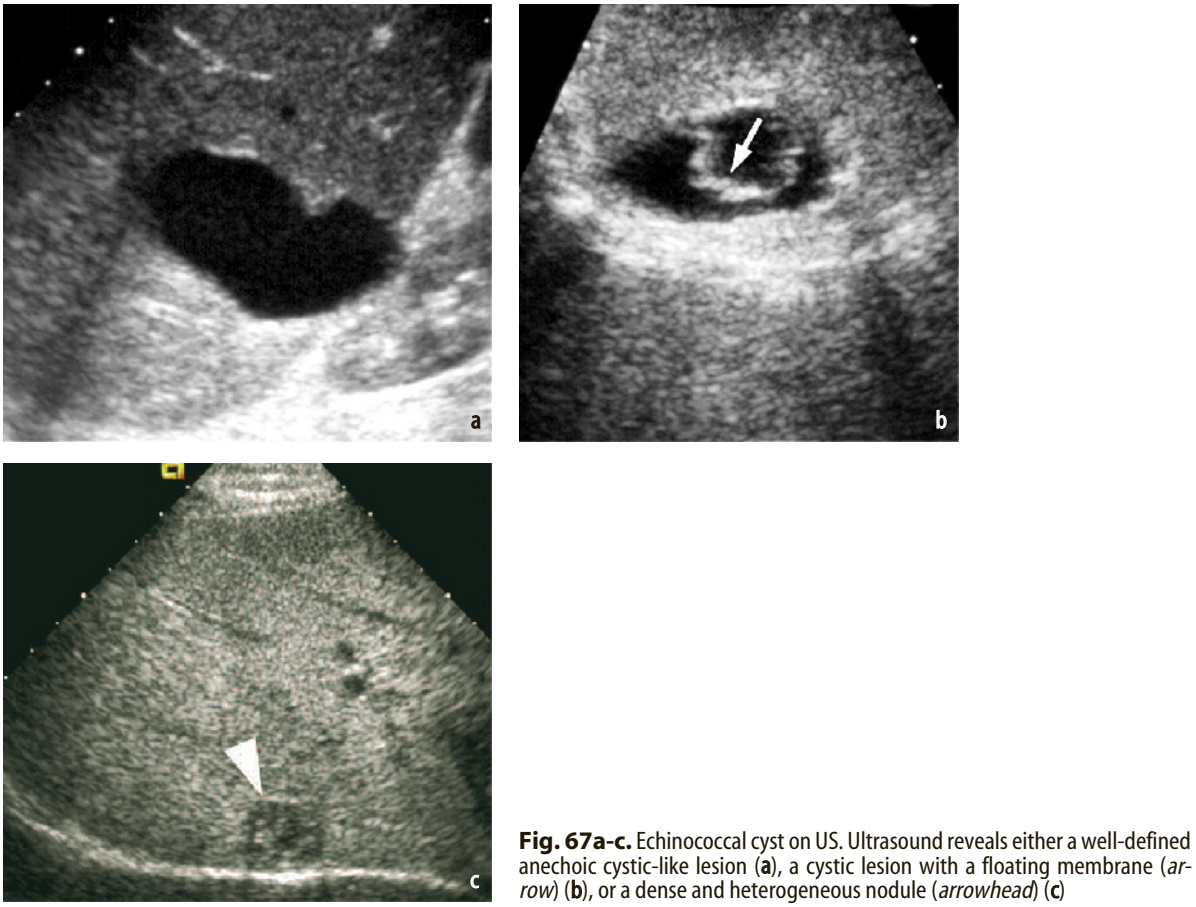

Fig. 67a-c. Echinococcal cyst on US. Ultrasound reveals either a well-defined anechoic cystic-like lesion (**a**), a cystic lesion with a floating membrane (*arrow*) (**b**), or a dense and heterogeneous nodule (*arrowhead*) (**c**)

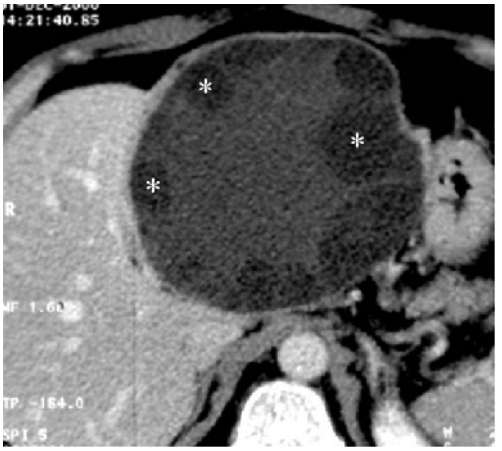

Fig. 68. Echinococcal cyst on CT. CT after contrast medium administration reveals a large well-delineated cystic lesion. Peripheral round areas of lower density (*asterisks*) are indicative of daughter cysts

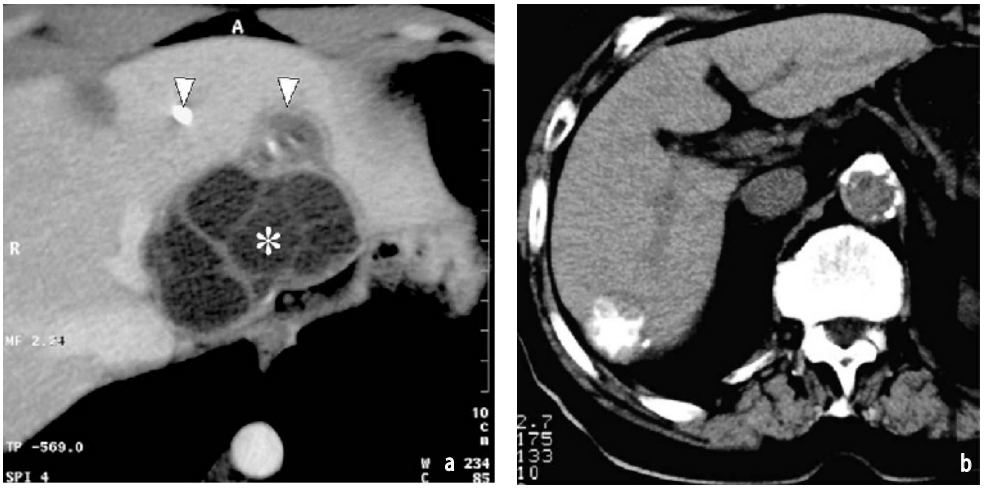

Fig. 69a, b. Echinococcal cyst on CT. CT after contrast medium administration (**a**) reveals a multilocular well-defined cystic lesion (*asterisk*) with thick hyperdense walls and septa. Additional nodules with a heterogeneous appearance and gross calcifications (*arrowheads*) can be seen around the bigger lesion. The almost complete replacement of the lesion by central calcification indicates the death of the cyst (**b**)

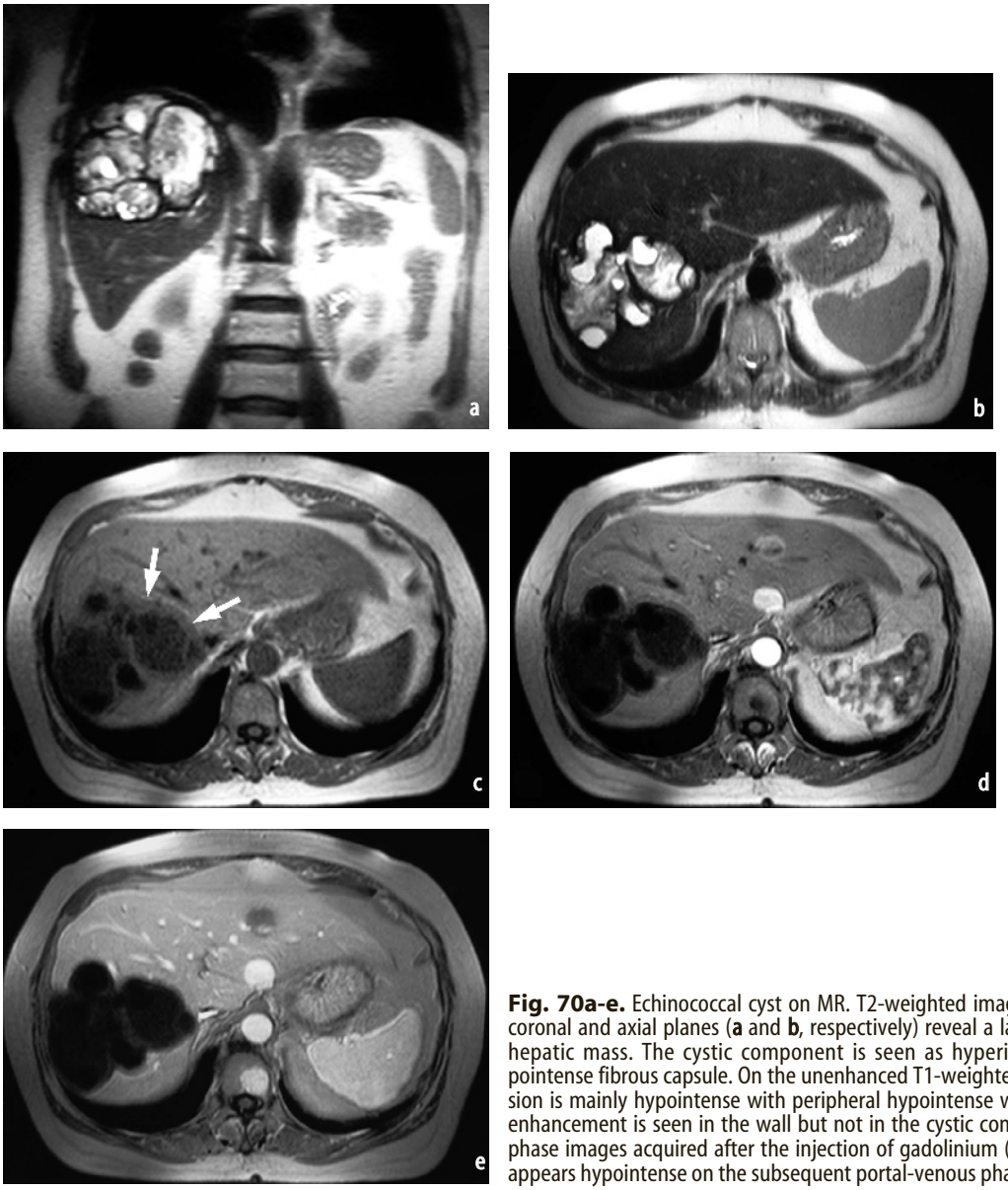

Fig. 70a-e. Echinococcal cyst on MR. T2-weighted images acquired in the coronal and axial planes (**a** and **b**, respectively) reveal a large multiloculated hepatic mass. The cystic component is seen as hyperintense with a hypointense fibrous capsule. On the unenhanced T1-weighted image (**c**), the lesion is mainly hypointense with peripheral hypointense wall (*arrows*). Slight enhancement is seen in the wall but not in the cystic component on arterial phase images acquired after the injection of gadolinium (**d**). The cystic mass appears hypointense on the subsequent portal-venous phase image (**e**)

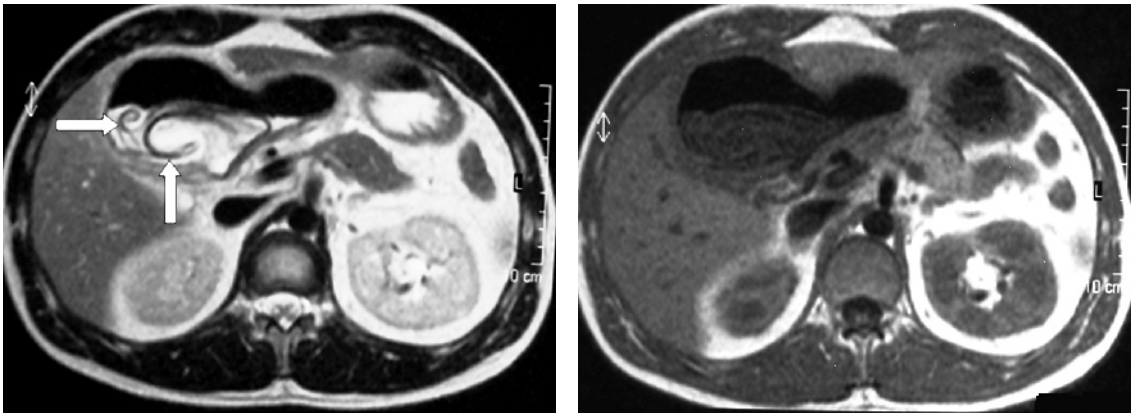

Fig. 71a, b. Complicated echinococcal cyst on MR. The T2- and T1-weighted images (**a** and **b**, respectively) reveal air within the upper portion of the echinococcal cyst and fluid level in the lower portion (duodenal fistula). A floating hypointense membrane can also be recognized (*arrows*)

71). Small cystic extensions from the main lesion are seen as peripheral areas of increased signal intensity on T2-weighted images and probably represent the active portions of the disease [52, 79].

References

1. Aibe H, Honda H, Kuroiwa T, et al. Sclerosed hemangioma of the liver. Abdom Imaging 2001;26:496-499
2. Allen DA. Focal infection processes. In: Ros PR, Bidgood WD (eds): Abdominal Magnetic Resonance Imaging. Mosby, 1993, 228-233
3. Arrive L, Flejou JF, Vilgrain V, et al. Hepatic adenoma: MR findings in 51 pathologically proved lesions. Radiology 1994;193:507-512
4. Ault GT, Wren SM, Ralls PW, et al. Selective management of hepatic adenomas. Am Surg 1996;62:825-829
5. Balci NC, Semelka RC, Noone TC, et al. Pyogenic hepatic abscess: MR findings on T1- and T2-weighted and serial Gadolinium-enhanced gradient-echo images. J Magn Reson Imaging 1999; 9:285-290
6. Barreda R, Ros PR. Diagnostic imaging of liver abscess. Crit Rev Diagn Imaging 1992;33:29-58
7. Basilico R, Blomley MJ, Harvey CJ, et al. Which continuous US scanning mode is optimal for the detection of vascularity in liver lesions when enhanced with a second generation contrast agent? Eur J Radiol 2002;41:184-191
8. Bianchi L. Glycogen storage disease I and hepatocellular tumors. Eur J Pediatr 1993;152 (Suppl 1):63-70
9. Bioulac-Sage P, Balabaud C, Wanless IR. Diagnosis of focal nodular hyperplasia. Not so easy. Am J Surg Pathol 2001;25:1322-1325
10. Blendis LM, Parkinson MC, Shilkin KB, et al. Nodular regenerative hyperplasia of the liver in Felty's syndrome. Q J Med 1974;43:25-32
11. Bluteau O, Jeannot E, Bioulac-Sage P, et al. Bi-allelic inactivation of TCF1 in hepatic adenomas. Nat Genet 2002;32:312-315
12. Bosniak MA, Ambos MA. Polycystic kidney disease. Semin Roentgenol 1975;10:133-143
13. Boulahdour H, Cherqui D, Charlotte F, et al. The hot spot hepatobiliary scan in focal nodular hyperplasia. J Nucl Med 1993;34:2105-2110
14. Brancatelli G, Federle MP, Grazioli L, et al. Benign regenerative nodules in Budd-Chiari syndrome and other vascular disorders of the liver: radiologic-pathologic and clinical correlation. Radiographics 2002;22:847-862
15. Brancatelli G, Federle MP, Grazioli L, et al. Focal nodular hyperplasia: CT findings with emphasis on multiphasic helical CT in 78 patients. Radiology 2001;219:61-68
16. Brancatelli G, Federle MP, Grazioli L, et al. Large regenerative nodules in Budd-Chiari syndrome and other vascular disorders of the liver: CT and MR imaging findings with clinicopathologic correlation. AJR Am J Roentgenol 2002; 178:877-883
17. Brancatelli G, Federle MP, Katyal S, et al. Hemodynamic characterization of focal nodular hyperplasia using three dimensional volume-rendered multidetector CT angiography. Am J Roentgenol 2002;179:81-85
18. Brancatelli G, Federle MP, Blachar A, Grazioli L, et al. Hemangioma in the Cirrhotic Liver: Diagnosis and Natural History. Radiology 2001;219:69-74
19. Buetow PC, Pantongrag-Brown L, Buck JL, et al. Focal nodular hyperplasia of the liver: radiologic-pathologic correlation. Radiographics 1996;16:369-388
20. Buffet C, Altman C. Nodular regenerative hyperplasia (in French). Gastroenterol Clin Biol 1994;18:123-132
21. Caremani M, Benci A, Maestrini R, et al. Abdominal cystic hydatid disease (CHD): classification of sonographic appearance and response to treatment. J Clin Ultrasound 1996;24:491-500

22. Chen YW, Jeng YM, Yeh SH, et al. P53 gene and Wnt signaling in benign neoplasms: beta-catenin mutation in hepatic adenoma but not in focal nodular hyperplasia. Hepatology 2002;36:927-935
23. Choi BI, Kim TK, Han JK, et al. Power versus conventional color Doppler sonography: comparision in the depiction of vasculature in liver tumors. Radiology 1996;200:55-58
24. Conter RL, Longmire WP Jr. Recurrent hepatic hemangiomas. Possible association with estrogen therapy. Ann Surg 1988;207:115-119
25. Dachman AH, Ros PR, Goodman ZD, et al: Nodular regenerative hyperplasia of the liver: clinical and radiologic observations. AJR Am J Roentgenol 1987;148:717-722
26. Flejou JF, Barge J, Menu Y, et al. Liver adenomatosis: an entity distinct from liver adenoma? Gastroenterology 1985;89:1132-1138
27. Friedman LS, Gang DL, Hedberg SE, et al. Simultaneous occurrence of hepatic adenoma and focal nodular hyperplasia: report of a case and review of the literature. Hepatology 1984;4:536-540
28. Fujihara T, Nagai Y, Kubo T, et al. Amebic liver abscess. J Gastroenterol 1996;31:659-663
29. Goldman IS, Farber BF, Brandborg LL. Bacterial and miscellaneous infections of the liver. In: Zakim D, Boyer TD (eds): Hepatology (3th ed). WB Sauders, Philadelphia, 1996, 1232-1242
30. Golli M, Van Nhieu JTV, Mathieu D, et al. Hepatocellular adenoma: color Doppler US and pathologic correlations. Radiology 1994;190:741-744
31. Goodman ZD, Ishak KG. Angiomyolipomas of the liver. Am J Surg Pathol 1984;8:745-750
32. Goodman ZD. Benign tumors of the liver. In: Okuda K, Ishak KG (eds): Neoplasms of the liver. Springer-Verlag, Tokyo, 1987, 105-125
33. Gorg C, Weide R, Schwerk WB, et al. Ultrasound evaluation of hepatic and splenic macroabscesses in the immunocompromized patient: sonographic patterns, differential diagnosis and follow-up. J Clin Ultrasound 1994;22:525-529
34. Grandin C, Van Beers BE, Robert A, et al. Benign hepatocellular tumors: MRI after superparamagnetic iron oxide administration. J Comput Assist Tomogr 1995;19:412-418
35. Grangier C, Tourniaire J, Mentha G, et al. Enhancement of liver hemangiomas on T1-weighted MR SE images by superparamagnetic iron oxide particles. JCAT 1994;18:888-896
36. Grazioli L, Alberti D, Olivetti L, et al. Congenital absence of portal vein with nodular regenerative hyperplasia of the liver. Eur Radiol 2000;10:820-825
37. Grazioli L, Federle MP, Ichikawa T, et al. Liver adenomatosis: clinical, histopathologic and imaging findings in 15 patients. Radiology 2000;216:395-402
38. Grazioli L, Morana G, Federle MP, et al. Focal nodular hyperplasia: morphologic and functional information from MR imaging with gadobenate dimeglumine. Radiology 2001;221:731-739
39. Grazioli L, Morana G, Kirchin MA, et al. MRI of focal nodular hyperplasia (FNH) with gadobenate dimeglumine (Gd-BOPTA) and SPIO (ferumoxides): an intra-individual comparison. Journal Magn Reson Imaging 2003;17:593-602
40. Grazioli L, Morana G, Kirchin MA,et al. Accurate differentiation of focal nodular hyperplasia from hepatic adenoma at gadobenate dimeglumine-enhanced MR imaging: prospective study. Radiology 2005;236:166-177
41. Groshar D, Ben-Haim S, Gips S, et al. Spectrum of scintigraphic appearance of liver hemangiomas. Clin Nucl Med 1992;17:294-299
42. Gurses N, Sungur R, Gurses N, et al. Ultrasound diagnosis of liver hydatid disease. Acta Radiol 1987;28:161-163
43. Halvorsen RA, Korobkin M, Foster WL, et al. The variable appearance of hepatic abscesses. AJR Am J Roentgenol 1984;142:941-946
44. Hammerstingl R, Vogl TJ, Schwarz W, et al. Contrast-enhanced MRI of focal liver lesions: differentiation and detection of primary and secondary liver lesions using Resovist-enhanced versus gadolinium-enhanced MRI in the same patient. Acta Radiol 1998;5(Suppl 1):75-79
45. Hawkins EP, Jordan GL, McGavran MH. Primary leiomyoma of the liver. Successful treatment by lobectomy and presentation of criteria for diagnosis. Am J Surg Pathol 1980;4:301-304
46. Heiken JP. Liver. In: Lee JKT, Sagal SS, Stanley RJ, et al (eds): Computed body tomography with MRI correlation (3rd ed). Lippincott-Raven, Philadelphia, 1998, 701-778
47. Hoffman A, Emre S, Verham R, et al. Hepatic angiomyolipoma: two case reports of caudate-based lesions and review of the literature. Liver Transplant Surg 1997;3:46-53
48. Hooper LD, Mergo PJ, Ros PR. Multiple hepatorenal angiomyolipomas: diagnosis with fat suppression, gadolinium-enhanced MRI. Abdom Imaging 1994;19:549-551
49. Ichikawa T, Federle MP, Grazioli L, et al. Hepatocellular adenoma: multiphasic CT and histopathologic findings in 25 patients. Radiology 2000;214:861-868
50. International Working Party. Terminology of nodular hepatocellular lesions. Hepatology 1995;22:983-993
51. Jacobs J, Birnbaum B. Computed tomography imaging of focal hepatic lesions. Semin Roentgenol 1995;30:308-323
52. Kalovidouris A, Gouliamos A, Vlachos L, et al. MRI of abdominal hydatid disease. Abdom Imaging 1994;19:489-494
53. Karhunen PJ. Benign hepatic tumours and tumour like conditions in men. J Clin Pathol 1986;39:183-188
54. Kawakatsu M, Vilgrain V, Belghiti J, et al, Association of multiple liver cell adenomas with spontaneous intrahepatic portohepatic shunt. Abdom Imaging 1994;19:438-440
55. Kew MC. Hepatic tumors and cysts. In: Feldman M, Scharschmidt BF, Sleisenger MH (eds): Sleisenger and Fordtran's Gastrointestinal and Liver disease (6th ed). WB Saunders, Philadelphia, 1998,1364-1387
56. Leen E, Angerson WJ, Yarmenitis S, et al. Multicenter clinical study evaluating the efficacy of SonoVue (BR 1), a new ultrasound contrast agent, in Doppler investigation of focal hepatic lesions. Eur J Radiol 2002;41:200-206

57. Leen E. The role of contrast enhanced ultrasound in the characterisation of focal liver lesions. Eur Radiol 2001;11(Suppl 3):27-34
58. Leese T, Farges O, Bismuth H. Liver cell adenomas: A 12 year-surgical experience from a specialist hepato-biliary unit. Ann Surg 1988;208:558-564
59. Leslie DF, Johnson CD, Johnson CM, et al. Distinction between cavernous hemangioma of the liver and hepatic metastases on CT: value of contrast enhancement patterns. AJR Am J Roentgenol 1995;164:625-629
60. Lewall DB. Hydatid disease. Biology, pathology, imaging and classification. Clin Radiol 1998;53:863-874
61. Lee KC, Yamazaki O, Hamda H, et al. Analysis of 69 patients with amebic liver abscess. J Gastroenterol 1996;31:40-45
62. Mathieu D, Vilgrain V, Mahfouz AE, et al. Benign liver tumors. Magn Reson Imaging Clin N Am 1997;5:255-288
63. McFarland EG, Mayo-Smith WW, Saini S, et al. Hepatic hemangiomas and malignant tumors: improved differentiation with heavily T2-weighted conventional spin-echo MR imaging. Radiology 1994;193:43-47
64. Missalek W. Ultrasonography in the diagnosis of amoebic liver abscess and its complications. Trop Doct 1992;22:59-63
65. Molina EG, Schiff ER. Benign solid lesions of the liver. In: Schiff's: Diseases of the liver. (8th ed), Vol. II. Lippincott-Raven 1999,1254-1257
66. Moreno-Merlo F, Wanless IR, Shimamatsu K et al. The role of granulomatous phlebitis and thrombosis in the pathogenesis of cirrhosis and portal hypertension in sarcoidosis. Hepatology 1997;26:554-560
67. Mortele KJ, Stubbe J, Praet M, et al. Intratumoral steatosis in focal nodular hyperplasia coinciding with diffuse hepatic steatosis: CT and MRI findings with histologic correlation. Abdom Imaging 2000;25:179-181
68. Mueller BU, Butler KM, Higham MC, et al. Smooth muscle tumors in children with human immunodeficiency virus infection. Pediatrics 1992;90:460-463
69. Murakami T, Nakamura H, Hori S, et al. Angiomyolipoma of the liver. Ultrasound, CT, MR imaging and angiography. Acta Radiol 1993;34:392-394
70. Murphy BJ, Casillas J, Ros PR, et al. The CT appearance of cystic masses of the liver. Radiographics 1989;9:307-322
71. Nakasaki H, Tanaka Y, Ohta M, et al. Congenital absence of the portal vein. Ann Surg 1989;210:190-193
72. Newlin N, Silver TM, Stuck KJ, et al. Ultrasonic features of pyogenic liver abscesses. Radiology 1981;139:155-159
73. Nguyen BN, Flejou JF, Terris B, et al. Focal nodular hyperplasia of the liver: a comprehensive pathologic study of 305 lesions and recognition of new histologic forms. Am J Surg Pathol 1999;23:1441-1454
74. Nishizaki T, Kanematsu T, Matsumata T, et al. Myelolipoma of the liver. Cancer 1989;63:930-934
75. Paley MR, Mergo PJ, Ros PR. Characterization of focal liver lesions with SPIO-enhanced T2WI: patterns of signal intensity and liver lesion contrast change. Radiology 1997;205:455-456
76. Patriarche C, Pelletier G, Attali P, et al. Ultrasonography, angiography, computed tomography and magnetic resonance in nodular regenerative hyperplasia of the liver: report of a pseudo-tumoral case. Radiat Med 1988;6:111-114
77. Paulson EK, McClellan JS, Washington K, et al. Hepatic adenoma: MR characteristics and correlation with pathologic findings. AJR Am J Roentgenol 1994;163:113-116
78. Pelletier G, Roche A, Boccaccio F, et al. Imaging of nodular regenerative hyperplasia of the liver. Study of 9 cases (in French). Gastroenterol Clin Biol 1988;12(10):687-690
79. Polat P, Kantarci M, Alper F, et al. Hydatic disease from head to toe. Radiographics 2003;23:475-494
80. Popescu I, Ciurea S, Brasoveanu V, et al. Liver hemangioma revisited: current surgical indications, technical aspects, results. Hepato-Gastroenterology 2001;48:770-776
81. Prayer LM, Schurawitzki HJ, Wimberger DM. Case report: lipoma of the liver— ultrasound, CT and MR imaging. Clin Radiol 1992;45:353-354
82. Ralls PW. Focal inflammatory diseases of the liver. Radiol Clin North Am 1998;36:377-389
83. Reddy KR, Schiff E. Approach to a liver mass. Semin Liver Dis 1993;13:423-435
84. Reed SL. Amebiasis: an update. Clin Infect Dis 1992;14:385-393
85. Reinertson TE, Fortune JB, Peters JC, et al. Primary leiomyoma of the liver: A case report and review of the literature. Dig Dis Sci 1992;37:622-627
86. Ribeiro A, Burgart LJ, Nagorney DM, et al. Management of liver adenomatosis: results with a conservative surgical approach. Liver Transpl Surg 1998;4:388-398
87. Ros PR, Helena M, Taylor HM, et al. Focal hepatic infections. In: Gore, Levine: Textbook of gastrointestinal radiology, 2nd edition. 1998:1569-1589
88. Ros PR. Computed tomography - pathologic correlation in hepatic tumors. In: Ferrucci JT, Mathieu DG (eds): Advances in hepatobiliary Radiology. CV Mosby, St. Louis, 1990,75-108
89. Rubin R, Lichtenstein G. Hepatic scintigraphy in the evaluation of solitary solid liver masses. J Nucl Med 1993;34:697-705
90. Saini S, Edelman RR, Sharma P, et al. Blood-pool MR contrast material for detection and characterization of focal hepatic lesions: initial clinical experience with ultrasmall superparamagnetic iron oxide (AMI-227). AJR Am J Roentgenol 1995;164:1147-1152
91. Sanfelippo PM, Beahrs OH, Weiland LH. Cystic diseases of the liver. Ann Surg 1974;179:922-925
92. Schima W, Saini S, Echeverri JA, et al. Focal liver lesions: characterization with conventional spin-echo versus fast spin-echo T2-weighted MR imaging. Radiology 1997;202:389-393
93. Semelka RC, Kelekis N, Sallah S, et al. Hepatosplenic fungal disease: diagnostic accuracy and spectrum of appearance of MR imaging. AJR Am J Roentgenol 1997;169:1311-1316
94. Semelka RC, Sofka CM. Hepatic hemangiomas. Magn Reson Imaging Clin N Am 1997;5:241-253
95. Shamsi K, De Schepper A, Degryse H, et al. Focular

nodular hyperplasia of the liver: radiologic findings. Abdom Imaging 1993;18:32-38
96. Sherlock S, Feldman CA, Moran B, et al. Partial nodular transformation of the liver with portal hypertension. Am J Med 1966;40:195-203
97. Shirkhoda A. CT findings in hepatosplenic and renal candidiasis. J Comput Assist Tomogr 1987;11:795-798
98. Soe KL, Soe M, Gluud S. Liver pathology associated with the use of anabolic-androgenic steroids. Liver 1992;12:73-79
99. Stromeyer FW, Ishak KG. Nodular transformation (nodular "regenerative" hyperplasia) of the liver. A clinicopathologic study of 30 cases. Hum Pathol 1981;12:60-71
100. Tanaka M, Wanless IR. Pathology of the liver in Budd-Chiari syndrome: portal vein thrombosis and the histogenesis of veno-centric cirrhosis, veno-portal cirrhosis, and large regenerative nodules. Hepatology 1998;27:488-496
101. Taylor K, Ramos I, Morse S, et al. Focal liver masses: differential diagnosis with pulsed Doppler US. Radiology 1987;164:643-647
102. Terayama N, Terada T, Hoso M, et al. Partial nodular transformation of the liver with portal vein thrombosis. A report of two autopsy cases. J Clin Gastroenterol 1995;20:71-76
103. Terkivatan T, De Wilt JH, De Man RA, et al. Management of hepatocellular adenoma during pregnancy. Liver 2000;20:186-187
104. Terris B, Flejou J, Picot R, et al. Hepatic angiomyolipoma. A report of four cases with immunohistochemical and DNA-flow cytometric studies. Arch Pathol Lab Med 1996;120:68-72
105. Trauner M, Stepan KM, Resch M, et al. Diagnostic problems in nodular regenerative hyperplasia (nodular transformation) of the liver. Review of the literature and report of two cases. Z Gastroenterol 1992;30:187-194
106. Verhaegen F, Poey C, Lebras Y, et al. X-ray computed tomographic tests in the diagnosis and treatment of amebic liver abscesses (in French). J Radiol 1996;77:23-28
107. Vilgrain V, Boulos L, Vullierme M, et al. Imaging of typical hemangioma of the liver with pathologic correlation. Radiographics 2000;20:379-397
108. Vogl TJ, Hammerstingl R, Schwarz W, et al. Superparamagnetic iron oxide—enhanced versus gadolinium-enhanced MR imaging for differential diagnosis of focal liver lesion. Radiology 1996;198:881-887
109. Wachsberg RH, Cho KC, Adekosan A. Two leiomyomas of the liver in an adult with AIDS: CT and MR appearance. J Comput Assist Tomogr 1994;18:156-157
110. Wanless I, Medline A. Role of estrogens as promoters of hepatic neoplasia. Lab Invest 1982;46:313-320
111. Wanless IR, Mawdsley C, Adams R, et al. On the pathogenesis of focal nodular hyperplasia of the liver. Hepatology 1985;5:1194-1200
112. Wanless IR, Albrecht S, Bilbao J et al. Multiple focal nodular hyperplasia of the liver associated with vascular malformations of various organs and neoplasia of the brain: a new syndrome. Mod Pathol 1989;2:456-462
113. Wanless IR, Liu JJ, Butany J. Role of thrombosis in the pathogenesis of congestive hepatic fibrosis (cardiac cirrhosis). Hepatology 1995;21:1232-1237
114. Wanless IR, Solt LC, Kortan P, et al. Nodular regenerative hyperplasia of the liver asociated with macroglobulinemia. Am J Med 1981;70:1203-1209
115. Wanless IR. Micronodular transformation (nodular regenerative hyplerplasia) of the liver: a report of 64 cases among 2500 autopsies and a new classification of benign hepatocellular nodules. Hepatology 1990;11:787-797
116. Wanless IR. Noncirrhotic portal hypertension: recent concepts. Prog Liver Dis 1996;14:265-278
117. Welch TJ, Sheedy PF 2nd, Johnson CM, et al. Radiographic characteristics of benign liver tumors: focal nodular hyperplasia and hepatic adenoma. Radiographics 1985;5:673-682
118. Yamashita Y, Ogata I, Urata J, et al. Cavernous hemangioma of the liver: pathologic correlation with dynamic CT findings. Radiology 1997;203:121-125

5

Hepatic Pseudolesions

CONTENTS

5.1 Pathophysiologic Background

The liver uniquely receives a dual blood supply; approximately 1000-1200 ml/min of blood arrives via the portal vein and approximately 400 ml/min arrives via the hepatic artery. In a non-cirrhotic liver, blood perfusion occurs at pressures of approximately 7 mmHg and 100 mmHg, via the portal vein and hepatic artery, respectively. Arterioportal parenchymal perfusion demonstrates the degree of reciprocity of the arterial and portal venous contributions by virtue of vascular flux through dynamic microcirculatory arterioportal shunts (APS), largely at the level of the portal triad by transplexal, transvasal, or even transtumoral routes [20, 24]. These shunts can transiently open under the influence of angiogenic modulators but are frequently related to a pathology that either compromises portal flow or increases arterial perfusion. APS can open to a further extent in response to significant portal blood flow reduction or stoppage, which in turn results in a compensatory increase of the arterial flow through the corresponding liver segments.

Connections between the intrahepatic vascular systems are not restricted to arterioportal communication but may also occur between the portal vein and the hepatic or systemic veins, as seen in conditions such as portal hypertension.

Transsinusoidal shunts are governed by an arteriolar inlet sphincter under the influence of angiogenic factors such as vascular endothelial growth factor (VEGF) and angioproteins. These shunts occur in Budd-Chiari syndrome, or may arise for no apparent reason or in response to focal infection or nodules of disease that compromise the portal perfusion of the subtended liver.

The peribiliary plexus or transplexal route is the most prominent venous system, and is composed of vessels that run around the lobular ducts. This system plays an important role when the portal vein is compromised.

Transvasal plexus often occurs in conjunction with peribiliary shunting and via the vasa vasorum of the portal vein. It most commonly occurs in the setting of portal vein occlusion or in cases of invasive hepatocellular carcinoma (HCC) [20].

Small areas of liver tissue may be supplied by another venous system, the “third inflow” which comprises aberrant veins that enter the liver directly, independently of the portal venous system. Such veins communicate with intrahepatic portal branches to various degrees and lead to focally decreased portal perfusion. However, little overall change in the hepatic arterial perfusion is seen. Because this hemodynamic state is persistent, focal metabolic changes are occasionally observed, typically as sparing in the fatty liver or as accumulations of fat [20].

5.1.1 Anatomic Variants of the Hepatic Circulation

Anatomic vascular variants of the hepatic circulation may involve the hepatic artery, the portal vein, and the hepatic veins, and may occur in the following manner:

A) The hepatic artery may have many collateral vessels including the pancreatic-duodenal arteries, the gastro-duodenal artery, and the phrenic inferior right artery. Collateral routes by aberrant hepatic arteries may originate from the superior mesenteric artery, the left gastric artery or by extrahepatic collateral arteries, such as the left gastroepiploic artery, the gastroduodenal artery, and the right gastric artery. Outside the celiac trunk, collateral flow may occur via the inferior phrenic artery [36].

B) The portal vein has variants and collateral vessels. Frequently, portal vein variants result in a "third inflow" in which aberrant veins that are not connected with the portal vein system enter the liver directly. These aberrant veins, which are not derived from the gut venous drainage, are poor in nutritional factors. The third inflow may involve the cystic vein, which drains the gallbladder bed, and the parabiliary venous system, which is within the hepatoduodenal ligament just anterior to the main trunk of the portal vein. The parabiliary venous system collects venous blood from the head of the pancreas, the distal part of the stomach, and the biliary system near the gallbladder [13, 32]. These veins usually join the main trunk of the portal venous system's major branches, but occasionally enter the liver directly around the porta hepatis, which sometimes results in isolated perfusion.
The epigastric-paraumbilical venous system is another variant of the portal vein and consists of small veins around the falciform ligament that drain the venous blood from the anterior part of the abdominal wall directly into the liver. These veins are roughly divided into three subgroups: the superior and inferior veins of Sappey that drain the upper and lower portions of the falciform ligament, respectively, and the vein of Burow [47]. When obstruction of the vena cava occurs, each of these veins may serve as collateral channels for blood flow into the liver.

C) There are numerous hepatic vein variants and accessories. Most hepatic vein variants drain directly into the inferior vena cava. These usually enter the vena cava on the right side both caudally and dorsally with respect to the level of the portal vein. The detection of these vessels is important in Budd-Chiari syndrome and also for surgical planning, since they represent the main drainage route from the right liver lobe [47].

5.1.2 Vascular Abnormalities

Due to the interrelationship between different vessels, when individual vessels become compromised, this immediately changes the blood flow in surrounding vessels (Fig. 1).

5.1.2.1 Portal Vein Compromise

A decrease in portal blood flow may occur in response to thrombosis, stenosis, or to compression of the main portal trunk or peripheral intrahepatic branches. On dynamic computer tomography (CT) or magnetic resonance (MR) studies of the liver, the decreased portal blood flow leads to areas of parenchymal enhancement during the arterial phase, referred to as transient hepatic attenuation difference (THAD). This area of enhancement, representing increased compensatory arterial flow, is no longer visible during the subsequent portal venous phase due to rapid equilibration of contrast density. Potential clinical problems associated with THAD are that focal liver lesions may be obscured if they are located within the areas of hyperattenuation, and that the THAD areas themselves may be mistaken for hypervascular lesions if they have a round or oval shape.

THAD are frequently seen around liver ab-

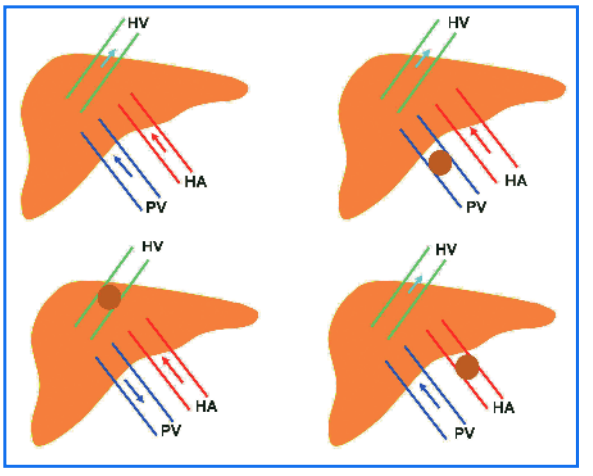

Fig. 1. Liver vessels. Schematic representation of the inter-relationship between different vessels in the liver, demonstrating changes in the blood flow when an individual vessel is compromised. (HA=Hepatic Artery, PV=Portal Vein, HV=Hepatic Veins)

scesses or acute cholecystitis and these may develop as a result of increased arterial perfusion deriving from local hyperemia related to the inflammatory process itself and/or because of locally reduced portal flow due to parenchymal compression by the lesion. In cirrhotic and non-cirrhotic patients, THAD are typically fan- or wedge-shaped and may be lobar, segmental, subsegmental, or subcapsular in location.

Another cause of reduced portal blood flow to the liver, especially at the periphery, is portal cavernoma [10].

5.1.2.2 Hepatic Artery Compromise

The hepatic arteries communicate with each other in the central portion of the liver and thus the blockage of these large arteries induces new routes of flow. However, acute obstruction of peripheral arterial flow does not induce recognizable changes in portal blood flow [43].

5.1.2.3 Hepatic Vein Compromise

When the hepatic vein is acutely obstructed, the portal vein becomes a draining rather than a supplying vein. The result is a compensatory increase in hepatic arterial flow as a result of functional portal flow elimination. Liver tumors may obstruct the hepatic vein, in which case prominent hepatic enhancement is induced at a site that corresponds to the area of obstructed hepatic venous drainage.

A reduction in the afferent blood flow via the hepatic vein is seen in Budd-Chiari syndrome. In the acute phase, the post-sinusoidal obstruction causes a severe reduction in the portal vein flow and a compensatory increase in the arterial flow delivered through the hepatic artery. Since blood flow is not able to perfuse the more peripheral liver areas properly, and because there is a pressure gradient between the arterial vessels and liver veins, functional intrahepatic APS develop, that may ultimately lead to complete flow reversal within the portal vein. In the latter phases of liver enhancement, the appearance of the parenchyma is characterized by stasis. This imaging finding is also seen in right side cardiac failure, and is ascribable to the same hemodynamic effects.

In the chronic phase of Budd-Chiari syndrome, an intrahepatic network of venous collateral vessels is prominent, which develops to bypass the obstruction. These abnormal vessels are more evident at the periphery, and are most prominent around the caudate lobe, due to its separate autonomous venous drainage [31].

5.2 Parenchymal Pseudolesions

Hepatic pseudolesions are non-neoplastic abnormalities which may be sub-divided into parenchymal pseudolesions and vascular pseudolesions. Parenchymal pseudolesions include focal fatty change, focal sparing, inflammatory pseudotumor, confluent fibrosis, pseudotumor hypertrophy and hepatic peliosis. Vascular pseudolesions, on the other hand, are non-neoplastic hepatic pseudolesions such as APS, THAD, and vascular abnormalities associated with Budd-Chiari syndrome.

Non-neoplastic abnormalities are clearly depicted with modern imaging techniques and arise principally due to blood flow abnormalities. These pseudolesions often occur focally and can be found in both cirrhotic and non-cirrhotic livers. The main clinical difficulty is to detect and discriminate these non-neoplastic lesions from benign and malignant hepatic neoplasms [32].

5.2.1 Focal Fatty Liver

Fatty liver infiltration is a common, metabolic complication of a variety of toxic, ischemic and infectious insults to the liver, such as obesity, diabetes mellitus, alcoholic liver disease, malnutrition, and chemotherapy. Other causes include hyperalimentation, inherited metabolic disturbance, inflammatory bowel disease, severe hepatitis, endogenous and exogenous steroid use, and pregnancy [1]. Generally, fat is deposited in response to different metabolic changes, such as increased hepatic synthesis of fatty acids (ethanol), decreased hepatic oxidation or utilization of fatty acids (carbon tetrachloride, tetracycline), impaired release of hepatic lipoproteins (steroids), or excessive mobilization of fatty acids from adipose tissue (alcohol, steroids). The prevalence of focal fatty infiltration of the liver increases significantly with advancing age; whereas it is uncommon in infants and young children, it is present in roughly 10% of the adult population [23].

There are both diffuse and focal forms of fatty liver infiltration. Approximately 30-40% of cases occur focally, either as solitary areas (10% of cases), or as multiple areas with a more widespread distribution (20-30% of cases). Most cases of fatty liver infiltration are of the diffuse type with a segmental, lobar, or irregular distribution. A common site of fatty liver infiltration is the ventro-medial portion of the medial segment adjacent to the falciform ligament [6]. Portal flow decrease leading to hepatic nutritional ischemia is a common finding at this site and it is this decrease in portal flow that induces the deposition of fat. Frequently, sys-

temic veins, such as the inferior vein of Saffey, supply this area in the absence of portal hypertension. Other common sites for the focal deposition of fat include subcapsular regions and the dorso-medial portion of the medial segment. When irregular fatty liver or multiple focal fat deposits are seen, they are typically distributed widely with no obvious relationship to vascular flow. In many cases fatty liver may be transient, appearing and disappearing comparatively rapidly. Moreover, it is often reversible with substance abstinence.

On ultrasound (US), a key indication for fatty liver infiltration is accentuation of the brightness of parenchymal echoes. While diffuse forms of fat infiltration typically have a homogeneous appearance, in some cases an extremely heterogeneous or pseudonodular appearance is noted, simulating diffuse nodularity. In the case of focal fatty infiltration, areas of fat deposition may be seen as solitary hyperechoic areas, multiple confluent hyperechoic areas, hyperechoic skip nodules, or irregular hyper- and hypoechoic areas (Fig. 2). Color Doppler examinations typically reveal no mass effect or vascular distortion (Fig. 3).

Some studies have examined the sensitivity and specificity of US for recognizing fat, as assessed on liver biopsy in patients suspected of having liver disease. Not surprisingly, the sensitivity of US imaging for the detection of fat increases with increasing degrees of steatosis. The mean sensitivity and specificity values vary from 60% to 90%, and from 80% to 95%, respectively. Unfortunately, US is not able to differentiate simple steatosis from non-alcoholic steatohepatitis, both of which may co-exist [17, 22].

On CT, the attenuation of the normal liver is generally 50-70 Hounsfield units (HU). Increased hepatic fat leads to a reduction of the mean hepatic attenuation. Whereas in mild cases the CT attenuation of the liver might approximate that of the spleen, in advanced cases the liver may appear particularly hypodense, albeit less dense than the portal and hepatic veins (Fig. 4). All forms of liver fat deposition (diffuse, lobar, irregular, and focal dis-

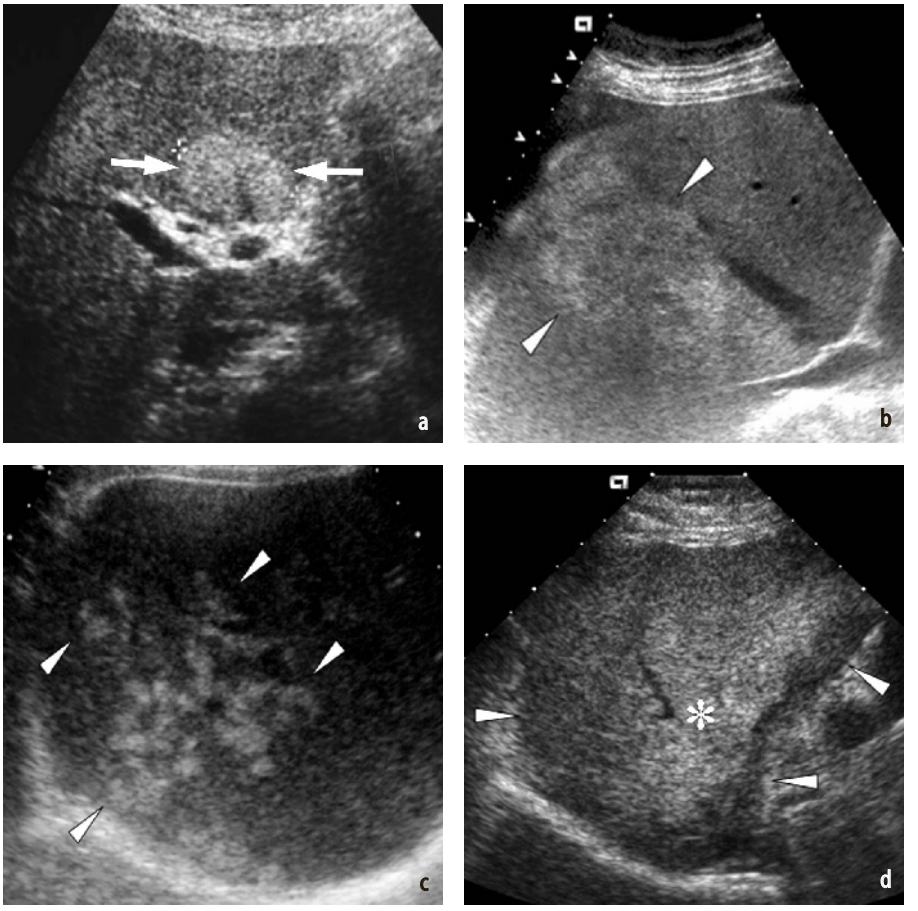

Fig. 2a-d. Focal fatty liver on US. On US examinations, focal fatty areas in the liver may appear with different patterns: (**a**) as hyperechoic nodules (arrows), (**b**) as multiple, confluent hyperechoic lesions (arrowheads), (**c**) as hyperechoic skip nodules (arrowheads), and finally (**d**) as irregular hyper- (asterisk) and hypoechoic areas (*arrowheads*)

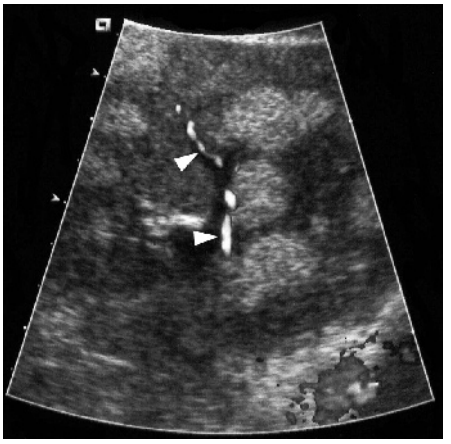

Fig. 3. Focal fatty liver on color Doppler US. On color Doppler evaluation, a vascular structure (*arrowheads*) courses, without distortion, between the hyperechoic nodules that represent focal fatty infiltration

tribution) are detectable on CT (Fig. 5). On unenhanced CT a diffuse distribution is seen as a general decrease of attenuation throughout the organ. Conversely, focal depositions of fat are identifiable as low-density, poorly demarcated, spherical or non-spherical areas that show no mass effect and which have a central core of inconspicuous hepatic tissue of normal density. However, multifocal fatty liver disease that simulates multiple lesions may also be seen (Fig. 6) [25].

On unenhanced T1- and T2-weighted MR imaging, fat deposition is typically characterized by slight hyperintensity relative to the normal liver parenchyma. Whereas conventional spin-echo sequences are relatively insensitive to fat deposition, the use of short tau inversion recovery (STIR) or other fat-suppression techniques may reveal the presence of fat deposition as areas of lower signal intensity. On the other hand, possibly the best imaging technique to detect and discriminate intracellular fat is chemical-shift imaging. On in-phase images, the signals from fat and water are additive, while on opposed-phase images the fat signal is subtracted from the water signal. Lesions or areas containing fat and water therefore show a loss of signal intensity on opposed-phase images when compared with in-phase images (Fig. 7).

On T1-weighted images acquired during the arterial phase of contrast enhancement after the bolus injection of a gadolinium contrast agent, focal fat depositions generally appear as isointense or slightly hypointense compared to the surrounding liver parenchyma, depending on the degree of steatosis (Fig. 8). Conversely, during the liver-specific hepatobiliary phase after Gd-BOPTA the typical appearance of focal fat depositions is slightly hypointense compared to the normal liver. This occurs because of "hepatocyte ballooning" which impedes the ability of the otherwise normal hepatocytes to take up Gd-BOPTA. This is particularly apparent on opposed-phase chemical shift imaging (Fig. 9).

With regards to diffuse fatty liver, this is typically seen during the liver-specific hepatobiliary phase after Gd-BOPTA administration, as a marked homogeneous increase in liver parenchyma signal intensity.

The appearance of focal fat areas on T2-weighted images after the administration of superparamagnetic iron oxide (SPIO) contrast agents is dependent on the Kupffer cell presence in the area of fatty change. Whereas some reports have suggested that fatty areas are not visible because of the overall marked decrease in signal intensity after SPIO accumulation [28], other studies have shown

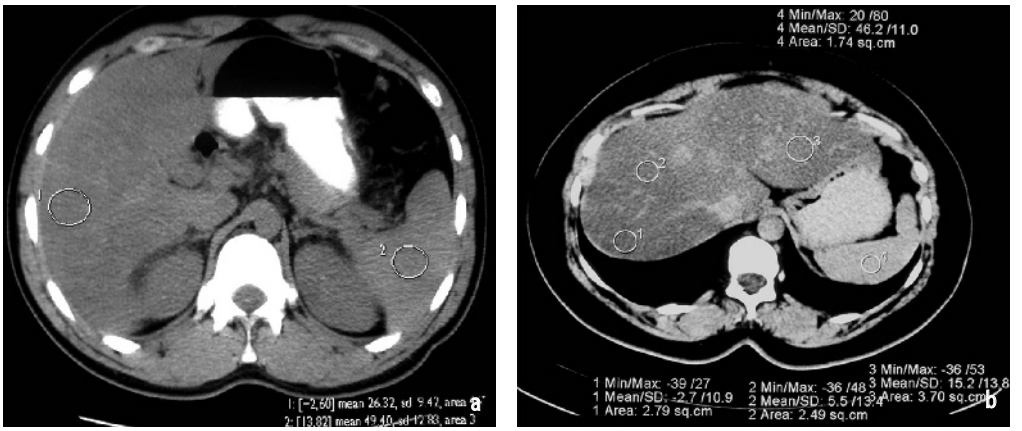

Fig. 4a, b. Focal fatty liver on CT. Pre-contrast CT scans show that in moderate forms of focal fatty liver (**a**) the ROI values of the liver are lower than those of the spleen. Conversely, in advanced focal fatty liver (**b**) the liver is markedly hypodense with ROI values near 0 HU. Note that in advanced focal fatty liver, vessels are seen as hyperdense compared with normal liver tissue

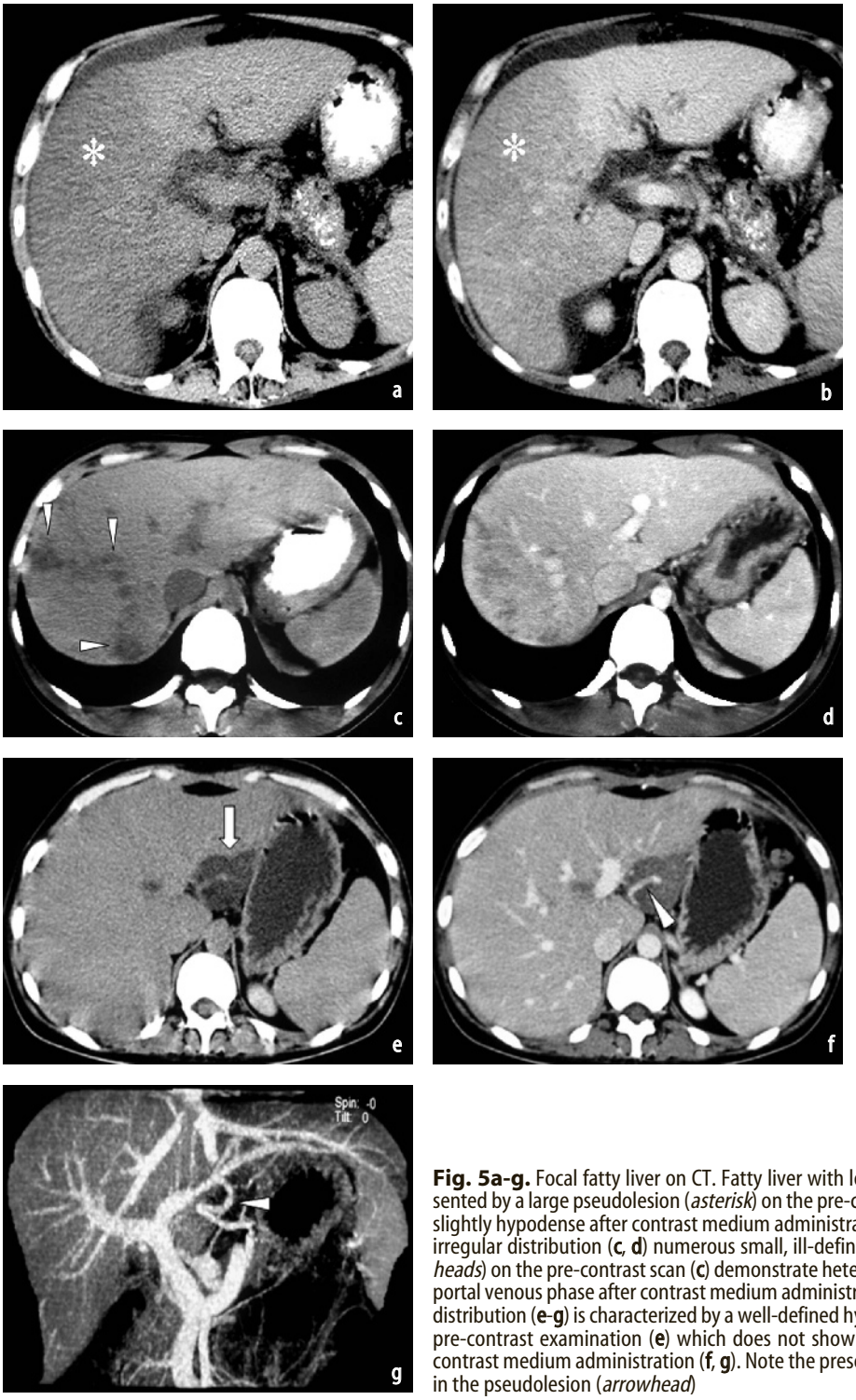

Fig. 5a-g. Focal fatty liver on CT. Fatty liver with lobar distribution (**a**, **b**) is represented by a large pseudolesion (*asterisk*) on the pre-contrast CT scan (**a**) that appears slightly hypodense after contrast medium administration (**b**). In focal fatty liver with irregular distribution (**c**, **d**) numerous small, ill-defined, hypodense nodules (*arrowheads*) on the pre-contrast scan (**c**) demonstrate heterogeneous enhancement in the portal venous phase after contrast medium administration (**d**). Fatty liver with a focal distribution (**e**-**g**) is characterized by a well-defined hypodense nodule (*arrow*) on the pre-contrast examination (**e**) which does not show significant enhancement after contrast medium administration (**f**, **g**). Note the presence of an aberrant vessel within the pseudolesion (*arrowhead*)

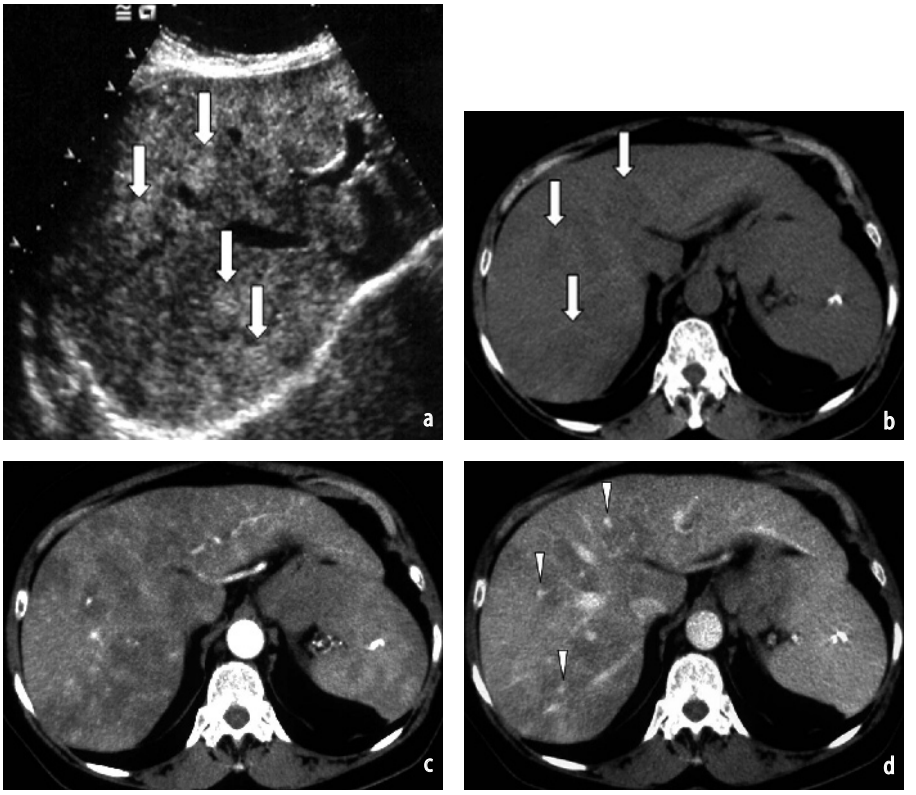

Fig. 6a-d. Multifocal fatty liver. On the US examination (**a**) multiple ill-defined, slightly hyperechoic nodules are detected (*arrows*). The corresponding pre-contrast CT scan (**b**) reveals numerous, ill-defined, slightly hypodense areas (*arrows*), which do not show significant enhancement during the arterial (**c**) and portal venous (**d**) phases after contrast medium injection. Note some vascular structures within the focal fatty areas (*arrowheads* in **d**)

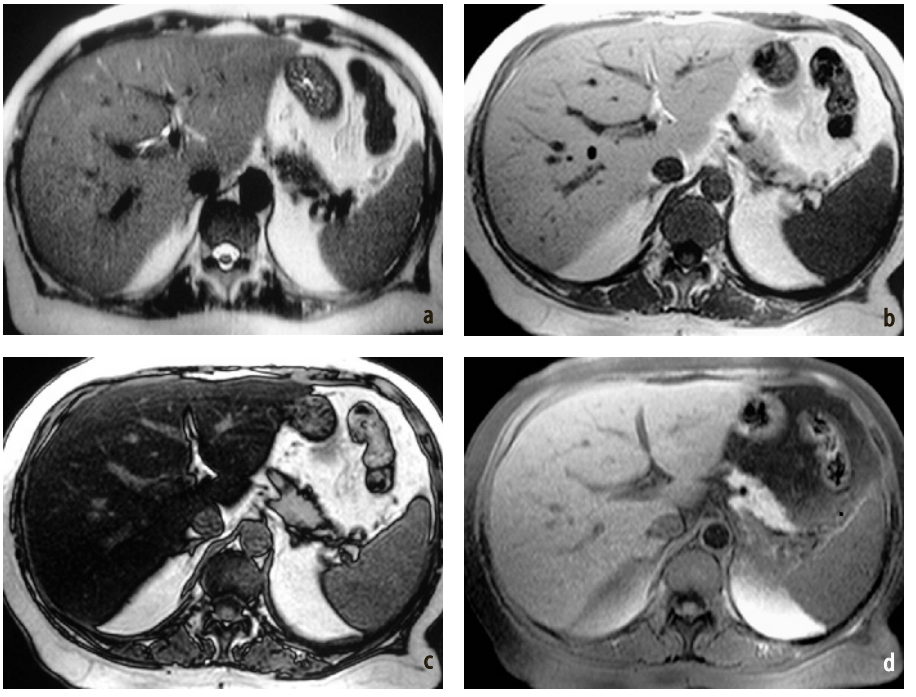

Fig. 7a-d. Diffuse fatty liver. On the pre-contrast HASTE T2-weighted image (**a**) and the GRE T1-weighted "in-phase" image (**b**) the signal intensity of the liver is homogeneously increased. Conversely, on the GRE T1-weighted "out-of-phase" image (**c**) the signal intensity is markedly and characteristically decreased. GRE T1-weighted fat suppressed sequences (**d**) are not sufficiently sensitive to small quantities of fat, and so the liver appears hyperintense as compared with the spleen

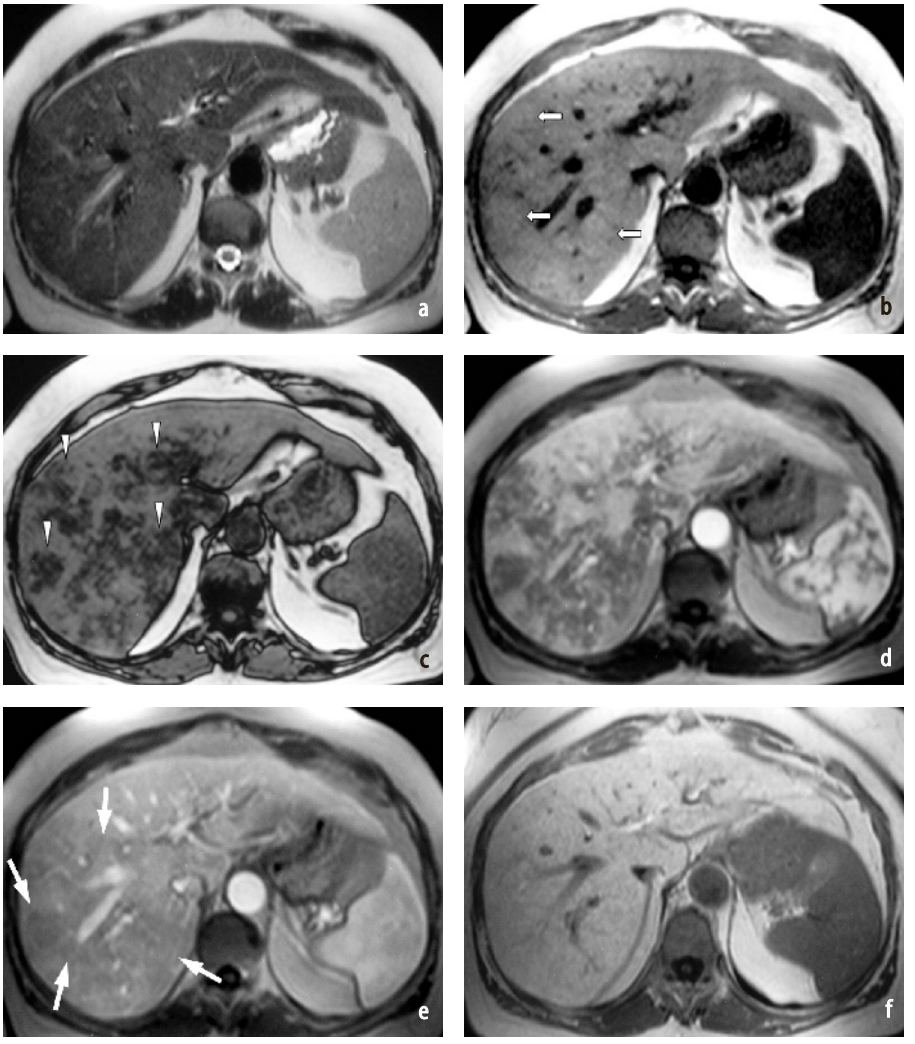

Fig. 8a-f. Focal fatty liver. On the pre-contrast T2-weighted image (**a**) the liver appears homogeneously, slightly hyperintense, whereas on the pre-contrast GRE T1-weighted "in-phase" image (**b**) it appears heteogeneous, and ill-defined slightly hyperintense areas (*arrows*) can be seen. The corresponding pre-contrast GRE T1-weighted "out-of-phase" image (**c**) shows diffuse hypointense areas (*arrowheads*) in both liver lobes indicating focal fatty infiltration. During the T1-weighted dynamic study after contrast agent administration, weak and heterogeneous intralesional enhancement can be detected in the arterial phase (**d**). Note that some vascular structures are clearly visible in the affected areas. In the portal venous phase (**e**), areas of focal fatty infiltration (*arrows*) appear as slightly hypointense compared to surrounding normal liver tissue. In the hepatobiliary phase after Gd-BOPTA administration (**f**) the liver is relatively homogeneous in appearance, although some of the areas of focal fatty infiltration show slightly decreased signal intensity. The signal intensity of these areas is relatively unchanged compared with the unenhanced images; however, these areas appear slightly hypointense because of the increased signal intensity of the surrounding normal liver tissue

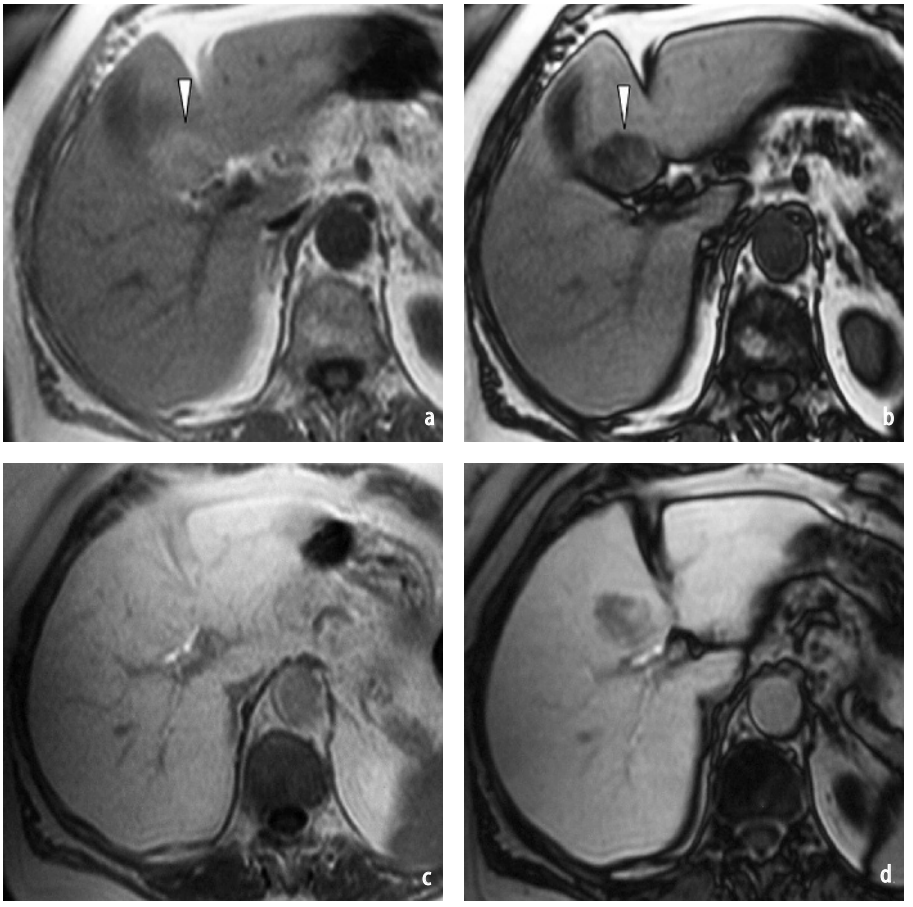

Fig. 9a-d. Focal fatty liver. An oval shaped, well-defined, slightly hyperintense area (*arrowheads*) in the posterior portion of segment IV can be detected on the pre-contrast GRE T1-weighted "in-phase" image (**a**). The lesion is heterogeneously hypointense on the pre-contrast GRE T1-weighted "out-of-phase" image (**b**). In the hepatobiliary phase after Gd-BOPTA administration (**c**, **d**) the area of focal fatty infiltration appears isointense on the T1-weighted "in-phase" image (**c**) and hypointense on the T1-weighted "out-of-phase" image (**d**). The decreased uptake of Gd-BOPTA is due to the altered metabolic function in the area of focal fatty infiltration

a decreased uptake of SPIO in non-diffuse areas of fat deposition [18].

While focal fat depositions may mimic the appearance of focal liver lesions, it is equally the case that focal fatty lesions such as lipoma and angiomyolipoma, but more frequently HCC or hepatic adenoma, may mimic focal fat. In order to distinguish focal fat depositions from lesions with fatty metamorphosis, the signal intensity on T2-weighted images, the prominent vascularity, the presence of intratumoral areas of hemorrhage or necrosis, specific imaging signs such as pseudocapsule, and the enhancement behavior after administration of liver-specific contrast agents should all be taken into account (Fig. 10).

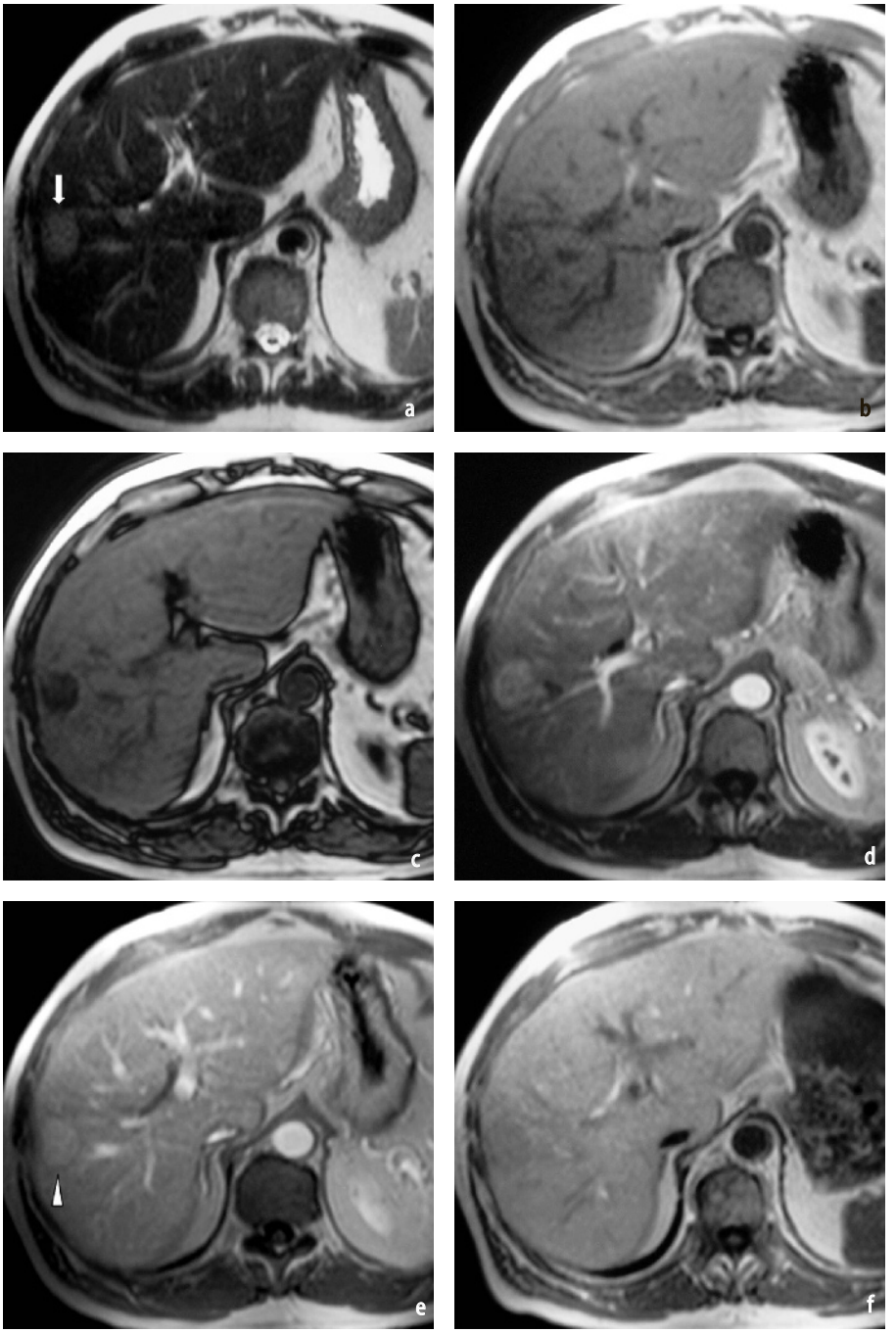

Fig. 10a-f. HCC with fatty metamorphosis. The pre-contrast Turbo SE T2-weighted image (**a**) and the corresponding GRE T1-weighted "in-phase" image (**b**) reveal a well-defined round nodule (*arrow*) which is slightly hyperintense and heterogeneously isointense compared to the normal liver parenchyma, respectively. The signal intensity is reduced on the GRE T1-weighted "out-of-phase" image (**c**) due to the fatty content of the lesion. On dynamic T1-weighted imaging after Gd-BOPTA administration (**d**, **e**) the lesion shows strong enhancement in the arterial phase (**d**) and a thin, hypointense pseudocapsule (arrowhead) in the portal venous phase (**e**). On the delayed hepatobiliary phase image (**f**) the nodule is slightly hypointense, suggesting that the lesion is malignant in nature. In this case, however, the neoplastic cells in the well-differentiated HCC still have some capability to take up Gd-BOPTA and to produce bile

5.2.2 Focal Spared Areas in Fatty Liver

Focal sparing of fatty infiltration most frequently occurs around the gallbladder and in the dorsomedial portion of the medial segment where supply to the hepatic parenchyma may derive from systemic veins such as the cystic vein of the gallbladder or an aberrant right gastric vein, rather than from the portal vein. Focal sparing can also occur adjacent to a tumor due to the presence of an arterioportal shunt or as a rim around an expansively growing tumor.

Unlike focal fat deposits, focal spared areas have a hypoechoic appearance on US. However, neither focal fat deposits, nor focal spared areas determine a mass effect with respect to vessels (Fig. 11).

On multiphasic CT, focal sparing has a hyperdense appearance that is variable with the amount of fatty liver infiltration. As in the case of focal fat infiltration, round areas of focal sparing may mimic hepatic tumors (Fig. 12).

On hepatobiliary phase T1-weighted MR images after the administration of Gd-BOPTA, focal sparing in fatty liver has an isointense or slightly hyperintense appearance (Fig. 13). A similar appearance is seen after the administration of other hepatobiliary agents such as Gd-EOB-DTPA or Mn-DPDP. Conversely, on T1- and T2-weighted images after SPIO administration, focal spared areas in fatty liver are seen as areas of relatively low signal intensity reflecting the relatively high uptake of SPIO in these areas compared with reduced uptake in fatty areas of the liver [18]. Whereas focal fatty infiltration and focal spared areas with a round, regular appearance may mimic hepatic tumors (Figs. 12, 13), irregular or diffuse areas of infiltration or sparing may obscure focal liver lesions (Fig. 14).

5.2.3 Inflammatory Pseudotumors

Hepatic inflammatory pseudotumor is an unusual and rare tumor-like condition that is increasingly recognized as an important differential diagnosis in patients presenting with liver masses. Synonyms used to define this lesion include xanthogranuloma, fibrous xantoma, plasmacellular granuloma, histiocytoma, pseudolymphoma, and plasmocytoma, all of which reflect the histologic components of the lesion. Most commonly, the condition occurs in children and in young men. Although the etiology is unknown, some authors have suggested obliterans phlebitis starting from the portal vein as a possible cause, with secondary biliary stasis and degeneration and necrosis of the biliary ducts, leading to periductal abscess or xanthogranuloma [27].

Macroscopically, the inflammatory pseudolesion is usually yellow-grey in color and solitary, although multifocal inflammatory pseudotumor of the liver has been described. The most frequent microscopic components are plasmacellular cells, although variable amounts of histiocytes, macrophages, fibromyoblasts, and fibrous tissue are also observed. Three histologic subtypes have been identified on the basis of the prevalence of single components, thus xanthogranulomatous type lesions have a histiocytic prevalence, plasmacellular type lesions contain mainly plasma cells, and sclerotic type lesions have a predominantly fibrotic component [46].

Typically, symptoms and laboratory findings indicate an acute inflammatory process, and recurrent pyogenic cholangitis is the most frequent clinical manifestation. Large lesions may cause a sensation of right upper abdominal quadrant fullness or discomfort, with malaise, fever and weight loss. Liver function tests sometimes demonstrate the elevation of alkaline phosphatase and γ-glutamyltransferase.

Features are non-specific on US, with lesions presenting as heterogeneously hypoechoic or mosaic patterns, similar to those observed in other focal liver neoplasms such as HCC [19]. Similarly, the appearance of an inflammatory pseudolesion is non-specific on unenhanced CT, with lesions invariably appearing hypodense. After contrast medium administration, an early intense and peripheral enhancement is usually followed by homogeneous, complete and persistent enhancement (Fig. 15). After a few minutes, peripheral enhancement and a hypodense core can be observed, the former comprising fibroblastic cells, and the latter chronic inflammatory cells [19].

On unenhanced T1-weighted MR images, inflammatory pseudotumor is typically hypointense, particularly in the central portion. Conversely, on T2-weighted images the lesion frequently demonstrates isointensity or slight hyperintensity (Fig. 16). However, the appearance is variable in relation to the histologic components: for example, slight hypointensity may be observed on T2-weighted images in lesions with a strong fibrotic predominance while a stronger hyperintense appearance is indicative of a greater predominance of inflammatory cells.

Early peripheral enhancement is typically seen on T1-weighted dynamic imaging after bolus injection of contrast agent, reflecting the cellular components and inflammatory changes within the lesion. Hepatobiliary phase imaging after administration of Gd-BOPTA or another hepatospecific contrast agent, frequently reveals a hypointense area representing the absence of hepatocytes within the lesion (Fig. 17) [19, 37].

A drop in signal on T2-weighted images after SPIO administration may reveal residual Kupffer cell function in liver parenchyma in and sur-

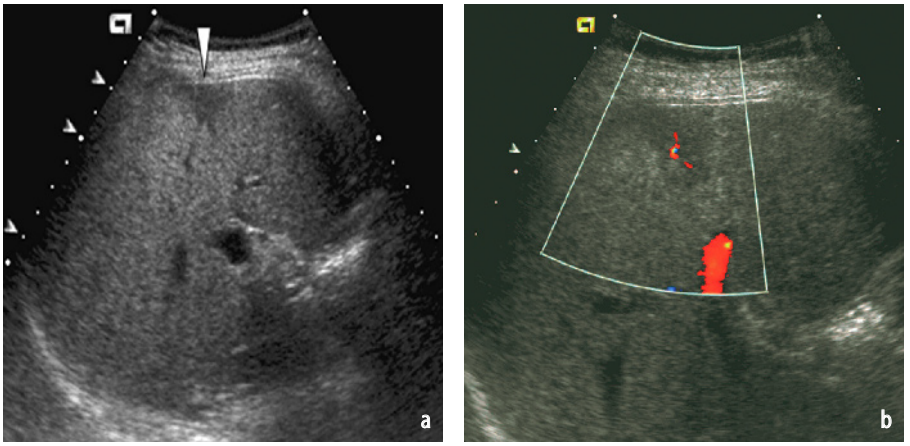

Fig. 11a, b. Focal sparing on US. B-mode US (**a**) reveals a hypoechoic area (*arrowhead*) with a triangular shape near the surface of the liver. On color Doppler US (**b**) an intralesional vessel is clearly visible. Note the absence of any mass effect. This is typical of focal sparing in fatty liver

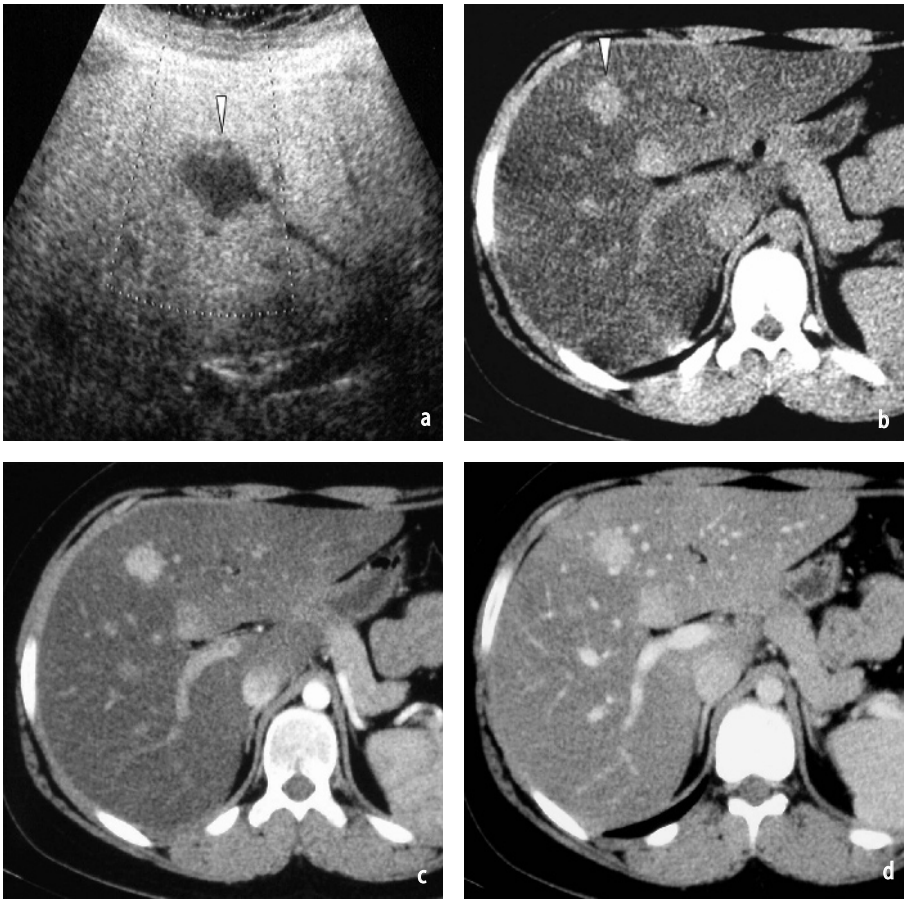

Fig. 12a-d. Focal sparing. Patient with Burkitt lymphoma after chemotherapy. On the US examination (**a**) the liver is extremely bright due to hepatic steatosis, and a round, hypoechoic nodule (*arrowhead*) is visible in segment IV of the liver. On the CT study (**b**-**d**) the lesion (*arrowhead*) does not show significant enhancement. This is indicative of focal sparing in fatty liver

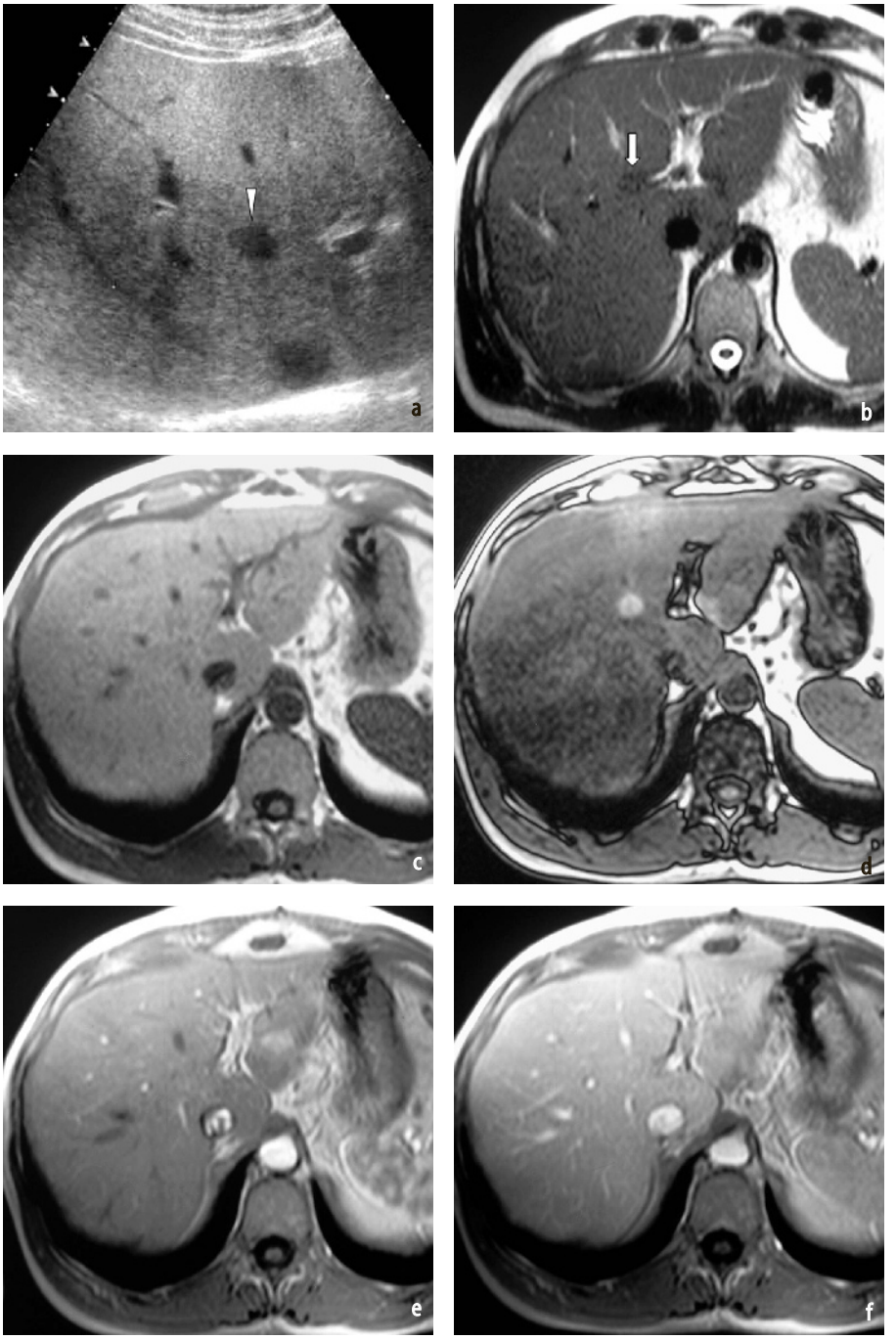

Fig. 13a-f. Focal sparing. Patient with history of breast cancer and chemotherapy. US evaluation (**a**) reveals an oval shaped, hypoechoic area (*arrowhead*) within a diffuse fatty liver. This is considered suspicious for metastasis. On the MR examination, this focal area (*arrow*) appears slightly hypointense on the pre-contrast TSE T2-weighted image (**b**), isointense on the GRE T1-weighted "in-phase" image (**c**), and hyperintense on the GRE T1-weighted "out-of-phase" image (**d**). On the dynamic images after Gd-BOPTA administration (**e**, **f**) the lesion does not reveal increased perfusion or wash-out. This is more indicative of an area of focal sparing in a fatty liver than of a metastasis

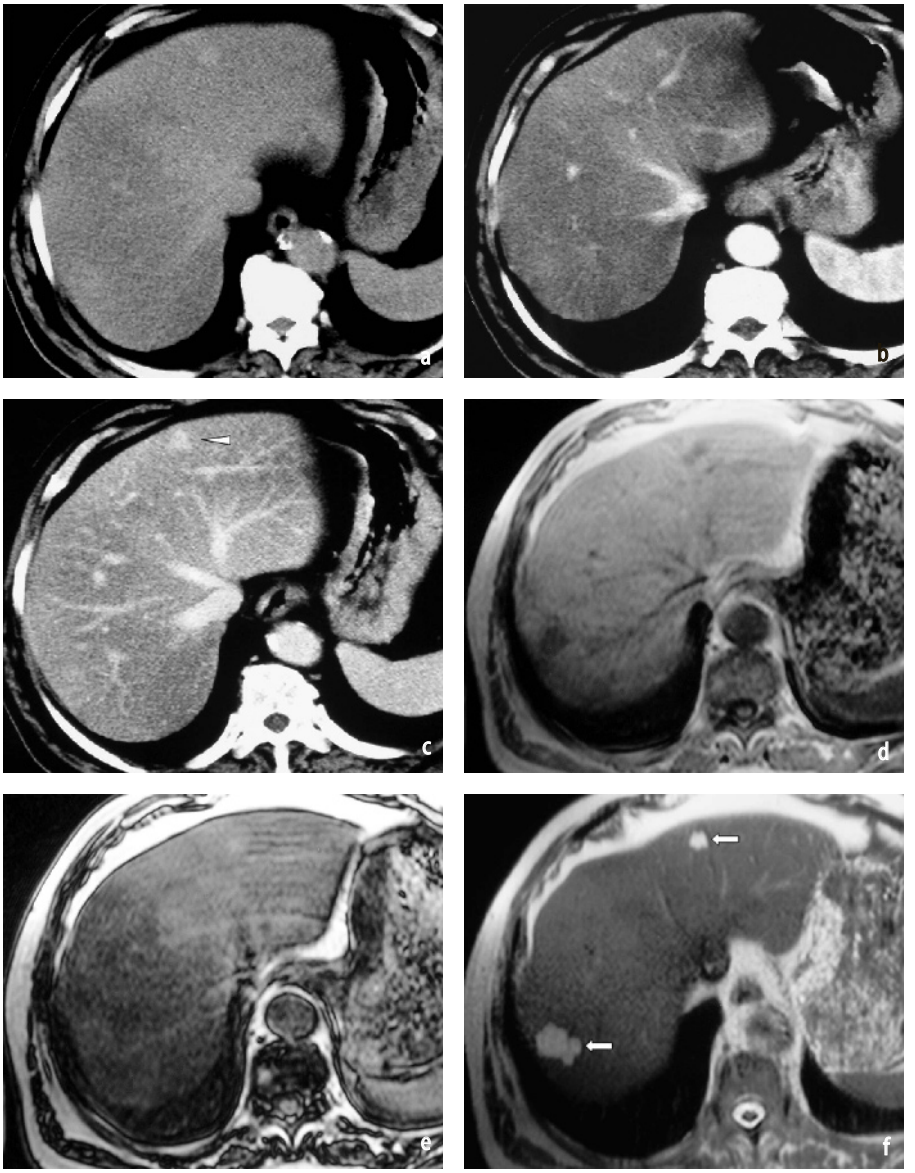

Fig. 14a-f. Focal fatty liver. Patient with history of renal cell carcinoma and chemotherapy. On the CT examination (**a**-**c**), and on the pre-contrast GRE T1-weighted "in-phase" and GRE T1-weighted "out-of-phase" images (**d**, **e**), the heterogeneous, diffuse fatty infiltration does not permit the confident definition of any lesion and in particular a small and ill-defined area (*arrowhead*) in liver segment II. On the corresponding HASTE T2-weighted image (**f**) two markedly hyperintense lesions (*arrows*) can be seen, and the signal intensity is suggestive of hemangioma

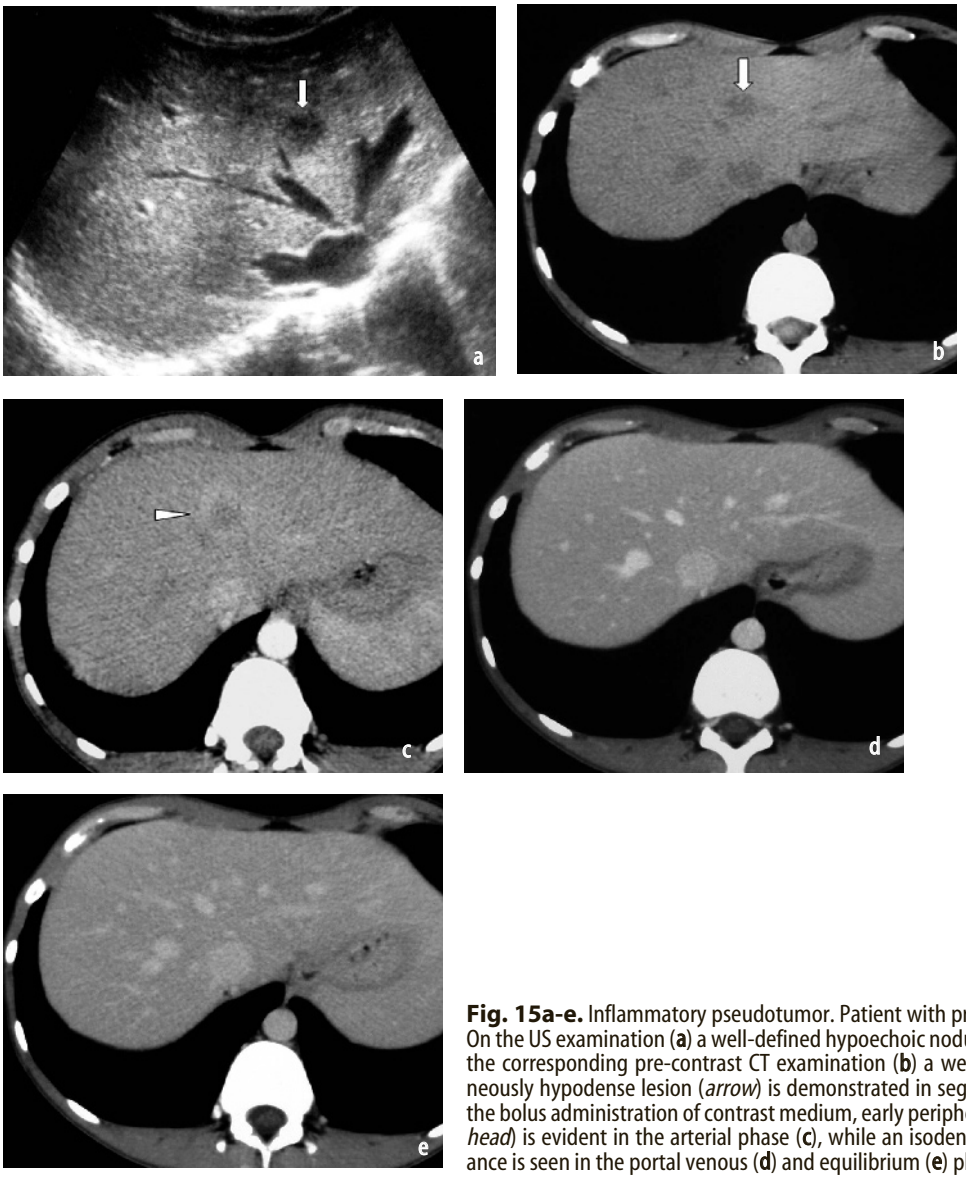

Fig. 15a-e. Inflammatory pseudotumor. Patient with primary immunodeficiency. On the US examination (**a**) a well-defined hypoechoic nodule (*arrow*) is detected. On the corresponding pre-contrast CT examination (**b**) a well-defined, oval, homogeneously hypodense lesion (*arrow*) is demonstrated in segment IV of the liver. After the bolus administration of contrast medium, early peripheral enhancement (*arrowhead*) is evident in the arterial phase (**c**), while an isodense homogeneous appearance is seen in the portal venous (**d**) and equilibrium (**e**) phases

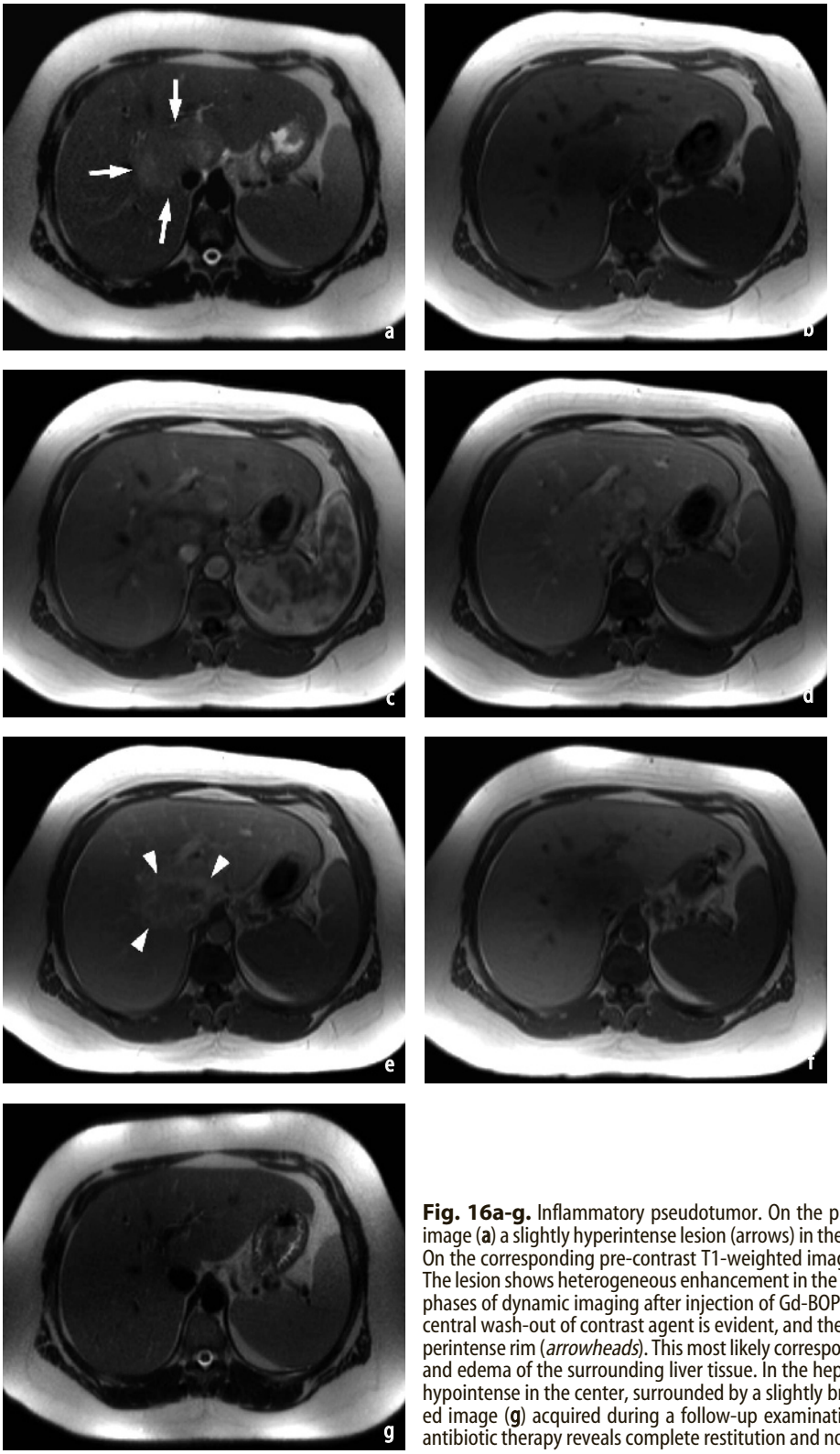

Fig. 16a-g. Inflammatory pseudotumor. On the pre-contrast HASTE T2-weighted image (**a**) a slightly hyperintense lesion (arrows) in the area of the liver hilum is visible. On the corresponding pre-contrast T1-weighted image (**b**) the lesion is hypointense. The lesion shows heterogeneous enhancement in the arterial (**c**) and portal venous (**d**) phases of dynamic imaging after injection of Gd-BOPTA. In the equilibrium phase (**e**) central wash-out of contrast agent is evident, and the lesion now demonstrates a hyperintense rim (*arrowheads*). This most likely corresponds to an inflammatory reaction and edema of the surrounding liver tissue. In the hepatobiliary phase (**f**) the lesion is hypointense in the center, surrounded by a slightly brighter rim. A HASTE T2-weighted image (**g**) acquired during a follow-up examination performed six months after antibiotic therapy reveals complete restitution and no residual tumor

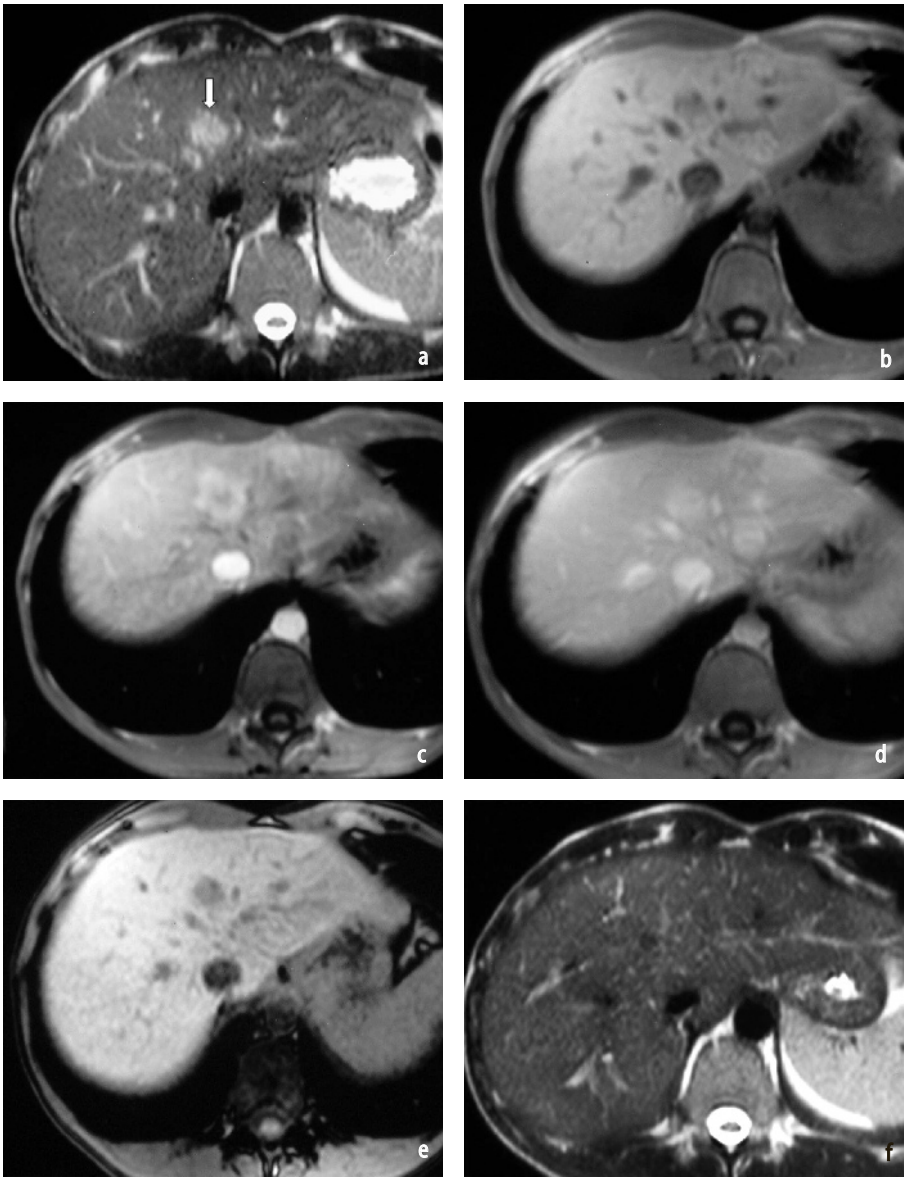

Fig. 17a-f. Inflammatory pseudotumor. Same case as demonstrated in Fig.15. On the pre-contrast T2-weighted sequence (**a**) and on the GRE T1-weighted image (**b**) the lesion (*arrow*) appears hyperintense and heterogeneously hypointense respectively, compared to the surrounding normal liver parenchyma. Enhancement is seen in the periphery of the lesion during the arterial phase (**c**) after Gd-BOPTA administration. During the portal venous phase (**d**), the lesion appears slightly hyperintense, particularly in the central portion. During the hepatobiliary phase (**e**) the nodule appears hypointense, due to the absence of hepatocytes. Follow-up MR imaging after six months (**f**) does not reveal any focal lesions

rounding the inflammatory pseudotumor. However, some authors have described lesions that show no SPIO particle uptake [37].

As it is difficult to diagnose inflammatory pseudotumor of the liver on MR imaging alone, supplemental lesion biopsy should also be performed [26].

5.2.4 Peliosis Hepatis

Peliosis hepatis is a rare entity characterized by blood-filled cystic cavities in the liver. Peliosis hepatis frequently develops in association with malignancies and chronic wasting diseases, such as tuberculosis. However, it has also been described in association with renal transplantation, hematological disorders and infection with human immunodeficiency virus (HIV), as well as in patients on long-term treatment with anabolic steroids, oral contraceptives, hormones, estrogen or Azathioprine. Regression is generally observed after such agents have been stopped or after appropriate antibiotic therapy [44, 45].

Macroscopically, peliosis is characterized by cystic dilated sinusoids filled with red blood cells and bound by cords of liver cells. Two varieties have been described: the phlebectatic type, in which the blood-filled spaces are lined with endothelium and are based on aneurysmal dilatation of the central veins, and the parenchymal type, in which the blood spaces are not lined with endothelium and are usually associated with hemorrhagic parenchymal necrosis. Peliosis can be differentiated from hemangioma by the presence of portal tracts within the fibrous stroma of the blood-filled spaces. Numerous theories have been proposed for the cause of peliosis hepatis, including outflow obstruction and hepatocellular necrosis leading to cystic blood-filled formations. Peliosis hepatis is usually found incidentally at autopsy but, rarely, it can cause hepatic failure or liver rupture with hemoperitoneum or shock. Patients sometimes have non-specific signs such as hepatomegaly and portal hypertension [44].

US findings are not specific for the diagnosis of peliosis hepatis; the hepatic echopattern is usually non-homogeneous with both hyperechoic and hypoechoic areas [30].

On CT images after the bolus administration of iodinated contrast material, these lesions usually appear initially hypodense, and become isodense over time [42].

On unenhanced T2-weighted MR images, peliosis hepatis frequently demonstrates high signal intensity similar to that seen in hemangioma. Conversely, low signal intensity is usually seen on unenhanced T1-weighted images. After gadolinium administration, the lesions may show homogeneous or heterogeneous hypervascularization depending on flow, and may appear iso- or hyperintense on portal venous and equilibrium phase images after Gd-BOPTA administration.

In the hepatobiliary phase after the administration of Gd-BOPTA, Mn-DPDP or Gd-EOB-DTPA, the lesion again appears hypointense because of the absence of hepatocytes within the cystic dilated sinusoids (Fig. 18).

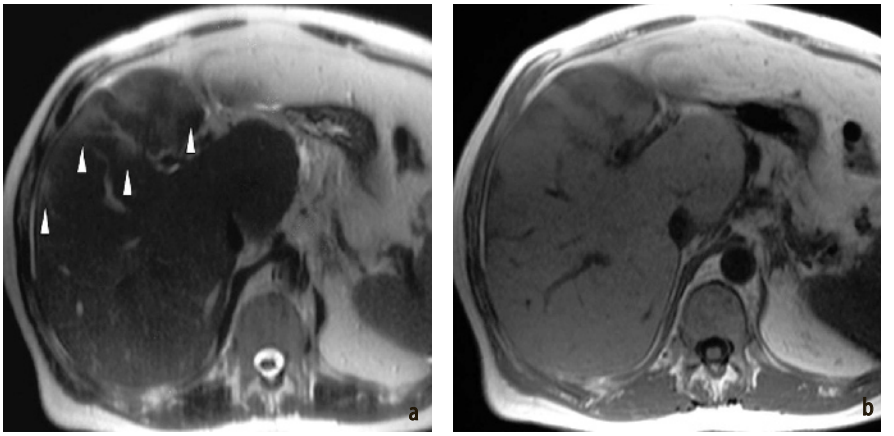

Fig. 18a-j. Peliosis hepatis. Patient with non-Hodgkin lymphoma during chemotherapy. The pre-contrast HASTE T2-weighted MR image (**a**) reveals multiple ill-defined areas (*arrowheads*) with high signal intensity. On the corresponding unenhanced GRE T1-weighted image (**b**) these areas have low signal intensity. During the dynamic evaluation after administration of Gd-BOPTA, the lesions show homogeneous hypervascularization in the arterial phase (**c**) and remain hyperintense during the portal venous (**d**) and equilibrium (**e**) phases. Because of the absence of hepatocytes within the dilated sinusoids, the lesions appear hypointense on T1-weighted (**f**) and T1-weighted fat-suppressed (**g**) images acquired during the hepatobiliary phase after Gd-BOPTA administration. A follow-up examination performed one year after chemotherapy (**h-j**) shows complete resolution of the parenchymal changes

→

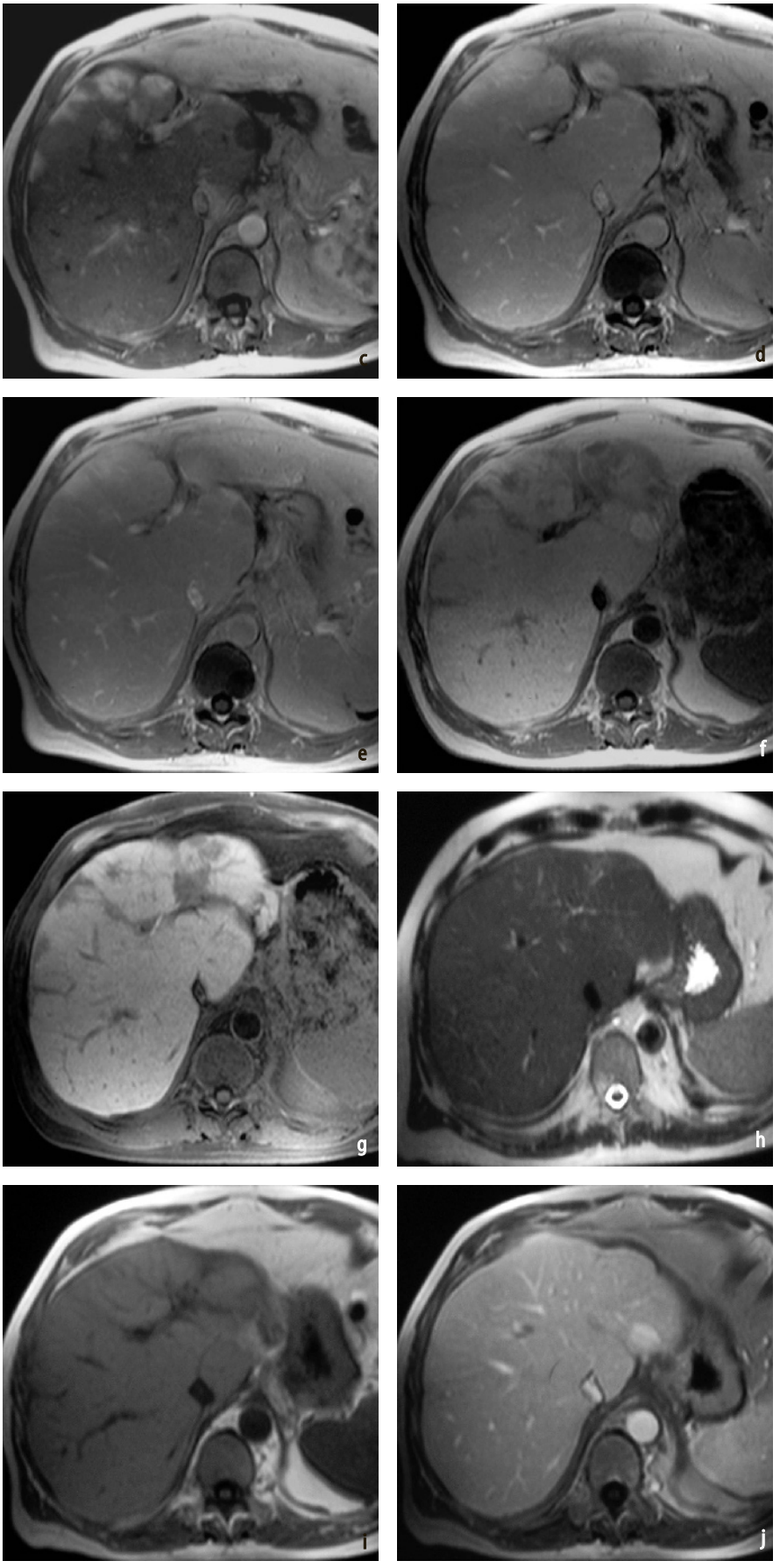
c
d
e
f
g
h
i
j

5.2.5 Confluent Hepatic Fibrosis

Confluent hepatic fibrosis is a mass-like fibrosis seen in approximately 15% of patients with advanced cirrhosis who are candidates for liver transplantation. The imaging findings of confluent fibrosis result in it being characterized due to its specific location in the liver, which is frequently the medial segment of the left and/or right lobe. Calcifications or dilatation of the biliary ducts are very rare.

Imaging techniques such as US are not specific for the diagnosis of confluent hepatic fibrosis; confluent fibrosis typically appears as an ill-defined hyperechoic, heterogeneous area, often with a pseudonodular aspect.

On unenhanced CT, confluent fibrosis often appears as a wedge-shaped focal area of low-density. After contrast material administration the lesion again demonstrates a low level of vascularity but may appear slightly hyperdense in the equilibrium or later phases due to the pooling effect of fibrotic tissue. Typical features such as retraction of the overlying liver capsule are evident on CT (Fig. 19).

Morphologic information on confluent fibrosis is available also after MR imaging, although the MR signal characteristics are not unique and do not permit accurate differentiation of this lesion from hepatic neoplasms. Whereas fibrotic tissue is typically hypointense with either a homogeneous or heterogeneous appearance on unenhanced T1- and T2-weighted images, confluent hepatic fibrosis appears as a region of lower signal intensity compared to that of the adjacent liver parenchyma on T1-weighted images, and as a region of higher signal intensity on T2-weighted and STIR images. The hyperintense appearance of confluent hepatic fibrosis on T2-weighted images reflects edema within the fibrotic area [40, 41].

The appearance of confluent fibrosis on dynamic phase images after the bolus injection of a gadolinium contrast agent is similar to that observed on CT, with hyperintensity typically seen during the equilibrium phase. During the hepatobiliary phase after the administration of a hepatospecific contrast agent, confluent fibrosis typically has a heterogeneously hypointense appearance due to the reduced number of hepatocytes (Fig. 20).

Confluent fibrosis on SPIO-enhanced T2-weighted images characteristically presents as a wedge-shaped area of high signal intensity with internal areas of low signal intensity. While the area of high signal intensity corresponds to the distribution of fibrosis, the low signal intensity regions reflect residual functioning liver parenchyma that is able to take up SPIO particles [33].

The differential diagnosis of confluent fibrosis in cirrhotic patients includes non-neoplastic processes such as segmental fatty liver or hepatic infarction and neoplastic processes such as infiltrative sclerosing HCC. Although irregular fatty infiltration may appear with variable shape and dis-

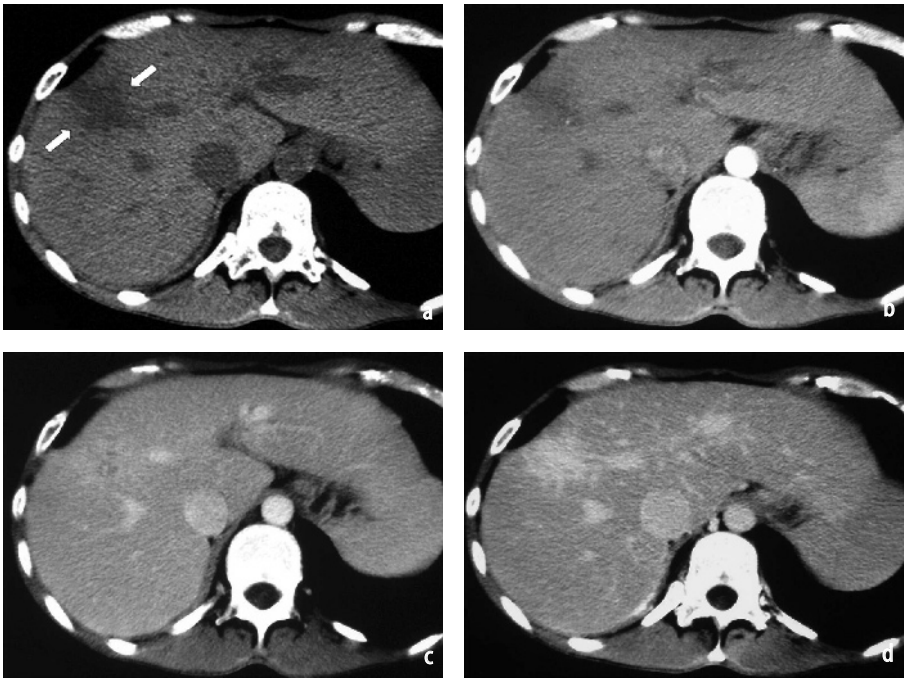

Fig. 19a-d. Confluent hepatic fibrosis. The pre-contrast CT scan (**a**) reveals a hypodense area (*arrows*) located in segment VIII of the liver, associated with capsular retraction. After contrast medium administration, this area shows minor enhancement in the arterial phase (**b**), while the density increases progressively in the portal venous (**c**) and equilibrium (**d**) phases

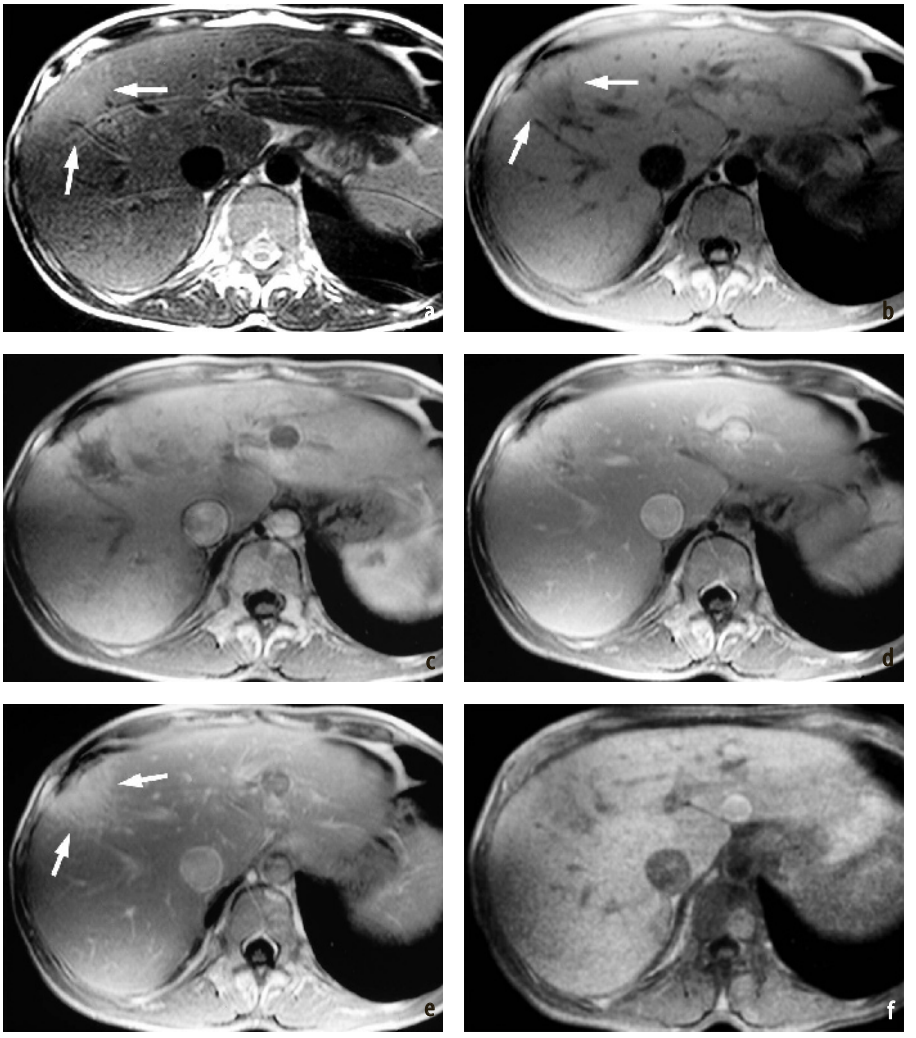

Fig. 20a-f. Confluent hepatic fibrosis. Same case shown in Fig.19. On the pre-contrast T2-weighted image (**a**) and on the GRE T1-weighted image (**b**) an area (*arrows*) located in segment VIII of the liver appears homogeneously, slightly hyperintense and heterogeneously, slightly hypointense, respectively. The enhancement behavior during the dynamic series after administration of Gd-BOPTA is similar to that seen on CT imaging: the area does not show significant enhancement on arterial phase images (**c**) but shows a progressive increase in signal intensity during the portal venous (**d**) and equilibrium (**e**) phases (*arrows*). On the hepatobiliary phase image (**f**) after injection of Gd-BOPTA this area appears slightly hypointense compared with the normal liver

tribution, the absence of capsular retraction or segmental shrinkage is often sufficient to distinguish this lesion from confluent fibrosis. Similarly, hepatic infarction can appear as a well-demarcated wedge-shaped area, but these areas typically show little or no enhancement. Moreover, hepatic infarction is rare in cirrhotic patients, occurring more frequently in patients with hematologic disorders after vascular surgery or transplantation. In the case of infiltrative sclerosing HCC, this lesion can be seen as a nearly wedge-shaped or peripheral band-like lesion, although it is usually hypervascular during the arterial phase of the dynamic study, showing wash-out in the portal venous phase. Moreover, HCC is frequently associated with a pseudocapsule and often contains areas of necrosis, hemorrhage or fatty metamorphosis within the lesion [40, 41].

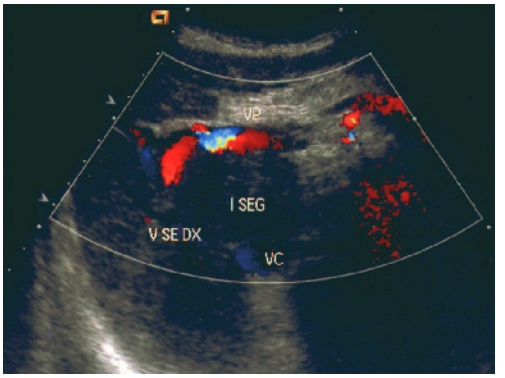

Fig. 21. Segmental hypertrophy. Patient with primary sclerosing cholangitis. Color Doppler US reveals prominent vascular structures located around segment I of the liver. This segment demonstrates a progressive increase in size due to atrophy of other segments affected by sclerosing cholangitis

5.2.6 Segmental Hypertrophy

In conditions such as cirrhosis, Budd-Chiari syndrome or primary sclerosing cholangitis the liver may be dysmorphic in appearance. In the chronic phase of Budd-Chiari syndrome, the abnormal vascularization tends to be located more peripherally and to be most prominent around the caudate lobe due to its separate autonomous venous drainage. Consequently, this liver portion may increase in volume.

In sclerosing cholangitis, atrophy and compensatory hypertrophy of the liver parenchyma are consequences of chronic obstruction of the segmental bile duct. This leads to atrophy of the affected segments and compensatory hypertrophy in other segments in which bile flow is maintained (Fig. 21). On CT and MR imaging the resulting liver hypertrophy appears more hyperdense and hyperintense on T1-weighted images respectively, compared to that of the surrounding parenchyma (Figs. 22, 23). In some cases the segmental hypertrophy has a pseudotumoral aspect.

5.2.7 Parenchymal Compression

Diaphragmatic compression of liver parenchyma due to contraction of diaphragmatic muscle bundles may create hypodense pseudonodular areas especially in segments VII and VIII of the liver. This is a typical occurrence at the time of the CT or MR examination when patients inspire deeply causing a focal increase in tissue pressure in the sub-capsular region. The result is a decrease in portal perfusion while the hepatic arterial perfusion remains relatively unchanged (Fig. 24).

Pseudolesions due to rib compression are observed in approximately 15% of patients, and are most commonly seen in the sub-capsular region of liver segments V and VI [47].

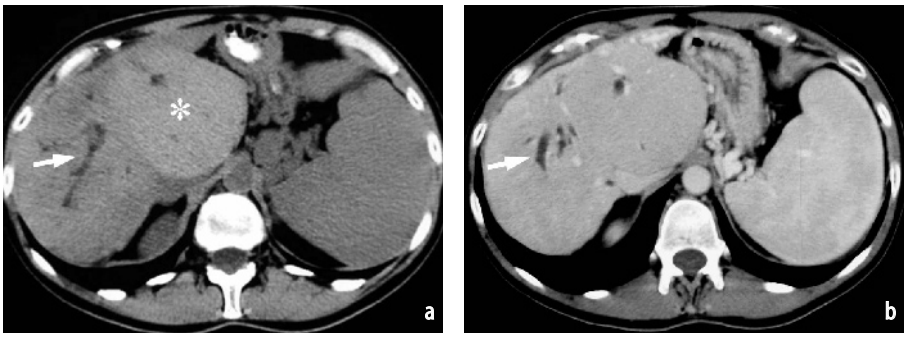

Fig. 22a, b. Segmental hypertrophy. Same case as demonstrated in Fig. 21. On the CT examination the liver is dysmorphic in appearance, with pseudotumoral hypertrophy of segment I (*asterisk*). This segment appears hyperdense on the pre-contrast image (**a**) as compared with the surrounding liver parenchyma that is affected by the sclerosing cholangitis. Note the dilatation of-bile ducts as typically seen in primary sclerosing cholangitis (*arrows*). On the post-contrast image (**b**) the hypertrophy shows normal perfusion and is seen with comparable density to the surrounding liver tissue

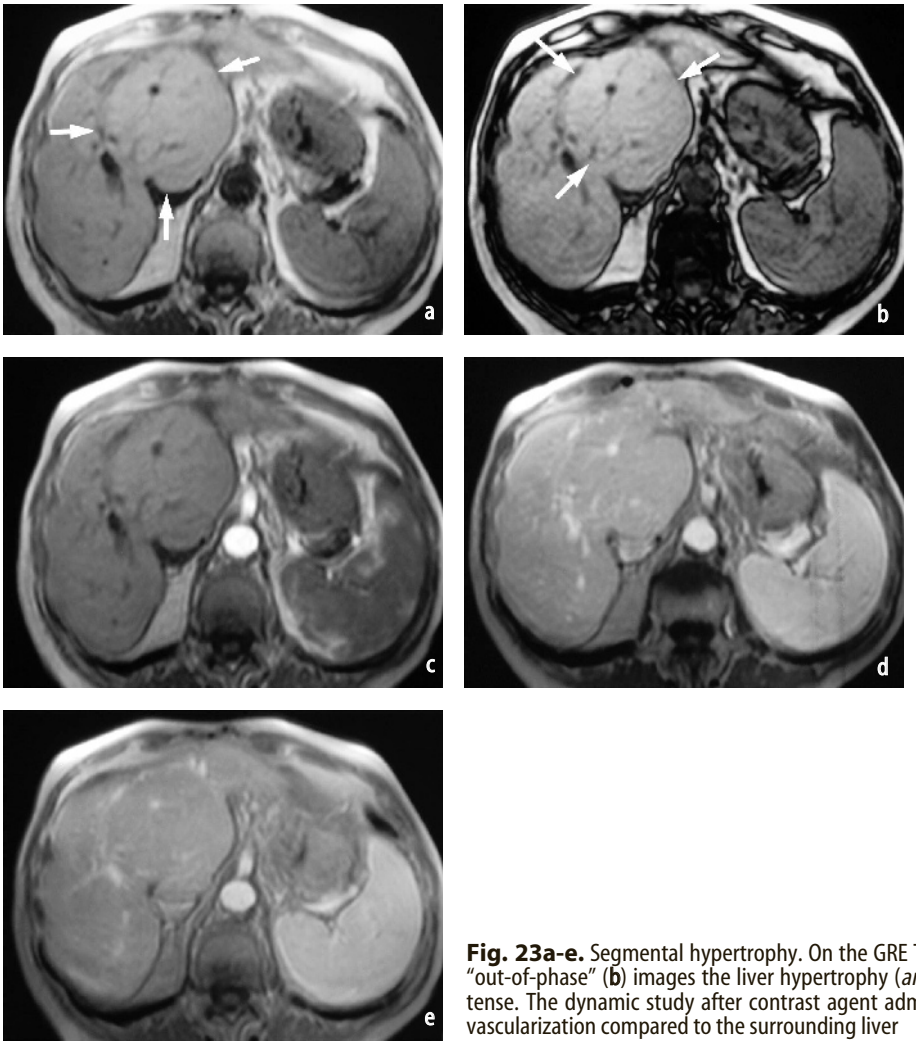

Fig. 23a-e. Segmental hypertrophy. On the GRE T1-weighted "in-phase" (**a**) and "out-of-phase" (**b**) images the liver hypertrophy (*arrows*) appears slightly hyperintense. The dynamic study after contrast agent administration (**c**-**e**) shows normal vascularization compared to the surrounding liver

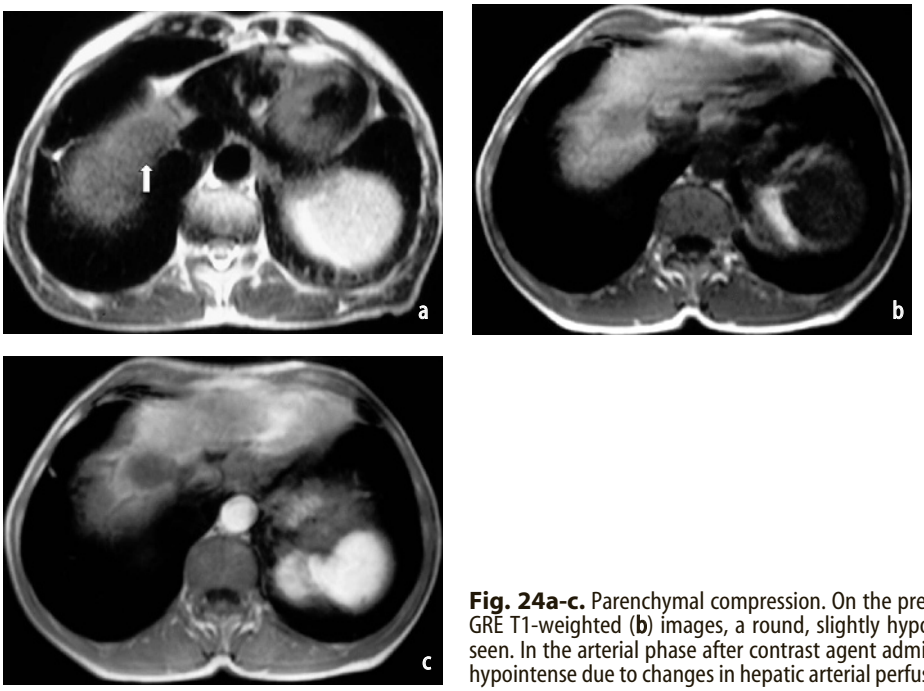

Fig. 24a-c. Parenchymal compression. On the pre-contrast T2-weighted (**a**) and GRE T1-weighted (**b**) images, a round, slightly hypointense lesion (*arrow*) can be seen. In the arterial phase after contrast agent administration (**c**) the area appears hypointense due to changes in hepatic arterial perfusion

5.3 Vascular Pseudolesions

5.3.1 Transient Hepatic Attenuation Differences (THAD)

THAD is associated with numerous intrahepatic vascular conditions, particularly intrahepatic shunts.

Intrahepatic shunts can be divided into arterioportal, arteriosystemic, and portosystemic, depending on the vascular connection. APS are the most common form of intrahepatic shunts, and are commonly associated with HCC or with iatrogenic causes, such as liver biopsy (Fig. 25) or radio-frequency (RF) ablation (Fig. 26). In APS a direct communication between the feeding arterial vessels of the neoplasm and the draining portal venules leads to increased arterial flow around the tumor [29].

Early enhancement of portal vein branches during the arterial phases of CT and MR dynamic studies is often indicative of APS. APS can sometimes be seen in association with small hemangiomas and seems to be related to the hyperdynamic vasculature of this tumor. APS are common in liver cirrhosis, due to the damaged hepatic flow (Figs. 27, 28), and can be a source of potential confusion with HCC, especially when they appear as small, round areas during the arterial phase (Figs. 29, 30).

Non-tumoral round APS show signal loss after SPIO administration, comparable to that occurring in the normal liver parenchyma. Homogeneous uptake of hepatospecific contrast agents such as Gd-BOPTA is generally observed, resulting in an isointense appearance relative to the normal parenchyma (Fig. 30 f, g) [48]. Well-differentiated small HCC may demonstrate the same enhancement behavior and the same uptake after SPIO and hepatospecific contrast agents. As a result, differential diagnosis may be difficult and biopsy or strict follow-up should be performed.

Direct communication between the portal vein and systemic veins results in intrahepatic portosystemic venous shunts. These are frequent in the setting of liver cirrhosis with portal hypertension, and may be accompanied by extrahepatic portosystemic collateral circulation.

THAD can be classified according to morphology (sectoral, segmental, and lobar), etiology (as a result of benign or malignant tumors, arterioportal shunting, liver cirrhosis, or venous thrombosis), or pathogenesis (due to low portal inflow, phlogosis, or sump effect). In the absence of a direct relationship to neoplasm, the most common cause of THAD is thrombosis of the portal vessels. The most frequent etiopathogenesis is therefore low portal inflow due to obstruction or compression of the portal vein [21]. Low portal inflow could be a result of APS. In this case, diversion of the portal flow by arterial flow under higher pressure results in relatively low portal flow and induces compensatory collateral arterial flow which intensifies and perpetuates the phenomenon. Thus, when THAD is related to APS there is no portal block, but rather a mixing of arterial and venous blood. This pathogenesis is frequently seen in hemangioma and HCC [9], as well as in arterial phenomena not associated with focal liver lesions.

Sectoral THAD are usually triangular in shape. If the lesion is present in the medial portion, low flow is induced by compression and the THAD is fan-shaped. However, if the lesion is central the low flow is usually related to thrombosis or APS and the THAD is wedge-shaped [21] (Fig. 31). On the other hand, it is well known that APS arising in the context of cirrhosis may produce THAD that sometimes display a round or pseudo-round morphology (the axial section of the conical shape may appear round or oval). Thus, THAD is poorly distinguishable from small HCC in cirrhotic patients, or from hypervascular metastases in non-cirrhotic patients [11]. Occasionally, THAD may occur as a prelude to an otherwise occult focal lesion [12] and can sometimes mask the underlying lesion.

5.3.2 Vascular Malformations

According to the Mullicken and Glowacki Classification, vascular malformations can be subdivided into: a) fast-flow forms, that comprise arteriovenous malformations and arterioportal fistulas, b) slow-flow forms, that comprise portosystemic shunts and venous as well as lymphatic malformations, and c) combined forms [38]. The vast majority of vascular pseudolesions are due to fast-flow form malformations.

5.3.2.1 Arteriovenous Malformations (AVMs)

AVMs are congenital abnormalities in the formation of blood vessels that shunt blood through direct arteriovenous connections, without neoplastic tissue between these anomalous vessels. Clinically, these congenital abnormalities can be observed in neonates with congestive heart failure, hepatomegaly, portal hypertension, and anemia, or in late childhood and in adults in the clinical setting of hereditary haemorrhagic teleangiectasia associated with congestive heart failure, hepatic is-

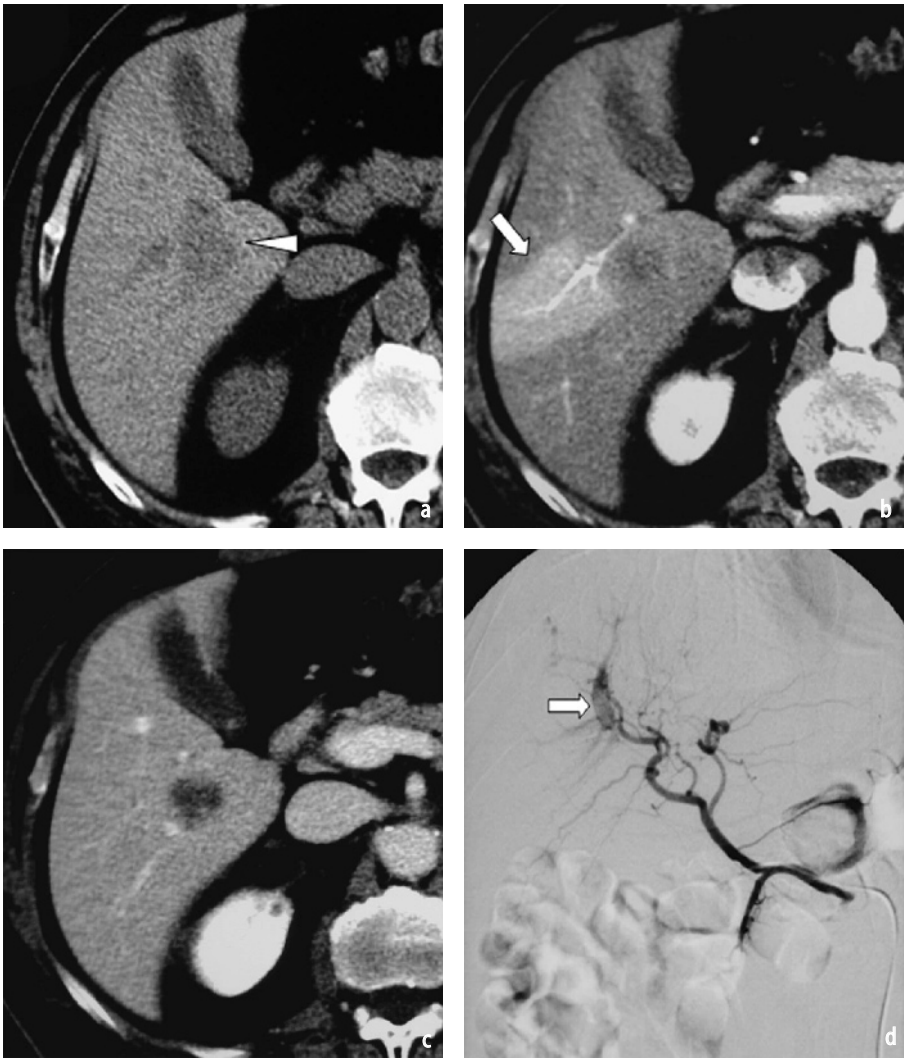

Fig. 25a-d. Arterioportal shunts. HCC after liver biopsy. On the pre-contrast CT scan (**a**) a hypodense, round, well-defined nodule (*arrowhead*) can be seen. In the arterial phase after contrast medium administration, a markedly hyperdense, triangular area (*arrow*) is visible near the nodule (**b**). In the portal venous phase (**c**) the area again appears isodense due to wash-out of contrast medium from this area and enhancement of the surrounding liver. Catheter angiography (**d**) confirms the presence of APS (*arrow*)

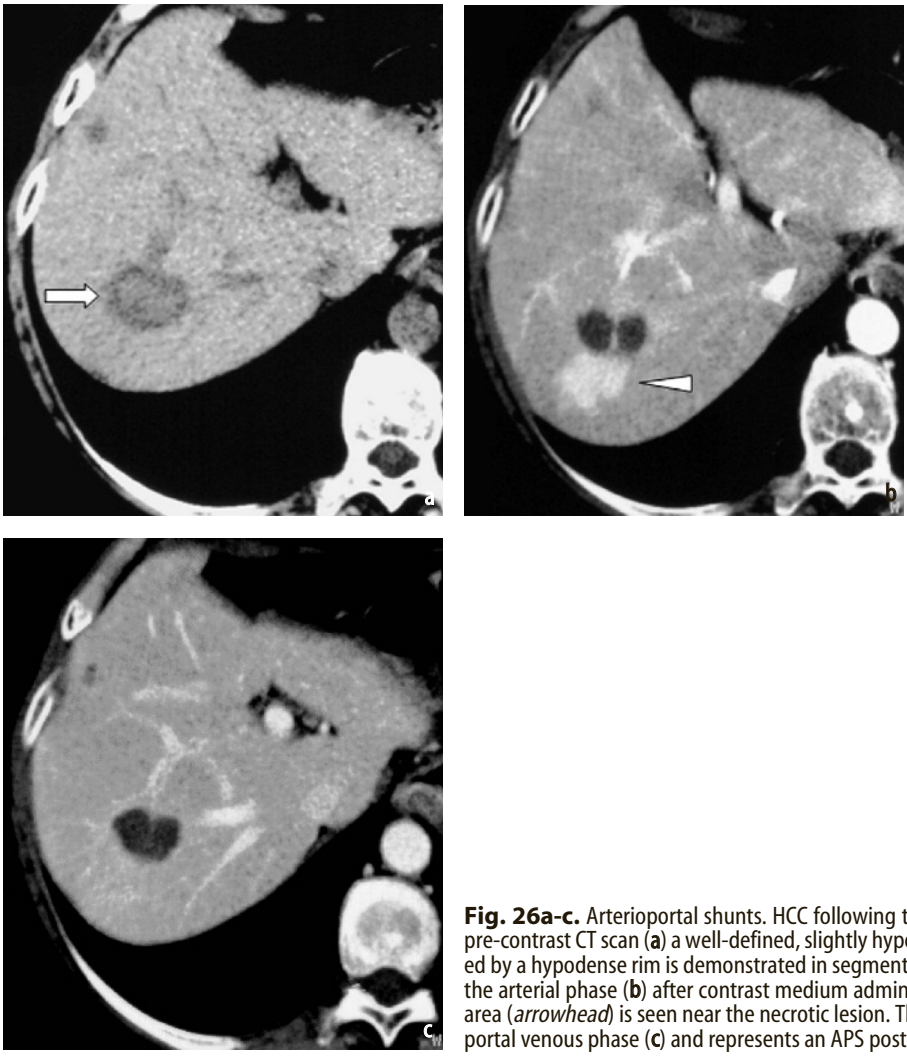

Fig. 26a-c. Arterioportal shunts. HCC following treatment by RF ablation. On the pre-contrast CT scan (**a**) a well-defined, slightly hypodense nodule (*arrow*) surrounded by a hypodense rim is demonstrated in segment VII of the right liver lobe. During the arterial phase (**b**) after contrast medium administration a markedly hyperdense area (*arrowhead*) is seen near the necrotic lesion. This area becomes isodense in the portal venous phase (**c**) and represents an APS post RF ablation

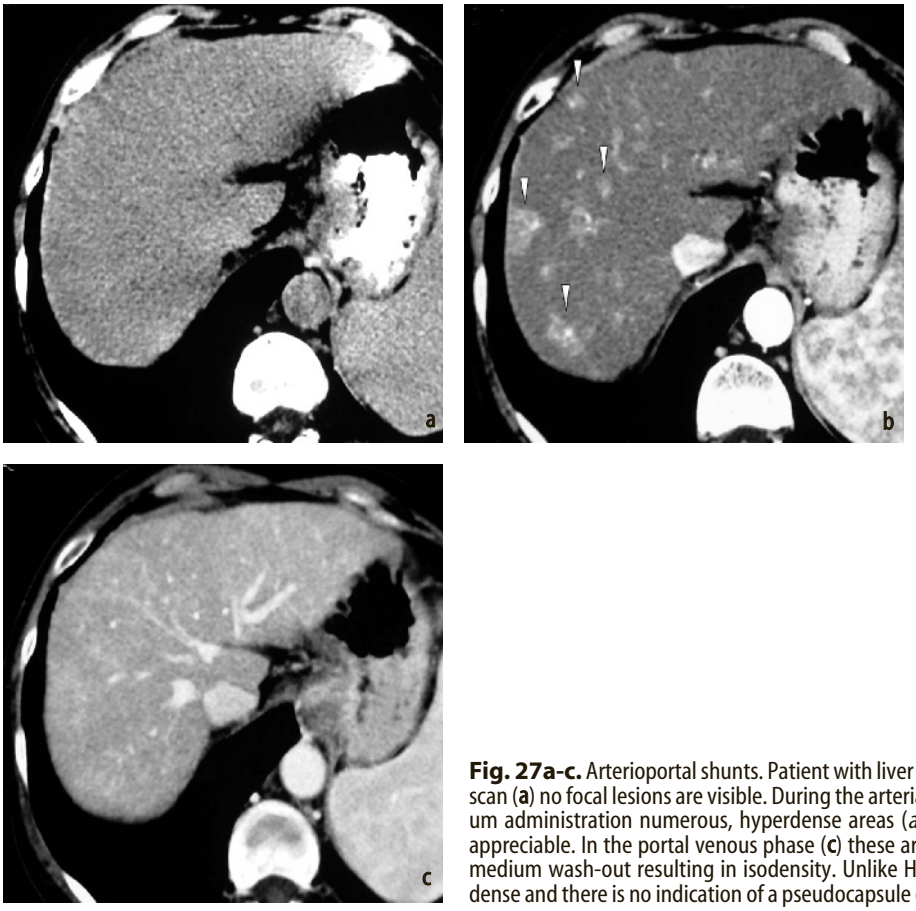

Fig. 27a-c. Arterioportal shunts. Patient with liver cirrhosis. On the pre-contrast CT scan (**a**) no focal lesions are visible. During the arterial phase (**b**) after contrast medium administration numerous, hyperdense areas (*arrowheads*) of variable size are appreciable. In the portal venous phase (**c**) these areas demonstrate rapid contrast medium wash-out resulting in isodensity. Unlike HCC, these lesions are not hypodense and there is no indication of a pseudocapsule on the portal venous phase scan

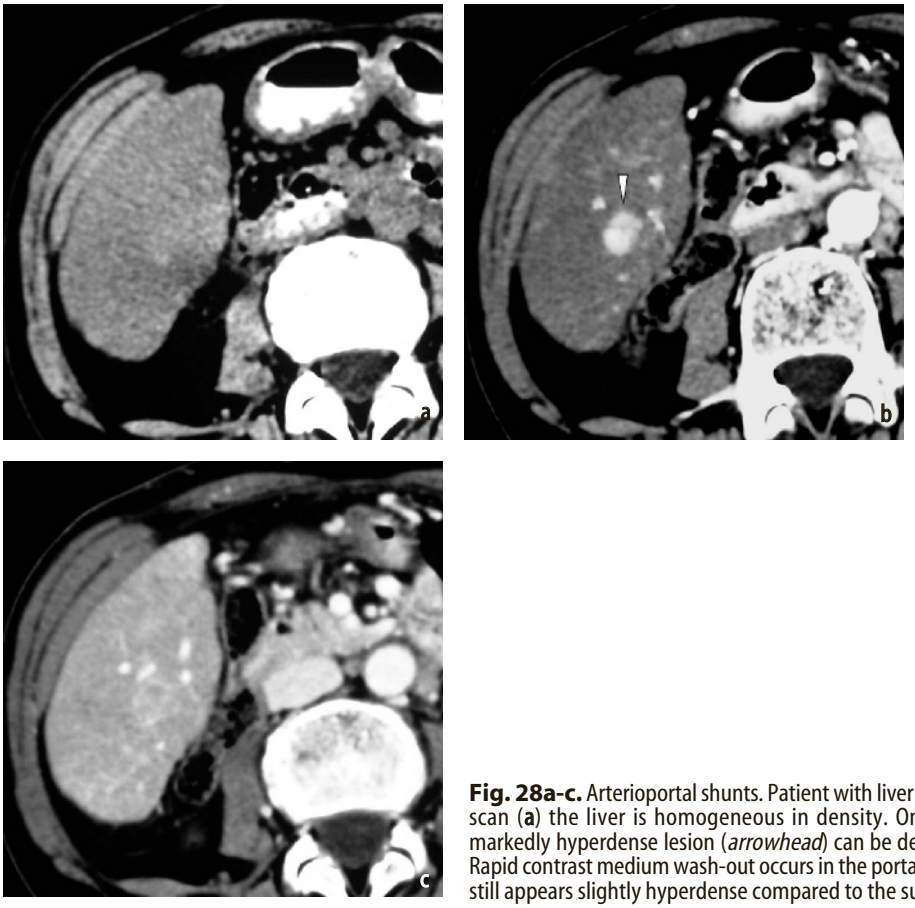

Fig. 28a-c. Arterioportal shunts. Patient with liver cirrhosis. On the pre-contrast CT scan (**a**) the liver is homogeneous in density. On the dynamic study, a round, markedly hyperdense lesion (*arrowhead*) can be detected in the arterial phase (**b**). Rapid contrast medium wash-out occurs in the portal venous phase (**c**) but the lesion still appears slightly hyperdense compared to the surrounding liver parenchyma

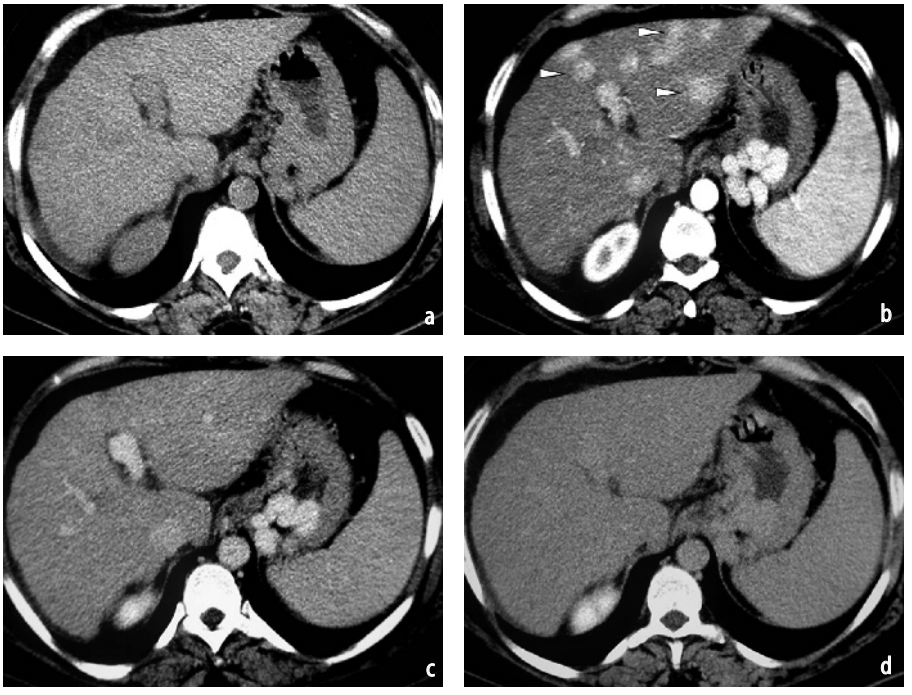

Fig. 29a-d. Arterioportal shunts. On the pre-contrast CT scan (**a**) no focal lesions are visible. On the arterial phase image (**b**) after contrast medium administration, several hyperdense lesions (*arrowheads*) with different shapes are visible in the left lobe of the liver. These areas appear isodense in the portal venous (**c**) and equilibrium (**d**) phases

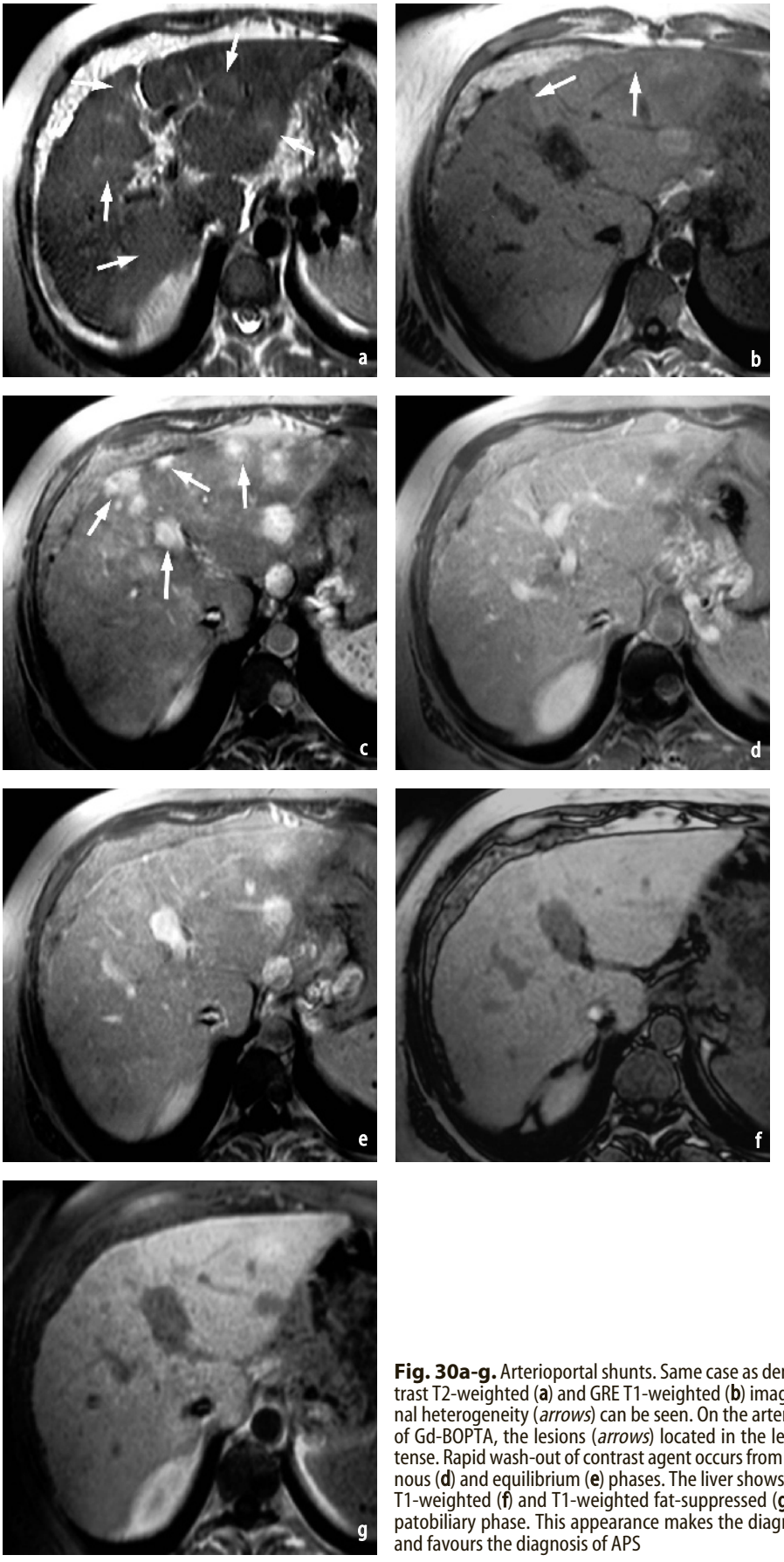

Fig. 30a-g. Arterioportal shunts. Same case as demonstrated in Fig. 29. On pre-contrast T2-weighted (**a**) and GRE T1-weighted (**b**) images, diffuse ill-defined areas of signal heterogeneity (*arrows*) can be seen. On the arterial phase image (**c**) after injection of Gd-BOPTA, the lesions (*arrows*) located in the left lobe appear markedly hyperintense. Rapid wash-out of contrast agent occurs from these lesions during the portal venous (**d**) and equilibrium (**e**) phases. The liver shows homogeneous signal intensity on T1-weighted (**f**) and T1-weighted fat-suppressed (**g**) images acquired during the hepatobiliary phase. This appearance makes the diagnosis of focal liver lesions unlikely and favours the diagnosis of APS

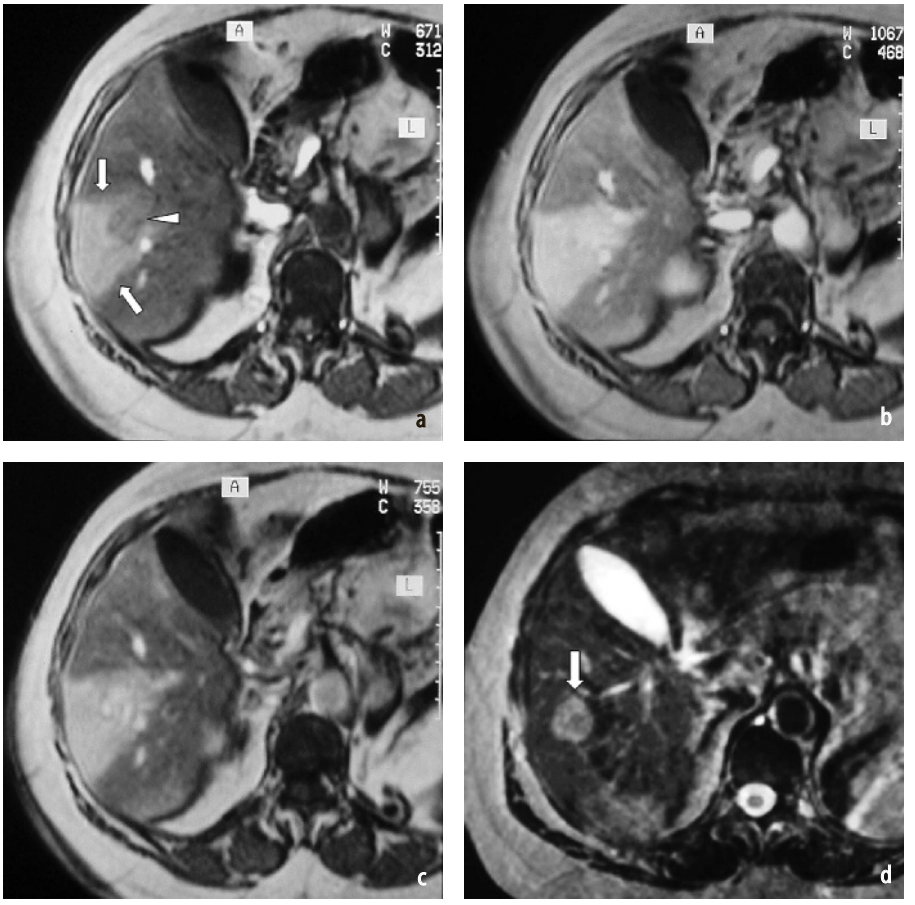

Fig. 31a-d. THAD, focal sparing and HCC. On the pre-contrast GRE T1-weighted "out-of-phase" image (**a**) a triangular area of focal sparing (*arrows*) is clearly demarcated in an otherwise diffuse steatosis of the liver. Within the focal sparing a round hypointense lesion (*arrowhead*) representing an HCC can be detected. On the arterial phase image (**b**) after contrast agent administration a THAD reproduces the triangular focal spared area. In the portal venous phase (**c**) the signal intensity in the focal spared area is similar to that observed in the pre-contrast phase, and the round lesion is not clearly visible. On the corresponding SE T2-weighted image (**d**) the focal spared area is not delineated, but a round hyperintense lesion (*arrow*) corresponding to the HCC is recognizable

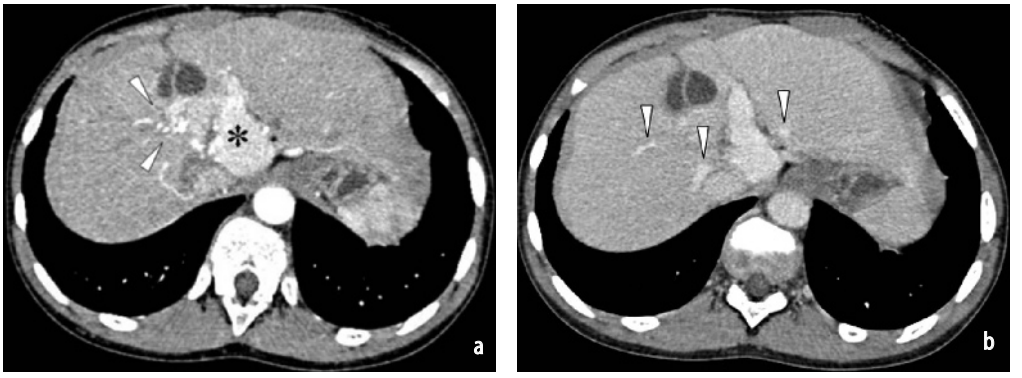

Fig. 32a, b. Arteriovenous malformations. On the arterial phase CT image (**a**), multiple, irregular and tortuous arterial vessels (*arrowheads*) are visible near the dome of the liver. The left portal branch (*asterisk*) is malformed, increased in size and shows early opacification. The portal vein is better delineated in the early portal venous phase (**b**) and further malformed venous vascular structures (*arrowheads*) are apparent surrounding the left portal branch

chemia, and portal hypertension [4, 7]. Frequently, AVMs may occur between the hepatic artery and the hepatic vein, as well as between the hepatic artery and the portal venous system.

On US, AVMs can appear as a nest of tortuous, enlarged, anechoic vessels located usually in one lobe of the liver. Color Doppler US generally demonstrates significant flow with high peak shifts both in arteries and veins, a low arterial resistive index (RI), and increased pulsatility of veins. In late stages of the disease, an arterialized spectral pattern can be seen in the hepatic veins [5].

On unenhanced CT, AVMs generally appear as hypoattenuating areas within the liver. In the arterial and early portal venous phases after contrast media administration these lesions enhance intensely and homogeneously. Thereafter, contrast medium equilibration results in a similar contrast density to that observed in the surrounding vascular structures (Fig. 32).

Typical findings on dynamic MR images of the liver for singular AVMs post-biopsy or surgery include a dilatation of the draining hepatic vein and an early enhancement of the hepatic veins during the arterial phase. Shunts between the hepatic artery and the portal venous system typically lead to increased portal venous pressure and thus to the usual findings of portal hypertension.

MR imaging is a very useful tool for distinguishing AVMs from hemangiomas. Specifically, signal hypointensity on T2-weighted images and the absence of progressive enhancement during the dynamic series of acquisitions after contrast agent administration make the diagnosis of AVM most probable (Fig. 33) [5, 8]. On MR angiography, AVMs are found with poor regional demarcation of the lesion, arteriovenous shunting, variable pooling of contrast material in vascular spaces, and no parenchymal blush.

5.3.2.2 Arterioportal Fistulas

Arterioportal fistulas may be acquired or congenital, and may have an intra- or extrahepatic location. Common causes of acquired arterioportal fistulas are cirrhosis and hepatic neoplasms, blunt or penetrating trauma, percutaneous liver biopsy, gastrectomy, transhepatic cholangiography, and biliary surgery (Fig. 34). In the case of congenital arterioportal fistulas, these are typically associated with hereditary hemorrhagic teleangectasia, biliary atresia, and Ehlers-Danlos Syndrome. Often asymptomatic within the first year of life, the first symptom of arterioportal fistula is usually portal hypertension associated with splenomegaly, hypersplenism, variceal formation, and ascites [2].

US with color Doppler is the most useful imaging technique for making the diagnosis of arterioportal fistula. At Doppler US, common features include enlargement of the hepatic artery and dilatation of the segment of the portal vein in which the fistula is located. In congenital arterioportal fistula, hepatofugal flow in the portal vein can be detected along with color speckling in the hepatic parenchyma adjacent to the fistula, which is due to vibration artifact [14].

Imaging features of arterioportal fistulas on dynamic CT and MR include marked enhancement of the main portal vein, segmental branches, or major tributaries, with attenuation or signal intensity approaching that of the aorta during the arterial phase. Perfusion anomalies of the surrounding liver parenchyma such as regional increases in arterial inflow as a response to inverted portal flow, and increased portal vein inflow due to the shunt itself, may also be observed [16]. Angiography is often indicated for possible embolization.

5.3.2.3 Hereditary Haemorrhagic Telangiectasia (HHT)

HHT, also called Rendu-Osler-Weber disease or Osler's disease, is a vascular, hereditary, autosomic dominant disorder that occurs with a frequency of approximately 10-20 cases/100,000 [15]. HHT is characterized by the presence of mucocutaneous or visceral angiodysplastic lesions, the latter most frequently seen in the liver, lung, brain, and gastrointestinal tract. Hepatic involvement accounts for 10-40% of cases and is characterized by the presence of intrahepatic shunts (arterioportal, arteriosystemic, venous portosystemic), diffuse telangiectases, and vascular mass-forming lesions [3]. AVMs are usually distributed diffusely throughout the liver and may be associated with enlargement of the hepatic artery and increased tortuousity of vessels in the liver hilum and in the central portions of the liver lobes. In Osler's disease, increased arterial perfusion of the liver tissue frequently leads to secondary nodular hypertrophy, which may be misinterpreted as a malignant hepatic tumor. These pseudotumors, as in focal nodular hyperplasia, represent a localized overgrowth of hepatocellular tissue and are not real liver tumors. Patients with hepatic involvement can be asymptomatic, but heart failure, portosystemic encephalopathy, cholangitis, portal hypertension, and cirrhosis have been reported [34].

Focal or diffuse changes in hepatic circulation are detectable on all of the imaging modalities. US, particularly in association with color Doppler, shows intrahepatic shunts with arterial and venous vessels frequently increased in size. However, this imaging method has comparatively low sensitivity

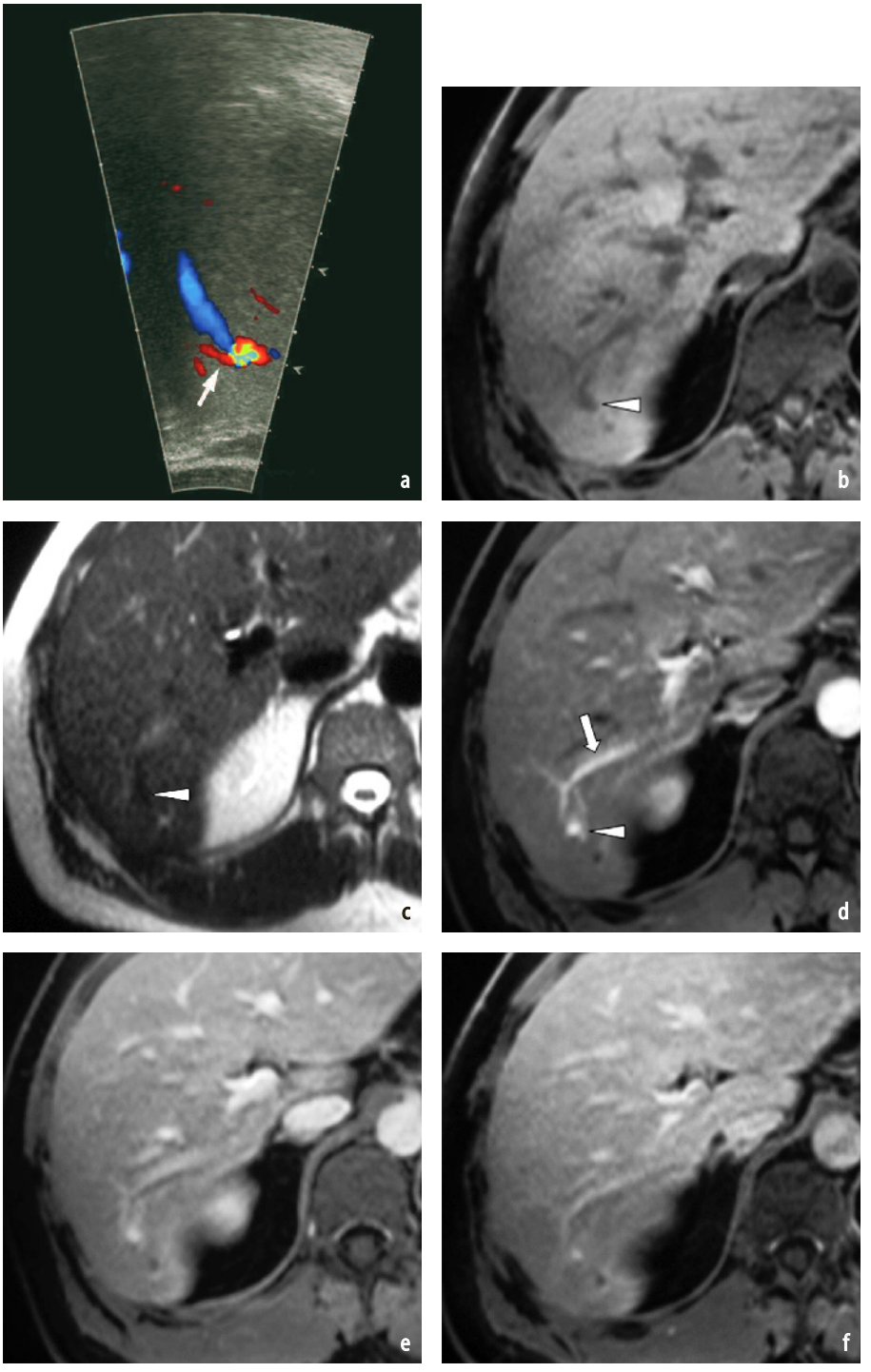

Fig. 33a-f. Arteriovenous malformations in a healthy young patient. An US scan (**a**) shows an abnormal communication (*arrow*) between an arterial branch and a venous vessel. On pre-contrast T1- and T2-weighted MR images (**b**, **c**) a small, hypointense area (*arrowheads*) is visible in the lower parts of segment VII of the liver. On the arterial phase image (**d**) the lesion (*arrowhead*) shows intense and homogeneous enhancement. Early enhancement of a right portal vein branch (*arrow*) is also evident. The lesion shows the same signal intensity as observed in surrounding vascular structures in the portal venous (**e**) and equilibrium (**f**) phases

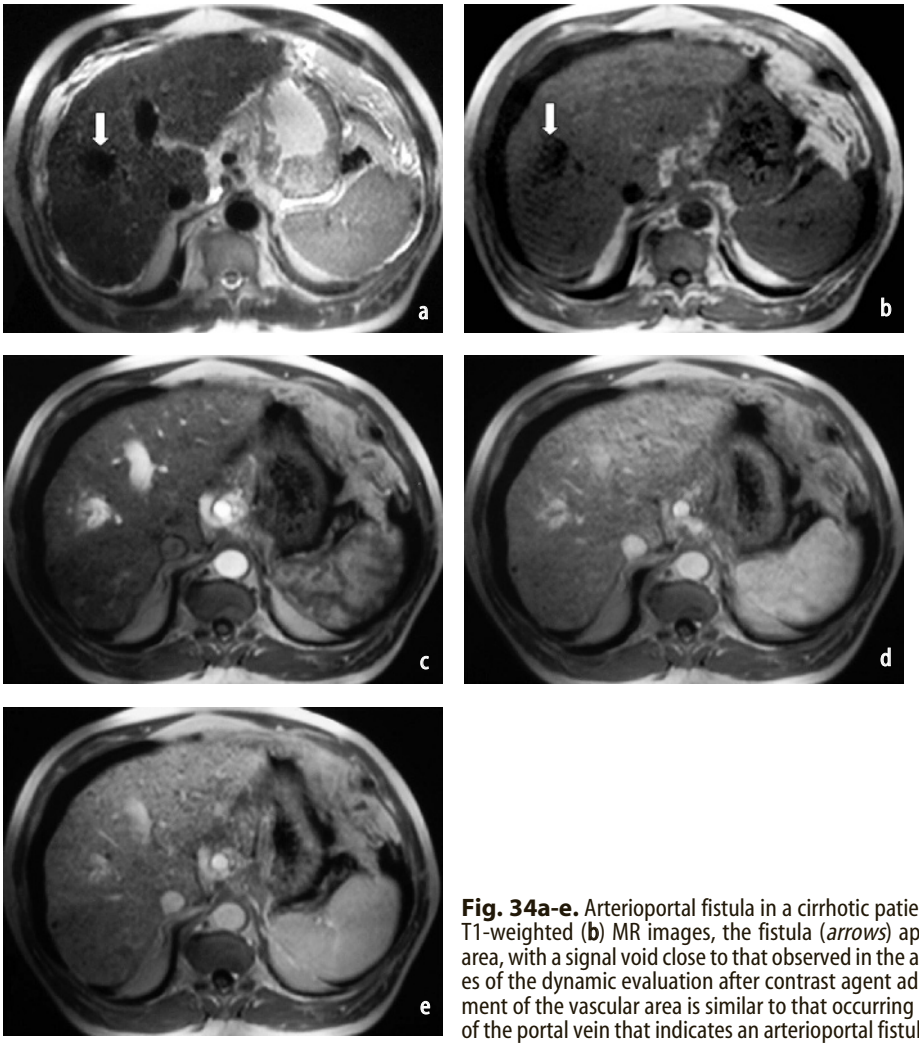

Fig. 34a-e. Arterioportal fistula in a cirrhotic patient. On the T2-weighted (**a**) and T1-weighted (**b**) MR images, the fistula (*arrows*) appears as a hypointense, round area, with a signal void close to that observed in the aorta and portal vein. In all phases of the dynamic evaluation after contrast agent administration (**c**-**e**) the enhancement of the vascular area is similar to that occurring in the aorta and the left branch of the portal vein that indicates an arterioportal fistula

and spatial resolution for demonstrating small arteriovenous shunts [39].

On multidetector CT, the possibility to perform a selective, multiphase study of hepatic vascular structures permits both arterial and venous vessels to be visualized. Hence, the visualization of arteriosystemic shunts is improved. Compared with conventional spiral CT, multidetector CT improves image quality, and permits better multiplanar and angiographic reconstruction. Consequently, the capability to identify and characterize the vascular lesions typical of HHT is improved [8]. Thus telangiectases, which are present in more than 60% of cases of HHT, are seen as small vascular spots that are readily recognizable on reconstructed multiplanar reformatted and maximum intensity projection (MIP) images. Likewise, large confluent vascular masses, which are present in about 25% of HHT cases, are seen as large shunts or multiple telangiectases that coalesce. In a recent study, multidetector CT (MDCT) was able to detect hepatic vascular alterations in about 80% of patients with a confirmed or suspected diagnosis of HHT [35]. In this study arterioportal shunts and arteriosystemic shunts were detected as the only vascular alterations in roughly 50% and 20% of patients, respectively, while both shunt types were detected in approximately 30% of patients.

On MR imaging, telangiectases appear as small hypo- to isointense lesions on unenhanced T1-weighted images and as iso- or hyperintense lesions on T2-weighted images (Fig. 35). Whereas arteriovenous shunts are poorly detected on unenhanced T1- and T2-weighted images, dilatated and tortuous vessels can usually be seen near the arteriovenous shunts.

Dynamic MR imaging reveals strong arterial phase enhancement and subsequent isointensity with the surrounding liver tissue in the portal venous and equilibrium phases. Normal enhancement of the affected tissue in the hepatobiliary phase can be noted with the use of contrast agents with hepatocellular properties such as Gd-BOPTA (Fig. 36).

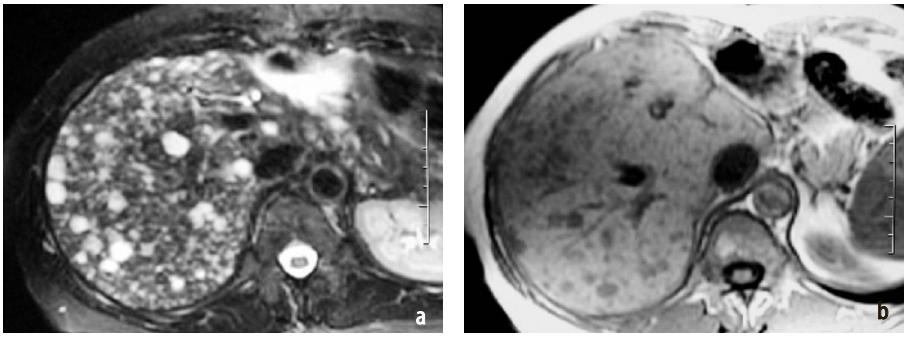

Fig. 35a, b. Hereditary haemorrhagic teleangiectasia. The pre-contrast T2-weighted fat-suppressed TSE image (**a**) reveals almost complete exchange of normal hepatic structure by diffuse small, round markedly hyperintense lesions. On the GRE T1-weighted image (**b**) the lesions demonstrate similar hypointensity to that observed in the vessels

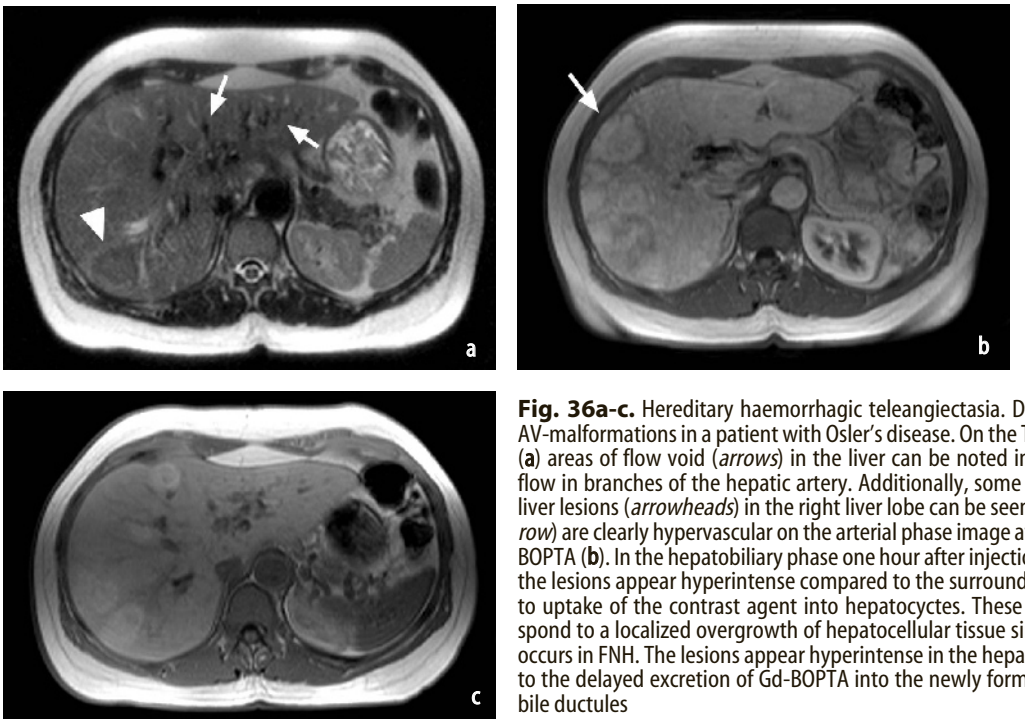

Fig. 36a-c. Hereditary haemorrhagic teleangiectasia. Diffusely distributed AV-malformations in a patient with Osler's disease. On the T2-weighted image (**a**) areas of flow void (*arrows*) in the liver can be noted indicating increased flow in branches of the hepatic artery. Additionally, some nodular-appearing liver lesions (*arrowheads*) in the right liver lobe can be seen. These lesions (*arrow*) are clearly hypervascular on the arterial phase image after injection of Gd-BOPTA (**b**). In the hepatobiliary phase one hour after injection of Gd-BOPTA (**c**), the lesions appear hyperintense compared to the surrounding liver tissue due to uptake of the contrast agent into hepatocyctes. These liver lesions correspond to a localized overgrowth of hepatocellular tissue similar to that which occurs in FNH. The lesions appear hyperintense in the hepatobiliary phase due to the delayed excretion of Gd-BOPTA into the newly formed and malformed bile ductules

References

1. Alpers DH, Sabesin SM, White HM. Fatty liver: biochemical and clinical aspects. In Schiff L, Schiff E (eds). Diseases of the liver, 7th edn. JB Lippincott, Philadelphia 1993
2. Altuntas B, Erden A, Karakurt C, et al. Severe portal hypertension due to congenital hepatoportal arteriovenous fistula associated with intrahepatic portal vein aneurysm. J Clin Ultrasound 1998; 26:357-360
3. Bernard G, Mion F, Henry L, et al. Hepatic involvement in hereditary hemorrhagic teleangiectasia: clinical radiological and hemodynamic studies of 11 cases. Gastroenterology 1993; 105:482-487
4. Boon LM, Burrows PE, Paltiel HJ, et al. Hepatic vascular anomalies in infancy: a twenty-seven-year experience. J Pediatr 1996; 129:346-354
5. Borner G, Peer S, Karner M, et al. Nontumorous vascular malformations in the liver: color Doppler ultrasonographic findings. J Ultrasound Med 2002; 21:187-197
6. Brawer MK, Austin GE, Lewin KJ. Focal fatty change of the liver, a hitherto poorly recognized entity. Gastroenterology 1980; 78:247-252
7. Burrows PE, Dubois J, Kassarjian A. Pediatric hepatic vascular anomalies. Pediatr Radiol 2001; 31:533-545
8. Buscarini E, Buscarini L, Civardi G, et al. Hepatic vascular malformations in hereditary hemorrhagic teleangiectasia: imaging findings. Am J Roentgenol 1994; 163:1105-1110
9. Chen JH, Chai JW, Huang CL, et al. Proximal arterioportal shunting associated with hepatocellular carcinoma: features revealed by dynamic helical CT. Am J Roentgenol 1999; 172:403-407
10. Chen WP, Chen JH, Hwang JI, et al. Spectrum of transient hepatic attenuation differences in biphasic helical CT. AJR Am J Roentgenol 1999; 172:419-424
11. Colagrande S, Carmignani L, Pagliari A, et al. Transient hepatic attenuation differences (THAD) not connected to focal lesions. Radiol Med 2002; 104:25-43
12. Colagrande S, Centi N, Carmignani N, et al. Meaning and etiopathogenesis of sectorial transient hepatic attenuation differences (THAD). Radiol Med 2003; 105:180-187
13. Couinaud C. The parabiliary venous system. Surg Radiol Anat 1988; 10:311-316
14. D'Agostino D, Orsi M. Congenital hepatic arterioportal fistula. J Pediatr Gastroenterol Nutr 1999; 29:487
15. Dakeishi M, Shioya T, Wada Y, et al. Genetic epidemiology of hereditary hemorrhagic teleangiectasia in a local community in the northern part of Japan. Hum Mutat 2002; 19:140-148
16. Gallego C, Velasco M, Marcuello P, et al. Congenital and acquired anomalies of the portal venous system. Radiographics 2002; 22:141-159
17. Gilmore IT, Burrohghs A, Murray-Lyon IM, et al. Indications, methods and outcomes of percutaneous liver biopsy in England and Wales: An audit by the British Society of Gastroenterology and the Royal College of Physicians of London. Gut 1995; 36:437-441
18. Hirohashi S, Ueda K, Uchida H, et al. Nondiffuse fatty change of the liver: discerning pseudo-tumor on MR images enhanced with ferumoxides. Initial observations. Radiology 2000; 217:415-420
19. Horiuchi R, Uccida T, Kojima T, et al. Inflammatory pseudotumor of the liver. Clinicopathologic study and review of the literature. Cancer 1990; 65:1583-1590
20. Itai Y, Matsui O. Blood flow and liver Imaging. Radiology 1997; 202:306-314
21. Itai Y, Saida Y, Irie T, et al. Intrahepatic portosystemic venous shunts: spectrum of CT findings in external and internal subtypes. J Comput Assist Tomogr 2001; 25:348-354
22. Joy D, Thava VR, Scott BB. Diagnosis of fatty liver disease: is biopsy necessary? European J Gastroenterology and Hepatology 2003; 15:539-543
23. Kammen BF, Pacharn P, Thoeni RF, et al. Focal fatty infiltration of the liver: Analysis of prevalence and CT findings in children and young adults. Am J Roentgenol 2001; 177:1035-1039
24. Kawasaki T, Carmichael FJ, Saldivia V, et al. Relationship between portal venous and hepatic arterial blood flows. Spectrum of response. Am J Physiol 1990; 259:1010-1018
25. Kemper J, Jung G, Poll LW, et al. CT and MRI findings of multifocal hepatic steatosis mimicking malignancy. Abdom Imaging 2002; 27:708-710
26. Kim SR, Hayashi Y, Kudo M, et al. Inflammatory pseudotumor of the liver in a patient with chronic hepatitis C: difficulty in differentiating it from hepatocellular carcinoma. Pathol Int 1999; 49(8):726-30
27. Krech RH, Erhaedt-Domagalski M, Neumann H. Inflammatory pseudotumor of the liver. Morphologic and cytophotometry studies and differential diagnosis. Pathologe 1995; 16(6):415-420
28. Kuwatsuru R, Brasch RC, Muhler A, et al. Definition of liver tumors in the presence of diffuse liver disease: comparison of findings at MR imaging with positive and negative contrast agents. Radiology 1997; 202:131-138
29. Lane MJ, Jeffrey B, Katz DS. Spontaneous intrahepatic vascular shunts: Am J Roentgenol 2000; 174:125-131
30. Lloyd RL, Lyons EA, Levi CS, et al. The sonographic appearance of peliosis hepatis. J Ultrasound Med 1982; 1:293-294
31. Mathieu D, Vasile N, Menu Y, et al. Budd-Chiari syndrome. Dynamic CT. Radiology 1987; 165:409-413
32. Matsui O, Takahashi S, Kadoya M, et al Pseudolesion in segment IV of the liver at CT during arterial portography: correlation with aberrant gastric venous drainage. Radiology 1994; 193:31-35
33. Matsuo M, Kanematsu H, Kondo T, et al. Confluent hepatic fibrosis in cirrhosis: ferumoxides-enhanced MR imaging findings. Abdom Imaging 2001; 26:146-148
34. Memeo M, Stabile Ianora AA, Scardapane A, et al. Hepatic involvement in hereditary hemorrhagic teleangiectasia: CT findings. Abdominal imaging 2004; 29:211-220
35. Memeo M, Stabile Ianora AA, Scardapane A, et al. Hereditary hemorrhagic teleangiectasia: study of hepatic vascular alterations with multi-detector row helical CT and reconstruction programs. Radiol Med 2005; 109:125-138

36. Michels NA. Newer anatomy of the liver and its variants blood supply and collateral circulation. Am J Surg 1966; 112:337-347
37. Mortele KJ, Wiesner W, De Hemptinne B, et al. Multifocal inflammatory pseudotumor of the liver: dynamic gadolinium-enhanced, ferumoxide-enhanced, and mangafodipir trisodium-enhanced MR imaging findings. Eur Radiol 2002; 12(2):304-308
38. Mullicken JB, Glowacki J. Hemangiomas and vascular malformations in infants and children: a classification based on endothelial characteristics. Plast Reconstr Surg 1982; 69:412-422
39. Naganuma H, Ishida H, Niizzawa M, et al. Hepatic involvement in Osler-Weber-Rendu Disease: findings on pulsed and color Doppler sonography. Am J Roentgenol 1995; 165:1421-1425
40. Ohtomo K, Baron RL, Dodd GD 3rd, et al. Confluent hepatic fibrosis in advanced cirrhosis: evaluation with MR imaging. Radiology 1993; 189:871-874
41. Ohtomo K, Baron RL, Dodd GD 3rd, et al. Confluent hepatic fibrosis in advanced cirrhosis: appearance at CT. Radiology 1993; 188:31-35
42. Pliskin M. Peliosis hepatis. Radiology 1975; 114:29-30
43. Ternberg JL, Butcher HR Jr. Blood flow relation between hepatic artery and portal vein obstruction. Science 1965; 150:1030-1031
44. Vignaux O, Legmann P, De Pinieux G, et al. Hemorrhagic necrosis due to peliosis hepatis: imaging findings and pathological correlation. Eur Radiol 1999; 9:454-456
45. Yanoff M, Rawson A. Peliosis hepatis: an anatomic study with demonstration of two varieties. Arch Pathol 1964; 77:159-165
46. Yoon KH, Ha HK, Lee JS, et al. Inflammatory pseudotumor of the liver in patients with recurrent pyogenic cholangitis: CT-histopathologic correlation. Radiology 1999; 211:373-379
47. Yoshimitsu K, Honda H, Kuroiwa T, et al. Unusual hemodynamics and pseudolesions of the non cirrhotic liver at CT. Radiographics 2001; 21:81-96
48. Yu JS, Rofsky NM. Magnetic resonance imaging of arterioportal shunts in the liver. Top Magn Reson Imaging 2002; 13:165-176

6

Imaging of Malignant Focal Liver Lesions

CONTENTS

6.1 Primary Malignant Liver Lesions

6.1.1 Hepatocellular Carcinoma

Hepatocellular carcinoma (HCC) is the most common primary hepatic malignancy and one of the most prevalent visceral malignances worldwide [21]. HCC usually occurs in the setting of cirrhosis with a known cause, such as chronic viral hepatitis or alcoholism. Regarding alcoholism as a cause of cirrhosis, it is thought that alcoholism promotes hepatic malignancies indirectly via its immunosuppressive effects. These effects facilitate the development of hepatitis B virus (HBV) and hepatitis C virus (HCV) infections. Furthermore, alcoholic cirrhosis is triggered by the well-known oxidative effects that deplete the anti-oxidative defense system [35]. Whereas in Asia HCC occurs almost exclusively in patients with chronic liver damage from hepatitis, in North America many patients develop HCC without cirrhosis or known risk factors [74]. In these latter patients it is possible that steroid hormones may play a role in carcinogenesis, as tumors occurring in non-cirrhotic livers have been associated with the use of exogeneous steroids such as anabolic steroids and oral contraceptives, as well as with genetic factors [52]. Environmental and dietary factors are known to play major etiological roles; in this context aflatoxins, nitrosamines, and other chemical carcinogens have been implicated in non-cirrhotic HCC [18, 22]. HCC is much more common among males than females. In high-incidence countries, the male-to-female ratio may be as high as 7 or 8 : 1, but in the United States, it is approximately 2 : 1 [57]. The occurrence of HCC increases progressively with age, although again this varies by country. Thus, in high-incidence countries, the mean age at diagnosis is in the third decade of life, while in low-incidence countries, it occurs 2 to 3 decades later. HCC is well documented in childhood; most childhood cases are associated with HBV infection or metabolic diseases, such as tyrosinemia [49].

Chronic liver disease, including liver cirrhosis, is one of the most important factors in HCC, which is characterized by the development of a spectrum of nodules ranging from benign regenerative nodules to overt HCC.

In carcinogenesis of the cirrhotic liver, the first step in the development of an overt HCC may be the formation of a benign regenerative nodule which then develops in a multistep fashion through the intermediate phases of ordinary low-grade dysplastic nodule (LGDN), high-grade dysplastic nodule (HGDN), and early HCC [90, 17].

Since dysplastic nodules (DNs) containing malignant foci and early well-differentiated HCC contain a great deal of fat, it has been postulated that fat deposition in dysplastic nodules is closely related to malignancy [53]. The same author reported that 20% of liver specimens resected with the diagnosis of HCC contained DNs and 40% of those DNs were HGDNs or DNs containing foci of HCC. The presence of DNs containing foci of HCC rep-

resents strong evidence that DNs are premalignant lesions [53].

Microscopically, HCC is composed of malignant hepatocytes that attempt to differentiate into normal liver structures, mimicking hepatocyte growth, but are unable to form normal hepatic acini. In well-differentiated HCC, tumor cells are difficult to distinguish from normal hepatocytes or hepatocytes in hepatocellular adenoma. Malignant hepatocytes may even produce bile. In other cases, there are microscopic variations, with HCC containing fat, tumoral secretions (large amounts of watery material), fibrosis, necrosis and amorphous calcification [73].

The most frequent pattern of HCC is the trabecular pattern, in which the tumor cells grow in thick cords that attempt to recapitulate the cell-plate pattern seen in normal liver tissue. The trabeculae are separated by vascular spaces with very little or no supporting connective tissue. Sometimes tumor secretions are in the center of the trabeculae, giving the tumor a pseudoglandular pattern. If the trabeculae grow together, they produce a solid pattern [71].

Macroscopically, there are also several patterns of growth. HCC is designated single or massive when there is a solitary small or large mass, with or without a capsule. Multiple separate nodules characterize multifocal HCC, the second most common pattern. The least common pattern of diffuse or cirrhotomimetic growth is multiple small tumoral foci distributed throughout the liver, mimicking nodules of cirrhosis. HCC is described as encapsulated when it is completely surrounded by a fibrous capsule. Encapsulated HCC has better prognosis due to its greater resectability. In general, vascular invasion of intrahepatic and perihepatic vessels is common in HCC [24, 86].

The symptoms associated with HCC include malaise, fever, abdominal pain, and weight loss, while jaundice is rare [86]. Often the neoplasm is detected in asymptomatic patients, and the liver function tests are normal or slightly altered except for elevation of α-fetoprotein levels. These values are high in more than 50% of cases and generally are considered suggestive of HCC when they exceed 200 ng/ml. Proteins produced by HCC may give rise to numerous paraneoplastic syndromes such as erythrocytosis, hypercalcemia, hypoglycemia and hirsutism [49]. Several investigators [74, 104] have consistently reported that HCC occurring in the non-cirrhotic liver has different features: patients are younger and are more likely to present with symptoms. Frequently, these patients have a single or dominant mass and have reduced mortality if liver resection is performed [95].

Ultrasound (US) is considered a screening method for patients at risk of HCC, and often detects neoplasms smaller than 2–3 cm (the so-called "small HCC"), even when α-fetoprotein levels are still normal. On US scans, the echogenicity of the HCC neoplasm varies with the size of the lesion. Thus, nodules smaller than 3 cm are usually well-defined, hypoechoic, and homogeneous, with posterior acoustic enhancement (Fig. 1). Conversely, lesions larger than 3 cm are often heterogeneous, with a mosaic or mixed pattern arising from a combination of areas of necrosis, hemorrhage, fatty degeneration and interstitial fibrosis (Fig. 2). In the diffuse form, tumor infiltration tends to cause a disruption of the hepatic echo structure [16]. When visible, the capsule of an encapsulated HCC usually appears as a thin, hypoechoic, peripheral band with characteristic lateral acoustic shadows [86].

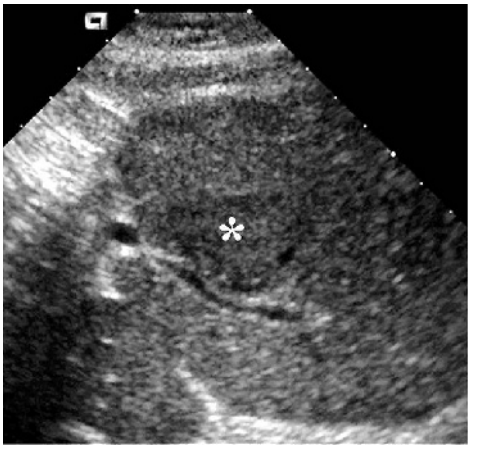

Fig. 1. Well-differentiated hepatocellular carcinoma. Ultrasound reveals a well-defined, homogeneous, and hypoechoic lesion (*asterisk*)

Color Doppler US sometimes reveals a "basket" pattern, which is indicative of hypervascularity and tumor shunting, and the "vessel within the tumor" pattern, with vessels that have peripheral-to-central directed flow (Fig. 3). Power Doppler US is often considered superior to color Doppler US for the depiction of vascular flow because of its high sensitivity to slow flow, lack of angle dependency, and absence of aliasing [59]. Recently, various harmonic imaging techniques, such as tissue harmonic imaging, harmonic power Doppler US, and color coded harmonic angiography, have been developed and used, also in combination with contrast media such as SonoVue, to improve the characterization of HCC.

The goal of contrast-enhanced US (CEUS) in cirrhotic patients is the differentiation of HCC from regerative nodules (RNs) and DNs (Fig. 4). On CEUS, the characteristic pattern of HCC is represented by an intense and fast peak of enhancement in the arterial phase, followed by a relatively quick wash-out (Fig. 5). Chaotic peritumoral and intralesional tortuous vessels may be seen in the arterial phase and feeding vessels can be identified in most cases [14, 48, 50].

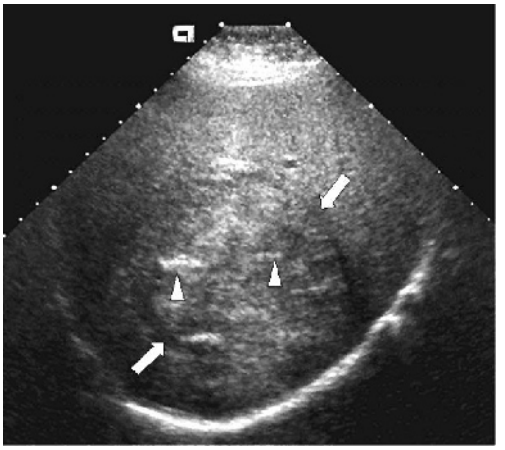

Fig. 2. Moderately-differentiated hepatocellular carcinoma. On ultrasound, the lesion is heterogeneous with hypoechoic and hyperechoic areas (*arrowheads*). A thin, hypoechoic rim corresponding to a pseudocapsule borders the lesion (*arrows*)

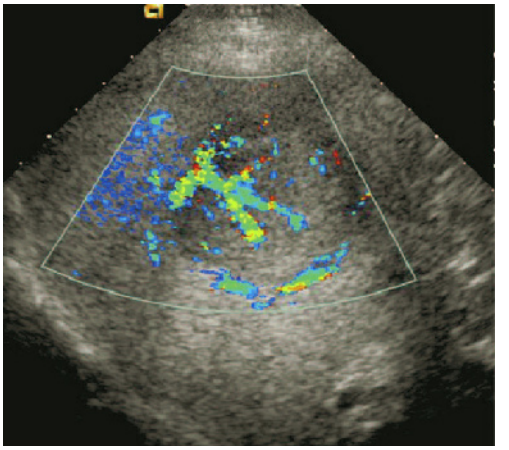

Fig. 3. Hepatocellular carcinoma on color Doppler. Color Doppler ultrasound reveals internal vascularization and a peritumoral hypervascular rim giving the characteristic 'basket' pattern. The vessels flow from the periphery through the center

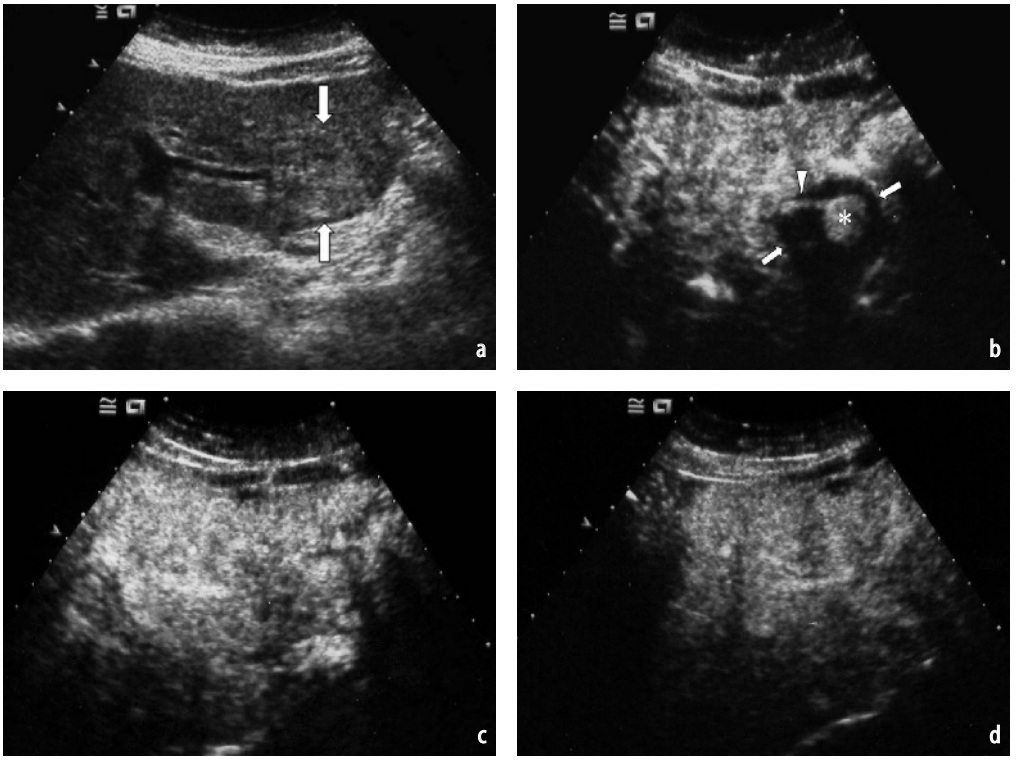

Fig. 4a-d. Dysplastic nodule with focus of hepatocellular carcinoma with SonoVue®. On the pre-contrast US scan (**a**), a heterogeneous isoechoic nodule is demonstrated (*arrows*). In the arterial phase of the dynamic evaluation after SonoVue® administration (**b**) the lesion (*arrows*) appears hypoechoic at the periphery with a hyperechoic central nodule representing a focus of hepatocellular carcinoma (*asterisk*). The feeding vessel supplying the hepatocellular carcinoma is also shown (*arrowhead* in **b**). The lesion becomes isoechoic in the portal-venous (**c**) and equilibrium (**d**) phases

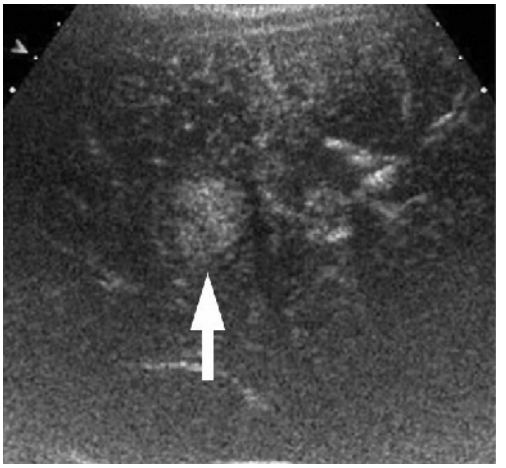

Fig. 5. Hepatocellular carcinoma on contrast-enhanced ultrasound: During the arterial phase, after the bolus injection of Sonovue®, the lesion shows intense and homogeneous enhancement, and becomes hyperechoic (*arrow*). Hyperechogenicity reflects the hypervascular nature of the tumor

On CT scans, the appearance of HCC depends largely on tumor size and histologic tumor grade, with low sensitivity for detection of small neoplasms that are difficult to differentiate from unopacified vessels [38]. Unenhanced CT scans often reveal a hypodense nodule. Occasionally, central areas of lower attenuation corresponding to tumor necrosis can be seen [51]. Small HCCs have a proportionately greater arterial hepatic blood supply and, as a result, they may be visible only on hepatic arterial phase images. They tend to demonstrate hyperattenuation on early arterial phase images and rapid wash-out in the subsequent portal-venous phase (Fig. 6) [76]. In larger lesions, the portal vein may also contribute significantly to the blood supply of the HCC, enabling its visualization on portal-venous phase images as well [45]. However, because large tumors may contain areas of hemorrhage or necrosis, they may be seen as either hyper- or hypoattenuating compared with the surrounding liver tissue during the arterial phase of hepatic enhancement, and as hypoattenuating in the portal-venous phase (Fig. 7). Nodular HCCs possess a peripheral capsule in about 50 to 80% of cases (Fig. 8) [32, 51, 70, 80].

Non-encapsulated tumors frequently appear as ill-defined, irregular, often hypervascular masses, showing a variable degree of vascular or bile duct infiltration (Fig. 9).

The role of CT in the detection of dysplastic nodules in the cirrhotic liver has been evaluated in several studies [37, 61]. These studies indicate that many DNs are isoattenuating to the adjacent liver parenchyma and thus cannot be detected on CT scans because the blood supply to these nodules is similar to that of the normal liver parenchyma.

On MR imaging, DNs are usually hyperintense on T1-weighted images, and iso- to hypointense on T2-weighted images. Conversely, HCCs are often hyperintense on T2-weighted images, and hypointense on T1-weighted images. However several studies [15, 54, 70] have stated that an accurate distinction between DNs and HCCs cannot usually be made on the basis of signal intensity characteristics on unenhanced MR, because of the overlapping signal intensities from multiple nodules.

DNs, particularly LGDNs, do not usually show significant arterial enhancement after the bolus injection of gadolinium contrast agents, however in about 5% of HGDNs arterial enhancement can be detected, possibly because of neoangiogenesis (Figs. 10, 11, 12). On delayed phase images acquired after the administration of hepatobiliary contrast agents, DNs generally show a contrast agent uptake similar to that observed in the surrounding parenchyma. Since DNs contain identical or slightly increased numbers of Kupffer cells compared to the normal liver parenchyma, they are not readily seen on T2-weighted fast spin-echo images acquired after the administration of superparamagnetic iron oxide (SPIO) contrast material [62].

Contrast-enhanced dynamic MR imaging is an important tool for differentiating DNs, DNs with a focus of HCC, and overt HCC (Fig. 13). Indeed, contrast-enhanced dynamic MR is useful for the detection and characterization of HCCs in general [69]. Generally, most HCCs, because of their hypervascular nature, are homogeneously hyperintense compared to the liver in the arterial phase, and hypointense in the portal-venous and equilibrium phases. Tumors smaller than 3 cm in diameter tend to show a homogeneous enhancement (Fig. 14), and in about 20% of cases are visible mainly in the arterial phase (Fig. 15).

Irregular mosaic-like or peripheral enhancement is usually seen in larger neoplasms, depending on the internal architecture [82, 106, 107].

In moderately differentiated trabecular or pseudo-glandular HCCs, a peak of enhancement is usually seen during the arterial phase, followed by a rapid decrease during the subsequent portal-venous and equilibrium phases. Gradually increasing enhancement over time is found in poorly-differentiated scirrhous HCCs, whereas minimal or no contrast enhancement is seen in small, well-differentiated neoplasms. Sometimes a mixture of variably-differentiated areas may be found in large HCCs (Fig. 16).

Dynamic MR imaging is also helpful for the assessment of HCC pseudocapsules (Figs. 10, 14). When present, HCC pseudocapsules containing abundant granulation tissue usually enhance

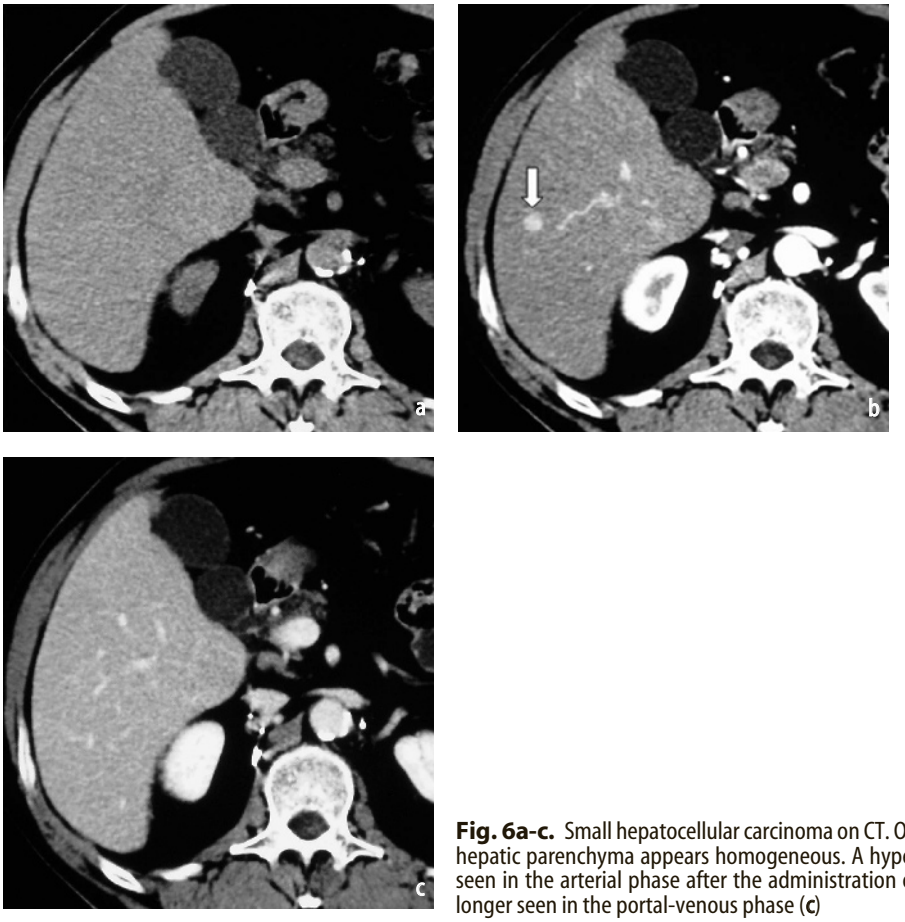

Fig. 6a-c. Small hepatocellular carcinoma on CT. On the unenhanced CT scan (**a**) the hepatic parenchyma appears homogeneous. A hypervascular nodule (*arrow*) can be seen in the arterial phase after the administration of contrast material (**b**) but is no longer seen in the portal-venous phase (**c**)

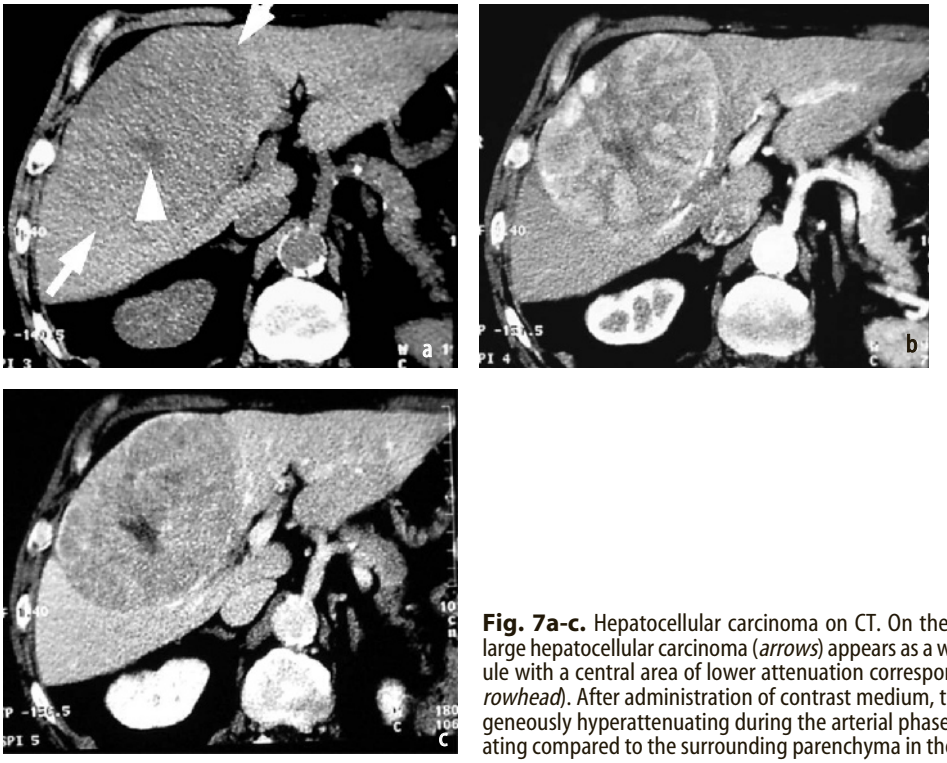

Fig. 7a-c. Hepatocellular carcinoma on CT. On the unenhanced CT scan (**a**), a large hepatocellular carcinoma (*arrows*) appears as a well-defined hypodense nodule with a central area of lower attenuation corresponding to tumor necrosis (*arrowhead*). After administration of contrast medium, the nodule is seen as heterogeneously hyperattenuating during the arterial phase (**b**), becoming hypoattenuating compared to the surrounding parenchyma in the portal-venous phase (**c**)

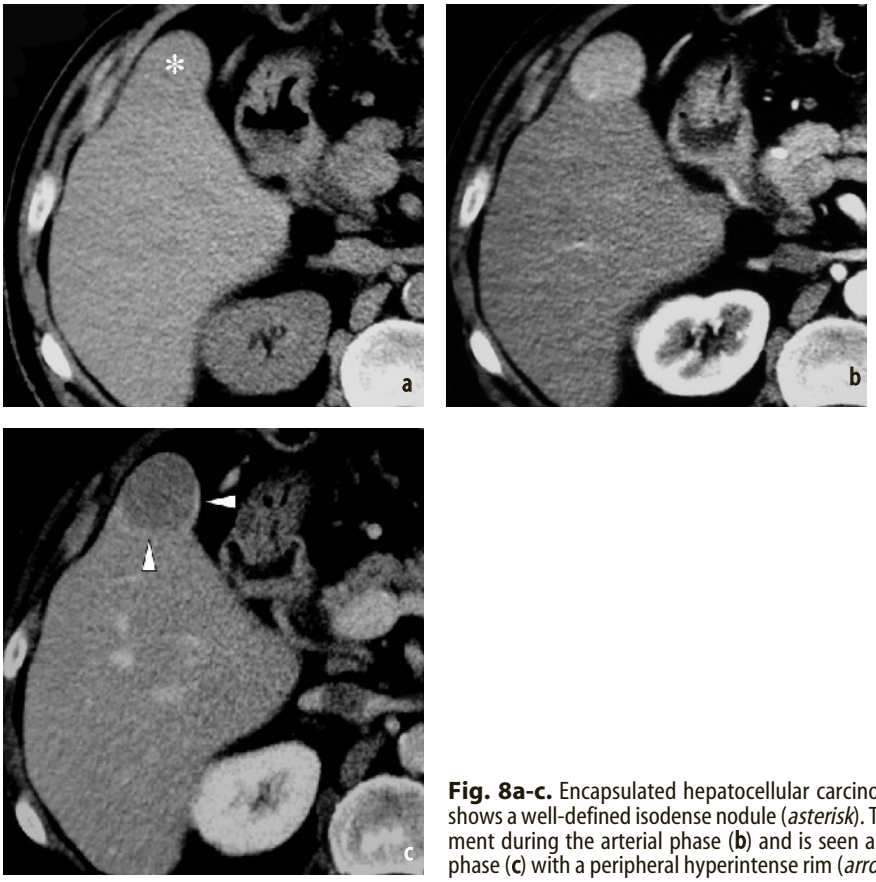

Fig. 8a-c. Encapsulated hepatocellular carcinoma. The unenhanced CT scan (**a**) shows a well-defined isodense nodule (*asterisk*). The lesion shows discrete enhancement during the arterial phase (**b**) and is seen as hypodense in the portal-venous phase (**c**) with a peripheral hyperintense rim (*arrowheads*)

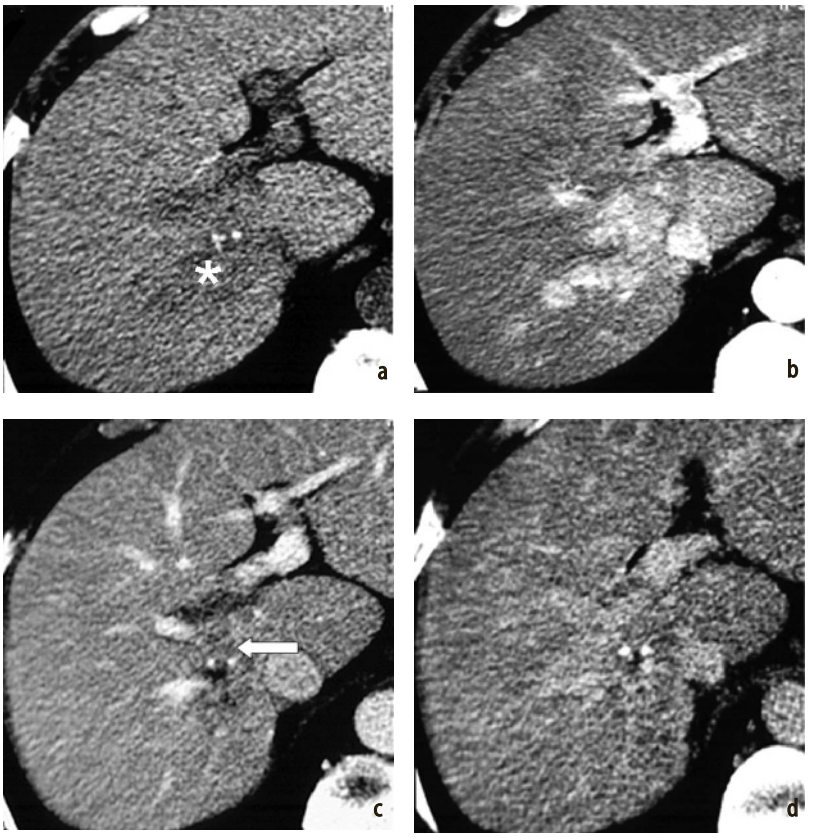

Fig. 9a-d. Non-encapsulated hepatocellular carcinoma. On the unenhanced CT scan (**a**) the nodule (*asterisk*) is seen as an ill-defined hypodense mass. The lesion enhances markedly during the arterial phase after the administration of contrast material (**b**) and subsequently shows right portal vein infiltration (*arrow*) in the portal-venous phase (**c**). During the equilibrium phase (**d**) the lesion becomes heterogeneously isodense

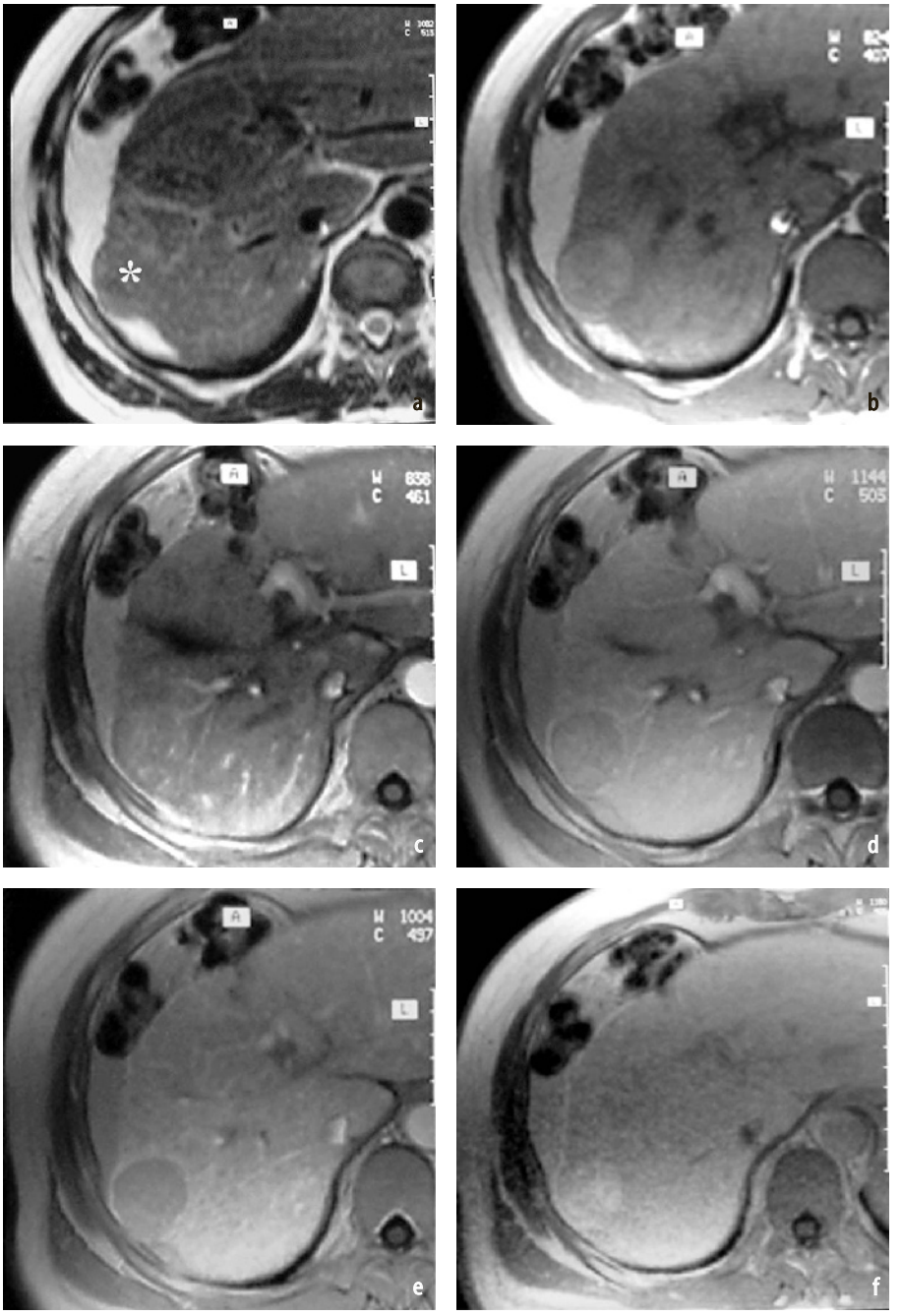

Fig. 10a-f. Dysplastic nodule. On the unenhanced T2-weighted image (**a**) the lesion (*asterisk*) is seen as isointense against the normal parenchyma, while on the corresponding T1-weighted image (**b**), it is seen as hyperintense. The lesion does not show significant enhancement on images acquired during the arterial phase after Gd-BOPTA administration (**c**), but reveals a thin enhancing peripheral rim during the portal-venous and equilibrium phases (**d** and **e**, respectively). In the delayed hepatobiliary phase (**f**) the dysplastic nodule demonstrates uptake of Gd-BOPTA

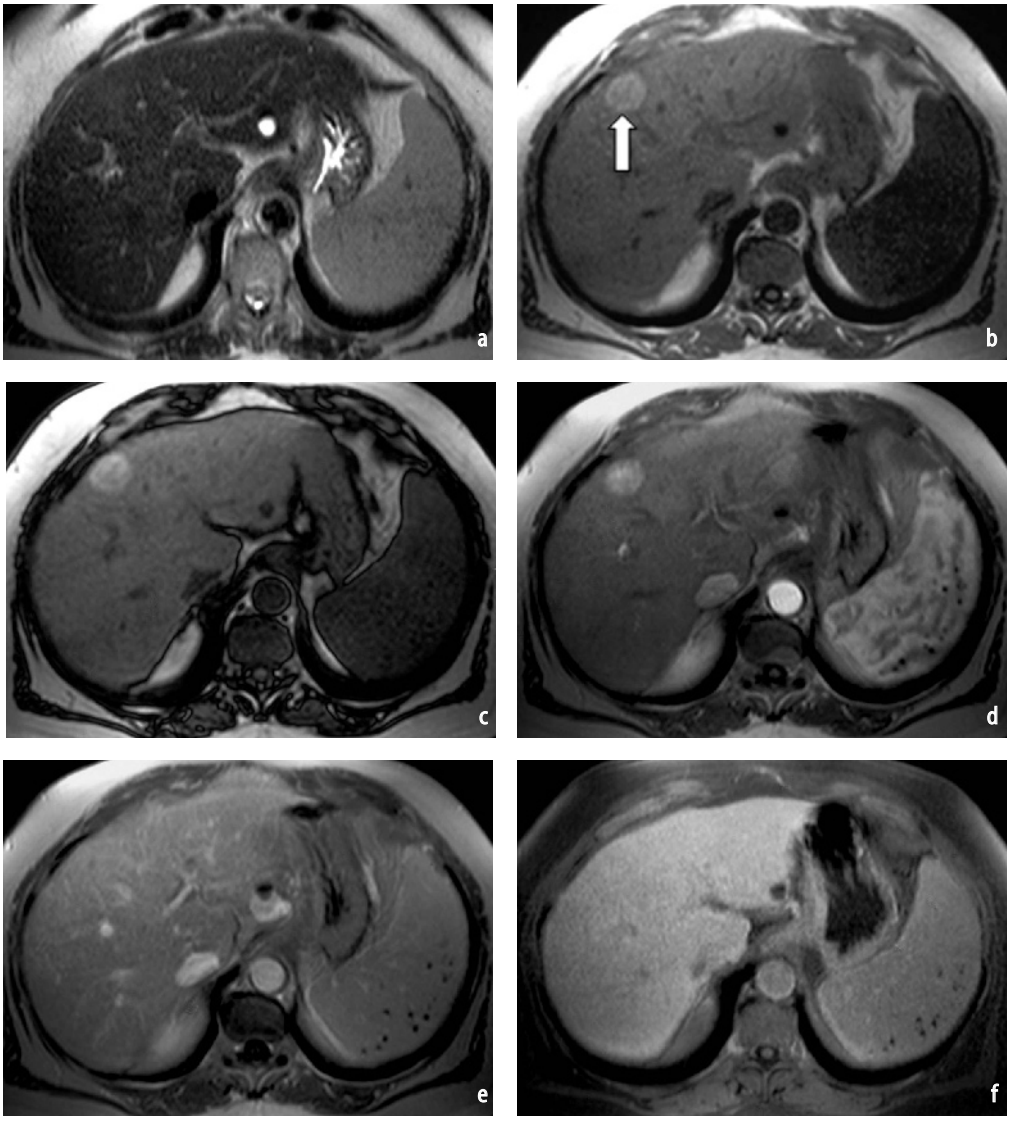

Fig. 11a-f. Dysplastic nodule. On the precontrast T2-weighted image (**a**) the lesion is isointense compared to the normal liver parenchyma, while on the GE T1-weighted "in-phase" (**b**) and "out-of-phase" (**c**) images the nodule (*arrow* in **b**) appears hyperintense due to an increased glycogen content. The nodule enhances during the arterial phase (**d**) after the bolus injection of hepatobiliary contrast agent Gd-BOPTA) but shows rapid wash-out of contrast agent during the subsequent portal-venous phase (**e**) rapid wash-out can be observed. On a T1-weighted fat suppressed GRE image in the delayed hepatobiliary phase (**f**) the lesion is isointense compared to the surrounding normal liver parenchyma

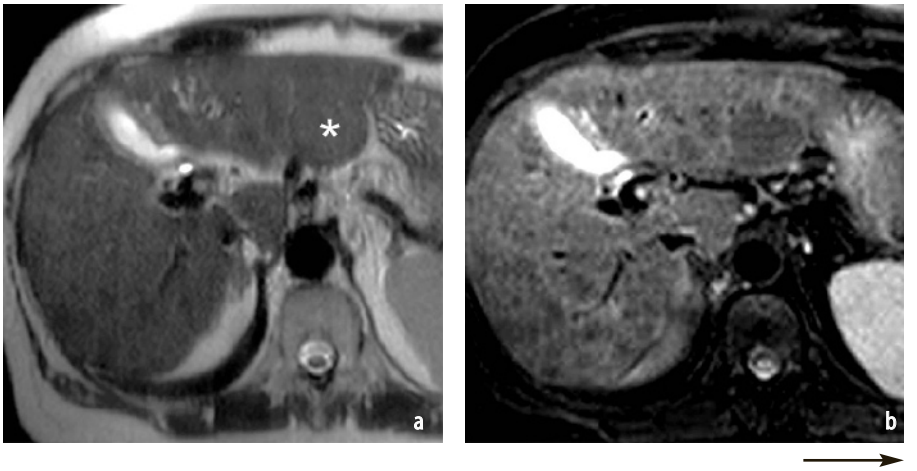

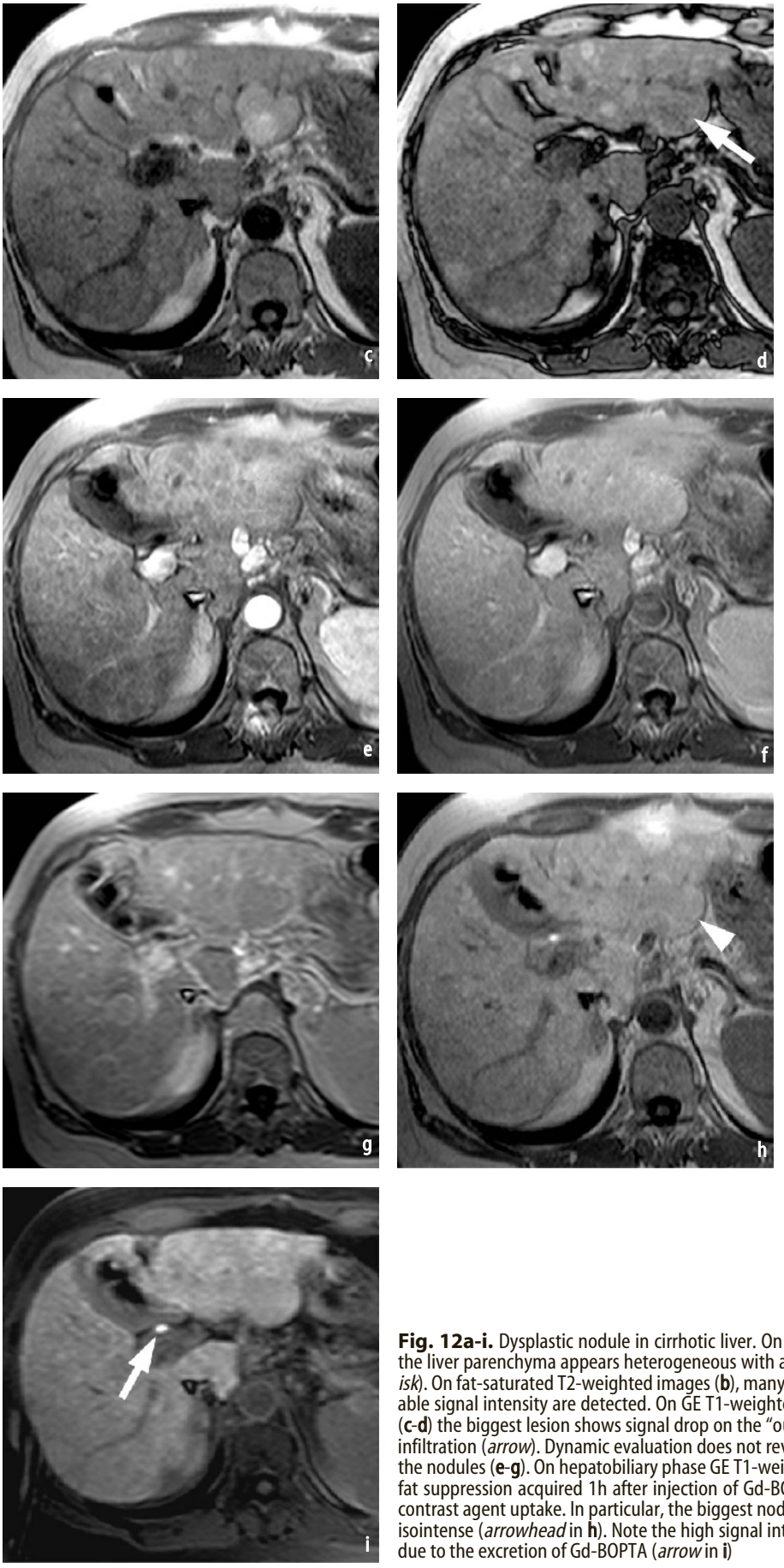

Fig. 12a-i. Dysplastic nodule in cirrhotic liver. On HASTE T2-weighted images (**a**) the liver parenchyma appears heterogeneous with a large isointense nodule (*asterisk*). On fat-saturated T2-weighted images (**b**), many hypointense nodules with variable signal intensity are detected. On GE T1-weighted in- and out-of-phase images (**c**-**d**) the biggest lesion shows signal drop on the "out-of-phase" image due to fatty infiltration (*arrow*). Dynamic evaluation does not reveal significant enhancement of the nodules (**e**-**g**). On hepatobiliary phase GE T1-weighted images with and without fat suppression acquired 1h after injection of Gd-BOPTA (**h**-**i**), many nodules show contrast agent uptake. In particular, the biggest nodule in the left liver lobe appears isointense (*arrowhead* in **h**). Note the high signal intensity in the common bile duct due to the excretion of Gd-BOPTA (*arrow* in **i**)

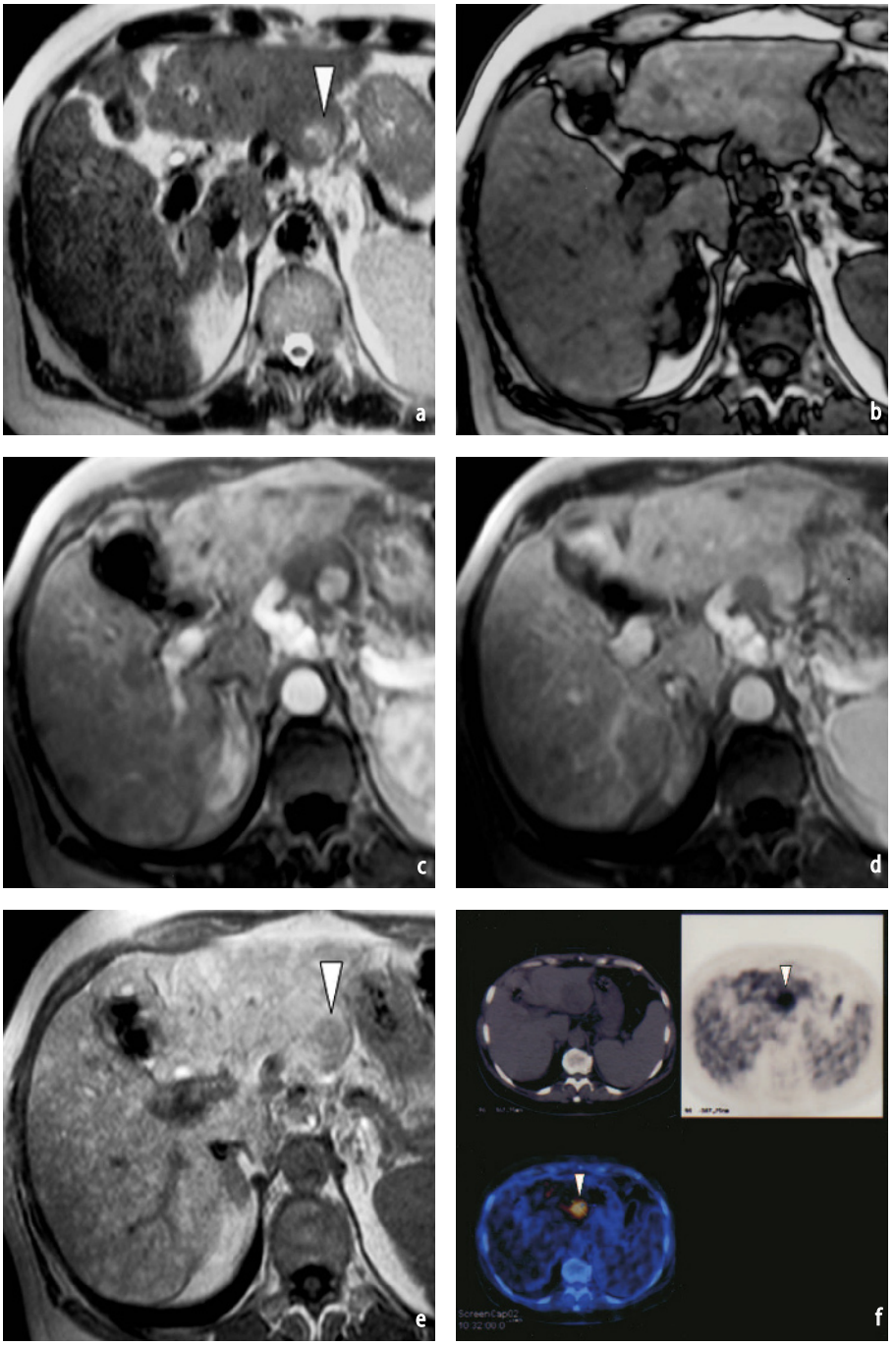

Fig. 13a-f. Dysplastic nodule with focus of hepatocellular carcinoma. This figure shows the same case as Fig.12, on a follow-up study one year later. On the precontrast T2- weighted image (**a**) the nodule now contains a heterogeneous hyperintense area (*arrowhead*) that appears slightly hypointense on the T1-weighted GE "out-of-phase" image (**b**). During the dynamic study after the bolus administration of Gd-BOPTA, the lesion shows enhancement of the internal portion in the arterial phase (**c**) with a "nodule within nodule" aspect. Discrete wash-out of contrast agent is apparent in the portal-venous phase (**d**). On the hepatobiliary phase T1-weighted image (**e**) the nodule is heterogeneous in signal intensity, the hypointense area (*arrowhead*) corresponds to a focus of hepatocellular carcinoma. A PET-CT scan (**f**) confirms the presence of a hot-spot area within the lesion (*arrowhead*)

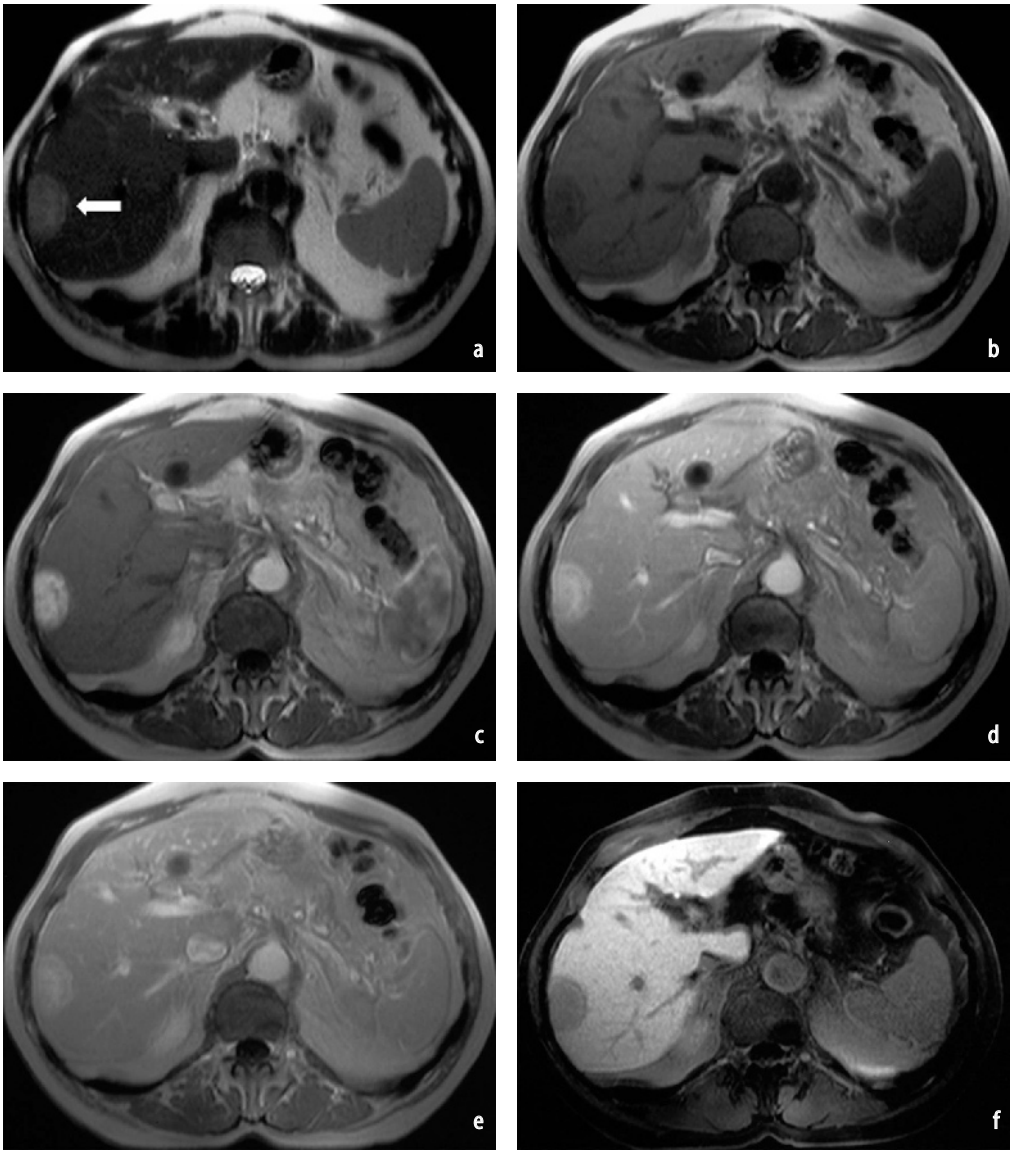

Fig. 14a-f. Hepatocellular carcinoma. On the unenhanced T2-weighted image (**a**) the lesion appears hyperintense (*arrow*), while on the unenhanced T1-weighted image (**b**) the nodule is slightly hypointense with a thin hypointense peripheral rim. In the arterial phase after the bolus administration of Gd-BOPTA (**c**) the mass becomes heterogeneously hyperintense due to hypervascularization, whereas the peripheral rim remains hypointense. In the portal-venous phase (**d**) the contrast agent persists within the lesion and the pseudocapsule becomes hyperintense as well. During the equilibrium phase (**e**) the nodule appears slightly hyperintense and well-circumscribed by a peripheral hyperintense pseudocapsule. In the delayed hepatobiliary phase (**f**) the neoplasm appears homogeneously hypointense and well-delineated, since unlike normal liver hepatocytes, the malignant hepatocytes of the hepatocellular carcinoma are unable to take up the contrast agent

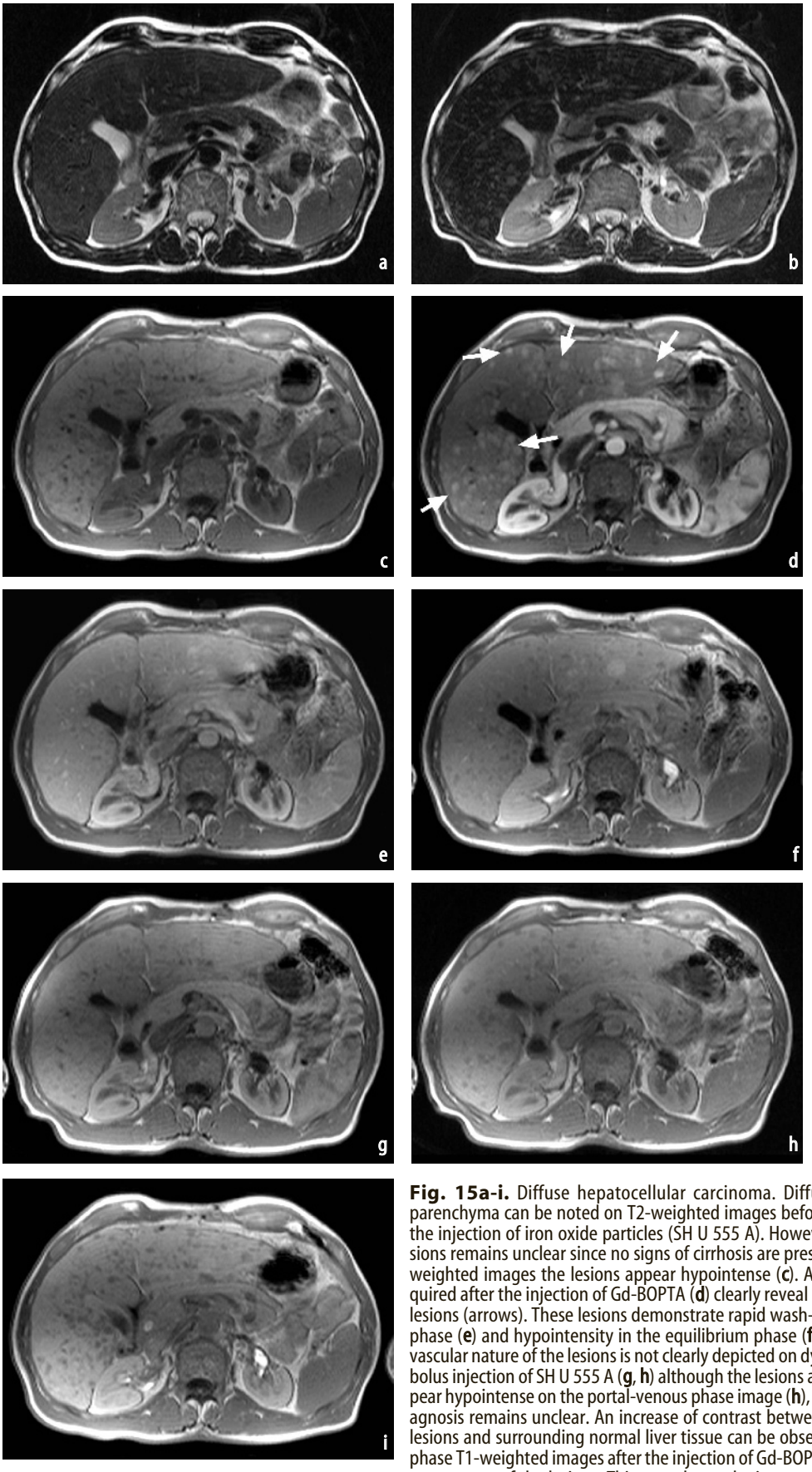

Fig. 15a-i. Diffuse hepatocellular carcinoma. Diffuse lesions in the liver parenchyma can be noted on T2-weighted images before (**a**) as well as after (**b**) the injection of iron oxide particles (SH U 555 A). However, the nature of the lesions remains unclear since no signs of cirrhosis are present. On unenhanced T1-weighted images the lesions appear hypointense (**c**). Arterial phase images acquired after the injection of Gd-BOPTA (**d**) clearly reveal numerous hypervascular lesions (arrows). These lesions demonstrate rapid wash-out in the portal-venous phase (**e**) and hypointensity in the equilibrium phase (**f**). In contrast, the hypervascular nature of the lesions is not clearly depicted on dynamic imaging after the bolus injection of SH U 555 A (**g**, **h**) although the lesions are more obvious and appear hypointense on the portal-venous phase image (**h**), hence the differential diagnosis remains unclear. An increase of contrast between the hypointense liver lesions and surrounding normal liver tissue can be observed (**i**) on hepatobiliary phase T1-weighted images after the injection of Gd-BOPTA, indicating the malignant nature of the lesions. This case shows the importance of dynamic imaging for differential diagnosis, since the only clue towards diagnosis in a patient without obvious signs of liver cirrhosis is the hypervascular nature of the lesions

prominently in the portal-venous phase. Thereafter, enhancement persists with signs of wash-out into the equilibrium phase due to slow flow in the abundant blood vessels that are present in fibrous tissue (Fig. 17) [32]. With regard to the delayed phase, several authors have shown that heterogeneous delayed retention of contrast agent in HCC is not specific to particular tumors, and may correspond to abundant fibrous stroma, as found in scirrhous HCC [28, 82].

In the delayed liver-specific phase after Gd-BOPTA, well-differentiated and moderately-differentiated HCCs show superior signal enhancement ratios to poorly differentiated HCCs [31, 64]. This is likely to be a consequence of the first two neoplastic forms retaining sufficient residual hepatocytic activity to take up Gd-BOPTA. These forms may also produce bile, which may also correlate with the degree of contrast enhancement. Nevertheless, fewer than 20% of well-differentiated and moderately-differentiated HCCs appear iso- or hyperintense on hepatobiliary phase images after administration of Gd-BOPTA (Fig. 18); most poorly-differentiated (Fig. 19) and large HCCs are hypointense compared to the normal liver on delayed, hepatobiliary phase images (see also Fig. 17).

SPIO agents are helpful for detecting small HCCs in cirrhotic livers. A recent report [40] investigated the relationship between the number of Kupffer cells in HCCs and DNs and the degree of SPIO uptake. This study showed that the ratio between the number of Kupffer cells in tumorous versus non-tumorous tissue decreased with the degree of cellular differentiation. Thus, the ratio of the signal intensity of the neoplastic lesion compared with that of the non-neoplastic area on SPIO-enhanced imaging correlated well with the number of Kupffer cells present (Figs. 20, 16).

On dynamic T1-weighted imaging after the bolus administration of SH U 555 A, the hypervascularity of HCC nodules can be visualized in the early arterial phase as a moderate hyperintense signal due to the T1-effect of this agent. Using a dynamic T2-weighted protocol, a sudden drop-out phenomenon can be observed in hypervascular HCCs after administration of SH U 555 A, with a rapid signal loss in the perfusion phase followed by a short increase in signal intensity. On the delayed phase images after administration of SH U 555 A, poorly-differentiated HCCs generally do not show significant contrast medium uptake and thus appear hyperintense (Fig. 21). Conversely, well-differentiated HCCs may show a variable degree of signal drop due to the presence of Kupffer cells within the lesion [34].

HCC generally do not show significant uptake of mangafodipir trisodium (Mn-DPDP) and thus appear as hypointense masses against enhanced normal parenchyma on mangafodipir-enhanced T1-weighted images [68]. However, well-differentiated HCCs may show uptake of Mn^{++} (Figs. 22, 23). Unfortunately, considering only the hepatobiliary phase, other malignant lesions, such as metastases of neuroendocrine tumors or benign lesions, such as hepatic adenoma or FNH, may also present a similar uptake, and thus differential diagnosis may be difficult. Although mangafodipir is sometimes employed to differentiate benign hepatocellular lesions from non-hepatocellular tumors, a dynamic imaging capability usually provides important additional information for the characterization of focal liver lesions (Fig. 24). Thus, dual MR contrast agents such as Gd-BOPTA or Gd-EOB-DTPA that allow both dynamic and hepatocyte-specific imaging may be of greater benefit.

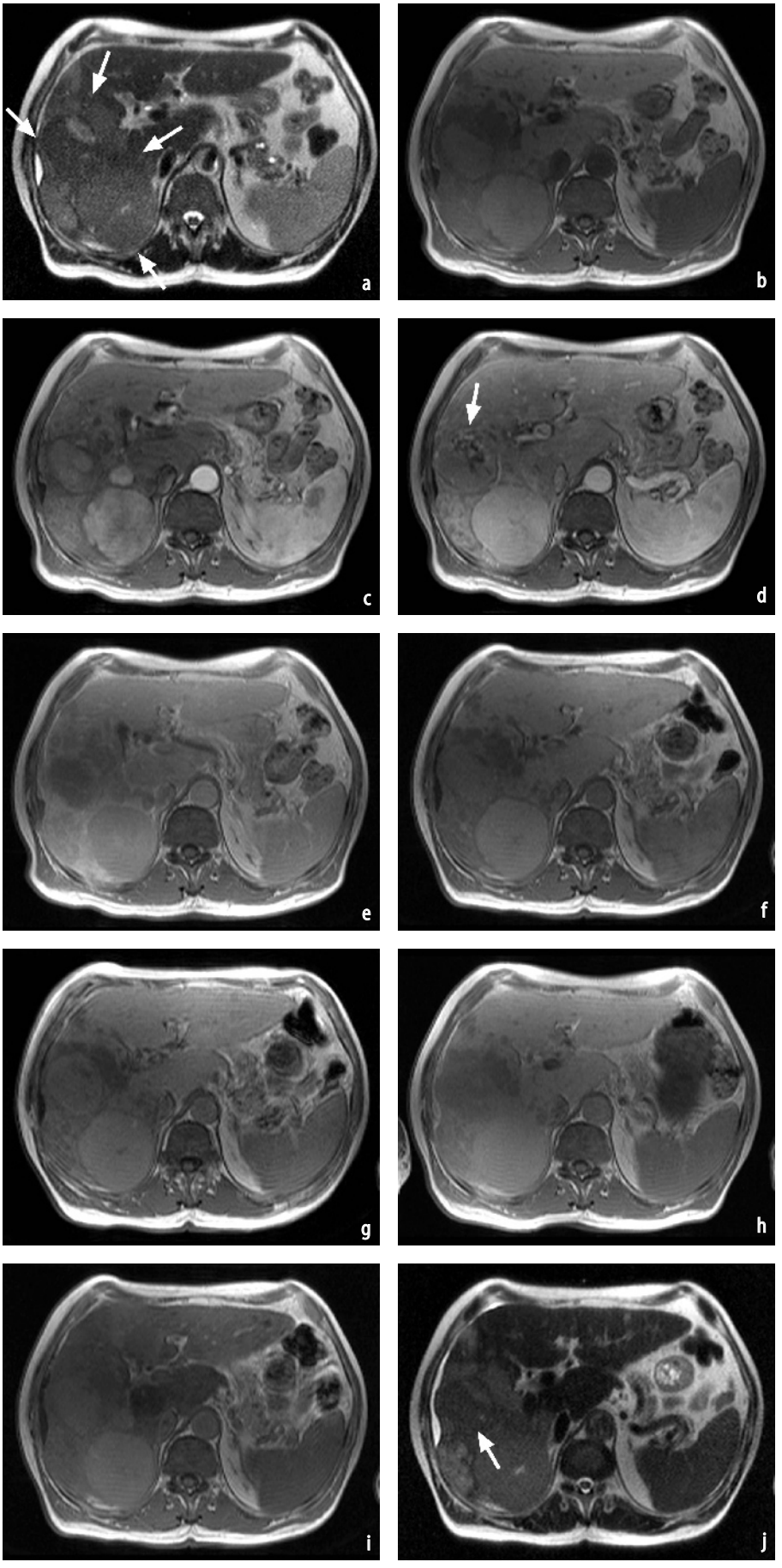
a
b
c
d
e
f
g
h
i
j

Fig. 16a-j. Hepatocellular carcinoma with different stages of differentiation. On unenhanced T2-weighted images (**a**) a large heterogeneously hyperintense lesion can be noted in the right liver lobe (*arrows*). On the corresponding T1-weighted image (**b**) the lesion again shows heterogeneous signal intensity with regions of hypo-, hyper- and isointensity. The hypervascularity of the lesion and the presence of numerous nodules is clearly depicted on arterial phase images after the bolus injection of Gd-BOPTA (**c**). In the portal-venous phase image (**d**), the more anterior aspect of the lesion demonstrates contrast agent wash-out (*arrow*), while the more posterior parts show contrast agent pooling. In the equilibrium phase (**e**) most of the lesion shows wash-out compared to normal liver tissue, thereby indicating a hepatocellular carcinoma. On arterial (**f**) and portal-venous (**g**) phase images after the injection of iron oxide particles (SH U 555 A) the hypervascular nature of the lesion cannot be appreciated to the same extent as after the application of a Gd-agent. In the hepatobiliary phase after the injection of Gd-BOPTA (**h**), parts of the lesion appear hypointense and others isointense compared to the surrounding liver tissue. This is indicative of both well-differentiated and undifferentiated areas of the hepatocellular carcinoma. The same holds true for iron oxide-enhanced T1-weighted (**i**) and T2-weighted (**j**) images in which parts of the lesion lose signal due to uptake of contrast agent by Kupffer cells (*arrow*) while other parts show higher signal intensity compared to normal liver tissue due to the lack of uptake

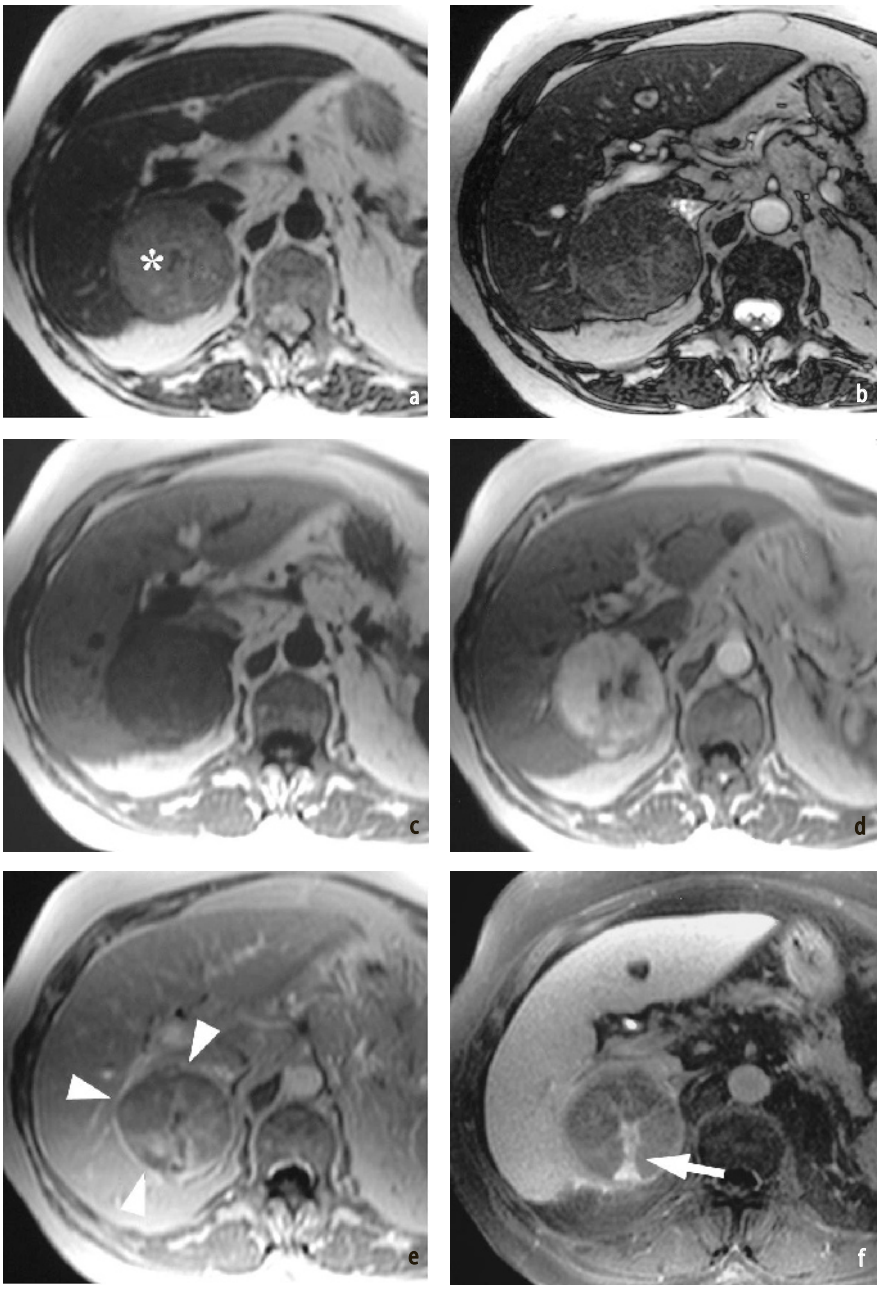

Fig. 17 a-f. Large hepatocellular carcinoma. On T2-weighted HASTE (**a**) and TrueFISP (**b**) images the hepatocellular carcinoma (*asterisk*) appears as a heterogeneous, slightly hyperintense mass. Conversely, on the unenhanced GE T1-weighted image (**c**) the lesion is seen as markedly hypointense. In the arterial phase, after the administration of Gd-BOPTA (**d**) the mass appears as heterogeneously hyperintense while in the portal-venous phase (**e**) it is heterogeneously hypointense with a well-defined peripheral hyperintense pseudocapsule (*arrowheads*). In the delayed hepatobiliary phase (**f**), the lesion is again hypointense due to the lack of contrast medium uptake by the malignant hepatocytes. A rim of intermediate signal intensity surrounds the lesion while central areas of necrosis show non-specific contrast agent retention (*arrow*)

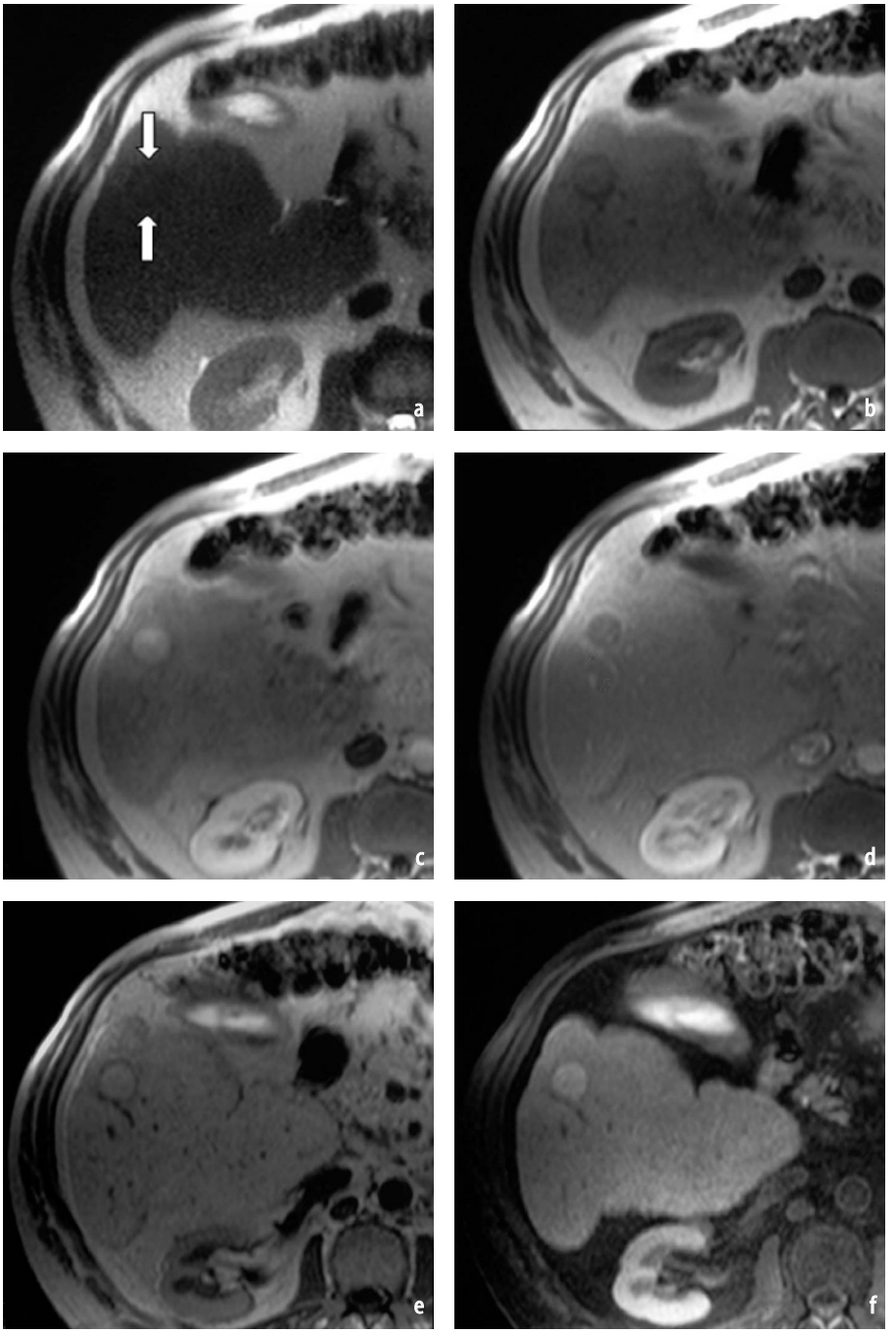

Fig. 18a-f. Well-differentiated hepatocellular carcinoma. On the precontrast T2-weighted image (**a**) the nodule (*arrows*) appears isointense compared to the normal liver parenchyma, with a thin peripheral rim. On the corresponding precontrast GE T1-weighted image (**b**) the lesion appears isointense with a hypointense rim. The lesion shows marked enhancement in the arterial phase (**c**) of the dynamic series after the bolus administration of Gd-BOPTA, followed by rapid wash-out of contrast agent in the portal-venous phase (**d**). Note that a hyperintense pseudocapsule is well demonstrated on the portal-venous phase scan. On the hepatobiliary phase GE T1-weighted (**e**) and T1-weighted fat suppressed images (**f**), the nodule is isointense and hyperintense respectively. This example demonstrates that the malignant cells in a well-differentiated hepatocellular carcinoma sometimes retain the ability to take up the contrast agent and to produce bile

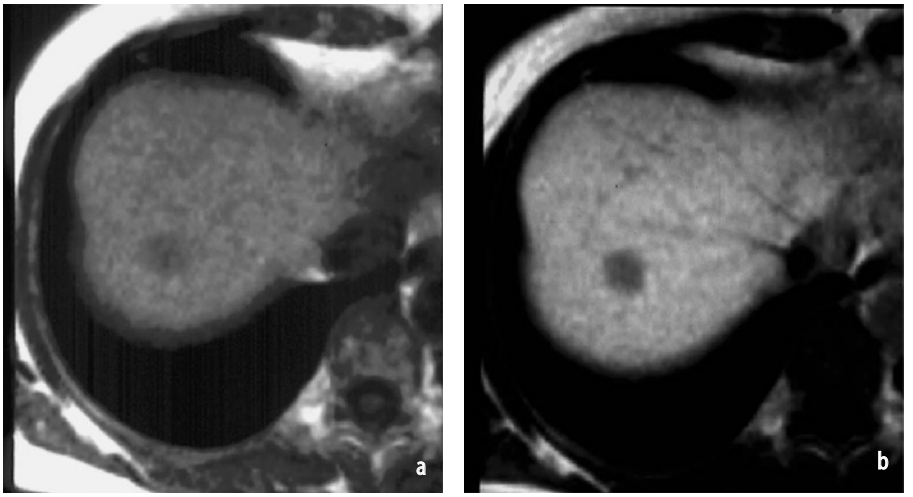

Fig. 19a, b. Poorly-differentiated hepatocellular carcinoma. On the unenhanced GE T1-weighted image (**a**) and on the image acquired during the delayed hepatobiliary phase after Gd-BOPTA administration (**b**) the nodule is seen as hypointense compared to the liver

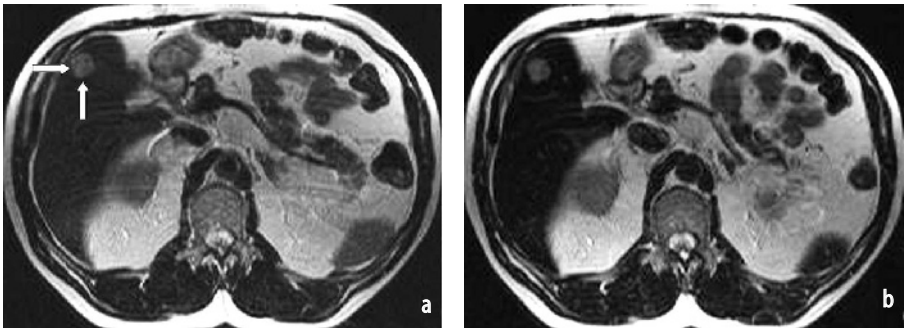

Fig. 20a, b. Hepatocellular carcinoma. On the unenhanced Turbo SE T2-weighted image (**a**) the nodule is well-defined and slightly hyperintense (*arrows*). On the image acquired during the delayed liver-specific phase after SPIO administration (**b**) the contrast-to-noise ratio is improved. The lesion does not show uptake of SPIO and remains hyperintense

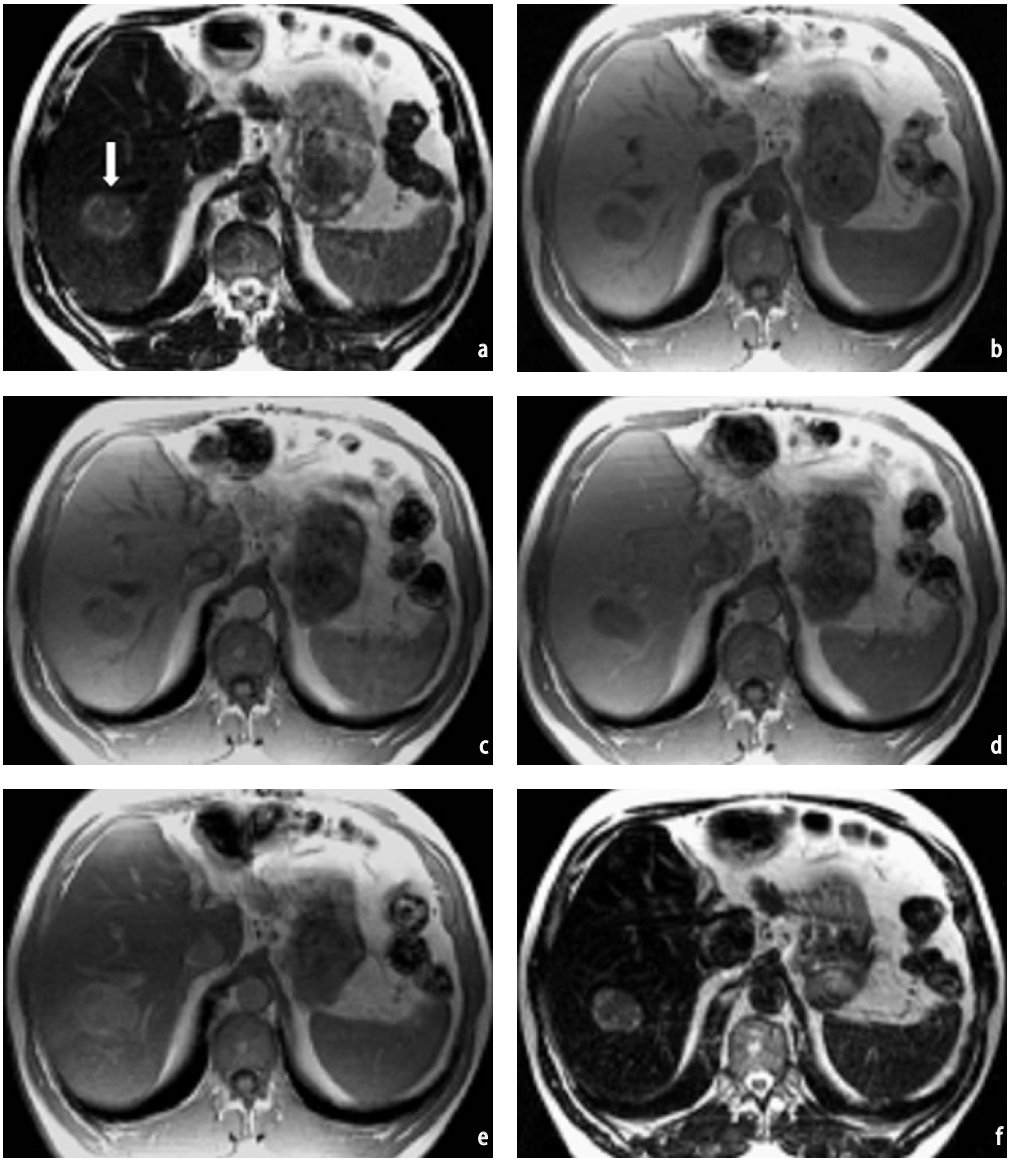

Fig. 21a-f. Poorly differentiated hepatocellular carcinoma with USPIO. On the precontrast T2-weighted image (**a**), a well-defined, round, slightly hyperintense nodule (*arrow*) is visible, while on the GRE T1-weighted sequence the lesion appears homogeneously hypointense (**b**). The dynamic evaluation after bolus injection of USPIO (**c**-**e**) reveals weak uptake of contrast medium, which is slightly more evident in the equilibrium phase (**e**). On a T2-weighted image acquired during the delayed liver specific phase after USPIO administration (**f**) the hepatocellular carcinoma appears hyperintense due to the lack of Kupffer cells within the lesion

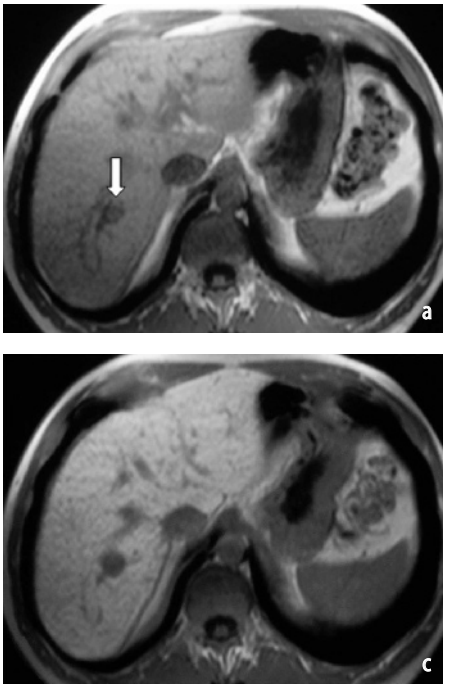

Fig. 22a-c. Hepatocellular carcinoma. The precontrast GRE T1-weighted image (**a**) reveals a small, well-defined hypointense nodule (*arrow*). The lesion (*arrow*) appears slightly hyperintense on the T2-weighted image (**b**). On the hepatobiliary phase image after Mn-DPDP administration (**c**) the nodule appears homogeneously hypointense compared to the surrounding normal liver parenchyma

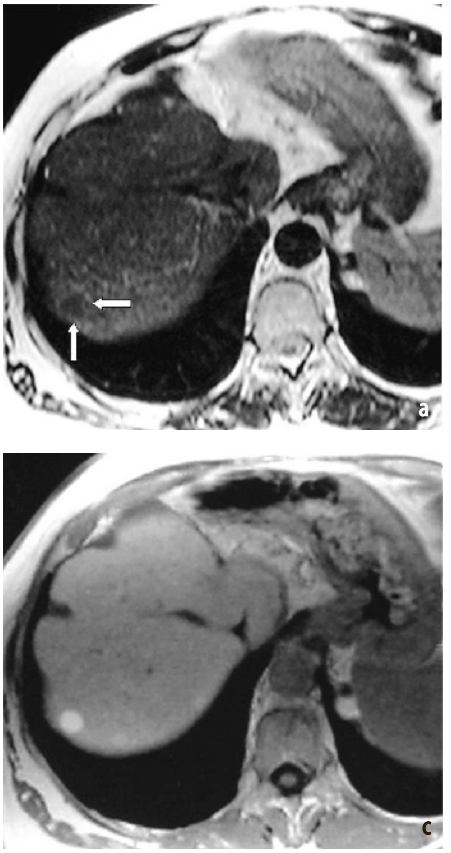

Fig. 23a-c. Hepatocellular carcinoma. On both the unenhanced T2-weighted image (**a**) and the unenhanced T1-weighted image (**b**) the nodule is slightly hypointense compared to the liver (*arrows* in **a**). The lesion is seen as strongly hyperintense on delayed phase images after mangafodipir administration (**c**) and no other lesions are visible

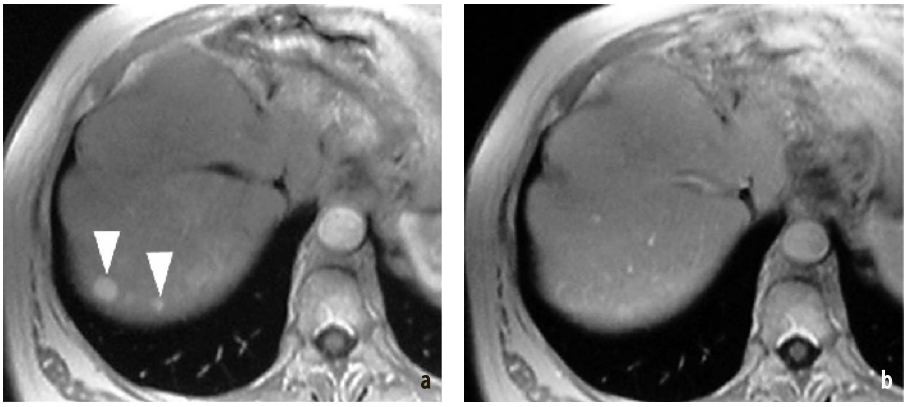

Fig. 24a, b. Hepatocellular carcinoma. The same case as presented in Fig. 23. In the arterial phase after the bolus administration of Gd-BOPTA (**a**), the lesion shows intense enhancement. Another small satellite nodule can be seen only in this phase of contrast enhancement (*arrowheads*). In the portal-venous phase (**b**) the larger lesion is seen as mildly hypointense with a slightly hyperintense rim, while the smaller lesion cannot be seen

6.1.2 Fibrolamellar Hepatocellular Carcinoma

Fibrolamellar hepatocellular carcinoma (FLC) is an uncommon tumor with clinical and pathological features different from those of hepatocellular carcinoma [19]. This neoplasm occurs predominantly in young adult patients, who have no history of cirrhosis or chronic liver disease [20]. Macroscopically, tumor size varies from 5 to 20 cm. The appearance of FLC is somewhat similar to that of focal nodular hyperplasia, with a central scar and multiple fibrous septa. Although hemorrhage is rare in FLC, necrosis and coarse calcifications have been reported in 20 to 60% of cases, especially in the central scar [20, 25, 39]. Most commonly, FLC is present as a solitary mass, although sometimes it may appear as bi-lobed or as a mass with small peripheral satellite lesions. Only rarely is FLC present as a diffuse multifocal mass. FLC lesions are usually intrahepatic, although sometimes pedunculated neoplasms may be found [97].

Histologically, FLC is composed of sheets of large polygonal tumor cells separated by abundant collagen bundles arranged in parallel lamellae. The tumor cells have a cytoplasm that is deeply eosinophilic and granular due to the presence of mitochondria. Sometimes FLCs contain bile [6, 72, 77].

The clinical presentation is variable, although patients commonly have abdominal pain, hepatomegaly, a palpable right upper quadrant abdominal mass, and cachexia [20]. Less frequently, the disease is accompanied by pain and fever, which simulates a liver abscess, gynecomastia in men, venous thrombosis, or jaundice. The gynecomastia is a result of the conversion of circulating androgens into estrogens by the enzyme aromatase, which is produced by the malignant hepatocytes.

Venous thrombosis can occur due to invasion of the hepatic venous system or the inferior caval vein. Alternatively, it may form part of a paraneoplastic syndrome (Trousseau syndrome). Jaundice is a very rare condition, and can be caused either by invasion or compression of the biliary vessels by the tumor or by compression of the biliary vessels by enlarged lymph nodes [1, 25].

The echostructure of this neoplasm is variable on US scans. Often the tumor contains both hyper- and iso-echogenic components, and thus is not homogeneous. The central scar, when present, is frequently seen as a central area of hyperechogenicity (Fig. 25) [10, 66].

On unenhanced CT images, FLC is usually seen as hypoattenuating compared to the liver and as well-defined with lobulated margins. Areas of low-density within the tumor correspond to the central scar or to necrosis and hemorrhage, while calcification may be seen in 15 to 30% of all central scars [39]. During the arterial and portal-venous phases after contrast material administration, FLC is predominantly, but heterogeneously, hyperattenuating

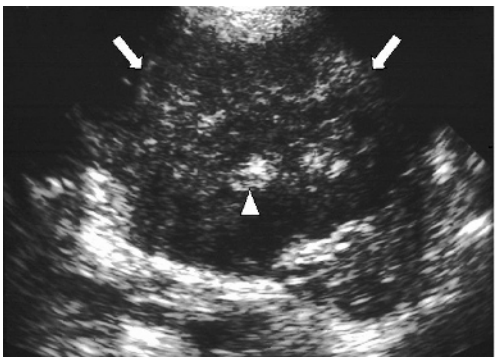

Fig. 25. Fibrolamellar carcinoma on US. Ultrasound reveals a heterogeneous hyper- to isoechoic lesion (*arrows*) with a hyperechoic central area (*arrowhead*) that corresponds to the central scar

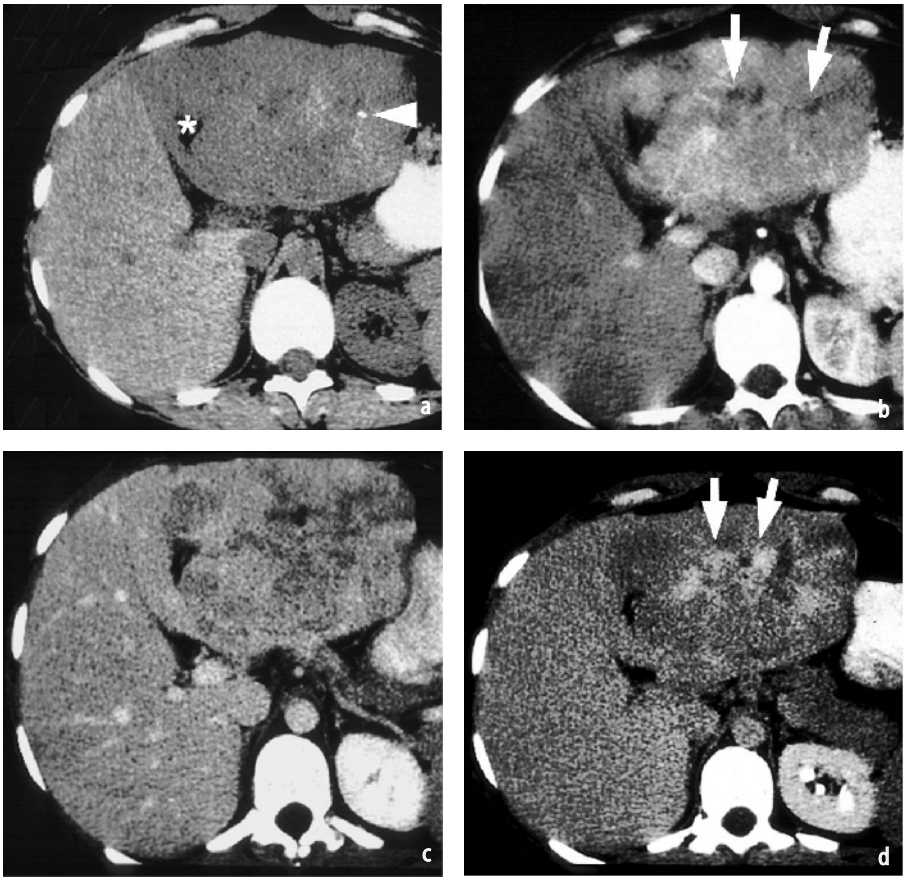

Fig. 26a-d. Fibrolamellar carcinoma on CT. On an unenhanced CT scan (**a**), the neoplasm appears as a hypodense mass compared to the liver, with coarse calcification (*arrowhead*) and a small area of necrosis (*asterisk*). On arterial and portal-venous phase images after the administration of contrast material (**b** and **c**, respectively), the nodule is seen as heterogeneously hyperattenuating with a hypodense central scar (*arrows* in **b**). In the delayed phase (**d**) the neoplasm is hypodense and the central scar hyperdense (*arrows*)

[39]. On delayed phase images, parts of the non-necrotic portions of the tumor, which mainly comprises fibrous tissue, may increase in attenuation relative to the liver [39]. The central scar usually shows minimal enhancement on arterial and portal-venous phase images and is best seen during the delayed phase (Fig. 26). The appearance of the lesion in the arterial and portal-venous phases reflects the enhancement of the cellular and vascular components of the tumor and the presence of fibrous and necrotic components. The relative homogeneity of the tumor observed on delayed images may indicate wash-out of contrast material from the more vascular areas, together with delayed enhancement of the fibrous lamellae (Fig. 27) [39, 96].

FLC is usually either hypointense or, rarely, isointense compared to the liver on T1-weighted MR images. On T2-weighted images, 90% of the lesions are hyperintense and the remaining 10% are isointense. The purely fibrous nature of the scar means that it is hypointense on both T1- and T2-weighted images (Fig. 28) [39].

FLC becomes heterogeneously hyperintense during the arterial phase after administration of gadolinium, and appears as isointense or slightly hypointense during the portal-venous and equilibrium phases (Fig. 29) [19, 39]. As on CT scans, the central scar shows minimal or no enhancement on hepatic arterial and portal-venous phase images, but may sometimes show persistent enhancement on equilibrium phase images (Fig. 30).

On images acquired during the hepatobiliary phase after Gd-BOPTA or mangafodipir trisodium administration, FLC usually appears as heterogeneously isointense or hypointense with areas of low signal intensity due to necrosis or, less frequently, hemorrhage (Fig. 31). Irregular hyperintense areas, if present, may be related to the presence of fibrotic components. The lack of enhancement on delayed phase images is helpful in distinguishing FLC from FNH (Fig. 32) [39].

FLC does not enhance significantly on SPIO-enhanced images. This absence of enhancement is helpful in distinguishing FLC from FNH in larger lesions, but may be less helpful in smaller lesions [66].

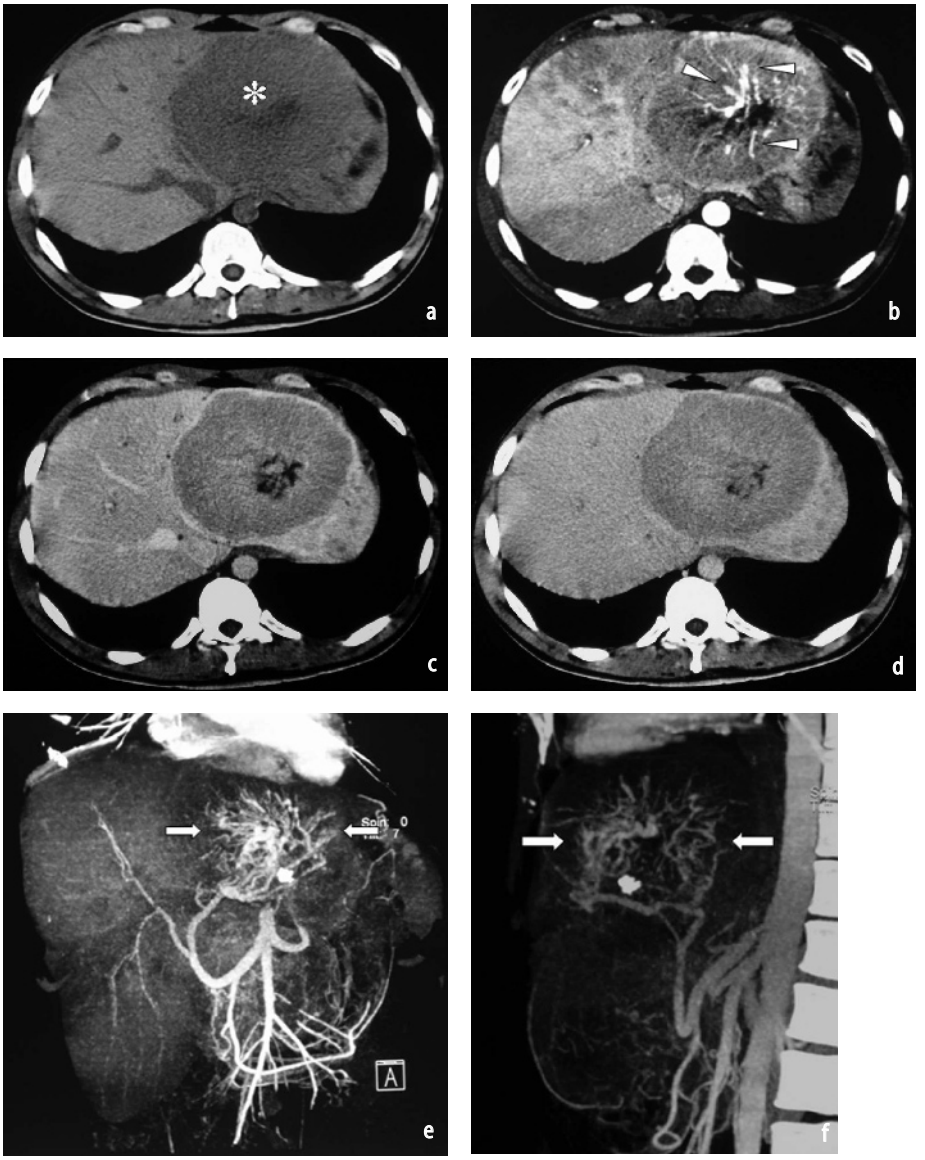

Fig. 27a-f. Fibrolamellar carcinoma on CT. On the precontrast CT scan (**a**) a large, heterogeneous lesion is demonstrated (*asterisk*). In the arterial phase (**b**) of the dynamic evaluation after contrast medium administration, markedly hyperdense intralesional vessels can be detected (*arrowhead*), and the lesion shows a heterogeneous density with a central hypodense scar. In the portal-venous phase (**c**) the mass is hypodense with a peripheral hyperdense capsule. The central scar remains hypodense in the portal-venous phase but demonstrates increased contrast density in the equilibrium phase (**d**). MIP reconstructions in coronal (**e**) and sagittal orientation (**f**) show the intratumoral vascularization (*arrows*)

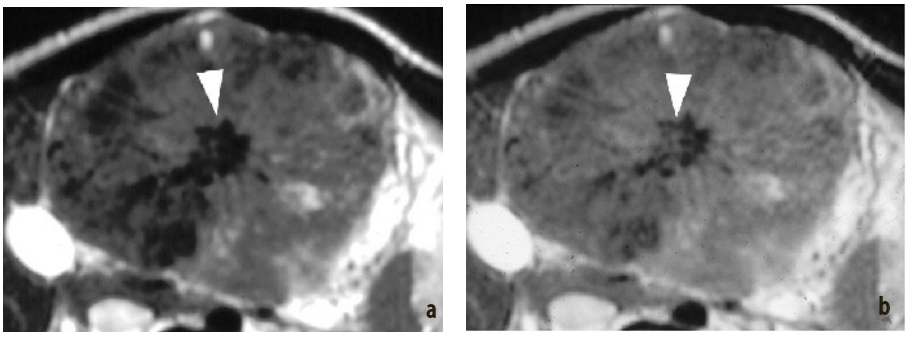

Fig. 28a, b. Fibrolamellar carcinoma. Unenhanced T1-weighted (**a**) and T2-weighted (**b**) images reveal a neoplasm that is hypointense and hyperintense compared to the normal parenchyma, respectively. On both images a hypointense central scar (*arrowhead*) is evident

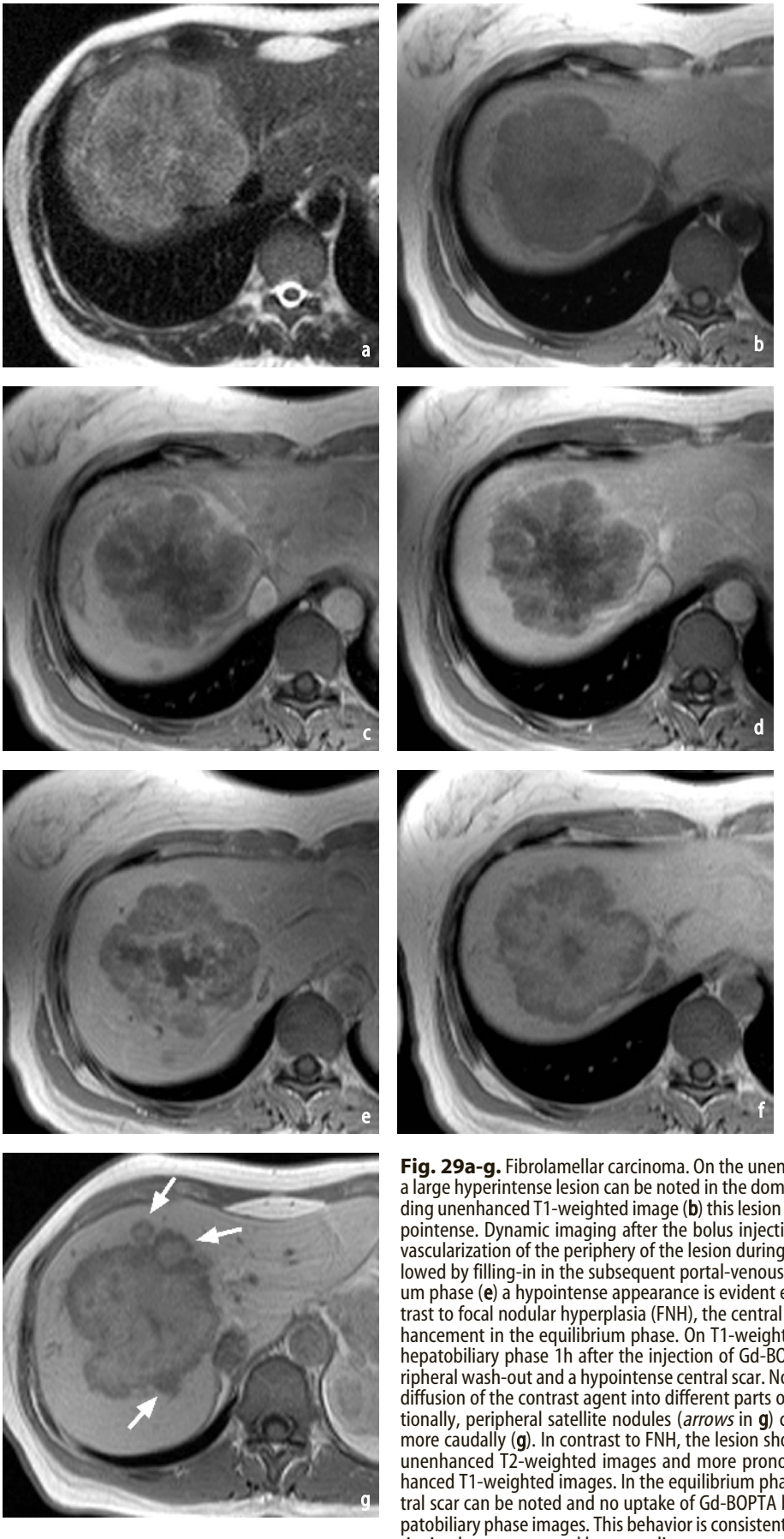

Fig. 29a-g. Fibrolamellar carcinoma. On the unenhanced T2-weighted image (**a**), a large hyperintense lesion can be noted in the dome of the liver. On the corresponding unenhanced T1-weighted image (**b**) this lesion appears as heterogeneously hypointense. Dynamic imaging after the bolus injection of Gd-BOPTA reveals hypervascularization of the periphery of the lesion during the initial arterial phase (**c**) followed by filling-in in the subsequent portal-venous phase (**d**). During the equilibrium phase (**e**) a hypointense appearance is evident even in peripheral areas. In contrast to focal nodular hyperplasia (FNH), the central scar of this lesion shows no enhancement in the equilibrium phase. On T1-weighted images acquired during the hepatobiliary phase 1h after the injection of Gd-BOPTA (**f**, **g**) the lesion shows peripheral wash-out and a hypointense central scar. Non-specific enhancement due to diffusion of the contrast agent into different parts of the lesion can be noted. Additionally, peripheral satellite nodules (*arrows* in **g**) can be seen in images acquired more caudally (**g**). In contrast to FNH, the lesion shows a higher signal intensity on unenhanced T2-weighted images and more pronounced hypointensity on unenhanced T1-weighted images. In the equilibrium phase no enhancement of the central scar can be noted and no uptake of Gd-BOPTA by the lesion is apparent on hepatobiliary phase images. This behavior is consistent with the presence of non-functioning hepatocytes and hence malignancy

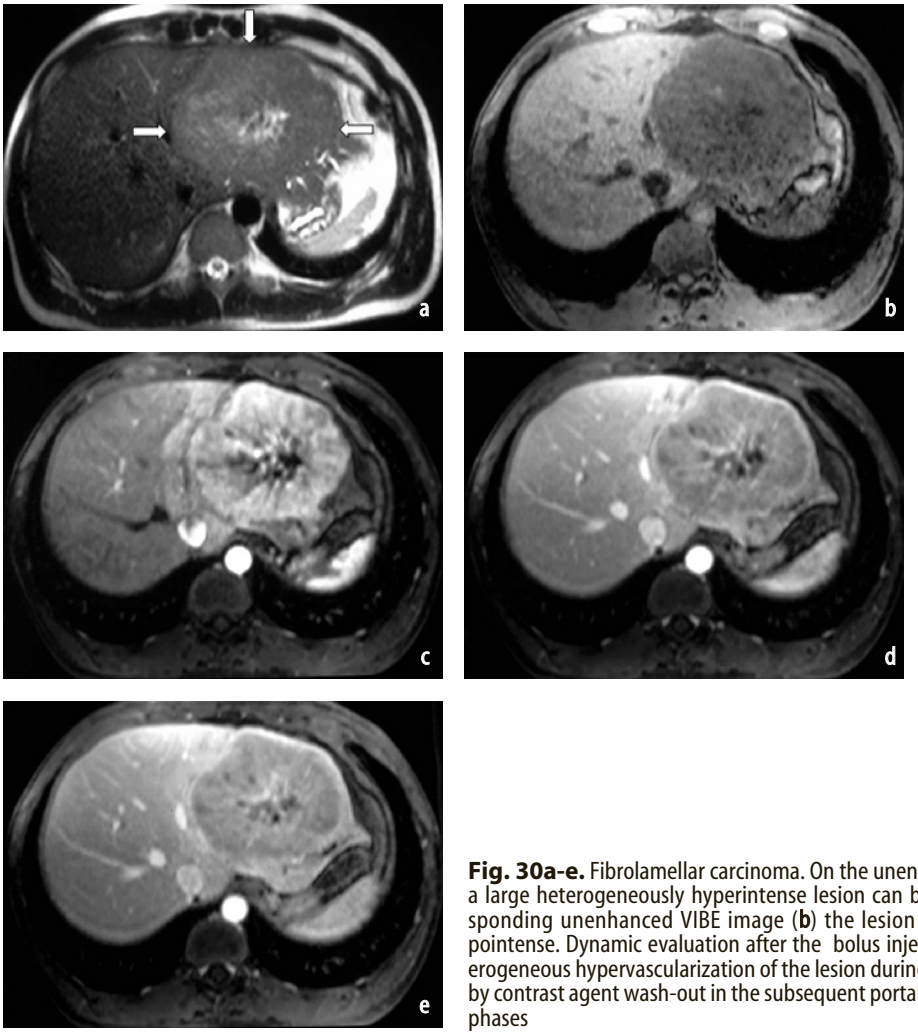

Fig. 30a-e. Fibrolamellar carcinoma. On the unenhanced T2-weighted image (**a**), a large heterogeneously hyperintense lesion can be seen (*arrows*). On the corresponding unenhanced VIBE image (**b**) the lesion appears heterogeneously hypointense. Dynamic evaluation after the bolus injection of Gd-BOPTA reveals heterogeneous hypervascularization of the lesion during the arterial phase (**c**) followed by contrast agent wash-out in the subsequent portal-venous (**d**) and equilibrium (**e**) phases

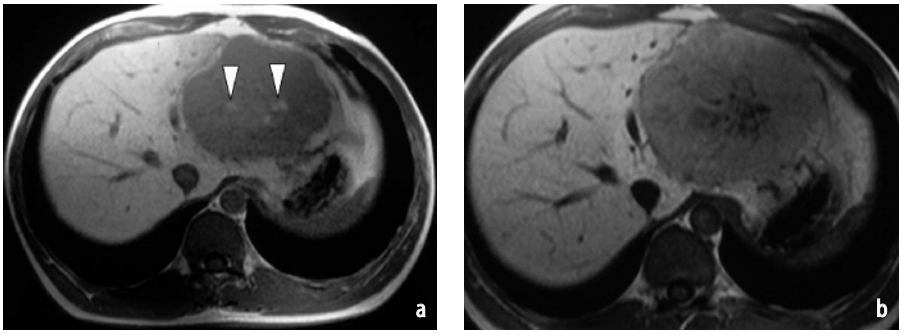

Fig. 31a, b. Fibrolamellar carcinoma after contrast agents. On the hepatobiliary phase after the injection of Gd-BOPTA (**a**) the lesion appears hypointense with a hyperintense central scar (*arrowheads*). In a similar way, the mass appears hypointense in the hepatobiliary phase after injection of Mn-DPDP with a markedly hypointense central area corresponding to the scar (**b**)

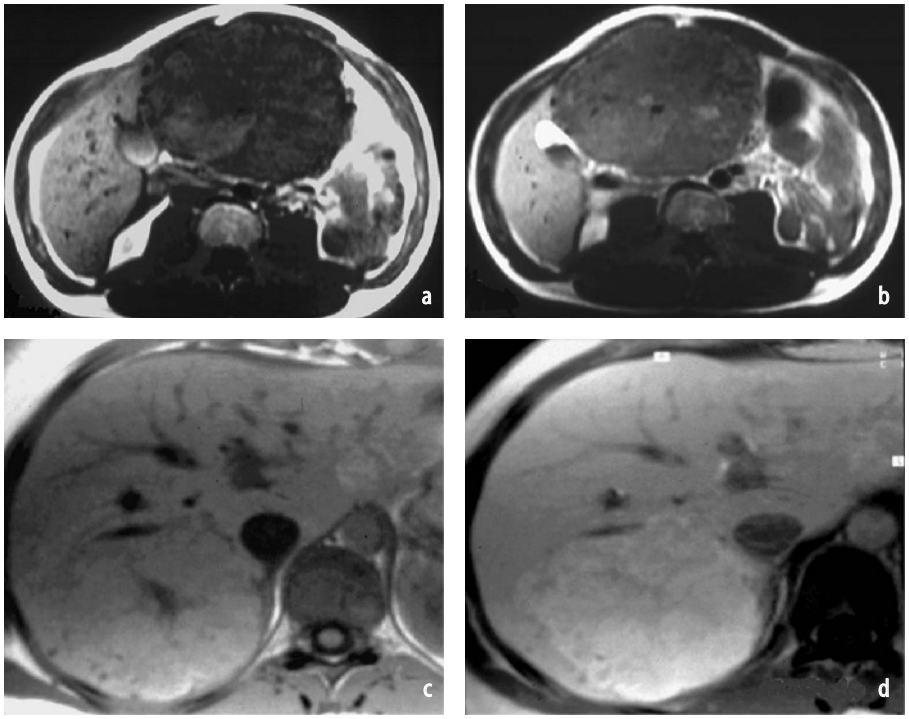

Fig. 32a-d. Fibrolamellar carcinoma after Gd-BOPTA. Fibrolamellar carcinomas do not show significant enhancement on delayed hepatobiliary phase images after the bolus administration of Gd-BOPTA (**a** and **b**, respectively). Conversely, focal nodular hyperplasia generally appears hyperintense on delayed liver-specific phase images after Gd-BOPTA due to the accumulation of contrast agent within the nodule and impaired biliary excretion (**c** and **d**, respectively)

6.1.3 Epithelioid Hemangioendothelioma

Epithelioid hemangioendothelioma (EHE) is a rare malignant hepatic neoplasm of vascular origin that develops in adults. It is more common in women than in men. No risk factors or specific causes have been identified [102].

Macroscopically, two different types of EHE have been described [27]. The nodular type represents an early manifestation of the disease. In the majority of cases there are multiple nodular lesions ranging in size from 1 to a maximum of 3 cm. Frequently, the nodules are found in both lobes of the liver and are located at sub-capsular sites in 50 to 65% of cases. Lesions adjacent to the capsule often cause capsular retraction [27]. The diffuse type of EHE develops in the later stages of the disease. It originates from the nodular type, with the nodules increasing in size until they finally coalesce, forming extensive peripheral lesions [67]. The route of lesion spread follows the hepatic veins or the different branches of the portal vein [26].

Histologically, EHE is composed of fibrous myxoid stroma with a relatively hypocellular center and two cell types: epithelioid and dendritic. The epithelioid cells stain positive for factor VIII-related antigen, indicating the vascular nature of this neoplasm which distinguishes it from metastasis. Intratumoral necrosis and hemorrhage are common [67].

The clinical manifestations are non-specific and variable, ranging from the complete absence of symptoms to hepatic failure. When present, the typical symptoms include right upper quadrant or epigastric discomfort or pain, weight loss, and weakness. Less common symptoms at initial presentation include jaundice, fever, and tiredness. Raised levels of serum alkaline phosphatase (AP) are found in approximately 70% of patients. Occasionally, rupture with hemoperitoneum may be present [41, 58]. Hepatomegaly and abdominal pain are present in 50 to 70% of cases.

On US, EHE is usually well-defined and hypoechoic, although hyperechoic examples are occasionally seen. Sometimes it is possible to find hypoechoic and hyperechoic lesions with a peripheral hypoechoic rim in the same patient (Fig. 33) [67]. Echo-color Doppler may show vascularization within the nodule. When the lesions appear hyperechoic, differential diagnosis with hemangioma is possible; capsular retraction in EHE, which is commonly not observed in hemangioma, is another important feature for differential diagnosis.

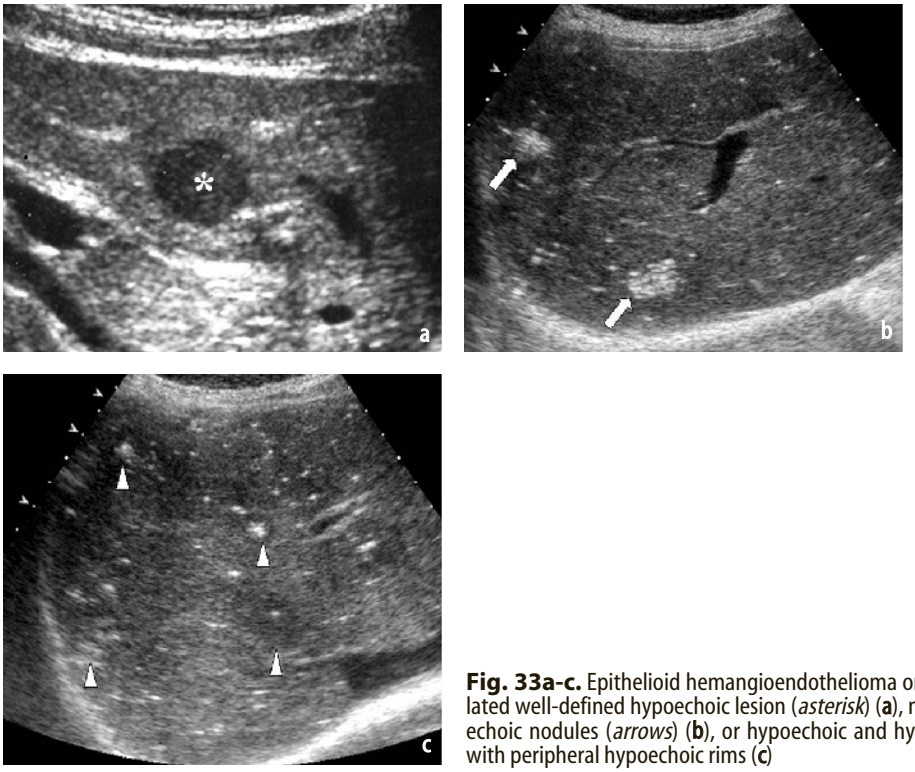

Fig. 33a-c. Epithelioid hemangioendothelioma on US. Ultrasound reveals an isolated well-defined hypoechoic lesion (*asterisk*) (**a**), numerous well-delimited hyperechoic nodules (*arrows*) (**b**), or hypoechoic and hyperechoic lesions (*arrowheads*) with peripheral hypoechoic rims (**c**)

On unenhanced CT images, the nodular type of EHE is of low attenuation, corresponding to myxoid stroma. After intravenous administration of contrast material, areas of high density can be observed in the periphery of the tumor, however, the center of the tumor shows very few or no contrast-enhancing areas [11, 67, 100]. In the diffuse type of EHE, CT scans reveal large, hypodense, diffuse areas throughout the liver extending toward the periphery. The outline is usually irregularly shaped. Focal calcifications within the tumor are found in about 20% of cases. Compensatory hypertrophy of unaffected liver segments, as well as splenomegaly, are common findings. The liver capsule is not usually affected, although confluent nodules may produce capsular retraction (Fig. 34). After intravenous administration of contrast material, enhancement at the periphery of the tumor can be observed, corresponding to a proliferating zone of active growth. Hypervascular areas, indicative of the vasoformative structure of the tumor or of a more distinct representation of blood vessels due to an obstruction of the portal vein, can sometimes be detected within the tumor [67, 100]. The tumor itself takes up only a small amount of contrast medium. During the delayed phase, the tumor becomes increasingly isodense, which makes it difficult to distinguish from normal liver tissue. Slightly ill-defined areas can be seen in the delayed phase (Fig. 35). However, the extension of the tumor is often better defined on unenhanced CT images [11].

The MR imaging features of EHE are similar to the CT findings: either peripheral nodules or larger confluent lesions are seen. The tumors are hypointense on T1-weighted images and hyperintense on T2-weighted images, although a hypointense center corresponding to calcification, necrosis and hemorrhage may be seen on both sequences. After intravenous administration of extracellularly distributed contrast material, moderate peripheral enhancement, progressive filling-in and delayed central enhancement can usually be seen, particularly in larger lesions. Peripheral wash-out can also be seen, which is useful for characterization. Lesions are generally seen as hypointense on delayed hepatobiliary phase images, compared to the surrounding liver parenchyma and to pre-contrast images after the administration of Gd-BOPTA (Fig. 36) [100].

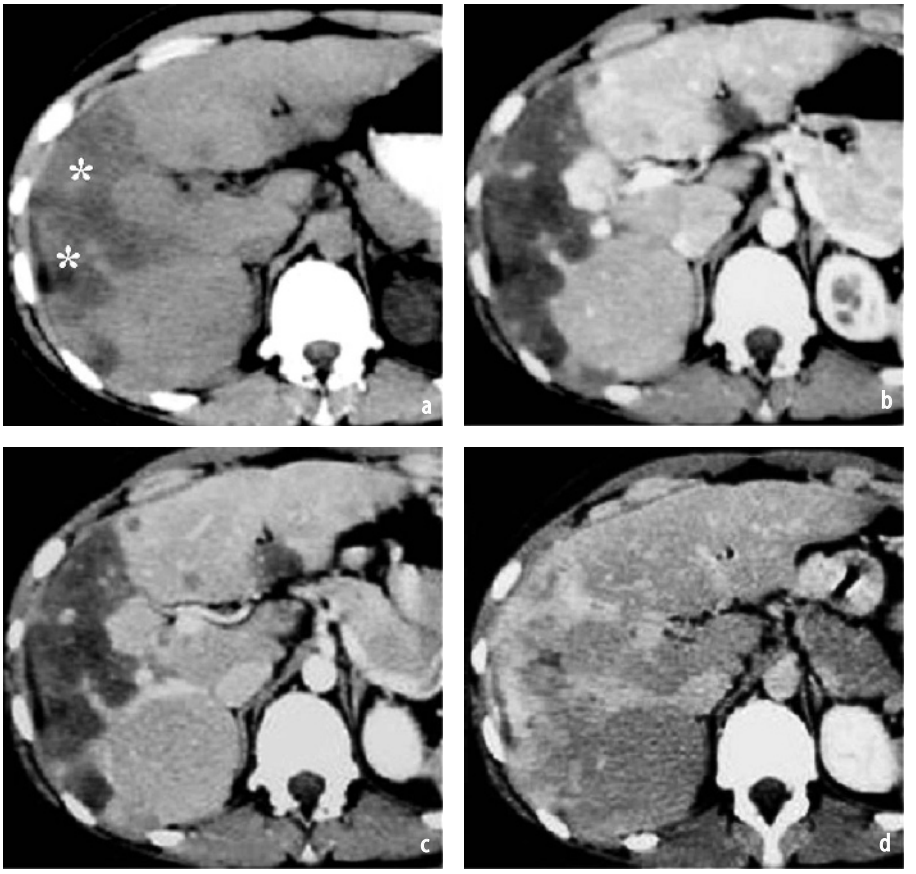

Fig. 34a-d. Epithelioid hemangioendothelioma on CT. Unenhanced CT (**a**) reveals large hypodense, confluent diffuse nodules (*asterisks*). Arterial (**b**) and portal-venous (**c**) phase images acquired after the administration of contrast material reveal enhancement at the periphery of the nodules but few contrast-enhancing areas at the center of the lesions. In the equilibrium phase (**d**) the nodules become heterogeneously hyperdense compared to normal liver, while compensatory hypertrophy and capsular retraction can be clearly seen

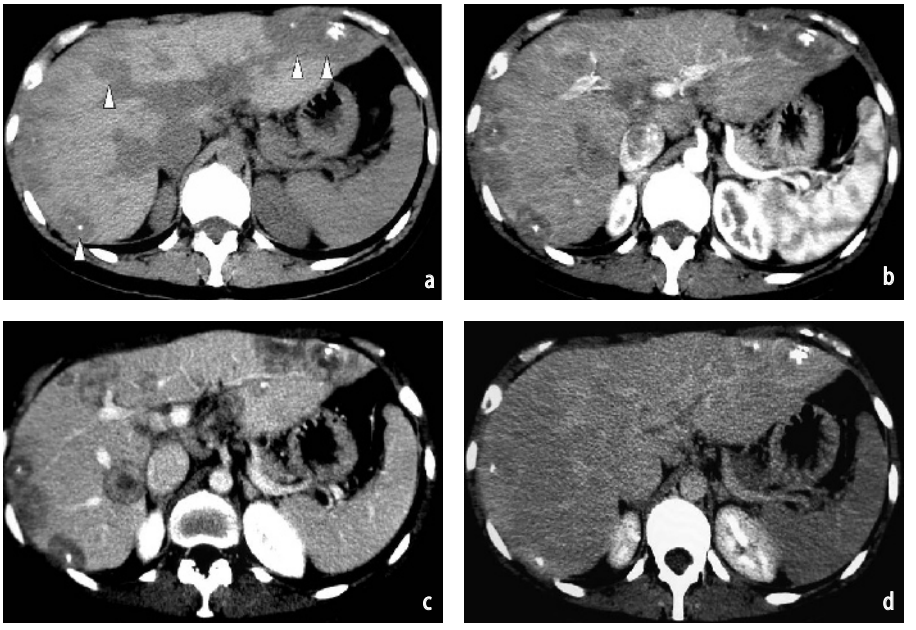

Fig. 35a-d. Epithelioid hemangioendothelioma (diffuse type). On unenhanced CT (**a**) several hypodense peripheral nodules (*arrowheads*) can be seen; several of these lesions show central calcification. Dynamic evaluation of these lesions after administration of contrast material reveals peripheral enhancement in the early post-contrast phases (**b** and **c**) but isodensity with the normal parenchyma on images acquired in the equilibrium phase (**d**)

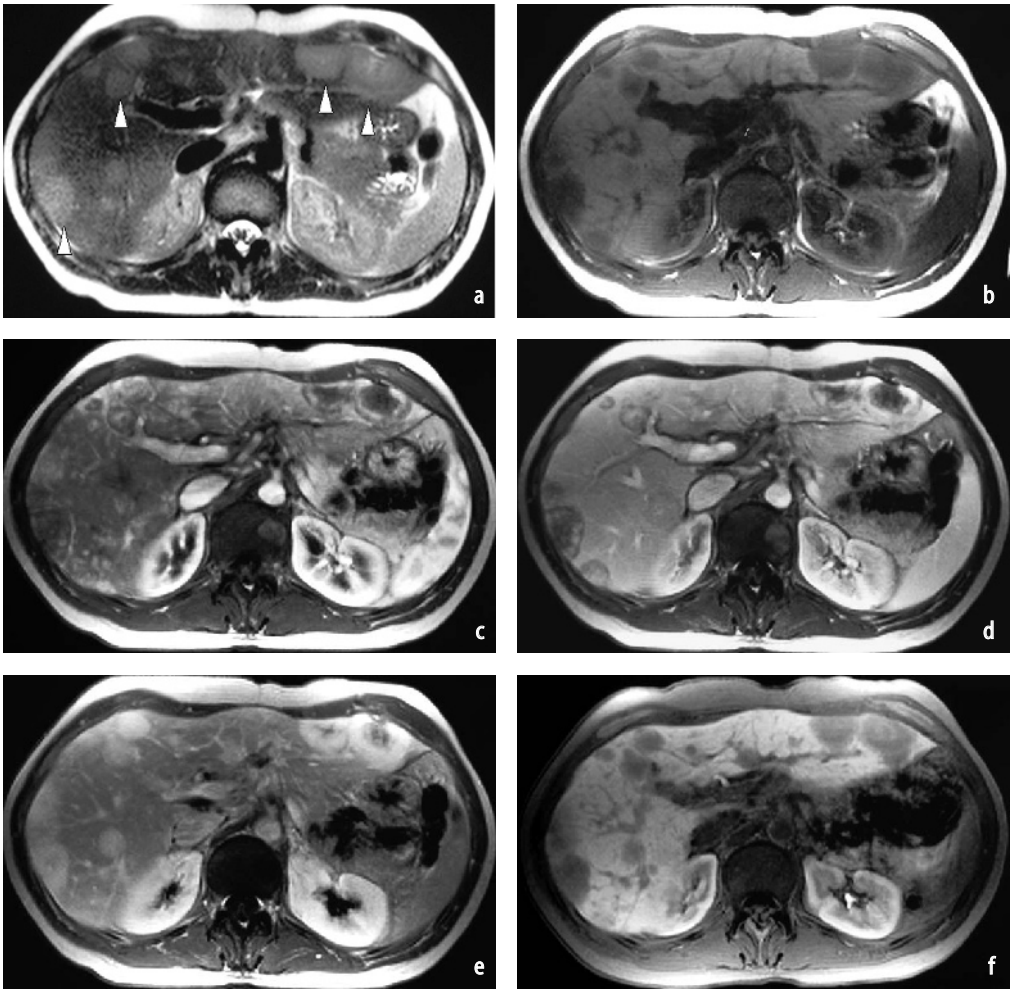

Fig. 36a-f. Epithelioid hemangioendothelioma. This figure shows the same case as Fig. 35. The lesions (*arrowheads*) are seen as hyperintense and hypointense on unenhanced T2-weighted (**a**) and T1-weighted (**b**) images, respectively. Peripheral enhancement and progressive filling-in of the lesions are seen on arterial (**c**) and portal-venous (**d**) phase images after the bolus injection of Gd-BOPTA. In the equilibrium phase (**e**) the lesions are seen as either completely or incompletely hyperintense against the normal parenchyma. Images acquired during the delayed hepatobiliary phase (**f**) show the lesions to be homogeneously hypointense compared to the normal liver

6.1.4 Hepatic Sarcomas

6.1.4.1 Angiosarcoma

Hepatic angiosarcoma (HAS) is a very rare neoplasm that occurs more frequently in males than in females and most typically in the seventh decade of life. In the general population, HAS accounts for only 1.8% of all primary hepatic neoplasms and is 30 times less common than HCC [43]. It is associated with previous exposure to toxins such as Thorotrast, vinyl chloride, arsenicals, steroids, radium and possibly copper [9, 99] and also with chronic idiopathic hemochromatosis [98] and von Recklinghausen disease [2]. Angiosarcoma represents approximately 25% of liver tumors in patients with proven thorium exposure. Although 40% of patients have hepatic fibrosis or cirrhosis at autopsy, the nature of the association between chronic liver disease and HAS is unknown. Further study is also required to delineate the cause of HAS in the remaining 60% of cases without a definitive etiologic association.

Histologically, HAS is composed of malignant endothelial cells lining vascular channels of variable size, from cavernous to capillary, which attempt to form sinusoids. Thorotrast particles can be found within the malignant endothelial cells in cases of Thorotrast-induced HAS [46].

Macroscopically, the majority of angiosarcomas present as multiple nodules, often with areas of internal hemorrhage. When present as a single, large mass, there is no capsule and frequently large cystic areas filled with blood debris [11].

The clinical presentation is non-specific, with abdominal pain, weakness and weight loss as fre-

quent complaints, and with hepatomegaly, ascites and jaundice as common findings. Liver function parameters are usually altered but no parameter or set of parameters is specific for the tumor. The occurrence of thrombocytopenia and disseminated intravascular coagulation is characteristic of HAS and may be related to the local derangement of clotting factors and blood cells by the tumor. Massive intra-abdominal hemorrhage is a complication which occurs in 25% of cases and is probably related to the high incidence of coagulation deficits and to the vascular nature of the neoplasm [44, 63].

On US scans, angiosarcomas are seen as either single or multiple hyperechoic masses. The echo architecture is usually heterogeneous due to the presence of hemorrhage of various ages [87].

CT images reveal the reticular pattern of deposition of Thorotrast extremely well in both liver and spleen. Circumferential displacement of Thorotrast in the periphery of a nodule is a characteristic finding of HAS. When there is no evidence of Thorotrast deposition, angiosarcomas present on unenhanced CT as single or multiple hypodense masses containing hyperdense areas of fresh hemorrhage. Many angiosarcomas are hypoattenuating compared to the liver on both arterial and portal-venous phase images after the administration of contrast material. However, a few lesions are hyperattenuating on arterial phase images, becoming isoattenuating on portal-venous phase images [81]. Centripetal contrast enhancement simulating the pattern of enhancement in hemangioma may occur. The earlier CT reports of angiosarcoma mimicking hemangioma can likely be attributed to imaging in a single temporal phase, often during the delayed phase of contrast enhancement, and to the evaluation of lesion enhancement relative to liver parenchyma rather than the aorta or hepatic artery. Temporal assessment by means of multiphasic helical CT of the various patterns of angiosarcoma enhancement in comparison with the pattern of normal vascular enhancement allows confident exclusion of the diagnosis of hemangioma [81].

On T1-weighted MR images, angiosarcomas are usually seen as hypointense with areas of hyperintensity corresponding to hemorrhage. Conversely, on T2-weighted images, the signal intensity is predominantly high, with areas of low signal [105]. Experience of contrast-enhanced MR imaging of HAS is very limited. On dynamic contrast-enhanced MR images, the enhancement pattern of HAS is usually different to that of cavernous hemangioma and similar to that observed with spiral CT [81]. Generally, diffuse or central enhancement is seen, although in some cases peripheral enhancement and centripetal filling-in of the lesion is observed. In these cases, irregular borders may contribute to the diagnosis. On equilibrium phase images, the lesion appears as a homogeneous, well-defined hyperintense mass (Fig. 37).

6.1.4.2 Undifferentiated Embryonal Sarcoma

Undifferentiated embryonal sarcoma (UES) is a very rare neoplasm in adult patients but is the fourth most common hepatic neoplasm in children, behind hepatoblastoma, hemangioendothelioma and hepatocarcinoma. Clinical and radiological findings for this lesion type are described in Chapter 10, "MR Imaging of the Liver in Pediatric Patients".

6.1.4.3 Hepatobiliary Rhabdomyosarcoma

Rhabdomyosarcoma (RMS) is the most common neoplasm of the biliary tree in children, but occurs only rarely in the adult population. Clinical and radiological findings for this neoplasm are described in Chapter 10, "MR Imaging of the Liver in Pediatric Patients".

6.1.4.4 Leiomyosarcoma, Malignant Fibrous Histiocytoma and Fibrosarcoma

These neoplasms are very rare tumors of the liver which usually occur in patients between 40 and 60 years of age, without gender predilection. Leiomyosarcoma is the most common of these lesions but to date only 54 cases have been described in the literature [29]. Microscopically, leiomyosarcomas originate from mesenchymal elements of the liver, and are composed of large smooth muscle spindle cells. Malignant fibrous histiocytoma was first described as a separate pathologic entity in the 1960s and 1970s. This lesion is composed of primitive cells that demonstrate partial histiocytic and fibroblastic differentiation. Finally, fibrosarcoma is a malignant tumor of soft tissue that is composed of undifferentiated cells derived from collagen-producing fibroblasts [42, 23]. Macroscopically, each of these lesions appears as a large, typically solitary mass in a non-cirrhotic liver. Sometimes it is possible to find necrotic and hemorrhagic areas.

On US these neoplasms appear as large, solid, and well-defined masses, with variable echo patterns depending on the degree of hemorrhage and necrosis. On CT, they appear as well-defined slightly hypodense, heterogeneous masses before contrast medium administration, and show progres-

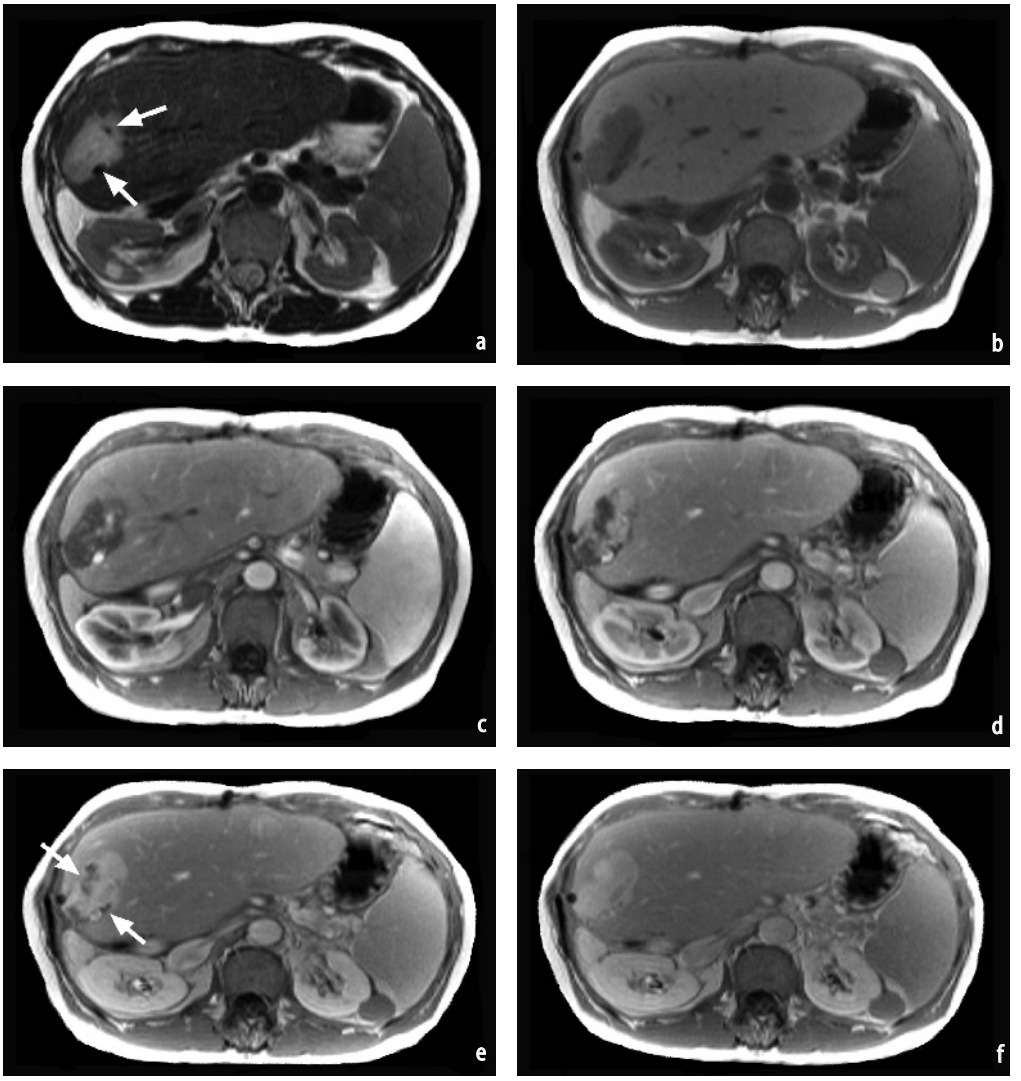

Fig. 37a-f. Angiosarcoma. The unenhanced T2-weighted image (**a**) reveals a high signal intensity mass with hypointense areas that represent large vessels with flow void (*arrows*). The signal intensity of the lesion is comparable to that seen with hemangioma. On the corresponding unenhanced T1-weighted gradient echo image (**b**), the mass is again sharply demarcated and shows homogeneous signal intensity. In contrast to hemangioma, enhancement is seen in central areas of the lesion on arterial phase images (**c**) with subsequent centrifugal filling-in of the lesion in the portal-venous phase (**d**). The peripheral areas of the lesion still do not show enhancement on T1-weighted images acquired 5 min after contrast agent injection (**e**) (*arrows*). However, by 10 min after contrast agent administration (**f**) homogeneous enhancement of the lesion can be observed, comparable to a hemangioma. The clue for diagnosis in this case is the centrifugal enhancement in the lesion rather than the nodular peripheral enhancement typically observed in hemangioma

sive enhancement after contrast medium administration which is more evident in the equilibrium phase. Areas of necrosis and hemorrhage are non-enhancing on post-contrast CT images.

These lesions demonstrate inconsistent signal intensity on pre-contrast T2- and T1-weighted MR images although frequently the signal is slightly hyperintense on T2-weighted images and hypointense on T1-weighted images compared with normal liver parenchyma. Typically, internal, hyperintense areas which correspond to necrosis and acute or subacute hemorrhage can be seen. After contrast agent administration, these neoplasms show a slight but often homogeneous enhancement compared to the surrounding normal liver parenchyma [65, 83].

6.2 Secondary Malignant Liver Lesions

6.2.1 Non-Hodgkin's Lymphoma and Hodgkin's Disease

Hepatic lymphoma is usually a secondary liver lesion that occurs in more than 50% of patients with Hodgkin's disease (HD) or non-Hodgkin's lymphoma [75]. Although primary hepatic lymphoma does exist, it is extremely rare because the amount of lymphatic tissue in the liver is very small, present only in the periportal spaces.

Primary hepatic lymphoma has been reported in middle-aged men infected with the human immunodeficiency virus, in patients under pharmacologic immunosuppression, and in organ transplant recipients. In the first two groups of patients, the lymphomatous process includes a spectrum of lymphoproliferation from benign B-cell hyperplasia to malignant monoclonal non-Hodgkin's lymphoma. An association has been identified between post-transplant lymphoproliferative disorders and Epstein-Barr virus infection. At the time of lymphoma diagnosis, more than 80% of post-transplant patients are infected with the Epstein-Barr virus [36, 94].

Whereas numerous miliary small nodules may be present in the liver in well-differentiated non-Hodgkin's lymphoma, in less well-differentiated non-Hodgkin's lymphomas, the lesions are often larger and more infiltrative. In Burkitt's lymphoma, subcapsular infiltration may also be found as a consequence of peritoneal spread [47].

In Hodgkin's lymphoma, the hepatic involvement may range from multiple small nodes to large infiltrations. This involvement occurs more frequently with lymphocyte depletion and mixed cellular subtypes than with the lymphocyte-rich subtype of HD. Concomitant peliosis hepatis may also be present [92].

Hepatic lymphoma initially spreads in the portal areas in which the majority of the lymphatic tissue is present [88]. In HD, a Reed-Sternberg variant cell-type can be detected microscopically. In non-Hodgkin's lymphoma the lymphocytic form tends to be miliary, whereas the large cell or hystiocytic varieties appear as nodular masses [47].

Clinically, patients with primary non-Hodgkin's lymphoma most often present with pain in the right upper abdominal quadrant or with hepatomegaly. Secondary lymphomas, as well as Hodgkin's lymphoma, may induce jaundice, fever and hepatomegaly, but unfortunately these signs are non-specific and in some cases may even result from chemotherapy [7].

On US, both Hodgkin's and non-Hodgkin's lymphoma commonly appear as single or multiple hypoechoic masses, often with indistinct margins. Multiple hypoechoic lesions may mimic the appearance of a diffuse infectious process such as candidiasis. In the diffuse lymphomatous form the echogenicity of the hepatic parenchyma may be normal or heterogeneous and the overall architecture of the liver may be altered. Occasionally, patients with non-Hodgkin's lymphoma have echogenic or target-like lesions [103]. If there is bleeding within the tumor, the ultrasonographic characteristics of a cyst may be seen [93].

On non-enhanced CT images, HD and non-Hodgkin's lymphoma generally appear as homogeneously hypodense, sharply marginated nodules. After contrast medium administration the lesions appear hypodense, although a weak enhancement may be detected (Fig. 38). In the miliary form, a diffuse decreased attenuation may be observed, which is indistinguishable from fatty infiltration [84].

On MR images, focal hepatic lymphoma is generally seen as homogeneously hypointense compared to the normal parenchyma on unenhanced T1-weighted images and hyperintense on T2-weighted images. Dynamic imaging after the administration of a gadolinium contrast agent typically reveals a hypointense appearance on arterial phase images, followed by homogeneous, delayed enhancement on portal-venous phase images and isointensity on equilibrium phase images (Figs. 39, 40). Susceptibility artifacts may be caused by hemorrhage in pre-treated focal infiltrations and may be more clearly delineated on fat-suppressed T1-weighted images [4]. Although lymphoma is readily distinguishable from normal liver, the difference in relaxation times from metastases and HCC is not significant.

In cases of diffuse infiltrative lymphoma, no significant differences are seen between normal liver parenchyma and the lymphomatous liver infiltration.

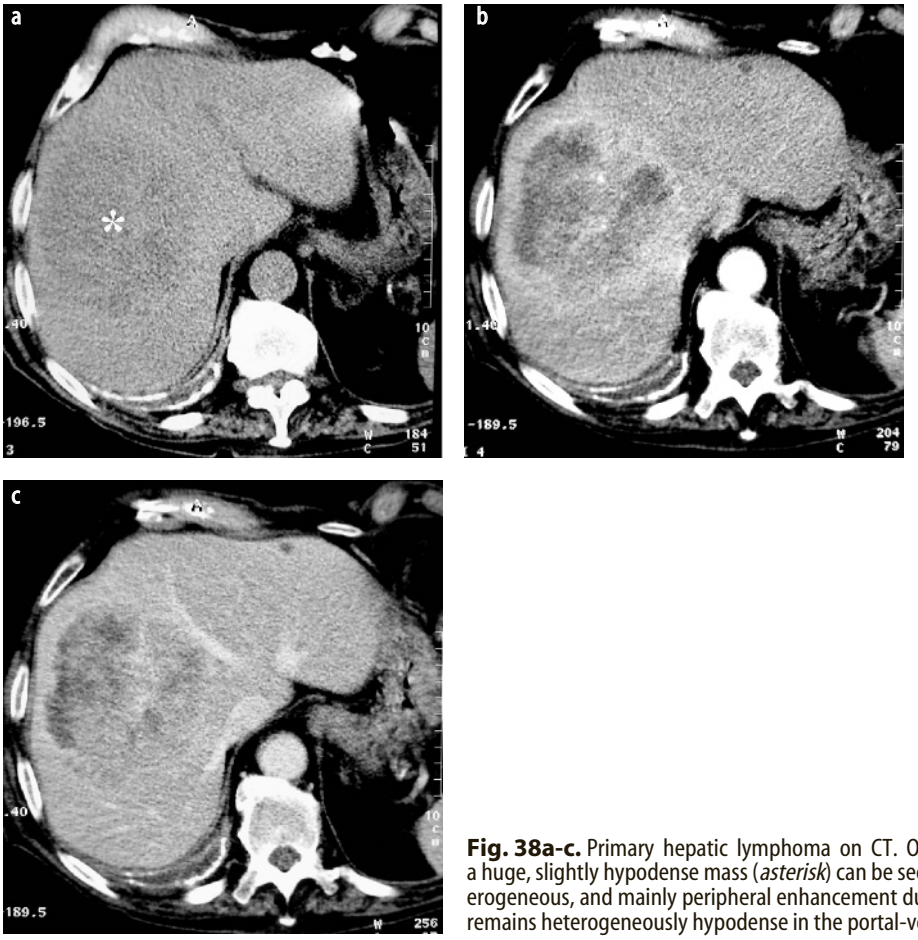

Fig. 38a-c. Primary hepatic lymphoma on CT. On the unenhanced CT image (**a**) a huge, slightly hypodense mass (*asterisk*) can be seen. The lesion shows weak, heterogeneous, and mainly peripheral enhancement during the arterial phase (**b**), and remains heterogeneously hypodense in the portal-venous phase (**c**)

6.2.2 Metastases

Metastases are the most common malignant focal liver lesions in the non-cirrhotic liver. However, metastases are relatively uncommon in the cirrhotic liver where HCC is more frequent. The liver is second only to regional lymph nodes as a site of metastatic disease; autopsy series of patients with primary tumors indicate that at the time of death, approximately 50% of patients have metastatic disease of the liver [78]. Although metastases can develop in the liver via hematogenous spread from most solid tumors, certain primary neoplasms are a particularly virulent cause of liver-dominant disease and often isolated liver metastases. These include colorectal cancer and neuroendocrine tumors, gastrointestinal sarcomas, uveal melanomas and other neoplasms [30].

The gross features of liver metastases vary. Lesions may be expansive, infiltrative, surface-spreading, or miliary, depending on the origin of the primary tumor. Within each of these categories, metastatic lesions may be massive, nodular, or diffuse and may range in size from less than 1 mm to many centimeters in diameter. Metastases from colon carcinoma usually appear as a few large nodules with central umbilication. Nodules from breast or lung carcinoma have an early central umbilication. Metastatic lesions of the miliary type are seen more frequently from breast, prostate or stomach cancers. Microscopically, metastases resemble the primary tumors. Fibrous reaction to the metastatic tumor is common in breast and pancreatic carcinomas, while a "fish flesh" texture is common in cellular and undifferentiated tumors such as small cell cancer, adenocarcinoma of the lung, non-Hodgkin's lymphoma, some sarcomas, and melanoma [30, 56]. Clinically, hepatomegaly is the most common finding, followed by ascites, jaundice, and varices [21].

On US, metastases to the liver usually take on one of the following appearances: hypoechoic, mixed echogenicity, target pattern, hyperechoic, cystic, heterogeneous or coarse echo texture without focal mass [3]. Most metastatic lesions exhibit a hypoechoic halo. This hypoechoic halo is composed of compressed normal liver parenchyma,

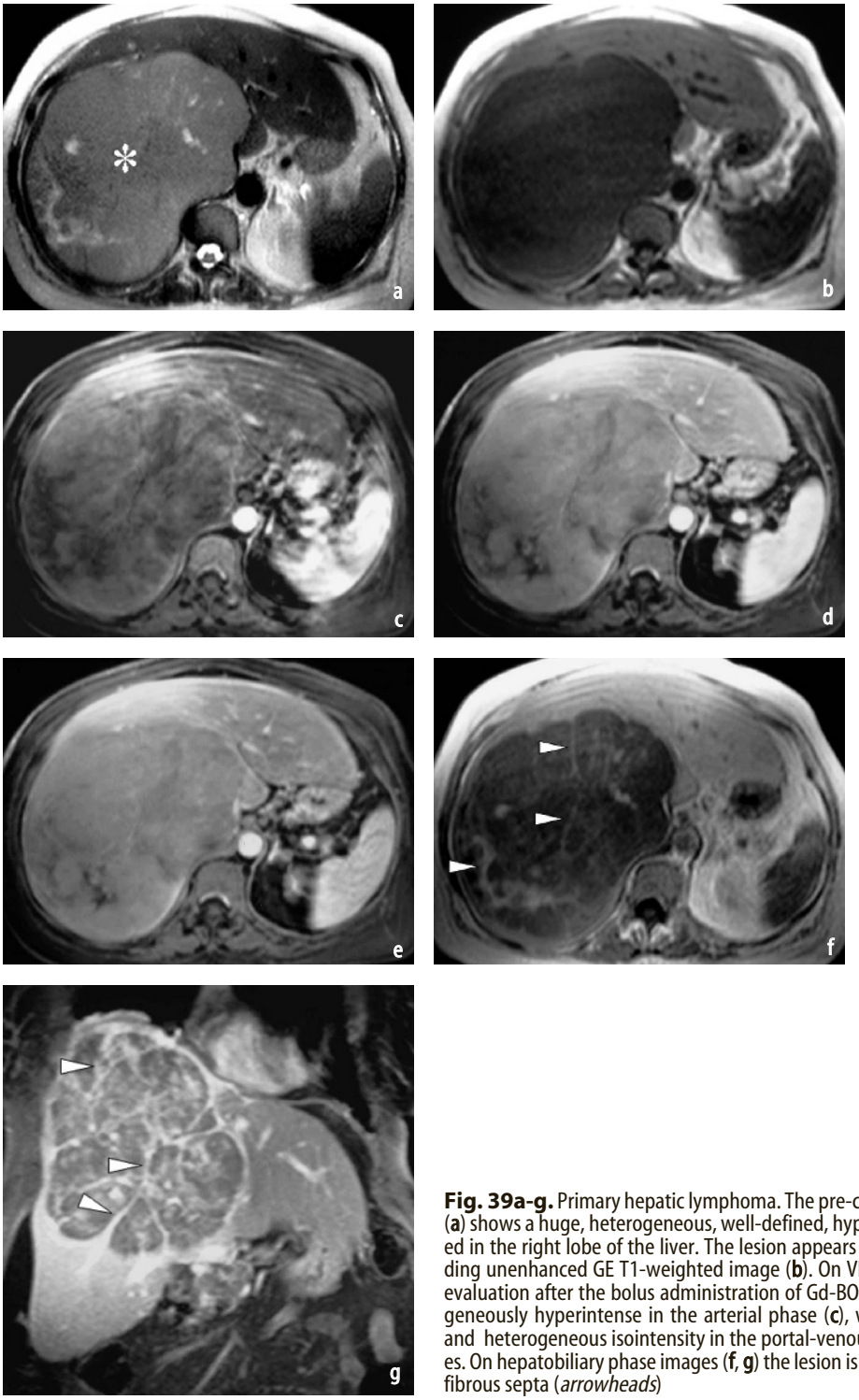

Fig. 39a-g. Primary hepatic lymphoma. The pre-contrast T2-weighted TSE image (**a**) shows a huge, heterogeneous, well-defined, hyperintense mass (*asterisk*) located in the right lobe of the liver. The lesion appears hypointense on the corresponding unenhanced GE T1-weighted image (**b**). On VIBE images during the dynamic evaluation after the bolus administration of Gd-BOPTA the mass becomes heterogeneously hyperintense in the arterial phase (**c**), with progressive enhancement and heterogeneous isointensity in the portal-venous (**d**) and equilibrium (**e**) phases. On hepatobiliary phase images (**f**, **g**) the lesion is hypointense with hyperintense fibrous septa (*arrowheads*)

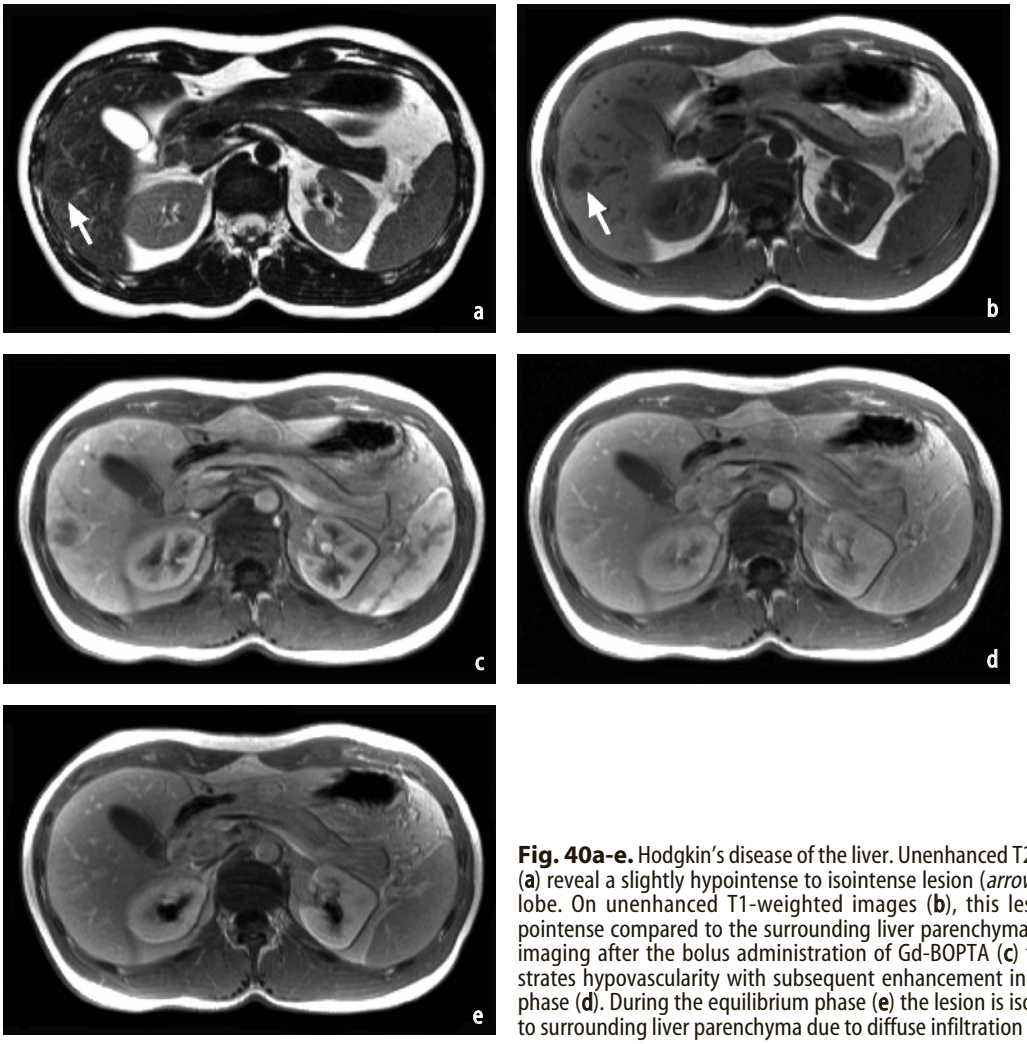

Fig. 40a-e. Hodgkin's disease of the liver. Unenhanced T2-weighted images (**a**) reveal a slightly hypointense to isointense lesion (*arrow*) in the right liver lobe. On unenhanced T1-weighted images (**b**), this lesion is clearly hypointense compared to the surrounding liver parenchyma. On arterial phase imaging after the bolus administration of Gd-BOPTA (**c**) the lesion demonstrates hypovascularity with subsequent enhancement in the portal-venous phase (**d**). During the equilibrium phase (**e**) the lesion is isointense compared to surrounding liver parenchyma due to diffuse infiltration

new proliferating tumor edema, and a rim of hypervascularity in the periphery of the lesion (Fig. 41). In addition to a halo, metastases may take on a target or bull's-eye appearance due to alternating layers of hyper- and hypoechoic tissue (Fig. 42). These three patterns are highly suggestive for malignancy [79]. Hypoechoic metastases tend to be hypovascular, and can be secondary to lymphoma, melanoma, breast or lung carcinoma. Hyperechoic metastases in many cases correspond to hypervascular lesions, and frequently arise from colon, renal, breast, and islet cell carcinomas (Fig. 43). Cystic metastases are rare, and include those from sarcomas, ovarian cancer (Fig. 44), colon cancer, and squamous cell carcinoma. Calcified metastases derive frequently from mucinous adenocarcinomas of the colon (Fig. 45), pancreas and ovary [79].

Liver metastases reveal neoangiogenetic phenomena. Microvessels are detected within the tumor, while macrovessels are rare within the lesion but are commonly found at the periphery of the nodules. The blood supply derives predominantly from arterial vessels rather than from the portal-venous system. Vascularization in general appears to be more conspicuous in small, non-necrotic nodules.

While color and power Doppler can demonstrate peripheral circulation of the lesions, detection of vascularization within the lesion is relatively rare.

Contrast-enhanced US in the arterial filling phase reveals that virtually all secondary lesions have an inflow that varies depending on the nature of the primary tumor and the presence of necrosis. A peripheral ring-shaped enhancement occurs in the arterial and portal-venous phases in about 50% of metastases with a diameter of less than 3 cm. Virtually all metastases have a hypoechogenic appearance in the portal-venous and late phases,

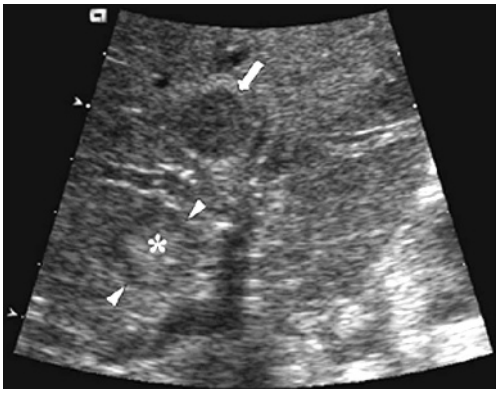

Fig. 41. Metastases with halo pattern. Ultrasound reveals a hyperechoic lesion (*asterisk*) surrounded by a regular hypoechoic rim (*arrowheads*). Another metastatic homogeneous hypoechoic nodule (*arrow*) coexists in the same patient

compared to the surrounding normal liver parenchyma (Fig. 46) [5].

Contrast-enhanced CT is widely used in the follow-up of secondary hepatic lesions. Since the majority of liver metastases are supplied by the hepatic artery and do not have a significant vascular supply from the portal system, most metastases are hypovascular relative to the normal liver parenchyma. These metastases nearly always demonstrate decreased attenuation compared to normal liver parenchyma on unenhanced CT scans. Non-contrast CT imaging is helpful for detecting calcifications, necrosis and hemorrhage within lesions, which occur in many types of metastases, most frequently from colon and ovarian cancers [79]. Hypovascular metastases are best seen during the portal-venous phase of contrast enhancement following the administration of contrast material when the normal liver parenchyma is maximally enhanced (Fig. 47) [55]. Hypovascular metastases most commonly arise from colon, stomach, pancreas, lung, breast, and cervix neoplasms.

On the other hand, hypervascular metastases tend to be more vascular than normal liver parenchyma and are best seen during the arterial phase of contrast enhancement when they are maximally enhanced. During the portal-venous phase these lesions are often isodense compared to the normal liver and are difficult to detect (Fig. 48). Metastases of this type include those derived from renal cell carcinoma, breast carcinoma, islet cell tumors, melanoma and sarcomas, pheochromocytoma, carcinoid and thyroideal carcinoma [8].

Regardless of the hypo- or hypervascular nature of the lesion, some experts consider that arterial phase imaging is essential for the visualization of metastases smaller than 1 cm in size. This is due to the fact that the predominant blood supply derives from the hepatic artery in small lesions [38]. Since small tumors do not usually outgrow their blood supply, they generally do not have necrotic, and thus hypovascular, central areas. Furthermore, visualization of the hyperdense rim of typical hypovascular lesions, such as colon carcinoma metastases, is frequently best achieved during the arterial phase [13]. The equilibrium phase, however, enables an evaluation of enhancement pattern and contrast wash-out and is thus important for lesion characterization. In this phase some metastases show central pooling and peripheral washout due to desmoplastic reaction and peripheral edema (Fig. 49).

The signal intensity of metastases varies con-

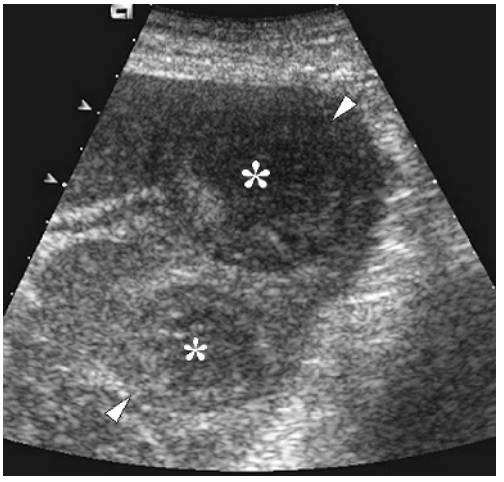

Fig. 42. Metastases with bull's-eye pattern. Ultrasound reveals two large nodular lesions (*asterisks*) with hyper- and hypoechoic peripheral layers (*arrowheads*)

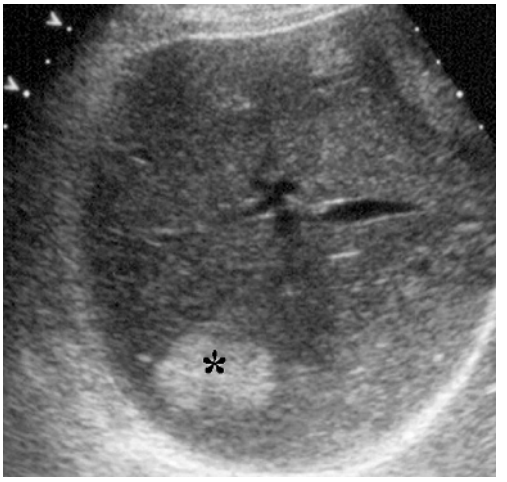

Fig. 43. Hyperechoic metastases from renal cancer. A large lobulated, homogeneous, hyperechoic nodule simulating a hemangioma can be seen in liver segment VII (*asterisk*)

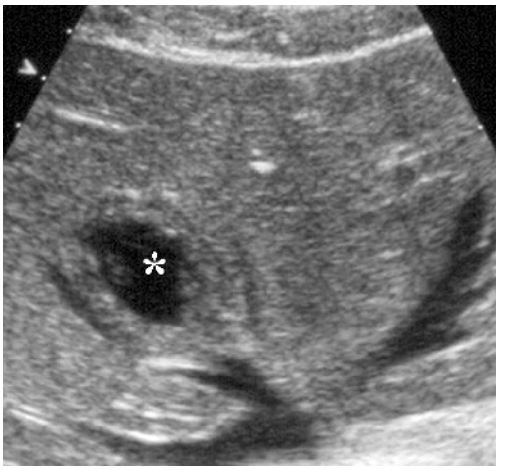

Fig. 44. Cystic metastases from ovarian cancer. An anechoic nodule with slighty irregular margins (*asterisk*) is surrounded by a thick hyperechoic and a thin hypoechoic rim

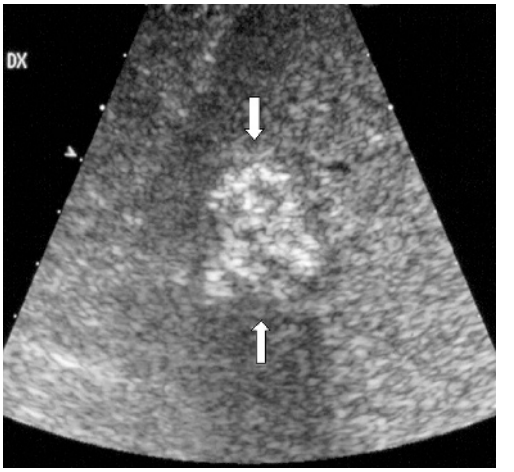

Fig. 45. Calcified metastases from colon cancer. Ultrasound reveals a nodular lesion with irregular margins (*arrows*) and numerous small calcifications with acoustic shadow

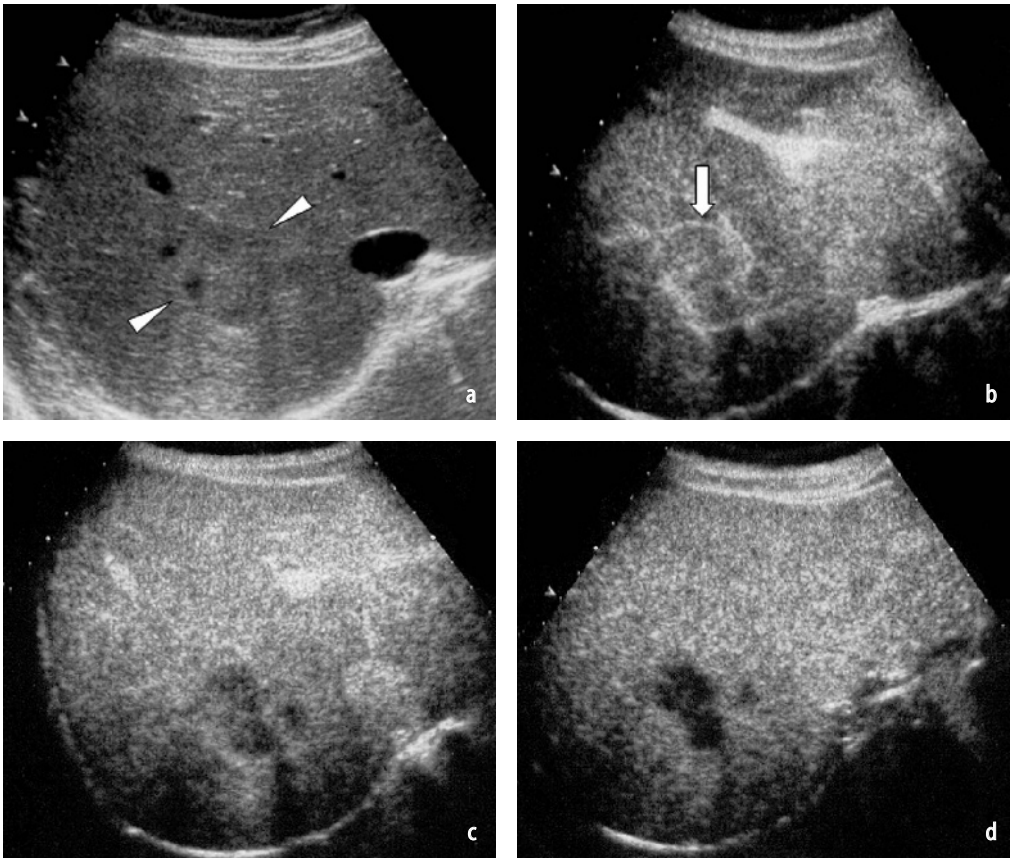

Fig. 46a-d. Metastasis from breast cancer. The pre-contrast US scan (**a**) reveals a heterogeneous, slightly hypoechoic nodule (*arrowheads*), located in segment VII of the right liver lobe. In the arterial phase of the dynamic evaluation after SonoVue® administration (**b**) the lesion shows homogeneous enhancement and a thin peripheral hyperechoic rim (*arrow*). Conversely, the lesion appears heterogeneously hypoechoic in the portal-venous (**c**) and equilibrium phases (**d**)

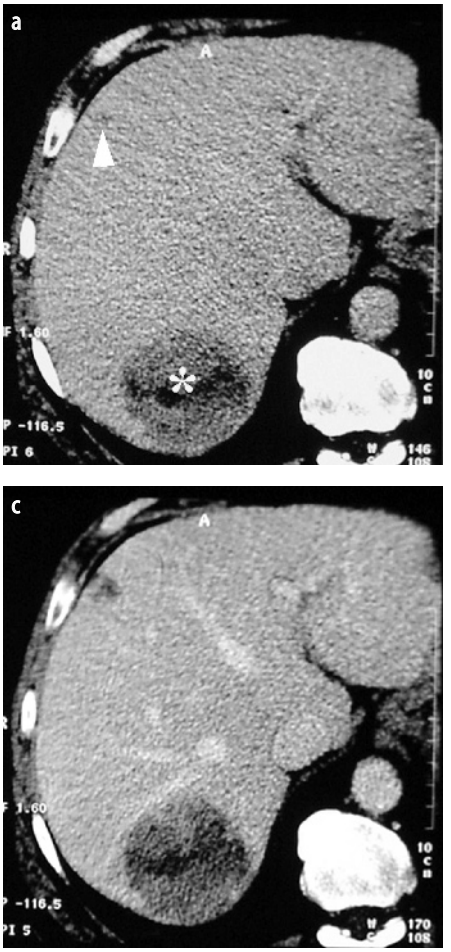

Fig. 47a-c. Hypovascular metastases from colon cancer. On unenhanced CT (**a**) a large heterogeneous hypodense lesion (*asterisk*) can be seen clearly. Another small ill-defined slightly hypodense lesion (*arrowhead*) is less clearly seen. During the arterial phase (**b**) the lesion shows less vascularity than the surrounding liver parenchyma. The lesions appear hypodense with increased conspicuity in the portal-venous phase (**c**)

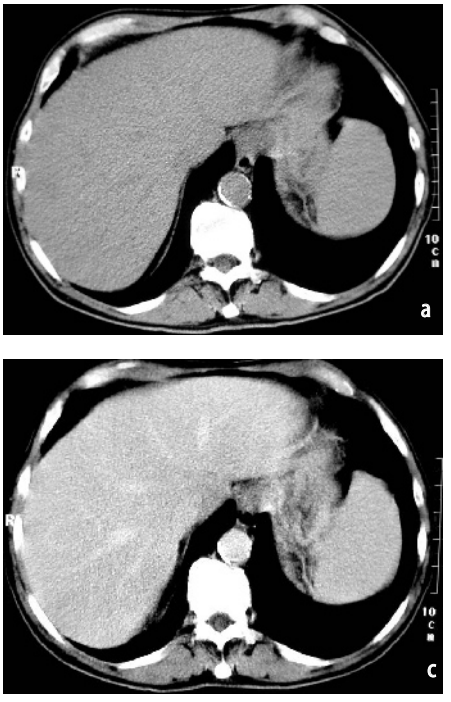

Fig. 48a-c. Hypervascular metastases from renal cancer. On unenhanced CT (**a**) no lesions are detected. During the arterial phase (**b**) two homogeneous hypervascular nodules (*arrowheads*) are seen. The nodules are isodense on the portal-venous phase image (**c**)

siderably on MR, depending on the degree of vascularity, necrosis, and hemorrhage. Generally, on unenhanced T1-weighted images metastases have low signal intensity compared to the surrounding parenchyma, but may demonstrate increased signal intensity whenever intralesional hemorrhage is present. On T2-weighted images, metastases usually demonstrate high signal intensity relative to the surrounding liver parenchyma, although the signal intensity is generally lower than that typically observed in hemangiomas and cysts. The presence of coagulative necrosis, fibrous tissue or calcifications decreases the signal intensity on T2-weighted images, while colliquative necrosis or edema leads to an increase of signal intensity (Fig. 50). For metastases from adenocarcinomas, a characteristic "doughnut" or "target" sign is often seen on T2-weighted images, in which a central hypointense area corresponding to necrosis is surrounded by a less hypointense area corresponding to the growth margins of the tumor.

During the arterial phase after the administration of an extracellularly-distributed contrast agent, weak peripheral heterogeneous enhancement can usually be seen, while nodular or globular enhancement patterns are rarely seen (Fig. 50). A hypointense rim caused by edema may delineate the lesion in the portal-venous and equilibrium phases (Fig. 51). Often, larger metastases demonstrate heterogeneous enhancement due to the presence of non-enhancing central necrotic areas (Fig. 50). On equilibrium phase T1-weighted images, lesions are typically heterogeneously hypointense, often with a characteristic "target", "halo", "peripheral wash-out" or "doughnut" appearance (Fig. 51). Hypervascular metastases are usually hypo- to isointense on unenhanced T1-weighted images and tend to reveal strong transient enhancement in the arterial phase followed by isointensity in the portal-venous and equilibrium phases (Fig. 52) [60].

The use of contrast agents with liver-specific properties is generally considered appropriate for both the detection and diagnosis of metastases. Both positive and negative contrast agents significantly improve detection capability compared to spiral CT [12, 33, 85, 91]. Dual contrast agents such as Gd-BOPTA and Gd-EOB-DTPA, which have both extracellular and hepatobiliary properties, enable improved characterization that can be particularly important in cases where benign and malignant lesions coexist in the same patient (Fig. 53).

On dynamic phase images the pattern of enhancement seen after Gd-BOPTA or after bolus injection of another Gd-chelate may provide useful information on the extent of tumor vascularization, and thus aid in tumor characterization (Fig. 54). Lesion detectability can also be improved on MR by the acquisition of liver-specific delayed scans after administration of Gd-BOPTA or other liver-specific contrast agents. The greatest improvement in detection has been observed for metastases smaller than 1 cm in diameter (Figs. 55, 56) [89].

With mangafodipir trisodium, metastases usually appear hypointense against a strongly enhanced normal liver (Fig. 57) [101]. In some cases, it is possible to observe a rim of peripheral enhancement surrounding the metastasis, which can be useful for discriminating metastases from other liver lesions such as cysts and hemangiomas [85]. Unfortunately, metastases from neuroendocrine tumors may show enhancement after mangafodipir trisodium. Moreover, some hemangiomas may be confused with metastases, due to the low signal intensity on T2-weighted images and hypointensity on delayed hepatobiliary phase T1-weighted images (Fig. 58).

SPIO contrast agents are particularly helpful for lesion detection. Due to the absence of Kupffer cells, metastases generally do not show significant signal drop after SPIO administration and thus appear as hyperintense nodules against a darkened normal liver (Fig. 59). However, the lack of a dynamic imaging capability means that SPIO agents often present the same problem as mangafodipir trisodium when the need is to differentiate between metastases and coexisting benign lesions. To a certain extent this problem, inherent to SPIO agents, may be overcome by USPIO agents for which both dynamic and late phase imaging is possible. Dynamic T1-weighted evaluation after SH U 555 A administration may reveal enhancement of liver metastases, most frequently at the periphery on arterial phase images (Fig. 60) [33].

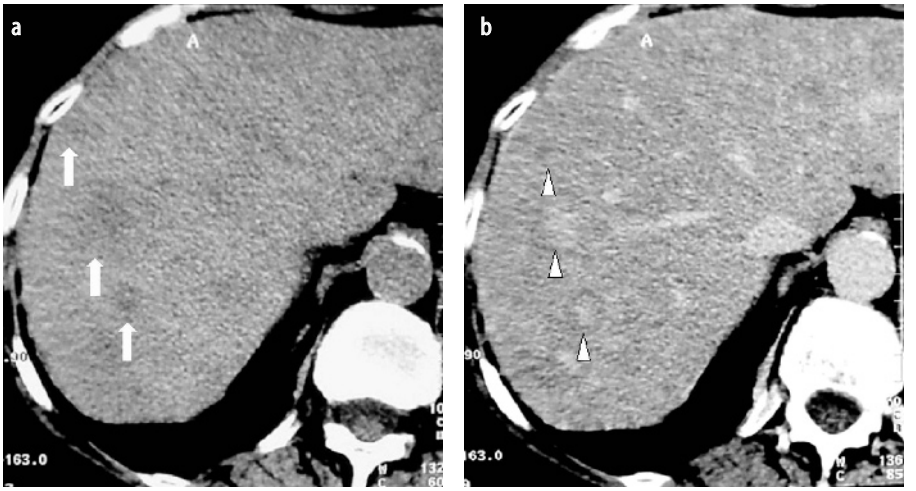

Fig. 49a, b. Metastases with central pooling from colon cancer. The unenhanced CT scan (**a**) shows numerous ill-defined hypodense nodules (*arrows*). In the equilibrium phase (**b**) the nodules demonstrate central contrast agent pooling and peripheral wash-out (*arrowheads*)

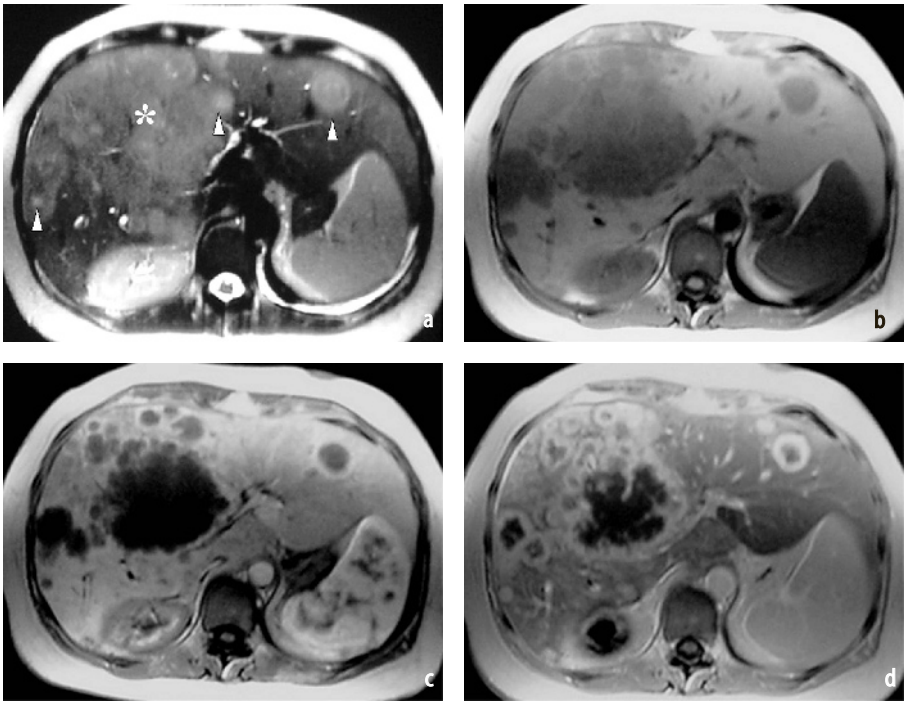

Fig. 50a-d. Metastases from gallbladder cancer. On the unenhanced Turbo SE T2-weighted image (**a**) and the GE T1-weighted image (**b**) the nodules (*arrowheads* in **a**) appear heterogeneously hyperintense and hypointense, respectively. Some nodules are confluent resulting in a large mass (*asterisk*). During the arterial phase after contrast agent administration (**c**) peripheral enhancement is evident in many nodules. These nodules are more conspicuous during the portal-venous phase (**d**)

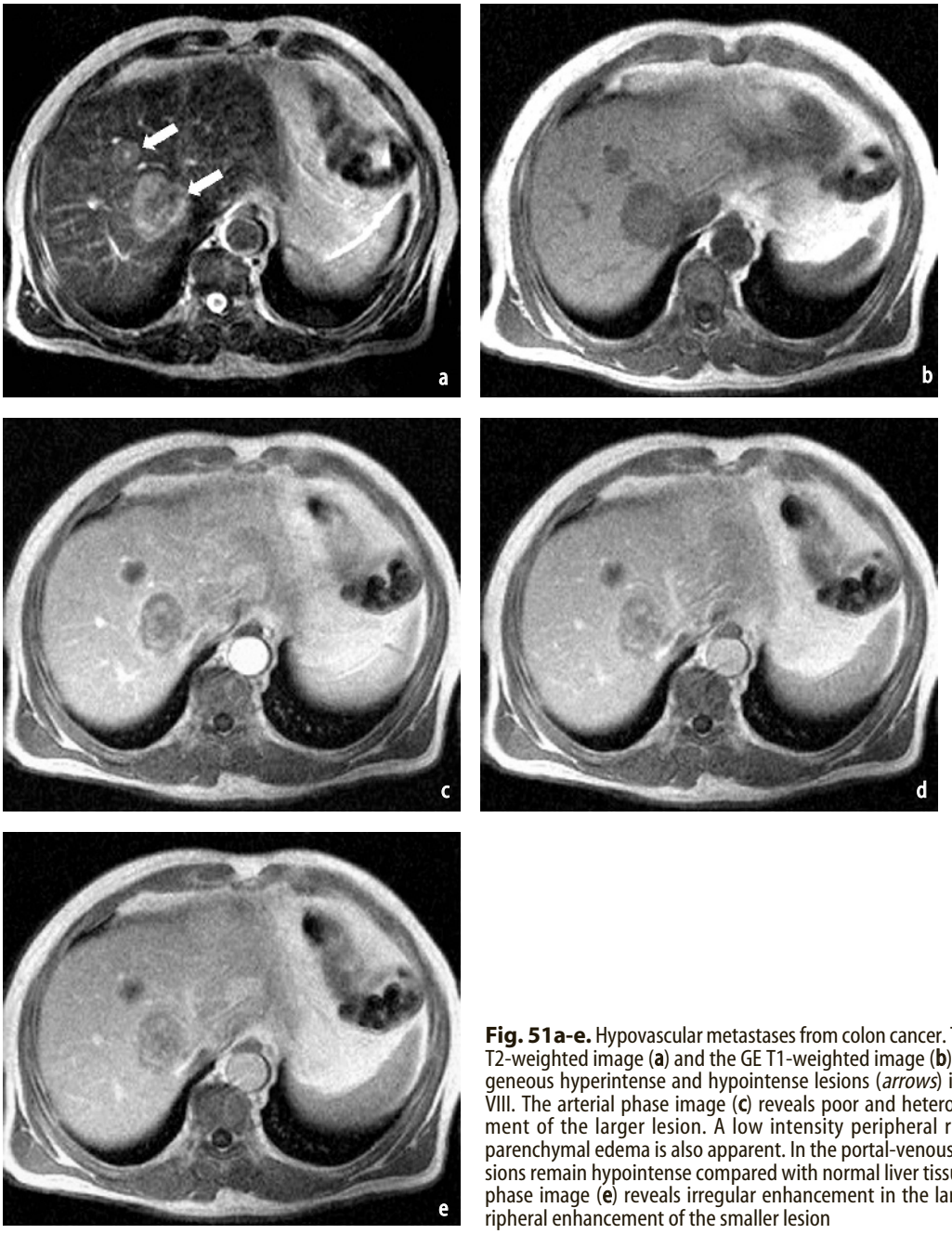

Fig. 51a-e. Hypovascular metastases from colon cancer. The unenhanced SE T2-weighted image (**a**) and the GE T1-weighted image (**b**) reveal two heterogeneous hyperintense and hypointense lesions (*arrows*) in segments IV and VIII. The arterial phase image (**c**) reveals poor and heterogeneous enhancement of the larger lesion. A low intensity peripheral rim due to hepatic parenchymal edema is also apparent. In the portal-venous phase (**d**), both lesions remain hypointense compared with normal liver tissue. The equilibrium phase image (**e**) reveals irregular enhancement in the larger lesion and peripheral enhancement of the smaller lesion

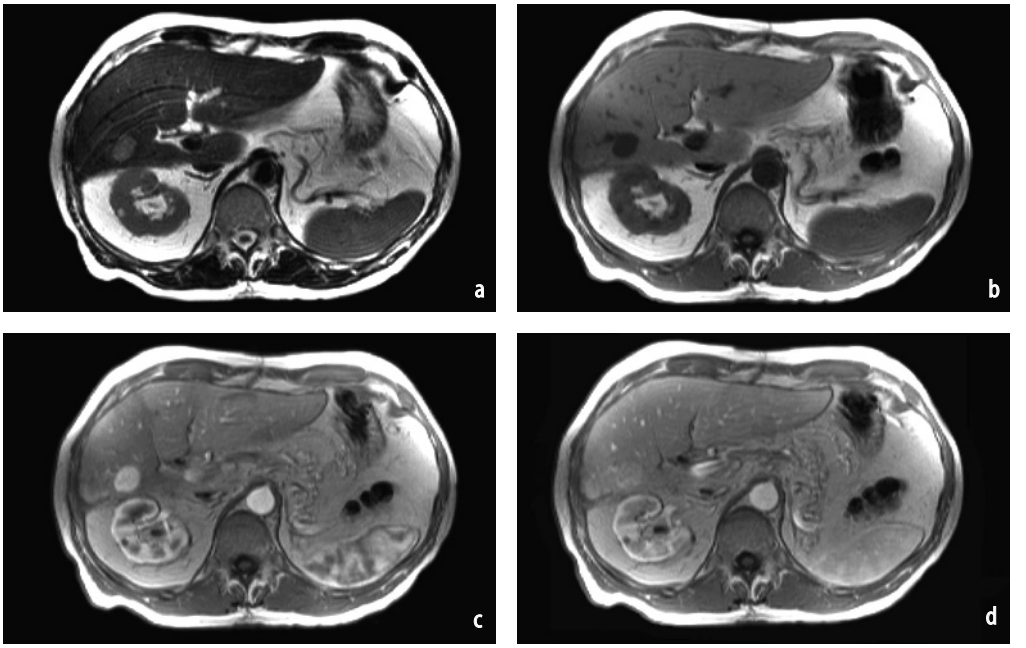

Fig. 52a-d. Hypervascular metastases from gastrinoma. On the unenhanced Turbo SE T2-weighted image (**a**) the nodule (white arrow) is seen as homogeneously hyperintense with distinct borders. The GE T1-weighted image (**b**) reveals a sharply demarcated, hypointense lesion with homogeneous signal intensity. During the dynamic study after the administration of gadolinium contrast agent, the lesion demonstrates initial strong homogeneous hypervascularization during the arterial phase (**c**) followed by isointensity in the portal-venous phase (**d**) due to rapid wash-out

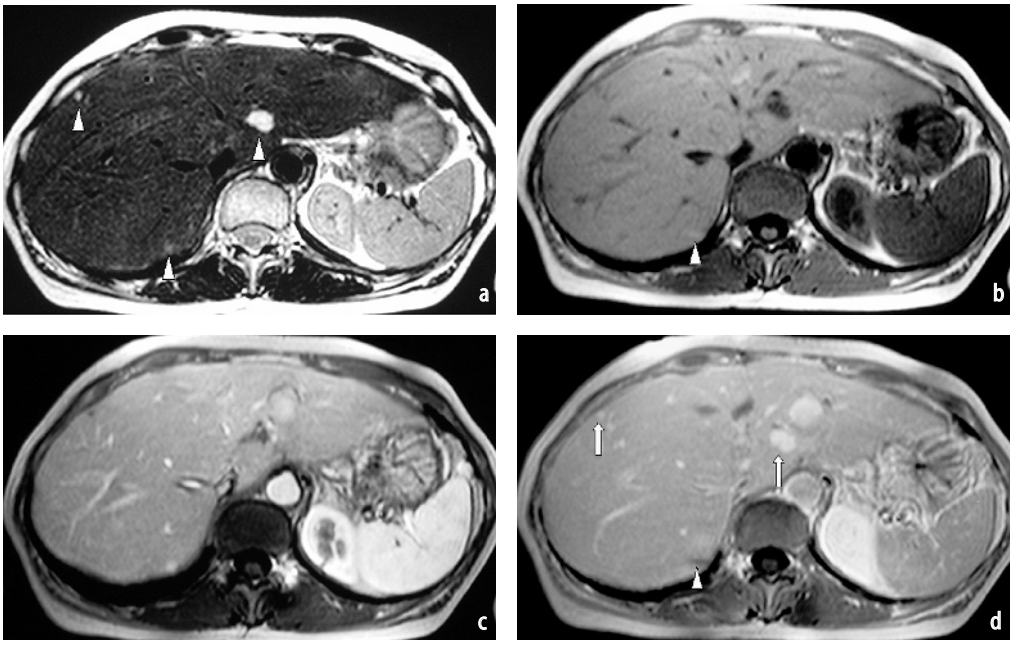

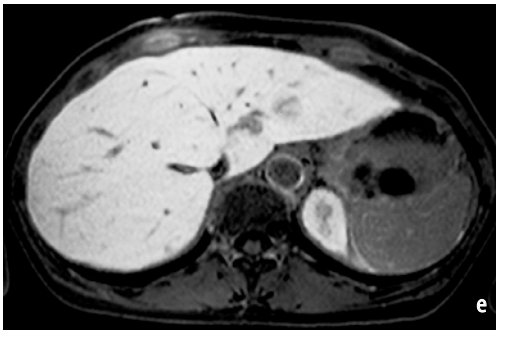

Fig. 53a-e. Detection and characterization of liver metastases from melanoma with Gd-BOPTA. On unenhanced Turbo SE T2-weighted images (**a**) three nodules (*arrowheads*) demonstrating different degrees of hyperintensity can be seen. On the GE T1-weighted image (**b**) two of these lesions are seen as hypointense while the third small nodule (*arrowhead*) appears slightly hyperintense. Dynamic evaluation (**c**, **d**) after Gd-BOPTA administration characterizes two lesions as hemangiomas (*arrows* in **d**), due to the presence of peripheral nodular enhancement, centripetal filling-in and complete filling-in. The metastatic lesion (*arrowhead* in **d**) shows homogeneous enhancement in the arterial phase (**c**) and wash-out in the equilibrium phase (**d**). While the metastasic lesion appears as an ill-defined hypointense nodule in the equilibrium phase, the hemangiomas are both hyperintense. Each of the lesions is seen as hypointense on the hepatobiliary phase image (**e**)

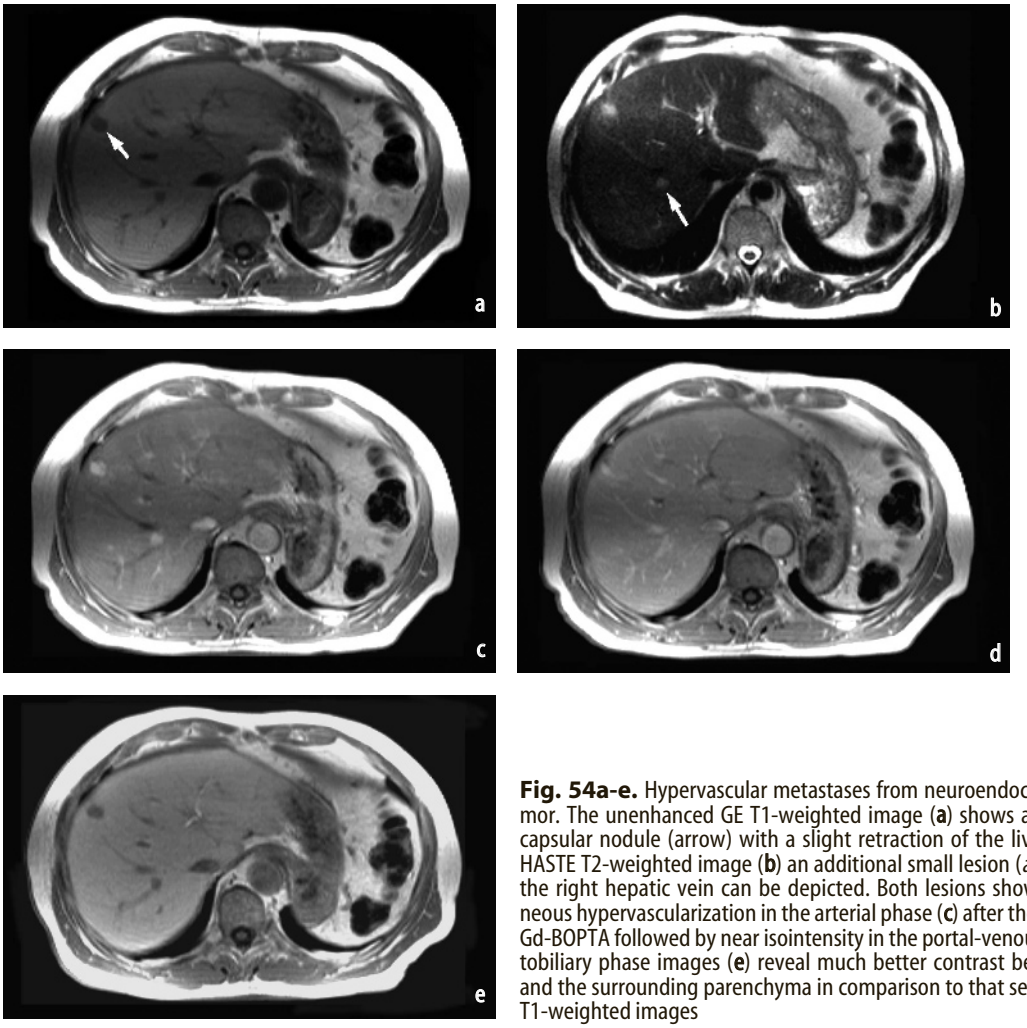

Fig. 54a-e. Hypervascular metastases from neuroendocrine pancreatic tumor. The unenhanced GE T1-weighted image (**a**) shows a hypointense subcapsular nodule (arrow) with a slight retraction of the liver surface. On the HASTE T2-weighted image (**b**) an additional small lesion (*arrows*) adjacent to the right hepatic vein can be depicted. Both lesions show strong homogeneous hypervascularization in the arterial phase (**c**) after the administration of Gd-BOPTA followed by near isointensity in the portal-venous phase (**d**). Hepatobiliary phase images (**e**) reveal much better contrast between the lesions and the surrounding parenchyma in comparison to that seen on unenhanced T1-weighted images

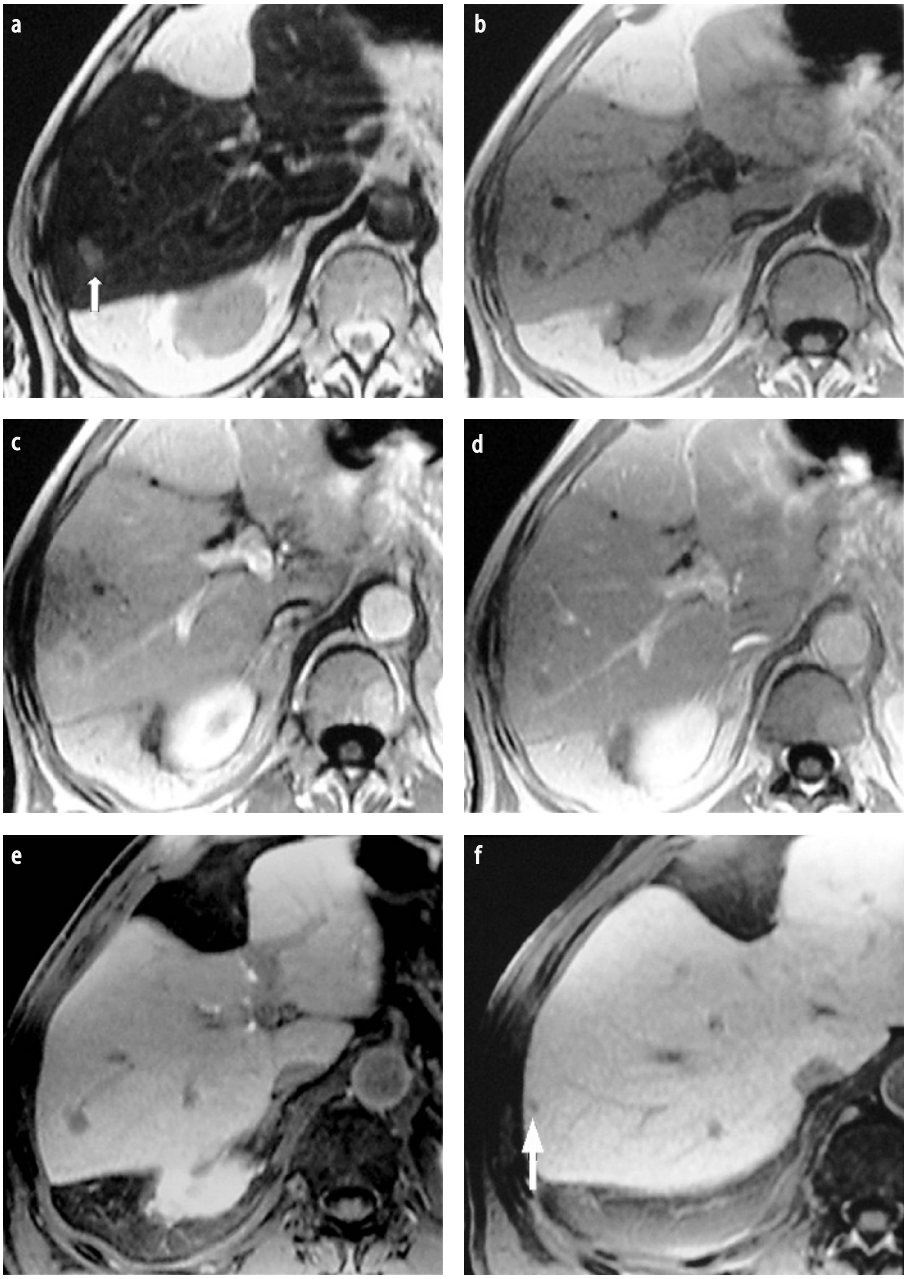

Fig. 55a-f. Metastases from endocrine tumor. A small, slightly hyperintense lesion (*arrow*) can be seen on the HASTE T2-weighted image (**a**). The lesion appears as hypointense on the unenhanced T1-weighted image (**b**). On dynamic imaging after the bolus administration of Gd-BOPTA the lesion demonstrates initial enhancement during the arterial phase (**c**) and wash-out in the portal-venous phase (**d**). On the hepatobiliary phase image (**e**) the nodule does not show any capacity to take up Gd-BOPTA and appears hypointense. Another very small nodule (*white arrow)* can be seen only in the hepatobiliary phase (**f**)

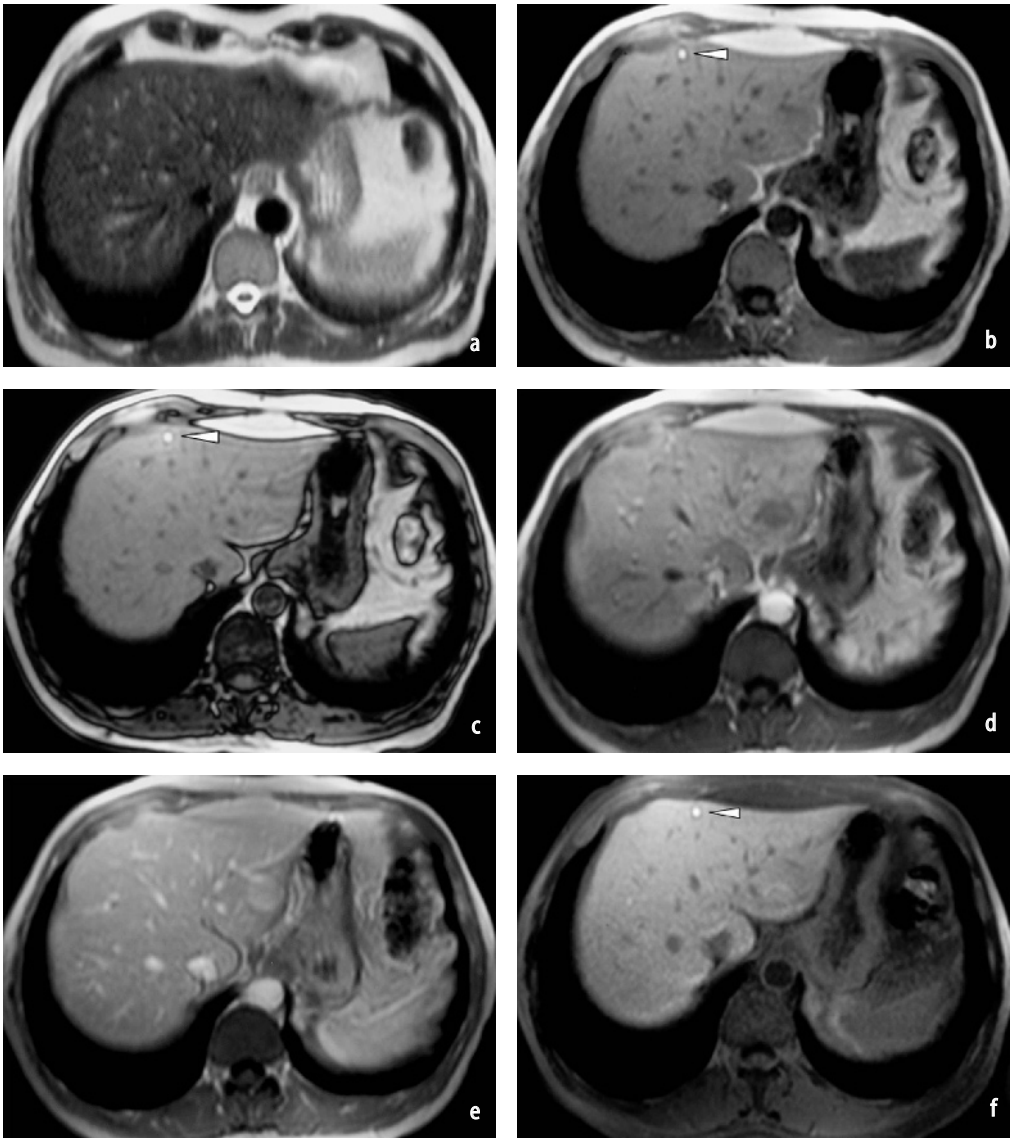

Fig. 56a-f. Metastases from melanoma. On the unenhanced T2-weighted HASTE sequence (**a**) no focal lesions can be detected. Conversely, a small, well-defined hyperintense nodule with a thin hypointense rim (*arrowhead*) is clearly depicted on the pre-contrast GE T1-weighted "in-phase" (**b**) and "out-of-phase" (**c**) images. The nodule is isointense compared to the surrounding liver during the dynamic study after the bolus administration of Gd-BOPTA (**d**-**e**). In the hepatobiliary phase (**f**) the lesion (*arrowhead*) again appears markedly hyperintense compared to the normal liver parenchyma due to presence of melanin

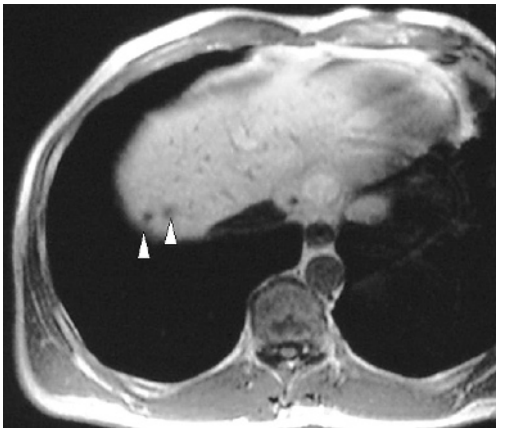

Fig. 57. Metastases from pancreatic cancer. After administration of mangafodipir the liver metastases (*arrowheads*) appear as hypointense nodules against the surrounding enhanced normal liver parenchyma

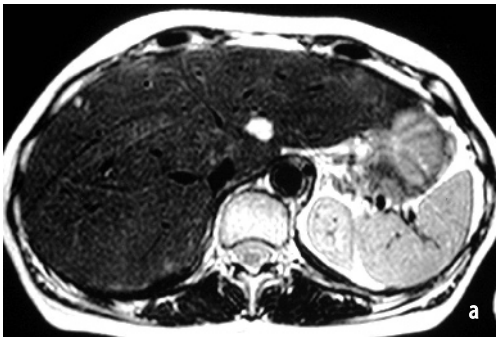

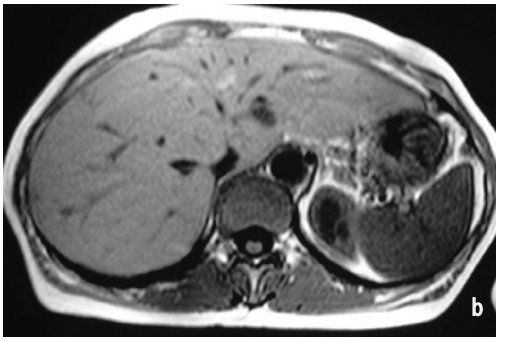

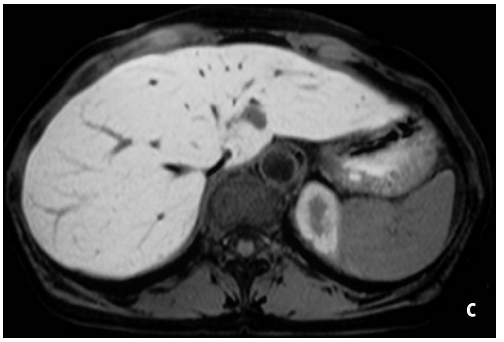

Fig. 58a-c. Metastases from melanoma. This figure shows the same case as Fig 53. All lesions are hypointense on the hepatobiliary phase image after the administration of mangafodipir. On the sole basis of the signal intensity on unenhanced and hepatobiliary phase images, it is difficult to distinguish metastases from hemangioma

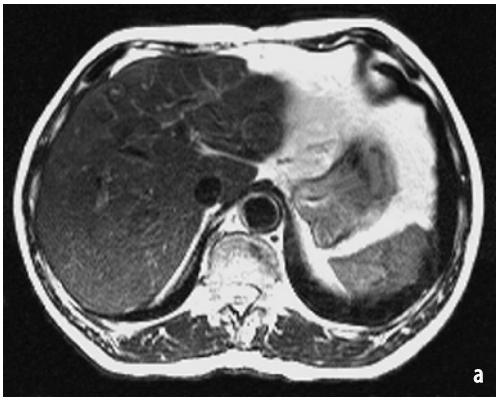

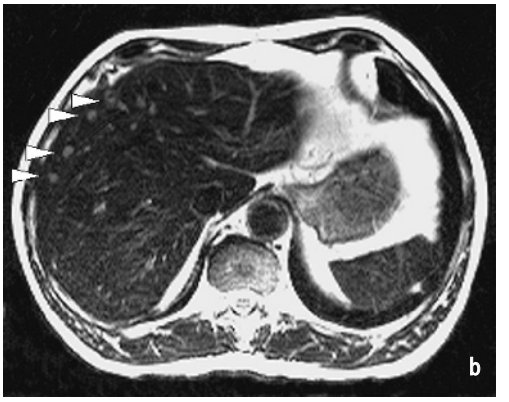

Fig. 59a, b. Metastases from colon cancer. Several small hyperintense nodules are demonstrated on the unenhanced Turbo SE T2-weighted image (**a**). After SPIO administration (**b**) the lesions (*arrowheads*) do not show a signal drop and are therefore better delineated. Additional nodules can also be seen

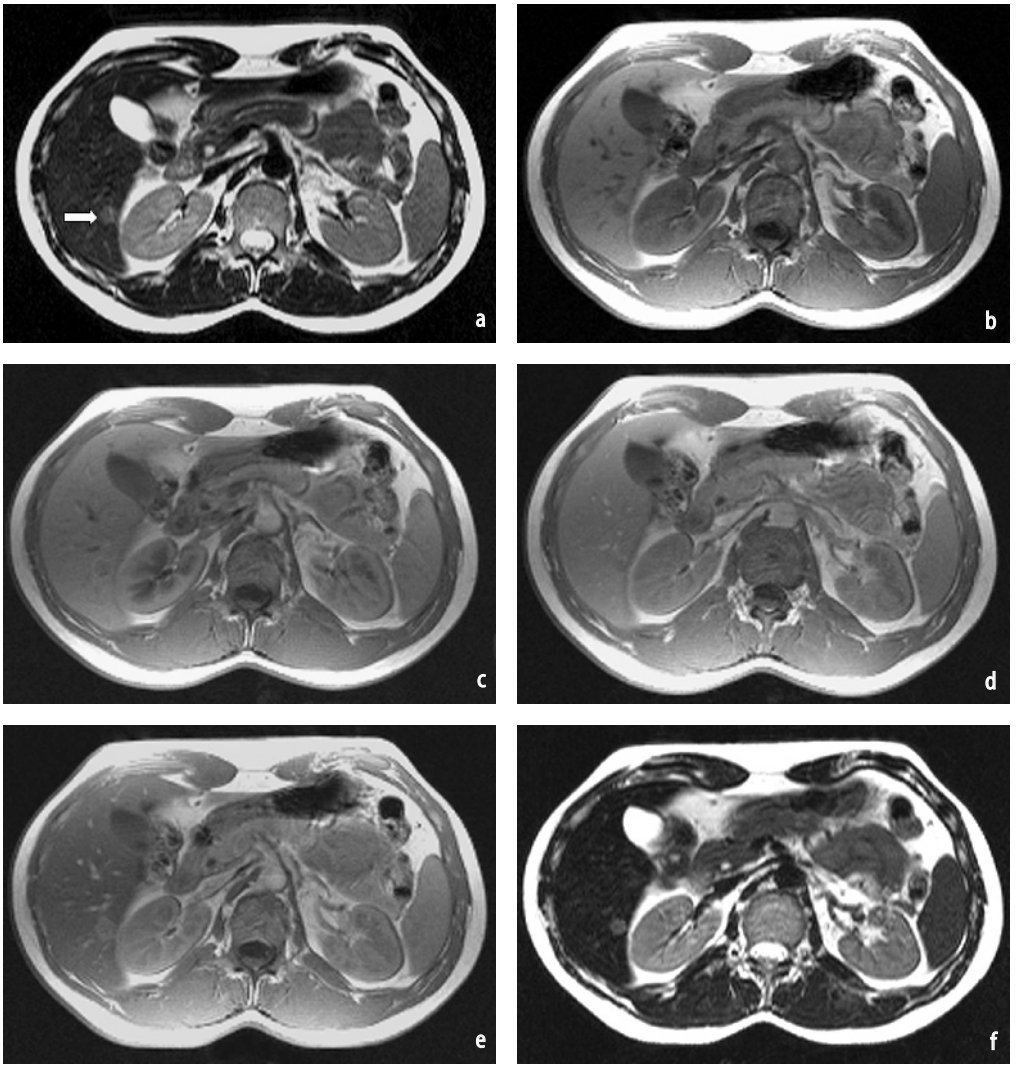

Fig. 60a-f. Metastases from melanoma. On the unenhanced Turbo SE T2-weighted image (**a**) a small hyperintense nodule (*arrow*) can be seen. On the GE T1-weighted image (**b**) the lesion is seen as hyperintense and well-delimited. On dynamic phase images after the bolus injection of SH U 555 A , the nodule does not show significant enhancement (**c**-**d**). On GE T1-weighted images acquired 10 min after SH U 555 A administration (**e**) the signal of the parenchyma is decreased compared to that of the lesion indicating the inability of the latter to take up USPIO . On the delayed phase Turbo SE T2-weighted image (**f**) the lesion appears brighter and better delineated compared to the unenhanced images

References

1. Agarwal VR, Takayama K, Van Wyk JJ, et al. Molecular basis of severe gynecomastia associated with aromatase expression in fibrolamellar hepatocellular carcinoma. J Clin Endocrinol Metab 1998;83:1797-1800
2. Andreu V, Elizalde I, Mallafre C, et al. Plexiform neurofibromatosis and angiosarcoma of the liver in von Recklinghausen Disease. Am J Gastroenterol 1997;92:1229-1230
3. Baker ME, Paulson EK. Hepatic metastatic disease. In: Meyers MA (ed): Neoplasms of the Digestive Tract: Imaging, Staging and Management. Philadelphia: Lippincott-Raven;1998:361-395
4. Bartolozzi C, Cioni D, Donati F, et al. Focal liver lesions: MR imaging-pathologic correlation. Eur Radiol 2001;11:1374-1388
5. Basilico R, Blomley MJ, Harvey CJ, et al. Which continuous US scanning mode is optimal for the detection of vascularity in liver lesions when enhanced with a second generation contrast agent? Eur J Radiol 2002;41:184-191
6. Berman MM, Libbey NP, Foster JH. Hepatocellular carcinoma. Polygonal cell type with fibrous stroma - an atypical variant with a favorable prognosis. Cancer 1980;46:1448-1455
7. Biemer JJ. Hepatic manifestation of lymphomas. Ann Clin Lab Sci1984;14:252-260
8. Bluemke DA, Soyer P, Fishman E. Helical (spiral) CT of the liver. Radiol Clin North Am 1995;33:863-886
9. Brady J, Liberatore F, Harper P, et al. Angiosarcoma of the liver: an epidemiology survey. J Natl Cancer Inst 1977;59:1383-1385
10. Brandt DJ, Johnson CD, Stephens DH, et al. Imaging of fibrolamellar hepatocellular carcinoma. AJR Am J Roentgenol 1988;151:295-299
11. Buetow PC, Buck JL, Ros PR, et al. Malignant vascular tumors of the liver: radiologic-pathologic correlation. Radiographics 1994;14:153-166
12. Caudana R, Morana G, Pirovano GP, et al. Focal Malignant hepatic lesions: MR imaging enhanced with gadolinium benzyloxypropionictetra-acetate (BOPTA) -preliminary results of phase II clinical application. Radiology 1996;199:513-520
13. Chen IY, Katz DS, Jeffrey RB, et al. Do arterial phase helical CT images improve detection or characterization of colorectal liver metastases? J Comput Assist Tomogr 1997;21(3):391-397
14. Chiao R, Mo L, Hall A, et al. B-mode blood flow imaging. AIUM Annual Convention, San Francisco, California, USA, April 2-5, 2000
15. Choi BI, Han JK, Hong SH, et al. Dysplastic nodules of the liver: imaging findings. Abdom Imaging 1999;24:250-257
16. Choi BI, Kim CW, Ham MC, et al. Sonographic characteristics of small hepatocellular carcinoma. Gastrointestinal Radiol 1989;14:255-261
17. Choi BI, Takayasu K, Han MC. Small hepatocellular carcinomas and associated nodular lesions of the liver: pathology, pathogenesis and imaging findings. AJR Am J Roentgenol 1993;160:1177-1187
18. Collier JD, Carpenter M, Burt AD, et al. Expression of mutant p53 protein in hepatocellular carcinoma. Gut 1994:35:98-100
19. Corrigan K, Semelka RC. Dynamic contrast-enhanced MR imaging of fibrolamellar hepatocellular carcinoma. Abdom Imaging 1995;20:122-125
20. Craig JR, Peters RL, Edmondson HA, et al. Fibrolamellar carcinoma of the liver: a tumor of adolescents and young adults with distinctive clincopathologic features. Cancer 1980;46:372-379
21. Fernandez MP, Redvanly RD. Primary hepatic malignant neoplasms. Radiol Clin North Am 1998;36:333-348
22. Enwonwu CO. The role of dietary aflatoxin in the genesis of hepatocellular cancer in developing countries. Lancet 1984;2:956-958
23. Enzinger FM, Weiss SW. Soft-tissue Tumors. Mosby Year-Book, St. Louis, 1983
24. Freeny PC, Baron RL, Teefey SA. Hepatocellular carcinoma: reduced frequency of typical findings with dynamic contrast-enhanced CT in a non-Asian population. Radiology 1992;182:143-148
25. Friedman AC, Lichtenstein JE, Goodman Z, et al. Fibrolamellar hepatocellular carcinoma. Radiology 1985;157:583-587
26. Fukayama M, Nihei Z, Takizawa T, et al. Malignant epithelioid hemangioendothelioma of the liver, spreading through the hepatic veins. Virchows Arch A Pathol Anat Histopathol 1984;404:275-287
27. Furui S, Itai Y, Ohtomo K, et al. Hepatic epithelioid hemangioendothelioma: report of five cases. Radiology 1989;171:63-68
28. Gabata T, Matsui O, Kadoya M, et al. Delayed MR imaging of the liver: correlation of delayed enhancement of hepatic tumors and pathologic appearance. Abdom Imaging 1998;23:309-313
29. Gates LK Jr, Cameron AJ, Nagorney DM, et al. Primary leiomyosarcoma of the liver mimicking liver abscess. Am J Gastroenterol 1995;90:649-652
30. Goodman ZD. Nonparenchymal and metastatic malignant tumors of the liver. In: Haubrich WS, Schaffner F, Berk JE (eds): Bockus Gastroenterology. Philadelphia: WB Saunders, 1995;2488-2500
31. Grazioli L, Morana G, Caudana R, et al. Hepatocellular carcinoma: correlation between gadobenate dimeglumine-enhanced MRI and pathologic findings. Invest Radiol 2000;35:25-34
32. Grazioli L, Olivetti L, Fugazzola C, et al. The pseudocapsule in hepatocellular carcinoma: correlation between dynamic MR imaging and pathology. Eur Radiol 1999;9:62-67
33. Hagspiel KD, Neidl KF, Eichenberger AC, et al. Detection of liver metastases: comparison of superparamagnetic iron oxide-enhanced and unenhanced MR imaging at 1.5 T with dynamic CT, intraoperative US and percutanous US. Radiology 1995;196:471-478
34. Hammerstingl R, Vogl TJ Schwarz W,. Contrast-enhanced MRI of focal liver lesions: differentiation and detection of primary and secondary liver lesions using Resovist-enhanced versus gadolinium-enhanced MRI in the same patient. Acad Radiol 1998;5(Suppl 1):75-79
35. Hardell L, Bengtsson NO, Jonsson U, et al. Aetiological aspects of primary liver cancer with special regard to alcohol, organic solvents and acute intermittent porphyria - an epidemiological investigation. Br J Cancer 1984;50:389-397
36. Harris KM, Schwartz ML, Slasky BS, et al. Posttransplantation cyclosporine-induced lymphoproliferative disorders: clinical and radiologic manifestations. Radiology 1987;162;697-700

37. Hayashi M, Matsui O, Ueda K, et al. Correlation between the blood supply and grade of malignancy of hepatocellular nodules associated with liver cirrhosis: evaluation by CT during intraarterial injection of contrast medium. AJR Am J Roentgenol 1999;172:969-976
38. Hollett MD, Jeffrey RB Jr, Nino-Murcia M, et al. Dual-phase helical CT of the liver: value of arterial phase scans in the detection of small (< or = 1.5 cm) malignant hepatic neoplasms. AJR Am J Roentgenol 1995;164:879-884
39. Ichikawa T, Federle MP, Grazioli L, et al. Fibrolamellar hepatocellular carcinoma: imaging and pathologic findings in 31 recent cases. Radiology 1999;213:352-361
40. Imai Y, Murakami T, Yoshida S, et al. Superparamagnetic iron oxide-enhanced magnetic resonance images of hepatocellular carcinoma: correlation with histological grading. Hepatology 2000;32:205-212
41. Ishak KG, Sesterhenn IA, Goodman ZD, et al. Epithelioid hemangioendothelioma of the liver: a clinicopathologic and follow-up study of 32 cases. Hum Pathol 1984;15:839-852
42. Ishak KG. Malignant mesenchymal tumors of the liver. In: Okuda K, Ishak KG (eds): Neoplasms of the liver. Springer Verlag, New York, 1988,121-156
43. Ishak KG. Mesenchymal tumors of the liver. In Okuda K, Peter RL (eds): Hepatocellular Carcinoma. John Wiley & Sons, New York, 1976,228-587
44. Ishak KG. Pathogenesis of liver iseases. In: Farber E, Philips MJ, Kaufman N (eds): International Academy of Pathology Monograph, No. 28, Williams & Wilkins, Baltimore, 1987,314-315
45. Itai Y, Matsui O. Blood flow and liver imaging. Radiology 1997;202:306-314
46. Ito Y, Kojiro M, Nakshima T, et al. Pathomorphologic characteristics of 102 cases of thorotrast-related hepatocellular carcinoma, cholangiocarcinoma, and hepatic angiosarcoma. Cancer 1988;62:1153-1162
47. Jaffe ES. Malignant lymphomas: pathology of hepatic involvement. Semin Liver Dis 1987;7:257-268
48. Jang HJ, Lim HK, Lee WJ, et al. Ultrasonographic evaluation of focal hepatic lesions: comparison of pulse inversion harmonic, tissue harmonic, and conventional imaging techniques. J Ultrasound Med 2000;19:293-299
49. Kew MC. Hepatic tumors and cysts. In: Feldman M, Scharschmidt BF, Sleisenger MH (eds): Sleisenger and Fordtran's Gastrointestinal and Liver Disease (6th ed). WB Saunders, Philadelphia, 1998,1364-1387
50. Kim AY, Choi BI, Kim TK, et al. Hepatocellular carcinoma: power Doppler US with a contrast agent - preliminary results. Radiology 1998;209:135-140
51. Kim T, Murakami T, Takahashi S, et al. Optimal phases of dynamic CT for detecting hepatocellular carcinoma: evaluation of unenhanced and triple-phase images. Abdom Imaging 1999;24:473-480
52. Kojiro M, Nakashima T. Pathology of hepatocellular carcinoma. In: Okuda K, Ishak KG (eds): Neoplasms of the Liver. Springer-Verlag, New York, 1987,81-104
53. Kojiro M. Hepatocellular nodular lesions. In: Kojiro M (ed): Pathology of Early Hepatocellular Carcinoma and Related Lesions. Medical Publishers, Tokyo, 1996;148-165
54. Krinsky GA, Lee VS, Theise ND, et al. Hepatocellular carcinoma and dysplastic nodules in patients with cirrhosis: prospective diagnosis with MR imaging and explanation correlation. Radiology 2001;219:445-454
55. Kuszyk BS, Bluemke DA, Urban BA, et al. Portal-phase contrast-enhanced helical CT for the detection of malignant hepatic tumors: sensitivity based on comparison with intraoperative and pathologic findings. AJR Am J Roentgenol 1996;166:91-95
56. LaBrecque DR. Neoplasia of the liver: focal nodular hyperplasia. In: Kaplowitz N (ed): Liver and Biliary Diseases (2nd ed): Williams & Wilkins, Baltimore, 1996, 391-438
57. Lai C, Gregory PB, Wu P, et al. Hepatocellular carcinoma in Chinese males and females: Possible causes for male predominance. Cancer 1987;60:1107-1110
58. Lauffer JM, Zimmermann A, Krahenbuhl L, et al. Epithelioid hemangioendothelioma of the liver. Cancer 1996:78(11):2318-2327
59. Lencioni R, Pinto F, Armillotta N, et al. Assessment of tumor vascularity in hepatocellular carcinoma: comparison of power Doppler US and color Doppler US. Radiology 1996;201:353-358
60. Lewis KH, Chezmar JL. Hepatic metastases. Magn Reson Imaging Clin N Am 1997;5:319-330
61. Lim JH, Cho JM, Kim EY, et al. Dysplastic nodules in liver cirrhosis: evaluation of hemodynamics with CT during arterial portography and CT hepatic arteriography. Radiology 2000;214:869-874
62. Lim JH, Choi D, Cho SK, et al. Conspicuity if hepatocellular nodular lesions in cirrhotic livers at ferumoxides-enhanced MR imaging: importance of Kupffer cell number. Radiology 2001;220:669-676
63. Locker GY, Doroshow JH, Zwelling LA, et al. The clinical features of hepatic angiosarcoma: a report of four cases and a review of the English literature. Medicine, (Baltimore) 1979;58:48-64
64. Manfredi R, Maresca G, Baron RL, et al. Delayed MR imaging of hepatocellular carcinoma enhanced by gadobenate dimeglumine (Gd-BOPTA). J Magn Reson Imaging 1999;9:704-710
65. Marti-Bonmati L, Ferrer D, Menor F, et al. Hepatic mesenchymal sarcoma: MRI findings. Abdom Imaging 1993;18:176-179
66. McLarney JK, Rucker PT, Bender GN et al. Fibrolamellar carcinoma of the liver: radiologic-pathologic correlation. Radiographics 1999;19:453-471
67. Miller WJ, Dodd GD 3rd, Federle MP, et al. Epithelioid hemangioendothelioma of the liver: imaging findings with pathologic correlation. AJR Am J Roentgenol 1992;159:53-57
68. Murakami T, Baron RL, Peterson MS, et al. Hepatocellular carcinoma: MR imaging with mangafodipir trisodium (Mn-DPDP). Radiology 1996;200:69-77
69. Murakami T, Kim T, Takamura M, et al. Hepatitis, cirrhosis and hepatoma. J Magn Reson Imaging 1998;8:346-358
70. Murakami T, Kim T, Takamura M, et al. Hypervascular hepatocellular carcinoma: detection with double arterial phase multi-detector row helical CT. Radiology 2001;218:763-767
71. Nakashima T, Kojiro M. Hepatocellular carcinoma: An Atlas of its Pathology. Springer-Verlag, Tokyo, 1987
72. Nerlich AG, Majewski S, Hunzelmann N, et al. Excessive collagen formation in fibrolamellar carcino-

ma of the liver: a morphological and biochemical study. Mod Pathol 1992;5:580-585
73. Noguchi S, Yamamoto R, Tatsuta M, et al. Cell features and patterns in fine-needle aspirates of hepatocellular carcinoma. Cancer 1986;58:321-328
74. Nzeako UC, Goodman ZD, Ishak KG. Hepatocellular carcinoma in cirrhotic and noncirrhotic livers: a clinico-histopathologic study of 804 North American patients. Am J Clin Pathol 1996;105:65-75
75. Ohsawa M, Aozasa K, Horiuchi K, et al. Malignant lymphoma of the liver. Report of five cases and review of the literature. Dig Dis Sci 1992;37:1105-1109
76. Oliver JH 3rd, Baron RL, Federle MP, et al. Detecting hepatocellular carcinoma: value of unenhanced or arterial phase CT imaging or both used in conjunction with conventional portal venous phase contrast-enhanced CT imaging. AJR Am J Roentgenol 1996;167:71-77
77. Orsatti G, Hytiroglou P, Thung SN, et al. Lamellar fibrosis in the fibrolamellar variant of hepatocellular carcinoma: a role for transforming growth factor beta. Liver 1997;17:152-156
78. Parker SL, Tong T, Bolden S, et al. Cancer statistics. CA Cancer J Clin 1997;47:5-27
79. Paulson EK. Evaluation of the liver for metastatic disease. Semin Liver Dis 2001;21(2):225-236
80. Peterson MS, Baron RL, Marsh JW, et al. Pretransplantation surveillance for possible hepatocellular carcinoma in patients with cirrhosis: epidemiology and CT-based tumor detection rate in 430 cases with surgical pathologic correlation. Radiology; 2000;217:743-749
81. Peterson MS, Baron RL, Rankin SC, et al. Hepatic angiosarcoma: findings on multiphasic contrast-enhanced helical CT do not mimic hepatic hemangioma. AJR Am J Roentgenol 2000;175:165-170
82. Peterson MS, Murakami T, Baron RL. MR imaging patterns of gadolinium retention within liver neoplasms. Abdom Imaging 1998;23:592-599
83. Pinson CW, Lopez RR, Ivancev K, et al. Resection of primary hepatic malignant fibrous histiocytoma, fibrosarcoma and leiomyosarcoma. South Med 1994;87:384-391
84. Rizzi EB, Schinina V, Cristofaro M, et al. Non-hodgkin's lymphoma of the liver in patients with AIDS: sonographic, CT and MRI findings. J Clin Ultrasound 2001;29:125-129
85. Rofsky NM, Earls JP. Mangafodipir trisodium injection (Mn-DPDP). A contrast agent for abdominal MR imaging. Magn Reson Imaging Clin N Am 1996;4:73-85
86. Ros PR, Murphy BJ, Buck JL, et al. Encapsulated hepatocellular carcinoma: radiologic findings and pathologic correlation. Gastrointest Radiol 1990;15:233-237
87. Ros PR, Taylor HM. Malignant Tumors of the liver. Textbook of gastrointestinal radiology, Vol II, second edition. Saunders, Philadelphia, 2000,1523-1568
88. Ros PR. Malignant liver tumors. In: Gore RM, Levine MS, Laufer I (eds): Gastrointestinal radiology. Saunders, Philadelphia, 1994,1897-1946
89. Runge VM, Lee C, Williams NM. Detectability of small liver metastases with gadolinium BOPTA. Invest Radiol 1997;32:557-565
90. Sakamoto M, Hirohashi S, Shimosato Y. Early stages of multistep hepatocarcinogenesis: adenomatous hyperplasia and early hepatocellular carcinoma. Hum Pathol 1991;22:172-178
91. Senéterre E, Taourel P, Bouvier Y, et al. Detection of hepatic metastases: ferumoxides-enhanced MR Imaging versus unenhanced MR Imaging and CT during arterial portography. Radiology 1996; 200:785-792
92. Sherlock S, Dooley J. Diseases of the liver and Biliary System (9th ed). Blackwell Scientific Publications, Oxford, 1993, 44-61
93. Shirkhoda A, Ros PR, Farah J, et al. Lymphoma of the solid abdominal viscera. Radiol Clin North Am 1990;28:785-799
94. Siskin GP, Haller JO, Miller S, et al. AIDS-related lymphoma: radiologic features in pediatric patients. Radiology 1995;196:63-66
95. Smalley SR, Moertel CG, Hilton JF, et al. Hepatoma in the noncirrhotic liver. Cancer 1988;62:1414-1424
96. Soyer P, Roche A, Levesque M, et al. CT of fibrolamellar hepatocellular carcinoma. J Computed Assist Tomogr 1991;15:533-538
97. Stevens WR, Johnson CD, Stephens DH, et al. Fibrolamellar hepatocellular carcinoma: stage at presentation and results of aggressive surgical management. AJR Am J Roentgenol 1995; 164:1153-1158
98. Sussman EB, Nydick I, Gray GF. Hemangioendothelial sarcoma of the liver and hemochromatosis. Arch Pathol 1974;97:39-42
99. Tamburro CH. Relationship of vinyl monomers and liver cancers: angiosarcoma and hepatocellular carcinoma. Semin Liver Dis 1984;4:158-169
100. Van Beers B, Roche A, Mathieu D, et al. Epithelioid hemangioendothelioma of the liver: MR and CT findings. J Comput Assist Tomogr 1992;16:420-424
101. Wang C, Ahlstrom H, Ekholm S, et al. Diagnostic efficacy of MnDPDP in MR imaging of the liver. A phase III multicentre study. Acta Radiol 1997;38:643-649
102. Weiss SW, Enzinger FM. Epithelioid hemangioendothelioma: a vascular tumor often mistaken for a carcinoma. Cancer 1982;50:970-981
103. Wernecke K, Peters PE, Kruger KG. Ultrasonographic patterns of focal hepatic and splenic lesions in Hodgkin's and non-Hodgkin's lymphoma. Br J Radiol 1987;60:655-660
104. Winston CB, Schwartz LH, Fong Y, et al. Hepatocellular carcinoma: MR imaging findings in cirrhotic livers and noncirrhotic livers. Radiology 1999;210:75-79
105. Worawattanakul S, Semelka RC, Kelekis NL, et al. Angiosarcoma of the liver: MR imaging pre- and post chemotherapy. Magn Reson Imaging 1997;15:613-617
106. Yamashita Y, Fan ZM, Yamamoto H, et al. Spin-echo and dynamic gadolinium-enhanced FLASH MR imaging of hepatocellular carcinoma: correlation with histopathologic findings. J Magn Reson Imaging 1994;4:83-90
107. Yu JS, Kim KW, Kim EK, et al. Contrast enhancement of small hepatocellular carcinoma: usefulness of three successive early image acquisitions during multiphase dynamic MR imaging. AJR Am J Roentgenol 1999;173:597-604

7

Imaging of the Biliary Tree and Gallbladder Diseases

CONTENTS

7.1 Introduction - Imaging Technique

The imaging techniques employed to evaluate the biliary system are usually selected on the basis of the diagnostic information required, the clinical presentation, and the body habitus. Although ultrasound (US) and computed tomography (CT) are the primary non-invasive imaging modalities for screening patients with biliary tree pathology, MR cholangiopancreatography (MRC) is rapidly assuming a more important role in non-invasive evaluation of the intra- and extrahepatic bile ducts. Percutaneous transhepatic cholangiography (PTC) and endoscopic retrograde cholangiopancreatography (ERCP) are able to provide detailed information on ductal anatomy and pathology through direct opacification of the bile ducts [72]. These techniques are also very useful as non-surgical therapeutic methods for biliary drainage, stent placement, stone removal and stricture dilatation.

US is generally used to screen patients with suspected biliary ductal disease. It is usually performed using the highest-frequency transducer at 3.5 MHz in obese patients and 5 MHz in thin patients. However, whereas the choledochal and common hepatic ducts can usually be seen, the intrahepatic ducts are rarely seen unless they are dilated. Usually the common hepatic duct and the common biliary duct are evaluated using parasagittal scans and appear as tubular hypoechoic structures. The common hepatic duct is identified anteriorly and laterally to the proximal main portal vein or the undivided right portal vein. The right hepatic artery passes between the posteriorly located portal vein and the anteriorly located common hepatic duct which can usually be measured at this level. The common bile duct is difficult to evaluate in the distal portion because of overlying gas in the duodenum and hepatic flexure. However, visualization can be improved by scanning the patient in a semi-erect position [67]. Color Doppler US is very helpful in distinguishing bile ducts from small hepatic vessels, especially in the left lobe where parallel branching hepatic anterior and portal veins may mimic dilated left intrahepatic ducts.

Frequently, US is able to visualize not only the dilated ducts in patients with biliary obstruction, but also the lesion associated with the duct dilatation. Biliary dilatation may also be observed in the absence of obstruction in patients who have undergone prior biliary surgery and cholecystectomy, or in subjects with resolved obstruction [54].

Whereas most abdominal US examinations are performed after prolonged fasting, the administration of a fatty meal prior to examination of the bil-

iary tree is an adjunctive maneuver that provides functional information in addition to increasing the accuracy of obstruction detection. Whereas a normal, non-obstructed duct decreases in size or does not change in caliber, an increase in caliber of 2 mm or more suggests some degree of ductal obstruction and the need for further evaluation [58].

On CT, bile ducts appear as water-dense tubular branching structures converging at the porta hepatis. The common hepatic duct and the common biliary ducts have a similar shape, and are generally visible within the hepatoduodenal ligament. The distal common biliary duct appears on cross-section as a circular, low-density structure in the pancreatic head. The normal hepatic duct on CT scans is 3-6 mm in diameter, and the common bile duct is 6-7 mm in diameter. Most CT examinations are performed in three phases (pre-contrast, arterial and portal-venous), frequently after the ingestion of 500-800 ml of water to distend the gastrointestinal tract.

Multi-detector computed tomography (MDCT) has greatly enhanced the capabilities of CT to assess the upper abdomen, and is increasingly proving useful for the evaluation of biliary duct disease. In addition, because the total length of the common bile duct can be delineated more completely, MDCT may be a more useful means of precisely defining the site and cause of biliary obstruction. This imaging modality permits precise evaluation of biliary tract abnormalities such as choledocholithiasis, hepatolithiasis, cholangiocarcinoma, extrinsic lesions obstructing the biliary tract, and congenital biliary tract anomalies [26].

MR imaging (MRI) has become more useful for biliary system imaging since the introduction of fast imaging strategies, gradient echo sequences, fast spin-echo sequences, and half-Fourier acquisition single-shot sequences (HASTE). MRC in association with morphologic imaging using T1- and T2-weighted sequences, has emerged as an accurate, non-invasive alternative to diagnostic endoscopic retrograde cholangiography (ERC) for the evaluation of diseases of the biliary tract [75].

MRC is performed using heavily T2-weighted sequences that depict the hyperintense fluid contained within the bile ducts with high signal intensity, whereas suppression of the signal of surrounding, non-fluid containing structures is achieved due to the long echo-time. MR images are acquired in the coronal and axial planes, typically with the use of a phase-array imaging coil to increase overall accuracy [48].

MRC is usually performed using a multisection technique involving the acquisition of multiple 1-3 mm thick source images of the pancreaticobiliary tract. Because of the orientation of the normal bile duct, the biliary tract is usually partially visualized on each of several images rather than visualized in its entirety on a single image. Although diagnostic decisions are usually made on the basis of the source images, three-dimensional (3D) images can be obtained with maximum intensity projection (MIP) and multiplanar reconstruction (MPR) techniques. Moreover, 3D images are able to provide a road map of the obstructed ductal system, delineate complex strictures, and assist in the planning of percutanous, surgical, and endoscopic procedures [19]. Another approach, which obviates the need for MIP post-processing, is to employ a single-shot projection technique to obtain a 30-70 mm thick image, during a three second acquisition.

The availability of MR contrast agents with hepatobiliary properties such as Gd-BOPTA, Mn-DPDP and Gd-EOB-DTPA, which are in part eliminated through the hepatobiliary system, permit the biliary tree to be visualized on T1-weighted images. This approach may prove useful for evaluating leakage from the biliary tree after hepatic resection or liver transplantation [21, 23].

7.2 Anatomy

7.2.1 Normal Anatomy

The liver is divided into the left and right lobe, and each lobe is divided into segments on the basis of its vascular anatomy and biliary drainage. The intrahepatic bile ducts generally follow the internal hepatic segmental anatomy. In the left lobe, a left medial segment duct and a left lateral segment duct normally join to form the main left hepatic duct. The right hepatic duct branches near its origin at the common hepatic duct. Frequently, the right hepatic duct has a dorso-caudal branch, draining the posterior segment of the right lobe, and a ventro-cranial branch, draining the anterior segment of the right lobe. Ductal drainage of the caudate lobe is variable and may be related to the left or right ductal system. The left and right hepatic ducts unite just outside the liver to form the common hepatic duct, which is usually 3-4 cm in length. The common hepatic duct courses ventrally and inferiorly with the hepatic artery and the portal vein from the porta hepatis in the hepatoduodenal ligament. The common hepatic duct joins the cystic duct to form the common bile duct that averages 6-7 cm in length. The common bile duct is divided into suprapancreatic, intrapancreatic, and ampullary segments, and enters the posterior-medial aspect of the second portion of the duodenum through a 1-2 cm long intramural tunnel terminating at the major duodenal papilla (Papilla of Vateri). The common bile duct in many

cases joins the pancreatic duct in the duodenal wall, and has a short common channel. The sphincter of Oddi surrounds the common channel and the choledochal sphincter surrounds the common bile duct from its entrance into the duodenal wall to its junction with the pancreatic duct. Microscopically, the extrahepatic ducts are composed mainly of elastic fibers, and are sparse in muscle fibers. This explains their change in size in response to fluctuations in intraductal pressure.

The gallbladder is an elliptical organ that straddles the intersegmental plane between liver segments IV and V. The gallbladder is divided into four parts: the fundus, the body, the infundibulum, and the neck. Usually the organ is attached to the liver by the parietal peritoneum. When relaxed, the normal gallbladder is approximately 10 cm long, 3-5 cm in diameter and has a capacity of approximately 50 ml. The gallbladder wall is usually 2-3 mm thick and composed of columnar epithelium. Lymphatic drainage of the gallbladder descends around the bile duct and involves cystic and pericholedochal lymph nodes. From the pericholedochal nodes the drainage continues to nodes found posterior to the pancreas, portal vein, and common hepatic artery, until finally the lymphatic flow reaches the lymph nodes of the interaortocaval region, celiac artery, and superior mesenteric artery. The gallbladder communicates with the common bile duct via the cystic duct, which is 2-4 cm in length, and contains tortuous folds known as the spiral valves of Heister near the neck of the gallbladder. The cystic duct usually joins the common hepatic duct approximately halfway between the porta hepatis and the ampulla of Vateri to form the common bile duct.

7.2.2 Biliary Tree and Gallbladder Anomalies

The primitive liver is composed of bipotential embryonic cells that can differentiate into either parenchymal or biliary cells. Biliary differentiation occurs when the embryonic cells are in contact with the mesenchyme surrounding the portal vein ramifications; this cell layer ultimately forms an epithelial cylinder called the ductal plate. Some segments of the cylindrical lumen form tubular structures that are gradually incorporated into the portal mesenchyme. This results in the portal triad acquiring a tubular bile duct surrounded by portal connective tissue. Abnormalities in ductal plate development can affect any level of the biliary tree, thereby explaining the diversity of congenital bile duct abnormalities [15].

Biliary tree malformations, with the exception of choledocal cysts, are often asymptomatic. Therefore the diagnosis is frequently not made until adulthood.

7.2.2.1 Choledochal Cyst and Cystic Dilatation of the Bile Duct

Choledochal cysts are anomalies of the biliary system characterized by dilatation of the extrahepatic or intrahepatic bile ducts. These anomalies are more frequent in females with a ratio of 4:1. In about 60% of cases the diagnosis is made in the first ten years of life, although choledochal cysts may become evident at any age (see Chap. 10, "MR Imaging of the Liver in Pediatric Patients", section 10.3.6, "Choledochal Cyst and Cystic Dilatation of the Bile Duct").

Choledochal cysts are considered to arise as a result of an anomalous junction of the pancreatic duct and common bile duct resulting in a long common channel [28]. This was first recognized in 1969 by Babbitt [4], who suggested that this long common channel allowed reflux of pancreatic enzymes into the common bile duct, with subsequent inflammation and weakening of the common bile duct wall with progressive dilatation.

Until recently, the Todani Classification [64] (Fig. 1) was used to categorize cystic dilatation of the biliary ducts. According to this classification, type I, the most common type, comprises cystic (IA), focal segmental (IB), and fusiform choledochal dilatations (IC); type II cysts are true diverticula arising from the common bile duct; type III cysts, also known as choledochoceles, are dilatations of the intraduodenal portion of the common bile duct; type IV cysts are multiple intra- and extrahepatic cysts (IVA) or multiple extrahepatic cysts (IVB); and type V choledochal cysts, also known as Caroli's disease, are multifocal cystic or saccular dilated intrahepatic bile ducts that may diffusely involve the liver, or less commonly involve only the left segment of the liver.

A more recent classification scheme, the Miyano Classification [47] (Fig. 2), now classifies choledochal cysts according to an association with the common channel. The disease is thus classified as:

1) associated with the common pancreatic bile duct: A (cystic), B (with intrahepatic biliary tree dilatation), C (fusiform),
2) without common pancreatic bile duct association: D (diverticula), E (sub-stenosis of the papilla with distal dilatation), F (intrahepatic dilatations – Caroli's disease).

Choledochal cysts typically vary from 1-10 cm, in size, although larger forms exist which may contain 5-10 l of bile. Histopathologically, the wall is usually thickened by inflammation and fibrosis, and is stained with bile; islets of cylindrical or columnar epithelium and intestinal metaplasia may be present.

The classic clinical triad of pain, a mass in the right upper abdominal quadrant and jaundice oc-

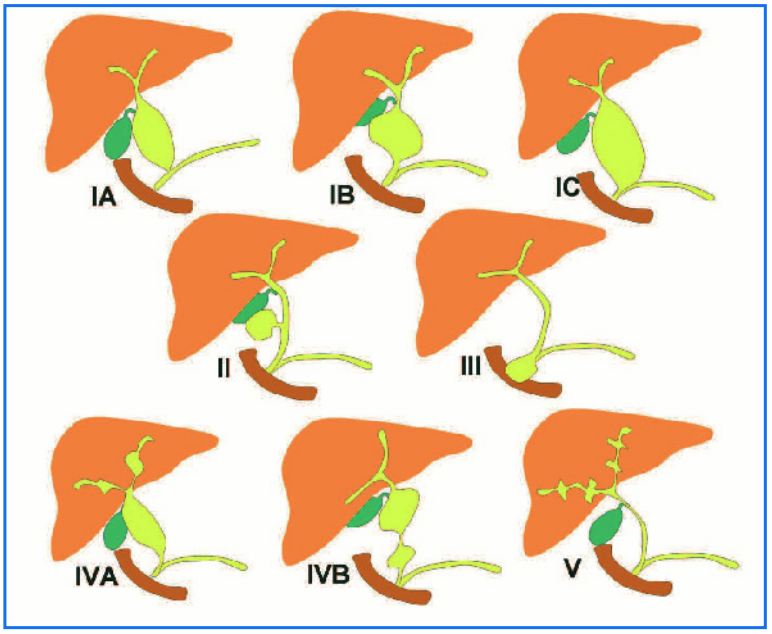

Fig. 1. Todani Classification of cystic dilatation of the biliary ducts

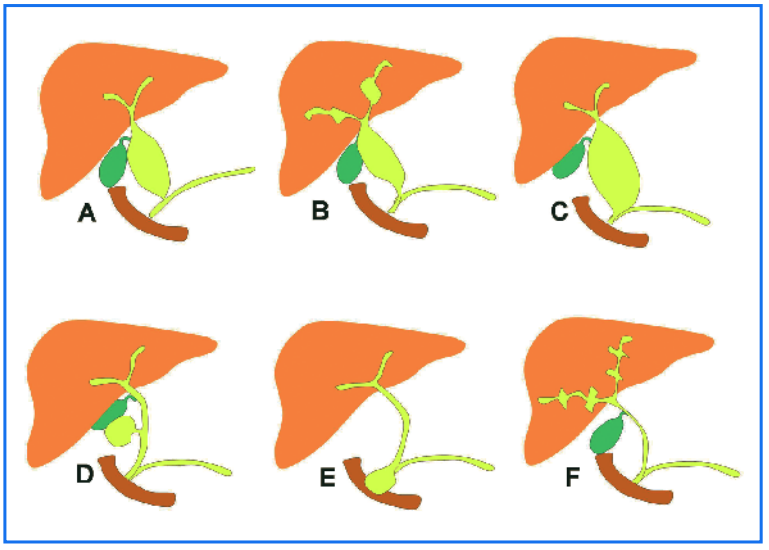

Fig. 2. Miyano Classification of cystic dilatation of the biliary ducts

curs in fewer than a third of patients with choledochal cysts. In newborns and infants, obstructive jaundice is the most common presentation, while in older children and adults the signs and symptoms are those of ascending cholangitis [65].

From the surgeon's point of view, road mapping is important for planning the operative approach to choledochal cysts. Information on the anomalous arrangement of the pancreaticobiliary duct system and the morphology of the duct is extremely important for determining the appropriate surgical procedure. Surgeons are concerned about the exact location of the pancreatic duct, the site of entry in the duodenum, and the length of the common channel.

At US these malformations appear as anechoic, hypoechoic fusiform or cystic lesions in the region of the porta hepatis, with communication to the biliary tree (Fig. 3). The gallbladder is always wellseparated from the cyst. Often it is possible to observe intraluminal sludge or stones within the biliary tree. Color-Doppler US shows the absence of vascularization within the cyst (Fig. 4). Unfortunately, the precise extent of cystic dilatation of the biliary system, the relationship of the cyst to the gallbladder and pancreatic duct, and the angle and site of the junction with the duodenum may be difficult to assess using US [36].

ERCP is frequently used to study the biliary tree in patients with choledochal cysts. However, it

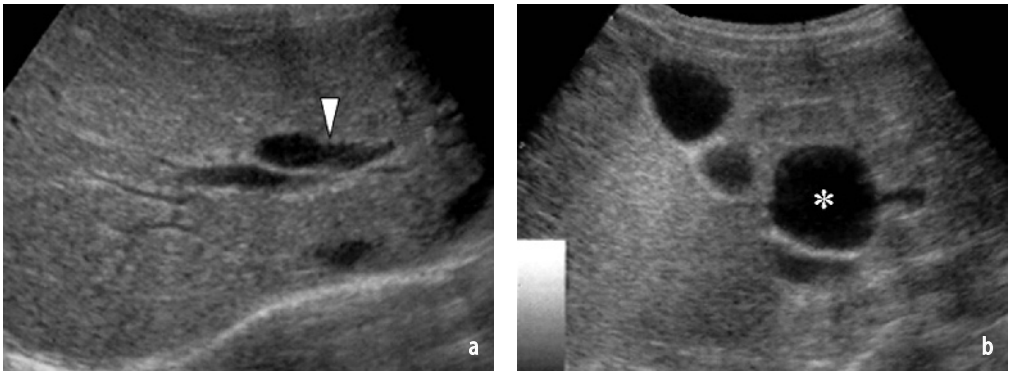

Fig. 3a, b. Choledochal cyst. US scans of choledochal cysts show an anechoic fusiform lesion (**a**, *arrowhead*) and a cystic lesion (**b**, *asterisk*) in the region of the liver hilum

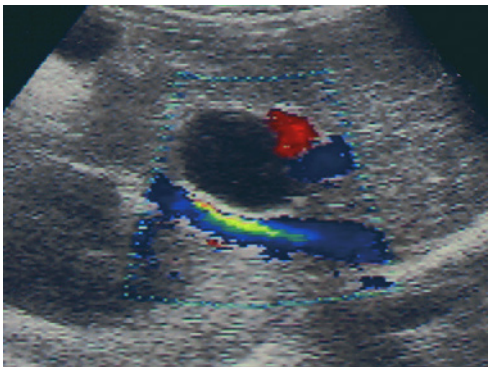

Fig. 4. Choledochal cyst. On Color Doppler US the choledochal cyst does not show any vascularization

is a diagnostic procedure that demands technical expertise and a number of safety measures, and it is not without complications. These include development of sepsis in an obstructed system, perforation of the viscera pancreatitis, and overdose of contrast agent.

At present, CT cholangiography (CTC) and increasingly, MRC, are effective non-invasive imaging alternatives to invasive cholangiography and ERCP, particularly in adult patients. MRC in particular appears to offer similar information to ERCP without the potential complications [45]. Both MRC and CTC offer comparable performance in establishing a diagnosis of choledochal cyst in pediatric patients [36].

MRC is based on imaging of stationary fluids on heavily T2-weighted pulse sequences. Since bile and pancreatic secretions have high signal intensity, choledochal cysts are characterized by a hyperintense tubular, fusiform or cystic structure (Fig. 5).

For the detection of intraductal stones CTC seems to be slightly superior to MRC. This could be related to the fact that the signal within the biliary tree is generated by the long T2 of bile. Since the T2 is shortened by protein plugs and stones, these may be more difficult to see on MRC compared to CTC. Nevertheless, when MRC is used, 2D reconstruction appears to be superior to 3D reconstruction for the detection of intraductal stones (Fig. 6).

7.2.2.2 Caroli's Disease

Caroli's disease, also known as communicating cavernous ectasia of the biliary tree, is a rare congenital disorder characterized by non-obstructive, saccular or fusiform dilatations of the intrahepatic bile ducts. It corresponds to type V of the Todani Classification and to type F of the Miyano Classification and occurs with equal frequency in males and females.

Two types of the disease have been described: the real, so-called "pure" type, and the more common type associated with congenital hepatic fibrosis. The less common pure form is characterized by saccular, digitate, or moniliform estasia of the intrahepatic bile ducts, with no other histologic abnormalities. The abnormalities typically predominate in one segment, usually in the left lobe, and may be diffuse or localized. The ectasias communicate freely with the bile ducts, promoting stasis and sludge formation, which can lead to lithiasis and cholangitis. Biliary infection and stones account for the usual presenting symptoms of fever and abdominal pain. Cholangiocarcinoma develops in approximately 5-10% of cases [46].

The more common form presents in childhood with abnormalities related to hepatic fibrosis and portal hypertension. In contrast to congenital hepatic fibrosis that arises due to the abnormal development of small interlobular bile ducts, the

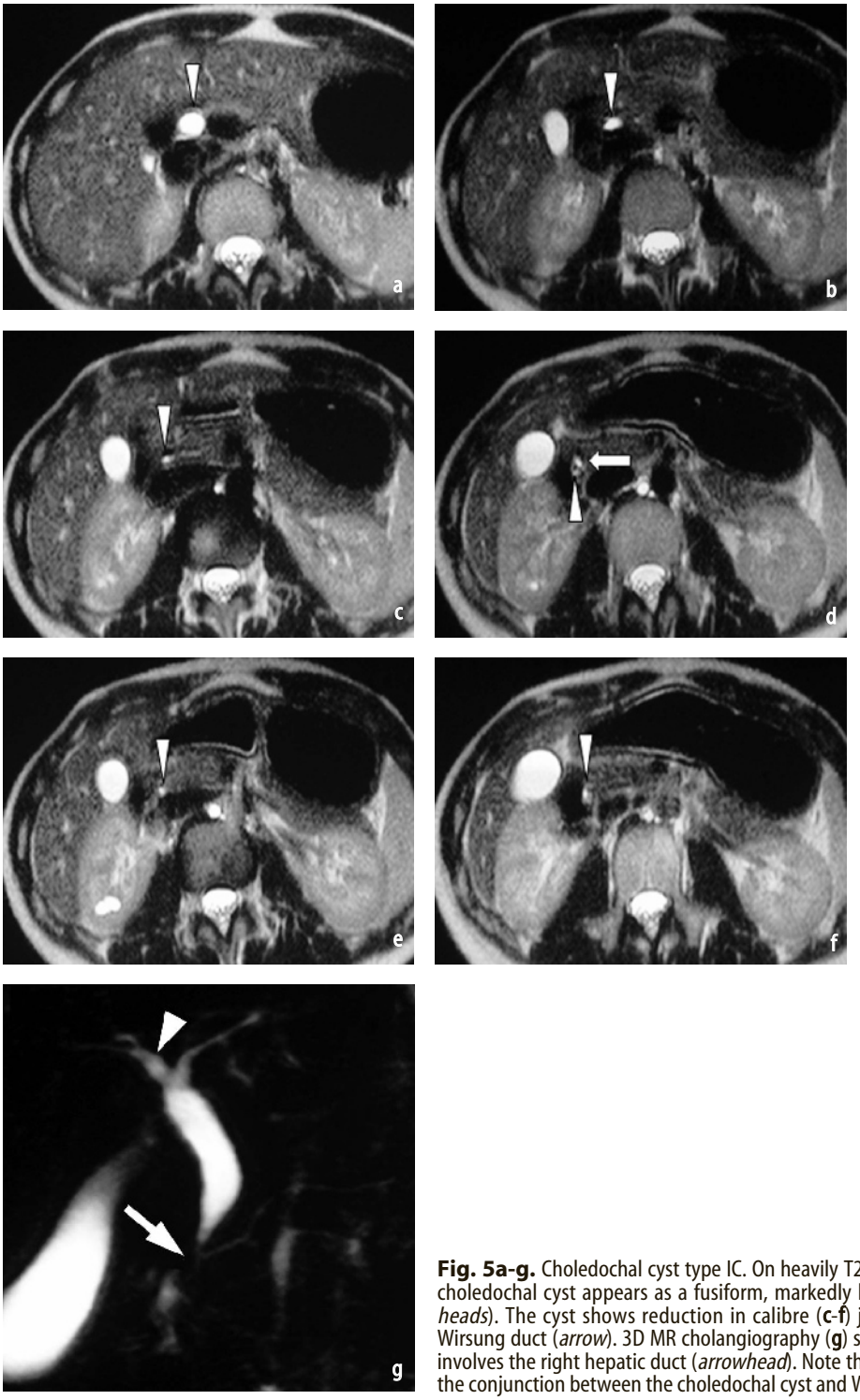

Fig. 5a-g. Choledochal cyst type IC. On heavily T2-weighted sequences (**a**-**f**), the choledochal cyst appears as a fusiform, markedly hyperintense structure (*arrowheads*). The cyst shows reduction in calibre (**c**-**f**) just above the union with the Wirsung duct (*arrow*). 3D MR cholangiography (**g**) shows the ductal dilatation that involves the right hepatic duct (*arrowhead*). Note the normal calibre (*arrow*) below the conjunction between the choledochal cyst and Wirsung duct

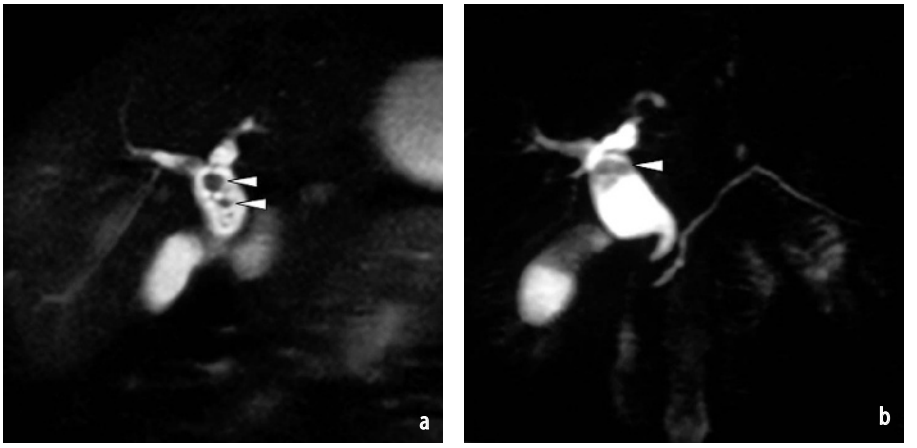

Fig. 6a, b. Choledochal cyst. 2D MR-cholangiography in coronal orientation (**a**) demonstrates a choledochal cyst and well-defined, round, hypointense intraductal structures (*arrowheads*) that correspond to stones. On 3D MR-cholangiography (**b**) the number and size of stones (*arrowhead*) is less accurately defined

more common form of Caroli's disease affects the large intrahepatic bile ducts. Histologically, intrahepatic bile duct ectasia and proliferation are associated with severe periportal fibroses. Compared with "pure" Caroli's disease, biliary duct dilatation is less marked in this form and cholangitis and biliary stone formation are usually absent. However severe problems may arise due to liver failure or complications associated with portal hypertension.

Proposed mechanisms for bile duct malformation include abnormal growth of the developing biliary epithelium and supporting connective tissue, and a lack of normal involution of the ductal plates that surround the portal tracts, resulting in epithelium-lined cysts surrounding the portal triads [34]. In the complex form, the genetic factor that causes the arrest in ductal plate remodeling seems to act not only during the early phase of embryogenesis, but also later during development of the more slender intrahepatic bile ducts and interlobular ducts. This results in the development of hepatic fibrosis at a more peripheral level of the biliary tree. Both forms of Caroli's disease can occur in combination with kidney abnormalities such as infantile polycystic kidney disease and medullary sponge kidney as well as other types of choledochal cysts. If all levels of the biliary tree are involved, features of both congenital hepatic fibrosis and Caroli's disease are present. This condition is often termed Caroli's syndrome [34, 41, 46].

Macroscopically, the intrahepatic cystic dilatations are round or lanceolate, from a few millimeters up to 5 cm in size, and may be separated by stretches of essentially normal duct. Microscopically, the dilated ducts frequently show chronic inflammation, and varying degrees of fibrosis and hyperplasia. Patients typically suffer from bouts or recurrent fever and pain, and jaundice may occur when sludge or stones block the common bile duct.

In the pure form of Caroli's disease, cholangiography reveals multiple communicating sacculi of the intrahepatic biliary tree. Stones are common and appear as filling defects. Bile duct strictures and wall irregularities may occur as a consequence of recurrent cholangitis. A similar appearance may be observed with magnetic resonance cholangiopancreatography (MRCP).

On US and CT examinations, the sacculi appear as well-defined intrahepatic cystic anechoic and hypodense areas, respectively (Fig. 7, 8). Color Doppler US usually reveals a characteristic "dot sign" related to the presence of portal vein branches at the periphery of the bile duct dilatation. The presence of stones and/or sludge may increase echogenecity and density, and the content may appear heterogeneous. Demonstration of communication between sacculi and the bile duct is important in distinguishing Caroli's disease from polycystic liver disease, but this is not easy to detect when the disease is in the early stages [46].

On MR imaging, the sacculi appear as homogeneously hypointense areas on T1-weighted images and as homogeneously hyperintense areas on T2-weighted images (Fig. 9). The signal intensity is generally homogeneous but may appear heterogeneous if stones, sludge, or phlogistic material are present within the sacculi and bile ducts (Fig. 10). In this latter situation, the surrounding liver parenchyma may also show changes in signal intensity [3]. MRCP is a valid tool for demonstrating

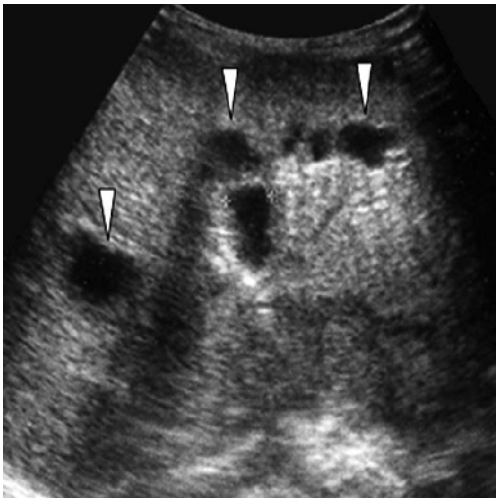

Fig. 7. Caroli disease. On US, round and tubular, hypoechoic structures (*arrowheads*) are visible

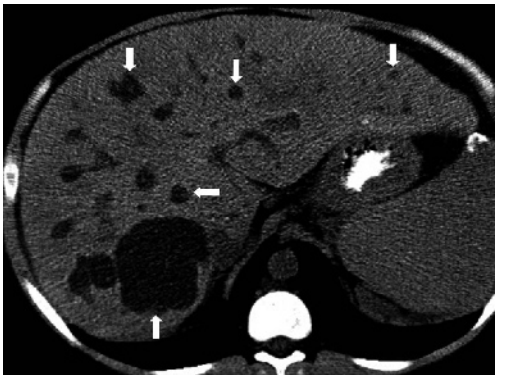

Fig. 8. Caroli disease. On unenhanced CT, numerous hypodense lesions (*arrows*) with variable shape can be seen in both lobes of the liver, but predominantly in the right liver lobe

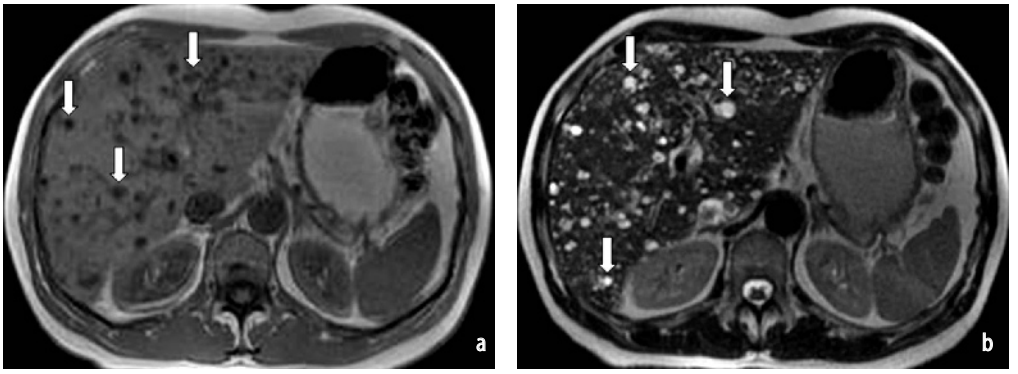

Fig. 9a, b. Caroli disease. On pre-contrast T1-weighted GRE (**a**) and T2-weighted TSE (**b**) images, diffuse intrahepatic round lesions (*arrows*), corresponding to intrahepatic sacculi, are homogeneously hypointense and homogeneously hyperintense, respectively

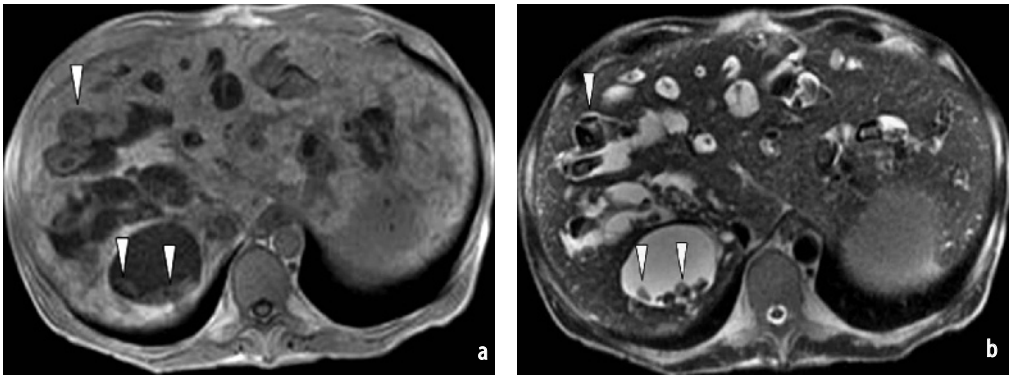

Fig. 10a, b. Caroli disease. Pre-contrast T1-weighted GRE (**a**) and T2-weighted TSE (**b**) images show heterogeneity within the sacculi (*arrowheads*) due to the presence of intraductal stones

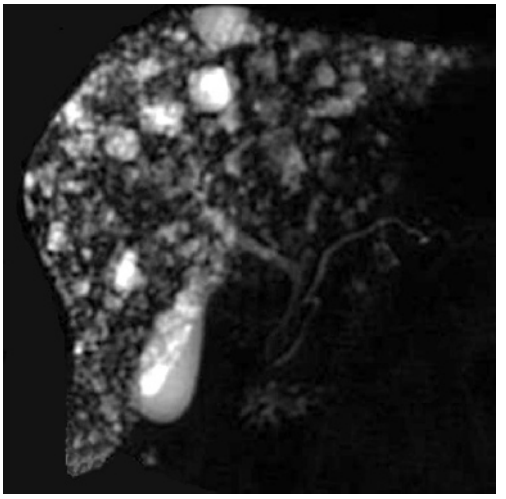

Fig. 11. Caroli disease on MRCP. Same case as demonstrated in Fig. 9. MRCP demonstrates diffuse, hyperintense, round and cystic lesions, distributed in both lobes of the liver, with a flower tree appearance

communication between sacculi and bile ducts (Fig. 11), which is positively demonstrated with Gd-BOPTA and other hepatobiliary contrast agents if contrast material is present within the sacculi and bile ducts during the hepatobiliary phase after administration (Fig. 12).

Differential diagnoses of Caroli's disease include primary sclerosing cholangitis, recurrent pyogenic cholangitis, and polycystic liver disease. Primary sclerosing cholangitis and recurrent pyogenic cholangitis may be associated with duct dilatation, stenosis, intrahepatic calculi, and malignancy. The ductal dilatation in primary sclerosing cholangitis is typically more isolated and fusiform than saccular (Fig. 13), and is not characteristic of Caroli's disease. Recurrent pyogenic cholangitis is the most difficult diagnosis to exclude because patients with pyogenic cholangitis present with sepsis and have intra- and extrahepatic biliary dilatation. Saccular dilatation favors the diagnosis of Caroli's disease because it is not typical in recurrent pyogenic cholangitis. Hepatic cysts of polycystic liver disease do not communicate with the bile ducts (see Fig. 54, Chapter 4).

7.2.2.3 Biliary Atresia

Biliary atresia is an obliterative cholangiopathy that may affect not only the extrahepatic but also the intrahepatic bile duct system, with complete obliteration or discontinuity of the hepatic or common bile ducts at any point from the porta hepatis to the duodenum. Obstruction of bile flow leads to cholestasis, progressive fibrosis, and ultimately, cirrhosis. The disorder occurs once every 10,000-15,000 live births and is more common in girls than in boys [5]. It accounts for approximately one third of all cases of prolonged neonatal cholestatic jaundice (see Chapter 10, "MR Imaging of the Liver in Pediatric Patients", Section 10.5.2, "Biliary Atresia").

Although factors such as developmental malformation, perinatal viremia (cytomegalovirus, rubella, retroviruses), and toxicity of bile constituents have been implicated, the actual cause of biliary atresia remains unknown [9, 22]. A single, unifying cause appears unlikely, and it seems more probable that there is etiologic heterogeneity that results in a progressive sclerosis; for example, an inflammatory process that affects the extrahepatic biliary tract leading to ductular luminal obliteration [5].

Biliary atresia occurs in two clinical forms, the embryonic or fetal type, and the perinatal type. The latter form is more frequent, and accounts for more than 60% of cases. The fetal variant may be associated with congenital malformations such as polysplenia, cardiovascular defects, abdominal situs inversus, intestinal malrotation, and anomalies of the portal vein and hepatic artery [22].

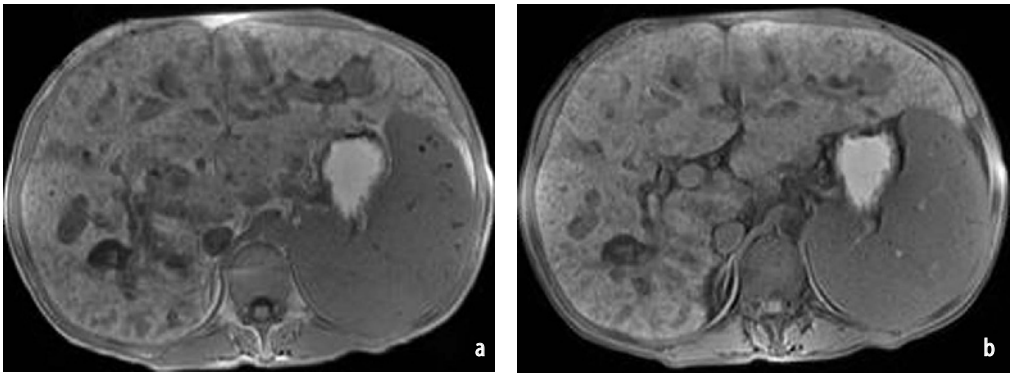

Fig. 12a, b. Caroli disease. On the unenhanced T1-weighted GRE image (**a**) the cystic sacculi are heterogeneously hypointense. On the T1-weighted GRE image (**b**) acquired during the hepatobiliary phase after the administration of Gd-BOPTA (0.1 mmol/kg BW) the cystic sacculi demonstrate an increase of signal intensity due to the presence of contrast agent within the cysts

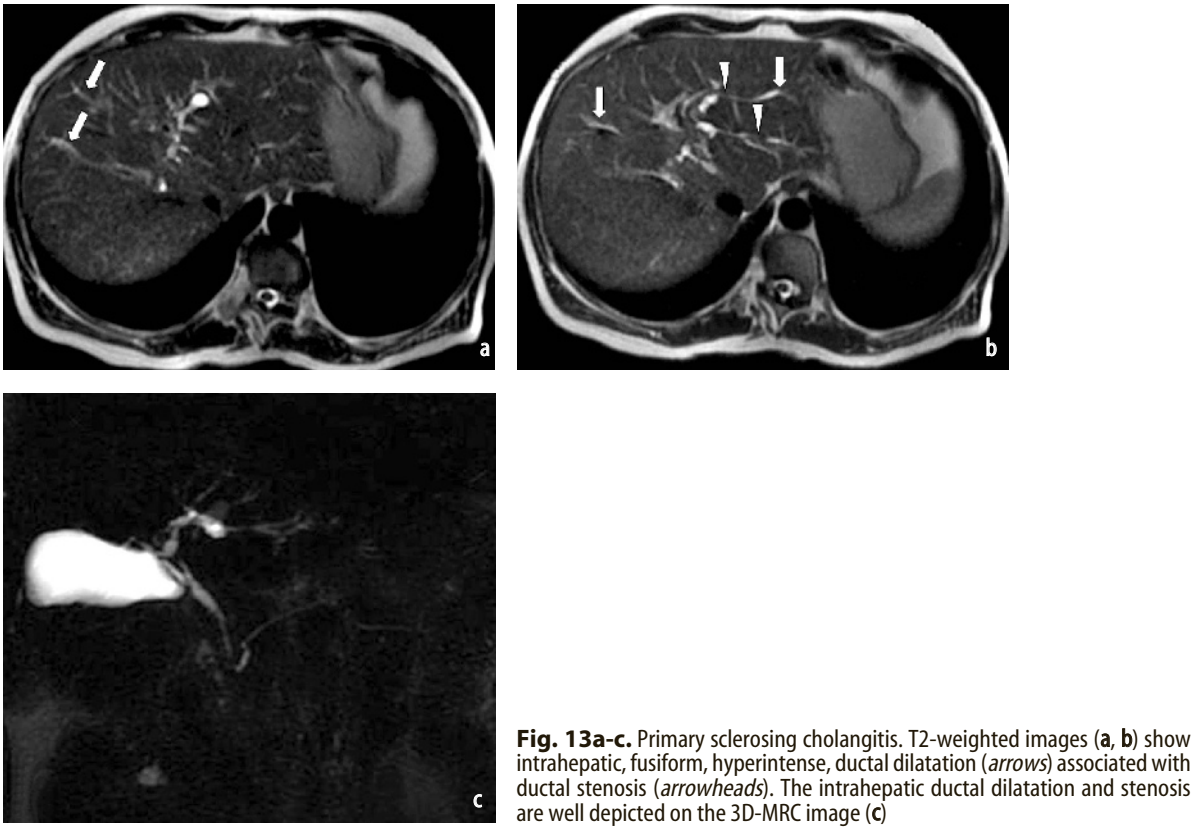

Fig. 13a-c. Primary sclerosing cholangitis. T2-weighted images (**a**, **b**) show intrahepatic, fusiform, hyperintense, ductal dilatation (*arrows*) associated with ductal stenosis (*arrowheads*). The intrahepatic ductal dilatation and stenosis are well depicted on the 3D-MRC image (**c**)

Biliary atresia can be classified in three ways according to the site of the obstruction:

- type I, obstruction at the level of the common bile duct;
- type II, obstruction at the level of common hepatic duct;
- type III, obstruction at the level of the porta hepatis.

The latter type is considerably more frequent and accounts for more than 90% of cases [9].

The macroscopic aspect of the liver varies according to the stage of the disease. At first it enlarges and is dark green in color, becoming finely nodular as cirrhosis develops. In untreated cases cirrhosis may take between 1 and 6 months after birth to develop. Microscopically, cholestasis, periportal ductal proliferation, and the presence of bile plugs in cholangioles and interlobular bile ducts are apparent. Fibrosis is progressive with a periportal and perilobular distribution. Linkage of portal areas is frequent and secondary biliary cirrhosis is a possible development [5]. In biliary atresia the liver parenchyma can be normal in structure, or demonstrate signs of biliary cirrhosis with a prominent hepatic artery.

Signs on US that may be related to biliary atresia include the shape and contractility of the gallbladder and the presence of the "triangular cord". In cases of biliary atresia, the gallbladder has a ghostlike appearance and these features have been described as the "gallbladder ghost triad" [25]. This consists of an atretic gallbladder of less than 1.9 cm in length, an absent or thinned smooth echogenic mucosal lining with indistinct walls, and a knobbly, irregular, or lobular contour (Fig. 14). A triangular- or tubular-shaped echogenic density on transverse or longitudinal scans represents a fibrous cone at the porta hepatis known as the triangular cord (Fig. 15). This focal hyperechogenicity associated with perivascular hyperechogenicity is related to progressive fibrosis and ductal sclerosis, and is very useful for the diagnosis of biliary atresia (Fig. 16) [12, 32].

Although scintigraphy is not used routinely, Technetium TC 99m iminodiacetic acid derivatives are rapidly excreted from the blood by hepatocytes and excreted into the bowel through the biliary system. With biliary obstruction, this material accumulates in the liver and none appears in the bowel (Fig. 17). When employed for imaging of infants, phenobarbital should be given for five days before the study. This is because phenobarbital increases bilirubin conjugation and excretion and has a choleretic effect, and thus enhances and accelerates the uptake of iminodiacetic acid analogues by the liver [17].

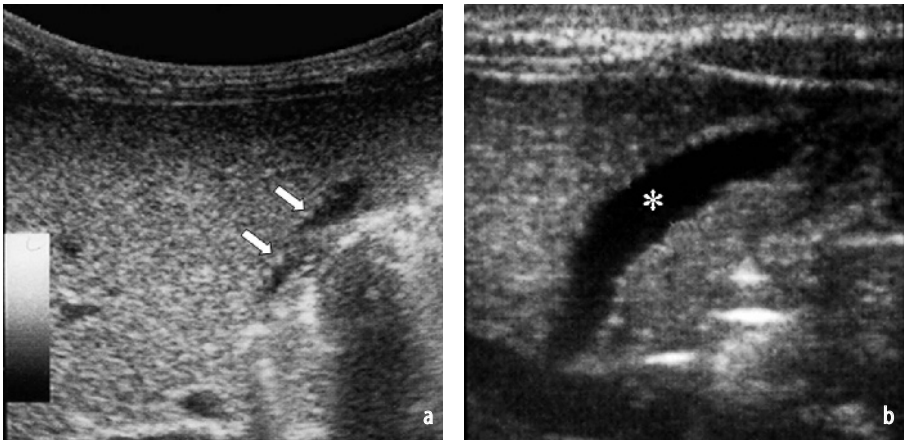

Fig. 14a, b. Biliary atresia. US scans of two different patients with biliary atresia show different gallbladder shapes. In (**a**) a very small, atretic gallbladder (*arrows*) is apparent, while in (**b**) an enlarged gallbladder (*asterisk*) with a thinned wall is seen

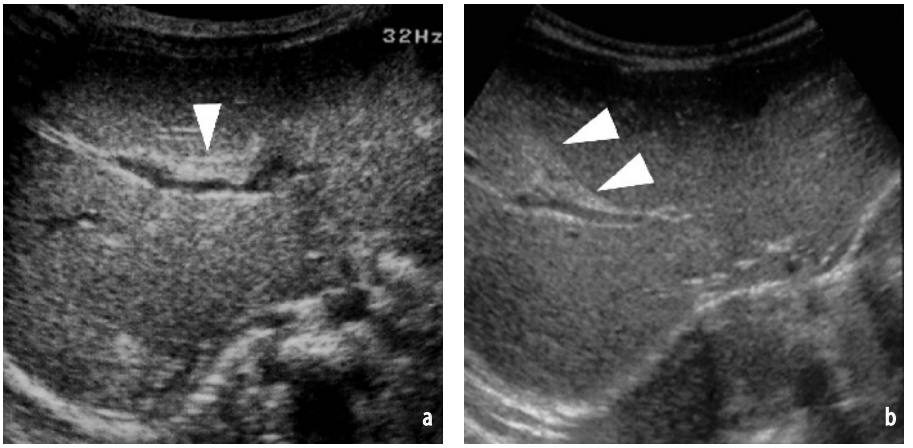

Fig. 15a, b. Biliary atresia. US scans show the triangular cord (*arrowheads*) as tubular (**a**) or triangular (**b**) hyperechoic tissue located at the porta hepatis

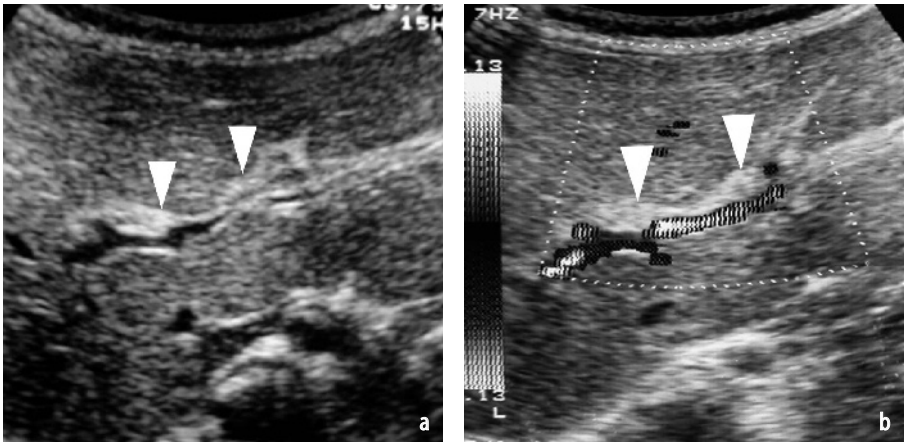

Fig. 16a, b. Biliary atresia. On US B-mode (**a**) and color Doppler US (**b**) scans, perivascular hyperechogenicity (*arrowheads*) corresponding to progressive fibrosis is clearly seen

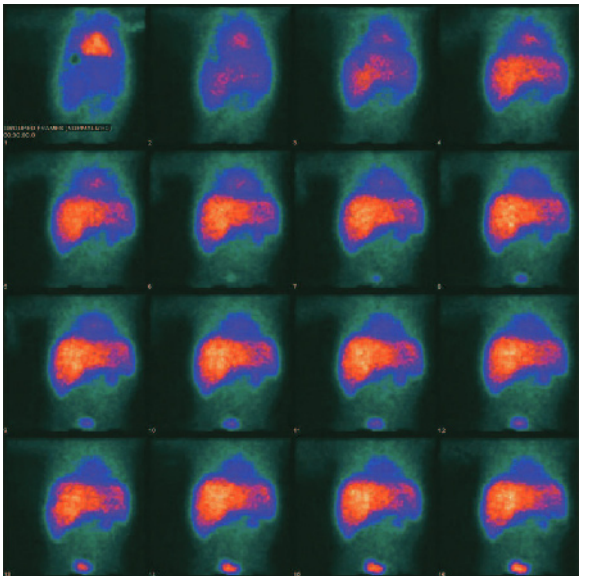

Fig. 17. Biliary atresia on scintigraphy. On Technetium 99m iminodiacetic scintigraphy scans, TC 99m is progressively accumulated in the liver and does not appear in the bowel

On T2-weighted MR imaging, moderately high signal intensity along the portal tract that extends peripherally from the porta hepatis correlates with periductal edema and inflammatory cell infiltration. Although biliary atresia can be reliably diagnosed on the basis of the lack of visualization of either the common bile duct or the common hepatic duct, findings on MRC should still be interpreted in relation to clinical information [22, 29, 52].

The prognosis of untreated biliary atresia is extremely poor, with death from liver failure usually occurring within two years. However, hepato-porto-enteroanastomy can restore bile flow in many cases if surgery is performed sufficiently quickly after diagnosis. Additional predictors of a poor outcome are caucasian race, the severity of the intrahepatic biliary cholangiopathy, the presence of cirrhosis on initial biopsy, and absence of ducts at the level of the liver hilus. The outcome correlates directly with the size of the bile duct remnants identified in the porta hepatis at surgery. Bile duct profiles of more than 150 mm and lined with columnar epithelium have been associated with a good surgical result [11, 24].

7.2.2.4 Agenesis of the Gallbladder

Failure of development of the caudal foregut diverticulum or failure of vacuolization after the solid phase of embryonic development results in agenesis of the gallbladder. In about two thirds of patients with gallbladder agenesis it is possible to observe other congenital anomalies, such as congenital heart lesions, polysplenia, imperforate anus, absence of one or more bones, and rectovaginal fistula [66].

Patients may be asymptomatic or present with right upper abdominal pain, jaundice, and vomiting. The preoperative diagnosis of gallbladder agenesis is difficult. Whereas imaging techniques such as US and CT may suggest the diagnosis, confirmation of gallbladder agenesis is usually an intraoperative finding, when its absence is discovered at cholangiography.

MR cholangiography can be considered an alternative non-invasive imaging method. The possibility of visualizing the biliary tree by means of 3D-reconstructions and to assess the absence of the gallbladder permits information to be acquired that is similar to that available by intraoperative cholangiography.

7.2.2.5 Duplication of the Gallbladder

Gallbladder duplication occurs when there is excessive budding of the caudal diverticulum. It is caused by incomplete revacuolization of the primitive gallbladder resulting in a persistent longitudinal septum that divides the gallbladder lengthwise. Gallbladder duplication may also occur due to the occurrence of separate cystic buds. Cholecystitis with cholelithiasis is a relatively frequent occurrence in these patients. The duplicated cystic ducts frequently enter the common bile duct separately, or alternatively, unite to form a common cystic duct. Less frequently they drain independently into the hepatic ducts.

US is not specific for the demonstration of this anomaly since entities such as choledochal cyst, bilobed gallbladder, and gallbladder diverticulum may mimic gallbladder duplication. MRC reliably demonstrates the presence of two gallbladders as hyperintense sacs, and can depict the type of drainage into the common bile duct [53].

7.2.2.6 Anomalies of Gallbladder Shape

Phrygian cap is the most common abnormality of gallbladder shape. The term “Phrygian cap” derives from a resemblance to folded hats worn in the ancient country of Phrygia. It is characterized by a fold or septum of the gallbladder between the body and fundus (Fig. 18). Although clinically unimportant, it may be mistaken on radiological examination for a stone or a pathological septum.

Multiseptate gallbladder is characterized by the presence of multiple internal septa of various sizes

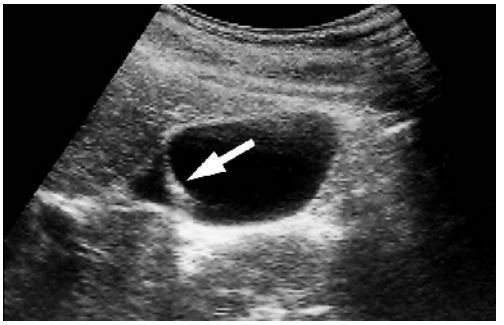

Fig. 18. Phrygian cap gallbladder. On US a hyperechoic septum (*arrow*) in the gallbladder is easily visible. This corresponds to a fold or septum of the gallbladder between the body and fundus

which divide the gallbladder lumen into several chambers. Although these chambers communicate with one another by means of one or more orifices, these septations may lead to stasis of bile and gallstone formation. On US, multiple, communicating, hyperechoic septations and locules can be seen bridging the gallbladder lumen with a honeycomb pattern [56].

MRC is not routinely performed for evaluation of this type of anomaly although it is able to demonstrate morphologic abnormalities and the internal septa.

7.3 Benign Biliary Neoplasms

7.3.1 Biliary Cystadenoma

Biliary cystadenoma is a rare cystic neoplasm that represents less than 5% of all intrahepatic cysts of biliary origin that arise from intra- and extrahepatic bile ducts [27]. This neoplasm may occur anywhere along the intra- or extrahepatic bile ducts, although about 80% of lesions are found partly or completely within the liver. The cause of biliary cystadenoma is unknown, although it could be related to a congenital anomaly of the biliary primitive bud.

This neoplasm can be classified as either a) cystadenoma with ovarian-like stroma, or b) cystadenoma without ovarian-like stroma. The variant without ovarian-like stroma is observed primarily in males and is considered more aggressive and more inclined to malignant degeneration. The form that develops predominantly in females has an ovarian-like stroma and follows an indolent course. Most lesions are more than 10 cm in diameter at diagnosis, with internal septa, and without solid components.

Microscopically, biliary cystadenoma has a mucin-secreting columnar epithelium lining the cysts. The lining cells have a pale eosinophilic cytoplasm and basally-oriented nuclei, typical of biliary-type epithelium. The epithelium is supported by a mesenchymal stroma which is compact and cellular [16].

Biliary cystadenoma is regarded as a pre-malignant tumor. Malignant transformation into cystadenocarcinoma may occur in up to 15% of cases. *In situ* carcinoma with papillary growth into the cysts may be the only lesion present although invasive adenocarcinoma may also be seen [35, 68].

Approximately 90% of these neoplasms occur in middle-aged women. When present, the symptoms are those of a growing abdominal mass. Right upper quadrant abdominal pain, occasionally irradiating to the scapula, is the main symptom [8].

On US, biliary cystadenoma is seen as a large hypoechoic, multiloculated cystic-like lesion with intralesional septa (Fig. 19). Occasionally mural nodules occur in benign cystadenoma, although these are more common within cystadenocarcinoma, in which they sometimes form a mass. Generally the liquid content is anechoic and homogeneous although complications such as hemorrhage or inflammation can increase the liquid echogenecity [33].

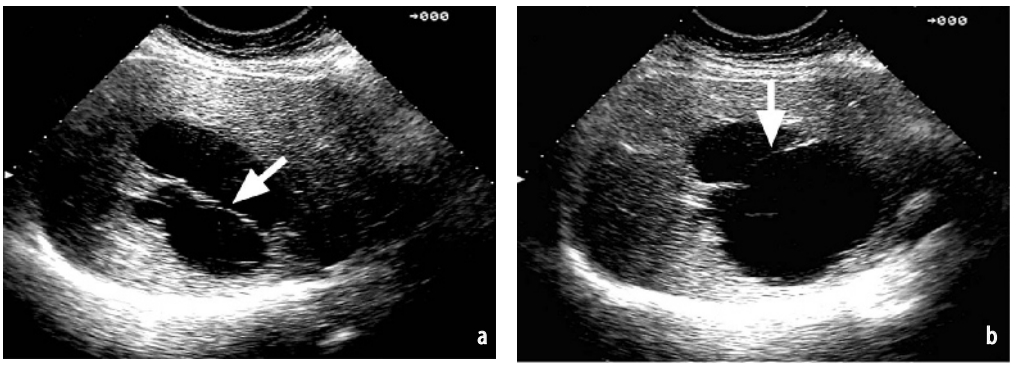

Fig. 19a, b. Biliary cystadenoma. US scans (**a**, **b**) reveal hypo- to anechoic lesions with thin septa (*arrows*)

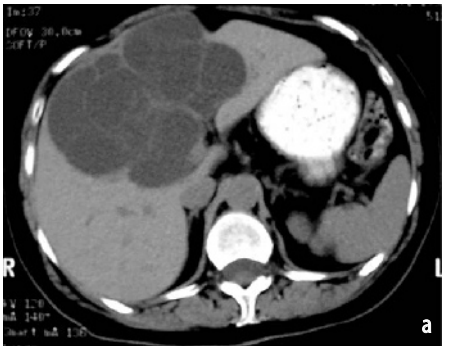

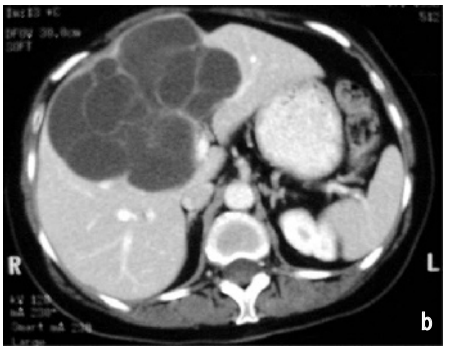

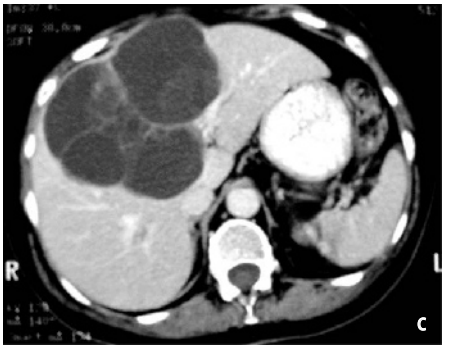

Fig. 20a-c. Biliary cystadenoma on CT. A hypodense lesion with thin septa is seen on the pre-contrast CT scan (**a**). The septa show enhancement after administration of iodinated contrast medium (**b**, **c**)

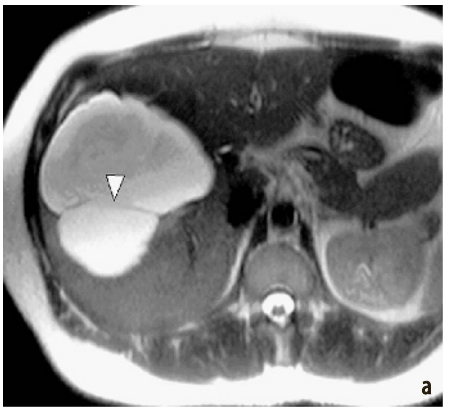

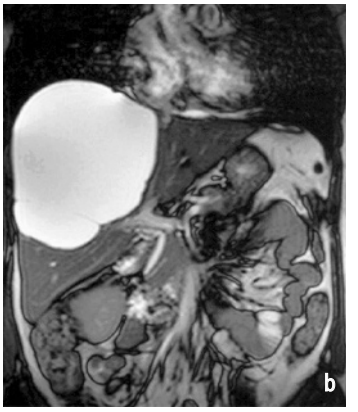

Fig. 21a, b. Biliary cystadenoma on MR. T2-weighted HASTE images acquired in the axial plane (**a**) and True-FISP images acquired in the coronal plane (**b**) reveal large, lobulated cystic lesions in the right liver lobe. The lesions are homogeneously hyperintense due to the fluid component and thin septa are visible (*arrowhead*)

On CT, these tumors are large, low-attenuating intrahepatic masses with lobulated margins and generally thin irregular walls with fibrous septa. Although the cystic parts of the lesions do not enhance following the intravenous administration of contrast material, the internal septations, mural nodules and papillary projections do show enhancement (Fig. 20) [1, 33].

On MR imaging, biliary cystadenoma appears as a multiloculated septated mass, whose signal intensity on T1- and T2-weighted images depends on the presence of solid ovarian-like stroma and the composition of the cystic fluid, which may be serous, mucinous, bilious, hemorrhagic, or a combination of these fluids (Fig. 21, 22). Low signal intensity within the wall on T2-weighted images may represent hemorrhage. Following the administration of intravenous contrast agents, the internal septations, mural nodules and papillary projections enhance [8]. On hepatobiliary phase images after administration of hepato-specific contrast agents, no contrast material is seen within the cystic cavities, and no significant accumulation is detected in the solid components. Thus the solid components are seen as hypointense areas compared with the surrounding liver parenchyma.

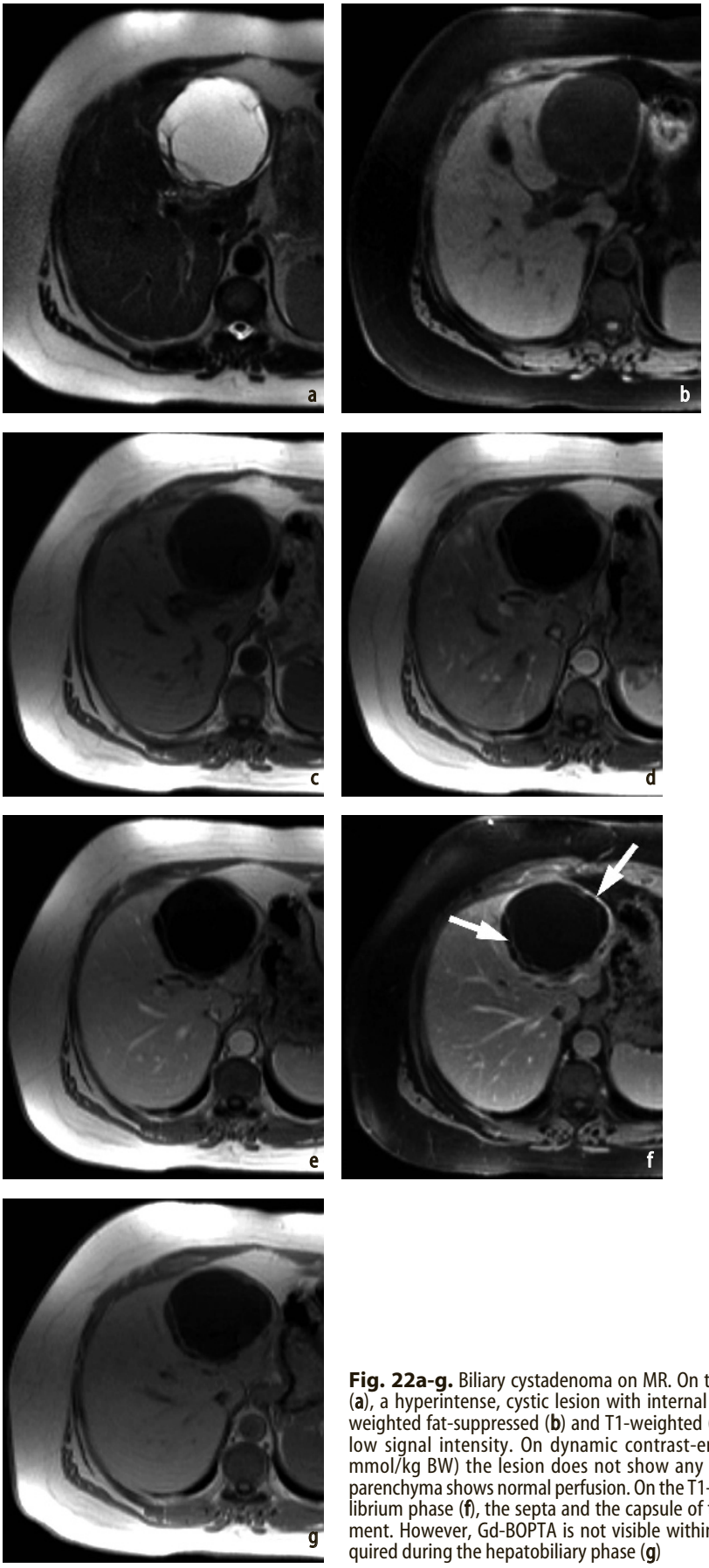

Fig. 22a-g. Biliary cystadenoma on MR. On the unenhanced T2-weighted HASTE image (**a**), a hyperintense, cystic lesion with internal septa is visible. On the corresponding T1-weighted fat-suppressed (**b**) and T1-weighted (**c**) images, the lesion shows homogeneous low signal intensity. On dynamic contrast-enhanced imaging (**d**, **e**) (Gd-BOPTA, 0.05 mmol/kg BW) the lesion does not show any vascularization and the surrounding liver parenchyma shows normal perfusion. On the T1-weighted fat-suppressed image in the equilibrium phase (**f**), the septa and the capsule of the lesion (*arrows*) show contrast enhancement. However, Gd-BOPTA is not visible within the lesion on the T1-weighted image acquired during the hepatobiliary phase (**g**)

7.3.2 Bile Duct Adenoma

This is a rare benign epithelial liver tumor which is mainly found incidentally at laparotomy or autopsy. Its maximal size often does not exceed 1-2 cm. Bile duct adenoma represents about 1% of all primary liver tumors. They occur both in children and elderly people, and may be present as solitary nodules or as multiple nodules throughout the liver [62].

Bile duct adenomas are typically located on the surface of the liver. Microscopically, small bile ducts lined by mucin-producing cells are embedded in a fibrous stroma. Based on immunhistochemical studies, the most likely pathogenesis is a reaction to a focal bile ductular injury. Histologically, bile duct adenomas comprise a mass of disorganized mature peribiliary gland acini and ductules within a variable amount of connective tissue stroma showing signs of chronic inflammation and collagenization. The composition of bile duct adenoma has resulted in it being termed a peribiliary gland hamartoma [6]. Although the tumor is benign in nature, there has been the suspicion of malignant transformation. Pathological differential diagnoses to be considered include bile duct hamartoma, cholangiocellular carcinoma, metastasis and hepatic granuloma.

On US, bile duct adenoma appears as a hyperechoic area with an acoustic shadow sometimes surrounded by a hyperechoic rim. Similar small hyperechoic liver lesions are hemangioma, focal nodular hyperplasia (FNH), hepatocellular carcinoma (HCC) and metastasis.

On unenhanced CT, bile duct adenoma is usually hypodense. However, the presence of calcifications may give the lesion a hyperdense appearance. On delayed contrast-enhanced CT, the lesions usually demonstrate heterogeneous enhancement, although homogeneous enhancement has also been described. The presence of fibrous stroma within the tumor results in the lesion demonstrating prolonged enhancement on contrast-enhanced CT.

The tumor is typically hypointense on unenhanced T1-weighted images and hyperintense on T2-weighted scans. Enhancement of bile duct adenomas on dynamic phase imaging after the injection of gadolinium contrast agent may be heterogeneous, ring-shaped or homogeneous. As in contrast-enhanced CT, the presence of fibrous stroma within the tumor leads to prolonged enhancement on post-contrast T1-weighted MR imaging.

Due to its small size and peripheral localization, bile duct adenoma is often difficult to detect. It should be included among the diseases to be differentiated from hyperechoic hepatic tumors on US and from hepatic tumors showing delayed enhancement on contrast-enhanced CT and MRI.

Bile duct adenomas can frequently be distinguished from other liver tumors by their smaller size, their localization beneath the liver capsule, and their prolonged enhancement [62].

7.3.3 Biliary Hamartoma

Biliary hamartoma is a benign neoplasm composed of a proliferation of small, round, normal-appearing ducts with cuboidal, slightly basophilic cells that have regular nuclei but lack any evidence of dysplasia or increased mitotic activity. In this lesion there is always a fibrous supporting stroma. This neoplasm occurs mainly in patients of older age, shows no sex predilection, and is often associated with adult polycystic kidney disease. The lesion may be up to 4 cm in diameter but most are 1 cm or less at diagnosis. An association between cholangiocellular carcinoma and multiple biliary hamartoma has been reported [43], and it has previously been considered a reactive process rather than a true neoplasm or malformation.

Biliary hamartoma is sometimes confused with bile duct adenoma but it is usually multiple and distributed throughout the liver, forming part of the spectrum of fibropolycystic diseases of the liver due to ductal plate malformation. Biliary hamartomas are asymptomatic and are therefore usually incidental findings at fine needle biopsy, laparotomy or autopsy.

Imaging findings are usually not specific since these lesions often mimic metastases or abscesses. Therefore biopsy is usually required for a definitive diagnosis.

On US, the typical form of the lesion is characterized by multiple, small, hypoechoic lesions that affect all segments of the liver giving a "honeycomb" pattern.

On pre-contrast CT images, numerous, round, small, hypodense lesions throughout the liver can be seen. These lesions usually do not show enhancement after contrast medium administration.

On pre-contrast T1- and T2-weighted MR images, lesions appear hypointense and hyperintense, respectively, and are generally well-defined (Fig. 23). The nodules do not show enhancement after administration of hepatospecific contrast agents, because the lesions are independent and do not communicate with the biliary system [50].

7.3.4 Biliary Papillomatosis

Biliary papillomatosis is an extremely rare condition characterized by the presence of multiple be-

Fig. 23. Biliary hamartoma. The MRC image reveals multiple, well-defined hyperintense round lesions (*arrowheads*) in both lobes of the liver

nign papillary adenomas in the bile ducts, that are similar to adenomas observed in the intestinal tract. Papillomas can be present in the intra- and extrahepatic bile ducts, including the common bile duct. The lesion can occasionally be found in the gallbladder and in the major pancreatic duct. The papillary excrescences are composed of mucus-secreting columnar epithelial cells supported by thin fibrovascular stalks. In some cases it is possible to observe variable degrees of structural and cytological atypia. Clinically, patients have episodes of obstructive jaundice, sepsis, and hemobilia [61]. A variable degree of biliary duct dilatation can be observed on imaging studies; in some cases intraductal tissue masses are present which may be variable in size.

7.4 Malignant Biliary Neoplasms

7.4.1 Cholangiocellular Carcinoma

Cholangiocellular carcinoma (CCC) is a primary malignant tumor arising from the bile duct epithelium and comprises 10-25% of all liver and biliary tract cancers. CCC is usually classified as intra- or extrahepatic based on the location of the involved ducts. Intrahepatic CCC can be further subdivided into peripheral and hilar. A tumor that arises peripheral to the secondary bifurcation of the left or right hepatic duct is considered a peripheral intrahepatic CCC, whereas a tumor that arises from one of the hepatic ducts or from the bifurcation of the common hepatic duct is considered to be a hilar CCC or "Klatskin tumor", according to Klatskin's description in 1965 (Fig. 24) [31]. Peripheral or lobular intrahepatic CCC arises from the epithelium of the internal wall of the small peripheral intrahepatic bile ducts and represents about 10% of all tumors. It tends to grow exophytically into the liver parenchyma as a large focal mass and may be polypoid or focally stenotic. Intrahepatic hilar CCC account for approximately 25% of all CCC and are usually scirrhous. Extrahepatic CCC account for approximately 65% of all CCC [31].

The liver cancer study group of Japan has recently proposed a new classification for intrahepatic CCC as mass-forming, periductal-infiltrating, or intraductal-growing based on their growth characteristics (Fig. 25) [42]. In the mass-forming type, the lesion may be solitary or multiple and possess satellite nodules around the main mass. The periductal infiltrating type of CCC grows

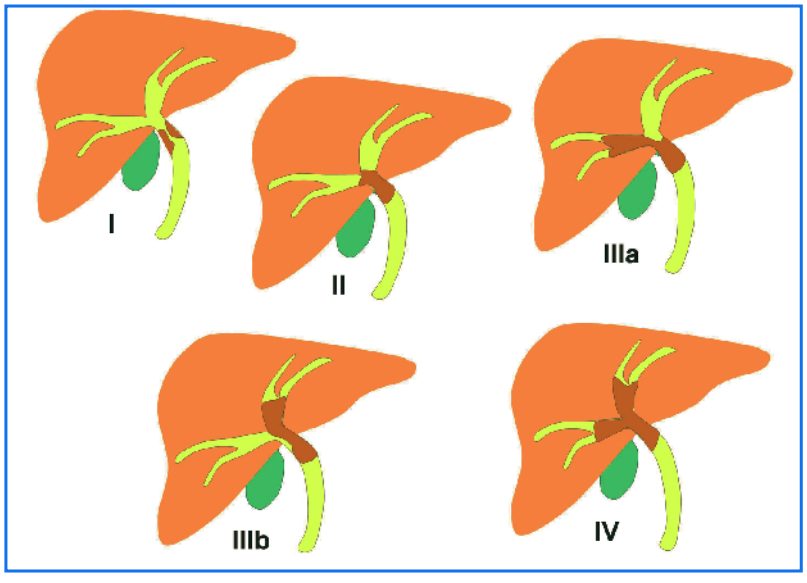

Fig. 24. Bismuth classification of hilar cholangiocellular carcinoma (*Klatskin tumors*)

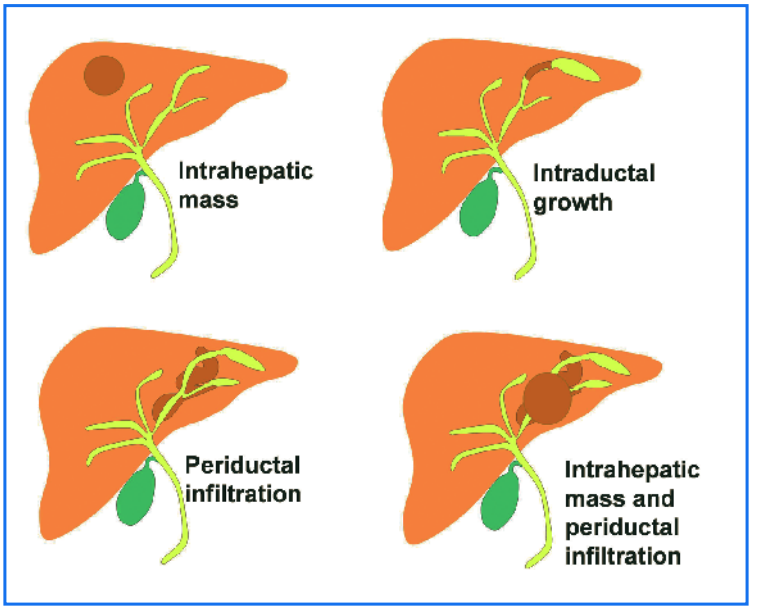

Fig. 25. Intrahepatic cholangiocellular carcinoma: new classification of the liver cancer study group of Japan

along the bile duct wall, resulting in concentric thickening of the wall along the bile duct leading to an elongated, spiculated, or branch-like appearance. The bile ducts are narrowed or nearly completely obstructed, and the involved segments vary in length. The intraductal-growing variant is characterized by the presence of intraluminal papillary tumors of the intra- or extrahepatic bile ducts associated with partial obstruction and dilatation of the bile ducts. The tumor fills sometimes and occludes the bile ducts.

Primary sclerosing cholangitis, choledochal cyst, familial polyposis, congenital hepatic fibrosis, infection with the Chinese liver fluke *Clonorchis sinensis*, and history of exposure to Thorotrast are risk factors for CCC [14, 38]. A mutation in the *p53* tumor suppressor gene has been demonstrated in peripheral-type CCC, in contrast to the k-*ras* mutations observed in lesions that affect the extrahepatic bile ducts [39, 63].

Patients diagnosed with CCC tend to be older than those with HCC; CCC occurs most frequently in patients in their sixth decade, although patients with risk factors may develop the neoplasm at a much younger age. CCC occurs slightly more frequently in men than in women.

The histologic variants of CCC include: adenocarcinoma, mixed CCC-HCC, squamous-, mucoepidermoid-, cystadeno- and granular cell carcinoma. Adenocarcinoma comprises 95% of the cases, and can range from well-differentiated mucin-producing, to poorly-differentiated [44]. Distinguishing morphological features allow further sub-classification of bile duct adenocarcinomas into papillary, sclerosing, and nodular variants. The sclerosing type is most common, followed by papillary and nodular cholangiocarcinoma [73].

The gross appearance of CCC is a grayish-white, firm/solid, fibrous mass. The cut section usually presents as sclerotic gray-white or pale white, with dense fibrous stranding. Typically, CCC has a large central core of fibrotic tissue that is relatively devoid of neoplastic cells. Cancer cells are mainly located at the periphery of the tumor. Daughter nodules can be found throughout the liver, both close to and distant from the main mass. Generally CCC is not highly vascularized, and hemorrhage and necrosis are uncommon.

CCC arising from the common bile duct appears as a rounded, relatively small intraluminal mass. It is usually located within the mid-extrahepatic biliary tree either at the distal common hepatic duct or at the common bile duct. The neoplastic cells have abundant connective tissue stroma and produce a variable desmoplastic reaction. The surrounding liver parenchyma is generally non-cirrhotic. Histologically, it is often difficult to distinguish CCC from metastases of adenocarcinoma. In more than 60-70% of cases, hilar or hepatoduodenal ligament lymph nodes are involved.

The clinical signs and symptoms are related to the site of origin of the tumor. In intrahepatic CCC, the symptoms are usually vague until the tumor is at an advanced stage when patients frequently present with anorexia, weight loss, abdominal pain, and a palpable mass in the upper abdomen. Fever may occur but is uncommon. Jaundice is rarely a presenting symptom in intrahepatic CCC, although it is common in hilar or ductal CCC [31]. There are no specific tumor markers for CCC, although elevations of serum carcinoembryonic antigen (CEA) and CA 19-9 are often found

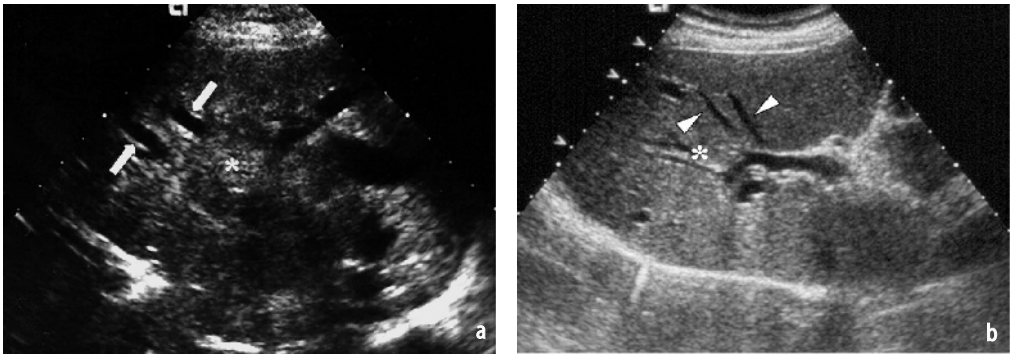

Fig. 26a, b. Hilar cholangiocellular carcinoma. US (**a**) reveals an ill-defined heterogeneous mass (*asterisk*) with dilated bile ducts (*white arrows*). An ill-defined infiltrative mass (*asterisk*) from the hilus through the hepatic parenchyma is also seen (**b**). Some bile ducts around the mass appear dilated (*white arrowheads*)

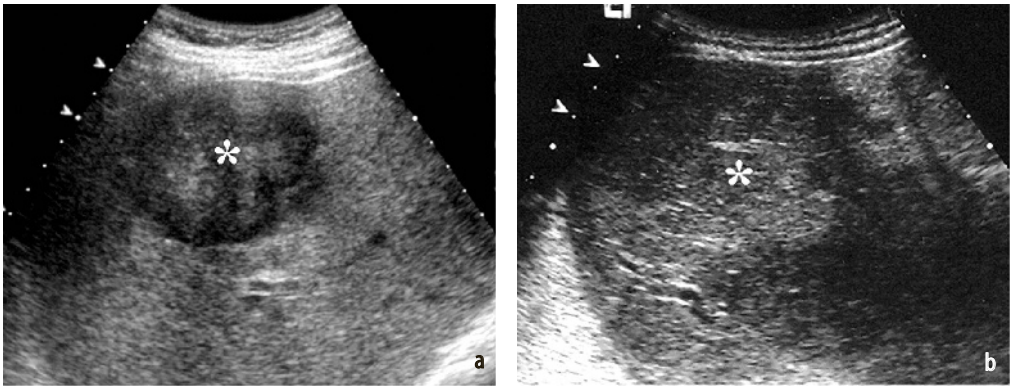

Fig. 27a, b. Peripheral cholangiocellular carcinoma . On US, the neoplasm (*asterisk*) appears as a well-defined heterogeneous nodule (**a**) or as an ill-defined mass (**b**) compared to the surrounding parenchyma

[71]. Elevation of alkaline phosphatase and γ-glutamyltransferase may be seen and patients may be hypoalbuminemic and mildly anemic.

On US scans, CCC may have mixed echogenicity or may be predominantly hypoechoic or hyperechoic. The sonographic features of Klatskin's tumor include duct dilatation, isolation of the right and left bile duct segments, mass or bile duct wall thickening at the hilus as well as lobar atrophy with crowded, dilated bile ducts. US is accurate for revealing the level of bile duct obstruction, but it shows tumor mass in only 20-70% of patients. When a mass is seen, it is usually poorly defined and echogenic, a reflection of the submucosal, scirrhous nature of this fibrotic neoplasm (Fig. 26) [10, 20].

Peripheral CCC may appear as an ill-defined mass with mixed echogenecity (Fig. 27) with or without segmental bile duct dilatation. A hypoechoic halo is observed in 33% of cases. Sometimes the central portion of the tumor appears hypoechoic due to the presence of necrosis. Hyperechoic spots with acoustic shadowing indicate the presence of calcifications. The infiltrative pattern of growth of CCC appears as diffuse architectural changes in the hepatic lobe. Satellite nodules may be seen. Color Doppler US shows scanty color signal because of CCC hypovascularity. This is a useful sign for the differential diagnosis of HCC, which is typically a hypervascular neoplasm. Focally stenotic or papillary CCC often cause segmental bile duct dilatation and may induce lobar atrophy if the location of the tumor is central.

CCC is usually hypodense or isodense relative to the normal liver parenchyma on unenhanced CT scans. After administration of contrast material, most CCC remain hypodense during the portal-venous phase but thereafter show enhancement on delayed phase images. This pattern of enhancement reflects the hypovascular, desmoplastic composition of most CCC; therefore, most lesions are better appreciated 15-20 minutes after contrast medium administration. Small necrotic regions are common in larger lesions. Segmental or diffuse bile duct dilatation is a common finding in hilar CCC (Fig. 28) [10].

Peripheral type CCC may simulate other hepatic neoplasms, such as metastases or hypovascular HCC. Its most common pattern consists of a hypodense ill-defined lesion on unenhanced CT scans, poor, rim-like enhancement during the arterial and portal-venous phases, and iso- or hyperdensity on delayed phase images (Fig. 29). Other factors such as the grade of the tumor, distribution of fibrosis, and contrast pooling can affect the delayed enhancement. Peripheral wash-out is another sign that can be seen on contrast-enhanced CT of peripheral CCC.

CCC is either isointense or hypointense relative to the normal liver on T1-weighted MR images, but may range from markedly to mildly hyperintense on T2-weighted images. The signal intensity of the tumor is variable, and depends on the amount of mucinous material, fibrous tissue, hemorrhage and necrosis within the tumor [70]. On dynamic T1-weighted MR images acquired after the intravenous administration of gadolinium, minimal or moderate incomplete enhancement is seen at the tumor periphery on early images, whereas progressive central contrast-enhancement is seen on later images (Fig. 30) [70].

The degree of enhancement varies with the type of tumor. Greater peripheral enhancement is noted in the early phases in large CCC, whereas greater enhancement is noted in the fibrous core of scirrhous CCC on delayed phase images (Fig. 31). Small, incidentally discovered intrahepatic CCC, as well as mixed CCC/HCC tumors can show intense, homogeneous enhancement during the arterial phase with prolonged enhancement on delayed phases due to marked hypervascularity [70, 74].

Generally, lesions show peripheral hypointensity and central iso- or hyperintensity on delayed phase images after the administration of contrast agents with liver-specific properties (Fig. 30, 31). However, the central area may also show incomplete enhancement. Satellite nodules are seen in about 10-20% of CCC cases and are chiefly responsible for the poor prognosis of this lesion (Fig. 32). Pooling of contrast within the tumor, and peripheral wash-out on delayed MR images are suggestive findings of CCC in non-cirrhotic patients. This characteristic enhancement pattern reflects the large amounts of fibrous tissue, neovascularity, and neoplastic cells at the periphery of the lesion.

A significant signal drop of the lesion is not detected after SPIO administration, and therefore the neoplasm appears significantly more hyperintense than normal liver parenchyma.

The use of MRC in conjunction with MRI permits the extent of the tumor in bile ducts to be determined. With this technique hilar obstruction and some segment dilatations can be easily diagnosed.

A common finding on all imaging techniques is the presence of lymphoadenopathy. Lymph nodes are typically large and round and hypoechoic, hypodense, and hypo- or hyperintense on US, CT, and MR studies, respectively, and show uptake of isotope on positron emission tomography (PET) examinations (Fig. 33).

7.4.2 Biliary Cystadenocarcinoma

Biliary cystadenocarcinoma is a rare cystic neoplasm that can arise within liver cysts, bile ducts, and in the context of polycystic liver disease. It also arises as a result of the malignant transformation of biliary cystadenoma. Since malignant degeneration of biliary cystadenoma may require as few as ten years, resection of cystadenoma is recommended.

As in biliary cystadenoma, there exists two forms of biliary cystadenocarcinoma, those with and those without ovarian-like stroma. Microscopically, the neoplasm may contain either mucinous or serous material although mucus is more common. These lesions are sometimes asymptomatic and are therefore discovered incidentally. More frequently patients present with pain, jaundice, nausea, and fever [51].

Unlike cystadenoma, biliary cystadenocarcinoma appears as a multiloculated complex cystic mass with irregular wall thickness, internal septations, and papillary projections on US and CT. MR imaging reveals irregular walls, internal septations, mural nodules and papillary projections within the lesion. The solid portions show enhancement after intravenous administration of gadolinium contrast agent [8].

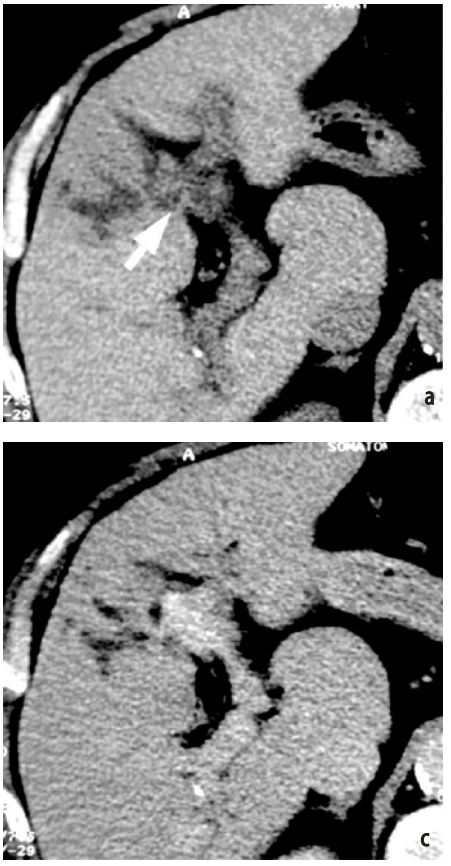

Fig. 28a-c. Hilar cholangiocellular carcinoma. On unenhanced CT (**a**) and early post-contrast dynamic phase CT (**b**), the neoplasm (*white arrows*) appears as an ill-defined hypodense mass located near the hilum. Bile duct dilatations (*arrowhead*) are also evident. On delayed phase images after contrast medium administration the lesion is seen as hyperattenuating (**c**)

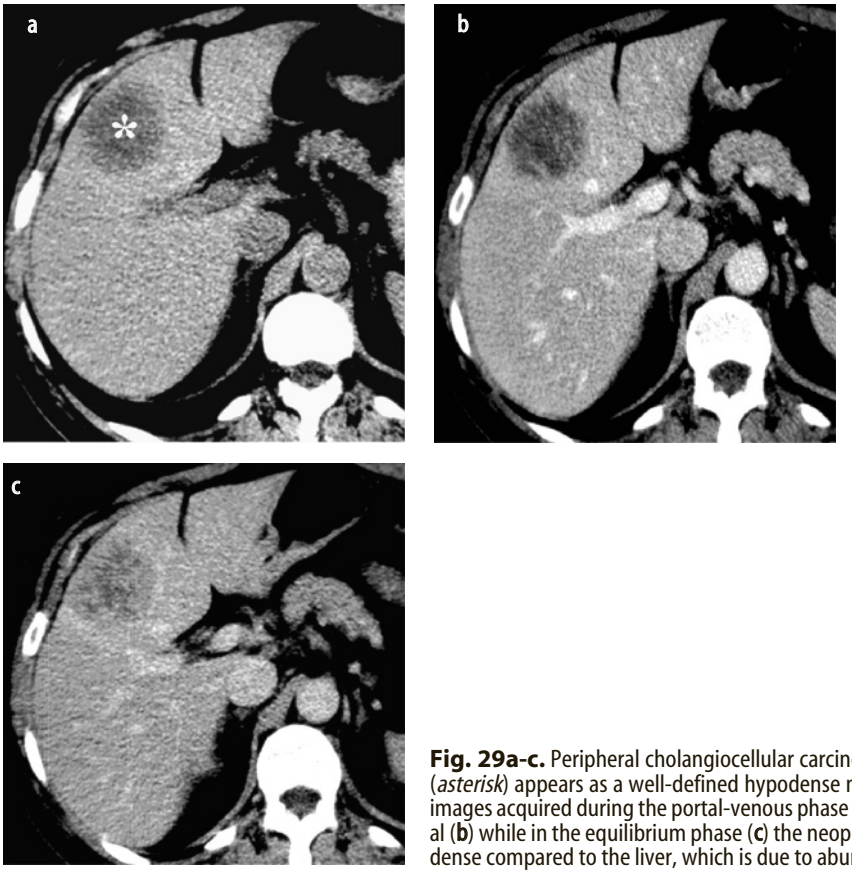

Fig. 29a-c. Peripheral cholangiocellular carcinoma. On unenhanced CT (**a**) the lesion (*asterisk*) appears as a well-defined hypodense mass. Minimal enhancement is seen on images acquired during the portal-venous phase after administration of contrast material (**b**) while in the equilibrium phase (**c**) the neoplasm is seen as heterogeneously hyperdense compared to the liver, which is due to abundant fibrotic desmoplastic reaction

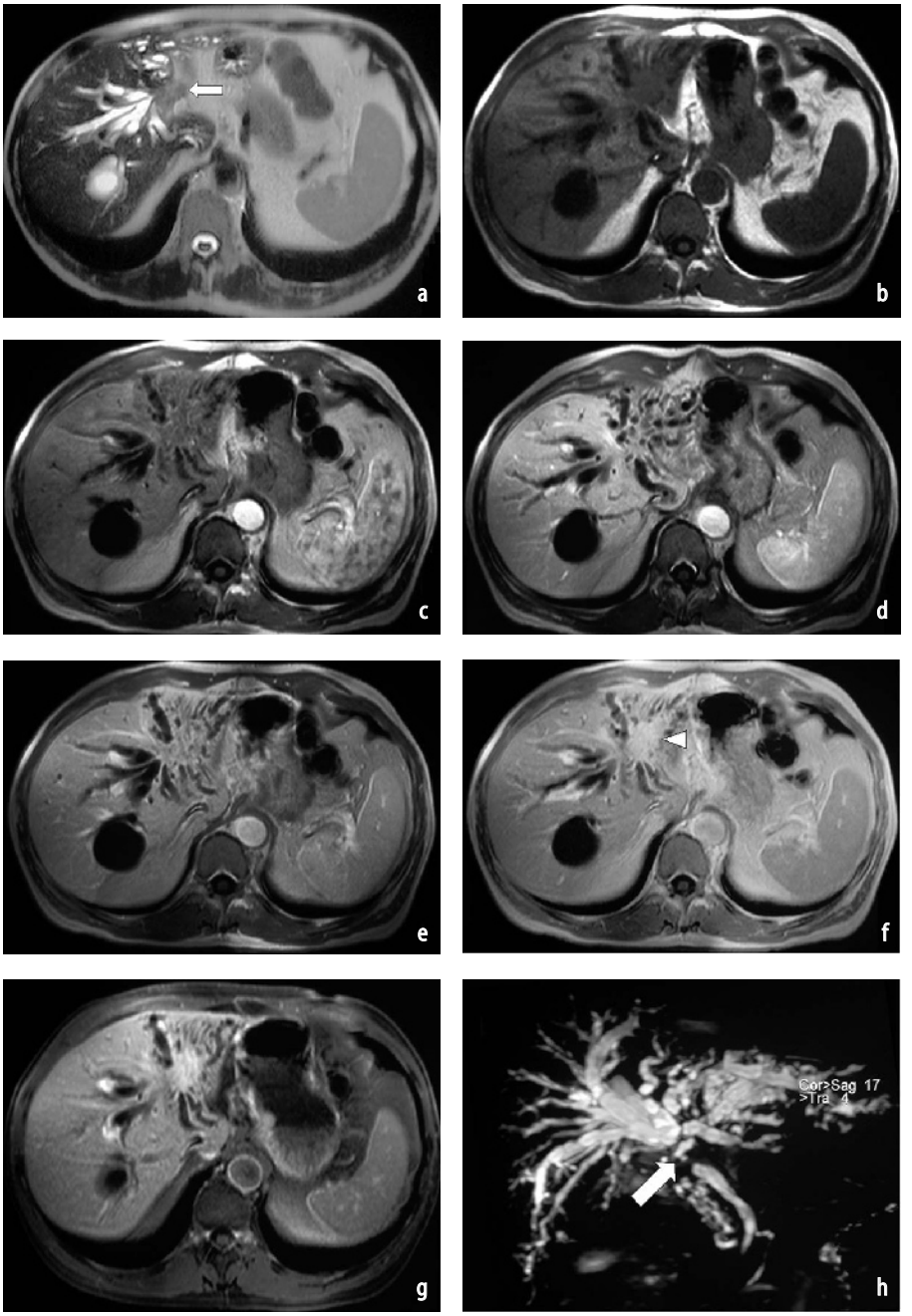

Fig. 30a-h. Hilar cholangiocellular carcinoma. On the unenhanced T2-weighted TSE image (**a**) the neoplasm (*white arrows*) appears slightly heterogeneously hyperintense compared to the normal liver and involvement of the bile duct system can be seen. On the unenhanced T1-weighted GRE image (**b**) the lesion appears as a slightly hypointense ill-defined mass. Poor enhancement is seen during the arterial phase after the bolus administration of Gd-BOPTA (**c**). However, desmoplastic reaction causes a progressive increase of contrast enhancement in subsequent acquisitions during the portal-venous and equilibrium phases (**d** and **e**, respectively). After 20 minutes the lesion (*arrowhead*) appears hyperintense (**f**). Due to the large amount of fibrotic tissue which causes non-specific contrast agent retention, the lesion retains this hyperintense appearance on images acquired one hour after Gd-BOPTA administration (**g**). Nevertheless, the presence of a hypointense peripheral rim indicates the malignant nature of the lesion. The involvement of hilar bile ducts (*arrow*) is clearly demonstrated with MRCP (**h**)

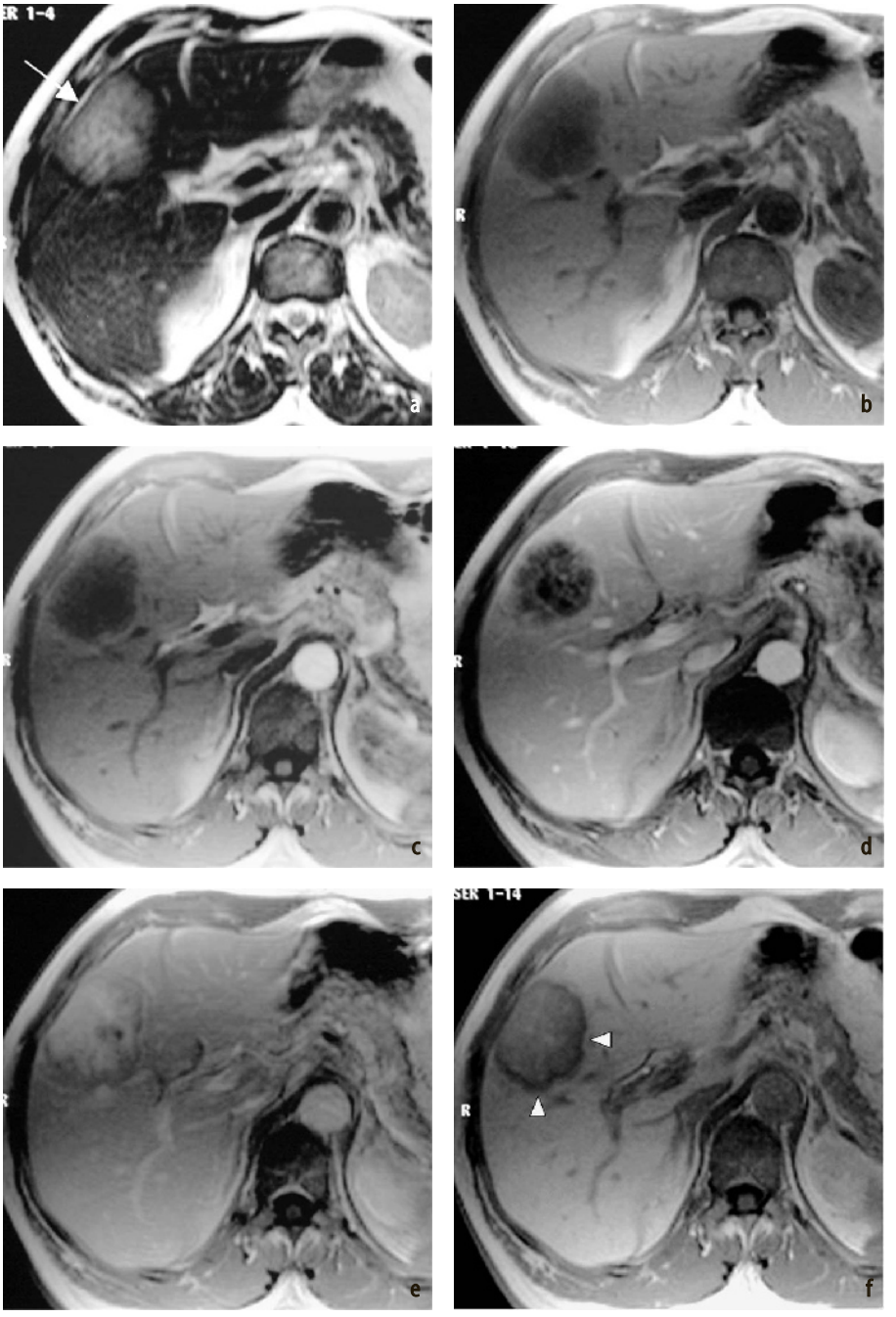

Fig. 31a-f. Peripheral cholangiocellular carcinoma. The neoplasm (*white arrow*) appears heterogeneously hyperintense on unenhanced T2-weighted images (**a**) and hypointense on unenhanced T1-weighted images (**b**). Moderate peripheral enhancement is seen on images acquired during the arterial (**c**) and portal-venous (**d**) phases after the administration of Gd-BOPTA. On the equilibrium and delayed phase images (**e** and **f**, respectively) the enhancement appears progressive and complete due to desmoplastic reaction. A hypointense rim (*white arrowheads*) indicating peripheral wash-out can be seen on the delayed-phase image

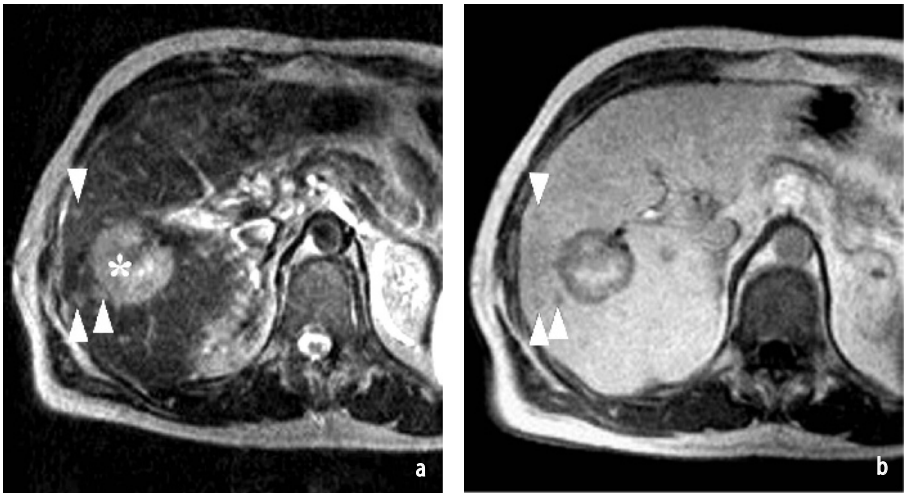

Fig. 32a, b. Cholangiocellular carcinoma. On the unenhanced T2-weighted image (**a**) a large heterogeneously hyperintense mass (*asterisk*) and numerous satellite nodules (*arrowheads*) can be seen. On the image acquired during the hepatobiliary phase after injection of Gd-BOPTA (**b**), the biggest nodule shows central enhancement and peripheral wash-out while the smaller satellite nodules (*arrowheads*) remain hypointense

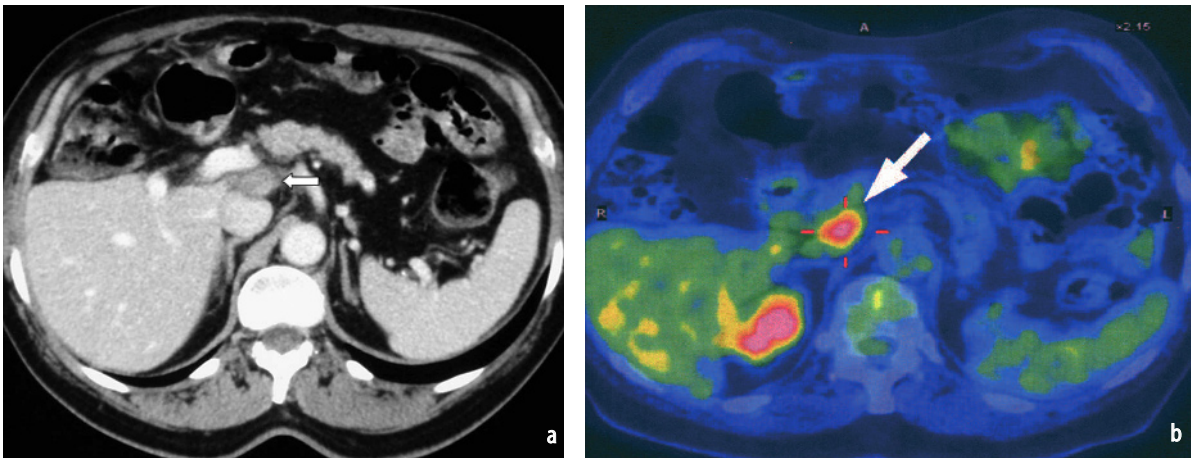

Fig. 33a, b. Cholangiocellular carcinoma. The post-contrast CT scan (**a**) shows a homogeneous, slightly hypodense, lymphoadenopathy (*arrow*) adjacent to the portal vein. The lesion is confirmed on the PET examination (**b**) as a nodule that shows isotope uptake (*arrow*)

7.5 Benign Neoplasms of the Gallbladder

7.5.1 Gallbladder Adenoma

Gallbladder adenoma is a rare benign neoplasm of glandular epithelium that is usually polypoid, single, and well-demarcated. The neoplasm is more common in middle-aged women and can also occur in children, although more rarely. Adenomas are classified as tubular, papillary, or tubulopapillary according to their pattern of growth. Microscopically they are classified as pyloric, gland type, intestinal type, and biliary type [2]. Gallbladder adenomas are usually small and asymptomatic, and are usually discovered incidentally during cholecystectomy. Occasionally, however, they can be large or multiple, with typical symptoms including upper right abdominal pain, jaundice, and vomiting. Sometimes adenomas of the gallbladder occur in association with Peutz-Jegher syndrome or Gardner's syndrome [2].

On US adenomas appear as homogeneously hyperechoic small, broad-based, non-shadowing, pedunculate or sessile polypoid defects (Fig. 34). These lesions do not move with gravitational maneuvers, and the echogenicity is inferior to that observed with stones.

In general, CT and MR imaging are not used for the diagnosis of gallbladder adenoma.

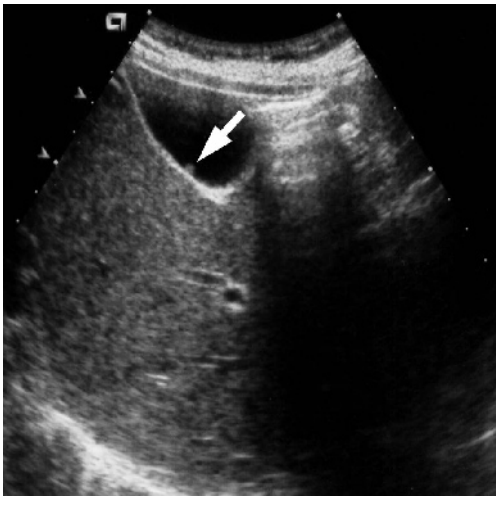

Fig. 34. Gallbladder adenoma. US reveals a small, well-defined, hyperechoic, sessile lesion (*arrow*)

7.6 Malignant Neoplasms of the Gallbladder

7.6.1 Gallbladder Carcinoma

Gallbladder carcinoma is the fifth most common malignancy of the gastrointestinal tract [37]. While there doesn't appear to be any difference between males and females in the incidence of gallbladder carcinoma, there are indications of demographic differences in the age of patients diagnosed with this neoplasm: in the United States the average age at diagnosis is about 70 years, while in India it is 40-50 years.

The four most important factors associated with the development of gallbladder carcinoma are genetic anomaly, gallstones, congenital abnormal choledocho-pancreatic junction, and porcelain gallbladder. With regards to genetic factors, a mutation of the k-*ras* gene, overexpression of the c-*erbB*-2 gene and decreased expression of the *nm*23 gene have been observed in patients with gallbladder carcinoma [13, 18]. An association between gallbladder carcinoma and gallstones is well known, and this causal relationship is the reason for performing cholecystectomy for cholelithiasis as a preventive measure for gallbladder carcinoma. Gallbladder carcinoma is associated with an abnormal choledocho-pancreatic junction because in this condition pancreatic juice can reflux into the common bile duct. The mixture of pancreatic juice and bile leads to chronic inflammation of the gallbladder with subsequent metaplasia, dysplasia, and carcinoma [30]. Finally, porcelain gallbladder, which is a diffuse calcification of the gallbladder wall, is also a predisposing factor: an estimated 22% of patients with porcelain gallbladder develop carcinoma [7, 55].

Approximately 60% of all neoplasms originate in the fundus of the gallbladder, while 30% originate in the body and 10% in the neck. Nearly 85% of primary carcinomas of the gallbladder are adenocarcinomas; the remainder are anaplastic or squamous cell carcinomas. The adenocarcinomas can be subdivided into various subtypes, including well-differentiated, papillary, intestinal, pleomorphic giant cell, poorly-differentiated small cell, and clear cell types.

Histologically, gallbladder carcinomas have three major patterns of presentation:

1) focal or diffuse thickening of the gallbladder wall;
2) polypoid mass originating in the gallbladder wall and projecting into the lumen;
3) mass obscuring or replacing the gallbladder, often invading adjacent liver, with or without multiple satellite nodules [59, 60].

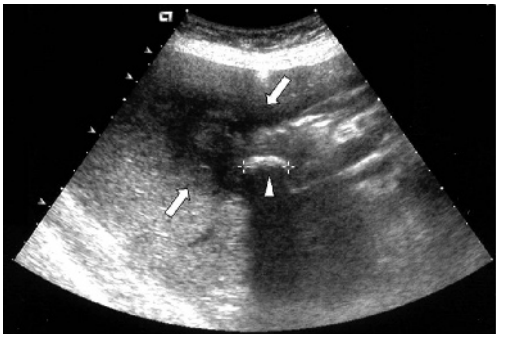

Fig. 35. Gallbladder carcinoma. US reveals an heterogeneous, hypo- and hyperechoic mass (*white arrows*) that replaces the gallbladder. A coarse stone with acoustic shadow can be seen within the mass (*arrowhead*)

Lymph node involvement is also a common finding in gallbladder carcinoma. Most patients with carcinoma of the gallbladder present with either acute cholecystitis or symptoms of malignancy, including constant right upper abdominal quadrant pain, malaise, weight loss, and jaundice. Patients sometimes have a long history of episodic cholecystitis. Gallbladder carcinoma is occasionally an incidental finding on abdominal imaging studies [40].

On US, gallbladder carcinomas may cause mild to marked mural thickening in a focal or diffuse pattern with irregular and mixed echogenicity. Carcinomas confined to the gallbladder mucosa may present as flat or slightly raised lesions with mucosal irregularities that are difficult to appreciate sonographically. On the other hand, polypoid carcinomas may be hyperechoic, hypoechoic, or isoechoic relative to the liver. These lesions are fixed to the gallbladder wall, and do not cause an acoustic shadow. Gallstones are usually present, in which case a large mass obscuring or replacing the gallbladder is a common presentation (Fig. 35). The echotexture of this manifestation is often complex with regions of necrosis and small amounts of pericholecystic fluid often present [60, 69]. Color Doppler US usually shows a hypovascular mass. However, a color signal may be seen at the periphery due to the hypervascularity of the peripheral components [69].

CT is inferior to US for evaluating the gallbladder wall for mucosal thickening or irregularity. Focal malignant wall thickening and polypoid cancer are both usually hyperdense on CT images acquired after the administration of intravenous contrast material. However, infiltrating carcinoma that replaces the gallbladder often shows irregular contrast enhancement with scattered regions of internal necrosis (Fig. 36) [60]. Invasion of the liver, satellite lesions, and bile duct dilatation are common findings in this form of gallbladder carcinoma [69].

The MR findings for gallbladder carcinoma are similar to those reported for CT. The tumor usual-

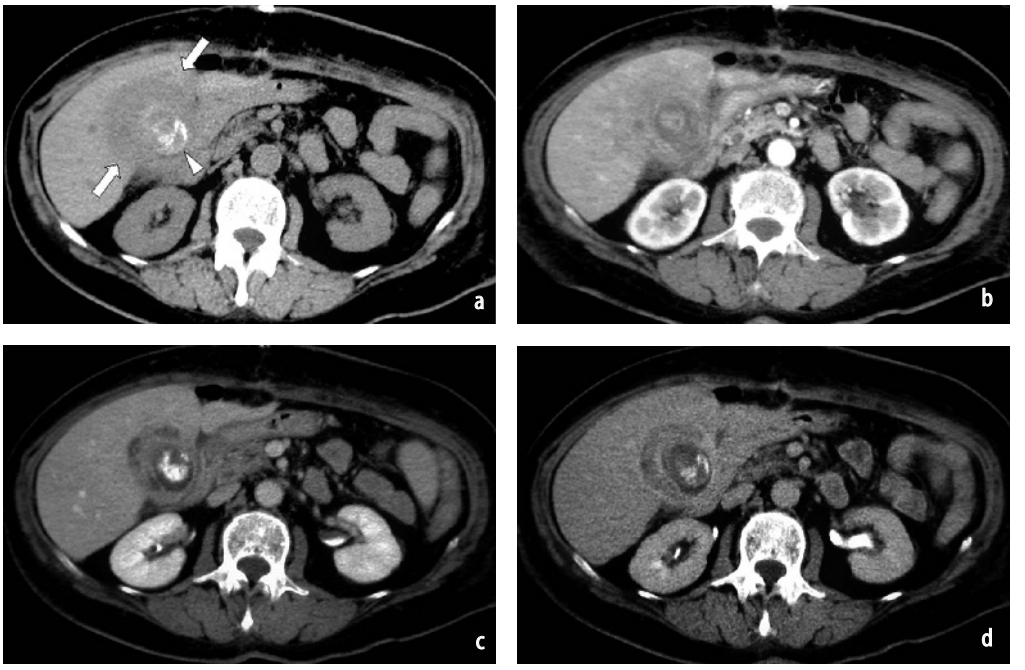

Fig. 36a-d. Gallbladder carcinoma on CT. Unenhanced CT (**a**) reveals an ill-defined slightly hypodense mass (*white arrows*) surrounding a coarse irregular, and heterogeneous stone (*white arrowhead*). In the arterial phase after contrast material administration (**b**) the neoplasm remains poorly-delineated and poorly-enhanced. In the portal-venous phase (**c**) the lesion appears heterogeneously isodense, but better defined against the normal liver. In the equilibrium phase (**d**) the neoplasm is more homogeneous and a thin hyperdense peripheral rim can be seen

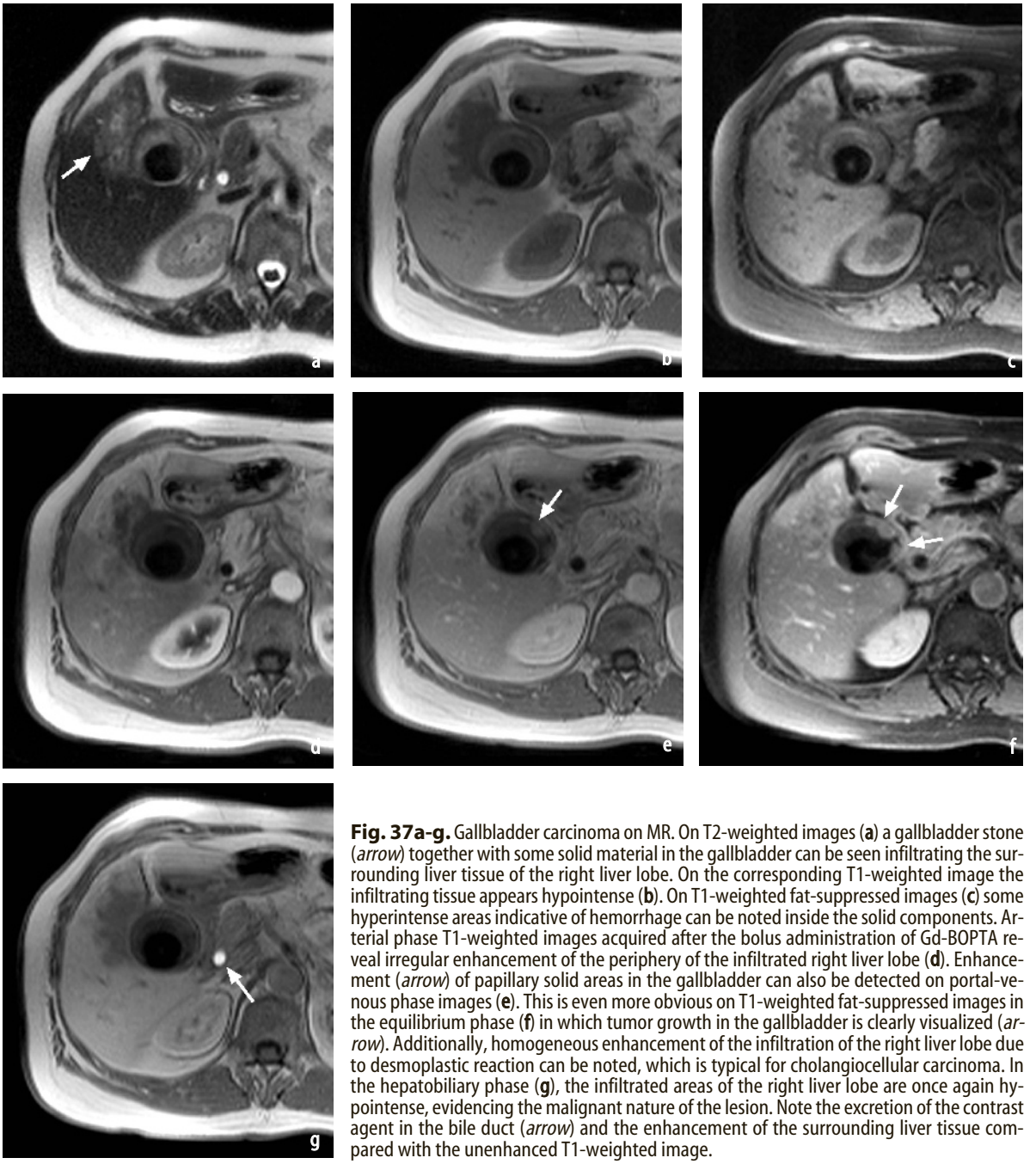

Fig. 37a-g. Gallbladder carcinoma on MR. On T2-weighted images (**a**) a gallbladder stone (*arrow*) together with some solid material in the gallbladder can be seen infiltrating the surrounding liver tissue of the right liver lobe. On the corresponding T1-weighted image the infiltrating tissue appears hypointense (**b**). On T1-weighted fat-suppressed images (**c**) some hyperintense areas indicative of hemorrhage can be noted inside the solid components. Arterial phase T1-weighted images acquired after the bolus administration of Gd-BOPTA reveal irregular enhancement of the periphery of the infiltrated right liver lobe (**d**). Enhancement (*arrow*) of papillary solid areas in the gallbladder can also be detected on portal-venous phase images (**e**). This is even more obvious on T1-weighted fat-suppressed images in the equilibrium phase (**f**) in which tumor growth in the gallbladder is clearly visualized (*arrow*). Additionally, homogeneous enhancement of the infiltration of the right liver lobe due to desmoplastic reaction can be noted, which is typical for cholangiocellular carcinoma. In the hepatobiliary phase (**g**), the infiltrated areas of the right liver lobe are once again hypointense, evidencing the malignant nature of the lesion. Note the excretion of the contrast agent in the bile duct (*arrow*) and the enhancement of the surrounding liver tissue compared with the unenhanced T1-weighted image.

ly has increased signal intensity relative to the liver on T2-weighted images and poorly-delineated contours. These lesions are either isointense or hypointense relative to the liver on T1-weighted images. The tumor generally shows poor and heterogeneous enhancement on dynamic phase imaging and often appears hyperintense on fat-suppressed T1-weighted images in the equilibrium phase [57]. On delayed hepatobiliary phase images after the administration of Gd-BOPTA, the tumor appears as a heterogeneous hypointense mass (Fig. 37). A significant signal drop is usually not seen after SPIO administration and the lesion is usually hyperintense compared to the normal liver parenchyma [57].

7.6.2 Gallbladder Carcinoid

Gallbladder carcinoid is a rare tumor that represents less than 1% of all digestive tract carcinoids. Patients are usually young or middle-aged adults and there is no clear sex predominance. Associa-

tions of gallbladder carcinoid with Zollinger-Ellison syndrome, multiple endocrine neoplasia, and carcinoid syndrome have previously been shown.

Macroscopically, these tumors appear as grey to yellow intramural nodules measuring from a few millimetres to 3-4 cm. The neoplastic cells are composed of uniform, small cells with eosinophilic granular cytoplasm. Most carcinoids are argyrophilic.

Small carcinoids of less than 1 cm are usually incidental findings in cholecystectomy specimens [49]. On imaging, gallbladder carcinoids manifest as polypoid masses that sometimes obstruct the cystic duct.

References

1. Agildere AM, Haliloglu M, Akhan O. Biliary cystadenoma and cystadenocarcinoma. AJR 1991; 156:1113
2. Albores-Saavedra J, Vardaman C, Vuitch F. Non-neoplastic polypoid lesions and adenomas of the gallbladder. Patho Ann 1993; 28:145-177
3. Asselah T, Ernst O, Sergent G, et al. Caroli's disease: a magnetic resonance cholangiopancreatography diagnosis. Am J Gastroenterol 1998; 93:109-110
4. Babbitt DP. Congenital choledochal cyst: new etiologic concept based on anomalous relationships of common bile duct and pancreatic bulb. Ann Radiol 1969; 12:231-240
5. Balistreri WF, Grand R, Suchy FJ, et al: Biliary atresia: current concepts and research directions. Hepatol 1996; 23:1682-1692
6. Bhathal PS, Hughes NR, Goodman ZD. The so-called bile duct adenoma is a peribiliary gland hamartoma. Am J Surg Pathol 1996; 20:858-864
7. Berk RN, Armbuster TG, Saltztein SL. Carcinoma in the porcelain gallbladder. Radiology 1973; 106:29-31
8. Buetow PC, Buck JL, Pantongrag-Brown L, et al. Biliary cystadenoma and cystadenocarcinoma: clinical-imaging-pathologic correlation with emphasis on the importance of ovarian stroma. Radiology 1995; 196:805-810
9. Caccia G, Ekema G, Falchetti D, et al. Atresia delle vie biliari: attualità e prospettive. Prospettive Pediatria 2004; 34:39-43
10. Campbell WL, Ferris JV, Holbert BL, et al. Biliary tract carcinoma complicating primary sclerosing cholangitis: evaluation with CT, cholangiography, US and MR imaging. Radiology 1998; 207:41-50
11. Chandra RS, Altman RP. Ductal remnants in extrahepatic biliary atresia: a histopathologic study with clinical correlation. J Pediatr 1978; 93:196-200
12. Choi SO, Park WH, Lee HJ, et al. "Triangular cord": a sonographic finding applicable in the diagnosis of biliary atresia. J Pediatr Surg 1996; 31:363-366
13. Chow NH, Huang SM, Chan SH, et al. Significance of c-erbB-2 expression in normal and neoplastic epithelium of biliary tract. Anticancer Res 1995; 15:1055-9
14. Coffey RJ, Wiesner RH, Beaver SJ, et al. Bile duct carcinoma: a late complication of end-stage primary sclerosing cholangitis. Hepatology 1984; 14:1056-1059
15. Desmet VJ. Pathogenesis of ductal plate abnormalities. Mayo Clin Proc 1998; 73:80-89
16. Devaney K, Goodman ZD, Ishak KG. Hepatobiliary cystadenoma and cystadenocarcinoma: a light microscopic and immunohistochemical study of 70 cases. Am J Surg Pathol 1994; 18:1078-1091
17. Donaldson JS. Disease of the pediatric gallbladder and biliary tract. In: Gore, Levine (Eds) Textbook of gastrointestinal radiology. WB Saunders Company, second edition 2000,2140-2147
18. Fujii K, Yasui W, Shimamoto F, et al. Immunohistochemical analysis of nm23 gene product in human gallbladder carcinomas. Virchows Arch 1995; 426:355-9
19. Fulcher AS, Turner MA, Capps GW. MR cholangiography: technical advances and clinical applications. Radiographics 1999; 19:25-41
20. Garber SJ, Donald JJ, Lees WR. Cholangiocarcinoma: ultrasound features and correlation with survival. Abdom Imaging 1993; 18:66-69
21. Goyen M, Barkhausen J, Debatin JF, Kuhl H, Bosk S, Testa G, Malago M, Ruehm SG. Right-lobe living related liver transplantation: evaluation of a comprehensive magnetic resonance imaging protocol for assessing potential donors. Liver Transpl 2002; 8(3):241-50
22. Kahn E. Biliary atresia revisited. Pediatr Dev Pathol 2004; 7(2):109-24
23. Kapoor V, Peterson MS, Baron RL, et al. Intrahepatic biliary anatomy of living adult liver donors: correlation of mangafodipir trisodium-enhanced MR cholangiography and intraoperative cholangiography. Am J Roentgenol 2002; 179(5):1281-6
24. Kasai M, Suzuki S. A new operation for "noncorrectable" biliary atresia: Hepatic portoenterostomy. Shujutsu 1959; 13:733-739
25. Kendrick APAT, Phua KB, Ooi BC, et al. Biliary atresia: making the diagnosis by the gallbladder ghost triad. Pediatr Radiol 2003; 33:311-315
26. Kim HC, Park SH, Park SI, et al. Three-dimensional reconstructed images using multidetector computed tomography in evaluation of the biliary tract: an illustrative review. Abdom Imaging 2004; 29:472-478
27. Kim K, Choi J, Park Y, et al. Biliary cystadenoma of the liver. J Hepatobiliary Pancreat Surg 1998; 5:348-352
28. Kim MJ, Han SJ, Yoon CS, Kim JH, Oh JT, Chung KS, Yoo HS. Using MR cholangiopancreatography to reveal anomalous pancreaticobiliary ductal union in infants and children with choledochal cysts. AJR Am J Roentgenol 2002; 179(1):209-14
29. Kim MJ, Park YN, Han SJ, et al. Biliary atresia in neonates and infants: triangular area of high signal intensity in the porta hepatis at T2-weighted MR cholangiography with US and histopathologic correlation. Radiology 2000; 215:395-401
30. Kimura K, Ohto M, Saisho H, et al. Association of gallbladder carcinoma and anomalous pancreaticobiliary ductal union. Gastroenterology 1985; 89:1258-1265
31. Klatskin G. Adenocarcinoma of the hepatic duct at its bifurcation within the porta hepatis. Am J Med 1965; 38:241-256
32. Kobt MA, Kobt A, Sheba MF, et al. Evaluation of the triangular cord sign in the diagnosis of biliary atresia. Pediatrics 2001; 108:416-420
33. Korobin M, Stephens DH, Lee JKT, et al. Biliary cys-

tadenoma and cystadenocarcinoma: CT and sonographic findings. AJR 1989; 153: 507-511
34. Krause D, Cercueil JP, Dranssart M, et al. MRI for evaluating congenital bile duct abnormalities. JCAT 2002; 26(4):541-552
35. Kyungsik K, Jinsub C, Youngnyun P, et al. Biliary cystadenoma of the liver. J Hepatobiliary Pancreat Surg 1998; 5:348-352
36. Lam WWM, Lam TPW, Saing H, et al: MR cholangiography and CT cholangiography of pediatric patients with choledochal cysts. AJR 1999; 173:401-405
37. Landis SH, Murray T, Bolden S, et al. Cancer statistics. Cancer 1999; 49:8-31
38. Lee JH, Yang HM, Bak UB, et al. Promoting role of Clonorchis sinensis infection on induction of cholangiocarcinoma during two-step carcinogenesis. Korean J Parasitol 1994; 32:13-18
39. Levi S, Urbano-Ispizua A, Gill R, et al. Multiple k-ras codon 12 mutations in cholangiocarcinomas demonstrated with a sensitive polymerase chain reaction technique. Cancer Res 1991; 51:3497-502
40. Levin B. Gallbladder carcinoma. Ann Oncol 1999; 10:129-130
41. Levy AD, Rohrmann CA, Murakata LA, et al. Caroli's disease: Radiologic spectrum with pathologic correlation. AJR 2002; 179:1053-1057
42. Liver Cancer Study Group of Japan. The general rules for the clinical and pathological study of primary liver cancer, 4th ed. Kanehara, Tokyo 2000
43. Luo TY, Itai Y, Eguchi N, et al. Von Meyenburg complexes of the liver: imaging findings. J Comput Assist Tomogr 1998; 22(3):372-8
44. Marcos-Alvarez A, Jenkins RL. Cholangiocarcinoma. Surg Oncol Clin North Am 1996; 5:301-316
45. Matos C, Nicaise N, Deviare J, et al. Choledochal cysts: comparison of findings at MR cholangiopancreatography and endoscopic retrograde cholangiopancreatography in eight patients. Radiology 1998; 209:443-448
46. Miller WJ, Sechtin AG, Campbell WL, Pieters PC. Imaging findings in Caroli's disease. AJR 1995; 165:333-337
47. Miyano T, Yamataka A. Choledochal cysts. Curr Opin Pediatr 1997; 9(3):283-288
48. Miyazaki T, Yamashita Y, Tsuchigame T, et al: MR cholangiopancreatography using HASTE (half-Fourier acquisition single-shot turbo spin-echo) sequences. AJR 1996; 166:1297-1303
49. Modin IM, Sandor A. An analysis of 8305 cases of carcinoid tumors. Cancer 1997; 79:813-829
50. Mortele B, Mortele K, Seynaeve P, et al. Hepatic bile duct hamartomas (von Meyenburg Complexes): MR and MR cholangiography findings. J Comput Assist Tomogr 2002; 26(3):438-43
51. Nakajima T, Sugano I, Matsuzaki O, et al. Biliary cystadenocarcinoma of the liver: a clinicopathologic and histochemical evaluation on nine cases. Cancer 1992; 69:2426-32
52. Norton KI, Glass RB, Kogan D, et al. MR cholangiography in the evaluation of neonatal cholestasis: Initial results. Radiology 2002; 222:687-691
53. Ozgen A, Akata D, Arat A, et al. Gallbladder duplication: imaging findings and differential consideration. Abdom Imaging 1999; 24:285-288
54. Parulekar SG. Gallbladder and bile ducts. In: McGahan JP, Goldberg BB (eds): Diagnostic ultrasound - a logical approach. Lippincott-Raven, Philadelphia 1998,175-224
55. Polk HC. Carcinoma and the calcified gallbladder. Gastroenterology 1966; 50:582-585
56. Saddik D. Multiseptate gallbladder: incidental diagnosis on ultrasound. Australas Radiol 1998; 42:374-376
57. Sagoh T, Itoh K, Togashi K, et al. Gallbladder carcinoma: evaluation with MR imaging Radiology 1990; 174:131-136
58. Simeone JF, Mueller PR, Ferrucci JT Jr, et al. Sonography of the bile ducts after a fatty meal: an aid in detection of obstruction. Radiology 1982; 143:211-215
59. Sons HU, Borchard F, Joel BS. Carcinoma of the gallbladder: autopsy findings in 287 cases and review of the literature. J Surg Oncol 1985; 28:199-206
60. Soyer P, Gouhiri M, Boudiaf M, et al. Carcinoma of the gallbladder: imaging features with surgical correlation. AJR 1997; 169:781-784
61. Taguchi J, Yasunaga M, Kojiro M, et al. Intrahepatic and extrahepatic biliary papillomatosis. Arch Pathol Lab Med 1993; 117:944-947
62. Tajima T, Honda H, Kuroiwa T, Yoshimitsu K, Irie H, Aibe H, Taguchi K, Masuda K. Radiologic features of intrahepatic bile duct adenoma: A look at the surface of the liver. J Comput Assist Tomogr 1999; 23(5):690-695
63. Terada T, Shimizu K, Izumi R, et al. P53 expression in formalin-fixed, paraffin-embedded archival specimens of intrahepatic cholangiocarcinoma. Retrieval of p53 antigenicity by microwave oven heating of tissue section. Mod Pathol 1994; 7:249-52
64. Todani T, Watanabe Y, Narusue M, et al. Congenital bile duct cysts. Am J Surg 1977; 134: 263-9
65. Todani T. Choledochal cysts and pancreatobiliary maljunction. In: Balistreri WF, Ohi R, Todani T, Tsushida Y (eds): Hepatobiliary, pancreatic and splenic disease in children: medical and surgical management. Elsevier Science 1997,261-286
66. Vijay KT, Kocher HH, Koti RS, et al. Agenesis of gallbladder - a diagnostic dilemma. J Postgrad Med 1996; 42:80-82
67. Wachsberg RH, Kim KH, Sundaram W. Sonographic versus endoscopic retrograde cholangiographic measurement of the bile duct revisited: importance of the transverse diameter. AJR 1998; 170:669-674
68. Wheeler DA, Edmonson HA. Cystadenoma with mesenchymal stroma (CMS) in the liver and bile ducts. A clinicopathologic study of 17 cases, 4 with malignant change. Cancer 1985; 56:1434-1445
69. Wilbur AC, Sagireddy PB, Aizenstein RI. Carcinoma of the gallbladder: color Doppler ultrasound and CT findings. Abdom Imaging 1997; 22:187-190
70. Worawattanakul S, Semelka RC, Noone TC, et al. Cholangiocarcinoma: spectrum of appearances on MR images using current techniques. Magn Reson Imaging 1998; 16:993-1003
71. Yamanaka N, Okamoto E, Ando T, Oriyama T, Fujimoto J, Furukawa K, Tanaka T, Tanaka W, Nishigami T. Clinicopathologic spectrum of resected extraductal mass-forming intrahepatic cholangiocarcinoma. Cancer 1995; 76:2449-2456
72. Yedlicka JW, Tadararthy SM, Letourneau JG, et al. Interventional techniques in the hepatobiliary sys-

tem. In: Castaneda-Zuniga WR (ed): Interventional Radiology (3rd ed). William & Wilkins, Baltimore 1997,1439-1573
73. Yeo CJ, Pitt HA, Cameron JL. Cholangiocarcinoma. Surg Clin North Am 1990; 70:1429-1447
74. Yoshida Y, Imai Y, Murakami T, et al. Intrahepatic cholangiocarcinoma with marked hypervascularity. Abdom Imaging 1999; 24:66-68
75. Zech CJ, Schoenberg SO, Helmberger T. Cross-sectional imaging of biliary tumors: current clinical status and future developments. Eur Radiol 2004; 14:1174-1187

8

Comparison of Available Contrast Agents for the Imaging of Specific Liver Lesions

CONTENTS

8.1 Introduction

A practical approach to the characterization of focal hepatic lesions by computed tomography (CT) and magnetic resonance (MR) has traditionally focused on the distribution of conventional iodine and gadolinium (Gd) chelates to extracellular fluid spaces. This approach facilitates both the detection and characterization of lesions, the latter relying upon the recognition of distinctive patterns of enhancement of liver lesions. On the basis of their handling of these contrast agents, lesions are broadly classified as being hypervascular, hypovascular or as having delayed persistent enhancement (See Chap. 3, "Contrast Agents for Liver Imaging", section 3.3, "Radiologic Classification of Focal Liver Lesions on MRI").

Hypovascular lesions include clearly avascular lesions such as cysts and abscesses, and also tumors that demonstrate only marginal peripheral enhancement, if any, compared to the surrounding liver parenchyma. The majority of metastases to the liver are hypovascular lesions from primary sources such as the colon, lung, and pancreas. The few primary sites from which hypervascular liver metastases derive include renal, thyroid, neuroendocrine (pancreatic islet cell), and sarcoma. Breast and melanoma metastases to the liver may be vascular, but generally less so than those of other tumors. Imaging of hypovascular tumors at dynamic SonoVue-enhanced ultrasound (US), iodine-enhanced CT or dynamic Gd-enhanced MR relies on imaging the liver before and during peak enhancement in order to maximize liver-lesion contrast before the equilibrium phases are reached.

The group of hypervascular liver lesions includes a wide number of lesion types, ranging from physio-pathologic to pathologic. Among these are benign and malignant lesions of both hepatocellular and non-hepatocellular origin. Enhancement characteristics can help narrow a differential diagnosis or, in many cases, achieve a definitive diagnosis.

Other lesions may be classified as demonstrating delayed persistent enhancement. This group of lesions principally comprises capillary and cavernous forms of hepatic hemangioma, although cholangiocellular carcinoma (CCC) also falls into this category, especially when an abundant fibrotic reaction is present. Additionally, some metastases from colon cancer may have a fibrotic component and thus appear with delayed central enhancement.

On hepatobiliary phase images after Gd-BOPTA, Gd-EOB-DTPA and Mn-DPDP, hepatocellular lesions may appear iso-, hyper- or hypointense compared to the normal liver parenchyma, de-

pending on whether the lesion has preserved hepatocellular activity, modified pathways of biliary excretion, or poor or absent hepatocyte activity, respectively. Similarly, hepatocellular lesions on reticuloendothelial phase images after administration of superparamagnetic iron oxide (SPIO) agents may appear iso-, hypo- or hyperintense. Iso- and hypointensity reflect a signal drop due to the presence of abundant and functioning Kupffer cells. Conversely, lesion hyperintensity reflects scarce or absent Kupffer cell activity.

Non-hepatocellular lesions such as metastases and hemangiomas generally appear hypo- and hyperintense, respectively, on hepatobiliary phase and reticuloendothelial phase images. (For a description of the characterization of liver lesions by unenhanced and contrast-enhanced MR imaging using different contrast agents see also: Chap. 3, section 3.3, "Radiologic Classification of Focal Liver Lesions on MRI").

8.2 Benign Focal Liver Lesions of Hepatocellular Origin

8.2.1 Focal Nodular Hyperplasia (FNH)

The cellular structure of FNH is similar to that of the normal hepatic parenchyma apart from the presence of an abnormal biliary system. Since FNH contains the same elements as normal liver but with a disordered architecture, it mimics the appearance of normal liver and may be difficult to detect using any of the imaging modalities without exogenous contrast agents. On unenhanced MR imaging, the lesion is iso- to hypointense compared to normal liver on T1-weighted images, frequently with a hypointense central fibrous scar. On T2-weighted images it is isointense to mildly hyperintense compared to normal liver, with a hyperintense central scar. On dynamic Gd-enhanced T1-weighted images, the lesions show intense enhancement in the arterial phase that washes out rapidly on portal-venous and subsequent equilibrium phase images. A key characteristic of this enhancement is a homogeneous appearance (other than the central scar) which aids in differentiating these lesions from fibrolamellar hepatocellular carcinoma.

Typical of fibrous tissue, the central scar is slower to allow entry of extracellular-type contrast materials and slower to allow wash-out. This leads to a characteristic hypointense appearance on early arterial phase images but an iso- to hyperintense appearance on portal-venous and equilibrium phase images due to a prolonged retention of contrast agent compared to the wash-out from normal liver parenchyma. This can be very helpful in differentiating the central scar of FNH from the tumor necrosis often seen in malignant tumors.

Although Gd-enhanced MRI is considered the most sensitive method for the characterization of FNH, atypical features can frequently confound interpretation: in a recent study 86% of small (< 3 cm) FNH did not have a visible scar on unenhanced or enhanced dynamic phase scans [6]. Similar findings have been reported for CT [13]. Although the absence of a scar in small FNH cannot be considered "atypical", it may make it more difficult to distinguish these lesions from other hypervascular neoplasms on dynamic imaging alone. Hence, the availability of MR contrast agents with liver-specific properties may be helpful for the accurate characterization of FNH.

Gd-BOPTA and Gd-EOB-DTPA offer the possibility to perform both dynamic and delayed phase imaging, unlike conventional Gd agents and some SPIO agents. Gd-BOPTA-induced enhancement of FNH on T1-weighted dynamic phase imaging is indistinguishable from that of conventional non-specific Gd agents (Fig. 1). Thereafter, Gd-BOPTA offers the advantage over conventional agents of permitting additional hepatobiliary phase T1-weighted imaging (Fig. 2). On these delayed T1-weighted images, substantial enhancement is usually noted within the parenchyma of the vast majority of FNH lesions indicating the presence of functioning hepatocytes able to take up Gd-BOPTA. Conversely, the central scar, which is the principal site of biliary metaplasia, appears consistently hypointense.

FNH lesions typically appear iso- or hyperintense compared to the surrounding liver parenchyma on hepatobiliary phase images after Gd-BOPTA, with three different patterns of enhancement frequently observed: homogeneous, peripheral or heterogeneous [6]. Similar findings have been observed with mangafodipir trisodium (Fig. 3) [3], although the inability to perform dynamic imaging with this agent is an obvious limitation (see Chap. 4, Figs. 23, 25).

Since FNH lesions usually contain Kupffer cells and are thus able to take up SPIO and ultrasmall superparamagnetic iron oxide (USPIO) particles, the lesions typically demonstrate reduced signal intensity (SI) on delayed post-iron oxide T2-weighted images (Fig. 4). However, this finding is not specific, as well-differentiated HCC may also take up iron oxide particles, although usually to a lesser extent. Moreover, the amount and distribution of Kupffer cells within the nodules can vary and yield different patterns of signal decrease: some small FNH (< 3 cm) show a homogeneous signal drop similar to that observed in the surrounding parenchyma, while large FNH may show a heterogeneous signal drop. The central scar does

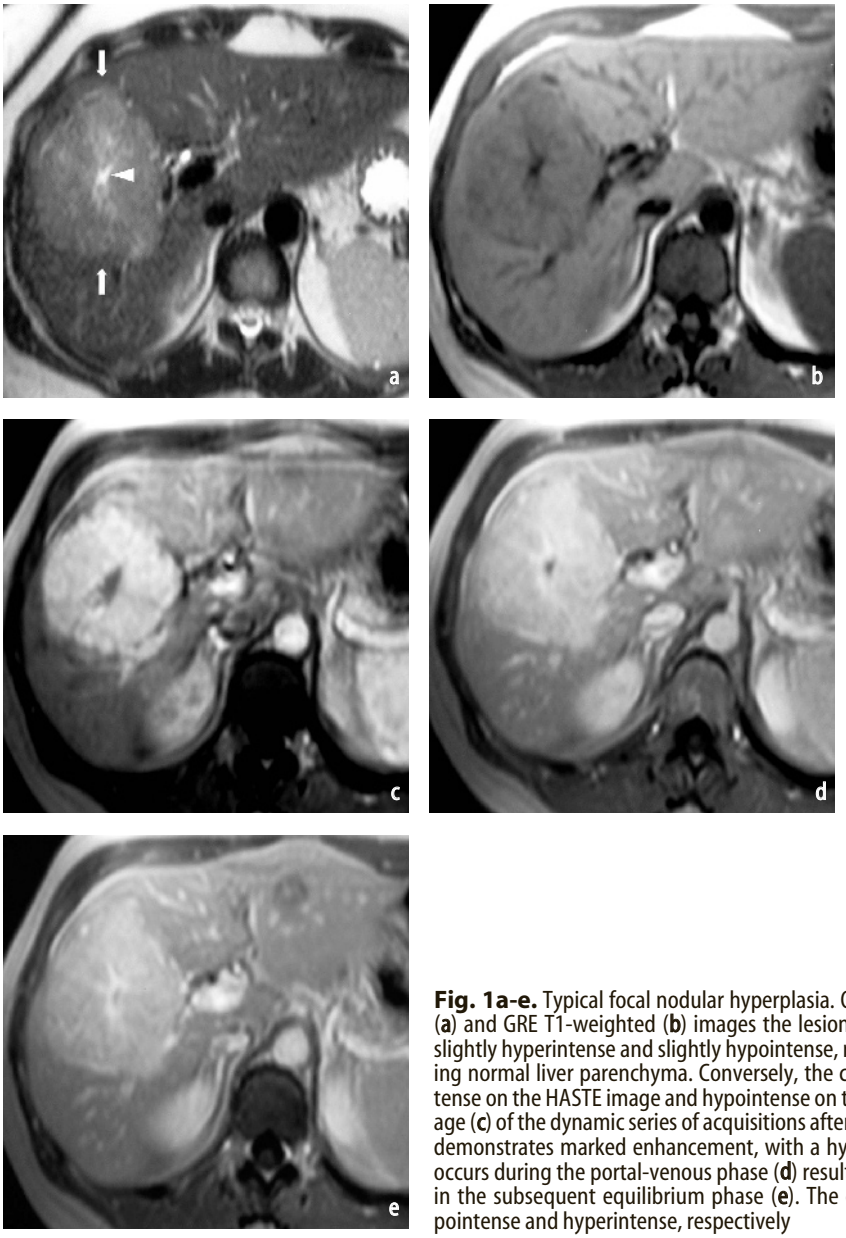

Fig. 1a-e. Typical focal nodular hyperplasia. On the pre-contrast HASTE T2-weighted (**a**) and GRE T1-weighted (**b**) images the lesion (*arrows* in **a**) appears homogeneously slightly hyperintense and slightly hypointense, respectively, compared to the surrounding normal liver parenchyma. Conversely, the central scar (*arrowhead* in **a**) is hyperintense on the HASTE image and hypointense on the GRE image. On the arterial phase image (**c**) of the dynamic series of acquisitions after administration of Gd-BOPTA, the lesion demonstrates marked enhancement, with a hypointense central scar. Rapid wash-out occurs during the portal-venous phase (**d**) resulting in an almost isointense appearance in the subsequent equilibrium phase (**e**). The central scar during these phases is hypointense and hyperintense, respectively

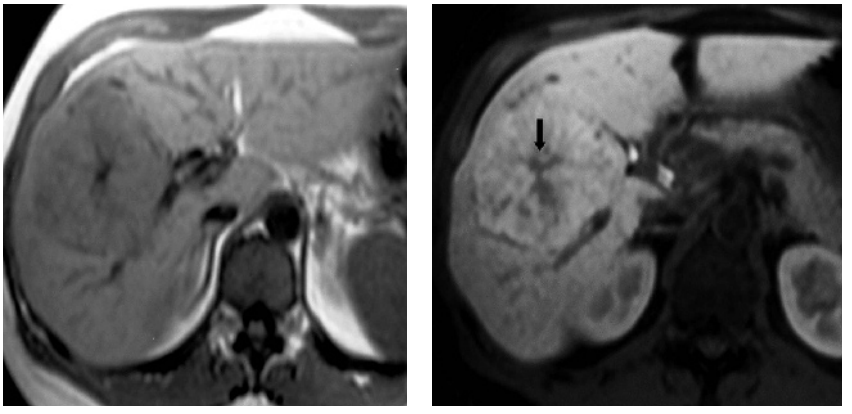

Fig. 2a, b. Typical focal nodular hyperplasia after Gd-BOPTA. Same case as Fig. 1. On the pre-contrast GRE T1-weighted image (**a**) the lesion appears homogeneously slightly hypointense compared to the normal liver parenchyma. In the hepatobiliary phase after Gd-BOPTA administration (**b**), the lesion appears hyperintense due to the uptake of Gd-BOPTA by normal hepatocytes. Conversely, the central scar is still hypointense (*arrow*)

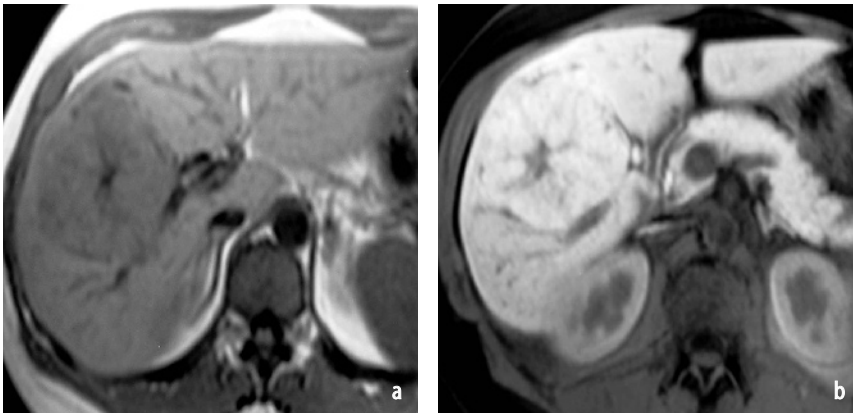

Fig. 3a, b. Typical focal nodular hyperplasia after Mn-DPDP. Same case as Fig. 1 and 2. On the pre-contrast GRE T1-weighted image (**a**) the lesion appears homogeneously slightly hypointense. In the hepatobiliary phase after Mn-DPDP administration (**b**), the lesion appears isointense with a hypointense central scar, similar to the appearance after Gd-BOPTA administration

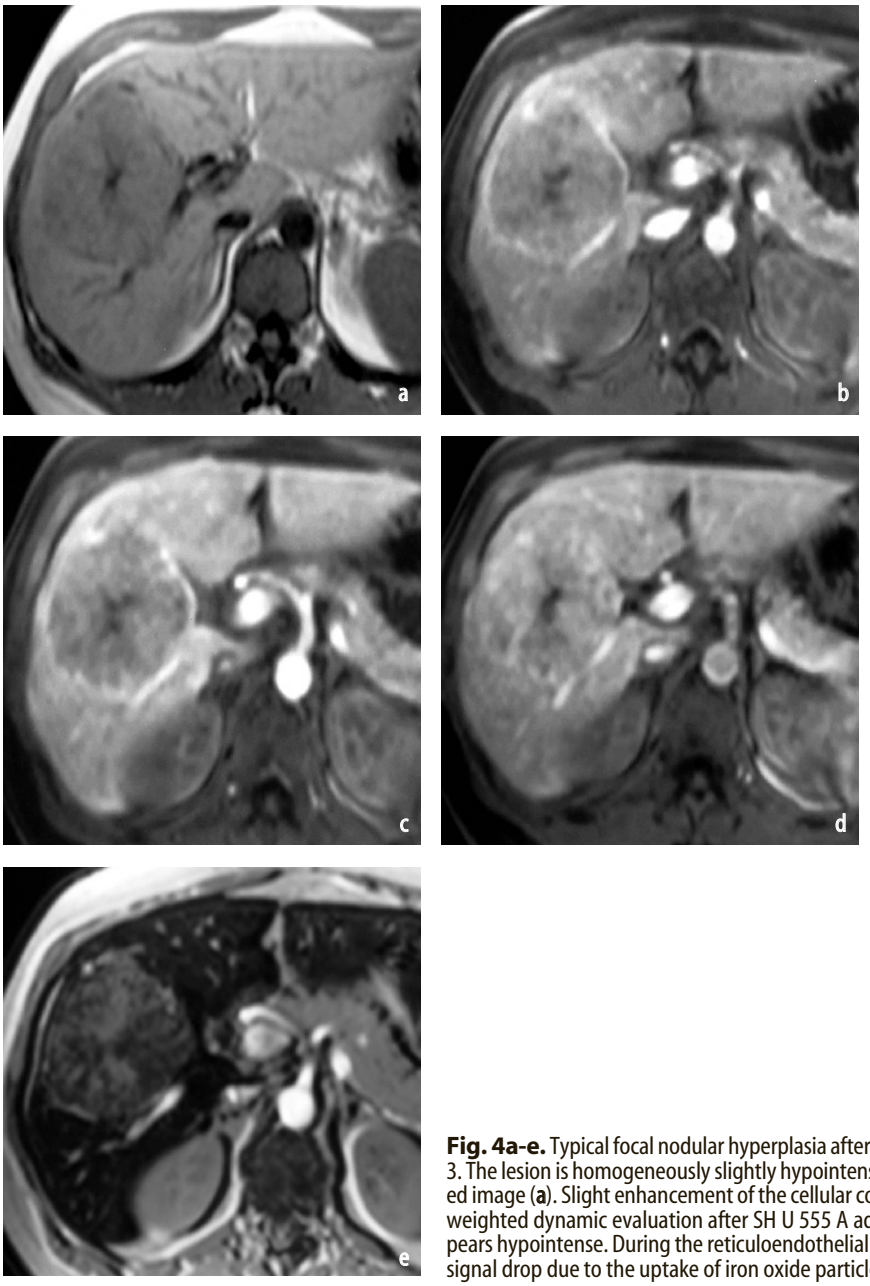

Fig. 4a-e. Typical focal nodular hyperplasia after SH U 555 A. Same case as Fig. 1, 2 and 3. The lesion is homogeneously slightly hypointense on the pre-contrast GRE T1-weighted image (**a**). Slight enhancement of the cellular components can be seen during the T1-weighted dynamic evaluation after SH U 555 A administration (**b**-**d**), while the scar appears hypointense. During the reticuloendothelial phase (**e**) the nodule shows a discrete signal drop due to the uptake of iron oxide particles by Kupffer cells within the lesion

not contain Kupffer cells and is therefore usually seen as a hyperintense central stellate area that corresponds to the high signal area seen on precontrast T2-weighted images. The possibility of performing dynamic phase T1-weighted imaging is an added advantage of the USPIO agents (Fig. 4).

A recent intraindividual comparison of Gd-BOPTA and ferumoxides in 50 patients with 83 FNH revealed that whereas all 83 (100%) FNH were seen during the examination with Gd-BOPTA, only 62 FNH were seen during the examination with ferumoxides [8]. Importantly, Gd-BOPTA detected, and was able to diagnose correctly, all 17 FNH in 12 patients with previous neoplasia, while ferumoxides was able to detect only nine of these 17 lesions (52.9%) and to accurately characterize only seven (Fig. 5).

8.2.2 Nodular Regenerative Hyperplasia (NRH)

NRH of the liver is not a specific entity but is a secondary and non-specific tissue adaptation to a heterogeneous distribution of blood flow. NRH is characterized by multiple monoacinar regenerative nodules without fibrous septa. The lesions are not usually visible until a confluent macroaggregation of sufficient size has been achieved. NRH occurs in 5-6% of individuals over 80 years of age and with increased frequency in patients with Budd-Chiari syndrome, systemic arthritis, polymyalgia rheumatica, massive tumor infiltration, mineral oil deposition and other disorders of liver blood flow [31, 33].

On unenhanced MR imaging, NRH displays a broad spectrum of SI characteristics and may appear hypo-, iso- or hyperintense compared to the normal liver parenchyma on T1- and T2-weighted images [31]. On dynamic phase MR imaging with Gd-BOPTA and other extracellularly-distributed Gd agents, about 90% of these lesions appear hyperintense during the arterial phase and iso- or slightly hyperintense during the portal venous and equilibrium phases [31].

As in the case of FNH, NRH demonstrates abnormal biliary system drainage, which does not derive from or communicate with that in the surrounding normal liver parenchyma. Consequently, like FNH these lesions appear iso- or hyperintense compared to the surrounding liver parenchyma in the hepatobiliary phase after both Gd-BOPTA and Gd-EOB-DTPA. A peripheral hypointense rim is often seen in the biggest nodules, which represents ischemic areas with focal peripheral steatosis (Fig. 6, 7).

These lesions also appear iso- or hyperintense compared to the surrounding liver parenchyma in the hepatobiliary phase after mangafodipir trisodium (Fig. 8).

The appearance of NRH after SPIO administration has not yet been fully described. However, because NRH typically contains abundant functioning Kupffer cells, its behavior can be expected to be similar to that of FNH (Fig. 9).

8.2.3 Hepatocellular Adenoma (HA)

Hepatocellular adenoma (HA) consists of plates or cords of cells that are larger than normal hepatocytes and may contain large amounts of glycogen and lipid. Lipid accumulation is responsible for the characteristic yellow appearance of the cut surface of adenomas at pathology, and evidence of lipid on CT or MR imaging can be suggestive in diagnosing HA. The plates are separated by dilated sinusoids, which are thin-walled capillaries perfused by arterial pressure, while a portal venous supply is lacking. A tumor capsule may be present (see Chap. 4, Figs. 40, 41).

Kupffer cells are often found in HA but may be reduced in number and function. Even though HA have functioning hepatocytes they lack bile ducts, a key histologic feature that distinguishes these lesions from FNH [20]. For this reason, bilirubin metabolism is blocked within HA, as confirmed by the absence of bile within resected lesions.

The appearance of HA on unenhanced MR imaging has been variously described as hyper-, iso-, and hypointense [1, 24]. Areas of increased SI on T1-weighted MR images can result from fat and hemorrhage while low SI areas correspond to necrosis, old hemorrhage or calcifications [24]. Some 47%-74% of HA are predominantly hyperintense on T2-weighted images while the remainder are iso- or hypointense. Most lesions are heterogeneous, demonstrating a combination of hyper- and hypointensity on T2-weighted images due to hemorrhage and necrosis. One third of HA have a peripheral rim corresponding to a fibrous capsule [1] that is typically hypointense on T1- and T2-weighted images.

Dynamic Gd-enhanced MR imaging can reveal early arterial enhancement, which is usually homogeneous and intense in non-complicated and small (< 5 cm) HA. However, in large lesions or in lesions with previous hemorrhage, the arterial enhancement may be heterogeneous (see Chap. 4, Fig. 42). On portal venous phase images, this early enhancement usually fades, revealing an iso- or hypointense lesion.

Since HA lack bile ducts, there is altered hepatocellular transport compared to normal hepatocytes. Thus, while HA may contain functioning hepatocytes able to take up Gd-BOPTA, the absence of an intracellular transport gradient due to the lack of active transport across the sinusoid mem-

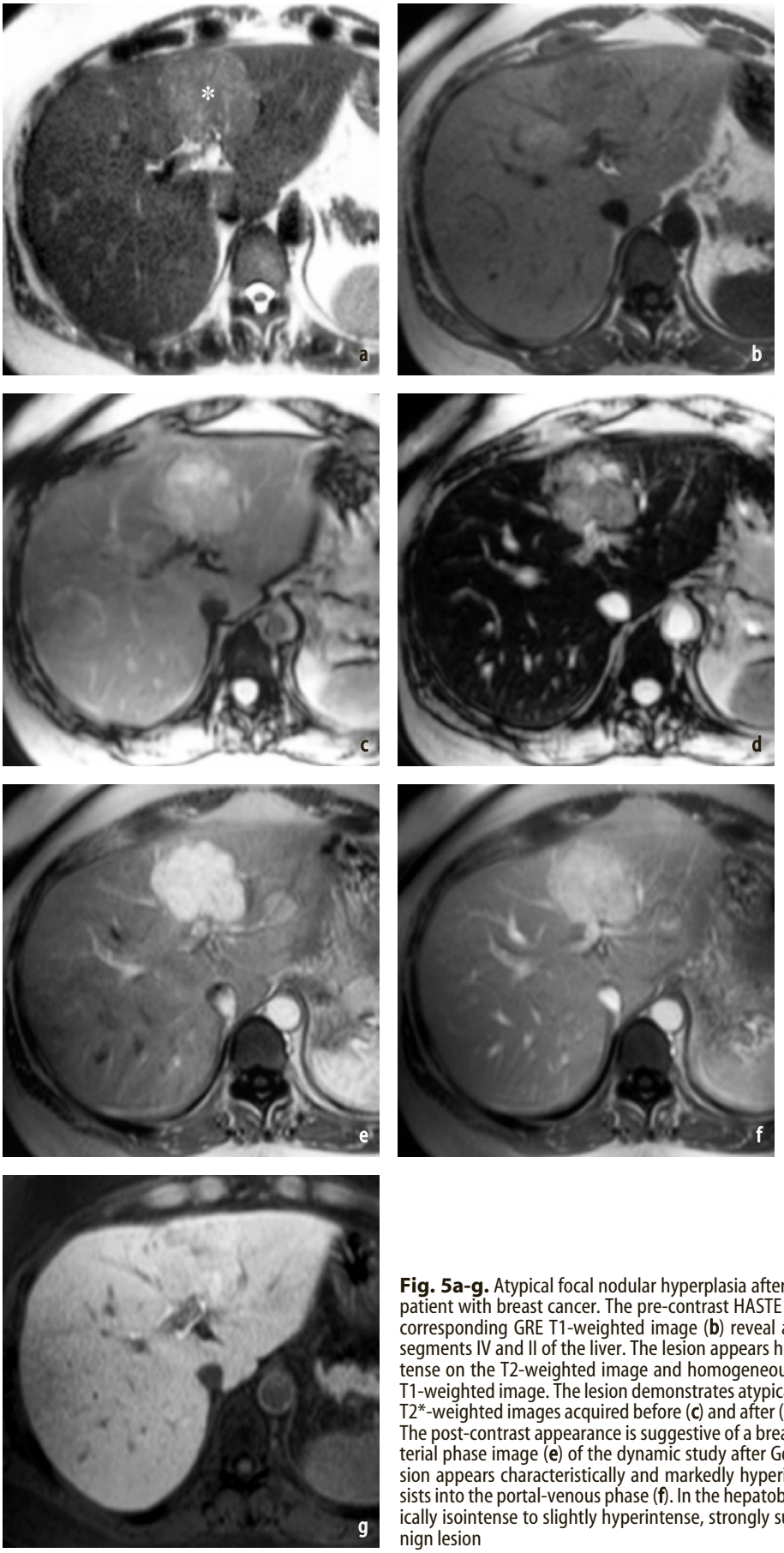

Fig. 5a-g. Atypical focal nodular hyperplasia after SH U 555 A and Gd-BOPTA in a patient with breast cancer. The pre-contrast HASTE T2-weighted image (**a**) and the corresponding GRE T1-weighted image (**b**) reveal a large nodule (*asterisk* in **a**) in segments IV and II of the liver. The lesion appears homogeneously slightly hyperintense on the T2-weighted image and homogeneously slightly hypointense on the T1-weighted image. The lesion demonstrates atypical nodular hyperintensity on the T2*-weighted images acquired before (**c**) and after (**d**) administration of SH U 555 A. The post-contrast appearance is suggestive of a breast cancer metastasis. On the arterial phase image (**e**) of the dynamic study after Gd-BOPTA administration, the lesion appears characteristically and markedly hyperintense. The enhancement persists into the portal-venous phase (**f**). In the hepatobiliary phase (**g**) the lesion is typically isointense to slightly hyperintense, strongly suggesting the presence of a benign lesion

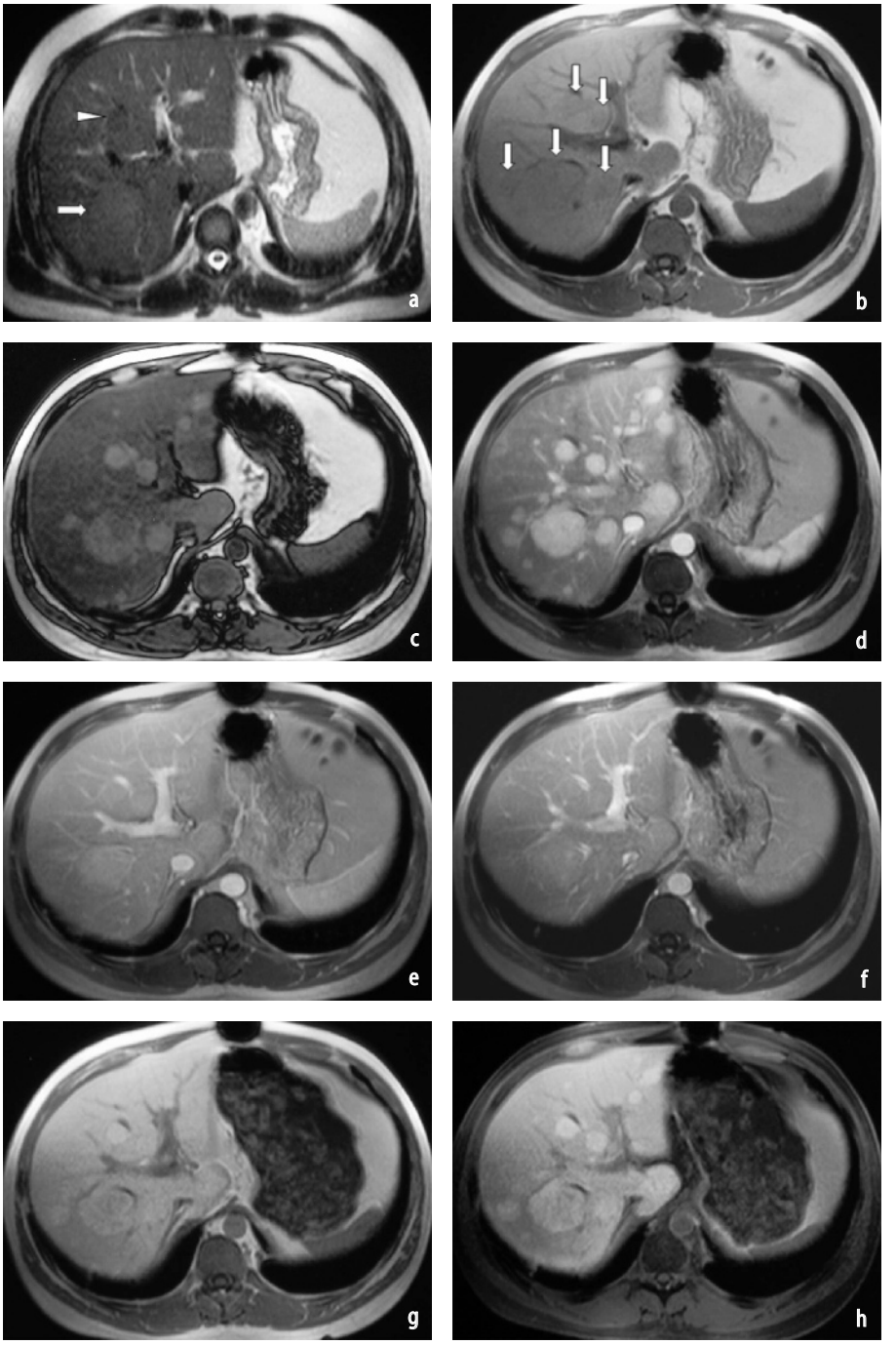

Fig. 6a-h. Nodular regenerative hyperplasia after Gd-BOPTA in a patient with previous testicular cancer. A large slightly hyperintense nodule (*arrow*) and a smaller round hypointense nodule (*arrowhead*) are visible on the pre-contrast TSE T2-weighted image (**a**). On the corresponding pre-contrast GRE T1-weighted "in-phase" image (**b**), numerous slightly hypointense nodules (*arrows*) are visible. These lesions appear slightly hyperintense in a diffuse fatty liver on the pre-contrast GRE T1-weighted "out-of-phase" image (**c**). The lesions show marked and homogeneous enhancement on the arterial phase image (**d**) of the dynamic study after Gd-BOPTA administration, followed by rapid wash-out in the portal venous (**e**) and equilibrium (**f**) phases. In the hepatobiliary phase (**g**, **h**) the lesions appear slightly hyperintense, due to the abnormal biliary system drainage which results in a reduced rate of bile elimination.

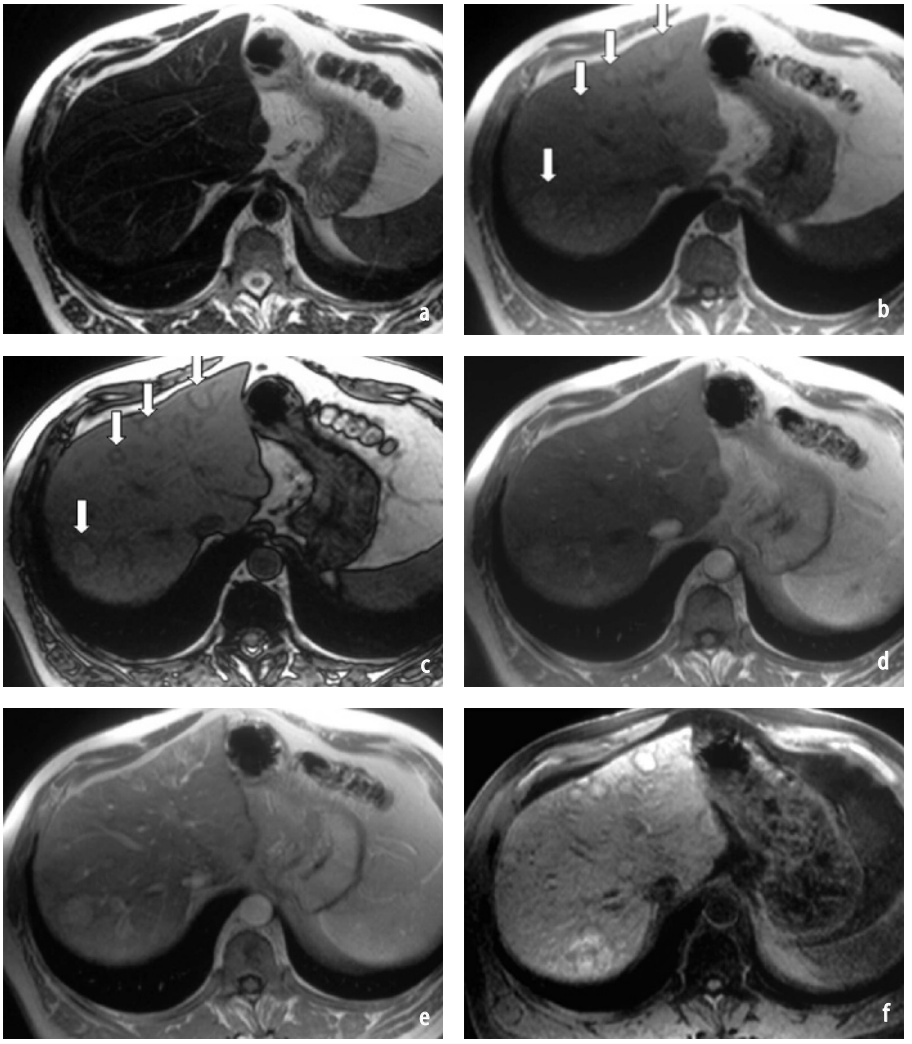

Fig. 7a-f. Nodular regenerative hyperplasia after Gd-BOPTA. No liver lesions are visible on the pre-contrast TSE T2-weighted image (**a**). Conversely, the pre-contrast GRE T1-weighted "in-phase" (**b**) and "out-of-phase" (**c**) images reveal numerous slightly hyperintense nodules (*arrows*) surrounded by a thin hypointense rim. During the dynamic evaluation after Gd-BOPTA administration (**d**, **e**) the lesions show weak enhancement, which is more evident in the portal venous phase (**e**). In the hepatobiliary phase (**f**), multiple well-defined hyperintense lesions with a thin hypointense peripheral rim can be seen

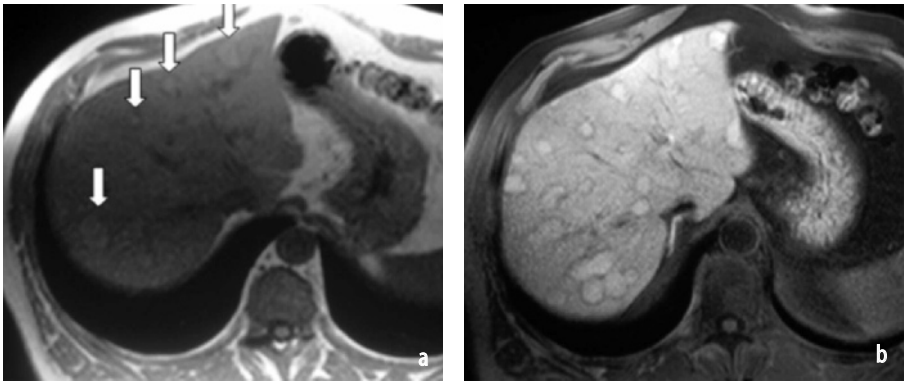

Fig. 8a, b. Nodular regenerative hyperplasia after Mn-DPDP. Same case as Fig. 7. The pre-contrast GRE T1-weighted image (**a**) reveals numerous slightly hyperintense nodules (*arrows*) surrounded by a thin hypointense rim. In the hepatobiliary phase after Mn-DPDP administration (**b**), the nodules are homogeneously hyperintense due to uptake of Mn^{++} into the lesion, similar to the appearance after Gd-BOPTA

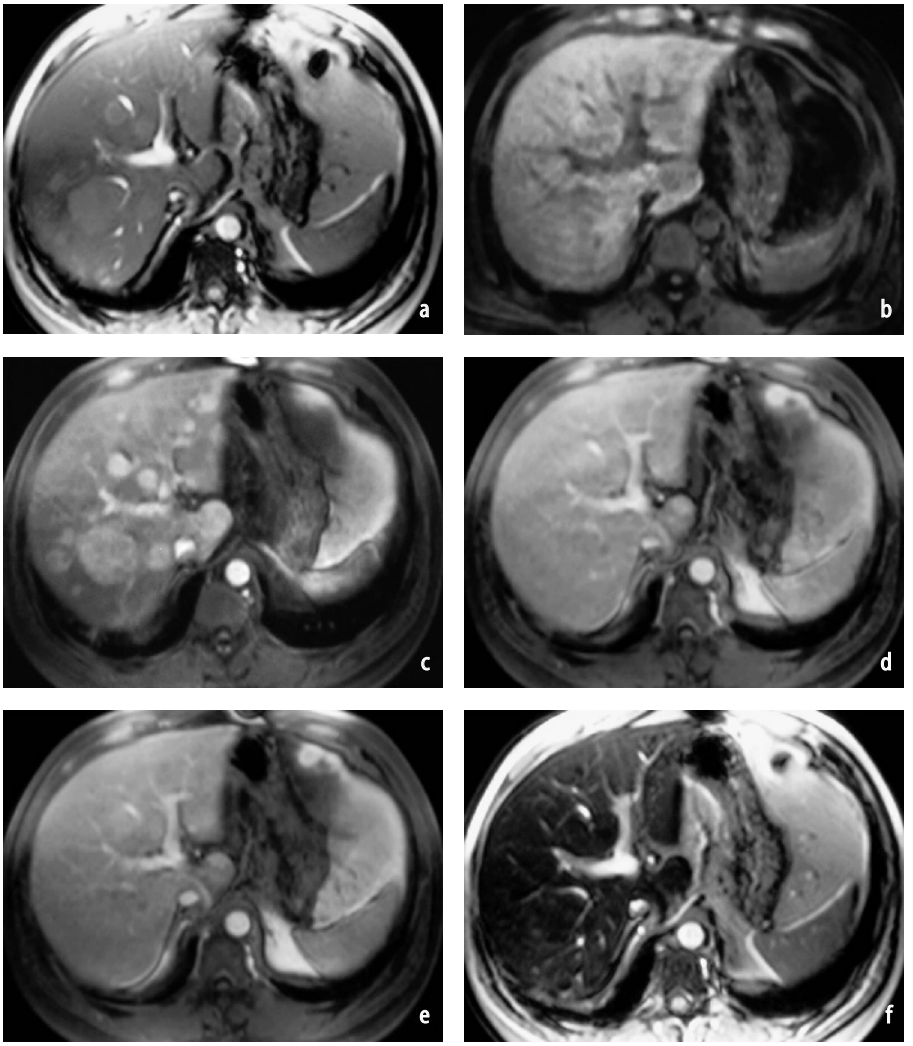

Fig. 9a-f. Nodular regenerative hyperplasia after SH U 555 A. Same case as Fig. 6. The pre-contrast T2*-weighted image (**a**) reveals numerous slightly hyperintense nodules. Conversely, no lesions are visible on the pre-contrast T1-weighted VIBE image (**b**). In the arterial phase (**c**) of the dynamic study after SH U 555 A administration, numerous well-defined hyperintense lesions are visible. These lesions demonstrate rapid contrast wash-out in the portal venous (**d**) and equilibrium (**e**) phases. In the reticuloendothelial phase (**f**) the nodules show a marked signal drop due to the uptake of iron oxide particles by Kupffer cells, similar to the observation in FNH

brane results in these lesions appearing hypointense on delayed hepatobiliary phase images against normal enhanced liver parenchyma in which enhancement derives from the presence of Gd-BOPTA in both the hepatocytes and adjacent biliary system. This has proven a highly accurate means of differentiating HA from FNH [7].

HA typically appear iso- or hyperintense on delayed hepatobiliary phase images after mangafodipir trisodium administration because the Mn^{++} ion non-specifically enters the HA lesion hepatocytes via ionic channels. Unfortunately, since a similar enhancement pattern is seen with FNH, the accurate differentiation of these lesions is not possible using this contrast agent (Figs. 10, 11).

Due to the variable number and activity of Kupffer cells in different HA, variable uptake of SPIO particles occurs, leading to a different appearance on post-contrast T2-weighted images (Figs. 12 , 13) [7]. Uptake of SPIO particles in HA may also be due to pooling of the contrast agent within the peliosis-like dilated vessels.

In liver adenomatosis, which is characterized by the presence of multiple adenomas in the same patient, the lesions may appear small or large, non-complicated or complicated. Moreover, some nodules may appear with fatty metamorphosis while others may have a homogeneous appearance. For these reasons the enhancement behavior typically varies for different lesions (Fig. 14).

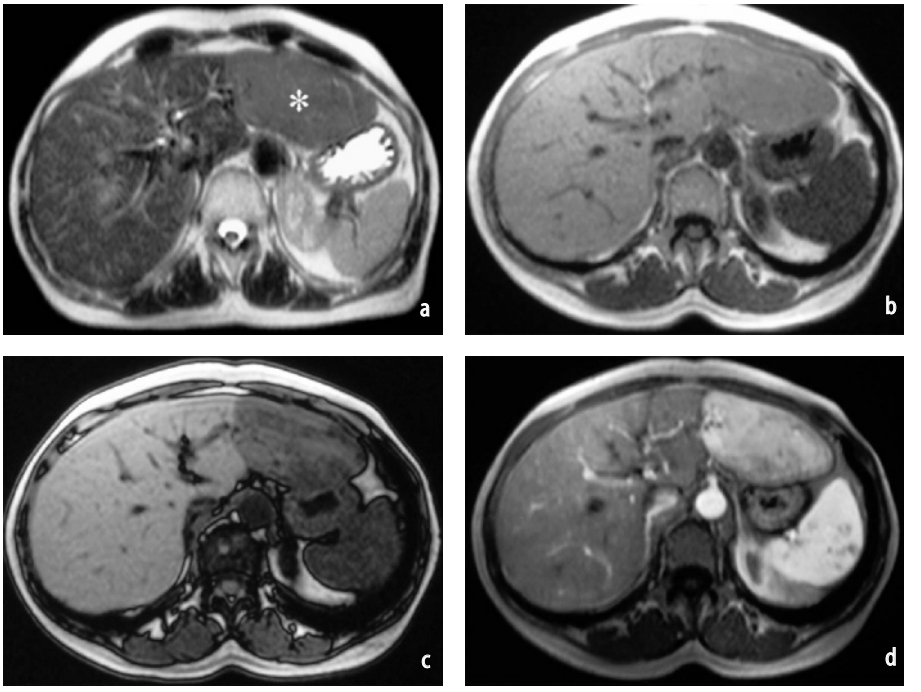

→

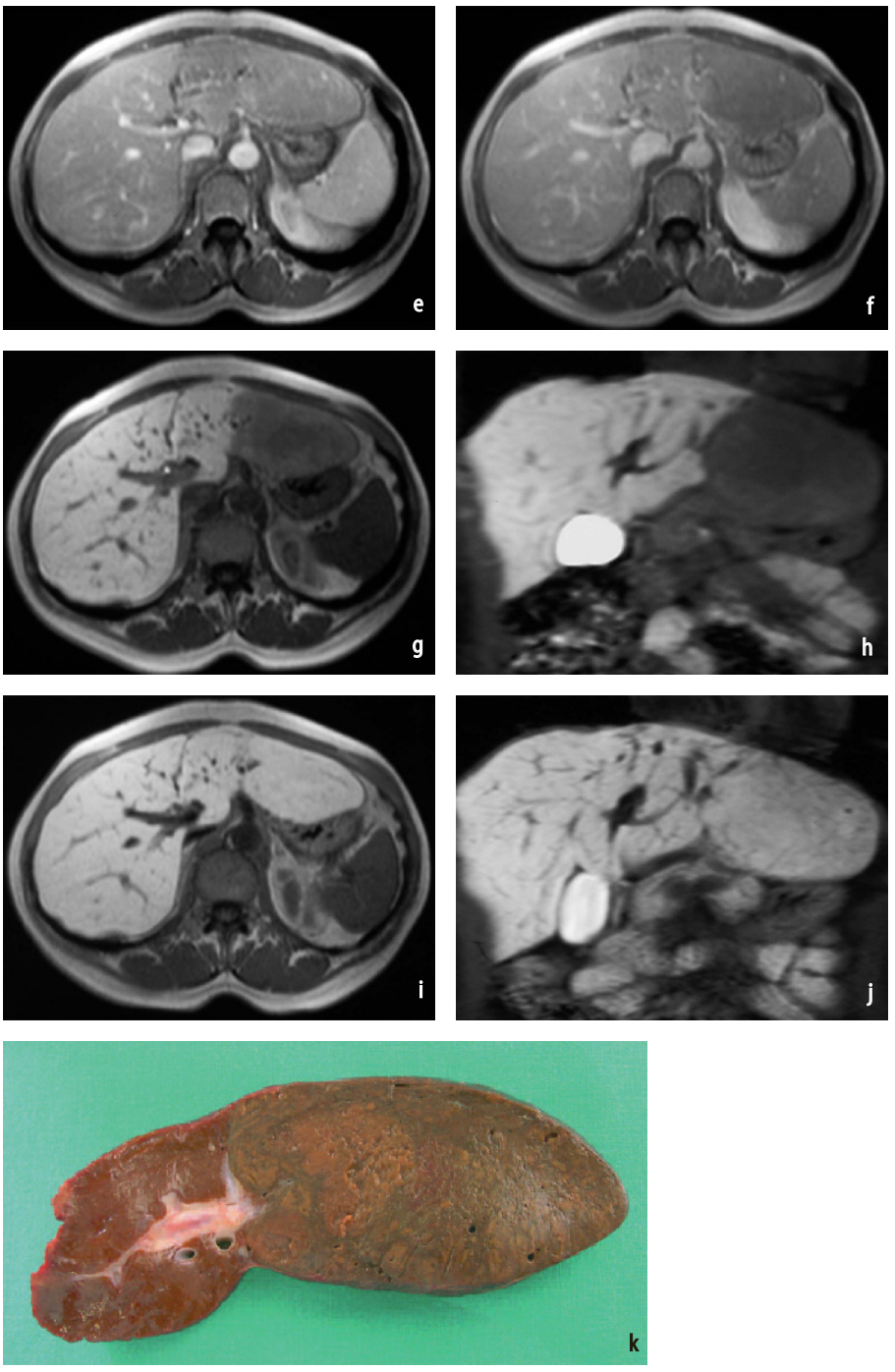

Fig. 10a-k. Non-complicated hepatic adenoma after Gd-BOPTA and Mn-DPDP. A large nodule (*asterisk*), located in the left lobe of the liver, appears slightly hyperintense on the pre-contrast TSE T2-weighted image (**a**), isointense on the pre-contrast GRE T1-weighted "in-phase" image (**b**) and homogeneously hypointense on the GRE T1-weighted "out-of-phase" image (**c**). The lesion demonstrates homogeneous enhancement in the arterial phase (**d**) of the dynamic series after administration of Gd-BOPTA, followed by rapid wash-out in the portal venous (**e**) and equilibrium (**f**) phases. The lesion is hypointense in the hepatobiliary phase after Gd-BOPTA administration (**g**, **h**) due to a decreased hepatocyte uptake of Gd-BOPTA as well as to the absence of bile ductules. Conversely, the lesion is isointense compared to the normal liver parenchyma on hepatobiliary phase images (**i**, **j**) after the administration of Mn-DPDP. This is due to the fact that Mn^{++} ions non-specifically enter the hepatocytes of the lesion via ionic channels. The gross specimen (**k**) shows a heterogeneous, well-defined, non-hemorrhagic and non-necrotic mass

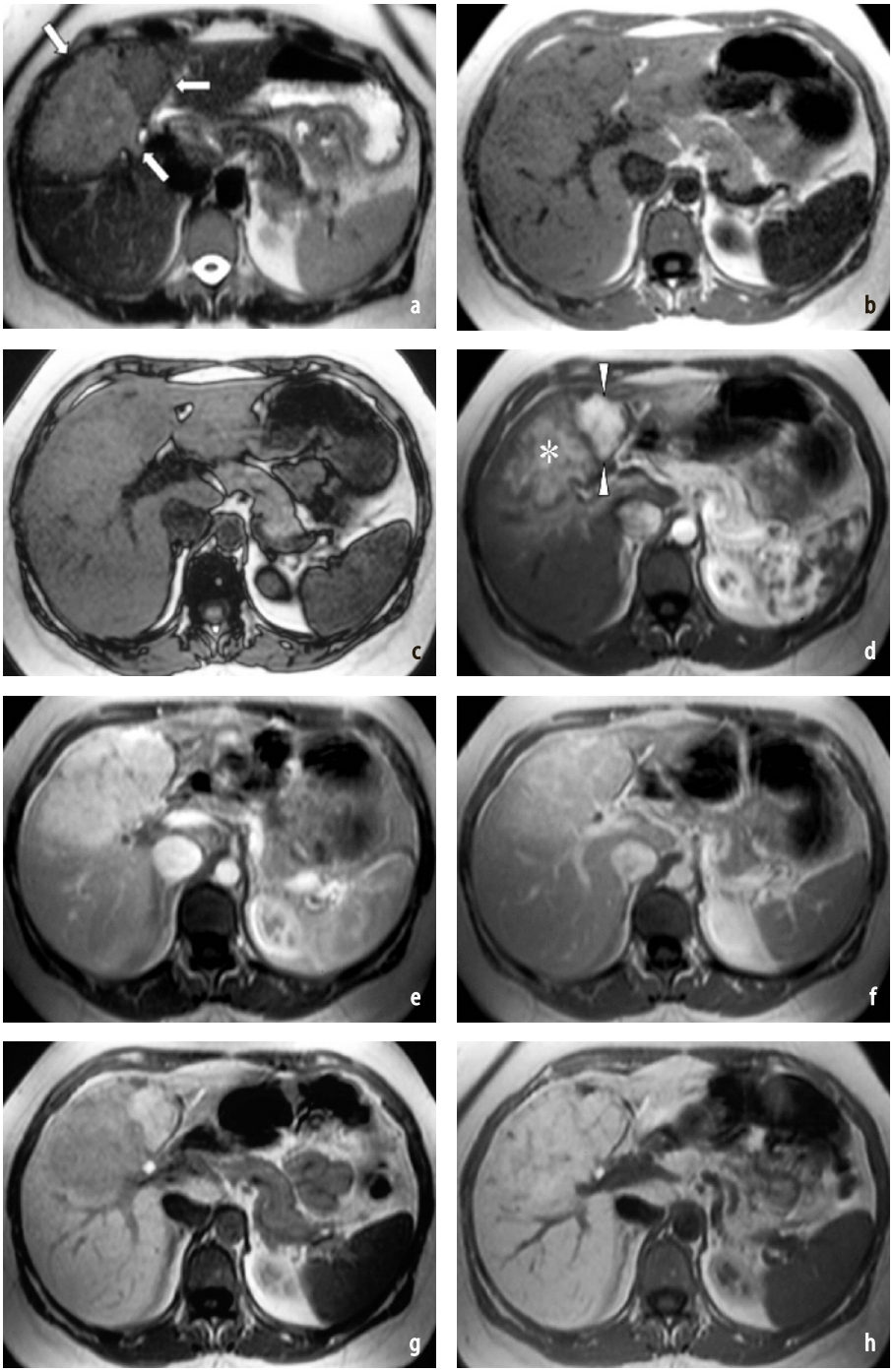

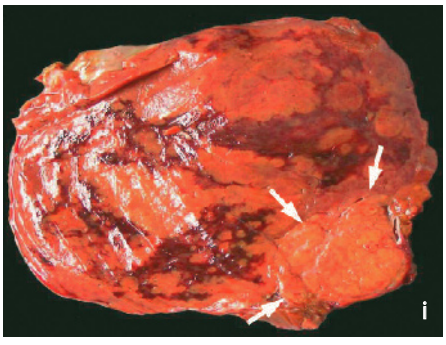

Fig. 11a-i. Coexisting hepatic adenoma and focal nodular hyperplasia after Gd-BOPTA and Mn-DPDP. The pre-contrast TSE T2-weighted image (**a**) reveals a large lesion (*arrows*) with heterogeneous signal intensity indicative of two different nodules. On the corresponding pre-contrast GRE T1-weighted "in-phase" (**b**) and "out-of-phase" (**c**) images, the lesion is isointense compared to the surrounding liver parenchyma. Unusual enhancement behavior is noted on dynamic phase images after the bolus injection of Gd-BOPTA (**d**-**f**). On the arterial phase image (**d**) the larger nodule (*asterisk*) appears slightly hyperintense while the smaller nodule (*arrowheads*) appears strongly hyperintense compared to the normal liver parenchyma. In the portal venous phase (**e**) both nodules appear homogeneously hyperintense with rapid wash-out of enhancement noted in the equilibrium phase (**f**). In the hepatobiliary phase after Gd-BOPTA administration (**g**) the larger nodule is markedly hypointense while the smaller nodule is slightly hyperintense. The enhancement behavior of the two nodules is characteristic for HA and FNH, respectively. In the hepatobiliary phase after Mn-DPDP administration (**h**), both nodules are isointense compared to the surrounding liver, indicating non-specific entry of Mn^{++} ions into hepatocytes. The gross specimen (**i**) confirms the different composition of the lesions: the FNH has a more homogeneous appearance (*arrows*) while the HA has a heterogeneous appearance due to hemorrhagic areas

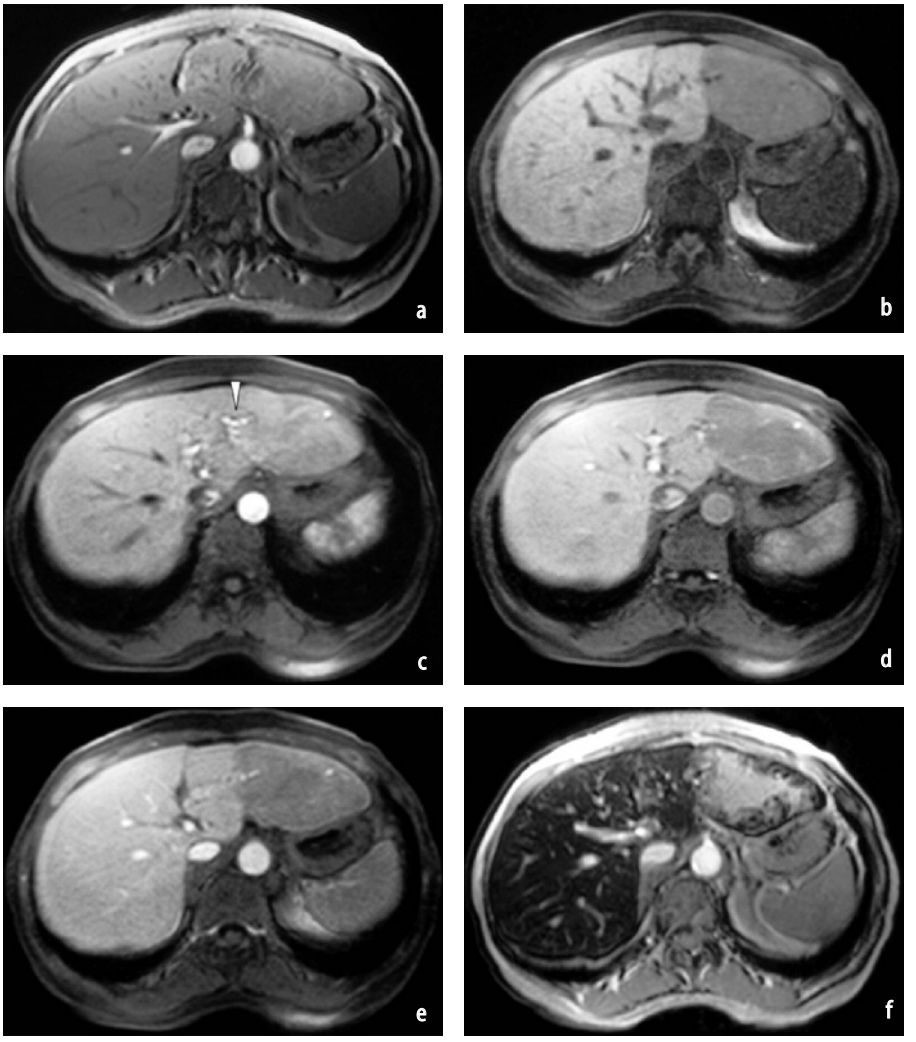

Fig. 12a-f. Non complicated hepatic adenoma after SH U 555 A. Same case as shown in Fig. 10. The lesion is isointense compared to the liver on the pre-contrast T2*-weighted image (**a**) and homogeneously hypointense on the pre-contrast VIBE image (**b**). The lesion is homogeneously enhanced in the arterial phase (**c**) of the dynamic evaluation after administration of SH U 555 A. Note the presence of feeding vessels (*arrowhead*). The lesion appears hypointense in the subsequent portal venous (**d**) and equilibrium (**e**) phases. In the reticuloendothelial phase (**f**) the lesion shows heterogeneous uptake of iron oxide particles characterized by a peripheral drop in signal

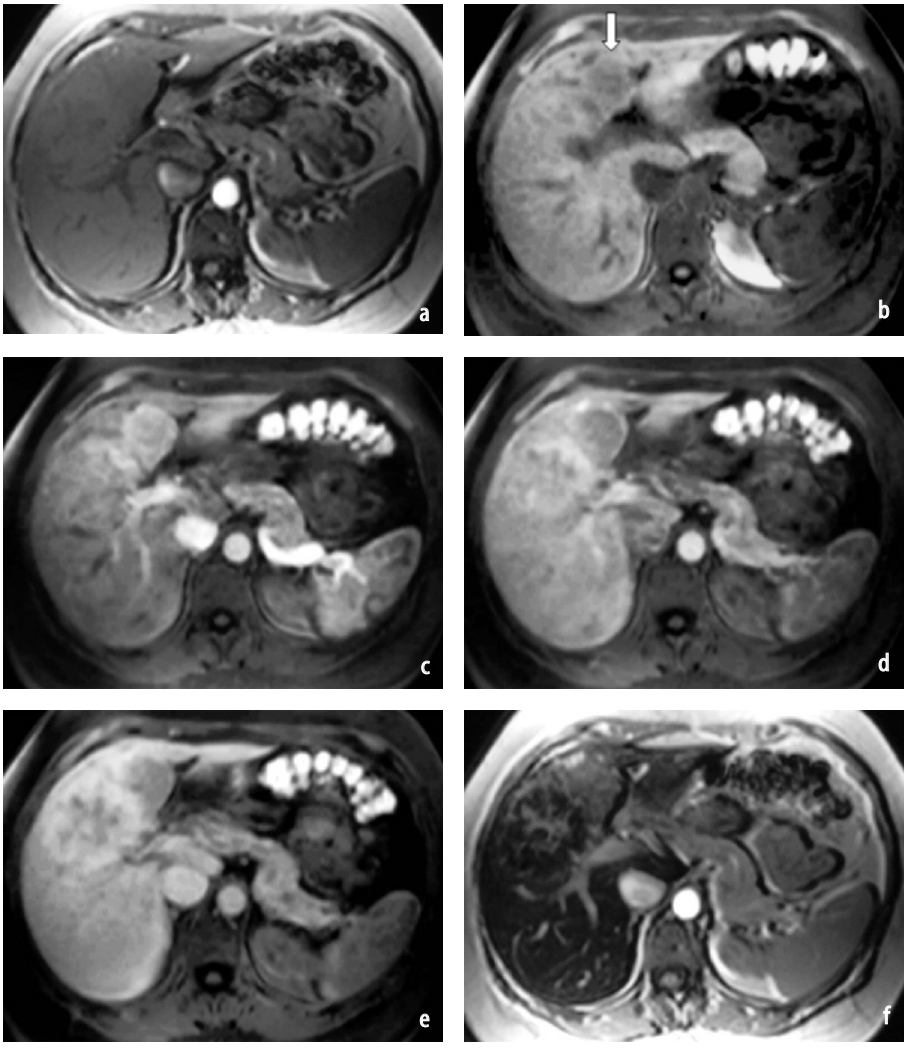

Fig 13a-f. Coexisting hepatic adenoma and focal nodular hyperplasia after SH U 555 A. Same case as Fig. 11. The lesion appears isointense on the pre-contrast T2*-weighted image (**a**), while on the VIBE image (**b**) the smaller nodule appears isointense at the periphery and hypointense in the central portion (*arrow*). On the arterial phase image (**c**) of the dynamic series after the administration of SH U 555 A, the bigger nodule appears slightly heterogeneously hyperintense while the smaller nodule is homogeneously hyperintense. In the portal venous (**d**) and equilibrium (**e**) phases the FNH (smaller nodule) appears hypointense, while the HA remains heterogeneously slightly hyperintense. In the reticuloendothelial phase (**f**) both lesions show a signal drop due to the presence of Kupffer cells, however the signal drop is less pronounced in the smaller FNH nodule

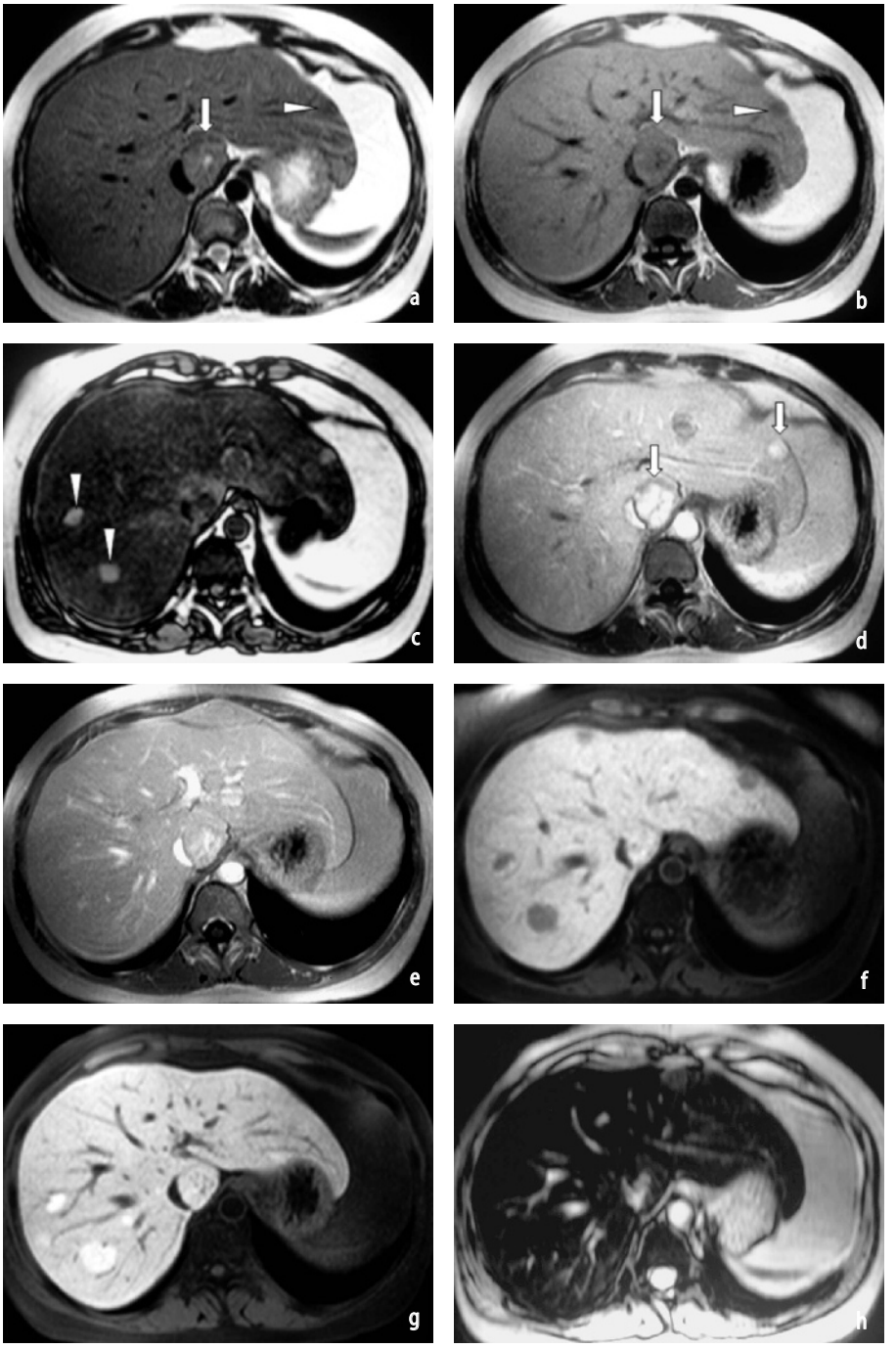

Fig. 14a-h. Liver adenomatosis and FNH after Gd-BOPTA, Mn-DPDP and SPIO. The pre-contrast TSE T2-weighted image (**a**) and the GRE T1-weighted "in-phase" image (**b**) reveal a small, round, hypointense lesion (*arrowhead*) located in segment II of the liver. In segment I an isointense nodule (*arrow*) with a hyperintense (T2-weighted image) and hypointense (T1-weighted image) central scar is visible. On the pre-contrast GRE T1-weighted "out-of-phase" image (**c**) the small nodule in segment II appears hyperintense while two other hyperintense lesions (*arrowheads*) are visible in the right lobe. The lesion located in segment I appears slightly hyperintense. During the arterial phase after Gd-BOPTA administration (**d**) the nodules (*arrows*) in segments II and I appear markedly hyperintense; conversely the two nodules located in the right lobe are isointense. In the portal venous phase (**e**) all the lesions appear isointense. On the hepatobiliary phase image (**f**) acquired after Gd-BOPTA administration, several hypointense nodules, suggestive of HA, are visible. The nodule in segment I of the liver appears isointense, which is suggestive of FNH. After Mn-DPDP administration (**g**) some hyperintense nodules are visible in the right lobe of the liver, while the nodules located in segments II and I appear isointense. On the reticuloendothelial phase image (**h**) after SPIO administration all the nodules are isointense compared to the normal liver, due to the presence of Kupffer cells within the lesions. This case illustrates that HA is more easily differentiated from FNH with Gd-BOPTA

8.3 Malignant Focal Liver Lesions of Hepatocellular Origin

8.3.1 From Regenerative Nodules to Hepatocellular Carcinoma (HCC)

According to the terminology established by an International Working Party in 1994, there are three steps in the development of HCC: regenerative nodule, dysplastic nodule (low-grade; high-grade; with focus of HCC) and small (< 2 cm) HCC.

Regenerative nodules are benign lesions with an exclusive portal venous blood supply. Low-grade dysplastic nodules, on the other hand, show slight cytologic atypia with mainly large cell changes, while high-grade dysplastic nodules are considered pre-malignant lesions. The development of new non-triadal arterial flow to small HCC and dysplastic nodules can result in some enhancement of dysplastic nodules at contrast-enhanced CT and MR and thus simulate HCC. However, this is comparatively rare [11, 17]. Small foci of carcinoma can be found in about one third of high-grade dysplastic nodules. When elements of HCC are found in lesions smaller than 2 cm in size, they are termed "small HCC".

Dysplastic nodules are commonly encountered pathologically in severe cirrhosis. However, only about 15% of such nodules are detected at MR imaging. When visualized, dysplastic nodules are typically hyperintense on T1-weighted images and hypointense on T2-weighted images [14]. However, since most are not seen, the most common appearance is therefore isointense compared to the surrounding liver parenchyma. Although arterial phase enhancement can increase the sensitivity for characterization of dysplastic nodules, this is at the expense of decreased specificity because of the overlap with the much more commonly seen arterial phase enhancement in HCC.

The nature of nodular regeneration in cirrhosis, and the development of dysplastic nodules may lead to additional false-positive diagnoses of HCC. MR imaging is now widely considered the most successful imaging modality for differentiating regenerative and dysplastic nodules from HCC. Regenerating nodules may have altered SI depending on whether or not they contain hemosiderin. Regenerating nodules without hemosiderin are typically iso- to slightly hyperintense on T1-weighted images and iso- or mildly hypointense on T2-weighted images. Those with hemosiderin are more hypointense on T2-weighted images due to their iron content (Fig. 15, 16). While dysplastic nodules have been reported to have low SI foci on T2-weighted images, and slightly hyperintense foci on T1-weighted images, most dysplastic nodules remain isointense with the cirrhotic liver, and it is generally only large, occasional dysplastic nodules that are identified at MR. The signal changes in dysplastic nodules also reflect the accumulation of iron and hemosiderin products (Fig. 17).

The macroscopic appearance of HCC has been classified as expanding, spreading and multifocal. On the basis of histological differentiation they can be classified as belonging to one of four grades, from I to IV. A frequent occurrence in small HCC is fatty degeneration. However, while this is seen microscopically, it is only rarely appreciated at imaging.

The formation of a pseudocapsule around the lesion (constructed usually from connective fibrous tissue) and of a septum within the tumor is frequently observed in larger HCC. This may derive from an interaction between tumor and host liver and may interfere with the growth and invasion of the HCC [9]. The internal septation process as well as the heterogeneity inherent within larger lesions due to macroscopic fat accumulation, hemorrhage, necrosis, and fibrosis creates a relatively characteristic 'mosaic' appearance (see Chapter 6, Fig. 16, 17) [29].

Kupffer cells are usually present in HCC. Although the number of Kupffer cells tends to be lower in cancerous compared to non-cancerous tissue, particularly as the tumor size increases and histologic grade decreases, there are typically few differences in Kupffer cell number in small well-differentiated HCC and non-cancerous tissues.

Many factors affect the visualization of primary HCC during unenhanced and/or contrast-enhanced MR imaging of the liver: the dimensions, composition and degree of vascularization of the lesion, and the functionality of the normal hepatic parenchyma and the residual hepatic function of the neoplastic cells themselves. Unfortunately such factors vary from patient to patient, often making the behavior of a given HCC lesion difficult to predict. Studies aimed at correlating the appearance of HCC on MR imaging with the pathologic characteristics of the lesion reflect the difficulty in drawing firm conclusions on the behavior of such lesions [5].

A large number of usually small HCC are isointense on T1- and T2-weighted imaging. When visualized, HCC typically appear mildly to moderately hyperintense at turbo spin echo (TSE) T2-weighted and/or short TI inversion-recovery (STIR) imaging. On T1-weighted images, increased SI correlates more strongly with a well-differentiated histologic grade than does iso- or hypointensity [22]. Hyperintensity on T1-weighted images is related to several factors, such as fatty metamorphosis, glycogen, clear cells and copper.

Dynamic T1-weighted imaging during the arte-

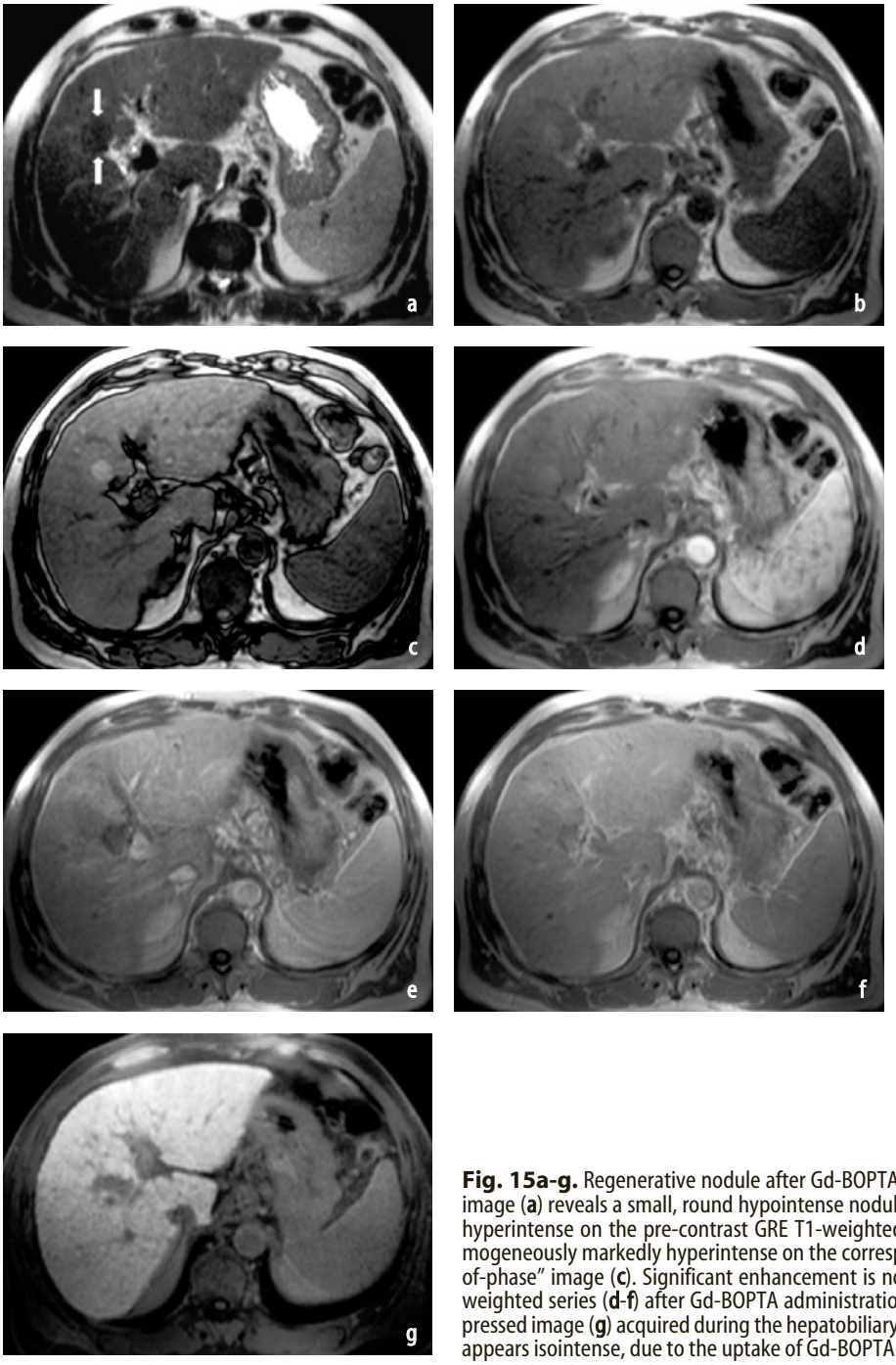

Fig. 15a-g. Regenerative nodule after Gd-BOPTA. The pre-contrast T2-weighted image (**a**) reveals a small, round hypointense nodule (*arrows*). The lesion is slightly hyperintense on the pre-contrast GRE T1-weighted "in-phase" image (**b**) and homogeneously markedly hyperintense on the corresponding GRE T1-weighted "out-of-phase" image (**c**). Significant enhancement is not seen during the dynamic T1-weighted series (**d**-**f**) after Gd-BOPTA administration. On the T1-weighted fat-suppressed image (**g**) acquired during the hepatobiliary phase, the regenerative nodule appears isointense, due to the uptake of Gd-BOPTA

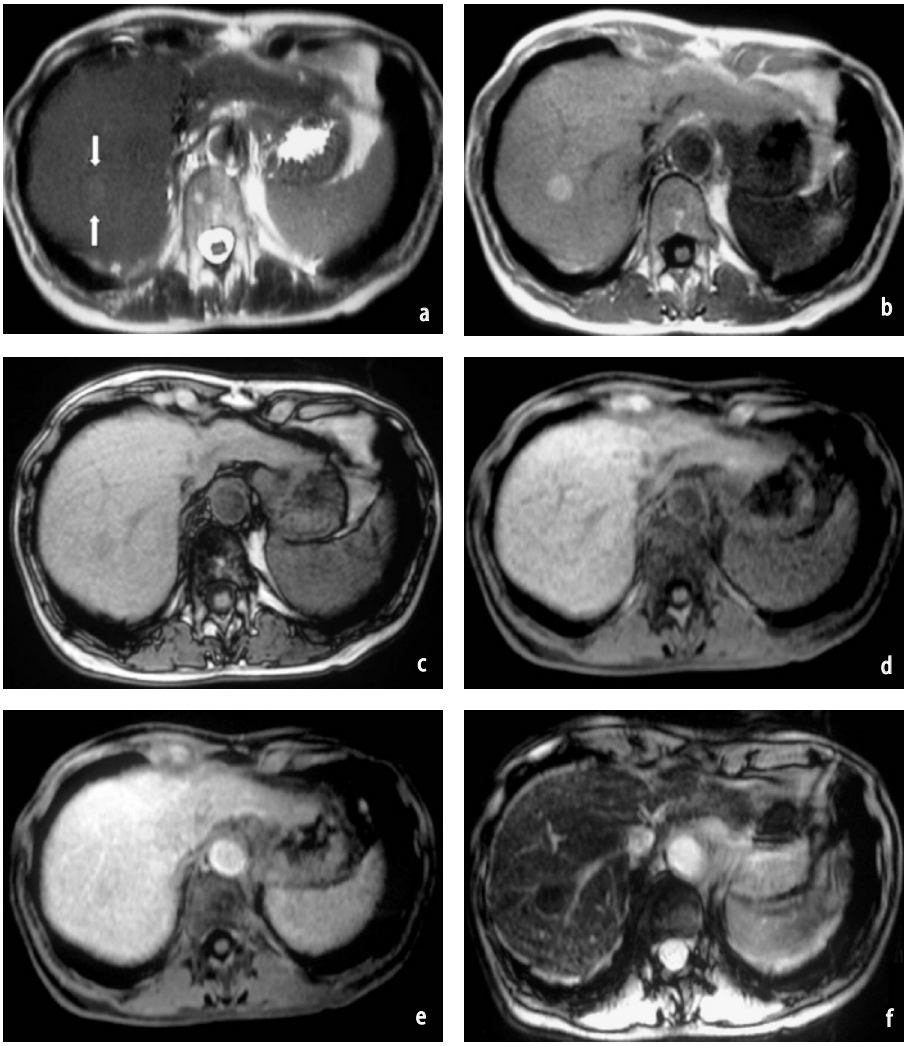

Fig. 16a-f. Regenerative nodule after SH U 555 A. On the pre-contrast HASTE T2-weighted image (**a**) a round, well-defined slightly hyperintense nodule (*arrows*) with a thin hypointense rim is visible. On the pre-contrast GRE T1-weighted "in-phase" image (**b**) the lesion appears homogeneously hyperintense, while on the corresponding GRE T1-weighted "out-of-phase" image (**c**) it appears slightly hypointense. On the pre-contrast VIBE image (**d**) the lesion appears isointense compared to the surrounding normal liver parenchyma. During the arterial phase after SH U 555 A injection (**e**) the nodule does not show enhancement, while in the reticuloendothelial phase (**f**) the lesion shows significant signal drop, which indicates a benign lesion containing Kupffer cells

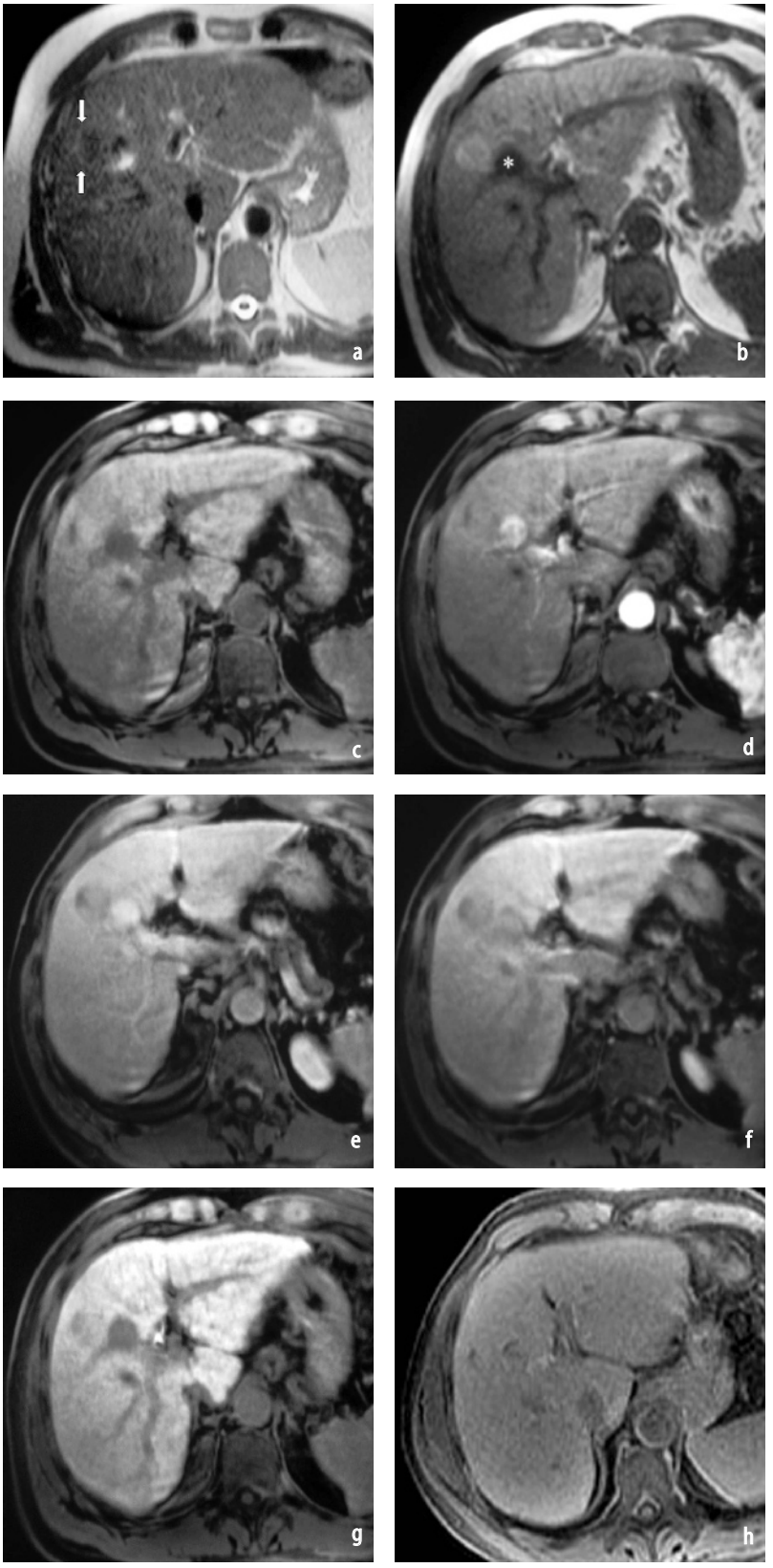

Fig. 17a-h. Dysplastic nodule after Gd-EOB-DTPA and Gd-BOPTA. The pre-contrast T2-weighted image (**a**) reveals a slightly hypointense lesion (*arrows*) located in segment VIII of the liver. On the pre-contrast GRE T1-weighted image (**b**) the nodule appears hyperintense, while on the pre-contrast VIBE image (**c**) it appears slightly hyperintense, coexisting with a round, vascular malformation near the right branch of the portal vein (*asterisk* in **b**). The solid lesion does not show evident enhancement on the arterial phase image (**d**) acquired during the dynamic study after Gd-EOB-DTPA administration. During the portal venous (**e**) and equilibrium (**f**) phases the lesion appears heterogeneously hypointense. In the hepatobiliary phase after Gd-EOB-DTPA (**g**), the nodule is slightly hypointense compared to the normal liver parenchyma. On the hepatobiliary phase image (**h**) acquired after Gd-BOPTA administration the nodule is isointense with respect to the surrounding liver parenchyma

rial phase is important for the detection of small HCC, because these may be occult at other pulse sequences and on portal venous and equilibrium phase images (Fig. 18). As HCC is a hypervascular lesion, characterized by abundant neoangiogenesis, these lesions typically demonstrate arterial enhancement at dynamic imaging. The enhancement is mainly intense and homogeneous in small non-necrotic lesions, while it may appear heterogeneous and less intense in large necrotic or hemorrhagic nodules. In about 10% of cases HCC may appear hypointense (Figs. 19, 20). Contrast agent wash-out during the portal venous phase is also typical of HCC.

The pseudocapsule of HCC usually appears hypointense on unenhanced T1- and T2-weighted images. On enhanced MR imaging with Gd-based contrast agents, enhancement of the pseudocapsule is seen principally on portal venous phase images although initial enhancement may be seen in the late arterial phase. As is typical of fibrous tissues, the enhancement usually persists into the equilibrium phase. Contrast agent wash-out from the lesion parenchyma means that the capsule is usually more prominent in the equilibrium phase [9].

Whereas dynamic phase imaging of HCC with Gd-BOPTA and Gd-EOB-DTPA gives similar results to that seen with conventional Gd agents, delayed phase imaging reveals a number of different enhancement patterns, with both iso-, hypo- and hyperintense patterns possible (Figs. 19, 20, and see Chap. 6, Fig. 16). Generally, moderately-differentiated lesions tend to enhance to a greater extent on delayed images than well-or poorly-differentiated lesions [5]. In a recent retrospective analysis of 94 HCC evaluated with Gd-BOPTA, 89.4% were hypointense in the delayed phase, compared with only 3.2% and 7.4% that were hyper- and isointense, respectively [5] (Figs. 21, 22). Elsewhere it has been shown that well- and moderately-differentiated HCC demonstrate superior signal enhancement ratios to poorly-differentiated HCC on images acquired at 0.5 Tesla at 60-120 min after Gd-BOPTA administration [18]. This finding reflects the retention of sufficient hepatocytic activity in these lesions to allow take-up of Gd-BOPTA. In this regard, a significant correlation has been observed between the presence of intra-lesional bile and the degree of lesion enhancement after Gd-BOPTA administration [5, 18].

HCC typically show heterogeneous enhancement with the hepatobiliary agent mangafodipir trisodium [21]. Well-differentiated HCC enhance to a greater extent than poorly-differentiated HCC. A rim-like enhancement on mangafodipir trisodium–enhanced MR images may be indicative of peritumoral infiltration of malignant cells into neighboring normal liver parenchyma resulting in intermingling of malignant cells with normal functioning hepatocytes in the peripheral region. However, such a finding has also been reported for CCC and metastases and may be due to compression of the surrounding normal liver tissue.

Post-mangafodipir trisodium MR imaging has been shown to result in a more accurate differentiation between benign (FNH) and malignant (HCC) hepatocellular tumors than unenhanced MR imaging alone, although overlapping enhancement behavior is more common with this agent than with Gd-based hepatobiliary agents [3]. On delayed images after mangafodipir trisodium infusion, most moderate and well-differentiated lesions are hypointense (Fig. 23).

HCC lesions generally do not show a significant decrease in SI after administration of SPIO contrast agents, although SI loss has been seen in some individual HCC [12].

The conspicuity of HCC after SPIO depends on differences in the number of Kupffer cells between the lesion and the surrounding liver. Typically, moderately- or poorly-differentiated HCC show large differences in the number of Kupffer cells compared to the surrounding liver and thus demonstrate a high contrast-to-noise ratio at SPIO-enhanced MR imaging, particularly in cirrhotic livers (see Chap. 6, Figs. 21a, 21f). Dysplastic nodules and most well-differentiated HCC, on the other hand, contain nearly the same number of Kupffer cells as the surrounding cirrhotic hepatic parenchyma and therefore are not well-depicted on T2-weighted MR images [12]. Focal HCC degeneration within dysplastic nodules can be detected with SPIO agents as areas of hyperintensity which do not show significant signal drop in comparison with the surrounding dysplastic non-neoplastic portion. This results in a typical "nodule in nodule" appearance (Fig. 24).

As regards the detection of HCC, there are conflicting reports as to whether dynamic Gd-enhanced MR imaging or SPIO-enhanced imaging is preferable. Tang et al. [30] found significantly more lesions on Gd-enhanced MR images than on SPIO-enhanced MR images in 53 patients (97 of 103 versus 80 of 103, $P < 0.01$) (see Chapter 6, Fig.15) whereas Vogl et al. [32] detected more HCC lesions with SPIO-enhanced MR imaging than with dynamic Gd-enhanced MR imaging. Pauleit et al. [23] found that unenhanced and Gd-enhanced MR imaging was significantly more sensitive and accurate than SPIO-enhanced imaging for the detection of small HCC but that SPIO-enhanced imaging was superior for the detection of large HCC, albeit non-significantly. Analysis of all HCC revealed no significant differences for Gd- and SPIO-enhanced imaging.

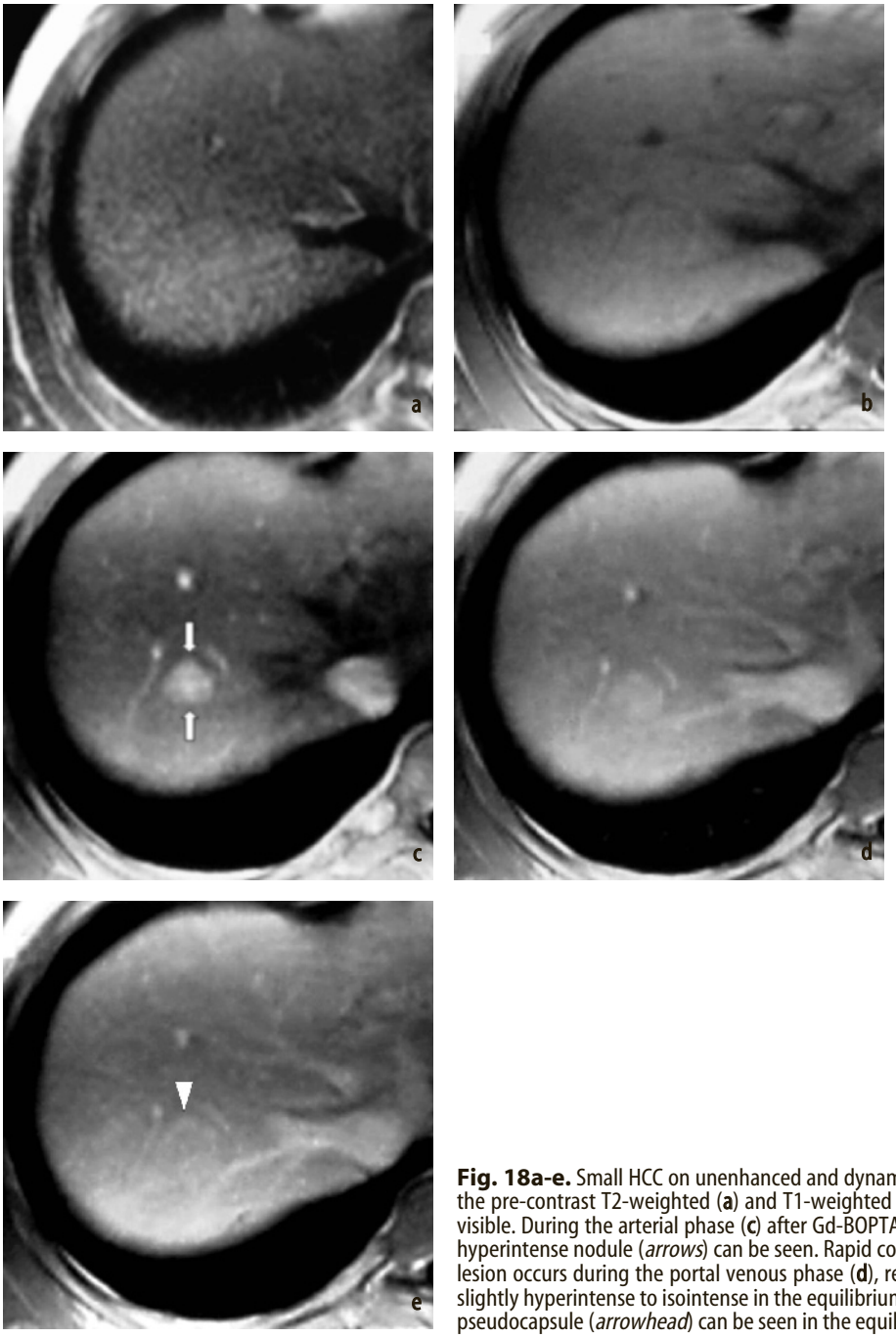

Fig. 18a-e. Small HCC on unenhanced and dynamic imaging after Gd-BOPTA. On the pre-contrast T2-weighted (**a**) and T1-weighted (**b**) images, no focal lesions are visible. During the arterial phase (**c**) after Gd-BOPTA administration, a well-defined hyperintense nodule (*arrows*) can be seen. Rapid contrast agent wash-out from the lesion occurs during the portal venous phase (**d**), resulting in the lesion appearing slightly hyperintense to isointense in the equilibrium phase (**e**). A thin hyperintense pseudocapsule (*arrowhead*) can be seen in the equilibrium phase

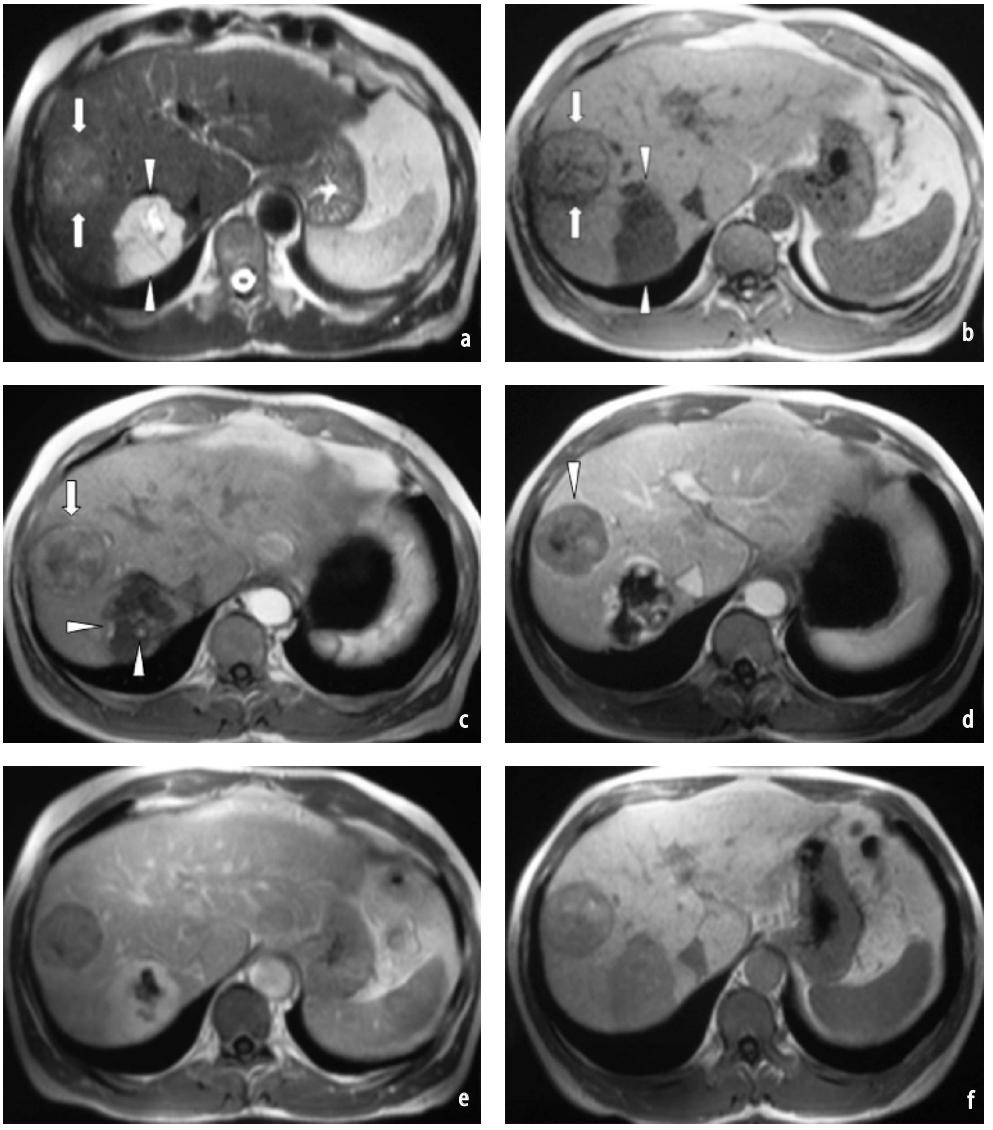

Fig. 19a-f. Hypovascular HCC and cavernous hemangioma after Gd-BOPTA. On the pre-contrast T2-weighted image (**a**) a round heterogeneous, slightly hyperintense nodule (*arrows*) and a heterogeneously hyperintense lesion (*arrowheads*) can be seen. The corresponding pre-contrast GRE T1-weighted image (**b**) reveals a well-defined heterogeneous, slightly hypointense nodule (*arrows*), and a homogeneously hypointense lesion (*arrowheads*) (**b**). On the arterial phase image (**c**) of the dynamic series after Gd-BOPTA injection, the round nodule (*arrow*) shows weak and irregular enhancement, while an initial nodular peripheral enhancement (*arrowheads*) can be observed in the other lesion. This latter behavior is suggestive of hemangioma. On the portal venous (**d**) and equilibrium (**e**) phase images the cavernous hemangioma shows progressive centripetal enhancement, while the round nodule appears consistently hypointense with a thin hyperintense pseudocapsule (*arrowhead* in **d**). This enhancement pattern is suggestive for HCC. Both lesions are heterogeneously hypointense on the delayed hepatobiliary phase image (**f**)

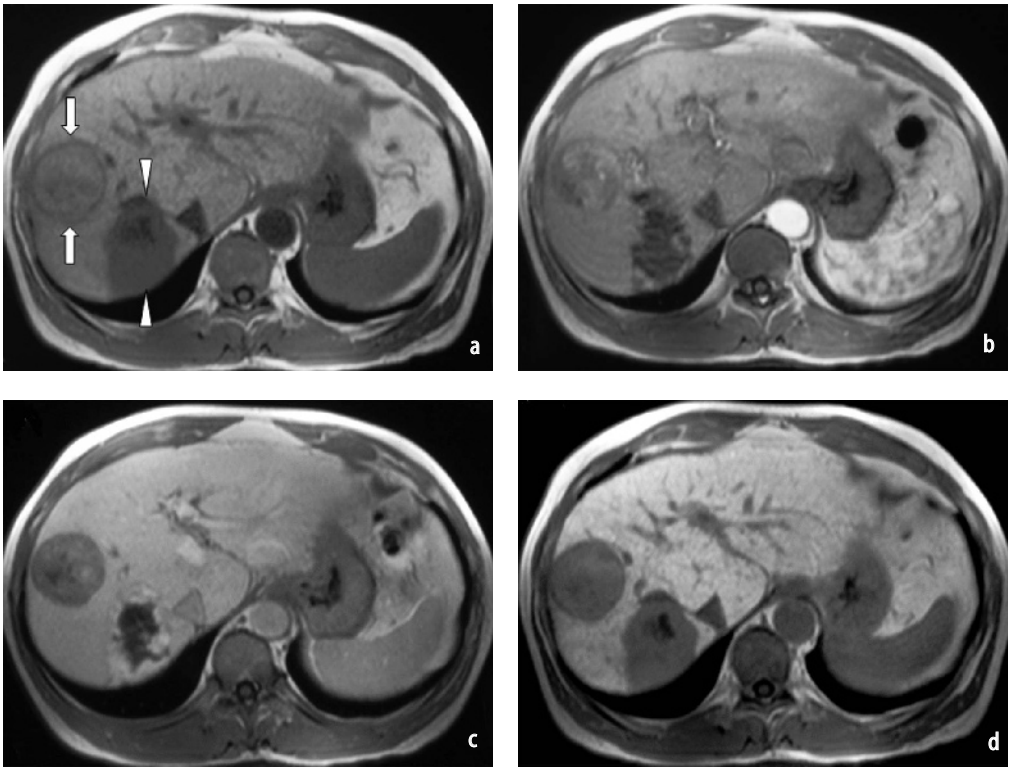

Fig. 20a-d. Hypovascular HCC and cavernous hemangioma after Gd-EOB-DTPA. Same case as shown in Fig. 19. The pre-contrast GRE T1-weighted image (**a**) reveals a well-defined heterogeneous, slightly hypointense nodule (*arrows*) and a homogeneously hypointense lesion (*arrowheads*). During the dynamic study after Gd-EOB-DTPA administration (**b**, **c**), the enhancement behavior is similar to that observed after Gd-BOPTA administration. Likewise, both lesions appear hypointense compared to the normal liver during the hepatobiliary phase (**d**) after Gd-EOB-DTPA administration

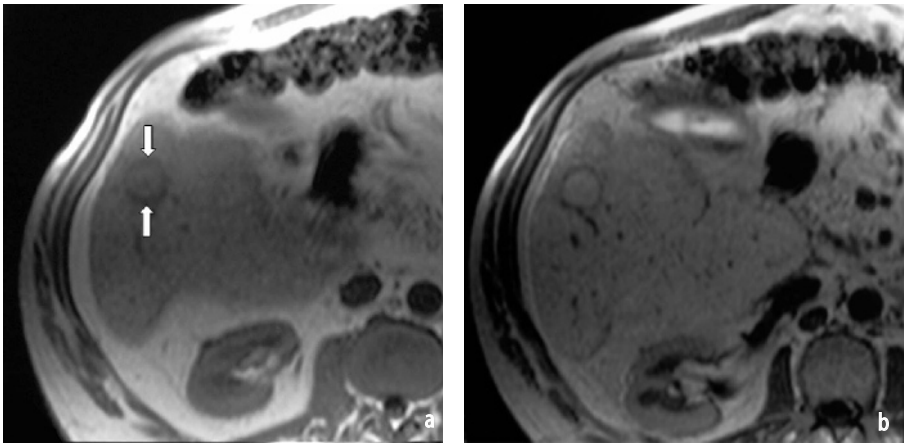

Fig. 21a, b. Well-differentiated HCC after Gd-BOPTA. The pre-contrast GRE T1-weighted image (**a**) reveals an isointense nodule (*arrows*) with a thin peripheral hypointense rim. In the hepatobiliary phase after Gd-BOPTA administration (**b**), the nodule is slightly hyperintense compared to the normal liver parenchyma. The malignant cells in the well-differentiated HCC retain the ability to take up Gd-BOPTA

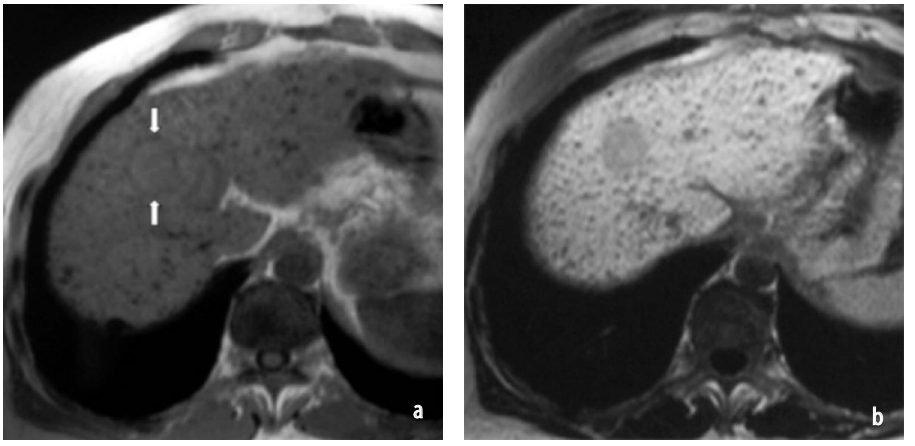

Fig. 22a, b. Poorly-differentiated HCC in liver cirrhosis after Gd-BOPTA. The pre-contrast GRE T1-weighted image (**a**) reveals a homogeneously isointense nodule (*arrows*) with a thin peripheral hypointense rim. Note the micronodular transformation of the liver by advanced cirrhosis. In the hepatobiliary phase after Gd-BOPTA administration (**b**), the nodule appears homogeneously hypointense compared to the normal liver parenchyma. In poorly-differentiated HCC the malignant cells are not able to take up Gd-BOPTA

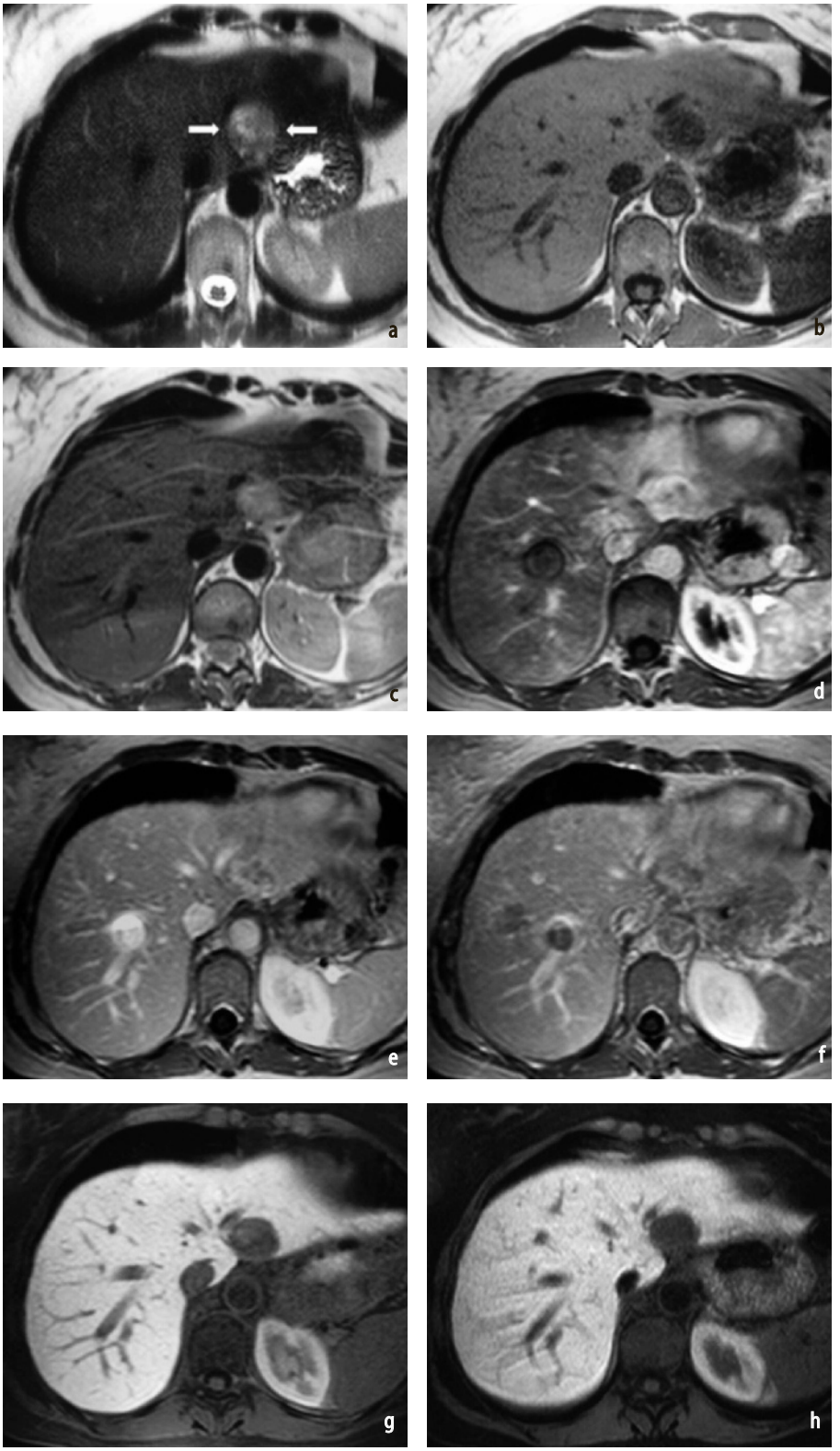

Fig. 23a-h. Moderately-differentiated HCC after Gd-BOPTA and Mn-DPDP. The pre-contrast HASTE T2-weighted image (**a**) reveals a round, heterogeneously hyperintense nodule (*arrows*). On the pre-contrast GRE T1-weighted "in-phase" (**b**) and "out-of-phase" (**c**) images the lesion appears hyper- and hypointense, respectively, compared to the normal liver parenchyma. On the arterial phase image (**d**) of the dynamic series after Gd-BOPTA injection, the nodule demonstrates marked and heterogeneous enhancement. Rapid wash-out of contrast agent is noted in the subsequent portal venous (**e**) and equilibrium (**f**) phases. In the hepatobiliary phase after Gd-BOPTA (**g**) and Mn-DPDP (**h**) administration the lesion is hypointense due to the lack of contrast agent uptake by the malignant hepatocytes

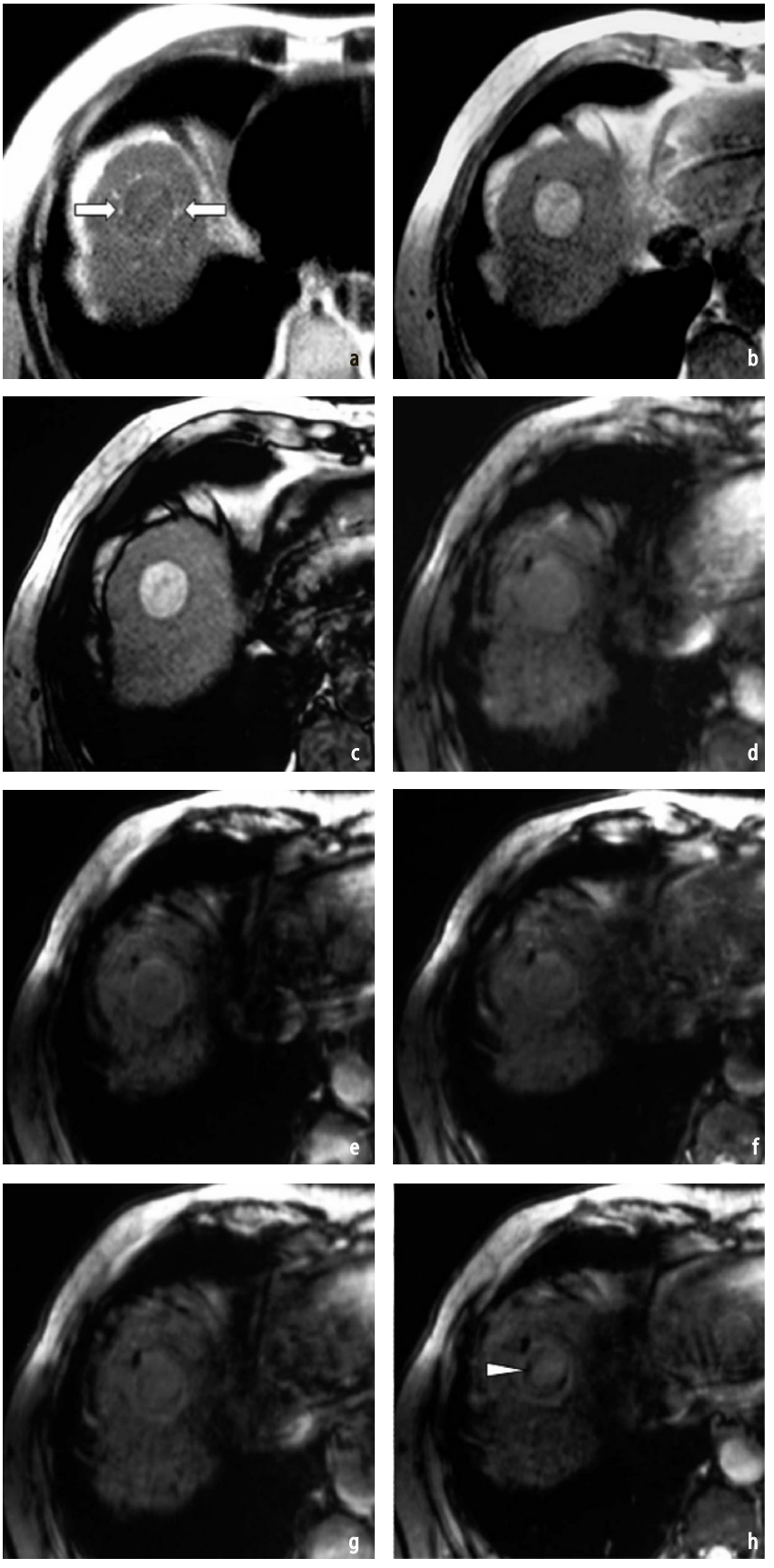
a
b
c
d
e
f
g
h

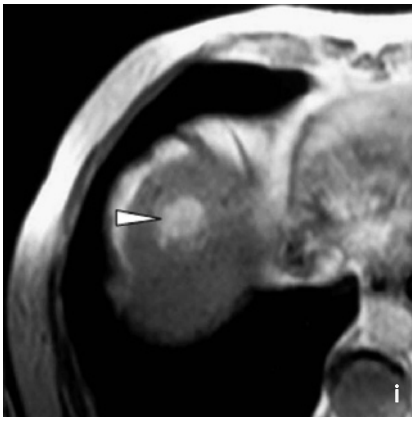

Fig. 24a-i. Dysplastic nodule and focal HCC degeneration after SH U 555 A. The pre-contrast HASTE T2-weighted image (**a**) reveals a round, well-defined slightly hypointense nodule (*arrows*). On the pre-contrast GRE T1-weighted "in-phase" (**b**), "out-of-phase" (**c**), and VIBE (**d**) images, the lesion appears hyperintense, most likely due to glycogen content. Only minimal enhancement is seen on images acquired during the dynamic series after SH U 555 A administration (**e**-**g**) although a thin and complete hyperintense peripheral rim is clearly visible. The VIBE image (**h**) acquired during the delayed phase reveals an intra-lesional round, slightly hyperintense nodule (*arrowhead*). A corresponding delayed GRE T1-weighted image (**i**) reveals a marked hyperintensity of the intranodular lesion (*arrowhead*), giving it the "nodule within a nodule" aspect suggestive of focal HCC in a dysplastic nodule

8.4 Benign Focal Liver Lesions of non-Hepatocellular Origin

8.4.1 Cavernous and Capillary Hemangioma

Hemangiomas represent tortuous caverns of blood-filled spaces that are usually well-circumscribed, ranging in size from a few millimeters to more than 20 cm. Microscopically, they are composed of multiple vascular channels lined by a single layer of endothelial cells supported by a thin, fibrous stroma.

Small (typically < 2 cm) hemangiomas that show complete and immediate filling with contrast material during the initial arterial phase have been referred to as capillary hemangiomas, but this distinction is without any clinical indication. Such small 'flash-filling' hemangiomas can simulate a vascular neoplasm if only the arterial phase characteristics are considered. However, the enhancement usually persists into the portal venous and delayed phases in capillary hemangiomas while contrast material wash-out usually occurs from small vascular tumors, rendering these lesions iso- or hypoattenuating/intense on later phases compared to the normal liver.

On cut sections, larger hemangiomas are almost always heterogeneous with areas of fibrosis, necrosis and cystic change; sometimes abundant fibrous tissue completely replaces the lesion.

Marked hyperintensity on T2-weighted images has historically been relied upon to establish the diagnosis of hemangioma particularly when using a long echo time (TE) (~ 120 ms). This is generally a useful technique, although high SI on heavily T2-weighted sequences with long TE may occasionally be seen in cystic tumors and uncommonly in hypervascular metastases from sarcoma, islet cell tumor, pheochromocytoma, carcinoid and renal cell carcinoma. On pre-contrast T1-weighted images hemangiomas are most commonly seen as well-defined and slightly hypointense with lobulated borders. In the majority of cases the combination of T2-weighted and serial dynamic T1-weighted Gd images allows a confident diagnosis of hemangioma [19, 27].

The dynamic imaging characteristics of hemangiomas after administration of Gd-BOPTA and Gd-EOB-DTPA are the same as with conventional Gd agents. Specifically, peripheral nodular enhancement which progresses centripetally to uniform enhancement is typical for cavernous haemangiomas, whereas rapid and complete enhancement during the arterial phase is typical for smaller capillary haemangiomas. Hemangiomas usually appear hypointense compared to the surrounding liver parenchyma on delayed phase images after these agents, as well as on delayed images after mangafodipir trisodium infusion (Fig. 25).

Because hemangiomas generally do not contain Kupffer cells, reticuloendothelial uptake of SPIO particles does not occur. However, uptake of USPIO particles does occur because of their blood-pool effect, resulting in a loss of SI on USPIO-enhanced T2-weighted images. Dynamic

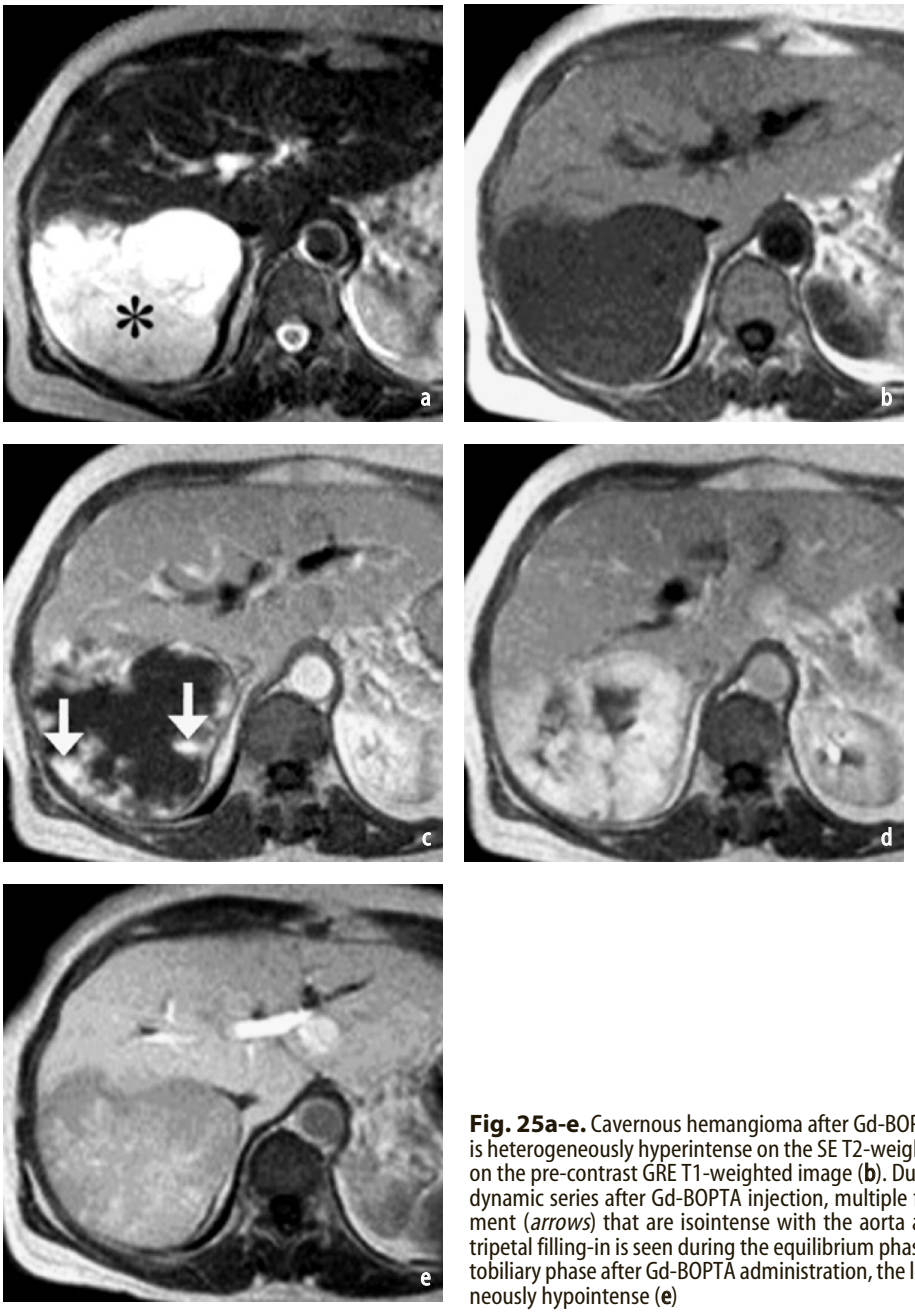

Fig. 25a-e. Cavernous hemangioma after Gd-BOPTA. The hemangioma (*asterisk*) is heterogeneously hyperintense on the SE T2-weighted image (**a**) and hypointense on the pre-contrast GRE T1-weighted image (**b**). During the arterial phase (**c**) of the dynamic series after Gd-BOPTA injection, multiple focal areas of nodular enhancement (*arrows*) that are isointense with the aorta are seen in the periphery. Centripetal filling-in is seen during the equilibrium phase (**d**). During the delayed hepatobiliary phase after Gd-BOPTA administration, the lesion appears slightly heterogeneously hypointense (**e**)

phase T1-weighted imaging after administration of SH U 555 A reveals the hyperintense globular enhancement and centripetal filling-in that is typical of dynamic phase imaging after administration of Gd contrast agents. Hemangiomas frequently appear hyperintense on delayed images acquired 10 min after SPIO administration [26] (see Chap. 4, Fig.12).

8.5 Malignant Focal Liver Lesions of non-Hepatocellular Origin

8.5.1 Hypervascular Metastases

Hypervascular metastases derive from highly vascular tumors such as carcinoid, islet cell tumor, renal carcinoma, thyroid carcinoma, pheochromocytoma, melanoma, and breast carcinoma. On unenhanced T1-weighted images these lesions are usually hypointense, while on T2-weighted images they are slightly hyperintense and/or heterogeneous in SI compared to the background liver tissue. Some hypervascular metastases may have higher SI on T2-weighted images and thus mimic hemangiomas (Fig. 26) [16].

Whereas hypovascular lesions are best imaged during the portal venous phase, maximum enhancement of vascular metastases usually occurs during the arterial phase after Gd injection. In the portal-venous phase these lesions usually show some rapid peripheral wash-out which, on subsequent images, results in a hypointense halo appearance. Hence, lesion characterization is best performed during the equilibrium phase, when the pattern of enhancement and degree of contrast agent wash-out can be determined [16]. Larger hypervascular metastases receive arterial blood more in the periphery of the lesion than in the less perfused center, and may therefore demonstrate a peripheral rim of enhancement.

The dynamic enhancement patterns on Gd-BOPTA and Gd-EOB-DTPA–enhanced dynamic MR imaging is the same as that seen with conventional Gd-based contrast agents. However, whereas the SI between liver and lesions thereafter equilibrates with conventional Gd-based agents, on delayed hepatobiliary phase images after Gd-BOPTA and Gd-EOB-DTPA, all metastases demonstrate marked hypointensity compared to the surrounding enhanced normal liver parenchyma (Fig. 27) [2]. Although some retention of contrast agent may occasionally be observed in the necrotic center of the lesion on delayed images, repetition of the delayed sequence at 2 to 3 h post-injection when complete washout from the interstitial space has occurred is usually sufficient to confirm that this central enhancement is not due to hepatocytic accumulation (Figs. 28, 29).

Hypervasuclar metastatic lesions typically appear hypointense compared to the surrounding liver parenchyma also after infusion of mangafodipir trisodium. However, uptake of Mn^{++} and a resulting hyperintense appearance has been observed after mangafodipir trisodium infusion in hepatic metastases from non-functioning endocrine tumors of the pancreas [25].

On SPIO-enhanced T2- or T2*-weighted images, hypervascular metastases appear hyperintense compared to the low SI of the surrounding normal liver parenchyma due to the lack of any significant uptake of SPIO particles [10, 28] (Fig. 30).

8.5.2 Hypovascular Metastases

Hypovascular metastases are the most frequent malignancies in the liver. In the United States, colon cancer is the most common primary site and approximately 50,000 cases of hepatic colorectal metastases are encountered annually.

Lesion detection is size-related, with lesions smaller than 1 cm being difficult to identify with conventional techniques. Unfortunately, a post-mortem assessment of the size of liver metastases has shown that the ratio between metastases larger than 1 cm and those smaller than 1 cm is approximately 1:1.6 for metastases of colorectal adenocarcinoma and 1:4 for other liver metastases [4]. Therefore an ability to accurately detect and characterize metastases under 1 cm in size is clearly warranted in order to accurately detect and stage the tumor extent within the liver.

Hypovascular metastatic lesions tend to be round in shape although metastases larger than 3 cm from colorectal adenocarcinoma commonly have a cauliflower aspect. The SI of these metastases is lower than that of surrounding hepatic tissue on unenhanced T1-weighted images and typically moderately higher on T2-weighted images. A hypointense peripheral rim around tumor nodules may be seen on T2-weighted images in about 25% of colorectal hepatic metastases. The histopathologic changes associated with this rim include compression of hepatic parenchyma, hepatocellular atrophy, fibrosis, inflammation, and congested sinusoids.

It remains a matter for debate whether the detection of hypovascular metastases is improved on contrast-enhanced images using conventional Gd agents compared to unenhanced images. On the other hand, even hypovascular tumors may show some enhancement that occasionally helps to detect or characterize the lesion. On hepatic arterial

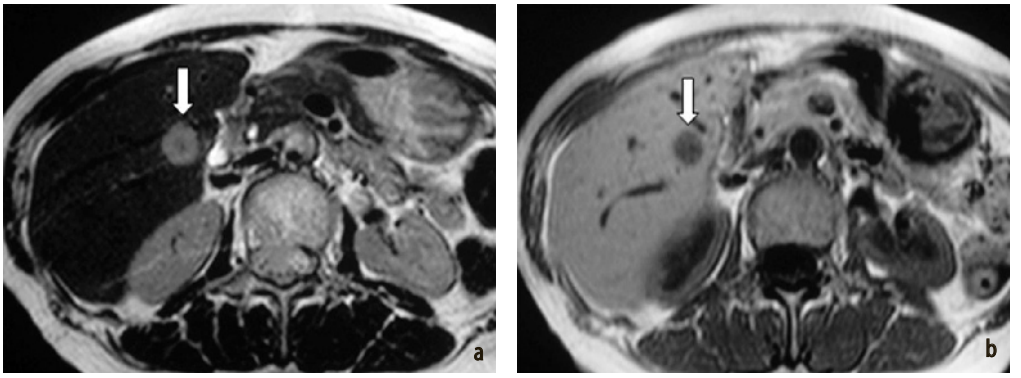

Fig. 26a, b. Metastases from cholangiocellular carcinoma on unenhanced imaging. The pre-contrast T2-weighted image (**a**) reveals a round, well-defined, hyperintense lesion (*arrow*) in segment VI of the liver. On the corresponding pre-contrast GRE T1-weighted image (**b**) the lesion (*arrow*) is homogeneously hypointense

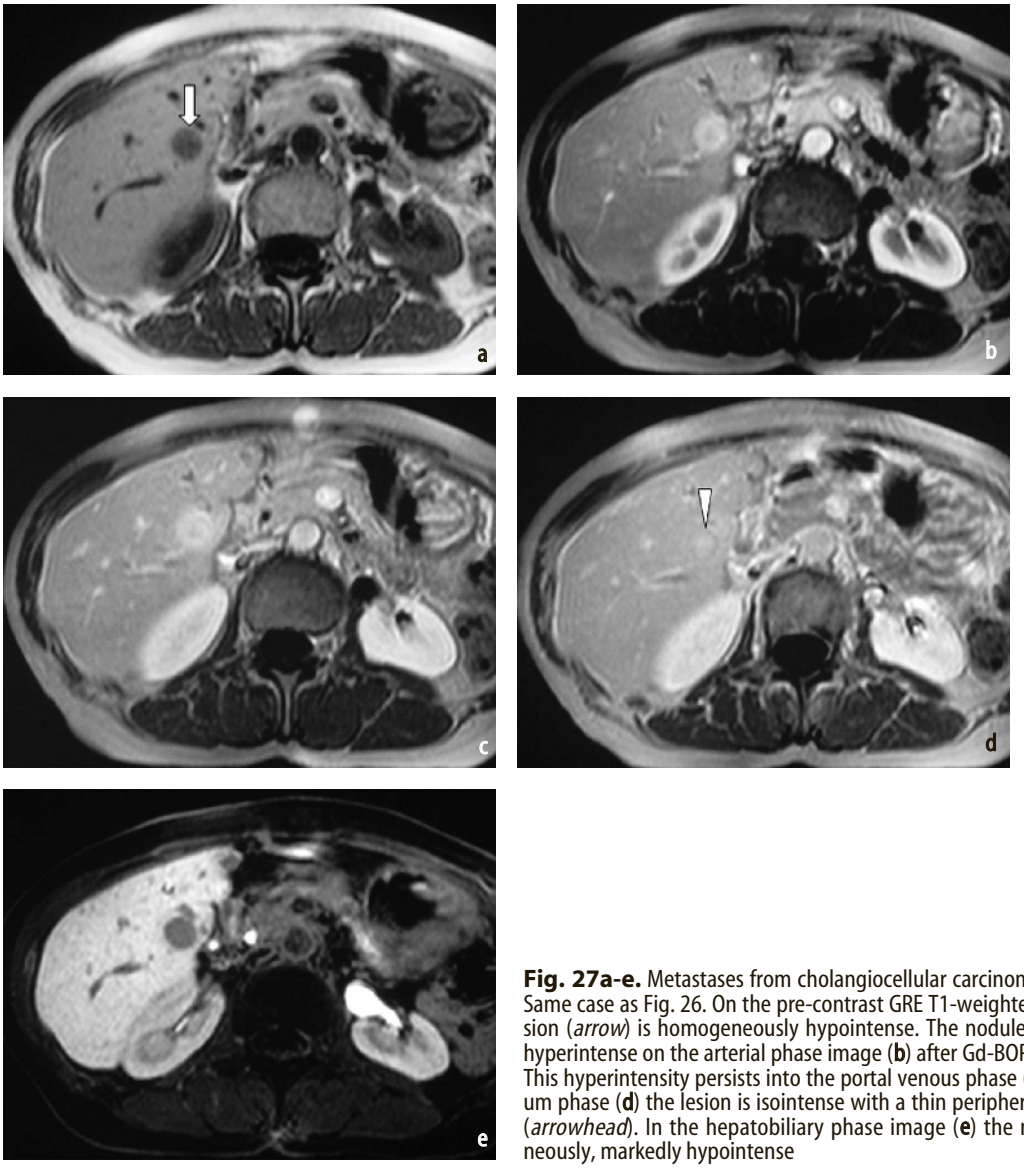

Fig. 27a-e. Metastases from cholangiocellular carcinoma after Gd-BOPTA. Same case as Fig. 26. On the pre-contrast GRE T1-weighted image (**a**) the lesion (*arrow*) is homogeneously hypointense. The nodule appears markedly hyperintense on the arterial phase image (**b**) after Gd-BOPTA administration. This hyperintensity persists into the portal venous phase (**c**). In the equilibrium phase (**d**) the lesion is isointense with a thin peripheral hypointense rim (*arrowhead*). In the hepatobiliary phase image (**e**) the nodule is homogeneously, markedly hypointense

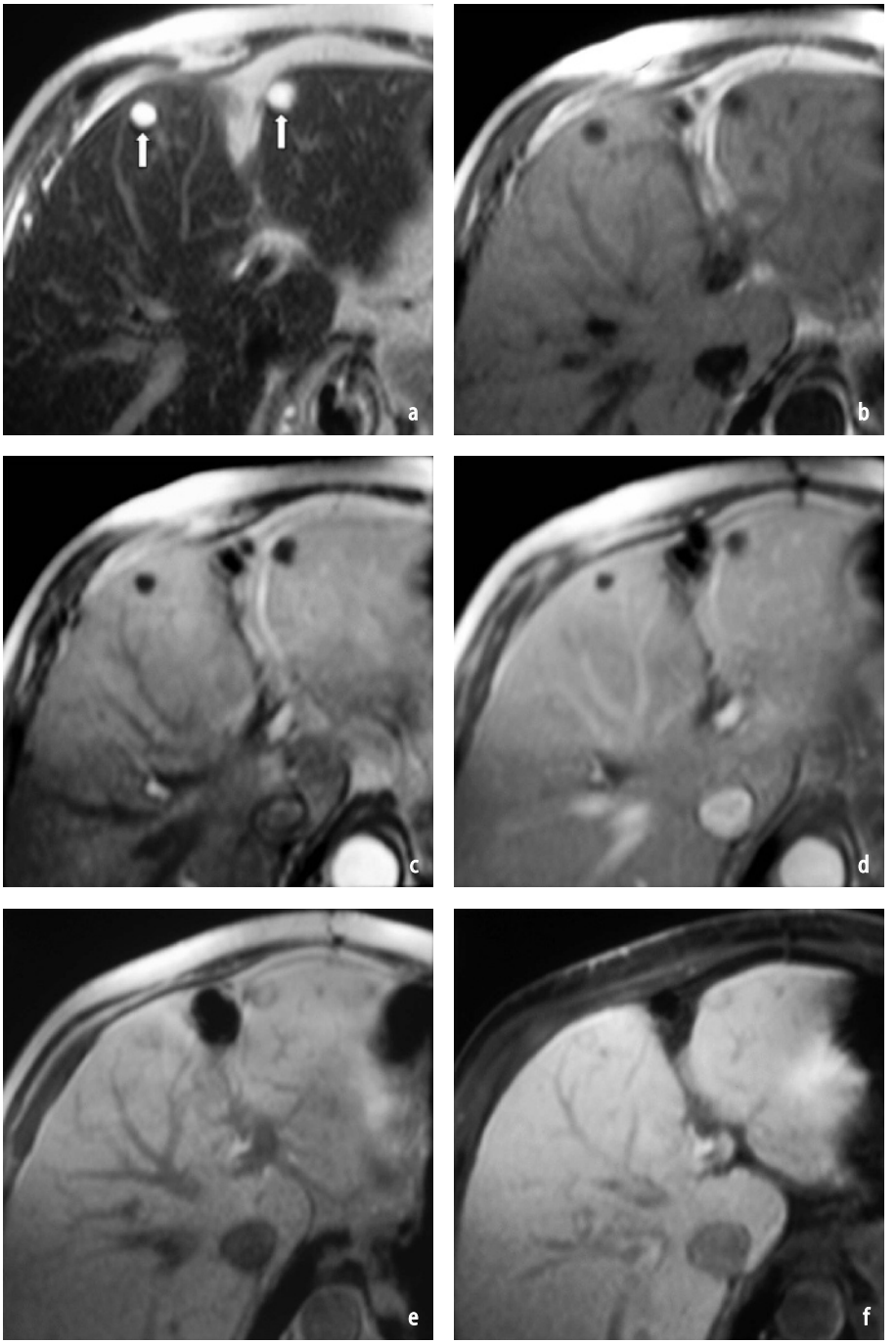

Fig. 28a-f. Metastases from gastrointestinal stromal tumor (GIST) after Gd-EOB-DTPA. On the pre-contrast T2-weighted image (**a**), two round, well-defined, markedly hyperintense lesions (*arrows*) can be seen in segments IV and II of the liver. On the pre-contrast GRE T1-weighted image (**b**) the nodules appear homogeneously hypointense. No enhancement is seen on arterial (**c**) and portal venous (**d**) phase images acquired during the dynamic series after Gd-EOB-DTPA administration, indicating large necrotic components within the lesions. In the hepatobiliary phase (**e**-**f**) 20 min after injection of contrast agent, the nodules appear isointense with a thin hypointense peripheral rim. This is due to non-specific intra-lesional pooling of the contrast agent in the necrotic components

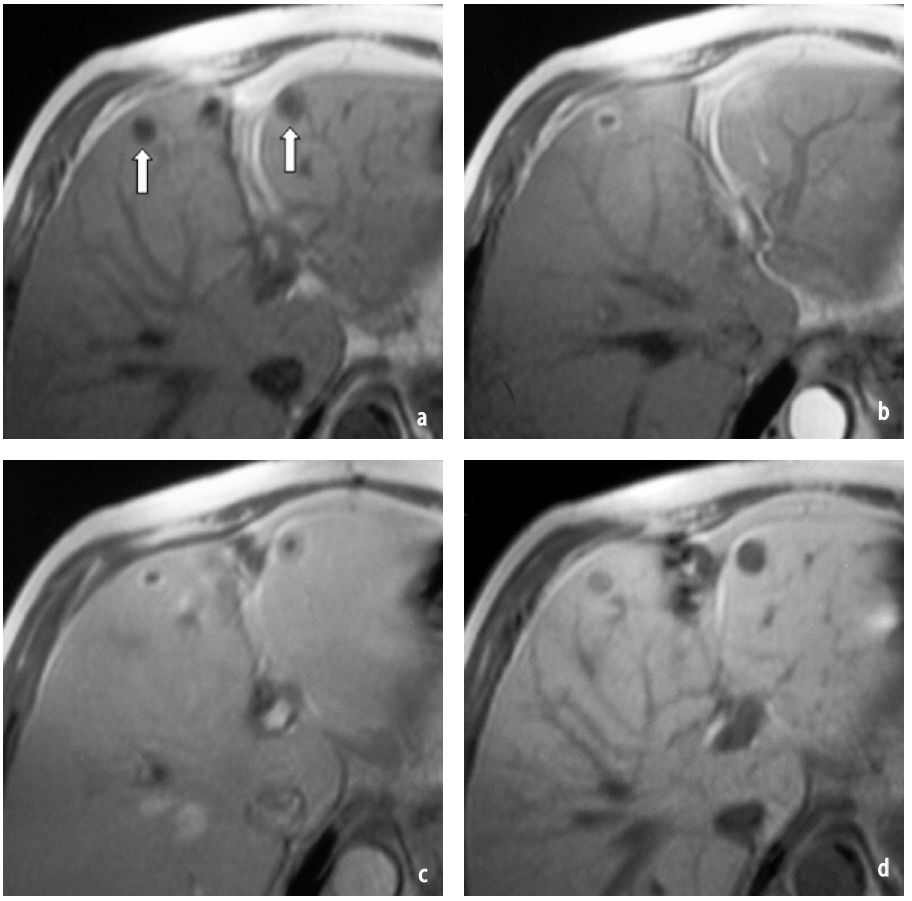

Fig. 29a-d. Metastases from gastrointestinal stromal tumor (GIST) after Gd-BOPTA. Same case as Fig. 28. On the pre-contrast GRE T1-weighted image (**a**) the nodules (*arrows*) appear homogeneously hypointense. In the arterial phase (**b**) of the dynamic series after Gd-BOPTA administration the nodules appear hypointense and are surrounded by a hyperintense peripheral rim. Partial wash-out is apparent on the portal venous phase image (**c**). In the hepatobiliary phase (**d**) 1 h after contrast agent administration, the lesion located in segment IV of the liver appears slightly hypointense, due to non-specific intra-lesional pooling of the contrast agent in the necrotic components of the lesion. The lesion in segment II appears homogeneously hypointense

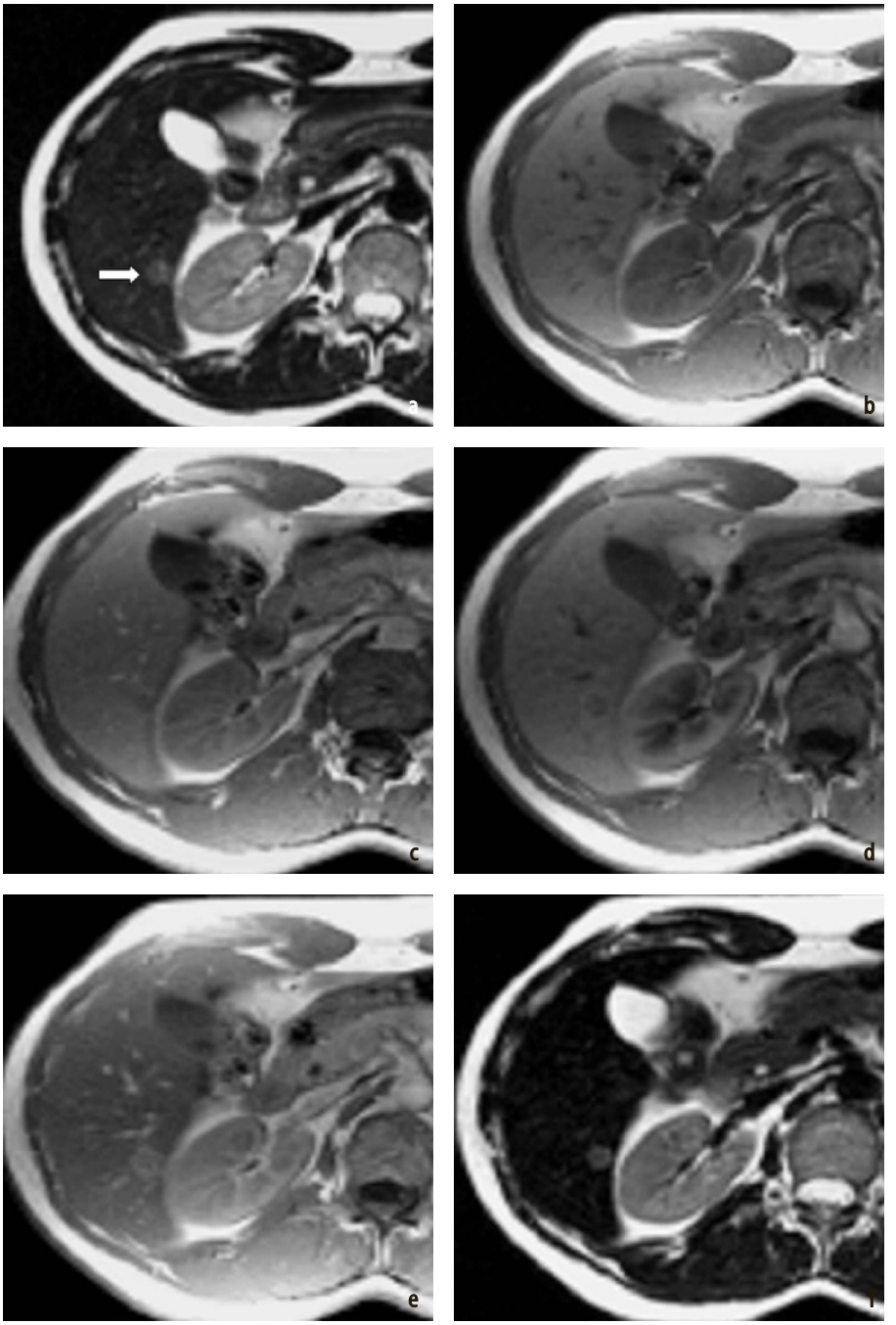

Fig. 30a-f. Metastases from malignant melanoma after SH U 555 A. The pre-contrast TSE T2-weighted image (**a**) reveals a small, round hyperintense nodule (*arrow*) in segment VI of the liver. On the corresponding pre-contrast GRE T1-weighted image (**b**), the lesion is hypointense. During the dynamic study after injection of SH U 555 A (**c**-**e**), the nodule shows weak and progressive enhancement, mainly in the equilibrium phase (**e**), and a thin peripheral hyperintense rim is easily visible. In the reticuloendothelial phase (**f**) the lesion appears hyperintense, due to the lack of uptake of SH U 555 A since there are no functioning Kupffer cells in the lesion

phase images metastases can show a fleeting ring enhancement that blurs the margins of the lesion. This corresponds to desmoplastic reaction, inflammatory infiltration and vascular proliferation in the tumor-liver parenchymal margin. The enhancement progresses centrally with concomitant peripheral wash-out. In the equilibrium phase around 10 min after administration of contrast agent, some lesions may show a peripheral hypointense rim ("peripheral wash-out" sign).

Dynamic phase imaging after Gd-BOPTA administration reveals identical enhancement patterns to those seen with conventional extracellular Gd-based contrast agents. Since the lesions are unable to take up Gd-BOPTA they appear as homogeneously hypointense on delayed T1-weighted images [2]. For metastases showing desmoplastic reaction, an accumulation of Gd-BOPTA in the fibrotic part may be observed, which can remain for several hours. In these cases, the observation of a peripheral hypointense halo is highly suggestive of the malignant nature of the lesion (Fig. 31).

The enhancement pattern after mangafodipir trisodium is similar to that after Gd-BOPTA; an increase of the liver-to-lesion contrast-to-noise ratio occurs because of the lack of Mn^{++} uptake (Fig. 32).

Since metastases do not contain Kupffer cells, the contrast-to-noise ratio and hence lesion detection and conspicuity is improved after SPIO injection when compared to unenhanced T2-weighted images (Fig. 33) [28].

Due to the non-specific behavior of malignant liver lesions after SPIO injection, some authors have proposed a dual contrast study in order to improve lesion characterization. With this approach, pre- and post-SPIO images are obtained, followed, after bolus injection of a conventional Gd agent, by multiphasic dynamic T1-weighted GRE images. Contrast agents such as Gd-BOPTA and Gd-EOB-DTPA, which inherently have both dynamic extracellular characteristics and delayed hepatospecific characteristics, have clear advantages over such an approach.

8.5.3 Cholangiocellular Carcinoma (CCC)

Cholangiocellular carcinoma (CCC) is usually classed as "intrahepatic" or "extrahepatic" depending on the site of origin. Intrahepatic cholangiocarcinoma (ICC) is a malignant neoplasm arising from the epithelium of the intrahepatic bile ducts and represents approximately 10% of all CCC. Hilar (Klatskin's) and bile duct cholangiocarcinomas account for the remaining 90% of the lesions. The neoplasm is usually a large, firm mass and in 10-20% of cases there are several satellite nodules around the main lesion. Pathologically, the stroma can contain extremes of dense fibrous material or mucinous glandular material or a combination of both. The pattern that predominates has a substantial impact on the imaging appearance. Variable amounts of central necrosis may be present within the tumor, especially in large lesions, although hemorrhage is rare.

On pre-contrast T1-weighted images CCC is generally iso- to hypointense relative to the normal liver. Conversely, on T2-weighted images the SI of the tumor ranges from markedly hyperintense to mildly hyperintense. Tumors with a high fibrous content tend to have lower SI on T2-weighted images, while those with high mucin content tend to have very high SI [34].

On serial dynamic T1-weighted images enhanced with conventional Gd agents, CCC usually show minimal or moderate incomplete rim enhancement at the tumor periphery on arterial phase images with progressive central contrast enhancement on portal venous and early equilibrium phase images [34]. Rarely, small homogeneously enhancing tumor nodules that simulate HCC can be seen on arterial phase imaging. Contrast enhancement is frequently better seen on portal venous and delayed equilibrium phase images in CCC with dense fibrous stroma [15].

Imaging with Gd-BOPTA is similar to imaging with conventional non-specific Gd-based contrast agents during the dynamic phase of contrast enhancement. However, delayed imaging with Gd-BOPTA during the hepatobiliary phase reveals contrast enhancement in the fibrotic areas of the lesion. The degree of enhancement depends on the type of CCC: greater peripheral enhancement is noted in large CCC, whereas stronger enhancement in the fibrous core is noted in the case of "scirrhous" CCC [35].

Significant uptake of Mn^{++} mangafodipir trisodium infusion is not observed on delayed T1-weighted images and hence the lesions generally appear hypointense. However, some peripheral rim enhancement may be observed. The hepatobiliary phase after administration of liver-specific contrast agents may add useful information for the identification of small satellite lesions.

Analogously, no significant uptake is observed after SPIO administration due to the absence of Kupffer cells within CCC. Consequently, there is increased liver-to-lesion contrast-to-noise ratio on delayed T2-weighted images.

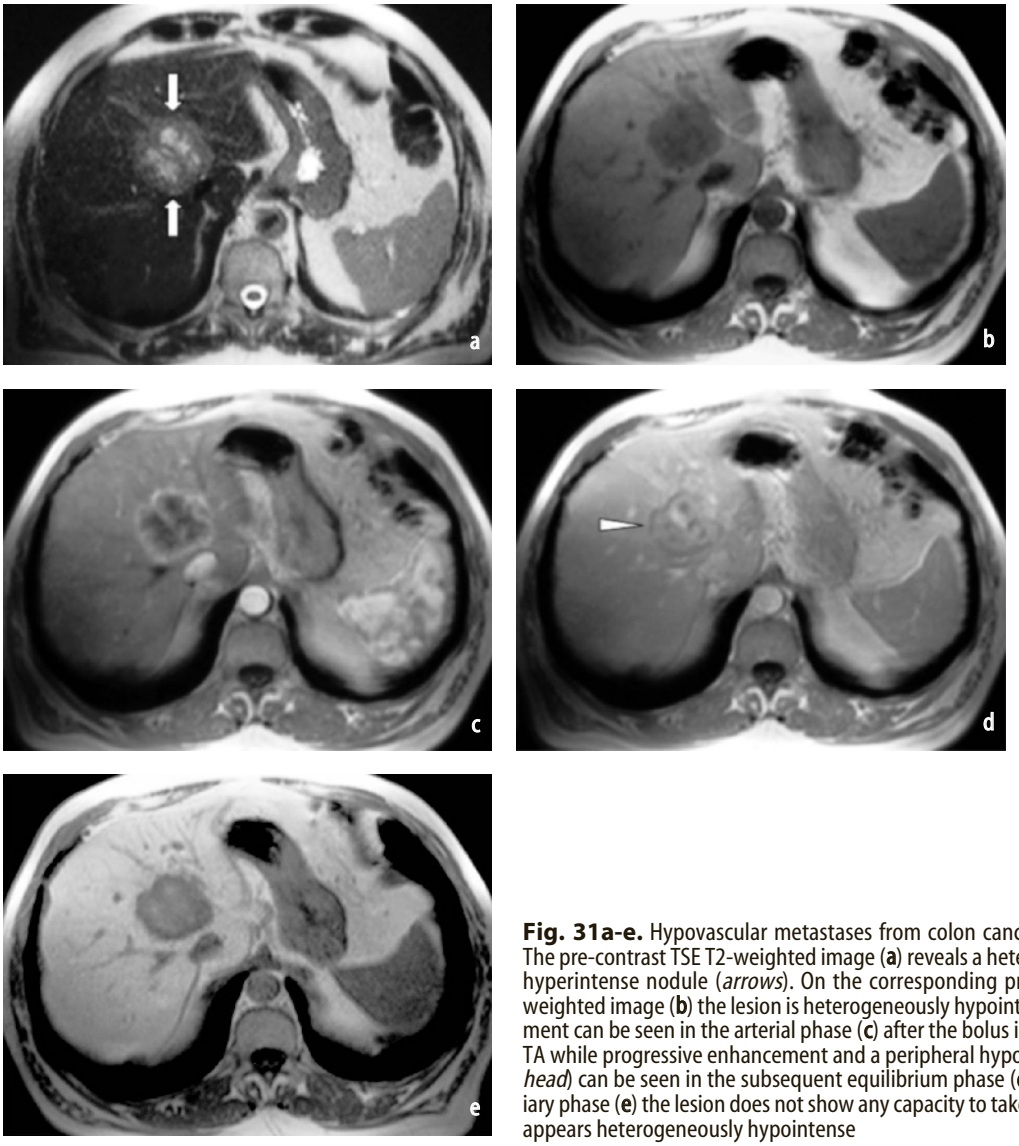

Fig. 31a-e. Hypovascular metastases from colon cancer after Gd-BOPTA. The pre-contrast TSE T2-weighted image (**a**) reveals a heterogeneous, slightly hyperintense nodule (*arrows*). On the corresponding pre-contrast GRE T1-weighted image (**b**) the lesion is heterogeneously hypointense. Rim enhancement can be seen in the arterial phase (**c**) after the bolus injection of Gd-BOPTA while progressive enhancement and a peripheral hypointense rim (*arrowhead*) can be seen in the subsequent equilibrium phase (**d**). In the hepatobiliary phase (**e**) the lesion does not show any capacity to take up Gd-BOPTA, and appears heterogeneously hypointense

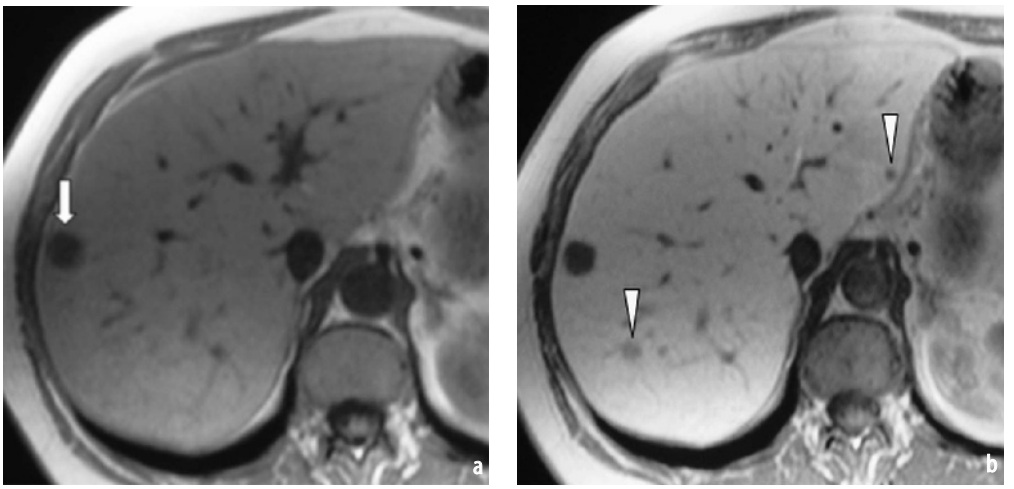

Fig. 32a, b. Metastases from cholangiocellular carcinoma after Mn-DPDP. The pre-contrast GRE T1-weighted image (**a**) reveals a small, round, homogeneously hypointense nodule (*arrow*). In the hepatobiliary phase after Mn-DPDP administration (**b**), the nodule is better delineated and appears markedly hypointense. Two additional small lesions (*arrowheads*) can be seen on the post-contrast image

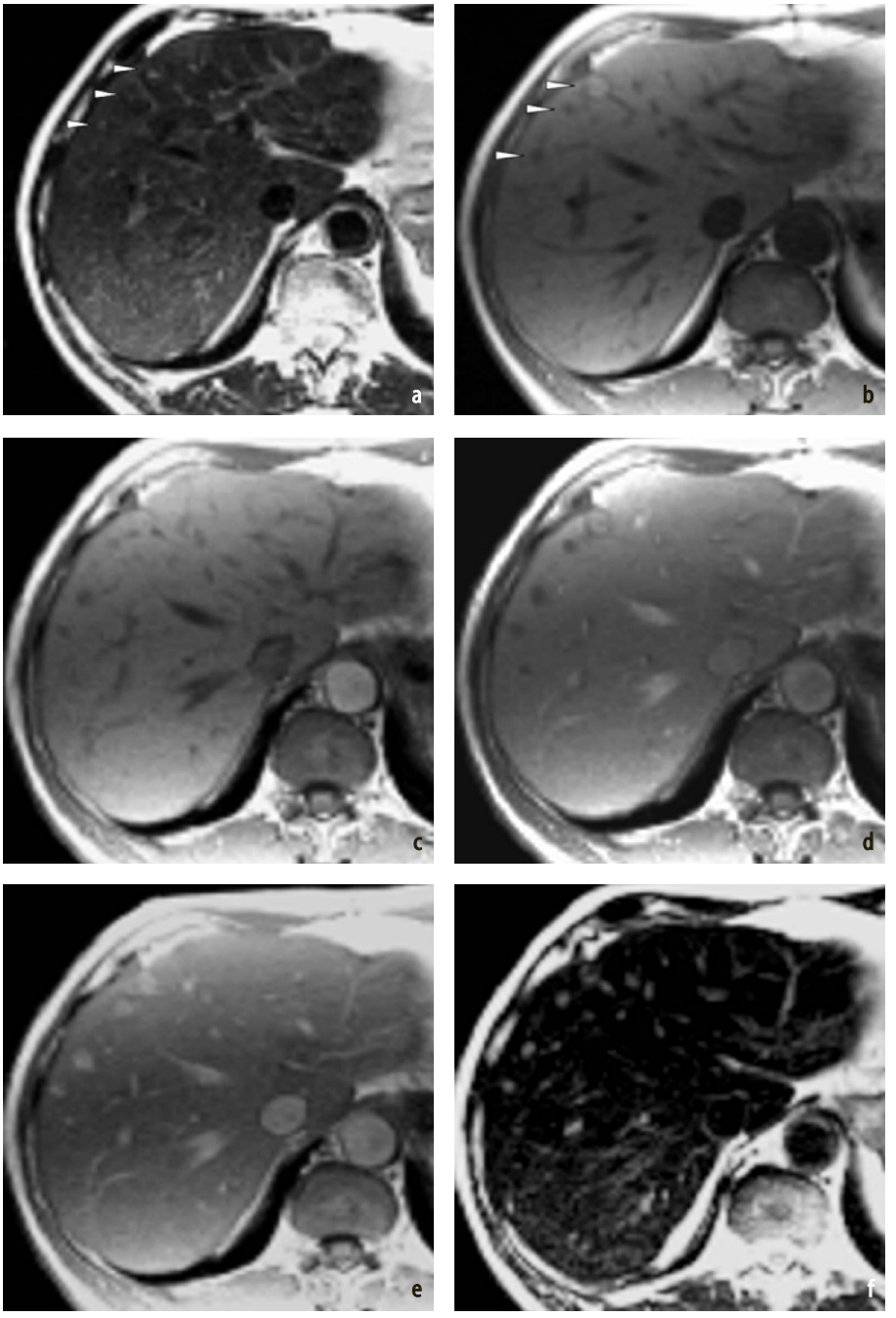

Fig. 33a-f. Metastases from colon cancer after SH U 555 A. On the pre-contrast TSE T2-weighted image (**a**), several small, slightly hyperintense nodules (*arrowheads*) can be seen. Conversely, on the pre-contrast GRE T1-weighted image (**b**) the lesions (*arrowheads*) are heterogeneous in appearance, presenting as either hypo- or hyperintense. In the arterial (**c**) and portal venous (**d**) phases of the dynamic evaluation after SH U 555 A administration, the nodules do not show significant enhancement. Conversely, in the equilibrium phase (**e**) they appear homogeneously hyperintense. In the reticuloendothelial phase (**f**) the lesions do not show significant signal drop, and are therefore better delineated. Additional nodules can also be seen

8.6 Summary

In summary, tumors of the liver exhibit variable appearances on MR. The key to accurately detecting and characterizing liver lesions is the proper use of the variety of MR contrast agents now available for clinical use. An understanding of the underlying pathology and histology of the spectrum of liver tumors and how these affect the appearance on unenhanced and contrast-enhanced MR images is also important in order to optimize diagnostic potential.

References

1. Arrive L, Flejou JF, Vilgrain V, et al. Hepatic adenoma: MR findings in 51 pathologically proved lesions. Radiology 1994; 193: 507-512
2. Caudana R, Morana G, Pirovano GP, et al. Focal Malignant hepatic lesions: MR imaging enhanced with Gadolinium Benzyloxypropionictetra-acetate (BOPTA)-preliminary results of phase II clinical application. Radiology 1996; 199: 513-520
3. Coffin CM, Diche T, Mahfouz A, et al. Benign and malignant hepatocellular tumors: Evaluation of tumoral enhancement after mangafodipir trisodium injection on MR imaging. Eur Radiol 1999; 9: 444-449
4. Goodman ZD. Nonparenchymal and metastatic malignant tumors of the liver. In: Haubrich WS, Schaffner F, Berk JE (eds): Bockus Gastroenterology Philadelphia: WB Saunders, 1995: 2488-2500
5. Grazioli L, Morana G, Caudana R, et al. Hepatocellular carcinoma. Correlation between gadobenate Dimeglumine-enhanced MRI and pathologic findings. Invest Radiol 2000; 35 (1): 25-34
6. Grazioli L, Morana G, Federle MP, et al. Focal nodular hyperplasia: Morphologic and functional information from MR imaging with gadobenate dimeglumine. Radiology 2001; 221: 731-739
7. Grazioli L, Morana G, Kirchin MA Schneider G. Accurate differentiation of Focal Nodular Hyperplasia from Hepatic Adenoma at Gadobenate Dimeglumine-enhanced MR imaging: prospective study. Radiology 2005; 236: 166-177
8. Grazioli L, Morana G, Kirchin MA, et al. MR imaging of focal nodular hyperplasia (FNH) with gadobenate dimeglumine (Gd-BOPTA) and SPIO (Ferumoxides): An intra-individual comparison. J Magn Reson Imaging 2003; May;17(5): 593-602
9. Grazioli L, Olivetti L, Fugazzola C, et al. The pseudocapsule in hepatocellular carcinoma: correlation between dynamic MR imaging and pathology. Eur Radiol 1999; 9: 62-67
10. Hagspiel KD, Neidl KFW, Eichenberger AC, et al. Detection of liver metastases: comparison of superparamagnetic Iron oxide-enhanced and unenhanced MR imaging at 1.5 T with dynamic CT, intraoperative US, and percutanous US. Radiology 1995; 196: 471-478
11. Hayashi M, Matsui O, Ueda K, et al. Correlation between the blood supply and grade of malignancy of hepatocellular nodules associated with liver cirrhosis: evaluation by CT during intraarterial injection of contrast medium. AJR 1999; 172: 969-976
12. Imai Y, Murakami T, Yoshida S, et al. Superparamagnetic iron oxide-enhanced magnetic resonance images of hepatocellular carcinoma: correlation with histological grading. Hepatology 2000; 32: 205-212
13. Kopp AF, Heuschmid M, Claussen CD. Multidetector helical CT of the liver for tumor detection and characterization. Eur Radiol 2002; 12: 745-752
14. Krinsky GA, Lee VS, Theise ND, et al. Hepatocellular carcinoma and dysplastic nodules in patients with cirrhosis: prospective diagnosis with MR imaging and explanation correlation. Radiology 2001; 219: 445-454
15. Lacomis JM, Baron RL, Oliver JH, Federle MP, Nalesnik M. Cholangiocarcinoma: Delayed CT contrast enhancement patterns. Radiology 1997;203:98-104
16. Lewis KH, Chezmar JL. Hepatic metastases. Magn Reson Imaging Clin North Am 1997; 5: 319-330
17. Lim J H, Cho JM, Kim EY, et al. Dysplastic nodules in liver cirrhosis: evaluation of homodynamic with CT during arterial portography and CT hepatic arteriography. Radiology 2000; 214: 869-874
18. Manfredi R, Maresca G, Baron RL, et al. Delayed MR imaging of hepatocellular carcinoma enhanced by gadobenate dimeglumine (Gd-BOPTA). J Magn Reson Imaging 1999; 9: 704-710
19. McFarland EG, Mayo-Smith WW, Saini S, et al. Hepatic hemangiomas and malignant tumors: improved differentiation with heavily T2-weighted conventional spin-echo. MR imaging Radiology 1994; 193:43-47
20. Molina EG, Schiff ER. Benign solid lesions of the liver. In: Schiff's Diseases of the liver (8th edition) Vol II. Lippincott-Raven 1999, 53:1254-1257
21. Murakami T, Baron RL, Peterson MS, et al. Hepatocellular carcinoma: MR imaging with mangoafodipir trisodium (Mn-DPDP). Radiology 1996; 200: 69-77
22. Murakami T, Kim T, Takamura M, et al. Hepatitis, cirrhosis, and hepatoma. J Magn Reson Imaging 1998; 8: 346-358
23. Pauleit D, Textor J, Bachmann R, et al. Hepatocellular Carcinoma: detection with gadolinium-and ferumoxides-enhanced MR imaging of the liver. Radiology 2002; 222(1): 73-80
24. Paulson EK, McClellan Js, Washington K, et al. Hepatic adenoma: MR characteristic and correlation with pathologic findings. AJR Am J Roentgenol 1994; 163:113-116
25. Rofsky NM, Earls JP. Mangafodipir trisodium injection (Mn-DPDP). A contrast agent for abdominal MR imaging. Magn Reson Imaging Clin N Am 1996; 4: 73-85
26. Saini S, Edelman RR, Sharma P et al. Blood-pool MR contrast material for detection and characterization of focal hepatic lesions: initial clinical experience with ultrasmall superparamagnetic iron oxide (AMI-227). AJR 1995; 164: 1147-1152
27. Schima W, Saini S, Echeverri JA, et al. Focal liver lesions: characterization with conventional spin-echo T2-weighted MR imaging. Radiology 1997; 202:389-394

28. Senéterre E, Taourel P, Bouvier Y, et al. Detection of hepatic metastases: Ferumoxides-enhanced MR Imaging versus unenhanced MR Imaging and CT during arterial portography. Radiology 1996; 200: 785-792
29. Stevens WR, Gulino SP, Batts KP, et al. Mosaic pattern of hepatocellular carcinoma: histologic basis for a characteristic CT appearance. J Comput Assist Tomogr 1996; 20:337-342
30. Tang Y, Yamashita Y, Arakawa A, et al. Detection of hepatocellular carcinoma arising in cirrhotic livers: comparison of gadolinium-and ferumoxides-enhanced MR imaging. AJR Am J Roentgenol 1999; 172(6): 1547-1554
31. Vilgrain V, Lewin M, Vons C, et al. Hepatic nodules in Budd-Chiari syndrome: Imaging features. Radiology 1999; 210:443-450
32. Vogl TJ, Hammerstingl R, Schwarz W, et al. Magnetic resonance imaging of focal liver lesions. Comparison of the superparamagnetic iron oxide resovist versus gadolinium-DTPA in the same patient. Invest Radiol 1996; 31: 696-708
33. Wanless IR. Micronodular transformation (nodular regenerative hyperplasia) of the liver: A report of 64 cases among 2500 autopsies and a new classification of benign hepatocellular nodules. Hepatology 1990; 11: 787-797
34. Worawattanakul S, Semelka RC, Noone TC, et al. Cholangiocarcinoma: spectrum of appearances on MR images using current techniques. Magn Reson Imaging 1998; 16: 993-1003
35. Yoshida Y, Imai Y, Murakami T, et al. Intrahepatic cholangiocarcinoma with marked hypervascularity. Abdom Imaging 1999; 24: 66-68

9

Imaging of Diffuse Liver Disease

CONTENTS

9.1 Steatosis Hepatis

Accumulation of fat within hepatocytes is commonly found in diabetic or obese patients or in patients who have been exposed to ethanol or other chemical toxins. In addition, in patients with advanced malignant neoplasms, fatty changes of the liver may be present due to poor nutrition and the hepatotoxic effects of chemotherapy. In most cases, fatty liver is associated with elevated levels of hepatic transaminases [48, 74].

Fatty changes are distributed either diffusely, giving rise to a patchy pattern, or are present as focal lesions. Frequently, the deposition of fat in the liver reflects regional differences in perfusion. Regions with a decreased portal flow accumulate less fat than areas that have normal or increased perfusion [2].

Generally, fatty changes of the liver have a characteristic pattern. In cases of entire fatty infiltration of the liver, the medial segment of the left lobe adjacent to the falciform ligament tends to accumulate fat, while the other side of the medial segment adjacent to the portal vein usually does not show any pathological changes [78]. A characteristic wedge-shape in certain regions of the liver is frequently indicative of fatty infiltration. Unfortunately, these findings are not sufficiently specific to enable a definitive diagnosis. With computed tomography (CT) imaging, the absence of a mass effect and the presence of normal vascular structures within the focal fatty lesions can be considered helpful for diagnosis, particularly in very large lesions. With magnetic resonance imaging (MRI), conventional T1-weighted spin-echo sequences are relatively insensitive to fatty infiltration, with differences in signal intensity (SI) of only 5-15% between normal liver tissue and tissue containing at least 10% triglycerides.

T2-weighted images, moreover, are especially insensitive to fatty infiltration. Thus, the diagnosis of a diffuse or focal fatty infiltration of the liver is based upon the exclusion of a focal or diffuse pathological process. In particular, comparison of CT scans that show regions of decreased attenuation with T2-weighted MR images that show no pathological changes, and T1-weighted images that depict a slightly bright lesion, may indicate fatty infiltration. With the evolution of chemical shift imaging, an accurate differential diagnosis of fatty lesions in the liver is now possible. Thus, fatty infiltration of the liver no longer represents a major diagnostic problem for MRI [32, 77].

In chemical shift imaging, the signal from water and fat is separated on the basis of differences in resonance frequency. This allows an absolute diagnosis of focal or diffuse fatty infiltration. Apart

from the case of lipoma of the liver, out-of-phase images are more sensitive for the detection of fatty liver than fat suppressed images. The intensity on out-of-phase images is determined from the absolute value of water intensity minus the fat intensity. Thus, whereas most tissues (including fat) appear similar on in-phase and out-of-phase images, fatty liver will be noticeably darker. If, for example, in a given case of focal fatty infiltration, fat accounts for 10% of the lesion's SI and water accounts for 90% on in-phase images, fat suppression, assuming that the fat signal is totally suppressed, will lead to an image in which the lesion still has 90% of the signal. However, if out-of-phase imaging is applied, using the same repetition time (TR) as on in-phase images, the SI of the lesion will drop to 80% of the in-phase signal (90% water signal minus 10% fat signal) thereby making it easier to detect the signal drop on MR images.

In the case of liver lipoma which contains only fat, the signal of the lesion will not change to any noticeable extent on out-of-phase images. On the other hand, the SI of the lesion will drop significantly on fat suppressed images (Fig. 1-3).

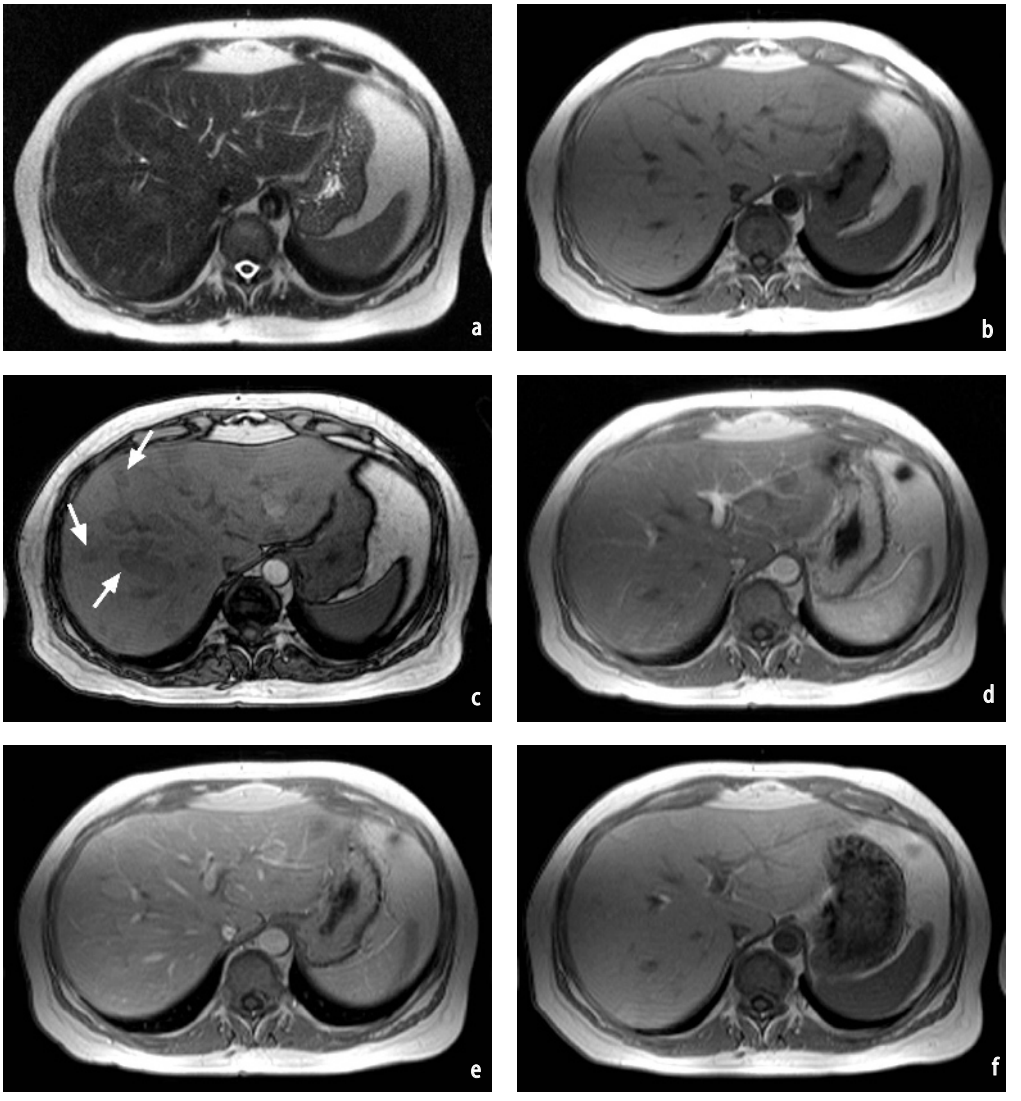

Fig. 1a-f. Diffuse focal fatty infiltration of the liver. A 54-year old female patient six months after high-dose chemotherapy for breast cancer. A follow-up CT study showed multiple hypodense liver lesions suspected to be metastases. Whereas T2-weighted (**a**) and T1-weighted (**b**) unenhanced images showed hardly any SI variations, out-of-phase images (**c**) show diffusely distributed hypointense areas (*arrows*). On dynamic and delayed imaging at arterial phase (**d**), portal-venous phase (**e**) and hepatobiliary phase (**f**) after Gd-BOPTA (0.05 mmol/kg BW), no regional changes of hepatic blood flow and no differences in Gd-BOPTA uptake can be seen, indicating that no focal liver lesions are present. Overall, MRI allows the diagnosis of diffuse focal fatty infiltration of the liver following high-dose chemotherapy

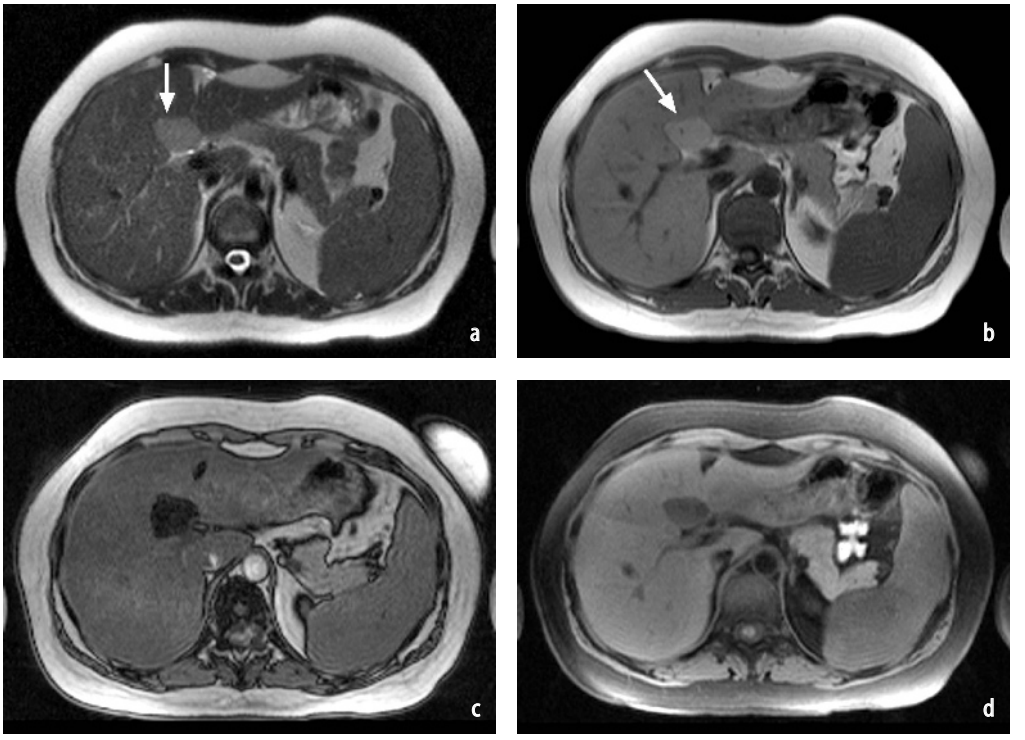

Fig. 2a-d. Focal fatty infiltration of the liver in the area of the portal vein bifurcation in a 62-year old female patient with a history of sigmoid colorectal cancer. Routine follow-up US detected a focal liver lesion near the liver hilum, indicative of a metastasis of colorectal carcinoma. Both T2-weighted (**a**) and T1-weighted (**b**) MR images reveal a focal hyperintense liver lesion (*arrows*). The high SI on both T1-weighted and T2-weighted images makes the diagnosis of a liver metastasis of colorectal carcinoma unlikely. Both out-of-phase (**c**) and fat suppressed T1-weighted (**d**) images reveal a significant drop in SI, which allows the accurate diagnosis of focal fatty infiltration of the liver. In this case, the high fat content means that even fat suppressed T1-weighted images show a significant drop in SI compared to the normal parenchyma

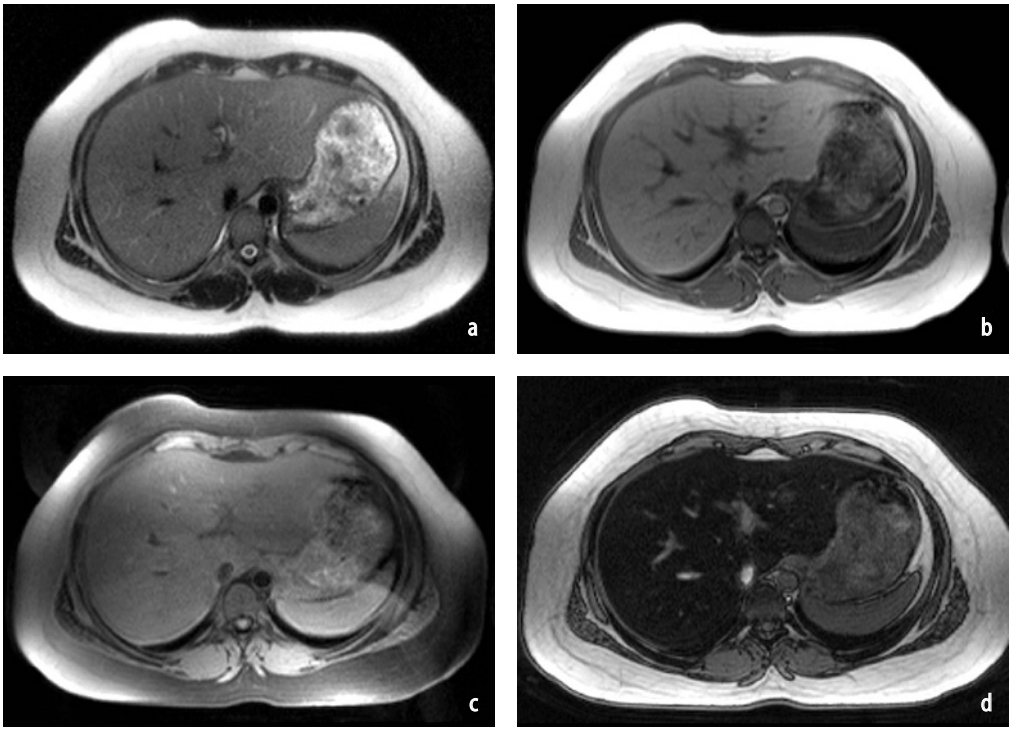

Fig. 3a-d. Diffuse fatty liver in a 26-year old obese female patient. Both T2-weighted (**a**) and T1-weighted (**b**) unenhanced images reveal an unusually high SI of the liver parenchyma. In this case, fat suppressed T1-weighted imaging (**c**) does not allow the diagnosis of diffuse fatty liver because the SI of the liver is not markedly different from that on T1-weighted images without fat suppression. However, out-of-phase images (**d**) readily allow the diagnosis of diffuse fatty liver because of the dramatic reduction of liver parenchymal SI

9.2 Inflammatory Disease

9.2.1 Viral Hepatitis

Acute viral hepatitis is diagnosed primarily by clinical or serological examination; cross-sectional imaging is not normally part of the primary diagnostic approach. Typical MR findings in acute viral hepatitis are hepatomegaly combined with edema of the liver capsule. In fulminant forms of acute viral hepatitis, diffuse or focal necrosis may be detected on MR images.

In patients suffering from chronic hepatitis, cross-sectional imaging, especially MRI, is performed to determine the presence of cirrhosis or ascites and to screen for the presence of hepatocellular carcinoma (HCC). A region of high SI surrounding the portal vein branches can frequently be found on T2-weighted images in patients suffering from acute or chronic active hepatitis, but is considered a non-specific sign [38]. In addition, diffuse or regional high signal areas can be identified on T2-weighted images [58, 59].

Patients with viral hepatitis typically have enlarged lymph nodes at the liver hilum presenting as solitary or confluent. However, in contrast to lymph node metastasis, the portal veins and other structures are not compressed and maintain their shape.

9.2.2 Sclerosing Cholangitis

Sclerosing cholangitis is a disease that affects the intra- and extrahepatic biliary system. Although it may have a variety of pathogenic origins, the histopathological changes are generally comparable. The biliary tracts, in particular, are affected by an intense inflammatory fibrosis [10]. Additionally, enlarged lymphatic nodules localized in the liver hilum may be found. Although the hepatic parenchyma usually presents as normal, a fulminate form of sclerosing cholangitis may occur, leading to liver failure and portal hypertension [80].

Typical findings with MRI are diffusely distributed regions of biliary dilatation and areas of periportal inflammation. These features are best distinguished on heavily T2-weighted images when the biliary dilatation presents as areas showing a fluid-equivalent signal localized along branches of the portal veins. On the other hand, periportal inflammation shows decreased SI on T1-weighted images, while a signal intermediate between that of liver tissue and bile is seen on T2-weighted images. These imaging findings are typically localized in the liver hilum and accompany the intrahepatic portal tracts surrounding the portal vein branches, but not the hepatic veins, which are unaffected by the disease. For the differential diagnosis of sclerosing cholangitis, periportal inflammation, biliary obstruction, hepatitis and periportal neoplasm all have to be taken into consideration.

Patients suffering from sclerosing cholangitis frequently develop an occult thrombosis of the main or segmental portal vein as a result of the periportal inflammatory process. This may subsequently lead to a segmental atrophy [9, 28] (Fig. 4). Another important finding in sclerosing cholangitis is the increased risk of developing cholangiocarcinoma (CCC). For this reason imaging studies should always focus on the detection of focal lesions as well (Fig. 5).

9.2.3 Radiation-Induced Hepatitis

Due to its size and anatomical location in the abdomen, the liver is frequently affected secondarily by radiation therapy of extrahepatic malignancies. Within six months of radiation injury, diffuse edema of the liver can be seen, appearing as increased SI on T2-weighted images and decreased SI on T1-weighted images [68].

Portal flow is generally reduced in patients with radiation injured regions of the liver, and, as in the case of patients with concomitant fatty infiltration, the deposition of fat in these areas is usually reduced [22].

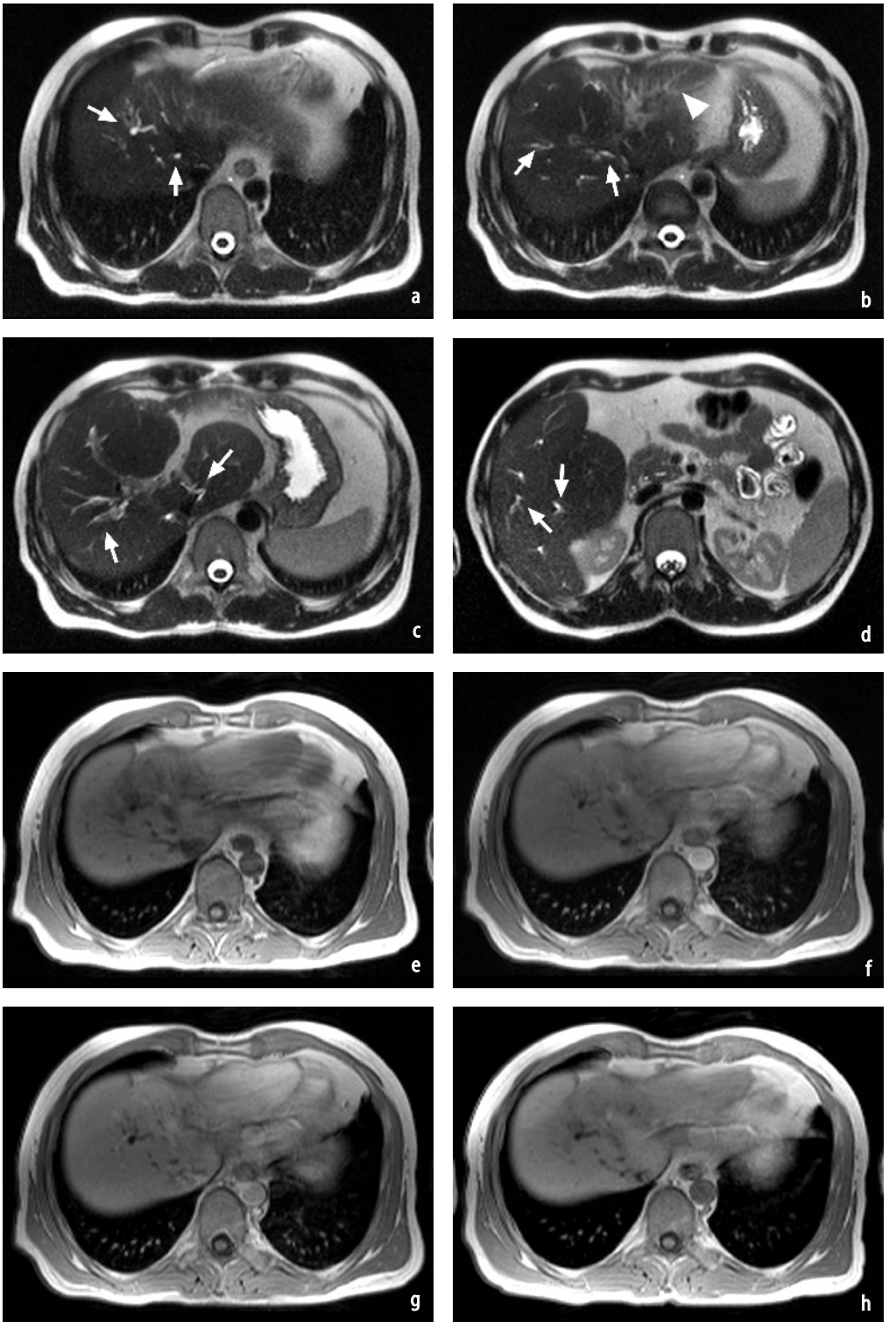

Fig. 4a-h. Primary sclerosing cholangitis. T2-weighted images (**a**-**d**) show diffusely distributed regions of biliary dilatation (*arrows*) as well as segmental atrophy (*arrowhead* in **b**) of segments II and III of the liver. Due to the already advanced stage of the disease, hypertrophy of segment I (**c**) can be detected. Unenhanced T1-weighted images (**e**) reveal decreased SI of the liver parenchyma. Irregular enhancement due to inflammatory changes can be seen on T1-weighted dynamic imaging in the arterial phase (**f**) and portal-venous phase (**g**). In the hepatobiliary phase after injection of 0.05 mmol/kg BW Gd-BOPTA (**h**), a patchy pattern can be detected that corresponds to the affected areas of liver parenchyma where uneven uptake and excretion of Gd-BOPTA has occured

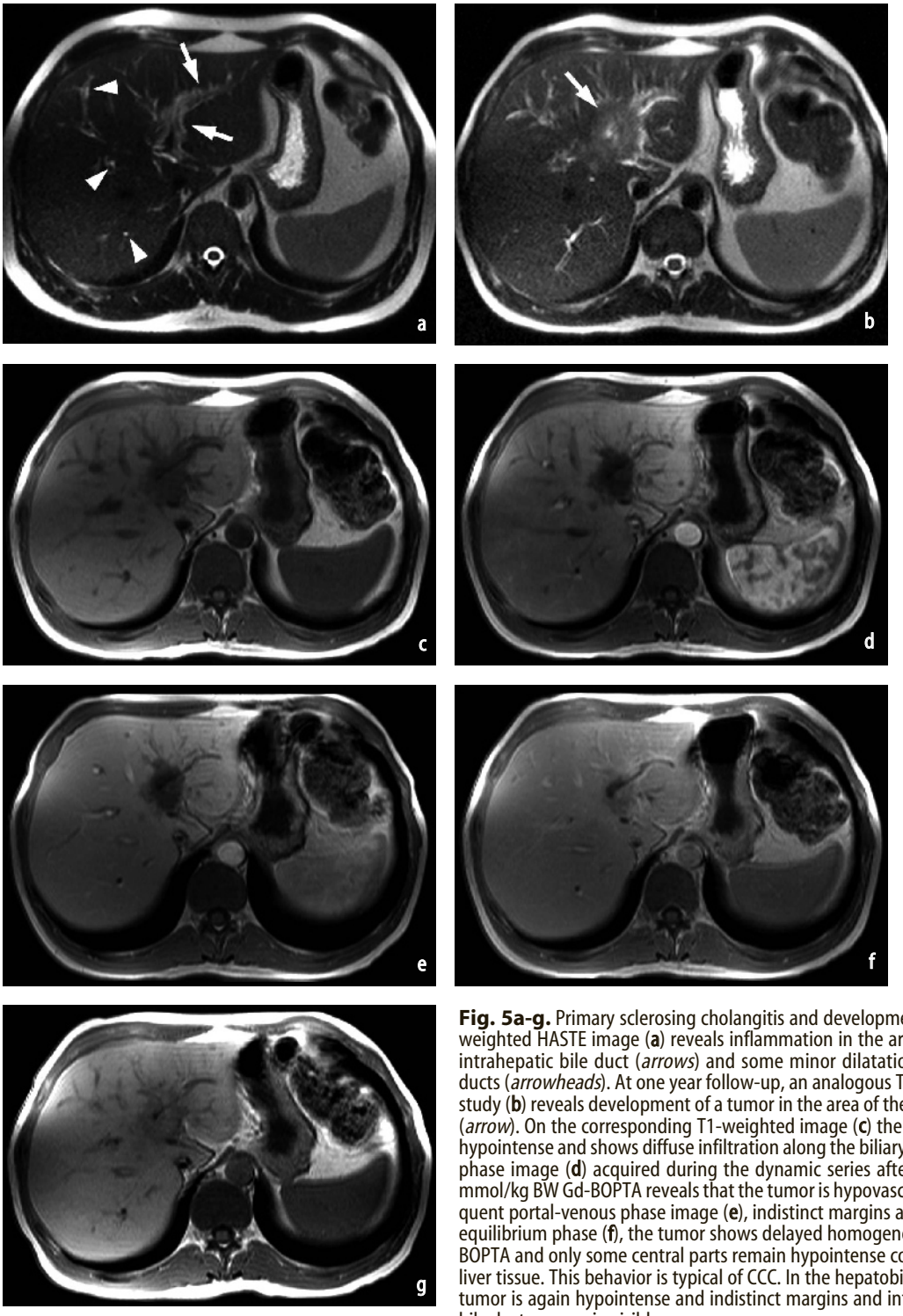

Fig. 5a-g. Primary sclerosing cholangitis and development of CCC. The T2-weighted HASTE image (**a**) reveals inflammation in the area of the left main intrahepatic bile duct (*arrows*) and some minor dilatations of intrahepatic ducts (*arrowheads*). At one year follow-up, an analogous T2-weighted HASTE study (**b**) reveals development of a tumor in the area of the biliary bifurcation (*arrow*). On the corresponding T1-weighted image (**c**) the tumor is markedly hypointense and shows diffuse infiltration along the biliary tracts. The arterial phase image (**d**) acquired during the dynamic series after injection of 0.05 mmol/kg BW Gd-BOPTA reveals that the tumor is hypovascular. On the subsequent portal-venous phase image (**e**), indistinct margins are apparent. In the equilibrium phase (**f**), the tumor shows delayed homogeneous uptake of Gd-BOPTA and only some central parts remain hypointense compared to normal liver tissue. This behavior is typical of CCC. In the hepatobiliary phase (**g**), the tumor is again hypointense and indistinct margins and infiltration along the bile ducts are again visible

9.3 Cirrhosis

Hepatic cirrhosis is a disease that leads to irreversible fibrosis of the parenchyma. It is localized in the spaces between the portal tracts and destroys the normal hepatic architecture. However, the development of cirrhosis in patients suffering from viral hepatitis is frequently inhibited by treatment with interferon [14].

Generally, diagnosis of liver cirrhosis is achieved by histological examination of a liver biopsy, whereas imaging is performed to determine the anatomical distribution of the disease.

Typical features of advanced hepatic cirrhosis on diagnostic imaging are nodular contours and enlargement of the caudate lobe and lateral segment of the left lobe, combined with atrophy of the right lobe [26, 59]. However, regional hypertrophy of certain liver segments, such as the caudate lobe, and atrophy of the right lobe are less likely to occur in alcohol-induced liver cirrhosis, which is one of the more frequent causes of cirrhosis [24].

As liver atrophy seems to be localized around the portal vein and the liver hilum, an empty region in the gallbladder fossa is typically seen, which contains periportal fat. Although cirrhosis affects the entire organ, the actual volume of fibrous scar tissue is very small compared with the whole liver volume and thus it has little influence on the relaxation times of hepatocellular tissue. For this reason, cirrhosis alone is difficult to depict on MRI [25].

However, as liver cirrhosis is often accompanied by hepatitis or inflammation, cirrhotic livers frequently show prolonged T1 and/or T2 relaxation times [66].

Furthermore, cirrhotic livers tend to accumulate iron, which leads to decreased hepatic SI. Frequently, the distortion and nodular appearance of intrahepatic vessels is helpful for the diagnosis of cirrhosis on MR images.

Similarly, the decreased caliber of segmental veins compared with the intrahepatic inferior caval vein can be interpreted as a sign of liver cirrhosis [42] (Fig. 6).

9.3.1 Regenerative Nodules

Regenerative nodules frequently arise in cirrhotic livers as a result of heterogeneous regeneration in the grossly distorted liver architecture. These lesions, which are usually less than 5 mm in diameter, show a heterogeneous pattern on MR images. Larger regenerative nodules, measuring more than 5 mm in diameter, can be found in about one third of cirrhotic livers, while nodules larger than 10 mm only occur in about 10% of cases [72].

Regenerative nodules on ultrasound (US) and CT may mimic neoplasms such as HCC, a misinterpretation frequently underlined by the fact that intrahepatic vessels are displaced by mass effects. MRI is superior for the diagnosis of regenerative nodules because of its better soft tissue contrast. The typical nodular pattern which is due to inflammatory fibrous septa surrounding each regenerative nodule is best depicted on mildly T2-weighted images [49].

Approximately 25% of regenerative nodules show an increased deposition of iron compared to surrounding normal liver cells [65]. Hence, their identification as regions with decreased SI on T2-weighted or T1-weighted gradient echo images is improved [64].

Furthermore, the contrast between the fibrous septa and the normal liver parenchyma can be increased by the application of exogenous iron oxide-based contrast agents [18].

As liver cirrhosis with regenerative nodules may also occur in patients suffering from fatty infiltration or presenting with fatty regenerative nodules, out-of-phase T1-weighted imaging is often appropriate to clarify the diagnosis. Since re-

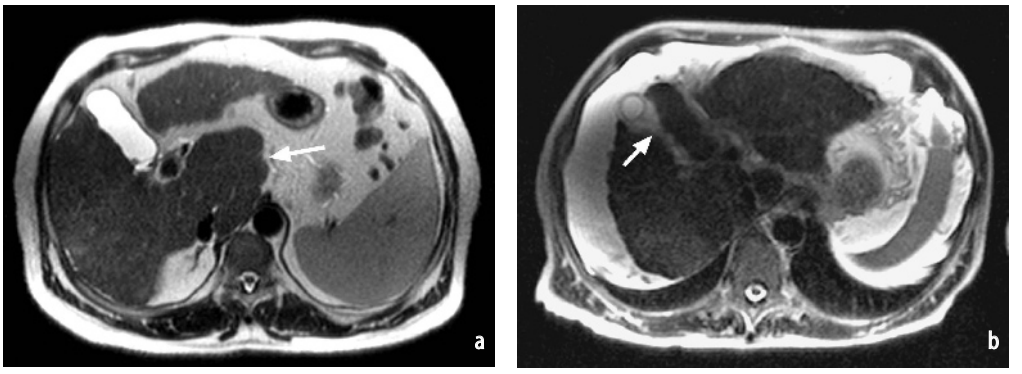

Fig. 6a, b. Typical findings in hepatic cirrhosis. T2-weighted images (**a**, **b**), show nodular contours of the surface of the liver, enlargement of the caudate lobe (*arrow* in **a**), ascites and atrophy of the right liver lobe with subsequent hypertrophy of the left lobe. Additionally, a typically empty region in the gallbladder fossa (*arrow* in **b**) can be depicted, corresponding to periportal fat

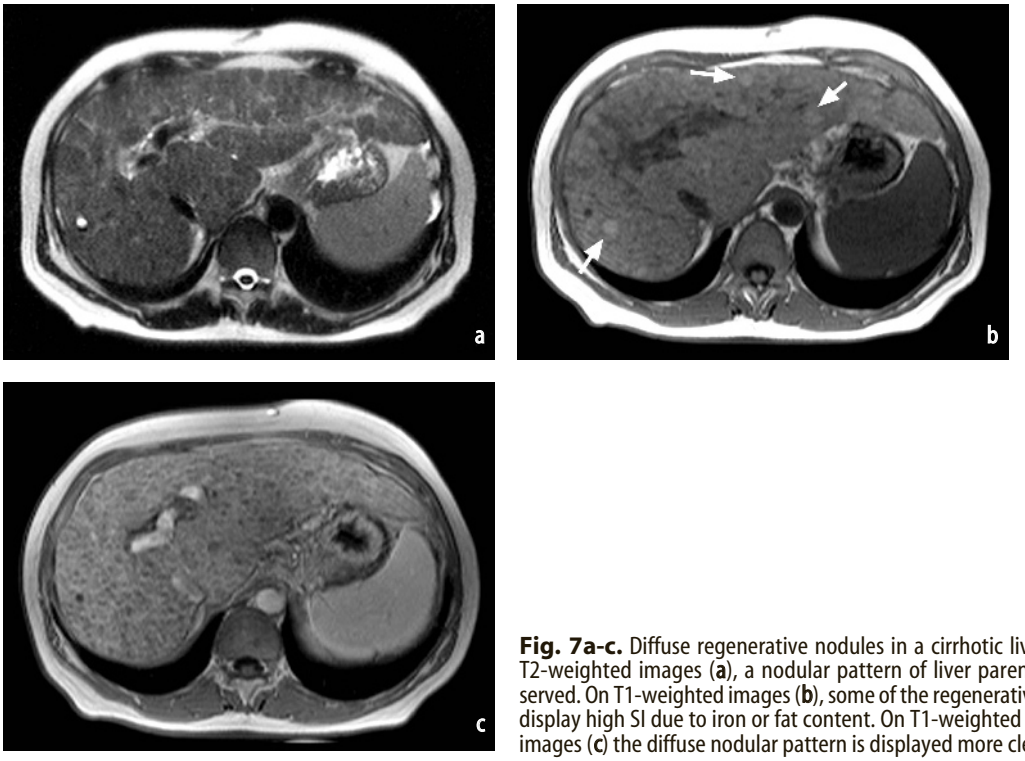

Fig. 7a-c. Diffuse regenerative nodules in a cirrhotic liver. On moderately T2-weighted images (**a**), a nodular pattern of liver parenchyma can be observed. On T1-weighted images (**b**), some of the regenerative nodules (*arrows*) display high SI due to iron or fat content. On T1-weighted contrast-enhanced images (**c**) the diffuse nodular pattern is displayed more clearly

generative nodules consist of normal hepatic cells, MRI is the imaging modality of choice to exclude HCC, which can usually be differentiated from regenerative nodules due to its increased SI on T2-weighted images. In some cases, regenerative nodules may appear as slightly hyperintense on T1-weighted sequences. This is particularly the case when the signal of the surrounding liver parenchyma is reduced due to fibrosis and in cases in which the nodules have accumulated fat [39] (Fig. 7).

Regenerative nodules should be distinguished from nodular regenerative hyperplasia, which is characterized by multiple hyperplastic nodules occurring in a non-cirrhotic liver. These nodules may sometimes mimic cirrhosis, however, they do not show the tendency to accumulate fat or iron [13].

9.3.2 Portal Hypertension

Portal hypertension is frequently a systemic complication of liver cirrhosis, however different pathologies such as obstruction at the post-sinusoidal (e.g. hepatic vein), sinusoidal (e.g. cirrhosis) or pre-sinusoidal (e.g. portal vein) level may also cause portal hypertension [27].

The most common cause of portal hypertension is liver cirrhosis. Associated complications include variceal bleeding, ascites and splenomegaly. A primary consequence of the increased pressure in the portal tract is dilatation of vessels. Later, as a result of the development of porto-systemic shunting, the blood flow to the liver diminishes and the size of the portal vessels is again reduced. Increased porto-systemic shunting results in less effective metabolism of absorbed nutrients and accumulation of toxic metabolites such as ammonia in the blood. This may lead to the clinical manifestations of hepatic encephalopathy. As decreased portal flow correlates with the presence of liver atrophy, porto-systemic shunting or portal hypertension contributes to the further regression of liver parenchyma in patients suffering from cirrhosis [35].

An important consequence of portal hypertension is the development of esophageal varices, the rupture of which, either spontaneously or as a result of vomiting, may lead to life-threatening hemorrhage. Esophageal varices are the result of porto-systemic shunting through the lienal vein to the left gastric (coronary) veins, which secondarily drain to thoracic veins such as the vena azygos or hemiazygos [79].

Concomitant varices in the spleno-renal venous system and the paraumbilical venous net, as well as the presence of anorectal shunts, may reduce the risk of rupture of the esophageal varices, but at the increased risk of hepatic encephalopathy [43].

Therapy of esophageal varices consists of sclerotherapy or surgical intervention to create alternative porto-systemic shunts. Esophageal varices are usually well depicted on T1-weighted or flow sensitive gradient echo images; these are localized

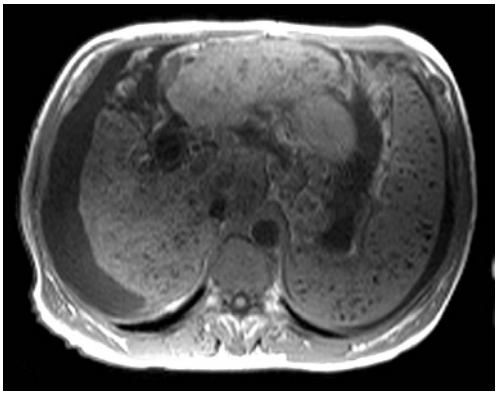

Fig. 8. Gamna-Gandy bodies of the spleen in a patient with portal hypertension due to liver cirrhosis. The T1-weighted image shows diffuse low signal intensity lesions in the spleen, representing siderotic nodules arising due to portal hypertension. Additionally, typical signs of liver cirrhosis including ascites, hypertrophy of the left liver lobe and liver segment I, and concomitant hypotrophy of the right liver lobe can be seen

anterior to the aorta at the level of the diaphragmatic hiatus [7].

Flow sensitive MRI can give results comparable to those of digital subtraction angiography and endoscopy. As the neighboring aorta and heart may induce pulsatile artifacts, low flip angles or electrocardiogram (ECG) gating should be used for gradient echo sequences. However, if esophageal varices are not seen, then dilated left gastric veins in the gastro-hepatic ligament may indicate the diagnosis.

Whereas spleno-renal shunts, retroperitoneal shunts and puborectal shunts are difficult to demonstrate on ultrasonography, they are well visualized using MR angiography techniques. Moreover, reversed flow in the central portion of the splenic vein can be considered diagnostic [50].

Paraumbilical shunting may be best diagnosed by following the left portal vein to the superficial veins at the umbilicus through the ligamentum teres hepatis. Dilated veins adjacent to the abdominal wall have a characteristic spider-web appearance, called caput medusae.

In patients with large gastroepiploical veins along the greater curvature of the stomach, esophageal varices induced by a single splenic vein occlusion (e.g. caused by pancreatitis), should be taken into account as a differential diagnosis.

Enlargement of the gastroepiploic veins can be considered a specific sign of splenic vein occlusion since they are not present in patients with portal hypertension in whom splenic veins are patent. In contrast, occlusion of the splenic vein can be excluded as a primary cause of portal hypertension in patients with paraumbilical varices. However, gastroesophageal and retroperitoneal collaterals may be seen in both conditions [36].

Portal vein velocity and flow volume may be ascertained on MRI using two-dimensional phase contrast techniques. With this imaging modality, increased portal flow is frequently seen in patients with cirrhosis in cases of recompensation. On the other hand, decreased or even reversed flow within the portal tract has been demonstrated in patients suffering from severe cirrhosis [63].

A thickened gallbladder wall is frequently found in patients with cirrhosis, independent of the primary diseases of the gallbladder.

Further clinical manifestations of portal hypertension are ascites and splenomegaly. So-called Gamna-Gandy bodies, representing siderotic nodules within the spleen, can arise in patients with portal hypertension and may be detected on T2-weighted or contrast-enhanced T1-weighted MRI [54] (Fig. 8).

9.4 Iron Overload

Since the liver is a central organ of digestive and reticuloendothelial function, it is heavily involved in the deposition and distribution of iron. Accumulated iron in the liver originates both from intestinally absorbed dietary iron and particulate iron from damaged erythrocytes. Normally, accumulated iron in the liver is metabolized and delivered to the bone marrow in order to be used for red blood cell production. However, several diseases which increase the uptake of intestinal iron or the liberation of physiologically bound iron may lead to an excessive accumulation of iron in the liver.

As iron reduces the T2 and T2* relaxation times significantly, MRI is a sensitive and specific imaging modality for the depiction of iron overload and its anatomical distribution. The most frequent diseases that lead to an increased accumulation of iron in the liver are hemochromatosis, siderosis (due to transfusional iron overload), hemolysis and cirrhosis. In addition to an examination of the liver, whole body MRI may be helpful to evaluate the underlying disease by revealing the pattern of increased iron accumulation in extrahepatic tissues.

9.4.1 Hemochromatosis

Hemochromatosis is a disease caused by an increased intestinal absorption of dietary iron, bound as ferritin or hemosiderin, and is characterized by excessive parenchymal iron accumulation [29].

The primary organs affected by hemochromatosis are the liver, pancreas and heart. Thus, liv-

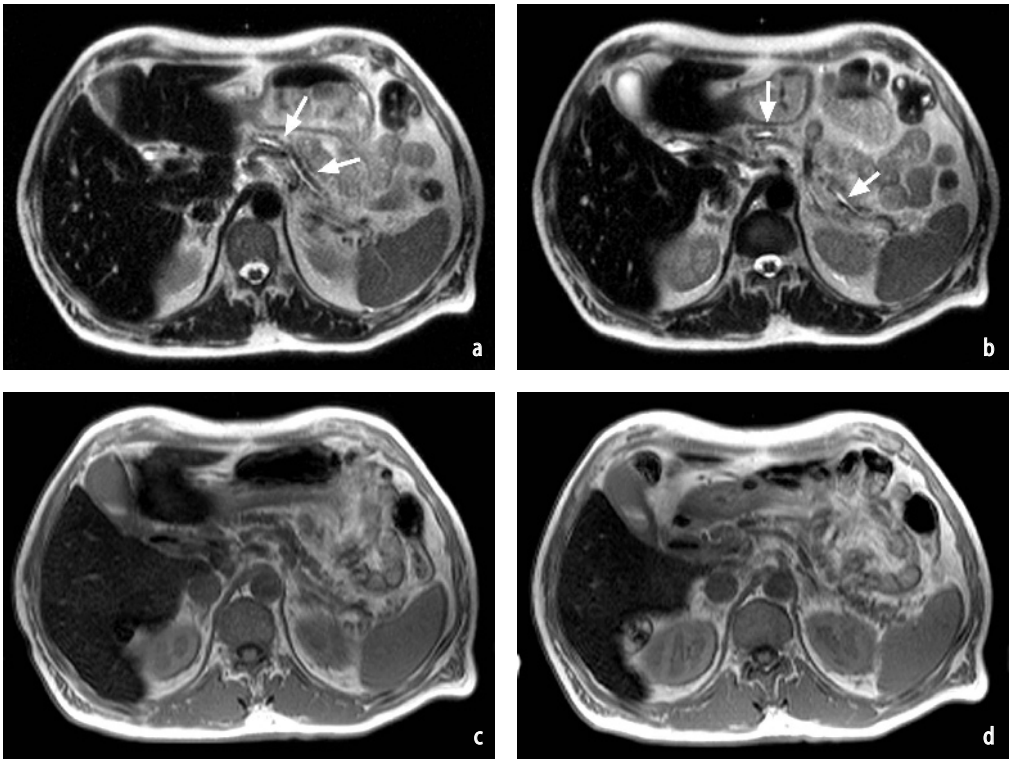

Fig. 9a-d. Longstanding hemochromatosis. The liver and pancreas show decreased SI on T2-weighted (**a**, **b**) and T1-weighted (**c**, **d**) images, while the spleen demonstrates essentially normal SI. Note that the atrophy of the pancreas is displayed best on T2-weighted images (*arrows*). As a result of the atrophy, this patient with longstanding disease developed diabetes mellitus

er cirrhosis, diabetes mellitus and cardiomyopathy frequently occur in untreated patients. Patients with longstanding disease and liver cirrhosis are significantly more at risk of developing HCC, thereby worsening their overall prognosis. Additional clinical manifestations include dermal hyperpigmentation, decreased libido and a slightly increased incidence of extrahepatic malignancies.

In general, menstruating women tend to show only a moderate development of the disease [47].

Patients with hemochromatosis also demonstrate decreased reticuloendothelial function and thus iron storage is mainly limited to the hepatic parenchyma [40]. In contrast, patients without hereditary hemochromatosis who ingest massive amounts of iron demonstrate both parenchymal and reticuloendothelial iron overload.

Hemochromatosis should be differentiated from hemosiderosis, in which increased accumulation of iron arises due to transfusional iron overload, typically in patients with hematological diseases who need regular blood transfusions. In patients with hemosiderosis, iron accumulates primarily in the reticuloendothial cells of the liver and spleen, while hepatocytes, pancreas and other parenchymal organs are relatively excluded. This difference is of major importance since parenchymal overload has more toxic consequences. However, an accumulation of iron within liver cells may also be seen in certain patients after massive blood transfusions [16, 46].

Since in most cases hemochromatosis is a primary genetic disease, familial screening should be performed in order to detect early liver cirrhosis or HCC. Moreover, the prognosis of patients with hemochromatosis can be improved significantly by reducing serum iron levels by means of repeated phlebotomy [3].

As measurements of serum iron levels and ferritin are not specific and CT findings do not provide satisfactory results, a definitive diagnosis has to be obtained by means of histological examination [58].

Since iron decreases the T2 relaxation time, hemochromatosis is seen as areas of decreased SI on T2- or T2*-weighted MR images [55]. In addition to the liver, the pancreas and heart are also affected. Therefore, the suspicion of hemochromatosis can be confirmed if each of these organs demonstrates decreased SI on MR images. Parenteral iron accumulation (e.g. in transfusional iron overload), can be excluded as the pathogenic factor in hemochromatosis if the spleen presents with a normal SI (Fig. 9).

In normal individuals the liver parenchyma shows increased SI compared with the skeletal muscles on all sequences. As skeletal muscles are not affected by hemochromatosis, they represent a suit-

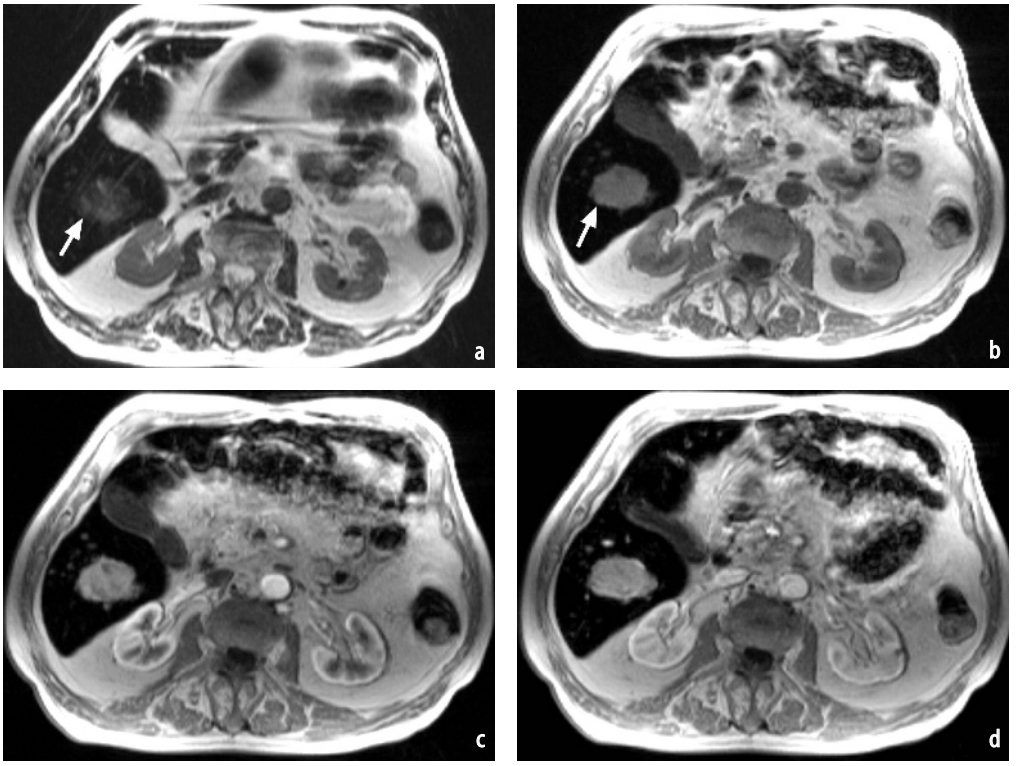

Fig. 10a-d. A 74-year old male patient with longstanding hemochromatosis, significantly elevated AFP levels and HCC. The unenhanced T2-weighted (**a**) and T1-weighted (**b**) images reveal decreased SI of the liver parenchyma and a hyperintense liver lesion (*arrows*) in the right liver lobe. In this case, iron deposition in the hepatocytes serves as an intrinsic contrast agent enabling the HCC to appear with high SI since iron storage does not take place in the tumor cells. With dynamic imaging after injection of Gd-BOPTA, strong hypervascularity of the lesion can be seen in the arterial phase (**c**) and portal-venous phase (**d**), clearly suggesting the presence of a HCC

able reference tissue to interpret and quantify the decreased signal of affected liver parenchyma [12].

In the early stages of the disease the SI of the pancreas remains normal, particularly in menstruating women. However, as the disease progresses, the signal within the pancreatic tissue decreases. This is particularly evident in symptomatic hemochromatosis. Since MRI is able to demonstrate the progression of iron accumulation and the clearing of hepatic iron, it may possibly serve as a monitoring modality in place of the histological follow-up examinations performed at present.

Cirrhosis of the liver frequently occurs in patients suffering from untreated hemochromatosis. With MRI, hemochromatosis may be detected due to the fact that fibrous septa demonstrate increased SI compared to the low SI of the parenchyma. However, in many cases of hemochromatosis-induced cirrhosis, a micronodular pattern is present that is difficult to visualize on MRI [64].

As dysplastic liver cells in HCC do not tend to accumulate iron to the same extent as liver parenchyma in hemochromatosis, HCC usually appear with high SI compared to the low SI of liver tissue. However, similar high signal areas are generally seen on all sequences for most focal liver lesions in cases of hepatic iron overload (Fig. 10).

Liver transplantation is usually indicated for patients with hemochromatosis and advanced liver cirrhosis (Fig. 11). Although the transplanted organ also tends to accumulate iron, the hepatotoxic effect of the accumulation develops over a long time and so prognosis is significantly improved. Interestingly, patients suffering from hemochromatosis may serve as donors for liver transplantation because the transplanted liver rapidly clears the accumulated iron [15].

9.4.2 Siderosis

In patients suffering from transfusional siderosis, the liver shows a similar decrease in SI as that seen in hemochromatosis. However, transfusional siderosis can easily be distinguished by examination of the SI of the spleen and pancreas. While the spleen demonstrates decreased SI in patients with transfusional siderosis, it usually does not show any SI decrease in cases of hemochromatosis. In contrast, the pancreas usually demonstrates a significant drop of SI in cases of hemochromatosis, but remains unchanged in patients with transfusional siderosis; only in cases of extreme transfusional

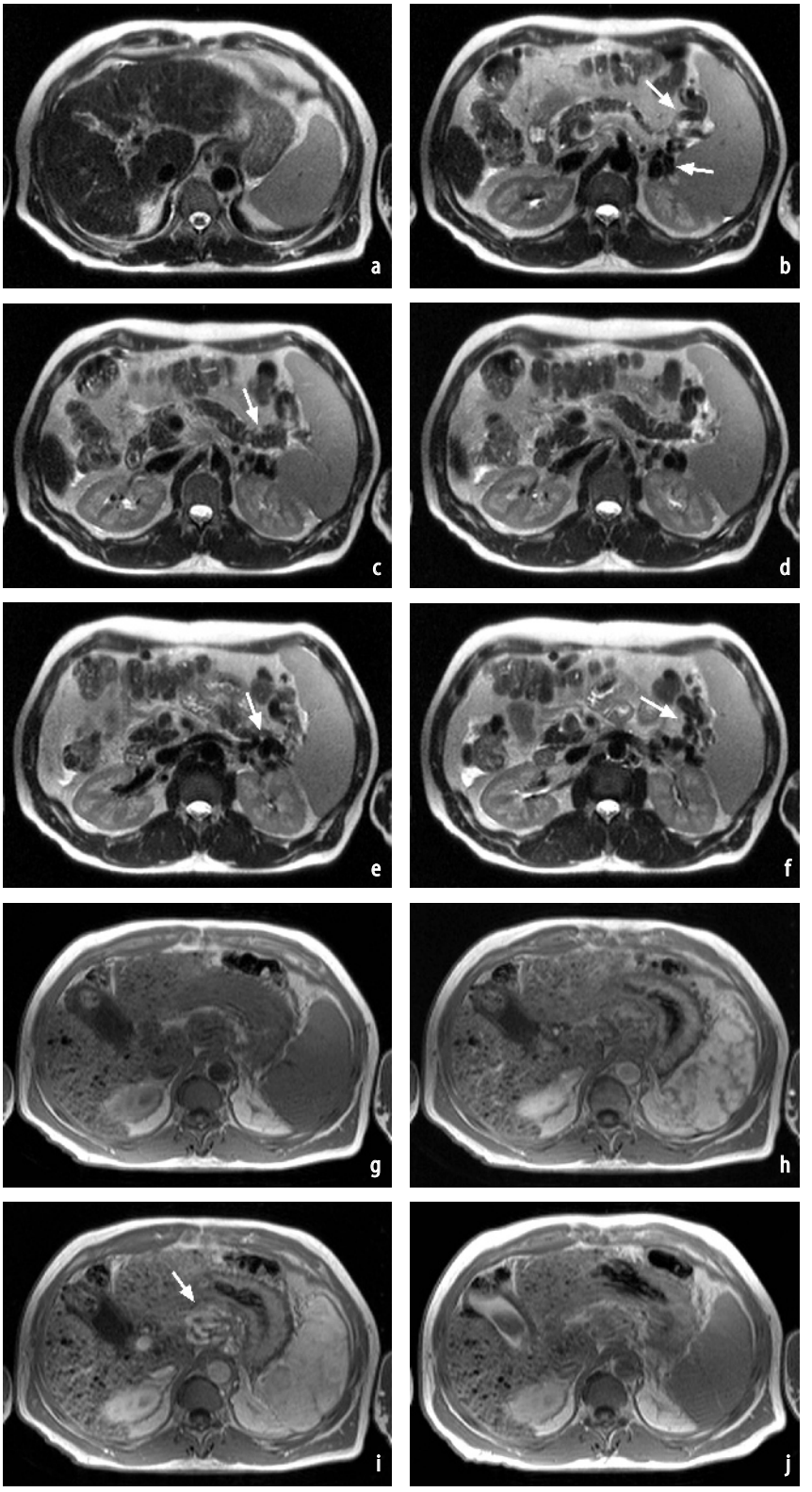

Fig. 11a-j. Patient with longstanding hemochromatosis and subsequent development of liver cirrhosis and portal hypertension. The T2-weighted images (**a**-**f**) show typical signs of liver cirrhosis with hypertrophy of liver segment I and a nodular surface of the liver. Due to the already advanced liver cirrhosis, the SI of the liver parenchyma is not as low as in cases of hemochromatosis without cirrhosis since the inflammatory changes in cirrhosis increase the SI of the liver. However, a decreased SI of the pancreatic tissue (**b**-**d**) can be noted together with the beginnings of pancreatic atrophy. The spleen is enlarged and multiple collateral vessels in the splenic hilum can be depicted, draining into the left renal vein (**b**-**f**) (*arrows*). On pre-contrast T1-weighted images (**g**), multiple small areas of low SI can be noted that correspond to areas of increased iron storage. The nodular appearance of the cirrhotic liver is much more obvious on dynamic images after Gd-BOPTA, shown here in the arterial phase (**h**) and portal-venous phase (**i**). Additionally, irregular portal-venous collaterals (*arrow*) can be seen near the small curvature of the stomach on the portal-venous phase image (**i**). Only a slight increase of liver parenchymal SI can be noted on the hepatobiliary phase image (**j**), although excretion of Gd-BOPTA into the gall bladder is evident

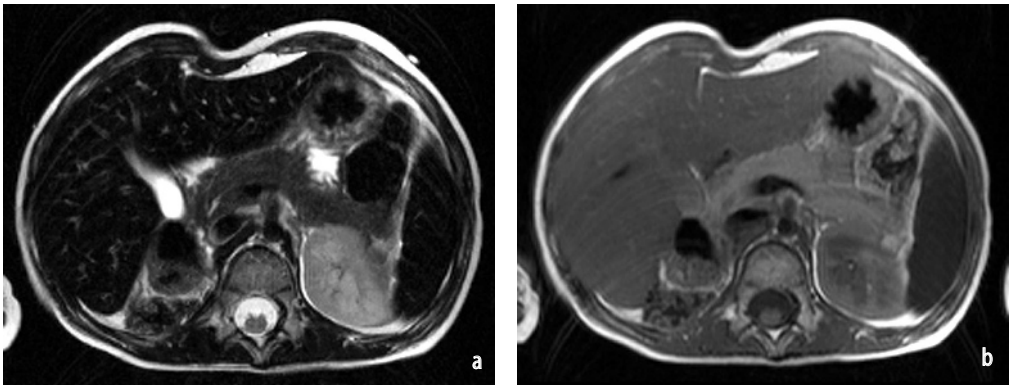

Fig. 12a, b. Transfusional siderosis in a 7-year old boy after multiple blood transfusions and chemotherapy for right-sided nephroblastoma. Both T2-weighted (**a**) and T1-weighted (**b**) images reveal decreased SI of the liver and spleen, while the SI of the pancreas is unaffected. This is due to the presence of iron storage in the macrophages of the spleen and liver, rather than in hepatocytes, as occurs in hemochromatosis (see Fig. 13)

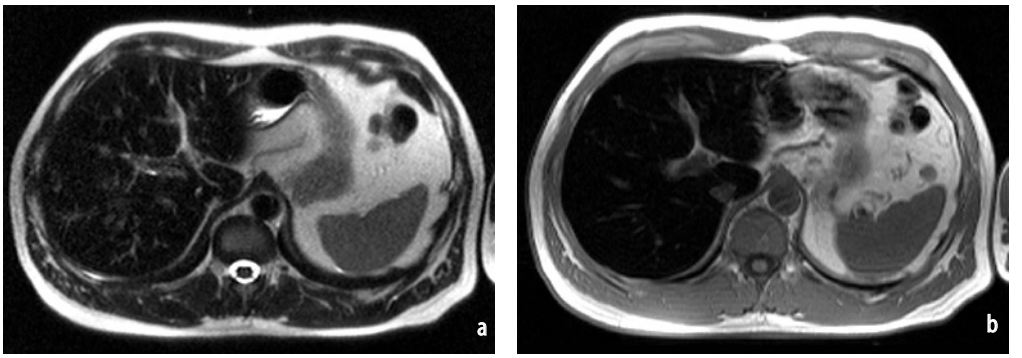

Fig. 13a, b. Hemochromatosis. Both T2-weighted (**a**) and T1-weighted (**b**) images reveal a dramatically decreased SI of the liver parenchyma while the SI of the spleen remains normal. This permits the differential diagnosis of transfusional siderosis (see Fig. 12) to be excluded since the SI of the spleen is also affected in transfusional siderosis

iron overload (i.e. after transfusion of >100 units of blood) is the SI of the pancreas affected [55].

Comparable findings are observed with cardiac MR imaging. Whereas no changes in imaging characteristics are seen in the myocardium of patients with transfusional siderosis, in cases of hemochromatosis the myocardium usually demonstrates decreased SI.

Transfusional siderosis frequently occurs in patients suffering from hematological diseases in which erythrocyte transfusion needs to be performed regularly [52].

In addition, parenteral iron overload may occur in patients with rhabdomyolysis in which the bound iron of myoglobin is liberated into the blood and absorbed secondarily by reticuloendothelial cells [53] (Fig. 12, 13).

9.4.3 Iron Overload in Liver Cirrhosis

A mild accumulation of iron is frequently found in cirrhotic livers, particularly if the cirrhosis is induced by alcohol abuse. However, since the SI of the parenchyma is not greatly reduced in such cases, the misdiagnosis of hemochromatosis, in which the parenchyma demonstrates a massive reduction of SI, can be avoided [4].

9.4.4 Hemolysis

Systemic accumulation of iron may be caused by hemolysis in which hemoglobin is liberated from red blood cells. While extravascular (e.g. splenic) hemolysis leads to a reticuloendothelial deposition of iron, intravascular hemolysis causes hepatocellular accumulation, since the released hemoglobin binds to plasma haptoglobin, which is taken up by hepatocytes. If the serum hemoglobin level exceeds the transport capacity of haptoglobin, it is filtered through renal glomeruli, reabsorbed and stored within proximal convoluted tubule epithelial cells. For this reason, intravascular hemolysis is characterized by an accumulation of iron in the liver and renal cortex, but not in the spleen. Dis-

eases which lead to intravascular hemolysis and thus show this characteristic imaging pattern include paroxysmal nocturnal hemoglobinuria and sickle cell disease [61].

9.5 Vascular Pathologies

9.5.1 Portal Vein Thrombosis

The etiology of portal vein thrombosis falls into the Virchow trias, comprising reduced blood flow within the vessel, changes in the consistency of blood which affects flow properties, and pathologies of the vessel wall. Thus, etiological factors of portal vein thrombosis are slow flow secondary to cirrhosis, obstruction of the vessel by porto-hepatic lymphadenopathy, direct invasion by cancer, inflammatory changes secondary to pancreatitis, sclerosing cholangitis, abdominal infections, polycytemia vera and benign masses [1, 45, 51, 75].

While portal vein thrombosis often occurs in cases of HCC, it may also be the result of other primary or secondary neoplasms of the liver.

In cases of portal vein occlusion, portal perfusion is maintained due to the periportal collateral veins. With progression, the draining collaterals dilate while the thrombosed portal vein retracts to form a "cavernous transformation" which on US may be misinterpreted as patency of the portal vein [44, 76].

MRI is an accurate method to non-invasively depict portal-venous blood flow, intraluminal thrombus and collateral circulation and can be generally carried out without the administration of contrast medium. Moreover, as it is not restricted by body habitus, ascites or abdominal gas, it is superior to duplex sonography [19, 34, 67, 81, 82].

MRI not only aids in the diagnosis of portal vein thrombosis, but also in the planning of shunt surgery and hepatic transplantation, and in the monitoring of shunt patency following surgery [5, 17, 60].

Patency of the portal vein can be interpreted on spin-echo images by the demonstration of a flow void within the vessel. However, increased SI is frequently seen at the confluence of the splenic and the mesenteric veins. In cases of portal vein occlusion, the thrombosis is usually isointense compared to the liver parenchyma on T1-weighted images, and hyperintense on T2-weighted images [34].

A diagnosis of portal vein thrombosis is likely when the lesion is present on all sequences with comparable size and shape. The suspicion of portal vein thrombosis may be confirmed or excluded following acquisition of flow sensitive gradient echo images [56].

Chronic occlusion of a branch of the portal vein may be accompanied by segmental atrophy and compensatory hypertrophy of other segments [35].

Tumoral obstruction of lobal or segmental portal branches may present on T2-weighted images as wedge-shaped regions of increased SI. In such cases the apex usually points to the obstructing tumor, and therefore, MR images should be examined carefully [31].

In livers with preexisting fatty infiltration, the area affected by segmental portal vein obstruction shows a decreased accumulation of fat, as fat deliverance correlates with portal flow [2] (Fig. 14).

9.5.2 Budd-Chiari Syndrome (Acute, Chronic)

Budd-Chiari syndrome is defined as an obstruction of the venous outflow from the sinusoidal bed of the liver. It leads to portal hypertension, ascites and progressive hepatic failure [57].

The treatment of Budd-Chiari syndrome depends on the cause of the obstruction and, hence, careful examination of the hepatic veins, the inferior caval vein (ICV) and the right atrium is necessary [37, 73]. For example, a membranous occlusion of the ICV is a common cause of obstruction in the Asian population. In such cases, membranectomy should be performed. On the other hand, if a solitary occlusion of the ICV is present without the hepatic veins being affected, a shunting from the ICV to the right atrium should be the primary treatment of choice.

If only the hepatic veins are obstructed, a shunt between the superior mesenteric vein and the ICV, a so-called "mesocaval shunt", may be inserted to lower the pressure in the portal-venous system. On the other hand, when both the ICV and the hepatic veins are occluded, the appropriate therapy would be a bypass from the superior mesenteric vein to the right atrium, a so-called "mesoatrial shunt". For patients in whom a neoplasm is the primary cause of Budd-Chiari syndrome, extensive surgery is often contraindicated.

Given the different therapeutic approaches available, accurate imaging in Budd-Chiari syndrome not only serves for diagnosis but should also indicate the most appropriate therapy for the patient. Ultrasonography may be used to detect hepatic vein occlusion (Fig. 15), however, the ICV is not reliably visualized on ultrasonography and ascites in Budd-Chiari syndrome may interfere with the appropriate depiction of the hepatic confluence [41].

In contrast, MRI, which is not affected by the individual constitution of the patient, represents a non-invasive imaging modality for the evaluation

of both the intra- and extrahepatic vascular anatomy in Budd-Chiari syndrome and the possible intra- or extrahepatic causal pathologies [38].

However, if portocaval shunting is planned, the examination frequently has to be completed by means of venography in order to determine the presence or absence of a significant pressure gradient across the ICV. Even if a patent ICV is demonstrated by non-invasive imaging modalities, a pressure gradient may be present, in most cases due to hypertrophy of the caudate lobe. In such cases, portocaval shunting is contraindicated and shunting should be performed from the portal-venous system to either the right atrium or the left inferior pulmonary vein [5, 60, 61].

Vascular findings. MR imaging is an accurate modality for the demonstration of the diverse pattern of vascular changes indicative of Budd-Chiari syndrome. Frequently, a significant reduction in caliber or a complete absence of hepatic veins may be found or, alternatively, newly arising intrahepatic collateral veins with a comma-like shape may be seen. Other findings include a constriction of the intrahepatic ICV or, less commonly, the hepatic veins appear patent but do not show any connection to the ICV. Since thrombus formation in the hepatic veins may be located some centimeters from the ICV, patent central hepatic veins and a normal hepatic confluence may be seen.

MRI not only permits the diagnosis of Budd-Chiari syndrome but may also reveal the etiological cause. For example, it is possible to visualize an obstruction of the ICV or the right atrium caused by neoplasms, such as primary sarcomas of the vein, or tumors of the liver, kidney or adrenal gland, and the resulting tumor thrombus formation.

Increased coagulability of the blood causing thrombosis of the hepatic veins (such as in polycytemia vera or paroxysmal nocturnal hemoglobinuria), may be identified by MRI. In patients with polycytemia vera, a diffusely decreased intensity of the bone marrow together with splenomegaly can point to the diagnosis. In patients suffering from paroxysmal nocturnal hemoglobinuria, an SI decreased in the liver and renal cortex but normal in the spleen is observed [57, 69].

Morphologic features. In most cases of Budd-Chiari syndrome, the hepatic venous outflow is not eliminated completely since a variety of accessory hepatic veins may drain above or below the principal site of obstruction. The most frequent accessory site of venous drainage occurs at the inferior right hepatic vein and the veins of the caudate lobe that drain directly into the inferior portion of the ICV. Additional collaterals draining to other systemic veins may be present, such as the azygos and the vertebral and/or intercostal veins which show characteristic enlargement if present. Reversed flow in some portal vein branches may occur, since connections between the portal and the hepatic veins are relatively common [62, 70]. However, the main portal flow usually remains antegrade [30]. Since some hepatic venous drainage is usually preserved for the caudate lobe and for central portions of the right and left liver lobes, a compensatory hypertrophy of the caudate lobe may develop. However, this may lead to a secondary obstruction of the ICV. Although subcapsular hepatic veins may also contribute to collateral blood flow, the resulting venous drainage is usually insufficient to prevent peripheral atrophy of the liver.

In patients with a completely obstructed venous outflow, shunting is performed from the hepatic veins and arteries to the portal veins, which thereafter demonstrate reversed flow [11].

As a result of collateral venous drainage, Budd-Chiari syndrome is typically associated with peripheral hepatic atrophy and, conversely, caudate and central hypertrophy which, together, may lead to a displacement of the porta hepatis towards the anterior portion of the liver [20]. These morphological changes can be visualized on MRI, together with a clear depiction of the occluded liver veins. Other findings include regional differences in liver SI due to central lobular necrosis and hepatocellular fat or iron content. Dynamic MR imaging of acute Budd-Chiari syndrome after bolus injection of extracellular contrast agents (Fig. 16) frequently reveals atypical parenchymal enhancement, which indirectly indicates the presence of increased vascular resistance. Unlike patients with liver cirrhosis, patients with acute Budd-Chiari syndrome demonstrate acute clinical symptoms and a large tender liver without signs of nodular changes. However, in chronic disease, nodular regenerative hyperplasia may develop which may lead to the misdiagnosis of liver cirrhosis [33] (Fig. 17).

Another disease leading to hepatic venous obstruction is the so-called "hepatic veno-occlusive disease". This is often caused by chemotherapy, especially after bone marrow transplantation [8]. In this disease, the post-sinusoidal venules are usually obstructed while the major hepatic veins and ICV do not show pathological changes and remain patent (Fig. 18). Since diagnosis by means of MRI is difficult in most cases, confirmation needs to be established either by histopathological examination of a biopsy or by wedge hepatic venography. Dynamic CT and MR imaging of the liver in the arterial and portal-venous phases may indicate an increased arterial perfusion of the affected regions and a prolonged liver transit time of the contrast agent [60] (Figs. 19, 20).

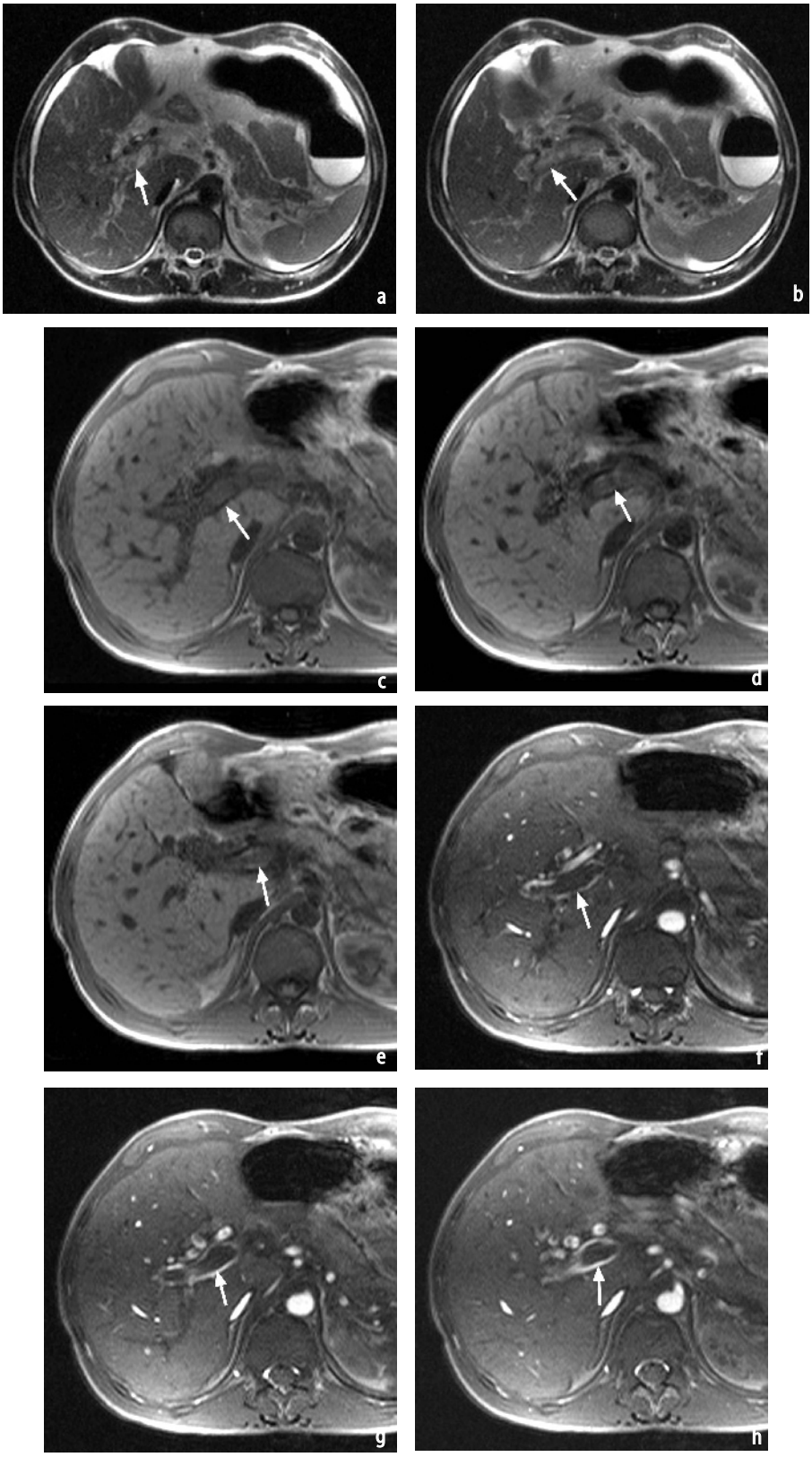

Fig. 14a-r. Subacute portal vein thrombosis. T2-weighted images (**a**, **b**) reveal intermediate to high SI in the area of the portal vein without any flow void (*arrows*). Additionally, perihepatic and perisplenic ascites can be noted. On T1-weighted images (**c**-**e**), again no flow void in the portal vein can be noted although a mass with hypointense and hyperintense areas (*arrows*) does seem to be present in the portal vein. Flow sensitive gradient echo images (**f**-**k**) clearly depict a thrombus within the portal vein (*arrows*) with some residual peripheral flow indicated by a peripheral high SI rim. The thrombosis can be followed to the confluence of the mesenteric and splenic veins. Irregular enhancement of the liver parenchyma can be noted on arterial phase images after contrast agent injection (**l**-**n**). On portal-venous phase images (**o**-**r**), again the thrombus in the portal vein is clearly depicted and can be followed into the periphery (*arrow*). Note that the mesenteric vein is also occluded (**r**, *arrow*)

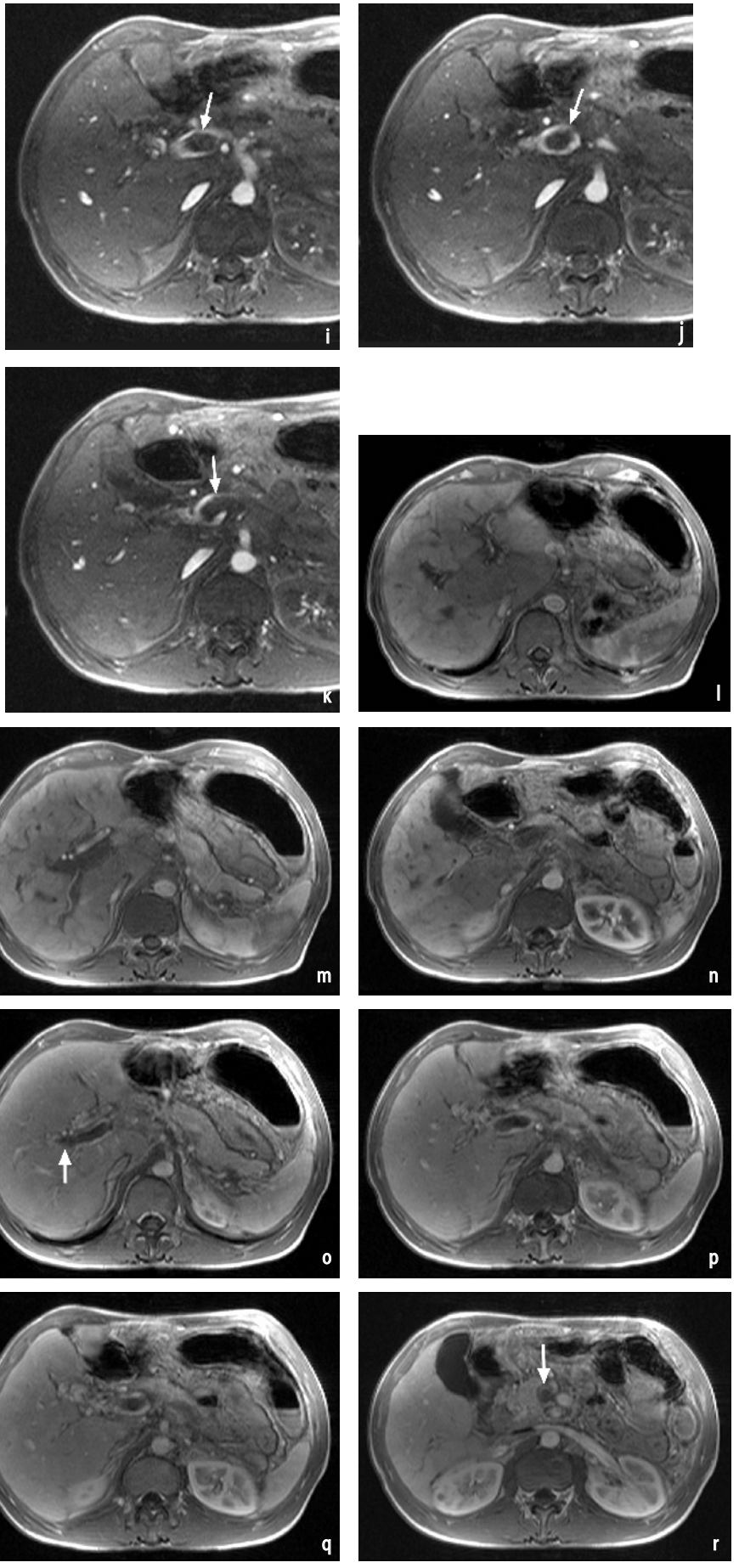
i
j
k
l
m
n
o
p
q
r

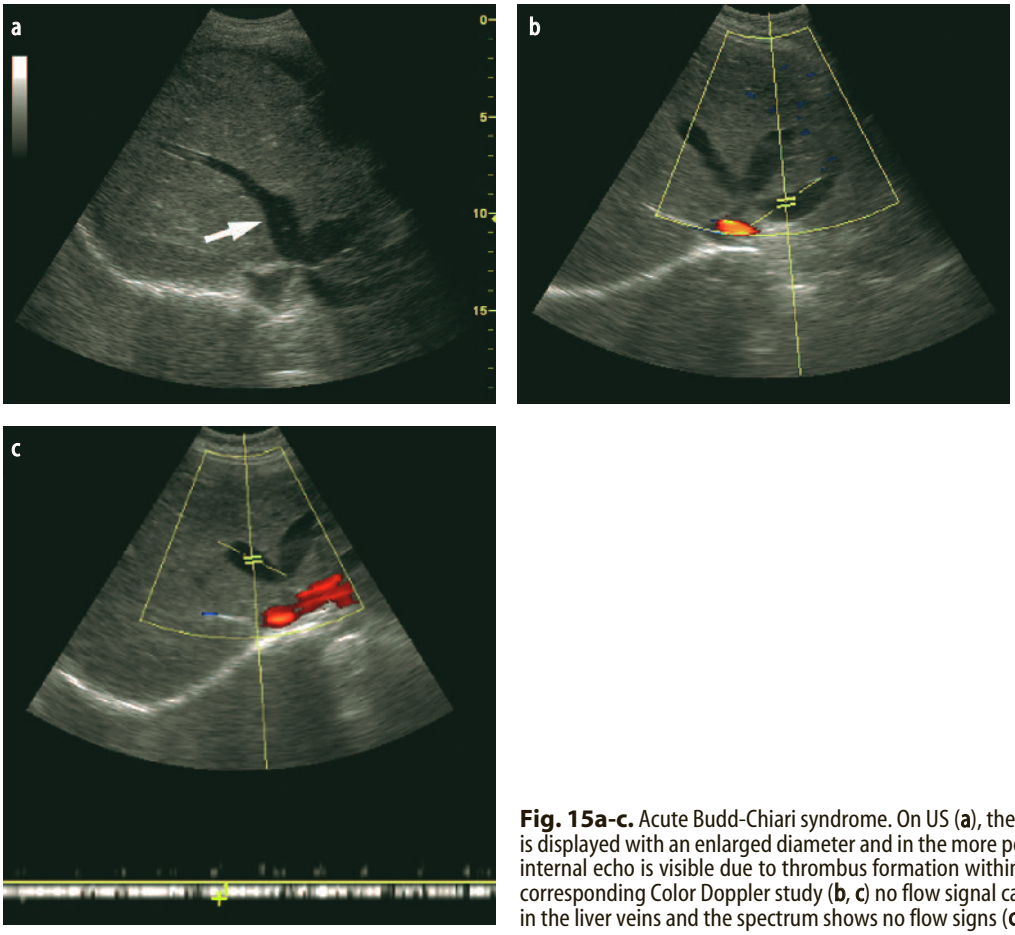

Fig. 15a-c. Acute Budd-Chiari syndrome. On US (**a**), the middle hepatic vein is displayed with an enlarged diameter and in the more peripheral parts some internal echo is visible due to thrombus formation within the vessels. On the corresponding Color Doppler study (**b**, **c**) no flow signal can be detected within the liver veins and the spectrum shows no flow signs (**c**)

Fig. 16a-j. Acute Budd-Chiari syndrome. T2-weighted images (**a**, **b**) reveal diffuse swelling of the liver and perihepatic and perisplenic ascites. The large intrahepatic liver veins show no signs of flow void and the periphery of the liver parenchyma, especially in the right liver lobe, shows increased SI. On the corresponding T1-weighted images (**c**, **d**), again the liver veins are depicted only as small hypointense bands and low SI areas (*arrows*) can be noted in the more caudal parts of the liver. On contrast-enhanced images during the arterial phase (**e**, **f**), only enhancement of the periphery of the liver can be seen (*arrows*). The more central parts do not show obvious enhancement due to increased vascular resistance. Still no enhancement of portal-venous branches is visible on the portal-venous phase images (**g**, **h**), although enhancement of the central parts of the liver can now be noted. Homogenous enhancement of the left liver lobe and central parts of the right liver lobe is more apparent on equilibrium phase images (**i**, **j**). Peripheral hypointense areas (*arrows*) can still be depicted in the right liver lobe in this phase. These areas correspond to liver necrosis due to acute Budd-Chiari syndrome

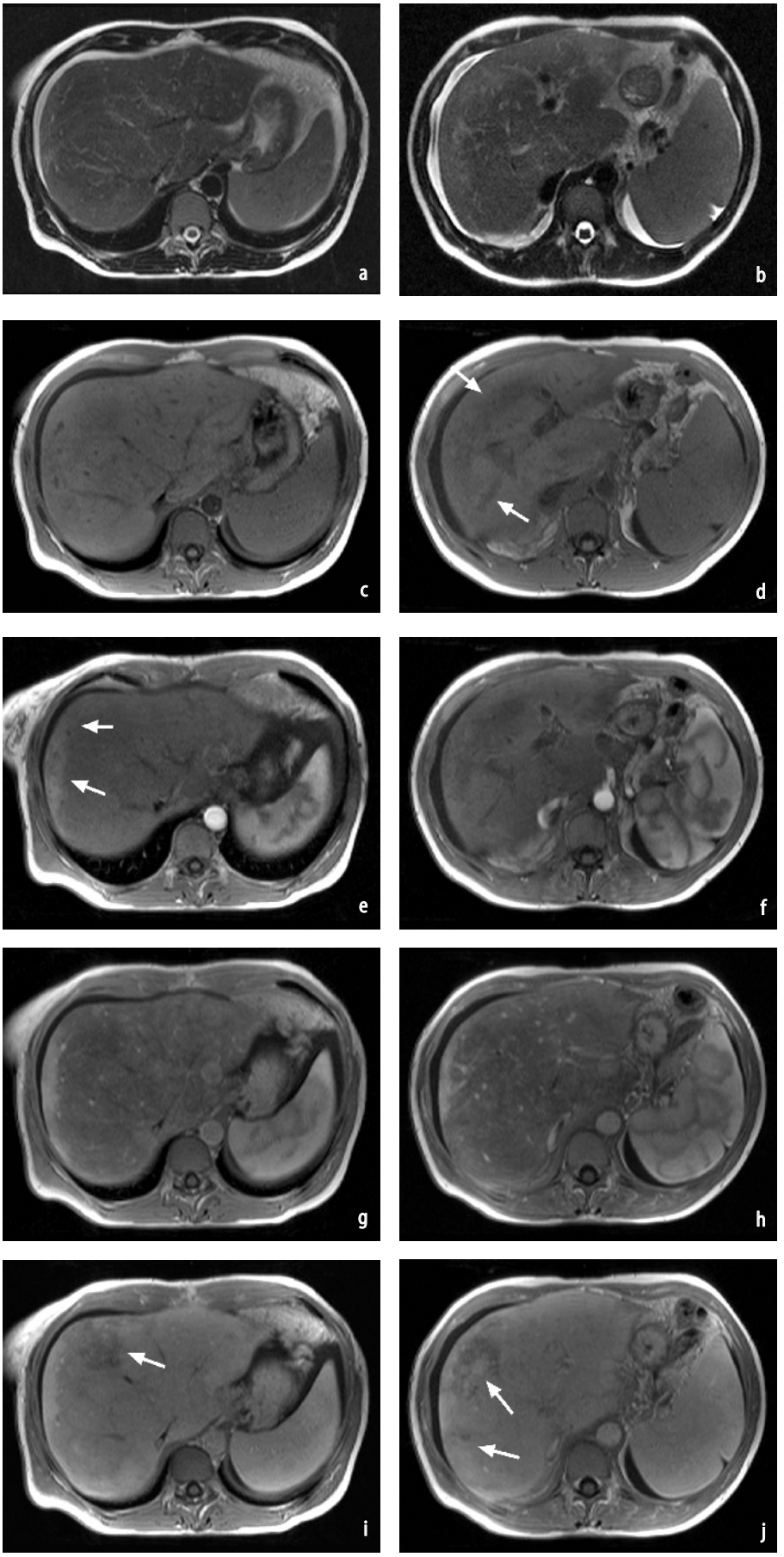
a
b
c
d
e
f
g
h
i
j

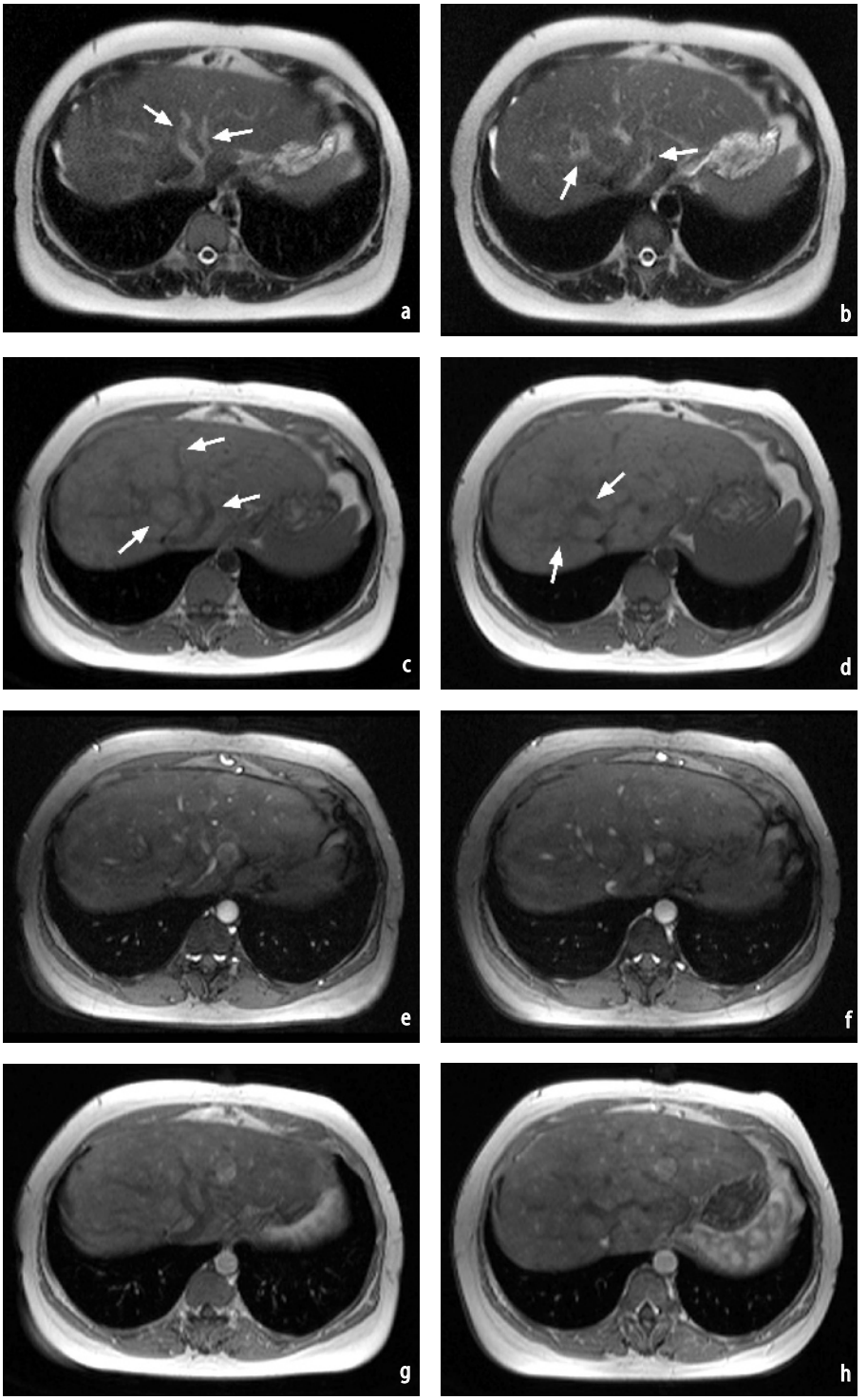
a
b
c
d
e
f
g
h

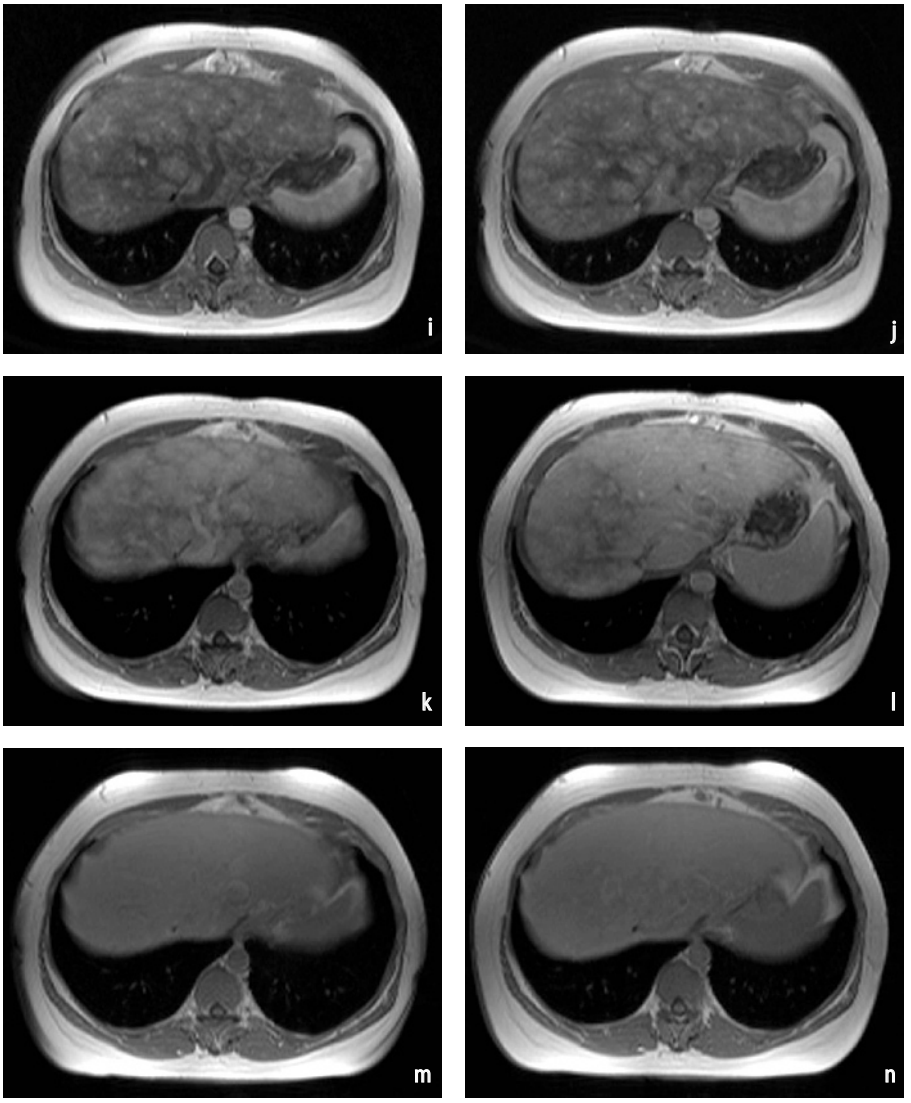

Fig. 17a-n. Longstanding Budd-Chiari syndrome. Unenhanced T2-weighted images (**a**, **b**) reveal a comma-like shape of the intrahepatic collateral veins (*arrows*) that is typical of Budd-Chiari syndrome. These veins (*arrows*) appear with low SI on unenhanced T1-weighted images (**c**, **d**) due to flow void, and show a flow signal on flow sensitive gradient echo sequences (**e**, **f**). As in the case of acute Budd-Chiari syndrome (see Fig. 16), delayed enhancement of the liver can be noted on dynamic imaging. Although diffuse enhancement of the liver parenchyma can already be observed on arterial phase images (**g**, **h**), full homogeneous enhancement is not yet seen even on portal-venous phase images (**i**, **j**). On the other hand, nodular enhancement due to regenerative processes is visible. Some hypointense areas in the liver parenchyma are still apparent on images acquired 5 min after contrast agent injection (**k**, **l**) indicating decreased blood flow. Isointensity with the surrounding liver tissue is finally observed on images acquired 15 min after contrast agent administration (**m**, **n**)

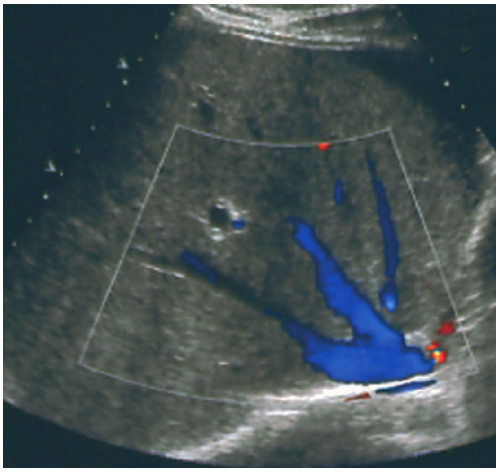

Fig. 18. Hepatic veno-occlusive disease in a 21-year old patient during chemotherapy for acute lymphoblastic leukemia. On Color Doppler US, the right hepatic vein is narrowed, however the ICV and hepatic veins are patent

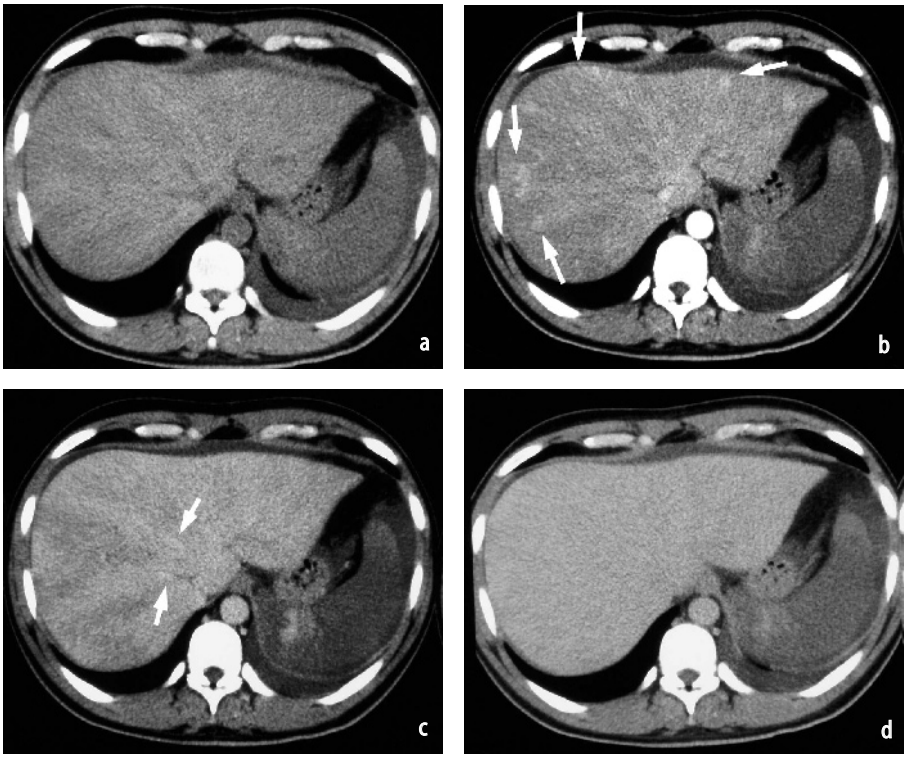

Fig. 19a-d. Hepatic veno-occlusive disease. Same case as demonstrated in Fig. 18. On the unenhanced CT scan (**a**), the liver parenchyma shows heterogeneous density and streaky hypodense areas. In the arterial phase after contrast medium administration (**b**), the liver shows heterogeneous enhancement with some peripheral areas (*arrows*) of increased arterial perfusion. On the portal-venous phase scan (**c**), again the streaky signal of the liver parenchyma is visible and the liver veins are poorly delineated (*arrows*). The diameter of the hepatic veins seems to be reduced and splenic infarction is apparent. Perfusion-related differences in density of the liver parenchyma cannot be visualized in the equilibrium phase (**d**)

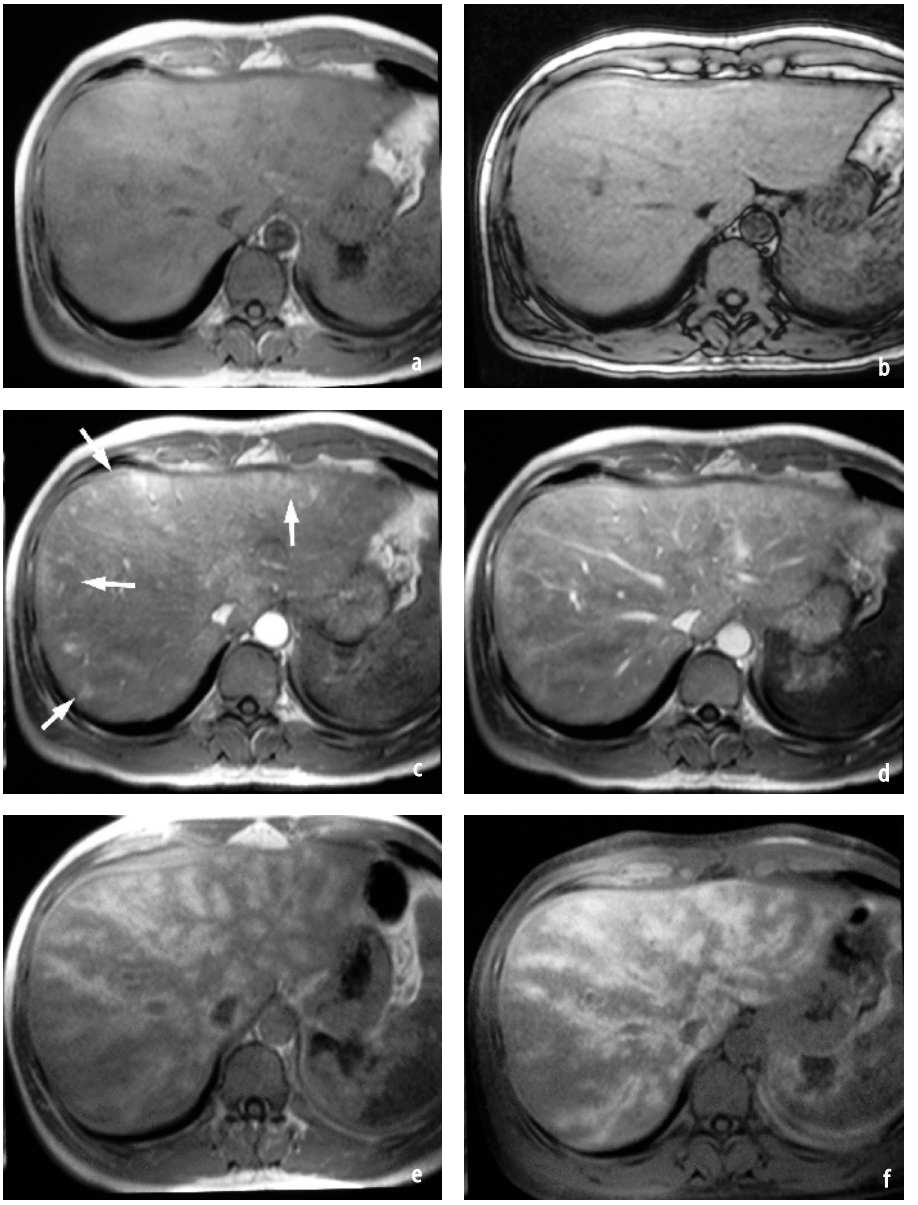

Fig. 20a-f. Hepatic veno-occlusive disease. Same case as demonstrated in Fig. 18 and 19. On the pre-contrast T1-weighted image (**a**), the liver shows heterogeneous SI with some areas of increased signal and other areas of decreased signal. The T1-weighted out-of-phase image (**b**) reveals that these differences of SI are not related to fatty liver, since no signal drop is observed. The hepatic veins near the confluence are patent. On the arterial phase image (**c**) after the bolus injection of Gd-BOPTA (0.1 mmol/kg BW), the liver shows heterogeneous, predominantly peripheral arterial perfusion (*arrows*), most likely related to increased intrahepatic resistance. In the portal-venous phase (**d**), the liver veins are contrasted but a very heterogeneous enhancement of the liver parenchyma is seen, with large, streaky areas of decreased perfusion. Note the missing enhancement of large areas of the spleen due to splenic infarction. The T1-weighted (**e**) and T1-weighted fat suppressed (**f**) images acquired in the hepatobiliary phase reveal streaky enhancement of the liver with preferential uptake of Gd-BOPTA in the peri-venous liver tissue. Uptake of Gd-BOPTA in more distant areas of the liver is considerably more limited due to veno-occlusive disease

9.5.3 Arterio-Venous Malformations

Arterio-venous (AV) malformations of the liver are rare and are caused either iatrogenically in liver biopsy and liver surgery, or are distributed diffusely in patients with hereditary hemorrhagic teleangiectasia (HHT; "Osler's disease") [23]. In general, AV-malformations may occur between the hepatic artery and the hepatic vein, as well as between the hepatic artery and the portal-venous system.

Typical findings on dynamic MR images of the liver for singular AV-malformations post-biopsy or surgery include a dilatation of the draining hepatic vein and early enhancement of the hepatic veins (Fig. 21). Shunts between the hepatic artery and the portal-venous system typically lead to increased portal-venous pressure and thus to the usual findings of portal hypertension [21].

In contrast, AV-malformations in Osler's disease are diffusely distributed throughout the liver and may be associated with enlargement of the hepatic artery and increased tortuousity of the vessels in the liver hilum and in the central portions of the liver lobes. In Osler's disease, increased arterial perfusion of the liver tissue leads frequently to secondary nodular hypertrophy that may be misinterpreted as a malignant hepatic tumor. These pseudotumors, as in focal nodular hyperplasia (FNH), represent a localized overgrowth of hepatocellular tissue and are not real liver tumors. Dynamic MRI reveals that these lesions show strong arterial phase enhancement and subsequent isointensity with the surrounding liver tissue in the portal-venous and equilibrium phases. Normal enhancement of the affected tissue in the hepatobiliary phase can be noted with the use of contrast agents with hepatocellular properties such as Gd-BOPTA [71] (Fig. 22).

Severe cases of AV shunting in Osler's disease may lead to right heart failure and, at present, the only curative treatment is liver transplantation [6].

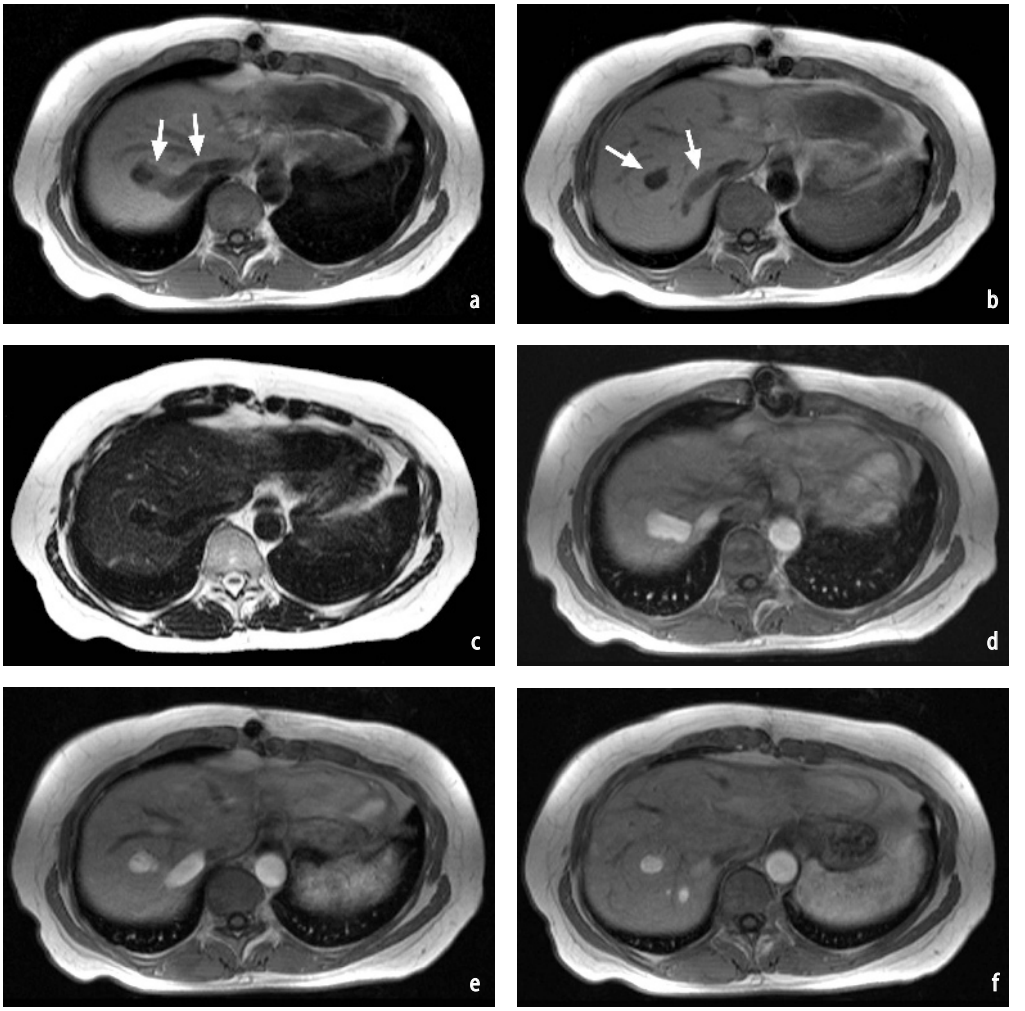

Fig. 21a-f. AV shunt of the liver. Unenhanced T1-weighted images (**a**, **b**) reveal dilatation of the draining hepatic veins in AV shunting (*arrows*). The corresponding T2-weighted image (**c**) again reveals flow void in the vessels. Early enhancement of the draining liver veins indicating an AV malformation can be depicted clearly on early arterial phase images (**d**-**f**) after intravenous injection of paramagnetic contrast agent

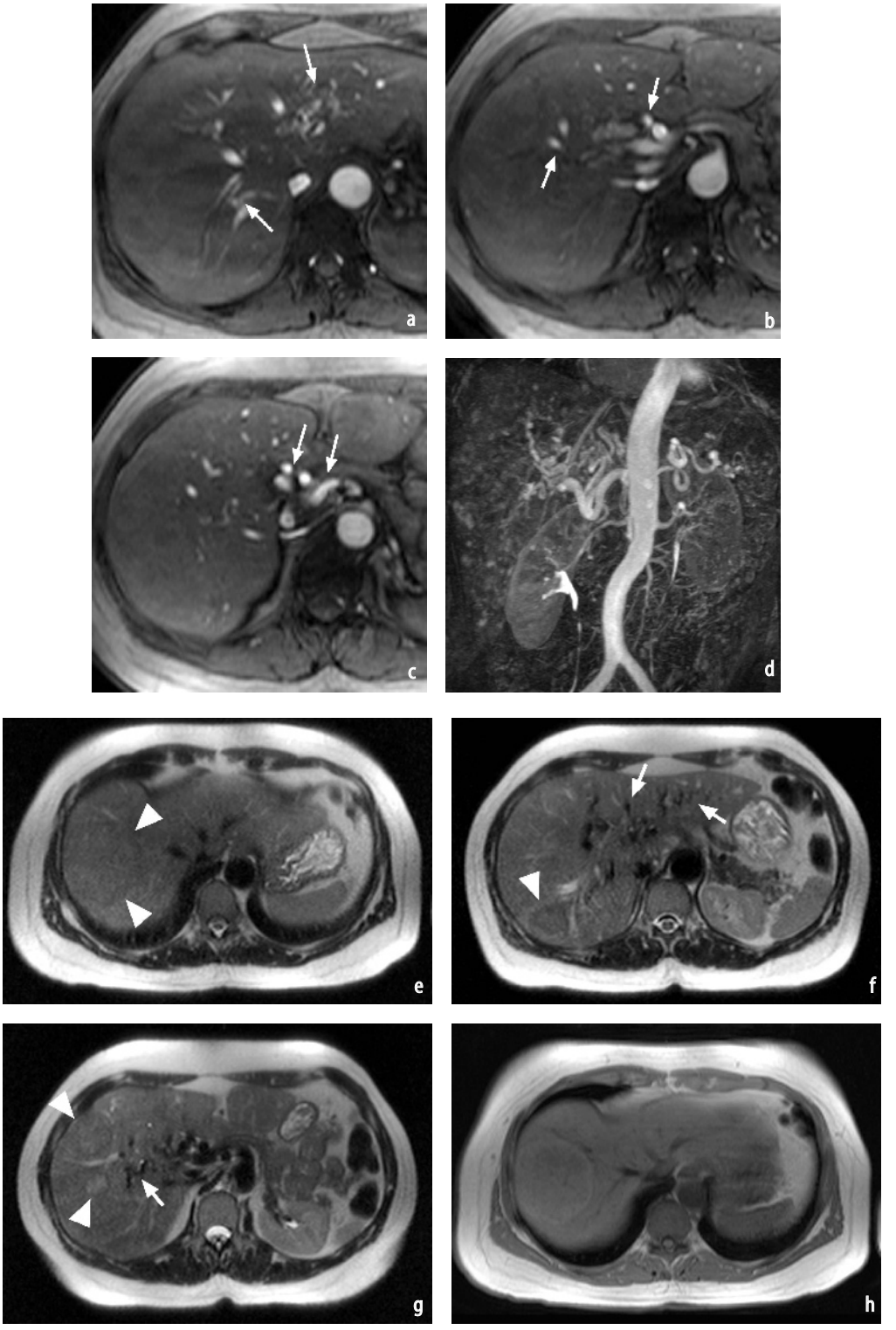

Fig. 22a-r. Diffusely distributed AV-malformations in a patient with Osler's disease and development of hyperplastic nodules. Flow sensitive gradient echo images (**a**-**c**) reveal enlarged tortuous vessels in the liver hilum and in the more centrally located liver parenchyma (*arrows*), indicating increased flow in the hepatic artery. On contrast-enhanced MRA (**d**), the dilatation of the hepatic artery is even more obvious. Again, the tortuous vessels and diffusely distributed small AV malformations in the liver are observed. On T2-weighted images (**e**-**g**) areas of flow void in the liver can be noted, indicating increased flow in branches of the hepatic artery (*arrows*). Additionally, some nodular-appearing liver lesions (*arrowheads*) in the right liver lobe can be seen. On pre-contrast T1-weighted images (**h**-**j**) these liver tumors show an almost isointense SI compared with the surrounding liver tissue. However, in the arterial phase after injection of Gd-BOPTA (**k**-**m**) these liver lesions (*arrows*) are clearly hypervascular. On portal-venous phase images (**n**, **o**) the lesions are isointense with the surrounding liver tissue. In the hepatobiliary phase one hour after injection of Gd-BOPTA (**p**-**r**), the lesions appear hyperintense compared to the surrounding liver tissue due to uptake of Gd-BOPTA into hepatocyctes. These liver lesions correspond to a localized overgrowth of hepatocellular tissue similar to that which occurs in FNH. The lesions appear hyperintense in the hepatobiliary phase due to the delayed excretion of the contrast agent into the newly formed bile ductules

→

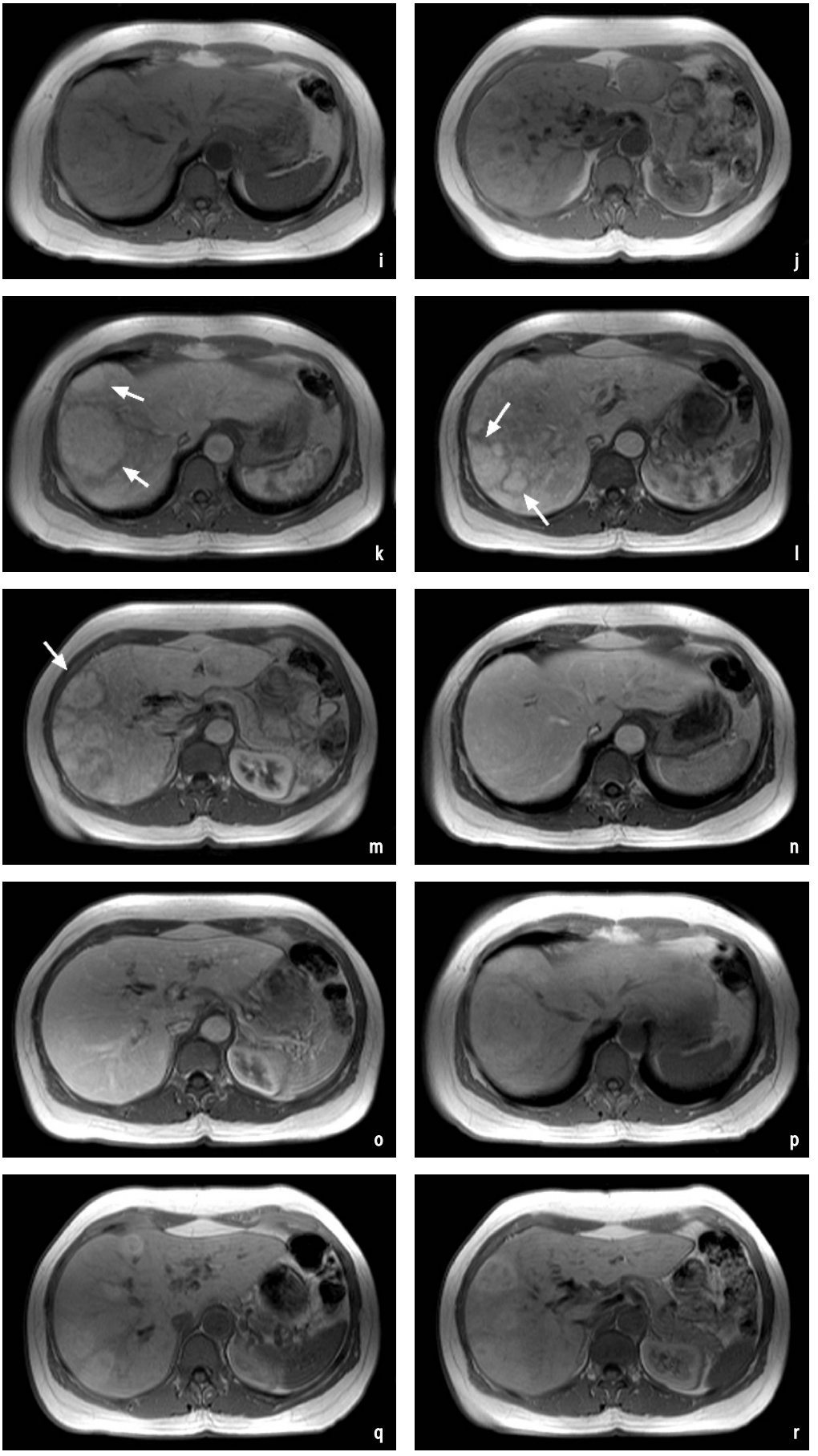
i
j
k
l
m
n
o
p
q
r

References

1. Alpern MB, Rubin JM, Williams DM, Capek P. Porta hepatis: duplex Doppler US with angiographic correlation. Radiology 1987 Jan;162(1 Pt 1):53-6
2. Arai K, Matsui O, Takashima T, Ida M, Nishida Y. Focal spared areas in fatty liver caused by regional decreased portal flow. AJR Am J Roentgenol 1988 Aug;151(2):300-2
3. Bassett ML, Halliday JW, Powell LW. Genetic hemochromatosis. Semin Liver Dis 1984 Aug;4(3):217-27
4. Bassett ML, Halliday JW, Powell LW. Value of hepatic iron measurements in early hemochromatosis and determination of the critical iron level associated with fibrosis. Hepatology 1986 Jan-Feb;6(1):24-9
5. Bernardino ME, Steinberg HV, Pearson TC, Gedgaudas-McClees RK, Torres WE, Henderson JM. Shunts for portal hypertension: MR and angiography for determination of patency. Radiology 1986 Jan;158(1):57-61
6. Boillot O, Bianco F, Viale JP, Mion F, Mechet I, Gille D, Delaye J, Paliard P, Plauchu H. Liver transplantation resolves the hyperdynamic circulation in hereditary hemorrhagic telangiectasia with hepatic involvement. Gastroenterology 1999 Jan;116(1):187-92
7. Brady TM, Gross BH, Glazer GM, Williams DM. Adrenal pseudomasses due to varices: angiographic-CT-MRI-pathologic correlations. AJR Am J Roentgenol 1985 Aug;145(2):301-4
8. Brown BP, Abu-Yousef M, Farner R, LaBrecque D, Gingrich R. Doppler sonography: a noninvasive method for evaluation of hepatic venocclusive disease. AJR Am J Roentgenol 1990 Apr;154(4):721-4
9. Caldwell SH, Hespenheide EE, Harris D, de Lange EE. Imaging and clinical characteristics of focal atrophy of segments 2 and 3 in primary sclerosing cholangitis. J Gastroenterol Hepatol 2001 Feb; 16(2):220-4
10. Chapman RW, Arborgh BA, Rhodes JM, Summerfield JA, Dick R, Scheuer PJ, Sherlock S. Primary sclerosing cholangitis: a review of its clinical features, cholangiography, and hepatic histology. Gut 1980 Oct;21(10):870-7
11. Chawla Y, Dilawari JB, Mitra SK, Khanna SK. The porta-splenic venous system in the Budd-Chiari syndrome. Trop Gastroenterol 1988 Jan-Mar;9(1):14-7
12. Chezmar JL, Nelson RC, Malko JA, Bernardino ME. Hepatic iron overload: diagnosis and quantification by noninvasive imaging. Gastrointest Radiol 1990 Winter;15(1):27-31
13. Dachman AH, Ros PR, Goodman ZD, Olmsted WW, Ishak KG. Nodular regenerative hyperplasia of the liver: clinical and radiologic observations. AJR Am J Roentgenol 1987 Apr;148(4):717-2
14. Di Bisceglie AM, Martin P, Kassianides C, Lisker-Melman M, Murray L, Waggoner J, Goodman Z, Banks SM, Hoofnagle JH. Recombinant interferon alfa therapy for chronic hepatitis C. A randomized, double-blind, placebo-controlled trial. N Engl J Med 1989 Nov 30;321(22):1506-10
15. Dietze O, Vogel W, Braunsperger B, Margreiter R. Liver transplantation in idiopathic hemochromatosis. Transplant Proc 1990 Aug;22(4):1512-3
16. Dolbey CH. Hemochromatosis: a review. Clin J Oncol Nurs 2001 Nov-Dec;5(6):257-60
17. Edelman RR, Zhao B, Liu C, Wentz KU, Mattle HP, Finn JP, McArdle C. MR angiography and dynamic flow evaluation of the portal-venous system. AJR Am J Roentgenol 1989 Oct;153(4):755-60
18. Elizondo G, Weissleder R, Stark DD, Guerra J, Garza J, Fretz CJ, Todd LE, Ferrucci JT. Hepatic cirrhosis and hepatitis: MR imaging enhanced with superparamagnetic iron oxide. Radiology 1990 Mar;174(3 Pt 1):797-801
19. Finn JP, Edelman RR, Jenkins RL, Lewis WD, Longmaid HE, Kane RA, Stokes KR, Mattle HP, Clouse ME. Liver transplantation: MR angiography with surgical validation. Radiology 1991 Apr;179(1):265-9
20. Fisher B, Szuch P, Levine M, Saffer E, Fisher ER. The intestine as a source of a portal blood factor responsible for liver regeneration. Surg Gynecol Obstet 1973 Aug;137(2):210-4
21. Garcia-Tsao G, Korzenik JR, Young L, Henderson KJ, Jain D, Byrd B, Pollak JS, White RI Jr. Liver disease in patients with hereditary hemorrhagic telangiectasia. N Engl J Med 2000 Sep 28;343(13):931-6
22. Garra BS, Shawker TH, Chang R, Kaplan K, White RD. The ultrasound appearance of radiation-induced hepatic injury. Correlation with computed tomography and magnetic resonance imaging. J Ultrasound Med 1988 Nov;7(11):605-9
23. Geisthoff UW, Schneider G, Fischinger J, Plinkert PK. Hereditary hemorrhagic telangiectasia (Osler´s disease). An interdisciplinary challenge. HNO 2002 Feb;50(2):114-28
24. Giorgio A, Amoroso P, Lettieri G, Fico P, de Stefano G, Finelli L, Scala V, Tarantino L, Pierri P, Pesce G. Cirrhosis: value of caudate to right lobe ratio in diagnosis with US. Radiology 1986 Nov;161(2):443-5
25. Goldberg HI, Moss AA, Stark DD, McKerrow J, Engelstad B, Brito A. Hepatic cirrhosis: magnetic resonance imaging. Radiology 1984 Dec;153(3):737-9
26. Goyal AK, Pokharna DS, Sharma SK. Ultrasonic diagnosis of cirrhosis: reference to quantitative measurements of hepatic dimensions. Gastrointest Radiol 1990 Winter;15(1):32-4
27. Groszmann RJ, Atterbury CE. The pathophysiology of portal hypertension: a basis for classification. Semin Liver Dis 1982 Aug;2(3):177-86
28. Hadjis NS, Adam A, Blenkharn I, Hatzis G, Benjamin IS, Blumgart LH. Primary sclerosing cholangitis associated with liver atrophy. Am J Surg 1989 Jul;158(1):43-7
29. Holland HK, Spivak JL. Hemochromatosis. Med Clin North Am 1989 Jul;73(4):831-45
30. Hosoki T, Kuroda C, Tokunaga K, Marukawa T, Masuike M, Kozuka T. Hepatic venous outflow obstruction: evaluation with pulsed duplex sonography. Radiology 1989 Mar;170(3 Pt 1):733-7
31. Itai Y, Ohtomo K, Furui S, Minami M, Yoshikawa K, Yashiro N. Lobar intensity differences of the liver on MR imaging. J Comput Assist Tomogr 1986 Mar-Apr;10(2):236-41
32. Itai Y, Ohtomo K, Kokubo T, Makita K, Okada Y, Machida T, Yashiro N. CT and MR imaging of fatty tumors of the liver. J Comput Assist Tomogr 1987 Mar-Apr;11(2):253-7
33. Kane R, Eustace S. Diagnosis of Budd-Chiari syn-

drome: comparison between sonography and MR angiography. Radiology 1995 Apr;195(1):117-21
34. Levy HM, Newhouse JH. MR imaging of portal vein thrombosis. AJR Am J Roentgenol 1988 Aug;151(2):283-6
35. Lorigan JG, Charnsangavej C, Carrasco CH, Richli WR, Wallace S. Atrophy with compensatory hypertrophy of the liver in hepatic neoplasms: radiographic findings. AJR Am J Roentgenol 1988 Jun;150(6):1291-5
36. Marn CS, Glazer GM, Williams DM, Francis IR. CT-angiographic correlation of collateral venous pathways in isolated splenic vein occlusion: new observations. Radiology 1990 May;175(2):375-80
37. Martin LG, Henderson JM, Millikan WJ Jr, Casarella WJ, Kaufman SL. Angioplasty for long-term treatment of patients with Budd-Chiari syndrome. AJR Am J Roentgenol 1990 May;154(5):1007-10
38. Matsui O, Kadoya M, Takashima T, Kameyama T, Yoshikawa J, Tamura S. Intrahepatic periportal abnormal intensity on MR images: an indication of various hepatobiliary diseases. Radiology 1989 May;171(2):335-8
39. Matsui O, Kadoya M, Kameyama T, Yoshikawa J, Arai K, Gabata T, Takashima T, Nakanuma Y, Terada T, Ida M. Adenomatous hyperplastic nodules in the cirrhotic liver: differentiation from hepatocellular carcinoma with MR imaging. Radiology 1989 Oct;173(1):123-6
40. McLaren GD, Muir WA, Kellermeyer RW. Iron overload disorders: natural history, pathogenesis, diagnosis and therapy. CRC Crtit. Rev. Clin. Lab. Sci. 1984; 19:205-266.
41. Menu Y, Alison D, Lorphelin JM, Valla D, Belghiti J, Nahum H. Budd-Chiari syndrome: US evaluation.Radiology 1985 Dec;157(3):761-4
42. Mitchell DG. MR imaging of cirrhosis and its complications. Abdom Imaging 2000 Sep-Oct;25(5):455
43. Mostbeck GH, Wittich GR, Herold C, Vergesslich KA, Walter RM, Frotz S, Sommer G. Hemodynamic significance of the paraumbilical vein in portal hypertension: assessment with duplex US. Radiology 1989 Feb;170(2):339-42
44. Nakao N, Miura K, Takahashi H, Miura T, Ashida H, Ishikawa Y, Utsunomiya J. Hepatic perfusion in cavernous transformation of the portal vein: evaluation by using CT angiography. AJR Am J Roentgenol 1989 May;152(5):985-6
45. Nelson RC, Lovett KE, Chezmar JL, Moyers JH, Torres WE, Murphy FB, Bernardino ME. Comparison of pulsed Doppler sonography and angiography in patients with portal hypertension. AJR Am J Roentgenol 1987 Jul;149(1):77-81
46. Niederau C, Strohmeyer G. Strategies for early diagnosis of haemochromatosis. Eur J Gastroenterol Hepatol 2002 Mar;14(3):217-21
47. Niederau C, Fischer R, Sonnenberg A, Stremmel W, Trampisch HJ, Strohmeyer G. Survival and causes of death in cirrhotic and in noncirrhotic patients with primary hemochromatosis. N Engl J Med 1985 Nov 14;313(20):1256-62
48. Nomura F, Ohnishi K, Ochiai T, Okuda K. Obesity-related nonalcoholic fatty liver: CT features and follow-up studies after low-calorie diet. Radiology 1987 Mar;162(3):845-7
49. Ohtomo K, Itai Y, Ohtomo Y, Shiga J, Iio M. Regenerating nodules of liver cirrhosis: MR imaging with pathologic correlation. AJR Am J Roentgenol 1990 Mar;154(3):505-7
50. Parvey HR, Eisenberg RL, Giyanani V, Krebs CA. Duplex sonography of the portal-venous system: pitfalls and limitations. AJR Am J Roentgenol 1989 Apr;152(4):765-70
51. Patriquin H, Lafortune M, Burns PN, Dauzat M. Duplex Doppler examination in portal hypertension: technique and anatomy. AJR Am J Roentgenol 1987 Jul;149(1):71-6
52. Powell LW, Bassett ML, Halliday JW. Hemochromatosis: 1980 update. Gastroenterology 1980 Feb;78(2):374-81
53. Rupert SA. Pathogenesis and treatment of rhabdomyolysis. J Am Acad Nurse Pract 2002 Feb; 14(2):82-87
54. Sagoh T, Itoh K, Togashi K, Shibata T, Nishimura K, Minami S, Asato R, Noma S, Fujisawa I, Yamashita K, et al. Gamna-Gandy bodies of the spleen: evaluation with MR imaging. Radiology 1989 Sep; 172(3):685-7
55. Siegelman ES, Mitchell DG, Rubin R, Hann HW, Kaplan KR, Steiner RM, Rao VM, Schuster SJ, Burk DL Jr, Rifkin MD. Parenchymal versus reticuloendothelial iron overload in the liver: distinction with MR imaging. Radiology 1991 May;179(2):361-6
56. Silverman PM, Patt RH, Garra BS, Horii SC, Cooper C, Hayes WS, Zeman RK. MR imaging of the portal-venous system: value of gradient-echo imaging as an adjunct to spin-echo imaging. AJR Am J Roentgenol 1991 Aug;157(2):297-302
57. Stanley P. Budd-Chiari syndrome.Radiology 1989 Mar;170(3 Pt 1):625-7
58. Stark DD, Bass NM, Moss AA, Bacon BR, McKerrow JH, Cann CE, Brito A, Goldberg HI. Nuclear magnetic resonance imaging of experimentally induced liver disease. Radiology 1983 Sep;148(3):743-51
59. Stark DD, Goldberg HI, Moss AA, Bass NM. Chronic liver disease: evaluation by magnetic resonance. Radiology 1984 Jan;150(1):149-51
60. Stark DD, Hahn PF, Trey C, Clouse ME, Ferrucci JT Jr. MRI of the Budd-Chiari syndrome. AJR Am J Roentgenol 1986 Jun;146(6):1141-8
61. Tabbara IA. Hemolytic anemias. Diagnosis and management. Med Clin North Am 1992 May; 76(3):649-68
62. Takayasu K, Moriyama N, Muramatsu Y, Goto H, Shima Y, Yamada T, Makuuchi M, Yamasaki S, Hasegawa H, Hojo K. Intrahepatic venous collaterals forming via the inferior right hepatic vein in 3 patients with obstruction of the inferior vena cava. Radiology 1985 Feb;154(2):323-8
63. Tamada T, Moriyasu F, Ono S, et al. Portal blood flow: measurement with MR imaging. Radiology 1989 Dec;173(3):639-44
64. Terada T, Nakanuma Y. Iron-negative foci in siderotic macroregenerative nodules in human cirrhotic liver. A marker of incipient neoplastic lesions. Arch Pathol Lab Med 1989 Aug;113(8):916-20
65. Terada T, Nakanuma Y. Survey of iron-accumulative macroregenerative nodules in cirrhotic livers. Hepatology 1989 Nov;10(5):851-4
66. The Clinical NMR Group. Magnetic resonance imaging of parenchymal liver disease: a comparison with ultrasound, radionuclide scintigraphy and X-

ray computed tomography. Clin Radiol 1987 Sep;38(5):495-502
67. Torres WE, Gaylord GM, Whitmire L, Chuang VP, Bernardino ME. The correlation between MR and angiography in portal hypertension. AJR Am J Roentgenol 1987 Jun;148(6):1109-13
68. Unger EC, Lee JK, Weyman PJ. CT and MR imaging of radiation hepatitis. J Comput Assist Tomogr 1987 Mar-Apr;11(2):264-8
69. Valla DC. Hepatic vein thrombosis (Budd-Chiari syndrome). Semin Liver Dis 2002 Feb;22(1):5-14
70. Van Beers B, Pringot J, Trigaux JP, Dautrebande J, Mathurin P. Hepatic heterogeneity on CT in Budd-Chiari syndrome: correlation with regional disturbances in portal flow. Gastrointest Radiol 1988;13(1):61-6
71. Varma DG, Schoenberger SG, Kumra A, Agrawal N, Robinson AE. Osler-Weber-Rendu disease: MR findings in the liver. J Comput Assist Tomogr 1989 Jan-Feb;13(1):134-5
72. Wada K, Kondo F, Kondo Y. Large regenerative nodules and dysplastic nodules in cirrhotic livers: a histopathologic study. Hepatology 1988 Nov-Dec;8(6):1684-8
73. Wang ZG, Zhu Y, Wang SH, Pu LP, Du YH, Zhang H, Yuan C, Chen Z, Wei ML, Pu LQ, et al. Recognition and management of Budd-Chiari syndrome: report of one hundred cases. J Vasc Surg 1989 Aug;10(2):149-56
74. Wanless IR, Lentz JS. Fatty liver hepatitis (steatohepatitis) and obesity: an autopsy study with analysis of risk factors. Hepatology 1990 Nov;12(5):1106-10
75. Wanless IR, Peterson P, Das A, Boitnott JK, Moore GW, Bernier V. Hepatic vascular disease and portal hypertension in polycythemia vera and agnogenic myeloid metaplasia: a clinicopathological study of 145 patients examined at autopsy. Hepatology 1990 Nov;12(5):1166-74
76. Weltin G, Taylor KJ, Carter AR, Taylor CR. Duplex Doppler: identification of cavernous transformation of the portal vein. AJR Am J Roentgenol 1985 May;144(5):999-1001
77. Wenker JC, Baker MK, Ellis JH, Glant MD. Focal fatty infiltration of the liver: demonstration by magnetic resonance imaging. AJR Am J Roentgenol 1984 Sep;143(3):573-4
78. White EM, Simeone JF, Mueller PR, Grant EG, Choyke PL, Zeman RK. Focal periportal sparing in hepatic fatty infiltration: a cause of hepatic pseudomass on US. Radiology 1987 Jan;162(1 Pt 1):57-9
79. Widrich WC, Srinivasan M, Semine MC, Robbins AH. Collateral pathways of the left gastric vein in portal hypertension. AJR Am J Roentgenol 1984 Feb;142(2):375-82
80. Wiesner RH, LaRusso NF. Clinicopathologic features of the syndrome of primary sclerosing cholangitis. Gastroenterology 1980 Aug;79(2):200-6
81. Williams DM, Cho KJ, Aisen AM, Eckhauser FE. Portal hypertension evaluated by MR imaging. Radiology 1985 Dec;157(3):703-6
82. Zirinsky K, Markisz JA, Rubenstein WA, Cahill PT, Knowles RJ, Auh YH, Morrison H, Kazam E. MR imaging of portal-venous thrombosis: correlation with CT and sonography. AJR Am J Roentgenol 1988 Feb;150(2):283-8

10

MR Imaging of the Liver in Pediatric Patients

CONTENTS

10.1 Introduction

In order of frequency, the liver accounts for approximately 6% of all abdominal tumors, and is third after the kidneys and adrenal glands for the occurrence of abdominal neoplasms in pediatric subjects. Hepatic tumors may be either primary or metastatic; the non-hepatic primary neoplasms that metastasize most frequently to the liver are Wilms' tumor, neuroblastoma, lymphoma and leukemia. Of the primary hepatic tumors, roughly two thirds are malignant in nature.

From the point of view of classification, malignant primary hepatic neoplasms can be distinguished on the basis of their cells of origin and the patient's age at onset. Concerning the cells of origin, liver cancers can be divided into epithelial and mesenchymal neoplasms. The liver malignancies of epithelial origin are more common and include hepatoblastoma (HB) and hepatocellular carcinoma (HCC). Those of mesenchymal origin comprise mainly sarcomas, i.e. angiosarcoma, myxoid mesenchymal sarcoma and rhabdomyosarcoma. These latter neoplasms are usually undifferentiated, although differentiated forms may occasionally develop.

The age of onset is an important classification parameter. Up to the age of five, the principal liver malignancies are HB and metastases of Wilms' tumor or neuroblastoma. In children older than five years of age, the most frequent neoplasms are HCC, undifferentiated embryonal sarcoma, fibrolamellar carcinoma and metastases (Table 1).

As in adult patients, other clinical parameters, such as signs, symptoms and α-fetoprotein (AFP) levels, are relevant factors to consider when radiologically assessing liver malignancy in pediatric subjects.

The fundamental role of imaging is to establish the extent of the lesion and its relationship with the liver's lobular and segmental anatomy, as well as with the vascular structures. This is essential in the preoperative work-up not only because surgery is often the treatment of choice, but also because of the need to monitor the neoplasm's response to chemotherapy and radiotherapy. A wide range of diagnostic methods are available to meet these objectives, including ultrasound (US), computed tomography (CT), magnetic resonance imaging (MRI) and angiography.

Though it is rarely used, direct x-ray of the ab-

Table 1. Classification of liver neoplasms in relation to age

Under five years of age	Over five years of age
Hepatoblastoma	Hepatocellular carcinoma
Hemangioendothelioma	Undifferentiated embryonal sarcoma
Mesenchymal hamartoma	Fibrolamellar carcinoma
Metastases from Wilms' tumor or neuroblastoma	Metastases
Sarcoma	Adenoma

domen can reveal hepatomegaly, elevation of the diaphragm, dislocation of the intestinal loops and the presence of calcifications, although this latter sign is non-specific.

US can identify the solid or cystic nature of a neoplasm, although the echo structure of solid lesions provides little information concerning its histology; in this context the use of Color Doppler US can help to ascertain the degree and type of vascularization.

CT and MR imaging are fundamental and irreplaceable tools for the diagnostic assessment of liver neoplasms in pediatric subjects because of their high accuracy in determining the full extent and resectability of a lesion. Of these two imaging modalities, MRI is usually the preferred technique because of the better soft tissue contrast and, importantly, because of the absence of ionizing radiation.

Due to the small size and frequent non-compliance of pediatric subjects, the techniques employed for liver imaging in these patients need to be adapted from those routinely employed in the adult population.

10.2 Techniques in Pediatric Liver Imaging

The results of pediatric liver CT and MR imaging depend mainly on good sedation and thus an interdisciplinary approach to evaluation is necessary. Significant changes in the examination method are needed in both helical CT and MRI when dealing with pediatric patients.

The CT protocol typically requires image acquisition during the arterial and portal-venous phases and also, whenever necessary, the equilibrium phase. The slice thickness is typically 5 mm or less with a pitch ranging from 1 to 1.5. The contrast medium is usually administered in quantities of 2 ml/kg, either by means of a mechanical injection method or by manual injection, depending on the caliber of the vein used for access. The arterial phase usually begins 10-15 sec after injecting the bolus of contrast medium, while the portal-venous phase begins immediately after the conclusion of the arterial phase, generally after a delay of 20-40 sec. In the event of a suspected malignant neoplasm, the chest must also be examined to check for the presence of lung metastases.

MRI examinations typically involve acquisition of T1- and T2-weighted spin echo (SE) or turbo spin echo (TSE) sequences in axial and coronal orientation, and T2-weighted fast spin echo (FSE) or, preferably, single-shot sequences in the axial plane. If necessary, gradient echo (GRE) images can also be acquired to examine vascular structures. In addition, T1-weighted fat-suppressed images should be acquired to evaluate the fat content of lesions. This can be important for the evaluation of teratoma in children. Generally, the slice thickness should be 5 mm or less with an interslice gap of less than 10%.

In order to optimize imaging results, different techniques of respiratory gating can be applied in children. Either an external trigger signal from a breathing belt or navigator techniques can be used to overcome motion artifacts from breathing. Alternatively, motion insensitive single shot T2-weighted HASTE sequences or motion insensitive T1-weighted spoiled GRE single shot sequences can be applied for imaging the pediatric abdomen and liver. For further details and limitations of these techniques, please refer to Chapter 1.

After the administration of a gadolinium (Gd)-based contrast agent, GRE images can be acquired at different time points. Typically, these are acquired in the axial orientation and usually with fat suppression. The arterial phase image of liver perfusion in pediatric patients should be acquired approximately 10-15 sec after the start of contrast agent injection. The portal venous phase follows at approximately 20-30 sec post-injection. Generally the acquisition time for the entire liver should be below 15 sec. Since there are no restraints on MRI regarding radiation exposure, the T1-weighted sequence should be repeated continuously 4 or 5 times to reliably achieve all phases of liver perfusion. In addition to dynamic imaging of the liver, steady state imaging should be performed in the equilibrium phase after contrast agent injection. Usually, this is performed using T1-weighted and T1-weighted fat-suppressed imaging sequences [89].

Contrast enhanced MR angiography (CE-MRA) can very precisely evaluate the arterial and

venous vascular anatomy of the liver in pediatric patients, but this method is usually reserved for cases requiring detailed preoperative vascular mapping or for cases in which chemo-embolization is required. To achieve maximum results, MRA studies should be performed under general anesthesia and controlled ventilation to allow for a sufficient breath-hold interval to acquire a high resolution contrast-enhanced 3D dataset.

10.3 Benign Liver Lesions in Pediatric Patients

10.3.1 Infantile Hemangioendothelioma (IHE)

IHE is the most common benign liver tumor in children. It is a vascular tumor derived from endothelial cells that proliferate and form vascular channels. IHE is relatively common and accounts for 10-15% of all childhood hepatic tumors [24]. Ninety percent of IHE are discovered within the first six months of life and females are affected more than males.

IHE are usually multiple or diffuse; a solitary lesion is an uncommon variant [59]. The nodules vary from a few millimeters to 15 cm or more in size. Typically, they are round, red-brown and spongy or white-yellow with fibrotic predominance in mature cases [82]. Microscopically, IHE represent a proliferation of small vascular channels lined by endothelial cells. Cavernous areas, as well as foci of hemorrhage, thrombosis, fibrosis and calcification, are common. The multinodular type may also involve other organs, as well as the skin [43].

Clinical findings, if present, may include hepatomegaly, congestive heart failure, thrombocytopenia caused by the trapping of platelets by the tumor (Kasabach-Meritt syndrome), and occasionally rupture with hemoperitoneum [53]. In symptomatic cases, as often occurs with the diffuse form (Fig. 1), treatment modalities include steroid administration, chemo- and radiotherapy, embolization or ligation of the hepatic artery and resection.

The natural history of IHE is benign, and lesions tend to regress gradually over a period of

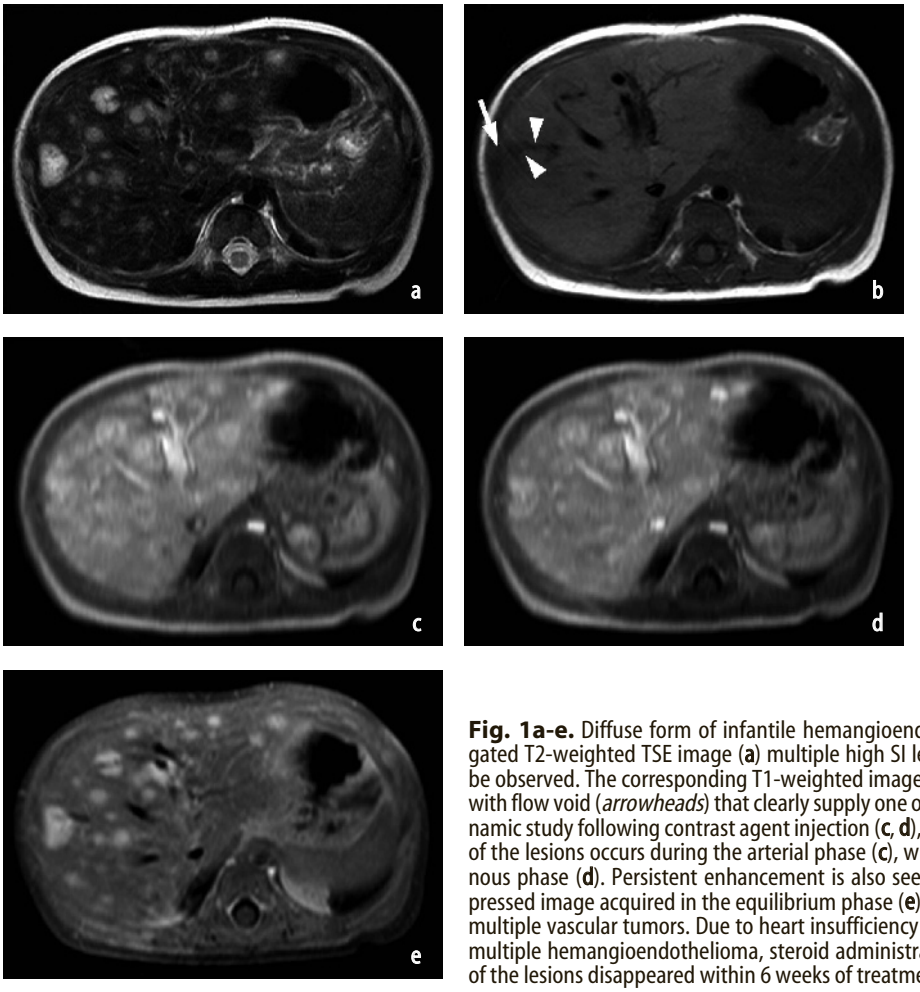

Fig. 1a-e. Diffuse form of infantile hemangioendothelioma. On the respiratory gated T2-weighted TSE image (**a**) multiple high SI lesions throughout the liver can be observed. The corresponding T1-weighted image (**b**) reveals some larger vessels with flow void (*arrowheads*) that clearly supply one of the lesions (*arrow*). On the dynamic study following contrast agent injection (**c**, **d**), early and strong enhancement of the lesions occurs during the arterial phase (**c**), which persists into the portal venous phase (**d**). Persistent enhancement is also seen on the T1-weighted fat-suppressed image acquired in the equilibrium phase (**e**), which points to a diagnosis of multiple vascular tumors. Due to heart insufficiency caused by the shunt flow from multiple hemangioendothelioma, steroid administration was performed and most of the lesions disappeared within 6 weeks of treatment

months [72]. However, malignant transformation of IHE into angiosarcoma may occur on rare occasions.

The ultrasonographic features of IHE are varied. Typically, there is a complex liver mass with large, draining hepatic veins [101]. Single or multiple lesions may be seen, and the lesions may range from hypoechoic to hyperechoic. These lesions may involute slowly over a period of months and develop increased echogenicity [21, 72].

On unenhanced CT examinations, IHE appear as hypodense masses with or without calcifications [74]. Early enhancement of the edge of the mass with variable delayed central enhancement is usually seen after administration of contrast medium [74].

Vascular channels and cyst-like components, which are usually well-defined, determine the hypointensity of the lesions on unenhanced T1-weighted MR images. On T2-weighted images the lesions usually appear homogeneously hyperintense, although some hypointense areas indicative of hemorrhage, thrombosis, fibrosis or calcification may be present (Fig. 2). After contrast agent administration, intense, peripheral enhancement or, less frequently, globular enhancement may be seen. Complete or incomplete filling-in during the portal-venous and equilibrium phases is also observed. On delayed phase images after Gd-BOPTA, IHE tend to be iso- or hypointense compared to the surrounding liver parenchyma (Fig. 3) [69, 72].

10.3.2 Focal Nodular Hyperplasia (FNH)

FNH in children is a very rare benign hepatic tumor [16, 48, 55] (Fig. 4). The characteristics of FNH in children do not differ from those in adults in terms of pathogenesis, macroscopic and microscopic morphology, prognosis and therapeutic consequences (see Chapt. 4 "Imaging of Benign Focal Liver Lesions", section 4.1.2, "Focal Nodular Hyperplasia"). Likewise, the radiologic characteristics of pediatric FNH are indistinguishable from those of FNH in adult subjects.

10.3.3 Hepatocellular Adenoma (HA)

HA in the pediatric age group occurs very rarely, although a steroid-associated form is increasingly being recognized in patients after corticoid therapy. As in the case of FNH, the gross pathologic features and radiologic characteristics of HA in pediatric patients resemble those of HA in adults (see Chapt. 4, "Imaging of Benign Focal Liver Lesions", section 4.1.3, "Hepatocellular Adenoma").

10.3.4 Hemangioma

Although hemangioma of infancy (HOI) is the most common benign tumor of childhood, occurring most frequently in the head and neck region and involving the skin, hepatic hemangioma in the pediatric age group is rare. However, when present, the pathologic and radiologic features of this lesion are similar to those of adult liver hemangioma (see Chapt. 4, "Imaging of Benign Focal Liver Lesions", section 4.1.1, "Hepatic Hemangioma"). The most important differential diagnoses in this context are angiosarcoma and IHE of the liver.

Whereas solitary hepatic hemangioma in the pediatric age group is a rare occurrence, multiple hemangiomas in the context of viscerocutaneous hemangiomatosis (Fig. 5) may be found in the liver. Multifocal cutaneous hemangiomas (generally defined as five or more) have a "localized" type of morphology and a well-recognized potential for concomitant visceral hemangiomas. The term "disseminated neonatal hemangiomatosis" has been used to describe this uncommon presentation of several hundreds of small, multifocal hemangiomas of the skin in association with extracutaneous, most commonly hepatic hemangiomas [35].

Hepatic hemangiomas in this context may manifest with coagulopathy, heart failure, and/or respiratory distress. Internal hemorrhage is also of significant concern with hemangiomas in hepatic or gastrointestinal locations. Often patients become symptomatic shortly after birth. Therapeutic options for hepatic and gastrointestinal hemangiomas may include surgical resection, embolization, corticosteroids, and interferon-α [8]. Imaging findings are similar to the findings in adults, although rapid filling is more common in the pediatric forms (Fig. 5).

10.3.5 Mesenchymal Hamartoma

Mesenchymal hamartoma is an uncommon lesion accounting for about 10% of all childhood liver tumors. It most likely represents a localized abnormality of ductal plate development that precedes birth; it is therefore usually considered a benign cystic developmental lesion rather than a true neoplasm. It occurs almost exclusively in young children (average age: 15 months) with a male to female ratio of approximately 2:1. Children typically present with progressive abdominal enlargement, and an association with polycystic kidney disease, congenital hepatic fibrosis and biliary hamartoma has been described.

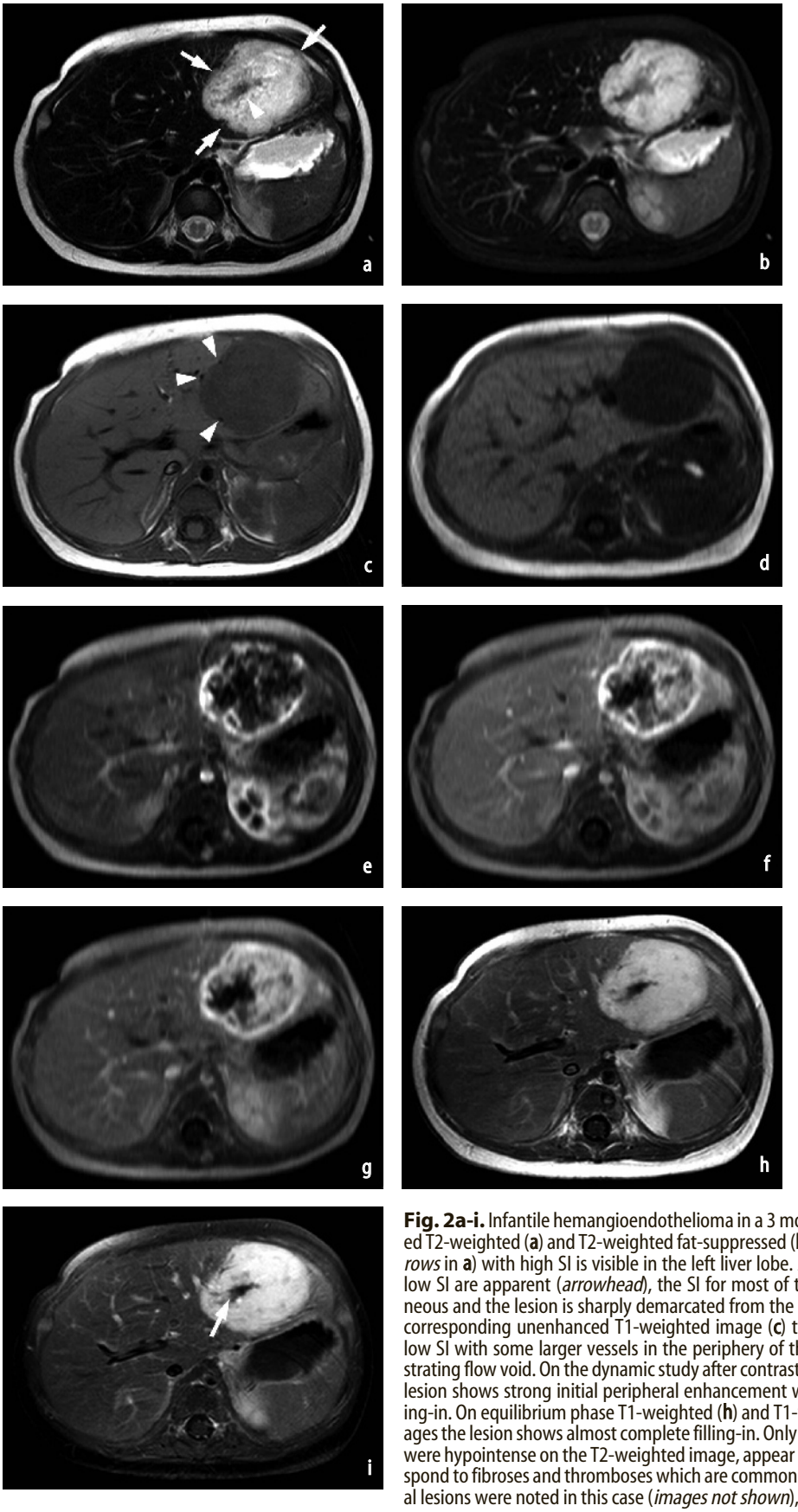

Fig. 2a-i. Infantile hemangioendothelioma in a 3 month old girl. On respiratory gated T2-weighted (**a**) and T2-weighted fat-suppressed (**b**) TSE images, a large lesion (*arrows* in **a**) with high SI is visible in the left liver lobe. Although some central areas of low SI are apparent (*arrowhead*), the SI for most of the lesion is relatively homogeneous and the lesion is sharply demarcated from the surrounding liver tissue. On the corresponding unenhanced T1-weighted image (**c**) the lesion shows homogeneous low SI with some larger vessels in the periphery of the lesion (*arrowheads*) demonstrating flow void. On the dynamic study after contrast agent administration (**d**-**g**), the lesion shows strong initial peripheral enhancement with subsequent centripetal filling-in. On equilibrium phase T1-weighted (**h**) and T1-weighted fat-suppressed (**i**) images the lesion shows almost complete filling-in. Only the central parts (*arrow*), which were hypointense on the T2-weighted image, appear hypointense. These areas correspond to fibroses and thromboses which are common findings in larger IHE. Additional lesions were noted in this case (*images not shown*),which confirmed the diagnosis

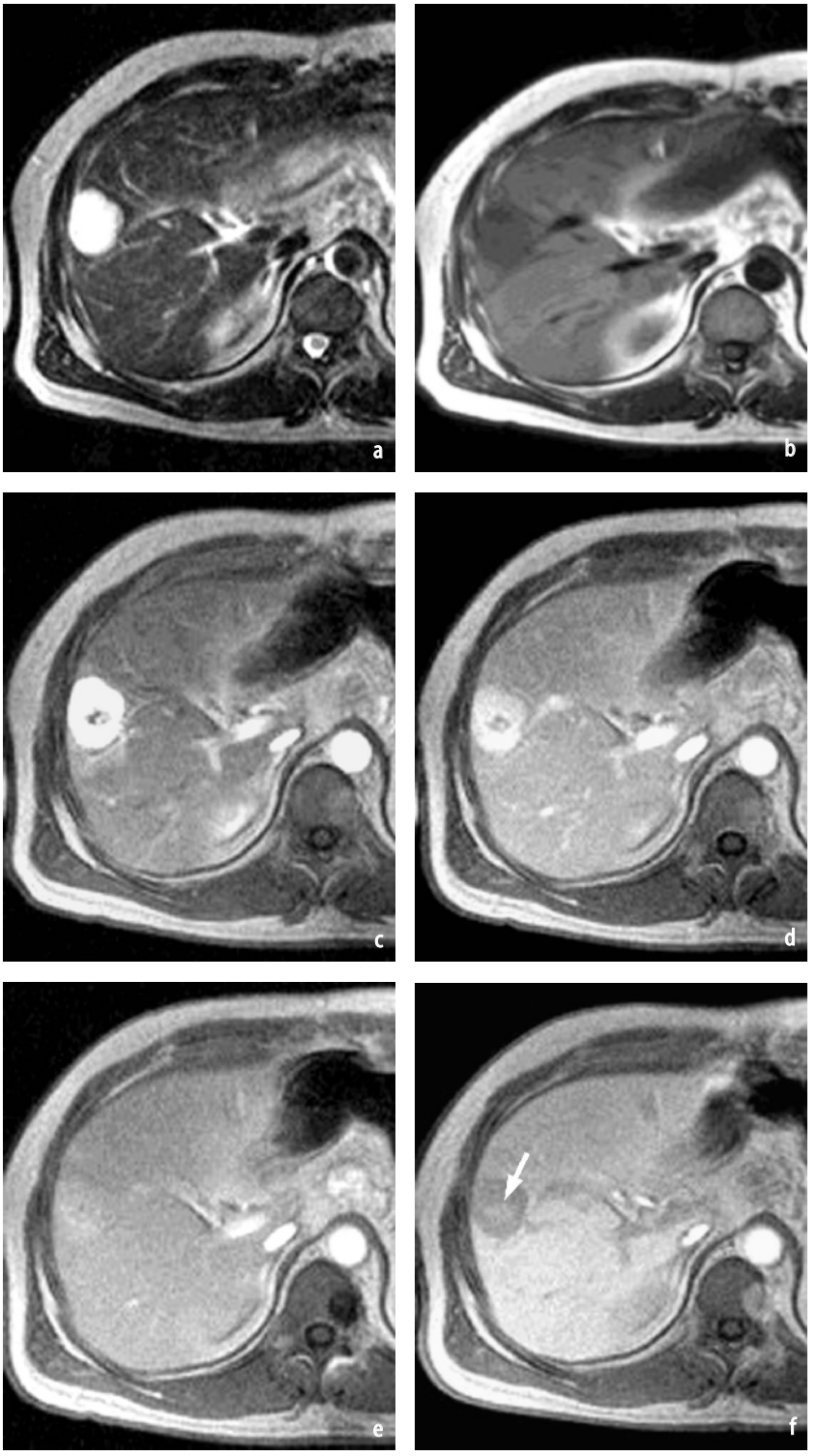

Fig. 3a-f. Infantile hemangioendothelioma. The nodule is homogeneously hyperintense compared to the adjacent liver tissue on the pre-contrast T2-weighted image (**a**), and is hypointense on the pre-contrast T1-weighted image (**b**). Dynamic phase imaging after the administration of Gd-BOPTA reveals peripheral intense enhancement during the arterial phase (**c**), incomplete filling-in during the portal venous phase (**d**) and complete filling-in during the equilibrium phase (**e**). The nodule is well-defined and hypointense with central contrast agent pooling (*arrow*) on the delayed hepatobiliary phase image (**f**)

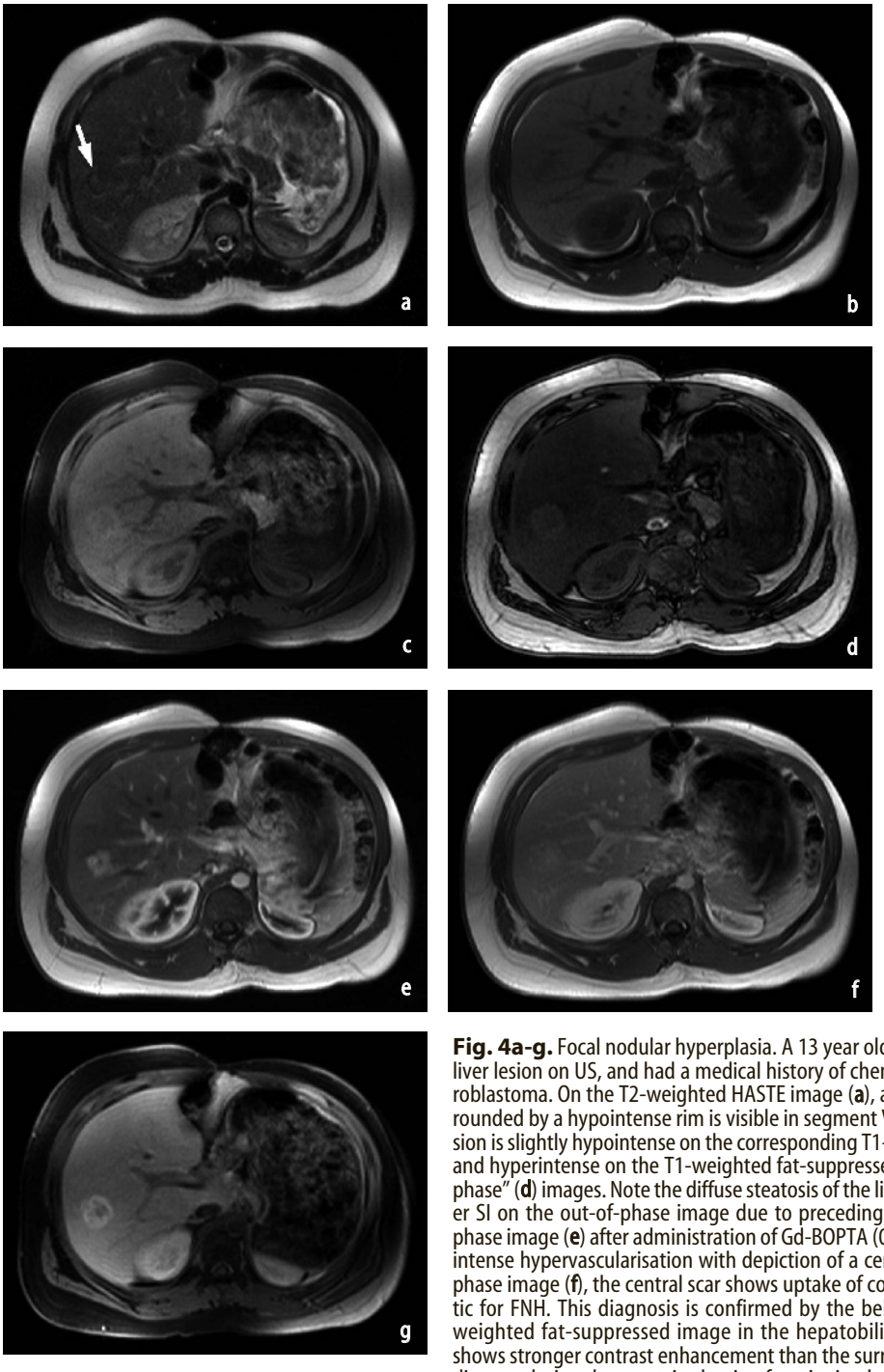

Fig. 4a-g. Focal nodular hyperplasia. A 13 year old boy presented with an unclear liver lesion on US, and had a medical history of chemotherapy and surgery for neuroblastoma. On the T2-weighted HASTE image (**a**), an isointense lesion (*arrow*) surrounded by a hypointense rim is visible in segment VII of the right liver lobe. The lesion is slightly hypointense on the corresponding T1-weighted "in-phase" image (**b**), and hyperintense on the T1-weighted fat-suppressed (**c**) and T1-weighted "out-of-phase" (**d**) images. Note the diffuse steatosis of the liver indicated by the reduced liver SI on the out-of-phase image due to preceding chemotherapy. On the arterial phase image (**e**) after administration of Gd-BOPTA (0.05 mmol/kg), the lesion shows intense hypervascularisation with depiction of a central scar. On the portal venous phase image (**f**), the central scar shows uptake of contrast agent; this is characteristic for FNH. This diagnosis is confirmed by the behavior of the lesion on the T1-weighted fat-suppressed image in the hepatobiliary phase, in which the lesion shows stronger contrast enhancement than the surrounding (**g**) liver tissue. This indicates a lesion that contains benign functioning hepatocytes and abnormal biliary drainage. This is the characteristic feature of FNH

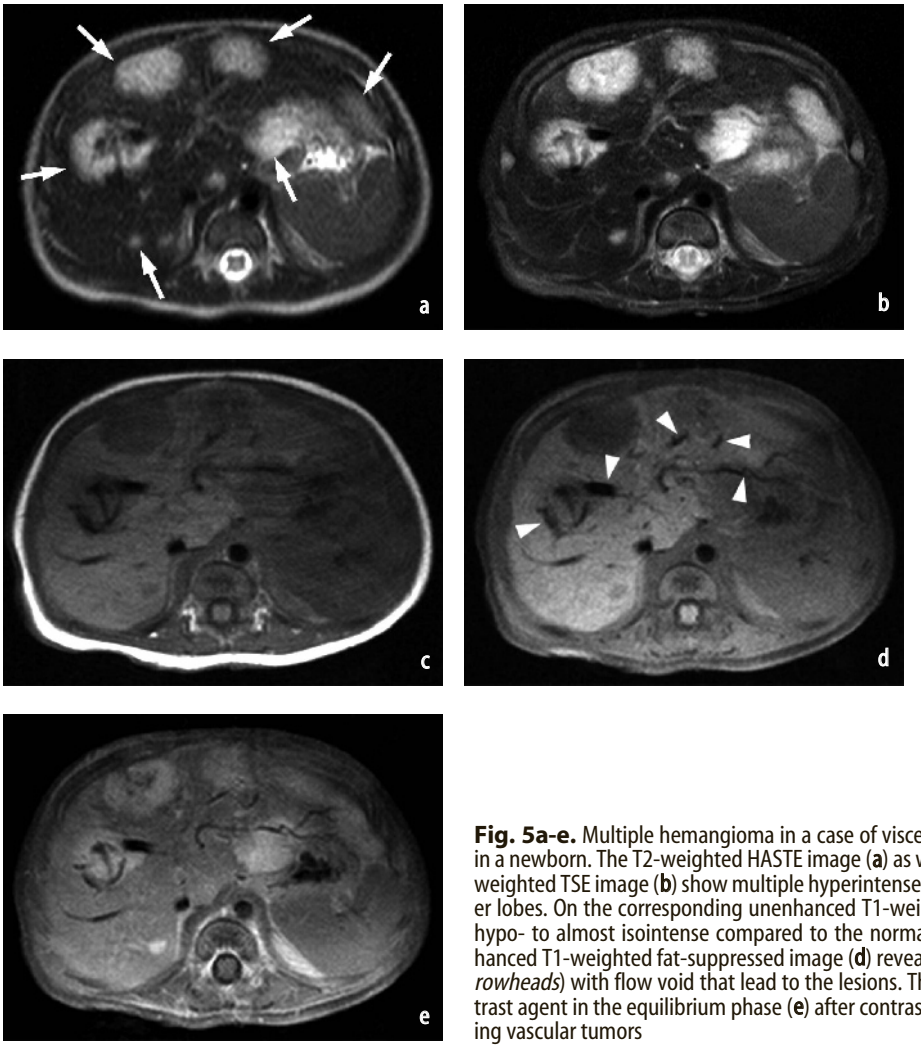

Fig. 5a-e. Multiple hemangioma in a case of viscerocutaneous hemangiomatosis in a newborn. The T2-weighted HASTE image (**a**) as well as the respiratory gated T2-weighted TSE image (**b**) show multiple hyperintense lesions (*arrows* in **a**) in both liver lobes. On the corresponding unenhanced T1-weighted image (**c**) the lesions are hypo- to almost isointense compared to the normal liver parenchyma. The unenhanced T1-weighted fat-suppressed image (**d**) reveals multiple tortuous vessels (*arrowheads*) with flow void that lead to the lesions. The lesions show pooling of contrast agent in the equilibrium phase (**e**) after contrast agent administration, indicating vascular tumors

On imaging studies mesenchymal hamartoma is a large, predominantly cystic mass frequently measuring 15 cm or more in diameter at the time of diagnosis. The tumors are generally well-defined and encapsulated or pedunculated. Cysts are present in 80% of cases [40].

On cut sections, mesenchymal hamartomas have either a solid appearance reflecting a mesenchymal predominance, or a multiloculated cystic appearance reflecting a cystic predominance. Histologically, the tumor consists of the cystic remnants of portal triads, hepatocytes and fluid-filled mesenchyma [80]. Extramedullary hematopoiesis is commonly present. Malignant transformation of mesenchymal hamartoma has not yet been reported and surgical excision is usually curative.

On US, a mesenchymal hamartoma has the appearance of a large cyst with internal septa (cystic appearance), or, less commonly, as a smaller cyst with thick septa (mesenchymal appearance).

On CT, the tumor appears as a well-defined mass with central hypodense areas and internal septa. Both solid and cystic components may be distinguished, although calcifications have not been reported. Both the septa and the solid components enhance following the administration of contrast material [80].

The MR appearance of mesenchymal hamartoma depends on the predominance of the stromal and cystic components. For lesions with a stromal predominance, the signal intensity (SI) on T1-weighted images is lower than that of the normal liver, because of increased fibrosis. Conversely, if the cystic component predominates, the appearance is similar to that of other cystic masses with marked hyperintensity on T2-weighted images. Multiple septa traversing the tumor can be seen, indicating that the lesion is not a simple cyst [80].

The SI of the different locules may vary, indicating different concentrations of proteinaceous material. After the injection of contrast agent, both the mesenchymal component and the septa enhance in a manner similar to that observed on CT.

10.3.6 Choledochal Cyst and Cystic Dilatation of the Bile Duct

Choledochal cysts are anomalies of the biliary system characterized by dilatation of the extra- or intrahepatic bile ducts (see Chapt. 7, "Imaging of the Biliary Tree and Gallbladder Diseases", section 7.2.2.1, "Choledochal Cyst and Cystic Dilatation of the Bile Duct"). Although choledochal cysts may become evident at any age, diagnosis is made within the first ten years of age in about 60% of cases. They are more frequent in females than in males with a ratio of about 4:1.

In newborns and infants, obstructive jaundice is the most common clinical presentation, while in older children and adults the signs and symptoms are those of ascending cholangitis [3, 96].

US is usually the first imaging modality to diagnose a choledochal cyst in pediatric patients. The appearance of these malformations is similar to their appearance in adult patients and the same limitations apply regarding visualization of the full extent of cystic dilatation, the relationship of the cyst to the gallbladder and pancreatic duct, and the angle and site of junction with the duodenum. In young children this may be related to the presence of gas in the bowel [50].

Although endoscopic retrograde cholangiopancreatography (ERCP) has been reported to be safe in infants and small children suspected of having choledochal cyst, CT and MR cholangiography (MRC) are frequently used as alternative imaging techniques [50]. Of these techniques, MRC is the preferred modality in pediatric patients because it offers similar information to ERCP without the potential complications inherent in the latter procedure and without the need for ionizing radiation [57].

Bile and pancreatic secretions have high SI on MRC performed with heavily T2-weighted pulse sequences. With these sequences choledochal cysts can usually be seen as hyperintense tubular, fusiform or cystic structures (Fig. 6).

Unfortunately, the signal-to-noise ratio is reduced in small patients, and image quality is frequently sub-optimal because of respiratory motion artifacts associated with the need to acquire images using non breath-hold sequences. These limitations render imaging of non-dilated pancreatic ducts and intrahepatic ducts more difficult and explain why the quality of MRC images is often inferior to that of CT cholangiography (CTC) images in some patients [50]. The availability of respiratory triggering may overcome many of the drawbacks associated with non breath-hold sequences and permit satisfactory imaging of even non-dilated bile ducts. Similarly, single-shot fast SE sequences have been shown to be effective for imaging of the biliary tree in infants and children unable to hold their breath [44].

The use of secretin further improves bile duct visualization in pediatric subjects. This is because the secretin increases pancreatic juice secretion, which increases the pancreatic duct visualization, particularly at the distal portion. This may be important for visualization of the common channel.

10.3.7 Inflammatory Pseudotumor

Inflammatory pseudotumor, also called inflammatory myofibroblastic tumor or plasma cell granuloma, is a rare lesion that affects both children and adults [91, 97]. Histologically, it is characterized by a proliferation of spindle-shaped cells, myofibroblasts mixed with inflammatory plasma cells, lymphocytes, and, occasionally, histiocytes (see Chapt. 5, "Hepatic Pseudolesions", section 5.2.3, "Inflammatory Pseudotumors"). The lesion arises in a variety of tissues and organs including the lungs, mesentery of the intestines, omentum, stomach, and liver [36, 87]. The lesion is generally considered to be benign, but some inflammatory pseudotumors may recur or metastasize, and some patients die of the disease. On the other hand, it is known that some inflammatory pseudotumors regress and completely resolve without treatment [27].

An inflammatory reaction is believed to cause inflammatory pseudotumor. Affected patients have varying degrees of non-specific symptoms and inflammatory responses, such as fever, impaired growth, leukocytosis, anemia, thrombocytosis, hypergammaglobulinemia, and an increase in the erythrocyte sedimentation rate or C-reactive protein (CRP). In some patients, inflammatory pseudotumor arises after trauma, surgery, or infection.

The radiologic findings for inflammatory pseudotumor are non-specific on all imaging modalities. On US, lesions typically present heterogeneously hypoechoic or mosaic patterns that are similar to those observed for other focal liver neoplasms [36].

The lesion is usually hypodense on unenhanced CT but presents an early intense and peripheral enhancement immediately after contrast medium administration, followed by homogeneous, complete and persistent enhancement. Thereafter peripheral enhancement and a hypodense core can often be observed. These features are due to the presence of fibroblastic cells and chronic inflammatory cells, respectively [30, 36].

The signal characteristics on MRI are similarly non-specific [27]. On unenhanced T1-weighted MR images inflammatory pseudotumor is often hypointense in the central portion, while on T2-weighted images the lesion frequently demonstrates isointensity or slight hyperintensity (Fig. 7).

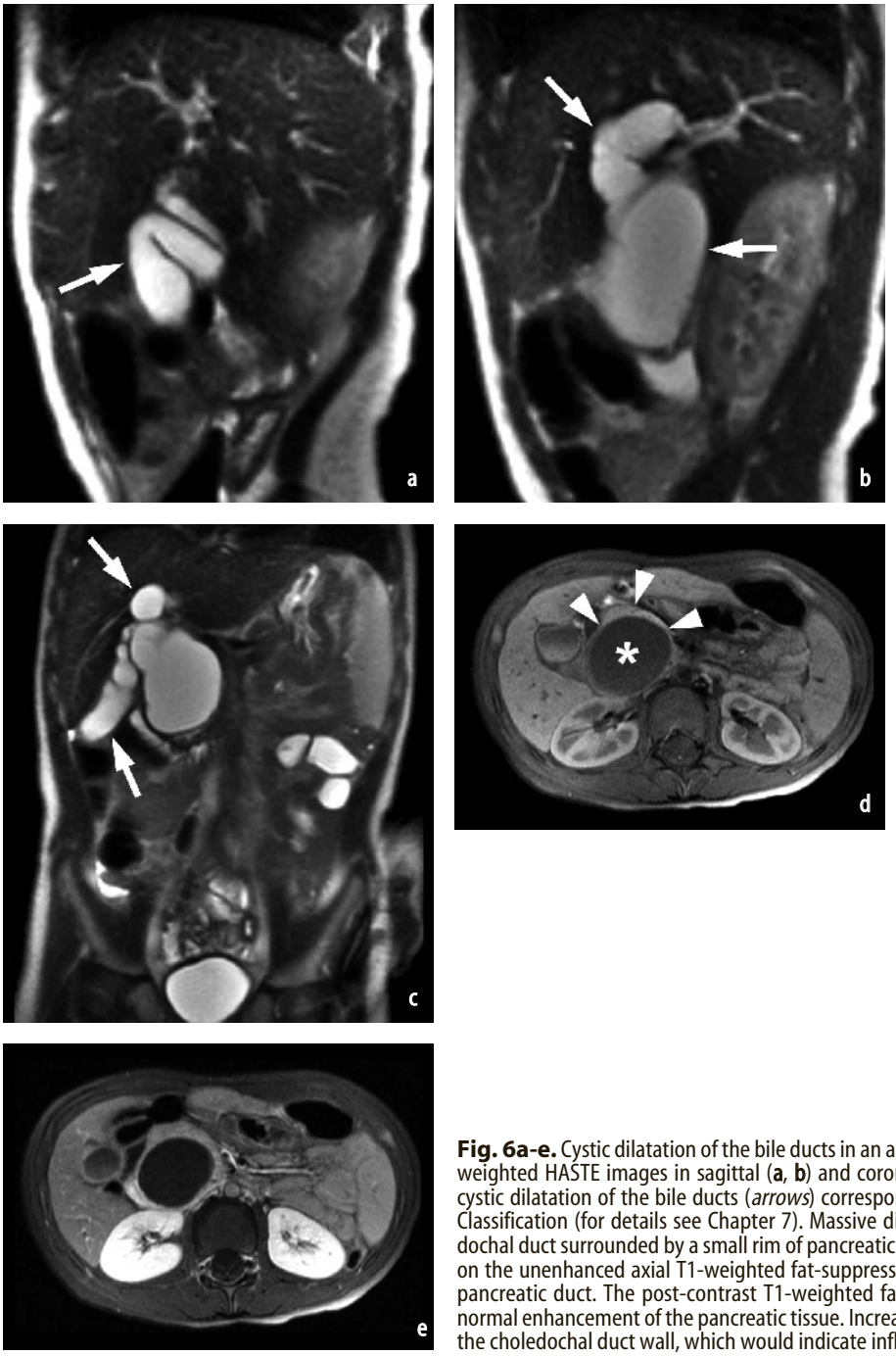

Fig. 6a-e. Cystic dilatation of the bile ducts in an asymptomatic 3 year old. The T2-weighted HASTE images in sagittal (**a**, **b**) and coronal (**c**) orientation demonstrate cystic dilatation of the bile ducts (*arrows*) corresponding to type IVa of the Todani Classification (for details see Chapter 7). Massive dilatation (*asterisk*) of the choledochal duct surrounded by a small rim of pancreatic tissue (*arrowheads*) is apparent on the unenhanced axial T1-weighted fat-suppressed image (**d**) at the level of the pancreatic duct. The post-contrast T1-weighted fat-suppressed image (**e**) reveals normal enhancement of the pancreatic tissue. Increased enhancement of the wall of the choledochal duct wall, which would indicate inflammation, is not seen

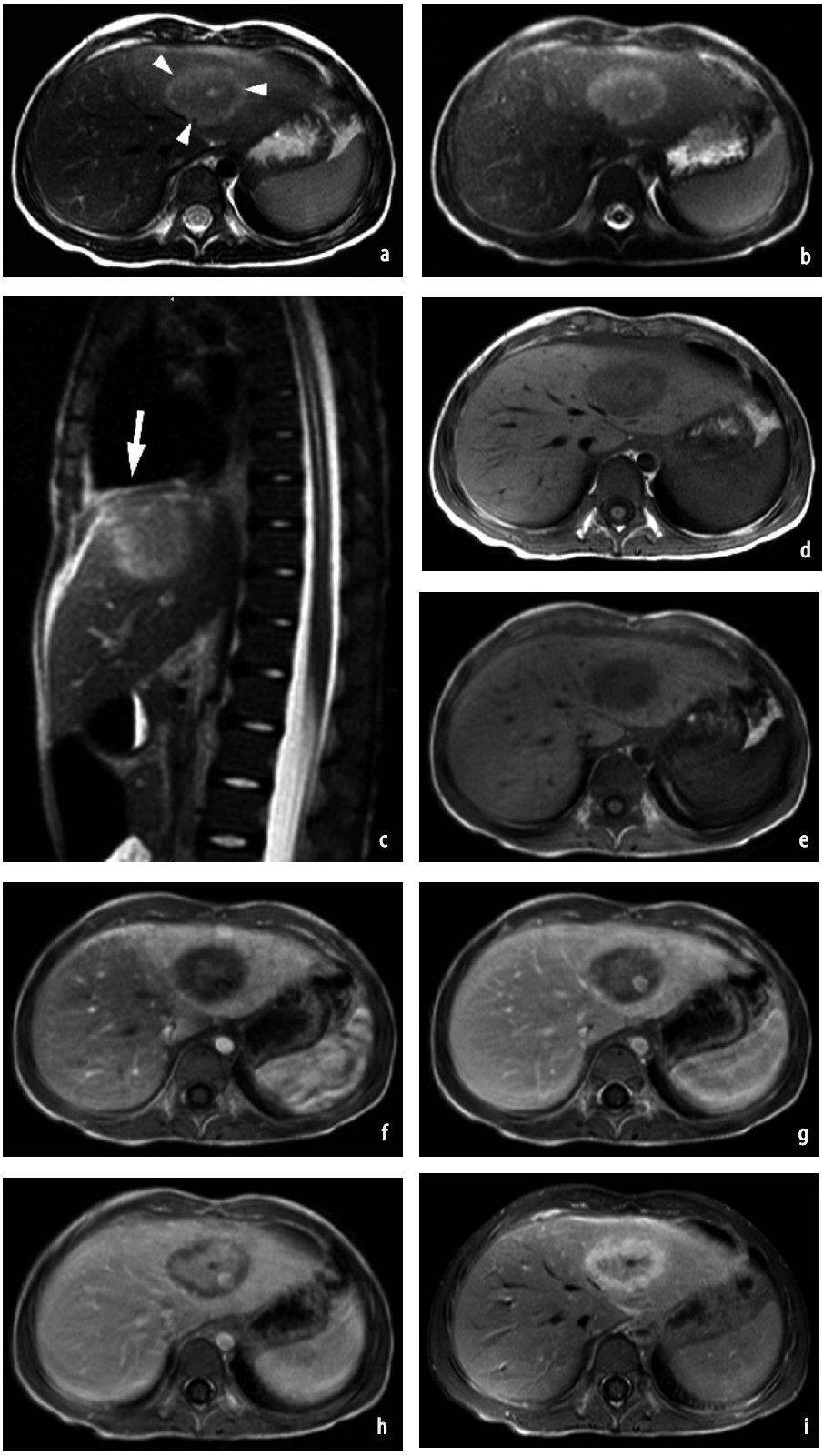

Fig. 7a-i. Inflammatory pseudotumor of the liver. On the T2-weighted respiratory-gated TSE image (**a**) and on the single-shot T2-weighted HASTE image (**b**) the lesion demonstrates slight hyperintensity with a hyperintense rim (*arrowheads* in **a**). The corresponding single-shot HASTE image in sagittal orientation (**c**) shows pleural reaction (*arrow*) neighbouring the lesion. On the unenhanced T1-weighted image (**d**), the inflammatory pseudotumor is hypointense. Peripheral enhancement is seen on the T1-weighted dynamic images (**e**-**h**) after the bolus injection of contrast agent; this reflects the cellular components and inflammatory changes within the lesion. On the T1-weighted fat-suppressed image in the equilibrium phase (**i**), a hyperintense rim surrounding the lesion is seen together with enhancement of the central portions of the lesion. The hyperintense rim is due to edema of the surrounding liver tissue

However, the appearance on T2-weighted images may vary in relation to the histologic components: a strong fibrotic predominance may result in slight hypointensity compared to the normal liver parenchyma while a greater predominance of inflammatory cells may produce a stronger hyperintense appearance. Early peripheral enhancement is typically seen on T1-weighted dynamic imaging after the bolus injection of Gd contrast agent. This reflects the cellular components and inflammatory changes within the lesion. In the equilibrium phase a hyperintense rim may be seen due to edema of the surrounding liver tissue. During this phase the central portions of the lesion are typically hyperintense [65].

10.4 Malignant Liver Lesions in Pediatric Patients

10.4.1 Hepatoblastoma (HB)

HB is the most common primary hepatic malignancy in children and represents approximately 45% of all pediatric liver neoplasms. It is generally detected in children younger than five years of age; in roughly 66% of cases the mean age for detection is one year. From an etiological point of view, a correlation has been observed with prematurity, with a gestational age of <37 weeks, and with a birth weight of <1000 g. Other risk factors are trisomy 18, hemi-hypertrophy, Beckwith-Wiedemann syndrome, familial adenomatous polyposis, fetal alcoholic syndrome, maternal use of gonadotropin, and maternal exposure to metals or petroleum products [47, 74, 89]. Liver cirrhosis is not considered a risk factor.

HB can be considered the infantile form of HCC. Histological classification divides HB into two main types: a pure epithelial form and a mixed epithelial-mesenchymal form. The pure epithelial form includes fetal, embryonal, macrotrabecular and undifferentiated small cell variants. Fetal epithelial HB is composed of cells that are smaller than normal hepatocytes and which have an eosinophilic cytoplasm. They have a relatively low nucleus to cytoplasm ratio and although some nucleoli are present, mitoses are rare and growth occurs with a compact trabecular pattern. The embryonal variant has a high nucleus to cytoplasm ratio, a basophilic cytoplasm and ductal elements with cells that can form acini, tubules and pseudorosettes. Mitoses are frequent in this form of HB. The macrotrabecular form is a variant comprising a recurrent combination of both the fetal and the embryonal cell types in cords or plaques. The cell dimensions of this form frequently exceed those of normal hepatocytes. The anaplastic small cell type of HB is composed of typically round or oval cells that may be fusiform but which always have a high mitotic index. Infiltration of the adjacent hepatocytes is normally observed, with vascular invasion and necrosis.

The mixed epithelial-mesenchymal form contains an epithelial component identical to that of epithelial HB, plus a mesenchymal component with osteoid, chondroid and rhabdomyoblastic elements. It is often associated with areas of calcification, hemorrhage and necrosis [34, 90].

The histological classification of HB carries marked prognostic implications; the survival rate for patients with the pure fetal variant is 90%, compared with 54% for the mixed form and 33% for the embryonal variant. Unfortunately the survival rate for patients with the anaplastic variant is 0% [13].

HB frequently presents as a single, large, bulky mass, most often in the right lobe of the liver. Macroscopically, its appearance varies according to the histological type: epithelial HB has a typically homogeneous appearance whereas the mixed form possesses calcifications, fibrotic bands and osteoid and cartilaginous material, and is consequently more heterogeneous in appearance [83].

The nodules may sometimes be multiple, in which case they may affect both lobes of the liver. A diffuse variant involving the whole organ has been reported but is less common. The presence of multifocal nodules, diffuse involvement, and vascular invasion is encountered in approximately 50% of cases overall and is indicative of unresectability and a worse prognosis. In 30% of cases, remote metastases are detected; the organs most often involved are the lung, kidney, brain and abdominal lymph nodes [46].

The variable presentation of HB means that the lesion can be defined as belonging to one of two categories according to the potential risk: (1) *standard risk hepatoblastoma* for patients with single or apparently multifocal neoplasms involving no more than three hepatic segments in the absence of metastases and extrahepatic abdominal involvement, (2) *high risk hepatoblastoma* with neoplastic disease extending to four or more liver segments and evidence of extrahepatic spread [90]. HB can be seen, albeit infrequently, in older children, in which case it tends to have clinical and anatomopathological characteristics in common with HCC and the prognosis is worse than in children of younger age. In older children HB may acquire macrotrabecular features similar to the trabecular characteristics of HCC, with vascular invasion and recurrence, as well as cholangiocellular differentiation [90].

Approximately 50% of children with HB are symptom-free; the diagnosis is often made during a medical check-up due to the incidental finding of a palpable mass or an increase in abdominal circumference. Abdominal pain, fever, loss of appetite and weight loss are reported in 25% of patients, whereas jaundice occurs in fewer than 10% of cases [89, 90].

In addition to histological type, factors that suggest the likely evolution of the disease include the number of lesions, the presence of metastases, and - of considerable relevance - the level of α-fetoprotein (AFP).

AFP is a protein produced exclusively in the fetal liver that disappears from the serum in the first few weeks of life. Its values rise in the presence of certain tumors, such as HB, HCC and endodermal breast tumors, and it is occasionally found in the serum of patients with pancreatic and gastric carcinoma. AFP positivity in pediatric HB and HCC is much higher than in adult HCC, with high values being detected in 96% of cases. The values of this tumor marker are indicative of a worse prognosis when they are higher than 1,000,000 ng/mL or lower than 100 ng/mL. The reason for such low values in the latter case, which corresponds to undifferentiated neoplasm, is that the cells are too immature and malignant to produce the protein [98]. High values of human chorionic gonadotropin (HCG) are sometimes observed and in these cases HB is associated with signs of early puberty. Thrombocytosis is also present in 93% of cases [34].

Prognosis and long-term survival depend on the feasibility of completely resecting the tumor, hence the fundamental role of imaging diagnostics in accurately assessing the extent of the neoplasm and its relationship with the intra- and extra-hepatic vascular structures.

The correct diagnosis and staging of HB, and its assignation to the correct risk category, can be achieved using most imaging modalities. A straightforward standard abdominal x-ray, however, reveals alterations that are generally non-specific. This approach merely shows a solid mass or calcifications (in 50% of cases) and therefore contributes little towards the distinction between benign and malignant lesions. The areas of calcification probably represent dystrophic calcifications in necrotic portions of the lesion [62].

US findings vary according to the histological type. Masses are normally well-defined, multilobulated and septate. The epithelial variant of the tumor is normally homogeneously hypo- or hyperechogenic while the mixed form invariably presents as a heterogeneous mass with hyper- and hypoechogenic areas that reflect calcification and tumor necrosis, respectively. Color Doppler assessment is very sensitive to the rich neo-vascularization of the tumor (Fig. 8) [5, 90].

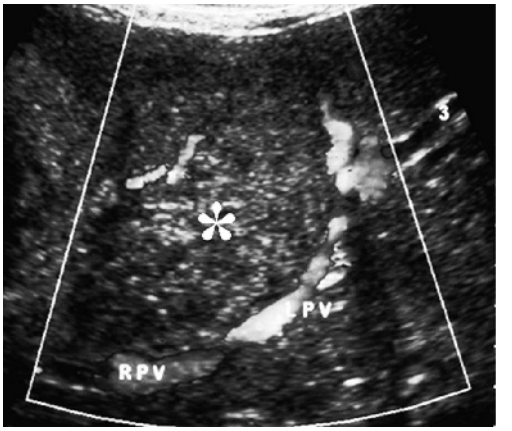

Fig. 8. Hepatoblastoma. Color Doppler US reveals a slightly hyperechoic and hypervascular mass (*asterisk*). An impression of the portal vein (PV) and of the right branch of the portal vein (RPV) can be seen

CT is of fundamental importance for the staging of HB, not only to assess the intrahepatic extension of the neoplasm correctly and thus decide on its resectability or non-resectability, but also to determine the presence or absence of metastases to the abdomen and chest. In the latter case, a further problem is posed by the frequent presence of atelectasis in the lower thoracic portions that may confound or mask lung nodes. For this reason it is often necessary to repeat the scans in the prone position. This method is also necessary during follow-up [90].

During the staging procedure, the SIOPEL protocol of June 1998 [90] recommends performing the examination before and after the administration of intravenous contrast medium. Prior to the administration of contrast medium the epithelial variant of HB is typically homogeneously hypodense and any calcifications that are present are usually small and punctiform (Fig. 9). Conversely, the mixed form of HB tends to be more heterogeneous (Fig. 10), often with larger and coarser calcifications. After injection of contrast medium, HB typically demonstrates enhancement during the arterial phase, which subsequently fades in the portal venous phase. Enhancement may be patchy and is usually inferior to that of the healthy parenchyma. A peripheral ring or hyperdense septa may be apparent in the late phase. This is due to the stromal component [34, 89, 90].

On MR imaging the SI of the tumor varies in relation to the histological type. Epithelial HB is seen as hypointense on T1-weighted images (Fig. 11) and as hyperintense on T2-weighted images. As in CT, the mixed form is much more heterogeneous due to the variable presence and extent of necrosis, hemorrhage and fibrosis. In this variant, hypointense bands and high signal areas are often

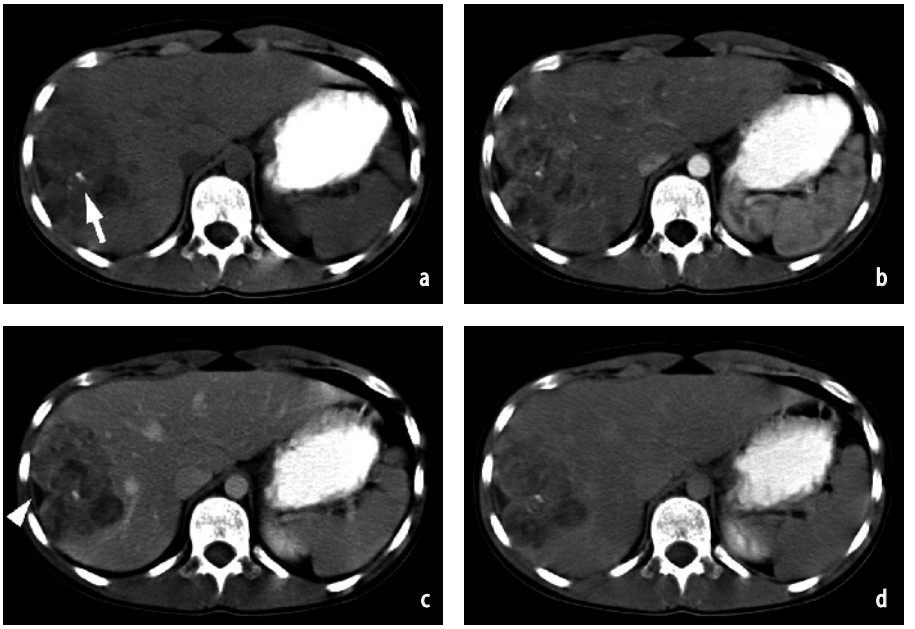

Fig. 9a-d. Hepatoblastoma (*epithelial variant*). The unenhanced CT scan (**a**) reveals a homogeneously hypodense lesion with a small and punctiform calcification (*arrow*). The lesion shows enhancement in the arterial phase after contrast medium administration (**b**) and washout of the contrast medium in the portal-venous (**c**) and equilibrium (**d**) phases. Note the retraction of the liver capsule (*arrowhead* in **c**)

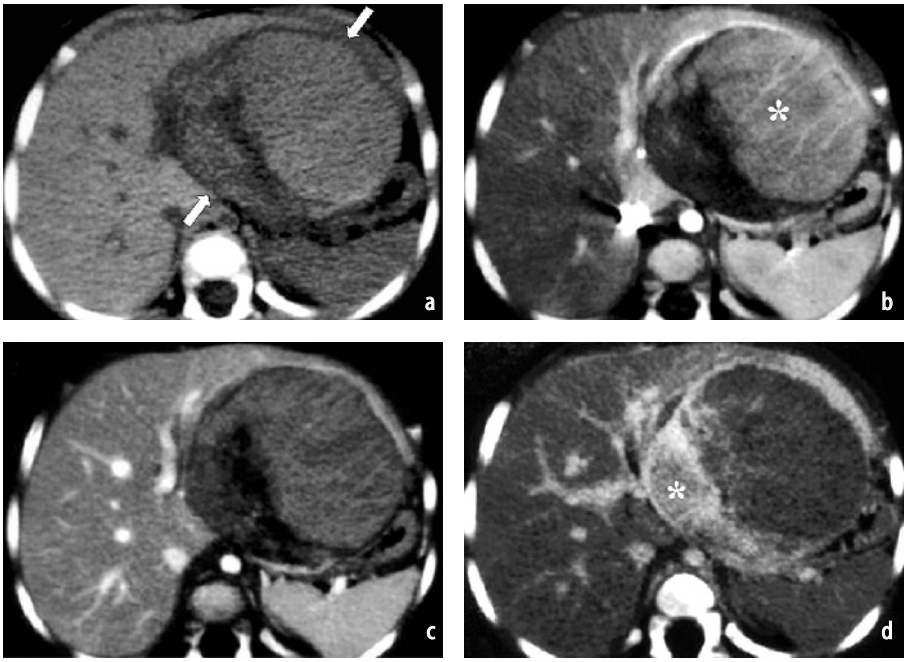

Fig. 10a-d. Mixed hepatoblastoma. On the unenhanced CT scan (**a**) the neoplasm (*arrows*) is heterogeneously iso- and hypodense. During the arterial phase after contrast material administration (**b**), the cellular component of the lesion (*asterisk*) enhances. However, this becomes hypodense in the portal-venous (**c**) and delayed (**d**) phases. Conversely, the stromal component (*asterisk* in **d**) enhances markedly in the delayed phase

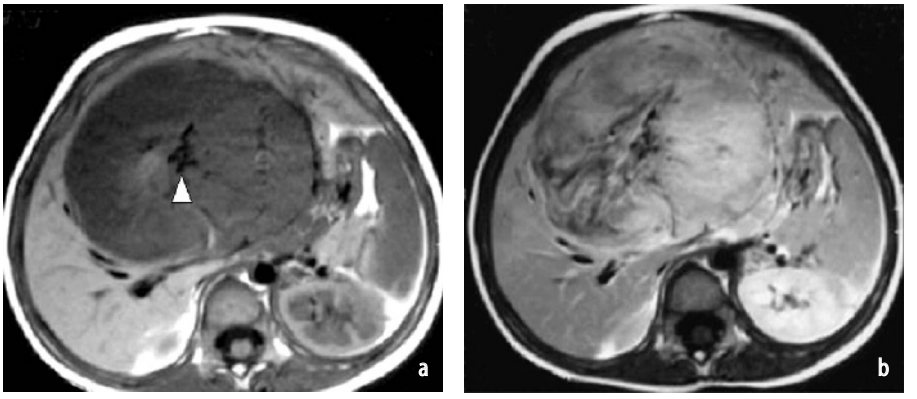

Fig. 11a, b. Hepatoblastoma. The unenhanced T1-weighted image (**a**) reveals a large, well-defined, lobulated hypointense mass with a small central area of lower SI (*arrowhead*) that corresponds to calcification. After contrast agent administration (**b**), the neoplasm demonstrates early, inhomogeneous enhancement

observed on both T1- and T2-weighted images, the latter being due to areas of hemorrhage. Unfortunately, calcifications cannot be diagnosed reliably using this technique. Unenhanced GRE T1-weighted sequences permit evaluation of the vascular components of both the tumor and the healthy parenchyma [34, 75].

Early enhancement and rapid wash-out are typical features of HB on post-contrast dynamic phase imaging (Fig. 12) [89]. In the arterial phase most lesions appear as heterogeneously hyperintense due to the presence of fibrotic and necrotic areas. Thereafter, in the portal-venous and equilibrium phases, the neoplasm is isointense and hypointense, respectively, with hyperintense areas corresponding to the stromal component. In the delayed hepatobiliary phase after the injection of Gd-BOPTA, the lesion is usually heterogeneously hypo- or isointense (Fig. 13).

Catheter angiography can reveal malignant tumoral neo-vascularization, vascular distortion and stretching, and invasion or encompassing of the portal vein or hepatic artery; occasionally it can also visualize a characteristic spoke wheel pattern due to the presence of multiple septa and fibrous bands [34]. Unfortunately, catheter angiography requires the use of ionizing radiation which is not ideal in young children. The availability of 3D CE-MRA has recently been shown to permit accurate preoperative evaluation of the liver vasculature in children with HB [33, 71].

10.4.2 Hepatocellular Carcinoma

HCC is the second most common malignant liver tumor of infancy. Whereas hepatoblastoma typically occurs in children under five years of age, HCC demonstrates two peak periods of onset, one between four and five years of age and the other between 12 and 14 years of age [74]. Etiological and predisposing factors for HCC include glycogenosis types I, III, IV, VI and IX, galactosemia, thyroxinosis, biliary cirrhosis secondary to atresia of the bile ducts, and hepatitis B or C viral infection. The incidence of HCC is slightly greater among boys [34, 90].

Histologically, pediatric HCC is composed of cells with an increased volume, a polygonal shape, abundant granules, acidophilic and glycogen-rich cytoplasm and an acidophilic nucleolus. The histological features are similar to those described for HCC in adult subjects (see Chapt. 6, "Imaging of Malignant Focal Liver Lesions", section 6.1.1, "Hepatocellular Carcinoma").

A variety of substances, such as Mallory bodies, AFP and α-1-antitrypsin, can be produced by the neoplastic hepatocytes. Adipose and glycogenic components may also be detectable in the cell cytoplasm. If the adipose component is abundant, the tumor is referred to as a hepatic clear cell carcinoma [51, 83].

Macroscopically, three different growth patterns may be observed. The lesion may be a massive solitary mass which may or may not be encapsulated. The multifocal variant is characterized by the presence of numerous distinct, sometimes confluent nodules that can simulate metastases. Finally, the less common diffuse form can involve the whole liver and is characterized by multiple small neoplastic foci that mimic the regeneration nodules of cirrhosis. Necrosis is sometimes extensive and can lead to the formation of cysts. HCC is defined as encapsulated when it is contained in a peripheral ring composed of fibrous tissue [29, 34, 58, 61].

At diagnosis, the most common clinical symptoms and signs are anorexia, fever, abdominal pain,

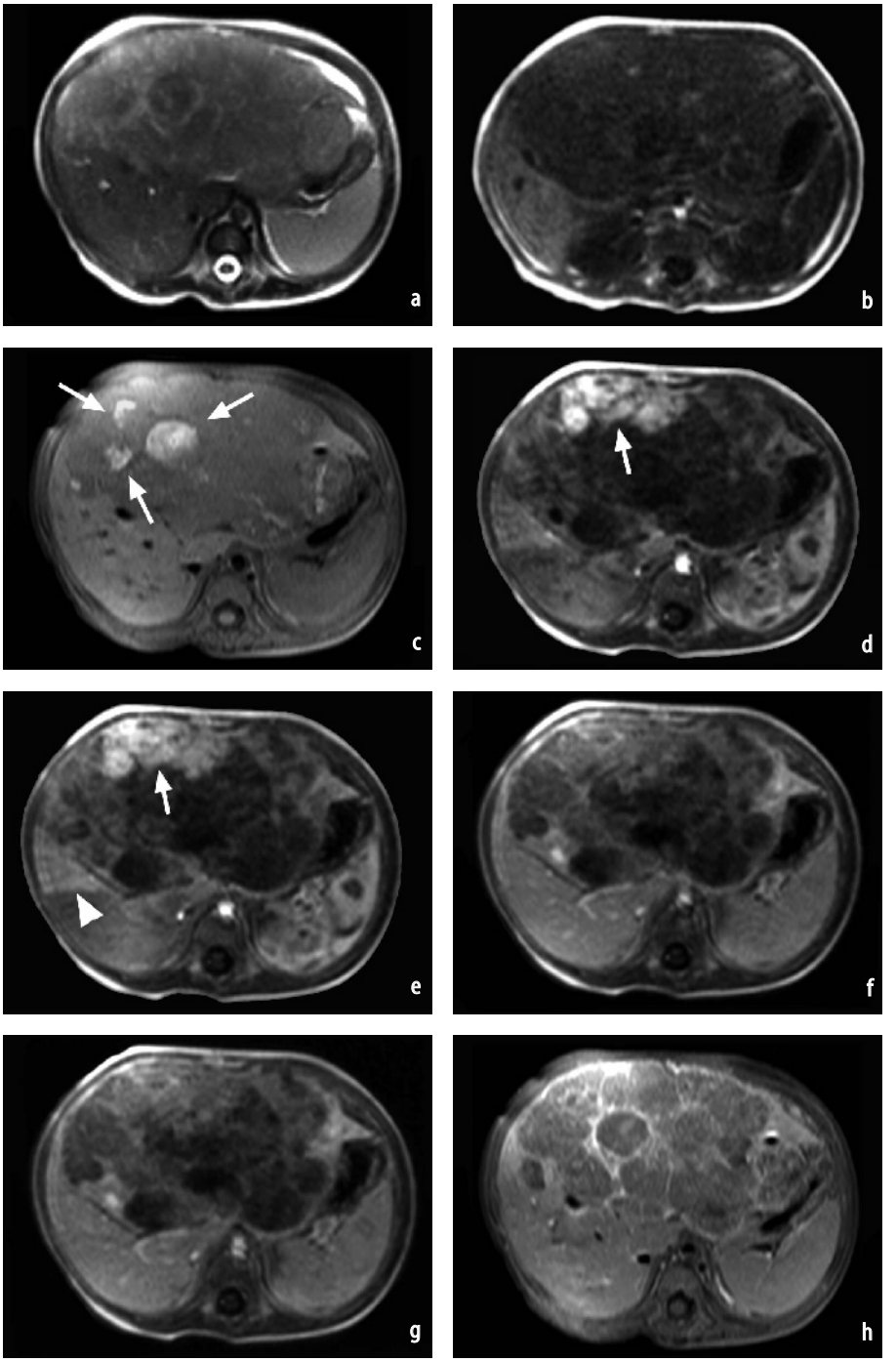

Fig. 12a-h. Hepatoblastoma in a 2 year old girl. A slightly hyperintense lesion compared with the surrounding liver tissue can be seen on the unenhanced T2-weighted image (**a**). On the unenhanced T1-weighted image (**b**), the lesion is revealed as a giant inhomogeneous hypointense mass with small areas of hyperintensity indicative of hemorrhage. The unenhanced T1-weighted fat-suppressed image (**c**) more clearly reveals the areas of high SI (*arrows*) indicative of hemorrhage and regressive changes. The lesion appears slightly hypointense in comparison to the normal liver parenchyma. On dynamic imaging after the bolus administration of Gd-BOPTA (**d**-**g**), the more ventrally located parts of the lesion show hypervascularity (*arrows* in **d** and **e**), whereas most of the remaining parts show only slightly inhomogeneous contrast agent uptake. Due to the mass effect of the lesion, inhomogeneous perfusion of the remaining liver tissue can also be noted (*arrowhead* in **e**). T1-weighted fat-suppressed images acquired during the delayed hepatobiliary phase (**h**) reveal inhomogeneous uptake of Gd-BOPTA. The lesions have a multinodular appearance with hypointense areas indicative of regressive changes

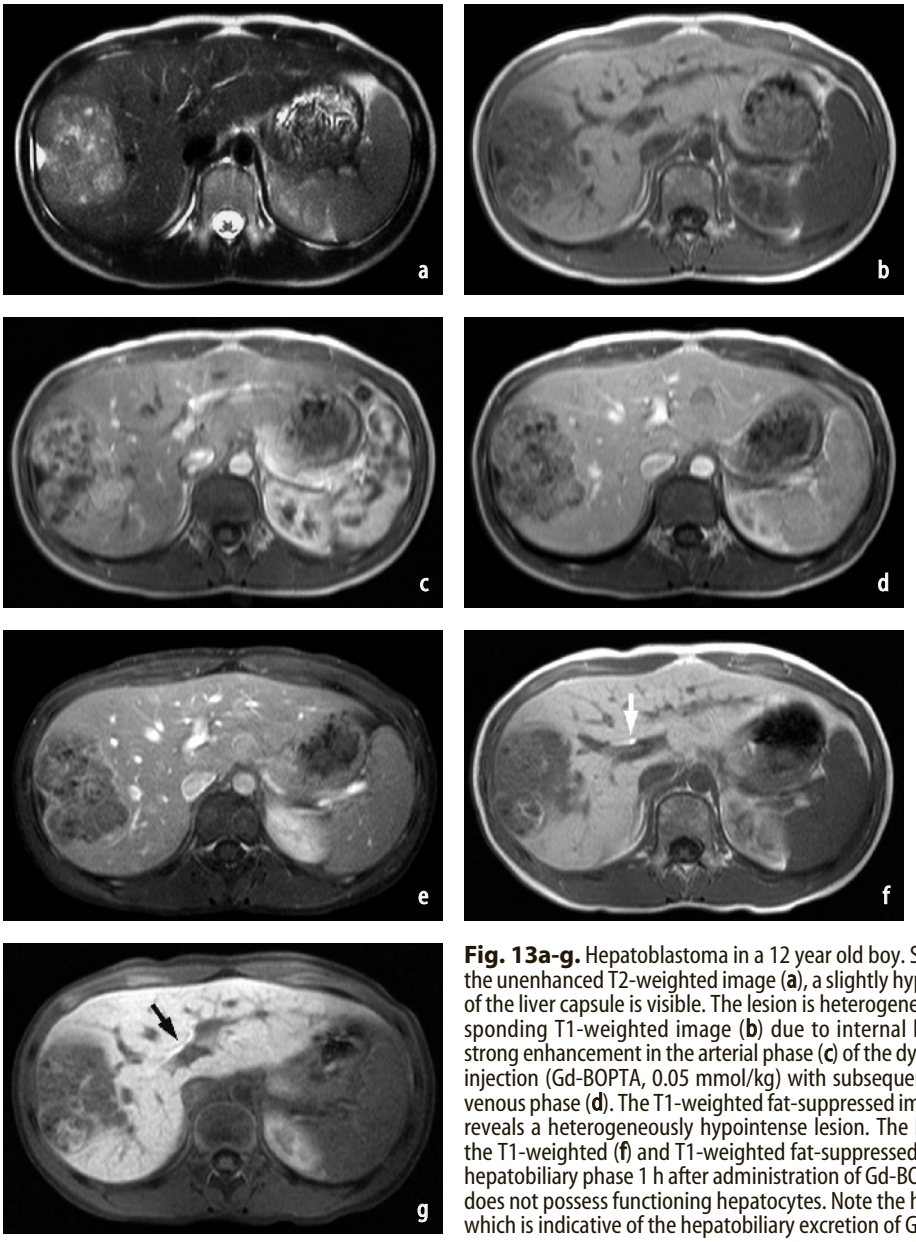

Fig. 13a-g. Hepatoblastoma in a 12 year old boy. Same case as shown in Fig. 9. On the unenhanced T2-weighted image (**a**), a slightly hyperintense lesion with retraction of the liver capsule is visible. The lesion is heterogeneously hypointense on the corresponding T1-weighted image (**b**) due to internal hemorrhage. The lesion shows strong enhancement in the arterial phase (**c**) of the dynamic study after contrast agent injection (Gd-BOPTA, 0.05 mmol/kg) with subsequent early wash-out in the portal-venous phase (**d**). The T1-weighted fat-suppressed image in the equilibrium phase (**e**) reveals a heterogeneously hypointense lesion. The lesion is clearly hypointense on the T1-weighted (**f**) and T1-weighted fat-suppressed (**g**) images acquired during the hepatobiliary phase 1 h after administration of Gd-BOPTA. This indicates a tumor that does not possess functioning hepatocytes. Note the high SI of the bile ducts (*arrows*), which is indicative of the hepatobiliary excretion of Gd-BOPTA

jaundice, and hepatomegaly; at times, its onset can be violent and sudden, with acute abdominal pain and hemoperitoneum due to rupture of the tumor or to rupture or erosion of the superficial vessels. The AFP values are high in more than 50% of cases and generally exceed 1000 ng/mL [7, 34, 89].

The prognosis for HCC is worse than that for HB, with a survival rate between 15% and 30%. This is due primarily to the large number of cases in which the cancer is multifocal or unresectable [89].

The appearance of HCC on US, CT and MR imaging is described in Chapter 6, "Imaging of Malignant Focal Liver Lesions", section 6.1.1, "Hepatocellular Carcinoma".

10.4.3 Fibrolamellar Carcinoma (FLC)

FLC is a slow-growing neoplasm of unknown etiology with different clinical and pathological features of HCC and HB. It is frequently detected in patients of adolescent age and has no predilection for either gender [19]. It generally occurs in the non-cirrhotic liver with normal AFP levels. There are no known risk factors and the prognosis is better than for HCC due to the better chances of surgical resection.

The most common symptoms are the same as those encountered in adult patients: abdominal pain, hepatomegaly, anorexia, weight loss, and less frequently, pain, fever and jaundice. In two out of three cases a mass is appreciable in the right hypochondrium.

As with HCC, the imaging features of FLC on US, CT and MR imaging in pediatric subjects are largely indistinguishable from those in adult subjects (see Chapt. 6, "Imaging of Malignant Focal Liver Lesions", section 6.1.2, "Fibrolamellar Hepatocellular Carcinoma").

10.4.4 Undifferentiated Embryonal Sarcoma (UES)

UES was first recognized as a clinical pathological entity in 1978 [93]. This neoplasm had previously been attributed various terms, including embryonal sarcoma, primary sarcoma, fibromyxosarcoma, and malignant mesenchymoma. Although rare, UES is the fourth most frequent hepatic neoplasm in infancy after HB, hemangioendothelioma and HCC.

UES occurs predominantly in children between six and ten years of age [22], although it has also been known to affect adults [9]. The incidence is almost the same in males and females [25, 47, 52].

Histologically, UES is composed of undifferentiated fusiform cells resembling primitive embryonal cells, and myxoid stroma [38]. A relationship has been suggested between UES and mesenchymal hamartoma [23]. However, these two neoplasms are distinguished not only by their histology, but also by their time of onset and clinical presentation: mesenchymal hamartoma is typically observed in small children, aged between four months and two years, whereas UES occurs in older children. Moreover, whereas the former is symptom-free, UES is usually symptomatic [25].

Macroscopically, UES presents as a large mass, located more frequently in the right lobe of the liver. It is often well-defined and sometimes complete with a pseudo capsule; it can reach 20 cm in diameter and may contain cystic, hemorrhagic and/or necrotic areas, as well as having a cellular component. The cystic variants are more frequent than the solid forms and reflect the rapid growth of the neoplasm [64, 81].

UES frequently presents as a palpable abdominal mass with or without pain, fever, jaundice and weight loss [25, 64, 89]. Sometimes, the tumor may rupture, leading to acute abdominal crisis [82]. There are no reliable changes in laboratory data, although mild leukocytosis and anemia may be seen in 50% of cases and elevated liver enzymes in 30% of cases. Typically, serum AFP levels are normal [20, 99].

In cases of UES, the prognosis depends on the possibility of achieving complete resection of the neoplasm. Although this is often difficult, when combined with adjuvant chemotherapy it offers the best chance of cure [99, 100].

On US this neoplasm can present either as a hypoechogenic mass with multiple hyperechogenic septa of variable thickness, or as an echogenic lesion containing numerous small cystic collections. This diversity of echostructure depends on the greater or lesser prevalence of the myxoid, solid, and hemorrhagic or necrotic components [9, 41, 64, 81, 89].

At CT imaging, UES generally presents as a large intrahepatic mass that has lower attenuation than the surrounding liver parenchyma. The abundant myxoid matrix of the tumor may be the cause of the hypodense appearance on CT. Conversely, lesions with higher-density contain hemorrhagic, necrotic or solid material. In some cases, a dense, peripheral enhancing thin rim corresponding to the fibrous pseudocapsule may be depicted on CT images. Likewise, hyperdense septations may also be seen in some cases [64, 81].

The MR findings are related to the cystic degeneration and the hemorrhagic-necrotic components of the tumor. On unenhanced T1-weighted images the neoplasm is typically hypointense due to cystic degeneration, with areas of higher SI reflecting hemorrhagic events. On T2-weighted images the SI reflects the cystic or solid predomi-

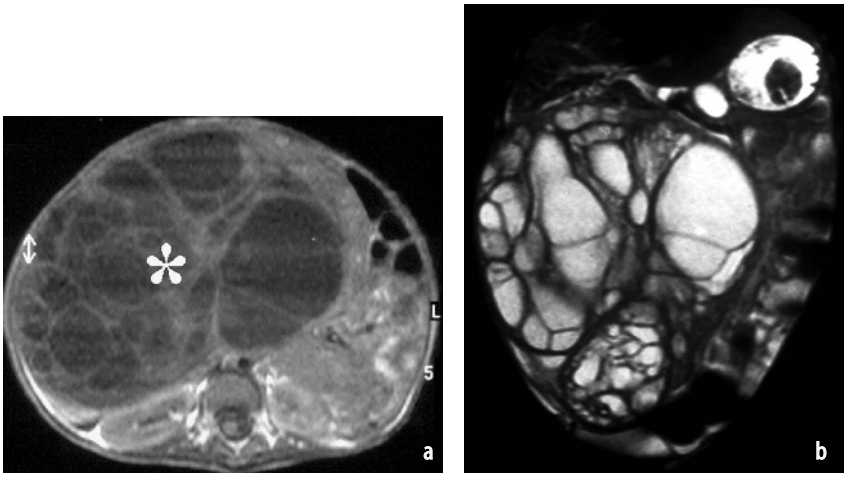

Fig. 14a, b. Undifferentiated embryonal sarcoma. On the unenhanced T1-weighted image (**a**), a large cystic septated lesion (*asterisk*) involving a large part of the liver can be seen. On the coronal T2-weighted image (**b**), the mass appears hyperintense and multiloculated

nance of the lesion, with marked signal hyperintensity in the case of a cystic lesion (Fig. 14). The fibrous pseudocapsule and septations, if present, are typically hypointense on both T1- and T2-weighted images [10, 81, 89, 105].

Catheter angiography generally reveals a hypo- or avascularized neoplasm and the extent of vascularization is inversely proportional to the cystic transformation. There are signs of macro-aneurysms, arterio-venous shunts, and stasis of the contrast medium in the solid portion of the tumor. Though these angiographic aspects are non-specific, the macro-aneurysms observed in the vascularization of the neoplasm have not been reported in any other hepatic malignancies, apart from UES [105].

10.4.5 Hepatobiliary Rhabdomyosarcoma (RMS)

Although RMS is the most common neoplasm of the biliary tree in children, it is a rare disease, accounting for approximately 1% of all RMS in pediatric patients. RMS usually occurs in children of about three years of age and is rarely seen after the first decade of life. There may be a slight predominance among males [84].

Although the early histological classification of RMS was different in the United States [37] and Europe [12], a universal classification now exists [66]. Hepatobiliary RMS in childhood can be of the embryonal or botryoid types [84]. It may arise in the liver or intrahepatic bile ducts [54] in intrahepatic cysts [85], the gallbladder [60], the cystic duct [49], the extrahepatic bile duct [49], the ampulla [14], or in choledochal cysts [73].

Microscopically, RMS contains spindle cell tumors in a myxoid stroma. A few cells have eosinophilic cytoplasmic tails resembling rhabdomyoblasts with or without cross striations [38]. Macroscopically, RMS tends to be well-demarcated from the surrounding tissue with a "pushing" margin. The mean diameter at diagnosis is usually about 8 cm [38, 84].

The most common clinical features are jaundice and abdominal distension. Pain, nausea, vomiting and fever are less frequent. AFP values are normal [84, 85].

US typically reveals biliary dilatation and an intraductal mass [28, 32]. Although the portal vein may be displaced by a large tumor, portal vein thrombosis has not been described. Larger masses may have fluid, cystic areas within them, possibly reflecting tumor necrosis [63]. When the tumor arises in the liver, there may be no distinguishing US features (Fig. 15). Color Doppler US may reveal numerous abnormal tumor arteries with low resistive index [79]. The same is seen on catheter angiography, indicating a malignant neoplasm (Fig. 16).

CT also reveals an intraductal mass with or without biliary dilatation (Fig. 17). Hypodense and heterogeneous attenuation patterns have been described [32] and areas of low attenuation within the tumor may be present [14, 54, 63, 73]. Enhancement patterns after the administration of contrast material have been described as strong heterogeneous, incomplete globular, mild and none [79], indicating that enhancement may be variable.

RMS is generally hypointense on unenhanced T1-weighted MR images and moderately or markedly hyperintense on T2-weighted images.

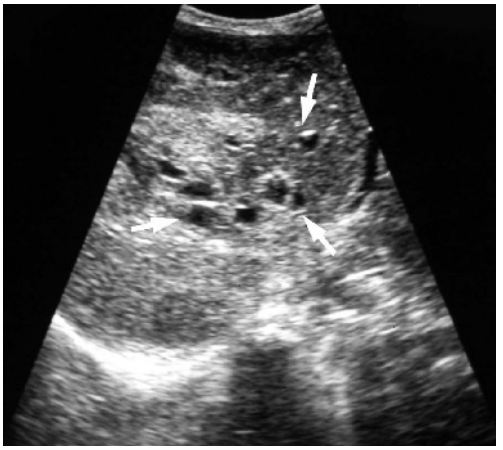

Fig.15. Hepatobiliary rhabdomyosarcoma. US reveals a large mass with internal cystic areas (*arrows*) that reflect tumor necrosis and dilated bile ducts

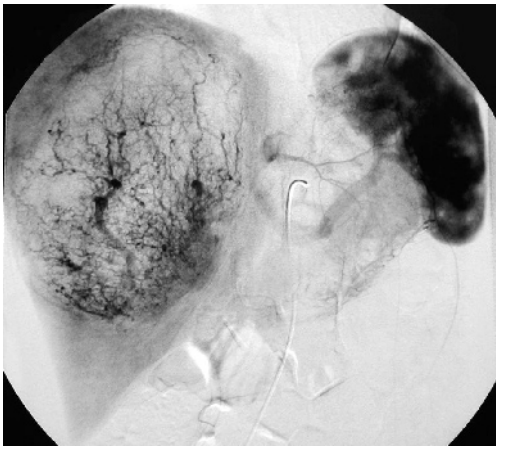

Fig. 16. Hepatobiliary rhabdomyosarcoma. Catheter angiography demonstrates numerous abnormal tumor vessels, indicative of a malignant liver tumor, within a hepatobiliary rhabdomyosarcoma

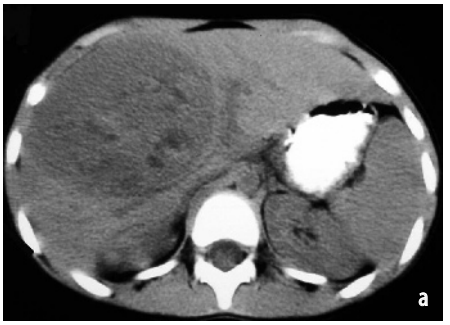

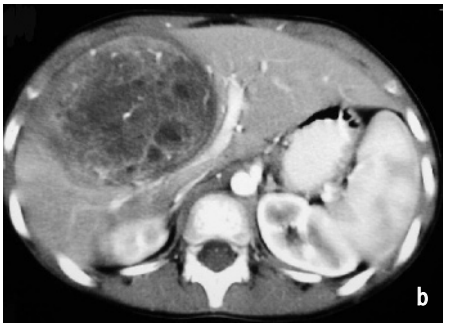

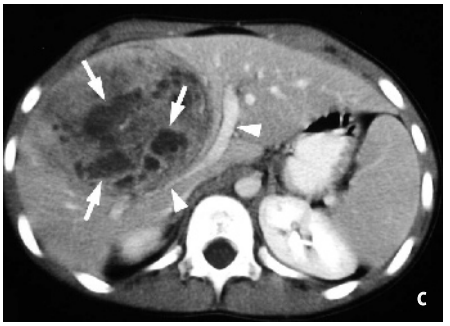

Fig. 17a-c. Hepatobiliary rhabdomyosarcoma. The unenhanced CT image (**a**) shows a hypodense tumor with heterogeneous attenuation pattern. Low attenuation areas are apparent within the tumor. Following the injection of contrast medium, the tumor shows heterogeneous enhancement in the arterial phase (**b**) with depiction of multiple irregular vessels within the tumor. In the portal-venous phase (**c**) most of the tumor shows wash-out of contrast medium resulting in a more heterogeneous appearance. Multiple cystic areas within the tumor (*arrows*) and displacement of the portal vein by the tumor (*arrowheads*) can be noted

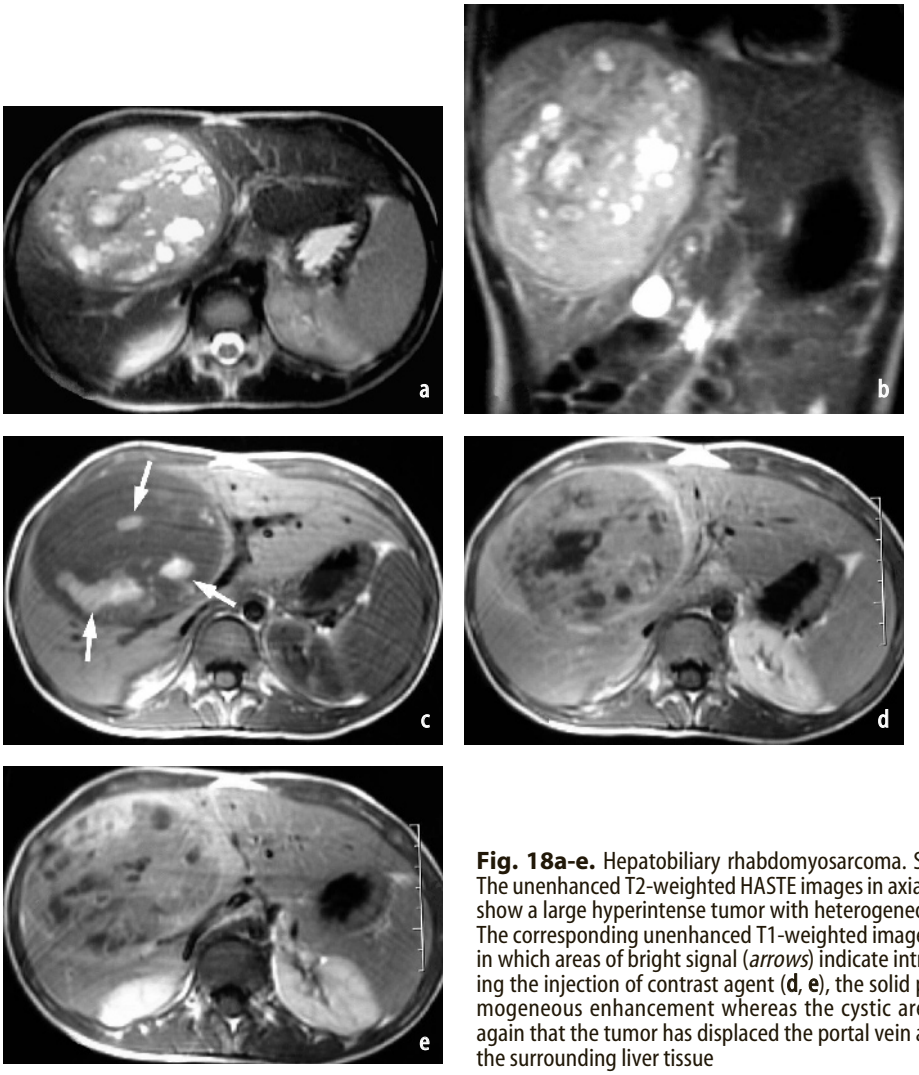

Fig. 18a-e. Hepatobiliary rhabdomyosarcoma. Same case as shown in Fig. 17. The unenhanced T2-weighted HASTE images in axial (**a**) and coronal (**b**) orientation show a large hyperintense tumor with heterogeneous SI and multiple cystic areas. The corresponding unenhanced T1-weighted image (**c**) reveals a tumor with low SI in which areas of bright signal (*arrows*) indicate intratumoral hemorrhage. Following the injection of contrast agent (**d**, **e**), the solid portions of the tumor show homogeneous enhancement whereas the cystic areas remain hypointense. Note again that the tumor has displaced the portal vein and is sharply demarcated from the surrounding liver tissue

Following the administration of a Gd contrast agent, intense but inhomogeneous contrast enhancement is usually seen (Fig. 18) [79].

10.4.6 Hepatic Angiosarcoma (HAS)

HAS is an extremely rare neoplasm in pediatric subjects, with only a few dozen cases having been reported. HAS is frequently considered to be the malignant form of IHE [1]. In this regard, exposure to comparatively high levels of arsenic, both during pregnancy and in the postnatal period, has been shown to contribute to the onset of HAS in the presence of IHE [26].

The mean age of onset of HAS in children is four years. Histologically, this neoplasm is composed of malignant endothelial cells lining vascular channels of various dimensions, which tend to form sinusoids. Macroscopically, two forms of HAS can develop: a multifocal or multinodular form (Fig. 19, 20), and a large, solitary mass. Both forms are associated with areas of necrosis and hemorrhage [10].

The clinical signs are non-specific, with progressive abdominal distension and a palpable mass in the right hypochondrium, often associated with abdominal pain, asthenia and weight loss. Hemorrhagic ascites is a common sign and hemoperitoneum is sometimes observed. This is a complication related to the vascular nature of the neoplasm on the one hand, and to the resulting thrombocytopenia on the other. The neoplasm usually presents with normal serum AFP values [10, 83].

Imaging findings for HAS in pediatric subjects on US, CT and MRI can be considered similar to those for the adult form of the lesion (see Chapt. 6, "Imaging of Malignant Focal Liver Lesions", section 6.1.4.1, "Angiosarcoma").

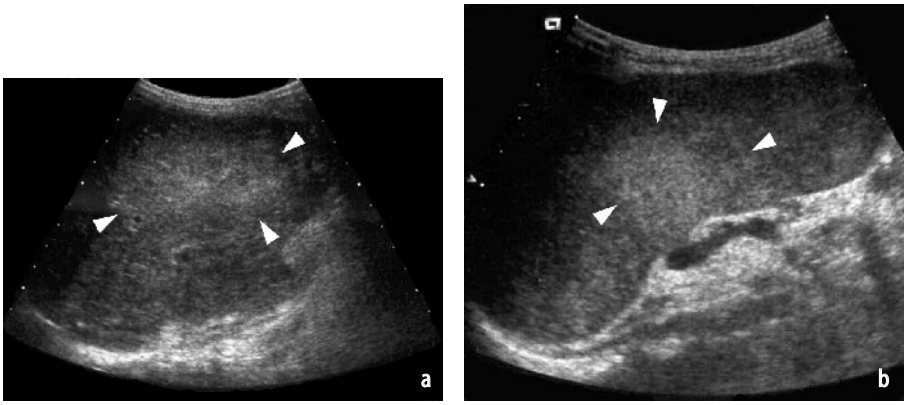

Fig. 19a, b. Angiosarcoma. US images (**a**, **b**) reveal a multinodular tumor growth which forms a large mass (*arrowheads*). The borders of the involved region are indistinct and small satellite lesions are visible

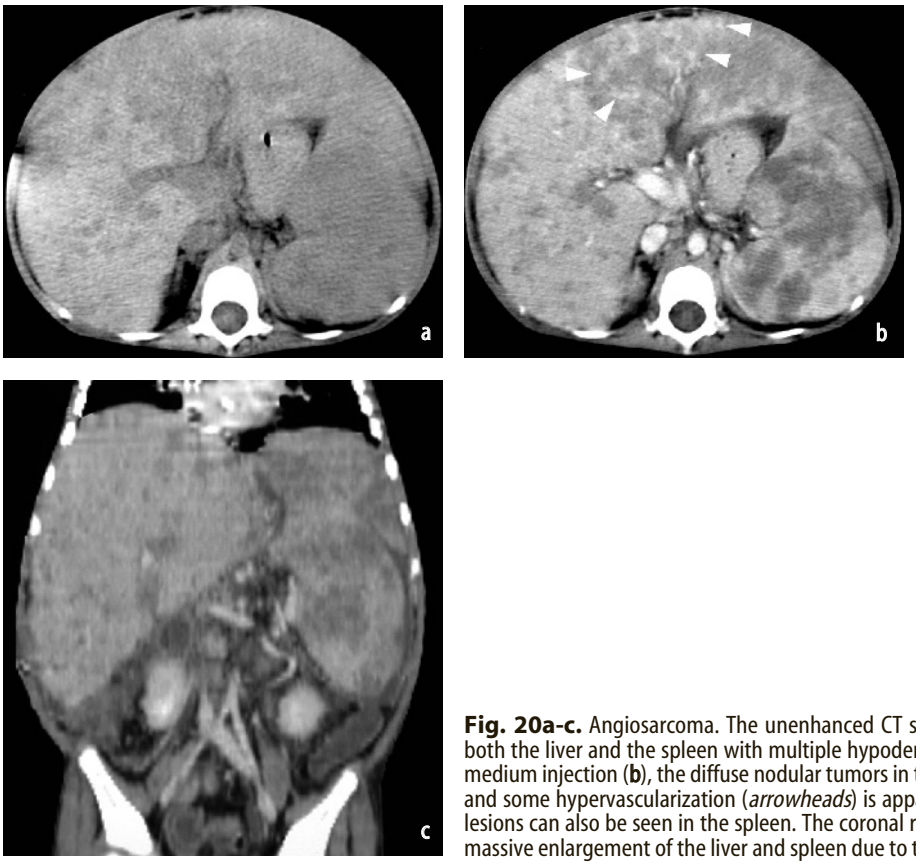

Fig. 20a-c. Angiosarcoma. The unenhanced CT scan (**a**) reveals enlargement of both the liver and the spleen with multiple hypodense nodules. Following contrast medium injection (**b**), the diffuse nodular tumors in the liver are much more evident and some hypervascularization (*arrowheads*) is apparent in the periphery. Multiple lesions can also be seen in the spleen. The coronal reconstruction (**c**) highlights the massive enlargement of the liver and spleen due to tumor infiltration

10.4.7 Hodgkin's and Non-Hodgkin's Lymphoma (NHL), Burkitt Lymphoma

Primary lymphoma of the liver is a very rare malignancy with a frequency of about 0.016% of all cases of NHL. The most frequent form of primary liver lymphoma is diffuse large B-cell NHL which occurs primarily in immunodeficient patients. To determine the primary nature of a hepatic lesion, systemic lymphoproliferative disease should first be ruled out.

Secondary liver involvement as a result of Hodgkin's lymphoma and NHL is more frequent. In advanced cases the incidence varies from 25-50%.

Typical symptoms include weight loss, fever and night sweats, while physical examination often reveals asthenia, hepatomegaly, jaundice and ascitis. Obstructive jaundice may occur as a late manifestation of NHL resulting from encasement of the common bile duct by the tumor. Imaging studies usually reveal a solitary mass in the liver although multiple masses may occur, albeit less frequently.

Primary lymphoma is usually hypoechoic or anechoic on US and hypodense on CT. On pre-contrast T2-weighted MR imaging, most lesions are homogeneously hyperintense with a SI that is comparable to or higher than that of the spleen (Fig. 21). Other lesions, however, may be isointense on T2-weighted images but appear as slightly hypointense on T1-weighted images (Fig. 22). Generally, the SI of lymphoma is comparable on "in-phase" and "out-of-phase" T1-weighted images. Lymphomas typically do not show significant enhancement on arterial phase images after the administration of Gd contrast agents, although a slight increase in SI may sometimes be seen in the late portal-venous phase. However, most lesions are isointense with the normal liver parenchyma on T1-weighted images acquired during the equilibrium phase. The SI of lymphomas that have a periportal distribution is non-specific, which may lead to an initial misdiagnosis of metastasis [17, 31] (Fig. 23).

Most patients are treated with chemotherapy, although some physicians employ a multimodal approach involving additional surgery and radiotherapy. Although the prognosis is variable, a good response may be achieved if aggressive combination chemotherapy is performed early after onset [18, 39, 56, 67, 76].

Burkitt's lymphoma is a mature B-cell lymphoma associated with Epstein-Barr-virus that is characterized by rapid proliferation and a propensity for extranodal sites of involvement such as the gastrointestinal tract and central nervous system. It affects primarily children and young adults. Since sonography is often the first imaging procedure performed in these patients, knowledge of the wide range of sonographic appearances is helpful for the recognition of Burkitt's lymphoma.

Burkitt's lymphoma appears to be curable in a high proportion of cases if treated with aggressive multiagent chemotherapy regimens. The use of autologous stem cell transplantation appears to benefit patients who have had chemotherapy-sensitive relapses [6, 106].

10.4.8 Metastases

Primary neoplasms that metastasize most frequently to the liver in the pediatric age group are Wilms' tumor, neuroblastoma, lymphoma and leukemia (Fig. 24). In contrast to liver metastases in adults, metastases to the liver in pediatric patients are much more uncommon. However, with regard to imaging studies, the same imaging characteristics are observed as in adult patients. Further details can be found in Chapter 6, "Imaging of Malignant Focal Liver Lesions", section 6.2.2, "Metastases".

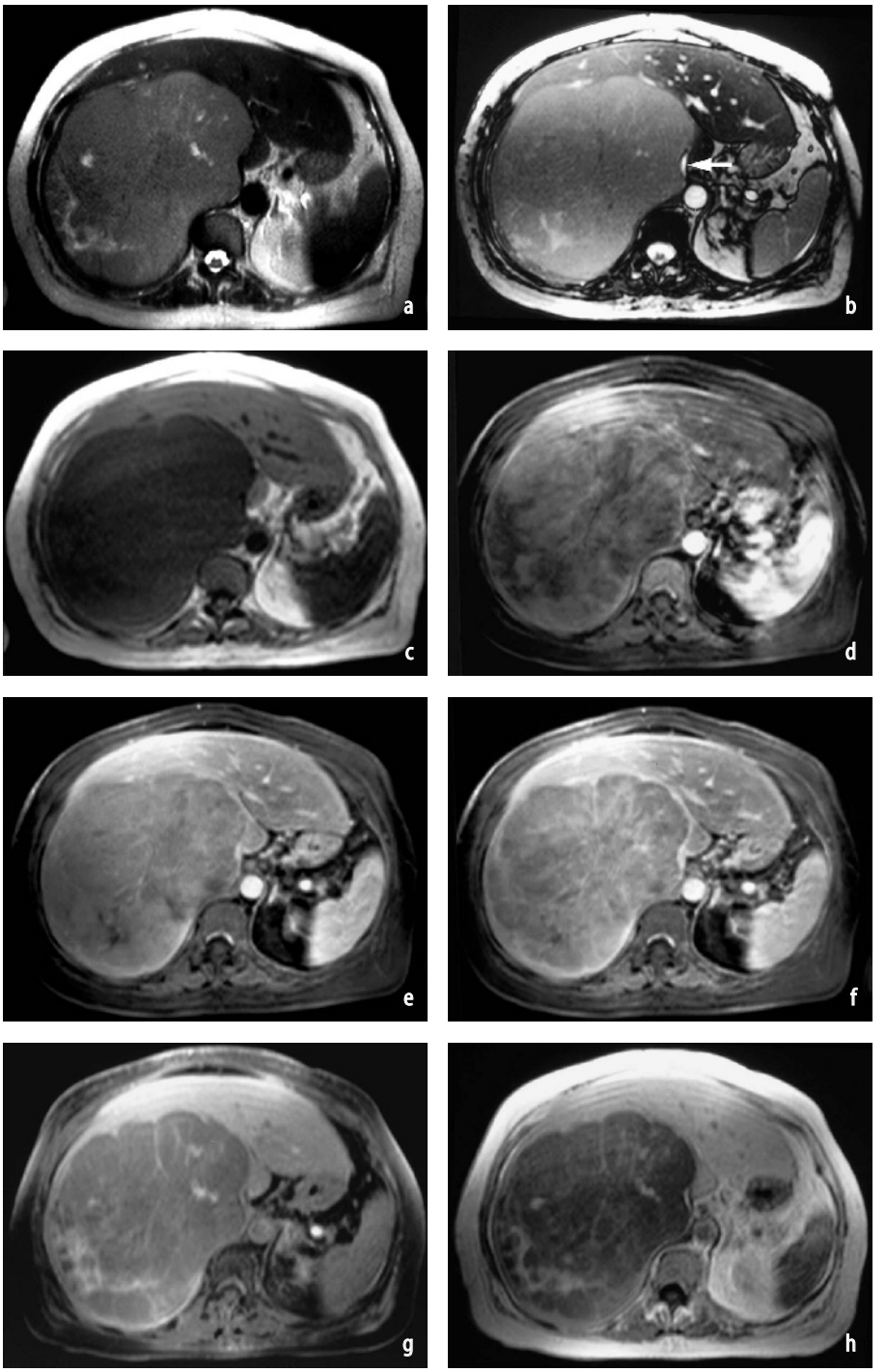

Fig. 21a-h. Primary hepatic large cell lymphoma. The T2-weighted image (**a**) reveals a giant hyperintense, sharply demarcated mass in the right liver lobe. Displacement of the portal vein (*arrow*) can be seen on the true FISP image (**b**). The lesion is homogeneously hypointense on the unenhanced T1-weighted image (**c**) and shows slight but homogeneous enhancement on T1-weighted fat-suppressed dynamic images following the bolus injection of Gd-BOPTA (**d**-**f**). The tumor is again hypointense on T1-weighted fat-suppressed (**g**), and T1-weighted (**h**) images acquired during the hepatobiliary phase after injection of Gd-BOPTA. Distinct tumor margins are again depicted clearly

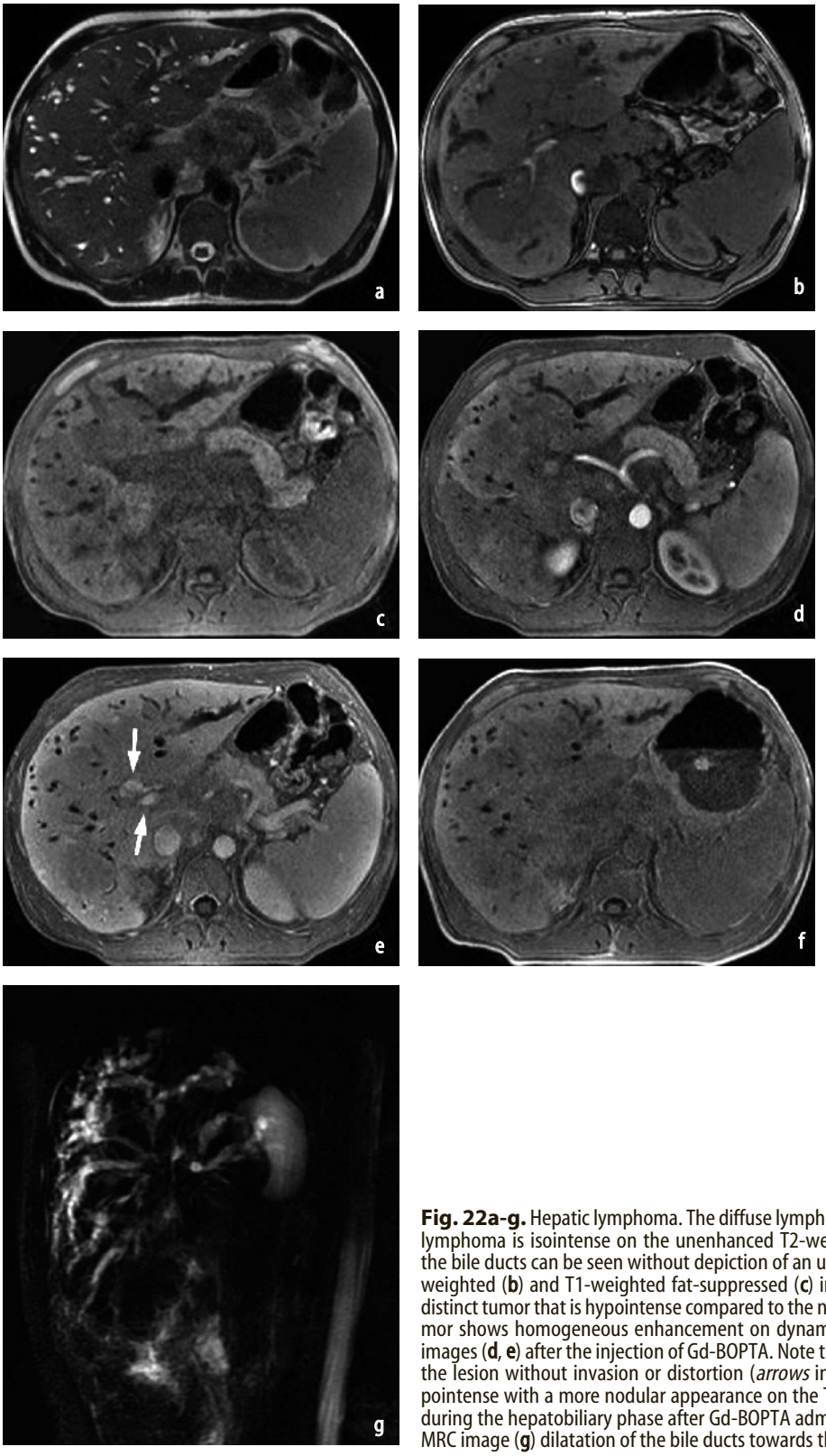

Fig. 22a-g. Hepatic lymphoma. The diffuse lymphomatous form of non-Hodgkin's lymphoma is isointense on the unenhanced T2-weighted image (**a**). Dilatation of the bile ducts can be seen without depiction of an underlying mass. Conversely, T1-weighted (**b**) and T1-weighted fat-suppressed (**c**) images reveal the presence of a distinct tumor that is hypointense compared to the normal liver parenchyma. The tumor shows homogeneous enhancement on dynamic T1-weighted fat-suppressed images (**d**, **e**) after the injection of Gd-BOPTA. Note that veins can be seen traversing the lesion without invasion or distortion (*arrows* in **e**). The tumor is markedly hypointense with a more nodular appearance on the T1-weighted image (**f**) acquired during the hepatobiliary phase after Gd-BOPTA administration. On a corresponding MRC image (**g**) dilatation of the bile ducts towards the liver hilum is visible

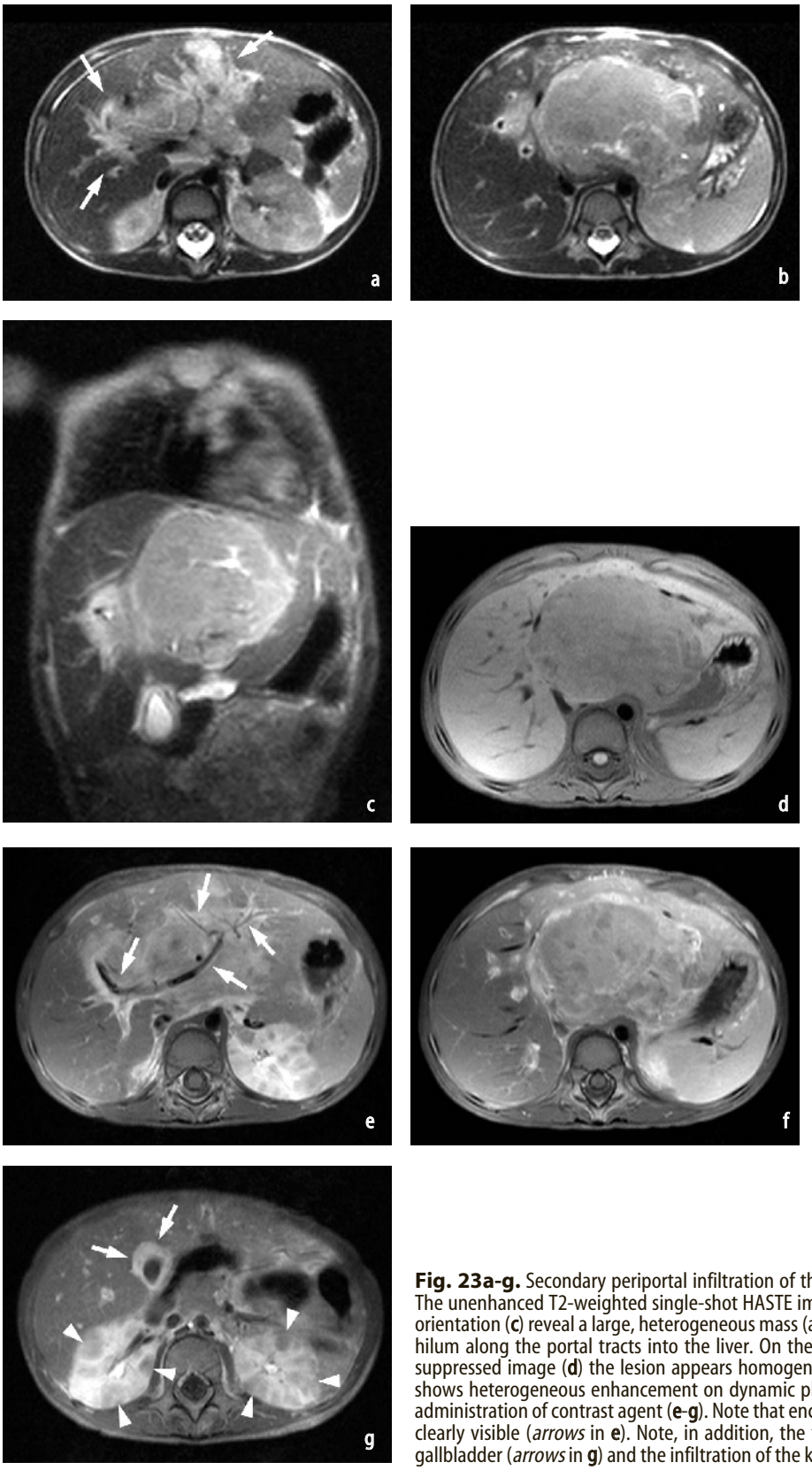

Fig. 23a-g. Secondary periportal infiltration of the liver by a Burkitt lymphoma. The unenhanced T2-weighted single-shot HASTE images in axial (**a**, **b**) and coronal orientation (**c**) reveal a large, heterogeneous mass (arrows in a) infiltrating from the hilum along the portal tracts into the liver. On the unenhanced T1-weighted fat-suppressed image (**d**) the lesion appears homogeneously hypointense. The lesion shows heterogeneous enhancement on dynamic phase images acquired after the administration of contrast agent (**e**-**g**). Note that encasement of the portal vessels is clearly visible (*arrows* in **e**). Note, in addition, the tumor masses surrounding the gallbladder (*arrows* in **g**) and the infiltration of the kidneys (*arrowheads* in **g**)

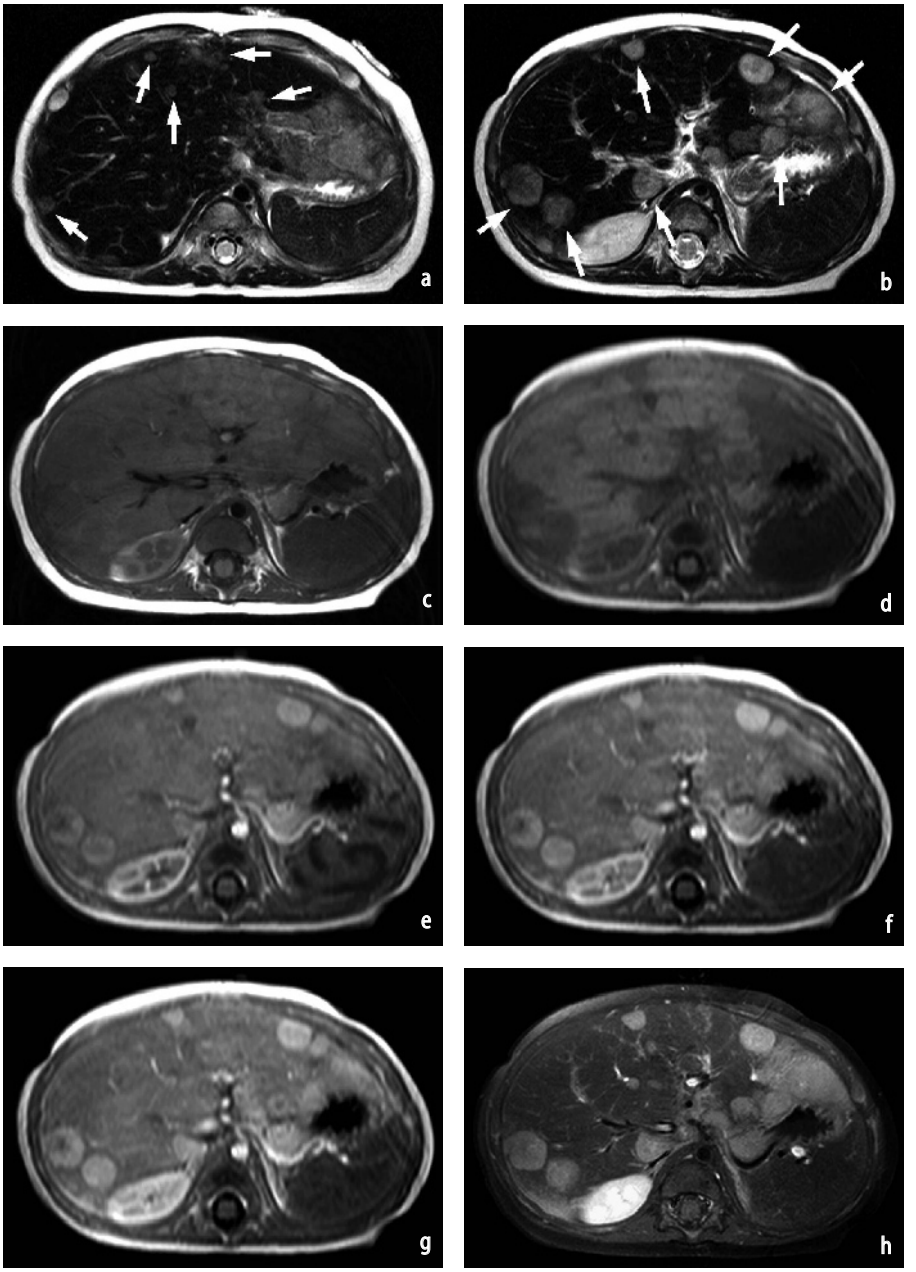

Fig. 24a-h. Liver metastases from neuroblastoma. The unenhanced T2-weighted images (**a**, **b**) reveal multiple, diffusely distributed hyperintense lesions (*arrows*) throughout the liver. The lesions appear slightly hypointense on the corresponding unenhanced T1-weighted image (**c**). Dynamic contrast-enhanced T1-weighted images (**d**-**g**) acquired after the bolus injection of contrast agent reveal the hypervascular nature of the metastases and contrast agent pooling. On the T1-weighted fat-suppressed image in the equilibrium phase (**h**) the lesions have homogeneous high SI and are clearly demarcated from surrounding liver tissue

10.5 Diffuse Liver Disease in Pediatric Patients

10.5.1 Steatosis

Whereas focal fatty infiltration of the liver is present in roughly 10% of the adult population, it is uncommon in infants and young children. However, its prevalence increases with age. The most frequent underlying causes in children are malnutrition with or without diabetes mellitus, obesity (Fig. 25), metabolic diseases and chemotherapy (Fig. 26).

As in the adult population, there are both diffuse and focal forms of fatty liver infiltration. Approximately 30-40% of cases occur focally, either as solitary areas (10% of cases) or as multiple areas with a more widespread distribution (20-30% of cases). Most cases of fatty liver infiltration are of the diffuse type with a segmental, lobar, or irregular distribution. More details on imaging of fatty liver are given in Chapter 5, "Hepatic Pseudolesions".

10.5.2 Biliary Atresia

The causes and clinical presentation of biliary atresia in pediatric subjects are as described in Chapter 7, "Imaging of the Biliary Tree and Gallbladder Diseases", section 7.2.2.3, "Biliary Atresia".

Most infants with biliary atresia are chemically jaundiced from birth. Jaundice is obstructive in type, with dark urine and pale stools. Initially, the infants have hepatomegaly with minimal or no splenomegaly. Later, progressive fibrosis and subsequent cirrhosis (Fig. 27) lead to all the complications of portal hypertension [11]. Cholestasis with prolonged conjugated hyperbilirubinemia of more than 4.5 mg/dL is typical. Usually, the jaundiced patients also have increased levels of serum γ-glutamyltransferase.

US is frequently employed for screening infantile cholestasis. The imaging characteristics on US are as described in Chapter 7, "Imaging of the Biliary Tree and Gallbladder Diseases", section 7.2.2.3, "Biliary Atresia".

MRC is a well-established non-invasive modality used to define the biliary system in children. Biliary atresia can be diagnosed reliably on the basis of the non-visualization of either the common bile duct or the common hepatic duct (Fig. 27). Nevertheless, MRC findings must be interpreted in relation to clinical information [45, 68].

The prognosis of untreated biliary atresia is extremely poor, with death from liver failure usually occurring within two years. Whereas hepato-porto-enteroanastomy can restore bile flow in most infants, the technique is usually not curative. With this surgical procedure, the timing of the surgery correlates with outcome. Thus, while bile flow is successfully re-established in more than 80% of infants if surgery is performed within 90 days of birth, the benefit of surgery gradually decreases if surgery is performed after 90 days [15, 42].

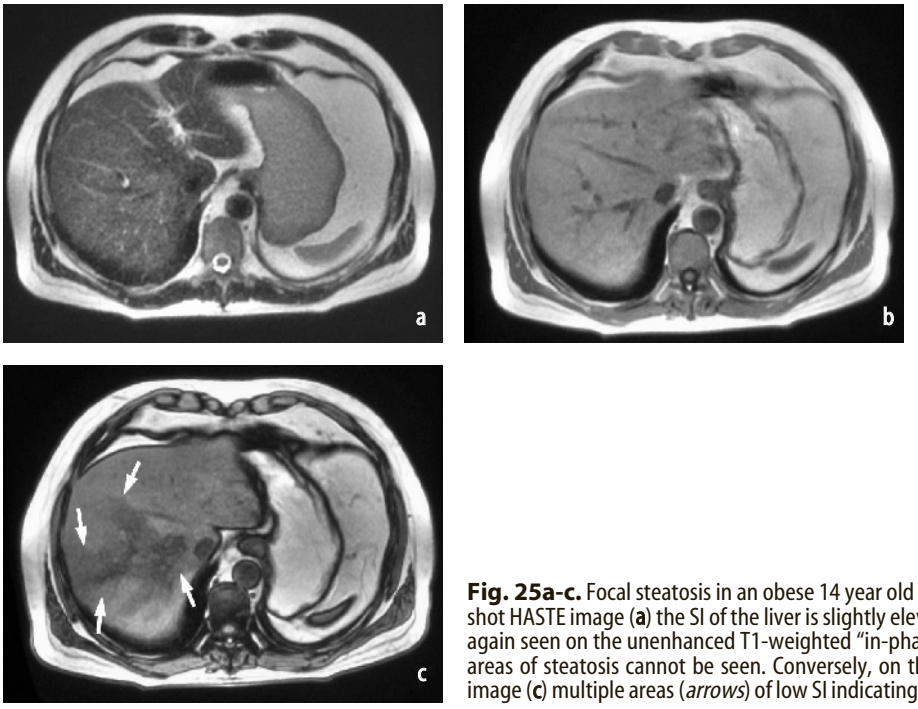

Fig. 25a-c. Focal steatosis in an obese 14 year old boy. On the T2-weighted single shot HASTE image (**a**) the SI of the liver is slightly elevated. Increased SI of the liver is again seen on the unenhanced T1-weighted "in-phase" image (**b**) although distinct areas of steatosis cannot be seen. Conversely, on the T1-weighted "out-of-phase" image (**c**) multiple areas (*arrows*) of low SI indicating focal steatosis can be identified

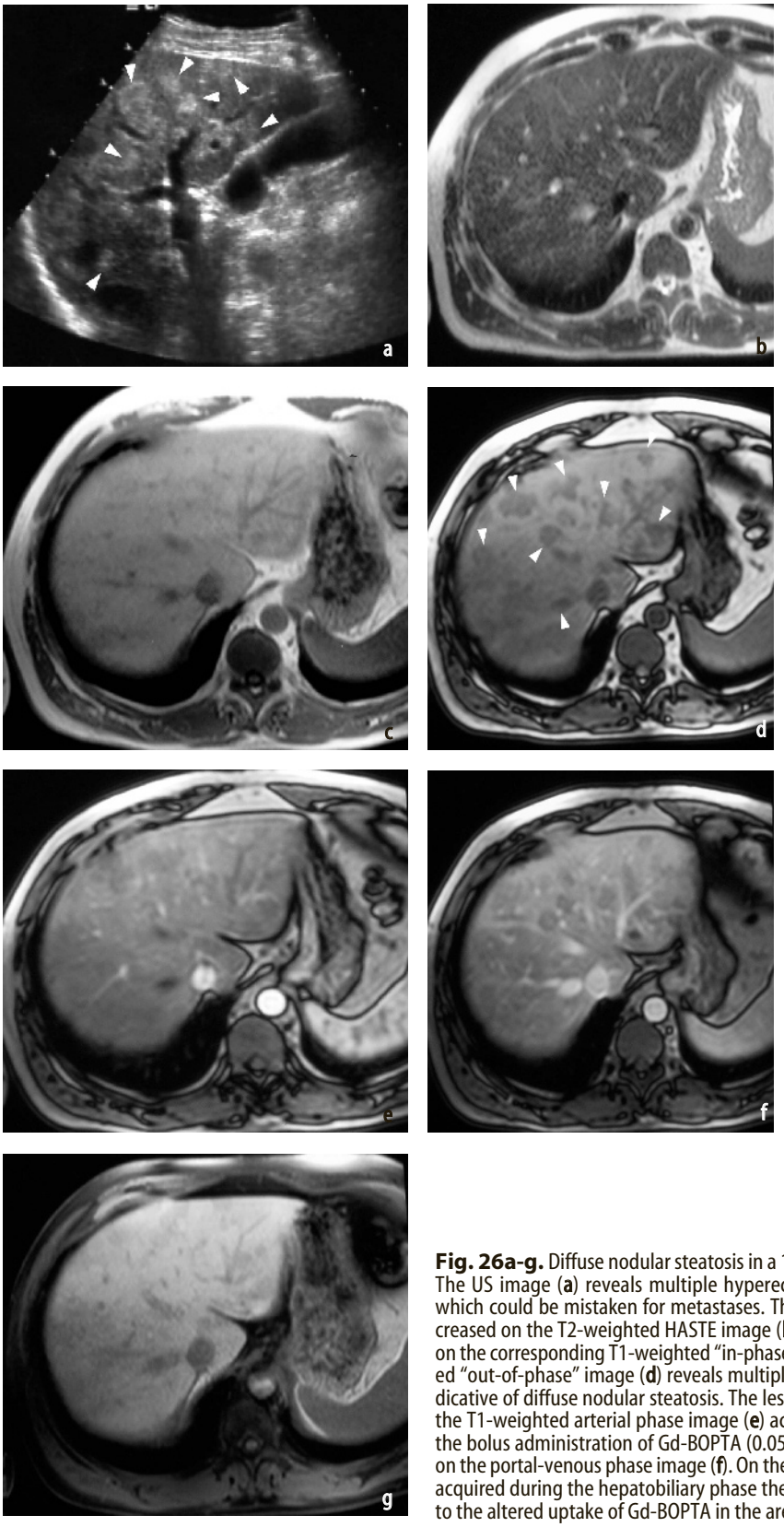

Fig. 26a-g. Diffuse nodular steatosis in a 14 year old patient post-chemotherapy. The US image (**a**) reveals multiple hyperechoic lesions (*arrowheads*) in the liver which could be mistaken for metastases. The SI of the liver is heterogeneously increased on the T2-weighted HASTE image (**b**), but more homogeneously increased on the corresponding T1-weighted "in-phase" image (**c**). Conversely, the T1-weighted "out-of-phase" image (**d**) reveals multiple hypointense lesions (*arrowheads*) indicative of diffuse nodular steatosis. The lesions do not show any enhancement on the T1-weighted arterial phase image (**e**) acquired during the dynamic phase after the bolus administration of Gd-BOPTA (0.05 mmol/kg) and are clearly hypointense on the portal-venous phase image (**f**). On the T1-weighted fat-suppressed image (**g**) acquired during the hepatobiliary phase the lesions show slightly decreased SI due to the altered uptake of Gd-BOPTA in the areas of nodular steatosis

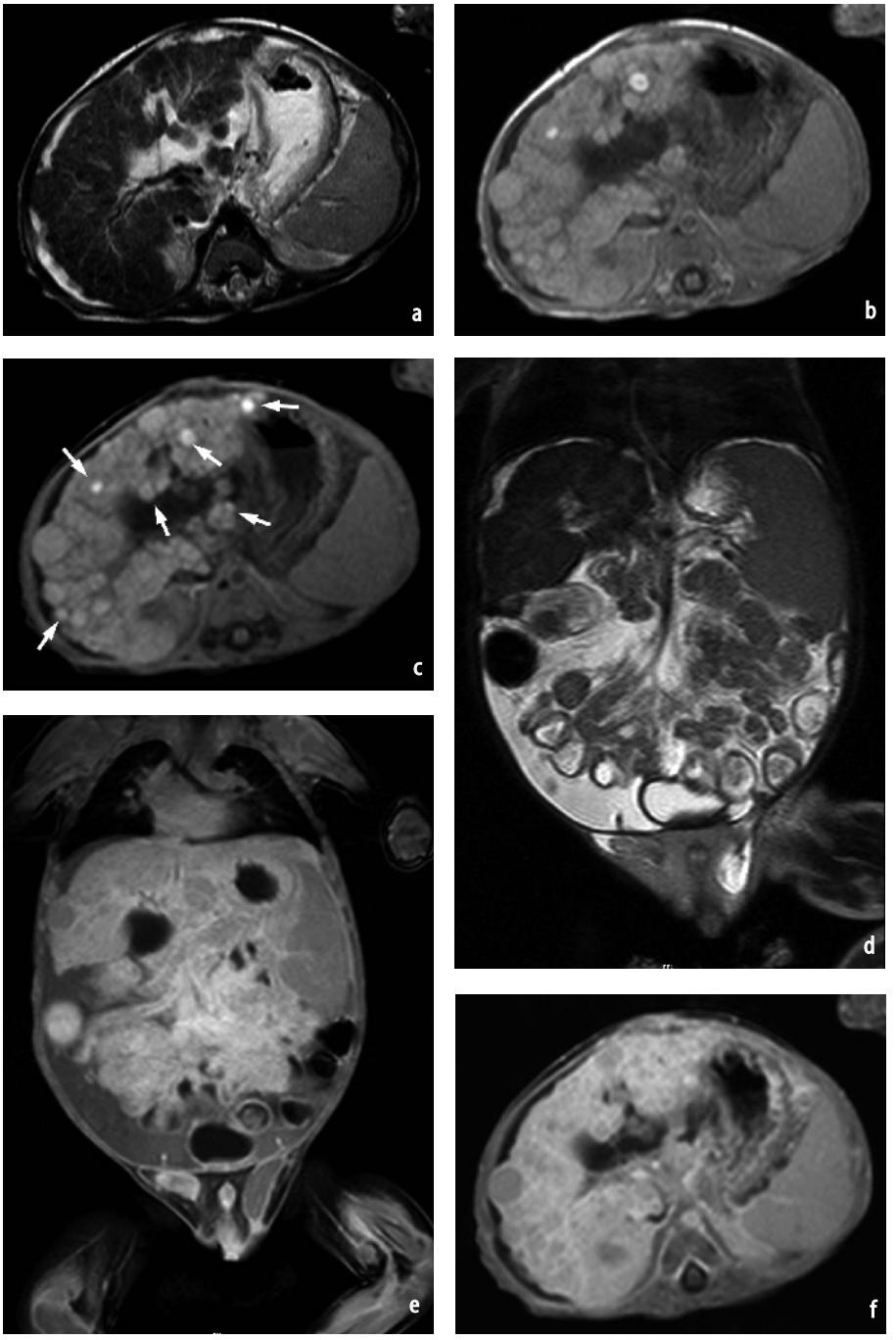

Fig. 27a-f. Biliary cirrhosis in a 4 month old child. The respiratory gated T2-weighted image (**a**) reveals liver cirrhosis with multiple regenerative nodules. Note the absence of any intra- or extrahepatic bile ducts. On the corresponding T1-weighted (**b**) and T1-weighted fat-suppressed (**c**) images multiple regenerative nodules (*arrows*) are visible as areas of increased SI due to iron storage. The T2-weighted HASTE sequence in coronal orientation (**d**) reveals the characteristic complications of liver cirrhosis, such as portal hypertension and massive ascites. Following contrast agent administration (**e**, **f**) the regenerative nodules are seen as hypointense whereas the cirrhotic tissue shows prolonged enhancement

10.5.3 Liver Fibrosis

Congenital hepatic fibrosis is part of the spectrum of hepatic cystic diseases, and is characterized by aberrant bile duct proliferation and periductal fibrosis. More details on this disease are given in Chapter 4, "Imaging of Benign Focal Liver Lesions", section 4.1.5, "Cysts".

In typical congenital hepatic fibrosis, cysts are not visible due to their very small size. Hepatic involvement in patients with polycystic kidney disease occurs in approximately 30-50% of cases. Clinically, the majority of patients present in childhood, when congenital hepatic fibrosis predominates with bleeding, varices and other manifestations of portal hypertension. In patients with predominating polycystic liver disease, the lesions are usually identified incidentally. Approximately 70% of patients with polycystic liver disease also have adult polycystic kidney disease. Congenital hepatic fibrosis is also related to Caroli's disease.

10.5.4 Storage Disease, Metabolic Diseases

A considerable number of metabolic diseases cause liver injury in infants and children. In many cases, the liver is the sole organ clinically affected by the metabolic disease. In other metabolic diseases, other organs/tissues are affected but liver disease still constitutes a major cause of morbidity and mortality. Some of the diseases are relatively common. For instance, α-1-antitrypsin deficiency affects approximately 1 in 1,800 live births, while the incidence of cystic fibrosis is as high as 1 in 1,700 in some populations. Taken together, genetic/metabolic liver diseases account for approximately 30% of children who undergo liver transplantation.

In most cases, metabolic diseases affecting the liver ultimately lead to cirrhosis. Typically, the imaging findings in these cases are similar to those in adults in whom liver cirrhosis arises for other reasons. In other cases, however, the findings may be more subtle. Frequently hepatomegaly or fatty liver is the main finding during the early stages of disease.

Alpha-1-antitrypsin Deficiency. Alpha-1-antitrypsin deficiency is the most common metabolic liver disease affecting children [94]. It also predisposes adults to HCC and causes emphysema, particularly in adults who smoke cigarettes. Recent studies have provided further information about the biochemical basis of the deficiency, and about the cellular mechanisms that account for the wide variation in phenotypic expression of liver disease. These studies have shown that this disease is prototypic for many genetic diseases associated with misfolded proteins and disturbances in the fundamental cellular pathways that respond to misfolded proteins, or stressors [95]. Recent studies have also provided evidence for the feasibility of chemoprophylaxis with a novel class of compounds called "chemical chaperones" that may have broad applicability to metabolic liver disease.

Glycogen Storage Disease. Another of the more common metabolic liver diseases is glycogen storage disease (GSD), a group of disorders that are associated with glycogen accumulation in the liver and other tissues due to specific defects in glycogenolysis. In this disease, mainly GSD type Ia is of interest with regard to imaging studies, since hepatomegaly with development of liver cell adenoma is a common finding. In GSD type Ia, there is developmental delay, hypoglycemia, metabolic acidosis, elevated triglycerides and uric acid levels in the blood, hepatomegaly, hepatic adenomas (Fig. 28), and HCC due to defects in the catalytic subunit of glucose-6-phosphatase. In GSD type Ib, the patients also have neutrophil dysfunction and recurrent infections due to a primary defect in a microsomal glucose-6-phosphate transporter. In GSD type III, in which there is a defect in the glycogen debrancher enzyme, hepatomegaly occurs but liver dysfunction is rare. In GSD type IV, in which there is deficiency of the glycogen branching enzyme, there is progressive liver dysfunction and liver failure. GSD type VI is due to defects in liver phosphorylase kinase. Nutritional therapy and the use of dietary cornstarch have had a major impact on GSD type Ia, whereas cytokine therapy has recently provided marked improvement in the lives of patients with GSD type Ib.

Wilson's Disease. A third common form of metabolic liver disease in children is Wilson's disease. It is a progressive disorder characterized by abnormalities of the motor system, psychiatric symptoms, and hepatic disease resulting in cirrhosis. A specific defect in copper transport results in progressive accumulation of copper in target tissues which leads to cirrhosis. Although copper is paramagnetic, substantial changes in liver SI are not found in patients with Wilson's disease. The main findings are liver cirrhosis and sometimes SI changes in the brain, especially the nucleus lenticularis, in which the concentration of copper may be much higher than in the liver.

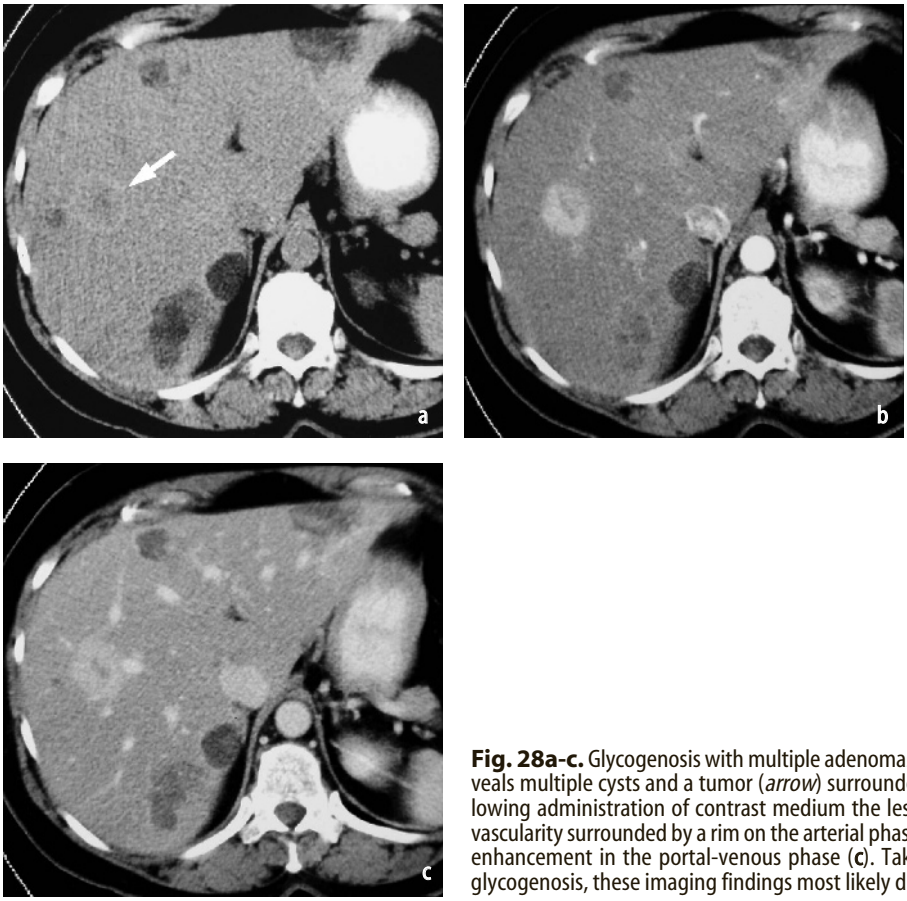

Fig. 28a-c. Glycogenosis with multiple adenomas. The unenhanced CT scan (**a**) reveals multiple cysts and a tumor (*arrow*) surrounded by a hyperdense capsule. Following administration of contrast medium the lesion demonstrates strong hypervascularity surrounded by a rim on the arterial phase scan (**b**), followed by persistent enhancement in the portal-venous phase (**c**). Taken together with the history of glycogenosis, these imaging findings most likely depict liver adenoma

References

1. Alt B, Hafez R, Trigg M et al. Angiosarcoma of the liver and spleen in an infant. Pediatr Pathol Lab Med 1985; 4:331-339
2. Apicella PL, Mirowitz SA, Weinreb JC. Extension of vessels through hepatic neoplasms: MR and CT findings. Radiology 1994; 191:135–136
3. Babbitt DP. Congenital choledochal cyst: new etiologic concept based on anomalous relationships of common bile duct and pancreatic bulb. Ann Radiol 1969; 12:231-240
4. Bartolozzi C, Cioni D, Donati F, et al. Focal liver lesions: MR imaging-pathologic correlation. Eur Radiol 2001; 11:1374-1388
5. Bates SM, Keller MS, Ramos IM, et al. Hepatoblastoma: detection of tumor vascularity with Duplex Doppler US. Radiology 1990; 176:505-507
6. Bociek, RG. Adult Burkitt's lymphoma. Clinical Lymphoma 2005; 6(1),11-20
7. Boechat MI, Kangarloo H, Ortega J, et al. Primary liver tumors in children: comparison of CT and MR imaging. Radiology 1988; 169:727-732
8. Boon LM, Burrows PE, Paltiel HJ, et al. Hepatic vascular anomalies in infancy: a twenty-seven year experience. J Pediatr 1996; 129:346-354
9. Buetow PC, Buck JL, Pantongrag-Brown L, et al. Undifferentiated (embryonal) sarcoma of the liver: pathologic basis of imaging findings in 28 cases. Radiology 1997; 203:779-783
10. Buetow PC, Buck JL, Ros PR, et al. Malignant vascular tumors of the liver: radiologic-pathologic correlation. Radiographics 1994; 14:153-166
11. Caccia G, Ekema G, Falchetti D, et al. Atresia delle vie biliari: attualità e prospettive. Prospettive in Pediatria 2004; 34:39-43
12. Caillaud JM, Gerard-Marchant R, Marsden HB, van Unnik AJ, Rodary C, Rey A, Flamant F. Histopathological classification of childhood rhabdomyosarcoma: a report from the International Society of Pediatric Oncology pathology panel. Med Pediatr Oncol 1989; 17:391-400
13. Canceller A, Blanchard H, Champagne J, et al. Surgical resection and chemotherapy improve survival rate for patients with hepatoblastoma. J Ped Surg 2001; 36:755-759
14. Caty MG, Oldham KT, Prochownik EV. Embryonal rhabdomyosarcoma of the ampulla of Vater with long-term survival following pancreaticoduodenectomy. J Pediatr Surg 1990; 25:1256-1258
15. Chandra RS, Altman RP. Ductal remnants in extrahepatic biliary atresia: a histopathologic study with clinical correlation. J Pediatr 1978; 93:196-200
16. Cheon JE, Kim WS, Kim IO, Jang JJ, Seo JK, Yeon

KM. Radiological features of focal nodular hyperplasia of the liver in children. Pediatr Radiol 1998; 28:878-883
17. Coakley FV, O'Reilley EM, Schwartz LH, Panicek DM, Castellino RA. Non-Hodgkin lymphoma as a cause of intrahepatic periportal low attenuation on CT. J Comput Assist Tomogr 1999; 23:726–728
18. Coenegrachts, KAD , Vanbeckevoort, DA , Deraedt, KB , Van Steenbergen, WC. MRI findings in primary non-Hodgkin's lymphoma of the liver. Journal Belge de Radiologie 2005; 88(1):17-19
19. Craig JR, Peters RL, Edmondson HA, et al. Fibrolamellar carcinoma of the liver. A tumor of adolescents and young adults with distinctive clinicopathologic features. Cancer 1980; 46:372-379
20. Craig JR. Mesenchymal tumors of the liver. Diagnostic problems for the surgical pathologist. Pathology 1994; 3:141-160
21. Dachman AH, Lichtenstein JE, Friedman AC, Hartman DS. Infantile hemangioendothelioma of the liver: a radiologic-pathologic-clinical correlation. AJR 1983; 140:1091-1096
22. Davey MS, Cohen MD. Imaging of gastrointestinal malignancy in childhood. Radiol Clin North Am 1996; 34:717-742
23. DeMaioribus CA, Lally KP, Sim K et al. Mesenchymal hamartoma of the liver : a 35 year review. Arch Surg 1990; 125:598-600
24. Dehner LP. Hepatic tumors in the pediatric age group: a distinctive clinicopathologic spectrum. Perspect Pediatr Pathol 1978; 4:217-268
25. Donnelly LF, Bisset GS. Pediatric Hepatic Imaging. Radiol Clin N Am 1998; 36:413-427
26. Falk H, Herbert JT, Edmonson L, et al. Review of childhood hepatic angiosarcoma - elevated environmental arsenic exposure in one case. Cancer 1981; 47:382-391
27. Flisak ME, Budris DM, Olson MC, et al. Inflammatory pseudotumor of the liver: Appearance on MRI. Clin Imaging 1994; 18:1-3
28. Friedburg H, Kauffmann GW, Bohm N, Fiedler L, Jobke A. Sonographic and computed tomographic features of embryonal rhabdomyosarcoma of the biliary tract. Pediatr Radiol 1984; 14:436-438
29. Fujita T, Honjo K, Ito K, et al. High resolution dynamic MR imaging of hepatocellular carcinoma with a phased-array body coil. Radiographics 1997; 17:315-331
30. Fukuya T, Honda H, Matsumata T, et al. Diagnosis of inflammatory pseudotumor of the liver: Value of CT. Am J Roentgenol 1994; 163:1087-1091
31. Gazelle GS, Lee MJ, Hahn PF, Goldberg MA, Rafaat N, Mueller PR. US, CT and MRI of primary and secondary liver lymphoma. J Comput Assist Tomogr 1994; 18:412-415
32. Geoffray A, Couanet D, Montagne JP, Leclere J, Flamant F. Ultrasonography and computed tomography for diagnosis and follow-up of biliary tract rhabdomyosarcomas in children. Pediatr Radiol 1987; 17:127-131
33. Haliloglu M, Hoffer FA, Gronemeyer SA, et al. 3D Gadolinium-enhanced MRA: evaluation of hepatic vasculature in children with hepatoblastoma. J Magn Reson Imaging 2000; 11:65-68
34. Helmberger TK, Ros PR, Mergo PJ et al. Pediatric liver neoplasms: a radiologic-pathologic correlation. Eur Radiol 1999; 9:1339-1347
35. Holden KR, Alexander F. Diffuse neonatal hemangiomatosis. Pediatrics 1970; 46:411-421
36. Horiuchi R, Uchida T, Kojima T, et al. Inflammatory pseudotumor of the liver: Clinicopathologic study and review of the literature. Cancer 1990; 65:1583-1590
37. Horn RC, Enterline HT. Rhabdomyosarcoma: a clinicopathological study and classification of 39 cases. Cancer 1958; 11:181-199
38. Horowitz ME, Etcubanas E, Webber BL, Kun LE, Rao BN, Vogel RJ, Pratt CB. Hepatic undifferentiated (embryonal) sarcoma and rhabdomyosarcoma in children. Cancer 1987; 59:396-402
39. Hsu CF, Ko SF, Hsiao CC, Shieh CS, Huang CC, Huang FC. Obstructive jaundice as the presenting manifestation of Burkitt's lymphoma in a 4-year-old boy. Journal of the Formosan Medical Association 2003; 102(2):105-108
40. Ishak KG, Rabin L. Benign tumors of the liver. Med Clin North Am 1975; 59:995-1013
41. Joshi SW, Merchant NH, Jambhekar NA. Primary multilocular cystic undifferentiated (embryonal) sarcoma of the liver in childhood resembling hydatid cyst of the liver. Br J Radiol 1997; 70:314-316
42. Kasai M, Suzuki S. A new operation for "noncorrectable" biliary atresia: Hepatic portoenterostomy. Shujutsu 1959; 13:733-739
43. Kew MC. Hepatic tumors and cysts. In: Feldman M, Scharschmidt BF, Sleisenger MH (eds): Sleisenger and Fordtran's Gastrointestinal and Liver disease (6th ed.). WB Saunders, Philadelphia 1998,1364-1387
44. Kim MJ, HN SJ, Yoon CS, et al. Using MR cholangiopancreatography to reveal anomalous pancreaticobiliary ductal union in infants and children with choledocal cysts. AJR 2002; 179:209-214
45. Kim MJ, Park YN, Han SJ, et al. Biliary atresia in neonates and infants: triangular area of high signal intensity in the porta hepatis at T2-weighted MR cholangiography with US and histopathologic correlation. Radiology 2000; 215:395-401
46. King SJ, Babyn PS, Greenberg ML, et al. Value of CT in determining the resectability of hepatoblastoma before and after chemotherapy. Am J Roentgenol 1993; 160:793-798
47. Kirks DR, Griscom NT. Hepatobiliary tumors. Practical Pediatric Imaging. Diagnostic Radiology of Infants and Children. Lippincott-Raven 1998, 954-969
48. Lack EE, Ornvold K. Focal nodular hyperplasia and hepatic adenoma: a review of eight patients in the pediatric age group. J Surg Oncol 1986; 33:129-135
49. Lack EE, Perez-Atayde AR, Schuster SR. Botryoid rhabdomyosarcoma of the biliary tract: report of five cases with ultrastructural observations and literature review. Am J Surg Pathol 1981; 5:643-652
50. Lam WWM, Lam TPW, Saing H, et al. MR cholangiography and CT cholangiography of pediatric patients with choledochal cysts. AJR 1999; 173:401-405
51. Lanza G. Tumori del fegato e dei dotti biliari intraepatici: Carcinomi. Anatomia Patologica Sistematica, seconda edizione, Ed. Piccin: 738-740
52. Leuschner I, Schmidt D, Harms D. Undifferentiated sarcoma of the liver in childhood: morphology, flow cytometry, and literature review. Human Pathol 1990,21:68-76
53. Levick CB, Rubie J. Hemangioendothelioma of the liver simulating congenital heart disease in infants. Arch Dis Child 1953; 28:49-51

54. Linstedt-Hilden M, Brambs HJ. Two different manifestations of botryoid sarcoma (embryonal rhabdomyosarcoma) of the biliary tree. Bildgebung 1994; 61:40-43
55. Luks FI, Yazbeck S, Brandt ML, Bensoussan AL, Brochu P, Blanchard H. Benign liver tumors in children: a 25-year experience. J Pediatr Surg 1991; 26:1326-1330
56. Maher MM, McDermott SR, Fenlon HM. Imaging of primary non-Hodgkin's lymphoma of the liver. Clin Radiol 2001; 56:295-301
57. Matos C, Nicaise N, Deviare J, et al. Choledocal cysts: comparison of findings at MR cholangiopancreatography and endoscopic retrograde cholangiopancreatography in eight patients. Radiology 1998; 209:443-448
58. Matricardi L, Lovati R, Provezza A, et al. Ecografia. L'epatocarcinoma: diagnostica per immagini e terapia interventistica, Ed. Lint: 14-32
59. McLean RH, Moller JH, Warwick WJ. Multinodular haemangiomatosis of the liver in infancy. Pediatrics 1972; 49:563-573
60. Mihara S, Matsumoto H, Tokunaga F, Yano H, Ota M, Yamashita S. Botryoid rhabdomyosarcoma of the gallbladder in a child. Cancer 1982; 49:812-818
61. Miller FH, Butler RS, Hoff FL, et al. Using triphasic helical CT to detect focal hepatic lesions in patients with neoplasms. Am J Roentgenol 1998; 171:643-649
62. Miller JH, Gates GF, Stanley P. The radiologic investigation of hepatic tumors in childhood. Radiology 1977; 124:451-458
63. Miller JH, Greenspan BS. Integrated imaging of hepatic tumors in childhood. Part I: Malignant lesions (primary and metastatic). Radiology 1985; 154:83-90
64. Moon WK, Kim WS, Kim IO, et al. Undifferentiated embryonal sarcoma of the liver: US and CT findings. Pediatr Radiol 1994; 24:500-503
65. Mortele KJ, Wiesner W, DeHemptinne B, et al. Multifocal inflammatory pseudotumor of the liver: dynamic gadolinium-enhanced, ferrumoxides-enhanced, and mangafodipir trisodium-enhanced MR imaging findings. Eur Radiol 2002; 12(2):304-308
66. Newton WA Jr, Gehan EA, Webber BL, Marsden HB, van Unnik AJ, Hamoudi AB, Tsokos MG, Shimada H, Harms D, Schmidt D, et al. Classification of rhabdomyosarcoma and related sarcomas. Cancer 1995; 76:1073-1085
67. Noronha V, Shafi NQ, Obando JA, Kummar S. Primary non-Hodgkin's lymphoma of the liver. Critical Reviews in Oncology/Hematology 2005; 53(3):199-207
68. Norton KI, Glass RB, Kogan D, et al. MR cholangiography in the evaluation of neonatal cholestasis: Initial results. Radiology 2002; 222:687-691
69. O'Neil J, Ros PR. Knowing hepatic pathology aids MRI of liver tumors. Diagn Imaging 1989; 19:58-67
70. Ohsawa M, Aozasa K, Horiuchi K, et al. Malignant lymphoma of the liver. Dig Dis Sci 1992; 37:1105-1109
71. Oue T, Fukuzawa M, Kusafuka T, et al. Transcatheter arterial chemoembolization in the treatment of hepatoblastoma. J Ped Surg 1998; 33:1771-1775
72. Pardes JG, Bryan PJ, Gauderer MW. Sponteneous regression of infantile hemangioendotheliomatosis of the liver. J Ultrasound Med 1982; 1:349-353
73. Patil KK, Omojola MF, Khurana P, Iyengar JK. Embryonal rhabdomyosarcoma within a choledochal cyst. Can Assoc Radiol J 1992; 43:145-148
74. Pobiel RS, Bisset III GS. Pictorial essay: imaging of liver tumors in the infant and child. Pediatr Radiol 1995; 25:495-506
75. Power C, Ros PR, Stoupis C, et al. Primary liver neoplasms: MR imaging with pathologic correlation. Radiographics 1994; 14:459-482
76. Ramos G, Murao M, DeOliveira BM, DeCastro LPF, Viana MB. Primary hepatic non-Hodgkin's lymphoma in children: A case report and review of the literature. Medical and Pediatric Oncology 1997; 28(5):370-372
77. Rizzi EB, Schinina V, Cristofaro M, et al. Non-Hodgkin's lymphoma of the liver in patients with AIDS: sonographic, CT and MRI findings. J Clin Ultrasound 2001; 29:125-129
78. Robinson PJA. The characterization of liver tumors by MRI. Clin Radiol 1996; 51:749-761
79. Roebuck DJ, Yang WT, Lam WW, Stanley P. Hepatobiliary rhabdomyosarcoma in children: diagnostic radiology. Pediatr Radiol 1998; 28:101-108
80. Ros PR, Goodman ZD, Ishak KG, Dachman AH, Olmsted WW, Hartman DS, Lichtenstein JE. Mesenchymal hamartoma of the liver: radiologic-pathologic correlation. Radiology 1986; 158:619-624
81. Ros PR, Olmsted WW, Dachman AH, et al. Undifferentiated (embryonal) sarcoma of the liver: radiologic pathologic correlation. Radiology 1986; 160:141-145
82. Ros PR, Rasmussen JF, Li KCP. Radiology of malignant and benign liver tumors. Curr Probl Diagn Radiol 1989; 18:95-155
83. Ros PR, Taylor HM. Malignant Tumors of the liver. Textbook of gastrointestinal radiology, second edition. 2000,1523-1568
84. Ruymann FB, Raney RB Jr, Crist WM, Lawrence W Jr, Lindberg RD, Soule EH. For the Intergroup Rhabdomyosarcoma Study of CCSG and POG. Rhabdomyosarcoma of the biliary tree in childhood: a report from the Intergroup Rhabdomyosarcoma Study. Cancer 1985; 56:575-581
85. Schweizer P, Schweizer M, Wehrmann M. Major resection for embryonal rhabdomyosarcoma of the biliary tree. Pediatr Surg Int 1994; 9:268-273
86. Semelka RC, Bagley AS, Brown DE, Kroeker MA. Malignant lesions of the liver identified on T1- but not T2-weighted MR images at 1.5 T. J Magn Reson Imaging 1994; 4:315–318
87. Shek TWH, Ng IOL, Chan KW: Inflammatory pseudotumor of the liver: Report of four cases and review of the literature. Am J Surg Pathol 1993; 17:231-238
88. Shirkhoda A, Ros PR, Farah J, et al. Lymphoma of the solid abdominal viscera. Radiol Clin North Am 1990; 28:785-799
89. Siegel MJ. Pediatric liver imaging. Seminars in liver disease 2001; 21:251-269
90. SIOPEL III: liver tumor studies. International society of pediatric oncology: Hepatoblastoma and hepatocellular carcinoma 1998
91. Souid AK, Ziemba MC, Dubansky AS, et al. Inflammatory myofibroblastic tumor in children. Cancer 1993,72:2042-2048
92. Soyer P, Roche A, Levesque M. Fibrolamellar hepatocellular carcinoma presenting with obstructive jaundice. A report of two cases. Eur J Radiol 1991; 13:196-198

93. Stocker JT, Ishak KG. Undifferentiated (embryonal) sarcoma of the liver. Report of 31 cases. Cancer 1978; 42:336-348
94. Sveger T. Liver disease in alpha-1-antitrypsin deficiency detected by screening of 200,000 infants. N Engl J Med 1976; 294:1216–21
95. Teckman JH, Qu D, Perlmutter DH. Molecular pathogenesis of liver disease in alpha-1-antitrypsin deficiency. Hepatology 1996; 24:1504–16
96. Todani T. Cholecochal cysts and pancreatobiliary malfunction. In Balistreri WF, Ohi R, Todani, Tsushida Y (eds.): Hepatobiliary, pancreatic and splenic disease in children: medical and surgical managment. Elsevier Science, 1997:261-286
97. Treissman SP, Gillis DA, Lee CLY, et al. Omental-mesenteric inflammatory pseudotumor: Cytogenetic demonstration of genetic changes and monoclonality in one tumor. Cancer 1994; 73:1433-1437
98. Tsuchida Y, Ikeda H, Suzuki N, et al. A case of well-differentiated, fetal-type hepatoblastoma with very low serum alpha-fetoprotein. J Ped Surg 1999; 34:1762-1764
99. Walker NI, Horn MJ, Strong RW, et al. Undifferentiated (embryonal) sarcoma of the liver. Pathologic findings and long-term survival after complete surgical resection. 1992; 69:52-59
100. Webber EM, Morrison KB, Pritchard SL et al. Undifferentiated (embryonal) sarcoma of the liver: results of clinical management in one center. J Ped Surg 1999; 34:1641-1644
101. Weiner SN, Parulekar SG. Scintigraphy and ultrasonography of hepatic hemangioma. Radiology 1979; 132:149-153
102. Weinreb JC, Brateman L, Maravilla KR. Magnetic resonance imaging of hepatic lymphoma. Am J Roentgenol 1984; 143:1211–1214
103. Wernecke K, Peters PE, Kruger KG. Ultrasonographic patterns of focal hepatic and splenic lesions in Hodgkin's and non-Hodgkin lymphoma. The British Journal of Radiology 1987; 60:655-660
104. Yamashita Y, Namimoto Y, Mitsuzaki T, Takahashi K. MR imaging of the liver: comparison between single shot echo-planar and half Fourier rapid acquisition with relaxation enhancement sequences. Radiology 1998; 207:331–337
105. Yoon Y, Kim JKK, Kang KH. Hepatic undifferentiated embryonal sarcoma: MR findings. J Comput Assist Tomogr 1997; 21:100-102
106. Zuti, S, Rouse, GA, DeLange, M, Agness, M. Burkitt's lymphoma: A spectrum of sonographic findings. Journal of Diagnostic Medical Sonography 1993; 9(1),19-23

11

Imaging of the Liver Post-Surgery and/or Post-Ablative Therapy

CONTENTS

11.1 Introduction

The liver is a common site of metastatic disease, which occurs following initial spread to the lymph nodes. It is the most common site of metastatic disease from primary cancer within the abdomen because it is the first major organ reached by venous blood draining from the intestinal tract. For patients with systemic spread of metastases, curative treatment is generally not possible and general chemotherapeutic approaches for treatment are indicated. On the other hand, if the liver remains the only site of metastatic disease, surgical resection may represent the only means of cure. Unfortunately, the average survival of patients with untreated hepatic metastases is between 2 and 8 months [19].

Only about 30% of patients with hepatic metastases represent cases suitable for surgical resection, even when intervention is performed in centers with expertise in hepatic surgery. Thus, there has been growing interest in interstitial approaches aimed at destroying liver metastases *in situ*. Local ablative therapeutic approaches include thermotherapy and chemotherapy and are alternatives to major surgery. Each of these has the advantage of being repeatable in cases of recurrent metastatic lesions [1].

Thermotherapeutic approaches to tumor reduction include the application of physical energy in radio-frequency (RF) ablation, laser-induced interstitial therapy (LITT) and cryotherapy. Chemotherapeutic approaches include the local instillation of drugs, alcohol injection, chemotherapeutic drug instillation and regional transarterial chemoembolization (TACE) [22].

11.2 Surgical Resection

The role of surgical resection in the treatment of hepatic metastases of primary colorectal carcinomas is well-recognized and may contribute to the five year survival of 25% to 37% of affected patients [9]. However, the approach to the surgical treatment of hepatic metastases from primary tumors other than colorectal cancer is less obvious, and is highly dependent upon the type of primary tumor. Nevertheless, a reported five year survival rate of 21% after resection of metastases from non-colorectal carcinomas can be considered comparable to that for metastases from colorectal carcinomas [12]. While outstanding results are obtained when metastases from neuroendocrine tumors are resected, less favorable results are frequently obtained from the resection of metastases from gastric or breast cancer.

As only about 30% of the patient population with hepatic metastatic disease is eligible for liver resection, preoperative magnetic resonance imaging (MRI) provides detailed information for surgical therapy planning, as it can help determine the number and location of intrahepatic lesions [32]. Exact anatomic description of the tumor spread in correlation with the segmental distribution and the course of major hepatic vascular structures is es-

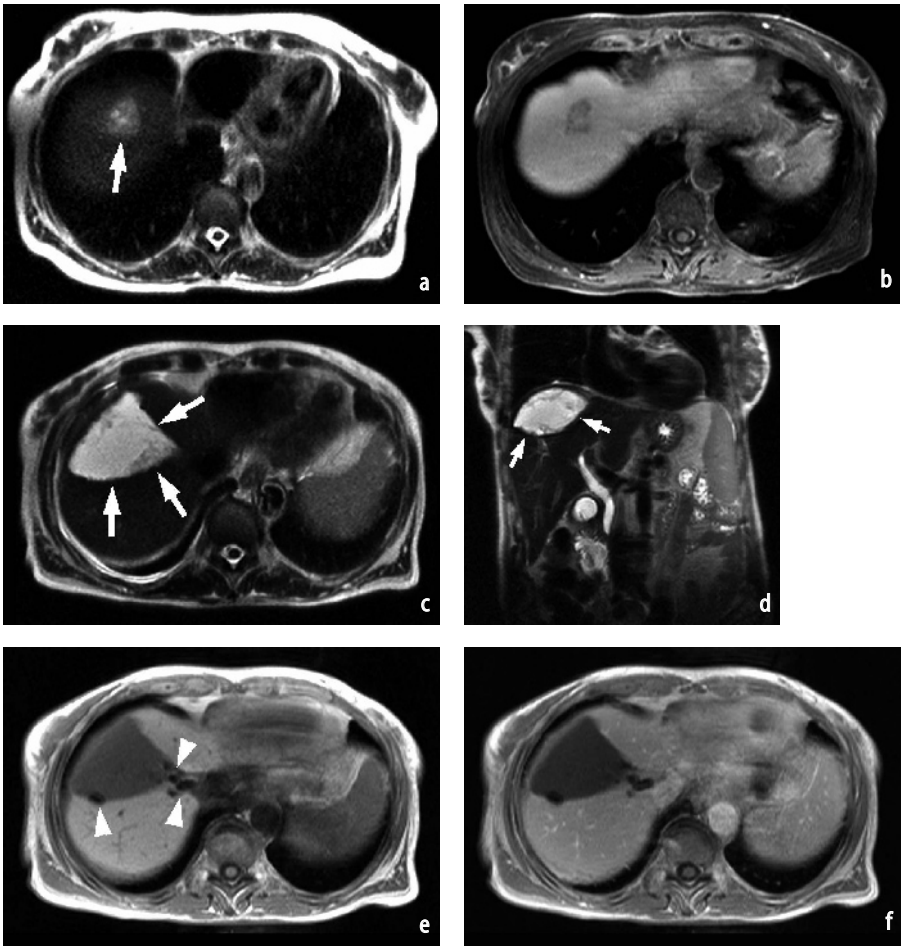

Fig. 1a-f. Pre- and post-surgical imaging in a patient with liver metastases from colorectal cancer and postoperative bilioma formation. The preoperative imaging studies show a metastasis with high SI on the T2-weighted image (**a**, *arrow*) and typical peripheral wash-out on the contrast-enhanced T1-weighted fat-suppressed image post-injection of Gd-BOPTA (**b**). On post-surgical imaging, three weeks after resection of the liver metastases (**c**-**f**), a triangular defect from atypical resection of the lesion is visible on axial (**c**) and coronal (**d**) T2-weighted HASTE images (*arrows*). The resulting defect is filled with a high SI fluid, which aspiration showed to be a bilioma formation. Note susceptibility artifacts from surgical clips on the unenhanced T1-weighted image (**e**, *arrows*). In the equilibrium phase post-contrast agent injection (0.05 mmol/kg BW Gd-BOPTA) no enhancing rim surrounding the defect is visible, which excludes an inflammatory process or abscess formation

sential. Infiltration of central hilar vascular structures such as the portal vein, hepatic artery and central hepatic bile ducts almost always excludes a possible treatment by liver resection. Moreover, extrahepatic tumor growth and infiltration into adjacent organs should be carefully evaluated.

Post-operative MRI of the liver within the first four weeks is helpful for the detection of surgical complications such as hematoma or abscess formation, perfusion disturbances or bilioma formation. Bilioma or abscess formations are characterized by a hypo- to hyperintense signal on T1-weighted images and by typically high signal intensity on T2-weighted images. A lack of central enhancement is seen both with bilioma and abscess formations, however if a pronounced peripheral enhancement, indicating an abscess wall, can be identified, the patient may require interventional drainage or surgical revision (Fig. 1). As regards bilioma formations, follow-up studies are advised since some bilioma formations resolve spontaneously with time. In the case of port-surgical biliary leaks, the precise location of the leak can frequently be accertained with the use of MR contrast agents such as Gd-BOPTA that are excreted in part through the hepatobiliary system. In this regard, T1-weighted images acquired during the hepatobiliary phase at around 2h after injection will usually reveal the location of the leak through contrast extravasation at the site of bile duct damage.

In most cases, surgical resection involves the removal of two or more liver segments and post-surgical follow-up imaging does not differ greatly from pre-surgical imaging. However, if the borders of the resected liver lesions are within 2 cm of the resection margin, special attention should be paid to the neighboring areas at follow-up. Using T1-weighted imaging, detailed evaluation of the

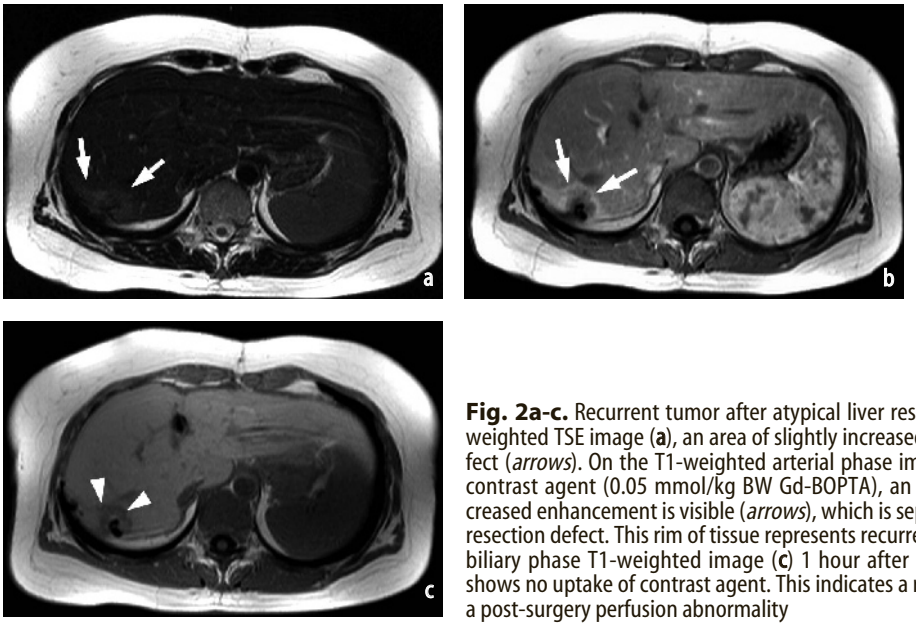

Fig. 2a-c. Recurrent tumor after atypical liver resection. On the unenhanced T2-weighted TSE image (**a**), an area of slightly increased SI surrounds the resection defect (*arrows*). On the T1-weighted arterial phase image (**b**) after bolus injection of contrast agent (0.05 mmol/kg BW Gd-BOPTA), an irregular shaped margin of increased enhancement is visible (*arrows*), which is separated by a tissue rim from the resection defect. This rim of tissue represents recurrent tumor which on the hepatobiliary phase T1-weighted image (**c**) 1 hour after contrast agent administration, shows no uptake of contrast agent. This indicates a recurrent tumor rather than just a post-surgery perfusion abnormality

resection margins is sometimes difficult due to susceptibility artifacts caused by surgical clips (Fig. 1e). Follow-up evaluations may also be difficult in cases of atypical resection. Likewise, when liver lesions are enucleated with a margin of 2-3 cm a clear identification of the resection margins may not always be possible. Additionally, signal intensity on unenhanced T1-weighted and T2-weighted images as well as on T1-weighted dynamic imaging may be influenced by hemorrhage, seroma formation, inflammation and ischemia of surrounding liver tissue, particularly during the first one to two months after resection. Thus follow-up imaging is usually best performed at three or more months after resection, in order to minimize the influence of post-surgical changes. In such cases, hyperintense nodular regions on T2-weighted images, hypointense areas on unenhanced T1-weighted images and irregular vascularization on T1-weighted dynamic images is usually indicative of a recurrent tumor (Fig. 2). Since the majority of patients develop recurrent metastases after surgical resection, careful restaging is mandatory.

Furthermore, in post-surgical follow-up imaging, special care should be taken to detect intrahepatic or intraperitoneal seeding of tumor cells from surgery. This is particularly important in instances of atypical resection of liver metastases.

11.3 Radio-Frequency (RF) Ablation

RF ablation of focal liver lesions uses an alternating current at frequencies above 250 kHz, induced by mono- or bipolar probes. This is used to generate heat and thus destroy tissue without causing stimulation of nerves or muscles. The slow application of electrical energy with low current density leads to the heating and eventual dehydration of cells and, thereafter, to the degeneration of collagenous structures and proteins [6].

Multiple probe arrays or cooled-tip RF electrodes with 2-3 cm of exposed metal tip, both of which are connected to a frequency generator (up to 200 Watts), are usually used to deliver the RF energy to the tissue. During the ablation procedure, a thermocouple measures the local temperature, and tissue impedance is monitored continuously while the generator output is increased slowly to 950 - 1100 mA. Careful monitoring is necessary in order to prevent the tissue from boiling and subsequently carbonizing. Thus, if the impedance increases by > 10 Ohm, the current needs to be reduced until stable impedance is again observed [5]. The standard RF application generally lasts for 12-25 minutes and results in typical coagulation necrosis diameters of 2.5-3.7 cm. The maximum diameter reached is 7 cm [18, 33].

Histologically, ablated areas consist of necrotic tumor tissue surrounded by necrotic liver tissue. The safety margin of surrounding necrotic liver tissue should have a thickness of > 1 cm, corresponding to the surgical resection borders. This zone is encircled by a homogeneous rim of edematous inflammatory tissue of variable thickness, which is maximal at about two weeks after the intervention [34].

In cases of complete tumor destruction, T2-weighted MR images acquired post-RF ablation typically show an area of low signal intensity

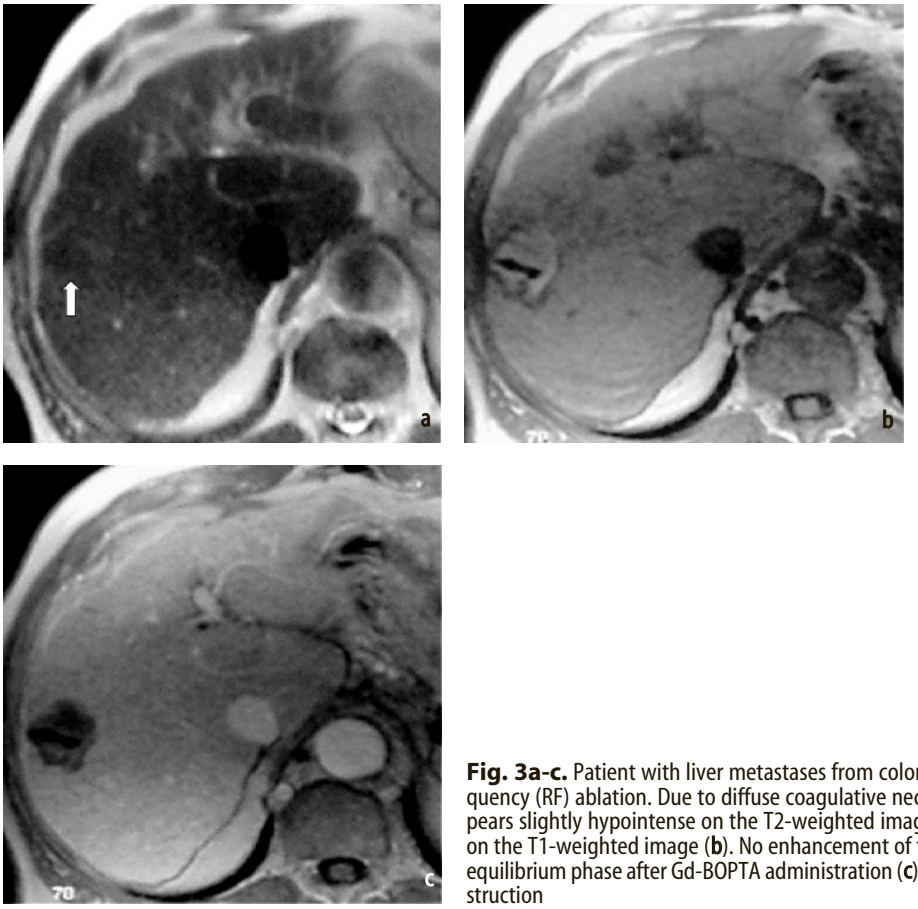

Fig. 3a-c. Patient with liver metastases from colon cancer treated with radio-frequency (RF) ablation. Due to diffuse coagulative necrosis, the RF-lesion (*arrow*) appears slightly hypointense on the T2-weighted image (**a**) and slightly hyperintense on the T1-weighted image (**b**). No enhancement of the RF-lesion is seen during the equilibrium phase after Gd-BOPTA administration (**c**), indicating complete tumor destruction

which corresponds to necrotic tumor and liver tissue. A hyperintense rim encircling this area represents edematous liver and granulation tissue. Conversely, treated lesions typically present as hyperintense with a hypointense rim on unenhanced T1-weighted images (Fig. 3). In the equilibrium phase following the injection of an extracellular Gd-chelate, T1-weighted images of completely destroyed liver lesions reveal a hypointense, non-perfused central area that is surrounded by a thin hyperintense rim (Fig. 4). The increased peripheral enhancement in completely destroyed liver lesions reflects the inflammatory reaction as well as sinusoidal obstruction and portal-venous perfusion at the edge of the ablated area. Typically, the peripheral wash-out that is characteristic of viable liver metastases, is not observed in completely RF-destroyed liver metastases.

On the other hand, if hyperintense irregular or nodular foci are detected on T2-weighted images, together with irregularity or interruption of the enhancement at the boundaries, or enhancement within the lesion on post-contrast T1-weighted images, this could indicate residual tumor or local tumor regrowth. Similarly, signs of peripheral wash-out in areas of the RF ablation should be interpreted as possible tumor regrowth or residual tumor tissue (Fig. 5). Wedged-shaped arterial perfusion as an expression of arterioportal shunting can sometimes complicate the evaluation of the surrounding normal liver tissue [35].

Commonly described complications of RF ablation are: hemorrhage, central bile duct injury, intraperitoneal abscess formation and, rarely, burning injuries of adjacent organs such as bowel, stomach or kidney. Due to the high sensitivity of MR imaging, major complications are easily detected.

Hemorrhage is detected on T1-weighted fat supressed images with intermediate to high SI depending on when the bleeding occurred. In RF ablation special attention should be paid not only to complications such as hemorrhage and inflammation, but also to intrahepatic diffusion of the tumor and to seeding along the puncture canal within the liver and abdominal wall.

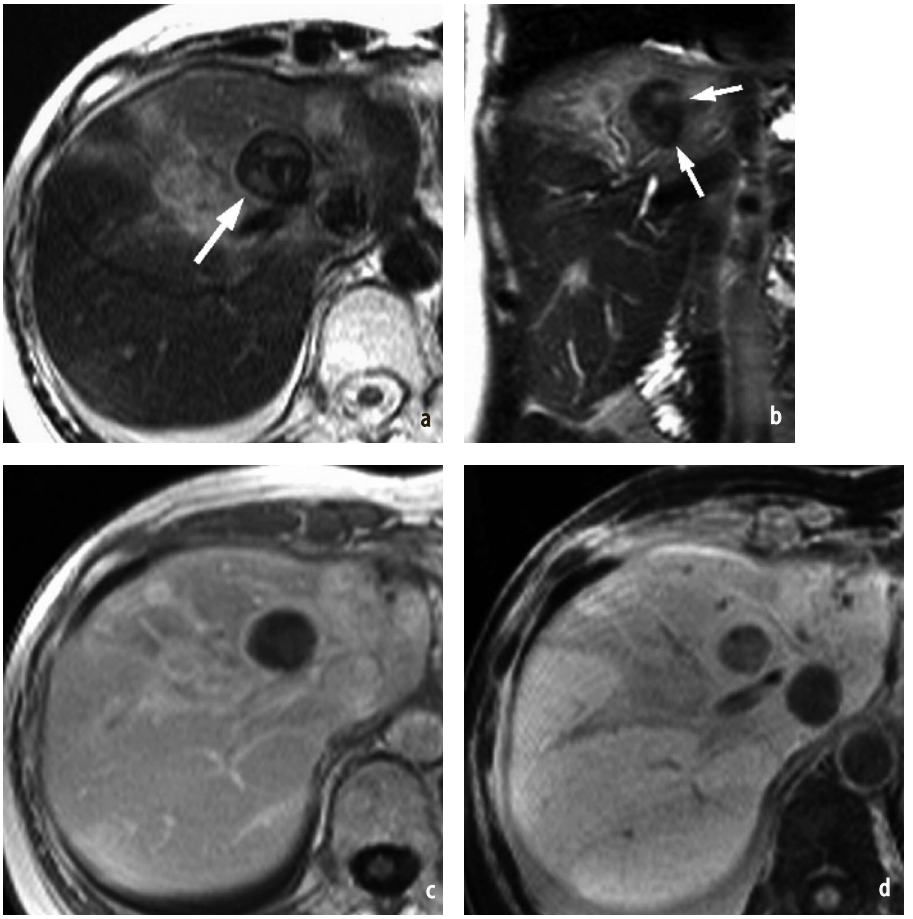

Fig. 4a-d. Patient with solitary metastasis of breast cancer treated with radio-frequency (RF) ablation. Imaging was performed three days after ablation. On the unenhanced T2-weighted HASTE images in axial (**a**) and coronal (**b**) orientation, the RF-lesion (*arrows*) shows a low SI, surrounded by a rim of even lower SI. Note the inflammation of the surrounding liver parenchyma, which has an increased SI. These changes are most likely caused by impairment of hepatic perfusion due to RF-ablation. In the equilibrium phase (**c**) after contrast agent injection (0.05 mmol/kg BW Gd-BOPTA), T1-weighted images show a closed, hyperintense rim surrounding the lesion. The lesion itself demonstrates no enhancement, indicating complete tumor destruction. In the hepatobiliary phase one hour after Gd-BOPTA administration (**d**), heterogeneous contrast agent uptake of the liver tissue surrounding the RF-lesion is demonstrated, the lesion shows no enhancement and is sharply demarcated from the surrounding liver

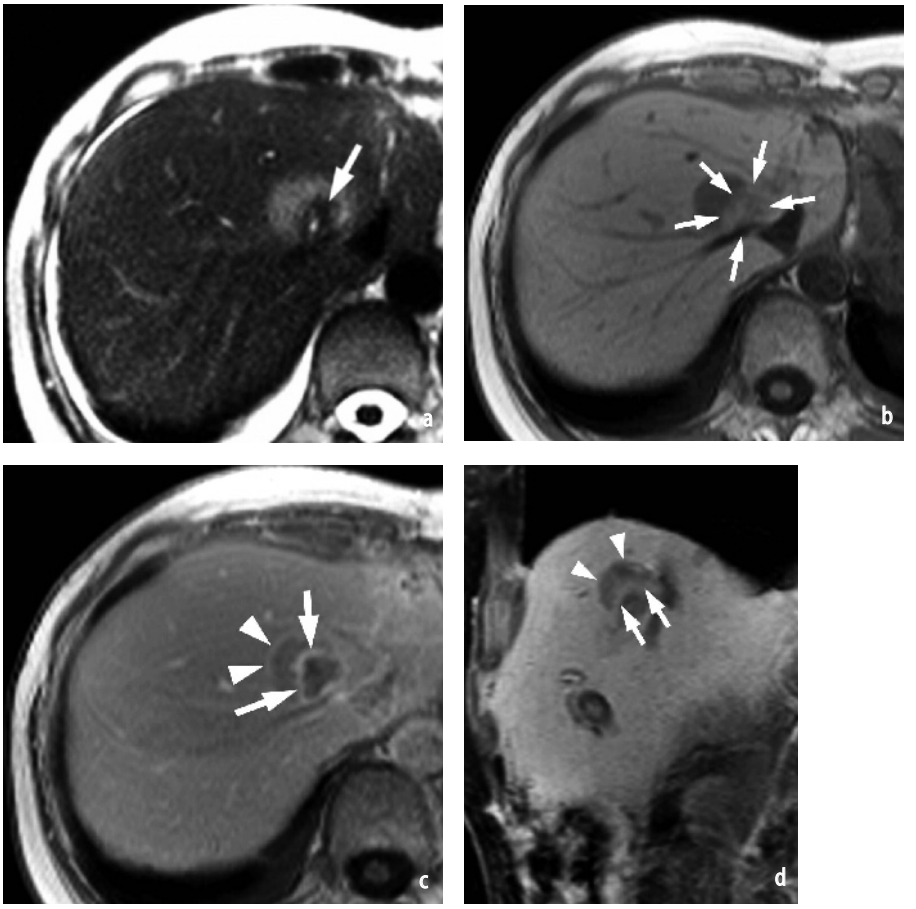

Fig. 5a-d. Incomplete RF-ablation of a liver metastasis from colorectal carcinoma. The unenhanced T2-weighted HASTE image (**a**) shows tissue with increased SI surrounding the hypointense RF-lesion (*arrow*). On the corresponding T1-weighted image (**b**) the RF-lesion has a slightly increased SI (*arrows*), whereas the residual tumor tissue is depicted with a low SI. After contrast agent injection (0.05 mmol/kg BW Gd-BOPTA) the T1-weighted equilibrium phase image (**c**) shows a hyperintense rim surrounding the RF-lesion (*arrows*). Similarly a rim separates the residual tumor tissue from the surrounding liver parenchyma (*arrowheads*). A coronal T1-weighted fat-suppressed image in the hepatobiliary phase after contrast agent injection (**d**) clearly demonstrates residual tumor tissue (*arrowheads*) separated from the RF-lesion by a hyperintense rim (*arrows*)

11.4 Laser-Induced Interstitial Therapy (LITT)

Interstitial laser-induced hyperthermia is based on the conversion of laser light into heat. This is typically performed using a Nd:YAG laser at a wavelength of 1064 nm. The technique involves the invasive insertion of a laser catheter into the lesion using a light-conducting quartz fiber. To avoid early carbonization around the tip of the optic fiber, a closed cooling system based on circulating saline solution decreases the temperature peak around the applicator tip [23]. The success of the treatment is highly dependent upon the optimal positioning of the laser applicator in the center of the lesion. Hence, precise monitoring during therapy is mandatory. The conversion of laser light into heat in LITT results in cell death followed by coagulative necrosis and secondary degeneration. Subsequent atrophy results in tumor shrinkage with minimal damage to surrounding structures. During the procedure, monitoring of thermo-induced signal changes in the treated tissue is possible on the basis of T1-weighted fast low angle GRE sequences in which a rise of the temperature is represented by a signal decrease [24].

The size of the heated volume depends on the power of the laser, the irradiation time and the optical and thermal characteristics of the treated tissue. Frequently, lesions with a diameter of up to 5 cm can be treated successfully [21].

T2-weighted MR images acquired approximately two to three months after LITT intervention typically reveal a hyperintense lesion surrounded by a hypointense rim. No enhancement of the lesion should be seen on T1-weighted equilibrium phase images acquired after injection of a Gd-chelate (Fig. 6).

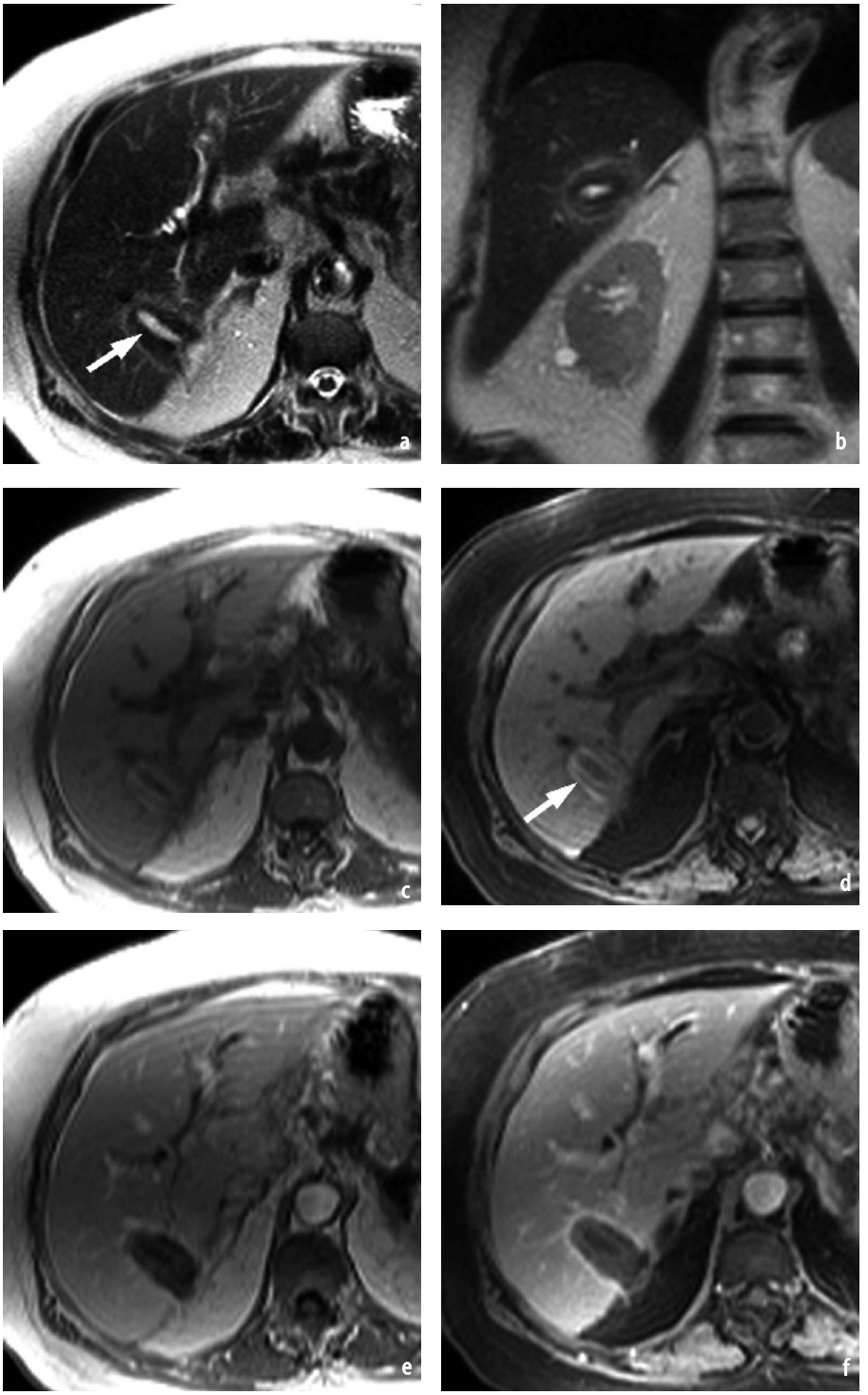

Fig. 6a-f. Patient with metastases from colorectal cancer treated by LITT intervention. The T2-weighted HASTE images in axial (**a**) and coronal (**b**) orientation demonstrate a hyperintense lesion (*arrow*), surrounded by some hypointense tissue which again is demarcated from the normal liver parenchyma by a hyperintense rim. On the corresponding T1-weighted (**c**) and T1-weighted fat suppressed images (**d**) the more peripheral parts of the lesion show signs of hemorrhage (*arrow* in **d**). On T1-weighted (**e**) and T1-weighted fat suppressed (**f**) images, acquired during the equilibrium phase after contrast agent injection, the lesion is distinguished from surrounding liver tissue by a hyperintense rim. The absence of contrast agent uptake in the center of the lesion indicates complete tumor destruction

Local tumor recurrence should be considered if T2-weighted images reveal nodular areas of medium to high signal intensity within the hypointense rim surrounding the lesion, or if nodular regions within the hyperintense necrosis, which differ from the signal intensity of the necrosis itself, can be detected. The same applies for contrast-enhanced T1-weighted images in which recurrent tumor growth is indicated if enhancement is seen in central areas of the lesion or if enhancing peripheral nodular structures are detected [2, 23, 25].

11.5 Cryotherapy

Cryosurgery is defined as local tumor destruction in situ caused by the rapid freezing of tumor cells. Cryosurgery was introduced as an ablative technique mainly in patients with prostatic malignancies and, in some centers, also for the treatment of patients with liver metastases and primary liver tumors such as hepatocellular carcinoma (HCC).

Since cryotherapy does not destroy the walls of large vessels such as the inferior caval vein or large liver veins and portal branches, this approach is particularly well-suited to the treatment of unresectable lesions located near these vessels.

Frequently, resection and cryotherapy are combined during a single invasive procedure. Moreover, cryosurgery is appropriate as an adjunct to liver surgery (so-called "edge cryotherapy") in cases in which a very close or histological-positive resection margin is anticipated. During this procedure, flat cryoprobes are positioned at the resection edge of the remaining liver and adequate freezing is performed to a depth of at least 1.5 cm into the liver tissue.

The mechanism of tumor cell destruction in cryotherapy depends on the location of the tumor tissue in relation to the cryoprobe. In areas close to the cryoprobe temperatures rapidly fall to −190 °C, causing ice crystals to form within and around the cells. Subsequent thawing and rehydration results in rupture of the cell membrane and hence tissue death. At distances slightly further from the cryoprobe, the temperature drops more slowly and ice forms within the small vessels. Since cell membranes impede intracellular ice crystal formation in this case, the parenchymal cells dehydrate to equilibrate the resulting chemical gradient. This results in cellular disintegration and expansion of the blood vessels, which rupture upon thawing, resulting in tissue hypoxia. Thus, cell death in cryotherapy is a combination of intra- and extracellular ice crystal formation, cellular dehydration, rupture of small vessels and hypoxia from small vessel destruction [10, 20]. Cellular damage can be increased by repeated application of consecutive freeze-thaw cycles [28].

Cryotherapy within the liver has experienced a renaissance with the availability of intraoperative ultrasound (US) as a real-time control for the ablative procedure. Nevertheless, the expansion of the forming ice ball cannot be detected opposite the ultrasound transducer, since the ice front orientated towards the transducer builds a reflection wall with a "shadow zone" behind it [26]. MR imaging can overcome this disadvantage, showing excellent contrast between ice formation and unaffected perfused liver tissue on the basis of decreased T2 relaxation time of the frozen tissue [27].

As a result of the histopathologic changes, lesions after cryotherapy may show signs of hemorrhage on unenhanced T1-weighted and T1-weighted fat-suppressed images and appear hyper- or rarely isointense on T2-weighted images. On contrast-enhanced T1-weighted images, the destroyed tissue is seen as a hypovascular region. In cases of complete tumor destruction, contrast-enhanced T1-weighted images acquired during the equilibrium phase reveal a hypointense lesion typically surrounded by a closed hyperintense rim, most likely formed by fibrovascular granulation tissue (Figs. 7, 8). If this rim is interrupted, the site of the interruption should be considered as indicating residual or recurrent tumor, since typically neither a homogeneous rim nor evidence of edema is seen in unaffected tumor tissue. Often the size of the resulting cryo-lesions remains relatively stable for three to six months. Thereafter lesions begin to shrink until they are either no longer visible or can be identified only by the presence of a small scar (Fig. 9) [2, 26].

11.6 Loco-Regional Drug Application

11.6.1 Percutaneous Ethanol Injection (PEI)

Several studies have shown that PEI is an effective alternative to surgery in cases of small HCC. Tumor cell destruction is achieved by alcohol-induced immediate coagulative necrosis of the affected tissue as a consequence of protein denaturation and cellular dehydration [16].

The maximum diameter of HCC lesions that can be treated successfully by PEI is approximately 3 cm. Larger lesions are less amenable to treatment with this technique because the ethanol distributes less homogeneously, resulting in incomplete necrosis of the lesion. This applies equally for the treatment of liver metastases where PEI is of limited effectiveness for local tumor control [8].

T2-weighted MR images acquired post-PEI

typically demonstrate areas of markedly decreased signal intensity, corresponding to regions of ethanol-induced coagulative necrosis. The possibility of tumor recurrence should be considered if an area of increased signal intensity is observed within the lesion. However, in rare cases, necrosis with high signal intensity may be observed in the center of the lesion. This is indicative of liquefactive necrosis and should be borne in mind for differential diagnosis.

Contrast-enhanced T1-weighted images in the equilibrium phase reveal a hypovascular area.

Recurrent or residual tumor should be considered if enhancement is detected within three to six months post-therapy (Fig. 10) [11, 17]. In cases of treated HCC, special attention should be paid to early enhancing areas in the arterial phase of the dynamic series of acquisitions since early enhancement is highly indicative of recurrent tumor.

On post interventional T1-weighted images a fan-shaped hypointense area of normal liver tissue adjacent to the treated HCC with a corresponding hyperintense signal on T2-weighted images can sometimes be observed and might be mistaken for residual tumor. This area, which typically enhances strongly on T1-weighted images after administration of contrast agent, represents pathologic changes in the normal liver tissue as a toxic reaction to the injected ethanol. Awareness of such abnormalities is important for the correct evaluation of therapeutic efficacy [29].

11.6.2 Regional Transarterial Chemoembolization (TACE)

Neither systemic or local chemotherapy nor chemoembolization are primary techniques normally used with the aim of curing liver metastases. They are mainly considered a second-line treatment in patients with metastases of colorectal carcinoma.

On the other hand TACE is frequently used for curative treatment of HCC, especially in Asia.

TACE therapy is based on the differential blood supply of normal liver tissue and hepatic tumors. Whereas arterial perfusion accounts for about 25% of the blood supply in normal liver parenchyma, it may account for as much as 95% in hepatic neoplasms, depending on the histology of the tumor. Thus, solid liver tumors are frequently accessible to arterial embolization and/or intra-arterially applied chemotherapy, while surrounding liver tissue is not affected to the same extent due to its mainly portal venous blood supply. The direct superselective arterial application of chemotherapeutics leads to an increased concentration of the chemotherapeutic drug within the lesion with a concomitant reduction of systemic side effects [3].

Typically, chemoembolization involves the injection of an emulsion of iodized oil (e.g. lipiodol) followed by a chemotherapeutic drug (e.g. doxorubicin) and embolization particles applied via an arterial catheter that is advanced into the segmental or subsegmental arteries that feed the tumor tissue.

Chemoembolization may lead to a partial reduction of tumor volume which may secondarily allow surgical resection or interventional ablation in the case of inaccessible tumors. Frequently it is performed in cases in which systemic chemotherapy is ineffective and in cases of therapy-resistant pain arising from dilatation of the liver capsule [21, 30].

TACE is generally contraindicated in a number of situations: when significant reduction of synthetic liver function is apparent, when 75% or more of the liver tissue is affected by the neoplasm, in cases of ascites where the Karnowski Index is less than 50%, and in cirrhotic livers when the liver parenchyma unaffected by the tumor has an increased arterial supply. Additionally, TACE may only be performed in cases of portal-venous obstruction if sufficient collaterals are present [14].

MRI is increasingly being used for follow-up studies in patients after injection of iodized oil. MRI is generally preferred to computed tomography (CT) for post-TACE imaging since the high concentration of lipiodol within the tumor can make it very difficult to recognize possible disease recurrence on CT imaging. This is due to the hyperdensity of lipiodol which tends to mask the hypervascular areas of residual or recurrent tumor which are also hyperattenuating after injection of iodinated contrast material [13, 31].

Follow-up imaging after TACE is possible between the first week and approximately two to three months after the procedure. If T1-weighted dynamic imaging is performed within the first week after TACE, the increased signal intensity seen in tumor nodules that accumulate lipiodol can sometimes make it difficult to detect residual hypervascular tumor tissue (Fig. 11). On the other hand, persistent lipiodol retention for more than four weeks indicates therapeutic effectiveness. Decreased signal intensity on T2-weighted images may also be observed within one week of treatment. However, remaining areas of higher signal intensity on T2-weighted images may not necessarily indicate residual tumor tissue, since the T2 relaxation time is also influenced by early concomitant modifications, such as ischemia, hemorrhage, edema and initial colliquative necrosis [4, 31].

Whereas early follow-up after TACE is often inconclusive for the detection of recurrent tumor, follow-up T2-weighted and arterial phase con-

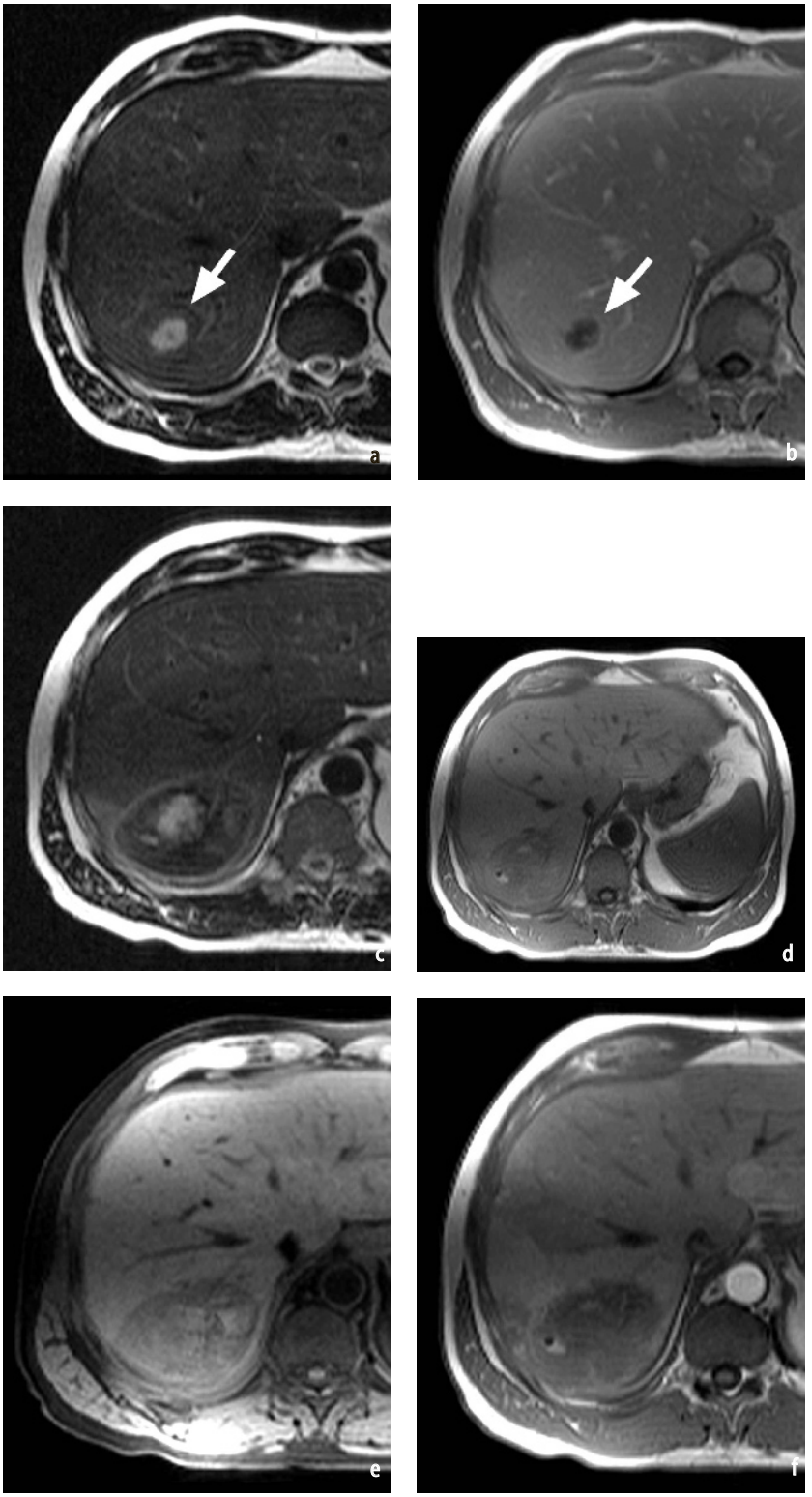
a
b
c
d
e
f

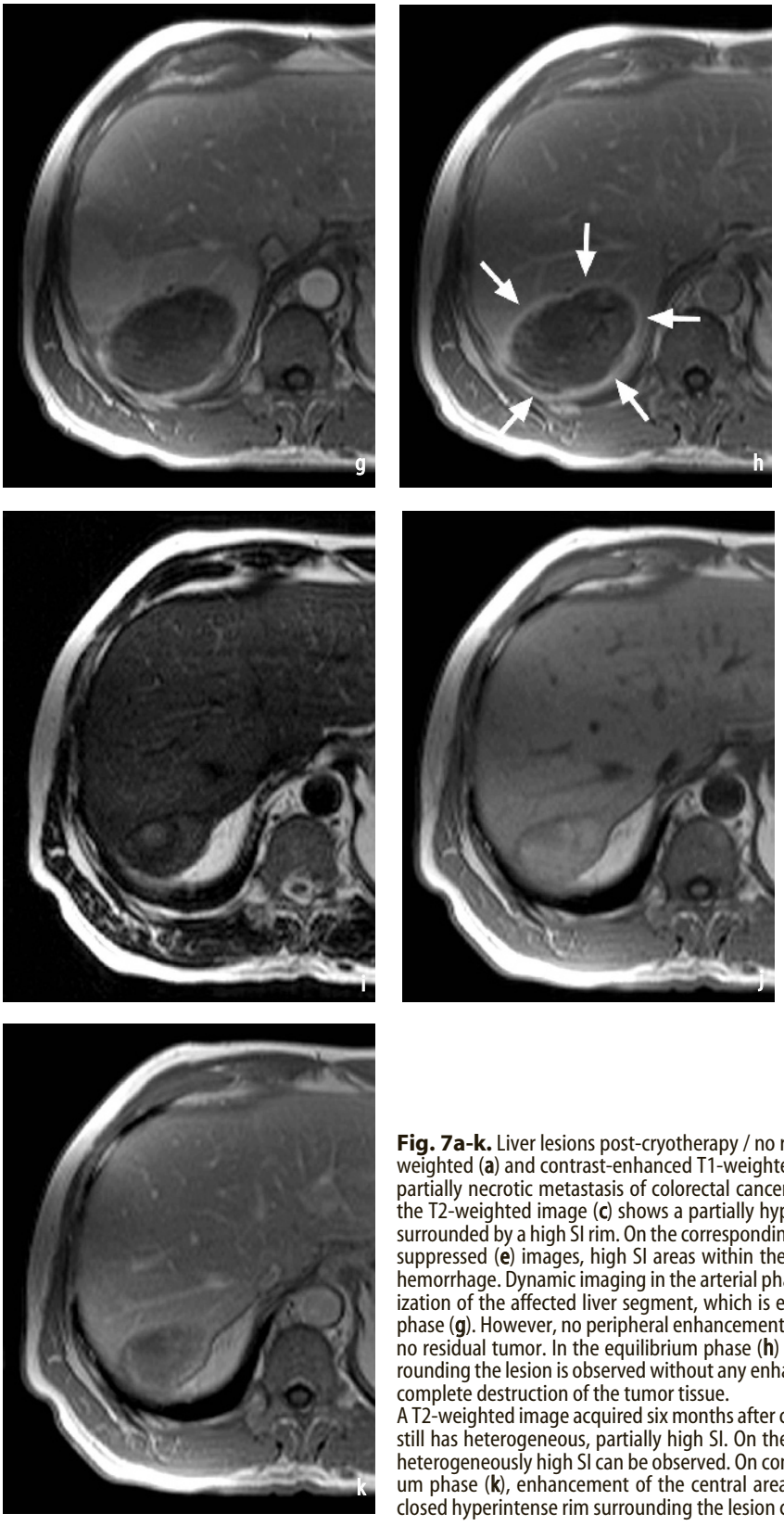

Fig. 7a-k. Liver lesions post-cryotherapy / no residual tumor. Pre-cryotherapy, the T2-weighted (**a**) and contrast-enhanced T1-weighted equilibrium phase (**b**) images show a partially necrotic metastasis of colorectal cancer (*arrows*). One week after cryotherapy, the T2-weighted image (**c**) shows a partially hyperintense, partially hypointense region surrounded by a high SI rim. On the corresponding T1-weighted (**d**) and T1-weighted fat-suppressed (**e**) images, high SI areas within the cryolesion can be detected, indicating hemorrhage. Dynamic imaging in the arterial phase (**f**) reveals segmental hypervascularization of the affected liver segment, which is even more obvious in the portal-venous phase (**g**). However, no peripheral enhancement of the cryolesion is detected, indicating no residual tumor. In the equilibrium phase (**h**) a closed hyperintense rim (*arrows*) surrounding the lesion is observed without any enhancement of central areas. This indicates complete destruction of the tumor tissue.
A T2-weighted image acquired six months after cryotherapy (**i**) shows that the cryolesion still has heterogeneous, partially high SI. On the corresponding T1-weighted image (**j**), heterogeneously high SI can be observed. On contrast-enhanced images in the equilibrium phase (**k**), enhancement of the central areas of the lesion is still not visible and a closed hyperintense rim surrounding the lesion can still be seen

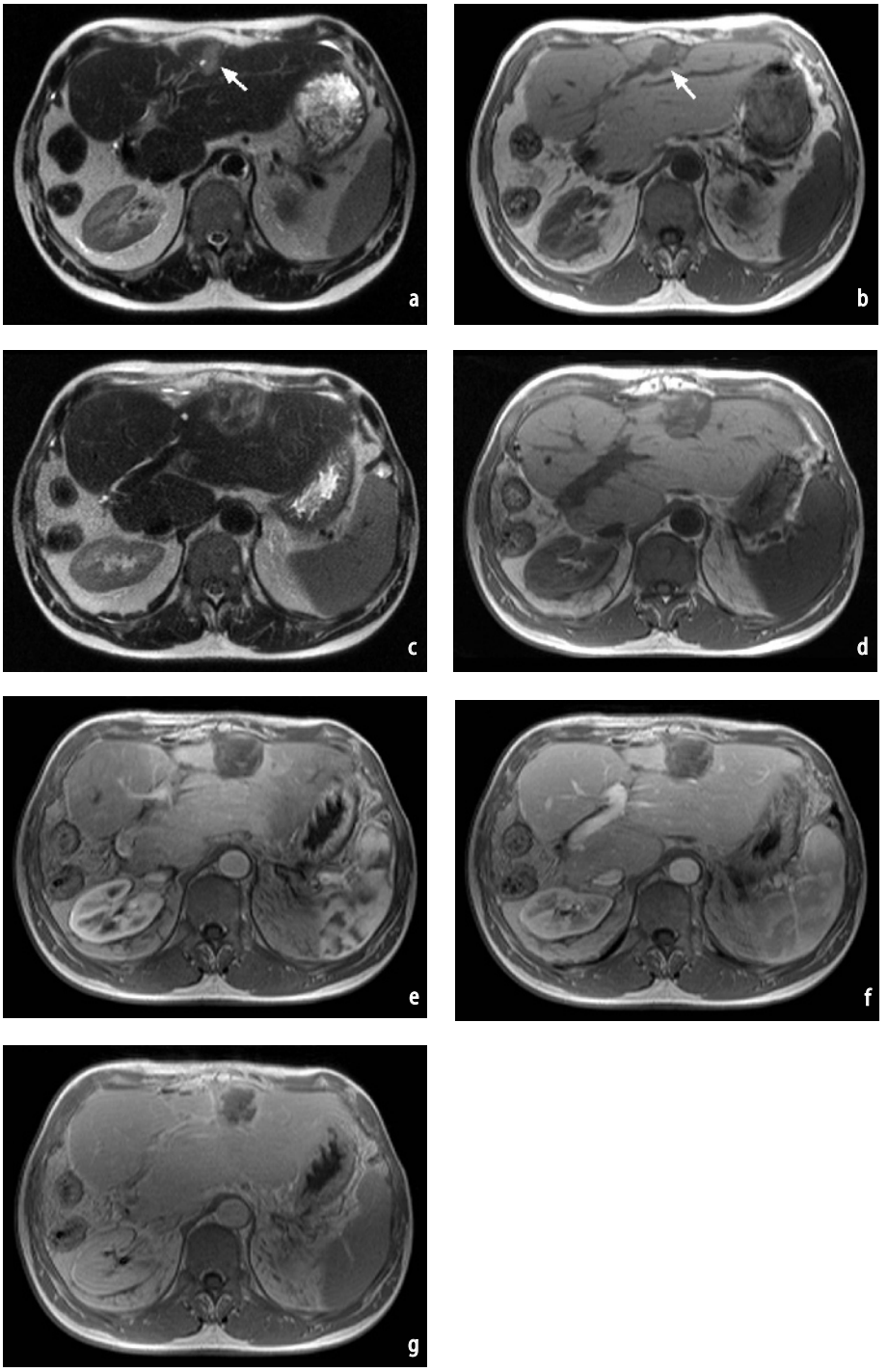

Fig. 8a-g. Liver lesion post-cryotherapy showing no residual tumor in a patient with previous liver resection.
On the unenhanced T2-weighted (**a**) and T1-weighted (**b**) images pre-cryotherapy, a metastasis (*arrows*) can be seen in the left liver lobe. Note that the patient underwent previous right hemi-hepatectomy. The T2-weighted image (**c**) acquired one month following cryotherapy, shows a heterogeneous, predominantly high SI lesion. On the T1-weighted image (**d**), this lesion is hypointense with some high SI areas indicative of hemorrhage. On dynamic imaging, segmental hypervascularization can again be noted in the arterial phase (**e**) with homogeneous signal in the portal-venous phase (**f**). The equilibrium phase image (**g**) again shows a closed hypervascular rim surrounding the lesion, indicating complete destruction of the metastasis

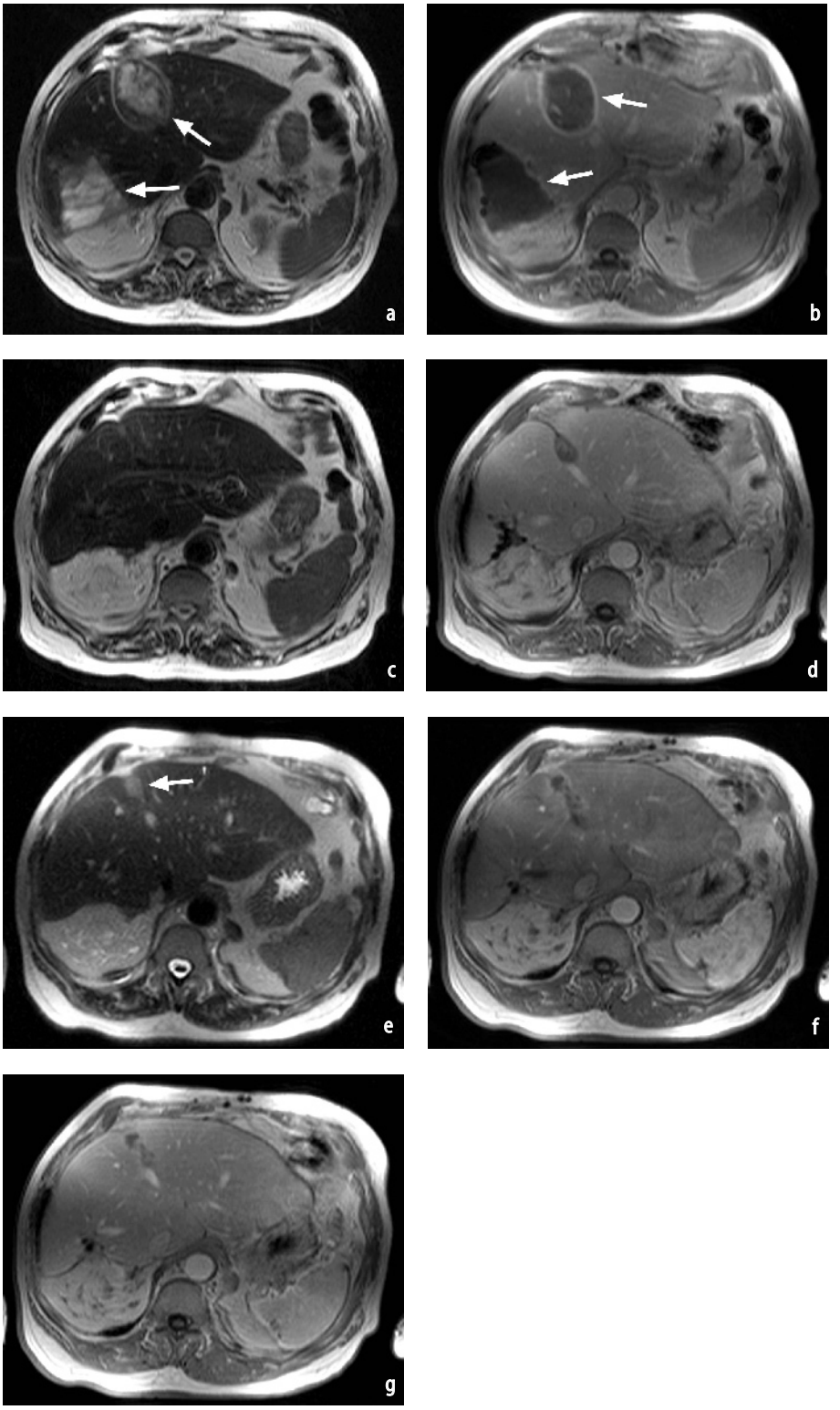

Fig. 9a-g. Patient post-cryotherapy demonstrating late recurrent disease. T2-weighted (**a**) and contrast-enhanced T1-weighted equilibrium phase (**b**) images acquired three weeks after cryotherapy show two large cryolesions (*arrows*). Hyperintense rims surrounding the lesions are apparent on the T1-weighted equilibrium phase image (**b**). Significant reduction of the size of the cryolesion can be noted on both T2-weighted (**c**) and contrast-enhanced T1-weighted equilibrium phase (**d**) images acquired six months post-cryotherapy. No signs of residual tumor or local recurrence are apparent. However, on a T2-weighted image acquired 12 months post-cryotherapy (**e**), again a homogeneous high SI lesion (*arrow*) in the area of one of the former cryolesions can be seen. On the corresponding T1-weighted image in the arterial phase after contrast agent injection (**f**), an irregular peripheral enhancement of the affected region is evident. In the equilibrium phase (**g**), no hyperintense rim can be observed. Taken together, these observations indicate local recurrent disease

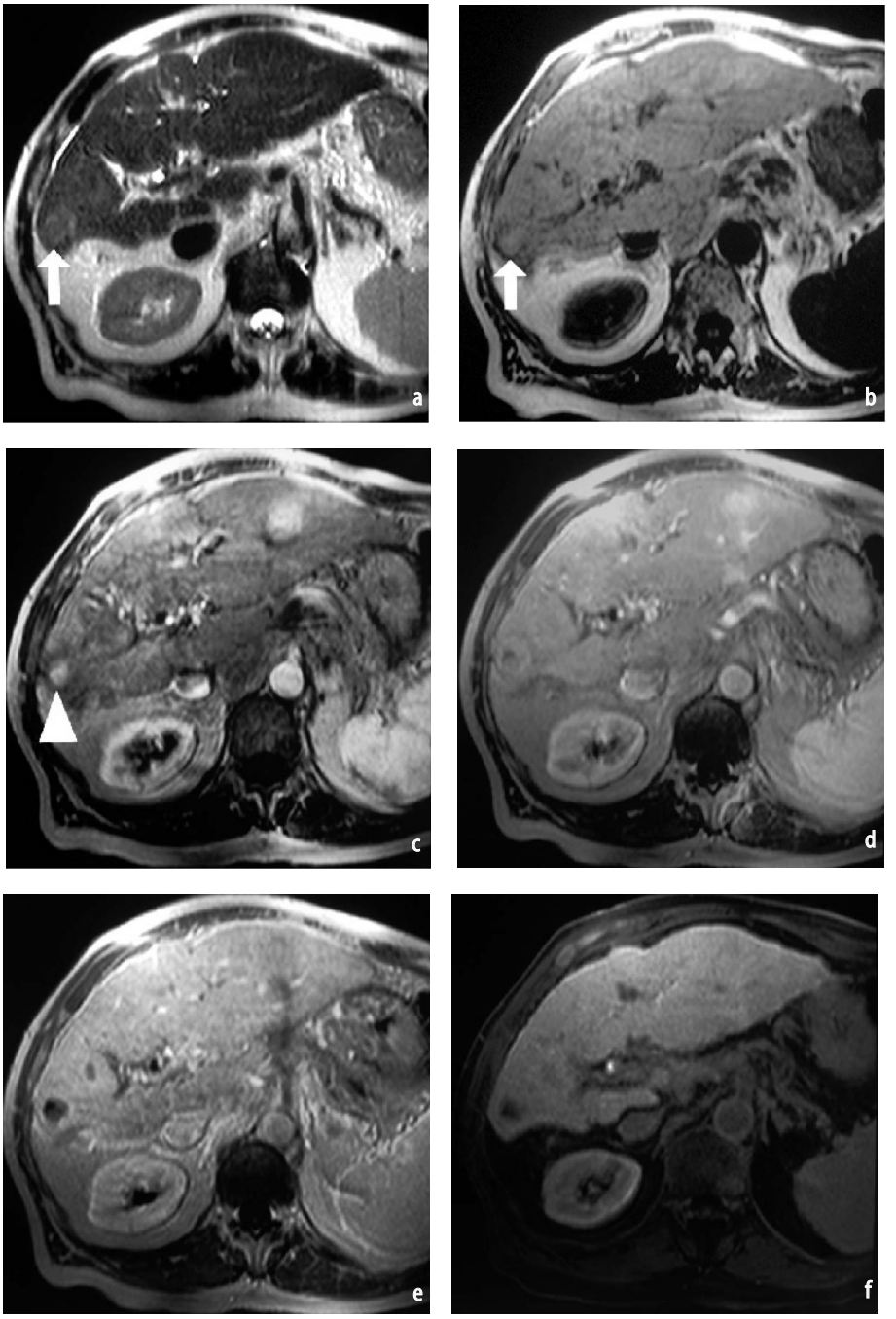

Fig. 10a-f. HCC post-percutaneous ethanol injection (PEI) / residual tumor. The nodule (*arrow*) appears hypointense with slightly hyperintense peripheral areas on the T2-weighted image (**a**) and hyperintense on the T1-weighted image (**b**) after PEI treatment. A focal hypervascular area (*arrowhead*), representing focal residual tumor, is seen during the arterial phase after the bolus injection of Gd-BOPTA (**c**). The portal-venous and equilibrium phase images (**d** and **e**, respectively) reveal contrast agent wash-out from the residual tumor and an overall hypointense appearance. The delayed hepatobiliary phase image (**f**) indicates that the residual tumor does not significantly take up Gd-BOPTA. This case is typical of residual tumor in HCC treated by percutaneous ethanol injection. The arterial phase image after contrast agnet injection is most sensitive for the detection of residual or recurrent tumor in cases of HCC or other hypervascular lesions

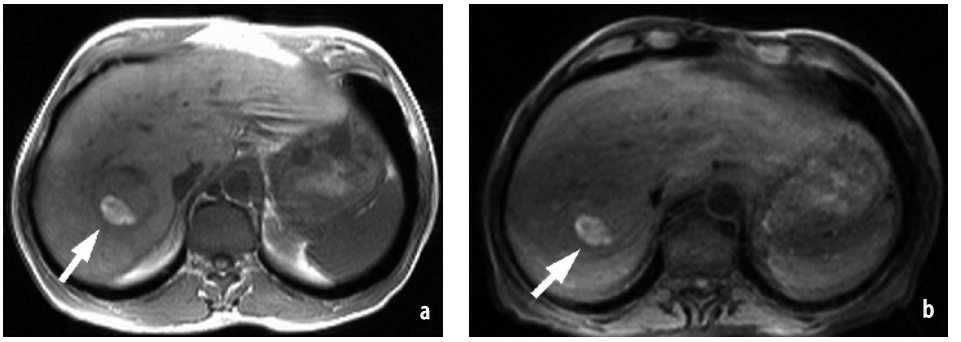

Fig. 11a, b. T1-weighted (**a**) and T1-weighted fat-suppressed (**b**) imaging of an HCC within the first week after TACE. Increased SI is seen within the treated tumor nodule due to accumulation of lipiodol (*arrows*). This can make it difficult to detect residual hypervascular tumor tissue on dynamic Gd-enhanced liver imaging

trast-enhanced T1-weighted MRI performed two to three months after therapy is very sensitive for detecting or excluding recurrent tumors. Typically, a reduction of the T2 relaxation time, resulting in a decrease of signal intensity, can be observed in completely destroyed tumors on T2-weighted images acquired two to three months post-TACE. At this time-point, the decreased T2-weighted signal intensity is more likely to be a result of coagulative necrosis induced by TACE than an effect of lipiodol [15].

Completely destroyed tumors are similarly depicted as areas of low signal intensity on T1-weighted images. Thus, dynamic imaging after the injection of Gd-based contrast agents is very sensitive for the detection of tumor recurrence, especially in hypervascular lesions such as HCC, since good contrast between the necrosis and viable tumor can be achieved (Fig. 12). Two to three months after treatment, areas of high signal intensity on T2-weighted images and hypervascular areas on contrast-enhanced T1-weighted dynamic arterial phase images can be considered as indicative of tumor recurrence [4, 31].

11.7 Multimodality Treatment of Hepatic Lesions

Only about 30% of patients with hepatic metastatic disease are suitable for hepatic resection. The majority of patients with liver metastases or primary malignant liver tumors are not candidates for this therapeutic approach due to advanced hepatic tumor spread [1]. To overcome this dilemma, a multi-modality treatment approach involving combined surgical, interventional, focal ablative and chemotherapeutic methods has been proposed to achieve a better five year patient survival.

With the development of focal ablative procedures, including local application of cold, heat, or drugs to destroy tumor tissue, a functional tissue sparing method has been developed. In patients with bilobar tumor spread, these new techniques allow for a combined therapeutic approach with open surgical liver resection of one liver lobe, in combination with focal ablative therapies such as cryotherapy, laser- or radio-frequency induced thermal tumor destruction in the contralateral lobe in order to pre-

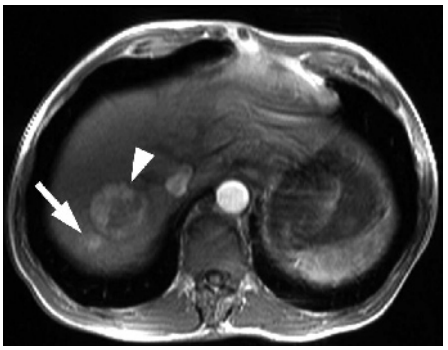

Fig. 12. Recurrent HCC post-TACE. Three months post-TACE therapy of an HCC, recurrent hypervascularization of the treated area is visible (*arrowhead*) on a T1-weighted arterial phase image after Gd-injection. In addition, a satellite lesion adjacent to the treated lesion is visible (*arrow*)

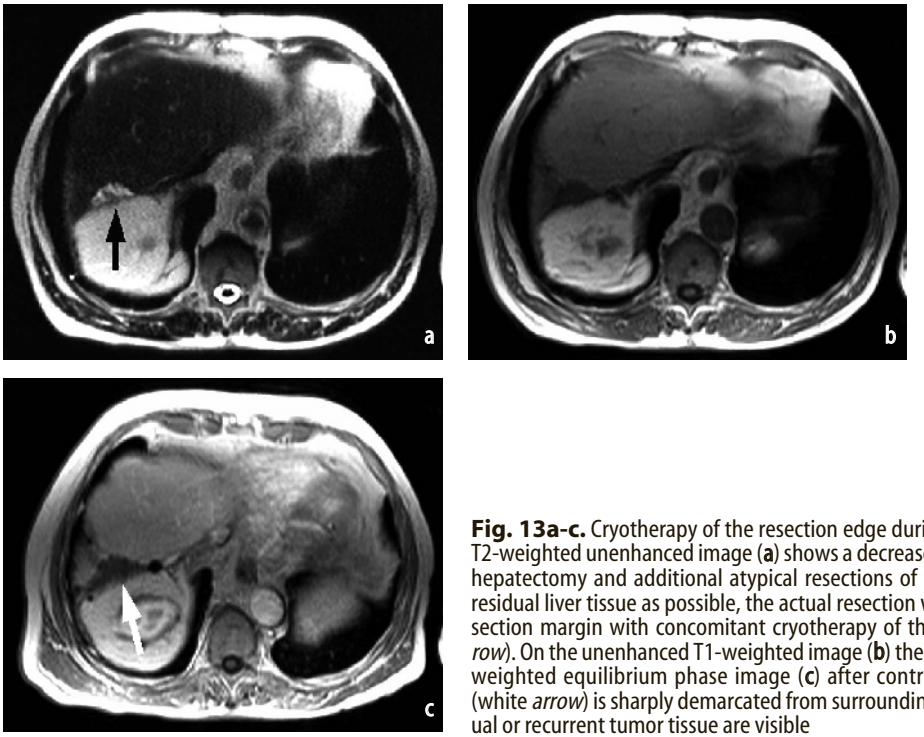

Fig. 13a-c. Cryotherapy of the resection edge during atypical liver resection. The T2-weighted unenhanced image (**a**) shows a decreased size of the liver due to hemihepatectomy and additional atypical resections of metastases. To spare as much residual liver tissue as possible, the actual resection was performed with a small resection margin with concomitant cryotherapy of the resection margins (black *arrow*). On the unenhanced T1-weighted image (**b**) the lesion shows low SI. On the T1-weighted equilibrium phase image (**c**) after contrast agent injection the lesion (white *arrow*) is sharply demarcated from surrounding liver tissue. No signs of residual or recurrent tumor tissue are visible

serve the functional surrounding liver tissue [36, 37]. To achieve this objective, precise pretherapeutic imaging is necessary to characterize the tumor's location, size and segmental distribution, in order to allow accurate planning of the therapeutic strategy. In some cases the calculation of tumor volume in relation to residual liver parenchyma might be helpful to determine the post-operative outcome in terms of liver function [38]. The method of intraoperative or interventional preconditioning of one liver lobe, for example, gives a better functional result after hepatic resection or thermal therapy [39]. The liver lobe to be preserved can be stimulated to regenerate by selective interventional occlusion of one portal venous branch on the opposite side. The volume increase can be detected precisely by MR volume calculation [38, 40].

Surgical resection of hepatic tumors should be performed if the lesion is surrounded by healthy liver tissue in order to leave a resection safety margin of 1 cm. Tumor locations near larger blood vessels or bile duct structures may make it difficult to achieve this safety margin. Therefore, cryotherapy of the resection edge with a specially designed flattened cryo-probe can be performed as a therapeutic adjunct to achieve tumor-free resection margins [41-43]. On post-operative MR imaging the resulting cryonecrosis is characterized by a flattened elliptical area (Fig. 13) with identical peripheral imaging features as endohepatic cryotherapy. Criteria for detection of residual tumor should be applied analogously.

In the large proportion of patients not suitable for curative treatment, systemic or intra-arterial chemotherapy has been established as a second-line therapy to achieve prolonged patient survival. Nevertheless, the five year survival of patients with colorectal carcinoma undergoing conventional chemotherapeutic treatment with 5-fluorouracil and leucovorin has proven to be very poor [44]. Newer strategies using a combination of irinotecan, oxaliplatin and modified delivery regimes have demonstrated better response rates [45]. This improved efficacy not only results in prolonged patient survival, but in some patients also offers the possibility of a curative treatment by surgery after down-staging [46]. Another strategy of preinterventional tumor downsizing is neoadjuvant transarterial chemoembolization. With the combination of chemotherapeutic drugs (e.g. mitomycin) and embolization materials such as microspheres and lipiodol, a significant reduction in tumor volume is possible which then allows treatment options with curative intention, such as surgical resection or focal ablative techniques. Nevertheless, further prospective randomized trials are needed to evaluate this strategy [24]. In this setting, MRI plays an important role in characterizing tumor volume and perfusion before and after neoadjuvant therapy in order to accurately evaluate the effectiveness of treatment and to evaluate the possibility of subsequent curative treatment.

References

1. Bown SG. Phototherapy in tumors. World J Surg 1983; 7:700-9
2. Braga L, Semelka RC, Pedro MS, et al. Post-treatment malignant liver lesions. MR imaging. Magn Reson Imaging Clin N Am 2002; 10:53-73
3. Chen HS, Gross JF. Intra-arterial infusion of anticancer drugs: theoretic aspects of drug delivery and review of responses. Cancer Treat Rep 1980; 64:31-40
4. De Santis M, Torricelli P, Cristani A, et al. MRI of hepatocellular carcinoma before and after transcatheter chemoembolization. J Comput Assist Tomogr 1993; 17(6):901-8
5. De Santis M, Alborino S, Tartoni PL, Torricelli P, Casolo A, Romagnoli R. Effects of lipiodol retention on MRI signal intensity from hepatocellular carcinoma and surrounding liver treated by chemoembolization. Eur Radiol 1997; 7:10-6
6. Desinger K, Stein T, Tschepe J, Müller G. Investigation on radio-frequency current application in bipolar technique for interstitial thermotherapy (RF-ITT). Minim Invasive Med 1996; 7:92-97
7. Dromain C, de Baere T, Elias D, et al. Hepatic tumors treated with percutaneous radio-frequency ablation: CT and MR imaging follow-up. Radiology 2002; 223:255-62
8. Ebara M, Ohto M, Sugiura N, Kita K, Yoshikawa M, Okuda K, Kondo F, Kondo Y. Percutaneous ethanol injection for the treatment of small hepatocellular carcinoma. Study of 95 patients. J Gastroenterol Hepatol 1990; 5(6):616-26
9. Gayowski TJ, Iwatsuki S, Madariaga JR, Selby R, Todo S, Irish W, Starzl TE. Experience in hepatic resection for metastatic colorectal cancer: analysis of clinical and pathologic risk factors. Surgery 1994; 116(4):703-10; discussion 710-711
10. Lee F, Bahn DK, McHugh TA, Onik GM, Lee FT Jr. US-guided percutaneous cryoablation of prostate cancer.Radiology 1994; 192(3):769-76
11. Lencioni R, Bartolozzi C, Caramella D, Di Coscio G. Management of adenomatous hyperplastic nodules in the cirrhotic liver: US follow-up or percutaneous alcohol ablation? Abdom Imaging 1993; 18(1):50-5
12. McCarter MD, Fong Y. Metastatic liver tumors. Semin Surg Oncol 2000; 19(2):177-88
13. Murakami T, Nakamura H, Tsuda K, Nakanishi K, Hori S, Tomoda K, Mitani T, Kozuka T, Monden M, Wakasa K. Treatment of hepatocellular carcinoma by chemoembolization: evaluation with 3DFT MR imaging. AJR Am J Roentgenol 1993; 160(2):295-9
14. Pentecost MJ. Transcatheter treatment of hepatic metastases. AJR Am J Roentgenol 1993; 160(6):1171-5
15. Sakurai M, Okamura J, Kuroda C. Transcatheter chemo-embolization effective for treating hepatocellular carcinoma. A histopathologic study. Cancer 1984; 54(3):387-92
16. Shiina S, Tagawa K, Niwa Y, Unuma T, Komatsu Y, Yoshiura K, Hamada E, Takahashi M, Shiratori Y, Terano A, et al. Percutaneous ethanol injection therapy for hepatocellular carcinoma: results in 146 patients. AJR Am J Roentgenol 1993; 160(5):1023-8
17. Sironi S, De Cobelli F, Livraghi T, Villa G, Zanello A, Taccagni G, DelMaschio A. Small hepatocellular carcinoma treated with percutaneous ethanol injection: unenhanced and gadolinium-enhanced MR imaging follow-up. Radiology 1994; 192(2):407-12
18. Solbiati L, Goldberg SN, Ierace T, Livraghi T, Meloni F, Dellanoce M, Sironi S, Gazelle GS. Hepatic metastases: percutaneous radio-frequency ablation with cooled-tip electrodes. Radiology 1997; 205(2):367-73
19. Stangl R, Altendorf-Hofmann A, Charnley RM, Scheele J. Factors influencing the natural history of colorectal liver metastases. Lancet 1994; 343(8910):1405-10
20. Steele G Jr. Cryoablation in hepatic surgery. Semin Liver Dis 1994; 14(2):120-5
21. Vogl TJ, Muller PK, Mack MG, Straub R, Engelmann K, Neuhaus P. Liver metastases: interventional therapeutic techniques and results, state of the art. Eur Radiol 1999; 9(4):675-84
22. Vogl TJ, Mack MG, Muller PK, Straub R, Engelmann K, Eichler K. Interventional MR: interstitial therapy. Eur Radiol 1999; 9(8):1479-87
23. Puls R, Stroszczynski C, Gaffke G, Hosten N,Felix R, Speck U. Laser induced thermotherapy (LITT) of liver metastases: MR guided percutaneous insertion of an MRI-compatible irrigated microcatheter system using a closed high field unit. J Magn Reson Imaging 2003; 17:663-670
24. Vogl TJ, Mack MG, Balzer JO, Engelmann K, Straub R, Eichler K, Woitaschek D, Zangos S. Liver metastases: Neoadjuvant downsizing with transarterial chemoembolization before laser induced thermotherapy. Radiology 2003; 229:457-464
25. Isbert C, Ritz JP, Schilling A, Roggan A, Heiniche A, Wolf KJ, Müller G, Buhr HJ, Germer CT. Laser induced thermotherapy (LITT) of experimental liver metastasis-Detection of residual tumor using Gd-DTPA enhanced MRI. Lasers Surg Med 2002; 30:280-289
26. Tacke J, Adam G, Haage P, Sellhaus B, Großkortenhaus S, Günther RW. MR-guided percutaneous cryotherapy of the liver: In vivo evaluation with histologic correlation in an animal model. J Magn Reson Imaging 2001; 13:50-56
27. Butts K, Sinclair J, Daniel BL, Wansapura J, Pauly J. Temperature quantitation and mapping of frozen tissue. J Magn Reson Imaging 2001; 13:99-114
28. Mala T, Edwin B, Tillung T, Hol PC, Soreide O, Gladhaug I. Percutaneous cryoablation of colorectal liver metastases: potentiated by two consecutive freeze-thaw cycles. Cryobiology 2003; 46:99-102
29. Fujita T, Honjo K, Ito K, Arita T, Koike S, Takano S, Tamura S, Matsumoto T, Matsunaga N. Fan-shaped hepatic parenchymal damage after ethanol injection therapy for hepatocellular carcinoma: MRI appearances. Abdom Imaging 1999; 24:56-60
30. Maataoui A, Qian J, Vossoughi D, Khan MF, Oppermann E, Bechstein WO, Vogl TJ. Transarterial chemoembolisation alone and in combination with other therapies: A comparative study in an animal model. Eur Radiol 2005; 15:127-133
31. Guang YS, Sun L, Zhou XP, Li Xiao, Zheng XH. Hepatocellular carcinoma treated with interventional procedures: CT and MRI follow-up. World J Gastroenterol 2004; 10:3546-3548
32. Sasson AR, Sigurdson ER. Surgical treatment of liver metastases. Semin Oncol 2002; 29:107-118
33. Lencioni R, Crocetti L, Cioni D, Della Pina C, Bartolozzi C. Percutaneous radiofrequency ablation of hepatic colorectal metastases: Technique, indications, results and new promises. Invest Radiol 2004; 39:689-697
34. Antoch G, Vogt FM, Veit P, Freudenberg L, Blech-

schmid N, Dirsch O, Bockisch A, Forsting M, Debatin J, Kuehl H. Assessment of liver tissue after radiofrequency ablation: Findings with different imaging procedures. J Nucl Med 2005; 46:520-525
35. Dromain C, De Baere T, Elias D, Kuoch V, Ducreux M, Boige V, Petrow P, Roche A, Sigal R. Hepatic tumors treated with percutaneous radio-frequency ablation : CT and MR imaging follow up. Radiology 2002; 223:255-262
36. Brooks AJ, Wang F, Alfredson M, Yan TD, Morris DL. Synchronous liver resection and cryotherapy for colorectal metastases: survival analysis. Surgeon 2005; 3(4):265-8
37. Seifert JK, Springer A, Baier P, Junginger T. Liver resection or cryotherapy for colorectal liver metastases A prospective case control study. Int J Colorectal Dis 2005; 20(6):507-20
38. Vogl TJ, Straub R, Eichler K, Sollner O, Mack MG. Colorectal carcinoma metastases in liver: laser-induced interstitial thermotherapy–local tumor control rate and survival data. Radiology 2004; 230(2):450-8
39. Banga NR, Homer-Vanniasinkam S, Graham A, Al-Mukhtar A, White SA, Prasad KR. Ischaemic preconditioning in transplantation and major resection of the liver. Br J Surg 2005; 92(5):528-38
40. Liu H, Fu Y. Portal vein embolization before major hepatectomy. World J Gastroenterol 2005; 11(14):2051-4
41. Gananadha S, Daniel S, Zhao J, Morris DL. An experimental evaluation of ablation devices for the local treatment of the liver resection edge. Eur J Surg Oncol. 2005; 31(5):528-32
42. Shen P, Hoffman A, Howerton R, Loggie BW. Cryosurgery of close or positive margins after hepatic resection for primary and metastatic hepatobiliary malignancies. Am Surg 2002; 68(8):695-703
43. Gruenberger T, Jourdan JL, Zhao J, King J, Morris DL. Reduction in recurrence risk for involved or inadequate margins with edge cryotherapy after liver resection for colorectal metastases. Arch Surg 2001; 136(10):1154-7
44. Stangl R, Altendorf-Hofmann A, Charnley RM, Scheele J. Factors influencing the natural history of colorectal liver metastases. Lancet 1994; 343(8910):1405-10

12

MR Angiography in Liver Disease

CONTENTS

12.1 Introduction

Recent developments in magnetic resonance (MR) scanner hardware and the advent of fast three dimensional (3D) gradient echo sequences have rapidly advanced the role of MR imaging for the evaluation of abdominal vasculature. Nowadays it is possible to accurately image both the arterial and venous vasculature of the abdomen and to acquire sufficient information to accurately detect and diagnose underlying pathologies of these vessels. In particular, depiction of anatomic variants of the arterial blood supply and demonstration of collateral circulation of the liver is easily performed non-invasively on contrast-enhanced MR angiography (CE MRA). The possibility to perform rapid time-resolved imaging permits evaluation of both the arterial and portal-venous systems in the same session, thereby rendering CE MRA a one-stop-shop for the work-up of patients with suspected vascular disease of the liver. The rapid improvements in CE MRA methodology permit accurate non-invasive evaluation of potential living donors and of patients scheduled for liver transplantation.

12.2 Technique

MRA does not require extensive patient preparation prior to the examination. Patients are not required to fast before the examination; on the contrary, high-caloric meals prior to the examination may increase the splanchnic flow, thereby improving the depiction of small branching arteries. On the other hand, physiological peristalsis may cause motion artifacts in some patients; this can be reduced by application of glucagon or N-butyl-scopalamine.

Imaging is usually performed with the patient in the supine position in the magnet. Typically, a body array surface coil that covers the abdomen is used. The arms should be elevated above the head in order to avoid aliasing artifacts. For accurate injection of contrast agent, an intravenous feed should be placed in the right antecubital vein. For most examinations the contrast agent and saline flush should be injected at a minimum flow rate of 2 ml/sec in order to achieve a sufficiently tight contrast agent bolus [25].

12.2.1 Time-of-Flight MRA

In order to achieve adequate signal in the vessels of interest, time-of-flight MR angiography (TOF MRA) generally requires the orthogonal acquisition of images. TOF MRA is therefore not suitable for depiction of the abdominal vasculature because of the typically tortuous course of the vessels. Although the proximal parts of the main abdominal branches in which most vascular pathologies are located may theoretically be assessed on TOF MRA, the long acquisition times for these sequences preclude the possibility of acquiring images in one breath-hold. Moreover, since flow in the aorta is perpendicular to that in the branching arteries, major artifacts which may mimic stenoses are common.

12.2.2 Phase-Contrast MRA

The abdominal vasculature may be evaluated with phase-contrast (PC) MRA using both two dimensional (2D) and 3D techniques [4, 14, 15, 21]. 2D PC MRA with electrocardiogram (ECG) or pulse triggering has been shown to provide functional information of the mesenteric vasculature [4, 14, 15, 21]. By segmenting the acquired phase with the cardiac cycle, quantitative measurements of flow velocity and volume may be acquired.

An important advantage of 3D PC MRA over 2D PC MRA is that images can be acquired in any plane [34]. However, due to the relatively long acquisition times, respiratory motion artifacts frequently impair the quality of the image. Moreover, image quality may be further reduced by ghost artifacts derived from inhomogeneous or turbulent flow during systole. Although this problem may be resolved by cardiac gating, this further increases the acquisition time without necessarily improving the image quality.

12.2.3 Contrast-Enhanced MRA

The acquisition of high quality images of the mesenteric vessels became feasible with the introduction of CE MRA [18, 26, 27]. Moreover, the technique permits the visualization of very small vessels that are not discernible using non-enhanced imaging techniques.

Imaging in the coronal plane permits evaluation of the aorta, splanchnic arteries and portal vein in one examination. A partition thickness of 3-5 mm is acceptable if zero padding is available for interpolation. In the absence of an interpolation algorithm, the slice thickness should be less than 3 mm. To evaluate stenotic disease of the celiac trunk or the proximal mesenteric arteries, imaging should be performed in the sagittal plane. Aliasing is not as severe for acquisitions in the sagittal plane, so it is possible to utilize a rectangular field-of-view with a high spatial resolution acquisition matrix (e.g. 512 x 256). If a slower MR system is used, it is advantageous to acquire images in the sagittal plane so that fewer sections or partitions are required to cover the aorta, celiac artery (CA), superior mesenteric artery (SMA), and inferior mesenteric artery (IMA). Imaging parameters should be adjusted to allow for image acquisition during breath-hold. Axial imaging may be useful if the primary goal is evaluation of the hepatic arteries, hepatic parenchyma or portal vein. However, one difficulty with the axial orientation is aliasing in the slice direction, which tends to be severe with the extremely short radio frequency (RF) pulses used in 3D CE MRA. To minimize aliasing, a coil should be used in which the cranial-dimension is only slightly larger than the caudal-dimension of the imaging volume. Fat saturation or chemically selective fat inversion pulses should also be considered. These will help minimize unwanted signal from pericardial and abdominal fat wrapping onto the image volume.

3D CE MRA datasets should be acquired before, during and after completion of intravenous contrast agent administration. Pre-contrast images should be checked to ensure that the imaging volume is positioned correctly. These images can also be used subsequently for digital subtraction to improve image contrast. Accurate timing of the contrast agent bolus is essential for arterial phase acquisitions. This can be achieved with automatic triggering (SmartPrep or Care Bolus), fluoroscopic triggering (Bolus Track) or by means of a test bolus to the mid-abdominal aorta. After arterial phase imaging, acquisition of a delayed image dataset is useful to show the portal-venous and hepatic venous anatomy. Arterial phase 3D CE MRA is best evaluated by first acquiring multiple overlapping maximum intensity projection (MIP) reconstructions in the coronal plane. Thereafter, reformations and subvolume MIP reconstructions can be prepared in perpendicular planes through each major abdominal aortic branch vessel, including the celiac trunk, and the SMA and IMA. It is also useful to assess the iliac arteries, especially the internal iliac arteries, as they may represent an important collateral pathway in patients with chronic mesenteric ischemia.

12.3 Imaging of the Arterial System

12.3.1 Normal Anatomy and Variants

The blood supply to the intra-abdominal organs derives from three major branches of the abdominal aorta: the celiac artery (CA), the SMA and the IMA. Although numerous anatomical variants exist, in the majority of cases CE MRA allows a detailed depiction of the typical and atypical vascular anatomy of the splanchnic vessels [2, 11, 17, 33]. Of principal interest for the arterial supply of the liver are the CA and the SMA, however, since collateral supply between the three major branches exists, all of these branches will be discussed (Fig. 1).

12.3.1.1 Celiac Artery (CA)

The CA is typically located at the level of the T12 to L1 vertebral body. It arises from the ventral part of the abdominal aorta and supplies the upper abdominal viscera. In about two thirds of patients the CA branches into the common hepatic artery, the splenic artery and the left gastric artery (Fig. 2). However, in the remaining one third of individuals, anatomical variants exist in which the common hepatic artery, the splenic artery and the left gastric artery arise from either the SMA or directly from the aorta.

The common hepatic artery divides into the proper hepatic artery and the gastroduodenal artery. In about 75% of cases the gastroduodenal artery thereafter branches into two further vessels; the right gastroepiploic artery and the superior pancreaticoduodenal artery. The superior pancreaticoduodenal artery forms an anastomosis with the inferior pancreaticoduodenal artery which derives from the SMA.

In about 50% of cases the proper hepatic artery divides into the left and right hepatic arteries. The remaining 50% of individuals show variants or accessory hepatic arteries. The main variants are shown in Fig. 3.

12.3.1.2 Superior Mesenteric Artery (SMA)

The SMA usually arises about 1 cm distal to the celiac artery at the anterior aspect of the aorta. In rare cases, a common single celio-mesenteric trunk is present. The first branch from the SMA is the inferior pancreaticoduodenal artery which forms an anastomosis with the superior pancreaticoduodenal artery deriving from the celiac artery. The jejunal and ileal branches arise from the proximal and left side of the SMA, forming multiple arcades. Right sided branches are the ileocolic artery, the right colic artery and the middle colic artery (Fig. 4).

A common variant is the origin of the right hepatic artery from the SMA or even the origin of the common hepatic artery from the SMA.

12.3.1.3 Inferior Mesenteric Artery (IMA)

The IMA arises from the abdominal aorta at approximately the level of the third lumbar vertebra. Compared to the other main abdominal branches

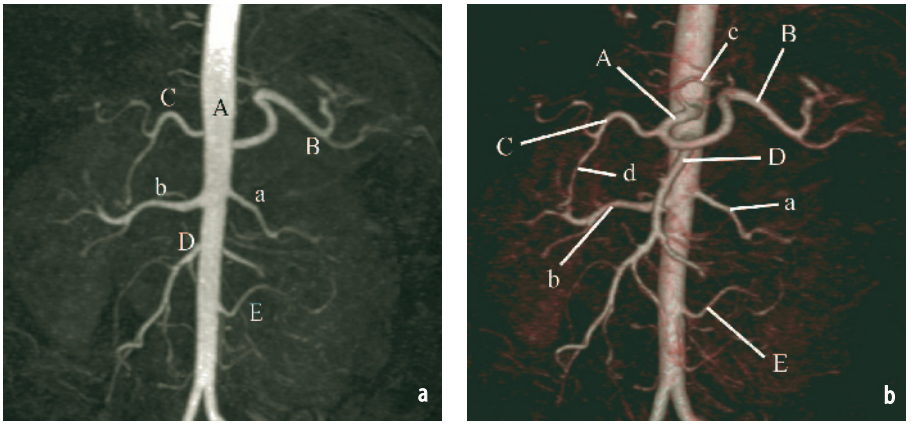

Fig. 1a, b. Maximum intensity projection (**a**) and volume rendered (**b**) displays of a 3D CE MRA dataset acquired in the early arterial phase demonstrate the arterial vascular anatomy of the abdomen. Beyond the aorta and both renal arteries, branches of the celiac trunk and the SMA are well-depicted.
A Celiac artery (CA). **B** Splenic artery. **C** Common hepatic artery. **D** Superior mesenteric artery (SMA). **E** Inferior mesenteric artery (IMA). **a** Left renal artery. **b** Right renal artery. **c** Left gastric artery. **d** Gastroduodenal artery.
From Magnetic Resonance Angiography, Schneider G. et al (eds.), p 233. Springer, 2005

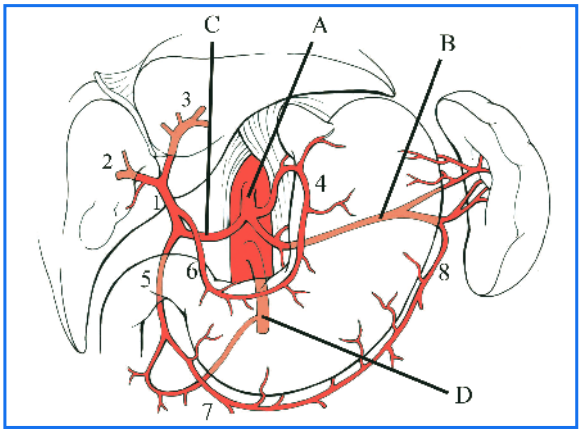

Fig. 2. Normal anatomy of the celiac trunk.
A Celiac artery (CA). **B** Splenic artery. **C** Common hepatic artery. **D** Superior mesenteric artery (SMA).
1 Proper hepatic artery. **2** Right hepatic artery. **3** Left hepatic artery. **4** Left gastric artery. **5** Gastroduodenal artery. **6** Right gastric artery. **7** Right gastroepiploic artery. **8** Left gastroepiploic artery.
From Magnetic Resonance Angiography, Schneider G. et al (eds.), p 232. Springer, 2005

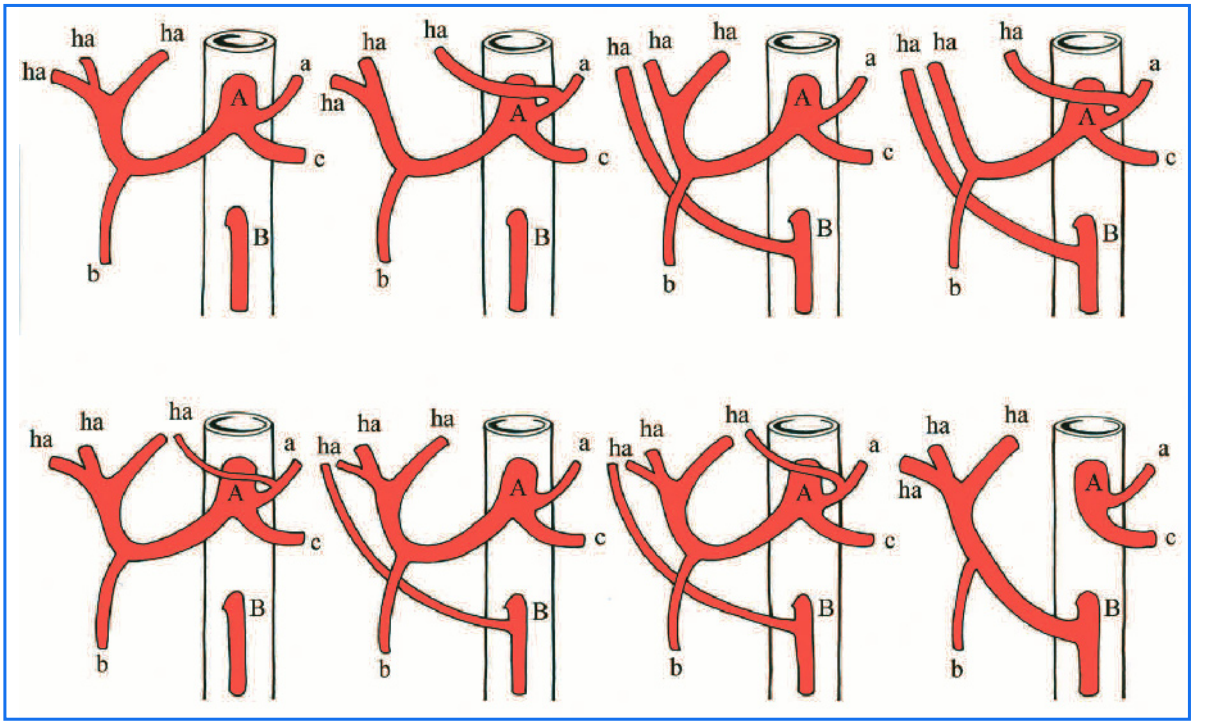

Fig. 3. Schematic representation of variants of the hepatic vasculature.
A Celiac artery (CA). **B** Superior mesenteric artery (SMA).
a Left gastric artery. **b** Gastroduodenal artery. **c** Splenic artery. **ha** Hepatic arteries
From Magnetic Resonance Angiography, Schneider G. et al (eds.), p 238. Springer, 2005

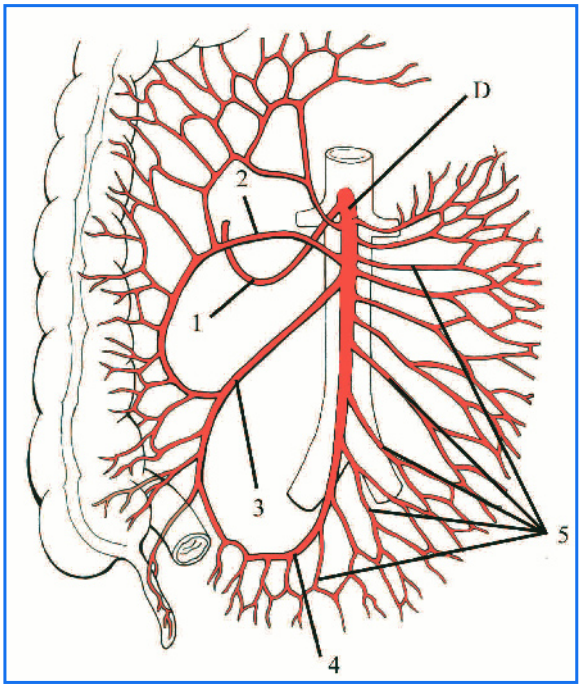

Fig. 4. Normal anatomy of the superior mesenteric artery.
D Superior mesenteric artery (SMA).
1 Gastroduodenal artery. **2** Medial colic artery. **3** Right colic artery. **4** Iliocolic artery. **5** Jejunal- and ilieal arteries.
From Magnetic Resonance Angiography, Schneider G. et al (eds.), p 232. Springer, 2005

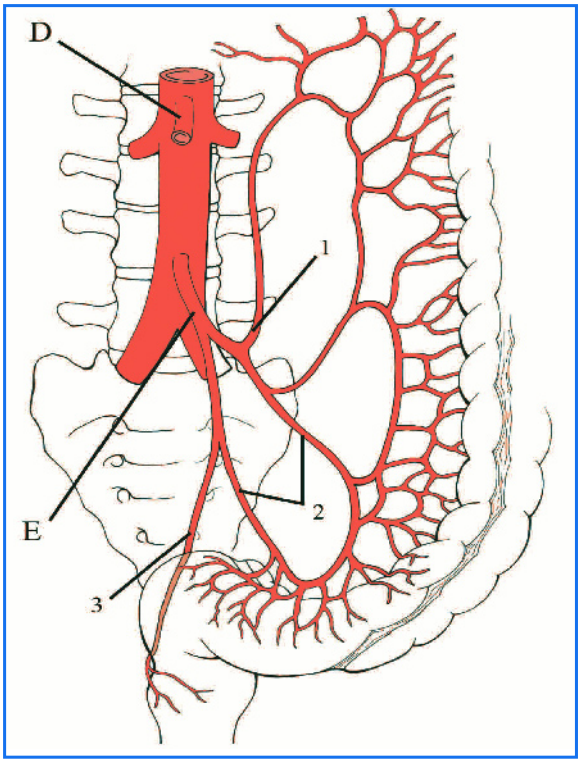

Fig. 5. Normal anatomy of the inferior mesenteric artery.
D Superior mesenteric artery (SMA). **E** Inferior mesenteric artery (IMA).
1 Left colic artery. **2** Sigmoid arteries. **3** Superior rectal artery.
From Magnetic Resonance Angiography, Schneider G. et al (eds.), p 232. Springer, 2005

it is a relatively thin vessel, measuring only 1-6 mm in diameter. For this reason the IMA is often difficult to depict on MRA.

The left colic artery usually represents the first branch of the IMA. This forms the so-called anastomosis of Riolan with the middle colic artery deriving from the SMA (Fig. 5). In cases of severe stenosis or occlusion of the SMA, this anastomosis can serve as a collateral supply for the SMA. Giving off the sigmoid branches, the IMA becomes the superior rectal artery.

Variations in the splanchnic arterial anatomy occur in more than 40% of patients (Fig. 3). For this reason, pre-operative vascular planning for hepatic resections, liver transplantations, resection of retroperitoneal masses, chemoinfusion pump placement, surgical shunting, or other abdominal operations may require accurate mapping of the visceral arterial anatomy. Generally, this is achieved by conventional angiography because of the fine detail needed to identify variations involving tiny arteries. However, to evaluate the origins of the splanchnic artery and major branches, 3D CE MRA is frequently sufficient.

The most common variation is a replaced (17%) or accessory (8%) right hepatic artery, most commonly from the SMA (Figs. 6, 7). Less common variations include the left hepatic artery arising from the left gastric artery (Fig. 8), the common hepatic artery arising from the SMA (2.5%) (Fig. 9) or directly from the aorta (2%) (Fig. 10), the left gastric artery arising from the aorta (1-2%) (Fig. 11), or a celio-mesenteric trunk (<1%). Other more complex variations may also occur.

Although the main indication for arterial imaging of the hepatic vasculature is the evaluation of vascular anatomy, there are other indications for which CE MRA may be helpful. For example, in the case of liver tumors such as pedunculated adenoma or focal nodular hyperplasia (FNH), preoperative CE MRA may help to optimize the therapeutic approach by displaying the arterial supply and venous drainage of the lesion (Fig. 12). Imaging of vascular pathologies such as aneurysms of the splanchnic arteries can also be performed in a non-invasive manner using CE MRA (Fig. 13) and therapeutic approaches, if necessary, can be planned.

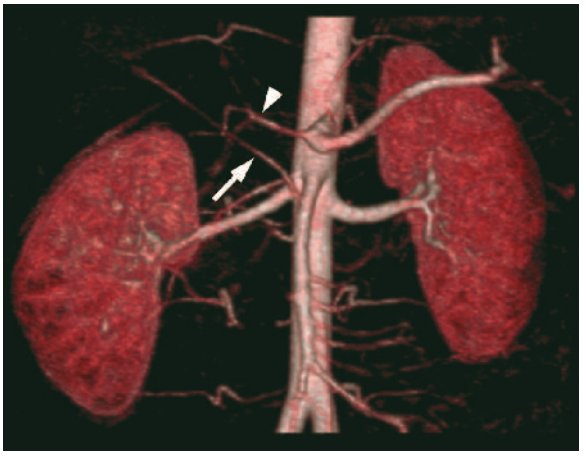

Fig. 6. A volume rendered 3D CE MRA (0.1 mmol/kg Gd-BOPTA) dataset shows an anatomic variation of the arterial supply of the liver in a patient with liver transplantation planned. Note that the right hepatic artery (*arrow*) branches from the SMA, whereas the left hepatic artery (*arrowhead*) branches from the celiac trunk. The small caliber of the vessels is the result of a longstanding inflammatory process that resulted in liver fibrosis

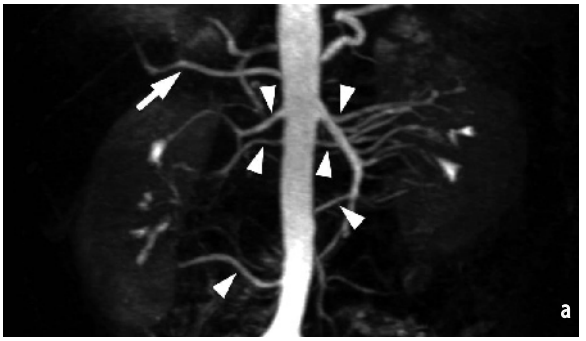

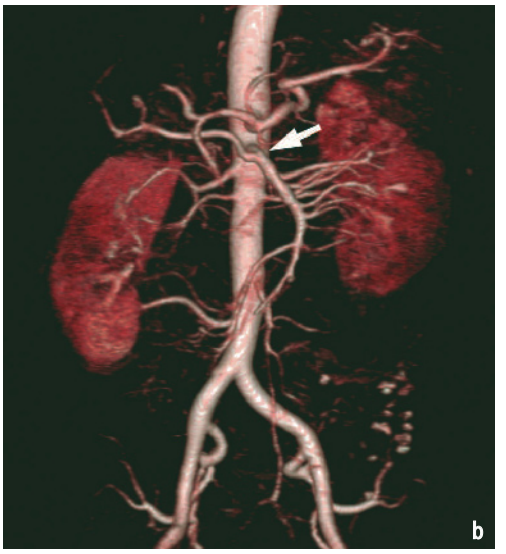

Fig. 7a, b. Whereas the MIP reconstruction (**a**) reveals multiple renal arteries (*arrowheads*) together with an obvious abnormal course of the right hepatic artery (*arrow*), the volume-rendered image (**b**) clearly displays the anatomic variation of a right hepatic artery originating from the SMA (*arrow*). This example shows that evaluation of vascular anatomy is sometimes easier on volume-rendered images than on MIP reconstructions

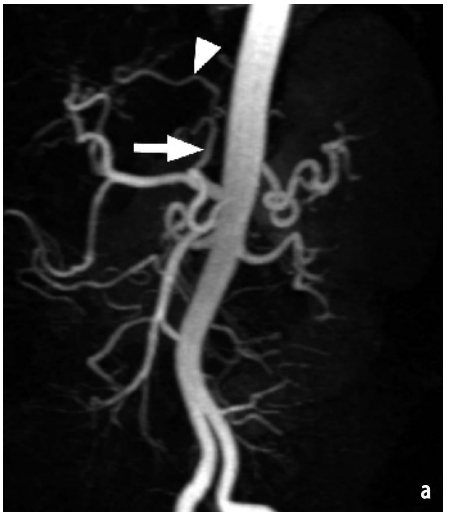

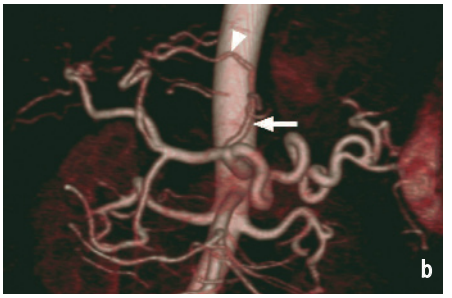

Fig. 8a, b. Left hepatic artery (*arrowhead*) arising from the left gastric artery (*arrow*) on a CE MRA (0.1 mmol/kg Gd-BOPTA) MIP reconstruction (**a**) and on a volume-rendered image (**b**). Note again that the vessels are better appreciated on the volume-rendered image

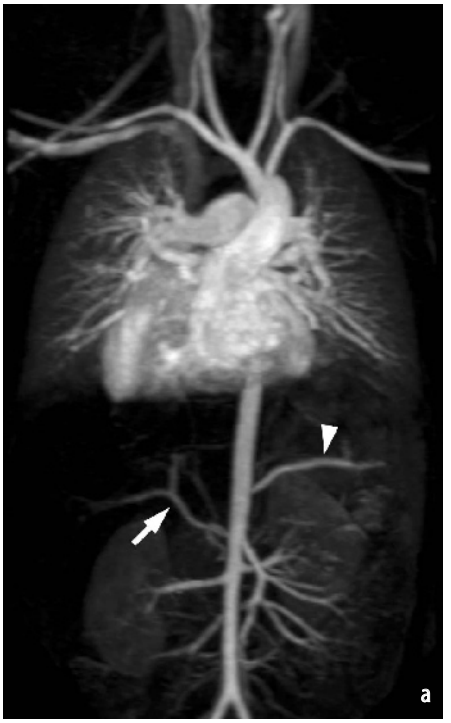

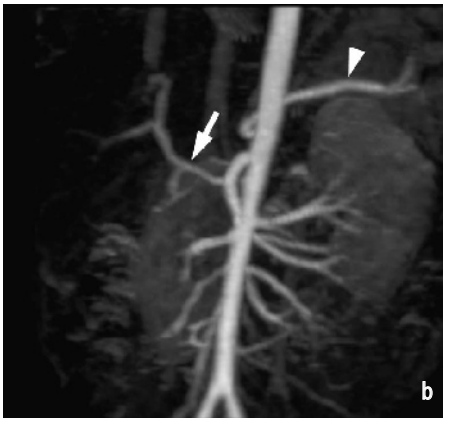

Fig. 9a, b. CE MRA in a 3 year old girl with transposition of the great arteries. Whole-body MIP reconstruction (**a**) reveals an abnormal course of the ascending aorta due to transposition of the great arteries and dextro-positio cordis. In addition, the splenic (arrowhead) and hepatic arteries (*arrow*) both seem to originate from the celiac trunk. However, a subvolume MIP reconstruction (**b**) clearly reveals that the common hepatic artery (*arrow*) branches from the SMA while the splenic artery (*arrowhead*) originates from the celiac trunk

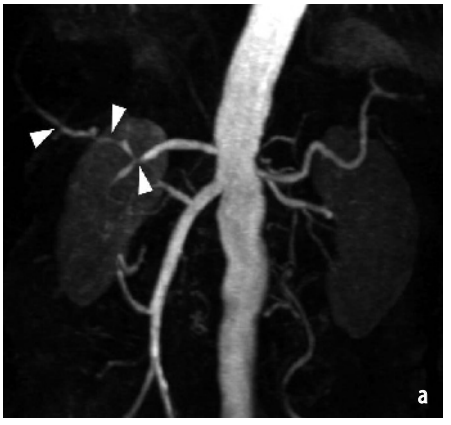

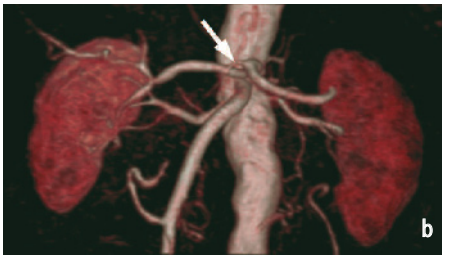

Fig. 10a, b. CE MRA (0.1 mmol/kg Gd-BOPTA) MIP reconstruction (**a**) reveals multiple stenoses (*arrowheads*) of the hepatic artery due to vasculitis. However, determining the origin of the hepatic artery is difficult. The corresponding volume-rendered image (**b**) reveals separate branching of the hepatic artery (*arrow*) from the aorta. Information regarding this anatomic variation is extremely important for planning liver transplantation

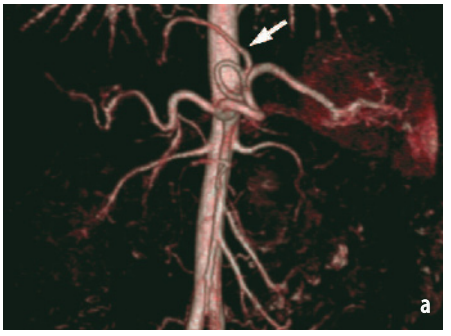

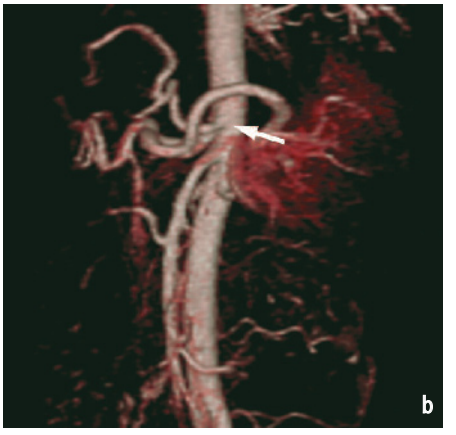

Fig. 11a, b. The volume-rendered image in AP-projection (**a**) demonstrates the left hepatic artery originating from the left gastric artery (*arrow*). The lateral view (**b**) reveals additional separate branching of the left gastric artery from the aorta (*arrow*)

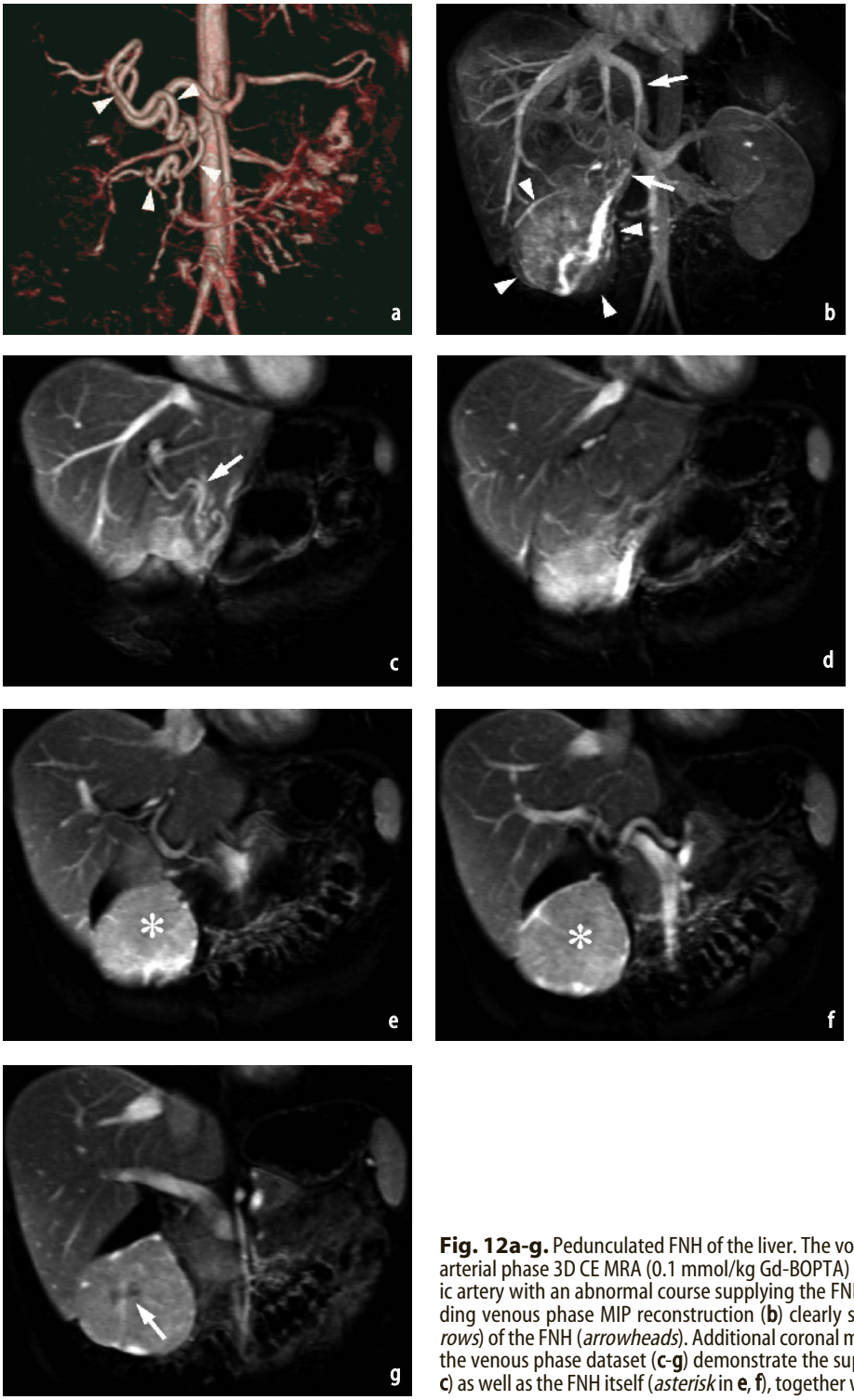

Fig. 12a-g. Pedunculated FNH of the liver. The volume-rendered image (**a**) of the arterial phase 3D CE MRA (0.1 mmol/kg Gd-BOPTA) dataset reveals a dilated hepatic artery with an abnormal course supplying the FNH (*arrowheads*). The corresponding venous phase MIP reconstruction (**b**) clearly shows the venous drainage (*arrows*) of the FNH (*arrowheads*). Additional coronal multiplanar reconstructions from the venous phase dataset (**c**-**g**) demonstrate the supplying hepatic artery (*arrow* in **c**) as well as the FNH itself (*asterisk* in **e**, **f**), together with the central scar (*arrow* in **g**)

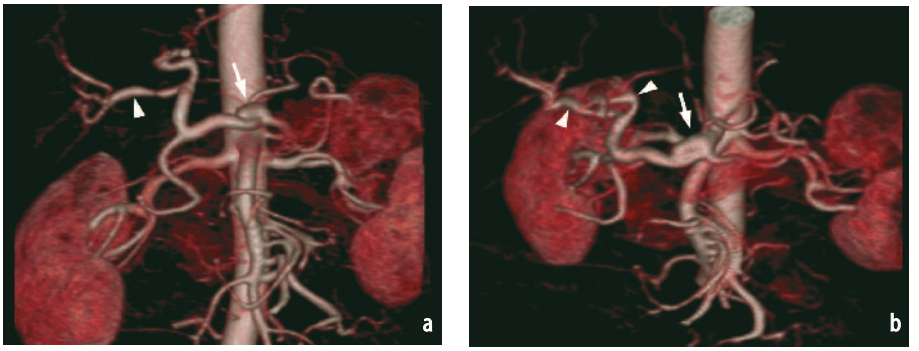

Fig. 13a, b. Volume-rendered images (**a**, **b**) in different orientations of a 3D CE MRA (0.1 mmol/kg Gd-BOPTA) dataset reveal multiple aneurysm formations in the celiac trunk (*arrow* in **b**) and hepatic arteries (*arrowheads*) due to systemic vascular disease

12.4 Imaging of the Portal-Venous System

3D CE MR portography is regarded as a safe, quick and robust imaging modality for evaluation of the portal-venous system. This technique has been shown to be advantageous compared to currently used techniques such as ultrasonography, catheter angiography, computed tomography (CT), and non-enhanced MR angiography with TOF and phase contrast (PC) techniques [22].

There are no major differences between MRA of the abdominal arterial system and MR portography in terms of patient management, coil selection and MR sequences. After acquisition of a precontrast coronal 3D gradient echo dataset, contrast agent is injected and image acquisition commences. Typically, image acquisition on MR portography is timed to the arterial vessel system with an additional acquisition delay of 40-60 sec after contrast agent injection prior to acquisition of the portal-venous dataset. At post-processing, the precontrast and CE arterial phase datasets are subtracted from the portal-venous phase dataset to enable visualization of the portal-venous system without arterial overlay. MIP reconstruction and multiplanar reformation techniques permit accurate evaluation of the portal-venous system.

The simultaneous availability of coronal source images permits demonstration of parenchymal lesions of the liver, pancreas, biliary tract and spleen. Precise and reliable assessment of the portal-venous system in patients with hepatic cirrhosis and portal hypertension is essential before liver transplantation, non-surgical transjugular shunting or surgical portosystemic shunting. In patients with portal hypertension and a history of gastroesophageal bleeding, it is mandatory to ascertain whether the portal-venous system is patent or if the portal vein or its main branches are thrombosed [28].

12.4.1 Normal Anatomy and Variants

The portal vein represents a confluence of the superior mesenteric vein (SMV) and the main splenic vein into which drains the pancreatic vein, left gastroepiploic vein, short gastric vein, and inferior mesenteric vein (IMV) (Fig. 14). The IMV receives its supply from the left colic, sigmoid and superior hemorrhoidal veins. It usually joins the splenic vein prior to the junction of the splenic vein with the SMV. The SMV receives its contribution from the jejunal, ileal, right colic, and middle colic veins. The right and left gastric veins usually drain directly into the portal vein.

The portal vein then divides into the right and left portal branches at the hepatic hilum. Approximately 50% of individuals demonstrate a bifurcation of the portal vein outside the liver capsule. A common anomaly of the portal-venous system is a trifurcation of the main portal vein, which occurs in about 8% of patients. In this case, the main portal vein divides into the right posterior segmental branch, the right anterior segmental branch and the left portal vein [11, 19].

12.4.2 Clinical Implications

3D CE MR portography permits accurate evaluation of the intra- and extrahepatic portal-venous system as well as the hepatic veins (Fig. 15). Due to the large field of view, the short time of acquisition, the lack of radiation, the non-invasive nature of the procedure and the low risk of complications, MR portography is regarded as superior to conventional catheter digital subtraction angiography (DSA). Clinical applications of 3D CE MR portography include the assessment of portal hypertension (portosystemic shunt, portal vein obstruction, hepatic vein obstruc-

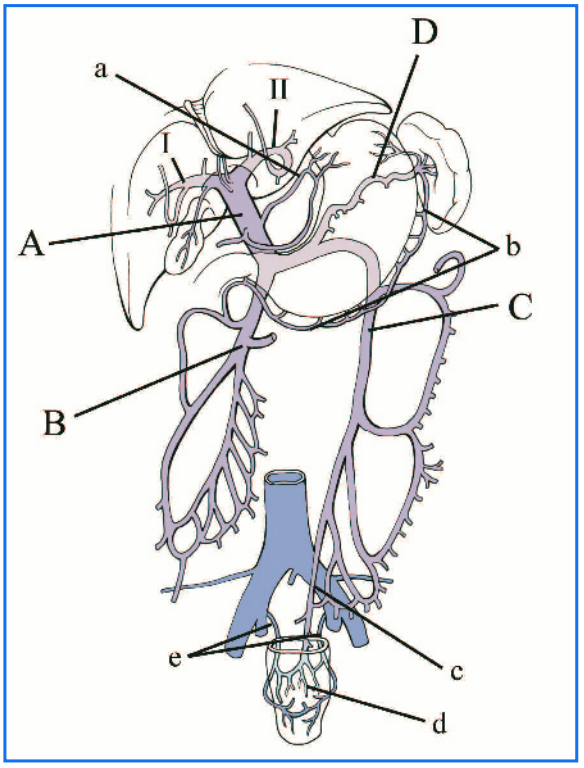

Fig. 14. Normal anatomy of the portal-venous system. **A** Portal vein. **B** Superior mesenteric vein (SMV). **C** Inferior mesenteric vein (IMV). **D** Lienal (splenic) vein. **I** Right branch of the portal vein. **II** Left branch of the portal vein. **a** Coronary and pyloric veins. **b** Right and left gastroepiploic veins. **c** Superior hemorrhoidal vein. **d** Hemorrhoidal plexus. **e** Middle and inferior hemorrhoidal veins. From Magnetic Resonance Angiography, Schneider G. et al (eds.), p 243. Springer, 2005

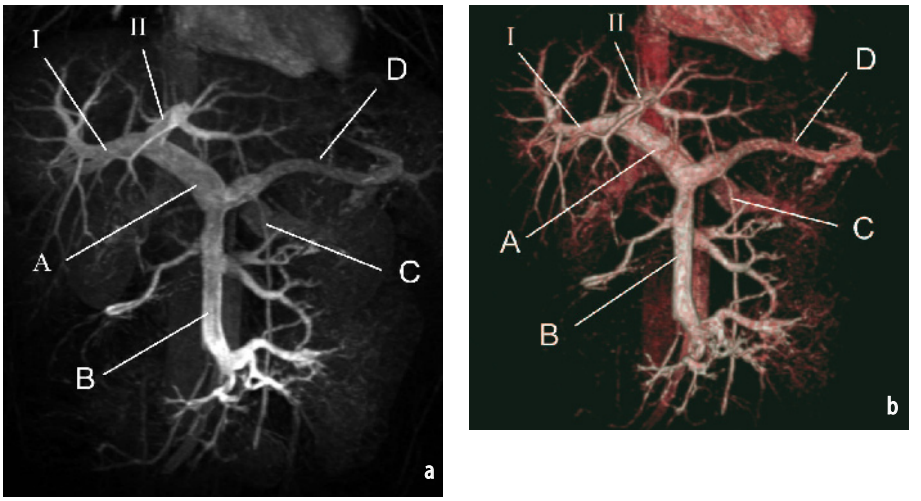

Fig. 15a, b. Normal anatomy of the portal-venous system on CE MRA MIP reconstruction (**a**) and volume-rendered image (**b**). **A** Portal vein. **B** Superior mesenteric vein (SMV). **C** Inferior mesenteric vein (IMV). **D** Lienal (splenic) vein. **I** Right branch of the portal vein. **II** Left branch of the portal vein

tion), hepatic encephalopathy, ascending portal thrombophlebitis, hepatocellular carcinoma (HCC) and pancreatobiliary tumors, gastrointestinal hemorrhage, and differentiation of splanchnic arterial disease from portal-venous disease [22, 33].

In patients with portal hypertension, 3D MR portography can be used to evaluate portosystemic shunts, hepatorenal collateral pathways, and obstruction of the portal or hepatic veins. In planning treatment for hepatic encephalopathy, it is important to identify the causative portosystemic shunt. In suspected cases of ascending portal thrombophlebitis, it is important to assess the severity of portal vein obstruction as well as portal collateral vessels. In patients with HCC or pancreatobiliary tumors, the presence or absence of portal vein invasion should be determined when planning treatment.

12.4.3 Evaluation in Liver Transplantation

Imaging proof of a patent portal vein is required in order for a patient to be placed on the liver transplant waiting list. Ultrasound (US) can image the portal vein, but is not 100% reliable. When US fails to adequately visualize the portal vein, 3D CE MRA offers a safe, accurate, and comprehensive assessment of portal-venous anatomy without requiring iodinated contrast medium [10, 12]. 3D CE MRA is also able to evaluate the splenic vein, SMV, IMV, inferior caval vein (ICV) and potential varices. Following liver transplantation, rising liver function tests may raise a suspicion of allograft ischemia. Since blood supply to the liver occurs primarily via the portal vein, this is the most important vessel to evaluate. The most common site of obstruction is at the anastomosis. Usually, anastomoses are easy to identify because of the caliber change between donor and recipient portal veins [23]. Stenosis of the transplant arterial anastomosis may be seen on the arterial phase of a portal-venous study, but its smaller size and often folded, tortuous course can make it difficult to assess. Occlusion of the transplant artery is important to detect because it results in ischemia to the donor common bile duct and can lead to biliary strictures and leaks. It is also important to assess the ICV since supra- and infrahepatic ICV anastomoses may also become narrowed and flow limiting.

12.4.4 Portal Vein Thrombosis and Cavernous Transformation

Thrombosis of the portal vein is a pathology that is frequently found in liver cirrhosis, pancreatitis, ascending portal thrombophlebitis or after sclerotherapy of a gastroesophageal varix [1]. In this condition it is important to acquire accurate information regarding portal-venous patency (Fig. 16). 3D CE MR portography provides detailed information not only about the location and length of portal vein obstruction, but also about portal collateral pathways (Fig. 17). Over time, a network of small collateral vessels develops to bypass the portal-venous occlusion. This network of collaterals, known as a cavernous transformation, is identified by its characteristic enhancement pattern in the hepatic hilum during the portal-venous and equilibrium phases of imaging (Fig. 18).

While color Doppler ultrasonography often fails to evaluate portal venous patency, 3D CE MR portography usually provides accurate information [7]. Furthermore, CE MRA can be used to assess surgical portosystemic shunts which are frequently placed to reduce portal-venous pressure. In this scenario CE MRA is used to evaluate the patency of the shunt (Fig. 19) and possible complications such as stenosis at the anastomosis.

12.4.5 Tumor Encasement

In patients with pancreatobiliary tumors, it is important to evaluate portal vein invasion before surgery. Whereas CT and DSA are often used for this purpose, 3D CE MR portography is also an accurate means to diagnose portal vein invasion [16, 30]. Invasion of the portal vein makes tumor resection with clear margins nearly impossible, thus removing the patient as a surgical candidate. Tumors in the pancreatic head may encase the SMV, portal vein, and medial splenic vein. Because these tumors cause biliary obstruction, they are usually detected quickly and are therefore more often resectable. Tumors in the body and tail of the pancreas cause less biliary obstruction and therefore frequently become larger before being detected. These tumors commonly occlude the splenic vein. Splenic vein occlusion has a tendency to produce short gastric varices which serve as venous collaterals. These can usually be seen on delayed images.

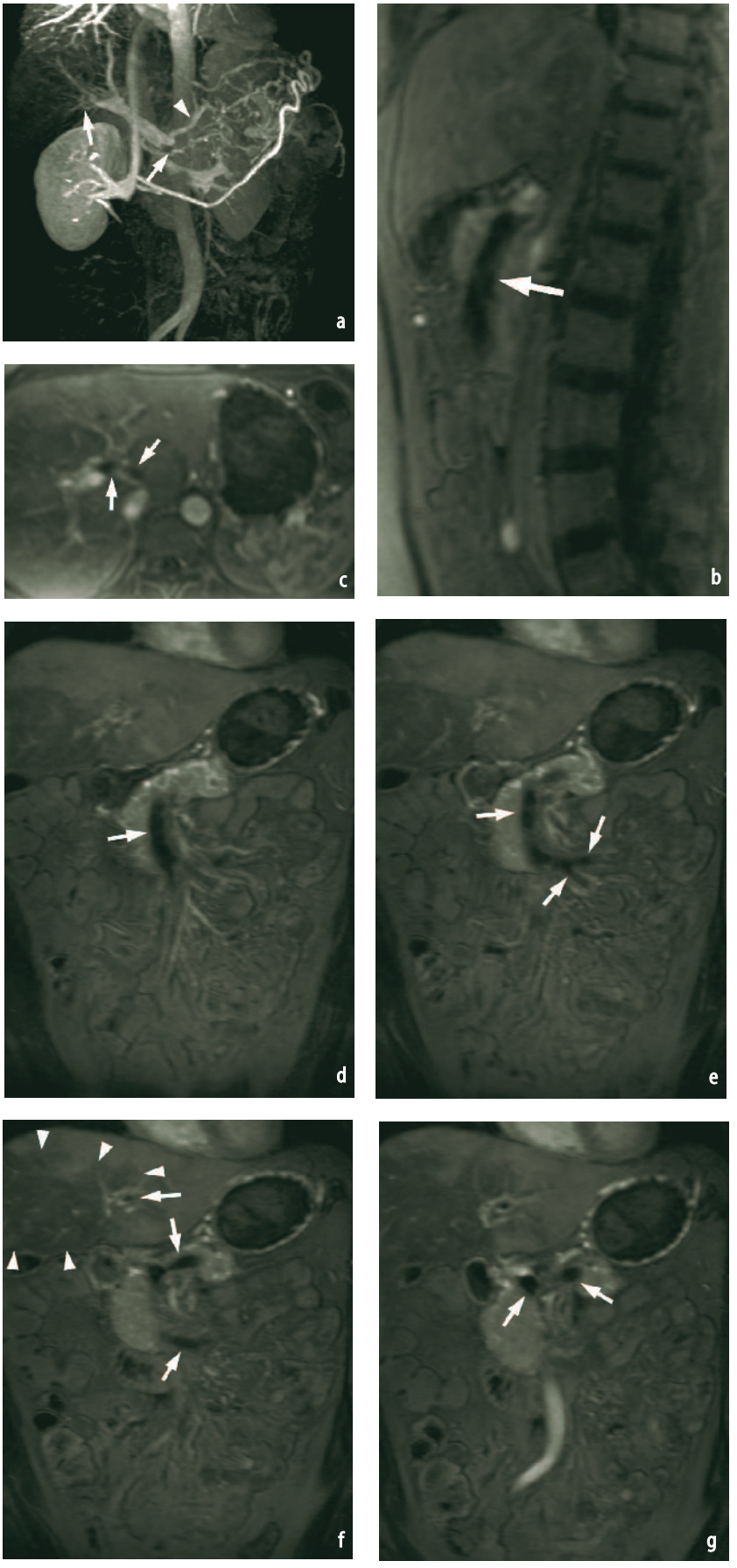
a
b
c
d
e
f
g

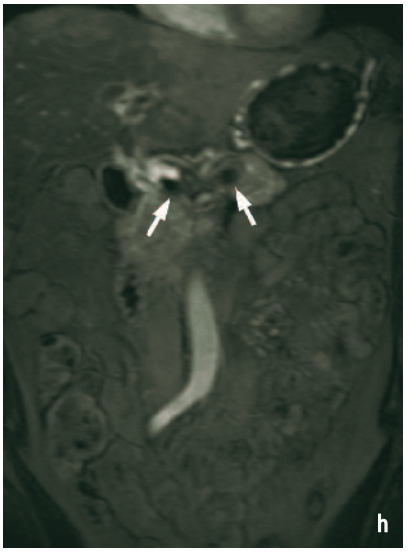

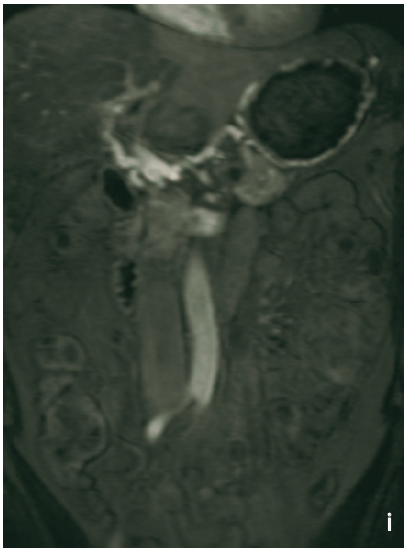

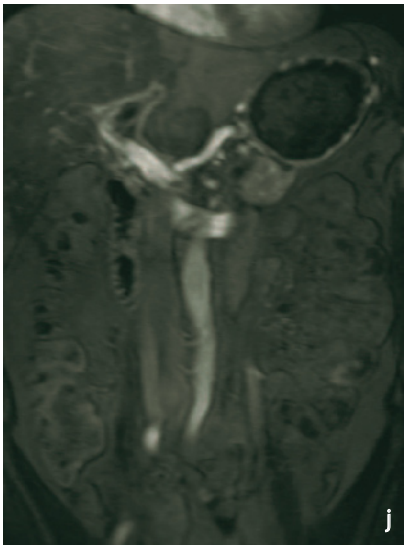

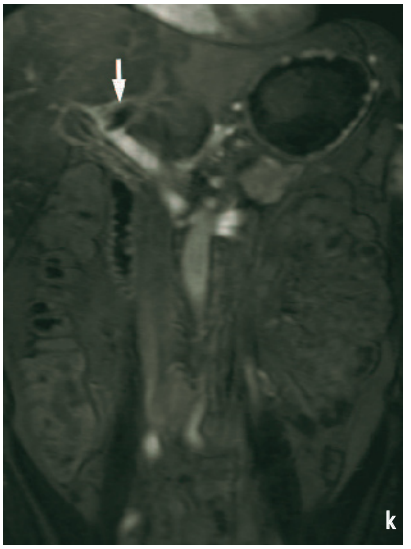

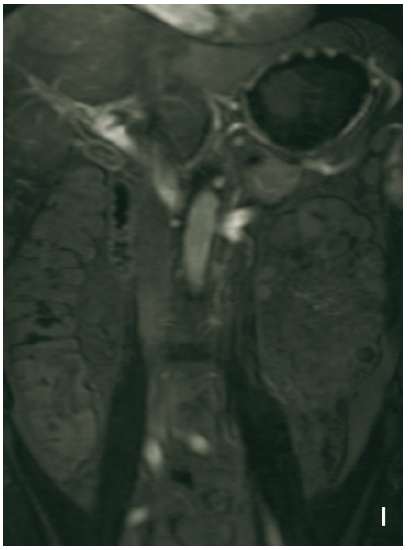

Fig. 16a-l. A 64 year old patient undergoing high dose chemotherapy, with portal vein thrombosis. The 3D CE MRA MIP reconstruction (**a**) in the portal-venous phase shows occlusion of the right branch of the portal vein (*arrows*). In addition, the portal vein is supplied by collaterals from the splenic vein (*arrowhead*), while the superior and inferior mesenteric veins are not displayed. To further evaluate the anatomic situation, sagittal (**b**), axial (**c**), and coronal (**d-l**) thick slab multiplanar reconstructions were prepared. The sagittal reconstruction reveals thrombus material in the superior mesenteric vein (*arrow* in **b**), while the axial reconstruction reveals additional thrombus material in the intrahepatic portions of the portal vein (*arrows* in **c**). The coronal reconstructions (**d-l**) reveal the full extent of the thrombosis, which affects the superior and inferior mesenteric veins as well as the splenic vein (*arrows*). Note the hypoperfusion of hepatic tissue due to peripheral portal vein thrombosis (*arrowheads* in **f**)

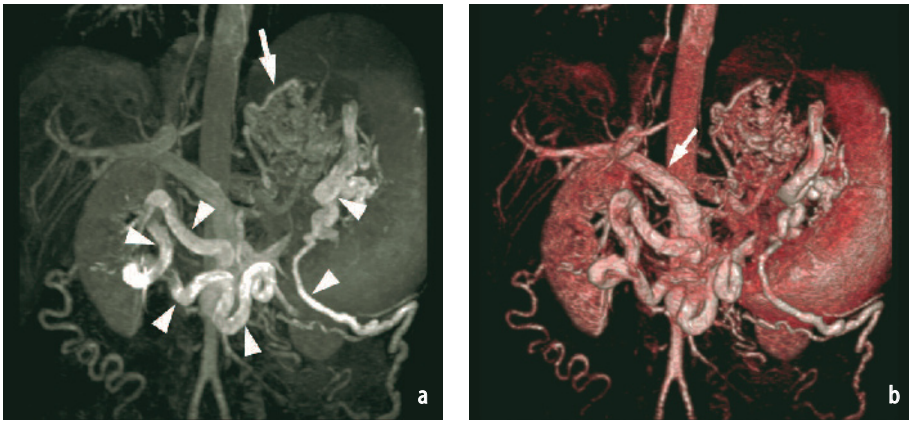

Fig. 17a, b. Extensive collateral mesenteric vessels in a patient after splenic vein thrombosis due to pancreatitis. Imaging was performed to rule out portal vein thrombosis.
The 3D CE MRA (0.1 mmol/kg Gd-BOPTA) MIP reconstruction (**a**) reveals an extensive number of collateral vessels (*arrow*) in the area of the gastric veins. In addition, collateral vessels (*arrowheads*) that drain blood from the splenic hilum to the abdominal wall and into the superior mesenteric vein are also visible. However, both the MIP reconstruction (**a**) and the volume-rendered image (**b**) reveal a patent portal vein with normal intrahepatic branching (*arrow* in **b**)

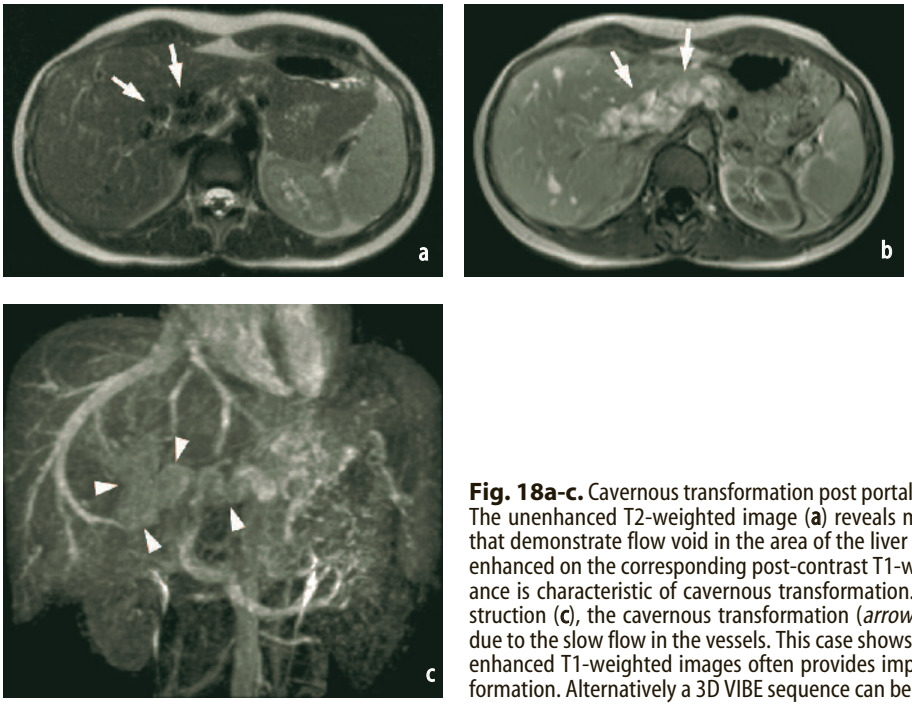

Fig. 18a-c. Cavernous transformation post portal vein occlusion.
The unenhanced T2-weighted image (**a**) reveals multiple dilated vessels (*arrows*) that demonstrate flow void in the area of the liver hilum. The vessels are markedly enhanced on the corresponding post-contrast T1-weighted image (**b**). This appearance is characteristic of cavernous transformation. On the 3D CE MRA MIP reconstruction (**c**), the cavernous transformation (*arrowheads*) is only faintly enhanced due to the slow flow in the vessels. This case shows that the acquisition of contrast-enhanced T1-weighted images often provides important additional diagnostic information. Alternatively a 3D VIBE sequence can be utilized

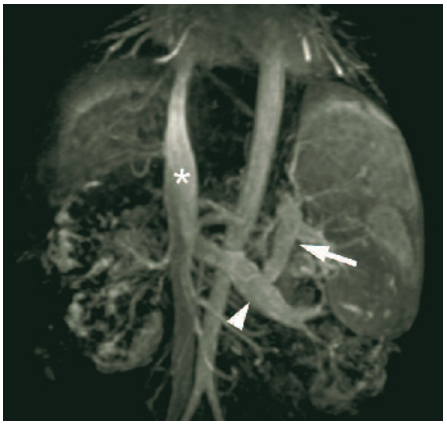

Fig. 19. Patent surgical spleno-renal shunt performed for lowering portal hypertension in a patient with liver fibrosis and recurrent bleeding from esophageal varices.
The 3D CE MRA study reveals a patent spleno-renal shunt with clear depiction of the vein graft (*arrow*), the left renal vein (*arrowhead*) and the ICV (*asterisk*)

12.5 Imaging of the Venous System

12.5.1 Normal Anatomy and Variants

The systemic venous architecture of the liver comprises three main venous vessels which drain into the ICV: the right hepatic vein, the middle hepatic vein and the left hepatic vein. In about 60% of individuals, the left hepatic vein and the middle hepatic vein form a common trunk which drains separately into the ICV. Normally, the right hepatic vein drains liver segments V-VII, the middle hepatic vein drains segments IV, V and VIII, and the left hepatic vein drains segments II and III. Venous drainage from segment I usually occurs directly into the ICV. This is considered the cause of hypertrophy of this segment in cirrhotic livers as result of an improved blood supply [13, 31].

12.5.2 Budd-Chiari Syndrome / Veno-Occlusive Disease

Budd-Chiari syndrome is a disorder characterized by hepatic outflow occlusion which has a variety of causes [9, 32]. In planning treatment, it is important to determine the location and length of hepatic outflow obstruction [20], and 3D CE MR portovenography is an accurate means of achieving this.

Heptatic outflow is also occluded in veno-occlusive disease. However, since it is the small intrahepatic veins that are affected in this disease, imaging findings frequently reveal larger liver veins that may have decreased calibre but which are nevertheless still patent.

Further details about these diseases and imaging examples can be found in Chapter 9, "Imaging of Diffuse Liver Disease".

12.6 Evaluation of Living Donors in Liver Transplantation

Resection of the liver from living donors for transplantation is a special surgical challenge. The success of the surgical procedure depends heavily on preoperative planning for which knowledge of the hepatic vasculature, as well as of the presence of hepatic neoplasms and their relationship to adjacent vessels, is crucial.

Conventional catheter angiography has long been considered the "gold standard" technique for evaluation of hepatic arterial anatomy. However, the morbidity and mortality associated with catheter angiography, coupled with the limitations of this procedure in demonstrating the hepatic venous anatomy, have provided impetus for the development of non-invasive methods [29]. Nowadays, CE MRA is increasingly considered a superior imaging modality for evaluating the hepatic vessels. Comprehensive information concerning the hepatic parenchyma as well as the complex arterial, venous and portal venous systems can today be obtained using a "one-stop-shop" examination.

Special care has to be taken when planning liver resection for living donor transplantation. As the rate of vascular abnormalities is comparatively high in the liver, accurate depiction of the arterial, venous and portal venous systems is important for successful resection of the graft as well as for replantation into the host. Knowledge of the relationship between intrahepatic neoplasms and adjacent vessels is also crucial for planning resection with tumor-free margins.

12.7 Segmental Anatomy of the Liver

The segmental anatomy of the liver is based on the vascular supply and drainage of the parenchyma. Until recently, classification of the liver lobes and sub-segments in the international literature was not uniform. Whereas British and American publications tended to follow the terminology of Goldsmith and Woodburne [8], in Europe and Japan the most common nomenclature used by radiologists and surgeons was based on the description of Couinaud and Bismuth [3, 5]. According to the terminology of Goldsmith and Woodburne [8], the liver comprises two liver lobes (left and right) separated by the middle hepatic vein, and four segments. While the right liver lobe consists of the right anterior and right posterior segments separated by the right hepatic vein, the left lobe is subdivided into the left medial and left lateral segments separated by the left hepatic vein.

Conversely, the classification of Couinaud and Bismuth [3, 5] describes a liver that is divided into a left and a right liver or hemiliver and sub-divided into four sectors and eight segments. Each of these eight segments is independent in terms of blood supply and biliary drainage. This allows for individual resection of a given segment without harm or alteration to the circulation of the remaining liver parenchyma. The left and right liver according to Couinaud and Bismuth correspond directly to the hepatic lobes described by Goldsmith and Woodburne [8]. The right hemiliver is further subdivided into a right paramedian sector and a right lateral sector consisting of two anterior

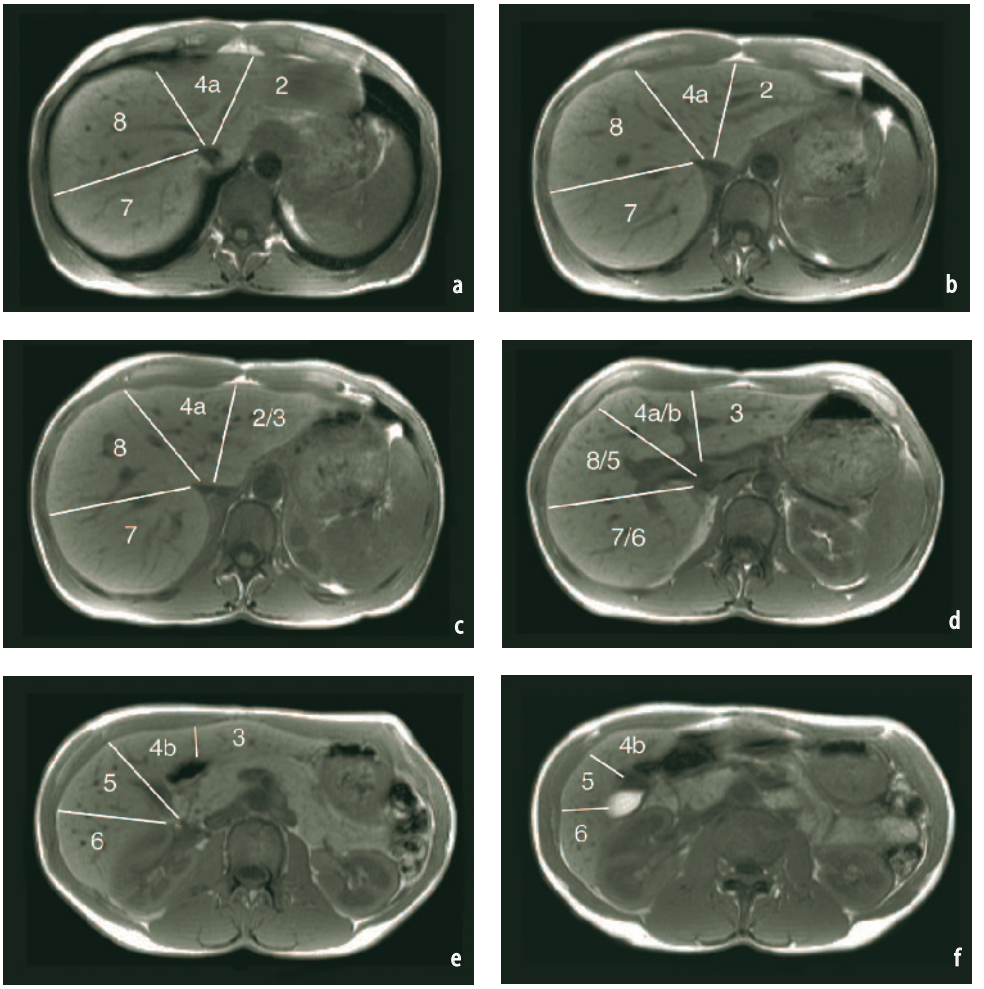

Fig. 20a-f. Segmental anatomy of the liver according to Couinaud and Bismuth

inferior and two posterior superior segments, respectively. Similarly, the left hemiliver comprises a left paramedian sector and a left lateral sector which are further sub-divided into anterior inferior and posterior superior segments.

The eight liver segments described by Couinaud and Bismuth [3, 5] are numbered clockwise based on a frontal view of the liver beginning with the posterior superior segment of the left paramedian sector, which corresponds to the caudate lobe, and ending with segment VIII which is consistent with the posterior superior segment of the right paramedian sector [6]. Today, the most common classification of liver segments is based on the Couinaud and Bismuth classification [3, 5].

Anatomically, the borders of the liver segments are well-defined, but show a wavy-shaped course [24]. However, in clinical routine, segmentation of the liver on cross-sectional CT and MR imaging is sharply demarcated and usually based on certain landmarks that define the underlying borders (Fig. 20). Based on these landmarks, the ICV is considered the center point for liver segmentation. A line from the ICV to the middle hepatic vein and the gallbladder separates the left and right hemilivers and the corresponding liver segments V/VIII and I/IVa, b, respectively. Whereas the axis between the ICV and right hepatic vein corresponds to the border between liver segments VI/VII and V/VIII, the line between the ICV, the left hepatic vein and the falciform ligament separates liver segments IVa and IVb from segments II and III.

Whereas liver segments VII, VIII, I, IVa and II are located at the posterior aspect of the imaged abdominal situs and above the level of the left and right main portal vein, segments VI, V, IVb and III are located inferior to the level of the main portal veins at the anterior aspect of the liver. Segment I corresponds to the caudate lobe.

References

1. Abbitt PL. Portal vein thrombosis: imaging features and associated etiologies. Curr Probl Diagn Radiol 1992;21:115-147
2. Baden JG, Racy DJ, Grist TM. Contrast-enhanced three-dimensional magnetic resonance angiography of the mesenteric vasculature. J Magn Reson Imaging 1999;10:369-375
3. Bismuth H. Surgical Anatomy and Anatomical Surgery of the Liver. World J Surg 1982;6:3-9
4. Burkart DJ, Johnson CD, Reading CC, et al. MR measurements of mesenteric venous flow: prospective evaluation in healthy volunteers and patients with chronic mesenteric ischemia. Radiology 1995; 194:801-806
5. Couinaud C. Le Foie. Etudes anatomiques et chirurgicales. Paris, Masson & Cie, 1957
6. Fasel JH, Gailloud P, Terrier F, Mentha G, Sprumont P. Segmental anatomy of the liver: a review and a proposal for an international working nomenclature. Eur Radiol 1996;6:834-7
7. Glassman MS, Klein SA, Spivak W. Evaluation of cavernous transformation of the portal vein by magnetic resonance imaging. Clin Pediatr 1993;32:77-80
8. Goldsmith NA, Woodburne RT. The surgical anatomy pertaining to liver resection. Surg Gynecol Obstet 1957;105(3):310-8
9. Gore RM. Vascular disorders of the liver and splanchnic circulation. In: Gore RM, Levine MS, Laufer I (eds). Textbook of gastrointestinal radiology. Saunders, Philadelphia 1994, 2018-2050
10. Goyen M, Barkhausen J, Debatin JF, Kuhl H, Bosk S, Testa G, Malago M, Ruehm SG. Right-lobe living related liver transplantation: evaluation of a comprehensive magnetic resonance imaging protocol for assessing potential donors. Liver Transpl 2002; 8:241-250
11. Hagspiel KD, Leung DA, Angle JF, Spinosa DJ, Pao DG, de Lange EE, Butty S, Matsumoto AH. MR angiography of the mesenteric vasculature. Radiol Clin North Am 2002;40:867-886
12. Lee VS, Morgan GR, Teperman LW, John D, Diflo T, Pandharipande PV, Berman PM, Lavelle MT, Krinsky GA, Rofsky NM, Schlossberg P, Weinreb JC. MR imaging as the sole preoperative imaging modality for right hepatectomy: a prospective study of living adult-to-adult liver donor candidates. Am J Roentgenol 2001;176:1475-1482
13. Lerut JP, Mazza D, van Leeuw V, Laterre PF, Donataccio M, de Ville de Goyet J, Van Beers B, Bourlier P, Goffette P, Puttemans T, Otte JB. Adult liver transplantation and abnormalities of splanchnic veins: experience in 53 patients. Transpl Int 1997;10:125-132
14. Li KCP, Hopkins KL, Dalman RL, et al. Simultaneous flow measurements within the superior mesenteric vein and artery with cine phase-contrast MR imaging: value in diagnosis of chronic mesenteric ischemia. Radiology 1995;194:327-330
15. Li KCP, Whitney WS, McDonnell C, et al. Chronic mesenteric ischemia: evaluation with phase-contrast cine MR imaging. Radiology 1994;190:175-179
16. McFarland EG, Kaufman JA, Saini S, Halpern EF, Lu DS, Waltman AC, Warshaw AL. Pre-operative staging of cancer of the pancreas: value of MR angiography versus conventional angiography in detecting portal venous invasion. Am J Roentgenol 1996;166:37-43
17. Meaney JF. Non-invasive evaluation of the visceral arteries with magnetic resonance angiography. Eur Radiol 1999;9:1267-1276
18. Meaney JFM, Prince MR, Nostrand TT, et al. Gadolinium-enhanced magnetic resonance angiography in patients with suspected chronic mesenteric ischemia. J Magn Reson Imaging 1997;7:171-176
19. Michels NA. Blood supply and anatomy of the upper abdominal organs. JB Lipincott Co, Philadelphia 1955
20. Murphy FB, Steinberg HV, Shires GT 3rd, Martin LG, Bernardino ME. The Budd-Chiari syndrome: a review. AM J Roentgenol 1986;147:9-15
21. Naganawa S, Cooper TG, Jenner G, et al. Flow velocity and flow measurement of superior and inferior mesenteric artery with cine phase contrast magnetic resonance angiography. Radiat Med 1994;12:213-220
22. Okumura A, Watanabe Y, Dohke M, Ishimori T, Amoh Y, Oda K, Dodo Y. Contrast-enhanced three-dimensional MR portography. Radiographics 1999 Jul-Aug;19(4):973-87
23. Pandharipande PV, Lee VS, Morgan GR, Teperman LW, Krinsky GA, Rofsky NM, Roy MC, Weinreb JC. Vascular and extravascular complications of liver transplantation: comprehensive evaluation with three-dimensional contrast-enhanced volumetric MR imaging and MR cholangiopancreatography. Am J Roentgenol 2001;177:1101-1107
24. Platzer W, Maurer H. On the segmental arrangement of the liver. Acta Anat (Basel) 1966;63:8-31
25. Prince MR, Grist TM, Debatin JF. Mesenteric Arteries. In: Prince MR, Grist TM, Debatin JF. 3D Contrast MR Angiography. Springer, Berlin, Heidelberg, New York 2003
26. Prince MR, Narasimham DL, Stanley JC, et al. Breathhold gadolinium-enhanced MR arteriography of the abdominal aorta and its major branches. Radiology 1995;197:785-792
27. Prince MR, Yucel EK, Kaufman JA, et al. Dynamic gadolinium-enhanced 3D abdominal MR arteriography. J Magn Reson Imaging 1993;3:877-881
28. Redvanly RD, Nelson RC, Stieber AC, Dodd GD 3rd. Imaging in the preoperative evaluation of adult liver-transplant candidates: goals, merits of various procedures, and recommendations. Am J Roentgenol 1995;164:611-617
29. Sahani D, Mehta A, Blake M, Prasad S, Harris G, Saini S. Preoperative Hepatic Vascular Evaluation with CT and MR Angiography: Implications for Surgery. Radiographics 2004;24:1367–1380
30. Smedby O, Riesenfeld V, Karlson B, Jacobson G, Lofberg A, Lindgren PG, Ahlstrom H. Magnetic resonance angiography in the resectability assessment of suspected pancreatic tumors. Eur Radiol 1997;7:649-653
31. Soyer P, Heath D, Bluemke DA, Choti MA, Kuhlman JE, Reichle R, Fishman EK. Three-dimensional helical CT of intrahepatic venous structures: comparison of three rendering techniques. J Comput Assist Tomogr 1996;20:122–127
32. Spritzer CE. Vascular disease and MR angiography of the liver. Magn Reson Imaging Clin N Am 1997;5:377-396
33. Vosshenrich R, Fischer U. Contrast-enhanced MR angiography of abdominal vessels: is there still a role for angiography? Eur Radiol 2002;12:218-230
34. Wasser MN, Geelkerken RH, Kouwenhoven M, et al. Systolically gated phase-contrast MRA of mesenteric arteries in suspected mesenteric ischemia. J Comput Assist Tomogr 1996;20:262-268

Subject Index

D

E

F

N

O

P

R

S

T

U

V

W